

Dissertation zur Erlangung des Doktorgrades  
Der Fakultät für Chemie und Pharmazie  
Der Ludwig-Maximilians-Universität München

DEVELOPMENT AND CHARACTERIZATION OF NOVEL  
INDIGOID CHROMOPHORES, PHOTOSWITCHES AND  
MOLECULAR MACHINERY

von

Christian Patrick Petermayer

aus

Reschitz, Rumänien

2019



Dissertation zur Erlangung des Doktorgrades  
Der Fakultät für Chemie und Pharmazie  
Der Ludwig-Maximilians-Universität München

DEVELOPMENT AND CHARACTERIZATION OF NOVEL  
INDIGOID CHROMOPHORES, PHOTOSWITCHES AND  
MOLECULAR MACHINERY

von

Christian Patrick Petermayer

aus

Reschitz, Rumänien

2019





*Erklärung:*

Diese Dissertation wurde im Sinne von § 7 der Promotionsordnung vom 1. Juli 2015 von Herrn Prof. Dr. Henry Dube betreut.

Eidesstattliche Versicherung:

Diese Dissertation wurde eigenständig und ohne unerlaubte Hilfe erarbeitet.

München, den 14.10.2019

.....  
Christian Patrick Petermayer

Dissertation eingereicht am:	14.10.2019
1. Gutachter:	Prof. Dr. Henry Dube
2. Gutachter:	Prof. Dr. Franz Bracher
Mündliche Prüfung am:	15.11.2019

This work was carried out from July 2015 to October 2019 under the guidance of Prof. Dr. Henry Dube at the Department of Chemistry of the Ludwig-Maximilians-Universität Munich.

First of all, I thank Prof. Dr. Henry Dube for giving me the opportunity to carry out my PhD in his group and for his guidance and support in the course of my scientific research.

I would like to express my appreciation to Prof. Dr. Franz Bracher for agreeing to be second reviewer of this thesis and thank all members of my defense committee – Prof. Dr. Henry Dube, Prof. Dr. Franz Bracher, Dr. Dorian Didier, Prof. Dr. Konstantin Karaghiosoff, Prof. Dr. Heinz Langhals and Prof. Dr. Oliver Trapp - for their interest shown in this manuscript by accepting to be referees.

I really would like to thank Veronika Werner, Edgar Uhl, Kerstin Hoffmann, Aaron Gerwien, Nicolai Bach, Thomas Bartelmann, Daria Berdnikova, Benjamin Regen-Pregizer Stefan Thumser and Henry Dube for carefully proofreading this manuscript.

I'd like to thank my collaboration partners Roland Wilcken, Eduardo Carrascosa and Daria Berdnikova for their scientific efforts and contributions to our projects.

I also thank Kristian Jordan, Florian Binder and all the numerous "Litstudenten" for their contributions to my research during their internships, bachelor's and master's theses.

Furthermore, I want to thank all past and present coworkers I have met in and before joining the Dube group.

First of all my friend and sole labmate Edgar "Edelbert" Uhl for more than four years within the exile labs "Nachtlabor" and "Stinkelabor" in which we had constructive and fruitful discussions about science and life. The numerous scientific experiments gave exciting insights in e.g. the pressure limits of sample vials, benumbing effects of various volatiles and the energetic potential of sound waves. I also thank him for his excellent taste in music, especially within frostbitten genres.

I also want to thank: (In order of appearance, somehow)

Manuel "Manul" Güntner for being an absolute mad lad.

Florian "Kinki" Kink for his words of wisdom and his awesome "Schweinebraten".

Monika "Monschelika" Schildhauer for her organizational and social skills and the hilarious discussions and pranks.

Sandra “Sandar” Wiedbrauk for fitting into a small locker, the good times and the funny “stuff” that constantly came up in the lab or during various festivities.

Ludwig “Luki” Huber for his critical thinking, whistling skills and his awesome “Anaconda” dancing moves.

Thomas “Tom” Bartelmann for his humorous comments, excellent taste in music and his twerking skills.

Stefan “Esteban” Thumser for all the scrap hunts, technical discussions and sweaty orthopedic cuddles.

Kerstin “Kerstian” Hoffmann for her uplifting spirit, her valuable scientific and social contributions to the group and her Romanian dancing skills.

Aaron “Flaivour” Gerwien for his inspiring enthusiasm for science, the valuable discussions, for posing as Cinderella at HGich.T and his flunky ball skills.

Nicolai “Boris” Bach for his competence during the day and mad partying skills at night.

Benjamin “Benni” Regen-Pregizer for his friendly mood, elaborate discussions and for implementing serious computational power into pieces of wood.

Sabrina “Brin0r” Hampel for her competence and cheerfulness in the lab, during parties, carnival festivities and recreational trips.

Mirko Wagner for participating in the night shifts within the 4<sup>th</sup> floor, his excellent taste in music, fruitful discussions and spontaneous partying skills.

Julian “Juuuuliaaan” Helberg for his scientific competence, rationality and helpfulness without limits concerning any topic and also for his beer-brewing and -drinking skills.

Andreas “Süßer Knopf” Bellan for his chemical knowledge, his lovely self and all the memorable stories that emerged during the last 10 years.

Markus “Chief” Müller for all the discussions, gaming- and partying sessions until dawn.

Nadja “Granaddl” Barl & Daniel “Schlingl” Hofmeister for their generousness and always enjoyable and relaxing company.

Gina “Natas” & Florian “Floh” & Jannis “Maximus” Achrainer for their caring support and unconditional helpfulness.

Elisabeth “Elli” & Stefan “Stopfi” & Franziska “Franzi” Gerstmeyr for the countless parties, festivals and adventures during the last 15 years.

Sebastian “Bäschdie” Meyer for always being there for me, within good and bad times, for naturally playing polyrhythmic guitar riffs in our band and being the “Wonnepoppen” that we all adore.

My band Stall Range “Stell Rage” for being a bunch of weirdos doing weird things.



Veronika “Vroniii” Werner for her knowledge, her endless love and support for me during difficult times within and outside the lab and for soon giving birth to our daughter.

Sorin “Soe” Petermayer for his guidance, tremendous knowledge and wisdom and for constantly pushing me to my limits, RIP.

Erika “Eribäri” Petermayer for her love, support and care for me during my whole life.

And last but not least Henry “HD” Dube for his trust in our group members and their self-sufficiency, the very flat hierarchies, all the spontaneous group seminars during lunch breaks, his very interesting taste in Austrian mumble rap and crowd surfing performances at HGich.T concerts. I want to emphasize his extraordinary skill in inspiring others for scientific problem settings and to expand one’s horizon in critical thinking and problem solving. The best motivation for spending days and nights in the lab is measurable progress achieved by applying newly acquired skills to create and observe at the edge of current knowledge. This kind of productive work environment without compulsory working hours was always supported by Henry without judgement, which I am grateful for.

Parts of this Ph.D. thesis have been published:

**Publications:**

*Hemiindigo: Highly Bistable Photoswitching at the Biooptical Window*

Christian Petermayer, Stefan Thumser, Florian Kink, Peter Mayer, Henry Dube

*J. Am. Chem. Soc.*, **2017**, 139, 42, 15060-15067.

Circular Dichroism Photoswitching with a Twist: Axially Chiral Hemiindigo

Christian Petermayer, Henry Dube

*J. Am. Chem. Soc.*, **2018**, 140, 42, 13558-13561.

*Twist and shine*

*Nature Reviews Chemistry*, **2018**, 2, 330.

*Reversible Photoswitching of Isolated Ionic Hemiindigos with Visible Light*

Eduardo Carrascosa\*, Christian Petermayer\*, Michael S. Scholz, James N. Bull, Henry Dube,  
Evan J. Bieske

*ChemPhysChem*, **2020**, 21, 680-685.

**Review Articles:**

*Indigoid Photoswitches: Visible light responsive molecular tools.*

Christian Petermayer, Henry Dube

*Acc. Chem. Res.* **2018**, 51, 1153-1163.

\* both authors contributed equally to this work

## Contributions:

Kristian Jordan	Synthesis and measurements of bulky acetylated hemiindigos ( <b>55</b> , <b>56</b> and <b>57</b> ) and their precursors ( <b>50</b> , <b>51</b> and <b>52</b> ) as well as of non-symmetric diarylated indigos ( <b>73</b> and <b>72</b> ) and respective precursors ( <b>74</b> , <b>75</b> and <b>77</b> ).
Florian Binder	Synthesis and identification of non-symmetric diarylated indigos ( <b>69</b> , <b>70</b> and <b>71</b> ) and respective precursors ( <b>19</b> , <b>68</b> and <b>74</b> ).
Florian Kink	Synthesis and identification of <b>2</b> , synthesis of <b>11</b> .
Stefan Thumser	Theoretical DFT calculations of <b>3</b> , <b>11</b> , <b>15</b> , <b>16</b> and <b>38</b> , technical support regarding computational chemistry.
Dr. Ludwig Huber	Synthesis of <b>63</b> .
Dr. Julian Helberg	Technical support regarding computational chemistry and bash scripting.
Dr. Eduardo Carrascosa	Time-resolved gas-phase measurements and DFT calculations of <b>80</b> , <b>81</b> and <b>82</b> , data interpretation and preparation of the manuscript " <i>Reversible Photoswitching of Isolated Ionic Hemiindigos with Visible Light</i> ".
Prof. Dr. Evan J. Bieske	Data interpretation and preparation of the manuscript " <i>Reversible Photoswitching of Isolated Ionic Hemiindigos with Visible Light</i> ".
Dr. Daria Berdnikova	Testing of photophysical properties upon binding to DNA of <b>34</b> , <b>81</b> , <b>98</b> , <b>100</b> , <b>101</b> , <b>102</b> , <b>104</b> , <b>105</b> , <b>106</b> , <b>108</b> , <b>109</b> , <b>110</b> and <b>112</b> .
Roland Wilcken	Transient measurements of <b>2</b> and scientific input regarding photophysics.

For my family

„Die Zensur ist das lebendige Geständnis der Großen, daß sie nur verdummte Sklaven treten,  
aber keine freien Völker regieren können. (...)“

JOHANN NEPOMUK NESTROY

(1801 - 1862)



# Table of Contents

<b>1</b>	<b>INTRODUCTION</b>	<b>1</b>
1.1	Photochemistry - A brief introduction .....	2
1.2	Indigo .....	11
1.3	Red-shifting of indigoid photoswitches .....	13
1.4	Switching of ECD responses.....	16
1.5	Molecular machines .....	17
<b>2</b>	<b>RESULTS AND DISCUSSION</b>	<b>24</b>
2.1	Hemiindigo - Improving the performance of photoswitches .....	26
2.2	Hemiindigo - Rationale of substitution patterns .....	30
2.2.1	Indoxyl fragment: N-H unsubstituted hemiindigo 9 .....	31
2.2.2	Indoxyl fragment: N-H acetylated hemiindigo 2 .....	34
2.2.3	Indoxyl fragment: N-H alkylation of hemiindigos.....	37
2.2.4	Stilbene fragment: Electron donating substituents.....	43
2.2.5	Indoxyl fragment: N-H alkylation of electron-rich hemiindigos .....	47
2.2.6	Indoxyl fragment: N-H arylation of electron-rich hemiindigos.....	54
2.2.7	Indoxyl fragment: Sterically demanding N-H arylations of electron-rich hemiindigos .....	56
2.2.8	Stilbene fragment: Extension of the aromatic system.....	59
2.2.9	Stilbene and indoxyl fragment: Push-pull effects .....	61
2.2.10	Central double bond: Substitution of the vinylic proton by a cyano group .....	63
2.2.11	Stilbene fragment: Electron withdrawing substituents .....	67
2.2.12	Stilbene fragment: Introduction of methyl groups in the <i>ortho</i> -position .....	68
2.2.13	Conclusion: Rationale of substitution patterns .....	75
2.2.14	Hemiindigo - Solvatochromism and the influence of water on hemiindigo chromophores.....	76

2.2.15	Hemiindigo - Effects of pH-modulation .....	78
2.2.16	Conclusion: Solvent, Water and pH influence .....	81
2.2.17	Hemiindigo - Photoswitching between photostationary states .....	82
2.2.18	Hemiindigo - Thermal bistabilities .....	87
2.2.19	First order kinetics without entering the equilibrium.....	87
2.2.20	First order kinetics with entering the equilibrium - <i>E/Z</i> isomerizations .....	94
2.2.21	Quantum yield determination.....	98
2.2.22	Benchmarking: Quantum yield determination of diarylethenes .....	99
2.2.23	Benchmarking: Quantum yield determination of the ring-opening photoreaction of diarylethene 35 using the <i>Riedle</i> setup.....	102
2.2.24	Benchmarking: Quantum yield determination of the ring-opening photoreaction of diarylethene 35 using the <i>Zinth</i> setup.....	108
2.2.25	Quantum yield determination for the photoisomerization reactions of hemiindigo 20 using the <i>Riedle</i> setup.....	111
2.2.26	Conclusion: Quantum yields .....	115
2.3	Chiral hemiindigos - Switching of ECD signals and control over atropisomerization speed and directionality .....	118
2.3.1	Chiral hemiindigos - Designing molecular gearboxes.....	118
2.3.2	Acetylated hemiindigos - First route for introduction of axial chirality .....	122
2.3.3	Synthesis of hemiindigos with axially chiral and achiral stilbene fragments .....	124
2.3.4	Introduction of a permanent stereocenter at the indoxyl fragment .....	141
2.3.5	<i>Ortho</i> -arylated hemiindigos - Second route for introduction of axial chirality .....	147
2.3.6	First generation of axially chiral arylated hemiindigos - Electronic effects on the stilbene fragment.....	150
2.3.7	Second generation of axially chiral arylated hemiindigos - Introduction of axially chiral stilbene fragments .....	163
2.3.8	Third generation of axially chiral arylated hemiindigos - Increasing the rotational barriers.....	187
2.3.9	Third generation of axially chiral arylated hemiindigos - Comparison of aliphatic signals and rotational barriers .....	207



2.3.10	Conclusion: Axially chiral hemiindigos .....	210
2.4	Indigo - From dye to molecular machines .....	212
2.4.1	Indigo - The aspect of thermochromism .....	212
2.4.2	Axially chiral indigos .....	223
2.4.3	Symmetric chiral indigos - First generation indigo 65.....	224
2.4.4	Symmetric chiral indigos - Second generation indigo 64 - Achiral aspects .....	233
2.4.5	Symmetric chiral indigos - Second generation indigo 64 - Assignment of <i>trans</i> isomers - NMR experiments.....	235
2.4.6	Symmetric chiral indigos - Second generation indigo 64 - Assignment of <i>trans</i> isomers - HPLC experiments.....	237
2.4.7	Symmetric chiral indigos - Second generation indigo 64 - Assignment of <i>trans</i> and <i>cis</i> isomers - ECD experiments .....	240
2.4.8	Symmetric chiral indigos - Second generation indigo 64 - Assignment of <i>trans</i> and <i>cis</i> isomers - DFT calculations .....	243
2.4.9	Non-symmetric chiral indigos - Second generation chimeric model compound indigo 70 - Disentanglement of chiral axes.....	247
2.4.10	Non-symmetric chiral indigos - First generation chimeric model compound indigo 69 - Disentanglement of chiral axes.....	251
2.4.11	Symmetric chiral indigos - Second generation indigo 64 - Experimental photophysical data .....	255
2.4.12	Symmetric chiral indigos - Second generation indigo 64 - Photoinduced <i>trans</i> to <i>cis</i> double bond isomerizations .....	256
2.4.13	Symmetric chiral indigos - Second generation indigo 64 - Low temperature NMR Data starting from the <i>syn-trans</i> -1 isomers .....	258
2.4.14	Symmetric chiral indigos - Second generation indigo 64 - Low temperature NMR Data starting from the <i>anti-trans</i> isomer .....	268
2.4.15	Symmetric chiral indigos - Second generation indigo 64 - Low temperature NMR Data - <i>Syn-trans</i> -1 to <i>anti-trans</i> kinetic analysis .....	277
2.4.16	Symmetric chiral indigos - Second generation indigo 64 - DFT overview .....	283
2.4.17	Symmetric chiral indigos - Second generation indigo 64 - DFT NMR.....	287
2.4.18	Symmetric chiral indigos - Second generation indigo 64 - <sup>1</sup> H-NMR-Shifts .....	291

2.4.19	Symmetric chiral indigos - Second generation indigo 64 - Photoinduced <i>syn-trans</i> -1 to <i>anti-trans</i> pumping.....	292
2.4.20	Symmetric chiral indigos - Second generation indigo 64 - Photoinduced unidirectional single bond motor.....	297
2.4.21	Symmetric chiral indigos - Second generation indigo 64 - Photoinduced unidirectional double bond motor .....	300
2.4.22	Symmetric chiral indigos - Second generation indigo 64 - Photoinduced and thermal extended Hula-Twist .....	303
2.4.23	Symmetric chiral indigos - Second generation indigo 64 - Photodriven extended Hula-Twist gear.....	307
2.4.24	Symmetric chiral indigos - Second generation indigo 64 - Overview of trajectories .....	309
2.4.25	Symmetric chiral indigos - Second generation indigo 64 - Temperature- and solvent dependence of cyclic trajectories .....	312
2.4.26	Symmetric chiral indigos - Second generation indigo 64 - Conclusion.....	313
2.4.27	Non-symmetric chiral indigos - Third generation chimeric indigo 71 .....	314
2.4.28	Non-symmetric chiral indigos - Third generation chimeric indigo 72 .....	322
2.4.29	Non-symmetric chiral indigos - Third generation chimeric indigo 73 .....	324
2.4.30	Conclusion: Axially chiral indigos .....	328
2.5	Ionic hemiindigos - Photoswitching of collision cross-sections in the gas phase - Introduction.....	331
2.5.1	Ionic hemiindigos - Synthesis .....	333
2.5.2	Ionic hemiindigos - Gas phase photoisomerization experiments.....	335
2.5.3	Ionic hemiindigos - ATD peak assignments and determination of isomeric yields upon irradiation in solution .....	338
2.5.4	Ionic hemiindigos - Photoisomerization action spectroscopy experiments .....	340
2.5.5	Ionic hemiindigos - Power dependence .....	342
2.5.6	Ionic hemiindigos - Conformer evaluation in the gas phase.....	343
2.5.7	Ionic hemiindigos - Conformational analysis in solution .....	345
2.5.8	Ionic hemiindigos - PSS UV-Vis spectra.....	349

2.5.9	Ionic hemiindigos - Evaluation of chain length effects .....	352
2.5.10	Conclusion: Ionic hemiindigos .....	358
2.6	Hemiindigos in water - Photoswitchable interactions with DNA / RNA biomolecules .....	361
2.6.1	Hemiindigos in water - Synthesis .....	363
2.6.2	Hemiindigos in water - Photoswitching of non-ionic compounds.....	370
2.6.3	Hemiindigos in water - Photoswitching of ionic compounds .....	382
2.6.4	Hemiindigos in water - DNA / RNA binding .....	390
2.6.5	Conclusion: Hemiindigos in water.....	396
2.7	Photophysics - Improvements on the accuracy, repeatability and convenience of measurements.....	398
2.7.1	Photophysics - Development of an “all-in-one” calculational <i>Excel</i> tool - 100% <i>Z / E</i> spectrum calculator .....	398
2.7.2	Photophysics - Development of an “all-in-one” calculational <i>Excel</i> tool - Photophysical data evaluation.....	410
2.7.3	Photophysics - Building of an inexpensive quantum yield determination setup .....	414
2.7.4	Photophysics - Building of an alternating irradiation device.....	419
2.7.5	Photophysics - Building of a cuvette holder for cryogenic ECD measurements.....	421
2.7.6	Conclusion: Photophysics .....	424
<b>3</b>	<b>EXPERIMENTAL SECTION</b>	<b>426</b>
3.1	General experimental .....	427
3.2	Indole precursors - Copper-catalyzed <i>N</i> -arylations.....	430
3.3	Indoxyl acetate precursors - Oxidative acetoxylation .....	435
3.4	Aldehyde precursors - $S_N2$ reactions.....	443
3.5	Condensation reactions of indoxyl acetates with aromatic aldehydes .....	445
3.6	Oxidative dimerization of arylated indoxyl acetates.....	468
3.7	Late stage substitutions at the indoxyl-nitrogen.....	479
3.7.1	<i>N</i> -Alkylations - $S_N2$ reactions .....	479

3.7.2	<i>N</i> -Arylations - <i>Buchwald-Hartwig</i> cross-couplings.....	500
3.7.3	<i>N</i> -Acetylations - Nucleophilic catalysis.....	505
3.7.4	Vicarious nucleophilic substitution at the central double bond.....	515
3.7.5	Quaternary ammonium salts - <i>Menschutkin</i> reactions.....	516
<b>4</b>	<b>SUMMARY</b>	<b>523</b>
4.1	Hemiindigo - Rationale of substitution patterns.....	524
4.2	Hemiindigo - Solvent, Water and pH influence.....	525
4.3	Quantum yields.....	526
4.4	Axially chiral hemiindigos.....	527
4.5	Axially chiral indigos.....	528
4.6	Ionic hemiindigos.....	529
4.7	Hemiindigos in water.....	530
4.8	Photophysics.....	531
<b>5</b>	<b>APPENDIX</b>	<b>532</b>
5.1	List of Abbreviations.....	533
5.2	Table of Figures.....	534
5.3	Table of Schemes.....	546
5.4	List of Tables.....	547
5.5	Table of Equations.....	548
5.6	References.....	549

# 1 INTRODUCTION

## Preface

When I started my PhD thesis in the *Dube* group in July 2015, my experience in the fields of photochemistry, physical chemistry and theoretical chemistry was very limited, as my previous internships and theses dealt with solid-state chemistry, inorganic primary explosives, polymers and synthetic metal organic chemistry.

This introduction is meant to give a brief overview of typical photophysical effects that occur within the excited states of matter. It also shows possibilities on how to convert photonic energy into chemical reactions and controllable molecular motions. The intention of this brief introduction is outlining some of the basic principles in photochemistry to chemists without a background in photophysics.

As photochemistry is a very interdisciplinary field that can range from synthetic chemistry to biology over molecular- / supramolecular dynamics and engineering to molecular computing to controlling of logical gates, only a few relevant aspects of the used photochemistry in this thesis can be implemented in this introduction.

## 1.1 Photochemistry - A brief introduction

### Biological aspects

The most prominent and important example of a photochemical reaction cascade is photosynthesis. Its two main biochemical pathways consist of harvesting photons to provide adenosine triphosphate (ATP) as chemical energy and nicotinamide adenine dinucleotide phosphate (NADP) as reducing agent for the conversion of carbon dioxide and water into energetically upcycled glucose and oxygen.<sup>[1, 2, 3]</sup> Without these complex reaction cascades, the sun's power to fuel life on earth would be mainly untapped in the ways we are aware of now. Another important photochemical reaction in biological systems is the vision of animals, which involves the *cis-trans* photoisomerization of retinal embedded in variable opsin proteins to convert photons with different wavelengths and intensities into electrical stimuli within the retina of the eye.<sup>[4, 5]</sup> Recently, the photochemical Hula-Twist mechanism - that was proposed in 1985 as underlying mechanism of this *cis-trans* isomerization of incorporated retinal - was directly evidenced to exist in a model system by our group.<sup>[6]</sup> However, for retinal itself, a recent time-resolved femtosecond x-ray crystallography study suggests an aborted bicycle pedal- instead of the Hula-Twist mechanism.<sup>[7]</sup> The biosynthesis of vitamin D<sub>3</sub> in animal skin is another photoinduced biosynthetic pathway that utilizes cholesterol as starting material and UV light. This biosynthetic pathway is crucial to many life forms as vitamin D<sub>3</sub> is only scarcely present in common food sources.<sup>[8]</sup>

### Absorption, fluorescence and phosphorescence

Color theory enthralled mankind for millennia and is also a major part of photophysics and -chemistry.<sup>[9]</sup> It describes the impression of dyes, chromophores and pigments to the human eye. Absorbance and luminescence are hereby the most commonly observed phenomena and can be described in detail by quantum theory.<sup>[10]</sup> Besides reflection and scattering, non-transparent matter shows at least absorption of photons in the visible spectrum of light, which can be understood as (internal) energy conversion of one or more photonic wavelengths with different intensities into phononic (heat), electrical or chemical energy.<sup>[11]</sup> This process subtracts the absorbed wavelengths from the incident light distribution and reflects the complementary color back to e.g. the opsins of the human eye.<sup>[5]</sup>

Luminescence can be observed in matter that does not dissipate external stimuli (Phononic excitation, photons, magnetic- or electric fields, electrons, hadrons...) thermally or chemically, leaving only emission of a photon as de-excitation pathway.<sup>[12]</sup> One prominent example of a commonly encountered luminescence phenomenon is photoluminescence, which can be categorized into fluorescence and phosphorescence. Fluorescence, for example, is encountered naturally by UV irradiation of calcium fluoride crystals or animal teeth.<sup>[13, 14]</sup> Whitening agents in textiles or quinine-containing beverages like tonic water also show fluorescent behavior under UV irradiation.

A theoretical approach to describe fluorescence uses the *Born-Oppenheimer* approximation in which the electronic structure of a vibrating molecule is treated with almost no mass compared to its nuclei with respectively almost infinite masses.<sup>[15]</sup> This becomes possible as electronic and nuclear motions usually take place at vastly different timescales, which facilitates solving the *Schrödinger* equation in the ground state but results in unreliable predictions for the excited states.<sup>[16, 17, 18]</sup> *Jablonski* diagrams (Figure 1), which also utilize the *Born-Oppenheimer* approximation, can be used to describe excited state behavior.<sup>[19, 20]</sup> These diagrams assign nuclei position on the abscissa and the energies of ground- and excited states on the ordinate. Vertical excitations between ground- and excited states symbolize the fast time-dependent change in electronic structure due to photon absorption within femtoseconds while the nuclei's positions are virtually frozen in position.

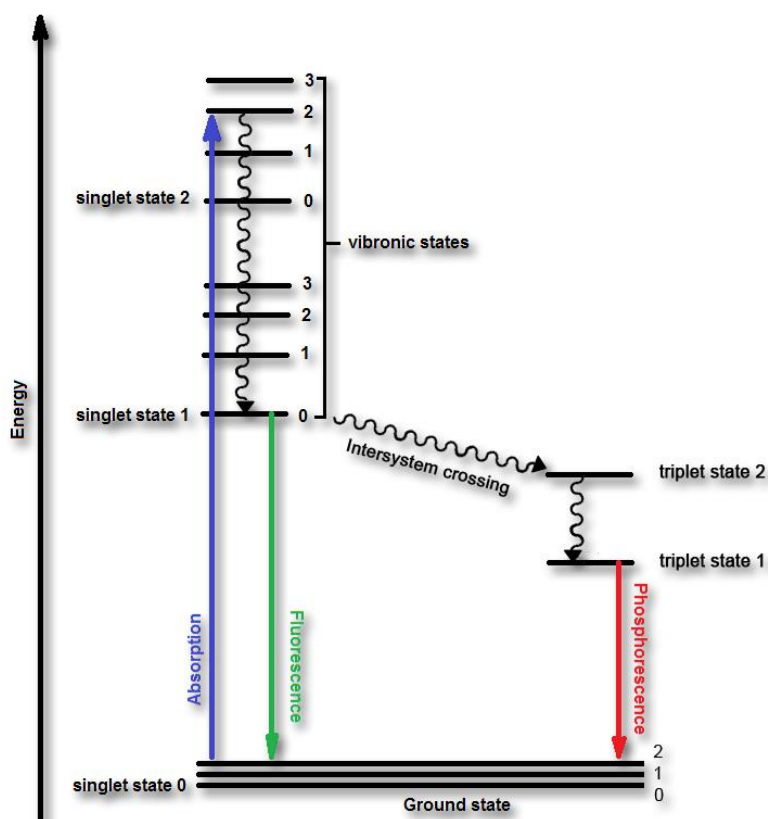


Figure 1: Simplified *Jablonski* diagram. Absorption of a photon results in excitation of the molecule e.g. into the singlet state 1 or 2 ( $S_1$  or  $S_2$ , blue arrow) within an accessible vibronic state. Lower lying vibronic states can be populated by phononic de-excitations, which can be simplified as cooling of an excited vibrating molecule towards a state of lower energy (wavy lines). The lowest energy vibronic mode of the excited state (here:  $S_{1-0}$ ) must be in phase with at least one vibronic mode  $x$  (in most cases not the lowest vibronic mode) of the ground state (singlet state 0 or  $S_0$ ) to emit a photon (fluorescence). This photon has the same energy as the energy gap between  $S_{1-0}$  and  $S_{0-x}$ . The same principle can be applied to the triplet states with the additional aspect that the required changes in spin polarization from triplet to singlet states are forbidden. This circumstance can trap molecules in long-lasting triplet states for time periods that extend fluorescent phenomena by several orders of magnitude.

The mechanism behind fluorescence consists of photon absorption into the electronic excited state and instead of thermal deactivation (internal conversion) to the electronic ground state, a photoemission pathway is taken, immediately emitting the photon within nanoseconds at a lower energy wavelength. Photon emission requires oscillations from the molecular nuclei, as the singlet state 1 and singlet state 0 need to experience an in-phase oscillation for this process.



Phosphorescence was first reported in 1602 by *V. Casciorolo* within barium sulfide and can also be observed on pilot / diving watch faces or on emergency exits that utilize phosphorescent paint. The mechanism of phosphorescence resembles fluorescent behavior with the exception that de-excitation takes place via intersystem crossing (see Figure 1). Here, the excited singlet state is converted into an intermediate triplet state by a forbidden change of spin polarization. This results in the longevity of the triplet state, which de-excites by emission of low energy photons over minutes, hours or days after the initial excitation.<sup>[19, 21]</sup>

### **From photochemistry to molecular machines**

The ability of photons to initiate or drive chemical reactions is a long and well known phenomenon. An early example of photochemistry is black-white photography where light sensitive silver bromide (yellow) coated plates are exposed to UV light through a lens system.<sup>[22]</sup> Photons catalyze the disproportion of the silver bromide to elemental silver (black) and bromide within the plate matrix. Fixation by eliminating residual silver bromide in the dark leaves the negative impression of the photographed image. Another example of a photochemical reaction starts with the UV light-induced homolytic dissociation of chlorine gas in presence stoichiometric amounts of hydrogen. The initially formed chlorine radicals react in chain propagation and termination reactions to form hydrogen chloride within an exothermic reaction cascade. The dissipated heat will further increase reaction kinetics and gas volume, leading to an exponential reaction profile, causing a detonation.<sup>[23]</sup>

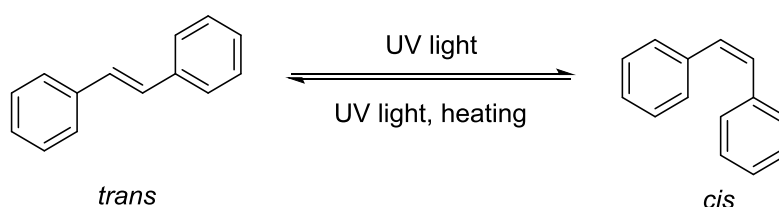
Modern applications of photochemistry and -physics consist of e.g. solar cells, photoredox catalysis and the emerging field of photoswitches and light driven molecular machinery.

Most inorganic solar cells use doped crystalline or amorphous semiconducting silicon to propagate photon induced charge separations.<sup>[24, 25]</sup> These accelerated charges can be harvested on adjacent electrodes to obtain a direct current source that becomes usable in all sorts of electronic devices upon respective conversion.

A prominent example of a photoredox catalyst is *tris*(bipyridine)ruthenium(II) chloride. In combination with common organocatalysts, new synthetic photon-driven methodologies based on single electron transfers can be derived.<sup>[26]</sup> One trait of photoredox catalysis is the ability to utilize catalytic amounts of photons to generate the desired products. This can be observed for the quantum yield (QY, QY = number of absorbed photons divided by the number of formed product molecules) of the single electron generation of *tris*(bipyridine)ruthenium(II) chloride.

This photoreaction supports a quantum yield of 2.8% but the catalytic nature of the reaction cascade allows for enlarged quantum yields with respect to the formed products by up to two orders of magnitude.<sup>[27, 28]</sup>

A research field that also vastly gains momentum is the development of photoswitches and light driven molecular machines. The first example of a photochemical transformation was reported with sunlight irradiation of  $\alpha$ -santonin crystals by *H. Trommsdorf*.<sup>[29]</sup> The incident light turned the crystals yellow before bursting due to substantial changes in crystal volume upon dimerization.<sup>[30]</sup> Likewise, a molecular photoswitch supports two or multiple isomeric forms that can be interconverted at least from one state to the other by light. One of the first known examples is the *trans* to *cis* double bond isomerization of stilbene by UV light (Scheme 1).<sup>[31, 32]</sup>



Scheme 1: Photoisomerization of *trans* stilbene to *cis* stilbene by irradiation with UV-light.

Another prominent photoswitchable molecular transformation is the light induced ring-opening and -closing reaction of e.g. diarylethenes,<sup>[33]</sup> spiropyranes<sup>[34]</sup> and *Stenhouse* adducts<sup>[35]</sup> (see Figure 2).

Most of the envisioned applications of photoswitches and light-driven molecular machinery reside in the fields of photopharmacology,<sup>[36, 37]</sup> sensing,<sup>[38, 39, 40]</sup> information processing,<sup>[41]</sup> materials science<sup>[42]</sup> and nanorobotics.<sup>[43, 44]</sup> The most prominent application of photoswitches to date is the sun-light induced tinting of sun glasses using spiropyranes as light responsive component.<sup>[45]</sup>

Photopharmacology describes the field in which an active pharmaceutical ingredient (API) is switched on at a specified location within an organism by preferably harmless (visible) light. This portrays another level of precise temporal and spatial control as the drug is only active at a desired tissue for precisely controlled time intervals. This is in contrast to common APIs that are unwanted and possibly dangerous (as metabolites) within other parts of the organism until conversion towards harmless derivatives by the organisms metabolism or excretion.<sup>[46, 47, 48, 49]</sup>

Advanced sensing applications consist e.g. of photoswitches that show fluorescent behavior in one isomeric form but not in the other.<sup>[39]</sup> For example, switchable spatial fluorescent

mapping of biological matrices can be utilized to trace dynamics within cells to visualize biological pathways.<sup>[50]</sup>

Digital molecular information processing strongly relies on interconvertible molecules with two or multiple different states to assemble logical devices such as memory, various logical gates (e.g. AND, XOR etc.), keypad locks or half-adders.<sup>[41]</sup> Quantum computing beyond 0's and 1's requires multiple states and readouts at desirably the smallest possible scale.<sup>[51]</sup>

Photoswitches can be used as a molecular scaffold to build light driven molecular motors, which are defined by their property of a unidirectional rotation around one bond or by traversing of different molecular states under continuous irradiation in a favored order and trajectory.<sup>[52, 53]</sup>

Incorporating molecular switches or motors within macromolecular scaffolds / -polymers or metal- / covalent organic frameworks can change the overall properties of these materials upon irradiation of light.<sup>[42]</sup>

With these tools on hand, artificial robots at the molecular scale can be envisioned.<sup>[43, 54]</sup> Photoswitches and molecular motors could be key tools not only to provide specific control of the principles of molecular motion motions but also to actively power them with high spatio-temporal precision.<sup>[55]</sup> Although known systems are far off from being assembled into artificial autonomous nanomachines,<sup>[56]</sup> the archetypes have already been created by nature: Enzymes, ribosomes, the cellular apparatus, intercellular communication, muscle tissue and nervous systems. The orchestration of these molecular machines and signal transducers leads to the possibility of complex life forms, all constantly utilizing their nanomachines to survive. The incorporation of a likewise complexity into a synthetic world is achievable in theory but surpasses human capabilities (at the moment).

## Overview of known photoswitchable scaffolds

Photoswitches and molecular motors / -machines use mainly *Z* / *E*- or *cis*-*trans* isomerizations and ring opening- / -closing mechanisms upon photoexcitation to switch from their global thermodynamic minimum to metastable states.<sup>[20, 57]</sup>

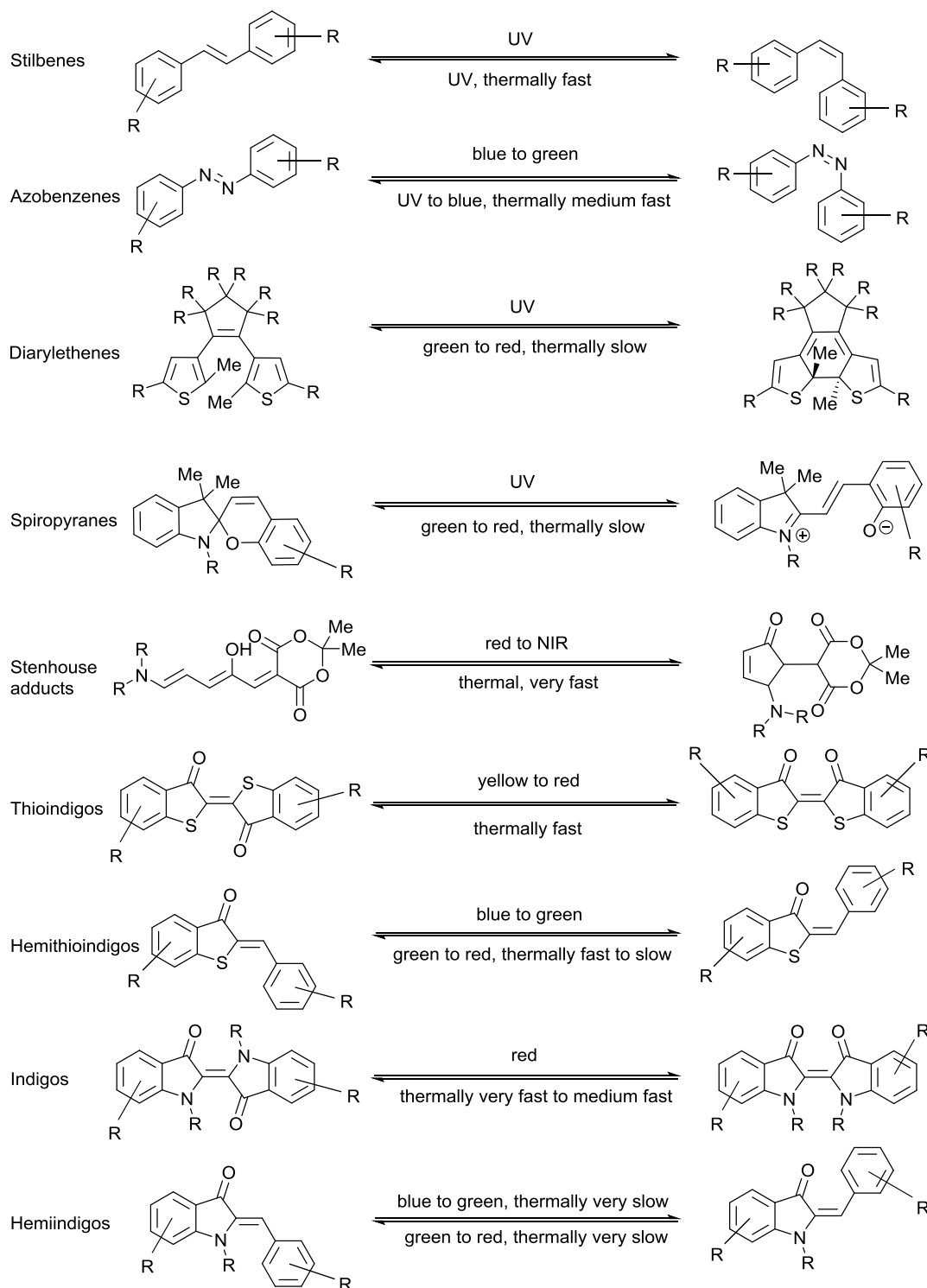


Figure 2: Overview of different classes of photoswitches. In general, thermodynamically stable forms are shown on the left, metastable products are shown on the right.

Rule-of-thumb performances with regard to red-shifted photoswitching and long thermal half-lives at 25 °C are shown for a respective isomerization direction. Very fast = ns to s, fast = s to min, medium fast = min to h, medium slow = h to days, slow = days to years, very slow = years to millennia. NIR = near infrared

Nowadays, photoswitching in general is explained by the excited state topology of the potential energy surface and its conical intersection towards the ground state potential energy surface, allowing for the generation of metastable products. The theory of conical intersections links the observation of short-lived excited states that do not deexcite via e.g. fluorescence to phononic molecular motion that leads to observable, metastable photoproducts.<sup>[20, 58, 59]</sup>

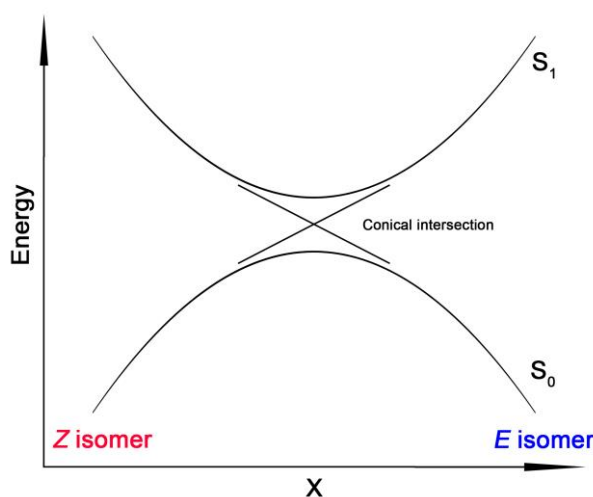


Figure 3: Simplified depiction of a conical intersection for a *Z* / *E* double bond isomerization, *X* represents the reaction coordinate. The excited state  $S_1$  rapidly de-excites towards the  $S_0$  state of the *Z*- or *E* isomer with a 1 to 1 probability.

Figure 3 also visualizes why achieving quantum yields beyond 50% is expected to be impossible for double bond isomerizations. This can be assumed if the incident photonic energy is completely converted into electronic excited state energy and only a singular, symmetric conical intersection is present within the potential energy surface. The latter is not necessarily the case as electrostatic- or steric bias in the excited state could influence the topology around the conical intersection. Conical intersections describe the often very fast formations of metastable photoproducts within few picoseconds very accurately.<sup>[20, 60]</sup> This indicates that after establishment of the excited state orbital structure, the molecular nucleic scaffold reacts to the changed electronic environment at a speed above the diffusion limit. If the instantly induced electronic structure change in the excited state favors the rearrangement of the molecular structure to a conical intersection that is intermediate to starting- and product structures, a

bifurcation towards two reaction paths that yield either the *Z*- or *E* isomers with equal probability is established. The conical intersection structure is populated more readily when one or multiple vibrational modes of the molecule already point towards the correct trajectory. This excited state then de-excites by directly forming either the starting material or the product species. In addition, hot ground states with a thermal bifurcation of the reaction coordinate can be used to explain the outcome of photoreactions towards the starting material or different products.<sup>[20, 58, 61]</sup>

## 1.2 Indigo

The synthesis<sup>[62]</sup> and structure<sup>[63]</sup> of indigo was first described by *Adolf von Baeyer* in 1870 and 1883. Indigo is still one of the most prominent dyes to date as its deep blue color and stability towards light and chemicals, accompanied by its low solubility, prevents it from being bleached out of dyed fabrics during wearing and washing. These properties also makes it unsuitable to directly apply indigo onto clothes, which is why it is reduced to its colorless and water soluble *leuco* form for dyeing processes. (Figure 4) Treated textiles can be left on air for *leuco* indigo to be re-oxidized to its blue form, which is now deeply embedded within the fibers. This indicates that the central double bond in this molecule plays a major role for its deep blue color.<sup>[64]</sup>

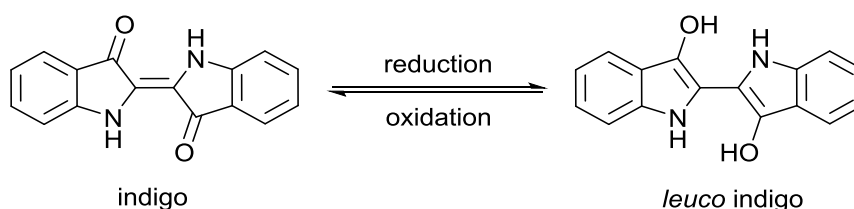


Figure 4: Indigo and its reduced *leuco* form.

Indigo is a quite intriguing dye as its deep blue color cannot be explained solely by the size of the conjugated system and is still not fully understood.<sup>[65, 66]</sup> When designing red-shifted dyes, the rationale consists in bringing the highest occupied molecular orbital (HOMO or  $S_0$ ) and the lowest unoccupied molecular orbital (LUMO or  $S_1$ ) closer together. This can be realized by incorporating an elongated aromatic system and placing a strong donor and a strong acceptor at its opposite ends. However, with indigo, all the amine donors and carbonyl acceptors are located adjacent to the central double bond. Multiple mesomeric forms, which exhibit electron donating pathways directly from one amine to the closest carbonyl or from one amine to the carbonyl opposite of the central double bond, can be proposed. All these possible excitation modes seem to contribute in bringing HOMO and LUMO closer together, resulting in a low energy absorption maximum at approximately 615 nm (red) that is perceived as the eponymous indigo blue.

Another extraordinary trait is the stability of indigo pigments towards irradiation, temperature, chemicals and dissolution. Destruction by photobleaching is prevented through excited state proton transfer (ESPT) which potentially can take place twice per molecule.<sup>[65]</sup> This dissipates the absorbed energy from the excited state not only through phononic radiation

of heat but also by dissociation of protons from the amine towards the carbonyl oxygen or the matrix, temporarily strengthening the hydrogen bonds within the structure.<sup>[67]</sup>

Strong intermolecular hydrogen bonding and *pi-pi* stacking lowers its solubility and hence the reactivity of indigo compared to indoles or indoxyls.<sup>[68]</sup>

Altogether, these characteristics are highly beneficial for indigo as a dye but utilizing it as *cis-trans* photoswitch in its nitrogen-unsubstituted form is impractical. Another drawback is the very low thermal bistability of its *cis* isomer as its half-life lies in the range of picoseconds, which makes it impossible to analyze without transient or cryogenic spectroscopic methods.

Additionally, it is known that substitution reactions of the amine protons cannot be carried out easily, as harsh reaction conditions are required and poor yields with many similar and inseparable side products can be expected.

Recent publications report actual photoswitching and thermal half-lives of the formed metastable *cis*-isomers ranging from minutes to hours at 25 °C for mono- and di-*N*-substituted indigo derivatives.<sup>[69]</sup> These findings suggest that suppression of the ESPT pathway is one of the most promising approaches for realizing efficient photoswitching properties of indigo and for diminishing ultrafast thermal back reactions from the *cis* to the *trans* state.<sup>[66]</sup>

### **This work**

In this work thermochromic effects on indigo derivatives were studied. The parent indigo scaffold was substituted by various symmetric and non-symmetric aryls on both nitrogen positions. Also, methyl groups were introduced on the indigo core adjacent to the nitrogen-aryl axes. Substitution in general led to good *trans* to *cis* photoswitching properties of several derivatives, especially at low temperatures. The properties beyond *trans* to *cis* photoswitching are outlined in Section 2.4.



### 1.3 Red-shifting of indigoid photoswitches

Most substituted indigo photoswitches can be addressed with red light at 620 nm, which is already an ideal property for biological applications, as low energy red light does not destroy cellular components unlike high energy UV light.<sup>[66, 69]</sup> Furthermore, deep tissue penetration is achieved by red light while blue or UV light is readily absorbed by prevalent molecules of biological entities. This can be demonstrated by a simple experiment shown in Figure 5 below.

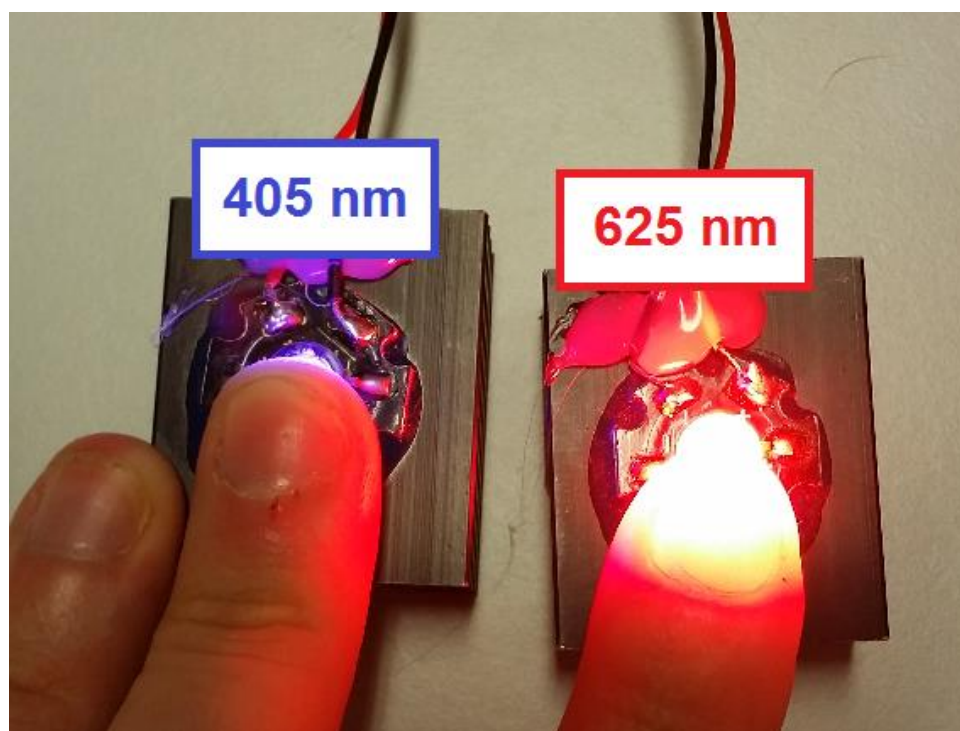


Figure 5: Irradiation of biological tissue with 405 nm (100 mW of light power, left) and 625 nm (130 mW of light power, right) light emitting diodes (LEDs). The lower measured power (~30%) for the LED on the left is not the main cause for the significant transmission difference ( $\gg 30\%$ ) when compared to the right.

However, thermal stabilities of indigo photoswitches still remain in the realm of nanoseconds to minutes at 37.5 °C.<sup>[66, 69]</sup> To address this shortcoming, the nitrogen atoms can be substituted by sulfur to form thioindigo, as *Adolf von Baeyer's* student, *Paul Friedländer* had shown in 1904.<sup>[70, 71]</sup> This violet dye is soluble in organic solvents and the metastable *cis* isomer shows thermal half-lives of several hours at ambient temperatures, depending on its substituents.<sup>[72]</sup> Further improvements regarding thermal stability are achieved by formal cleavage of the thioindigo chromophore at its central double bond and substitution with a hemistilbene.<sup>[41, 73]</sup> This leads to the class of hemithioindigo (HTI) derivatives, which overall exhibit long thermal

half-lives by sacrificing some of the red-shifted absorption of thioindigo. Electron donating substitutions at the stilbene fragment increase the red-shift of hemithioindigo while significantly lowering the thermal stabilities of the photoproducts.<sup>[73]</sup> To overcome these drawbacks, the nitrogen of the parent indigo chromophore was introduced again in this work to obtain hemiindigo (HI), which was also reported by *Adolf von Baeyer* in 1883.<sup>[63]</sup> The unsubstituted hemiindigo photoswitch is already red-shifted by 50 nm compared to the respective hemithioindigo and in contrast, electron donating substitutions at the stilbene fragment do not severely impede the thermal bistability of the chromophores.<sup>[74]</sup> Figure 6 summarizes the enhancements of thermal stability throughout various classes of indigoid photoswitches.

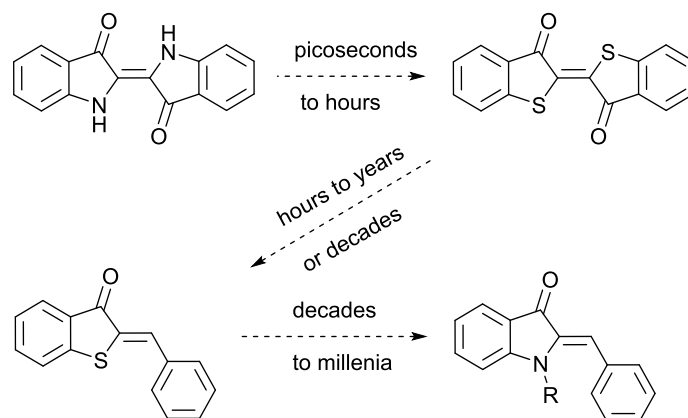


Figure 6: Overview of increasing thermal half-lives for different indigoid photoswitches at 25 °C.

### This work

Highly bistable and efficient photoswitching at the biooptical window is demonstrated with electron donor-substituted hemiindigo derivatives. The peak performance values throughout all derivatives of this class of photoswitches show almost quantitative switchability from 99% *Z*- to 98% *E* isomer content with low energy red- and green light between *Z* and *E* states with quantum yields of up to 49% and thermal half-lives up to 3400 years at 25 °C.<sup>[74, 75]</sup> Good to excellent switchability throughout all solvent polarities as well as in gas and polymer phase is maintained. Repeated photostationary state (PSS) switching over hundreds of cycles and photobleaching experiments over days showed good fatigue resistance of these compounds towards irradiation with high-energy blue light.<sup>[76]</sup>

The two main pitfalls of the photoswitching performance of hemiindigos are discussed. One factor that disrupts the photoswitchability is addition of significant amounts of *Brønsted* acid / base. Second, especially for electron donating substitutions at the stilbene fragment, pure water

poses also a problem, as no switching is observed without addition of a few drops or sometimes up to 20% of water miscible organic solvent, e.g. tetrahydrofuran, *N,N*-dimethylformamide or dimethyl sulfoxide. However, utilization of less electron-rich stilbene fragments makes it possible to obtain hemiindigos that show potent photoswitching in pure water.<sup>[40]</sup>

## 1.4 Switching of ECD responses

Enantiomerically pure chiral compounds twist the plane of polarized light by an angle  $\alpha$  respectively to the polarized input plane as intrinsic property.<sup>[77]</sup> A polarimeter can be used to measure  $\alpha$ , which is given as material constant for a specific concentration of enantiopure compound and used solvent.<sup>[78]</sup> Electronic circular dichroism (ECD) spectroscopy measures the wavelength dependency of this phenomenon and reports the ellipticity similar to UV-Vis spectroscopy with the unit mdeg (millidegrees) instead of a.u. (arbitrary units) for (chiral) absorptivity.<sup>[78]</sup>

The manipulation of ECD signals is not as straightforward as red-shifting chromophores because the complete geometry and constitution of the molecules in solution contributes to its ECD signal in an almost unpredictable way. Recent advances show photoswitches with attached chiral complexing domains, which change their ECD signal upon switching of the binding geometry of the metal.<sup>[79]</sup> Enantiomerically pure molecular motors exhibit changes in their ECD response when switching through different helicities within their rotation cycle.<sup>[80]</sup> These systems display changes in shape and intensity of their wavelength dependent ability to rotate a polarized plane of light. Regardless of the isomer distribution of the molecules, an ECD response is observed as long as no racemization occurs. Modulation of the entire ECD response between two photoswitchable isomers while maintaining absorptivity in the visible spectrum of light was not observed until recently.<sup>[75]</sup>

### This work

To address the previous point, introduction of (axial) chirality to the hemiindigo photoswitch<sup>[74]</sup> at the amine functionality leads to intriguing spectral observations, especially regarding its ECD responses. Derivatives bearing *ortho*-tolyl moieties have been synthesized and it was observed that the *Z* isomers show intense ECD spectra while the spectra of *E* isomers were diminished. Repeated cycling between *Z*- and *E* states could reliably recover the ECD signal while a decrease in intensity could be completely attributed to thermal atropisomerization of the axially chiral *ortho*-tolyl residue with only little photodegradation. This is the first observation of an ON-OFF circular dichroism switch that switches its ECD signal while maintaining absorbance in the same wavelength region.<sup>[75]</sup> The drawback of ECD signal loss caused by thermal atropisomerization could be reduced for one axially chiral hemiindigo derivative and even eliminated for a chiroptical switch supporting a permanent stereo center.

## 1.5 Molecular machines

By the time of writing, there is still controversy regarding the definition of molecular machines. *A. Coskun, M. Banaszak, R. D. Astumian, J.F. Stoddart and B. A. Grzybowski* state that switchable systems do not carry out work because they will retrieve their starting state by reversing the initial switching motion. A machine, in contrast, continuously performs work in form of driving chemical reactions or performing ongoing mechanical motion.<sup>[81]</sup>

A hotel elevator, for example, would not be considered as a machine from this point of view. If a person decides to ride to the 17<sup>th</sup> floor and notices that they forgot something in the lobby, the elevator will not have performed any work by arriving at the ground floor again, except overcoming mechanical friction and air resistance. Elevating a person to the 17<sup>th</sup> floor stores potential energy, which will be released when the person leaves again or eventually at the demolition of the building.

In this work a molecular machine is defined as an entity that converts different forms of energy into each other to carry out work (in principle) against an equilibrating force, e.g. lifting a weight onto a table to store potential energy against gravity.

At the macroscopic scale, motions often do not store energy directly but always have to overcome friction and the momentum of acceleration / deceleration. Macroscopic rotary motors are mostly attached to a winch, pinion and rack, gears or a pump to translate rotary motion into another rotary- / linear motion or into pressure. In order to achieve observable work, the machine must deliver enough force to induce a positional change or to reside in a higher state of energy, which can be used later on.

An electrical capacitor or accumulator, for example, wired to a generator with a diode in series would be considered as machine in this point of view, as turning of the DC generator would result in an electrical current that is forwarded by the diode and charges the capacitor until its saturation or voltage limit. Uncoupling of the generator shaft and shorting the diode would result in rotation of the shaft powered by the capacitor until all stored potential electrical energy is depleted.

A bistable photoswitch can be considered as a similar setup, with the thermodynamic minimum being the e.g. *Z*- or *E* state or respective equilibrium composition and a PSS constituting the charged form with a higher heat of formation and potentially strained geometry. The energy of the switch is slowly released by thermally overcoming the activation barrier towards the favored state or equilibrium. Shorting of the diode in the generator setup is equivalent to heating the photoswitch for faster retrieval of the stored potential energy.

The molecular motor published by *M. Güntner* provides a fully unidirectional rotation around the central double bond in four distinct steps (see Figure 7).<sup>[82]</sup> Starting from the thermodynamically most stable *Z*-(*S*)-(*P*) isomer a light induced double bond isomerization to the *E*-(*S*)-(*M*) isomer takes place. The metastable *E*-(*S*)-(*M*) form, is able undergo a thermal helix inversion, yielding the *E*-(*S*)-(*P*) isomer. This property is often described as thermal ratcheting as the photochemistry of the thermally obtained *E*-(*S*)-(*P*) derivative is entirely different from the *E*-(*S*)-(*M*) isomer and shows complete selectivity towards the *Z*-(*S*)-(*M*) product formation. The latter can also thermally invert its helicity, yielding the thermodynamically favored *Z*-(*S*)-(*P*) isomer and completing the unidirectional rotational cycle. The intermediates prevent a photochemical or thermal back reaction to an extent where the number of forward rotations entirely overcome the number of backward pathways.

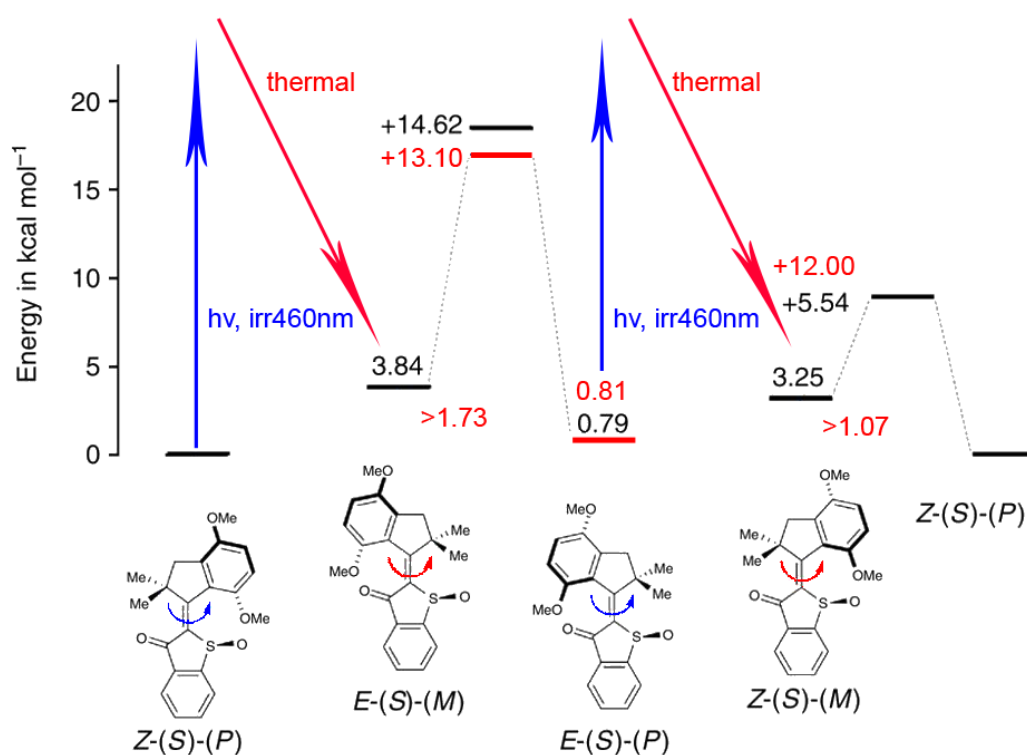


Figure 7: Energy profile of the unidirectional rotational cycle of the molecular motor as published by *M. Güntner*.<sup>[82]</sup> Black lines represent theoretically obtained values calculated at the MPW1K/6-31+G(d,p) level of theory, blue values indicate experimentally measured values.

Molecular setups as described by Figure 7 could make it possible for the motor to transport itself on a surface,<sup>[83]</sup> to drive molecular gears, racks or to act as winch or pump, which is already observed for natural molecular motors within cells, bacteria and higher life forms.

## This work

Axially chiral disubstituted indigo photoswitches were synthesized and characterized. One derivative in particular showed enrichment of the thermodynamically disfavored *anti-trans* state that was inaccessible by pure photochemistry starting from the *syn-trans* isomer as global minimum.

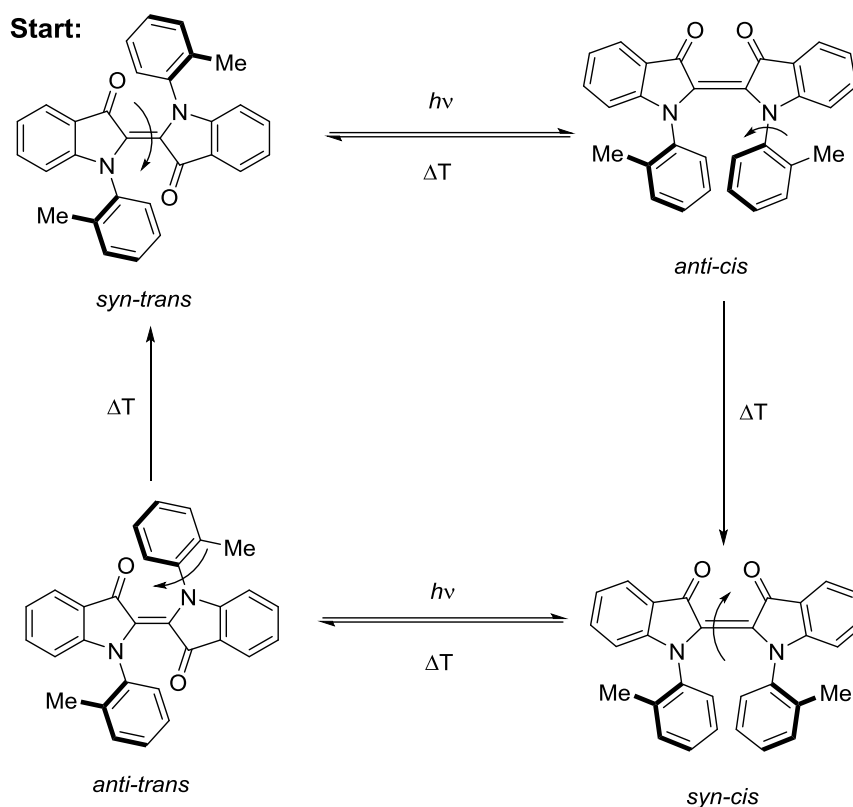


Figure 8: Simplified motional cycle of an axially chiral di-*N*-arylated indigo derivative.

Experimental data and theoretical evaluation supported the molecule in Figure 8 to undergo a photoinduced unidirectional two-step double bond rotation and a unidirectional four-step single bond rotation. The findings also suggest this setup to be a prospective molecular motor that can selectively modulate the rates of rotation of its two rotatable axes relatively to each other by changing the temperature of the sample. In addition, a combined photoinduced- and thermal Hula-Twist motion over three bonds can be proposed by observations via low temperature NMR spectroscopy. This also implies a geared motion between the photoinduced power stroke of the central double bond isomerization and the single bond rotation. Furthermore, the direction of the accumulation of *syn-trans* and *anti-cis* isomer can be selected and reversed by a temperature change from 25 °C to -50 °C. This highly intriguing molecular setup is proposed as the prospectively first known indigo-based molecular motor and the first molecular motor that can be fueled directly by red light.

- [1] M. Calvin, A. A. Benson, *The Path of Carbon in Photosynthesis*, *Science* **1948**, 107, 476.
- [2] R. Hill, *Oxygen Evolved by Isolated Chloroplasts*, *Nature* **1937**, 139, 881.
- [3] J. Ingenhousz, *Experiments upon vegetables discovering their great power of purifying the common air in the sunshine and of injuring it in the shade and at night*, **1779**.
- [4] G. Wald, *Carotenoids and the vitamin A cycle in vision*, *Nature* **1934**, 134, 65.
- [5] T. D. Lamb, *Gain and kinetics of activation in the G-protein cascade of phototransduction*, *Proc. Natl. Acad. Sci. U.S.A.* **1996**, 93, 566.
- [6] A. Gerwien, M. Schildhauer, S. Thumser, P. Mayer, H. Dube, *Direct evidence for hula twist and single-bond rotation photoproducts*, *Nature Communications* **2018**, 9, 2510.
- [7] P. Nogly, T. Weinert, D. James, S. Carbajo, D. Ozerov, A. Furrer, D. Gashi, V. Borin, P. Skopintsev, K. Jaeger, K. Nass, P. B ath, R. Bosman, J. Koglin, M. Seaberg, T. Lane, D. Kekilli, S. Br unle, T. Tanaka, W. Wu, C. Milne, T. White, A. Barty, U. Weierstall, V. Panneels, E. Nango, S. Iwata, M. Hunter, I. Schapiro, G. Schertler, R. Neutze, J. Standfuss, *Retinal isomerization in bacteriorhodopsin captured by a femtosecond x-ray laser*, *Science* **2018**, 361, 127.
- [8] W. F. Loomis, *Skin-pigment regulation of vitamin-D biosynthesis in man*, *Science* **1967**, 157, 501.
- [9] J. Itten, *Kunst der Farbe: Subjektives Erleben und objektives Erkennen als Wege zur Kunst*, Otto Maier Verlag, Ravensberg, **1961**.
- [10] J. Joly, *A quantum theory of colour vision*, *Proceedings of the Royal Society of London. Series B, Containing Papers of a Biological Character* **1921**, 92, 219.
- [11] H. Ley, * ber die Beziehungen zwischen Lichtabsorption und chemischer Konstitution bei organischen Verbindungen*, *Angew. Chem.* **1907**, 20, 1303.
- [12] P. W. Atkins, d. P. Julio, *Physikalische Chemie*, 4th ed., Wiley-VCH Verlag GmbH & Co. KGaA, **2006**.
- [13] J. Wisotzky, *Phosphorescence of teeth cooled in liquid nitrogen*, *The Journal of the American Dental Association* **1963**, 67, 392.
- [14] Y.-K. Lee, *Fluorescence properties of human teeth and dental calculus for clinical applications*, *Journal of biomedical optics* **2015**, 20, 40901.
- [15] M. Born, R. Oppenheimer, *Zur Quantentheorie der Molekeln*, *Annalen der Physik* **1927**, 389, 457.
- [16] E. Schr odinger, *An Undulatory Theory of the Mechanics of Atoms and Molecules*, *Phys. Rev.* **1926**, 28, 1049.
- [17] E. Schr odinger, *Quantisierung als Eigenwertproblem*, *Annalen der Physik* **1926**, 384, 361.
- [18] E. Schr odinger, *Quantisierung als Eigenwertproblem*, *Annalen der Physik* **1926**, 385, 437.
- [19] A. Jablonski, *Efficiency of Anti-Stokes Fluorescence in Dyes*, *Nature* **1933**, 131, 839.
- [20] F. A. Carey, R. J. Sundberg, *Photochemistry. In: Advanced Organic Chemistry. Advanced Organic Chemistry.*, Springer, Boston, MA, **2007**.
- [21] G. N. Lewis, M. Kasha, *Phosphorescence and the Triplet State*, *J. Am. Chem. Soc.* **1944**, 66, 2100.
- [22] M. Frizot, *Neue Geschichte der Fotografie*, Koenemann.com, **1998**.
- [23] H. Remane, W. Girnus, *Meilensteine der Chemie 2009*, *Nachrichten aus der Chemie* **2009**, 57, 11.
- [24] E. Becquerel, *M emoire sur les effets  lectriques produits sous l'influence des rayons solaires*, *Comptes Rendus* **1839**, 9, 561



- [25] R. S. Ohl, *Light-sensitive electric device* **1941**, US2402662A.
- [26] D. A. Nicewicz, D. W. C. MacMillan, *Merging Photoredox Catalysis with Organocatalysis: The Direct Asymmetric Alkylation of Aldehydes*, *Science* **2008**, 322, 77.
- [27] K. Nakamaru, *Synthesis, Luminescence Quantum Yields, and Lifetimes of Trischelated Ruthenium(II) Mixed-ligand Complexes Including 3,3'-Dimethyl-2,2'-bipyridyl*, *Bull. Chem. Soc. Jpn.* **1982**, 55, 2697.
- [28] M. A. Cismesia, T. P. Yoon, *Characterizing chain processes in visible light photoredox catalysis*, *Chemical Science* **2015**, 6, 5426.
- [29] H. Trommsdorf, *Über Santonin*, *Ann. Chem. Pharm.* **1834**, 11, 190.
- [30] A. Natarajan, C. K. Tsai, S. I. Khan, P. McCarren, K. N. Houk, M. A. Garcia-Garibay, *The Photoarrangement of  $\alpha$ -Santonin is a Single-Crystal-to-Single-Crystal Reaction: A Long Kept Secret in Solid-State Organic Chemistry Revealed*, *J. Am. Chem. Soc.* **2007**, 129, 9846.
- [31] J. Saltiel, *Perdeuteriostilbene. The Role of Phantom States in the cis-trans Photoisomerization of Stilbenes*, *J. Am. Chem. Soc.* **1967**, 89, 1036.
- [32] J. B. Birks, *The photo-isomerization of stilbene*, *Chem. Phys. Lett.* **1976**, 38, 437.
- [33] M. Irie, *Diarylethenes for Memories and Switches*, *Chem. Rev.* **2000**, 100, 1685.
- [34] G. Berkovic, V. Krongauz, V. Weiss, *Spiropyran and Spirooxazines for Memories and Switches*, *Chem. Rev.* **2000**, 100, 1741.
- [35] S. Helmy, F. A. Leibfarth, S. Oh, J. E. Poelma, C. J. Hawker, J. Read de Alaniz, *Photoswitching Using Visible Light: A New Class of Organic Photochromic Molecules*, *J. Am. Chem. Soc.* **2014**, 136, 8169.
- [36] K. Hull, J. Morstein, D. Trauner, *In Vivo Photopharmacology*, *Chem. Rev.* **2018**, 118, 10710.
- [37] W. A. Velema, W. Szymanski, B. L. Feringa, *Photopharmacology: Beyond Proof of Principle*, *J. Am. Chem. Soc.* **2014**, 136, 2178.
- [38] I. S. Park, Y.-S. Jung, K.-J. Lee, J.-M. Kim, *Photoswitching and sensor applications of a spiropyran-polythiophene conjugate*, *Chem. Commun.* **2010**, 46, 2859.
- [39] M. Ikegami, T. Arai, *Photochromic and Fluorescence Properties of a Hemiindigo in the Presence of Bovine Serum Albumin*, *Chem. Lett.* **2005**, 34, 492.
- [40] D. V. Berdnikova, *Visible-range hemi-indigo photoswitch: ON-OFF fluorescent binder for HIV-1 RNA*, *Chem. Commun.* **2019**, 55, 8402.
- [41] F. Kink, M. P. Collado, S. Wiedbrauk, P. Mayer, H. Dube, *Bistable Photoswitching of Hemithioindigo with Green and Red Light: Entry Point to Advanced Molecular Digital Information Processing*, *Chemistry – A European Journal* **2017**, 23, 6237.
- [42] J.-R. Colard-Itté, Q. Li, D. Collin, G. Mariani, G. Fuks, E. Moulin, E. Buhler, N. Giuseppone, *Mechanical behaviour of contractile gels based on light-driven molecular motors*, *Nanoscale* **2019**, 11, 5197.
- [43] S. Kassem, A. T. L. Lee, D. A. Leigh, V. Marcos, L. I. Palmer, S. Pisano, *Stereodivergent synthesis with a programmable molecular machine*, *Nature* **2017**, 549, 374.
- [44] S. M. Douglas, I. Bachelet, G. M. Church, *A Logic-Gated Nanorobot for Targeted Transport of Molecular Payloads*, *Science* **2012**, 335, 831.
- [45] B. Osterby, R. D. McKelvey, L. Hill, *Photochromic sunglasses: A patent-based advanced organic synthesis project and demonstration*, *J. Chem. Educ.* **1991**, 68, 424.
- [46] M. Borowiak, W. Nahaboo, M. Reynders, K. Nekolla, P. Jalinot, J. Hasserodt, M. Rehberg, M. Delattre, S. Zahler, A. Vollmar, D. Trauner, O. Thorn-Seshold, *Photoswitchable Inhibitors of Microtubule Dynamics Optically Control Mitosis and Cell Death*, *Cell* **2015**, 162, 403.

- [47] J. Broichhagen, J. A. Frank, D. Trauner, *A Roadmap to Success in Photopharmacology*, *Acc. Chem. Res.* **2015**, *48*, 1947.
- [48] P. Urban, S. D. Pritzl, D. B. Konrad, J. A. Frank, C. Pernpeintner, C. R. Roeske, D. Trauner, T. Lohmüller, *Light-Controlled Lipid Interaction and Membrane Organization in Photolipid Bilayer Vesicles*, *Langmuir* **2018**, *34*, 13368.
- [49] P. Glock, J. Broichhagen, S. Kretschmer, P. Blumhardt, J. Mücksch, D. Trauner, P. Schwille, *Optical Control of a Biological Reaction–Diffusion System*, *Angew. Chem. Int. Ed.* **2018**, *57*, 2362.
- [50] Z. Tian, A. D. Q. Li, *Photoswitching-Enabled Novel Optical Imaging: Innovative Solutions for Real-World Challenges in Fluorescence Detections*, *Acc. Chem. Res.* **2013**, *46*, 269.
- [51] E. National Academies of Sciences, Medicine, *Quantum Computing: Progress and Prospects*, The National Academies Press, Washington, DC, **2019**.
- [52] T. R. Kelly, H. De Silva, R. A. Silva, *Unidirectional rotary motion in a molecular system*, *Nature* **1999**, *401*, 150.
- [53] N. Koumura, R. W. J. Zijlstra, R. A. van Delden, N. Harada, B. L. Feringa, *Light-driven monodirectional molecular rotor*, *Nature* **1999**, *401*, 152.
- [54] J. Chen, S. J. Wezenberg, B. L. Feringa, *Intramolecular transport of small-molecule cargo in a nanoscale device operated by light*, *Chem. Commun.* **2016**, *52*, 6765.
- [55] W. R. Browne, B. L. Feringa, *Making molecular machines work*, *Nature Nanotechnology* **2006**, *1*, 25.
- [56] C. Song, Z.-G. Wang, B. Ding, *Smart Nanomachines Based on DNA Self-Assembly*, *Small* **2013**, *9*, 2382.
- [57] M. Kathan, S. Hecht, *Photoswitchable molecules as key ingredients to drive systems away from the global thermodynamic minimum*, *Chem. Soc. Rev.* **2017**, *46*, 5536.
- [58] W. Fuß, *Previtamin D: Z–E photoisomerization via a Hula-twist conical intersection*, *PCCP* **2019**, *21*, 6776.
- [59] B. Maerz, S. Wiedbrauk, S. Oesterling, E. Samoylova, A. Nenov, P. Mayer, R. de Vivie-Riedle, W. Zinth, H. Dube, *Making Fast Photoswitches Faster—Using Hammett Analysis to Understand the Limit of Donor–Acceptor Approaches for Faster Hemithioindigo Photoswitches*, *Chemistry – A European Journal* **2014**, *20*, 13984.
- [60] R. Wilcken, M. Schildhauer, F. Rott, L. A. Huber, M. Guentner, S. Thumser, K. Hoffmann, S. Oesterling, R. de Vivie-Riedle, E. Riedle, H. Dube, *Complete Mechanism of Hemithioindigo Motor Rotation*, *J. Am. Chem. Soc.* **2018**, *140*, 5311.
- [61] C. Redwood, M. Bayda, J. Saltiel, *Photoisomerization of Pre- and Provitamin D<sub>3</sub> in EPA at 77 K: One-Bond-Twist, Not Hula-Twist*, *The Journal of Physical Chemistry Letters* **2013**, *4*, 716.
- [62] A. Baeyer, A. Emmerling, *Reduction des Isatins zu Indigblau*, *Berichte der deutschen chemischen Gesellschaft* **1870**, *3*, 514.
- [63] A. Baeyer, *Ueber die Verbindungen der Indigogruppe*, *Berichte der deutschen chemischen Gesellschaft* **1883**, *16*, 2188.
- [64] H. Schmidt, *Indigo – 100 Jahre industrielle Synthese*, *Chem. unserer Zeit* **1997**, *31*, 121.
- [65] S. Yamazaki, A. L. Sobolewski, W. Domcke, *Molecular mechanisms of the photostability of indigo*, *PCCP* **2011**, *13*, 1618.
- [66] L. A. Huber, P. Mayer, H. Dube, *Photoisomerization of Mono-Arylated Indigo and Water-Induced Acceleration of Thermal cis-to-trans Isomerization*, *ChemPhotoChem* **2018**, *2*, 458.

- [67] H. S. Correa, E. Ortiz, V. H. Uc, I. D. B. Quintal, J. L. H. Avila, *Indigo stability: an ab initio study*, *Molecular Simulation* **2011**, 37, 1085
- [68] J. Seixas de Melo, A. P. Moura, M. J. Melo, *Photophysical and Spectroscopic Studies of Indigo Derivatives in Their Keto and Leuco Forms*, *The Journal of Physical Chemistry A* **2004**, 108, 6975.
- [69] C. Y. Huang, A. Bonasera, L. Hristov, Y. Garmshausen, B. M. Schmidt, D. Jacquemin, S. Hecht, *N,N'-Disubstituted Indigos as Readily Available Red-Light Photoswitches with Tunable Thermal Half-Lives*, *J. Am. Chem. Soc.* **2017**, 139, 15205.
- [70] P. Friedlaender, *Ueber Thionaphenderivate und Thioindigo*, *Justus Liebigs Annalen der Chemie* **1907**, 351, 390.
- [71] P. Friedländer, *Zeitschr. f. Farben- und Textilchemie* **1904**, 3, 333.
- [72] M. Dittmann, F. F. Graupner, B. Maerz, S. Oesterling, R. de Vivie-Riedle, W. Zinth, M. Engelhard, W. Lüttke, *Photostability of 4,4'-Dihydroxythioindigo, a Mimetic of Indigo*, *Angew. Chem. Int. Ed.* **2014**, 53, 591.
- [73] S. Wiedbrauk, H. Dube, *Hemithioindigo—an emerging photoswitch*, *Tetrahedron Lett.* **2015**, 56, 4266.
- [74] C. Petermayer, S. Thumser, F. Kink, P. Mayer, H. Dube, *Hemiindigo: Highly Bistable Photoswitching at the Biooptical Window*, *J. Am. Chem. Soc.* **2017**, 139, 15060.
- [75] C. Petermayer, H. Dube, *Circular Dichroism Photoswitching with a Twist: Axially Chiral Hemiindigo*, *J. Am. Chem. Soc.* **2018**, 140, 13558.
- [76] C. Petermayer, H. Dube, *Indigoid Photoswitches: Visible Light Responsive Molecular Tools*, *Acc. Chem. Res.* **2018**, 51, 1153.
- [77] B. Kahr, K. Claborn, *The Lives of Malus and His Bicentennial Law*, *ChemPhysChem* **2008**, 9, 43.
- [78] F. A. Carey, R. J. Sundberg, *Stereochemistry, Conformation, and Stereoselectivity*. In: *Advanced Organic Chemistry*. *Advanced Organic Chemistry*, Springer, Boston, MA, **2007**.
- [79] A. Homberg, E. Brun, F. Zinna, S. Pascal, M. Górecki, L. Monnier, C. Besnard, G. Pescitelli, L. Di Bari, J. Lacour, *Combined reversible switching of ECD and quenching of CPL with chiral fluorescent macrocycles*, *Chemical Science* **2018**, 9, 7043.
- [80] B. L. Feringa, *In Control of Motion: From Molecular Switches to Molecular Motors*, *Acc. Chem. Res.* **2001**, 34, 504.
- [81] A. Coskun, M. Banaszak, R. D. Astumian, J. F. Stoddart, B. A. Grzybowski, *Great expectations: can artificial molecular machines deliver on their promise?*, *Chem. Soc. Rev.* **2012**, 41, 19.
- [82] M. Guentner, M. Schildhauer, S. Thumser, P. Mayer, D. Stephenson, P. J. Mayer, H. Dube, *Sunlight-powered kHz rotation of a hemithioindigo-based molecular motor*, *Nat Commun* **2015**, 6, 8406.
- [83] T. Kudernac, N. Ruangsapapichat, M. Parschau, B. Maciá, N. Katsonis, S. R. Harutyunyan, K.-H. Ernst, B. L. Feringa, *Electrically driven directional motion of a four-wheeled molecule on a metal surface*, *Nature* **2011**, 479, 208.

## 2 RESULTS AND DISCUSSION

The main focus of this work consisted of the design and characterization of a novel class of high performing, thermally bistable, red-shifted photoswitches and their applicability in gaseous, liquid and solid phases. Subsequent endeavors headed at the utilization of these compounds for establishing control of molecular motion and / or chiral properties as well as entering the fields of biology and materials science.<sup>[74, 75, 76]</sup>

The main property of the investigated class of photoswitches is exhibited in the photo- or thermally induced *Z* / *E* or *E* / *Z* isomerization of the central double bond, shown in Figure 9.

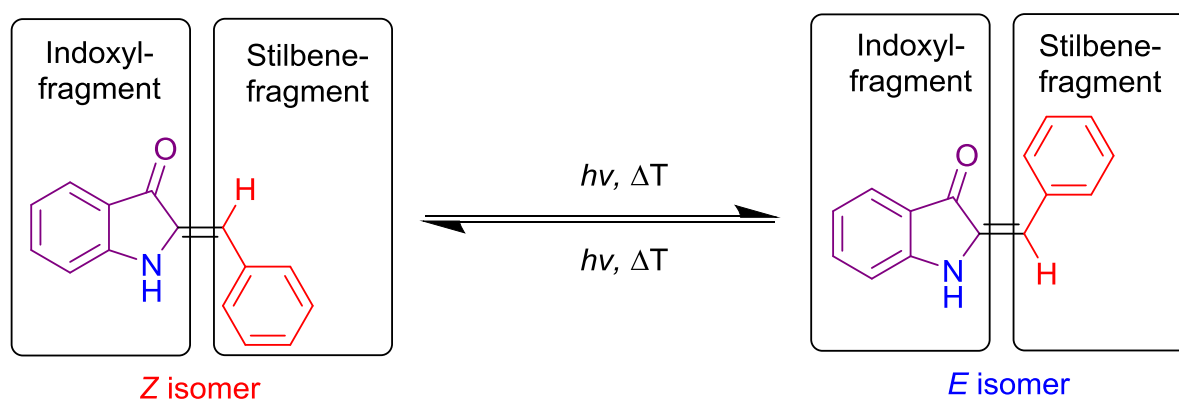


Figure 9: Nomenclature and fundamental switching processes of a hemiindigo photoswitch induced by visible light or thermal excitation.

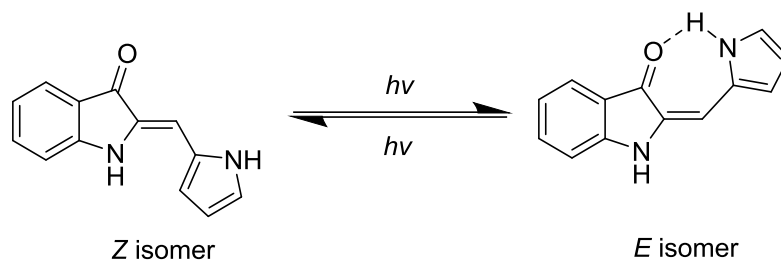
The two formal parts of the molecule are referred to as (hemi-)indigo or indoxyl fragment (left) and (hemi-)stilbene fragment (right). The two stable conformations, namely *Z*- and *E* isomer, differ vastly in their (photo-)physical properties and can be examined independently by common spectroscopic methods. The isomerization process also yields a rather large mechanical change with an expansive swing of the phenyl group when the indoxyl fragment is regarded as static. When the stilbene fragment is treated as fixed, a volume-demanding 180° rotation of the indoxyl fragment can be postulated. Linear and rigid substituents at the N-H or adjacent aromatic C-H position would experience extensive conformational changes upon switching because of their enhanced mechanical leverage. Such large geometrical changes makes *Z* / *E* double bond isomerizing switches viable in situations where substantial mechanical change is required. Examples are the photocontrol of binding affinities of small molecules to active sites in protein complexes or the opening / closing of ion channels within membranes.<sup>[46, 84]</sup> The red-shifted absorptions of hemiindigos makes them perfect candidates for the use inside bacteria, cells or biological tissues, as green and red light will not damage proteins or DNA. Long wavelength light is also beneficial for deep tissue penetration as it would not be absorbed

as readily as UV or blue light by skin.<sup>[66, 69]</sup> Another benefit of this class of photoswitches is their high thermal bistability, supporting half-lives over months or years even at physiological temperatures. Good photoquantum yields enable quick and efficient irradiation timeframes.

Normally, only the *Z* isomer is shown as *Lewis*-formula in this work for clarity. If not stated otherwise, only one *E* isomer with its respective enantio- or diastereomers can be formed.

## 2.1 Hemiindigo - Improving the performance of photoswitches

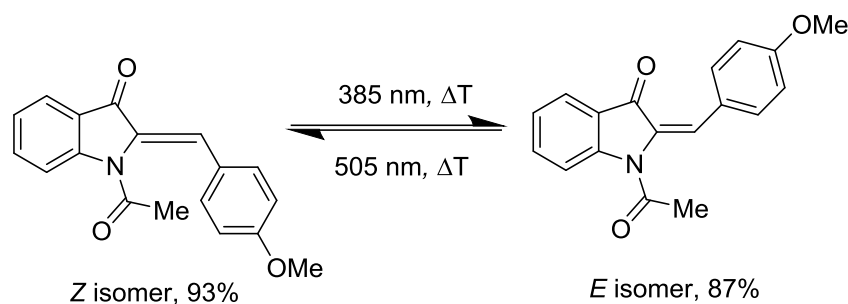
Hemiindigo was first described by *A. von Baeyer* in 1883 within one of his landmark publications “Über die Verbindungen der Indigogruppe”.<sup>[63]</sup> Its potential as photoswitch was untapped until research by *T. Arai et al.* in 1999 discovered the pyrrole-substituted hemiindigo **1** as viable photoswitch and fluorescence modulator in bovine serum albumin (Scheme 2).<sup>[39, 85]</sup>



Scheme 2: Photoisomerization of pyrrole-substituted hemiindigo **1** by *T. Arai*.

The challenge to find novel photoswitches with potentially improved performance characteristics compared to stilbenes, azobenzenes, diarylethenes, spiropyranes and *Stenhouse* adducts led to the synthesis of several hemiindigo derivatives, which was initially covered by the work of *F. Kink*. The first generation of hemiindigo photoswitches comprised a methoxy group attached to the stilbene fragment in *para*-position based on previous findings for hemithioindigo done by *S. Wiedbrauk*.<sup>[86]</sup> Different electron donating and withdrawing groups at the stilbene fragment of hemithioindigo showed the fastest switching characteristics of 2.4 picoseconds (ps) for the methoxy derivative, which was measured via time resolved UV-Vis spectroscopy by *R. Wilcken*.<sup>[86, 87]</sup> The resulting high thermal stabilities and good switching performance made this substitution pattern a good starting point for the related hemiindigo system. However, hemithioindigo behaves vastly different compared to hemiindigo, as the *para*-methoxy substituted molecule shows strong, rapidly decreasing fluorescence and majorly photodestruction over prolonged irradiation periods, probably caused by intermolecular excited state proton transfer (ESPT), which triggers unidentified side reactions.

This unfavorable behavior of hemiindigos can be overcome by substitution of the amine hydrogen by e.g. acetyl, as done by *F. Kink*. The obtained molecules **2** are stable towards irradiation and show high thermal bistabilities with barriers of about 33 kcal/mol.



Scheme 3: Photoswitching and thermal isomerization pathways of hemiindigo **2**.

Transient measurements done by *R. Wilcken* from the group of *E. Riedle* revealed photoisomerization speeds for this photoswitch of 2.1 ps, which is very similar to the corresponding methoxy-substituted hemithioindigo derivative.

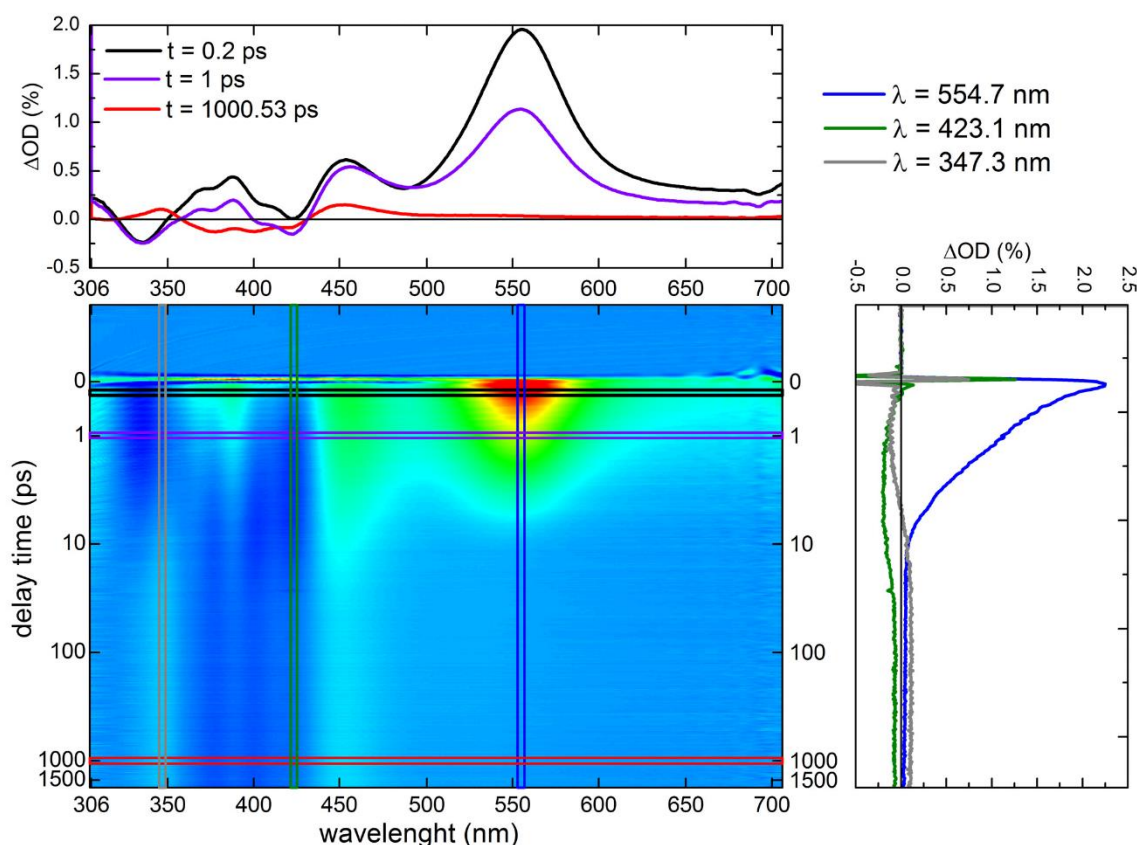
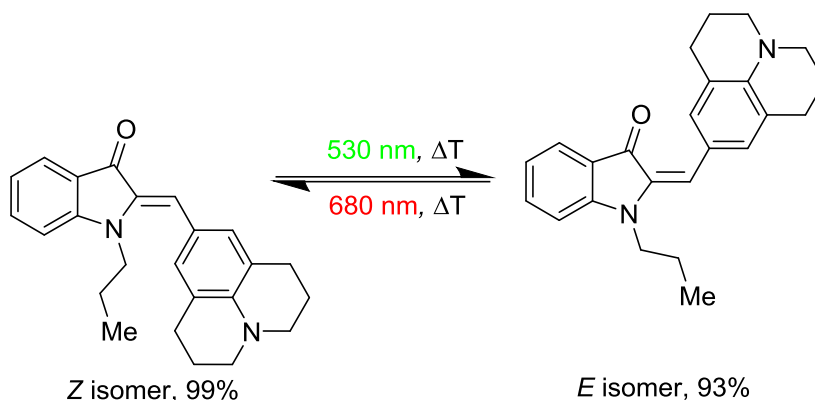


Figure 10: Transient absorption spectra of hemiindigo **2** recorded after 45 femtoseconds photoexcitation of the *Z* isomer with 400 nm light.

Electron donating groups like dimethyl amino or julolidine at the stilbene fragment in combination with alkyl-substitution of the NH proton result in a strong, solvent dependent red-shift of absorptions up to 100 nm for hemithioindigo and hemiindigo derivatives alike.



Scheme 4: Exemplary *Z* / *E* isomerization of hemiindigo **3** with nominal green 530 nm LED light to 93% *E* isomer and nominal red 680 nm LED light to 99% *Z* isomer in dimethyl sulfoxide. The *Z* isomer has a thermal half-life of 0.7 years and the *E* isomer of 0.9 years at 25 °C.

One drawback of red-shifted hemithioindigos is their overall low thermal stability and the significantly lowered thermal stability if substituents of increasing donor strength (and thus red-shifting capacity) are introduced. The energy barriers for the thermal double bond isomerizations in toluene solution decrease from 26.4 kcal/mol for the methoxy-substituted hemithioindigo **4** to 24.7 kcal/mol, for the dimethylamino derivative **5** to 21.4 kcal/mol for the julolidine derivative **6**. At the same time these energy barriers are sensitive to solvent dipole moment and decrease further with increasing polarity. Interestingly for hemiindigos the energy barriers remain significantly higher in the range of 25 - 30 kcal/mol within aprotic solvents for derivatives **7**, **8** and **3**.<sup>[74]</sup> This displays their seldom trait of red-shifted absorptions combined with high thermal bistability, which makes photoswitching switching accessible with low energy green and red light, which is highly favorable for biological applications. Quantum yields of approximately 20% for the *Z*- to *E*-photoisomerization and 10% for the *E*- to *Z*-photoisomerization within all solvent polarities ensure the practical efficiencies of the switching processes.



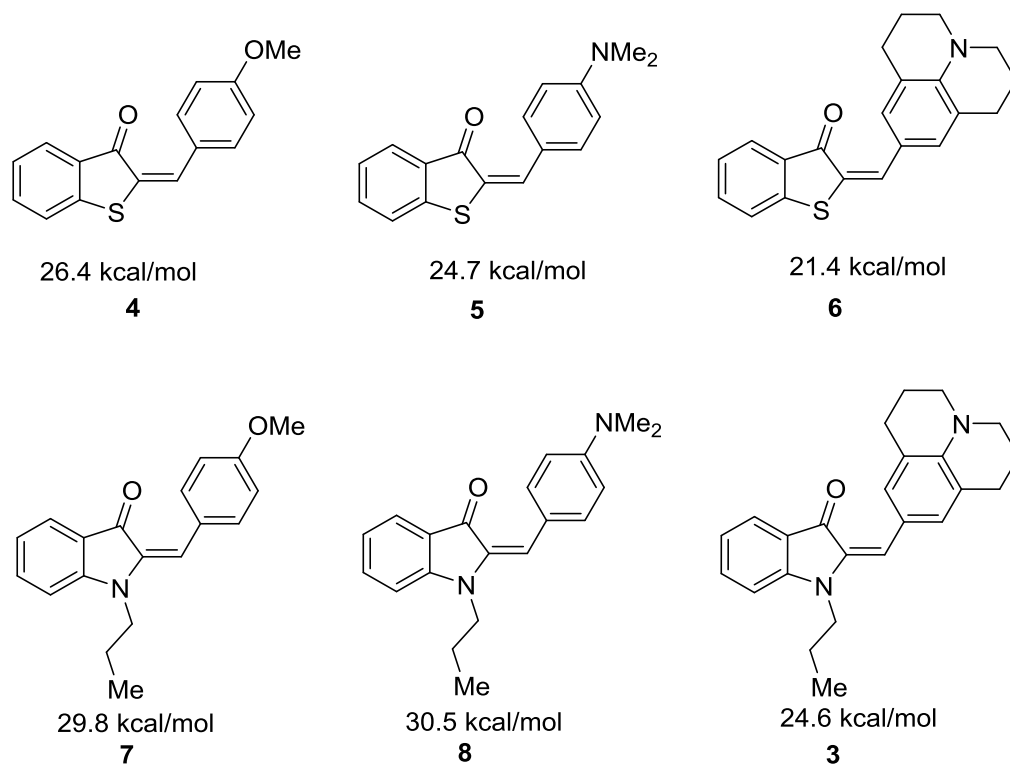


Figure 11: *Lewis*-formulas of hemithioindigos *E*-**4**, **5**, **6** (top) and hemiindigos *E*-**7**, **8**, **3** (bottom) and their free activation enthalpies  $\Delta G^*$  for the respective *E* to *Z* isomerizations in toluene.

## 2.2 Hemiindigo - Rationale of substitution patterns

The generalized rationale behind the substitution patterns for adjusting the photophysical properties of hemiindigo photoswitches is depicted below (Figure 12).

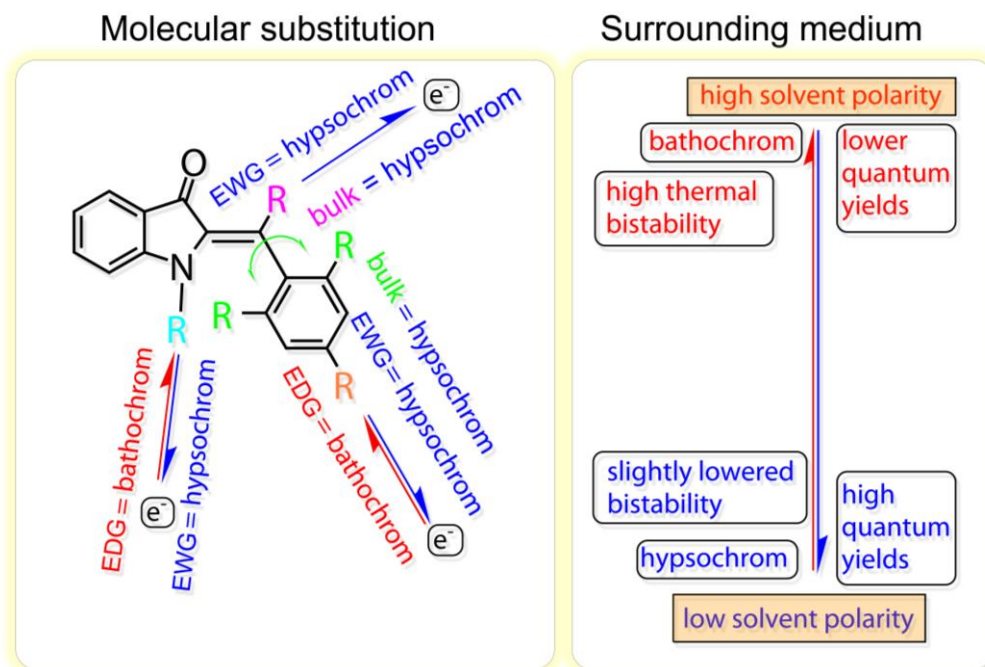
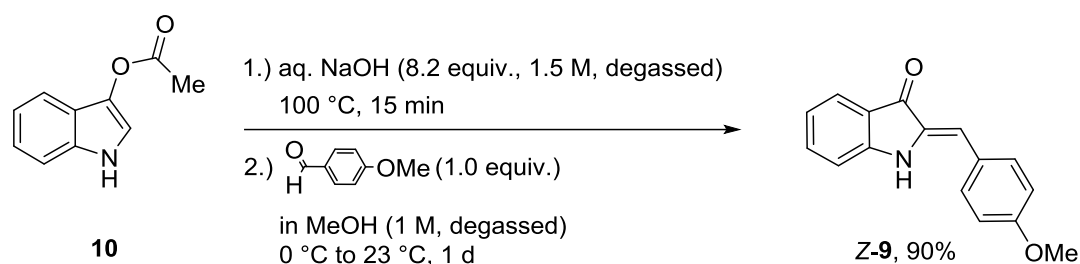


Figure 12: Rationale for the substitution and selection of solvents for tailoring hemiindigo photoswitches. EWG = Electron withdrawing group, EDG = electron donating group. Electron donating moieties at the N-R position result in red-shifted chromophores, the same can be seen for the *para*-position of the stilbene fragment. Electron withdrawing groups will result in blue-shifted absorptions, this includes the proton substitution at the central double bond. Introduction of bulk at the *ortho*-positions of the stilbene fragment or at the central double bond will result in twisting of the adjacent single bond and loss of *pi*-conjugation along the chromophore, which also blue-shifts absorptions. Polar solvents will red-shift absorptions and enhance thermal bistabilities while lowering quantum efficiencies upon switching. Apolar solvents will reverse these trends.

## 2.2.1 Indoxyl fragment: N-H unsubstituted hemiindigo **9**

The first investigated hemiindigo chromophore **9** was derived from hemithioindigo **4** by *S. Wiedbrauk*, which showed the fast transient switching behavior in the range of picoseconds.<sup>[59]</sup> The first experiments on hemiindigos were carried out in our group by *F. Kink*. Scheme 5 shows the applied synthetic procedure by *U. Burger et al.*<sup>[88]</sup>



Scheme 5: Condensation of indoxyl acetate and an aldehyde to obtain hemiindigo **9**.

Basic ester cleavage of indoxyl acetate **10** at 100 °C yields the indoxyl, which is immediately deprotonated in  $\alpha$ -position and leaves a deep green colored reaction mixture upon completion. After cooling to 0 °C, the nucleophilic carbanion attacks the aldehyde carbon under C-C bond formation with subsequent abstraction of water to yield the central double bond. Upon workup, hemiindigo **9** is obtained in a very good yield of 90% as orange crystalline squares (1-2 mm edge length).

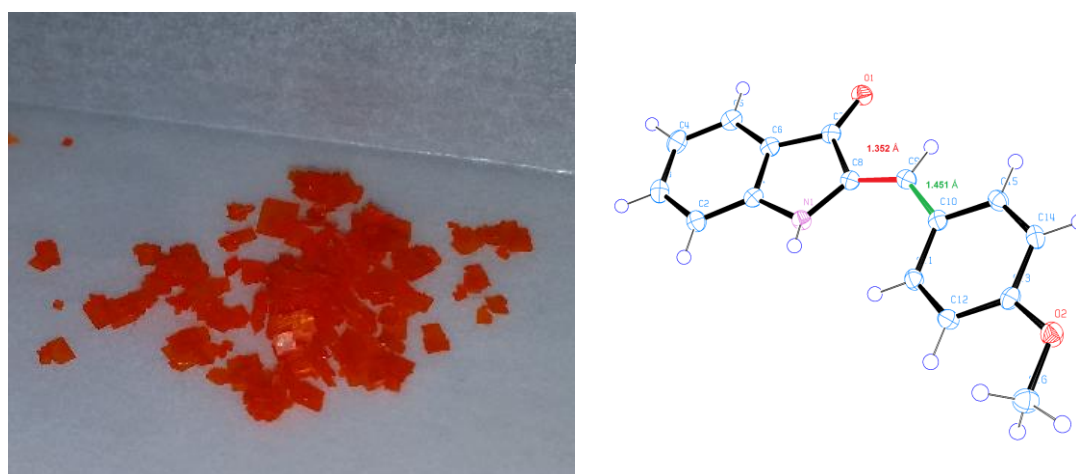


Figure 13: Crystals (left) and structure of hemiindigo **Z-9** (left) in the crystalline state. An almost planar conformation of the single bond with a dihedral angle of 9.26° for C8-C9-C10-C11 can be observed. The double bond (red) measures 1.352 Å in length and the stilbene single bond (green) at 1.451 Å.

However, the promising substitution of sulphur with nitrogen yielded a molecule with slightly enhanced red-shifted absorptions but with sub-par photophysical properties. Figure 15 shows the photoswitching behavior of hemiindigo **9** in apolar and polar solvents. Only N-H unsubstituted derivatives and neutral to moderate electron donors like methyl and methoxy groups in *para*-position of the stilbene fragment initially show strong fluorescent behavior, which is lost upon photoswitching or exposure to air at ambient temperatures (Figure 16). Irradiation with green light leads to significant destruction of the chromophore within minutes, which can be followed by the loss of absorption at the isosbestic point at 470 nm (toluene) and 500 nm (dimethyl sulfoxide) as exemplified for hemiindigo **9** in Figure 15. This might be caused by excited state proton transfer (ESPT), which could yield reactive intermediates that further destabilize the *Michael* system. These findings lead to a pronounced focus on substitution patterns containing *N*-substituted chromophores (see Section 2.2.3).

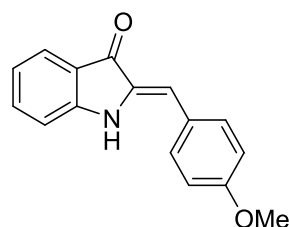


Figure 14: *Lewis*-formula of hemiindigo **9**.

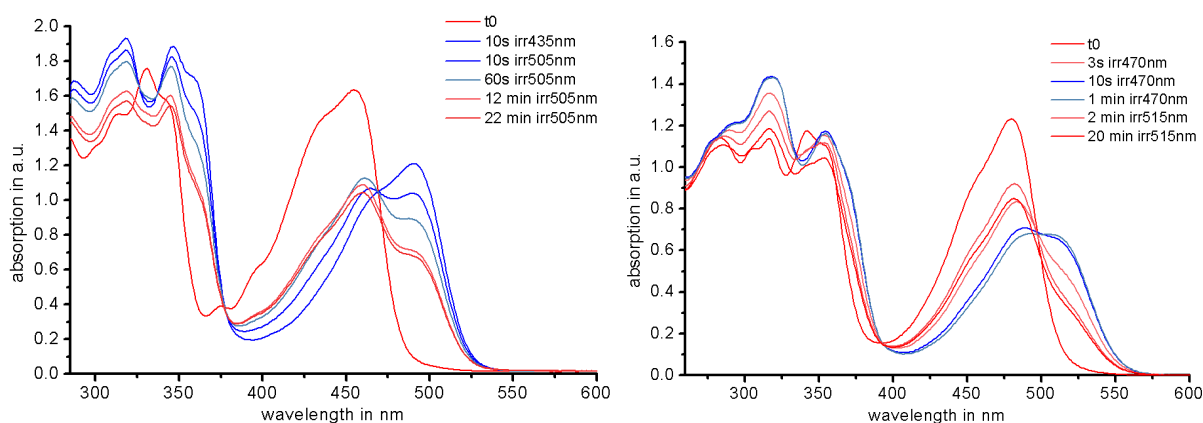


Figure 15: Photoswitching of hemiindigo **9** in toluene (left) and dimethyl sulfoxide (right) at different wavelengths. *Z* isomer enriched states are colored in red, *E* isomer enriched states are colored in blue. Comparable amounts of photodestruction can be seen over this broad range of solvent polarity. The estimated increase in isomeric yields of the *E* isomer in toluene can be attributed to the overall improved quantum yields of hemiindigos in apolar solvents, which is discussed in Section 2.2.25. Exact quantification of thermal bistabilities, isomeric ratios

and quantum efficiencies were not carried out as the constant degradation of this molecule would not yield accurate results.

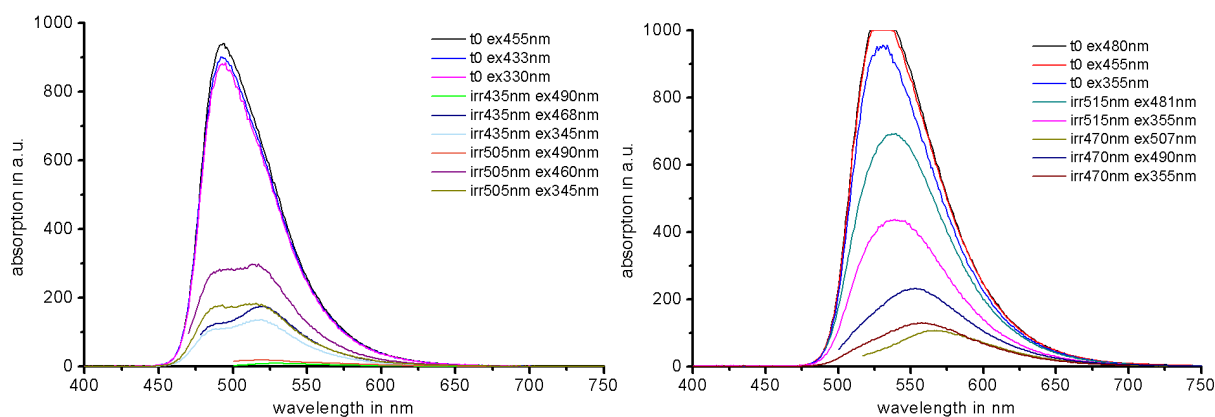


Figure 16: Fluorescence spectra of hemiindigo **9** in toluene (left) and dimethyl sulfoxide (right). This strong fluorescence is exclusive to N-H unsubstituted and stilbene *para*-proton, -methyl and -methoxy substituted hemiindigos. Fluorescence is lost upon photoswitching and by exposure to atmospheric conditions.

The N-H unsubstituted hemiindigos show complete recovery of the *Z* isomer exclusively upon heating, similar to hemithioindigos. However, substitution of the N-H proton shifts the *Z* state closer to the *E* state energetically, which results in thermodynamic equilibria with both isomeric states being populated.



The twisted single bond shown in green in Figure 17 contributes to the hypsochromic shift of the absorption by hindering the overall  $\pi$ -conjugation. This is generally beneficial for a greater separation of  $Z$  and  $E$  absorption bands, which is usually beneficiary for isomer accumulation in the photostationary state.

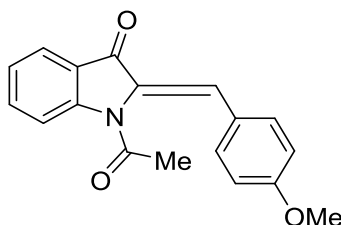


Figure 18: Lewis-formula of hemiindigo **2**.

Compared to hemiindigo **9**, the acetylated derivative **2** exhibits substantially differing properties with blue-shifted absorptions, no fluorescent behavior, very good photostability, good isomeric yields in the PSS, very high thermal bistability and a thermal  $Z/E$  isomer equilibrium at higher temperatures in toluene solution.

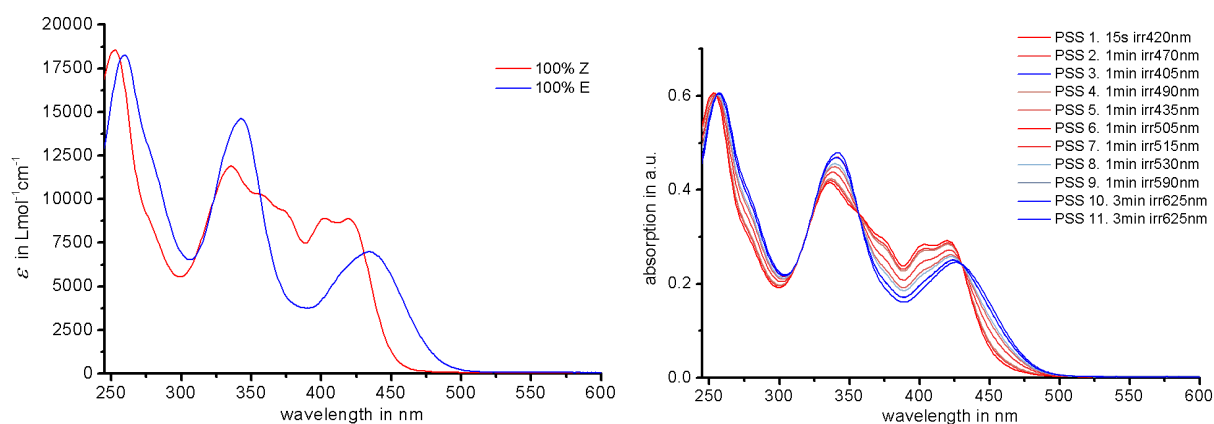


Figure 19: Molar absorption (left) and PSS (right) spectra of hemiindigo **2** in dichloromethane. A blue shifted absorption compared to the N-H substituted compound **9** can be observed resulting from acetylation of the indoxyl nitrogen (Figure 15). Defined isosbestic points can be seen at 260 nm, 320 nm, 360 nm and 430 nm, which indicates good photostability of this compound. Highest isomeric yields were obtained at 385 nm irradiation (88%  $E$  isomer) and at 505 nm irradiation (87%  $Z$  isomer). Energy barriers for thermal double bond isomerizations were determined to be 24.4 kcal/mol for the  $Z$  to  $E$  and 24.0 kcal/mol for the  $E$  to  $Z$  direction at 24 °C, which translates to thermal half-lives of 12.5 h and 24.5 h at 25 °C, for the respective isomers.

The relatively low thermal bistabilities of hemiindigo **2** can be attributed to the presence of small amounts of hydrochloric acid, which is a contaminant of the dichloromethane solvent. Filtration of the solvent through aluminium(III) oxide increased the measured energy barrier for thermal double bond isomerizations significantly, as shown for hemiindigo derivatives (Figure 20).

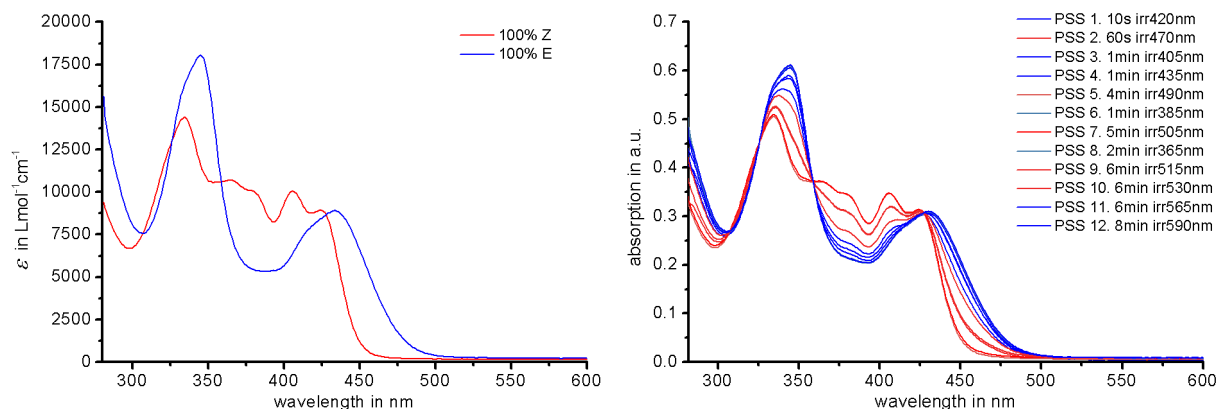


Figure 20: Molar absorption (left) and PSS (right) spectra of hemiindigo **2** in toluene. Almost similar absorption profiles can be observed compared to dichloromethane as solvent (Figure 19). The isosbestic points are well defined, verifying the photostability of this compound. Highest isomeric yields were obtained at 385 nm irradiation (89% *E* isomer) and at 490 nm irradiation (99% *Z* isomer). Energy barriers for thermal double bond isomerizations were determined to be 32.6 kcal/mol for the *Z* to *E* and 31.4 kcal/mol for the *E* to *Z* direction at 100 °C, which translates to thermal half-lives of 2895 years and 381 years at 25 °C, for the respective isomers.



### 2.2.3 Indoxyl fragment: N-H alkylation of hemiindigos

As the substitution of the N-H proton by an acetyl group yielded stable photoswitches, the next iteration of hemiindigo photoswitches was set to utilize electron donating substituents at the indoxyl nitrogen. The first experiments employing a methyl substituent were done by *F. Kink* and furnished difficult to purify and barely stable molecules. Nonetheless, reproduction and temporal purification of the unstable compounds was possible and a crystal structure for hemiindigo **13** in the *E* isomeric form could be obtained (Figure 21)

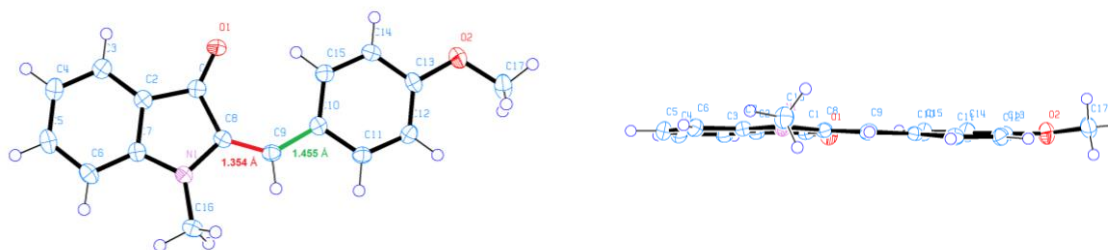


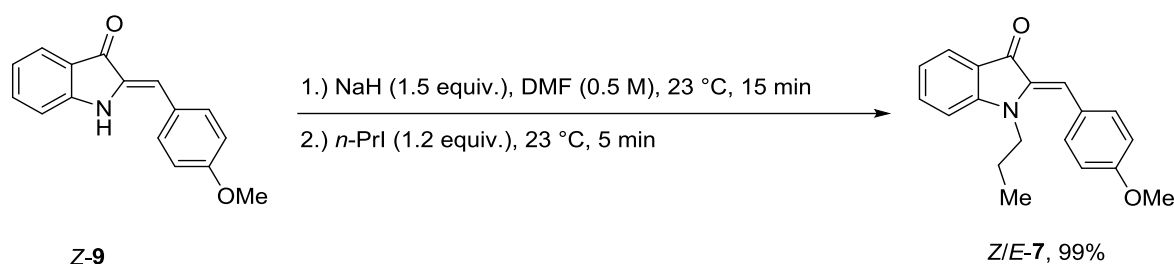
Figure 21: Structure of hemiindigo **13** in the crystalline state in its *E* isomeric form. Full planarity for the *E* isomer can be observed, which is seen for all hemiindigos with *ortho*-unsubstituted stilbene fragments. The double (red) and single bond (green) are elongated from 1.352 to 1.354 Å and 1.451 to 1.455 Å, respectively, compared to N-H substituted chromophore **2**. This can be caused by the +I effect of the methyl group or the overall electronically different *E* isomeric form.

The lack of photostability of hemiindigo **13** led to discardment of this substitution pattern.

An ethyl group was introduced instead to probe if an aliphatic substitution can be made feasible at all. Recrystallization of the *N*-ethyl substituted hemiindigo **14** at 100 °C in ethanol / water mixtures yielded the undesired molecule shown in Figure 22.



The introduction of electron donating aliphatic substituents was carried out according to procedures from V. Velezheva et al.<sup>[90]</sup>



Scheme 7: Alkylation of hemiindigo **9** via an  $S_N2$  mechanism to obtain compound **7** in excellent yields.

Deprotonation of the nitrogen proton by sodium hydride yielded a deep green solution. Dropwise addition of an electrophile creates orange reaction hot spots upon contact with the vigorously stirring solution, which indicates fast reaction kinetics. Small orange crystals could be obtained after workup (Figure 23).

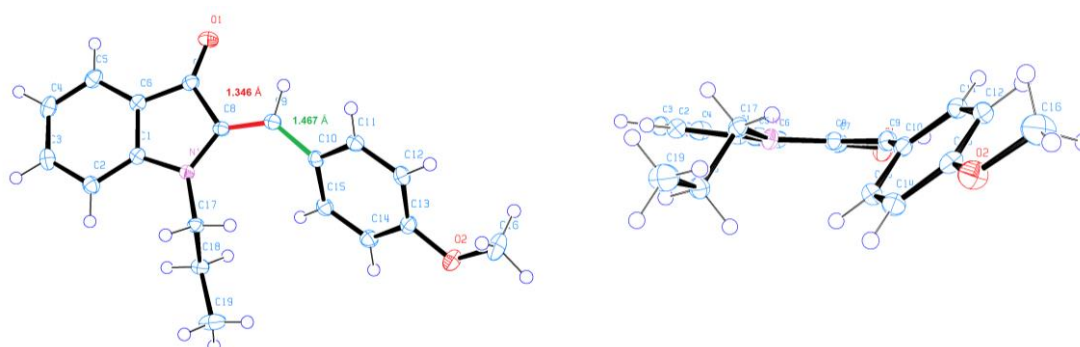


Figure 23: Structure of hemiindigo **7** in the crystalline state. The viewing angle on the right emphasizes the strong single bond twisting of the stilbene fragment. The stilbene single bond dihedral torsion angle amounts to  $43.47^\circ$  for C8-C9-C10-C15 in the *Z* isomeric state and the dihedral helical torsion angle amounts to  $8.73^\circ$  for C17-N1-C8-C9. The double bond (red) is contracted from 1.352 to 1.346 Å and the single bond (green) is highly elongated from 1.451 to 1.467 Å compared to the N-H unsubstituted chromophore **9**.

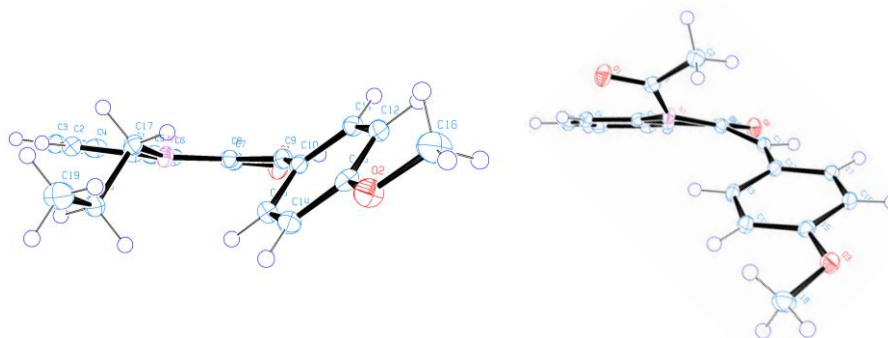


Figure 24: Comparison of helical torsion and stilbene single bond rotation for alkylated hemiindigo **7** (left) and acetylated hemiindigo **2** (right)

In the crystalline state, alkylated hemiindigo **7** (Figure 24, left) shows a stilbene single bond dihedral torsion angle of  $43.47^\circ$ , which is almost doubled compared to the  $23.24^\circ$  of the acetylated compound. This occurs at the cost of helical dihedral torsion, which is reduced from  $52.97^\circ$  to  $8.73^\circ$  for the alkylated compound **7** (Figure 24, left). This indicates increased protrusion of the acetyl substituent, as the amide bond tries to stay as planar as possible due to its drive to maximize *pi*-conjugation. Additionally, the electron withdrawal of the acetyl seems to increase the rigidity of the stilbene single bond, as bending of the indoxyl core for hemiindigo **2** is favored over a single bond rotation. The electron donating alkyl chain in hemiindigo **7** benefits the overall bathochromic absorption shift while the stronger out-of-plane twisting of the stilbene single bond in the *Z* isomeric state induces a hypsochromic shift. This brings both absorption bands for *Z* and *E* isomers further apart (i.e. increases photochromism), which increases obtainable isomeric yields upon continuous irradiation if differences in quantum yields and molar absorption coefficients are assumed to be non-variant.

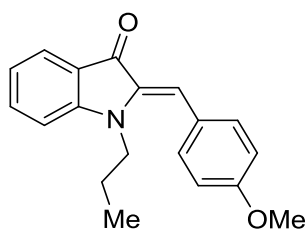


Figure 25: Lewis-formula of hemiindigo 7.

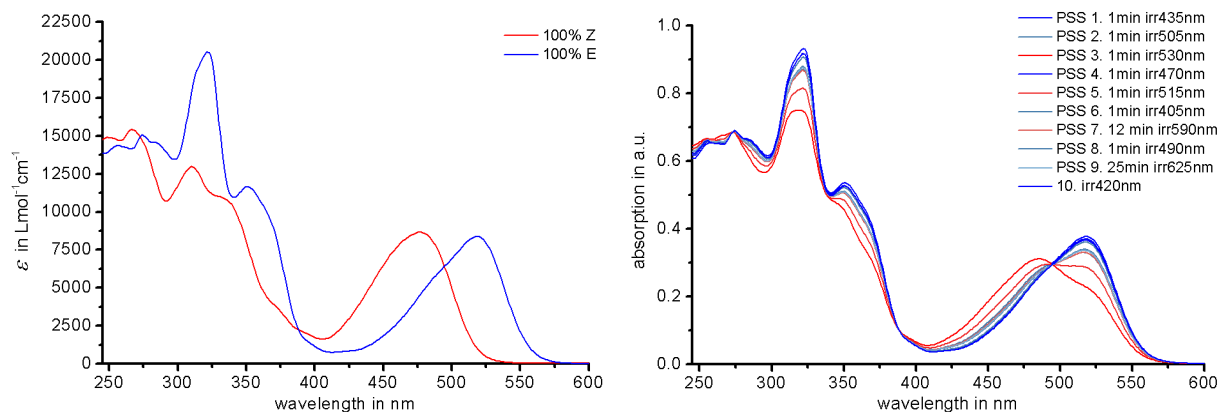


Figure 26: Molar absorption (left) and PSS (right) spectra of hemiindigo 7 in dichloromethane. The isosbestic points are well defined, verifying the photostability of this compound. Highest isomeric yields were obtained at 435 nm irradiation (96% *E* isomer) and at 565 nm irradiation (54% *Z* isomer). Energy barriers for thermal double bond isomerizations were determined to be 23.8 kcal/mol for the *Z* to *E* and 23.7 kcal/mol for the *E* to *Z* direction at 100 °C, which translates to thermal half-lives of 8.9 h and 7.5 h at 25 °C, for the respective isomers. Quantum yields were determined at  $17 \pm 3\%$  (449 nm) for *Z* to *E* and  $3.2 \pm 1\%$  (565 nm) for *E* to *Z* direction.

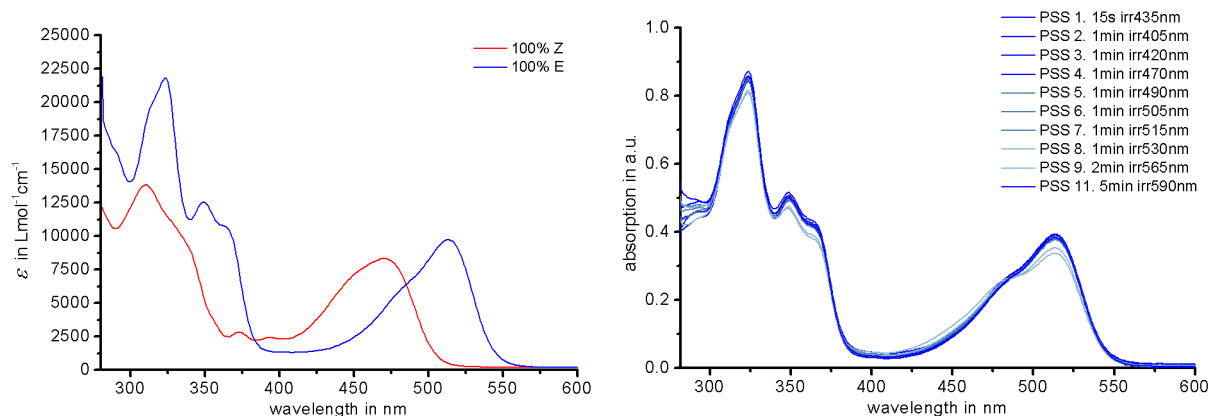
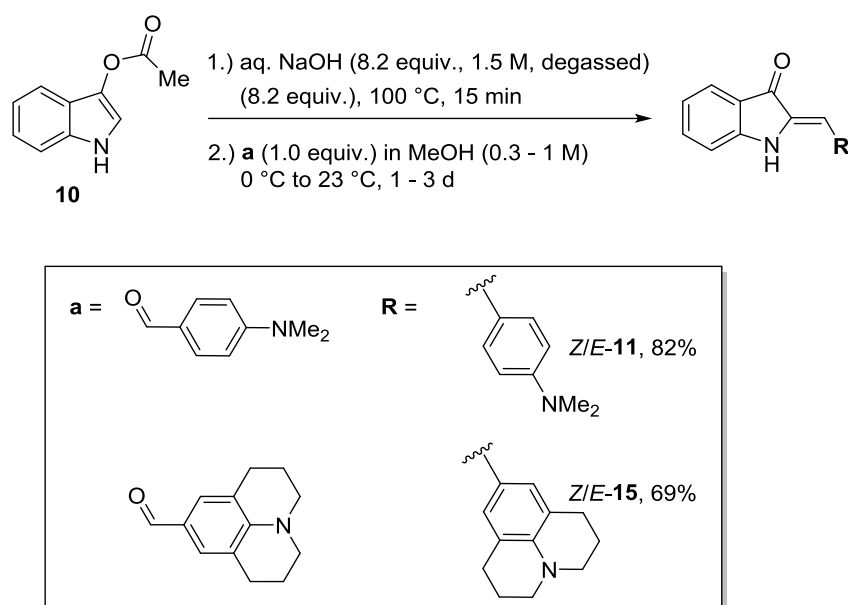


Figure 27: Molar absorption (left) and PSS (right) spectra of hemiindigo 7 in toluene. Similar spectra can be observed compared to dichloromethane as solvent (see Figure 26). The isosbestic points are well defined, verifying the photostability of this compound. Highest isomeric yields were obtained at 435 nm irradiation (97% *E* isomer) and at 530 nm irradiation (18% *Z* isomer). Energy barriers for thermal double bond isomerizations were determined to be 31.5 kcal/mol for the *Z* to *E* and 29.8 kcal/mol for the *E* to *Z* direction at 100 °C, which translates to thermal half-lives of 452 years and 25.6 years at 25 °C, for the respective isomers.

## 2.2.4 Stilbene fragment: Electron donating substituents

Another important position to tailor the photophysical properties of hemiindigo photoswitches is the *para*-position of the stilbene fragment. The acetylated methoxy derivative **2** has proven as reliable photoswitching system. However, proton or alkyl substitution suffered major drawbacks regarding their thermo- and photostability or applicability in apolar solvents. The *para*-methoxy derivatives were abandoned at this time in favor of the electron rich dimethylamino and julolidine derivatives.

To obtain these electron rich hemiindigos **11** and **15** and , a synthetic route that utilizes similar conditions as for the methoxy derivatives (see Scheme 5) by the procedure of *U. Burger et al.* was employed.



Scheme 8: Synthesis of hemiindigos **11** and **15** from indoxyl acetate **10** and electron-rich aldehydes in good to moderate yields. The products can be crystallized as violet needles (dimethylamino moiety) or red / green dichroic crystals (julolidine derivative).

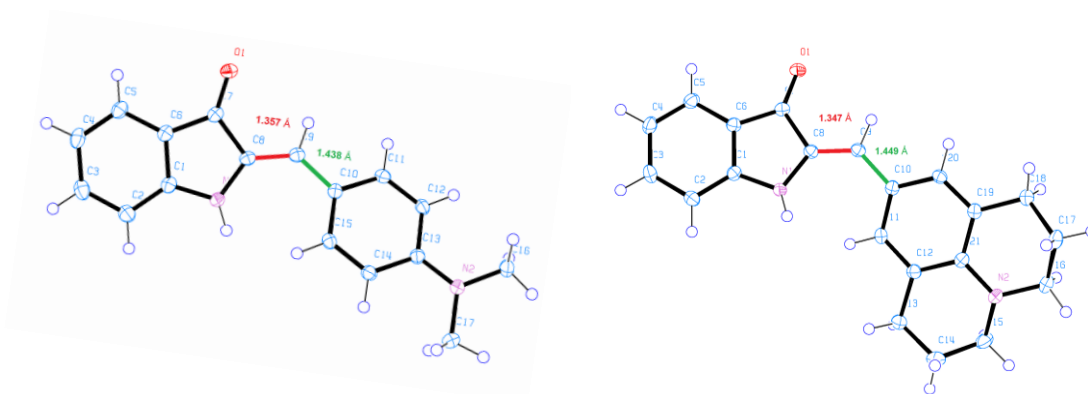


Figure 28: Structure of hemiindigo **Z-11** (left) and **Z-15** (right) in the crystalline state. Both derivatives remain planar in the *Z* form, as no bulk is introduced at the indoxyl nitrogen. The double (red) and single bond (green) lengths change from 1.352 to 1.357 to 1.347 Å and 1.451 to 1.438 to 1.449 Å for the methoxy, dimethylamino and julolidine derivatives **9**, **11** and **15**, respectively.



Figure 29: Dichroic crystals of hemiindigo **15** obtained in lengths from 5 to 10 mm. Adapted with permission from <sup>[74]</sup>. Copyright 2017 American Chemical Society.



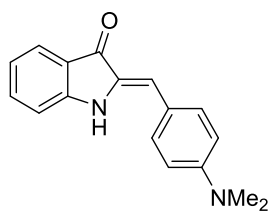
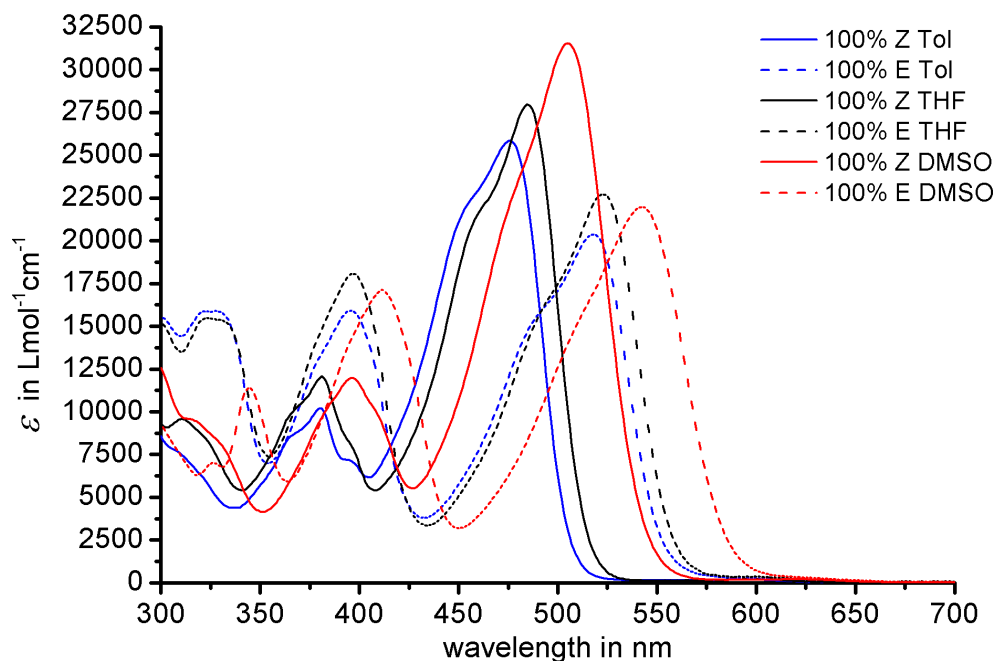
Figure 30: Lewis-formula of hemiindigo **11**.

Figure 31: Molar absorption spectra of pure *Z* and *E* isomers of **11** measured in solvents of increasing polarity (toluene, tetrahydrofuran and dimethyl sulfoxide). PSS and switching spectra are omitted for clarity reasons and can be found in the literature.<sup>[74]</sup> A clear correlation between rising solvent polarity and red-shift of absorptions can be observed, evidencing moderate solvatochromism. Adapted with permission from <sup>[74]</sup>. Copyright 2017 American Chemical Society.

Table 1: Photophysical properties of hemiindigo **11** in different solvents.

Solvent	$\phi_{ZE}/\%$ (at nm)	$\phi_{EZ}/\%$ (at nm)	Isomeric yield (LED nm)	$\Delta G^* Z/E$ /kcal mol <sup>-1</sup>	$\Delta G^* E/Z$ /kcal mol <sup>-1</sup>	$T_{1/2} Z$ at 25 °C	$T_{1/2} E$ at 25 °C
toluene	24 ± 2 (467)	9 ± 2 (600)	99% <i>Z</i> (617 nm)	-	24.1	-	15 h
			87% <i>E</i> (470 nm)				
THF	-	-	94% <i>Z</i> (617 nm)	-	24.5	-	1.2 d
			89% <i>E</i> (435 nm)				
DMSO	19 ± 2 (467)	11 ± 2 (600)	98% <i>Z</i> (617 nm)	-	26.9	-	70 d
			89% <i>E</i> (470 nm)				

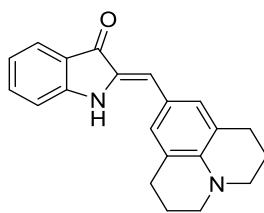
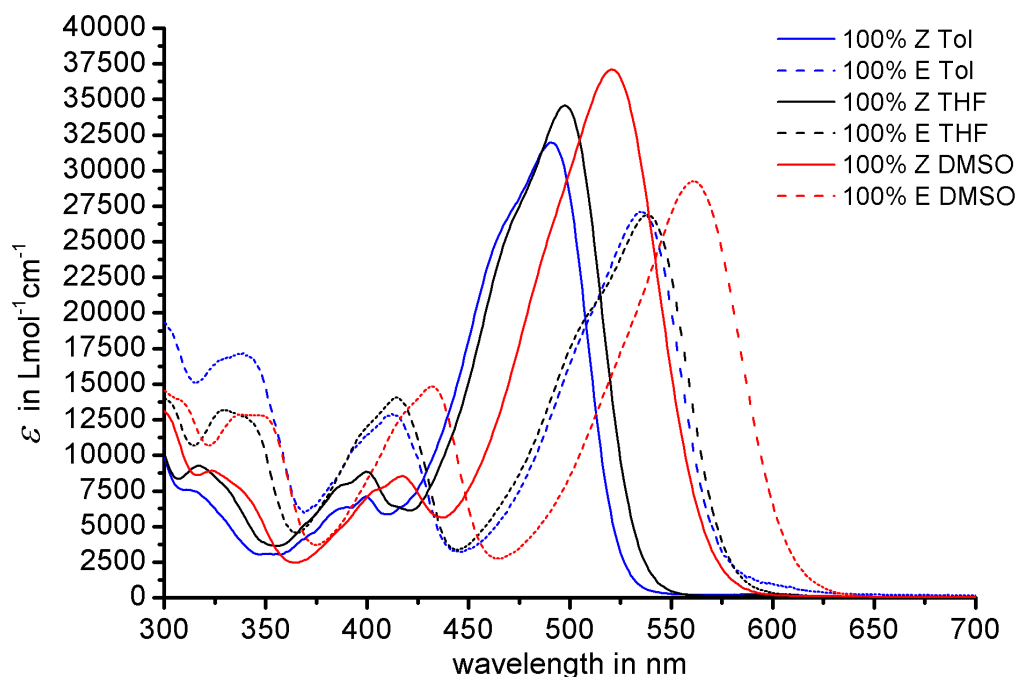
Figure 32: Lewis-formula of hemiindigo **15**.

Figure 33: Molar absorption spectra of pure *Z* and *E* isomers of **15** measured in solvents of increasing polarity (toluene, tetrahydrofuran and dimethyl sulfoxide). PSS and switching spectra are omitted for clarity reasons and can be found in the literature.<sup>[74]</sup> A clear correlation between rising solvent polarity and red-shift of absorptions can be observed, evidencing moderate solvatochromism. Adapted with permission from <sup>[74]</sup>. Copyright 2017 American Chemical Society.

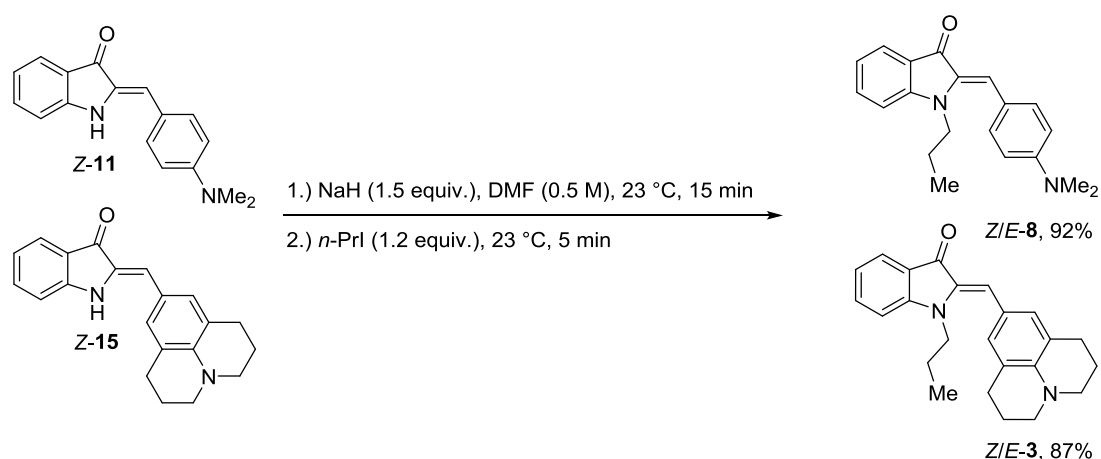
Table 2: Photophysical properties of hemiindigo **15** in different solvents.

Solvent	$\phi_{Z/E}/\%$ (at nm)	$\phi_{E/Z}/\%$ (at nm)	Isomeric yield (LED nm)	$\Delta G^* Z/E$ /kcal mol <sup>-1</sup>	$\Delta G^* E/Z$ /kcal mol <sup>-1</sup>	$T_{1/2} Z$ at 25 °C	$T_{1/2} E$ at 25 °C
toluene	–	–	99% <i>Z</i> (617 nm)	–	23.8	–	8.9 h
			83% <i>E</i> (470 nm)				
THF	–	–	99% <i>Z</i> (617 nm)	–	22.4	–	50 min
			90% <i>E</i> (470 nm)				
DMSO	16 ± 2 (467)	10 ± 2 (600)	95% <i>Z</i> (617 nm)	–	25.8	–	11 d
			81% <i>E</i> (505 nm)				

## 2.2.5 Indoxyl fragment: N-H alkylation of electron-rich hemiindigos

Substitution with electron donating substituents in *para*-position of the stilbene fragment proved as successful approach to improve the overall photophysical properties of hemiindigos, easily outperforming the *n*-propyl methoxy derivative **7** in every aspect except its higher thermal stability in some solvents.

Substitution of the N-H proton of the improved switches **11** and **15** is the next logical step and was carried out according to procedures from V. Velezheva et al.<sup>[90]</sup>



Scheme 9: Alkylation of *N*-protonated hemiindigos **11** and **15** via an S<sub>N</sub>2 mechanism to yield alkylated compounds **8** and **3**.

The respective hemiindigo photoswitches were obtained in good to very good yields. Deep violet crystals could be obtained in both cases.

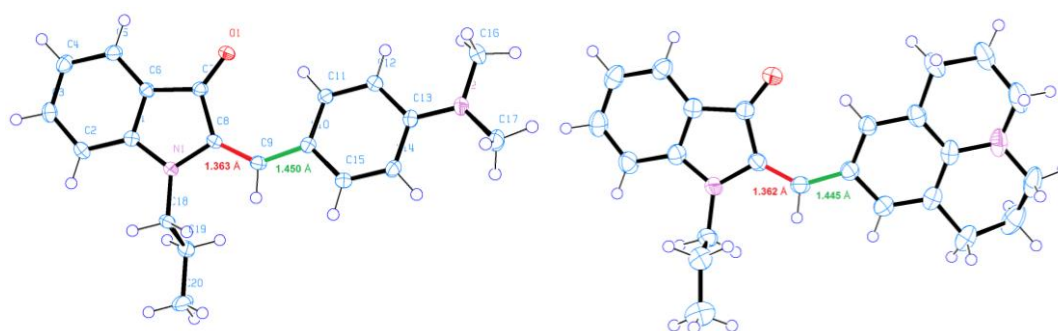


Figure 34: Structure of hemiindigo **E-8** (left) and **E-3** (right) in the crystalline state. Both derivatives remain planar in the *E* isomeric form. The double (red) and single bond (green) lengths change from 1.354 to 1.363 to 1.362 Å and 1.455 to 1.450 to 1.445 Å for the *N*-methyl methoxy, dimethylamino and julolidine derivatives **7**, **8** and **8**, respectively. A clear trend for stilbene-single-bond-shortening can be observed by increasing electron donor strength in the *para*-position.

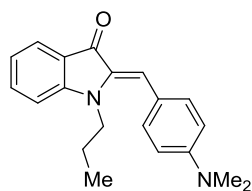
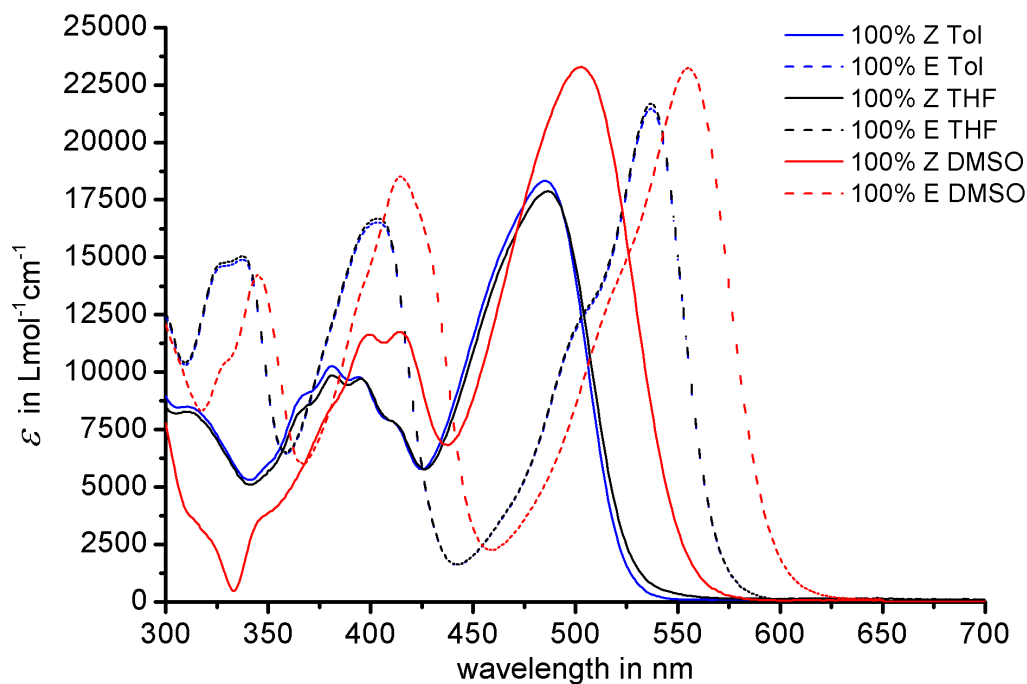
Figure 35: Lewis-formula of hemiindigo **8**.

Figure 36: Molar absorption spectra of pure *Z* and *E* isomers of **8** measured in solvents of increasing polarity (toluene, tetrahydrofuran and dimethyl sulfoxide). PSS and switching spectra are omitted for clarity reasons and can be found in the literature.<sup>[74]</sup> A clear correlation between rising solvent polarity and red-shift of absorptions can be observed, evidencing moderate solvatochromism. Adapted with permission from <sup>[74]</sup>. Copyright 2017 American Chemical Society.

Table 3: Photophysical properties of hemiindigo **8** in different solvents.

Solvent	$\phi_{Z/E}/\%$ (at nm)	$\phi_{E/Z}/\%$ (at nm)	Isomeric yield (LED nm)	$\Delta G^* Z/E$ /kcal mol <sup>-1</sup>	$\Delta G^* E/Z$ /kcal mol <sup>-1</sup>	$T_{1/2} Z$ at 25 °C	$T_{1/2} E$ at 25 °C
toluene	–	–	99% <i>Z</i> (617 nm)	30.3	30.5	60 a	83 a
			93% <i>E</i> (470 nm)				
THF	–	–	99% <i>Z</i> (625 nm)	28.0	27.8	1.2 a	0.9 a
			93% <i>E</i> (470 nm)				
DMSO	23 ± 2	9 ± 2	98% <i>Z</i> (617 nm)	28.2	28.7	1.7 a	4.0 a
	(467)	(600)	95% <i>E</i> (470 nm)				

The already established *n*-propyl substitution of the indoxyl N-H proton also benefits the hemiindigo photoswitches with electron donating stilbene substituents. Almost quantitative photoswitching upon irradiation with blue and red light in combination with very high thermal bistabilities (half-lives from 0.9 to 83 years) over a broad solvent polarity range and good quantum yields could be achieved for hemiindigo **8**.

Additional experiments were carried out to scrutinize the photostability of the compound.

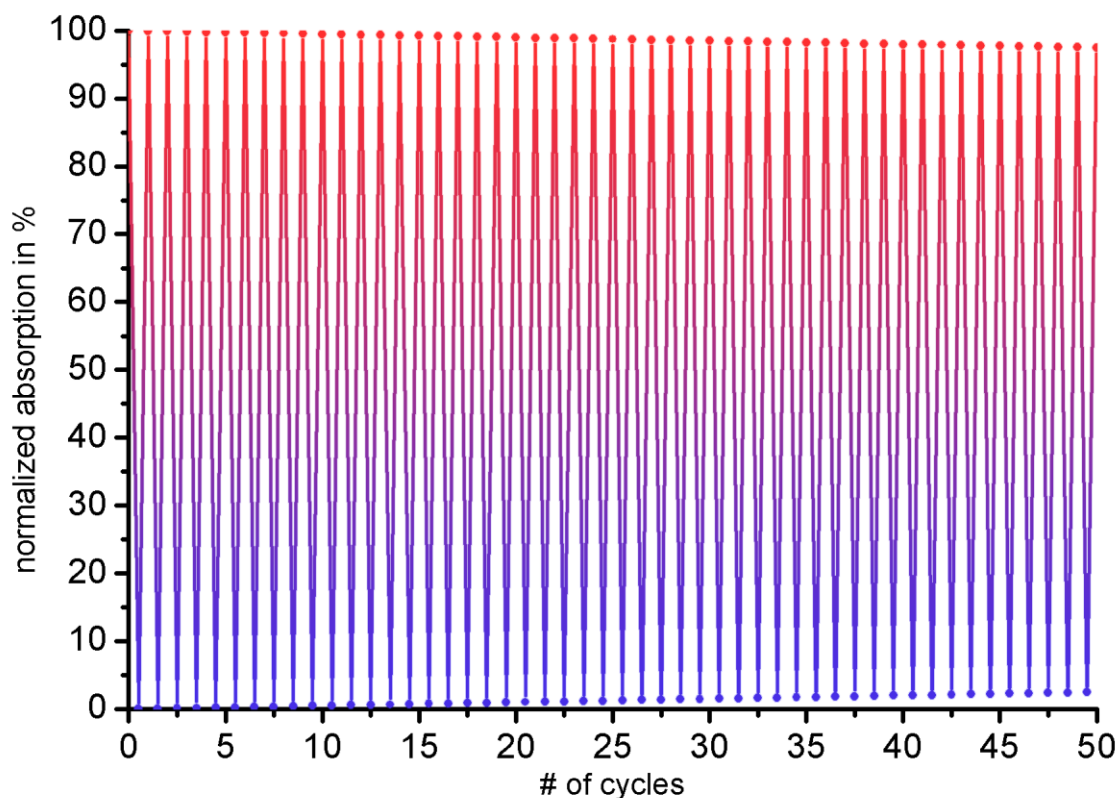


Figure 37: Prolonged photoswitching of hemiindigo **8** from *Z* PSS (590 nm) to *E* PSS (470 nm) and vice versa in dimethyl sulfoxide over 50 cycles. Only minor amounts of photodestruction could be observed. Adapted with permission from [76]. Copyright 2018 American Chemical Society.

Photoswitching of hemiindigo **8** in water could only be realized in mixtures containing four volumetric parts of water and one part of dimethyl sulfoxide, *N,N*-dimethylformamide or tetrahydrofuran. It is assumed that solely solubility played a role in this behavior as precipitation can be observed within the cuvette. Exemplary absorption spectra recorded during photoswitching are shown for clarity reasons, the complete data can be found in the literature.<sup>[74]</sup>

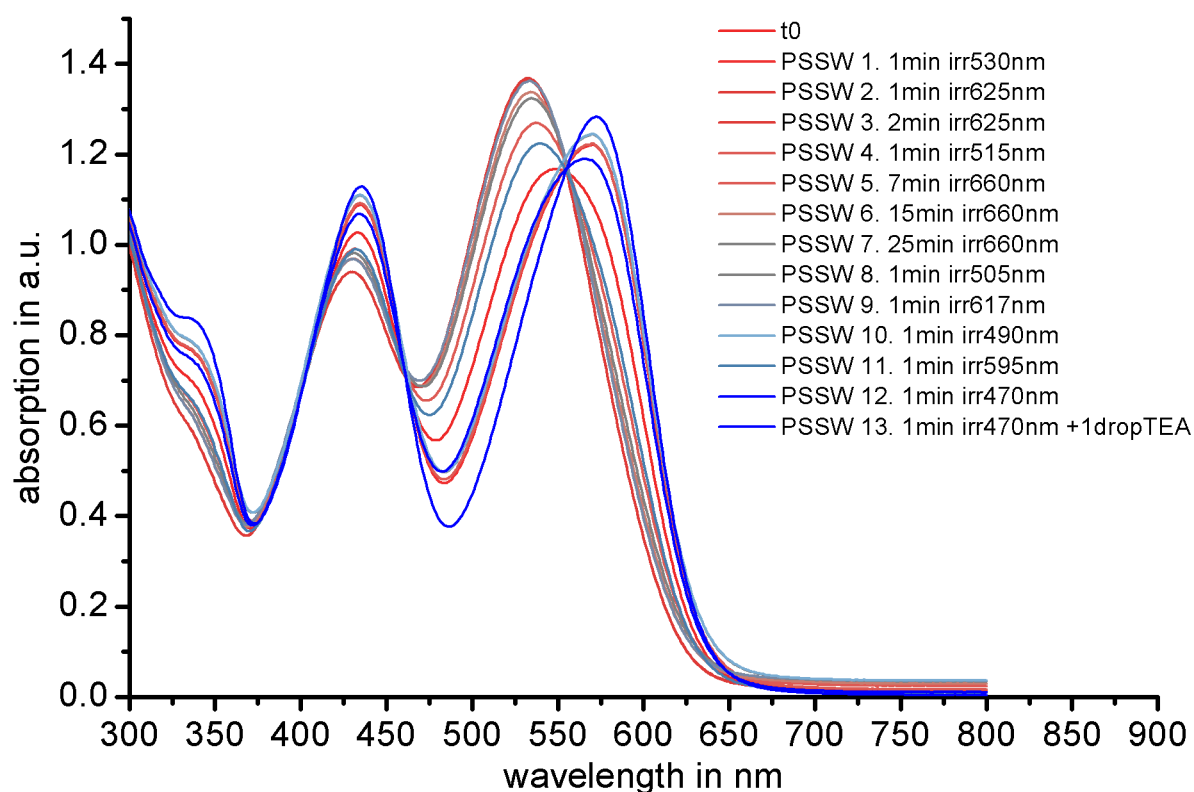


Figure 38: Absorption spectra during photoswitching of hemiindigo **8** in 4 / 1 water / *N,N*-dimethylformamide. Visually unhampered photoswitchability remains even at high water contents. Adapted with permission from <sup>[74]</sup>. Copyright 2017 American Chemical Society.

Nonetheless, the synthesis of ionic derivatives of hemiindigo **8** for gas phase experiments (see Section 2.5) proved that these compounds with electron rich *para*-substituted stilbene fragments do not photoswitch in pure water. However, *D. Berdnikova* rediscovered the previously abandoned *para*-methoxy stilbene substituted hemiindigo derivatives as useful motifs that remain switchable in pure water (see Section 2.6).

Experiments by *A. Gerwien* proved that hemiindigo **8** can be incorporated inside poly(methyl methacrylate) matrices by diffusion. This process preserves the photoswitchability of this compound within polymeric material and can be observed by the naked eye.

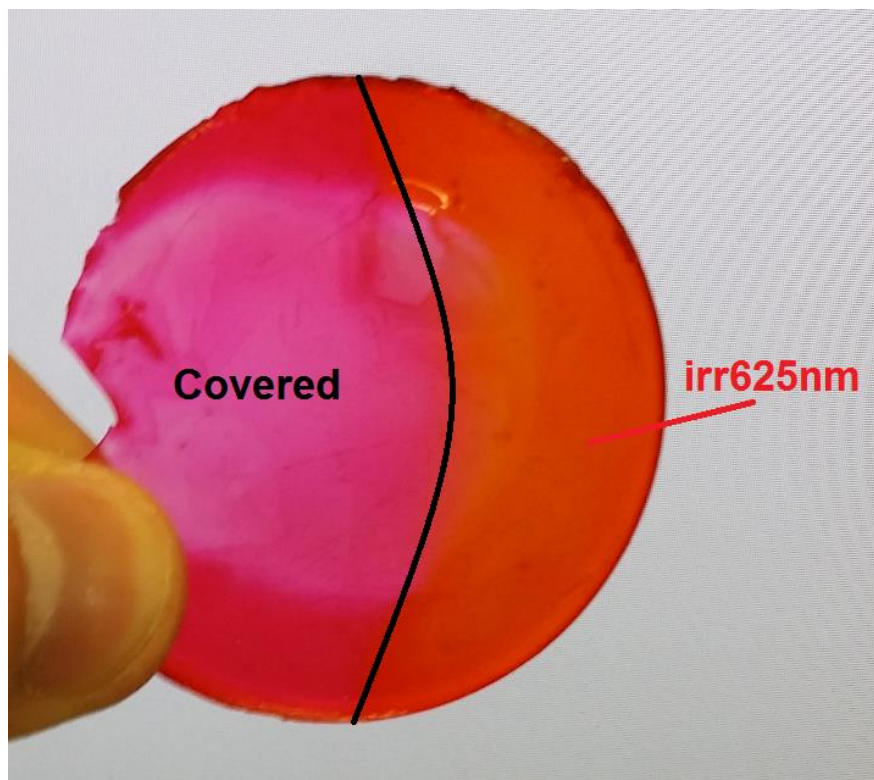


Figure 39: Poly(methyl methacrylate) piece treated with a solution of hemiindigo **8** in dichloromethane. Photoswitchability was preserved within the polymer. Experiments with UV curable clear resins for 3D printing by *Formlabs* were also successful, which makes it possible to print photoswitches favorably within translucent polymer materials.

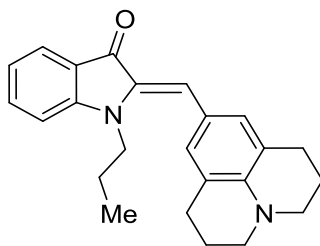
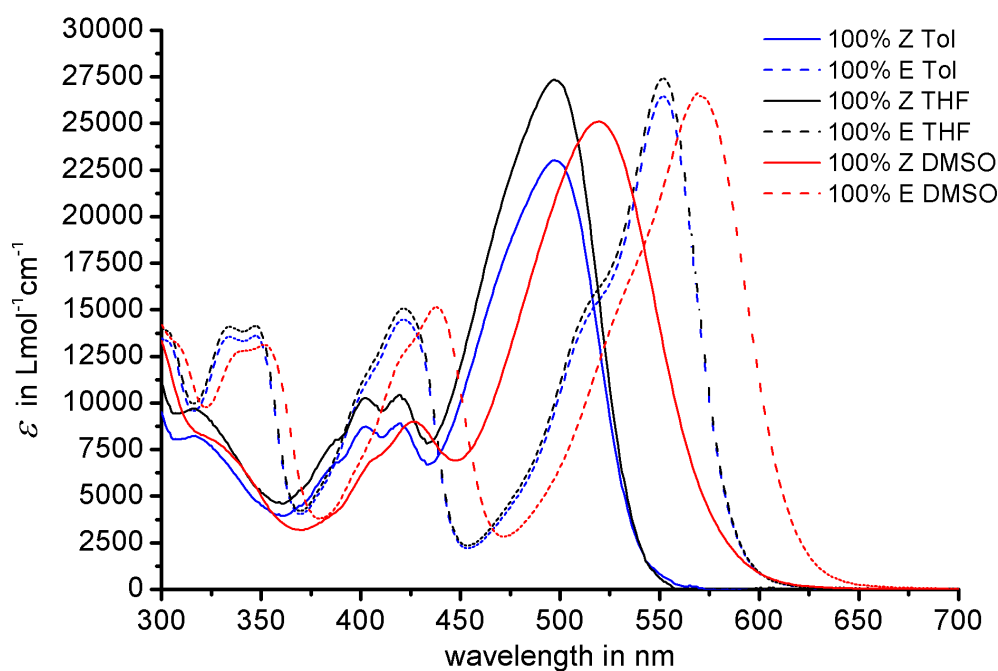
Figure 40: Lewis-formula of hemiindigo **3**.

Figure 41: Molar absorption spectra of pure *Z* and *E* isomers of **3** measured in solvents of increasing polarity (toluene, tetrahydrofuran and dimethyl sulfoxide). PSS and switching spectra are omitted for clarity reasons and can be found in the literature.<sup>[74]</sup> A clear correlation between rising solvent polarity and red-shift of absorptions can be observed, evidencing moderate solvatochromism. Adapted with permission from <sup>[74]</sup>. Copyright 2017 American Chemical Society.

Table 4: Photophysical properties of hemiindigo **3** in different solvents.

Solvent	$\phi_{Z/E}/\%$ (at nm)	$\phi_{E/Z}/\%$ (at nm)	Isomeric yield (LED nm)	$\Delta G^* Z/E$ /kcal mol <sup>-1</sup>	$\Delta G^* E/Z$ /kcal mol <sup>-1</sup>	$T_{1/2} Z$ at 25 °C	$T_{1/2} E$ at 25 °C
toluene	–	–	99% <i>Z</i> (617 nm)	24.5	24.6	1.2 d	1.4 d
			95% <i>E</i> (470 nm)				
THF	–	–	96% <i>Z</i> (617 nm)	28.3	28.6	2.0 a	3.4 a
			90% <i>E</i> (470 nm)				
DMSO	22 ± 2 (467)	7 ± 2 (600)	99% <i>Z</i> (680 nm)	27.7	27.8	0.7 a	0.9 a
			98% <i>E</i> (505 nm)				



Introducing an *n*-propyl group to hemiindigo **15** yields compound **3** with strongly red-shifted absorptions towards the biooptical window. This photoswitch can be addressed with low energy green and red light while maintaining almost quantitative photoisomerization yields in combination with high thermal bistability (half-lives from 1.2 days to 3.4 years) over a broad solvent polarity range. Also good quantum yields were measured for the photoisomerization in both *Z* to *E* and *E* to *Z* directions.

Photoswitching of hemiindigo **3** in water could only be realized in mixtures containing four volumetric parts of water and one part of dimethyl sulfoxide, *N,N*-dimethylformamide or tetrahydrofuran.

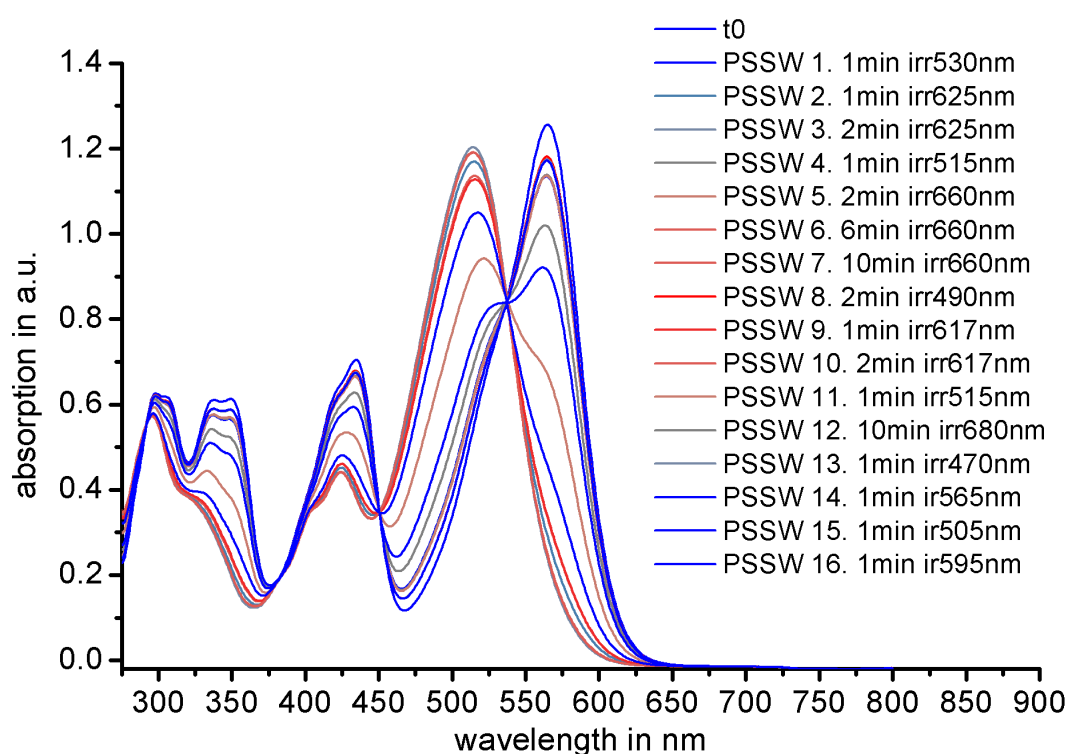
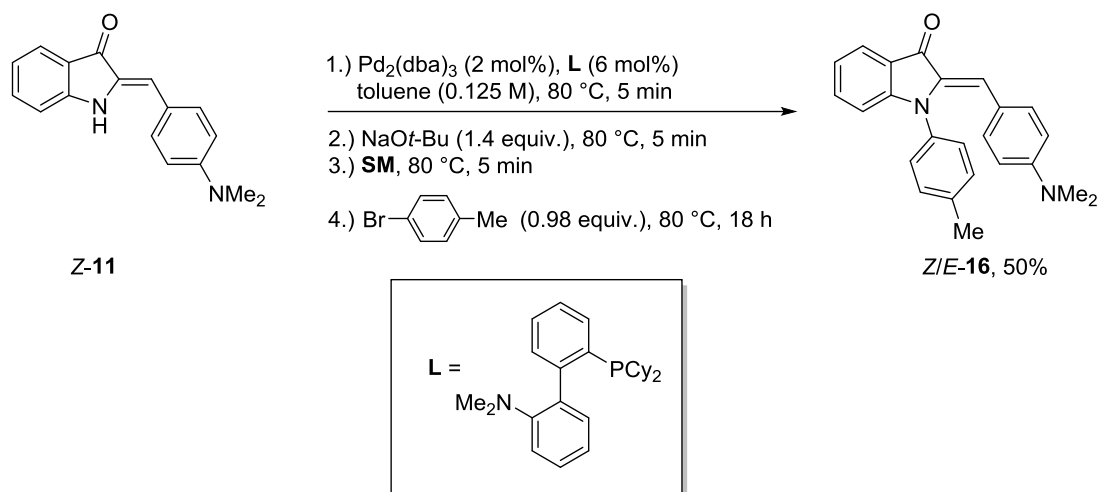


Figure 42: Photoswitching of hemiindigo **3** in 4 / 1 water / *N,N*-dimethylformamide. Excellent photoswitching performance can be observed even at high water contents. Adapted with permission from <sup>[74]</sup>. Copyright 2017 American Chemical Society.

As mentioned before, the synthesis of ionic derivatives of hemiindigo **3** for gas phase experiments (see Section 2.5) proved that the compounds with electron rich stilbene fragments do not switch in pure water. However, *D. Berdnikova* rediscovered the previously abandoned *para*-methoxy stilbene substituted hemiindigo derivatives as useful motifs that remain switchable in pure water (see Section 2.6).

## 2.2.6 Indoxyl fragment: N-H arylation of electron-rich hemiindigos

Another possibility in improving the performance of hemiindigo photoswitches was envisioned by further increasing the electron-donating strength at the indoxyl nitrogen. This can be achieved by introduction of an (electron-rich) aryl substituent. Preparation utilizing a palladium catalyzed *Buchwald-Hartwig* cross-coupling reaction according to *Old et al.* leads to late-stage arylated hemiindigo **16** in moderate yields.



Scheme 10: Palladium catalyzed *Buchwald-Hartwig* cross-coupling reaction of an electron-poor aromatic secondary amine, i.e. hemiindigo **11** and *para*-bromotoluene utilizing *DavePhos* as ligand **L**. **SM** = Starting Material.

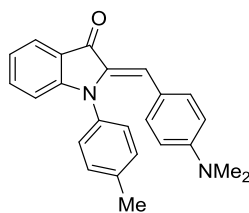
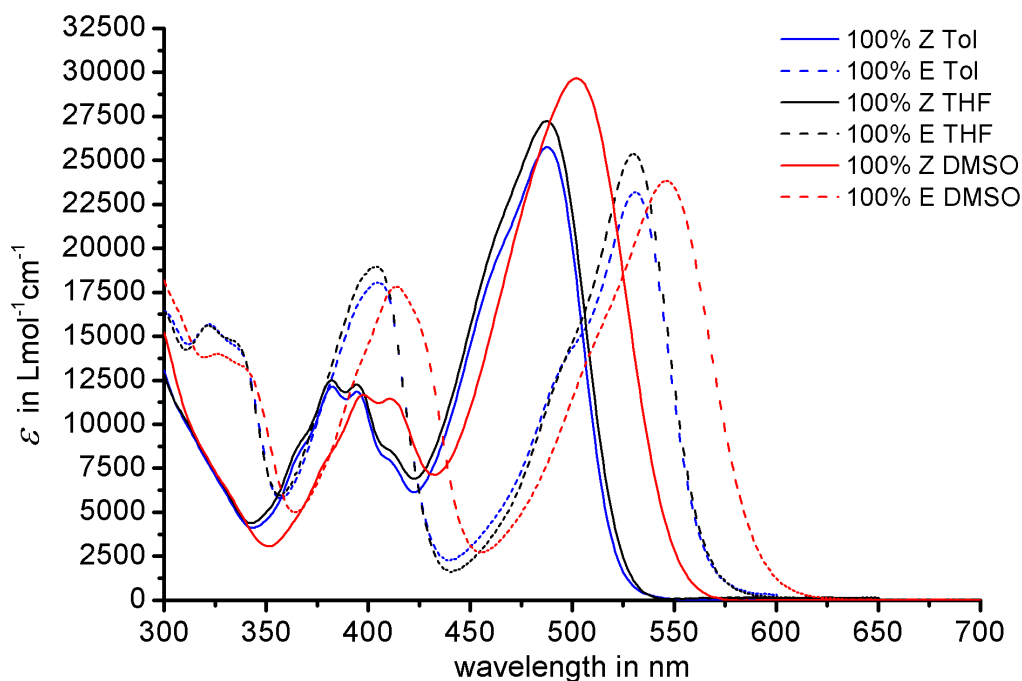
Figure 43: Lewis-formula of hemiindigo **16**.

Figure 44: Molar absorption spectra of pure *Z* and *E* isomers of **16** measured in solvents of increasing polarity (toluene, tetrahydrofuran and dimethyl sulfoxide). PSS and switching spectra are omitted for clarity reasons and can be found in the literature.<sup>[74]</sup> A clear correlation between rising solvent polarity and red-shift of absorptions can be observed, evidencing moderate solvatochromism. Adapted with permission from <sup>[74]</sup>. Copyright 2017 American Chemical Society.

Table 5: Photophysical properties of hemiindigo **16** in different solvents.

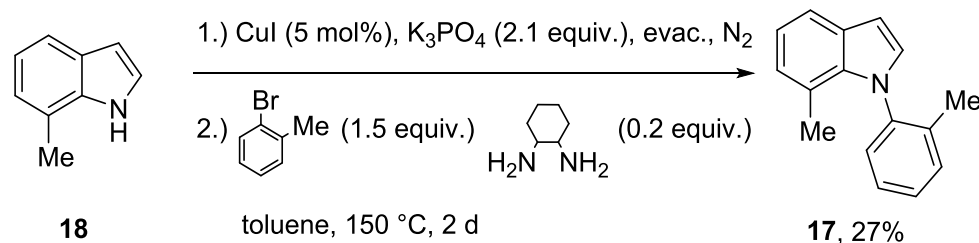
Solvent	$\phi_{Z/E}/\%$ (at nm)	$\phi_{E/Z}/\%$ (at nm)	Isomeric yield (LED nm)	$\Delta G^* Z/E$ /kcal mol <sup>-1</sup>	$\Delta G^* E/Z$ /kcal mol <sup>-1</sup>	$T_{1/2} Z$ at 25 °C	$T_{1/2} E$ at 25 °C
toluene	–	–	99% <i>Z</i> (617 nm)	30.5	30.5	77 a	77 a
			95% <i>E</i> (470nm)				
THF	–	–	98% <i>Z</i> (617 nm)	29.5	29.5	14 a	14 a
			86% <i>E</i> (470 nm)				
DMSO	22 ± 2	2 ± 1	93% <i>Z</i> (625 nm)	25.4	25.7	9 d	6 d
	(467)	(625)	97% <i>E</i> (470 nm)				

Introducing an *aryl* group to hemiindigo **11** yields compound **16** with strongly red-shifted absorptions towards the biooptical window. This photoswitch can be addressed with low energy green and red light while maintaining almost quantitative photoisomerization yields in combination with high thermal bistability (half-lives from 6.0 days to 77 years) over a broad solvent polarity range. Also good quantum yields were measured for the photoisomerization in both *Z* to *E* and *E* to *Z* directions.

## 2.2.7 Indoxyl fragment: Sterically demanding N-H arylations of electron-rich hemiindigos

As *N*-arylation with a symmetric *para*-tolyl residue led to photoswitching properties comparable to *n*-propylation, the unique possibility of substitution with a non-symmetric aryl moiety, i.e. an *ortho*-tolyl substituent at this position seemed very promising. The hereby introduced chiral axis along the N-C<sub>Aryl</sub> bond unveils interesting motional effects and adds several intriguing molecular properties (see Section 2.3 for further details). However, enforcing a strong twist of the chiral aryl axis was expected to already change the photophysical properties of hemiindigo in highly beneficial ways. An additionally introduced methyl group at the 7 position of indoxyl core also aides in forcing the *ortho*-tolyl axis further orthogonally towards the indoxyl plane.

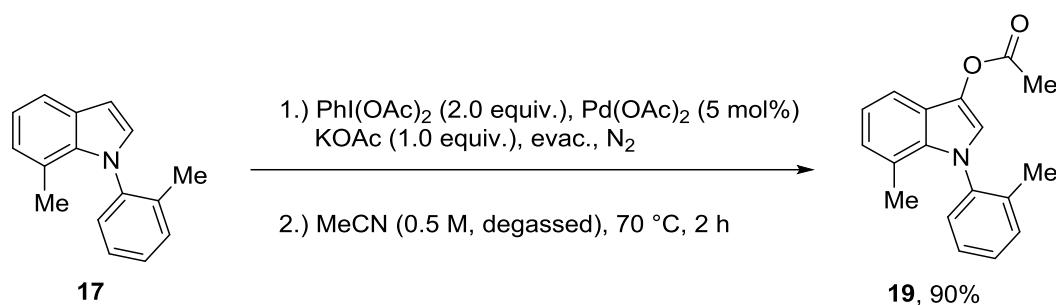
As the *Buchwald-Hartwig* type late stage arylation was not feasible with *ortho*-tolyl halides or with 7-methyl indoxyls under previously described conditions (Scheme 10), another synthetic route was established to gain access to these compounds. 7-Methyl-1-(*o*-tolyl)-1*H*-indole **17** was prepared according to the published procedure of *J. Antilla et al.* from **18** at elevated temperatures in pressure tubes.<sup>[91]</sup>



Scheme 11: Preparation of *N*-arylated indole **17**.

Chiral HPLC at 0 °C did not afford separation of rotamers, which indicates a low free activation enthalpy of the rotational axis below  $\Delta G^* = 20$  kcal/mol in apolar solvent.

7-Methyl-1-(*o*-tolyl)-1*H*-indol-3-yl acetate **19** was prepared from **17** according to the procedure by *P. Choy et al.*<sup>[92]</sup>

Scheme 12: Preparation of *N*-arylated indoxyl acetate **19**.

Hemiindigo **20** was prepared according to the same procedure as reported in Scheme 5 for the synthesis of hemiindigo **11**.

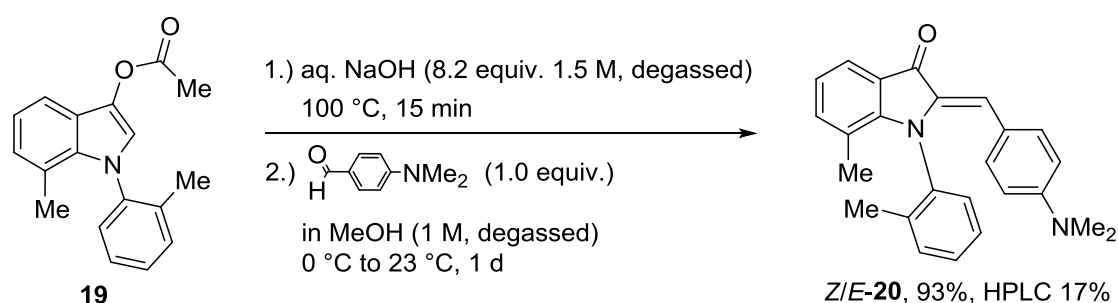
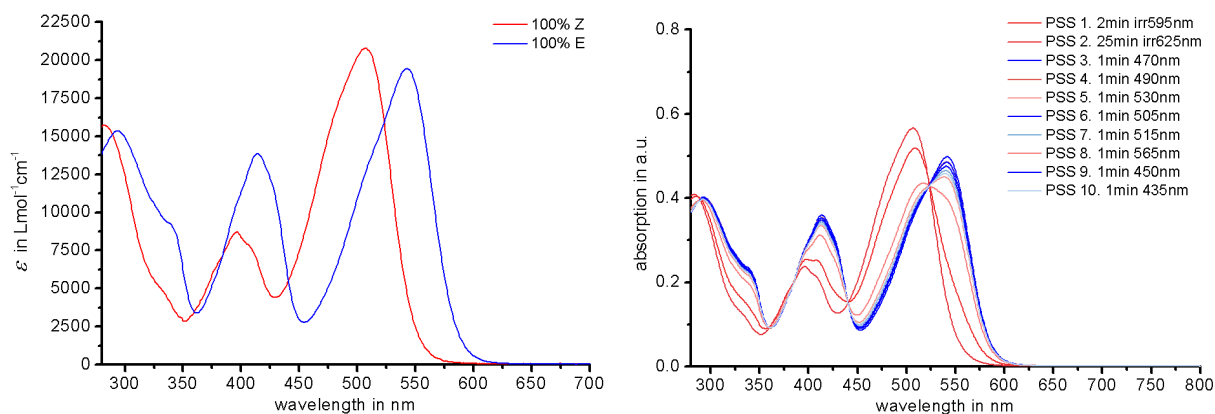
Scheme 13: Preparation of hemiindigo **20**. Low yields after HPLC separation are caused by injection loss and the collection of only one isomer peak.

Figure 45: Molar absorption spectra of pure isomers (left) and spectra recorded at the PSS at different wavelengths of irradiation PSS (right) spectra of hemiindigo **20** in dimethyl sulfoxide. The isosbestic points are well defined, verifying the photostability of this compound. Highest isomeric yields were obtained at 470 nm irradiation (93% *E* isomer) and at 625 nm irradiation (97% *Z* isomer). Energy barriers for thermal double bond isomerizations were determined to be 30.6 kcal/mol for the *Z* to *E* and 32.1 kcal/mol for the *E* to *Z* direction at 114 °C,

which translates to thermal half-lives of 99 years and 1140 years at 25 °C, for the respective isomers. Quantum yields were determined at  $33 \pm 2\%$  (467 nm) for *Z* to *E* and  $9 \pm 1\%$  (600 nm) for *E* to *Z* photoisomerizations. In 83 / 17 heptane / ethyl acetate, the quantum yields increase up to  $49 \pm 2\%$  (450 nm) for *Z* to *E* and  $12 \pm 2\%$  (520 nm) for *E* to *Z* photoisomerization. Adapted with permission from [75]. Copyright 2018 American Chemical Society.

Hemiindigo derivative **20** shows comparable or increased photophysical properties as hemiindigo **16** mainly because of the increased thermal bistabilities and quantum yields.

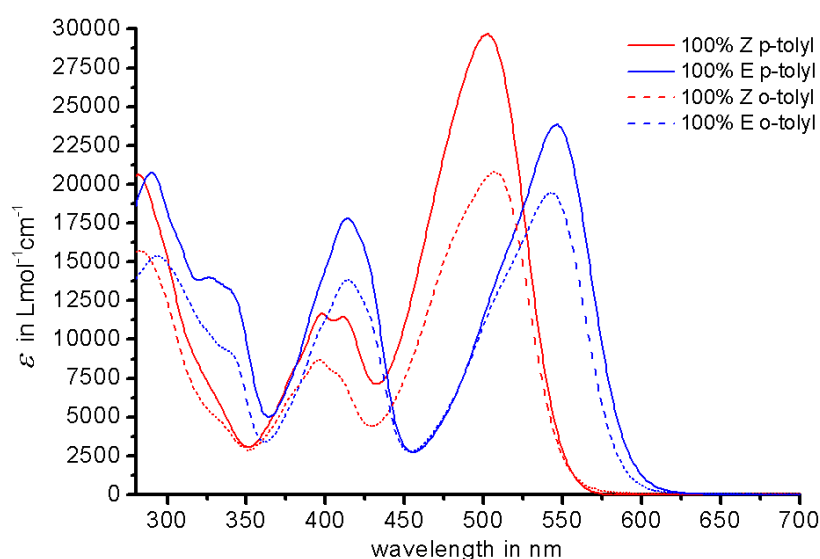


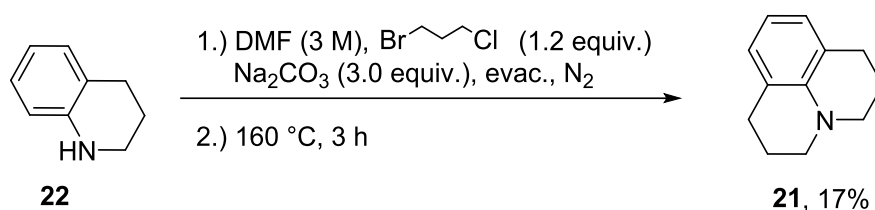
Figure 46: Comparison of molar absorption spectra for less twisted *para*-tolyl (**16**) and strongly twisted *ortho*-tolyl derivative **20** in dimethyl sulfoxide. No significant batho- or hypsochromic shift can be observed. Thus the wavelengths of absorption are mainly determined by the stilbene-fragment and much less so by the twisting of the *N*-indoxyl substituent. A reduction of  $\epsilon$  by 30% can be observed. However, this does not hamper the responsiveness of the twisted system, as even higher quantum yields are reported for hemiindigo **20**.

The increased thermal stability of the *Z* isomer with twisted *N*-aryl substitution can be explained by its decreased sterical interference with the stilbene fragment in the *Z* state compared to hemiindigo **16**. The *E* form, however, should not be largely influenced in its thermal stability by the substituents at the indoxyl nitrogen atom. Apparently, other factors also play an important role in increasing the thermal stability of the axially chiral hemiindigo derivative **20**.

These findings led to the idea of incorporating an enlarged aromatic system as stilbene fragment to achieve further red-shifted absorption in combination with enhanced thermal stabilities.

### 2.2.8 Stilbene fragment: Extension of the aromatic system

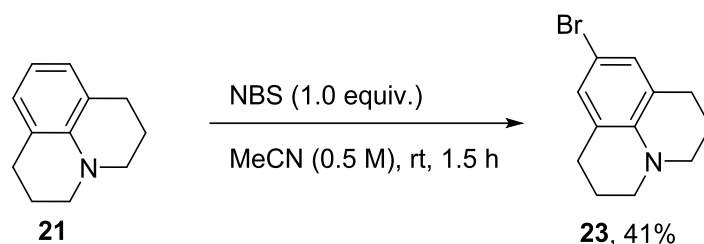
Julolidine **21** was prepared from **22** according to *H. Katajama et al.* (Scheme 14).<sup>[93]</sup>



Scheme 14: Cyclization reaction of 1,2,3,4-tetrahydroquinoline **22** and 1-bromo-3-chloropropane.

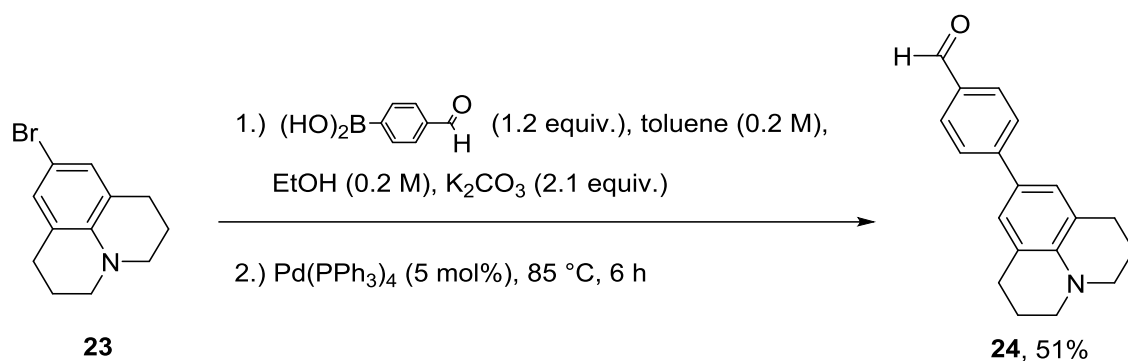
The poor isolated yield of the highly unstable product was caused by a second silica column chromatography attempt using 100% hexane as eluent, which led to degradation of the product. The preceding column with 9 / 1 hexane / ethyl acetate as eluent did not achieve satisfactory separation from by-products. The isolated compound turns from a clear, colorless oil to a brown mass within minutes upon exposure to air.

The subsequent bromination was carried out by using *N*-bromosuccinimide to yield compound **23**.

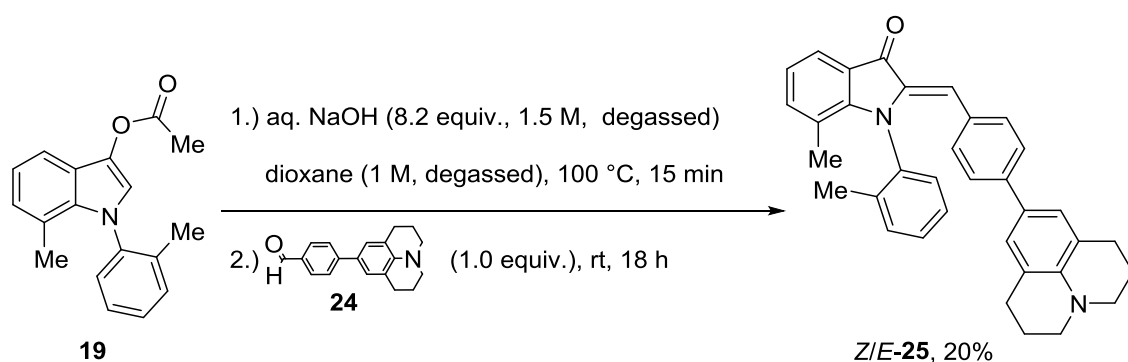
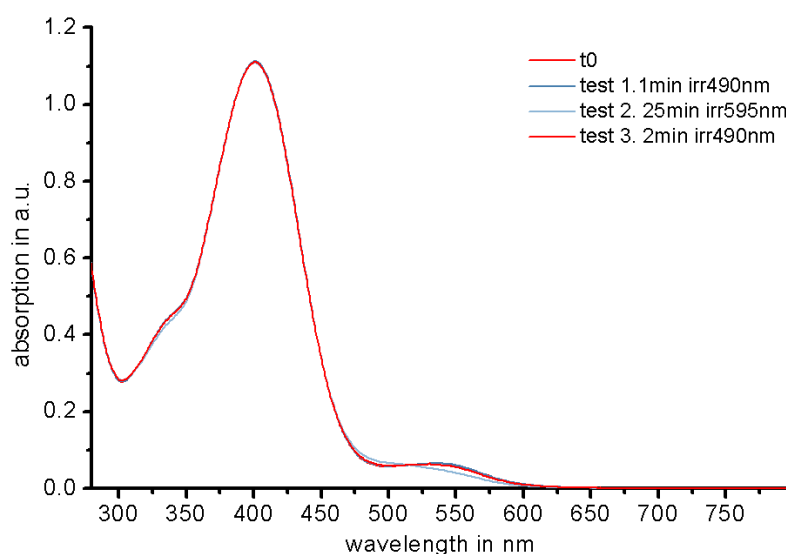


Scheme 15: Bromination of julolidine **21**.

The obtained product was not as sensitive as its precursor but still degrades within days on air. Subsequent *Suzuki* cross-coupling was carried out according to Scheme 16.<sup>[94]</sup>

Scheme 16: *Suzuki* cross-coupling of bromojulolidine **23** and 4-formylphenylboronic acid.

Condensation of the now stable aldehyde **24** with the arylated indoxyl acetate **19** was done according to a modified procedure of *U. Burger et al.* and yielded hemiindigo **25**.<sup>[88]</sup>

Scheme 17: Condensation reaction between arylated indoxyl acetate **19** and an extended electron-rich aldehyde **24**.Figure 47: UV-Vis spectrum of hemiindigo **25** in dimethyl sulfoxide.



No red-shift could be observed compared to **20**. The photoswitching performance was sub-par compared to dimethyl amino derivative **8**. Increasing the conjugated *pi*-system therefore did not seem to be feasible and this approach was abandoned at this time.

## 2.2.9 Stilbene and indoxyl fragment: Push-pull effects

To further scrutinize the push-pull effects on the indoxyl-nitrogen and stilbene fragment of the hemiindigo photoswitch, hemiindigo **12** was prepared according to Scheme 6. According to previous experiments, the acetyl group causes a hypsochromic shift of the chromophore while the dimethylamino moiety is responsible for a bathochromic shift. This molecule was synthesized to discern one dominating effect over the other and / or if a push-pull can be established that will benefit red-shifting.

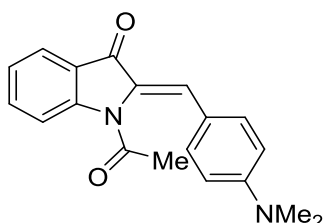


Figure 48: Lewis-formula of hemiindigo **12**.

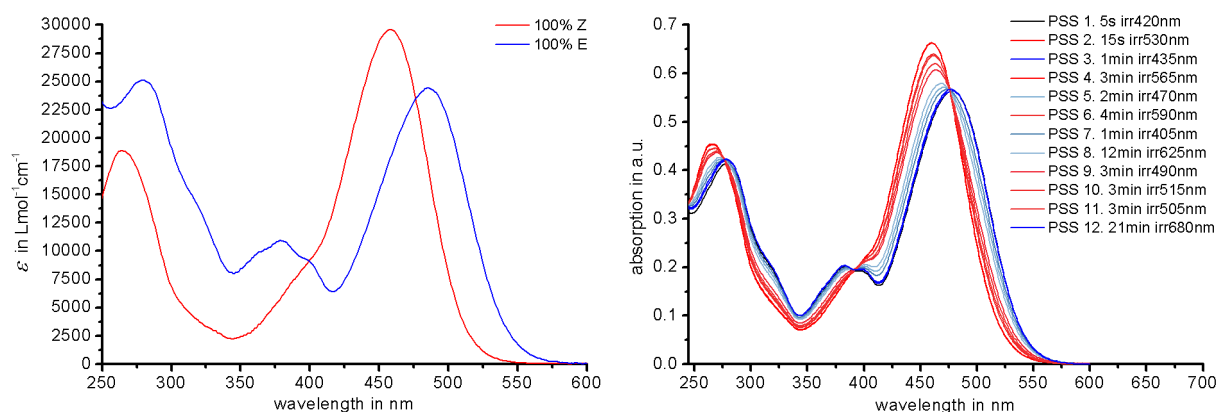


Figure 49: Molar absorption spectra of pure isomers (left) and spectra recorded at the PSS at different wavelengths of irradiation PSS (right) spectra of hemiindigo **12** in dichloromethane that was filtered through aluminium(III) oxide to reduce prevalent amounts of hydrochloric acid. The isosbestic points are well defined, verifying the photostability of this compound. Highest isomeric yields were obtained at 420 nm irradiation (79% *E* isomer) and at 625 nm irradiation (99% *Z* isomer). Energy barriers for thermal double bond isomerizations were determined to be 25.9 kcal/mol for the *Z* to *E* and 27.9 kcal/mol for the *E* to *Z*

direction at 100 °C, which translates to thermal half-lives of 13 days and 1 year at 25 °C, for the respective isomers.

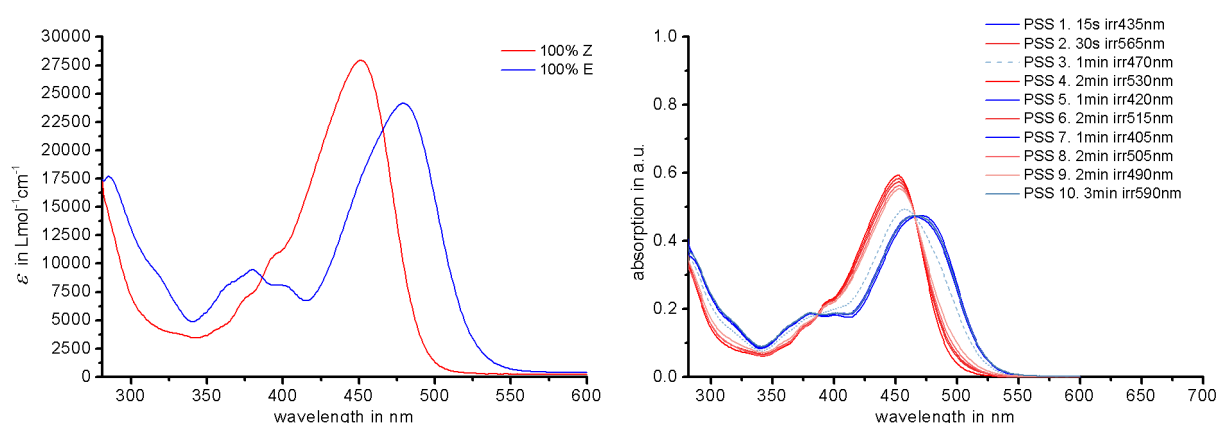
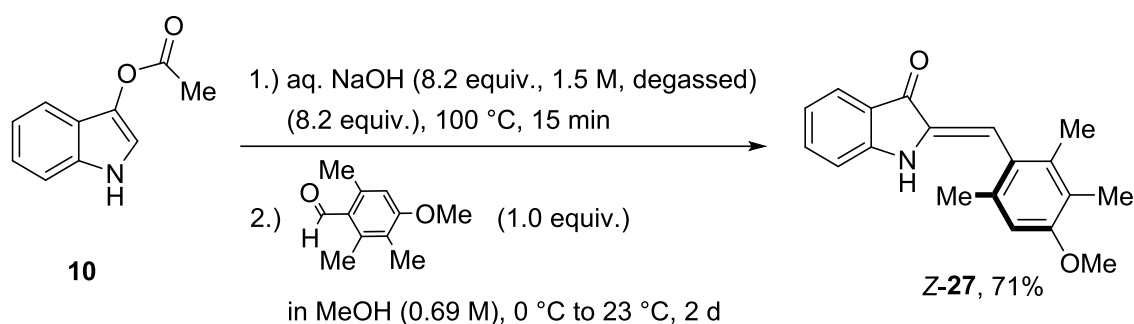


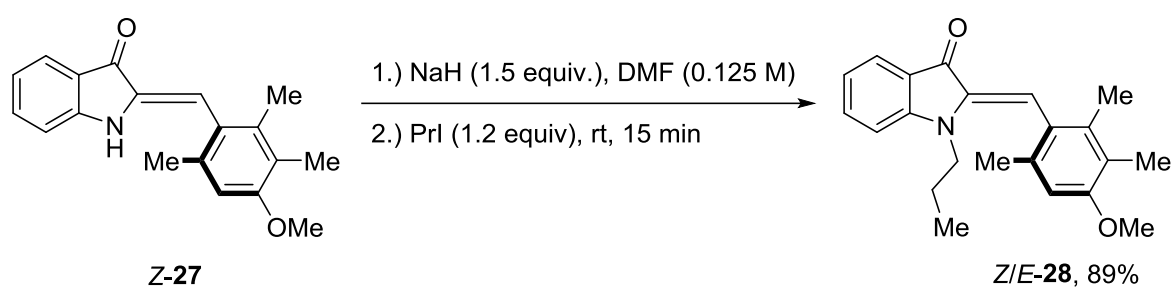
Figure 50: Molar absorption spectra of pure isomers (left) and spectra recorded at the PSS at different wavelengths of irradiation PSS (right) spectra of hemiindigo **12** in dichloromethane that was filtered through aluminium(III) oxide to reduce prevalent amounts of hydrochloric acid. The isosbestic points are well defined, verifying the photostability of this compound. Highest isomeric yields were obtained at 420 nm irradiation (77% *E* isomer) and at 530 nm irradiation (96% *Z* isomer). Energy barriers for thermal double bond isomerizations were determined to be 29.8 kcal/mol for the *Z* to *E* and 30.3 kcal/mol for the *E* to *Z* direction at 100 °C, which translates to thermal half-lives of 26 years and 60 years at 25 °C, for the respective isomers. Unprecedented behavior of this compound can be seen as the only intermediate *Z* / *E* composition is obtained with 470 nm irradiation (broken light blue line). For previous compounds, a more or less continuous distribution of PSS compositions was obtained when sweeping through all available wavelengths for irradiation. In this case, however, a sharp discrimination for wavelengths below 470 nm and above 470 nm can be observed, which strongly favor one or the other isomer in the PSS.

## 2.2.10 Central double bond: Substitution of the vinylic proton by a cyano group

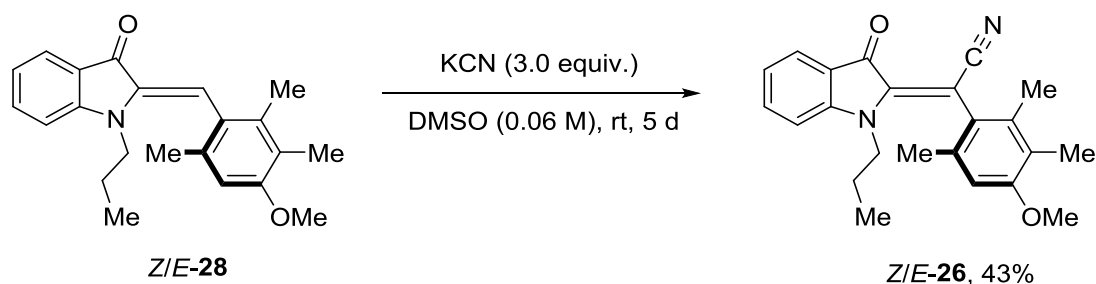
Substitution of the proton at the central double bond by a methyl group using diazomethane was proven feasible on hemithioindigo derivatives by *M. Schildhauer* and *K. Hoffmann*. This approach was unsuccessful on hemiindigo, as no reaction progress could be observed under similar conditions. However, nitrile could be successfully incorporated by following a procedure from *V. Velezheva et al.* to obtain compound **26** (Scheme 20). In order to obtain hemiindigo derivatives with potentially high atropisomerization barriers, hemiindigo **27** was synthesized starting from indoxyl acetate using the condensation conditions by *U. Burger et al.*<sup>[88]</sup>



Scheme 18: Condensation reaction of indoxyl acetate **10** and 4-methoxy-2,3,6-trimethylbenzaldehyde according to the procedure of *U. Burger et al.* to yield hemiindigo **27**.



Scheme 19:  $S_N2$  reaction of 1-propyl iodide with the deprotonated nitrogen of hemiindigo **27** according to the procedure of *V. Velezheva et al.* to yield compound **28**.<sup>[90]</sup>



Scheme 20: Vicarious  $S_NAr$  reaction of the protonated central double bond position of hemiindigo **28** with potassium cyanide according to the procedure of V. Velezheva *et al.* to yield hemiindigo **26**.<sup>[90]</sup>

The *ortho*-methyl substituents on the stilbene-fragment in hemiindigo **26** served as proof-of-concept for hindering the rotational barrier of the single bond connecting the stilbene moiety with the photoisomerizable double bond. The introduced non-symmetric stilbene fragment is needed for establishing a chiral axis along the hindered single bond, which should lead to two different enantiomeric rotamers. Further separation via HPLC and ECD measurements of the possibly enantiopure rotamers need to be carried out to verify the thermal stability of the chiral axis.

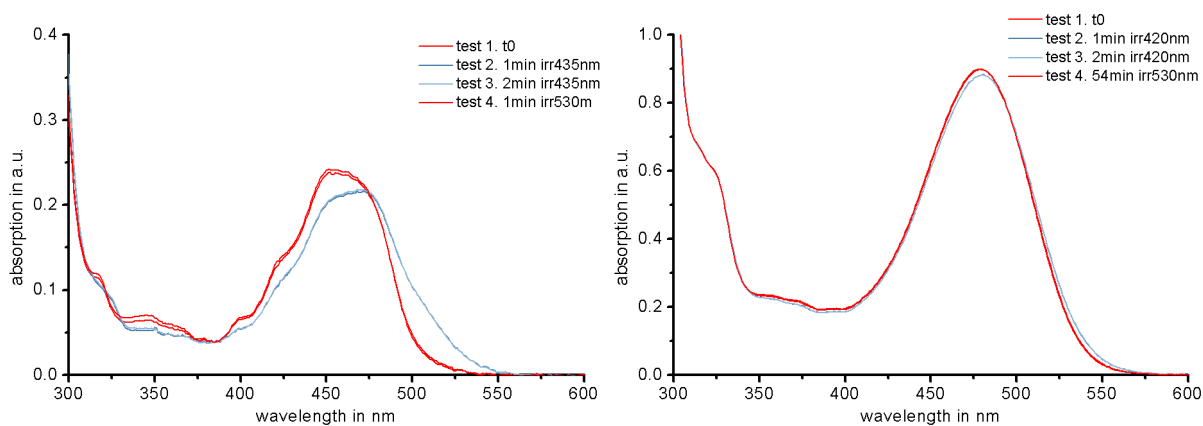


Figure 51: UV-Vis spectra of irradiation experiments on hemiindigo **26** in cyclohexane (left) and dichloromethane (right). Photoswitching can be seen in cyclohexane. The initial *Z* / *E* composition is switched with 435 nm LED light and can be recovered by irradiation with 530 nm. Little photoswitching is observed in dichloromethane, which was also assessed via NMR in Figure 53.

The photochromism is strongly reduced by the present substitution pattern in hemiindigo **26**. The overall red-shift of absorption is comparable to other twisted methoxy substituted hemiindigos (see Section 2.3.8). The low photoisomerization yields (Figure 51) can be

attributed to low photochromism in combination with poor quantum yields of *Z* and *E* isomers, which is why this substitution pattern was not studied further.

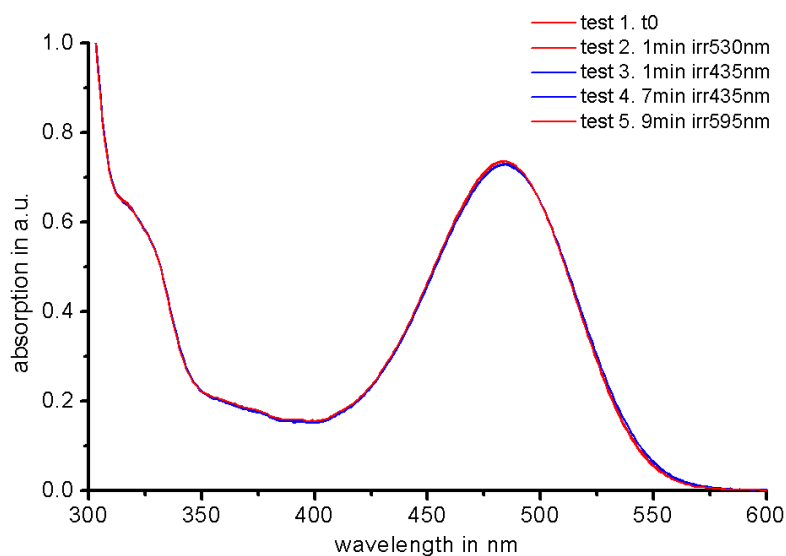


Figure 52: UV-Vis spectra of irradiation experiments on hemiindigo **26** in dimethyl sulfoxide. Little photoswitching can be seen. This kind of substitution pattern seems to perform poorly within polar solvents, in contrast to derivatives possessing only a threefold substituted double bond.

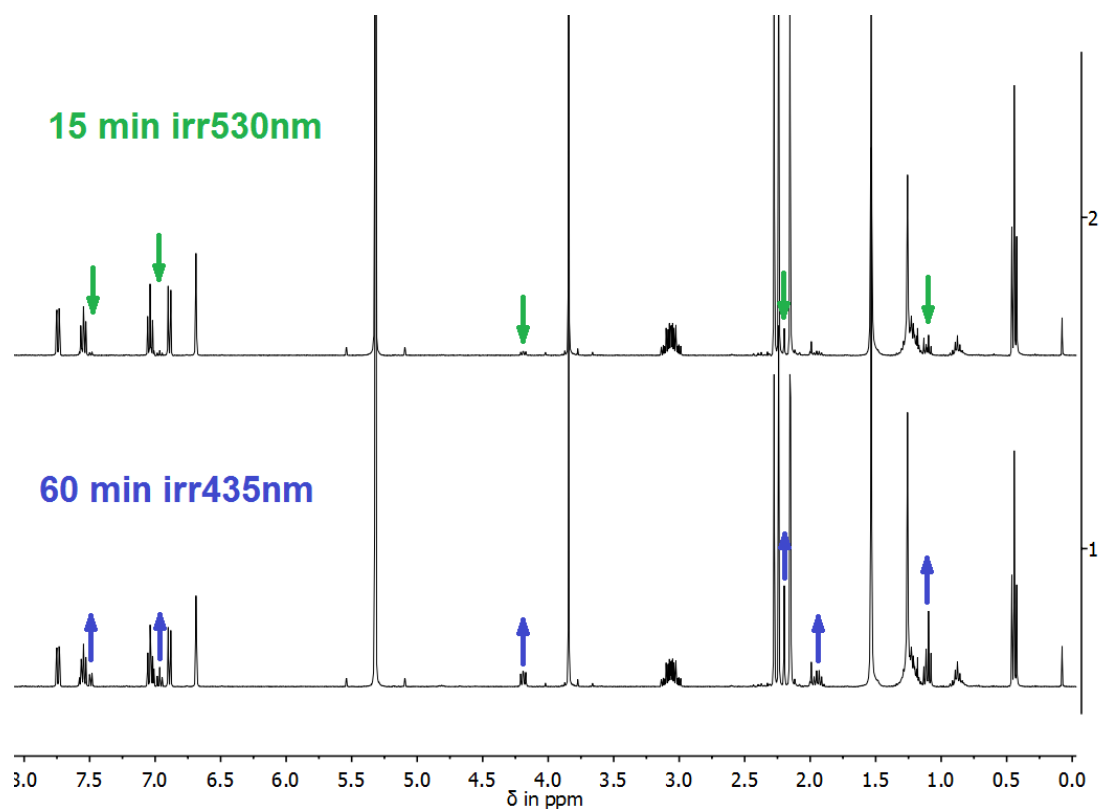


Figure 53:  $^1\text{H}$ -NMR spectra recorded during irradiation experiments on hemiindigo **26** in dichloromethane- $d_2$  at 25 °C, 400 MHz. The initial *Z* / *E* composition before

irradiation is the same as observed in the spectrum on top and is not shown. 91% of the *Z* isomer are present in the thermal equilibrium and photoswitching to 23% *E* isomer content is possible.

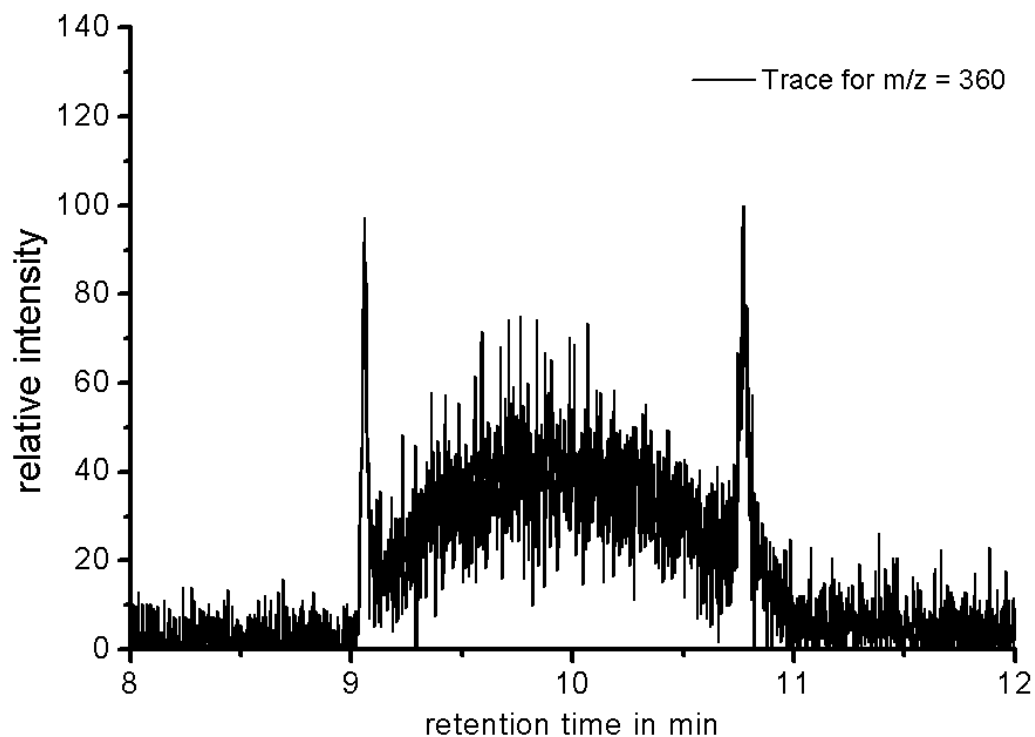


Figure 54: Chromatogram of hemiindigo **26** recorded via gas chromatography - mass spectrometry. Only the mass trace with an  $m/z$  of 360 corresponding to the product **26** is shown. Two distinct peaks connected by a streaking area can be observed at 300 °C, suggesting interconversion of *Z*- and *E* isomers during elution.

The effect observed in Figure 54 is unprecedented compared to other hemiindigo derivatives measured via the same methodology and conditions. Quantification of the thermal dynamics could be done by measurements at different elution temperatures utilizing the equations developed by *O. Trapp*.<sup>[95]</sup>

### 2.2.11 Stilbene fragment: Electron withdrawing substituents

As electron donating stilbene substituents led to very well performing, red-shifted photoswitches, electron withdrawing groups are expected to lead to blue-shifted absorptions. Hemiindigo **29** was synthesized to confirm these assumptions.

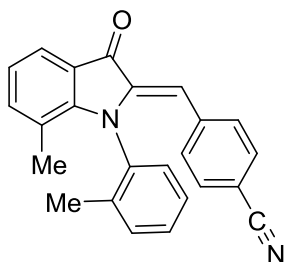


Figure 55: Lewis-formula of hemiindigo **29**.

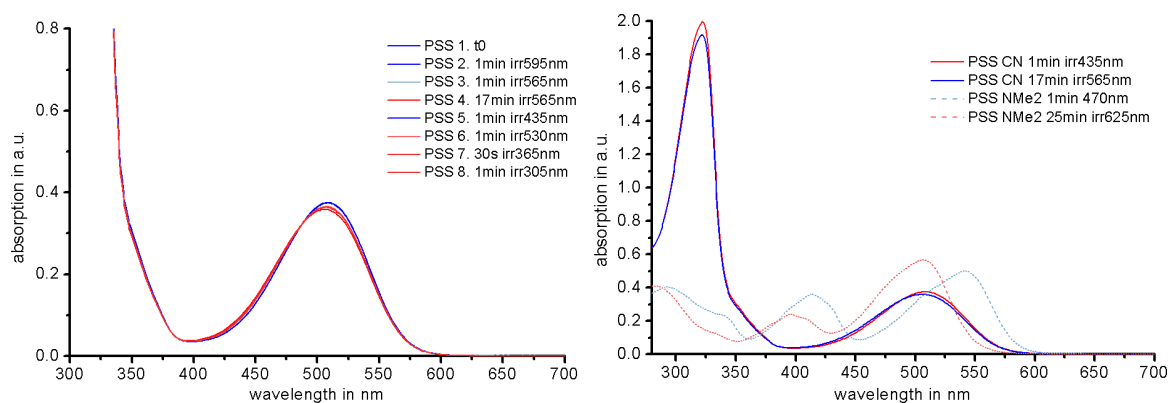


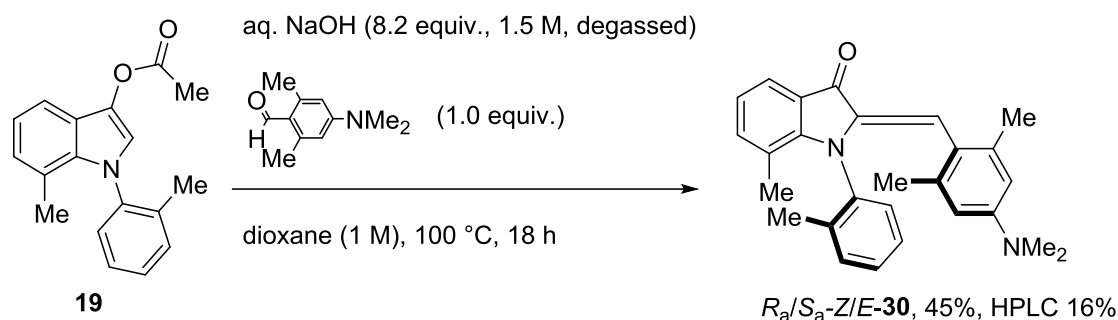
Figure 56: UV-Vis spectra of photoswitching experiments of hemiindigo **29** in dimethyl sulfoxide (left) and comparison to the dimethylamino derivative **20**. The absorption maximum of the *Z* isomer (red) is not shifted but the *E* isomer (blue) exhibits a hypsochromic shift beyond the most red-shifted *Z* isomer maximum.

The poor photoisomerization yields obtained for hemiindigo **29** can again be attributed to low photochromism in combination with poor quantum yields of *Z* and *E* isomers, which is why this substitution pattern was also not studied further.

Large changes of photophysical properties can be expected by introducing substituents at the stilbene *ortho*-positions. Bulky methyl groups should strongly twist the stilbene single bond out of the indoxyl plane. Conditions for the condensation of indoxyl acetate and the respective aldehyde have to be adjusted for this substitution pattern, as the steric demand requires increased temperatures for these compounds to react.

## 2.2.12 Stilbene fragment: Introduction of methyl groups in the *ortho*-position

The synthetic scheme according to *U. Burger et al.* was altered using dioxane as co-solvent and the starting materials are added prior to heating to 100 °C.<sup>[88]</sup> The reaction mixture was kept at 100 °C for 18 h to yield hemiindigo **30**.



Scheme 21: Preparation of hemiindigo **30** from indoxyl acetate **19**. Moderate to low yields were obtained after HPLC purification, which was caused by losses during injection and discarded fractions due to elution overlap with other compounds.

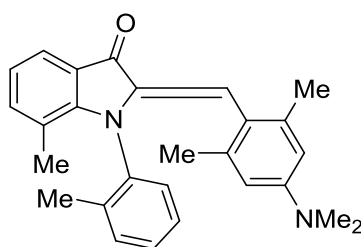


Figure 57: Lewis-formula of hemiindigo **30**.

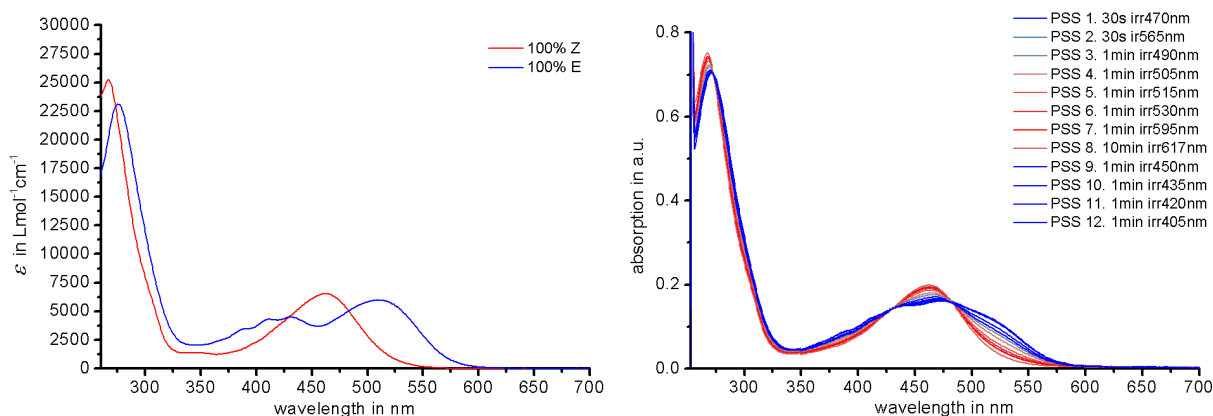


Figure 58: Molar absorption spectra of pure isomers (left) and spectra recorded at the PSS at different wavelengths (right) of hemiindigo **30** in dimethyl sulfoxide. The isosbestic points are well defined, verifying the photostability of this compound. Highest isomeric yields were obtained at 450 nm irradiation (56% *E* isomer) and



at 617 nm irradiation (96% *Z* isomer). Energy barriers for thermal double bond isomerizations were determined to be 30.5 kcal/mol for the *Z* to *E* and 31.7 kcal/mol for the *E* to *Z* direction at 114 °C, which translates to thermal half-lives of 78 years and 614 years at 25 °C, for the respective isomers. Quantum yields were determined at 12 ±2% (450 nm) for *Z* to *E* and 12 ±2% (520 nm) for *E* to *Z* direction. In 83 / 17 heptane / ethyl acetate the quantum yield rises to 33 ±2% (435 nm) for *Z* to *E* and is lowered to 10 ±2% (520 nm) for *E* to *Z* photoisomerizations. This increase in quantum yield of the *Z* isomer over the *E* isomer improves the photoisomerization yields to 98% *Z* isomer (530 nm) and 84% *E* isomer (435 nm) in apolar medium. Adapted with permission from [75]. Copyright 2018 American Chemical Society.

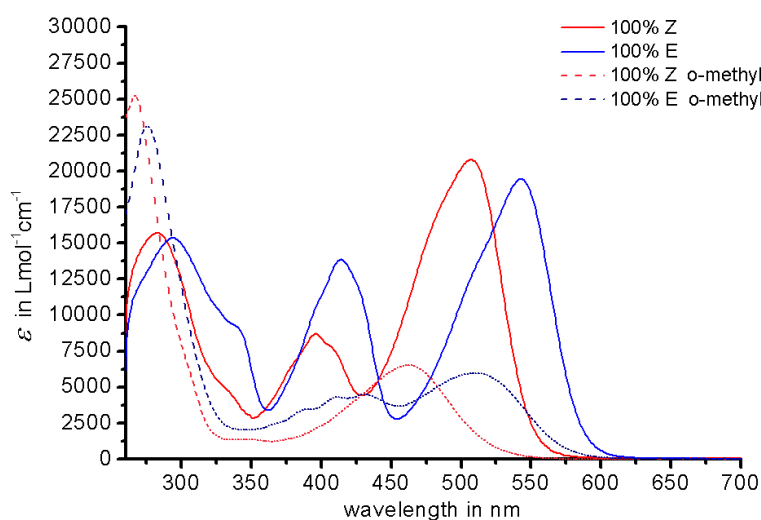
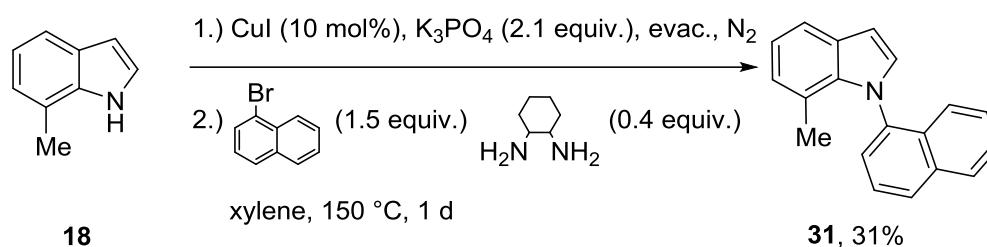


Figure 59: Comparison of molar absorption spectra for less (**20**) and highly stilbene single bond-twisted hemiindigo **30** in 83 / 17 heptane / ethyl acetate. A strong hypsochromic shift of the twisted derivative **30** can be observed and its molar absorptivity  $\epsilon$  is lowered by 70%.

The poor separation of *Z* and *E* absorption maxima is likely to be an important reason for the mediocre *E* isomeric yield of 56%. The thermal half-lives for hemiindigo **30** were slightly reduced from 99 years to 78 years for the *Z* isomer and from 1140 years to 614 years at 25 °C compared to hemiindigo **20**. The twisting of the stilbene single bond is not beneficial with regard to red-shifting the hemiindigo chromophore, increasing quantum yields or enhancing thermal bistabilities. Nonetheless, the derivatives with twisted *N*-aryl substituents and twisted stilbene single bond still remain potent and robust photoswitches. For details regarding their chiral properties, see Section 2.3.8.

The late stage arylation of 7-methyl indoxyls with 1-naphthyl halides was not feasible, therefore another synthetic route was established to gain access to the *N*-naphthyl-substituted compounds. 7-Methyl-1-(naphthalen-1-yl)-1*H*-indole **31** was prepared from **18** and 1-bromonaphthalene according to a procedure of *J. Antilla et al.* at elevated temperatures in pressure tubes.<sup>[91]</sup>



Scheme 22: Preparation of *N*-arylated indole **31**.

The naphthyl substituted indole **31** could be crystallized unlike the *N*-*ortho*-tolyl substituted indole **17**, which is a clear, colorless oil.

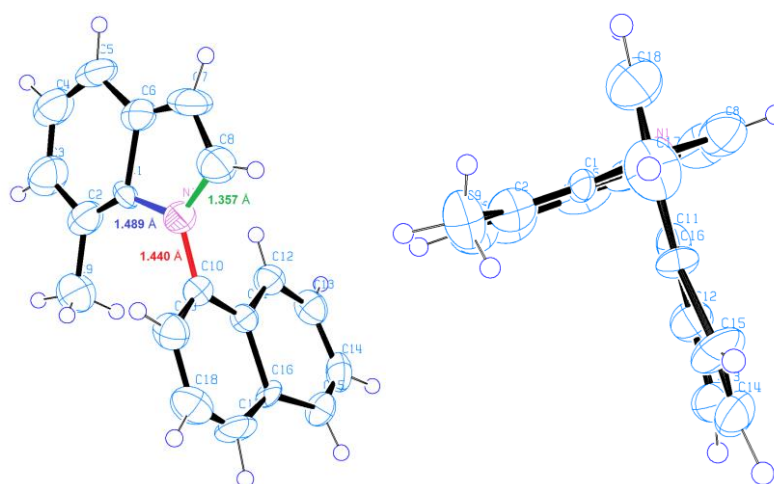
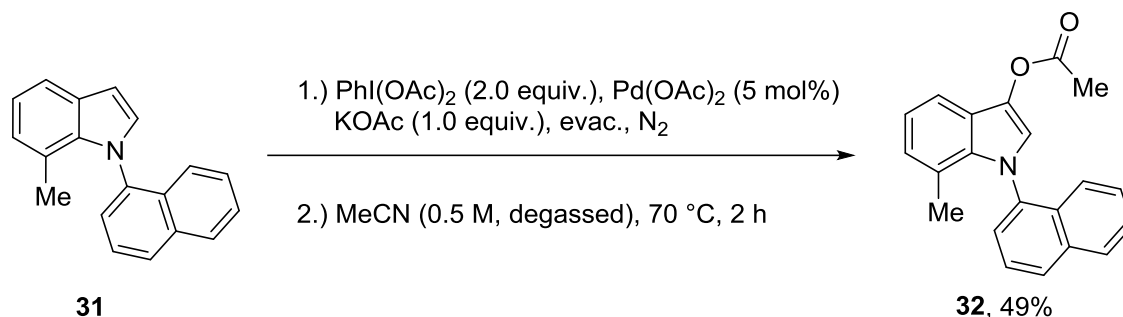


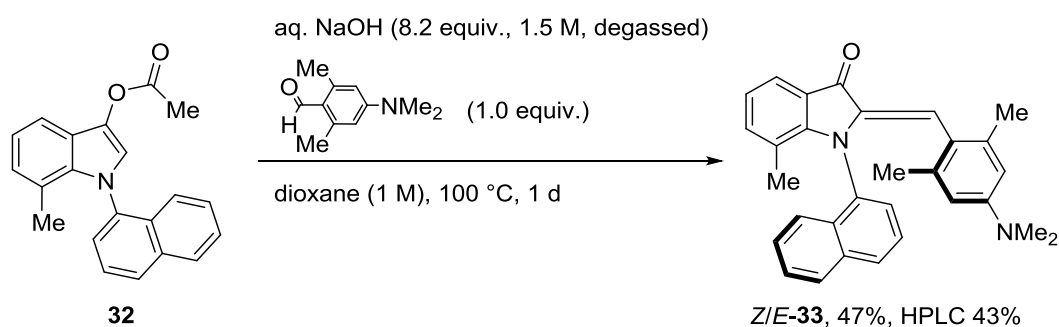
Figure 60: Structure of naphthylated indole **31** in the crystalline state. The perspective on the right emphasizes the nearly orthogonal planes of indole and naphthyl. The dihedral angle between the indole and naphthyl plane is close to 90° with 86.28° for the angle C8-N1-C10-C19. This proves that the introduction of the 7-methyl group alone twists the aryl axis to nearly its maximum in the crystalline state, which is also reproduced by DFT calculations (see Section 2.3.7). Chiral HPLC at 0 °C did not show a separation of rotamers for **31**, which indicates a low thermal stability of its rotational axis suggesting a rotational energy barrier of less than 20 kcal/mol.

7-Methyl-1-(naphthalen-1-yl)-1*H*-indol-3-yl acetate **32** was prepared from **31** according to a procedure reported by *P. Choy et al.*<sup>[92]</sup>



Scheme 23: Preparation of *N*-arylated indoxyl acetate **32**.

Hemiindigo **33** was prepared according to the modified procedure from *U. Burger et al.* used for the synthesis of hemiindigo **30**.<sup>[88]</sup>



Scheme 24: Preparation of hemiindigo **33** in moderate yields. Loss of substance during HPLC injection was minimized by recovery and re-injection of spilled material.

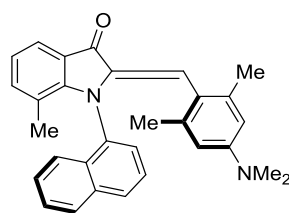
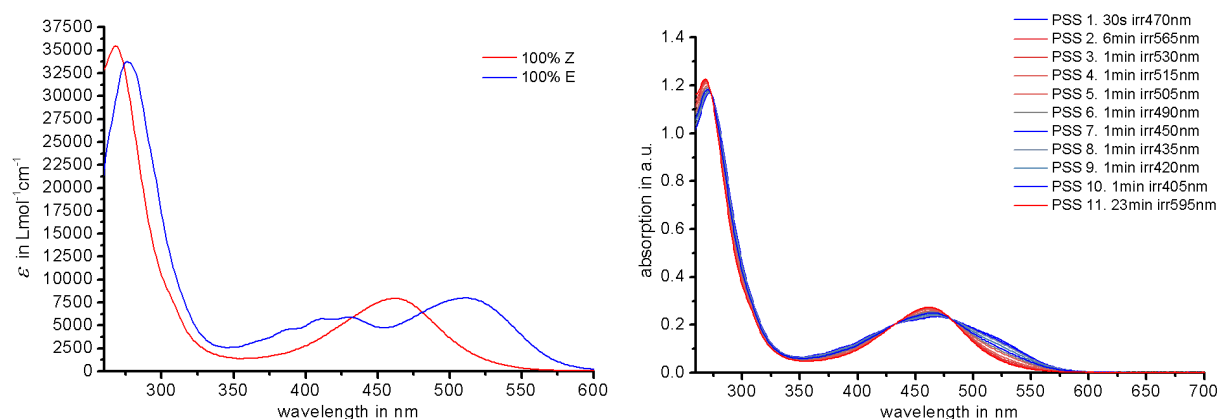
Figure 61: Lewis-formula of hemiindigo **33**.

Figure 62: Molar absorption spectra of pure isomers (left) and spectra recorded at the PSS at different wavelengths of irradiation PSS (right) spectra of hemiindigo **33** in dimethyl sulfoxide. The isobestic points are well defined, verifying the photostability of this compound. Highest isomeric yields were obtained at 450 nm irradiation (43% *E* isomer) and at 595 nm irradiation (98% *Z* isomer). Energy barriers for thermal double bond isomerizations were determined to be 31.8 kcal/mol for the *Z* to *E* and 32.7 kcal/mol for the *E* to *Z* direction at 114 °C, which translates to thermal half-lives of 750 years and 3427 years at 25 °C, for the respective isomers. Quantum yields were determined at  $5 \pm 1\%$  (450 nm) for *Z* to *E* and  $8 \pm 2\%$  (520 nm) for *E* to *Z* photoisomerizations. In 83 / 17 heptane / ethyl acetate, quantum yields were determined at  $27 \pm 2\%$  (435 nm) for *Z* to *E* and  $9 \pm 2\%$  (520 nm) for *E* to *Z* photoisomerizations. This increase in quantum yield of the *Z* isomer over the *E* isomer improves the photoisomerization yields to 98% *Z* isomer (530 nm) and 83% *E* isomer (435 nm) in apolar medium. Adapted with permission from <sup>[75]</sup>. Copyright 2018 American Chemical Society.

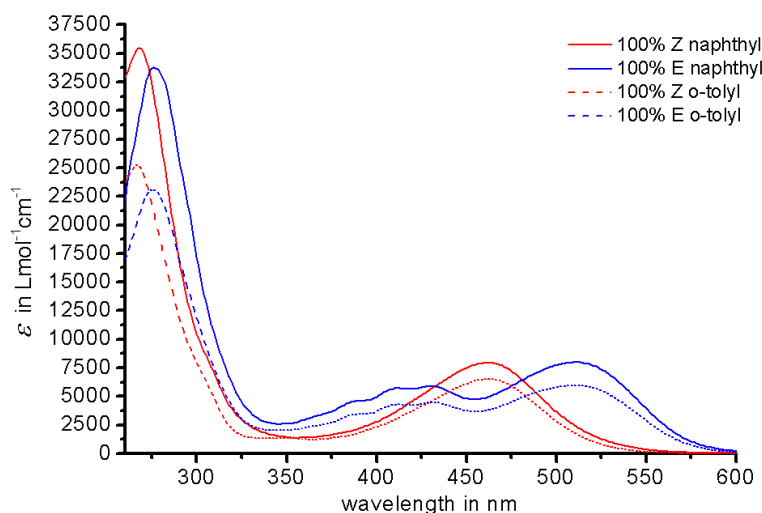


Figure 63: Comparison of molar absorption spectra of *N*-naphthyl substituted hemiindigo **33** and *N*-*ortho*-tolyl substituted hemiindigo **30**. The shape of absorption spectra is almost identical whereas the molar absorptivity  $\epsilon$  is increased by 20% for the naphthyl derivative.

The change from *ortho*-tolyl to naphthyl does not change the absorption profile significantly but drastically increases the thermal half-lives in between *Z* and *E* isomers by one order of magnitude for the *Z* isomer and by three times for the *E* isomer. This could be explained by the better sterical fit of the flat naphthyl residue between methyl group and twisted stilbene fragment compared to the sterically more demanding methyl group that protrudes the phenyl plane on both sides.

In summary the introduction of a spatially better fitting naphthyl group increased the thermal double bond isomerization half-lives significantly while not severely interfering with other photophysical parameters.

Incorporation and switching of this compound was also carried out within *Formlabs* clear photo curable polymer, which makes it possible to dissolve and 3D print this matrix with the functional switches inside. The procedure of incorporating soluble photoswitches into the viscous resin was first applied by A. Gerwien. The photoswitch is dissolved with a few drops of dichloromethane, added to the resin and stirred vigorously by hand. The resin is placed under high vacuum to evaporate the dichloromethane, which can cause bubbles upon polymerization. The desired amount of resin is put on a microscope sample carrier plate and two equally sized capillaries are used as spacers. Another carrier plate is pressed on top and the resin is polymerized with a 150 mW 405 nm LED for 5 minutes. The prepared plates can be analyzed within commercial UV-Vis and electronic circular dichroism (ECD) spectrometers.

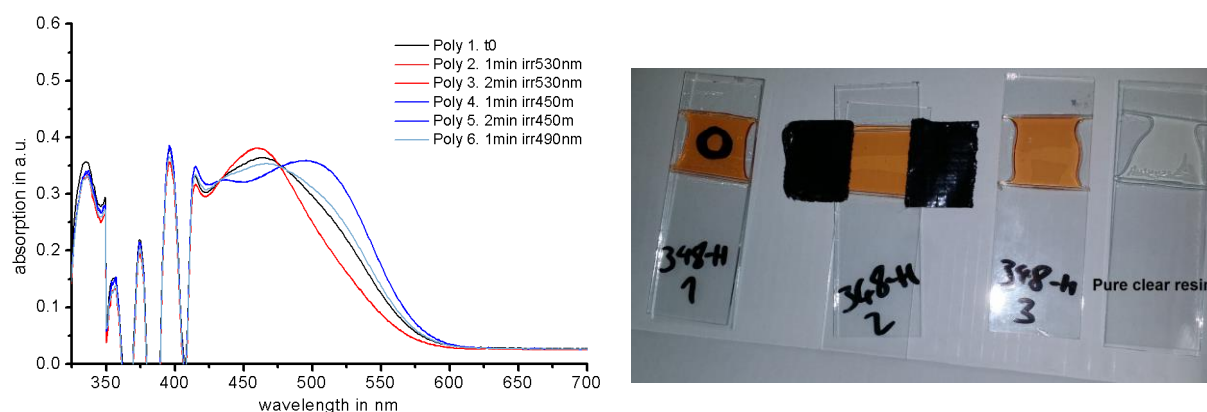


Figure 64: UV-Vis spectra of hemiindigo **33** dissolved in *Formlabs* clear resin (left) and photograph of prepared samples (right). Photoswitchability between >95% *Z* isomer and >83% *E* isomer can be seen, which equals the performance of hemiindigo **33** in apolar solvent mixtures of 87 / 13 heptane / ethyl acetate. The black circle on sample “348-H 1” served as positional marker for circularly polarized light (CPL) irradiations and ECD measurements.

As future perspective, the addition of enantiopure rotamers of hemiindigo **33** in these matrices can be examined with regard to changes of the thermal stability of the rotational aryl axes, allowing the measurements of precise kinetics in the polymer matrix and their comparison to solution experiments.

### 2.2.13 Conclusion: Rationale of substitution patterns

It could be shown that hemiindigos are a class of virtually unexplored, potent photoswitches supporting high photoisomerization ratios with blue over green to yellow and red light, high thermal bistabilities, good quantum yields and high tolerance of the photoreactions towards solvent polarity changes. The effects of different substitutions at the indoxyl- and stilbene fragments could be shown, with electron donating substituents being beneficial for red-shifted absorptions and twisted aryl axes at the indoxyl-nitrogen increasing thermal bistability while maintaining its red-shift. Increase of conjugation strength at the stilbene fragment did not yield desired red-shifted hemiindigos. The thermal bistabilities of *Z* and *E* isomers can be increased by electron withdrawing groups at the indoxyl nitrogen or by electron-neutral stilbene fragments. The thermal bistabilities of *N*-arylated hemiindigos profit from twisting of the *N*-aryl moiety and from decreasing sterical bulk between the indoxyl core methyl group and the stilbene fragment by substituting an *ortho*-tolyl group with a naphthyl group.

Further experiments on substitutions at the aromatic indoxyl positions have to be carried out, as DFT calculations show a large red-shift for nitro substituted derivatives (Figure 65).

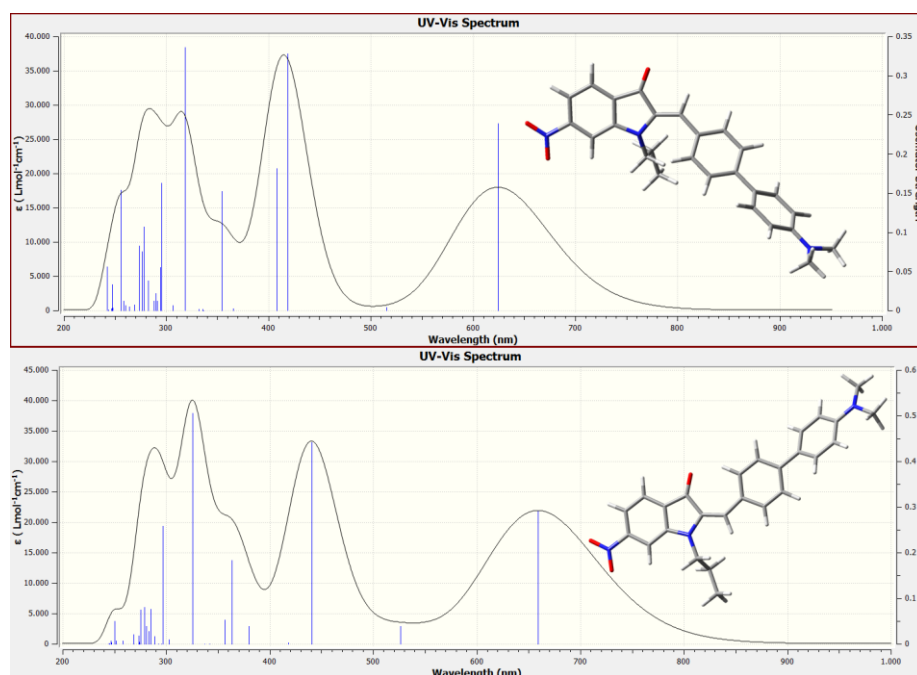


Figure 65: Calculated UV-Vis spectra at the B3LYP/6-311+G(d,p) level of theory, (TD-DFT, nstates = 30) for a potentially red-shifted hemiindigo derivative, *Z* isomer (top) and *E* isomer (bottom) are shown. Absorption maxima of 625 nm (*Z*) and 660 nm (*E*) can be observed, an increase towards longer wavelengths is expected for the experiment, as DFT calculations tend to underestimate the red-shift.<sup>[74]</sup>

## 2.2.14 Hemiindigo - Solvatochromism and the influence of water on hemiindigo chromophores

The following sections serve as a quick overview of the discussed results and methods throughout this work, starting with solvatochromism and photoswitchability of hemiindigos in water.

Regardless of structural modifications, hemiindigos exhibit strong solvatochromism but little thermochromism, which stands in contrast to the results on the parent indigo chromophore (see Section 2.1).

For the class of hemiindigo photoswitches, apolar solvents as well as the gas phase (see Section 2.5) show blue-shifted absorptions while polar organic solvents and their water mixtures exhibit strongly red-shifted absorptions for these compounds. This experimentally observed significant solvatochromism cannot be fully explained by the utilized DFT level of theory.<sup>[74]</sup>

It is highly desirable to operate molecular switches and machines in water, as it is the most abundant and likewise most important liquid for life on earth. Biological applications demand good solubility, photoswitchability and photostability of the utilized switch or machine to perform within or around cells or bacteria.

Hemiindigos exhibit very good overall photoswitching performance, but they display unpredictable behavior when water is used as (co-)solvent, especially for hemiindigos substituted with a 4-(dimethyl amino) phenyl or julolidine moiety as stilbene fragments. Proficient photoswitching could be observed for one cycle in water / polar organic solvent mixtures (up to 80 - 97%, v / v) with e.g. tetrahydrofuran, dimethylformamide or dimethyl sulfoxide as organic modifiers (see Figure 42 and literature<sup>[74]</sup>). At high water contents precipitation can be observed but no obvious decrease of photoisomerization efficiency could be tested at the time these measurements were carried out.

Introduction of a permanent charge tag (see Section 2.5) made electron rich hemiindigo derivatives **8** and **3** soluble in pure water, further proving their diminished switching behavior in this solvent. Insolubility could thus be excluded as the main reason for non-existent photoisomerization yields.

*D. Berdnikova* introduced a hydrophilic alkyl dimethylamino side chain to a phenylmethoxy substituted hemiindigo **34** and showed that photoswitching in water was feasible again, even when binding of the hemiindigo to RNA / DNA complexes occurs.<sup>[40]</sup> Controlling RNA -



protein interactions by visible light can serve as therapeutic handle within the emerging field of photopharmacology.<sup>[96]</sup>

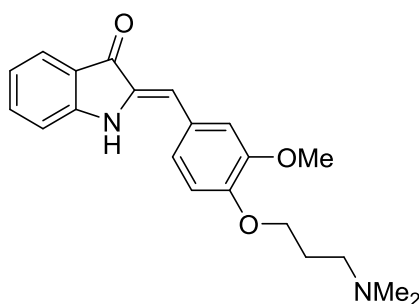


Figure 66: Hemiindigo derivative **34** was synthesized by *D. Berdnikova*. Photoswitching and unspecified binding to HIV-1 TAR RNA, HIV-1 RRE-IIB RNA and HIV-1 TAR Tat complexes with fluorescent responses could be shown.<sup>[40]</sup>

As part of a collaboration with *D. Berdnikova*, charge tagged hemiindigo derivatives without strongly electron donating stilbene fragments were synthesized and tested for their binding and switching properties on DNA and RNA (see Section 2.6).

The exact reason why electron donating stilbene fragments show no photoswitching behavior in water is still not understood to date. One possible explanation is excited state proton energy transfer (ESPT), as the basic amino functionalities abstract protons from remaining water molecules and cleaves the associated protons upon irradiation as deexcitation channel. Another possible theory is the ratio between an apolar biradical and a polar ionic state of the *Z* / *E* transition state structure at the central double bond. Electron donating stilbene fragments might favor an ionic state at the central double bond, which can be stabilized by water molecules. This might lower the thermal stabilities of the photoswitch to such an extent that no photoisomerization or distinct spectra of *Z* and *E* can be seen at ambient temperatures. Since low temperature experiments in water in its liquid state are not possible at ambient pressure, transient spectroscopy on a dimethylamino and a methoxy substituted hemiindigo would be the method of choice to confirm or disprove these theories. Addition of polar organic solvent restores photoswitchability in between *Z* and *E* isomers, which underlines this argument as the organic solvent shell displaces the water.

## 2.2.15 Hemiindigo - Effects of pH-modulation

Addition of *Brønsted* acids and -bases reduces photoswitchability in a reversible fashion by shifting the initial *Z* / *E* compositions towards a new equilibrium or by generating an intermediate protonated form. Strong changes in absorption and photochromic shifts can be observed upon protonation. Lower thermal stabilities (21 - 24 kcal/mol) in untreated dichloromethane compared to dichloromethane filtered through aluminium oxide (23 - 26 kcal/mol) can be observed as well.

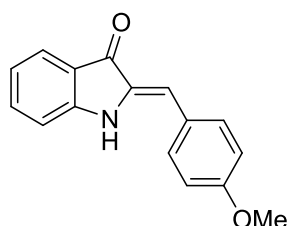


Figure 67: *Lewis*-formula of hemiindigo **9**.

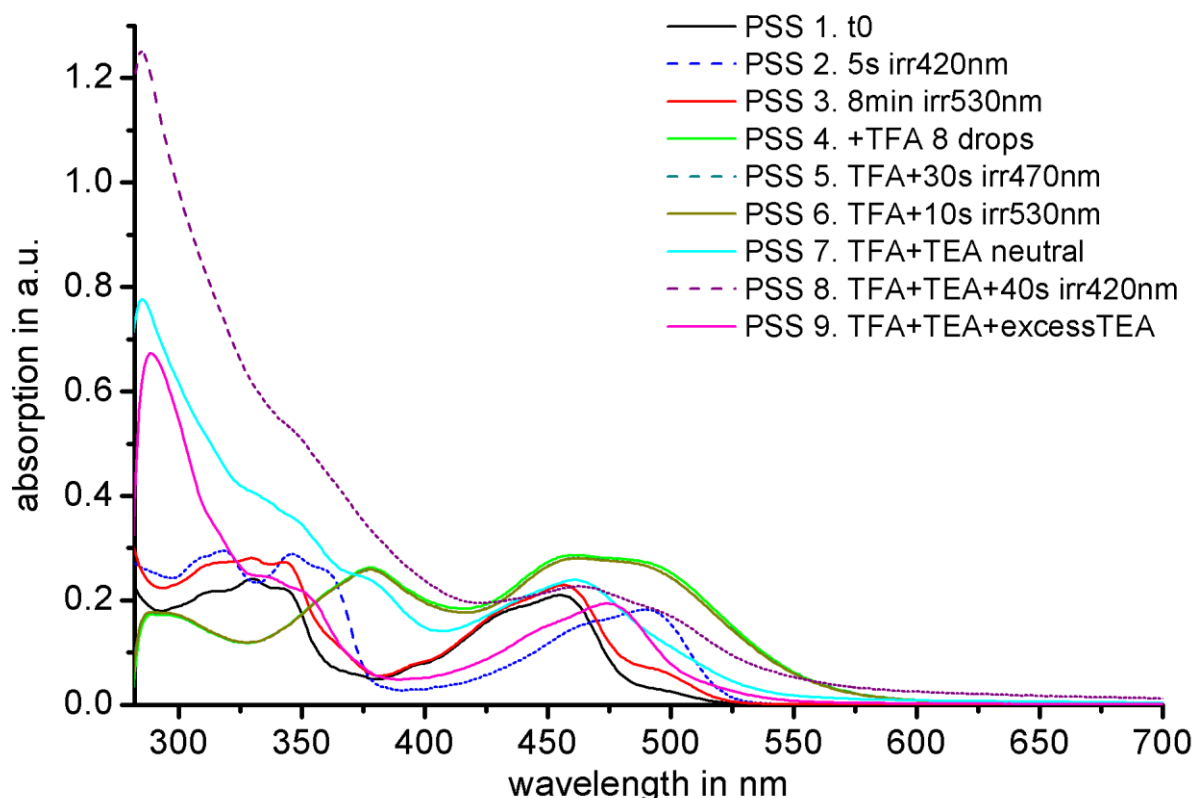


Figure 68: Impact of acids and base additions on the absorption of hemiindigo **9** in toluene. Photoswitchability without additives was ensured first (broken blue line and solid red line). Addition of 8 drops of trifluoroacetic acid to 2 mL of toluene volume yielded spectrum shown in green. Irradiation in this state did not induce

any spectral changes. This can be caused by low thermal barriers in between *Z* and *E* isomer or due to deexcitation trough ESPT. An increase of molar absorptivity can be seen although the photoswitch concentration was diluted throughout this experiment. Neutralizing the solution yielded the bright blue line. In this state photoswitchability could be restored (broken violet line). Addition of a few drops of triethylamine yielded the pink spectrum.

In summary, photoswitchability is lost for hemiindigo **9** when exposed to acids or excess base in organic solution.

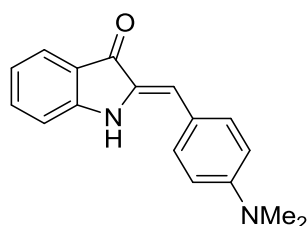


Figure 69: Lewis-formula of hemiindigo **11**.

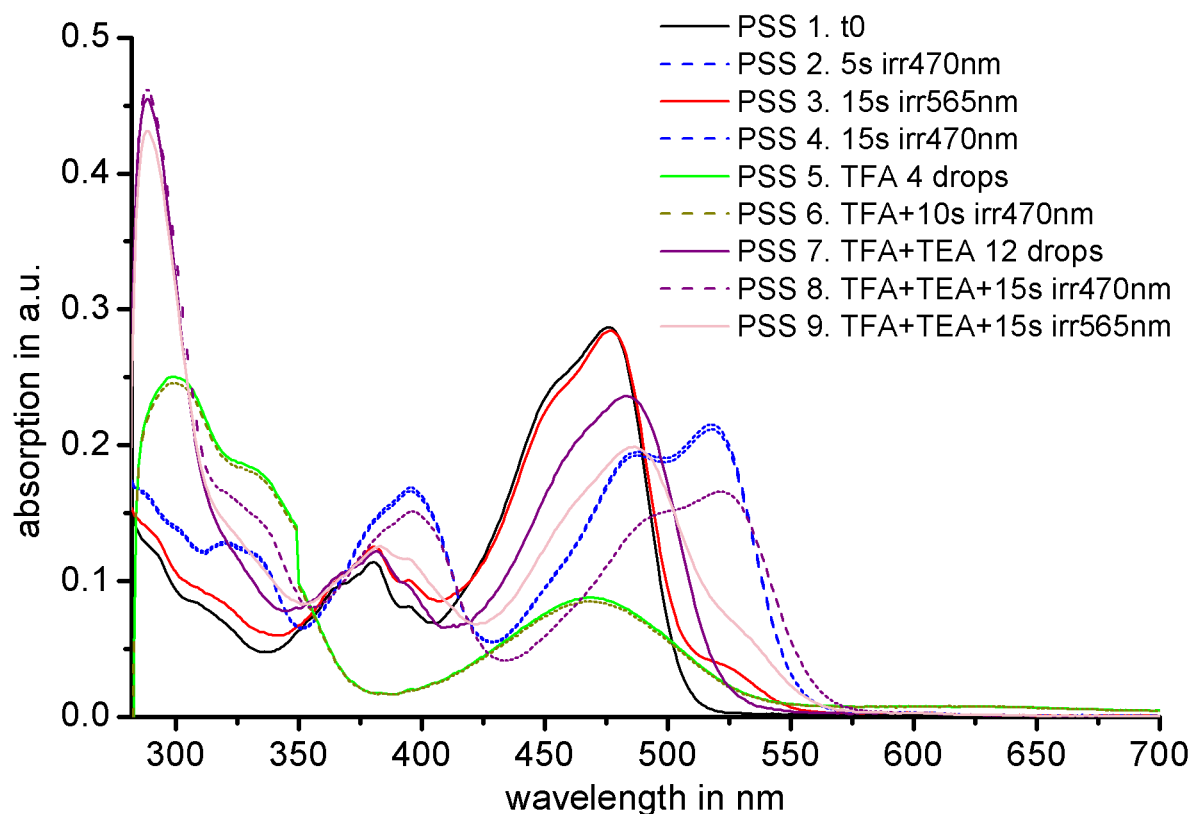


Figure 70: Impact of acids and base addition on the absorption of hemiindigo **11** in toluene. Photoswitchability without additives was ensured first (dashed blue line and solid red line). Addition of 4 drops of trifluoroacetic acid to 2 mL of toluene

solution yielded the spectrum shown in green. Irradiation in this state did not induce any spectral changes. This can be caused by low thermal barriers in between *Z* and *E* isomer or due to deexcitation through ESPT. A strong decrease of molar absorptivity can be seen as the photoswitch was not diluted by a factor of three by the small volumes of acid / base added. Excess triethylamine (violet line) restores proper photoswitchability (broken violet line, pink line) and results in a defined isosbestic point shifted by approximately 10 nm to the red part of the visible light spectrum compared to the neutral solution. A decrease in molar absorptivity by 20% can be observed.

The effect of acids can also be seen within measurements of thermal stabilities in dichloromethane. The remaining hydrochloric acid severely lowers the thermal *Z* / *E* isomerization barriers. For hemiindigo **8**, an energy barrier of 20.3 kcal/mol for the thermal *Z* to *E* and 20.6 kcal/mol for the thermal *E* to *Z* isomerization was measured. If dichloromethane is filtered through aluminium(III) oxide to remove residual acid in the solvent, the measured energy barriers amounted to 21.8 kcal/mol for the thermal *Z* to *E* and 21.9 kcal/mol for the thermal *E* to *Z* isomerization direction. Filtration increases the thermal half-life 18-fold for the *Z* isomer and 10-fold for the *E* isomer.

For hemiindigo **16**, an energy barrier of 20.7 kcal/mol for the thermal *Z* to *E* and 21.2 kcal/mol for the *E* to *Z* isomerization was measured. If dichloromethane is filtered through aluminium(III) oxide, the measured energy barriers amounted to 22.4 kcal/mol for the thermal *Z* to *E* and 24.1 kcal/mol for the thermal *E* to *Z* isomerization. The thermal half-life is also increased 18-fold for the *Z* isomer and 134-fold for the *E* isomer.

In conclusion, pure water as solvent and acidic / basic conditions are factors that decrease the photophysical performance of hemiindigo chromophores.

Methoxy derivatives (see Section 2.2.1) are able to overcome the inability to photoswitch in water at the cost of less red-shifted absorptions.

### 2.2.16 Conclusion: Solvent, Water and pH influence

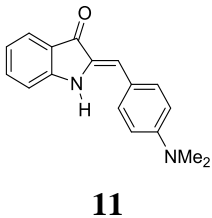
The effects of solvent polarity on hemiindigo photoswitches could be demonstrated. Generally, red-shift is increased and quantum yields are slightly decreased for polar solvents, these trends are reversed for apolar solvents, with few exceptions. Photoswitching in water can only be realized by addition of 2.5 - 30% of water miscible organic solvent for hemiindigos supporting electron rich stilbene fragments.<sup>[74]</sup> Water soluble, ionic hemiindigos can only photoisomerize if the stilbene fragment features weak electron donating groups like methoxy or methyl (see section 2.2.5 and Section 2.6 for details). Acidic or basic conditions do not show visible photoswitching of hemiindigo chromophores.

## 2.2.17 Hemiindigo - Photoswitching between photostationary states

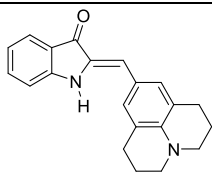
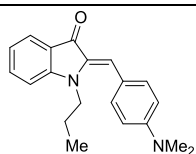
A photostationary state (PSS) is defined as the state of an irradiated sample where the isomeric ratio of e.g. *Z* and *E* isomers of a photoswitch does not change while intensity and wavelength of the irradiating light is held constant. The composition of isomers in a particular PSS represents the maximum obtainable isomeric yield for a specific irradiation condition and is a key photophysical property that depends on the following combined parameters, namely photochromism, molar absorptivities, quantum yields and thermal stabilities. A strong photochromism usually enables enrichment of specific isomers by selectively irradiating at wavelengths where only one isomer absorbs strongly using e.g. distinct wavelength distributions as emitted by LEDs or monochromatic laser light. High quantum yields and molar absorptivities will enhance the overall photoisomerization speed for a specific isomer. High thermal stabilities of all present isomers will prevent them from thermal interconversion towards their equilibrium concentration, which makes these species visible even for non-transient spectroscopic methods at ambient or elevated temperatures.

Hemiindigos exhibit very high isomer ratios in the PSS at different wavelengths reaching up to 99% *Z* and 98% *E* isomer for the best performing switches. The following Table 6 provides a brief selection of measured compositions in the PSS at different wavelengths.

Table 6: Isomer yields obtained in the PSS after *Z* / *E* and *E* / *Z* photoisomerization of the respective hemiindigo in different solvents at different wavelengths. Isomer yields were determined via UV-Vis measurements at  $\sim 2.5 \cdot 10^{-5}$  M concentration.

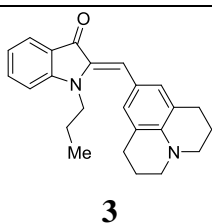
Hemiindigo	Solvent	Wavelength	% <i>E</i> isomer	% <i>Z</i> isomer	Duration
 <b>11</b>	toluene	470 nm	87	13	1 min
		490 nm	57	43	1 min
		505 nm	55	45	1 min
		515 nm	31	69	1 min
		530 nm	15	85	1 min
		565 nm	12	88	1 min
		590 nm	46	54	1 min
		617 nm	0.9	99	4 h
	THF	435 nm	89	11	1 min
		470 nm	87	13	1 min
		490 nm	69	31	1 min
		505 nm	68	32	1 min
		515 nm	44	56	2 min
		530 nm	28	72	1 min
	565 nm	17	83	1 min	

		595 nm	14	86	1 min
		617 nm	3.8	96	6 h
	DMSO	470 nm	89	11	1 min
		490 nm	84	16	1 min
		505 nm	85	15	1 min
		515 nm	75	25	1 min
		530 nm	73	27	1 min
		565 nm	48	52	1 min
		595 nm	13	87	1 min
		617 nm	2.0	98	4 h
	toluene	470 nm	83	17	10 s
		490 nm	61	39	30 s
		505 nm	61	39	30 s
		515 nm	46	54	30 s
		530 nm	35	65	30 s
		565 nm	22	78	30 s
		595 nm	7.7	92	5 min
		617 nm	0.5	99	1 h
	THF	470 nm	90	10	10 s
		490 nm	82	18	10 s
		505 nm	81	19	10 s
		515 nm	68	32	20 s
		530 nm	59	41	30 s
		565 nm	38	62	30 s
		595 nm	11	89	90 s
		617 nm	1.2	99	45 min
	DMSO	470 nm	81	19	5 s
		490 nm	81	19	10 s
		505 nm	81	19	5 s
		515 nm	77	23	5 s
		530 nm	75	25	5 s
		565 nm	59	41	10 s
		595 nm	25	75	20 s
		617 nm	4.9	95	3 min
		680 nm	9.3	91	5 h
	toluene	405 nm	71	29	5 min
		420 nm	81	19	5 min
		435 nm	92	8.0	5 min
		470 nm	93	7.0	5 min
		490 nm	87	13	5 min
		505 nm	84	16	5 min
		515 nm	73	27	5 min
		530 nm	55	45	5 min
		565 nm	38	62	5 min
		590 nm	2.0	98	15 min

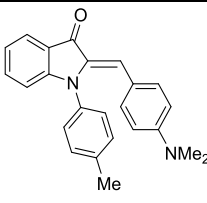
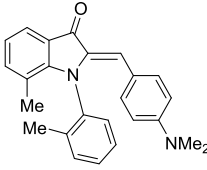
**15****8**

## 2.2.17 HEMIINDIGO - PHOTOSWITCHING BETWEEN PHOTOSTATIONARY STATES

		617 nm	0.7	99	4 h
		625 nm	1.9	98	4 h
	THF	405 nm	77	23	1 min
		420 nm	77	23	1 min
		435 nm	90	10	1 min
		470 nm	93	7.0	5 s
		490 nm	87	13	3 min
		505 nm	79	21	3 min
		515 nm	68	32	3 min
		530 nm	51	49	3 min
		565 nm	35	65	3 min
		590 nm	0.4	99	12 min
	DMSO	625 nm	0.4	99	10 min
		405 nm	73	27	1 min
		420 nm	71	29	1 min
		435 nm	79	21	1 min
		470 nm	95	5.0	1 min
		490 nm	90	10	1 min
		505 nm	90	10	2 min
		515 nm	83	17	2 min
		530 nm	82	18	2 min
		565 nm	61	39	2 min
		590 nm	6.9	93	5 min
		600 nm	4.2	96	10 min
		617 nm	1.7	98	30 min
		625 nm	3.8	96	1 h
	toluene	470 nm	95	5.0	5 s
		490 nm	91	9.0	10 s
		505 nm	91	9.0	10 s
		515 nm	82	18	15 s
		530 nm	77	23	15 s
		565 nm	54	46	30 s
		595 nm	12	88	60 s
		617 nm	0.5	99	20 min
	THF	470 nm	90	10	5 s
		490 nm	85	15	5 s
		505 nm	85	15	5 s
		515 nm	78	22	5 s
		530 nm	72	28	5 s
		565 nm	52	48	20 s
		595 nm	12	88	60 s
		617 nm	3.5	96	15 min
	DMSO	470 nm	96	4.0	5 s
		490 nm	97	3.0	5 s
		505 nm	98	2.0	10 s





		515 nm	94	6.0	5 s
		530 nm	93	7.0	5 s
		565 nm	77	23	5 s
		595 nm	36	64	5 s
		617 nm	5.0	95	40 s
		680 nm	0.1	99	4 h
 <p><b>16</b></p>	toluene	405 nm	71	29	1 min
		420 nm	82	18	1 min
		435 nm	95	5.0	15 s
		470 nm	95	5.0	1 min
		490 nm	89	11	2 min
		505 nm	85	15	2 min
		515 nm	72	28	2 min
		530 nm	51	49	2 min
		565 nm	38	62	30 s
		590 nm	2.3	98	3 min
	617 nm	0.4	99	1 h	
	THF	405 nm	61	39	1 min
		420 nm	72	28	1 min
		435 nm	84	16	1 min
		470 nm	86	14	5 s
		490 nm	77	23	2 min
		505 nm	74	26	2 min
		515 nm	63	37	2 min
		530 nm	37	63	3 min
		565 nm	36	64	3 min
590 nm		3.9	96	14 min	
DMSO	617 nm	1.6	98	2 h	
	405 nm	72	28	1 min	
	420 nm	70	30	1 min	
	435 nm	81	19	1 min	
	470 nm	97	3.0	1 min	
	490 nm	89	11	1 min	
	505 nm	89	11	2 min	
	515 nm	83	17	2 min	
	530 nm	81	19	2 min	
	565 nm	63	37	2 min	
	DMSO	435 nm	83	17	1 min
		450 nm	88	12	1 min
		470 nm	93	7	3 sec
		490 nm	90	10	1 min
		505 nm	90	10	1 min
		595 nm	25	75	5 min
		617 nm	7.7	92	80 min
		625 nm	6.8	93	2 h

## 2.2.17 HEMIINDIGO - PHOTOSWITCHING BETWEEN PHOTOSTATIONARY STATES

<b>20</b>		515 nm	85	15	1 min	
		530 nm	80	20	1 min	
		565 nm	67	33	1 min	
		595 nm	27	73	1 min	
		625 nm	2.7	97	25 min	
	Heptane/Ethyl	405 nm	77	23	1 min	
	acetate	420 nm	91	9.5	1 min	
	83/17	435 nm	96	4.3	2 sec	
		450 nm	95	4.7	1 min	
		470 nm	92	8.4	1 min	
		490 nm	76	24	1 min	
		505 nm	74	26	1 min	
		515 nm	53	47	1 min	
		530 nm	31	69	30 sec	
		565 nm	29	71	1 min	
		595 nm	68	32	7 min	
		600 nm	3.8	96	60 min	
	<b>30</b>	DMSO	305 nm	41	59	1 min
			365 nm	35	65	1 min
			385 nm	35	65	1 min
		405 nm	41	59	1 min	
		420 nm	47	53	1 min	
		435 nm	55	45	1 min	
		450 nm	56	44	1 min	
		470 nm	54	46	30 s	
		505 nm	30	70	1 min	
		515 nm	21	79	1 min	
		530 nm	16	84	1 min	
		565 nm	13	87	30 s	
		595 nm	12	88	1 min	
		617 nm	4.1	96	20 min	
Heptane/Ethyl		420 nm	82	18	1 min	
acetate		435 nm	84	17	5 sec	
93/7		450 nm	82	18	1 min	
		470 nm	68	32	1 min	
		530 nm	2.2	98	4 min	
<b>33</b>		DMSO	405 nm	26	74	1 min
		420 nm	31	69	1 min	
		435 nm	37	63	1 min	
		450 nm	43	57	1 min	
		470 nm	39	61	30 s	
		505 nm	17	83	1 min	
		515 nm	11	89	1 min	
		530 nm	6.4	94	1 min	

	565 nm	4.3	96	1 min
	595 nm	2.1	98	3 min
Heptane/Ethyl	405 nm	75	25	1 min
acetate	420 nm	82	18	1 min
87/13	435 nm	83	17	3 s
	450 nm	82	18	1 min
	470 nm	64	36	1 min
	505 nm	12	88	30 s
	515 nm	9.1	91	1 min
	530 nm	2.0	98	1 min
	565 nm	13	87	1 min
	595 nm	30	70	1 min

### 2.2.18 Hemiindigo - Thermal bistabilities

A high thermal bistability of photoproducts, which can be formed with low energy red light is a rare and highly sought after property of photoswitches. Mechanically rigid switching scaffolds often require high energy UV / blue light to populate their excited states.<sup>[53]</sup> Hemiindigos undergo photoisomerization with blue and green or green and red light with thermal half-lives of years to millennia at 25 °C. N-H unsubstituted hemiindigos thermally convert entirely to the *Z* isomeric form in the dark, in contrast to nitrogen substituted switches, as these form temperature- and solvent specific isomer equilibria. Racemization kinetics of axially chiral hemiindigos (see Section 2.3.6) to an equally distributed *R<sub>a</sub>*- / *S<sub>a</sub>* state are treated by first order kinetics.

### 2.2.19 First order kinetics without entering the equilibrium

The thermal stabilities of *Z* / *E* double bond isomerizations with 100% *Z* or 100% *E* isomer as thermodynamic minimum were determined via NMR or UV-Vis spectroscopy (see 2.2.3 and Section 2.2.7). Tightly sealed cuvettes were used for elevated temperature UV-Vis measurements and observation of clear isosbestic points proved no concentration changes during the measurements.

When the thermal isomerization is a unimolecular first order reaction and proceeds completely towards pure states, eq. 1 can be applied:

$$-\frac{d[\text{isomer excess}]}{dt} = k[\text{isomer excess}] \quad \text{eq. 1}$$

The rate constant  $k$  of the reaction is obtained by plotting  $\ln(c_{t0}/c_t)$  versus time, with  $c_{t0}$  being the initial excess of the starting isomer at  $t_0$  and  $c_t$  being the decreasing isomer excess at increasing time increments  $t$ . The slope of the graph gives the rate constant  $k$  for the isomerization of the respective hemiindigo  $Z/E$  isomers or atropisomers.

$$k = \frac{\ln\left(\frac{[\text{isomer excess}]_{t_0}}{[\text{isomer excess}]_t}\right)}{t} \quad \text{eq. 2}$$

The free activation enthalpy  $\Delta G^*$  for the process can be calculated from the rate constant  $k$  of the reaction (eq. 2) by using the *Eyring* equation (eq. 3):

$$k = \frac{k_B T}{h} e^{\frac{-\Delta G^*}{RT}} \quad \text{eq. 3}$$

with  $k_B =$  Boltzmann constant ( $1.381 \cdot 10^{-23} \text{ J} \cdot \text{K}^{-1}$ )

$T =$  temperature in K

$h =$  Planck constant ( $6.626 \cdot 10^{-34} \text{ J} \cdot \text{s}$ )

$k =$  rate constant of the reaction

eq. 3 can be rearranged to give eq. 4 and the numerical value of the rate constant  $k$  obtained from eq. 2 can be inserted:

$$\Delta G^* \text{ (in J mol}^{-1}\text{)} = 8.314 \cdot T \cdot \left[ 23.760 + \ln\left(\frac{T}{k}\right) \right] \quad \text{eq. 4}$$

This methodology was applied to atropisomers as well which were quantified by electronic circular dichroism (ECD) spectroscopy in heptane / ethyl acetate solutions at different temperatures and separately for  $Z$  and  $E$  isomers. Pure enantiomers were obtained prior to measurements by separation via chiral HPLC. Rotation of the *ortho*-tolyl or naphthyl fragments around their chiral hemiindigo N-C axis was observed as loss of the ECD signal over time since this rotation results in racemization of the samples. The quantification was carried out by adding the area in the ECD spectrum above and below the x-axis from e.g. 250 - 500 nm, which was set as 100%. However, the endpoint was set to 0% and not to the 50% equilibrium of the racemate, which is the correct value. This leaves the plotted  $k$  values underestimated by 50%, resulting in higher free activation enthalpies for thermal atropisomerization barriers (which is better in all presented cases). For the sake of consistency and comparability, the plots of the atropisomerization reactions are displayed with this systematic error in mind. The magnitude of this error is displayed in a calculational example (Table 7) for commonly measured thermal atropisomerization barriers for hemiindigo and indigo molecules:

Table 7: Overview of different incorrectly determined free activation enthalpies (exemplary values) and the respective correction of systematic error.

Incorrectly calculated $\Delta G^*$ [kcal/mol]	Incorrectly determined $k$ ( $s^{-1}$ )	Incorrectly calculated thermal half- life (25 °C)	Correctly calculated $\Delta G^*$ [kcal/mol]	Correctly determined $k$ ( $s^{-1}$ )	Correctly calculated thermal half- life (25 °C)
15	61.7	0.01 s	15.4	30.9	0.02 s
20	0.013	52 s	20.4	0.007	105 s
25	$2.85 \times 10^{-6}$	2.81 d	25.4	$1.42 \times 10^{-6}$	5.63 d
30	$6.13 \times 10^{-6}$	35.8 a	30.4	$3.06 \times 10^{-6}$	71.7 a

In principle, halving of the determined  $k$  value results in an increased free activation enthalpy of about 0.41 kcal/mol and doubled thermal half-lives for all cases, which is a significant improvement in stability compared to the initially reported values.

Exemplary plots are shown for the *E* to *Z* thermal central double bond isomerization of hemiindigo **15** in three different solvents. The complete data can be found in the literature.<sup>[74]</sup>

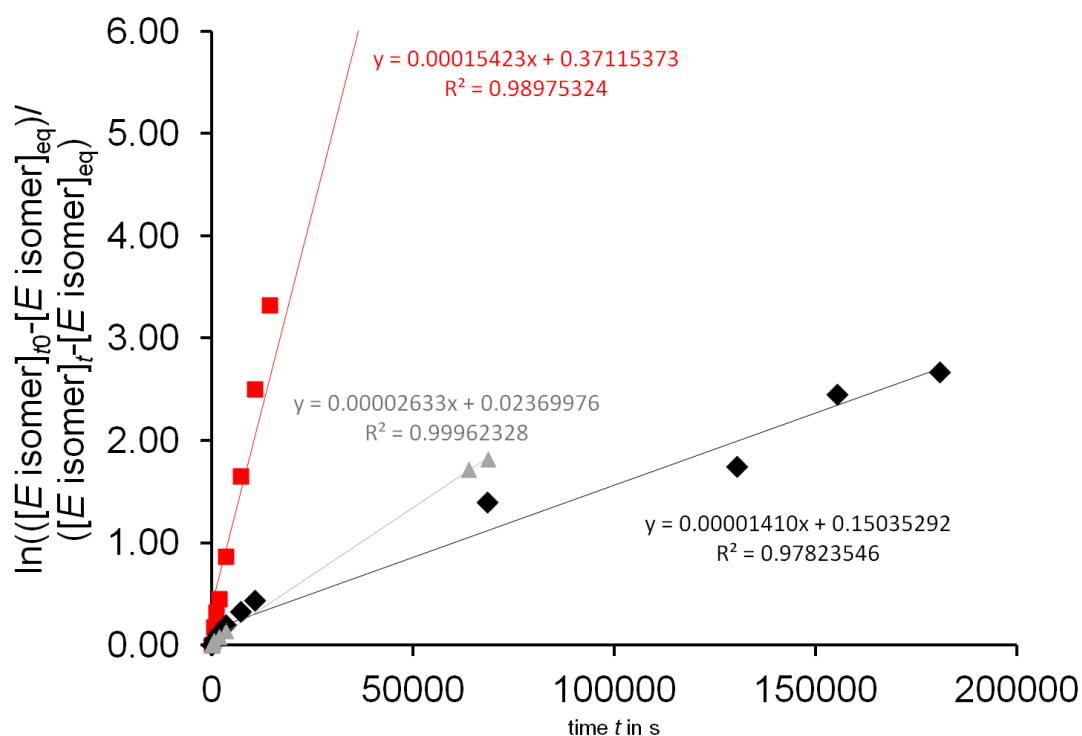
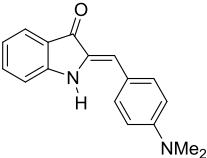
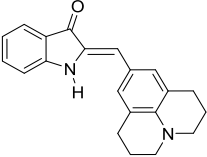


Figure 71: A first order kinetic analysis of the thermal *E* to *Z* isomerization of hemiindigo **15** in toluene (black, 22 °C), tetrahydrofuran (red, 25 °C), and dimethyl sulfoxide (grey, 51 °C) gives a linear relationship. The slope *m* can be translated into the rate constant *k* for this process. The corresponding Gibbs energies of activation are given in Table 8. Adapted with permission from <sup>[74]</sup>. Copyright 2017 American Chemical Society.

Table 8: Free activation enthalpies  $\Delta G^*$  and corresponding half-lives at 25 °C for the thermal *E* / *Z* as well as *Z* / *E* isomerizations of hemiindigos **11** and **15** without entering equilibria.

Hemiindigo	Solvent	Polarity - $E_T(30)^{[97]}$ /kcal $\text{mol}^{-1}$	$\Delta G^*$ (therm. <i>Z</i> / <i>E</i> equil.) /kcal $\text{mol}^{-1}$	$\Delta G^*$ (therm. <i>E</i> / <i>Z</i> equil.) /kcal $\text{mol}^{-1}$	Equilibra- tion half- life of pure <i>Z</i> isomer at 25 °C	Equilibra- tion half- life of pure <i>E</i> isomer at 25 °C	Thermo-dynamic % <i>E</i> /% <i>Z</i> equilibrium in the dark (at T in °C )
 <b>11</b>	toluene	33.9	-	24.1	-	15 h	0/100 (26)
	THF	37.4	-	24.5	-	1.2 d	0/100 (28)
	DMSO	45.1	-	26.9	-	70 d	0/100 (51)
 <b>15</b>	toluene	33.9	-	23.8	-	8.9 h	0/100 (22)
	THF	37.4	-	22.4	-	50 min	0/100 (25)
	DMSO	45.1	-	25.8	-	11 d	0/100 (51)

In contrast to N-H substituted hemiindigos, the unsubstituted species convert completely into their *Z* isomeric state, similar to many hemithioindigo derivatives.

To assess the thermal stability of the introduced chiral axes in the respective hemiindigo photoswitches **30** and **33**, the rotamers were separated via chiral HPLC at 0 °C. The absolute area of their ECD response was measured within an ECD spectrometer at defined temperatures and plotted against time to obtain kinetic datasets. An exemplary plot is given below for hemiindigo **30**. The complete data can be found in the literature.<sup>[74]</sup>

The obtained free activation enthalpies  $\Delta G^*$  for the thermal chiral axis racemization and corresponding extrapolated half-lives at 25 °C are given in Table 11.

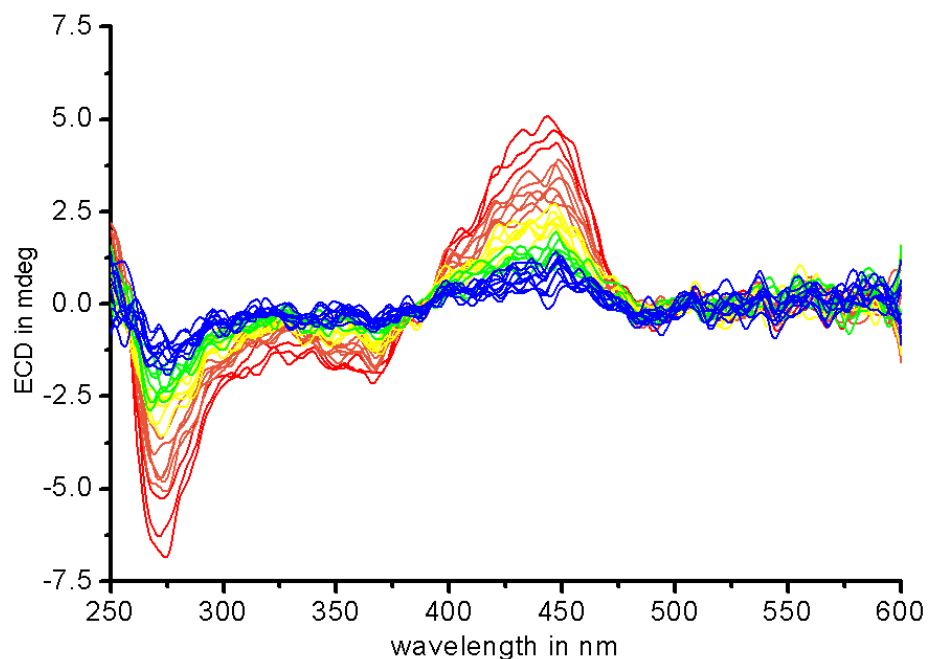


Figure 72: Exemplary illustration of the decaying ECD response of Z-( $R_a$ )-**30** at 40 °C in 93 / 7 heptane / ethyl acetate. The red spectrum with strongest ECD response represents  $t = 0$  s and was set to 100% (added absolute spectral area for positive and negative signals). Correspondingly, the blue spectrum with weakest ECD response represents  $t = 3720$  s at the end of measurement. Kinetic plots were conducted within these respective margins. Yellow and green represent intermediate time points within the measurement. Adapted with permission from [75]. Copyright 2018 American Chemical Society.



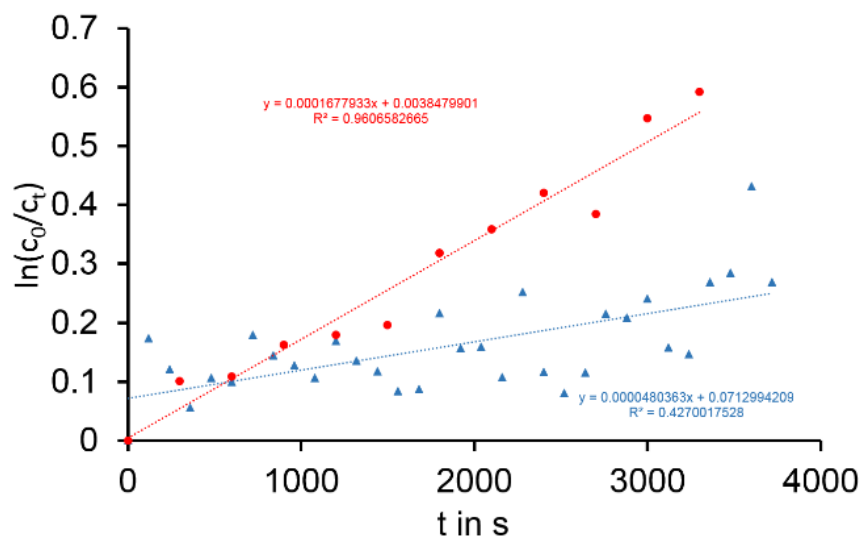


Figure 73: First order kinetic analyses of the thermal racemization via atropisomerization of hemiindigo **30** in 93 / 7 heptane / ethyl acetate in the dark. The slopes  $m$  can be translated into the rate constant  $k$  for each process. Racemization in the  $Z$  isomeric state (red, see also Figure 72) was measured at 40 °C and gives an energy barrier of 23.1 kcal/mol. Racemization in the  $E$  isomeric state (blue) was measured at 60 °C and proceeds over an energy barrier of 26.1 kcal/mol. Poor  $R^2$  values are based on bad signal to noise ratios caused by the weak ECD response of the  $E$  isomer. Adapted with permission from <sup>[75]</sup>. Copyright 2018 American Chemical Society.

An overview of obtained atropisomerization barriers is given in Table 11, Section 2.3.8.

The introduction of *ortho*-methyl substituents at the stilbene fragment increases the thermal stability of the *ortho*-tolyl chiral axis resulting in half-lives that range from seconds to days at 25 °C for hemiindigo **30**. This could be attributed to the twisting of the stilbene fragment around its single bond, interfering less with the *ortho*-tolyl moiety. Substitution of the *ortho*-tolyl moiety by a naphthyl residue raises the thermal half-lives further to days and months. This could be explained by the better fit of the naphthyl group in between the methyl group of the indoxyl core and the stilbene fragment.

## 2.2.20 First order kinetics with entering the equilibrium - E/Z isomerizations

The thermal *Z* to *E* or *E* to *Z* isomerizations of hemiindigos proceed mainly at elevated temperatures resulting in stable mixtures of isomers in specific equilibrium compositions. Measurements were performed via <sup>1</sup>H-NMR spectroscopy in deuterated dimethyl sulfoxide, toluene, tetrahydrofuran, dichloromethane or by UV-Vis spectroscopy in heptane / ethyl acetate mixtures.

NMR tubes were charged with 1.1 mg to 2.5 mg of the respective hemiindigo compound and 0.6 mL - 0.7 mL of deuterated solvent resulting in mM concentrations. The NMR tubes were irradiated at suitable wavelengths to accumulate a high percentage of the desired isomer. Subsequent heating of the samples was carried out in the dark at 60 - 114 °C and the thermal isomerization kinetics were followed by repeating <sup>1</sup>H-NMR measurements in determined time intervals (typically hours to days). Lower thermal stabilities ≤26 kcal/mol were quantified by UV-Vis spectroscopy at 24 - 82 °C in heptane / ethyl acetate mixtures or dichloromethane. In cases with barriers below 26 kcal/mol, data points were typically taken in shorter time intervals after the initial irradiation interval. After prolonged heating, the stable equilibrium concentrations of *Z* and *E* isomers were obtained from integration of indicative signals in the <sup>1</sup>H-NMR spectrum or from the known extinction coefficients and absolute absorption values of the *E* isomers in the red part of the absorption spectrum (where the absorption of *Z* isomers is approximately zero).

The thermal *E* / *Z* isomerization is a unimolecular reaction of first order and proceeds towards an equilibrium *E* / *Z*-isomer composition where both isomers are present as described by eq. 5:

$$\ln\left(\frac{[E \text{ isomer}]_{t_0} - [E \text{ isomer}]_{eq}}{[E \text{ isomer}]_t - [E \text{ isomer}]_{eq}}\right) = (k_{E/Z} + k_{Z/E})t \quad \text{eq. 5}$$

with  $[E \text{ isomer}]_{t_0}$  being the initial concentration of the *E* isomer at the time  $t = 0$ ,  $[E \text{ isomer}]_{eq}$  being the concentration of the *E* isomer at the equilibrium,  $[E \text{ isomer}]_t$  representing the concentration of the *E* isomer at specific times in the measurement  $t$ ,  $k_{E/Z}$  being the rate constant  $k$  of the *E* to *Z* isomerization,  $k_{Z/E}$  being the rate constant  $k$  of the *Z* to *E* isomerization, and  $t$  being the elapsed time. When plotting the logarithmic left part of eq. 5 versus time  $t$  the obtained slope  $m$  contains both rate constants for the isomerization reactions taking place. The rate constant  $k_{E/Z}$  can then be calculated according to eq. 6:

$$k_{E/Z} = \frac{m}{1 + \frac{[E \text{ isomer}]_{eq}}{[Z \text{ isomer}]_{eq}}} \quad \text{eq. 6}$$

when taking into account the law of mass action (eq. 7):

$$\frac{[E \text{ isomer}]_{eq}}{[Z \text{ isomer}]_{eq}} = \frac{k_{Z/E}}{k_{E/Z}} \quad \text{eq. 7}$$

likewise, the rate constant for  $k_{Z/E}$  can be calculated according to eq. 8:

$$k_{Z/E} = \frac{m}{1 + \frac{[Z \text{ isomer}]_{eq}}{[E \text{ isomer}]_{eq}}} \quad \text{eq. 8}$$

from the same kinetic plot (see Figure 74 for plots of the thermal  $E$  to  $Z$  and  $Z$  to  $E$  isomerizations of hemiindigo **20** in dimethyl sulfoxide as an example).

By rearranging the *Eyring* equation (eq. 3), the free activation enthalpy  $\Delta G^*$  can be calculated from the rate constants  $k_{E/Z}$  or  $k_{Z/E}$  of the reaction according to eq. 4.

The obtained free activation enthalpies  $\Delta G^*$  for the thermal  $Z / E$  as well as  $E / Z$  isomerizations of selected hemiindigos and the corresponding extrapolated half-lives at 25 °C are given in Table 9.

The obtained kinetic plot for hemiindigo **20** is shown exemplarily for clarity reasons. The full data can be found in the literature.<sup>[75]</sup>

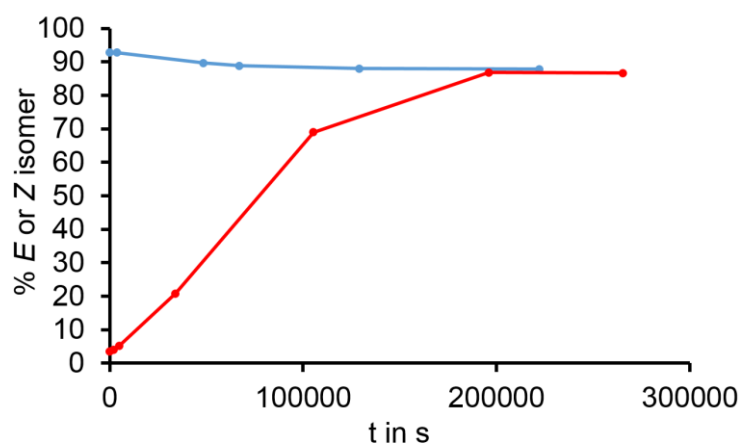


Figure 74: Kinetics of the thermal isomer interconversion of hemiindigo **20** at 103 °C in dimethyl sulfoxide- $d_6$  in the dark starting from either 92%  $E$ -**20** (blue) or 96%  $Z$ -**20** (red). After prolonged heating, a stable 87 / 13  $E / Z$  isomer mixture is obtained independently for both experiments. Adapted with permission from <sup>[75]</sup>. Copyright 2018 American Chemical Society.

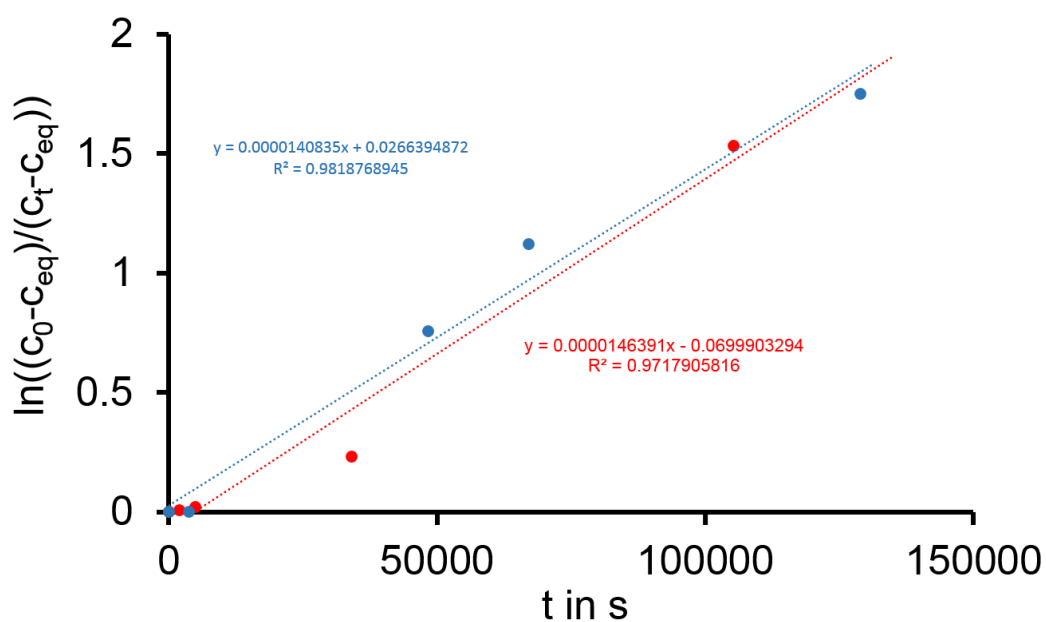
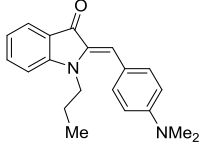
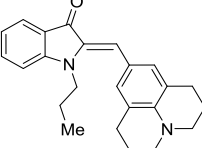
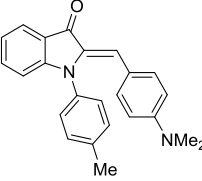
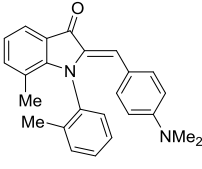
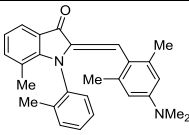
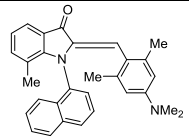


Figure 75: First order kinetic analysis of the thermal *E* to *Z* and *Z* to *E* isomerization of hemiindigo **20** in dimethyl sulfoxide-*d*<sub>6</sub> at 103 °C starting from either 92% *E*-**20** (blue) or 96% *Z*-**20** (red). After prolonged heating in the dark, a stable 87/13 *E/Z* isomer composition is observed in both experiments. Linearized plots according to eq. 5 are shown. The slopes *m* can be translated into the rate constant *k* for each isomerization direction. Analysis of the thermal *Z* to *E* equilibration reaction (red) gave energy barriers of 30.6 for *Z* / *E*- and 32.0 kcal/mol for the *E* / *Z* isomerizations. Analysis of the thermal *E* to *Z* equilibration reaction (blue) gave energy barriers of 30.6 for *Z* / *E*- and 32.1 kcal/mol for *E* / *Z* isomerizations, respectively. The close agreements of these two independent experiments can be seen by the almost similar slopes for the *Z* to *E* and *E* to *Z* isomerization experiments. Adapted with permission from <sup>[75]</sup>. Copyright 2018 American Chemical Society.

Table 9: Free activation enthalpies  $\Delta G^*$  for the thermal *Z* / *E* and *E* / *Z* isomerizations of selected hemiindigos and corresponding extrapolated half-lives at 25 °C.

Hemiindigo	Solvent	Polarity $E_T(30)^{[1]}$ $^{971}$ /kcal $\text{mol}^{-1}$	$\Delta G^*$ (therm. <i>Z</i> / <i>E</i> equil.) /kcal $\text{mol}^{-1}$	$\Delta G^*$ (therm. <i>E</i> / <i>Z</i> equil.) /kcal $\text{mol}^{-1}$	Equilibra- tion half- life of pure <i>Z</i> isomer at 25 °C	Equilibra- tion half- life of pure <i>E</i> isomer at 25 °C	Thermodynamic % <i>E</i> /% <i>Z</i> equilibrium in the dark (at T in °C )
 <b>8</b>	toluene	33.9	30.3	30.5	60 a	83 a	57/43 (100)
	THF	37.4	28.0	27.8	1.2 a	0.9 a	41/59 (63)
	DMSO	45.1	28.2	28.7	1.7 a	4.0 a	65/35
	DCM	40.7	20.3	20.6	87 s	144 s	(24)
	DCM/ $\text{Al}_2\text{O}_3$	40.7	21.8	21.9	18 min	22 min	(24)
 <b>3</b>	toluene	33.9	24.5	24.6	1.2 d	1.4 d	52/48 (52)
	THF	37.4	28.3	28.6	2.0 a	3.4 a	59/41 (63)
	DMSO	45.1	27.7	27.8	0.7 a	0.9 a	52/48 (52)
 <b>16</b>	toluene	33.9	30.5	30.5	83 a	83 a	50/50 (100)
	THF	37.4	29.5	29.5	15 a	15 a	50/50 (63)
	DMSO	45.1	25.4	25.7	6 d	9 d	40/60 (47)
	DCM	40.7	21.2	20.7	6.6 min	2.9 min	(24)
	DCM/ $\text{Al}_2\text{O}_3$	40.7	24.1	22.4	15 h	50 min	(24)
 <b>20</b>	DMSO	45.1	30.6	32.1	99 a	1140 a	87/13 (103)
	Hept/EA 83/17		26.4	27.1	30 d	104 d	77/23 (82)

	DMSO	45.1	30.5	31.7	78 a	614 a	87/13 (114)
<b>30</b>	<hr/>						
	DMSO	45.1	31.8	32.7	750 a	3427 a	77/23 (113)
<b>33</b>	<hr/>						

### 2.2.21 Quantum yield determination

The photochemical quantum yields of the  $Z/E$  and  $E/Z$  photoisomerization  $\phi_{Z/E}$  and  $\phi_{E/Z}$ , respectively were calculated as the ratio between the numbers of isomerized molecules  $n(Z)$  or  $n(E)$  and the number of absorbed photons  $n(h\nu)$  (eq. 9). The published instrumental setup from the group of *E. Riedle* was used for this purpose.<sup>[98]</sup>

$$\phi = \frac{n(h\nu)}{n(\text{molecules})} \quad \text{eq. 9}$$

The photochemical quantum yields  $\phi_{Z/E}$  and  $\phi_{E/Z}$  were determined using eq. 10:

$$\phi = \frac{V_{\text{sample}} \cdot N_A \cdot h \cdot c}{P_0 \cdot f \cdot \lambda_{\text{ex}}} \cdot m_0 \cdot \text{conc}_{\text{sample}} \quad \text{eq. 10}$$

$$\text{with } P_0 = (P_{\text{solv}} - P_{\text{sample}}) \text{ at } t_0 \text{ and } f = \frac{1 + R \frac{P_{\text{sample}}}{P_{\text{solv}}}}{1 - R}$$

where  $V_{\text{sample}}$  is the volume of the sample measured within a UV-Vis cuvette,  $N_A$  is Avogadro's constant ( $6.02214 \cdot 10^{23} \text{ mol}^{-1}$ ),  $h$  is Planck's constant ( $6.62607 \cdot 10^{-34} \text{ Js}$ ),  $c$  is the speed of light ( $2.99792 \cdot 10^8 \text{ ms}^{-1}$ ),  $R$  is the reflection coefficient of the cuvette (at the exit surface with a literature value of 0.0357),<sup>[98]</sup>  $\lambda_{\text{ex}}$  is the excitation wavelength in nm,  $\text{conc}_{\text{sample}}$  is the total concentration of the sample,  $m_0$  is the initial slope of the recorded photokinetic in  $\%Zs^{-1}$  or  $\%Es^{-1}$ . The value  $t_0$  represents the starting point of the measurement (i.e. = 0 s) and is linked to the sample  $Z_0/E_0$  composition of the system prior to irradiation.  $P_0$  represents the absorbed power by the sample and is calculated by subtraction of  $P_{\text{sample}}$  (which is the recorded power read-out at the thermal photometer in the presence of a sample filled cuvette under irradiation) from  $P_{\text{solv}}$ , which corresponds to the power read-out at the thermal photometer under irradiation

of a solely solvent-filled cuvette in place. The weighted initial power factor  $P_0f$  at  $t_0$  was calculated by plotting the relative concentration decrease (in %) of the prevalent species versus the increasing  $Pf$  values.  $P_0f$  was obtained at the 100% value of the abscissa of that plot (see Figure 83 and Figure 85). The potential loss in LED irradiation power on duty caused by warm-up was considered by plotting  $P_{\text{air,start}}$  and  $P_{\text{air,end}}$  against  $t_{\text{start}}$  and  $t_{\text{end}}$  in a linear fashion and consideration of this linear equation at every  $t$  and  $P_{\text{sample}}$  read-out. The slope  $m_0$  was obtained from a linear regression of the initial part of the concentration versus time plot, which is generated by plotting the increasing amount of produced isomer in % on the ordinate versus irradiation time  $t$  in s on the abscissa.

For all quantum yield measurements spectroscopic concentrations of  $1 \times 10^{-5} \text{ molL}^{-1}$  -  $7 \times 10^{-5} \text{ molL}^{-1}$  were used in toluene, dimethyl sulfoxide or heptane / ethyl acetate - the exact values are given in Table 10. The progress of photoisomerizations was followed using UV-Vis spectroscopy by taking into account the known extinction coefficients of both individual isomers. Quantum yields were measured using a 450 nm (*Prizmatix* high power LED coupled to glass fiber) or 467 nm LED for the *Z* to *E* photoisomerizations and a 520 nm (*Prizmatix* high power LED coupled to glass fiber) or 600 nm LED for the *E* to *Z* photoisomerizations. Data evaluation was carried out by the initial slope method.

For measurements in the *E* to *Z* photoisomerization direction the respective solutions were irradiated at a suitable wavelength to obtain the maximum possible content of *E* isomer prior to measurement. The same procedure was carried out to obtain the maximum PSS composition of the *Z* isomer for the quantum yield measurement of the *Z* to *E* photoisomerization direction (see Table 10).

### 2.2.22 Benchmarking: Quantum yield determination of diarylethenes

The photophysical quantum yield measurements for the model compound 4,4'-(perfluorocyclopent-1-ene-1,2-diyl)*bis*(3,5-dimethyl-2-phenylthiophene) **35** were carried out to demonstrate small intrinsic deviations of our quantum yield determination methodologies. This commercially available photoswitch exhibits quantitative switching behavior to its open form with 530 nm and a PSS consisting of 79% to its closed form, which was obtained by irradiation with a 254 nm UV lamp. The pure “ring-closed” isomer was obtained by separation from residual „ring-open“ isomer using reverse phase HPLC (Machery-Nagel VP 250/21 NUCLEODUR Sphinx RP 5  $\mu\text{m}$  column, 15 mLmin<sup>-1</sup>, 35 °C column temperature, 100% Acetonitrile, retention times: open form at 6.1 min), see chromatogram in Figure 76.

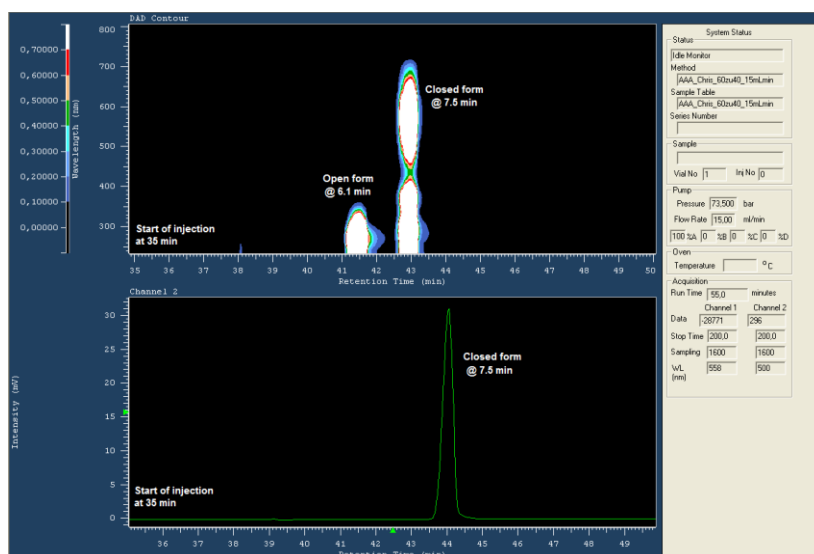


Figure 76: Chromatogram of the HPLC separation of diarylethene **35** in pure acetonitrile. 3D plot of the diode array detector (DAD, top), trace of the Vis detector at 500 nm (bottom). A baseline resolved separation could be obtained.

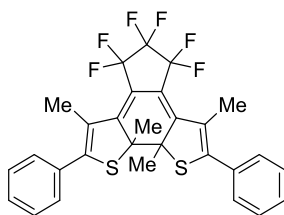


Figure 77: Lewis-formula of **35**.

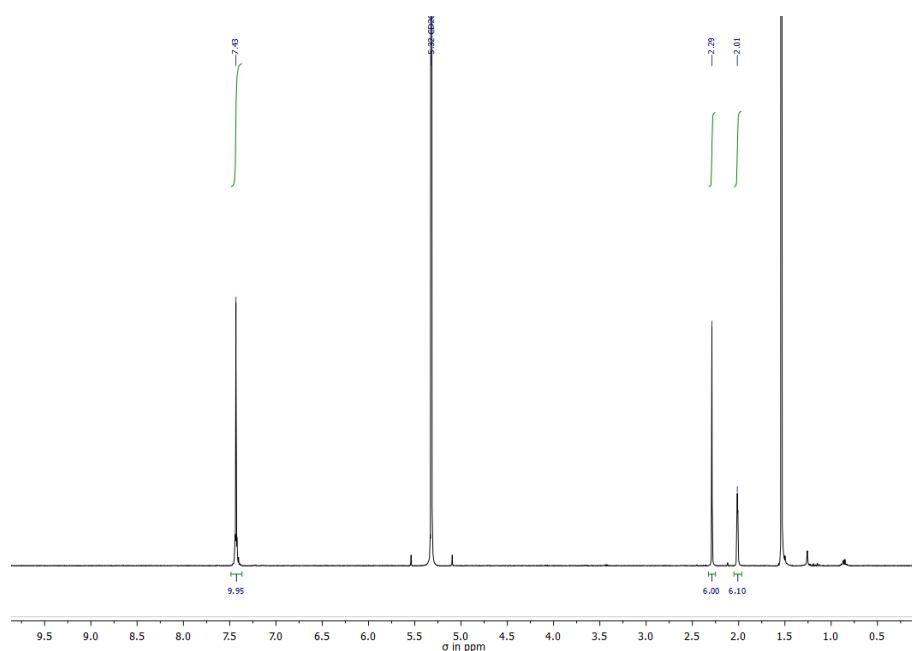


Figure 78:  $^1\text{H-NMR}$  spectrum of the HPLC separated diarylethene **35** (closed form) in dichloromethane- $d_2$ . No open form is visible.



The molar absorptivities were determined by weighing in 0.2738 mg of the compound on a *Sartorius* nanogram balance and dissolving the solid in 10 mL *n*-hexane.

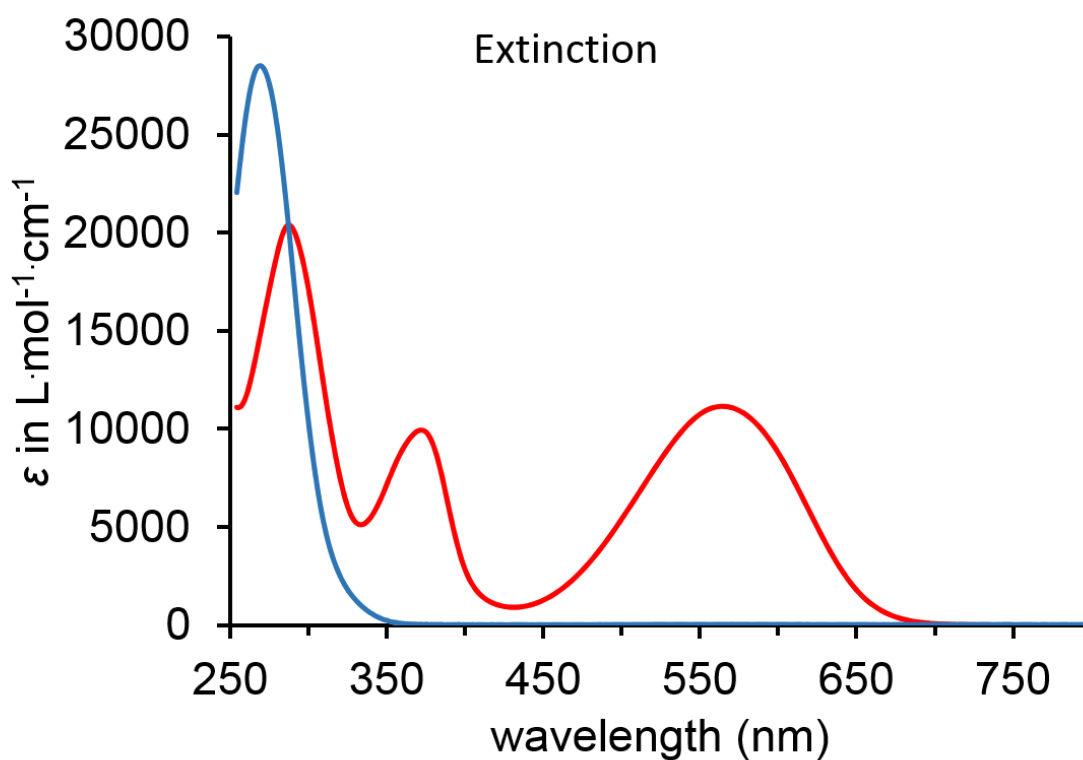


Figure 79: Molar absorption spectra of diarylethene **35** in *n*-hexane. The molar absorptions reported by *Sumi et al.* of 28400 Lmol<sup>-1</sup>cm<sup>-1</sup> at 268 nm for the open form and 10900 Lmol<sup>-1</sup>cm<sup>-1</sup> at 562 nm for the closed form match very well with the recorded data (28517 Lmol<sup>-1</sup>cm<sup>-1</sup> (blue) at 268 nm and 11123 Lmol<sup>-1</sup>cm<sup>-1</sup> at 562 nm (red)).

### 2.2.23 Benchmarking: Quantum yield determination of the ring-opening photoreaction of diarylethene 35 using the *Riedle* setup

Absorption spectra were recorded at different time points during irradiation of ring-closed diarylethene **35** (Figure 80) with a 520 nm LED light source. Power values  $P$  were obtained after irradiation lengths  $>15$  s at the end of each irradiation step (after this time interval the power reading is measured most accurately in correlation to the determined open / closed composition because of the slowness of the utilized power meter) and then used for the absorbed power versus composition plot. Further parameters to consider are: concentration of the sample were determined as  $conc_{\text{sample}} = 5.764 \cdot 10^{-5} \text{ molL}^{-1}$ , cuvette volume  $V_{\text{cuv}} = 2.82 \cdot 10^{-3} \text{ L}$ , power reading with pure solvent *n*-hexane  $P_{\text{solv}} = 3.400 \cdot 10^{-3} \text{ W} \pm 3.3 \cdot 10^{-6} \text{ W}$ , power reading of the LED at measurement start  $t_0$  in air  $P_{\text{air}(0)} = 3.680 \cdot 10^{-3} \text{ W}$  and at the end of the experiment  $P_{\text{air}(\text{end})} = 3.466 \cdot 10^{-3} \text{ W}$  after  $t_{\text{meas}} = 3420 \text{ s}$ .

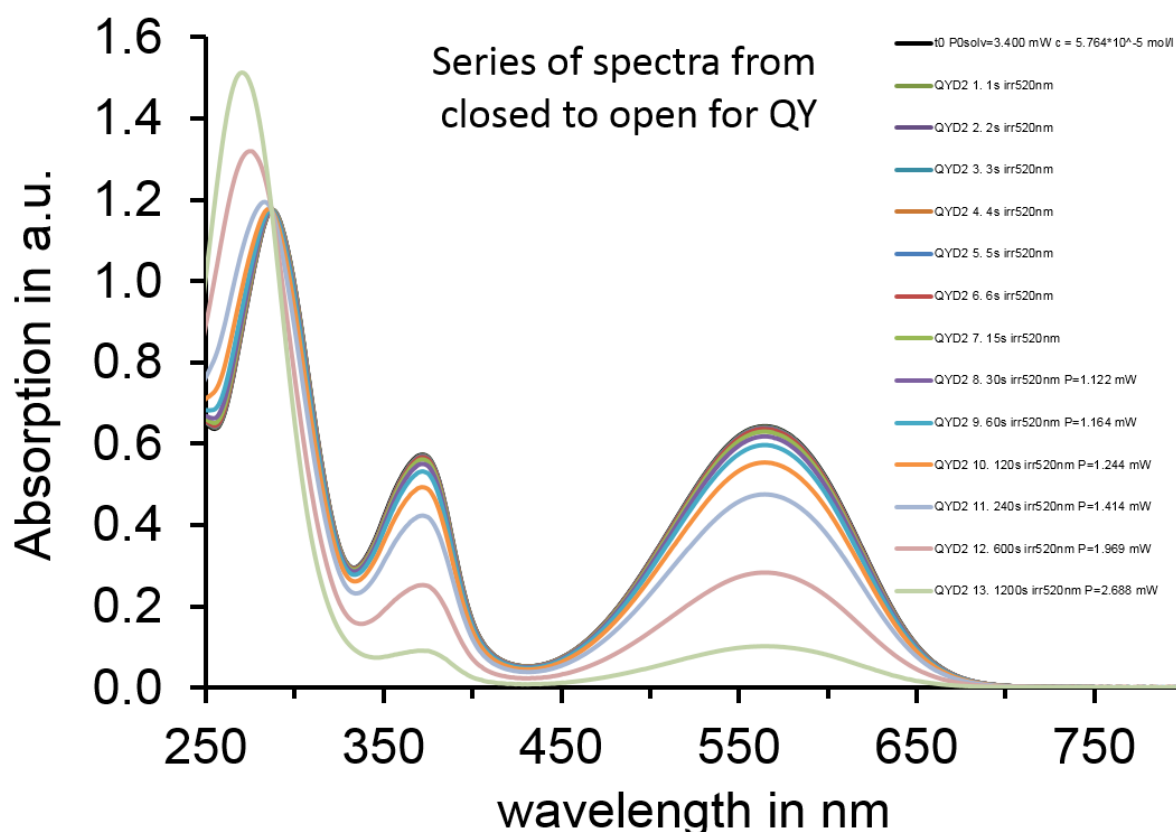


Figure 80: Photoisomerization progress of the ring-opening reaction of diarylethene **35** at different time points in *n*-hexane.

The individual spectra were translated into %open isomer using the known extinction molar absorptivities and were plotted versus time (Figure 81).

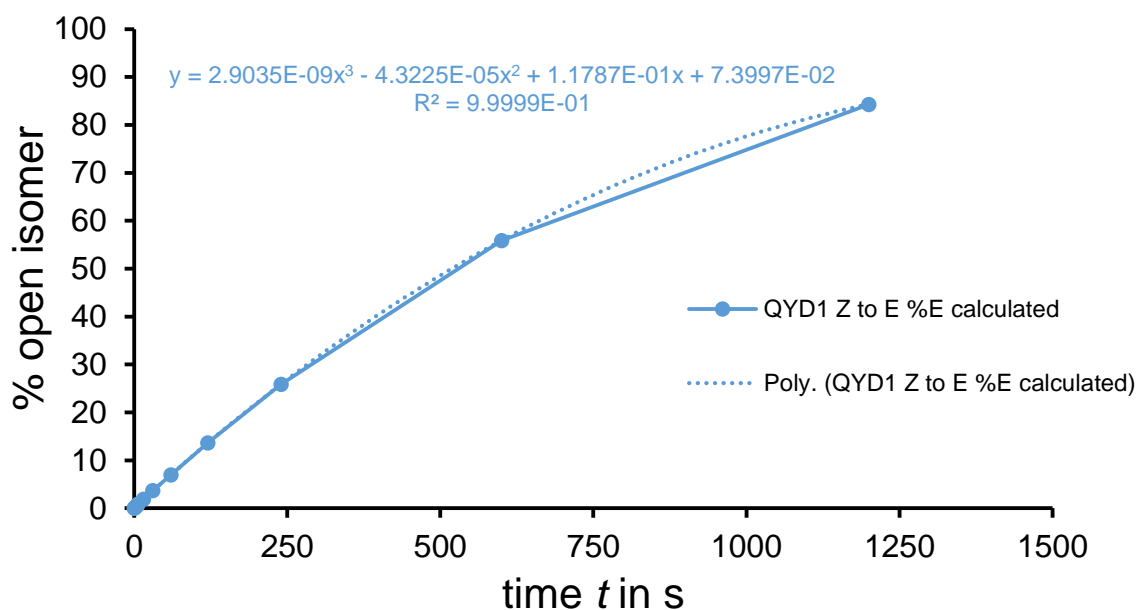


Figure 81: Recorded photokinetic (blue) and polynomial fit (dotted blue) during the photoswitching of diarylethene **35** from 100% closed to 80% open form in *n*-hexane.

Plotting the initial linear slope of the %open isomer  $m_0$  multiplied by the total concentration  $conc_{\text{sample}}$  versus time gives the turnover rate  $m_0 conc_{\text{sample}}$  in  $c_{(\text{open})}s^{-1}$  after linear regression as shown below (Figure 82).

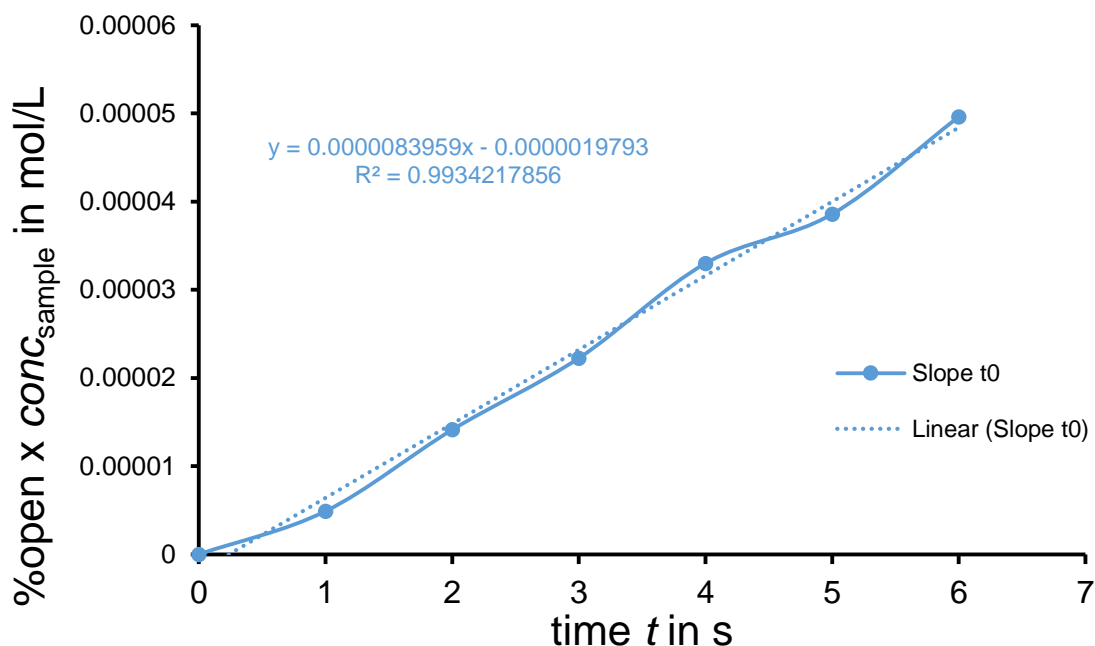


Figure 82: Starting points / linear segment of the photokinetic shown in Figure 81 measured during the photoswitching of diarylethene **35** from 100% closed to 8% open form in *n*-hexane

The transmitted power readings  $P_{\text{sample}}$  were translated into absorbed power  $P$  by the compound relatively to  $P_{\text{solv}}$ . The absorbed power  $P$  at different time points during measurements was plotted as a function of the closed isomer percentage to extrapolate the weighted initial power factor  $P_0f$  at the beginning of the measurement ( $t_0$ ) where the slow responsiveness of the power meter makes a direct measurement impossible (Figure 83). Furthermore, the thermal LED power drift (with active cooling) was considered by measuring the power values of the LED in air from start  $t_0$  to the end of the experiment. The thermal LED power drift was taken in consideration as described in Section 2.7.2 to increase precision and eliminate this systematic error margin.

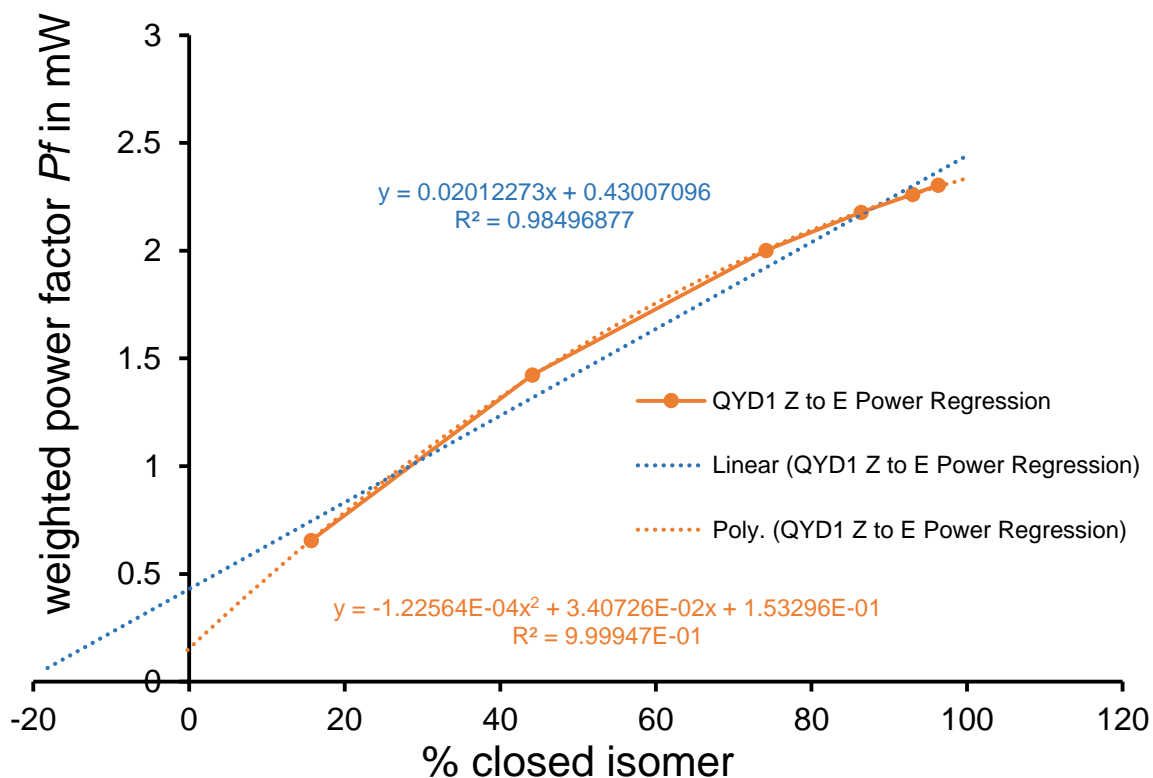


Figure 83: Regression of the weighted power factor versus the percentage of 100% closed diarylethene **35** in *n*-hexane to extrapolate the power value  $P_0f$  at the time  $t_0$ . Linear approximation (broken blue line) and polynomial fit (broken orange line) which improves the obtained quantum yield by 4.6% compared to the linear regression value.

Measured hemiindigos exhibit completely linear behavior in the  $P_0f$  versus %*E* or %*Z* plots until reaching their respective PSS. However, the power plot data points for diarylethene **35** differs from the linear fit, which gives  $P_0f = 2.443$  mW for 100% closed form. A polynomial fit of the data gives a  $P_0f$  value of 2.335 mW, which increases the quantum yield by 4.6% (relative value).

After inserting the extrapolated  $P_0f$  value at  $t_0$  (i.e. at 100% closed isomer) and the slope  $m_0$   $conc_{\text{sample}}$  value in eq. 11:

$$\phi = \frac{V_{\text{sample}} \cdot N_{\text{A}} \cdot h \cdot c}{P_0 \cdot f \cdot \lambda_{\text{ex}}} \cdot m_0 \cdot conc_{\text{sample}} \quad \text{eq. 11}$$

$$\text{with } P_0 = (P_{\text{solv}} - P_{\text{sample}}) \text{ at } t_0 \text{ and } f = \frac{1 + R \frac{P_{\text{sample}}}{P_{\text{solv}}}}{1 - R}$$

A quantum yield for the ring opening photoreaction of 2.69% was determined with the *Riedle* setup in *n*-hexane. This finding reproduces the reported quantum yield of 2.2% (eq. 12) by *Sumi et al.*<sup>[99]</sup> for irradiations at 520 nm according to:

$$\Phi_{\text{closed to open}} = 10^{\left(-2.67 + \frac{526}{520}\right)} \quad \text{eq. 12}$$

In a second independent measurement a 60 / 40 mixture of closed / open form of the diarylethene was used for the determination of the quantum yield for the photochemical ring opening reaction instead of the pure ring closed compound. Irradiation was done with a 520 nm LED. The measurement is shown in Figure 84 utilizing a fifth order polynomial fit from which the extrapolated initial slope  $m_0$  was derived.

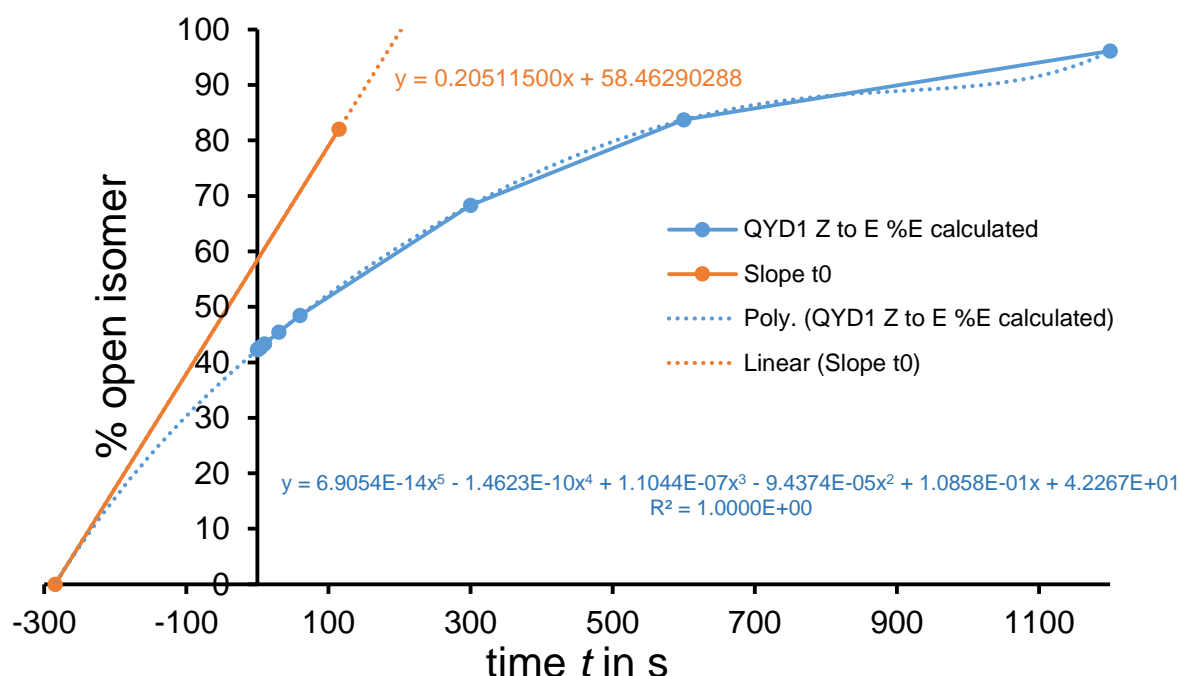


Figure 84: Quantum yield measurement, photokinetic, and polynomial fit for the ring-opening photoswitching reaction of diarylethene **35** at 520 nm irradiation starting from a 60% to 40% closed to open form mixture in *n*-hexane.

The concentration of the sample was  $conc_{\text{sample}} = 4.97 \times 10^{-5} \text{ molL}^{-1}$ , the volume of the cuvette was 2.5 mL, and the weighted power factor  $P_0f = 2.560 \text{ mW}$  was determined by extrapolation of measured power factors  $Pf$  during irradiation as described before (see Figure 85). With the obtained data, a quantum yield of 2.29% was determined in this case, which is in very good agreement with the literature value of 2.2%.<sup>[99]</sup>

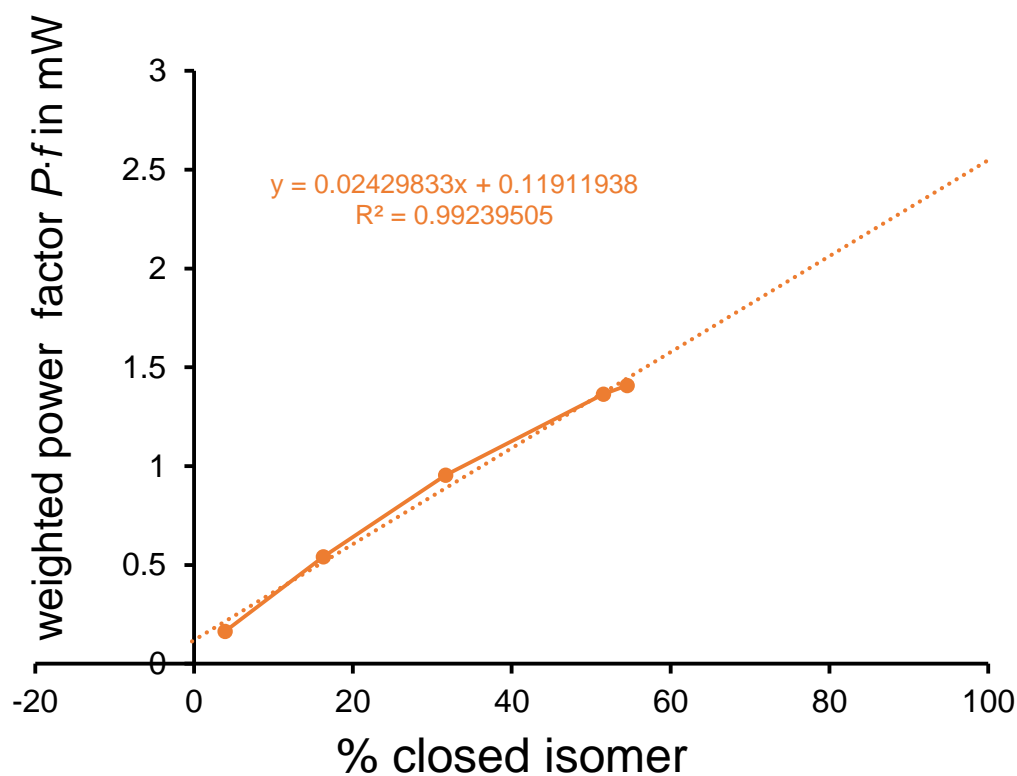


Figure 85: Regression to calculate the power value  $P_0f$  at the time  $t_0$  for the ring-opening photoswitching reaction of diarylethene **35** at 520 nm irradiation starting from a 60% to 40% closed to open form mixture in *n*-hexane. The linear approximation is shown in broken orange lines.

These experiments show that the intrinsic error is small for our methodology as starting from 60% closed form and starting from 100% closed form gave quantum yield values ranging from 2.29% and 2.69%, which is in good agreement to the 2.2% reported by literature.<sup>[99]</sup>

## 2.2.24 Benchmarking: Quantum yield determination of the ring-opening photoreaction of diarylethene 35 using the *Zinth* setup

With this method, the quantum yield was determined by directly irradiating the sample in the UV-Vis spectrometer with a monochromatic laser setup at 473 nm and concomitant continuous tracking of the changing absorption at one selected wavelength (650 nm in this case).<sup>[100]</sup> The obtained slope  $m$  of the initial “linear” segment with neglectable absorption of the ring-open isomer is defined by (eq. 13):

$$m = \sum \frac{\Delta \text{Abs}_{i,i-1}}{\Delta t_i} \quad i = 1, 2, \dots \quad \text{eq. 13}$$

The quantum yield  $\phi_{\text{closed/open}}$  can be determined according to eq. 14:

$$\phi_{\text{closed/open}} = \frac{V \cdot N_A \cdot h \cdot c}{P_{\text{abs}} \cdot \lambda_{\text{ex}} \cdot (\epsilon_{\text{open}} - \epsilon_{\text{closed}}) \cdot d} \cdot m \quad \text{eq. 14}$$

With  $V$  = sample volume in the cuvette (0.0018 L),  $P_{\text{abs}}$  = absorbed power by the sample ( $4.5 \times 10^{-5}$  W),  $\lambda_{\text{ex}}$  = irradiation wavelength ( $4.73 \times 10^{-7}$  m),  $(\epsilon_{\text{open}} - \epsilon_{\text{closed}})$  = difference in molar absorptivity of pure isomers at the read-out wavelength ( $-1954 \text{ Lmol}^{-1}\text{cm}^{-1}$  at 650 nm),  $m$  = slope of absorption change versus time,  $N_A$  = Avogadro constant ( $6.022 \times 10^{23} \text{ mol}^{-1}$ ),  $h$  = Planck constant ( $6.626 \times 10^{-34} \text{ J}\cdot\text{s}$ ) and  $d$  = thickness of cuvette (1 cm).

Linear regression of the initial part of the kinetic plot gave the slope  $m = -4.8836 \text{ s}^{-1}$  (Figure 86 below).



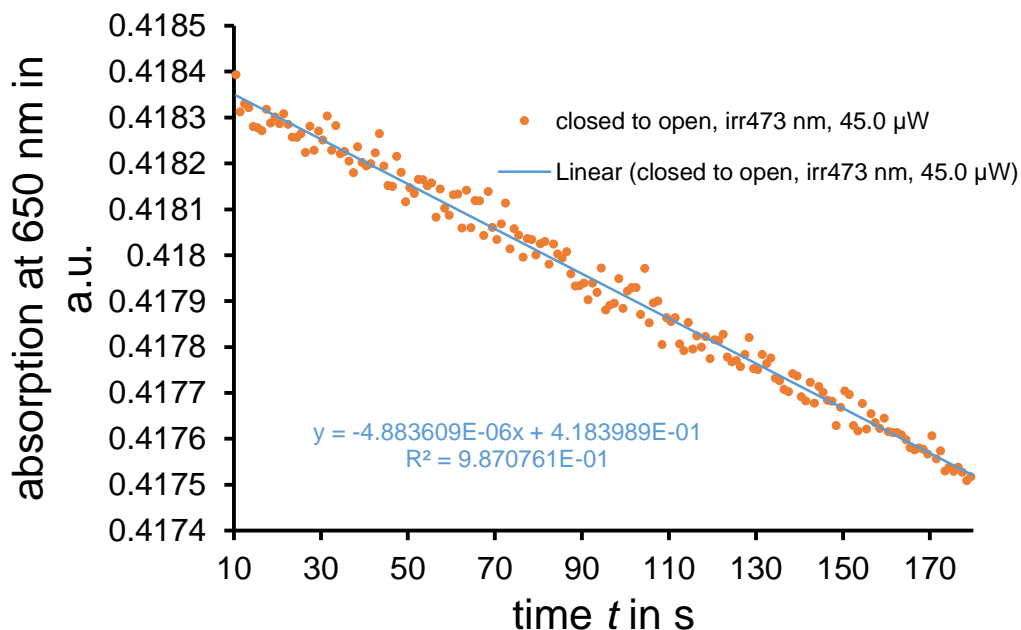


Figure 86: Initial linear part (orange) and slope (blue) for the photoisomerization from 100% closed to open form recorded with the *Zinth* laser setup. Only the part from 10 s to 180 s is shown, as the first seconds gave inaccurate results because of laser adjustment.

The full kinetic plot over 60 min including the fit to the initial slope drawn for comparison is given in Figure 87.

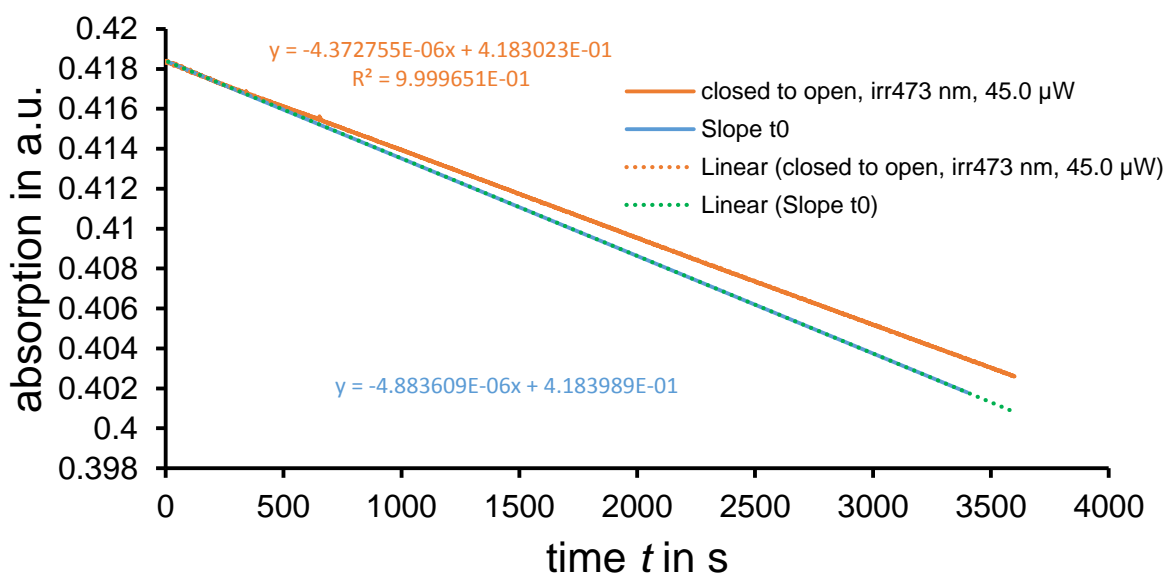


Figure 87: Complete plot for measurements (orange) and slope  $t_0$  (blue and green dotted line) for the photoisomerization from 100% closed to open form recorded with the *Zinth* laser setup. Slope  $t_0$  considers only the data points shown in Figure 86 and is added for comparison.

A red filter glass with the absorption characteristics shown in Figure 88 was used to minimize potential noise hitting the detector by reflections of the laser on the stirring bar. The absorption of the compound at the start and end of the measurement and the excitation / read out wavelengths are shown as well.

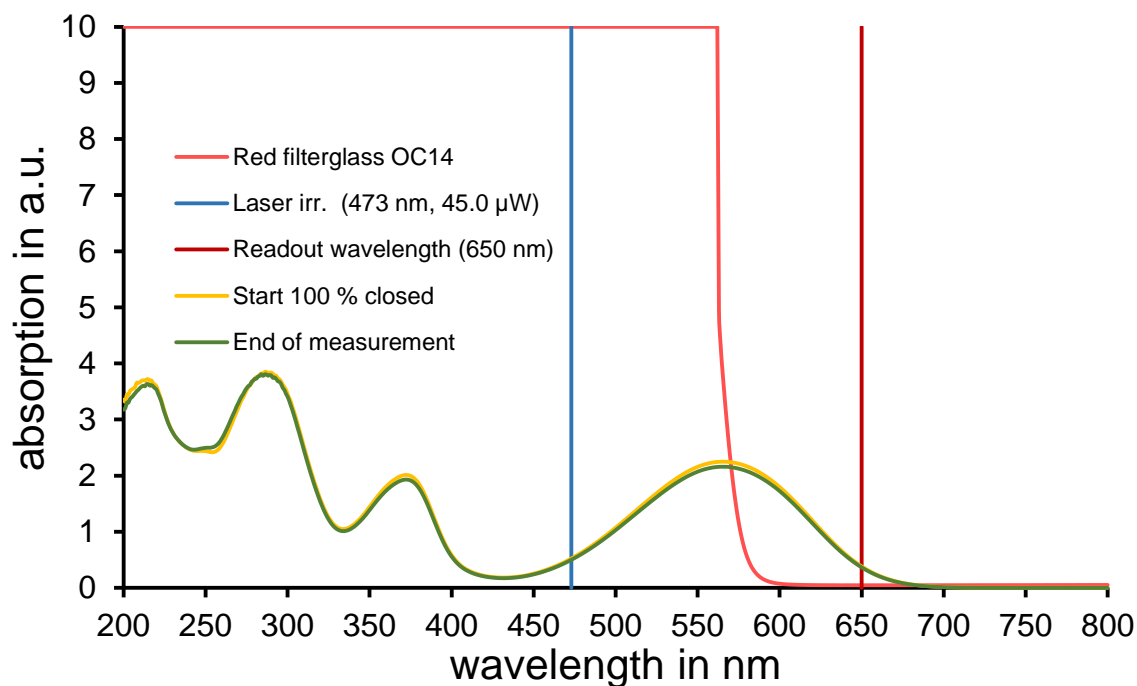


Figure 88: Overlay of the  $t_0$  spectrum of diarylethene **35** in *n*-hexane (yellow),  $t_{\text{end}}$  spectrum (green), irradiation wavelength (473 nm, blue), absorption profile of the low pass filter glass, which was installed between the irradiated cuvette and the detector and readout wavelength (650 nm dark red).

The measurement utilizes 473 nm laser light with 45.0  $\mu\text{W}$  of constant power output throughout the measurement which is completely absorbed by the sample. Measurement of a cuvette with a sample concentration of  $2.1409 \cdot 10^{-4} \text{ molL}^{-1}$  and 1.80 mL sample volume results in a quantum yield of 2.53%, which is in accordance to the previous measurements from the *Riedle* setup<sup>[101]</sup> (2.29%, 2.69%) and the reported literature value (2.2%).<sup>[99]</sup>

With these experiments we could show that the used methodology consistently delivers the reported quantum yields published by *Sumi et al.*<sup>[99]</sup>

## 2.2.25 Quantum yield determination for the photoisomerization reactions of hemiindigo **20** using the *Riedle* setup

Two quantum yield measurements are shown exemplarily for hemiindigo **20** in the following section. The complete data can be found in the literature.<sup>[74, 75]</sup>

The quantum yield measurement for the *Z* to *E* photoisomerization of hemiindigo **20** in 83 / 17 heptane / ethyl acetate at 450 nm started with a mixture of 95.9% *Z*-**20** and 4.1% *E*-**20**. The whole photoconversion kinetic was fitted with a fourth order polynomial and eq. 15 was obtained:

$$y = -2.1622 \times 10^{-7} x^4 + 1.2061 \times 10^{-4} x^3 - 2.4589 \times 10^{-2} x^2 + 2.3202x - 2.0972 \quad \text{eq. 15}$$

Extrapolation of the polynomial to  $y = \%E \text{ isomer} = 0$  gives  $x = -1.7618$ . Differentiation of eq. 15 gives eq. 16:

$$y' = -8.6488 \times 10^{-7} x^3 + 3.6183 \times 10^{-4} x^2 - 4.9178 \times 10^{-2} x + 2.3202 \quad \text{eq. 16}$$

Insertion of the  $x$  value at  $y = 0$  into eq. 16 gives the initial slope  $m_0 = 2.408\%Es^{-1}$  (see Figure 89). The initial power factor at  $t_0$   $P_{0f}$  for 0% *E* isomer was extrapolated to be 2.474 mW, resulting in a quantum yield  $\phi_{Z/E} = 49.26\%$

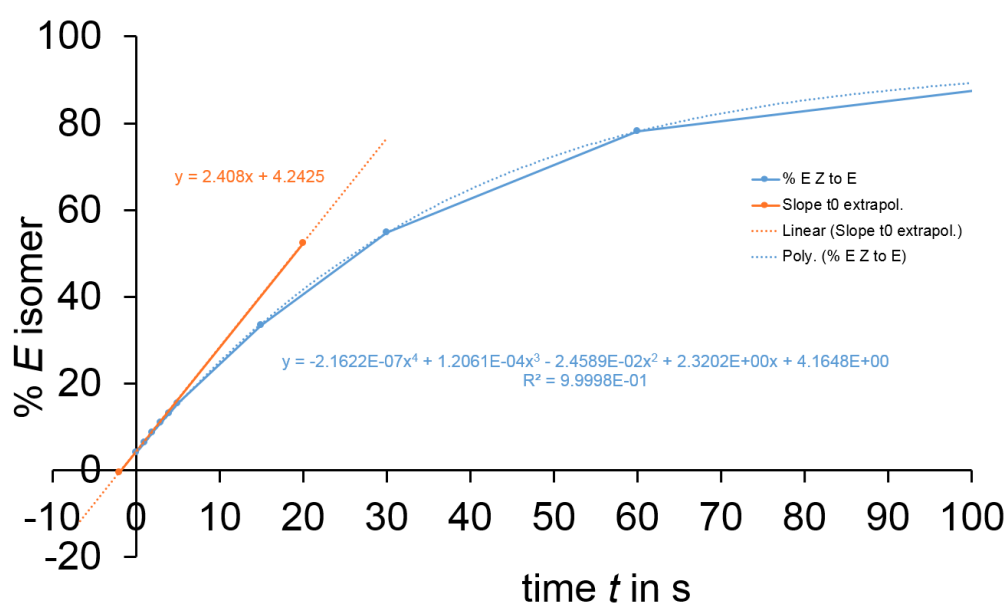


Figure 89: Quantum yield measurement of the *Z* to *E* photoisomerization of hemiindigo **20** in 83 / 17 heptane / ethyl acetate (blue dots) using a 467 nm LED for irradiation and starting from 95.9% *Z*-**20** and 4.1% *E*-**20**. The whole photoconversion

kinetic was fitted with a fourth order polynomial (blue broken line). The polynomial formula is given in blue. Extrapolation of the polynomial to  $y = \%E$  isomer = 0, differentiation and insertion of the corresponding x-value gives an initial slope  $m_0 = 2.408\%Es^{-1}$  (orange formula). Adapted with permission from [75]. Copyright 2018 American Chemical Society.

The quantum yield measurement for the *E* to *Z* photoisomerization of hemiindigo **20** in 83 / 17 heptane / ethyl acetate at 520 nm started with a mixture of 95.8% *E*-**20** and 4.2% *Z*-**20**. The whole photo conversion kinetic was fitted with a fourth order polynomial (eq. 17):

$$y = 5.2765 \times 10^{-10}x^4 + 8.9917 \times 10^{-8}x^3 - 7.5945 \times 10^{-4}x^2 + 4.5415 \times 10^{-1}x + 4.2489 \quad \text{eq. 17}$$

Extrapolation of the polynomial to  $y = \%Z$  isomer = 0 gives  $x = -9.2136$ . Differentiation of eq. 17 gives eq. 18:

$$y' = 2.1106 \times 10^{-9}x^3 + 2.6975 \times 10^{-7}x^2 - 1.5189 \times 10^{-3}x + 0.45415 \quad \text{eq. 18}$$

Insertion of the x value at  $y = 0$  into eq. 18 gives the initial slope  $m_0 = 0.4682\%Zs^{-1}$  (see Figure 90). The initial power factor at  $t_0$   $P_0f$  for 0% *Z* isomer was extrapolated to be 1.779 mW, resulting in a quantum yield  $\phi_{E/Z} = 11.54\%$ .

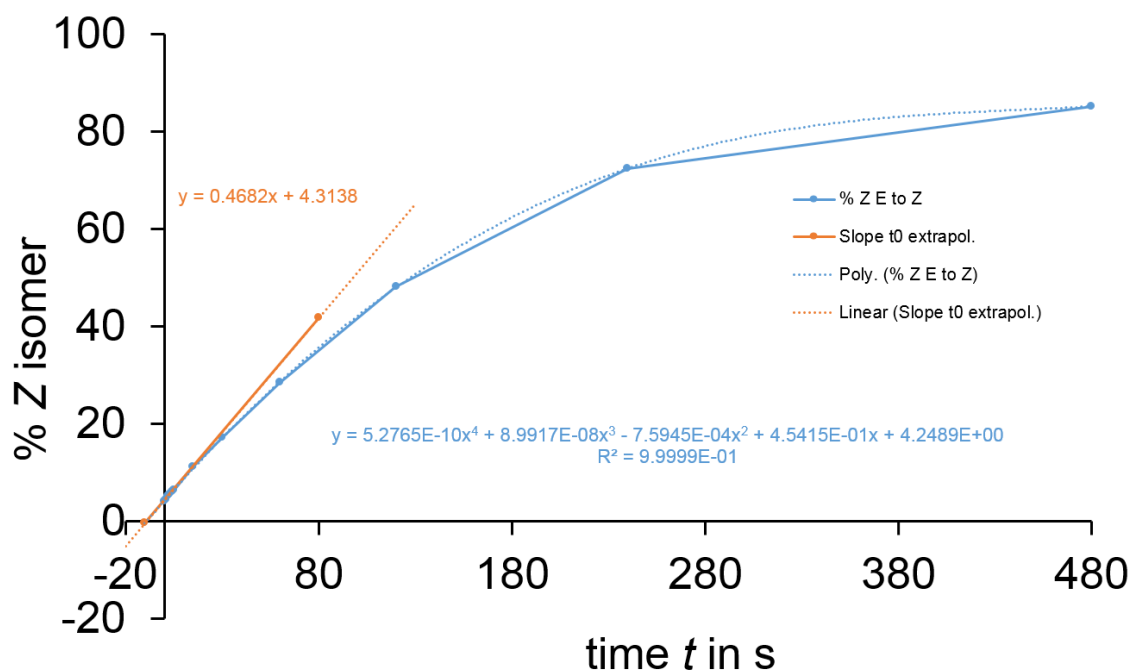
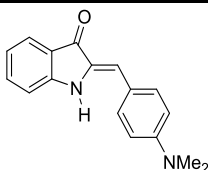


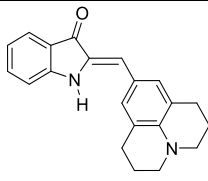
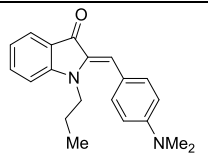
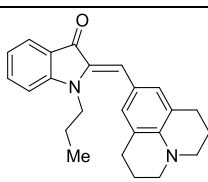
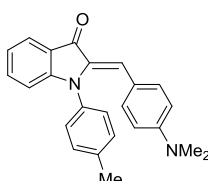
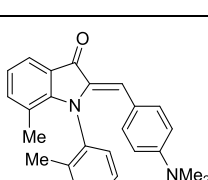
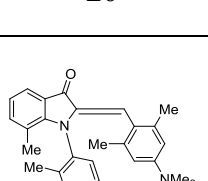
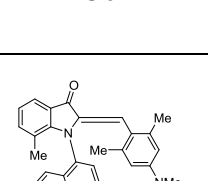
Figure 90: Quantum yield measurement of the *E* to *Z* photoisomerization of hemiindigo **20** in 83 / 17 heptane / ethyl acetate (blue dots) using a 520 nm LED for irradiation and starting from 95.8% *E*-**20** and 4.2% *Z*-**20**. The whole photoconversion kinetic was fitted with a fourth order polynomial (blue broken line). The polynomial formula is given in blue. Extrapolation of the polynomial to  $y = \%Z$  isomer = 0, differentiation and insertion of the corresponding  $x$ -value gives an initial slope of  $m_0 = 0.4682\%Zs^{-1}$  (orange formula). Adapted with permission from <sup>[75]</sup>. Copyright 2018 American Chemical Society.

An overview of selected quantum yield measurements is given in Table 10.

Table 10: Overview of measured quantum yields and experimental measurement parameters using the *Riedle* setup.

HI	Solvent	$\phi_{Z/E}/\%$ (at nm)	$\phi_{E/Z}/\%$ (at nm)	Conc. Sample in mol·L <sup>-1</sup>	V cuvette in mL	$P_0 f_{Z \text{ to } E}$ /E to Z in mW	$m_0$ in %E·s <sup>-1</sup> /%Z·s <sup>-1</sup>
 <b>11</b>	toluene	24 ±2 (467)	9 ±2 (600)	2.948x10 <sup>-5</sup>	2.5	3.978/0.5265	5.116/0.3262
	DMSO	19 ±2 (467)	11 ±2 (600)	3.449x10 <sup>-5</sup>	2.5	4.189/0.4557	3.547/0.27775
	DMSO	15 ±2 (565)	8 ±2 (565)	3.099x10 <sup>-5</sup>	2.5	2.299/3.622	2.125/1.8068
	*	DMSO	18 ±2 (473)	-	6.694x10 <sup>-5</sup>	1.8	0.158/-

2.2.25 QUANTUM YIELD DETERMINATION FOR THE PHOTOISOMERIZATION REACTIONS OF HEMIINDIGO 20 USING THE RIEDLE SETUP

	DMSO	16 ±2 (467)	10 ±2 (600)	2.123x10 <sup>-5</sup>	2.5	1.534/4.336	1.820/3.914
<b>15</b>							
	DMSO	23 ±2 (467)	9 ±2 (600)	2.602x10 <sup>-5</sup>	2.5	4.233/2.479	5.768/1.643
<b>8</b>							
	DMSO	22 ±2 (467)	7 ±2 (600)	1.862x10 <sup>-5</sup>	2.5	0.8107/2.469	1.493/1.895
<b>3</b>							
	DMSO	22 ±2 (467)	2 ±1 (625)	2.239x10 <sup>-5</sup>	2.5	1.185/0.1839	1.811/0.036
<b>16</b>							
	DMSO	33 ±2 (467)	9 ±2 (600)	2.4316x10 <sup>-5</sup>	3.26	1.724/1.138	2.835/0.6314
<b>20</b>	Hept./EA 83/17	49 ±2 (450)	12 ±2 (520)	7.3025x10 <sup>-5</sup>	2.50	2.474/1.779	2.408/0.4682
	DMSO	12 ±2 (450)	12 ±2 (520)	Z: 8.357x10 <sup>-5</sup> E: 9.385x10 <sup>-5</sup>	2.00	2.205/3.252	0.4415/0.7977
<b>30</b>	Hept./EA 93/7	34 ±2 (450)	10 ±2 (520)	9.2871 x10 <sup>-5</sup>	2.50	2.769/5.527	1.540/0.8274
	DMSO	5 ±2 (450)	8 ±2 (520)	3.4797x10 <sup>-5</sup>	2.50	2.589/2.164	0.5234/0.9035
<b>33</b>	Hept./EA 87/13	27 ±2 (450)	9 ±2 (520)	3.8782x10 <sup>-5</sup>	2.50	1.432/1.110	1.506/0.4215

\* Measurement using the *Zinth* setup utilizing a 473 nm laser.<sup>[86]</sup>

### 2.2.26 Conclusion: Quantum yields

A general trend towards higher quantum yields especially for the *Z* to *E* direction when changing from polar to apolar solvents can be observed. This could be explained by a highly polar excited state structure similar to charge-transfer (CT) states, which would be stabilized by a polar environment. Such CT states would lead to competing deexcitation channels, which reduce the photoisomerization quantum yield - similar to the twisted intramolecular charge transfer (TICT) state behavior of donor-substituted twisted hemithioindigos.<sup>[87, 102]</sup> In theory, if the conical intersection shows symmetric pathways towards *Z* or *E* isomer, the maximum obtainable quantum yield should amount 50%. However, sterical pre-twisting of a molecule or specific electronic structures can prearrange and favor the trajectory of the desired photoreaction leading to quantum yields beyond 50%. Rational design of quantum yield efficiencies is therefore very challenging, as these effects cannot be easily predicted.

The introduction of a twisted *ortho*-tolyl aryl axis (hemiindigo **20**) increases the *Z* to *E* quantum yield by 10% compared to the *para*-toluene axis supported by hemiindigo **16** and the *n*-propyl residue found with hemiindigo **8**. The significant drop of photoisomerization efficiency to 2% observed with hemiindigo **16** could be circumvented by remotely twisting the aryl axis away from the stilbene fragment. A possible explanation for this low quantum yield is the collision of the stilbene fragment with the *para*-tolyl residue which tries to planarize to extend its *pi*-conjugation towards the indoxyl core. With the twisted *N*-aryl axis in hemiindigo **20** its quantum yield rises 4.5-fold from 2 to 9%. This also indicates that the *E* to *Z* isomerization power stroke is barely able to twist the conjugated *para*-tolyl out of its way.

It would also be possible for the *para*-tolyl hemiindigo **16** to twist the stilbene fragment around its single bond, which can be discarded as this would cause a significant bathochromic shift, which cannot be observed compared to the *ortho*-tolyl derivative **20** (see Figure 46, Section 2.2.7 for comparison). These findings suggest that the torsion of the *N*-aryl axis is favored, while the stilbene single bond remains within the conjugated indoxyl plane. The stilbene fragment could be regarded as a torsion sensor that reports increased twisting with a bathochromic shift.

- [39] M. Ikegami, T. Arai, *Photochromic and Fluorescence Properties of a Hemiindigo in the Presence of Bovine Serum Albumin*, *Chem. Lett.* **2005**, 34, 492.
- [40] D. V. Berdnikova, *Visible-range hemi-indigo photoswitch: ON–OFF fluorescent binder for HIV-1 RNA*, *Chem. Commun.* **2019**, 55, 8402.
- [46] M. Borowiak, W. Nahaboo, M. Reynders, K. Nekolla, P. Jalinot, J. Hasserodt, M. Rehberg, M. Delattre, S. Zahler, A. Vollmar, D. Trauner, O. Thorn-Seshold, *Photoswitchable Inhibitors of Microtubule Dynamics Optically Control Mitosis and Cell Death*, *Cell* **2015**, 162, 403.
- [53] N. Koumura, R. W. J. Zijlstra, R. A. van Delden, N. Harada, B. L. Feringa, *Light-driven monodirectional molecular rotor*, *Nature* **1999**, 401, 152.
- [59] B. Maerz, S. Wiedbrauk, S. Oesterling, E. Samoylova, A. Nenov, P. Mayer, R. de Vivie-Riedle, W. Zinth, H. Dube, *Making Fast Photoswitches Faster—Using Hammett Analysis to Understand the Limit of Donor–Acceptor Approaches for Faster Hemithioindigo Photoswitches*, *Chemistry – A European Journal* **2014**, 20, 13984.
- [63] A. Baeyer, *Ueber die Verbindungen der Indigogruppe*, *Berichte der deutschen chemischen Gesellschaft* **1883**, 16, 2188.
- [66] L. A. Huber, P. Mayer, H. Dube, *Photoisomerization of Mono-Arylated Indigo and Water-Induced Acceleration of Thermal cis-to-trans Isomerization*, *ChemPhotoChem* **2018**, 2, 458.
- [69] C. Y. Huang, A. Bonasera, L. Hristov, Y. Garmshausen, B. M. Schmidt, D. Jacquemin, S. Hecht, *N,N'-Disubstituted Indigos as Readily Available Red-Light Photoswitches with Tunable Thermal Half-Lives*, *J. Am. Chem. Soc.* **2017**, 139, 15205.
- [74] C. Petermayer, S. Thumser, F. Kink, P. Mayer, H. Dube, *Hemiindigo: Highly Bistable Photoswitching at the Biooptical Window*, *J. Am. Chem. Soc.* **2017**, 139, 15060.
- [75] C. Petermayer, H. Dube, *Circular Dichroism Photoswitching with a Twist: Axially Chiral Hemiindigo*, *J. Am. Chem. Soc.* **2018**, 140, 13558.
- [76] C. Petermayer, H. Dube, *Indigoid Photoswitches: Visible Light Responsive Molecular Tools*, *Acc. Chem. Res.* **2018**, 51, 1153.
- [84] W. Szymański, J. M. Beierle, H. A. V. Kistemaker, W. A. Velema, B. L. Feringa, *Reversible Photocontrol of Biological Systems by the Incorporation of Molecular Photoswitches*, *Chem. Rev.* **2013**, 113, 6114.
- [85] M. Ikegami, T. Suzuki, Y. Kaneko, T. Arai, *Photochromism of Hydrogen Bonded Compounds*, *Molecular Crystals and Liquid Crystals Science and Technology. Section A. Molecular Crystals and Liquid Crystals* **2006**, 345, 113.
- [86] B. Maerz, S. Wiedbrauk, S. Oesterling, E. Samoylova, A. Nenov, P. Mayer, R. de Vivie-Riedle, W. Zinth, H. Dube, *Making fast photoswitches faster--using Hammett analysis to understand the limit of donor-acceptor approaches for faster hemithioindigo photoswitches*, *Chemistry* **2014**, 20, 13984.
- [87] S. Wiedbrauk, B. Maerz, E. Samoylova, A. Reiner, F. Trommer, P. Mayer, W. Zinth, H. Dube, *Twisted Hemithioindigo Photoswitches: Solvent Polarity Determines the Type of Light-Induced Rotations*, *J. Am. Chem. Soc.* **2016**, 138, 12219.
- [88] U. Burger, A. O. Bringhen, *Cyclization Studies with N-Munnich Bases of 2-Substituted Indoles*, *Helv. Chim. Acta* **1989**, 72, 93.
- [89] M. J. Moon, S. K. Lee, J. W. Lee, W. K. Song, S. W. Kim, J. I. Kim, C. Cho, S. J. Choi, Y. C. Kim, *Synthesis and structure-activity relationships of novel indirubin derivatives as potent anti-proliferative agents with CDK2 inhibitory activities*, *Bioorg. Med. Chem.* **2006**, 14, 237.
- [90] V. S. Velezheva, P. J. Brennan, V. Y. Marshakov, *Novel Pyridazino[4,3-b]indoles with Dual Inhibitory Activity against Mycobacterium tuberculosis and Monoamine Oxidase*, *J. Med. Chem.* **2004**, 47, 3455.



- [91] J. C. Antilla, A. Klapars, S. L. Buchwald, *The Copper-Catalyzed N-Arylation of Indoles*, *J. Am. Chem. Soc.* **2002**, *124*, 11684.
- [92] P. Y. Choy, C. P. Lau, F. Y. Kwong, *Palladium-catalyzed direct and regioselective C-H bond functionalization/oxidative acetoxylation of indoles*, *J. Org. Chem.* **2011**, *76*, 80.
- [93] H. Katayama, E. Abe, K. Kaneko, *Synthesis of julolidines from anilines*, *J. Heterocyclic Chem.* **1982**, *19*, 925.
- [94] N. Miyaura, A. Suzuki, *Stereoselective synthesis of arylated (E)-alkenes by the reaction of alk-1-enylboranes with aryl halides in the presence of palladium catalyst*, *J. Chem. Soc., Chem. Commun.* **1979**, 866.
- [95] O. Trapp, S. Bremer, S. K. Weber, *Accessing reaction rate constants in on-column reaction chromatography: an extended unified equation for reaction educts and products with different response factors*, *Analytical and Bioanalytical Chemistry* **2009**, 395, 1673.
- [96] C. M. Connelly, M. H. Moon, J. S. Schneekloth, *The Emerging Role of RNA as a Therapeutic Target for Small Molecules*, *Cell Chem Biol* **2016**, *23*, 1077.
- [97] C. Reichardt, *Solvatochromic Dyes as Solvent Polarity Indicators*, *Chem. Rev.* **1994**, *94*, 2319.
- [98] U. Megerle, R. Lechner, B. König, E. Riedle, *Laboratory apparatus for the accurate, facile and rapid determination of visible light photoreaction quantum yields*, *Photochem Photobiol Sci* **2010**, *9*, 1400.
- [99] T. Sumi, Y. Takagi, A. Yagi, M. Morimoto, M. Irie, *Photoirradiation wavelength dependence of cycloreversion quantum yields of diarylethenes*, *Chem Commun (Camb)* **2014**, *50*, 3928.
- [100] S. Wiedbrauk, B. Maerz, E. Samoylova, A. Reiner, F. Trommer, P. Mayer, W. Zinth, H. Dube, *Twisted Hemithioindigo Photoswitches: Solvent Polarity Determines the Type of Light-Induced Rotations*, *J. Am. Chem. Soc.* **2016**, *138*, 12219.
- [101] U. Megerle, R. Lechner, B. König, E. Riedle, *Laboratory apparatus for the accurate, facile and rapid determination of visible light photoreaction quantum yields*, *Photochem. Photobiol. Sci.* **2010**, *9*, 1400.
- [102] S. Wiedbrauk, B. Maerz, E. Samoylova, P. Mayer, W. Zinth, H. Dube, *Ingredients to TICT Formation in Donor Substituted Hemithioindigo*, *The Journal of Physical Chemistry Letters* **2017**, *8*, 1585.

## 2.3 Chiral hemiindigos - Switching of ECD signals and control over atropisomerization speed and directionality

The previously outlined rationale concerning viable substitution patterns of the hemiindigo chromophore lead to the development of highly bistable and red-shifted photoswitches that can be addressed with green and red light. These properties are favorable for their usage in life sciences, as harmful UV- or blue light is circumvented and longer wavelength light is generally absorbed less by biological tissues, allowing for deeper penetration of the generated light stimuli. Applications within the field of materials science are also imaginable, as the absorption window for orthogonal photoswitching is significantly enlarged.<sup>[74]</sup>

### 2.3.1 Chiral hemiindigos - Designing molecular gearboxes

The introduction of a chiral moiety or axis at the hemiindigo nitrogen and / or the stilbene fragment is a strategy to obtain molecular systems that could pose as potential molecular motors or geared molecular assemblies. The molecular setup of hemiindigo allows the substitution of chiral groups at the indoxyl nitrogen to be potentially driven by the power-stroke of the photoisomerization reaction. Several approaches were envisioned and are outlined below.

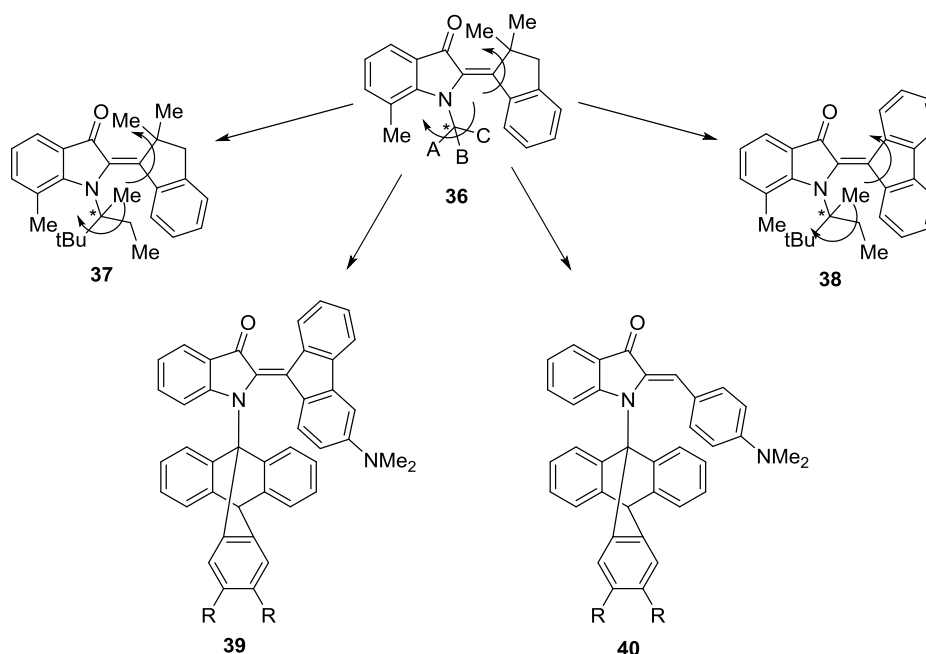


Figure 91: Initial design idea for a unidirectional molecular gearbox (top middle, **36**). A, B and C pose as different substituents to yield a stereocenter at the indoxyl nitrogen. Indanone (top left, **37**) and fluorenone (top right, **38**) stilbene fragments could be used as rigid paddles to drive the adjacent N-C axis. Triptycyl moieties

(bottom, **39** and **40**) could provide better geared engagement between the photochemically driven stilbene fragment and the coupled, mechanically driven, single bond rotation attached to the nitrogen.

Semi-empirical calculations at the PM6 level of theory were performed for the undecorated triptycyl fluorenone derivative by rotating of the dihedral angle at the central double bond (Figure 91, bottom left, **39**) to scrutinize its effect on the triptycyl moiety. Based on the calculations, a geared motion was predicted, in which the rotation of the double bond intermeshes with the triptycyl moiety. This leaves the possibility to create a light-driven gear box on the basis of a hemiindigo photoswitch.

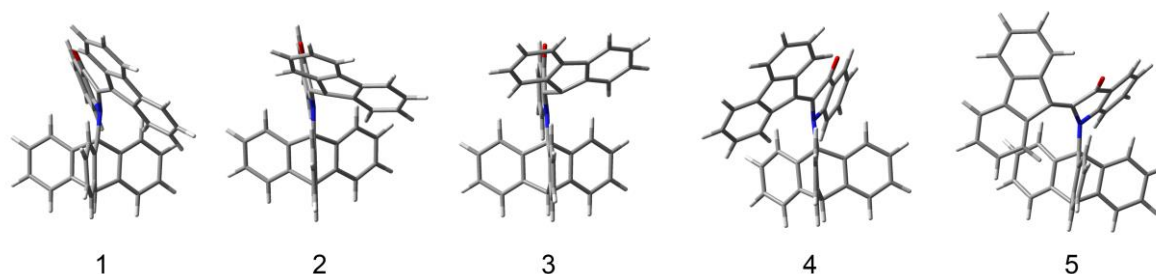
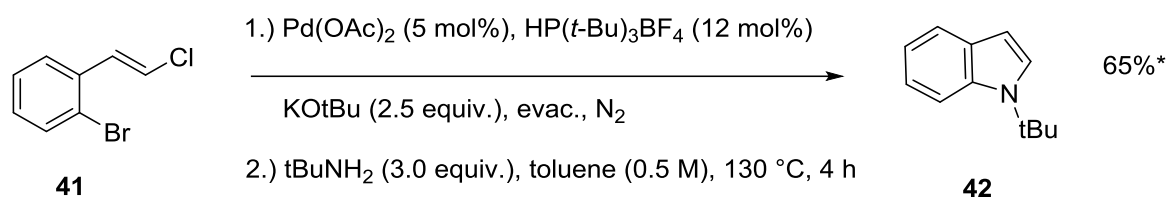


Figure 92: Sequence for a geared, photodriven motion of the triptycyl residue at the indoxyl nitrogen of a model hemiindigo chromophore. One intermeshing step is shown in the sequence from 1 - 5. Calculations were done at the PM6 level of theory, the central double bond was rotated in 90 steps of two degrees each for the full 180° rotation of the double bond.

The *N*-alkylated derivatives (Figure 91, top left and right) are difficult to synthesize as reaction conditions for a successful direct *N*-alkylation by tertiary alkyls could not be found for this chromophore. Therefore, introduction of the sterically more demanding triptycenes was not attempted.

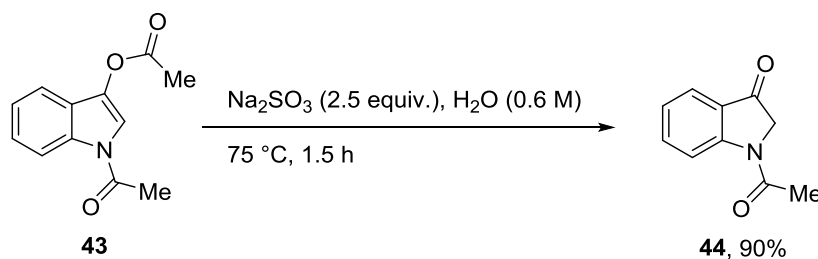
A synthesis described by A. Fletcher,<sup>[103]</sup> however, can circumvent these issues by introducing tertiary alkyls as primary amines to 1-bromo-2-(2-chlorovinyl)benzene **41** yielding indole **42** (Scheme 25).



Scheme 25: Introduction of tertiary alkyl substituents at the indole nitrogen atom. \* = yield reported in the literature.

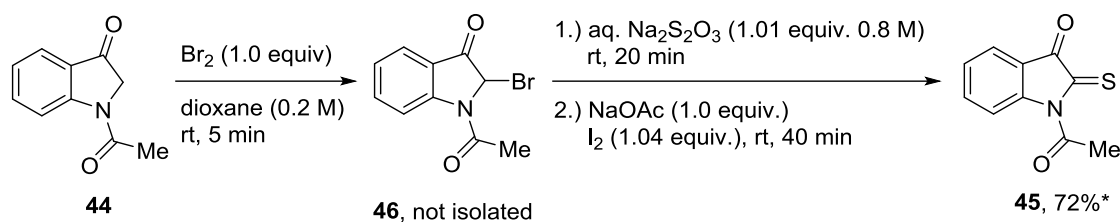
This reaction yields indoles, which can be acetylated to indoxyl acetates, one of the main precursors of hemiindigo photoswitches (see Section 2.2.7). However, viable reaction conditions to condensate ketones instead of aldehydes to indoxyl or indoxyl acetate have not been found yet. The common conditions for the related condensation reaction of ketones with benzothiophenones yielding hemithioindigos utilize boron trihalides as *Lewis*-acids. However, addition of *Lewis*-acids turns indoxyl containing reaction mixtures black within seconds even at -78 °C. This was observed for N-H and also N-R substituted indoxyl acetates or indoxyls, indicating a fast reaction of boron with the nitrogen-containing compounds forming undefined side-products. Piperidine or sodium hydroxide gave no productive reactivity in catalytic and stoichiometric conditions. Another approach towards the desired condensation products consists of strongly increasing the reactivity of the starting materials. This can be realized by an approach commonly used by the *Feringa* group, the *Barton-Kellogg* or *Staudinger*-type diazo-thioketone coupling.

The synthesis of the starting materials for a *Barton-Kellogg*-type coupling were tried with minor success, starting from indoxyl diacetate. The *N*-acetylated substitution was chosen as test reaction as it is already described in the literature.<sup>[104]</sup> The synthesis starts with an ester cleavage of **43** reported by *Shcherbakova et al.* and leads to the *N*-acetylated indoxyl precursor **44**.<sup>[105]</sup> In contrast to the literature, no further purification other than washing with water was necessary to obtain a clean product in very good yields.



Scheme 26: Synthesis of the *N*-acetylated indoxyl building block **44**.

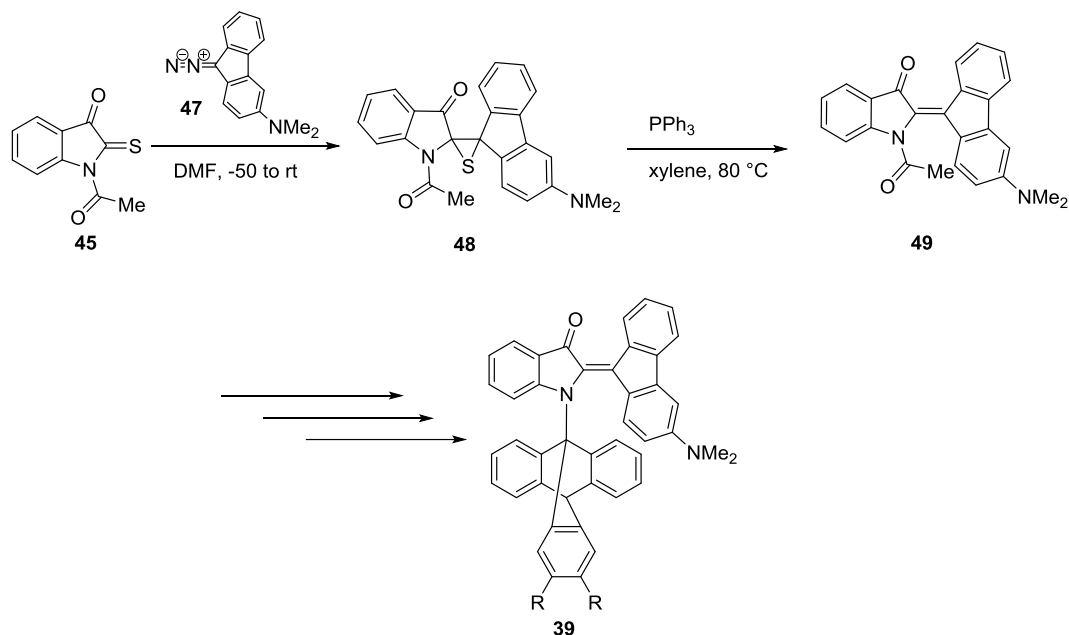
Subsequently, the synthesis of thioketone substituted indoxyl **45** by *V. Velezheva et al.* was carried out starting with a bromination of **44** giving **46** (Scheme 27).<sup>[104]</sup>



Scheme 27: Synthetic route to the 2-thioketone precursor. \* = yield reported by literature.<sup>[104]</sup>

The published route by *V. Velezheva et al.* towards the thioketone **45** did not yield the desired product as crystals but a non-purifiable violet slush.

However, the main target was the coupling reaction of the indoxyl thioketone **45** with a diazofluorenone derivative **47** reported by *M. Ramana* and is outlined below.<sup>[106]</sup> The exemplary conditions are the ones used by *N. Ruangsupapichat* to synthesize crowded olefin motor systems by the *Feringa* group and suggests a possible route to the desired products.<sup>[107]</sup>



Scheme 28: Proposed coupling conditions of the 2-thioketone indoxyl **45** by *V. Velezheva* with the diazofluorenone **47** by *M. Ramana* utilizing the conditions of *N. Ruangsupapichat* yielding intermediate **48** and model system **49** (top). The desired triptycyl derivative **39** is shown below.

These unsuccessful approaches lead to abandoning indanones and fluorenes as stilbene fragments in hemiindigo architectures. However, a geared motion might also be obtained by the photoinduced power stroke of a comparably simple phenyl dimethylamino moiety (Figure 91, **40**). The bulky alkyl substituents were also abandoned in favor of the bigger and more rigid triptycenes (Figure 91, **40**).

## 2.3.2 Acetylated hemiindigos - First route for introduction of axial chirality

To test the feasibility of constructing hemiindigo based molecular motors and machines, introduction of asymmetry into the molecular framework is a first necessity. To this end, introduction of axial chirality seemed to be a very interesting and straight forward possibility. A simple case is establishment of a chiral axis across the N-C bond of by acetylation to yield hemiindigo **2**. As evidenced by crystal structure data and theoretical assessment, the acetyl cannot fully planarize in the *Z* isomeric form for steric reasons (Section 2.2.2, Figure 17 and Figure 94).

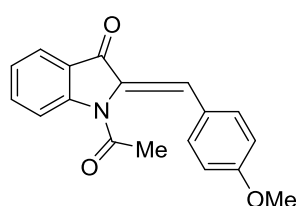


Figure 93: Lewis-formula of hemiindigo **2**.

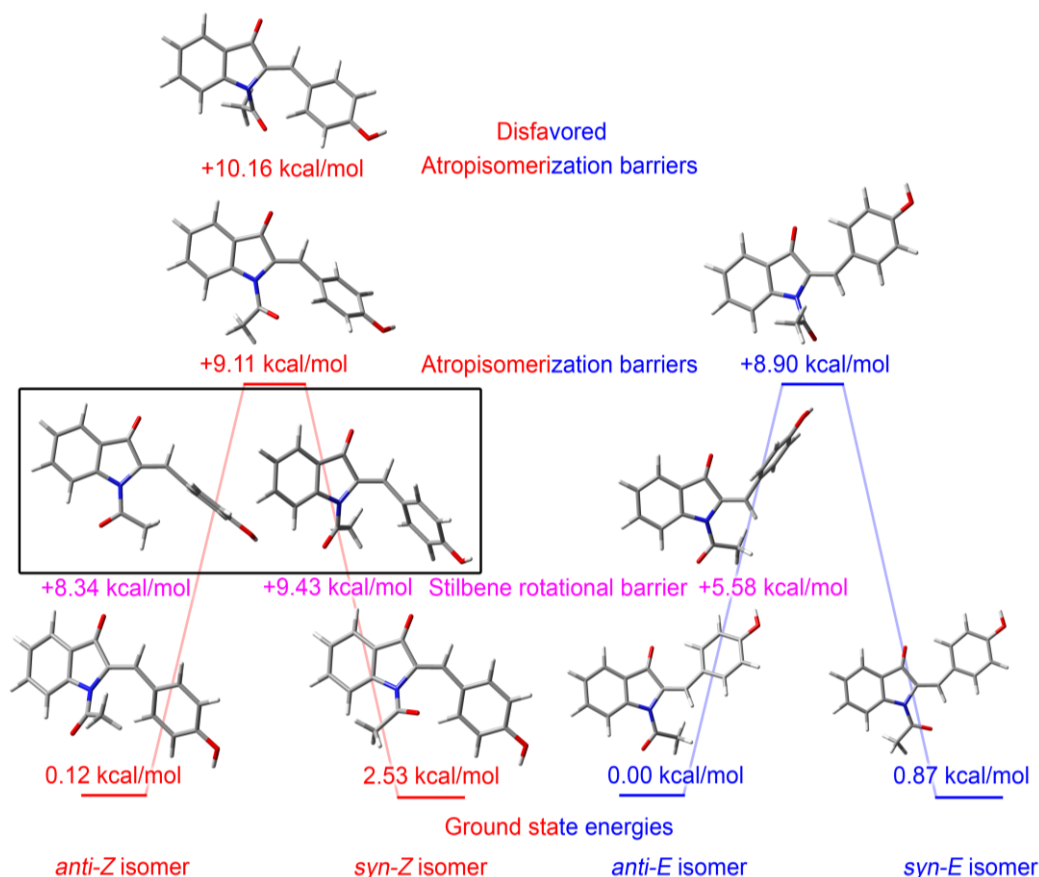


Figure 94: Calculated ground and transition state structures of hemiindigo **2** at the B3LYP/6-311+G(d,p) level of theory. Transition states for the atropisomerizations and the stilbene single bond rotations were found for *Z* and

*E* isomers. The disfavored transition state for the *E* isomer did not converge after several attempts and tweaks. The “+” sign in front of transition state values indicates the energy difference with respect to the lowest ground state of respective *Z* or *E* isomers. Structures in the box both correspond to the transition states of the stilbene rotational barriers of the *anti-Z*-isomer.

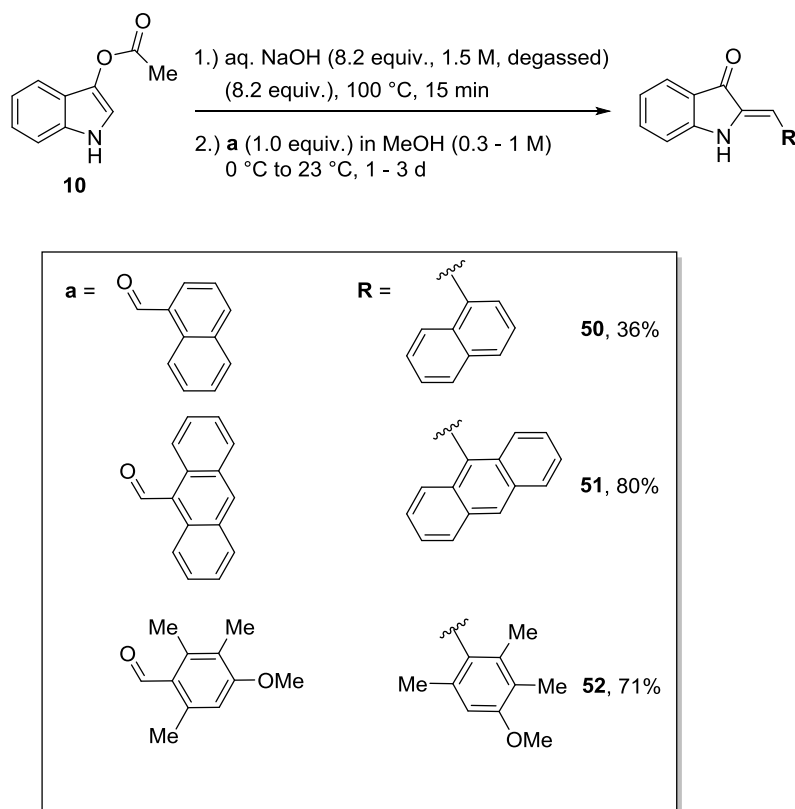
The amide bond in hemiindigo **2** tries to planarize as much as possible and is assumed to be reasonably stable towards rotation (see crystal structure in section 2.2.2, Figure 17), which should result in two diastereomers that should be visible as separate species at low temperatures. However, a splitting and / or intensity difference of the proton signals associated with the acetyl group could not be observed in the <sup>1</sup>H- and NOESY-NMR spectra. Irradiation of the solution with 470 nm over 3 hours to yield predominantly *Z* isomer did also not result in a second set of signals (not shown).

The calculations predicted very low energy barriers for the thermal rotation of the amide bonds in the electronic ground state, which explains why it was impossible to observe separate rotamers at 0 °C via chiral HPLC or <sup>1</sup>H-NOESY cross-peaks at -80 °C. One explanation would be that the methyl group is not bulky enough to lead to a high energy barrier of this rotation.

*K. Jordan* synthesized three different hemiindigos with sterically demanding and / or asymmetric stilbene fragments and functionalized the amine proton with bulky isobutyryl residues during his bachelor’s thesis.

### 2.3.3 Synthesis of hemiindigos with axially chiral and achiral stilbene fragments

Next, introduction of asymmetry via axially chiral stilbene fragments was scrutinized and hemiindigos **50**, **51** and **52** (Scheme 29) were synthesized and evaluated.



Scheme 29: Synthesis of hemiindigos with asymmetric and / or bulky stilbene fragments.

Synthesis of hemiindigos **50**, **51** and **52** from indoxyl acetate **10** with axially chiral and achiral stilbene fragments.

The naphthyl hemiindigo derivative **50** shows a strongly twisted stilbene fragment in the crystalline state (Figure 96), evidencing the presence of pronounced axial chirality in this structure. Unfortunately, the *N*-unsubstituted naphthalene derivative **50** (Figure 97) shows poor photoswitching properties and -stability towards irradiation, which is common for *N*-H unsubstituted hemiindigos without strong electron donors at the *para*-position of the stilbene fragment.



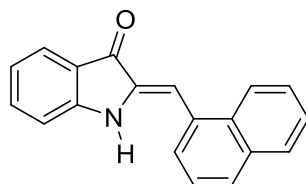


Figure 95: Lewis-formula of hemiindigo **50**.

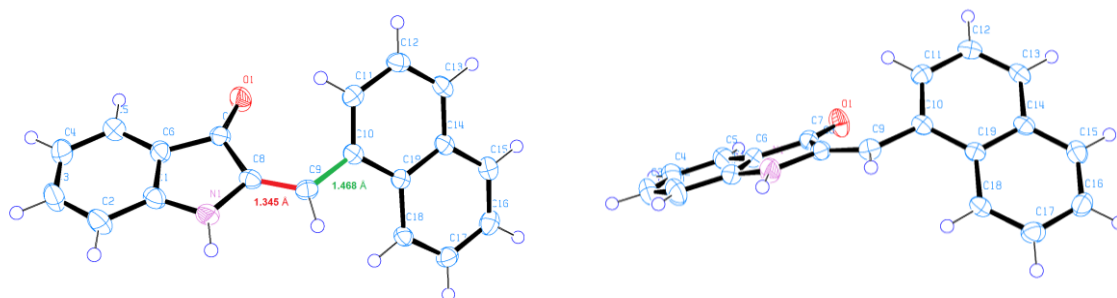


Figure 96: Structure of hemiindigo **50** in the crystalline state. The viewing angle on the right emphasizes the pronounced stilbene single bond twisting. The stilbene single bond dihedral torsion angle amounts to  $42.05^\circ$  for C8-C9-C10-C11 in the *E* isomeric state. The double bond (red) length amounts to  $1.345 \text{ \AA}$  and the single bond (green) to  $1.468 \text{ \AA}$ .

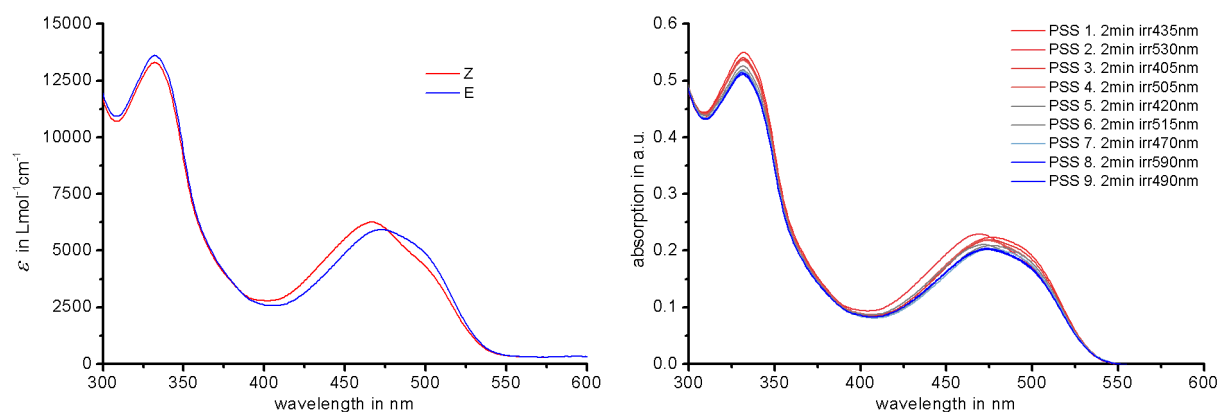


Figure 97: Molar absorption (left) and PSS (right) UV-Vis spectra of hemiindigo **50** in toluene. The isosbestic points are not well defined, verifying the photolability of this compound. The *Z* state cannot be recovered upon irradiation, which could be caused by a low quantum yield for the *E* to *Z* photoisomerization.

The characterization of the *N*-unsubstituted anthracene derivative **51** also revealed a pronounced out of conjugation twisting of the anthracene moiety compared to the indoxyl plane (Figure 99). Because of the symmetry of the anthracene moiety, no chiral axis is established. However, this compound can still be regarded as chiral because of the helicity induced by the twisting in the molecule. Given the expected low energy barrier for thermal helix inversion around the single bond, which connects the anthracene with the central double bond, this molecule is most likely prone to fast thermal racemizations. Again, sub-par photoswitching properties are observed for **51** most likely caused by similar effects as seen with hemiindigo **50**.

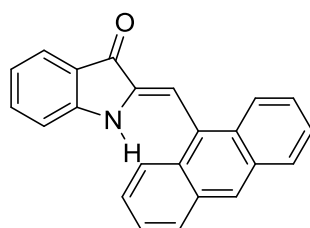


Figure 98: *Lewis*-formula of hemiindigo **51**.

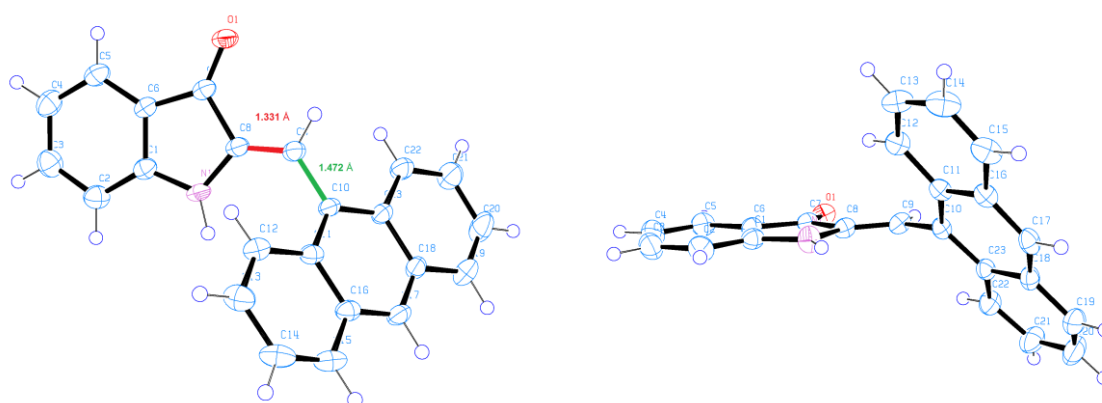


Figure 99: Structure of hemiindigo **51** in the crystalline state. The viewing angle on the right emphasizes the pronounced single bond twisting of the anthracene. The anthracene single bond dihedral torsion angle amounts to  $-59.61^\circ$  for C8-C9-C10-C11 in the *Z* isomeric state, which is about  $17^\circ$  larger than the value of the corresponding torsion angle in the *E* state of naphthyl derivative **50**. The double bond (red) length amounts to 1.331 Å and the single bond (green) to 1.472 Å. Comparison to the *E* form of the naphthyl derivative **50** does not allow for unambiguous conclusions as electronic effects in between *Z* and *E* form might outweigh the influence of the added phenyl core resulting in the observed torsional differences.

The characterization of the N-H unsubstituted anthracene derivative **51** also revealed similar, sub-par photoswitching properties caused by the same effects observed on hemiindigo **50**.

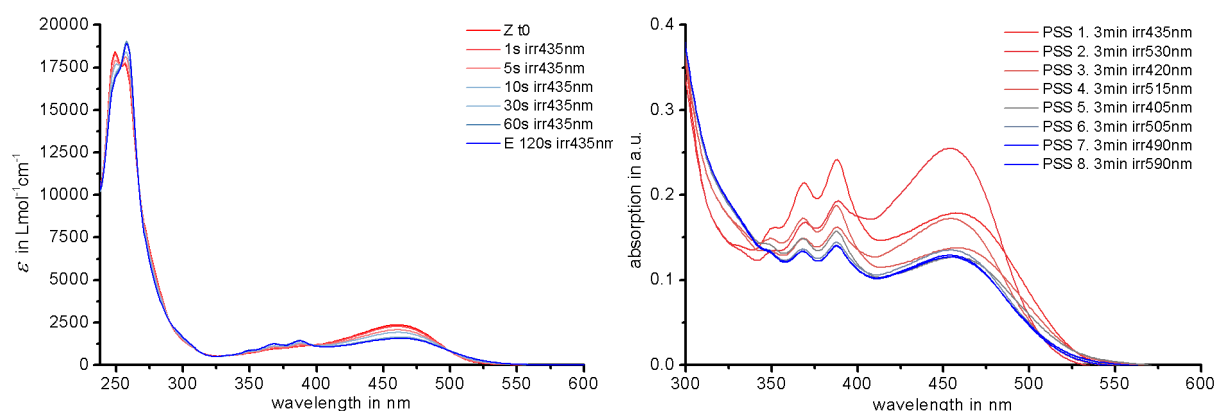


Figure 100: Molar absorption in dichloromethane (left) and PSS (right) UV-Vis spectra of hemiindigo **51** in toluene. The isosbestic points are well defined in dichloromethane, which is not true for toluene, verifying the solvent dependent photolability of this compound as mainly photodegradation can be observed in latter case.

Hemiindigo **52** (Figure 101) with non-symmetric stilbene fragment, which also bears a *para*-methoxy substituent, is highly twisted owed to the presence of *ortho*-methyl groups and possesses axial chirality (Figure 102). The stilbene fragments single bond dihedral torsion angle almost matches the  $59.61^\circ$  angle of the anthracene derivative **51**. An elongation from  $1.331 \text{ \AA}$  (double bond) and  $1.472 \text{ \AA}$  (single bond) compared to the anthracene derivative **51** can be observed, which could be explained by the sterically larger methyl groups. The expected increase in torsion for **52**, which does not take place, is compensated by elongation of the central double- and single bond.

This substitution pattern leads to significantly better photoswitching properties compared to the naphthyl and anthracene derivatives **50** and **51**. The photodegradation is reduced but photochromism and estimated isomer yields in the PSS are still worse compared to the *N* substituted derivatives. However, the three methyl groups and one methoxy group seem to introduce enough electron density towards the central double bond for the molecule to achieve a comparable photostability as the dimethylamino and julolidine derivatives.

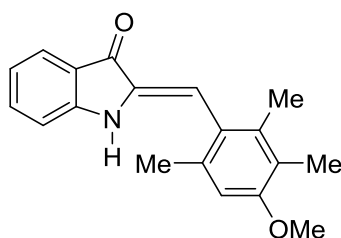


Figure 101: Lewis-formula of hemiindigo **52**.

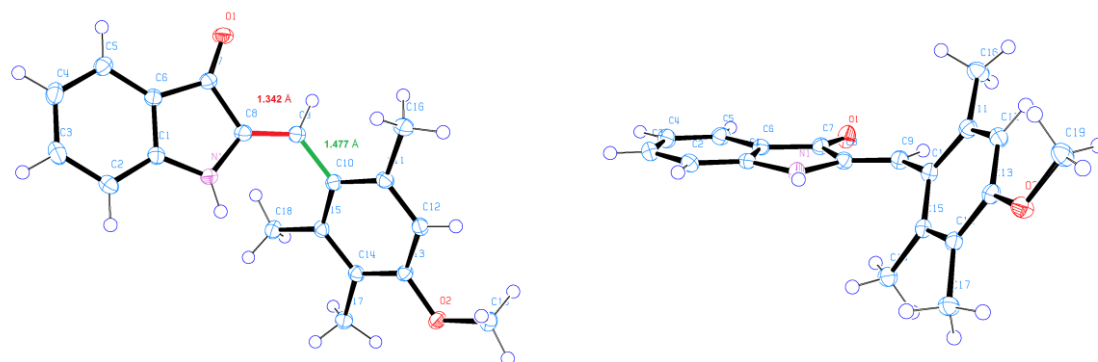


Figure 102: Structure of hemiindigo **52** in the crystalline state. The viewing angle on the right emphasizes the strong stilbene single bond twisting. The stilbene single bond dihedral torsion angle amounts to  $58.25^\circ$  for C8-C9-C10-C15 in the *Z* isomeric state, the double bond (red) length amounts to 1.342 Å and the single bond (green) to 1.477 Å.

The N-H unsubstituted di-*ortho* methylated asymmetric methoxy derivative **52** shows better photoswitching properties and photostability compared to the naphthyl and anthracene derivatives. The photodegradation is reduced compared to **50** and **51** but the photochromism and estimated PSS yields are not on par to the N-H substituted derivatives (see Section 2.2.5). However, the three methyl groups and one methoxy group seem to introduce enough electron density towards the central double bond for the molecule to achieve a comparable photostability as the dimethylamino and julolidine derivatives **11** and **15**.

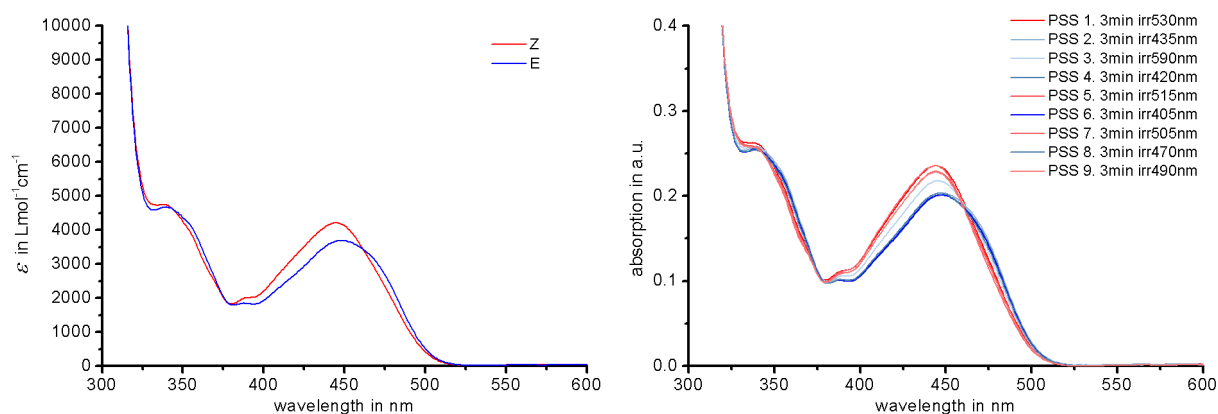
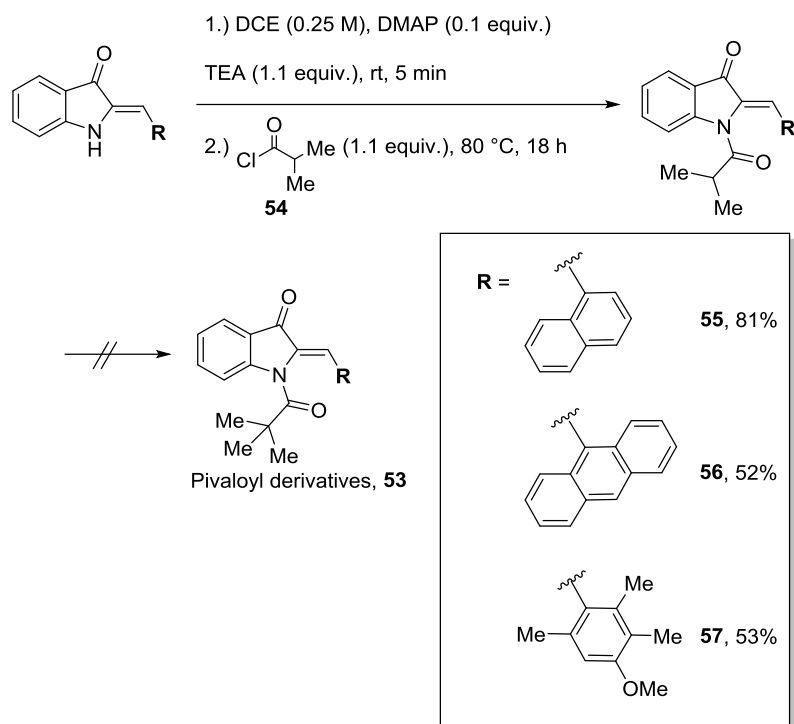


Figure 103: Molar absorption (left) and PSS (right) UV-Vis spectra of hemiindigo **52** in toluene. The isosbestic points are well-defined compared to previously synthesized derivatives **50** and **51** as viable photoswitchability can be observed.

The stilbene single bond dihedral torsion angle almost matches the  $59.61^\circ$  of the anthracene derivative **51**. An elongation from  $1.331 \text{ \AA}$  (double bond) and  $1.472 \text{ \AA}$  (single bond) compared the anthracene derivative **51** can be observed, which could be explained by the sterically larger methyl groups. The expected increase in torsion for **52**, which does not take place, is compensated by elongation of the central double- and single bond.

To yield a photoswitchable system that shows mechanical coupling of motions between two rotatable molecule parts, additional functionality was introduced at the indoxyl nitrogen of hemiindigos **50**, **51** and **52**. If amides are formed or chiral residues are used for this purpose, additional non-symmetric information is introduced into the molecules. Albeit this complicates the conformational analyses, this information is necessary for evidencing gearing processes and the trajectory of light induced and thermal motions.

Initially, the introduction of a pivaloyl residue was tested under varying conditions, which yielded highly unstable products **53** that could only be observed by immediate subsequent mass spectrometry analysis. Chromatographic purification did not provide the target compounds. The change to isobutyryl chloride **54** made desired products **55**, **56** and **57** obtainable in moderate to good yields.



Scheme 30: Introduction of an isobutyryl moiety via 4-dimethylaminopyridine (DMAP) mediated nucleophilic catalysis in dichloroethane (DCE) utilizing triethylamine (TEA) as base. The introduction of a pivaloyl residue did not yield products **53**.

A drawback of the isobutyryl substituent is the  $\alpha$ -acidic proton located at the isopropyl residue, which can be deprotonated by triethylamine and undergoes a nucleophilic attack on another isobutyryl chloride molecule. Also, this acylation reaction seems to be very specific towards the used solvent and base, as only chlorinated solvents and triethylamine as base showed any reaction progress. The change to sodium hydride as base or *N,N*-dimethylformamide, tetrahydrofuran, toluene or pyridine as solvents did not result in any significant product formation.

The main goal for the synthesis of these compounds was answering the question on how to decorate the photoswitchable hemiindigo chromophore to achieve observable feedback between the light-induced power stroke of the stilbene fragment and an asymmetric group in its proximity. The acyl groups were the only potential asymmetric groups with relatively high sterical demand that could be introduced at this time.

The naphthyl bearing hemiindigo **50** was acylated with isobutyric acid chloride yielding hemiindigo **55** (Figure 104) to explore the properties of two asymmetric units that can be switched from a close interaction in the *Z* isomer to no interaction in the *E* isomer. The  $^1\text{H-NMR}$  solution spectra showed no split signals of diastereomeric rotamers in either the *E* or *Z* isomeric state (Figure 105).

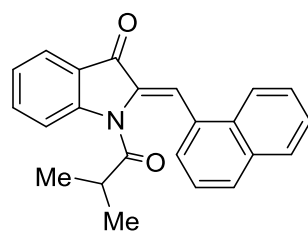


Figure 104: *Lewis*-formula of hemiindigo **55**.

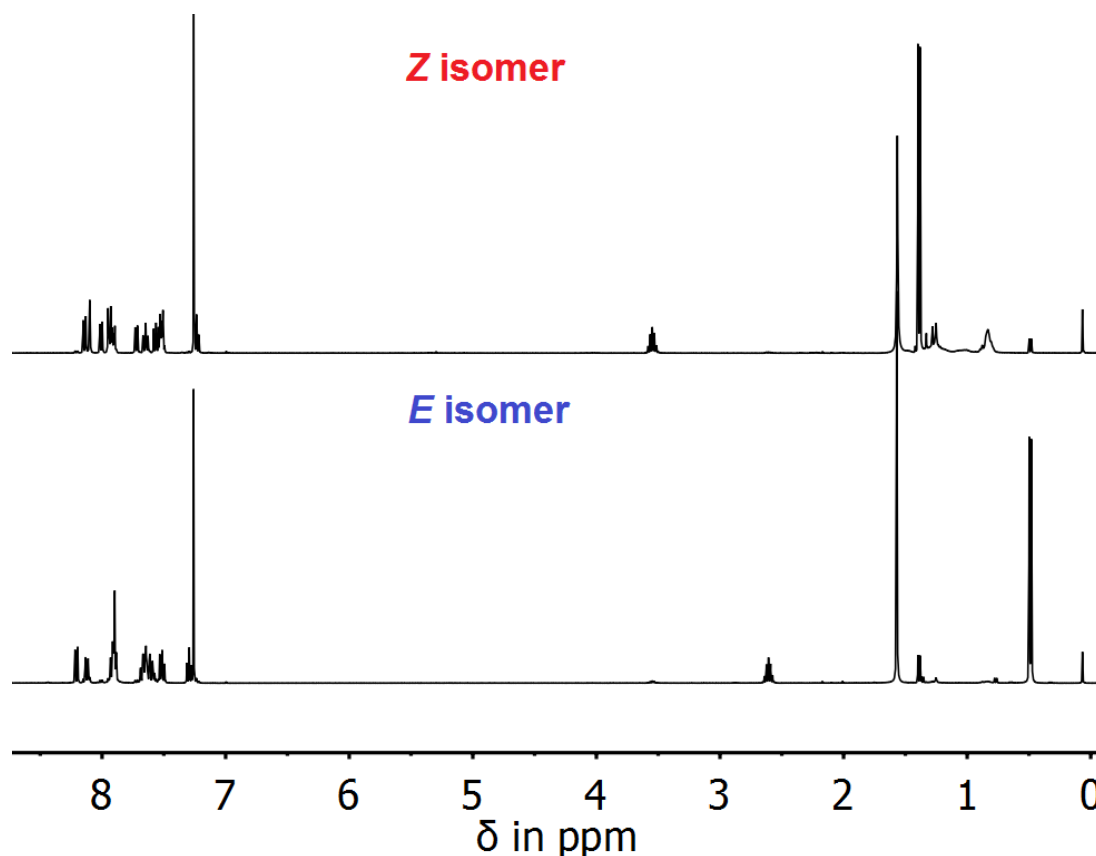


Figure 105:  $^1\text{H}$ -NMR spectrum of HPLC separated *Z* and *E* isomers of hemiindigo **55** in chloroform-*d* at 27 °C.

The lack of observing different diastereomeric rotamers of **55** in solution can be explained by the low energy barriers for rotation around the chiral axes in hemiindigo **55** single bond amounting to 8.32 kcal/mol for rotation of the naphthyl fragment in the *Z* state and 4.80 kcal/mol for the same rotation in the *E* isomeric state as calculated at the B3LYP/6-311+G(d,p) DFT level of theory (see Figure 106).

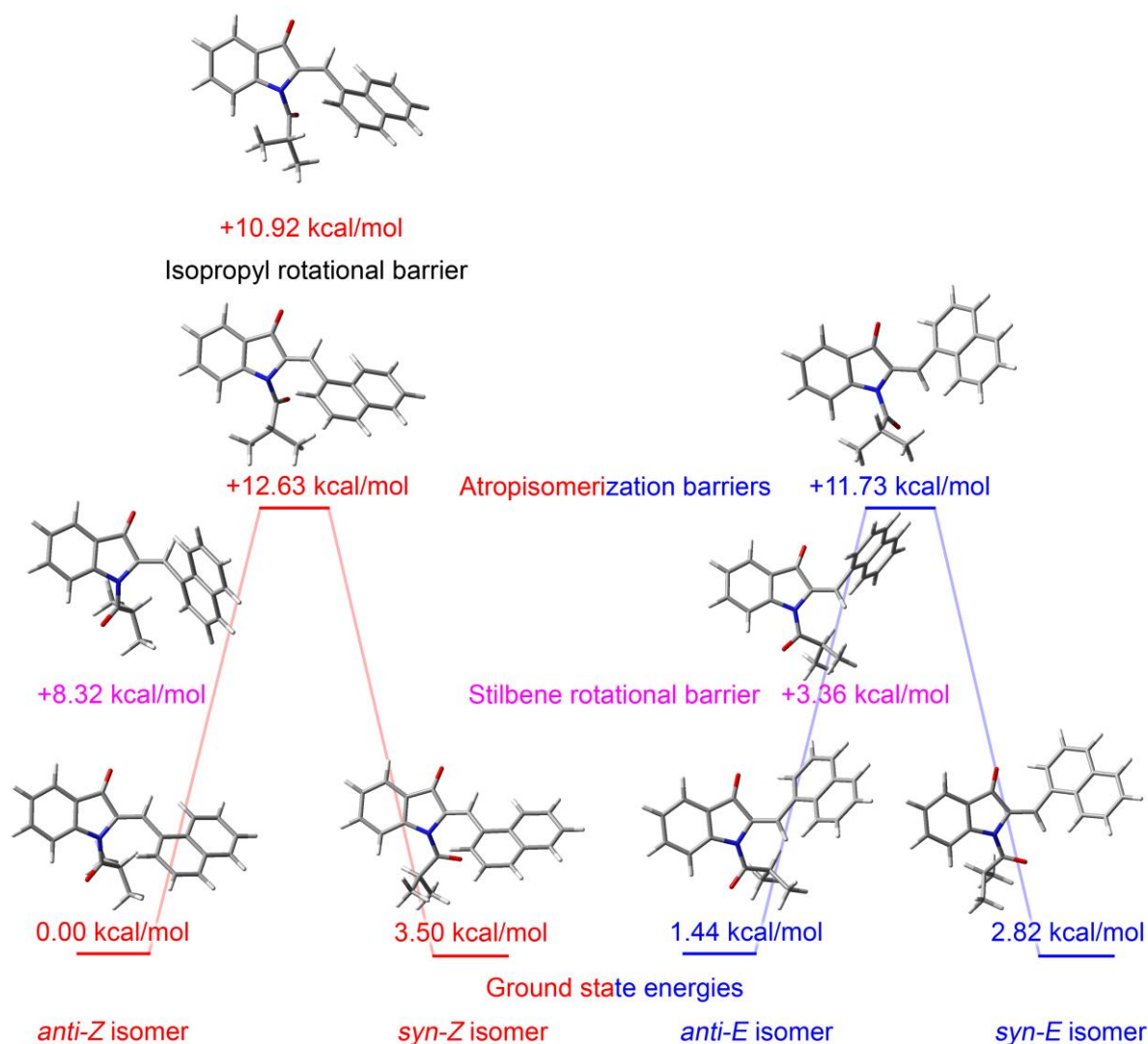


Figure 106: Calculated ground and transition state structures of hemiindigo **55** at the B3LYP/6-311+G(d,p) level of theory. Transition states for the atropisomerizations for *Z* and *E* isomers and the naphthyl single bond rotation for *anti*-diastereomers were found. The “+” sign in front of transition state values indicates the energy difference with respect to the lowest ground state of the respective *Z* or *E* isomers. The *syn*- transition states of the stilbene single bond rotation, however, did not converge after several attempts and tweaks. The isopropyl C-C single bond rotation and the methyl group rotation (+7.26 kcal/mol when adjacent to the carbonyl group, not shown) were found only for the *Z* isomer.

As freezing rotations with energy barriers this low is impossible at -80 or -105 °C, no split signals should be observable. Theoretically, the acyl rotation could be sufficiently slowed down at -105 °C and thus further experiments have to be carried out to scrutinize this system.



UV-Vis spectroscopy showed photoswitching into the *E* state but no photoisomerization back to the *Z* state, which renders **55** an impractical photoswitch in toluene (Figure 107).

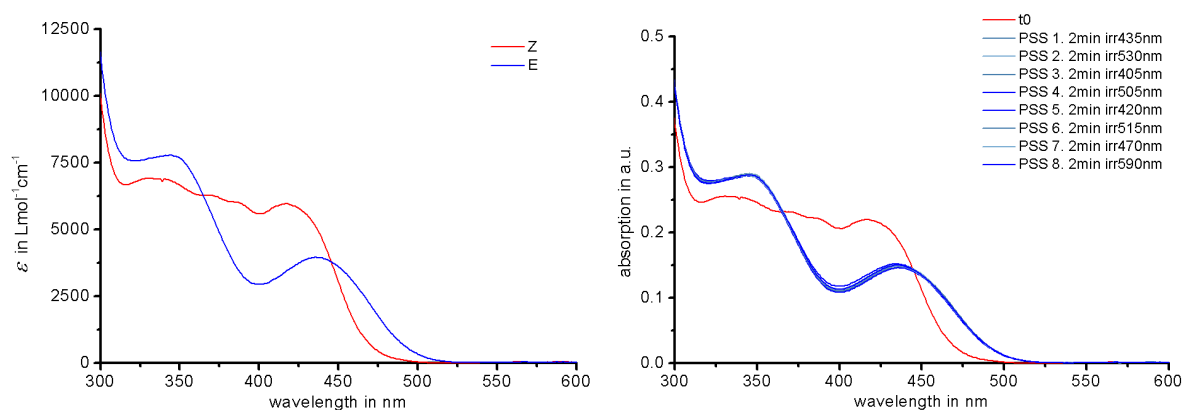


Figure 107: Molar absorption (left) and PSS (right) UV-Vis spectra of hemiindigo **55** in toluene. The isosbestic points are not well defined, verifying the photolability of this compound. The *Z* state cannot be recovered upon irradiation.

The inability to efficiently perform the photoinduced *E* to *Z* isomerization can also be observed for hemiindigo **7** in toluene (see Section 2.2.3). This can be caused by a poor quantum yield and / or by a weak power stroke towards the sterically more crowded *Z* isomer.

$^1\text{H-NMR}$  signal splitting cannot be expected for the acylated anthracene derivative **56** (Figure 108) at ambient temperatures as the amide single bond supports an expected rotational barrier below 13 kcal/mol (see Figure 107 for the naphthyl derivative **55**) to obtain stable rotamers. However, cooling to  $-80\text{ }^\circ\text{C}$  could be a successful approach and has yet to be tried for this compound.

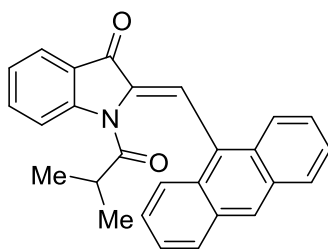


Figure 108: *Lewis*-formula of hemiindigo **56**.

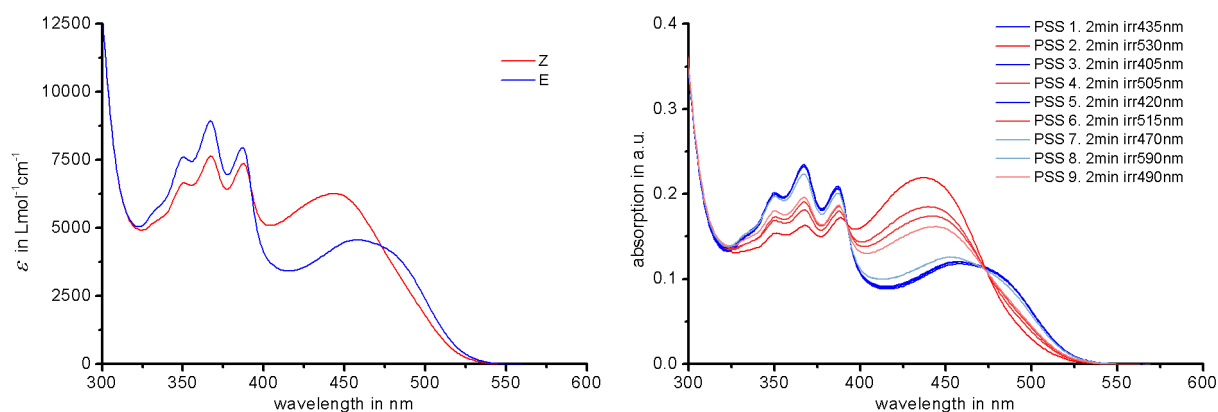


Figure 109: Molar absorption (left) and PSS (right) UV-Vis spectra of hemiindigo **56** in toluene. The isosbestic points are well defined, verifying the restored photostability of this compound after acylation. Photoswitching proceeds readily in both directions and a strong red-shift of about 60 nm compared to the naphthyl derivative **55** can be observed.

The often observed instability of N-H unsubstituted hemiindigos could be circumvented by acylation of the anthracene derivative **51**. Signal splitting could not be observed at ambient temperatures as the thermal *N*-acyl bond barrier is estimated to be below 16 kcal/mol.

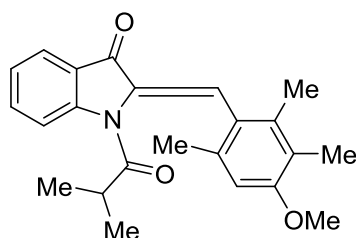


Figure 110: *Lewis*-formula of hemiindigo **57**.

The asymmetric di-*ortho*-methyl *para*-methoxy stilbene substituted hemiindigo **57** was also acylated to scrutinize the effects of the isobutyryl group on photoswitching within a hemiindigo with axially chiral stilbene fragment possessing considerable rotational barriers.

Hemiindigo **57** showed viable photoswitching with visible light in both *Z* to *E* and *E* to *Z* directions (Figure 111).

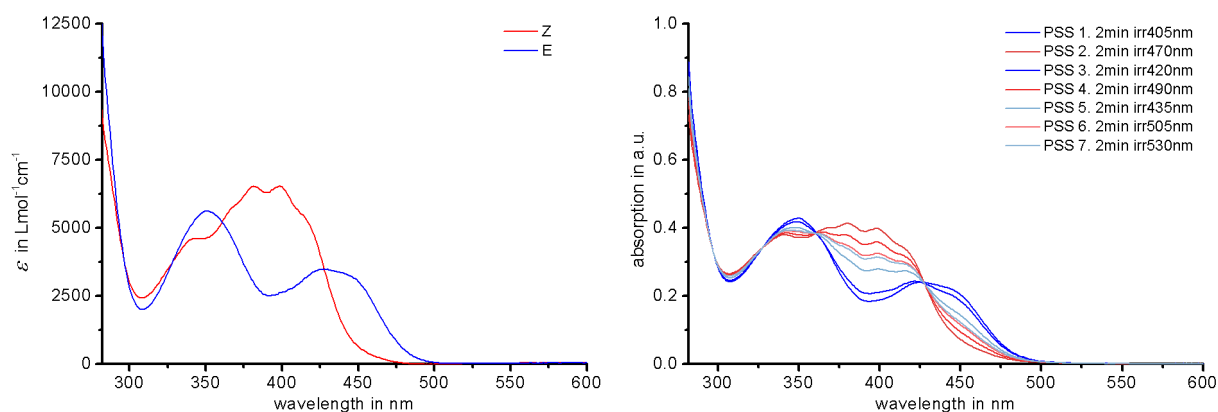


Figure 111: Molar absorption (left) and PSS (right) UV-Vis spectra of hemiindigo **57** in toluene. The isosbestic points are well defined, verifying the photostability of this compound. Photoswitching proceeds readily in both directions, a large blue-shift of approx. 60 nm can be observed compared to the anthracene derivative. A fine structure can be seen for the Z isomer, which can be attributed to multiple, discernable oscillation modes with smaller full widths at half maximum (FWHM).

Introduction of the *ortho*-methyl groups increases the single bond rotational barrier of the stilbene fragment significantly compared to the naphthyl compound **55**. This can be observed via  $^1\text{H-NMR}$  at ambient temperatures (Figure 112).

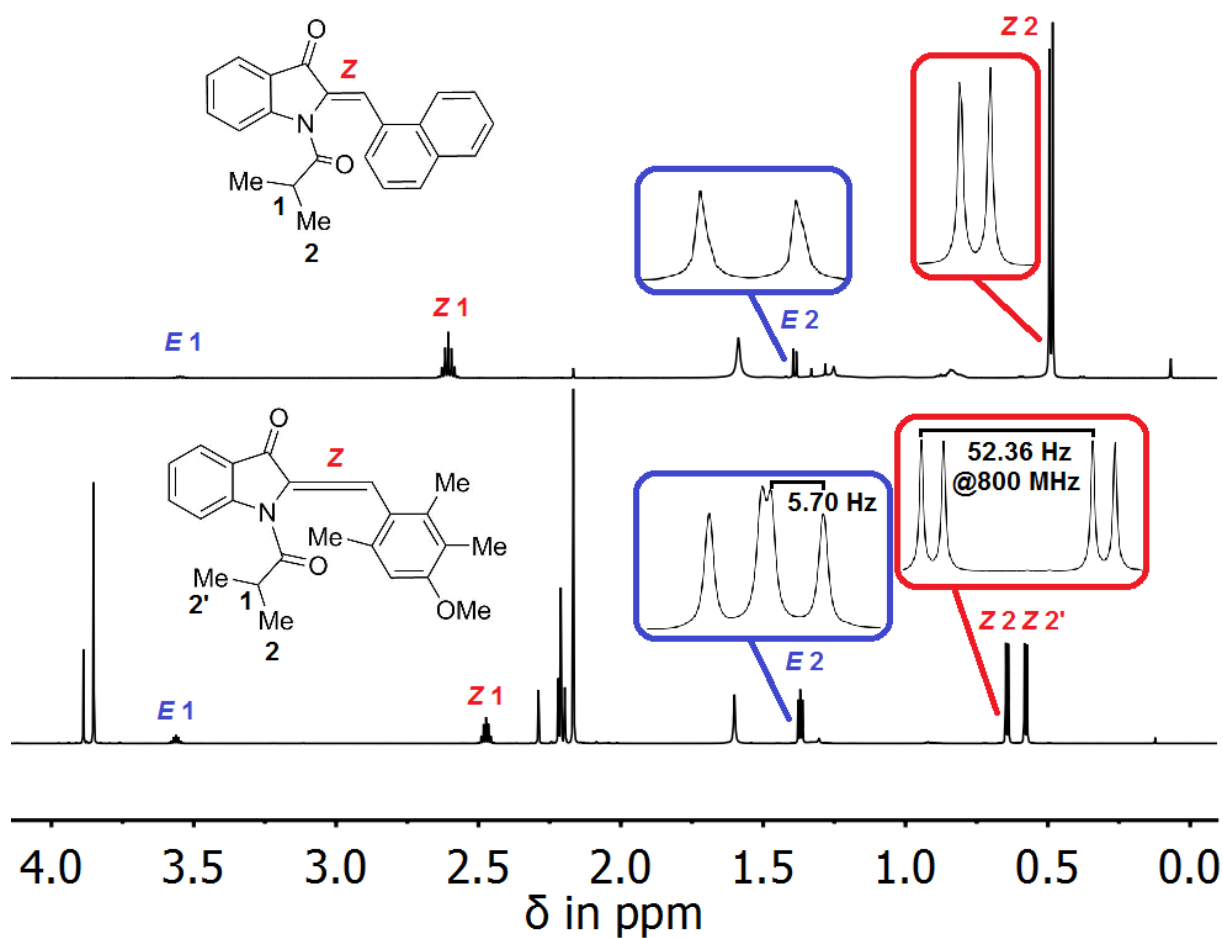


Figure 112: Comparison of <sup>1</sup>H-NMR spectra of hemiindigo **55** in chloroform-*d* (600 MHz, 27 °C) and **57** in dichloromethane-*d*<sub>2</sub> (800 MHz, 27 °C), only the aliphatic region is shown. A pronounced splitting of the isobutyryl methyl signals (2) can be observed which is enlarged in the *Z* state by almost one order of magnitude from 5.70 Hz to 52.36 Hz at 800 MHz NMR spectrometer frequency.

The splitting of the isobutyryl methyl signals (protons 2, Figure 112) observed for the *Z* and *E* isomers of hemiindigo **57** proves the existence of two rotamers for the stilbene single bond axis. The *N*-carbonyl axis is not locked and neither is the carbonyl-isopropyl axis, which can be evidenced by the lack of signal splittings for protons 1 (see assignments in Figure 112) in the *Z* and *E* isomeric forms. The fast dynamics cause protons 1 and 2 to appear completely symmetric towards the asymmetric stilbene fragment, as no other split signals can be observed at the NMR timescale at ambient temperatures. This observation will be crucial to understand the increasingly rigid systems in Section 2.3.6 later on. The twofold signal set of protons 2 can be attributed to the asymmetric environment introduced by the stilbene fragment. Even if the stilbene fragment is interconverting from one rotamer to the other, the induced chemical shift difference of the isobutyryl methyl groups remains the same on average as long as the rotation

is not exceeding the time scale of the NMR experiment. This is important to consider, as the rotational barrier of the stilbene fragment is estimated to be at 16 kcal/mol by DFT calculations, which is considered as free rotation at ambient temperatures. In fact, every rotational barrier in this system is free to interconvert at ambient temperatures. Signal splittings can be observed for **57** because atropisomerization of the stilbene fragment is within the NMR timescale under the utilized conditions. Hemiindigo **55** possesses a sterically less hindered naphthyl moiety and atropisomerization is consequently faster than the NMR time scale, which results in no split signals in this case.

Attempted separation of rotamers for hemiindigo **57** at 0 °C via chiral HPLC did yield one sharp peak and no separation. Molecules with rotational barriers as low as 20 kcal/mol could be previously separated and isolated utilizing this method. This experiment thus proves energy barriers of <20 kcal/mol for hemiindigo **57**. Besides enriching one rotamer and tracing its kinetics towards the racemate as done in Section 2.3.6, coalescence can be used to get accurate measurements of the rotational barriers. A variable temperature coalescence NMR experiment was conducted for hemiindigo **57** to directly obtain the energy barriers for the atropisomerization reaction (Figure 113).

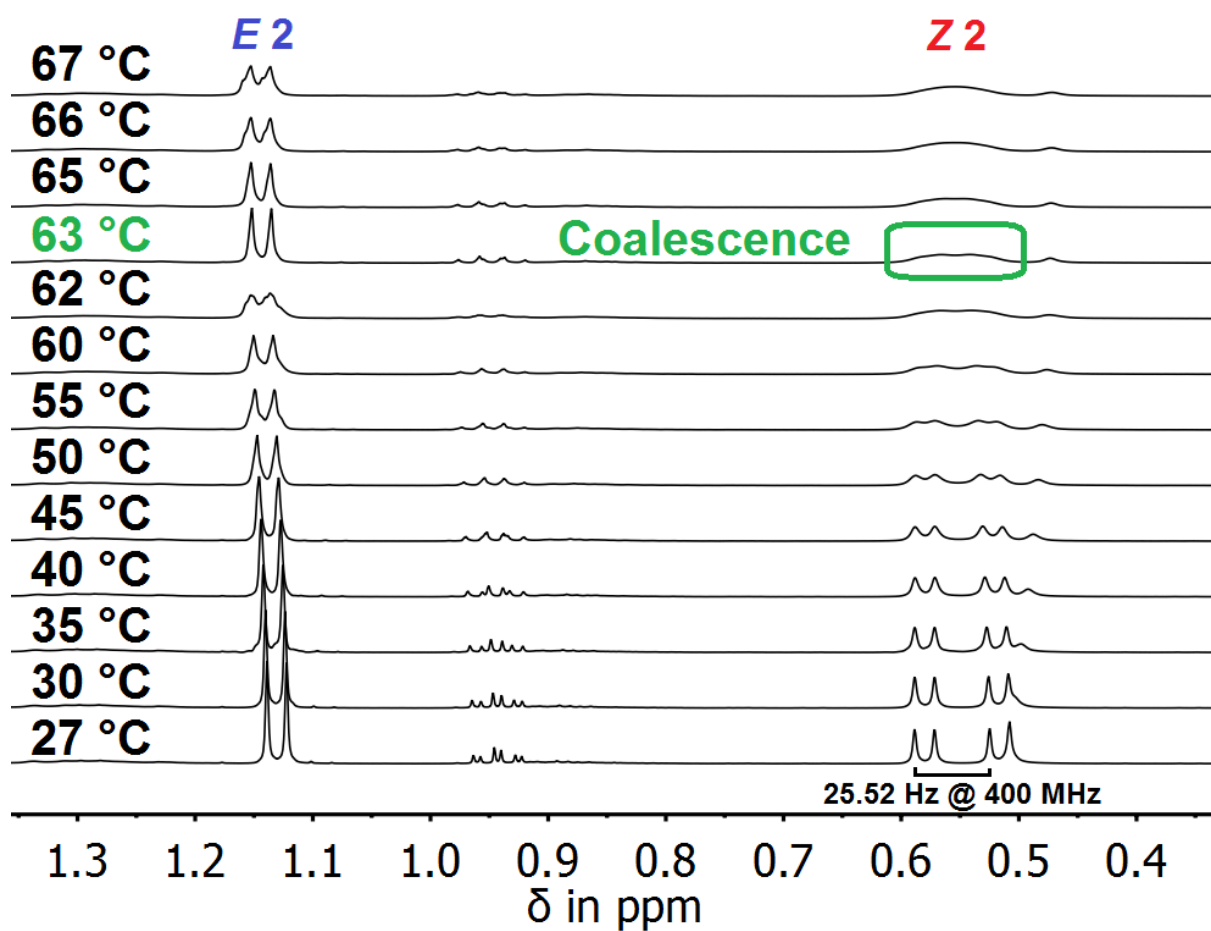


Figure 113: <sup>1</sup>H-NMR spectra of a mixture of *Z* and *E* isomers of hemiindigo **57** in toluene-*d*<sub>8</sub> measured at different temperatures on a 400 MHz NMR spectrometer.

The coalescence temperature is defined as the temperature where a signal splitting is barely discernable and can be inserted into eq. 19:

$$\Delta G = RT_c \left( 22.96 + \ln \left( \frac{T_c}{\Delta\nu} \right) \right) \quad \text{eq. 19}$$

Where  $T_c$  is the temperature of coalescence in K,  $\Delta\nu$  represents the maximum shift difference of split signals in Hz (typically measured at several different temperatures, which are far lower than the coalescence temperature to establish no further change in the signal splitting) and  $R$  equals the gas constant in  $\text{Jmol}^{-1}\text{K}^{-1}$ . With the experimentally determined values of  $\Delta\nu = 25.52$  Hz and  $T_c = 336.15$  K, the free activation enthalpy  $\Delta G^*$  can be determined at 71.37 kJ/mol or 17.06 kcal/mol, which translates to a thermal half-life of 0.36 s at 25 °C and is in very good agreement with the theoretical prediction for thermal atropisomerization of hemiindigo **57**. It is noteworthy that  $\Delta\nu$  is the divisor of the fraction in eq. 19, which correlates smaller chemical shift splittings to higher barriers. This means larger splittings correspond to lower barriers when the same coalescence temperature is determined. As the 400 MHz NMR device cannot resolve the shifts of split protons 2 in the *E* isomer and the only available 800 MHz NMR device is not equipped with a heatable probe head, the coalescence temperature of the *E* isomer could not be determined. If, hypothetically, the same coalescence temperature as in the *Z* isomer is assumed, the smaller signal splitting of 2.85 Hz (5.70 Hz divided by two for a 400 MHz spectrometer) is caused by a calculated free activation enthalpy of 77.50 kJ/mol or 18.52 kcal/mol, which translates to a thermal half-life of 4.3 s. Counterintuitively, photoswitching from the *E* state to the more sterically demanding *Z* state is inherently linked to lowered rotational barriers for partaking molecular entities. This is consistently shown for the chiral hemiindigos in Section 2.3.5 by experiment and theory.

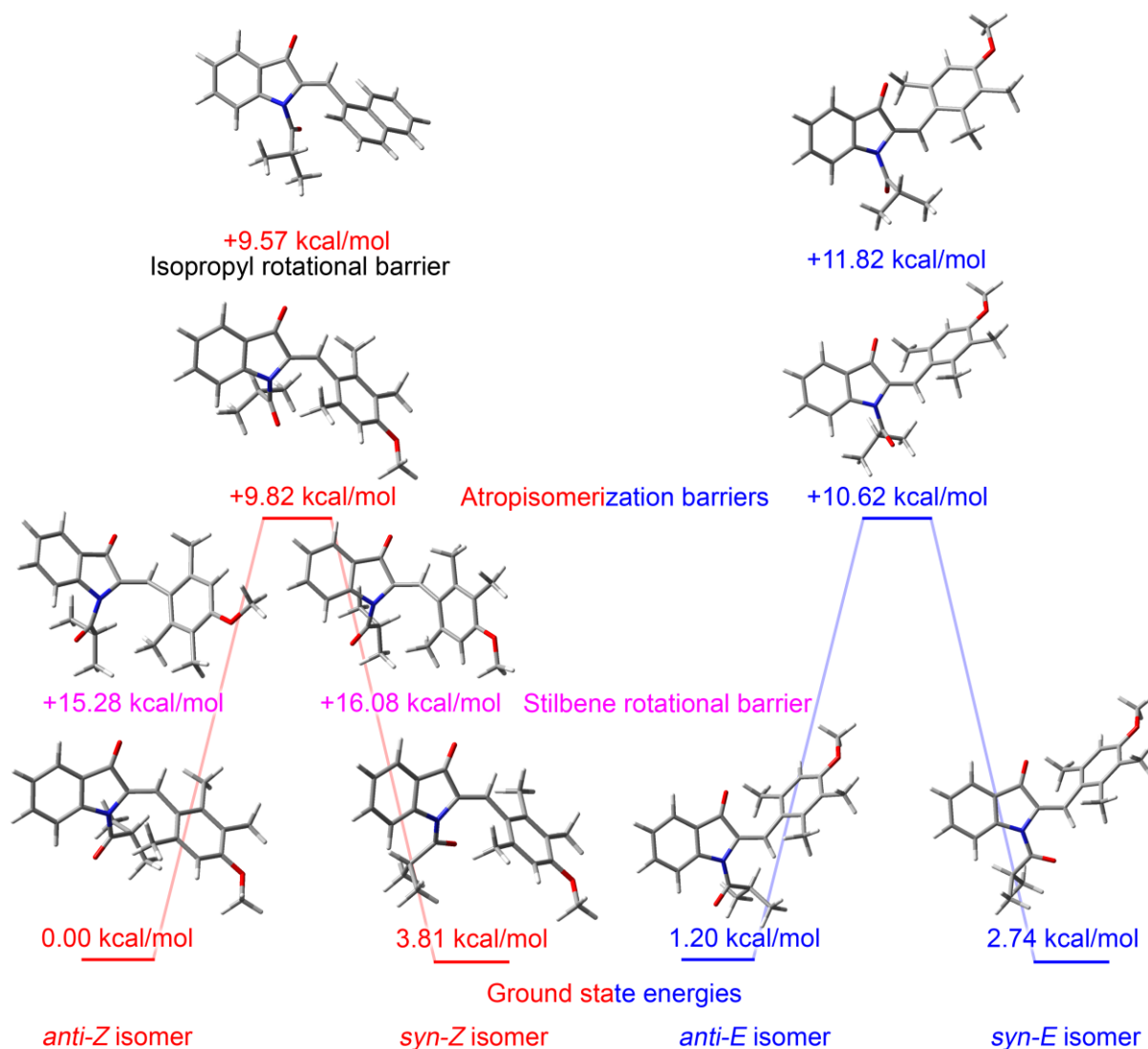


Figure 114: Calculated ground and transition state structures of hemiindigo **57** at the B3LYP/6-311+G(d,p) level of theory. Transition states for the atropisomerizations for *Z* and *E* isomers and two stilbene single bond rotation for the *anti-Z* isomer were found. The “+” sign in front of transition state values indicates the energy difference with respect to the lowest ground state of respective *Z* or *E* isomers. The *E*- transition states of the stilbene single bond rotation, however, did not converge after several attempts and tweaks. The isopropyl single bond rotation was found only for the *Z* isomer. The calculated value of the stilbene single bond rotation in the *Z* state is in good agreement to the experimentally determined value of 17.06 kcal/mol.

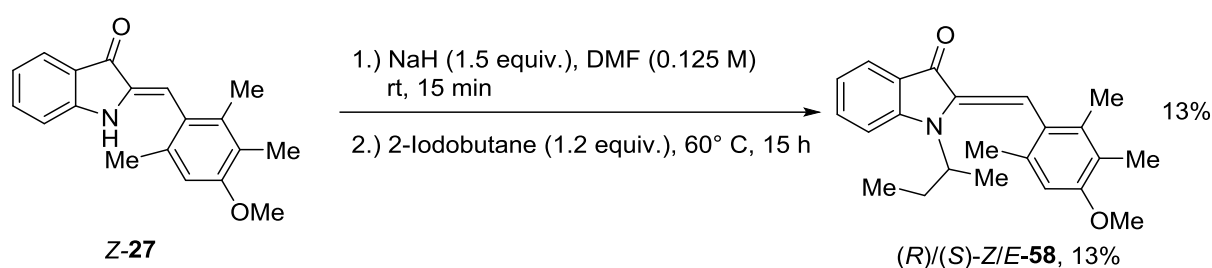
In hindsight, these molecules vastly helped understanding the underlying kinetic processes and the interpretation of NMR spectra of the chiroptical hemiindigo photoswitches presented in Section 2.3.7.



### 2.3.4 Introduction of a permanent stereocenter at the indoxyl fragment

After the introduction of non-symmetric acyl residues to the hemiindigo nitrogen atom resulting in axially- or helically chiral, yet thermally unstable rotamers, the N-H substitution of hemiindigo **27** with a residue bearing a permanent stereocenter was explored subsequently.

Hemiindigo **58** possesses a permanent stereocenter adjacent to the nitrogen atom and the already introduced non-symmetric di-*ortho* methyl *meta*-methyl *para*-methoxy stilbene fragment, which is responsible for introducing axial chirality to the molecule (Figure 116).



Scheme 31: Introduction of a secondary alkyl residue to the hemiindigo chromophore. Elevated temperatures are necessary for the reaction to progress and only low yields of **58** could be obtained.

For analysis of the chiroptical properties of hemiindigo **58** enantiomers were separated using chiral HPLC (Figure 115).

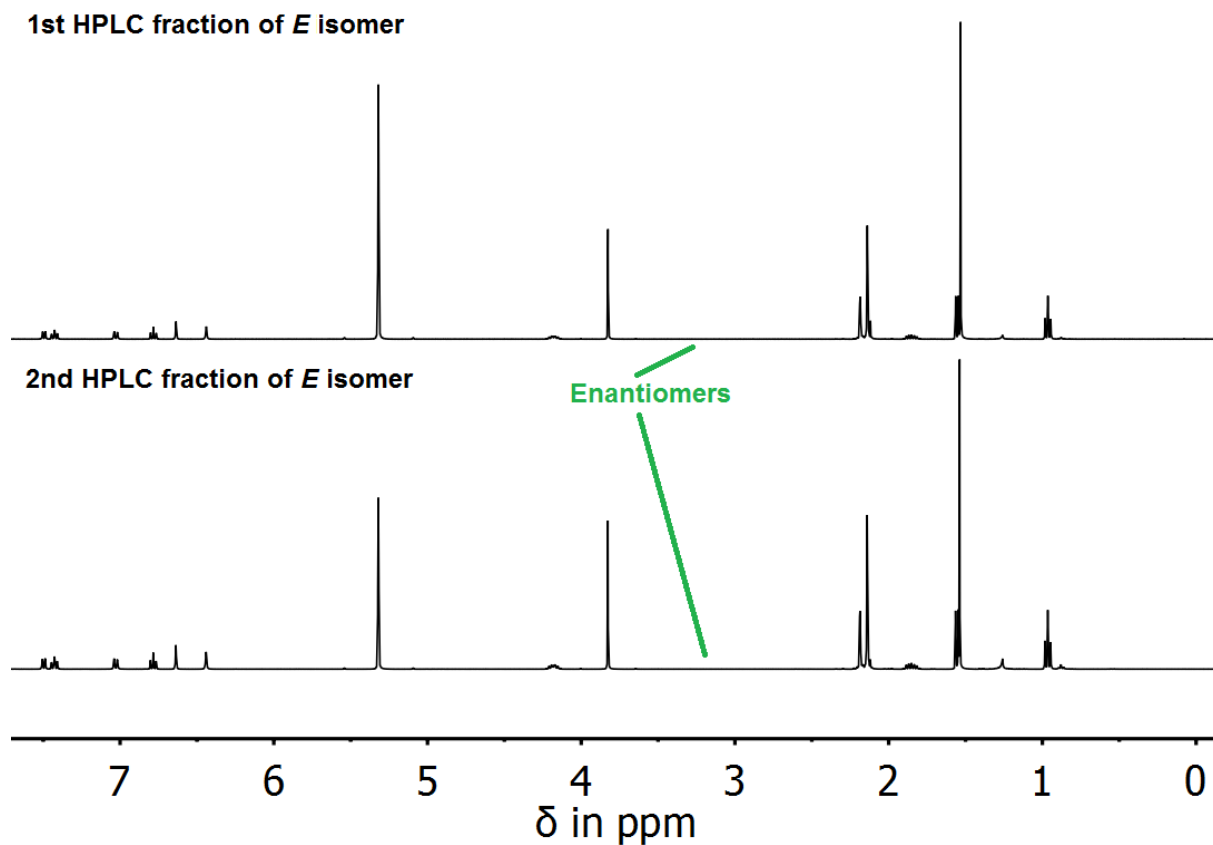


Figure 115:  $^1\text{H}$ -NMR spectra of enantiopure HPLC fractions of hemiindigo **58** in dichloromethane- $d_2$  at ambient temperatures. The matching signals prove the separated HPLC fractions to be enantiomers.

Crystals suitable for x-ray structural analysis were obtained for each enantiomer (Figure 116). Because of the absence of heavy atoms in the structure and overall quality of the crystals no absolute assignment of the stereoconfiguration could be made by these experiments.

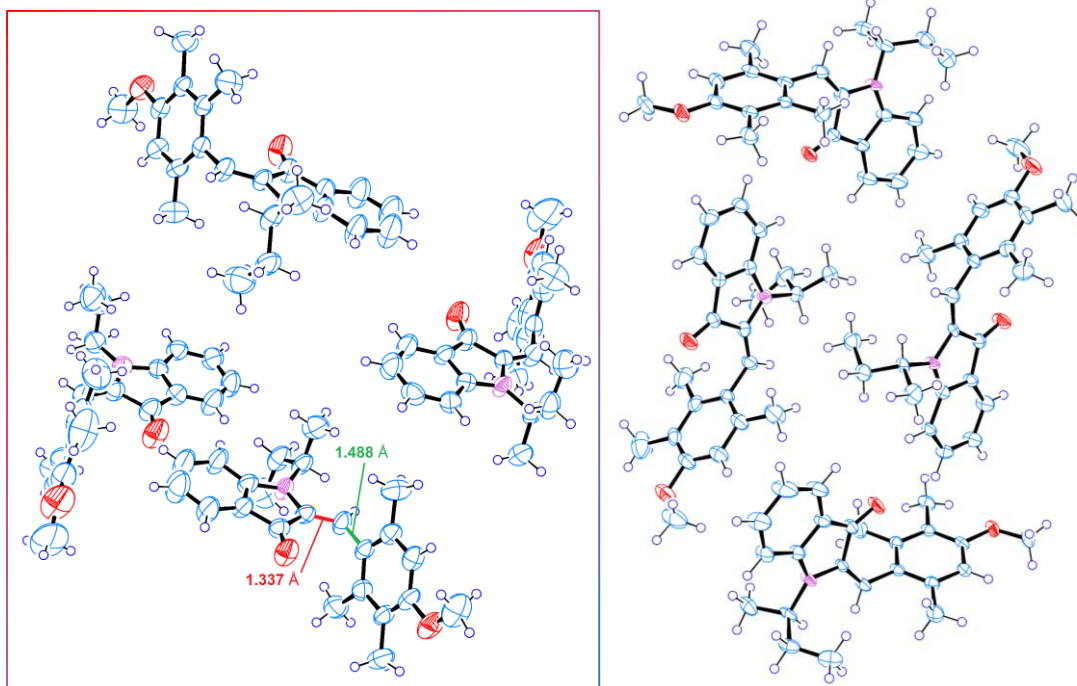


Figure 116: Structures of the enantiopure crystallization batches for *E* isomers of hemiindigo **58** in the crystalline state. The structure on the left (inside rectangle) was crystallized from the first enantiomeric fraction, the structure on the right from the second one, respectively. The chiral nature of the compound requires four molecules to determine its unit cell. Both crystal structures purposely show the *R* configuration at the stereocenter as the evaluation of the structural data done by *P. Mayer* was not unambiguous to assign the enantiomers to their respective stereodescriptors. This is generally difficult to achieve if the molecules do not contain at least one heavy atom, for example sulphur, or if only small crystals can be obtained. The stilbene single bond dihedral torsion angle amounts to  $78.20^\circ$  for C54-C55-C56-C57 in the *E* isomeric state. The double bond (red) length amounts to 1.337 Å and the single bond (green) to 1.488 Å.

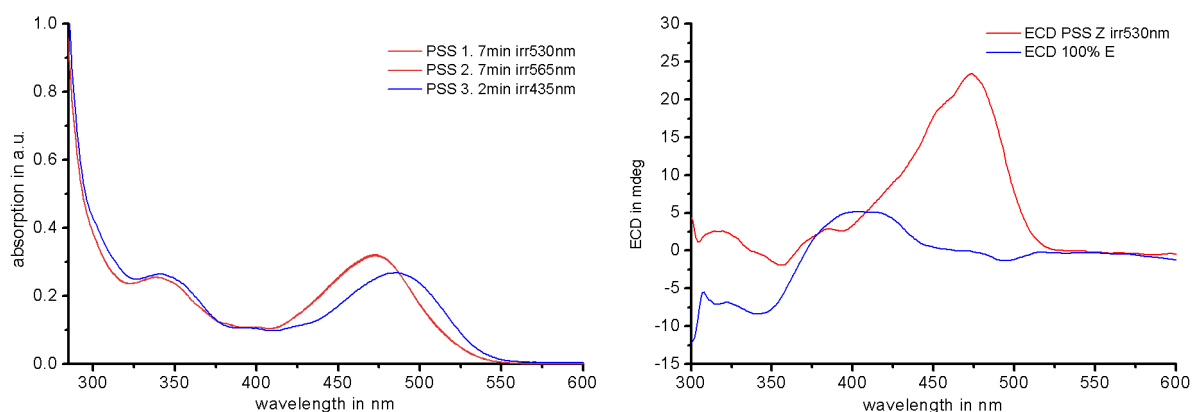


Figure 117: PSS (left) UV-Vis and ECD spectra of hemiindigo **58** in dimethyl sulfoxide. The isosbestic points are well defined, verifying the photostability of this compound after alkylation. Photoswitching proceeds readily in both directions. A red-shift of the absorption of approximately 40 nm can be observed compared to the absorption of the acylated derivative **57**. A strong modulation of the ECD signal can be seen in between *Z* and *E* isomer. Adapted with permission from [75]. Copyright 2018 American Chemical Society.

Hemiindigo **58** shows viable and fully reversible photoswitching with visible light and at the same time a strong modulation of its ECD signal in an ON/OFF manner (Figure 117).

Increased intramolecular twisting in the *Z* state compared to the less twisted *E* state causes the strong ECD modulation for this hemiindigo chromophore, which is explained in detail in Section 2.3.5. This made hemiindigo **58** a first prototype for the chiroptical switches portrayed in Section 2.3.8 with the added benefit of a permanent stereocenter that cannot be racemized thermally.

Experiments with circularly polarized light were carried out on this compound, see Figure 118 below.

The research field of absolute asymmetric synthesis also covers the prebiotic approach to explain the homochirality seen with *L*-amino acids and *D*-sugars within all lifeforms on earth. *B. Feringa*, *P. Hashim* and *K. Rijeesh* already showed that circularly polarized light (CPL) can deracemize chiral- or prochiral photoswitches to induce miniscule amounts of enantiomeric excess (ee).<sup>[108, 109, 110]</sup> With a chiroptical hemiindigo photoswitching system at hand, experiments were carried out on compound **58** observe deracemization by CPL irradiation and to potentially improve upon currently possible generation of ee.

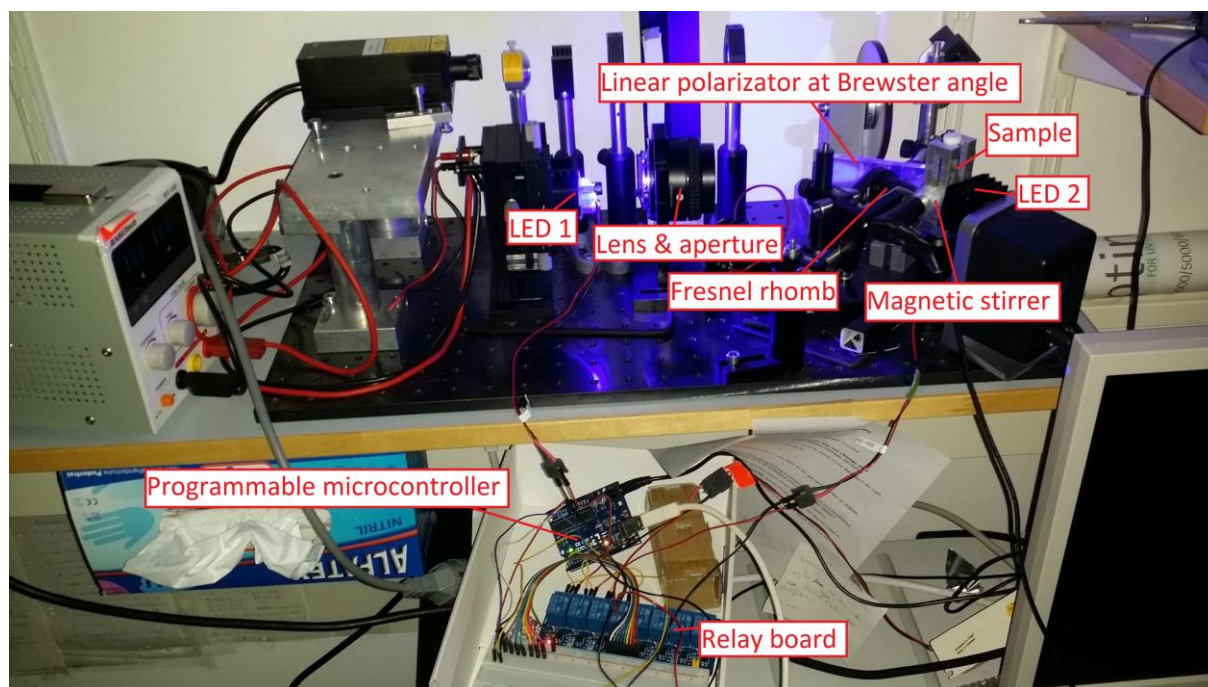


Figure 118: Setup for alternatively irradiating liquid samples with right or left handed circularly polarized light (CPL) and non-polarized light. LED 1 is focused with a lens on a stack of microscopy plates at the *Brewster* angle of  $56^\circ$ . The reflected linearly polarized light (LPL) was tested with sunglasses (which can pose as linear polarizers) and could be extinguished upon turning the glasses within the plane of the lens, which proved successful linear polarization. The addition of a *Fresnel* rhomb (which poses also as a quarter wave plate) with its optical axis turned at  $45^\circ$  to the light path led to a non-extinguishable ray of CPL. When another quarter wave plate (like the *Fresnel* rhomb) is added to the beam path, CPL is again transformed to extinguishable LPL, which proves the successful circular polarization of the LED light. A microcontroller can be used for actuating a relay board to run cyclic experiments where a sample is repeatedly irradiated with CPL and normal, unpolarized light to its initial state.

Irradiation of a racemic mixture of hemiindigo **58** with circularly polarized light did not yield any observable deracemization, which can be attributed to the relatively low sensitivity of the used ECD spectrometer or the wrong molecular setup. The fixed stereocenter might pose a problem as it cannot be interconverted to the other handedness by circularly polarized light, which made the deracemization process rely solely on the difference in ECD absorption and the associated difference in photoquantum efficiency. A molecular setup with chiral axes had to be developed for the circularly polarized light to prefer one enantiomeric rotamer over the other, resulting in population of one species and generating enantiomeric excess, in theory. Section 2.3.5 details the efforts towards this research field. However, the drawbacks of thermal racemization of the axially chiral axes can be prevented by the introduction of a permanent stereocenter, which was shown for hemiindigo **58**. This poses as a potential candidate for materials science, data applications with multiple read-outs or quantum computing without the drawbacks of a thermal racemization process and subsequent data loss as observed with the axially chiral derivatives.

### 2.3.5 *Ortho*-arylated hemiindigos - Second route for introduction of axial chirality

The chiral properties were disregarded in Section 2.2.7 as this section will explain them in full detail. To study the cooperativity, dynamics and properties of a chiral axis adjacent to a photoswitchable molecule part and to potentially improve approaches towards absolute asymmetric synthesis, an *ortho*-tolyl moiety was introduced to the hemiindigo chromophore.

Introduction of a chiral aryl axis to the hemiindigo photoswitch at the nitrogen position together with a methyl group at the 7 position of the indoxyl fragment, which functions as a bulky stopper, adds another rotational axis which can be photochemically controlled. The *ortho*-aryl and naphthyl residues together with di-*ortho*-substituted stilbene fragments yield photoswitchable systems that can gate the rotational speed of the chiral axis, control their rotational directionality towards racemization and modulate large amounts of the ECD signal in between *Z* and *E* isomeric states solely with visible light.

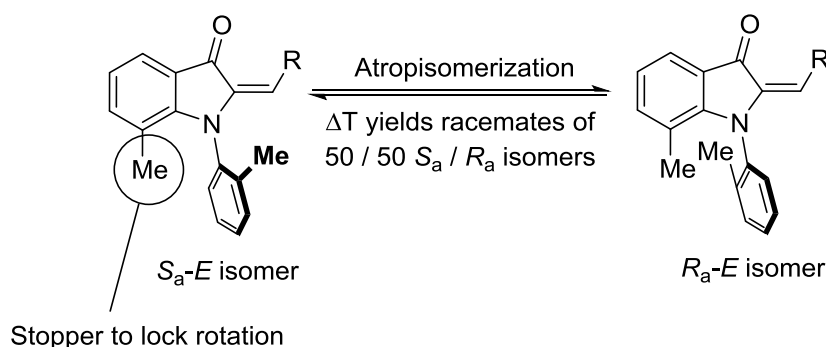


Figure 119: Design principles of axially chiral hemiindigo photoswitches. The chiral axis together with a methyl group in 7-position of the indoxyl core yield HPLC-separable rotamers for specific stilbene substitution patterns in *Z* and *E* isomeric forms.

The introduction of a twisted chiral aryl axis makes it possible to measure their free activation enthalpies and thermal half-lives.

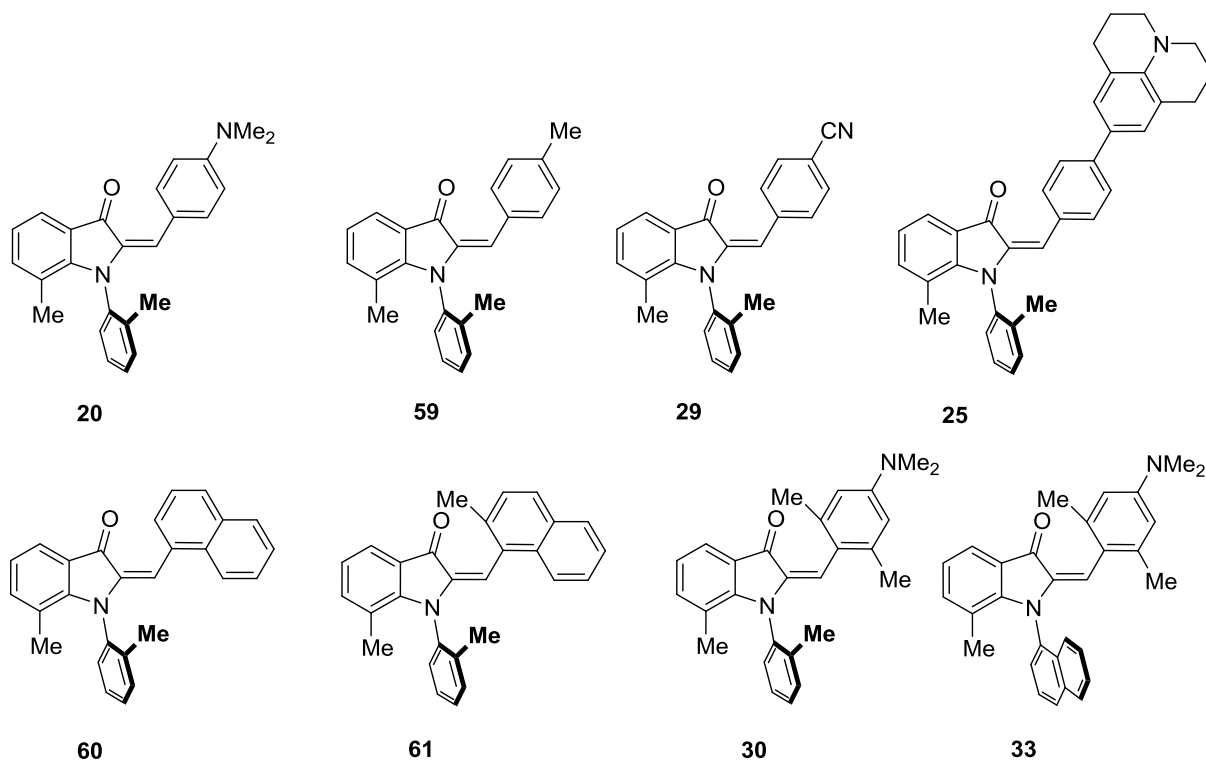


Figure 120: Overview of selected axially chiral hemiindigos **20**, **59**, **29**, **25**, **60**, **61**, **30** and **33**. Only respective *E* isomers are shown. The properties of compound **25** were discussed in Section 2.2.7, as no chiral HPLC separation was performed on this molecule.

Addition of *ortho*-methyl groups at the stilbene fragment (**30**) slightly lowers the thermal *Z* / *E* isomerization barriers compared to **20**. For the naphthalene derivative **33**, however, the *Z* / *E* barriers are improved significantly. In both cases this comes at the cost of red-shift, as the out-of-plane twisting of the stilbene fragment reduces the *pi*-delocalization of the chromophore. The hypsochromic shift manifests in a color change from orange / pink (**20**) to yellow / darker yellow (**30** and **33**) for respective *Z* / *E* isomers. The atropisomerization barriers are vastly improved upon twisting the stilbene single bond as well as by introduction of a naphthalene moiety seen for hemiindigo **33**. One explanation consists of a better fit of the flat naphthyl residue between the indoxyl methyl group and the stilbene fragment or central double bond proton compared to the protruding methyl group of the *ortho*-tolyl moiety. This is emphasized in the *Z* state, as a 3 kcal/mol atropisomerization barrier increase from *Z*- compared to *E* isomers can be observed, which is also well reflected by calculations at the B3LYP/6-311G+(d,p) level of theory.



Presented chiral hemiindigos were synthesized starting from 7-methyl indole **18** and *ortho*-bromotoluene via a copper(I) mediated cross coupling by a procedure of *J. Antilla et al.*<sup>[91]</sup> Elevated temperatures of 150 - 160 °C and pressure tubes or xylene were utilized instead of 110 °C and toluene where no reaction progress could be observed. Oxidative acetylation of the indole was performed according to *P. Choy et al.*<sup>[92]</sup> and the condensation of the obtained indoxyl acetate and aldehydes was carried out according to *U. Burger et al.*<sup>[88]</sup> with increased temperatures up to 100 °C. The detailed synthesis can be found in Section 2.2.7.

### 2.3.6 First generation of axially chiral arylated hemiindigos - Electronic effects on the stilbene fragment

The three discussed first-generation derivatives were brought forward to explore electron donating, neutral and electron withdrawing groups regarding the possible change in rotational properties of the *ortho*-tolyl substituent. This was done via chiral HPLC by separating the rotamers from each other with subsequent re-injection after the irradiation or thermal racemization of isolated species. After these preliminary results, ECD spectra of the enantiomers were recorded and photochemical- as well as thermal behavior was tested.

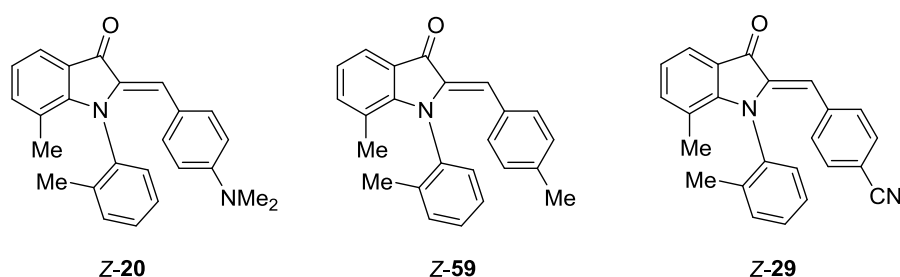


Figure 121: First generation of synthesized axially chiral hemiindigo derivatives **20**, **59** and **29**.

Photophysical properties regarding the *Z* / *E* isomerization of compounds **20** and **29** are discussed in detail in Section 2.2.7 and are omitted here.

Priorly, the conformation of hemiindigo **20** was investigated via <sup>1</sup>H-NMR spectroscopy. The *ortho*-tolyl axis is substantially twisted in the *Z* isomeric state with the aryl substituent at the indoxyl nitrogen being oriented in a perpendicular fashion to the indoxyl moiety. This leaves the aniline moiety not being able to planarize. This geometric arrangement is confirmed by the theoretical description and can be observed experimentally by the significantly upfield-shifted signals of aromatic- and aliphatic protons of the *ortho*-tolyl substituent compared to the corresponding signals for the *E* isomer (Figure 122) for hemiindigo **20**. In the *E* state of **20**, the aniline moiety can planarize completely, which reduces the overall twist in the molecule and increases conjugation of the *pi*-system.

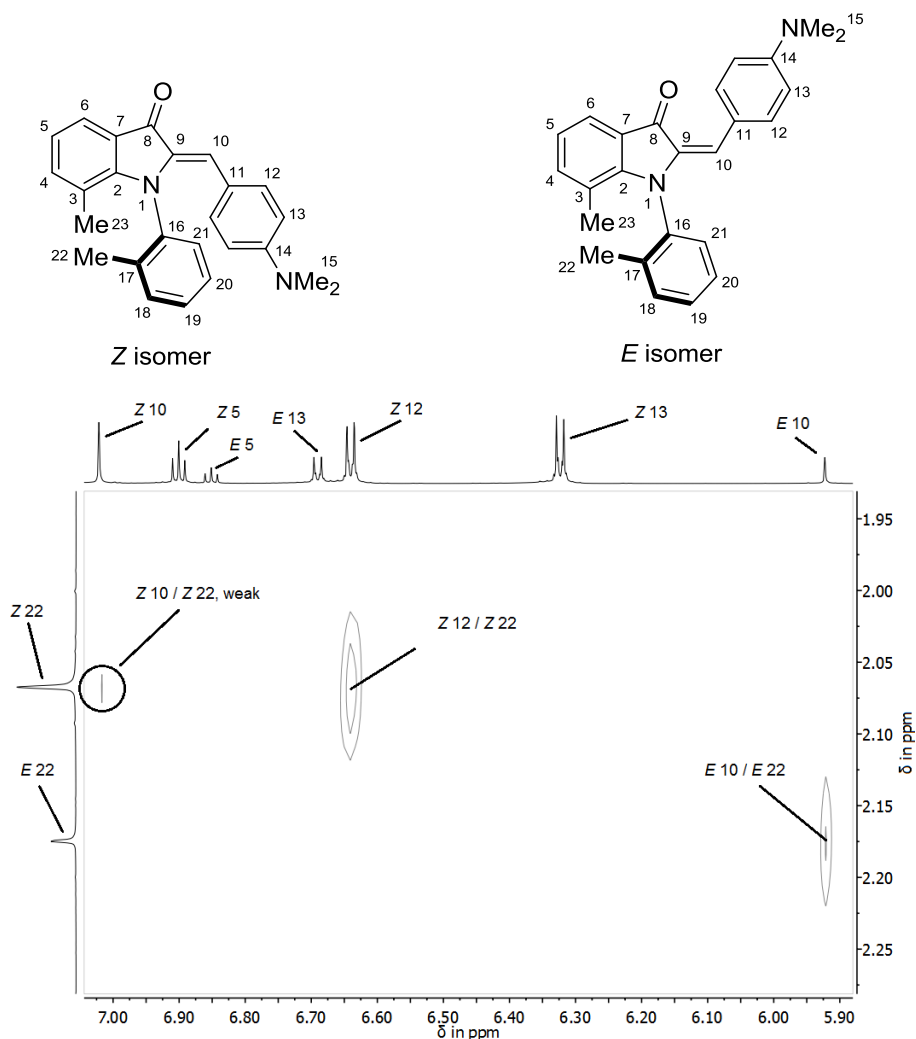


Figure 122: Section of the 2D  $^1\text{H}$ -NOESY NMR spectrum (dichloromethane- $d_2$ , 600 MHz, 27 °C) of hemiindigo **20**. An unambiguous assignment of the double bond configuration can be done with this spectrum. A strong NOE cross signal between Z 12 and Z 22 evidences the Z isomeric state. The strong NOE cross signal between proton E 10 and protons E 22 evidences the E isomer. The corresponding cross signal of Z 10 and Z 22 is very weak, indicating a farther distance of the methyl group associated to the *ortho*-tolyl residue to the double bond proton in the Z isomeric state.

2.3.6 FIRST GENERATION OF AXIALLY CHIRAL ARYLATED HEMIINDIGOS - ELECTRONIC EFFECTS ON THE STILBENE FRAGMENT

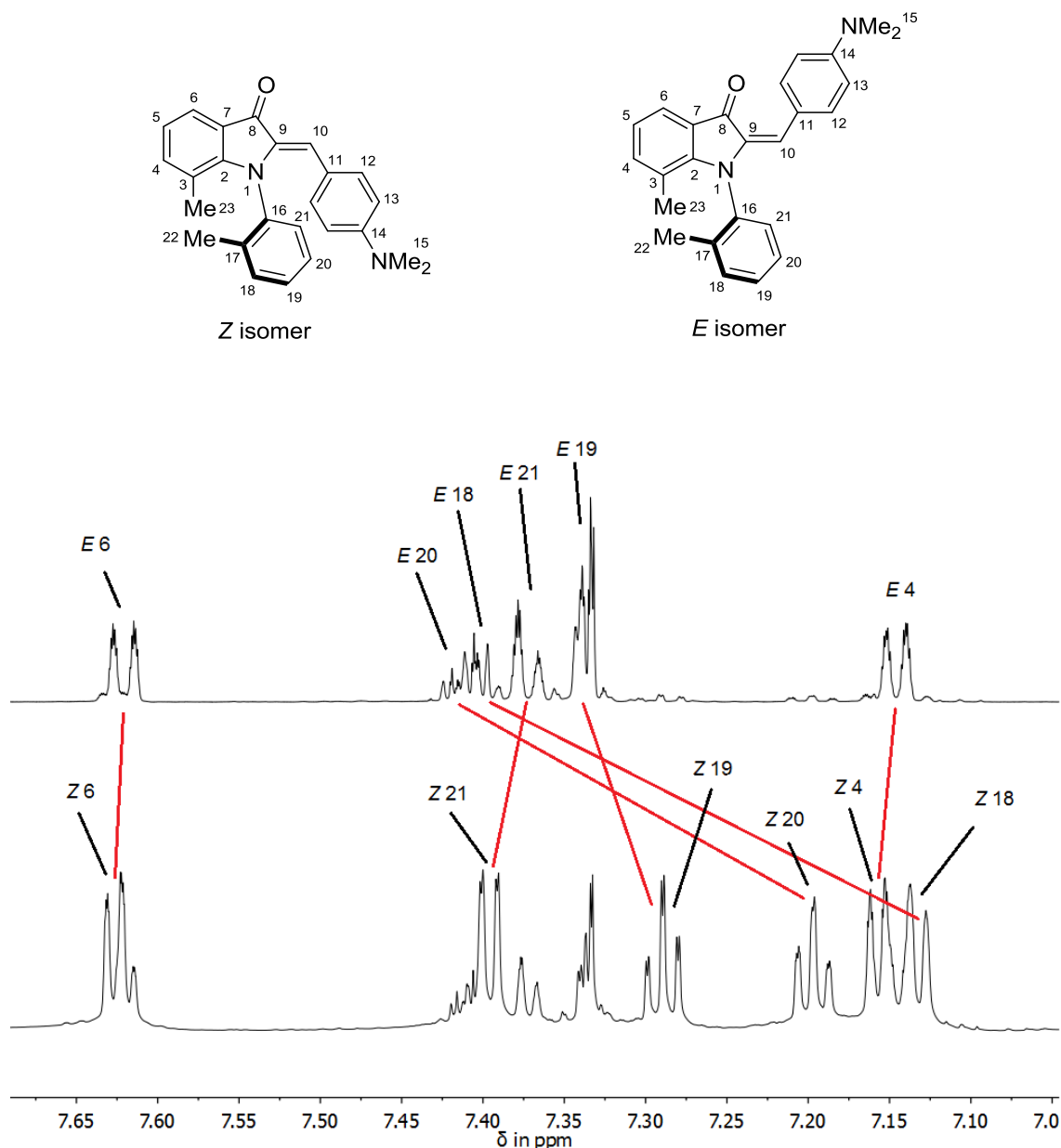


Figure 123: Aromatic section of the <sup>1</sup>H-NMR spectra (dichloromethane-*d*<sub>2</sub>, 800 / 600 MHz, 27 °C) of *E* (top) and *Z* isomer (bottom) enriched mixtures of hemiindigo **20**. Large upfield shifts can be observed upon transition from *E* to *Z* isomer, which indicate proximity of the shielding aniline ring-current to the chiral *ortho*-tolyl residue in the *Z* state. Adapted with permission from [75]. Copyright 2018 American Chemical Society.

In general, separation of rotamers was done via chiral HPLC (*Diacel Chiralpak IC* and / or *ID* columns, 5  $\mu\text{m}$  pore size, 10 mm inner diameter, 250 mm length, 8 mL/min flow rate at 0 °C) with heptane / ethyl acetate mixtures as eluents.

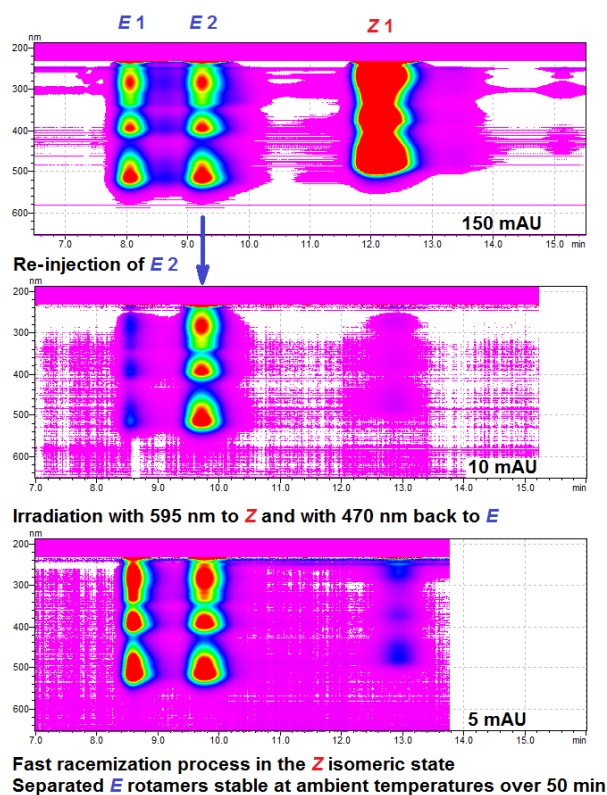


Figure 124: 3D UV-Vis Chromatograms of hemiindigo **20** on a chiral HPLC column recorded at 0 °C in 87 / 13 heptane / ethyl acetate. The peak intensity scale is given in mAU (milli a.u., arbitrary units).

Injection of a *Z* / *E* mixture gives three separable peaks, *E* 1 *E* 2 and *Z* 1. Collection and re-injection of *E* 2 gives the pure peak and some residual *E* 1 from fraction overlap. Irradiation of *E* 2 to the *Z* state and back to the *E* form gives *E* 1 and *E* 2 in a 1 to 1 racemic mixture. *E* 2 left in the dark did not racemize significantly (not shown).

### 2.3.6 FIRST GENERATION OF AXIALLY CHIRAL ARYLATED HEMIINDIGOS - ELECTRONIC EFFECTS ON THE STILBENE FRAGMENT

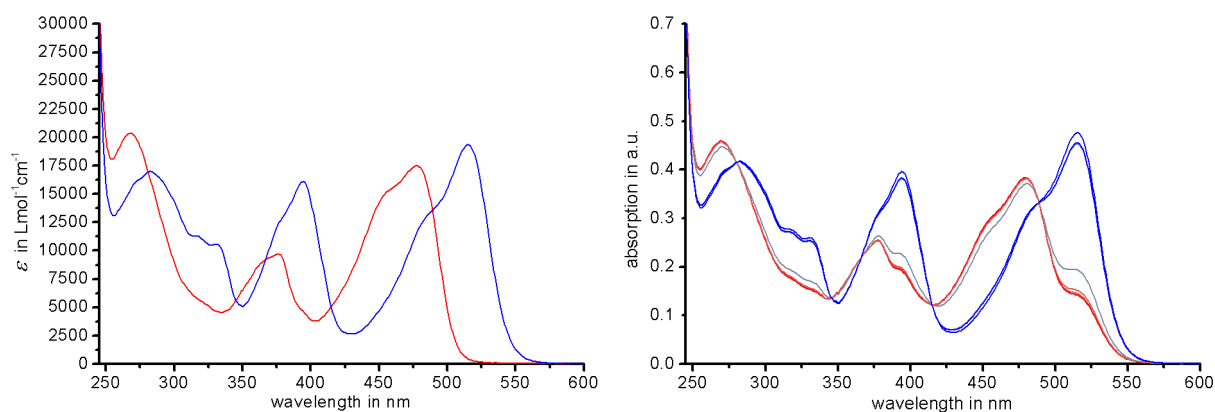


Figure 125: Molar absorption coefficients (left) of **20** in 83 / 17 heptane / ethyl acetate with the *Z* isomer shown in red and the *E* isomer in blue. Spectral changes recorded after different irradiation times show clear isosbestic points (right). Adapted with permission from [75]. Copyright 2018 American Chemical Society.

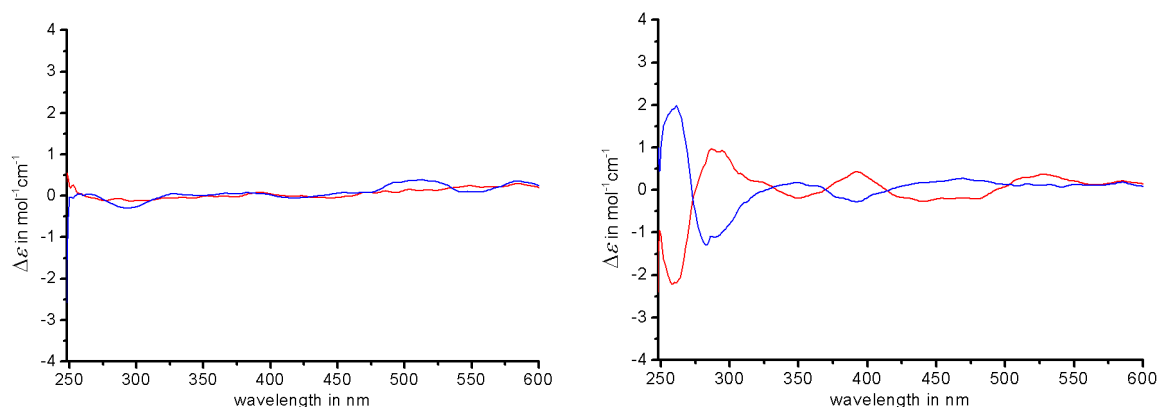


Figure 126: ECD spectrum measurement of *Z*-**20** at 25 °C (left). Because of the low energy barrier of 19.9 kcal/mol for atropisomerization via *N*-(indoxyl)-*o*-tolyl single-bond rotation (corresponding to a half-life of 43 s at 25 °C) the ECD signal has almost completely vanished at 0 °C. Molar ellipticity ECD spectra of *E*-**20** in 83 / 17 heptane/ethyl acetate at 25 °C (right), (*R*<sub>a</sub>)-*E*-**20** shown in blue, (*S*<sub>a</sub>)-*E*-**20** shown in red. Adapted with permission from [75]. Copyright 2018 American Chemical Society.

Samples at  $\sim 2.5 \cdot 10^{-5}$  M concentrations were irradiated at 0 °C or 23 °C and the ECD / UV-Vis spectra were recorded before and after irradiation steps.

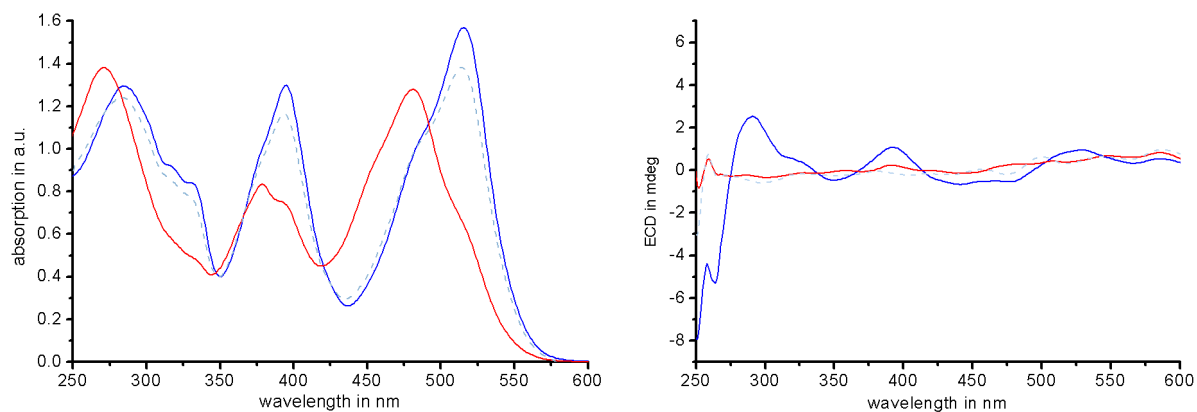


Figure 127: UV-Vis absorption (left) and ECD spectrum (right) of **20** in 83 / 17 heptane / ethyl acetate recorded for one switching cycle starting from pure (*R<sub>a</sub>*)-*E*-**20** (solid blue), which was photoisomerized to *Z*-**20** (5 min, 595 nm, solid red) and then switched back to *E*-**20** (1 min, 470 nm, light blue, dashed) in high isomeric yields at 23 °C. The low free activation enthalpy  $\Delta G^* = 19.9$  kcal/mol for thermal atropisomerization in the *Z* isomeric state leads to fast racemization in this state within ~2 minutes (thermal half-life of 43 s at 25 °C) under the applied measurement conditions. Consequently, the ECD signal is already lost in the *Z* isomeric state (right, red spectra) and photoisomerization back to the thermally more stable *E*-**20** therefore shows no leftover ECD signal for the *E* isomer (right, light blue, dashed line). Adapted with permission from <sup>[75]</sup>. Copyright 2018 American Chemical Society.

A cryogenic cuvette (see Figure 377, Section 2.7.5) was used to measure the decline in ECD response at -20 °C for a sample of *E* isomer that was *in situ* irradiated to the *Z* form at -80 °C.

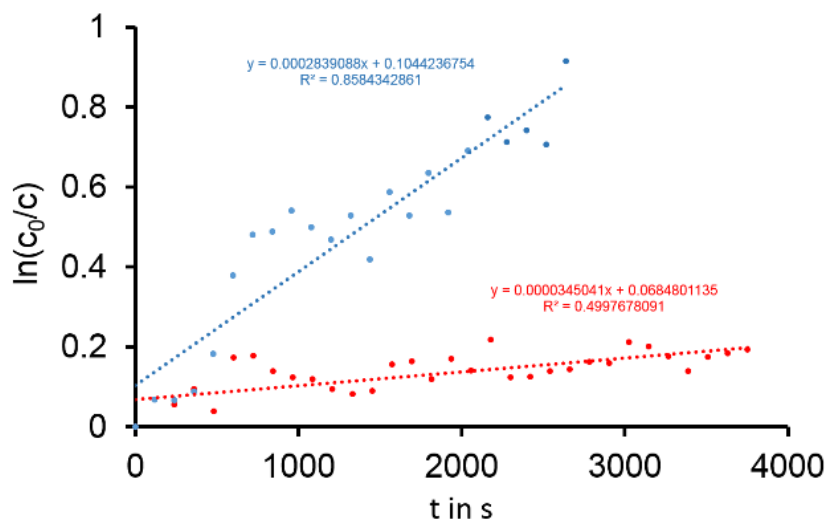


Figure 128: First order kinetic analyses of the thermal racemization via atropisomerization of hemiindigo **20** in 83 / 17 heptane / ethyl acetate in the dark. The slopes  $m$  can be translated into the rate constants  $k$  for each process. Racemization in the *Z* isomeric state (red) was measured at -20 °C and proceeds over an energy barrier of 19.9 kcal/mol. Racemization in the *E* isomeric state (blue) was measured at 40 °C and proceeds over an energy barrier of 23.4 kcal/mol. Poor R<sup>2</sup> values are based on bad signal to noise ratios caused by weak ECD responses. Adapted with permission from <sup>[75]</sup>. Copyright 2018 American Chemical Society.

DFT calculations were carried out to obtain further insight in the motional behavior of chiroptical hemiindigo photoswitches.



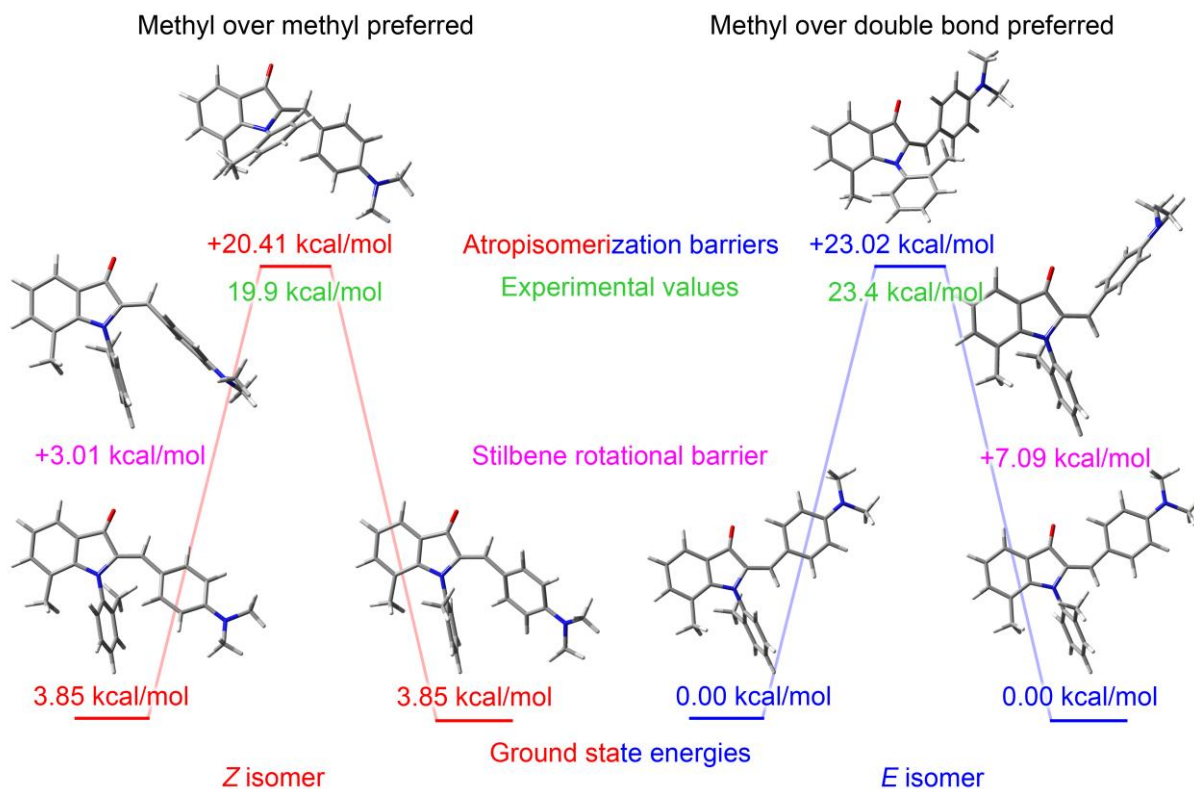


Figure 129: Calculated ground and transition state structures of hemiindigo **20** at the B3LYP/6-311+G(d,p) level of theory. Transition states for the atropisomerization and the stilbene single bond rotation were found. The disfavored atropisomerization transition states did not converge after several attempts and tweaks. The calculated energies are in good agreement to the experimental values. The “+” sign in front of transition state values indicates the energy difference with respect to the lowest ground state of respective *Z* or *E* isomers.

A by 3.5 kcal/mol lowered atropisomerization barrier for the *Z* isomers can be measured and confirmed by theory, which is in agreement to the previous findings during HPLC experiments. The stilbene single bond rotation barrier is also lowered by 4 kcal/mol in the *Z* state. The transition state structures suggest a rotation around the *ortho*-tolyl axis with its methyl group passing over the indoxyl core methyl group in the *Z* state while the *E* form prefers rotation of the methyl group over the central double bond. These findings show that gating of thermal barriers as well as their directionality are possible for these chiroptical photoswitches.

Benchmarking with different DFT functionals and the same 6-311+G(d,p) basis set yielded consistent results. The addition of GD3BJ dispersion to the B3LYP functional lowered the differences of ground and transition states, which is mainly observed for the  $\omega$ B97XD

functional as this functional is already parametrized to include dispersive and long range corrections. A reversal of ground state energies takes place by using this functional, which, however, describes the 13 / 87 *Z* / *E* thermal equilibrium composition in dimethyl sulfoxide less adequately than the other functionals. It has to be noted that the high solvent polarity of dimethyl sulfoxide can change the thermal equilibrium compared to non-polar solvents and calculations without solvent model.

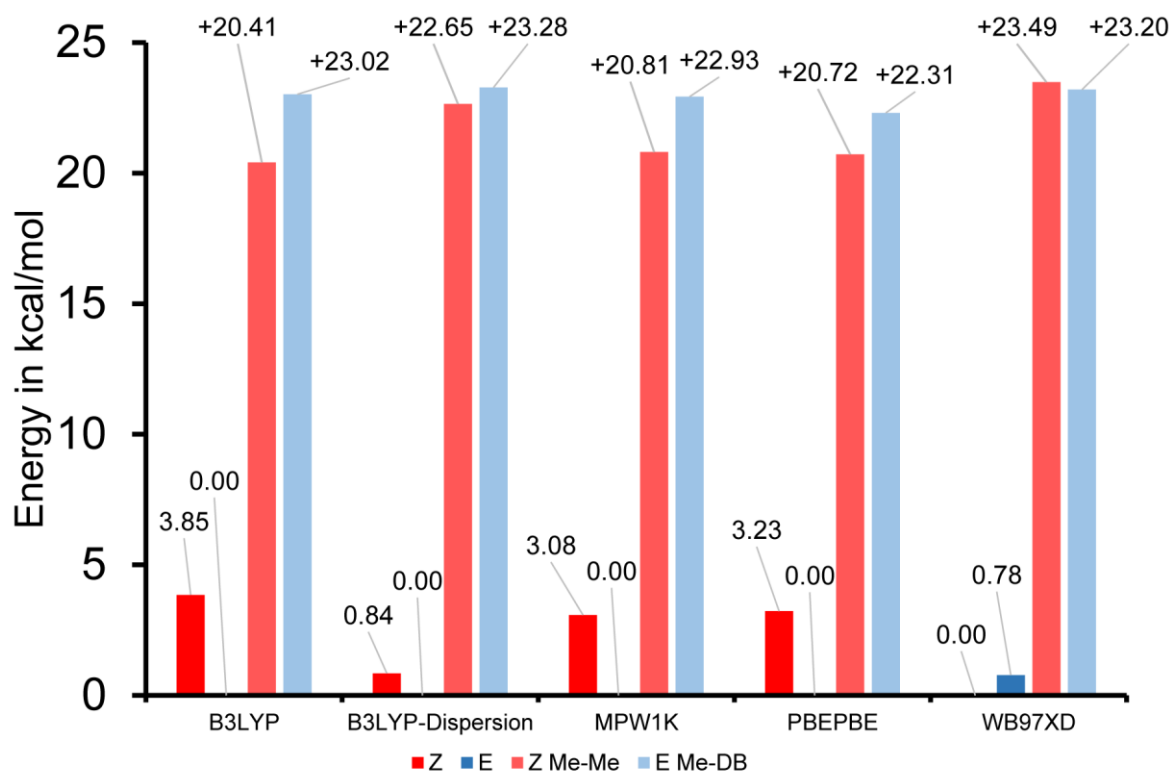


Figure 130: Benchmarking results for hemiindigo **20** using different DFT functionals for the 6-311+G(d,p) basis set. “Z” and “E” represent the ground states and “Z Me-Me” and “E Me-DB” the energetically lowest found transition state for the rotation around the *ortho*-tolyl axis with the respective double bond configuration (see Figure 129). The “+” sign in front of transition state values indicates the energy difference with respect to the lowest ground state of respective *Z* or *E* isomers.

For the *Z* isomer, a rotation of the chiral axis methyl over the indoxyl core methyl group is preferred for all functionals. In the *E* isomer, the bulky methyl group always takes the path over the central double bond. This stands in contrast to the observations for hemiindigo **30** and **33**. The dispersive and long range correction within the  $\omega$ B97XD functional gives the *Z* form as thermodynamic minimum and reverses the suggested directional behavior.

The theoretical evaluation of the isomeric and enantiomeric forms of hemiindigo **20** was successful and yielded very good results compared to the experiment. As it is not possible to

measure the rotational direction of the racemization process by common spectroscopies, theoretical calculations are the only way to obtain insight in the underlying transition states. It could be shown that gating of the thermal barriers by 3 kcal/mol as well as control over the racemization direction could be established.

The oddity of a lowered thermal barrier in the sterically more encumbered *Z* state can be explained by the influential stilbene fragment, which is forced towards planarity to regain mesomeric stabilization. This interferes with the twisted *ortho*-aryl axis as the protons on the edge of the stilbene fragment displace the *ortho*-aryl axis against the indoxyl core methyl group, elongating the *N*-aryl bond. This will lower the free activation enthalpy of the chiral axis and overcoming the indoxyl core methyl group is favored. *N*-aryl axis lengths in the transition state amount to 1.470 Å for *Z*- and 1.446 Å for *E* isomeric states, which further underlines this theory. This also means that the disfavored rotational direction for the *E* isomer, where the chiral axis methyl group passes over the indoxyl core methyl, supports an even higher rotational barrier than the favored 23 kcal/mol. Switching into the *Z* state does not only lower this barrier by the nominal 3 kcal/mol but by 3 + X kcal/mol compared to a methyl over methyl passing in the *E* state. However, the disfavored transition state in the *E* isomer did not converge after several attempts and tweaks at the utilized level of theory, giving no value for X and the total lowering of the rotational barrier

The *para*-methyl substituted hemiindigo **59** is regarded as neutral in terms of electron accepting or donating properties at the stilbene part.

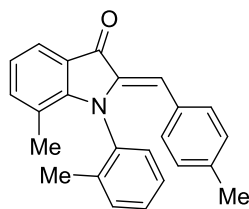


Figure 131: Lewis-formula of hemiindigo **59**.

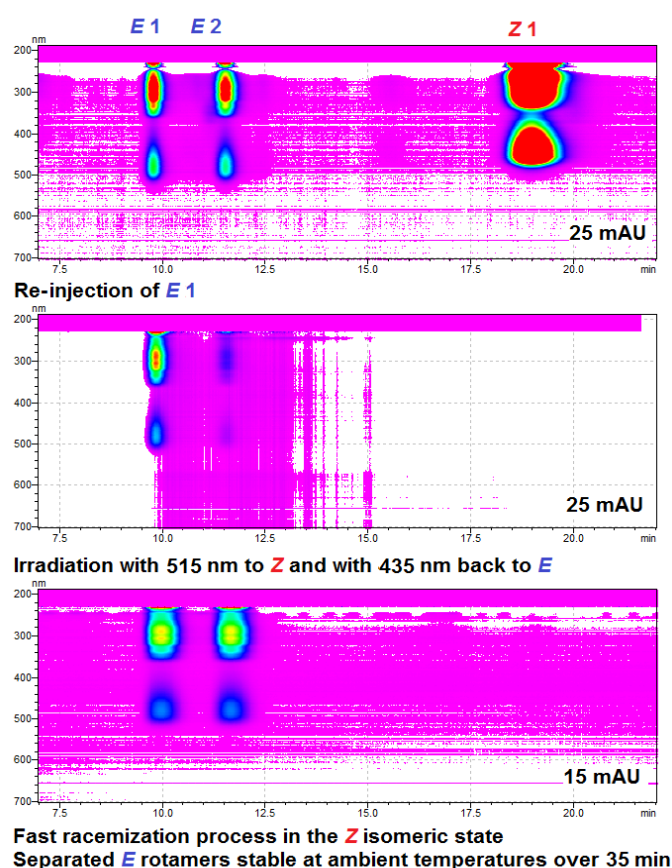


Figure 132: 3D UV-Vis Chromatograms of hemiindigo **59** on a chiral HPLC column (*Diacel Chiralpak IC*, 5 $\mu$ m, 8 mL/min) recorded at 0 °C in 95 / 5 heptane / ethyl acetate. Injection of a Z / E mixture gives three separable peaks, E 1 E 2 and Z 1. The peak intensity scale is given in mAU (milli a.u., arbitrary units).

Collection and re-injection of E 1 gives the pure peak and some residual E 2 from fraction overlap. Irradiation of E 1 to the Z state and back to the E form gives E 1 and E 2 in a 1 to 1 racemic mixture. E 1 left in the dark did not noticeably racemize, heating to 100 °C for 5 minutes, however, yielded the racemate (not shown). As the *para*-methyl derivative **59** did not show different chiral behavior compared to the electron-rich hemiindigo substitution **20**, investigation was not carried out further.

The *para*-cyano stilbene fragment substituted hemiindigo **29** represents an electron accepting derivative.

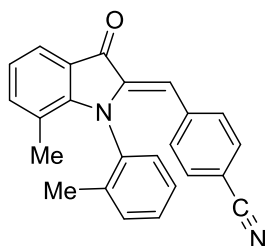


Figure 133: Lewis-formula of hemiindigo **29**.

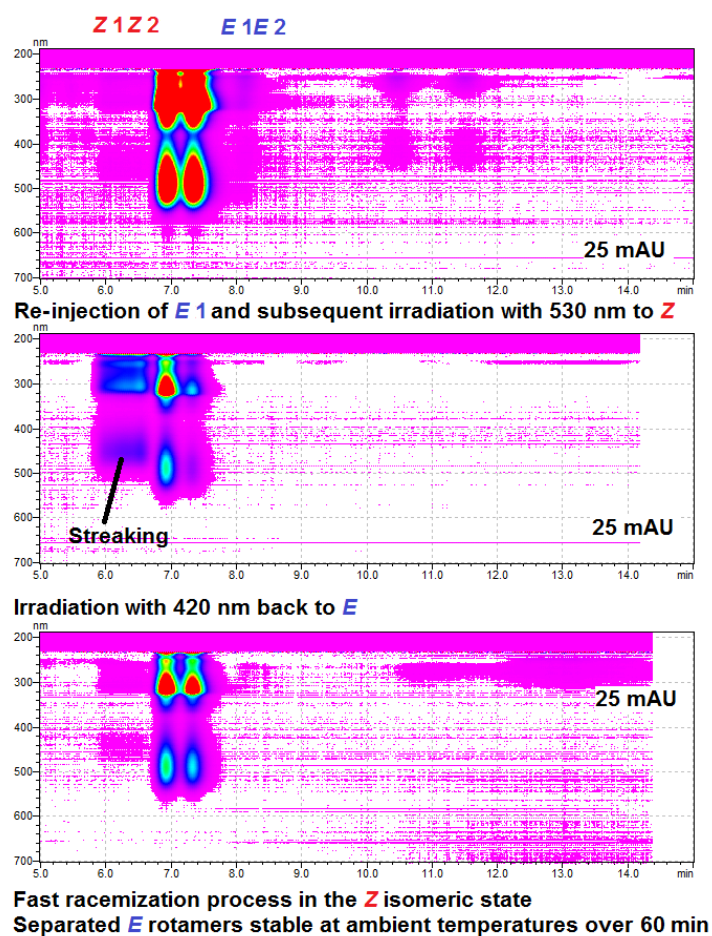


Figure 134: 3D UV-Vis Chromatograms of hemiindigo **29** on a chiral HPLC column (*Diacel Chiralpak IC*, 5 $\mu$ m, 8 mL/min) recorded at 0 °C in 83 / 17 heptane / ethyl acetate. Injection of a *Z* / *E* mixture gives mainly two separable peaks, *E* 1 and *E* 2. The peak intensity scale is given in mAU (milli a.u., arbitrary units).

Collection and re-injection of *E* 1 gives the pure peak and some residual *E* 2 from fraction overlap (not shown). Irradiation of *E* 1 to the *Z* state did yield peaks for the *Z* isomers, which show streaking at 0 °C, indicating a small rotational barrier for the chiral axis. The low *Z* isomer

yields can be caused by the already confirmed poor photoswitching behavior of **26**, see section 2.2.11. Irradiation back to the *E* form, however, restored the racemate, which is consistent to the dimethylamino and methyl derivatives. *E* 1 left in the dark did not noticeably racemize, heating to 100 °C for 20 minutes, however, yielded the racemate (not shown).

As this substitution pattern did also not show different chiral behavior besides its poor isomeric yields for the *Z* isomer after photoswitching, it was also not investigated further.

### 2.3.7 Second generation of axially chiral arylated hemiindigos - Introduction of axially chiral stilbene fragments

As the thermal barriers for the atropisomerizations seemed to be low for hemiindigo **20**, especially in the *Z* isomeric state, naphthyl moieties were introduced as stilbene fragment with the intent to stabilize the chiral axes. This should be observed by twisting of the stilbene fragment caused by sterical interference of the central double bond proton and the naphthyl proton and / or the *ortho*-methyl group, respectively. This twisting should reduce sterical strain at the *ortho*-tolyl chiral axis, increasing its rotational barriers. The introduction of two asymmetric units was also revisited, as previous molecules **55** and **57** did not show desired properties at ambient temperatures.

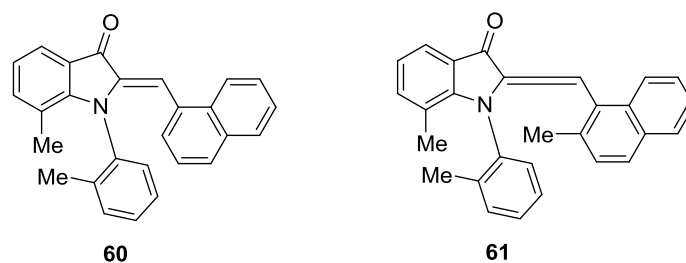


Figure 135: Second generation of synthesized axially chiral hemiindigo derivatives **60** and **61**.

2.3.7 SECOND GENERATION OF AXIALLY CHIRAL ARYLATED HEMIINDIGOS - INTRODUCTION OF AXIALLY CHIRAL STILBENE FRAGMENTS

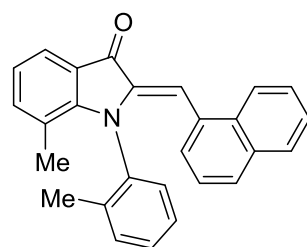


Figure 136: Lewis-formula of hemiindigo **60**.

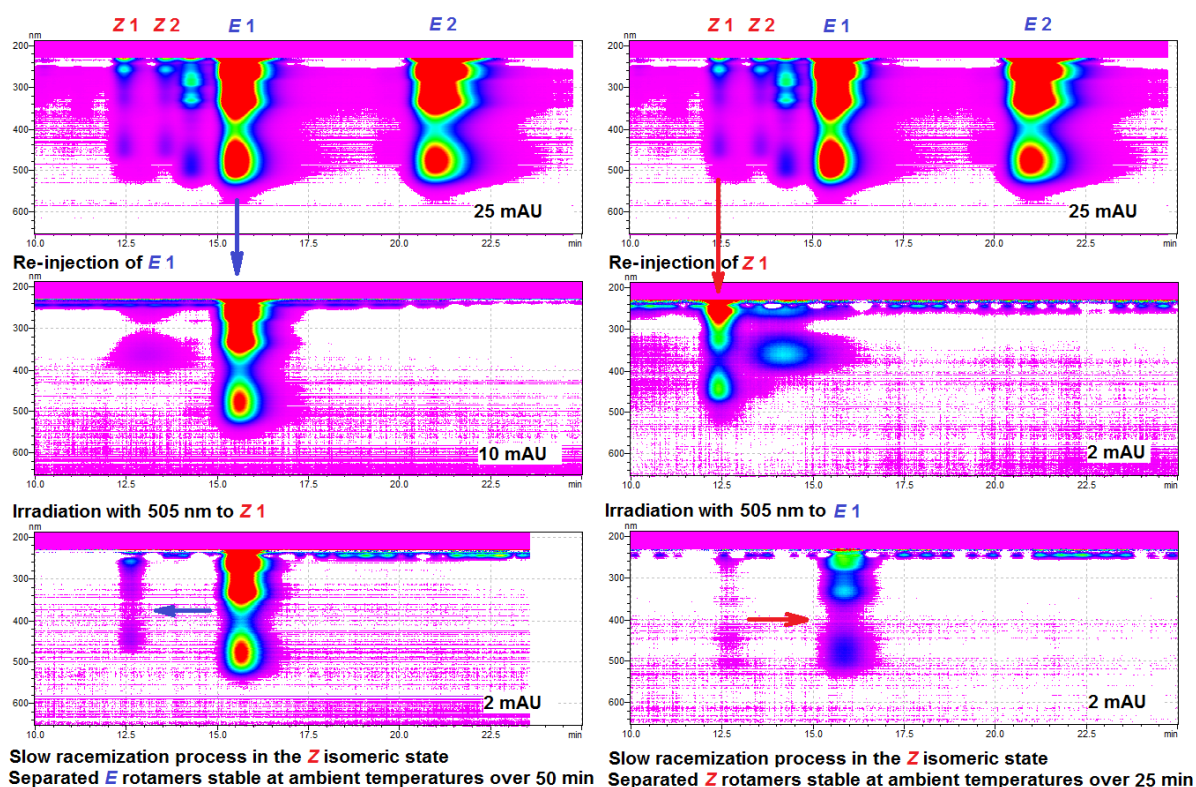


Figure 137: 3D UV-Vis Chromatograms of hemiindigo **60** on a chiral HPLC column (*Diacel Chiralpak IC*, 5 $\mu$ m, 8 mL/min) recorded at 0 °C in 95 / 5 heptane / ethyl acetate. Injection of a *Z* / *E* mixture gives four separable peaks, *Z* 1, *Z* 2, *E* 1 and *E* 2, which is a novelty compared to the previously synthesized hemiindigos substituted with chiral axes. The peak intensity scale is given in mAU (milli a.u., arbitrary units). Collection and re-injection of *E* 1 (left) gives the pure *E* peak. Collection and re-injection of *Z* 1 (right) gives the pure peak and some unknown side product, which is probably a residue from a previous run. Irradiation of *Z* 1 to the *E* state yielded the *E* 1 isomer almost quantitatively. *E* 1 and *Z* 1 left in the dark did not noticeably racemize, heating to 100 °C for 25 minutes, however, yielded the racemates (not shown).

Irradiation of *E* 1 to the *Z* state did only yield small amounts of the *Z* isomer because of poor choice of irradiation wavelength, as the PSS is already heavily *E* isomer enriched at 505 nm,



which is caused by the presumably very high quantum yield of this compound in apolar solvents. However, only the *Z* 1 isomer is obtained and not the racemic mixture of both, which shows that the photoisomerization itself does not racemize the chiral axis. This compound does not significantly racemize in its *Z* isomer at 0 °C in contrast to all previously examined hemiindigos substituted with chiral axes. As the introduction of naphthyl residues yielded stable chiral axes in both *Z* and *E* isomeric forms, it was possible to isolate and study these compounds via NMR, UV-Vis, ECD spectroscopy and X-ray crystallography.

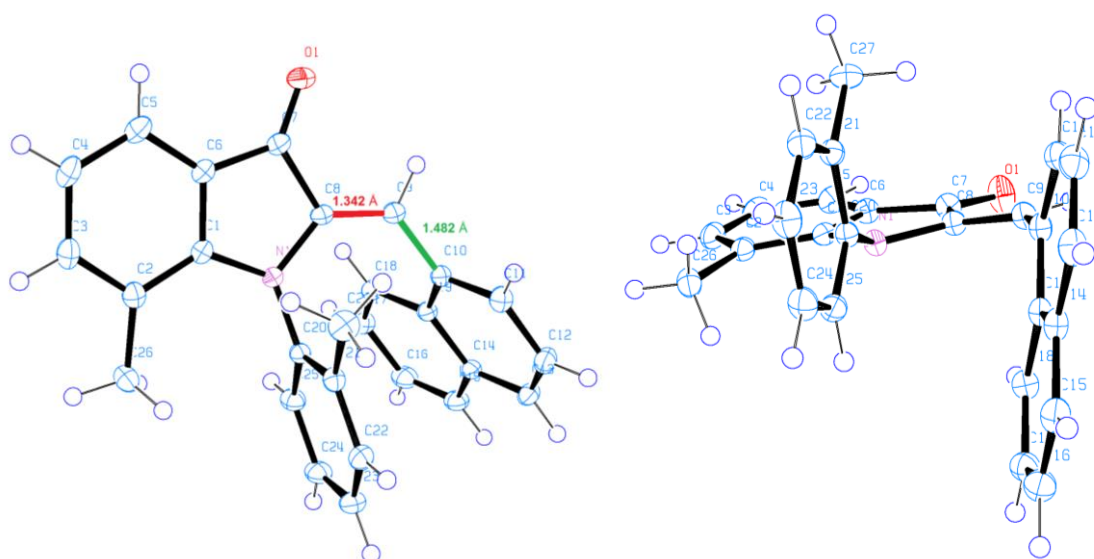


Figure 138: Structure of hemiindigo **60** in the crystalline state. The viewing angle on the right emphasizes the strong twisting of the naphthyl stilbene fragment and the *ortho*-tolyl chiral axis within the *Z* form. Latter is strongly twisted with a dihedral torsion angle of 102.71° for C25-C20-N1-C1. The twist around the stilbene single bond amounts to 72.49° for C8-C9-C10-C19. The length of the double bond (red) amounts to 1.342 Å and the single bond (green) amounts to 1.482 Å.

2.3.7 SECOND GENERATION OF AXIALLY CHIRAL ARYLATED HEMIINDIGOS - INTRODUCTION OF AXIALLY CHIRAL STILBENE FRAGMENTS

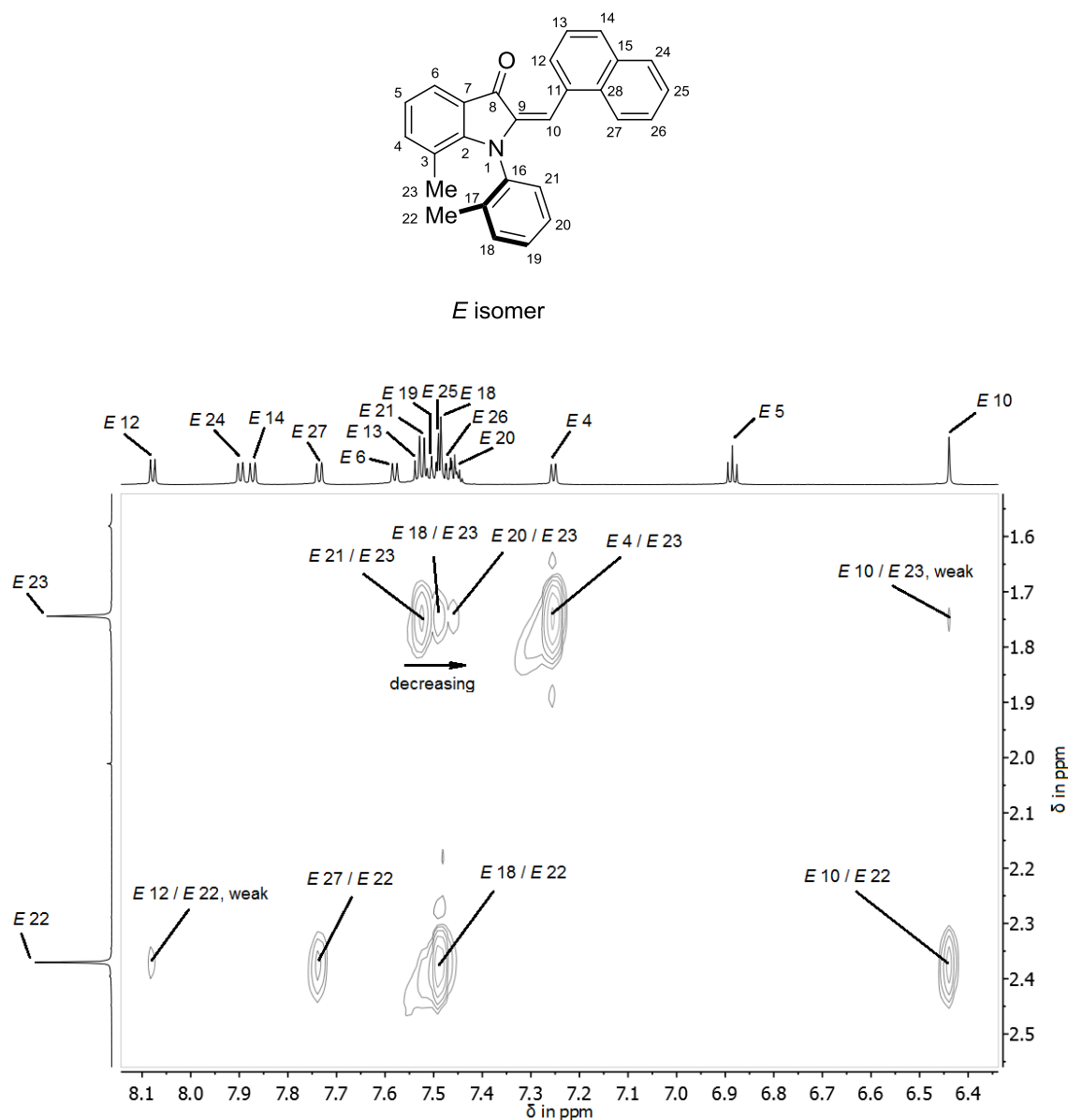


Figure 139: Section of the NOESY  $^1\text{H}$ -NMR spectrum (dichloromethane- $d_2$ , 800 MHz, 27 °C) of hemiindigo *E*-60. The strong NOE cross signal between proton *E* 10 and protons *E* 22 and the weak interaction between *E* 12 and *E* 22 suggest the *E* conformation. Cross signal *E* 27 / *E* 22 and the downfield shift of *E* 12 and *E* 27 suggest the naphthyl moiety to face away from the carbonyl oxygen while maintaining rotatability at the carbon-carbon single bond (weak signals *E* 12 / *E* 22). Cross signals *E* 21 / *E* 23, *E* 18 / *E* 23 and *E* 20 / *E* 23 exemplify the proximity of methyl group *E* 23 towards the ring system of the chiral aryl axis.

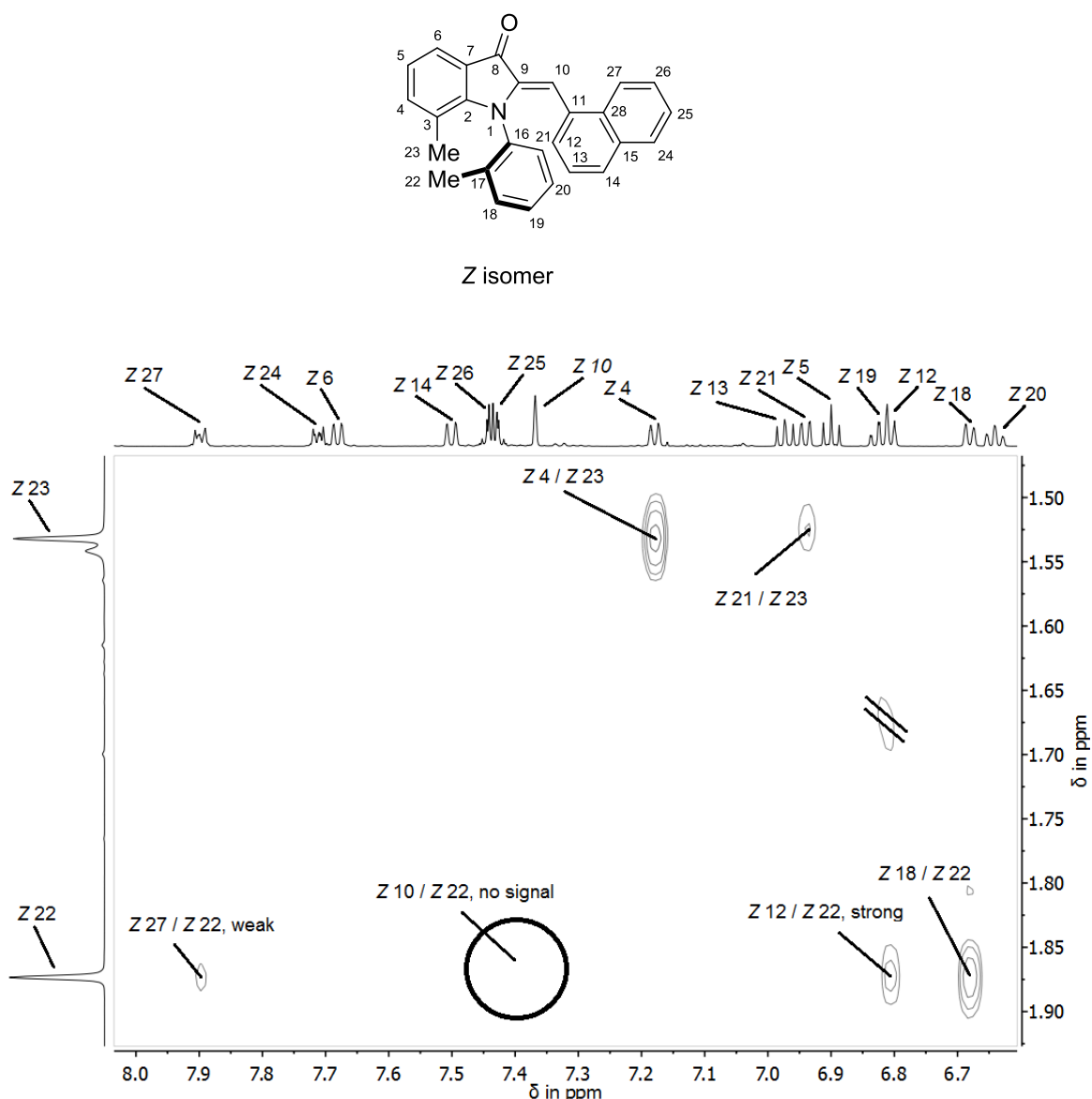


Figure 140: Section of the NOESY  $^1\text{H}$ -NMR spectrum (dichloromethane- $d_2$ , 600 MHz, 27°C) of hemiindigo Z-60. The missing NOE cross signal between proton Z 10 and protons Z 22 and the strong interaction between Z 12 and Z 22 suggest the Z conformation. Cross signal Z 27 / Z 22 suggests twisting of the stilbene and the downfield shift of Z 27 suggest the naphthyl moiety to face towards the carbonyl oxygen while maintaining rotatability at the carbon-carbon single bond. Signal Z 12 shows a strong upfield shift, hinting towards increased distance towards the carbonyl oxygen. Cross signal Z 21 / Z 23, exemplifies the proximity of methyl group Z 23 towards the ring system of the chiral aryl axis.

2.3.7 SECOND GENERATION OF AXIALLY CHIRAL ARYLATED HEMIINDIGOS - INTRODUCTION OF AXIALLY CHIRAL STILBENE FRAGMENTS

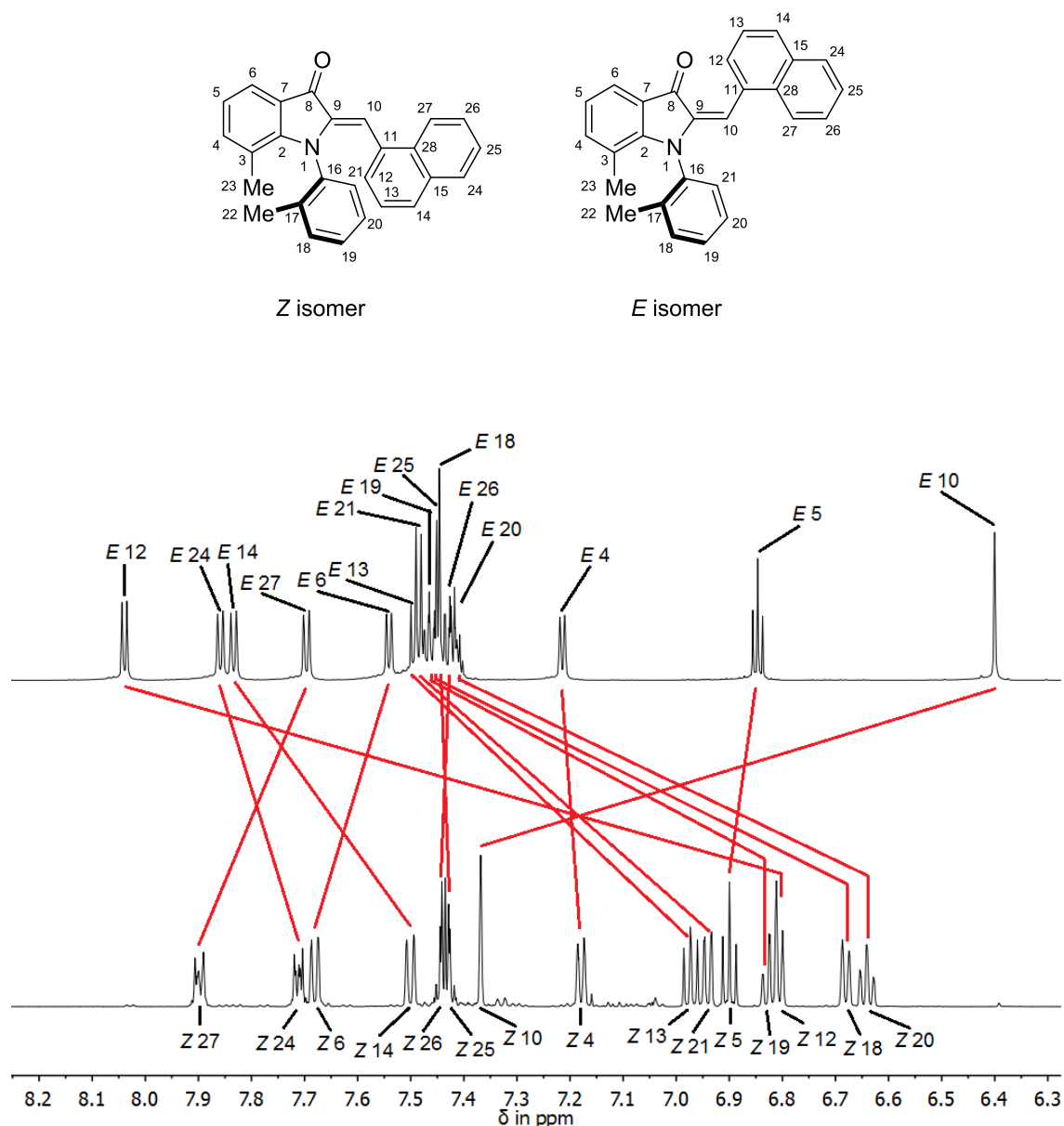


Figure 141: Section of the  $^1\text{H-NMR}$  spectra (dichloromethane- $d_2$ , 800 / 600 MHz, 27 °C) of *E* (top) and *Z* isomer (bottom) enriched mixtures of hemiindigo **60**. Strong chemical shifts can be observed upon transition from *E* to *Z* isomer, which indicates proximity of the stilbene ring current towards the *N*-aryl chiral axis in the *Z* state as the signals for the *E* isomer are separated from each other and tend to shift upfield in the *Z* isomer. The large upfield shifts of signals 12, 18, 19, 20 and 21 from *E* to *Z* and the downfield shift of signal 27 indicates transition from a mostly planar stilbene fragment in *E* configuration to pronounced twisting of the naphthalene in the *E* state.

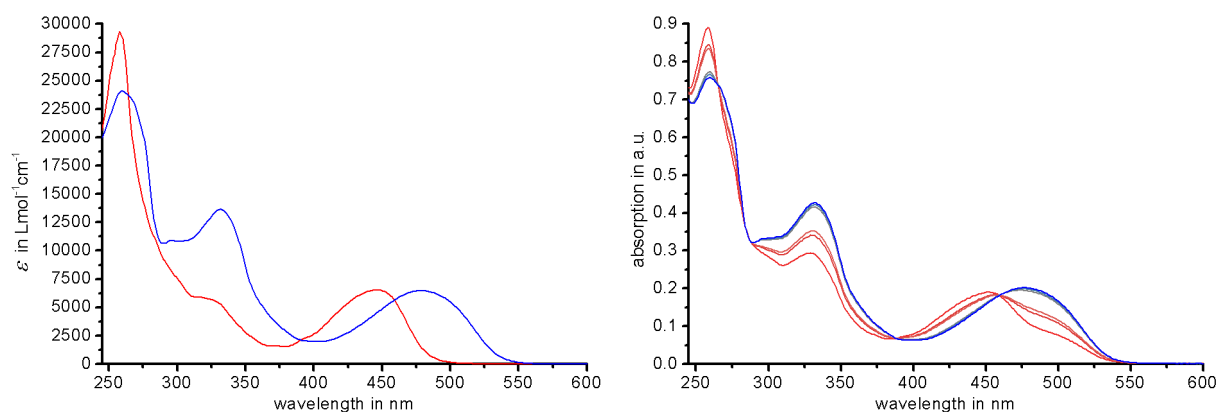


Figure 142: Molar absorption (left) and PSS (right) spectra of hemiindigo **60** in 95 / 5 heptane / ethyl acetate. The isosbestic points remain defined, verifying the photostability of this compound. Best isomeric yields were determined at 95% *E* isomer (435 nm) and 39% *Z* isomer (617 nm).

The low isomeric yield for the *Z* isomer of 39% is caused by the high difference in quantum yields for *Z* and *E* isomer. If a solution of the *Z* form is exposed to room light, large amounts of *E* isomer are generated immediately, which was not observed for any other hemiindigo so far.

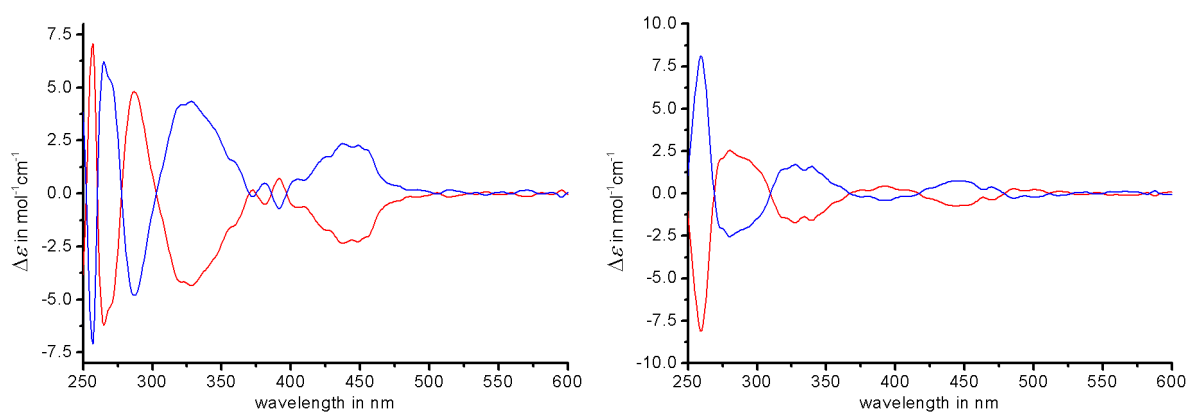


Figure 143: Molar electronic circular dichroism spectra of hemiindigo **60** for the *Z* (left) and *E* isomer (right) in 95 / 5 heptane / ethyl acetate at 0 °C. Fractions *Z* 1 and *E* 1 yielded the red spectra (*ortho*-tolyl  $S_a$  configurations) while *Z* 2 and *E* 2 yielded the blue spectra ( $R_a$  configurations).

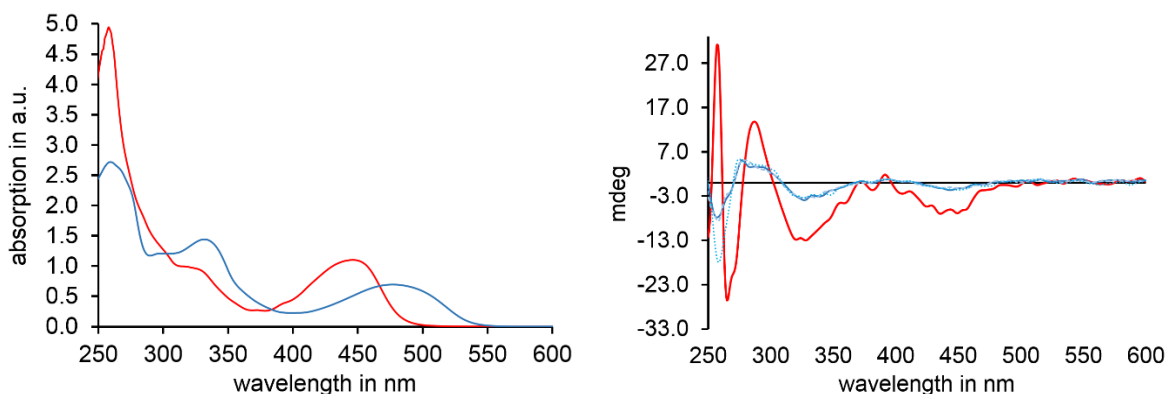


Figure 144: UV-Vis (left) and ECD spectrum (right) of **60** in 95 / 5 heptane / ethyl acetate after one cycle of switching of *E* (blue) and *Z* (red) isomers at 0 °C. Isomerization from *E* to *Z* was not feasible with all wavelengths available in this solvent mixture (irradiation in dimethyl sulfoxide yielded the *Z* isomer). The mediocre thermal barrier of the chiral aryl axis in the *Z* isomer (right, red) prevents racemization at 0 °C and irradiation from *Z* to the *E* isomer (blue) yielded almost exactly the ECD spectrum of the isolated pure *E* isomer (light blue, dotted line). Irradiation with 530 nm for 5 min did not yield the *Z* isomer but did also not change the ECD spectrum (light blue, dashed line). (*Z* to *E* irradiation: 2 min 470 nm)

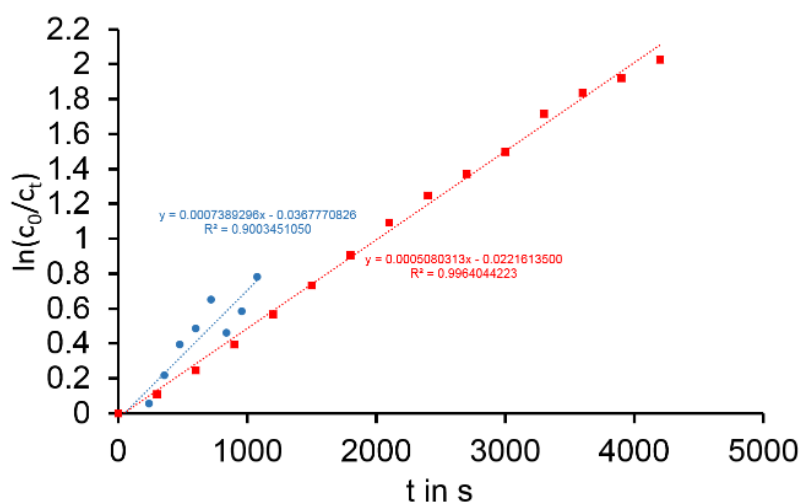


Figure 145: First order kinetic analyses of hemiindigo **60** in 95 / 5 heptane / ethyl acetate for the atropisomerization of *Z* isomer (red) and *E* isomer (blue). The data points are fitted with a linear relationship. The slope  $m$  can be translated into the rate constant  $k$  for this process. For the *Z* isomer, a rotational barrier of 21.7 kcal/mol was determined at 10 °C, which translates into a thermal half-life of 15 min at 25 °C. For the *E* isomer, a rotational barrier of 24.3 kcal/mol was determined at 60 °C, which translates into a thermal half-life of 21 h at 25 °C.

The introduction of a naphthyl group proved as a major success as all four forms of hemiindigo **60** could be isolated and examined. This was achieved due to the chiral aryl axis barrier reaching values over 21 kcal/mol, which makes handling of the compounds possible at 0 °C.

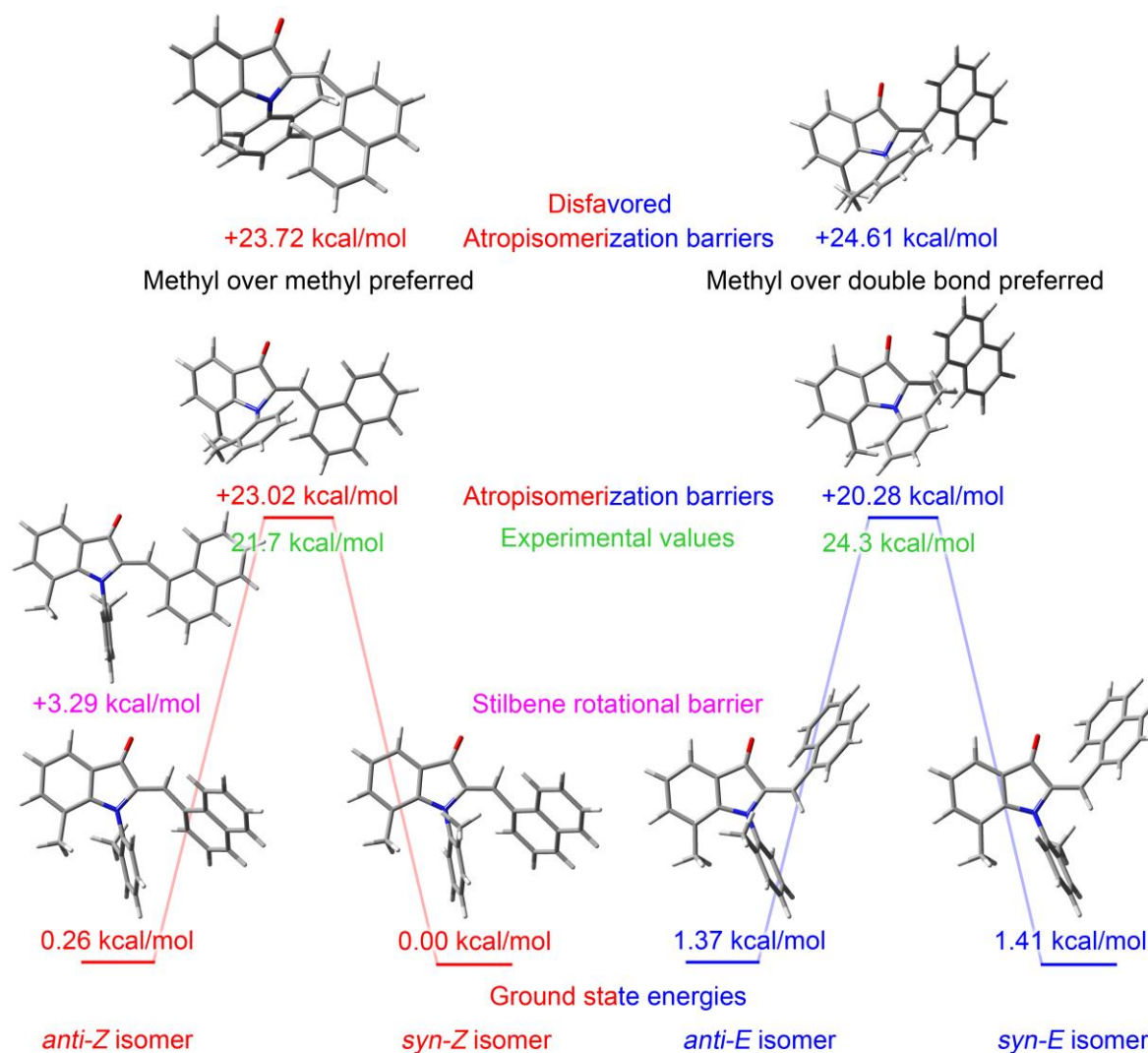


Figure 146: Calculated ground and transition state structures of hemiindigo **60** at the B3LYP/6-311+G(d,p) level of theory. All transition states for the atropisomerization and one for the stilbene single bond rotation were found. The transition state of the stilbene single bond did not converge after several attempts and tweaks. The “+” sign in front of transition state values indicates the energy difference with respect to the lowest ground state of respective *Z* or *E* isomers. The calculated energies are in good agreement to the experimental values for the *Z* isomer, however the lowest transition state of the *E* isomer is undershot by about 4 kcal/mol compared to the experimental values. The methyl-over-methyl

transition state is disfavored by 4 kcal/mol in the *E* isomer and the methyl over central double bond transition state is disfavored by 1 kcal/mol in the *Z* state. A by 2.6 kcal/mol lowered atropisomerization barrier for the *Z* isomers can be measured. The transition state structures suggest a rotation of the *ortho*-tolyl axis methyl group over the indoxyl core methyl group in the *Z* state while the *E* form prefers passing of the methyl group over its central double bond. These findings show that gating of thermal barriers as well as their directionality are possible for these chiroptical photoswitches.

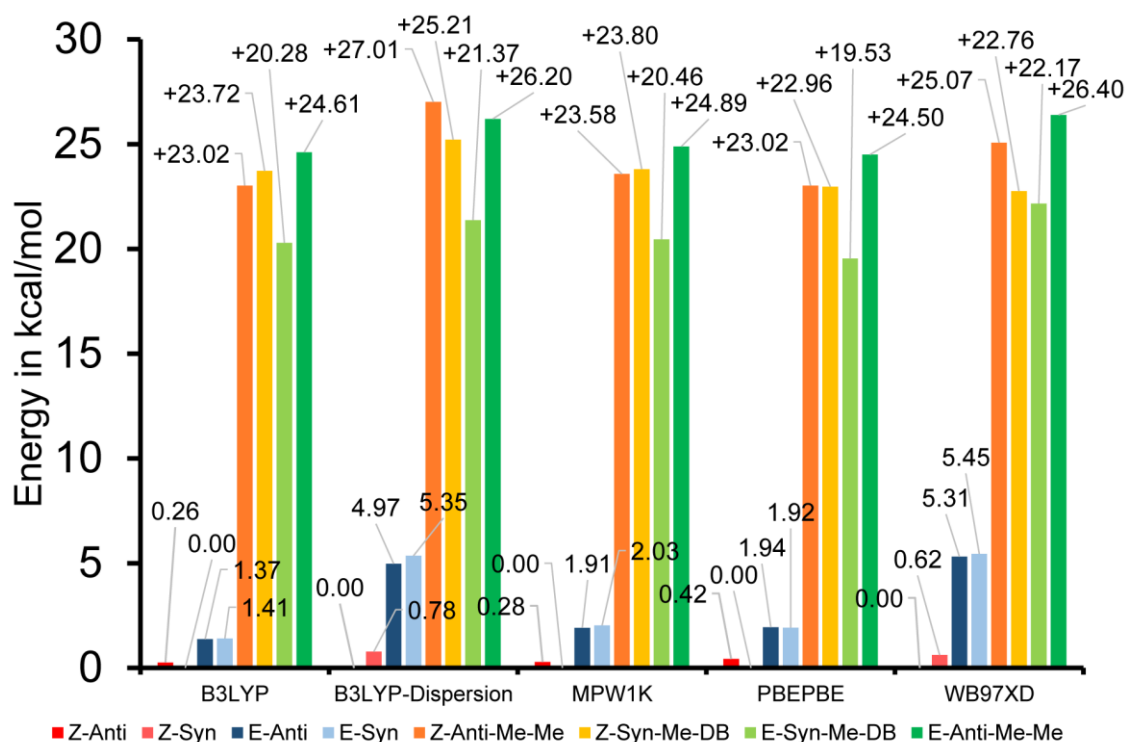


Figure 147: Benchmarking results for hemiindigo **60** using different DFT functionals for the 6-311+G(d,p) basis set. “Z-anti/syn” and “E-anti/syn” represent the ground states and “Z-Anti-Me-Me” and “E-Syn-Me-DB” the energetically lowest transition state for respective isomer and rotation pathway in all cases without dispersive corrections except for the PBEPBE functional. The “+” sign in front of transition state values indicates the energy difference with respect to the lowest ground state of respective *Z* or *E* isomers.

For the *E* isomer, a rotation of the chiral axis methyl over the central double bond is preferred for all functionals. In the *Z* isomer, the PBEPBE-, WB97XD- and B3LYP functional with GD3BJ dispersion favors a rotation of the methyl group over the central double bond. The B3LYP- and MPW1K functional suggest the rotation over the indoxyl methyl group by a small



margin, which stands in contrast to hemiindigo **30** and **33**. Disabling dispersive corrections yields very similar results for all functionals.

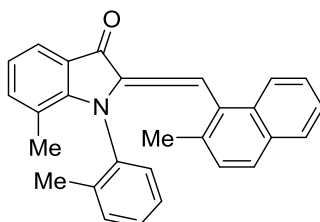


Figure 148: Lewis-formula of hemiindigo **61**.

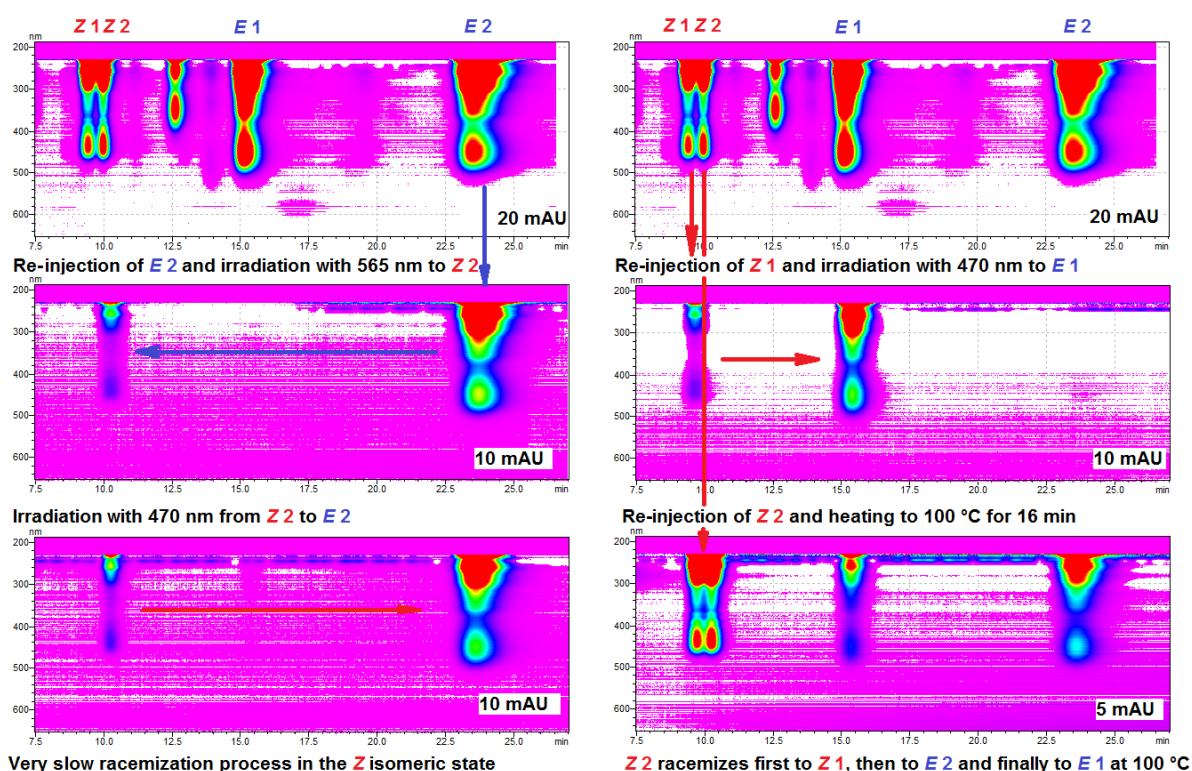


Figure 149: 3D UV-Vis Chromatograms of hemiindigo **61** on a chiral HPLC column (*Diacel Chiralpak IC*, 5  $\mu\text{m}$ , 8 mL/min) recorded at 0 °C in 95 / 5 heptane / ethyl acetate. Injection of a *Z* / *E* mixture gives four separable peaks, *Z* 1, *Z* 2, *E* 1 and *E* 2, which shows similar results to hemiindigo **60** with the addition that eight peaks were expected, see Figure 151. The peak intensity scale is given in mAU (milli a.u., arbitrary units).

Collection, irradiation with 565nm and re-injection of *E* 2 (left) gives the *E* 2 and only small amounts of the *Z* 2 peak because of the broad spectrum of this LED color. Irradiation of *Z* to the *E* state showed only small changes as the *E* isomer resides as major species. However, only the *Z* 2 and *E* 2 isomers are obtained. Collection, irradiation and re-injection of *Z* 1 (right) gives the pure *E* 1 peak. Collection and heating to 100 °C for 16 min of *Z* 2 yielded all isomers at

different intensities. The *Z* 1 isomer is formed first, followed by the *E* 2 isomer and lastly the *E* 1 isomer.

The high thermal barriers of hemiindigo **61** allow for easy separation and handling of isomers.

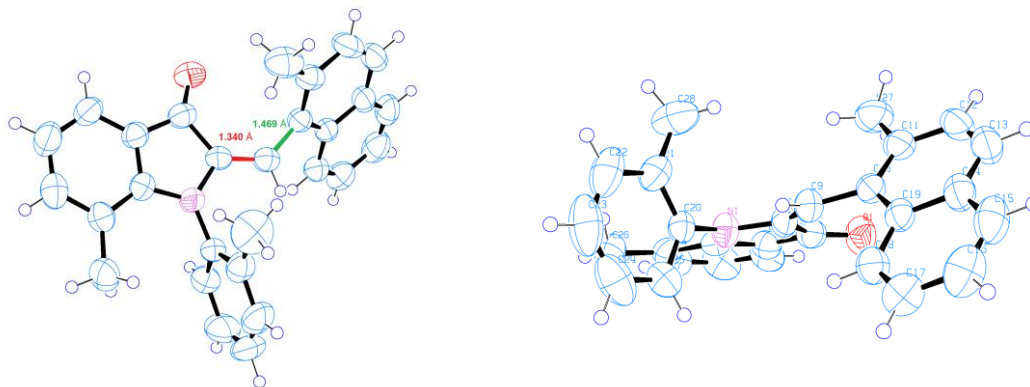


Figure 150: Structure of (*S<sub>a</sub>*)-(*S<sub>a</sub>*)-*anti-E*-**61** in the crystalline state. The *anti* form is defined by the higher oxidized carbon position in the phenyl ring opposing the *ortho*-tolyl methyl group. This means that in the *anti* form both methyl groups involved in axial chirality are configured *syn* to each other. The viewing angle on the right emphasizes the strong twisting of the naphthyl stilbene fragment and the *ortho*-tolyl chiral axis within the *E* form. Latter is strongly twisted with a dihedral torsion angle of 84.09° for C25-C20-N1-C1. The stilbene single bond is twisted by 53.58° for C8-C9-C10-C11. The length of the double bond (red) amounts to 1.340 Å and the single bond (green) amounts to 1.469 Å.

As one asymmetric chiral axis induces asymmetry in an adjacent symmetric part of the molecule, as seen with hemiindigo **60**, desymmetrization of this symmetric part will also split the signals of the initial asymmetric chiral axis. This can be observed for hemiindigo **61** via NMR spectroscopy.

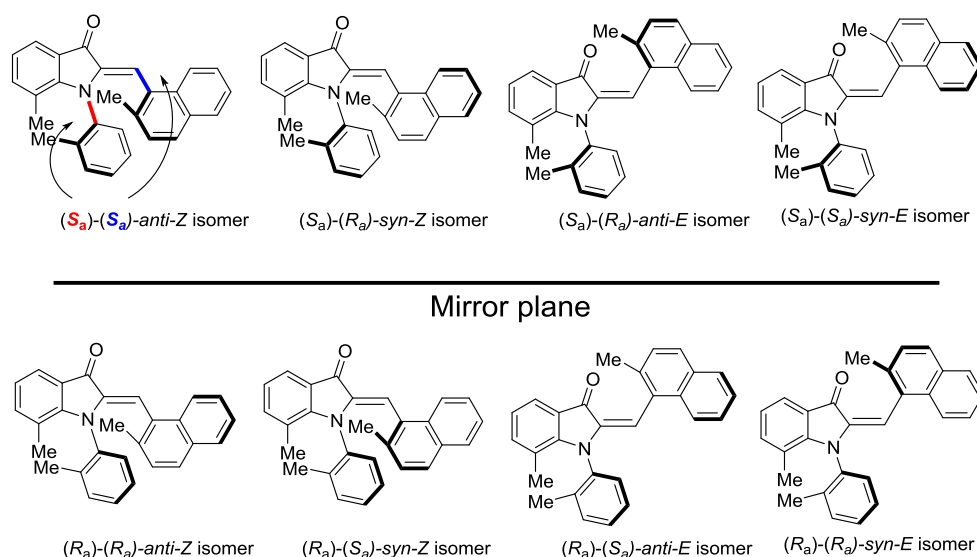


Figure 151: Overview of all possible conformations of hemiindigo **61**.

The ability to separate only four of the eight prevalent enantio- and diastereomers via chiral HPLC at 0 °C hints towards an unlocked stilbene single bond rotation barrier, as the used chiral HPLC column reliably separates between the  $R_a$ - and  $S_a$ -*ortho*-tolyl axes of all investigated hemiindigos so far. This means that *syn*- and *anti* diastereomers cannot be separated at the utilized conditions. NMR studies (Figure 152) confirm these assumptions, as the *Z* 1 and *Z* 2 as well as the *E* 1 and *E* 2 fractions show exactly the same spectra, respectively. This labels all of the isolated fractions as mixtures of *syn*- / *anti* diastereomers, which explains the large amount of visible signals to the additionally occurring two-fold signal splitting for each molecular part that experiences an asymmetric environment. This means a doubled signal set for all *ortho*-tolyl and naphthyl hydrogen and carbon signals is expected for each *syn* and *anti* diastereomer for every fraction *Z* 1, *Z* 2, *E* 1 and *E* 2. As enantiomers cannot be discerned via NMR without chiral alignment media,<sup>[111]</sup> the amounts of signals is reduced by half. This means that in theory a minimum of  $(10 * 2 + 7) * 2 = 54$  proton and  $(14 * 2 + 14) * 2 = 84$  carbon signals should be observable for non-helically twisted molecules. A maximum of  $(12 * 2 + 5) * 2 = 58$  proton and  $(18 * 2 + 10) * 2 = 92$  carbon signals should be observable for helically twisted molecules. These calculations are applicable for *Z* and *E* isomers each, doubling the theoretical amount of signals for isomeric *Z* / *E* mixtures.

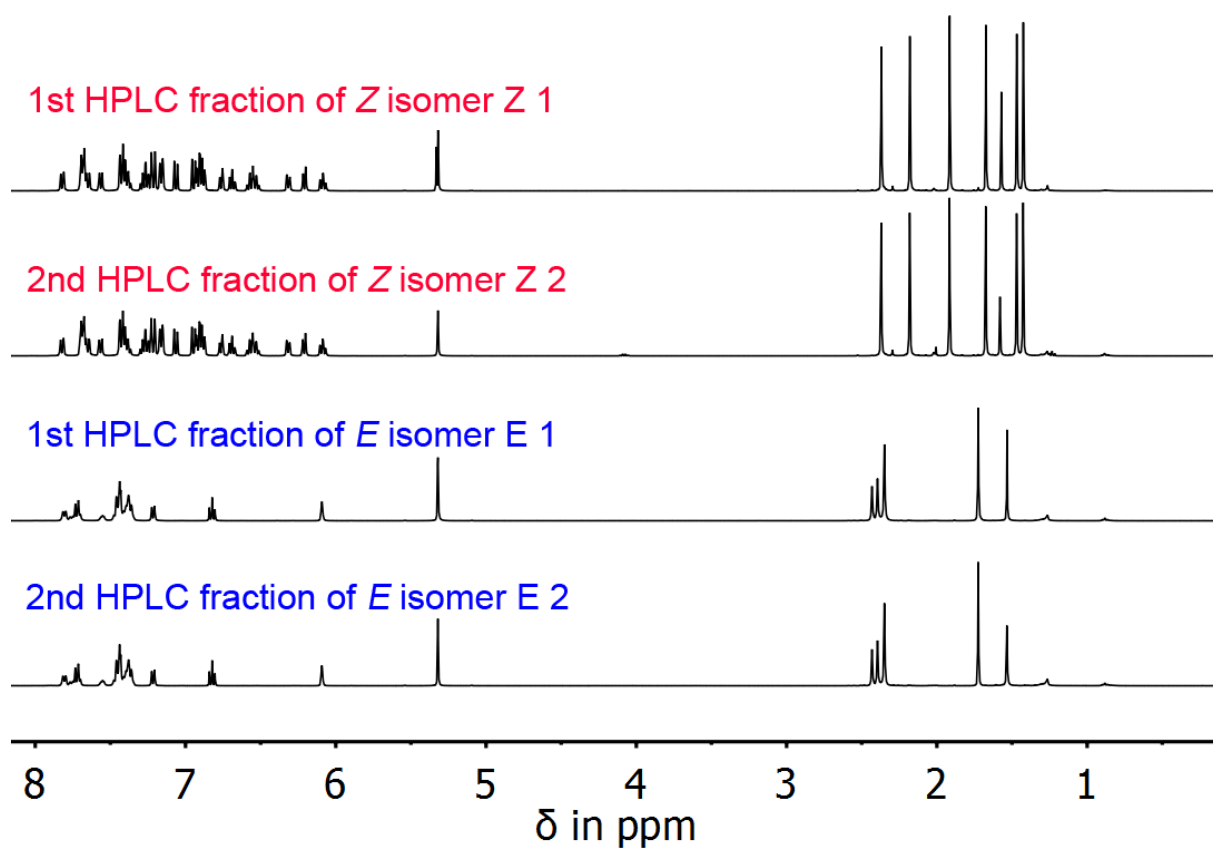


Figure 152: <sup>1</sup>H-NMR spectra (dichloromethane-*d*<sub>2</sub>, 600 MHz, 27 °C) of all four separable *Z* and *E* isomers of hemiindigo **61**. Six distinct methyl group signals can be observed for the *Z* isomer, three of them each belong to the respective *anti*- or *syn* diastereomers. In the *E* form, overlapping signals can be observed as the chemical shift between diastereomers is too small / similar to cause distinct signal shifts.

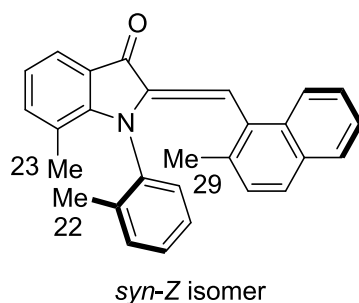


Figure 153: Lewis-formula of hemiindigo **61**.

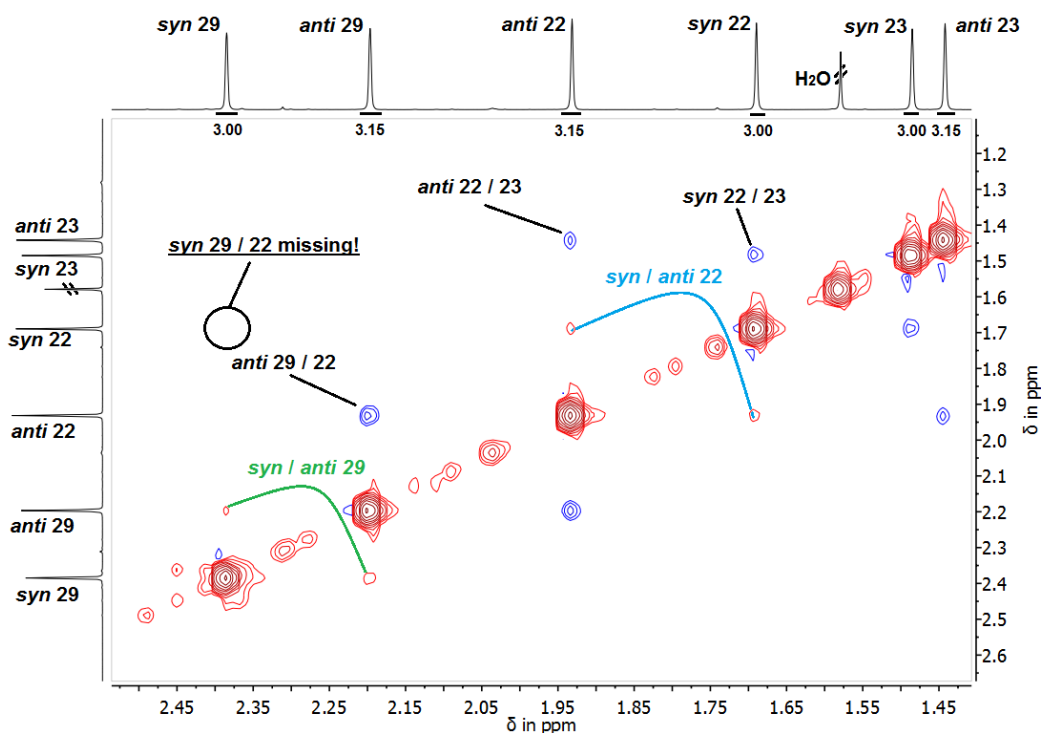


Figure 154:  $^1\text{H}$ -NOESY 2D NMR spectrum of *syn*- and *anti-Z*-**61** (dichloromethane- $d_2$ , 600 MHz, 27 °C). An unambiguous assignment can be made as cross-signal 22 / 23 is observable for *syn* and *anti* forms but signal 29 / 22 is only visible in the *anti* form in which both rotatable methyl groups are closest together. As NOESY and EXSY share the same pulse sequence, positive (red) signals between *syn* and *anti* forms prove an observable fast exchange of nuclei for these positions caused by the dynamics being faster than the used mixing time of 1.2 s.

The indicated red signals underline the rotatability of only the stilbene single bond, as one rotational flip around this axis will yield the other diastereomer while the *ortho*-tolyl axis remains stable. This explains why both signals 29 and 22 show the same positive cross-signal at the same intensity. The *anti* form is preferred by 5% over the *syn* isomer, which is also in accordance to the theoretical results (Figure 166). The  $^1\text{H}$ -NMR integrals are in accordance with the NOESY assignment.

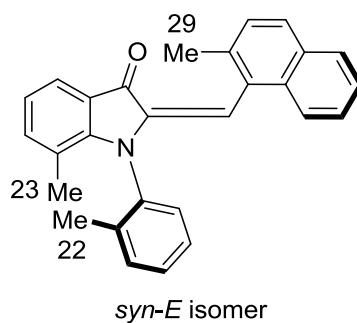


Figure 155: Lewis-formula of hemiindigo **61**.

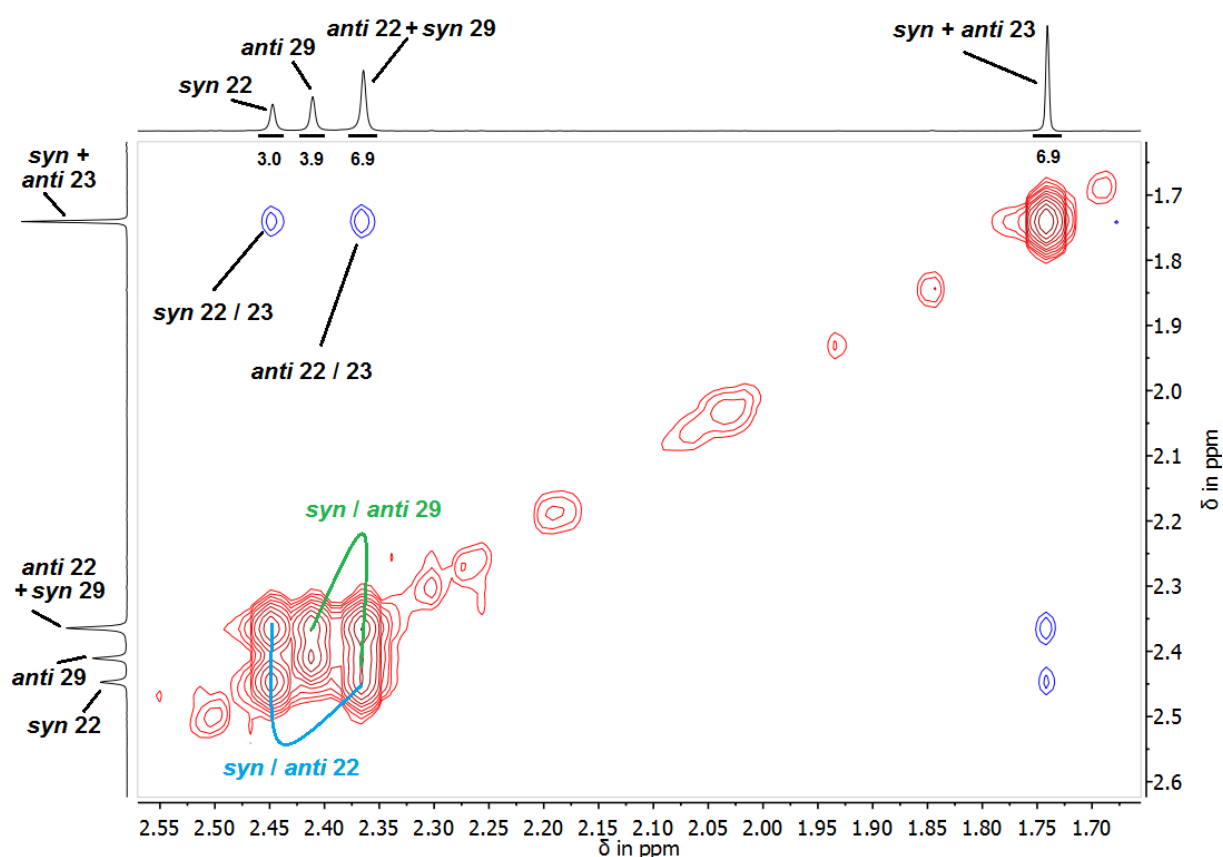


Figure 156:  $^1\text{H}$ -NOESY 2D NMR spectrum of *syn*- and *anti-E*-**61** (dichloromethane- $d_2$ , 600 MHz, 27 °C). An unambiguous *syn* / *anti* assignment cannot be made. However, the crystallized *E* isomer resides in the *anti* form (Figure 150), hinting towards its higher thermodynamic stability or crystal packing effects. The signals of 22 can be seen for the *syn*- and *anti* form and very pronounced positive (red) signals for *syn* to *anti* transitions of signals 22 and 29 can be observed. This proves faster dynamics of the stilbene single bond rotation in the *E* isomer compared to the *Z* state (see Figure 154).

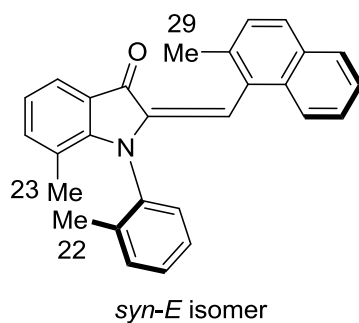


Figure 157: Lewis-formula of hemiindigo **61**.

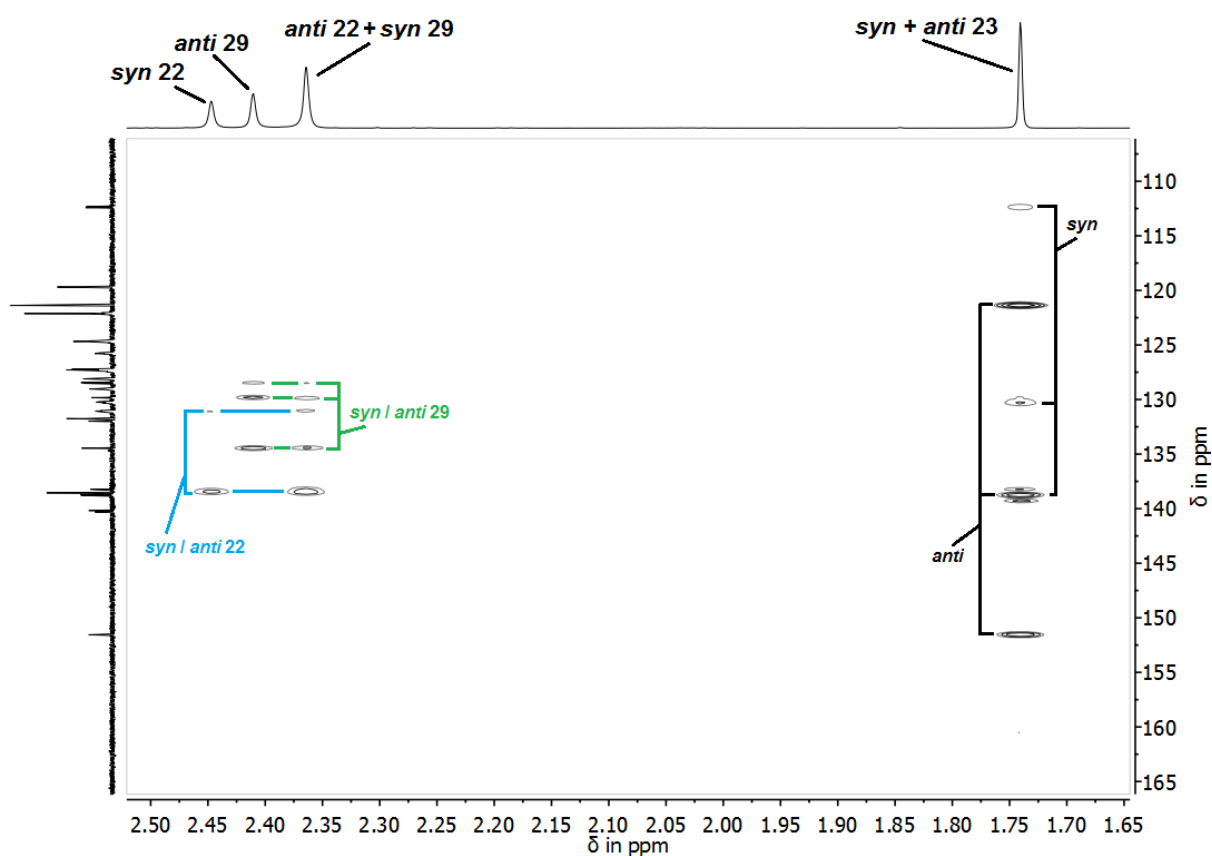


Figure 158:  $^1\text{H}$ -HSQC 2D NMR spectrum of *syn*- and *anti-E*-**61** (dichloromethane- $d_2$ , 600 MHz, 27 °C). An unambiguous *syn* / *anti* assignment cannot be made. However, the superimposing signals can be differentiated, suggesting the  $^1\text{H}$ -NOESY assignment regarding the positions of the methyl groups to be correct.

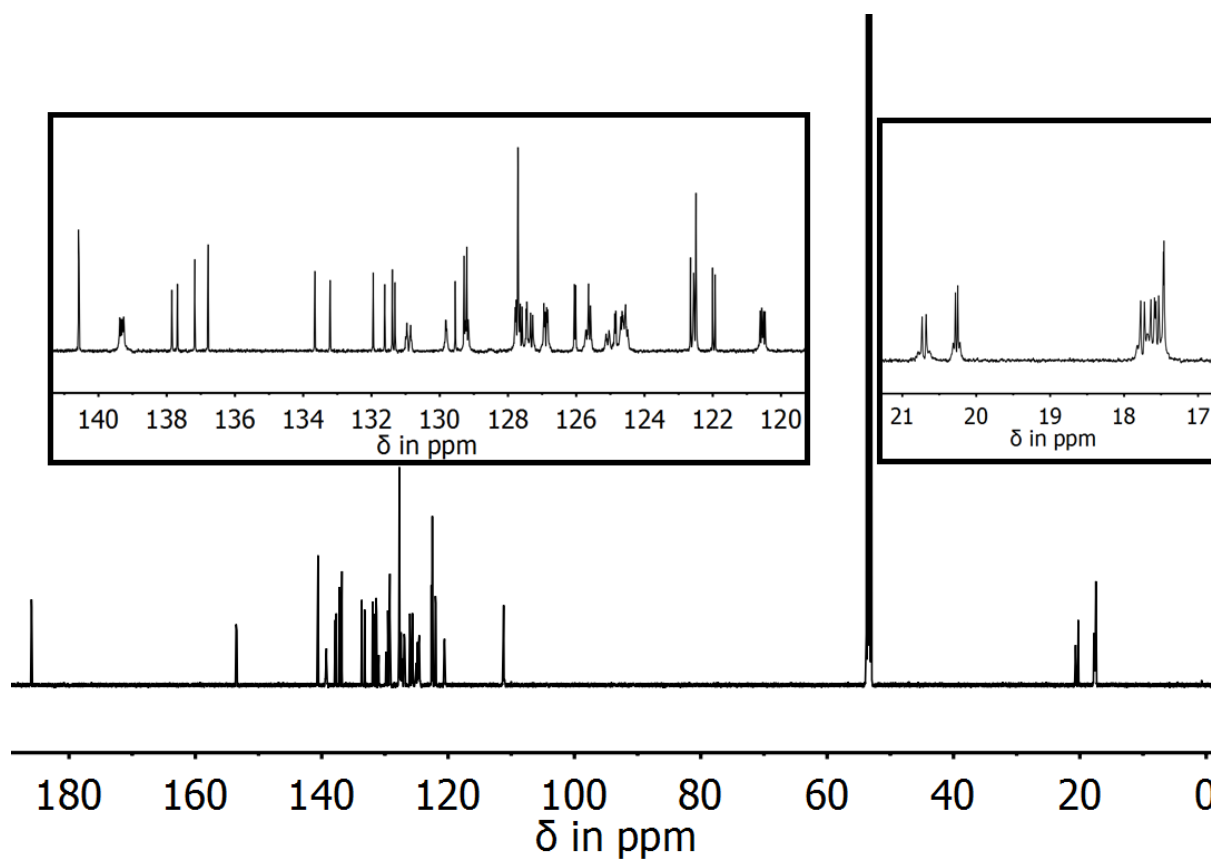


Figure 159:  $^{13}\text{C}$ -NMR spectrum of *syn*- and *anti*-**Z-61** (dichloromethane- $d_2$ , 600 MHz, 27 °C). The two insets above magnify the large amounts of signals and multiplets.

Six proton signals could be obtained for the methyl groups of these compounds while six respective multiplets are observed in the  $^{13}\text{C}$ -NMR spectrum. These signals show second order AA'BB' multiplet patterns comparable to *para*-substituted aromatic systems supporting unequal positions 1 and 4.



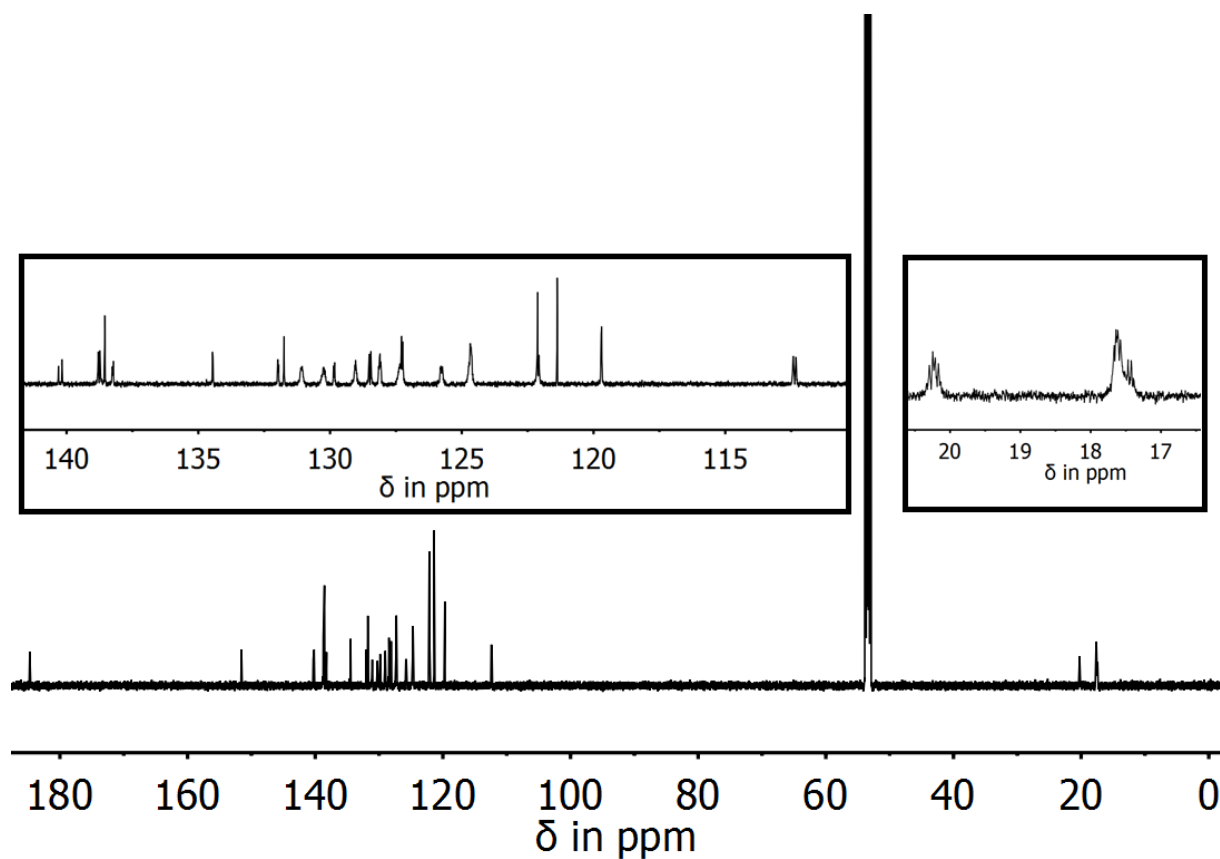


Figure 160:  $^{13}\text{C}$ -NMR spectrum of *syn*- and *anti*-*E*-**61** (dichloromethane- $d_2$ , 600 MHz, 27 °C). The insets above visualize the large amounts of signals and multiplets. Four proton signals could be obtained for the methyl groups of these compounds while two respective multiplets are observed in the  $^{13}\text{C}$ -NMR spectrum.

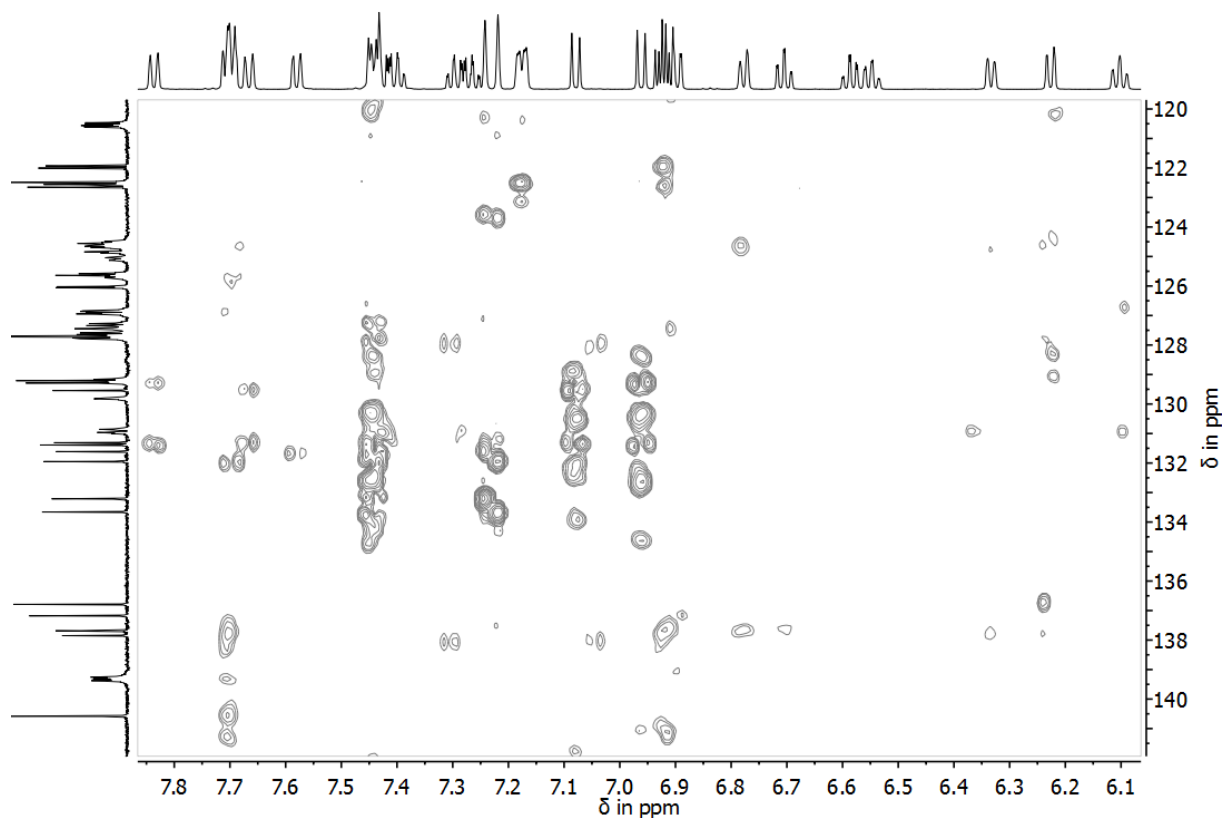


Figure 161: <sup>1</sup>H-HMBC 2D NMR spectrum of *syn*- and *anti*-**Z-61** (dichloromethane-*d*<sub>2</sub>, 600 MHz, 27 °C). An unambiguous assignment of all protons and carbons cannot be made, as interpretation by hand is impossible with this large amount of overlapping signals and ghost peaks which were observed with multiple sample preparations on 600 and 800 MHz NMR devices.

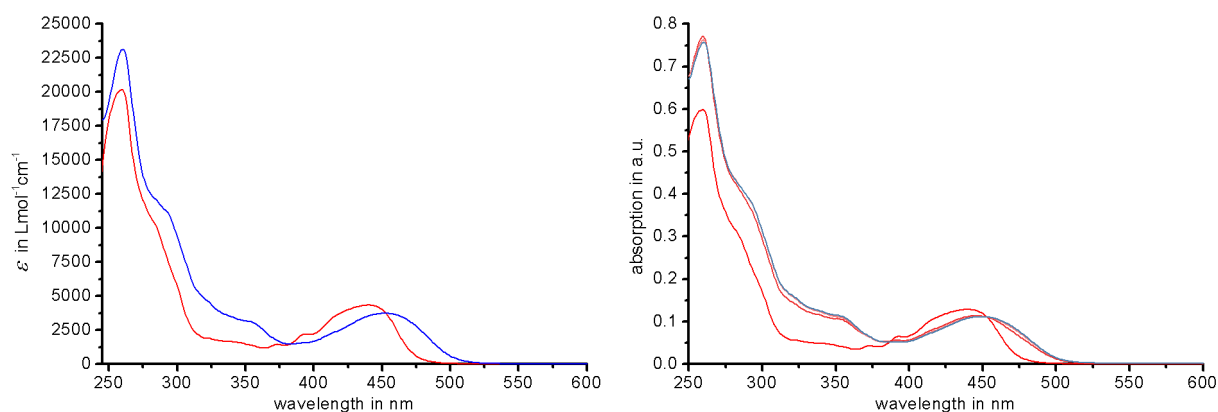


Figure 162: Molar absorption (left) and PSS (right) UV-Vis spectra of hemiindigo **61** in 95 / 5 heptane / ethyl acetate. The isosbestic points remain defined, verifying the photostability of this compound. Best isomeric yields were determined at 98% *E* isomer (470 nm) and 25% *Z* isomer (505 nm).

The low isomeric yield for the *Z* isomer of 25% is caused by the high difference in quantum yields for *Z* and *E* isomer. If the *Z* form is exposed to room light, large amounts of *E* isomer are generated immediately, which was also observed for hemiindigo **60**.

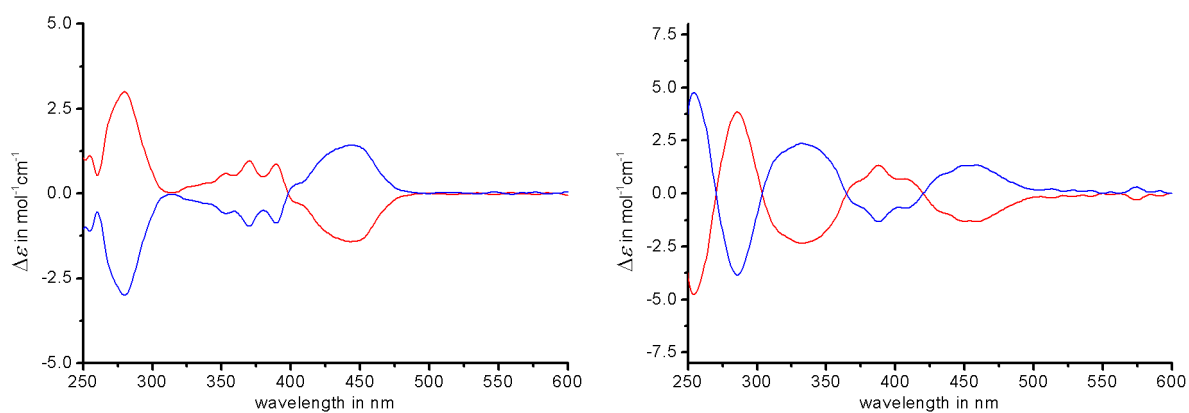


Figure 163: Molar electronic circular dichroism spectra of hemiindigo **61** for the *Z* (left) and *E* isomer (right) in 95 / 5 heptane / ethyl acetate at 0 °C. Fractions *Z* 1 and *E* 1 yielded the red spectra (*ortho*-tolyl  $S_a$  configurations) while *Z* 2 and *E* 2 yielded the blue spectra ( $R_a$  configurations).

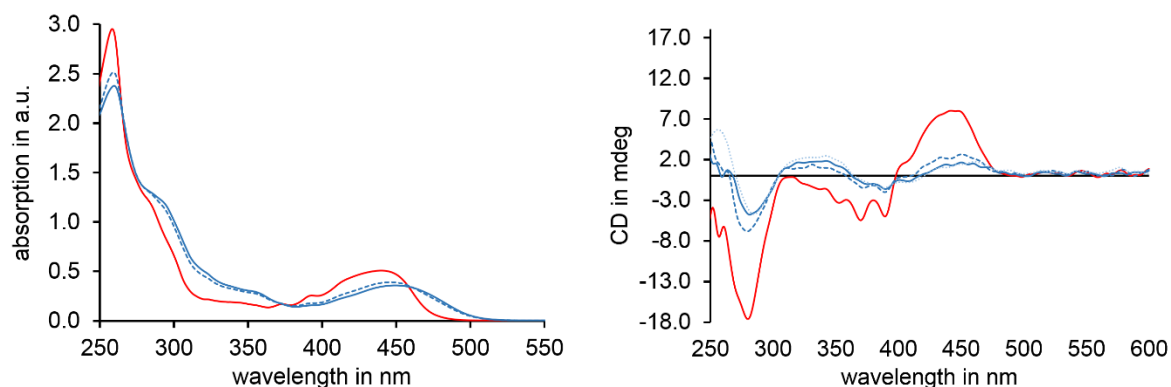


Figure 164: UV-Vis (left) and CD spectrum (right) of hemiindigo **61** in 95 / 5 heptane / ethyl acetate after one cycle of switching from *Z* (red) to *E* (blue) to little *Z* contents (blue, dashed line) at 0 °C. The high thermal barrier for the chiral aryl axis in the *Z* isomer (right, red) prevents racemization from 0 °C up to ambient temperatures and irradiation to the *E* isomer (blue) yielded almost exactly the ECD spectrum of the isolated pure *E* isomer (light blue, dotted line). Irradiation with 505 nm for 10 min did yield the *Z* isomer in low contents but did also not change the ECD spectrum (blue, dashed line), which shifts proportionally towards the *Z* state. (*Z* to *E* irradiation: 5 min 470 nm).

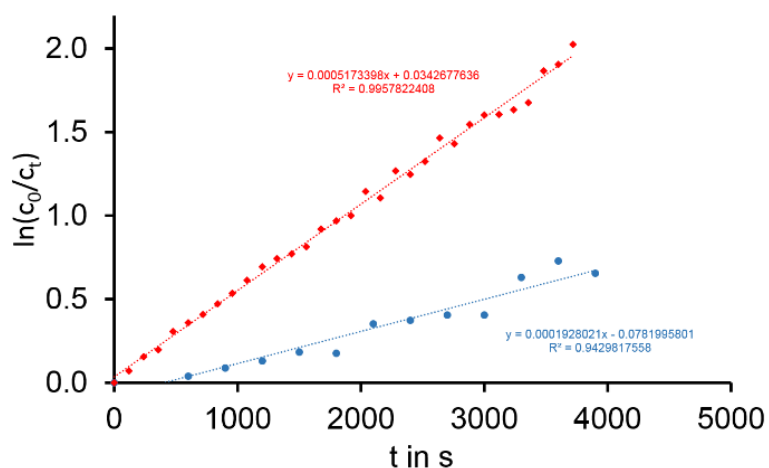


Figure 165: First order kinetic analyses of hemiindigo **61** in 95 / 5 heptane / ethyl acetate for the atropisomerization of *Z* isomer (red) and *E* isomer (blue). The data points are fitted with a linear relationship. The slope  $m$  can be translated into the rate constant  $k$  for this process. For the *Z* isomer, a rotational barrier of 24.6 kcal/mol was determined at 40 °C, which translates into a thermal half-life of 35 h at 25 °C. For the *E* isomer, a rotational barrier of 26.8 kcal/mol was determined at 80 °C, which translates into a thermal half-life of 59 d at 25 °C. Used formulas and equations can be found in Section 2.2.19.

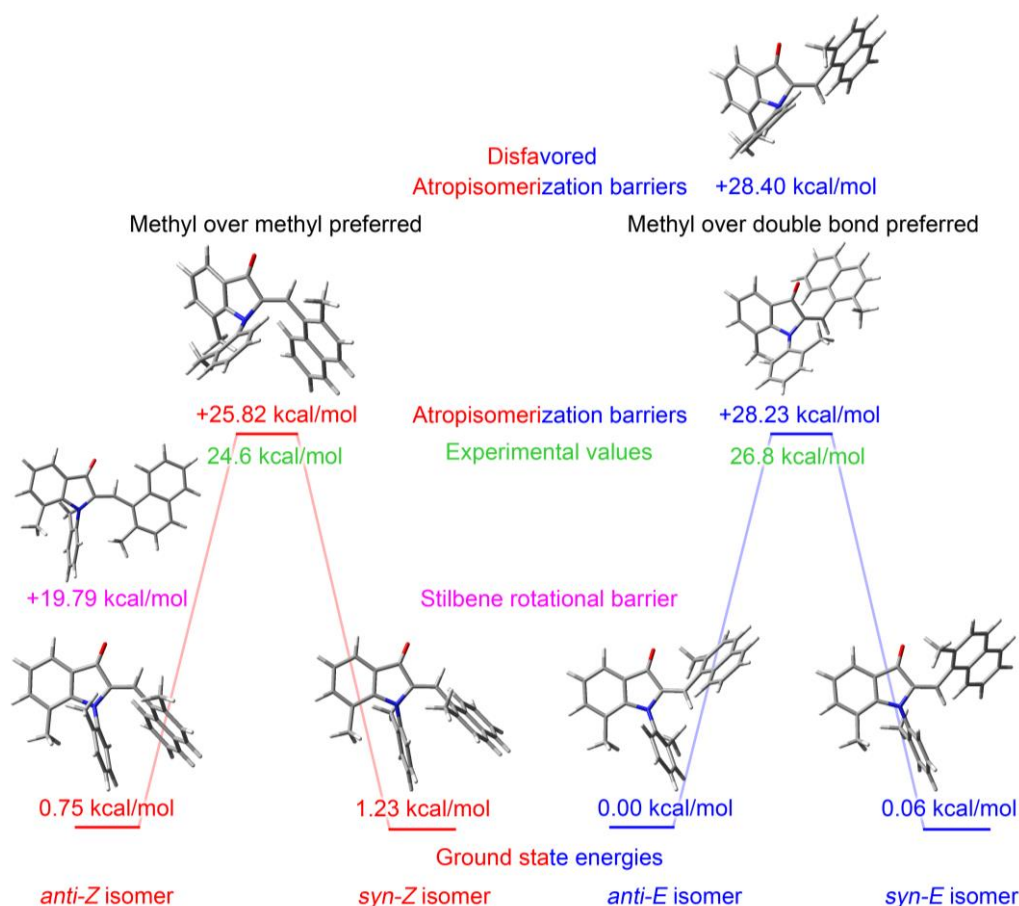


Figure 166: Calculated ground and transition state structures of hemiindigo **61** at the B3LYP/6-311+G(d,p) level of theory. Transition states for the atropisomerization and the stilbene single bond rotation were found. The disfavored atropisomerization transition state for the *Z* isomer and the stilbene rotation in the *E* isomer did not converge after several attempts and tweaks. The “+” sign in front of transition state values indicates the energy difference with respect to the lowest ground state of respective *Z* or *E* isomers.

The calculated energies are in good agreement to the experimental values for the *Z* and *E* isomer, however the lowest transition state of the *E* isomer is overshoot by about 1.5 kcal/mol compared to the experimental values. The methyl-over-methyl transition state differs only by 0.2 kcal/mol in the *E* isomer. The atropisomerization barrier is lowered by 2 kcal/mol in the *Z* state. The transition state structures suggest a rotation of the *ortho*-tolyl axis methyl group over the indoxyl core methyl group in the *Z* state while the *E* form prefers passing of the methyl group over its central double bond by a small margin. The stilbene fragment shows a relatively high rotational barrier of 19.79 kcal/mol, which is in good agreement to the NOESY NMR

experiments. These findings show that gating of thermal barriers is possible for these chiroptical photoswitches and that the design intents did work out towards the desired direction.

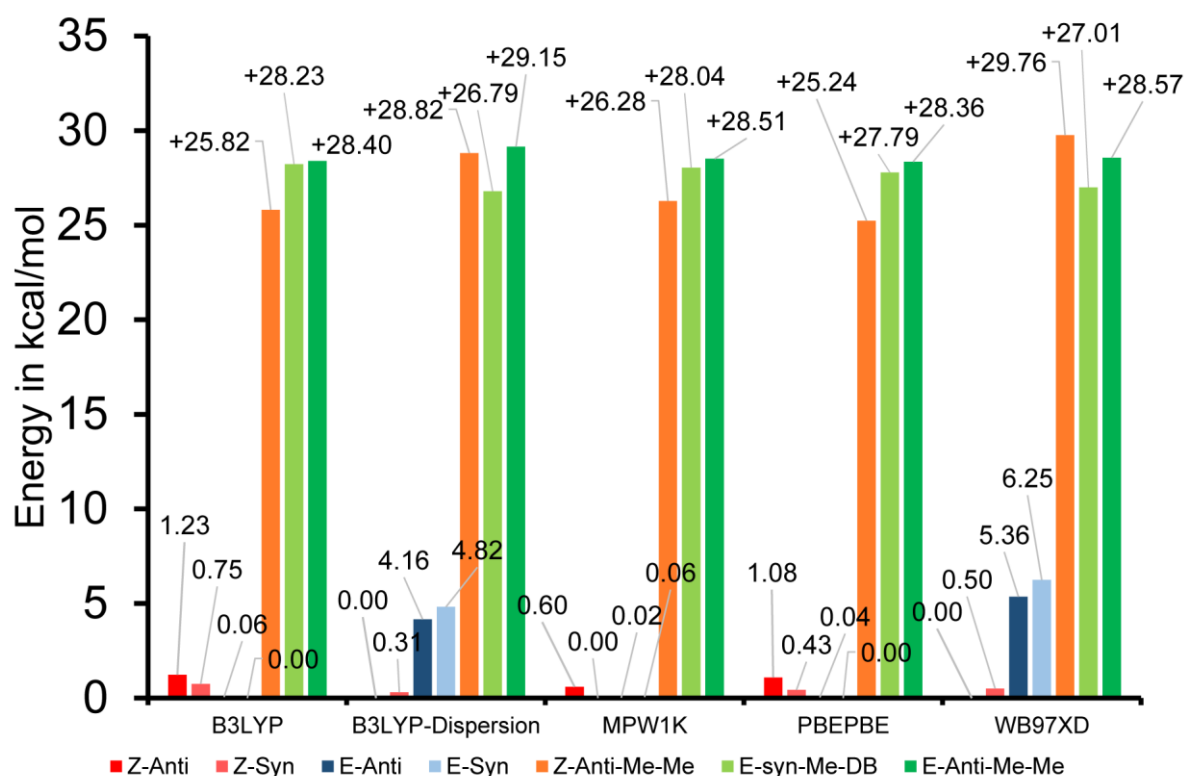


Figure 167: Benchmarking results for hemiindigo **61** using different DFT functionals for the 6-311+G(d,p) basis set. “Z-anti/syn” and “E-anti/syn” represent the ground states and “Z-Anti-Me-Me” and “E-Syn-Me-DB” the energetically lowest transition state for respective isomer and rotation pathway (see Figure 166). The “+” sign in front of transition state values indicates the energy difference with respect to the lowest ground state of respective *Z* or *E* isomers.

For the *E* isomer, a rotation of the chiral axis methyl over the central double bond is preferred for all functionals. For the *Z* state, only the methyl over methyl transition state could be found. The experimental value is in good agreement, however, an energetically lower transition state can possibly be found via DFT calculations, making an unambiguous suggestion on directionality impossible to date.

### 2.3.8 Third generation of axially chiral arylated hemiindigos - Increasing the rotational barriers

As increasing the sterical demand of the stilbene fragment yielded higher atropisomerization barriers for the *ortho*-tolyl axis in derivatives **60** and **61**, the third generation of axially chiral hemiindigos was synthesized.

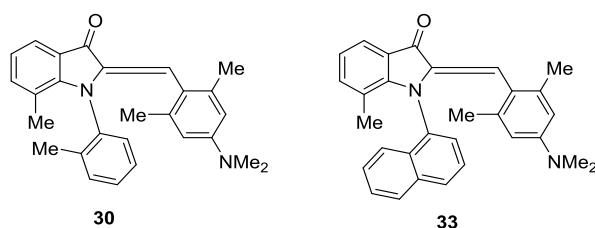


Figure 168: Third generation of axially chiral hemiindigos **30** and **33**.

Photophysical properties regarding the *Z* / *E* isomerization of compounds **30** and **33** are discussed in detail in Section 2.2.7 and are omitted here. HPLC runs and experiments are also not shown because **30** and **33** show the same observations as **61** but two different chiral columns (*Diacel Chiralpak IC* and *ID*) are needed to separate the rotamers of *Z* and *E* isomer, respectively.

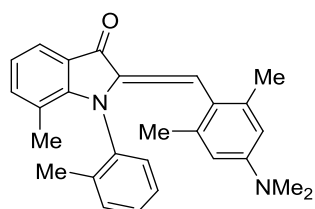


Figure 169: *Lewis*-formula of hemiindigo **30**.

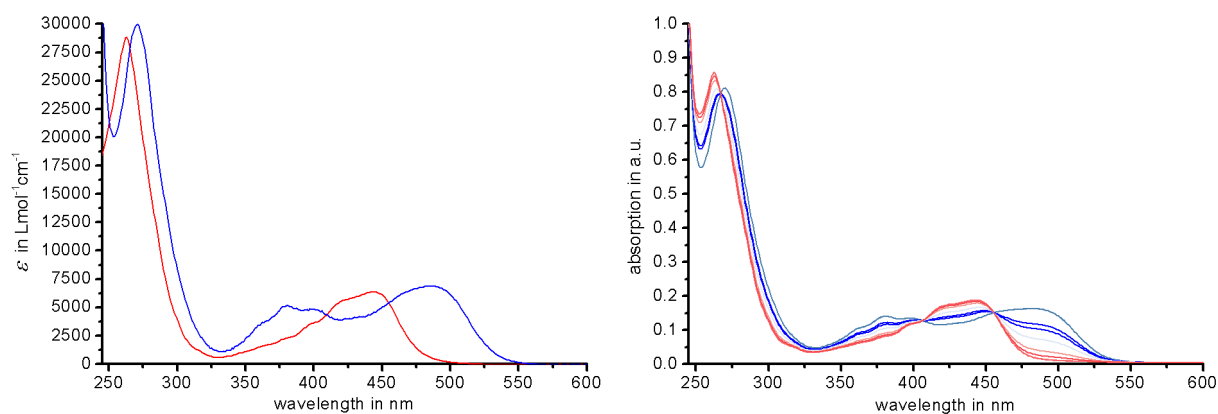


Figure 170: Molar absorption coefficients of **30** in 93 / 7 heptane / ethyl acetate (left) with the *Z* isomer shown in red and the *E* isomer in blue. Spectral changes recorded

after different irradiation times show clear isosbestic points (right). Adapted with permission from [75]. Copyright 2018 American Chemical Society.

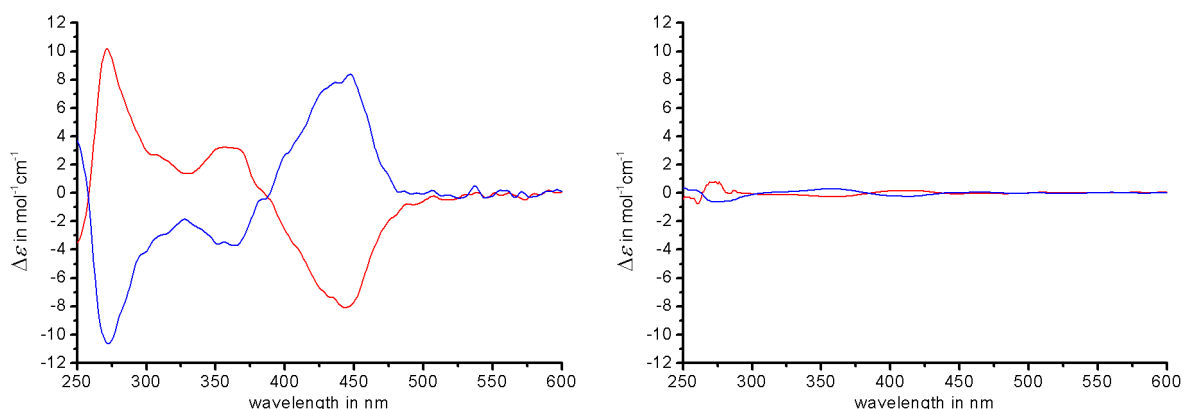


Figure 171: Molar ellipticity ECD spectra of **Z-30** in 93 / 7 heptane / ethyl acetate (left), (*R<sub>a</sub>*)-**Z-30** shown in blue, (*S<sub>a</sub>*)-**Z-30** shown in red. Molar ellipticity ECD spectra of **E-30** in 93 / 7 heptane / ethyl acetate (right), (*R<sub>a</sub>*)-**E-30** shown in blue, (*S<sub>a</sub>*)-**E-30** shown in red. Adapted with permission from [75]. Copyright 2018 American Chemical Society.

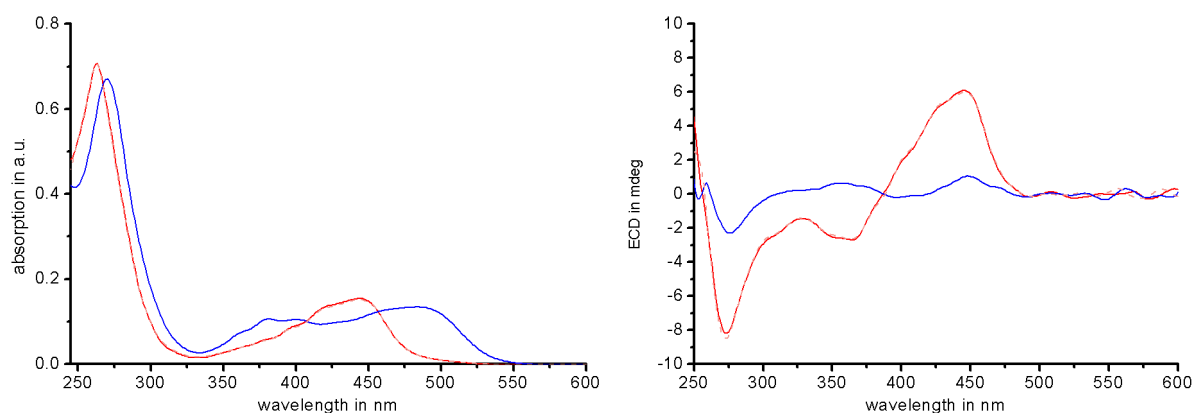


Figure 172: UV-Vis absorption (left) and ECD spectrum (right) of **30** in 93 / 7 heptane / ethyl acetate recorded for one switching cycle starting from pure (*R<sub>a</sub>*)-**Z-30** (solid red), which was photoisomerized to (*R<sub>a</sub>*)-**E-30** (1 min 435 nm, solid blue) and then switched back to (*R<sub>a</sub>*)-**Z-30** (1 min 530 nm, pale red, dashed) in high isomeric yields at 0 °C. The high free activation enthalpies  $\Delta G^* = 24.0$  kcal/mol for thermal atropisomerization in the *Z* isomeric state and  $\Delta G^* = 26.1$  kcal/mol in the *E* isomeric state prevent any racemization at 0 °C and even ambient temperatures. Therefore, the initial ECD spectrum of the pure *Z* isomer is fully recovered after a complete photoswitching cycle (solid red and pale red dashed



spectra). Adapted with permission from <sup>[75]</sup>. Copyright 2018 American Chemical Society.

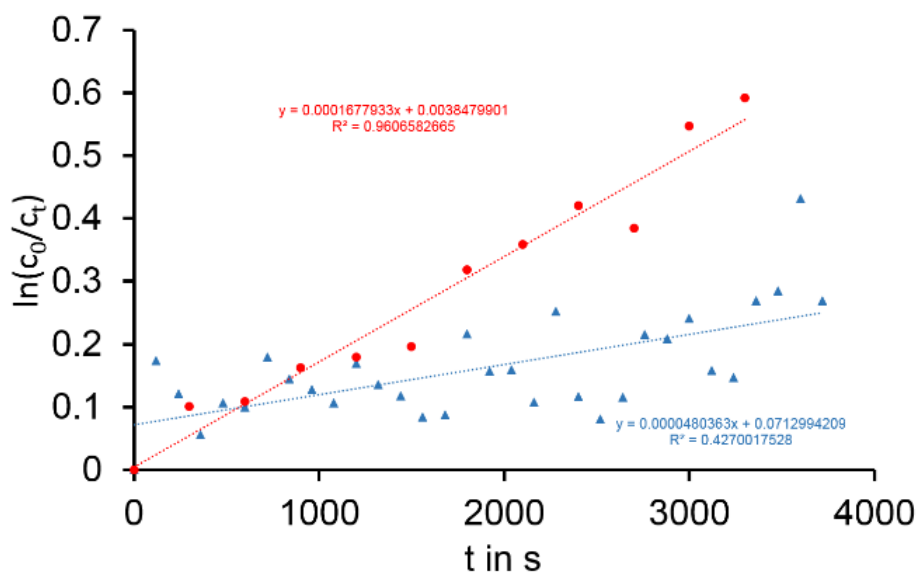


Figure 173: First order kinetic analyses of the thermal racemization via atropisomerization of hemiindigo **30** in 93 / 7 heptane / ethyl acetate in the dark. The slopes  $m$  can be translated into the rate constant  $k$  for each process. Racemization in the *Z* isomeric state (red, see also Figure 174) was measured at 40 °C and proceeds over an energy barrier of 23.1 kcal/mol. Racemization in the *E* isomeric state (blue) was measured at 60 °C and proceeds over an energy barrier of 26.1 kcal/mol. Poor  $R^2$  values are based on bad signal to noise ratios caused by the weak ECD response of the *E* isomer. Adapted with permission from <sup>[75]</sup>. Copyright 2018 American Chemical Society.

To further benchmark the photoswitchability of the now well-performing chiroptical photoswitches, cyclic irradiation experiments were carried out to examine the robustness of ECD photoswitching.

At first, hemiindigo **30** was photoswitched between *Z* and *E* isomeric state and the ECD spectra were recorded after a specific number of cycles (Figure 174). Details on the experimental low-temperature ECD spectrometer setup with *in situ* irradiation capabilities can be found in Section 2.7.5.

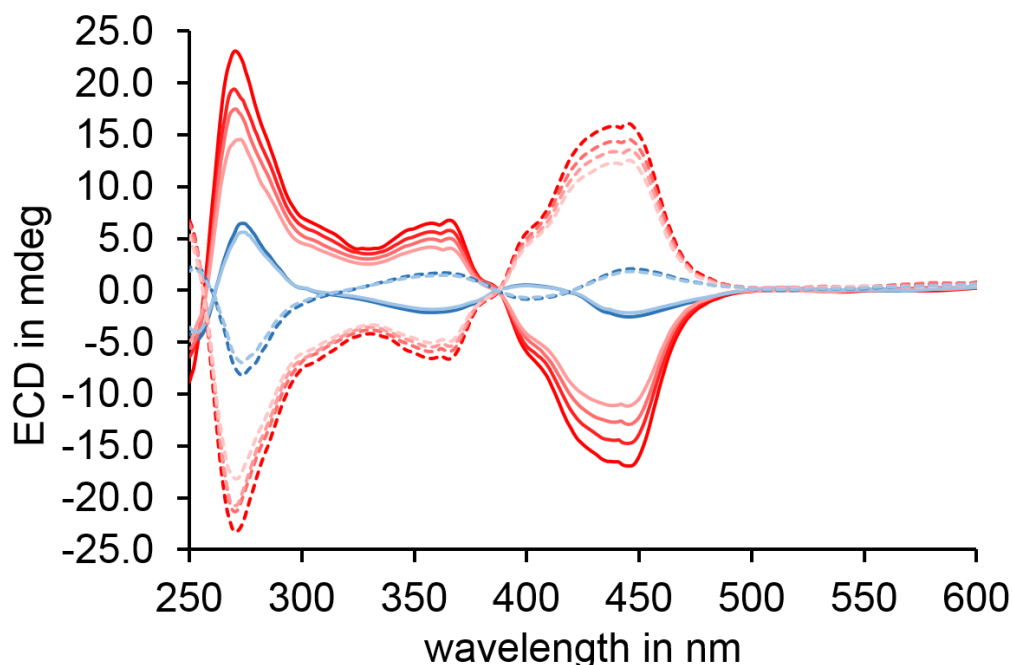


Figure 174: Repetitive photoswitching of the ECD spectrum of hemiindigo **30** (solid lines: ( $S_a$ ) configuration) and thermal decay of the ECD spectrum in the dark (broken lines: ( $R_a$ ) configuration) in 93 / 7 heptane / ethyl acetate. Spectra of *Z* isomers are shown in red and of *E* isomers in blue (light blue after 36 cycles / 90 minutes). The ( $S_a$ ) and ( $R_a$ ) configured samples were handled at 18 °C within an air-conditioned room. The ( $S_a$ )-**30** isomer was photoswitched 12 times between its two PSS' at 435 nm (30 s irradiation time at 260 mW per cycle to reach the PSS) and 505 nm (120 s irradiation time at 80 mW per cycle to reach the PSS) within 30 minutes. An ECD spectrum was recorded at this time interval and the procedure was repeated for two times (red solid line spectra, total of 36 photoswitching cycles within 90 min). The ( $R_a$ )-*Z*-**30** isomer was kept in the dark at 18 °C and was also measured in 30 min intervals to show the thermal racemization of the chiral axis (red broken line spectra). ECD measurements were conducted at 0 °C and samples were put on ice (0 °C) during transfer of samples and waiting times in complete darkness. The slightly faster decline of the photoswitched sample (red solid line spectra) results from additional heating effects of the LED irradiations, which were measured to result in 6.15 °C higher

sample temperature compared to the surrounding 18 °C. Adapted with permission from <sup>[75]</sup>. Copyright 2018 American Chemical Society.

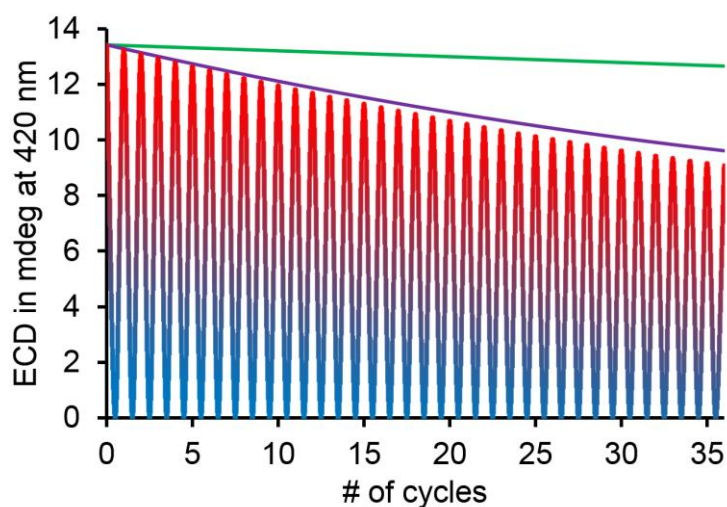


Figure 175: Repetitive photoswitching of the ECD spectrum of (*S<sub>a</sub>*)-**30** (red, see also Figure 174) and thermal decay of (*R<sub>a</sub>*)-**Z-30** (violet) in 93 / 7 heptane / ethyl acetate. Photoirradiation was performed at 24.15 °C (red for the *Z* state, blue for the *E* state). The ECD signal at 420 nm is used exemplarily because at this spectral position signal intensity for the PSS solution enriched in *E* isomer (84% *E-30* and 16% *Z-30* in the PSS at 435 nm) is zero. The thermal decay of the *Z-30* ECD signal was measured at 18 °C and then extrapolated to 24.15 °C to ensure comparability (solid violet line). The residual loss of ECD signal is attributed to irreversible photodegradation (green) over 36 photoswitching cycles and was determined from the corresponding experimental absorption spectra (5% after 36 cycles). Adapted with permission from <sup>[75]</sup>. Copyright 2018 American Chemical Society.

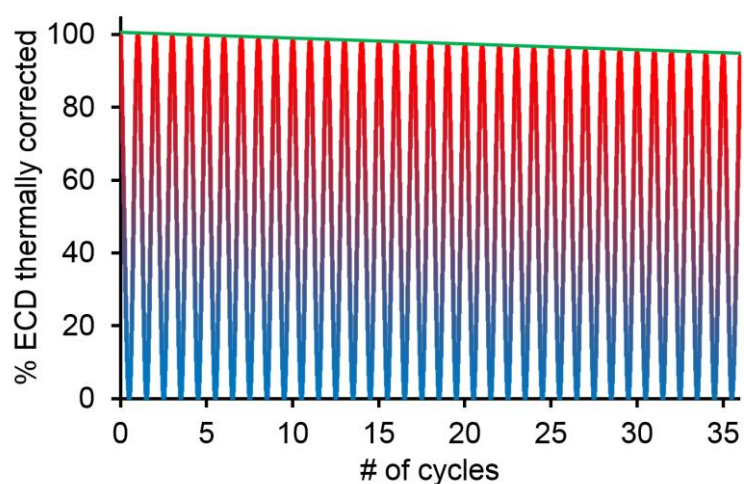


Figure 176: Fully reversible photoswitching of the ECD spectrum of ( $S_a$ )-**30** (red for the  $Z$  state, blue for the  $E$  state) in 93 / 7 heptane / ethyl acetate is seen after correction for thermal ECD decay of ( $S_a$ )- $Z$ -**30**. No racemization of the chiral  $N$ -indoxyl-*ortho*-tolyl axis by photoinduced double-bond isomerization is observed over 36 switching cycles excluding light induced coupled motions between the aniline fragment and the *ortho*-tolyl residue. Photodegradation is plotted in green for comparison. Adapted with permission from <sup>[75]</sup>. Copyright 2018 American Chemical Society.

A second ECD measurement at  $-20$  °C was designed to again confirm the sole dependency of the ECD decay within cyclic irradiation experiments.

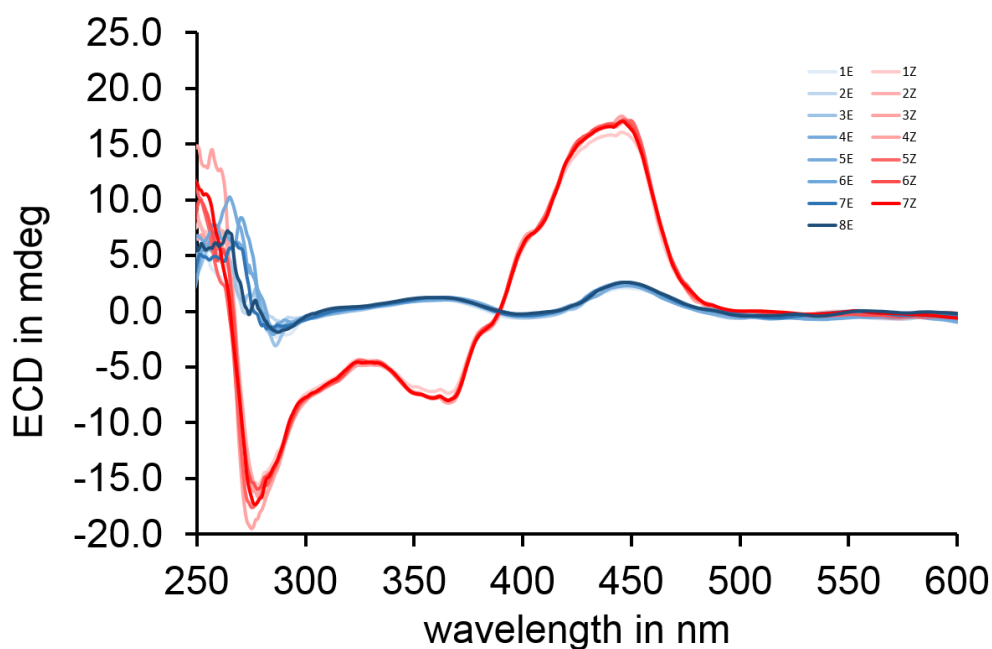


Figure 177: Repetitive photoswitching of the ECD spectrum of hemiindigo **30** (solid lines: ( $R_a$ ) configuration) 93 / 7 heptane / ethyl acetate. Spectra of  $Z$  isomers are shown in red and of  $E$  isomers in blue (light blue at the start). The ( $R_a$ ) configured sample was irradiated and measured at  $-20$  °C within a cryostat mounted inside the ECD spectrometer equipped with a glass fiber directly inserted into the sample cuvette inside the cryostat (see Section 2.7.5 for the newly built setup for this purpose). The ( $R_a$ )-**30** isomer was photoswitched 7 times between its two PSS' at 450 nm (10 s irradiation time at 193 mW per cycle to reach the PSS) and 520 nm (60 s irradiation time at 92 mW per cycle to reach the PSS). An ECD spectrum was recorded after every irradiation step. Adapted with permission from <sup>[75]</sup>. Copyright 2018 American Chemical Society.

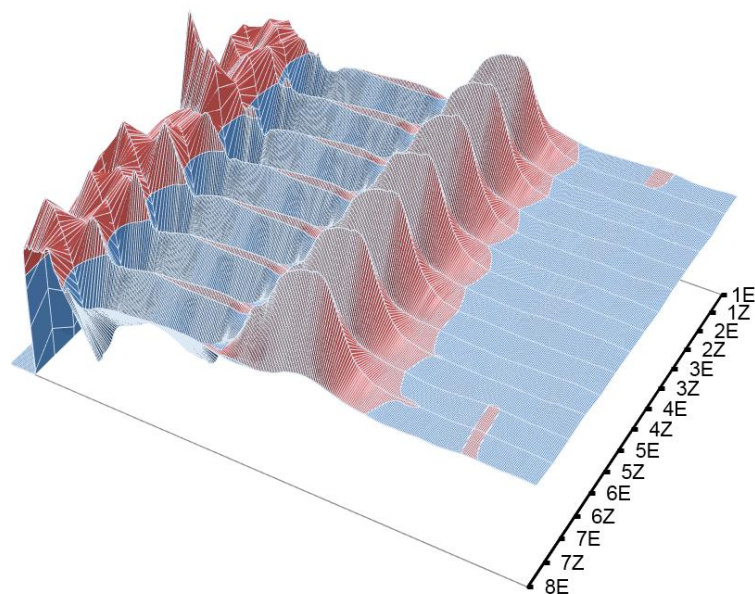


Figure 178: 3D plot showing modulation of the ECD of hemiindigo **30** by repetitive photoswitching between the PSS at 435 nm (weak signals) and the PSS at 520 nm (strong signals) at -20 °C. Adapted with permission from [75]. Copyright 2018 American Chemical Society.

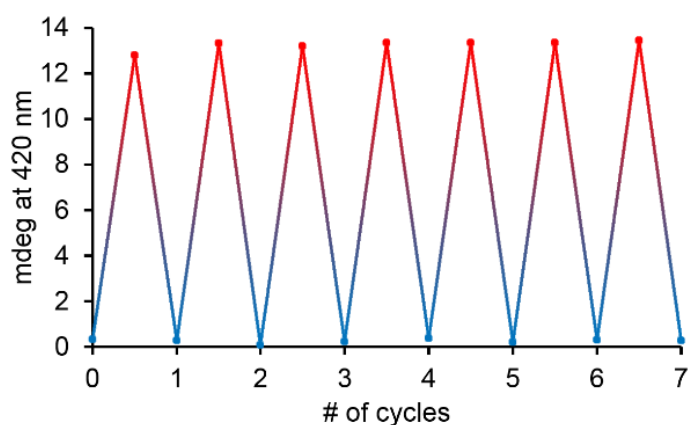


Figure 179: Repetitive photoswitching of the ECD spectrum of (*R<sub>a</sub>*)-**30** (red) in 93 / 7 heptane / ethyl acetate. Photoirradiation was performed at -20 °C (red for the *Z* enriched state at 520 nm, blue for the *E* enriched state at 450 nm). No thermal racemization or photodegradation could be observed over the course of the experiment at -20 °C. The ECD signal at 420 nm is used exemplarily because at this spectral position signal intensity for the PSS solution enriched in *E* isomer (83% *E*-**30** and 17% *Z*-**30** in the PSS at 450 nm) is almost zero. Adapted with permission from [75]. Copyright 2018 American Chemical Society.

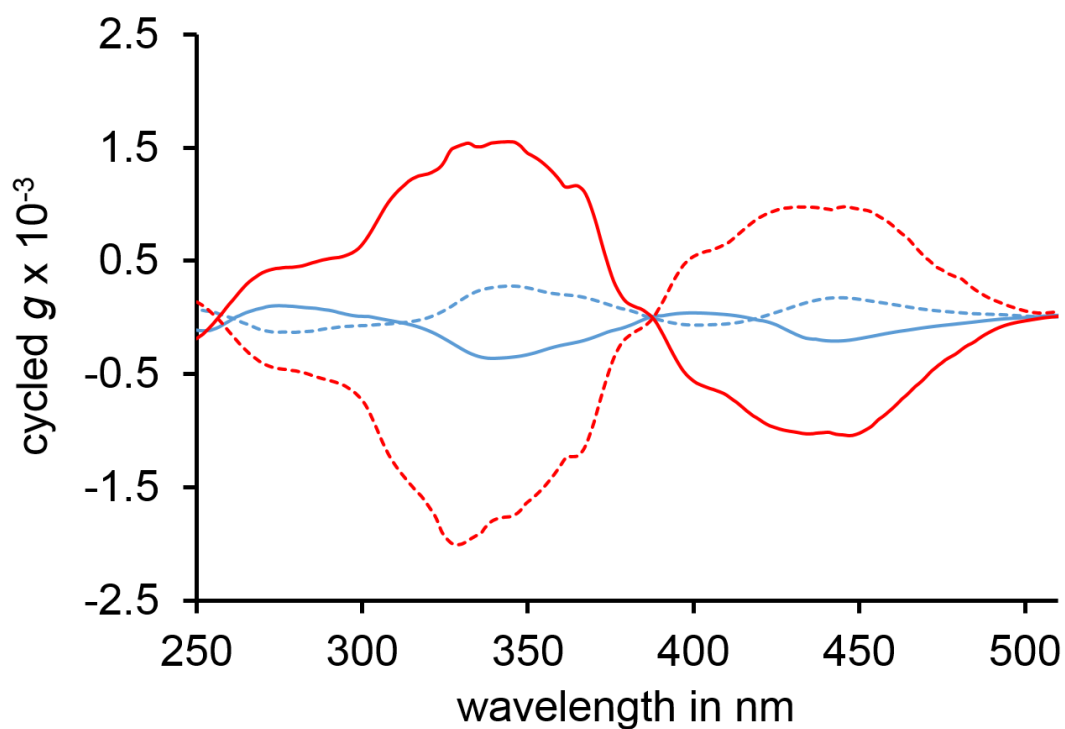


Figure 180: Photoswitching of the  $g$  factors of hemiindigo **30** in 93 / 7 heptane / ethyl acetate (blue:  $E$  isomers, red:  $Z$  isomers, solid lines:  $(S_a)$  configuration, broken lines:  $(R_a)$  configuration). Adapted with permission from <sup>[75]</sup>. Copyright 2018 American Chemical Society.

2.3.8 THIRD GENERATION OF AXIALLY CHIRAL ARYLATED HEMIINDIGOS - INCREASING THE ROTATIONAL BARRIERS

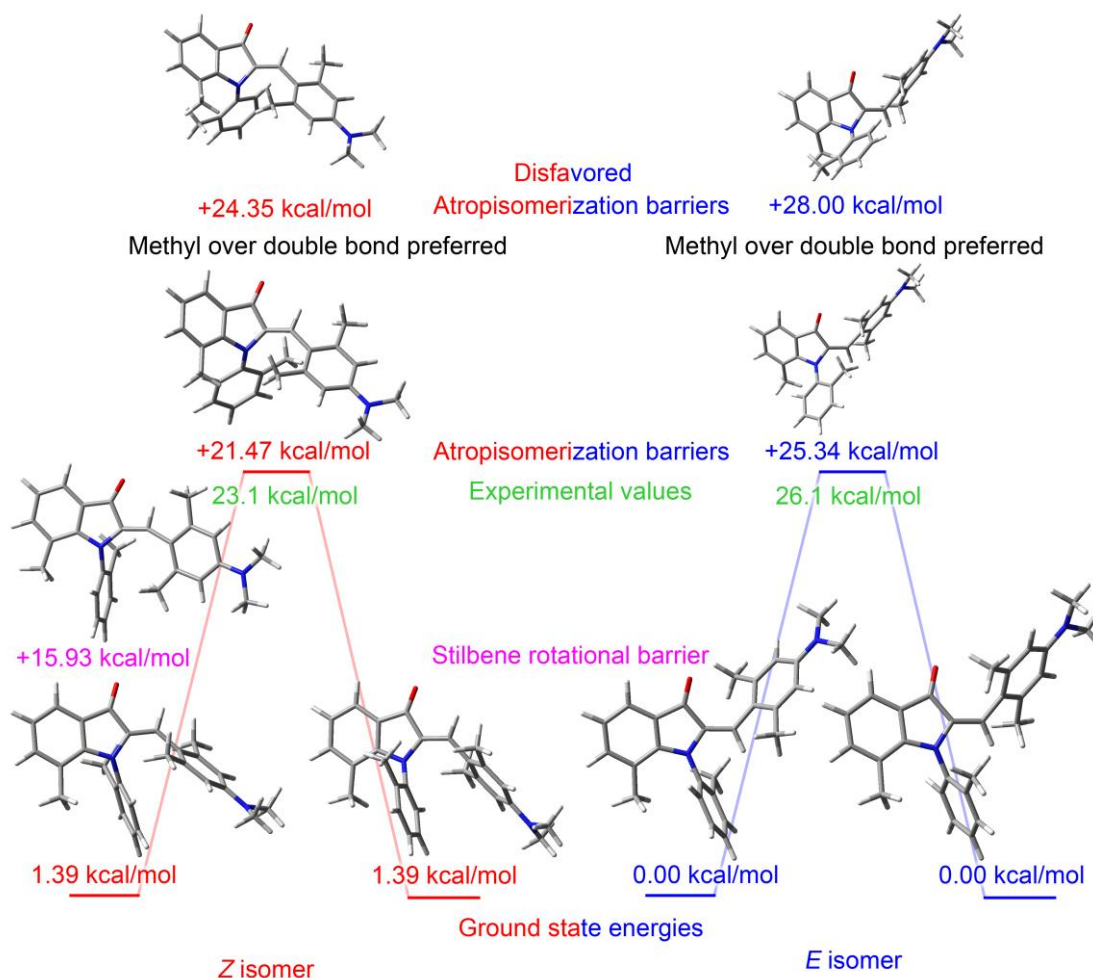


Figure 181: Calculated ground and transition state structures of hemiindigo **30** at the B3LYP/6-311+G(d,p) level of theory. Transition states for all atropisomerization and the stilbene single bond rotation in the Z state were found. The “+” sign in front of transition state values indicates the energy difference with respect to the lowest ground state of respective Z or E isomers.

The calculated energies are in good agreement to the experimental values for the Z and E isomer. A by 3 kcal/mol lowered atropisomerization barrier for the Z isomers can be measured. The transition state structures suggest a rotation of the *ortho*-tolyl axis methyl group over the central double bond is preferred in the Z state with the E form also passing over the central double bond. These findings show that gating of thermal barriers is possible for these chiroptical photoswitches and the trend for the directionality of the Z-**30** isomer could be reversed compared to other axially chiral hemiindigos.



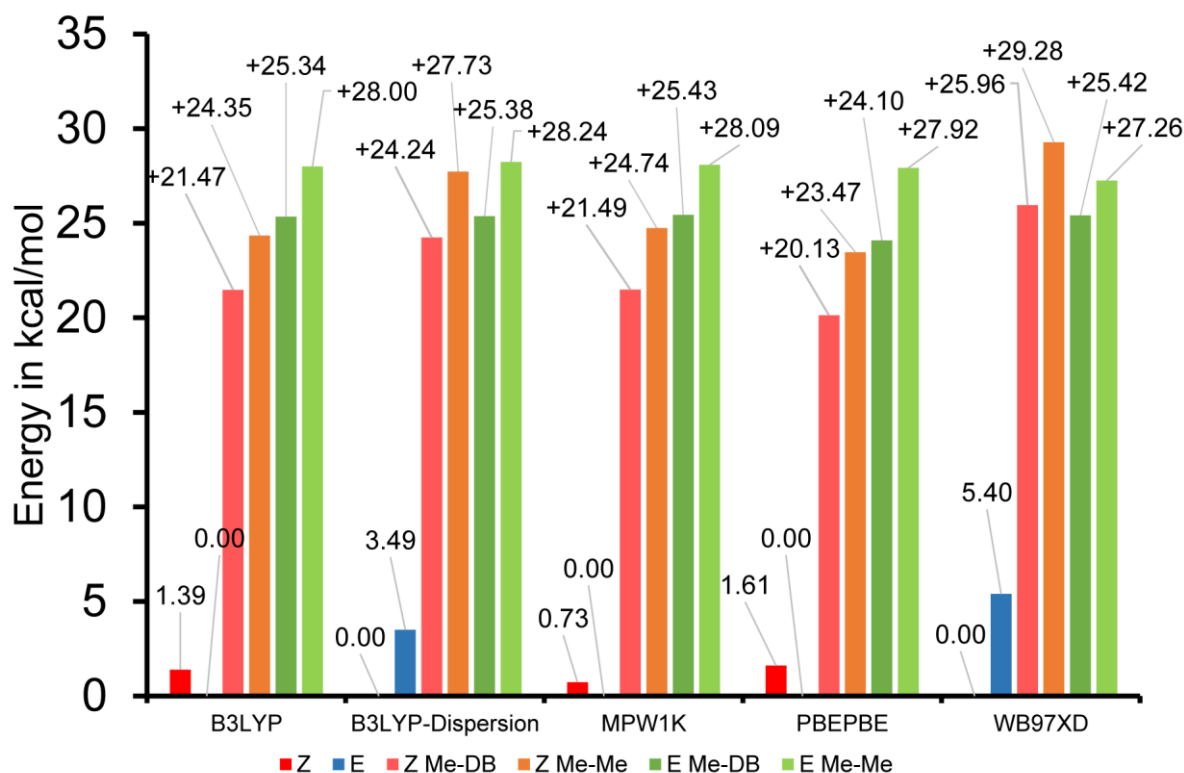


Figure 182: Benchmarking results for hemiindigo **30** using different DFT functionals for the 6-311+G(d,p) basis set. “Z” and “E” represent the ground states and “Z-Me-DB” and “E-Me-DB” the energetically lowest transition state for respective isomer and rotation pathway (see Figure 181). The “+” sign in front of transition state values indicates the energy difference with respect to the lowest ground state of respective *Z* or *E* isomers.

For *Z*- and *E* isomers of **30**, a rotation of the chiral axis methyl over the central double bond is preferred for all functionals. This stands in contrast to the change in directionality observed for hemiindigos **20**, **60** and **61**. The transition state energy is enlarged and the ground state energy is decreased for *Z* isomers when using the  $\omega$ B97XD- or B3LYP functional with GD3BJ dispersive corrections.

As hemiindigo **30** performed well under cyclic irradiation conditions, one way of enlarging sterical hindrance at the chiral axis and hence the atropisomerization barrier is the introduction of a naphthyl moiety. As second- and third generation chiroptical hemiindigo photoswitches are already heavily sterically crowded, especially in the *Z* form, naphthyl should occupy less space compared to *ortho*-tolyl while still being cumbersome when rotated.

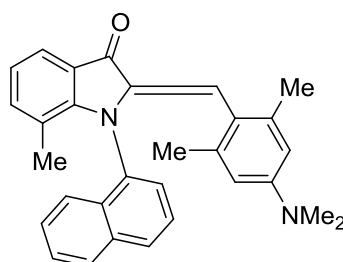


Figure 183: Lewis-formula of hemiindigo **33**.

The photophysical details were already discussed in Section 2.2.7, its chiroptical properties are subsequently highlighted in full detail.

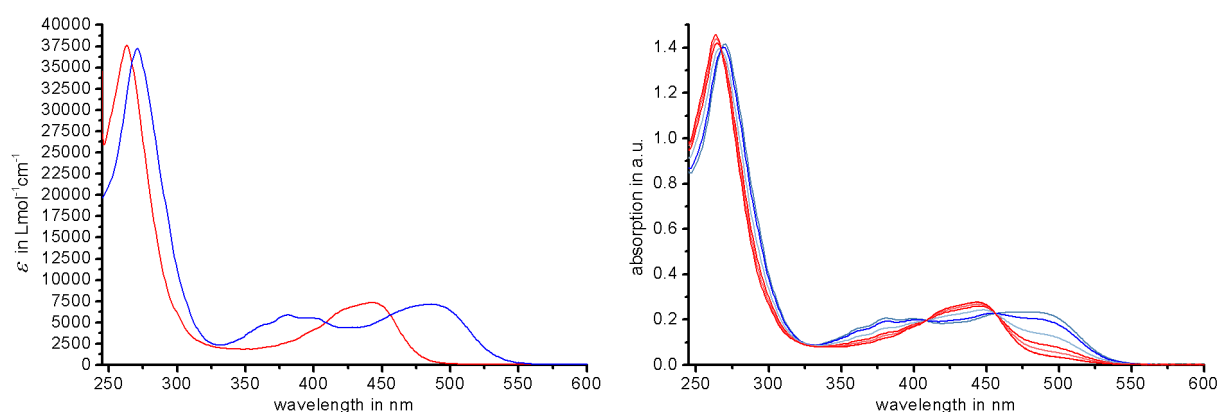


Figure 184: Molar absorption coefficients of **33** in 87 / 13 heptane / ethyl acetate (left) with the *Z* isomer shown in red and the *E* isomer in blue. Spectral changes recorded after different irradiation times show clear isosbestic points (right). Adapted with permission from <sup>[75]</sup>. Copyright 2018 American Chemical Society.

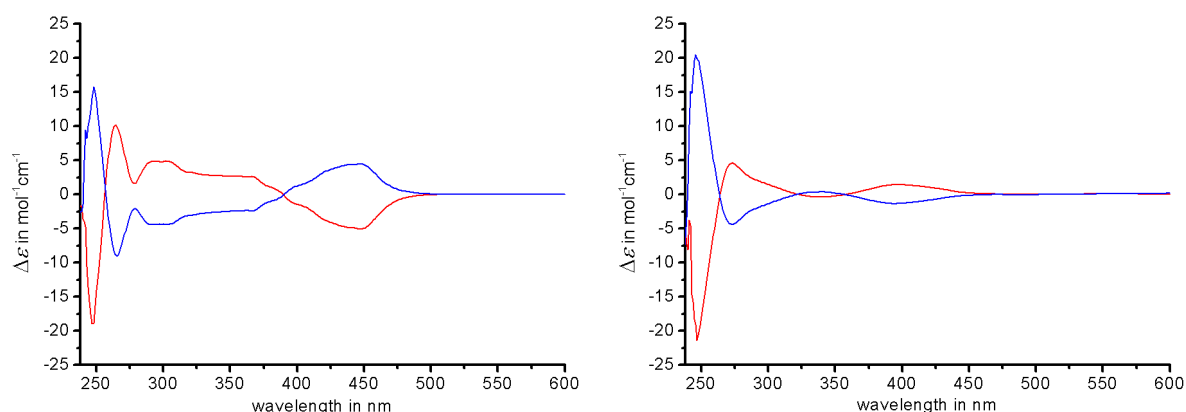


Figure 185: Molar ellipticity ECD spectra of **Z-33** (left) in 87 / 13 heptane / ethyl acetate, ( $R_a$ )-**Z-33** shown in blue, ( $S_a$ )-**Z-33** shown in red. Determination of the absolute configuration is based on the theoretical description. Molar ellipticity ECD spectra of **E-33** (right) in 87 / 13 heptane / ethyl acetate, ( $R_a$ )-**E-33** shown in blue, ( $S_a$ )-**E-33** shown in red. Adapted with permission from [75]. Copyright 2018 American Chemical Society.

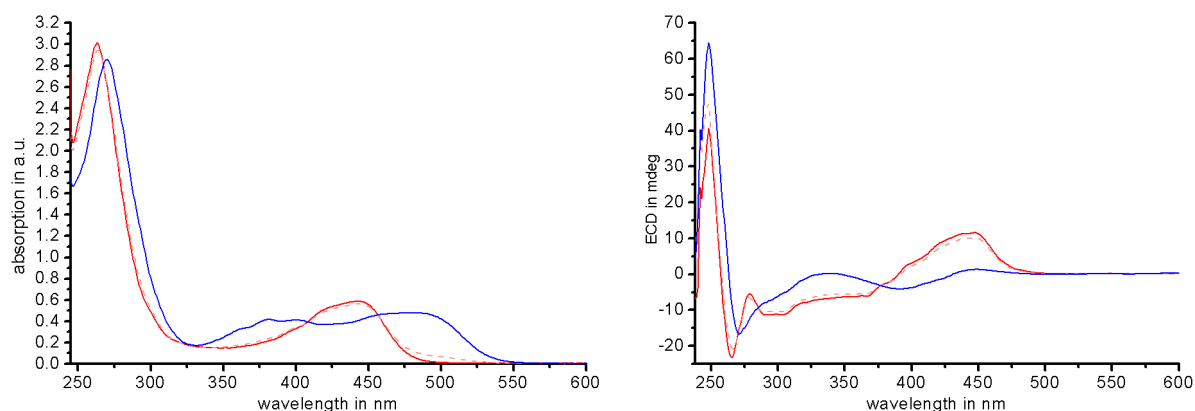


Figure 186: UV-Vis absorption (left) and ECD spectrum (right) of **33** in 87 / 13 heptane / ethyl acetate recorded for one switching cycle starting from pure ( $R_a$ )-**Z-33** (solid red), which was photoisomerized to ( $R_a$ )-**E-33** (30 s, 435 nm, solid blue) and then switched back to ( $R_a$ )-**Z-33** (2 min, 505 nm, pale red, dashed) in high isomeric yields at 0 °C. The further increased free activation enthalpies  $\Delta G^* = 24.8$  kcal/mol for thermal atropisomerizations in the *Z* isomeric state and  $\Delta G^* = 27.6$  kcal/mol in the *E* isomeric state prevent any racemization also at ambient temperatures. Therefore, the initial ECD spectrum of the pure *Z* isomer is fully recovered after a complete photoswitching cycle (solid red and pale red dashed spectra). Adapted with permission from [75]. Copyright 2018 American Chemical Society.

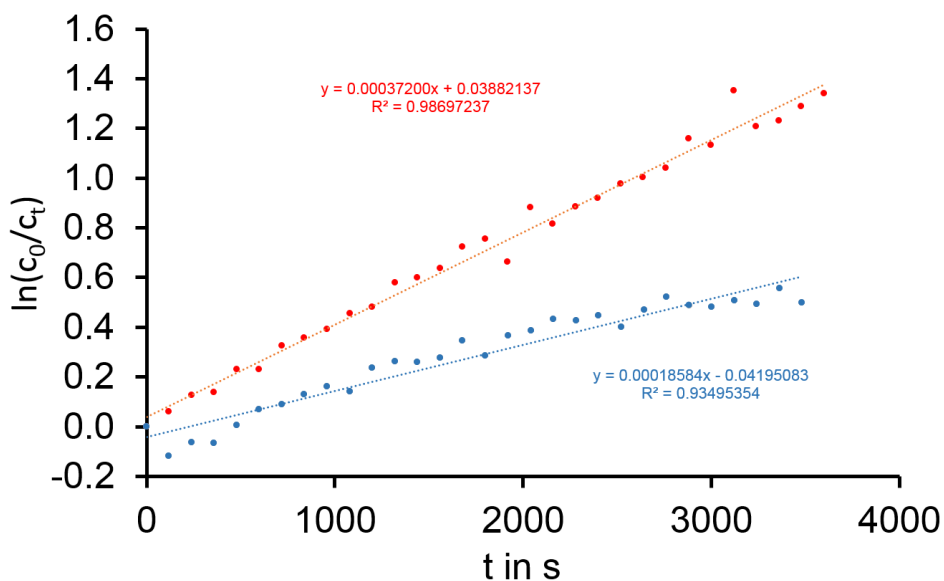
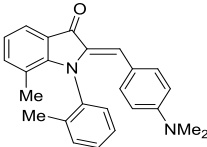
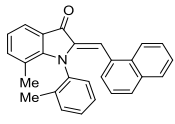
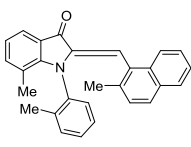
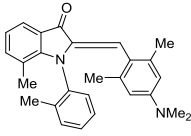
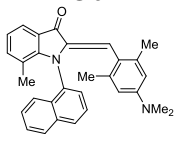


Figure 187: First order kinetic analyses of the thermal racemization via atropisomerization of hemiindigo **33** in 87 / 13 heptane/ethyl acetate in the dark. The slopes  $m$  can be translated into the rate constant  $k$  for each process. Racemization in the  $Z$  isomeric state (red) was measured at 40 °C and proceeds over an energy barrier of 24.8 kcal/mol. Racemization in the  $E$  isomeric state (blue) was measured at 90 °C and proceeds over an energy barrier of 27.6 kcal/mol. Adapted with permission from <sup>[75]</sup>. Copyright 2018 American Chemical Society.

Table 11: Free activation enthalpies  $\Delta G^*$  for thermal racemizations of the chiral axes of hemiindigos **20**, **30** and **33** measured separately for *Z* and *E* isomers in heptane / ethyl acetate mixtures. Corresponding half-lives in a = years, d = days, min = minutes and s = seconds were extrapolated to 25 °C.

Hemiindigo	Solvent	$\Delta G^*$ (therm. rac. <i>Z</i> isomer) /kcal mol <sup>-1</sup>	$\Delta G^*$ (therm. rac. <i>E</i> isomer) /kcal mol <sup>-1</sup>	Racemization half-life of pure <i>Z</i> isomer at 25 °C	Racemization half-life of pure <i>E</i> isomer at 25 °C
 <b>20</b>	Hept/EA 83/17	19.9	23.4	43 s	286 min
 <b>60</b>	Hept/EA 95/5	21.7	24.3	15 min	21 h
 <b>61</b>	Hept/EA 95/5	24.6	26.8	35 h	59 d
 <b>30</b>	Hept/EA 93/7	23.1	26.1	164 min	19.3 d
 <b>33</b>	Hept/EA 87/13	24.8	27.6	2.01 d	0.622 a

With significantly enlarged atropisomerization barriers at hand (compared to hemiindigo **20**), repeated photoswitching of the ECD response of hemiindigo **33** was carried out at 19.2 °C

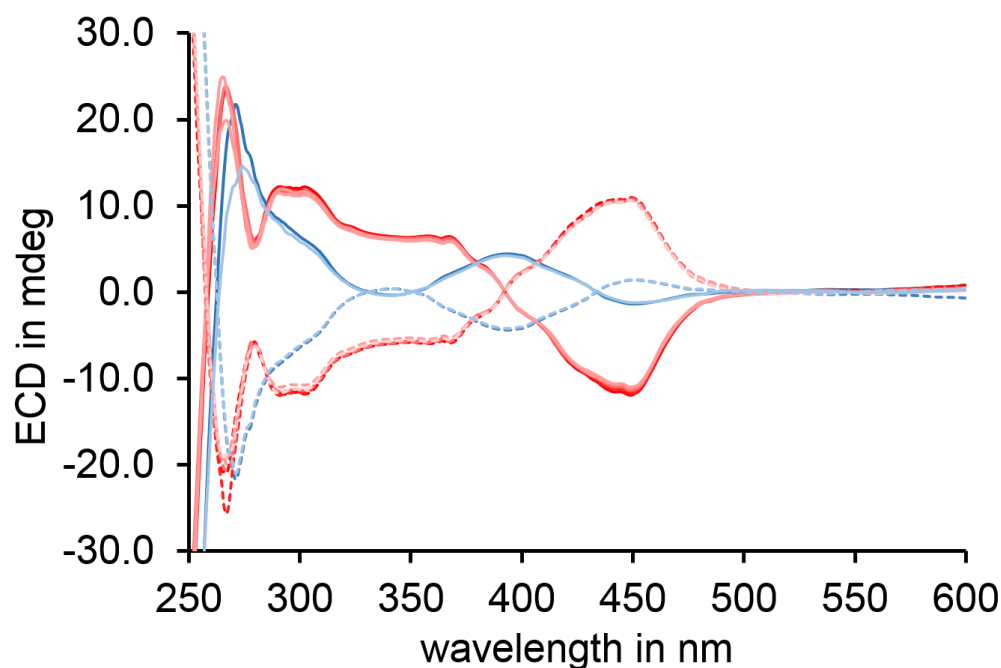


Figure 188: Repetitive photoswitching of the ECD spectrum of hemiindigo **33** (solid lines: ( $S_a$ ) configuration) and thermal decay of the ECD spectrum in the dark (broken lines: ( $R_a$ ) configuration) in 87 / 13heptane / ethyl acetate. Spectra of *Z* isomers are shown in red and of *E* isomers in blue (light blue after 160 cycles/120 min). The ( $S_a$ ) and ( $R_a$ ) configured samples were handled at 18 °C within an air-conditioned room. The ( $S_a$ )-**33** isomer was photoswitched 40 times between its two PSS' at 435 nm (7 s irradiation time at 260 mW per cycle to reach the PSS) and 505 nm (38 s irradiation time at 80 mW per cycle to reach the PSS) within 30 minutes. A spectrum was recorded after this time interval and this procedure was repeated for three times (red solid line spectra, total of 160 photoswitching cycles within 120 min). The ( $R_a$ )-*Z*-**33** isomer was kept in the dark at 18 °C and was also measured in 30 min intervals to show the thermal racemization of the chiral axis (red broken line spectra). ECD measurements were conducted at 0 °C and samples were kept at 22 °C during transfer of samples and waiting times in complete darkness. The slightly faster decline of the photoswitched sample (red solid line spectra) results from heat dissipation of the LEDs, which were measured to result in 1.23 °C higher sample temperature with respect to the surrounding 18 °C. A new fan equipped irradiation setup was built to cool LEDs and sample during irradiation and is depicted in Section 2.7.4. Adapted with permission from <sup>[75]</sup>. Copyright 2018 American Chemical Society.

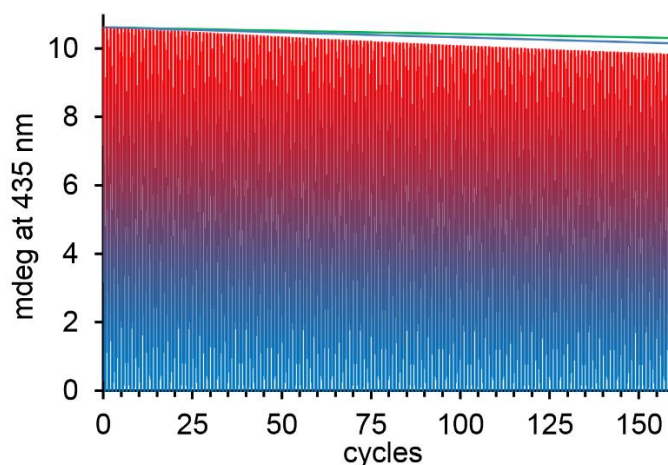


Figure 189: Repetitive photoswitching of the ECD spectrum of (*S<sub>a</sub>*)-**33** (red, see Figure 190), thermal decay of (*R<sub>a</sub>*)-**Z-33** (violet) extrapolated to 19.2 °C and photodegradation (green) in 87 / 13 heptane / ethyl acetate. Photoirradiation was performed at 19.2 °C (red for the *Z* state, blue for the *E* state). The ECD signal at 435 nm is used exemplarily because at this spectral position signal intensity for the PSS solution enriched in *E* isomer (83% *E-3* and 17% *Z-33* in the PSS at 435 nm) is close to zero. The thermal decay of the *Z-33* ECD signal was measured at 18 °C and extrapolated to the actual 19.2 degrees of the irradiation sample temperature (violet). The residual loss of ECD signal after correcting for thermal decay is attributed to irreversible photodegradation over 160 photoswitching cycles and amounts to 2% (green, derived from absorption loss during UV-Vis measurements). Adapted with permission from <sup>[75]</sup>. Copyright 2018 American Chemical Society.

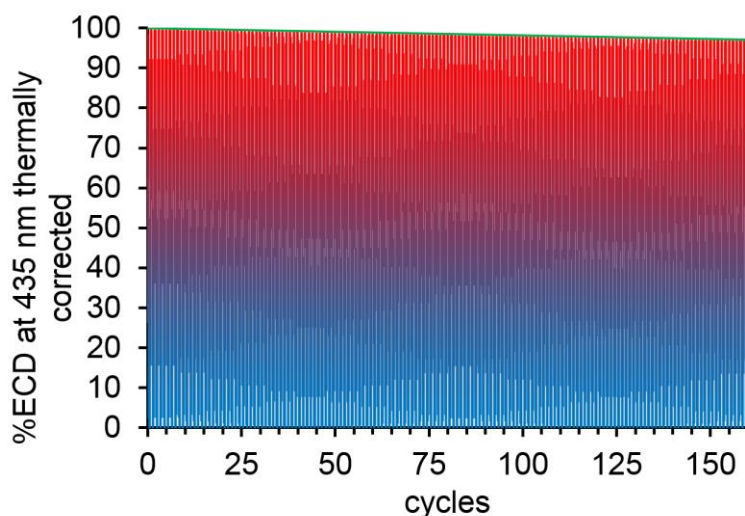


Figure 190: Fully reversible photoswitching of the ECD spectrum of (*S<sub>a</sub>*)-**33** in 83 / 17 heptane / ethyl acetate (red for the *Z* state, blue for the *E* state) is observed after

correction for thermal ECD decay of (*S<sub>a</sub>*)-**Z-33**. No racemization of the chiral *N*-indoxyl-naphthyl axis by photoinduced double-bond isomerization is observed over 160 cycles excluding light induced coupled motions between the aniline fragment and the naphthyl residue. Photodegradation is plotted in green for comparison. Adapted with permission from <sup>[75]</sup>. Copyright 2018 American Chemical Society.

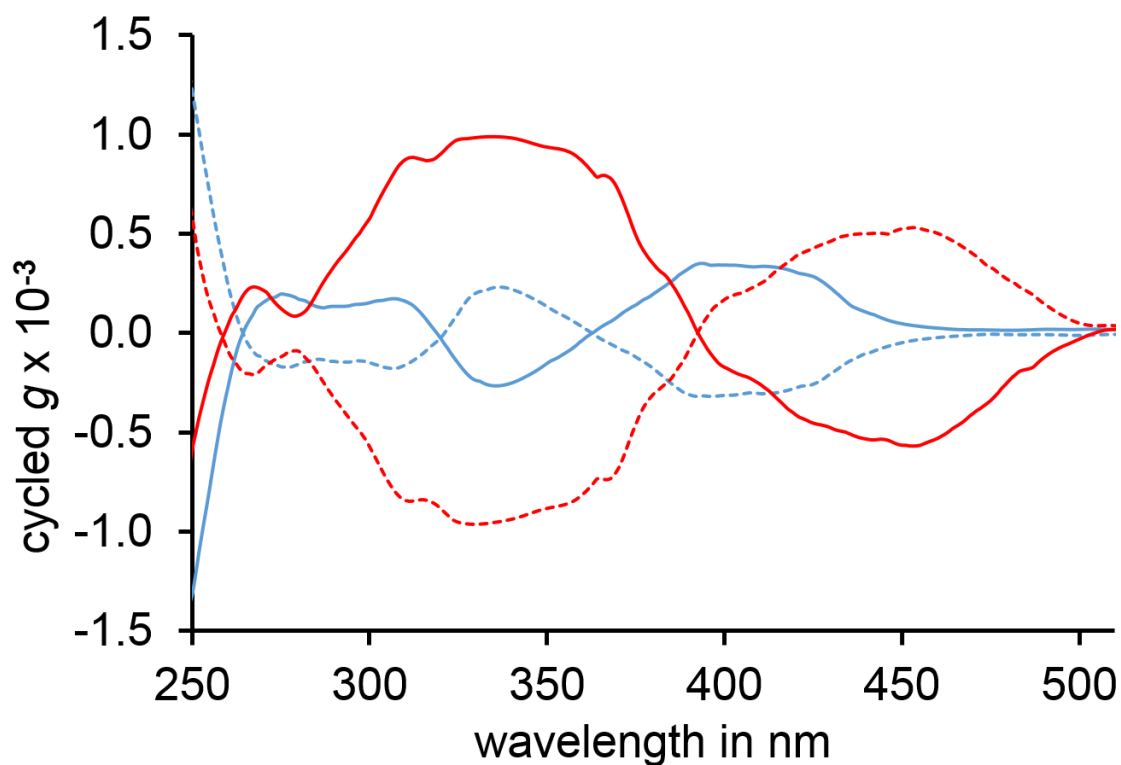


Figure 191: Photoswitching of the *g* factors of hemiindigo **33** in 83 / 17 heptane / ethyl acetate (blue: *E* isomers, red: *Z* isomers, solid lines: (*S<sub>a</sub>*) configuration, broken lines: (*R<sub>a</sub>*) configuration). Adapted with permission from <sup>[75]</sup>. Copyright 2018 American Chemical Society.



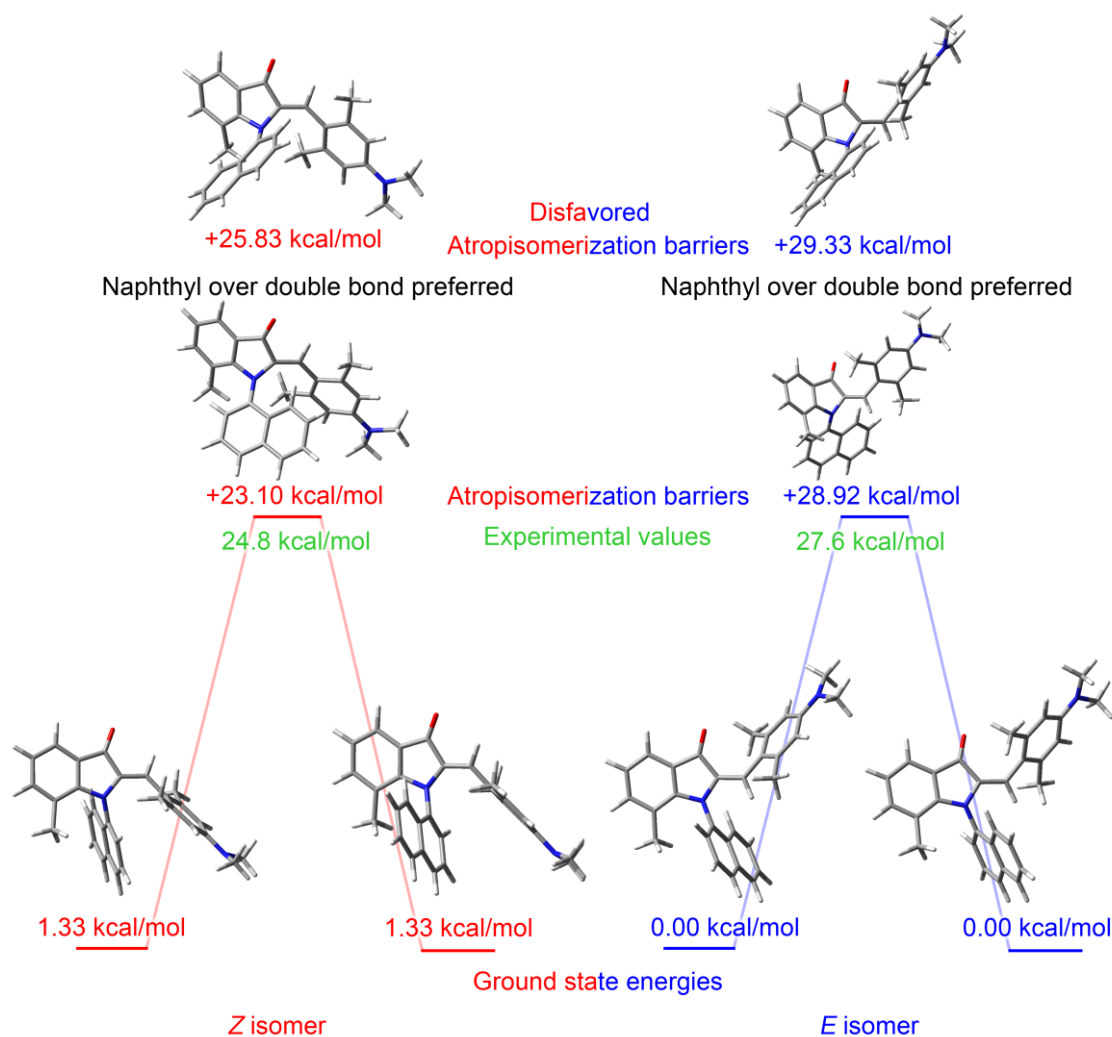


Figure 192: Calculated ground and transition state structures of hemiindigo **33** at the B3LYP/6-311+G(d,p) level of theory. Transition states for all atropisomerizations were found. The stilbene rotation transition states did not converge after several attempts and tweaks. The “+” sign in front of transition state values indicates the energy difference with respect to the lowest ground state of respective *Z* or *E* isomers.

The calculated energies are in good agreement to the experimental values. The naphthyl-over-methyl transition state is disfavored by 0.4 kcal/mol in the *E* isomer and by 2.7 kcal/mol in the *Z* state. A by 2.8 kcal/mol lowered atropisomerization barrier for the *Z* isomer can be measured. The transition state structures suggest a rotation of the naphthyl over the central double bond in both cases as seen with hemiindigo **30**. These findings show that gating of thermal barriers is possible for these chiroptical photoswitches and the trend for the directionality of the *Z*-**33** isomer could be reversed compared to other axially chiral hemiindigos **20**, **60** and **61**.

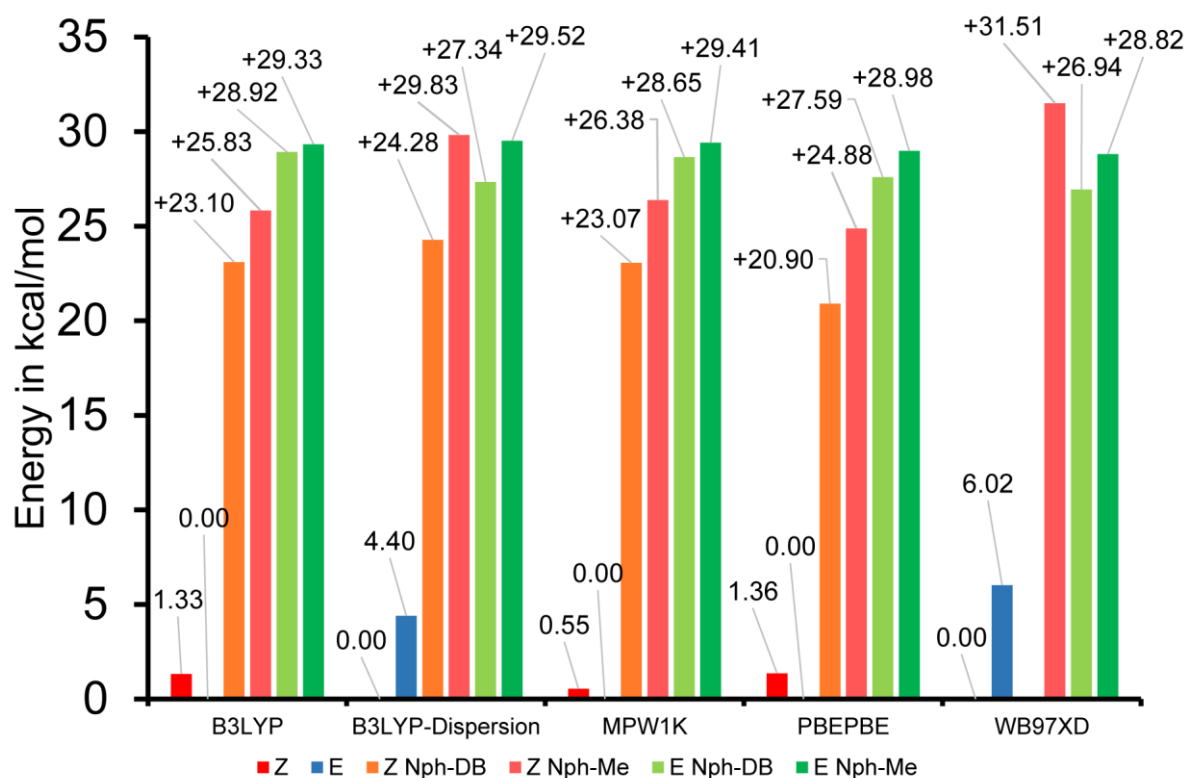


Figure 193: Benchmarking results for hemiindigo **33** using different DFT functionals for the 6-311+G(d,p) basis set. “Z” and “E” represent the ground states and “Z-Nph-DB” and “E-Nph-DB” the energetically lowest transition state for respective isomer and rotation pathway (see Figure 192). The “+” sign in front of transition state values indicates the energy difference with respect to the lowest ground state of respective *Z* or *E* isomers. The “Z-Nph-DB” transition state did not converge with the  $\omega$ B97XD functional after several attempts and tweaks.

For *Z* and *E* isomers, a rotation of the chiral axis naphthyl core over the central double bond is preferred for all functionals. This stands in contrast to the change in directionality observed for hemiindigos **20**, **60** and **61**. The transition state energy is enlarged and the ground state energy is decreased for *Z* isomers when using the  $\omega$ B97XD- or B3LYP functional with GD3BJ dispersive corrections.

### 2.3.9 Third generation of axially chiral arylated hemiindigos - Comparison of aliphatic signals and rotational barriers

A comparison of the aliphatic  $^1\text{H}$ -NMR signals for three axially chiral hemiindigos bearing symmetric stilbene fragments is given in Figure 194 below. **20** shows no split signals of the stilbene fragment, as its rotational single bond barrier was calculated at +6.86 kcal/mol (*Z*) and +7.09 kcal/mol, which shows no difference in chemical shift for protons off the single bond straight line. In the case of **30**, however, a doubled signal set in the *Z* isomer can be observed for methyl protons 24a and 24b, which is also seen for the aromatic protons and all respective carbons within the  $^{13}\text{C}$  spectrum. The single bond rotation barrier for the *Z* isomer was calculated at +17.32 kcal/mol, a similar rotational barrier was measured on the acylated *ortho*-methyl substituted hemiindigo **57** with +17.06 kcal/mol, which could also be measured via its coalescence in an  $^1\text{H}$ -NMR temperature sweep experiment (see Section 2.3.2, Figure 113). The same effect can be seen on hemiindigo **33** with the addition that the *E* isomer also shows signal splitting for the methyl signals, hinting towards an increased rotational barrier in the *E* isomeric state.

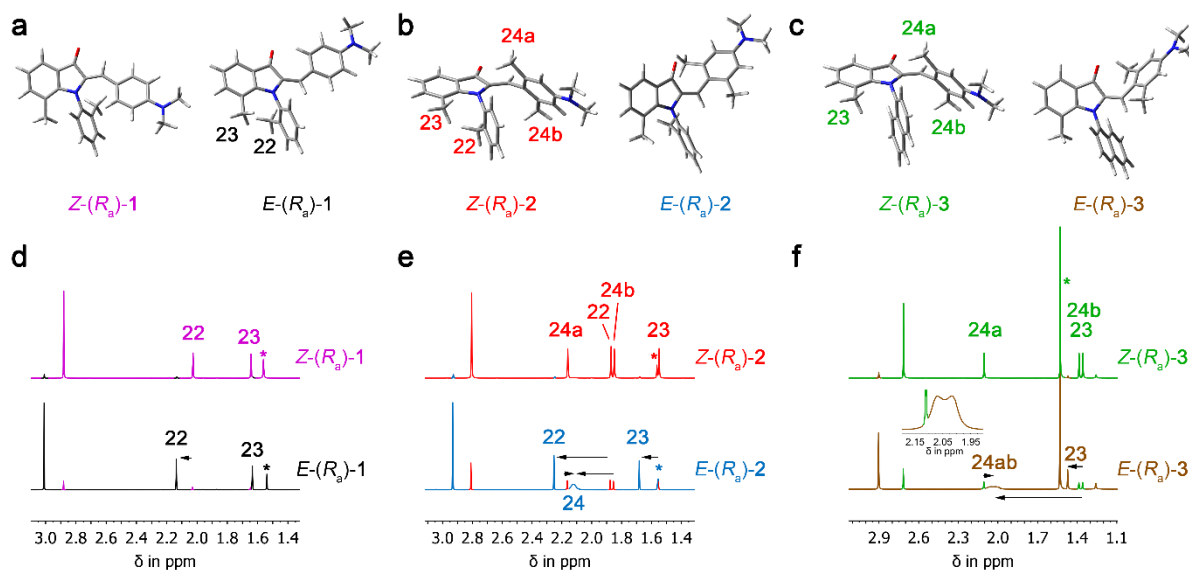


Figure 194: Conformational analysis of hemiindigos **20**, **30** and **33**. a) - c) Molecular structures of (*R<sub>a</sub>*)-*Z*- and (*R<sub>a</sub>*)-*E*-isomers of **20**, **30** and **33** from left to right optimized at the DFT B3LYP/6-311+G(d,p) level of theory. d) Aliphatic region of the  $^1\text{H}$  NMR spectrum (400 MHz, dichloromethane- $d_2$ , 27 °C) of *Z*-**20** (violet) and *E*-**20** (black). Indicative signals of the methyl groups are upfield shifted in *Z*-**20** compared to *E*-**20**. Signals of protons 24a and 24b are split and strongly

separated for **Z-30**. In the corresponding **E-30** isomer the signal of protons 24 are broadened. e) Aliphatic region of the  $^1\text{H}$  NMR spectrum of **Z-30** (red) and **E-30** (blue). Indicative signals of the methyl groups are upfield shifted in **Z-30** compared to **E-30**. f) Aliphatic region of the  $^1\text{H}$  NMR spectrum of **Z-33** (green) and **E-33** (brown). Indicative signals of the methyl groups are upfield shifted in **Z-33** compared to **E-33**. Signals of protons 24a and 24b are split and strongly separated for **Z-33**. In the corresponding **E-33** isomer the corresponding signals are also already split at ambient temperature (see inset 600 MHz, dichloromethane- $d_2$ , 27 °C). The “\*” symbol represents the water peak. Adapted with permission from <sup>[75]</sup>. Copyright 2018 American Chemical Society.

An overview of all measured free activation enthalpies  $\Delta G^*$  for the switches with symmetrical stilbene fragments is given in Figure 195:

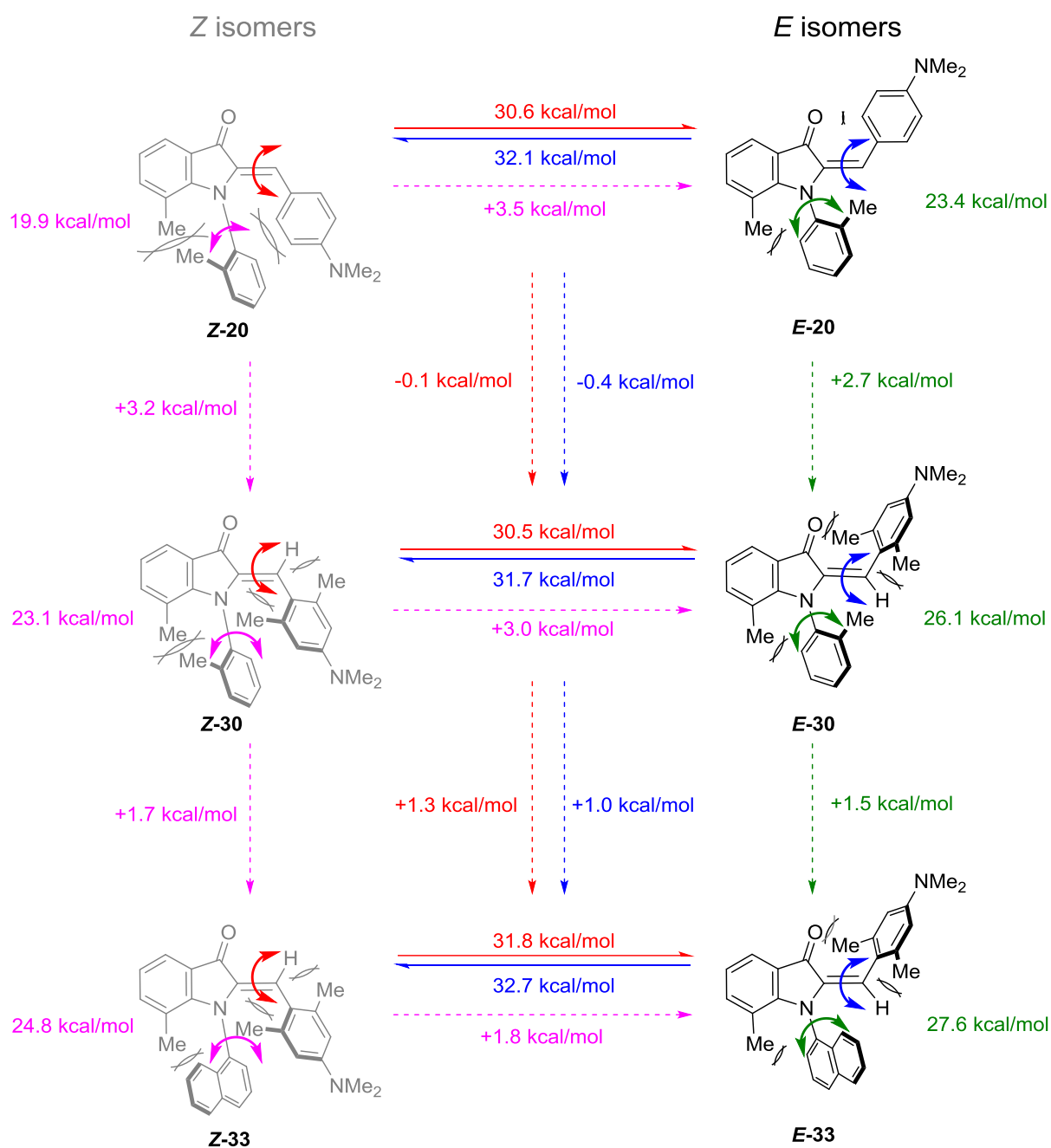


Figure 195: All atropisomerization and *Z*/*E* isomerization barriers for hemiindigos **20**, **30** and **33**. Changes are indicated with +/- over the respective arrows. A clear tendency towards higher atropisomerization barriers from **20** over **30** to **33** can be seen. A slight drop the *Z*/*E* isomerization barrier can be seen for hemiindigo **30** compared to **20** and **33**. Adapted with permission from [75]. Copyright 2018 American Chemical Society.

### 2.3.10 Conclusion: Axially chiral hemiindigos

The introduction of a chiral acyl or aryl axis on hemiindigo chromophores at the indoxyl nitrogen was tested with various substitution patterns to explore the influence of electronics and sterics on the photoswitching behavior and motion of the passive chiral axes.

First experiments were carried out with acyl residues as the *pi*-delocalization of the amide bond was thought to be stable enough for low temperature measurements. This could not be achieved and the low thermal barriers of this atropisomerization are only reported by theory. Changing the acetyl to an isobutyryl group increased the sterical bulk and yielded presumably higher rotational barriers as split signals could be observed via  $^1\text{H}$  NMR spectroscopy when sterically hindered, asymmetrical stilbene fragments are introduced to the hemiindigo photoswitch. This splitting, however, is not caused by the high rotational barrier of the isobutyryl group but by the averaged asymmetric environment induced by the stilbene fragment. The rotational barrier of the stilbene fragment could be determined via temperature dependent  $^1\text{H}$ -NMR coalescence measurements.

The introduction of a chiral aryl axis to the hemiindigo chromophore was done utilizing a novel synthetic route coupling sterically demanding 2-bromotoluene to 7-methyl indole as precursor. The resulting chiroptical switches were scrutinized via chiral HPLC,  $^1\text{H}$  NMR, UV-Vis and (low temperature) electronic circular dichroism (ECD) spectroscopy. In general, a by 3 kcal/mol lowered atropisomerization barrier for the *Z* isomers compared to the *E* isomers could be observed. For all non-*ortho* stilbene substituted derivatives, the calculated transition states of *Z* isomers show passing of the *ortho*-tolyl methyl group over the indoxyl core methyl group while *E* isomer transition states prefer rotation of said methyl group over the central double bond, introducing directionality of the thermal atropisomerization. Furthermore, a strong modulation of ECD signals could be observed between *Z* and *E* isomers for derivatives **30** and **33**. Cyclic experiments showed that the atropisomerization is not influenced by the photoswitching motion, making these materials viable chiroptical switches addressable by visible light. The drawback of the fast racemization of **33** in its *Z* state could be improved by the introduction of a naphthyl moiety which makes the chiroptical properties of these switches usable for prolonged times at 25 °C.

Derivative **58** (see Section 2.3.4) supports a permanent stereocenter and shows similar magnitudes of ECD modulation as derivatives **30** and **33** while maintaining its UV-Vis absorption profile. This type of compounds could be used for prolonged data storage applications beyond 1s and 0s and advanced chiroptical filter systems.

- [74] C. Petermayer, S. Thumser, F. Kink, P. Mayer, H. Dube, *Hemiindigo: Highly Bistable Photoswitching at the Biooptical Window*, *J. Am. Chem. Soc.* **2017**, *139*, 15060.
- [75] C. Petermayer, H. Dube, *Circular Dichroism Photoswitching with a Twist: Axially Chiral Hemiindigo*, *J. Am. Chem. Soc.* **2018**, *140*, 13558.
- [88] U. Burger, A. O. Bringhen, *Cyclization Studies with N-Munnich Bases of 2-Substituted Indoles*, *Helv. Chim. Acta* **1989**, *72*, 93.
- [91] J. C. Antilla, A. Klapars, S. L. Buchwald, *The Copper-Catalyzed N-Arylation of Indoles*, *J. Am. Chem. Soc.* **2002**, *124*, 11684.
- [92] P. Y. Choy, C. P. Lau, F. Y. Kwong, *Palladium-catalyzed direct and regioselective C-H bond functionalization/oxidative acetoxylation of indoles*, *J. Org. Chem.* **2011**, *76*, 80.
- [103] A. J. Fletcher, M. N. Bax, M. C. Willis, *Palladium-catalysed N-annulation routes to indoles: the synthesis of indoles with sterically demanding N-substituents, including demethylasterriquinone A1*, *Chem Commun (Camb)* **2007**, 4764.
- [104] V. S. Velezheva, A. I. Mel'man, Y. I. Smushkevich, V. I. Pol'shakov, O. S. Anisimova, *1-Acetyl-2-bromo-3-indolinone in nucleophilic substitution reactions and the synthesis of pyrrolo[3,2-b]indoles*, *Pharm. Chem. J.* **1990**, *24*, 917.
- [105] I. Shcherbakova, Y. Nikolyukin, *Indoloquinoline compounds as Calcium Channel Blockers*, **2007**, CA20072662185.
- [106] M. M. V. Ramana, P. V. Potnis, *A Simple Approach to the Synthesis of Fluoren-9-Ones*, *Synth. Commun.* **1995**, *25*, 1751.
- [107] N. Ruangsupapichat, M. M. Pollard, S. R. Harutyunyan, B. L. Feringa, *Reversing the direction in a light-driven rotary molecular motor*, *Nature Chemistry* **2011**, *3*, 53.
- [108] B. L. Feringa, R. A. van Delden, *Absolute Asymmetric Synthesis: The Origin, Control, and Amplification of Chirality*, *Angew. Chem. Int. Ed.* **1999**, *38*, 3418.
- [109] P. K. Hashim, R. Thomas, N. Tamaoki, *Induction of molecular chirality by circularly polarized light in cyclic azobenzene with a photoswitchable benzene rotor*, *Chemistry* **2011**, *17*, 7304.
- [110] K. Rijeesh, P. K. Hashim, S. I. Noro, N. Tamaoki, *Dynamic induction of enantiomeric excess from a prochiral azobenzene dimer under circularly polarized light*, *Chem Sci* **2015**, *6*, 973.
- [111] B. Luy, *Disinction of enantiomers by NMR spectroscopy using chiral orienting media*, *Journal of the Indian Institute of Science* **2010**, *90*, 119.

## 2.4 Indigo - From dye to molecular machines

The indigo chromophore is one of the oldest and most prominent dyes known to mankind and possesses strongly red-shifted absorptions. Recent works describe the feasibility of *cis* to *trans* photoswitching at the central double bond with red light for this chromophore.<sup>[66, 69]</sup> The two opposing nitrogen atoms - which can be accessed by substitution reactions - exhibit a large positional change upon photoisomerization respective to each other. This feature of indigo photoisomerization leads to interesting possibilities for non-symmetrical substitutions on the indigo core nitrogen atoms, potentially establishing complex motional cascades upon irradiation. With the steadily rising interest in the field of artificial molecular machines, finding and controlling of induced molecular motions becomes a necessity to peek inside the inner workings of these molecular setups.<sup>[55, 80, 81]</sup> Tuning of key parameters, like the type of driving force and stability of metastable states is crucial for addressability and access to spectroscopic evidence of transitional intermediates. Light as fuel is highly desirable, as it is waste-free, cheap and precisely controlled in temporal and spatial dimensions. Low energy red light is highly advantageous for biological applications as it offers deep tissue penetration and overall mild irradiation conditions, minimizing cellular damage. The indigo chromophore offers red-shifted absorptions in the 620 nm region and poses as an ideal candidate for red-shifted photoswitches upon substitution of its nitrogen protons.<sup>[66, 69]</sup> Single molecule artificial molecular motors and machines to date all rely on high energy UV- or blue to green light as fuel, which can be circumvented with the herein described prospective molecular motor based on the indigo chromophore.<sup>[53, 82, 112]</sup>

A short overview on the thermochromism of the indigo chromophore is given in the section below as the examination of the herein proposed indigo based motors and / or machines can only proceed with experiments at variable temperatures.

### 2.4.1 Indigo - The aspect of thermochromism

The investigation of the thermochromism of the indigo chromophore is crucial for the examination of the proposed indigo based motors and / or machines as the required experiments to elucidate their molecular movements have to be conducted at variable temperatures. Experiments on the (substituted) indigo chromophore resulted in the observation of intensity and wavelength modulation in their absorption spectra upon temperature change. This indicates thermochromic effects which could be demonstrated for the “naked” indigo chromophore as well as the derivatives below, which suggests thermochromism to be an intrinsic property of



the indigo scaffold. Precise measurements of molar absorptivities or isosbestic points should be done at well-defined and regulated temperatures, as lowering temperatures will enlarge and bathochromically shift the most red-shifted absorption maximum. The opposite effect can be seen by increasing the temperature beyond the ambient starting conditions. Photokinetic reaction rates should also be increased by enlarged molar absorptivities.

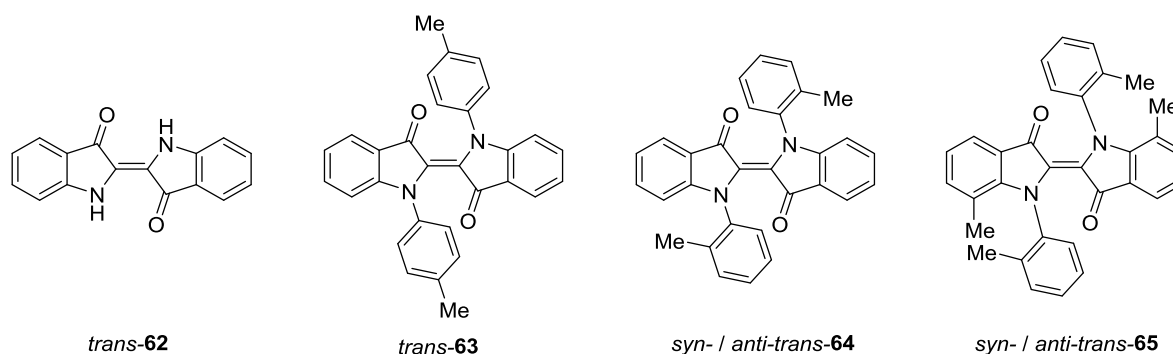


Figure 196: Overview of investigated compounds **62**, **63**, **64** and **65** regarding their UV-Vis spectra at different temperatures. Compound **63** was synthesized and characterized by *L. Huber*.<sup>[66]</sup> The *syn*- / *anti*-stereodescriptors are explained in detail within Section 2.4.5.

To date, thermochromism of indigo was not studied in detail. Publications by *K. Ramig* and *O. Lavinda et al.* suggest that the change in color intensity of indigo dyed cotton fibers results from the interaction of indigo with the fabric and / or solid state aggregation effects.<sup>[113, 114]</sup> In this work, the measurements on indigo derivatives in solution showed that a fabric / solid state phase is not needed for thermochromic effects, which suggests other, additional mechanisms to be responsible for the change in color intensity of indigo. Another publication by *G. Wyman* reports thermochromic effects on thioindigo.<sup>[115]</sup>

To obtain temperature dependent absorption spectra, a UV-Vis spectrophotometer was equipped with a temperature probe with external data logging fixated on the sample cuvette holder and a thermostat. Heating was implemented via thermostat, cooling was achieved by adding ice to the circulating water in the reservoir. A lag between temperature read-out and absorption response can be expected, as the heating / cooling ramp could not be precisely controlled. Starting points might differ from the initial 100% value as the depicted spectra and graphs only show the measurement progress upon heating / cooling and not the static plateau / equilibration period at the beginning or at the end of the measurement. Slower heating / cooling leaves more time for thermal equilibration of thermometer readout and sample equilibration and should be used for future experiments.

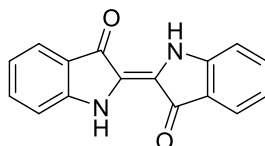
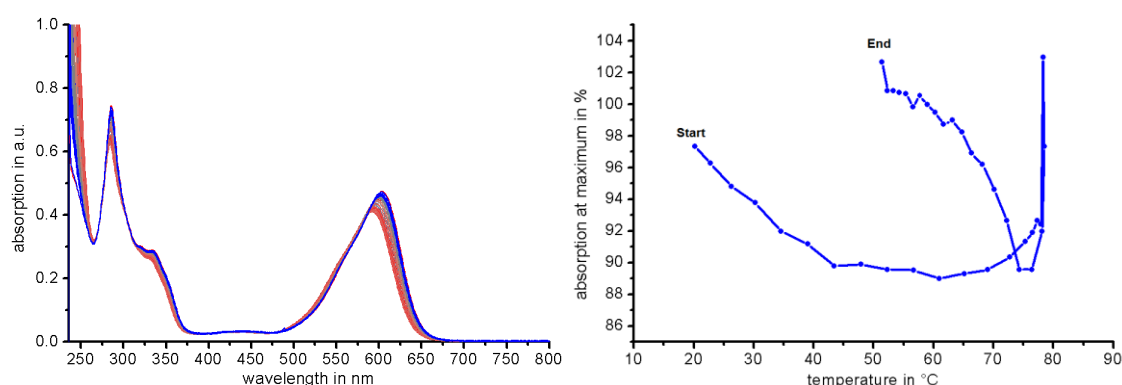
Figure 197: Lewis-formula of *trans*-indigo **62**.

Figure 198: UV-Vis spectra (left) and plot of absorption maximum (right) against temperature for the parent indigo **62** in chloroform. A thermochromic shift of about 20 nm can be seen. Also, a decline in absorption to about 60 °C can be observed with a subsequent sharp increase in absorbance starting at 78 °C probably caused by boiling chloroform. The initial absorbance is not lost upon cooling, but the higher values at the end can be explained by increasingly dissolved chromophore, as this compound tends to be very insoluble in most solvents.

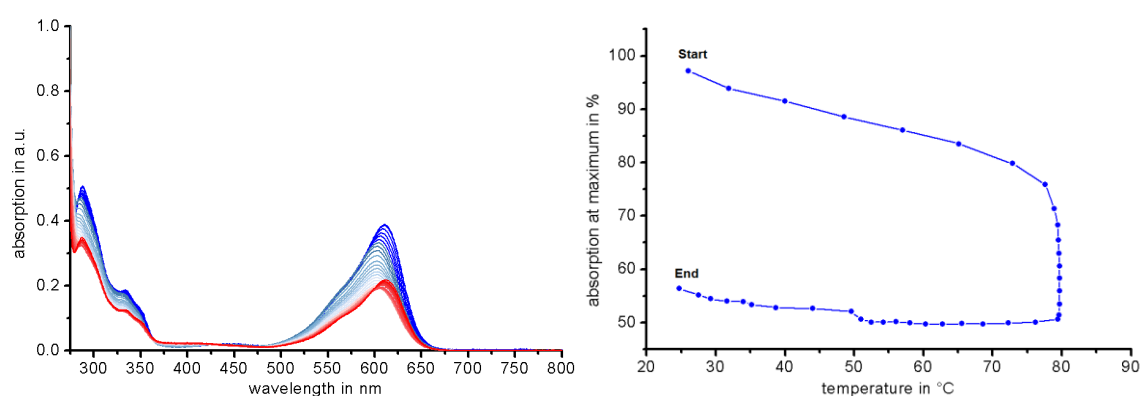


Figure 199: UV-Vis spectra (left) and plot of absorption maximum vs. temperature (right) for the parent indigo **62** in *N,N*-dimethylformamide. A thermochromic shift of about 10 nm can be seen. Also, a steady decline in absorption to 78 °C can be observed with a subsequent sharp drop in absorbance starting from 78 °C. The initial absorbance can be partially restored upon cooling, however, a permanent decline of 44% can be observed. This thermal degradation can also be observed for arylated derivatives for this solvent.

As irreversible thermal degradation of the indigo chromophores in *N,N*-dimethylformamide represents the major mechanism behind its absorption change, the results in other solvents suggest another cause for the observed effects. Twisting of the central double bond can be addressed via DFT calculations at the B3LYP/6-311+G(d,p) level of theory show how this twisting influences the absorption and electronic circular dichroism (ECD) spectra of indigo **62**.

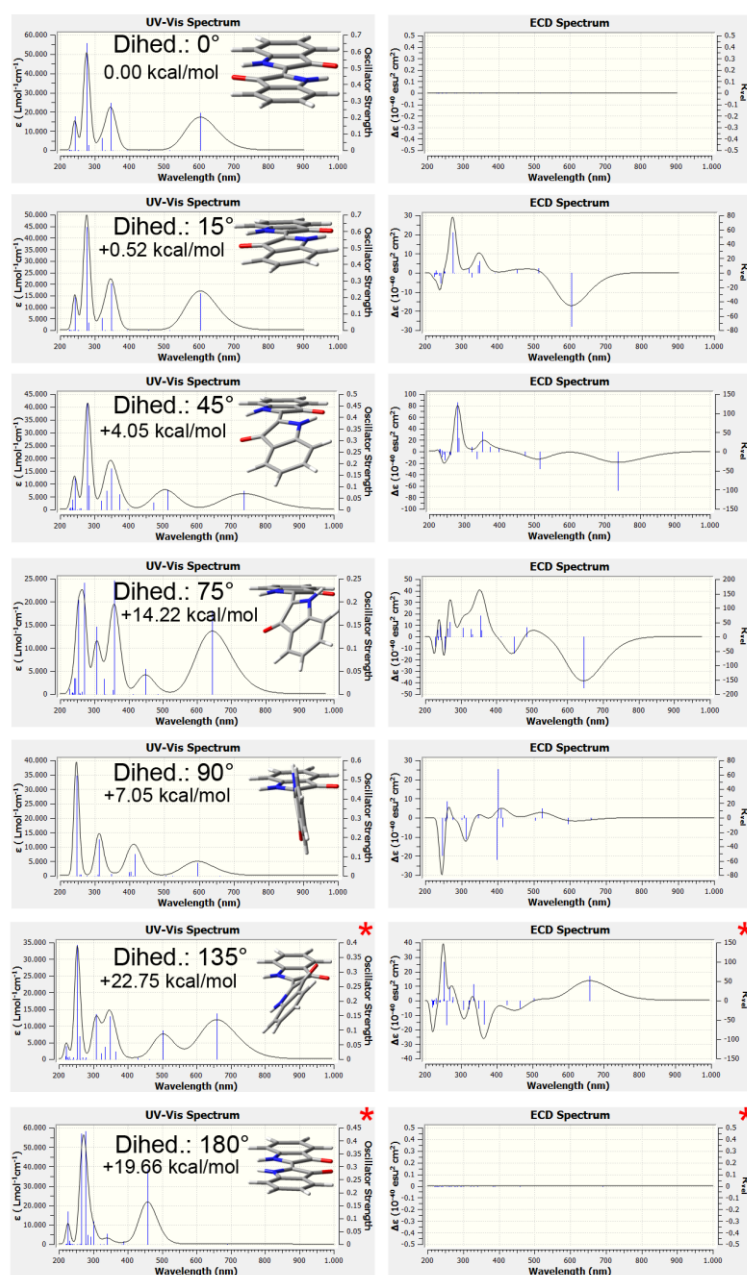


Figure 200: DFT calculations at the B3LYP/6-311+G(d,p) level of theory for indigo **62**, UV-Vis spectra including oscillator energies (left) and ECD spectra (right) were calculated using TD-DFT,  $n_{\text{states}} = 20$  or  $*$  = 30 (the other enantiomer was calculated for 135°). The *trans*-form of indigo represents its global minimum,

while dihedral torsion of the central double bond by  $180^\circ$  gives the *cis*-state. Incremental torsion in  $15^\circ - 45^\circ$  steps yields two red-shifted maxima for a  $45^\circ$  and a  $135^\circ$  torsion angle.

Generally, a pronounced loss of absorption is observed (see left intensity scale in Figure 200) when torsion is introduced to the indigo chromophore, which is the case for *N*-substituted derivatives. This supports the main experimental observation. An additional and bathochromically shifted oscillation with an absorption maximum of up to 740 nm can be observed for twisted derivatives, which contradicts the experiment at first (Figure 200). However, imaginary averaging of the two most red-shifted absorptions gives a slightly shifted absorption maximum at 600 nm, which is in accordance to the rather small hypsochromic shift within the experiment. These findings suggest restoration of planarity upon cooling, which can be experimentally seen for chiral indigo **64** (see Figure 208). The chiral indigo derivatives also show the same red-shifted ECD signals at 600 nm which are independent of the ECD absorptions of the chiral axes, see Section 2.4.9.

As the parent indigo chromophore does not permit a wide range of usable solvents, soluble *N*-substituted indigo chromophores were tested for their thermochromic properties. First, the di-*para*-tolyl-indigo **63** synthesized by *L. Huber* was investigated in chloroform, dimethylformamide and toluene to exclude possible effects of the chiral axes on the thermochromic behavior.

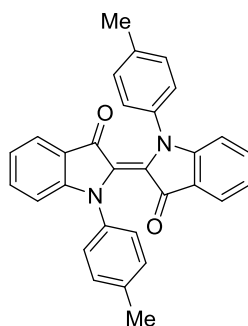


Figure 201: Lewis-formula of di-*para*-tolyl-indigo **63**.

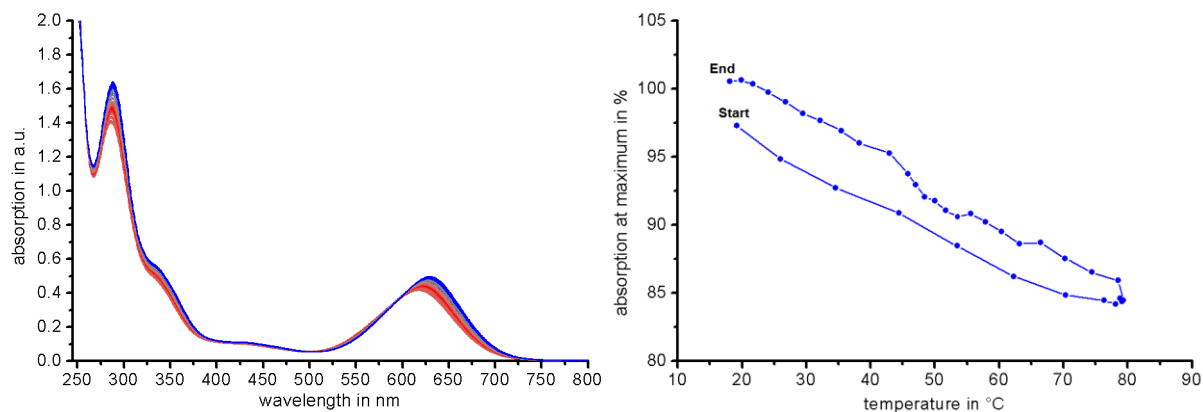


Figure 202: UV-Vis spectra (left) and plot of absorption maximum vs. temperature (right) for the di-*para*-tolyl substituted indigo **63** in chloroform. A thermochromic shift of about 30 nm can be seen. Also, a steady and linear decline in absorption to 80 °C can be observed. The initial absorbance can be completely restored upon cooling.

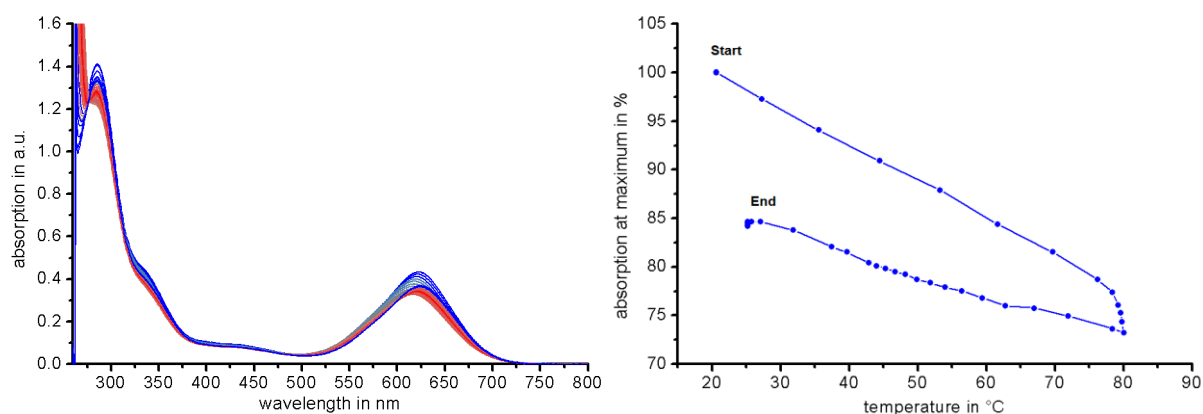


Figure 203: UV-Vis spectra (left) and plot of absorption maximum vs. temperature (right) for the di-*para*-tolyl substituted indigo **63** in *N,N*-dimethylformamide. A thermochromic shift of about 20 nm can be seen. Also, a steady decline in absorption to 80 °C can be observed. The initial absorbance can be partially restored upon cooling, although the same kind of loss of absorbance can be seen with the parent indigo chromophore **62** in *N,N*-dimethylformamide.

## 2.4.1 INDIGO - THE ASPECT OF THERMOCHROMISM

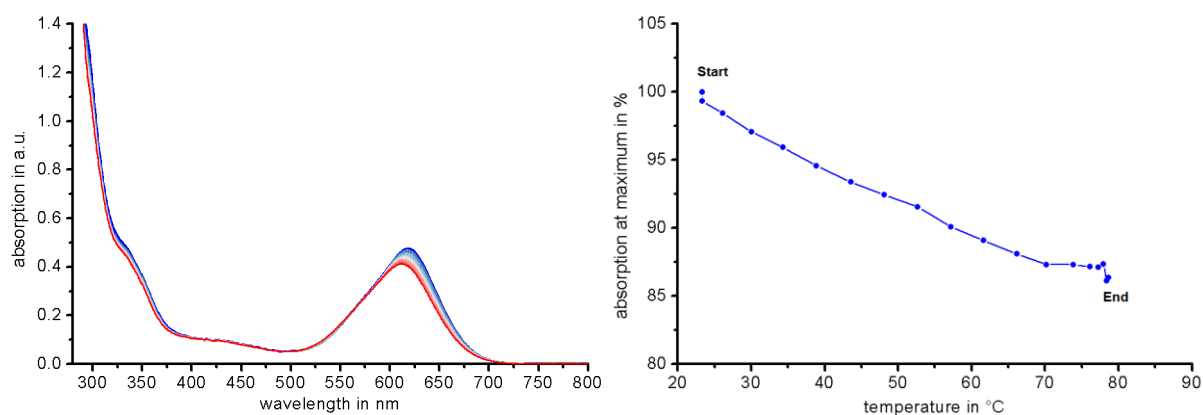
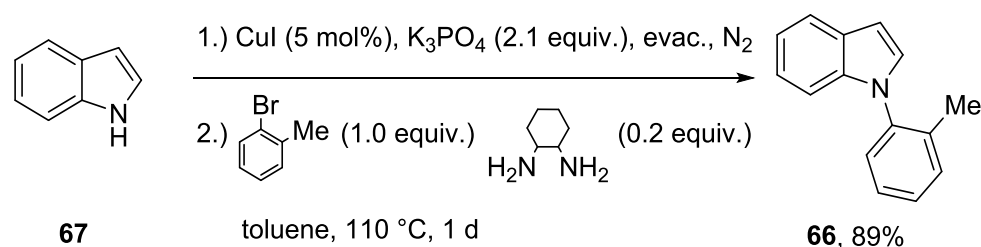


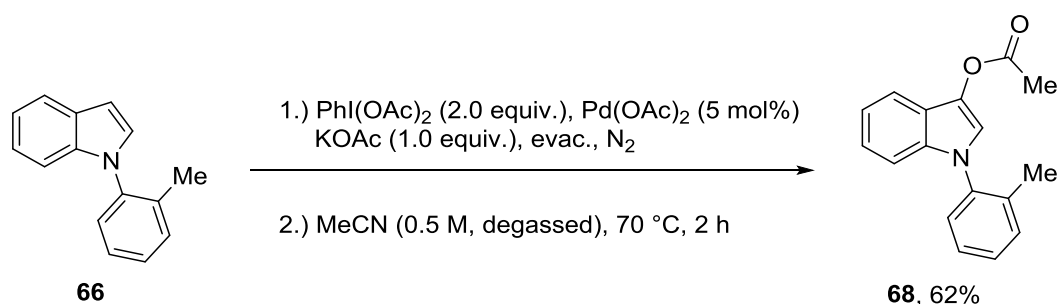
Figure 204: UV-Vis spectra (left) and plot of absorption maximum vs. temperature for the di-*para*-tolyl substituted indigo **63** in toluene. A thermochromic shift of about 20 nm can be seen. Also, a steady and linear decline in absorption to 80 °C can be observed.

To investigate chiral indigo derivatives and their thermochromism, non-symmetric substituents were introduced at the indoxyl-N atom. The precursor 1-(*o*-tolyl)-1*H*-indole **66** was prepared according to the published procedure of *J. Antilla et al.* from indole **67**.<sup>[91]</sup>



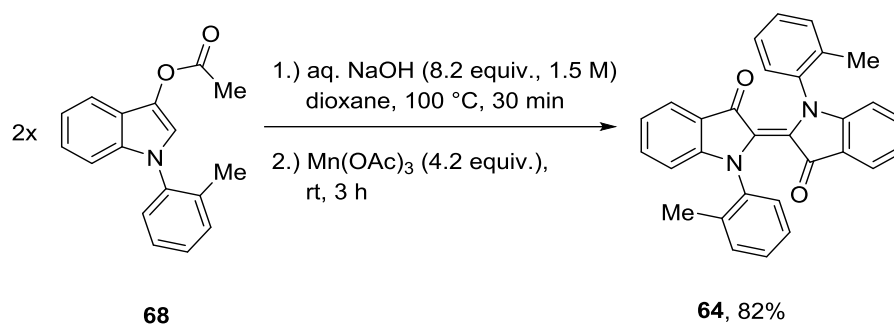
Scheme 32: Preparation of *N*-arylated indole **66**.

1-(*o*-tolyl)-1*H*-indol-3-yl acetate **68** was prepared from **66** according to the procedure by *P. Choy et al.*<sup>[92]</sup>



Scheme 33: Preparation of *N*-arylated indoxyl acetate **68**.

The synthesis of indigo **64** is shown in Scheme 34 below.



Scheme 34: Deacylation of indoxyl acetate **68** according to *U. Burger et al.*<sup>[88]</sup> with dioxane as co-solvent and subsequent oxidation with manganese(III) acetate to furnish indigo **64** in good yield.

Chiral indigo derivative **64** showed pronounced thermochromism as depicted in Figure 206 to Figure 209.

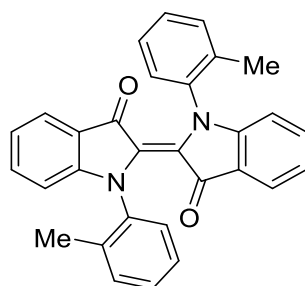


Figure 205: *Lewis*-formula of di-*ortho*-tolyl-indigo **64**.

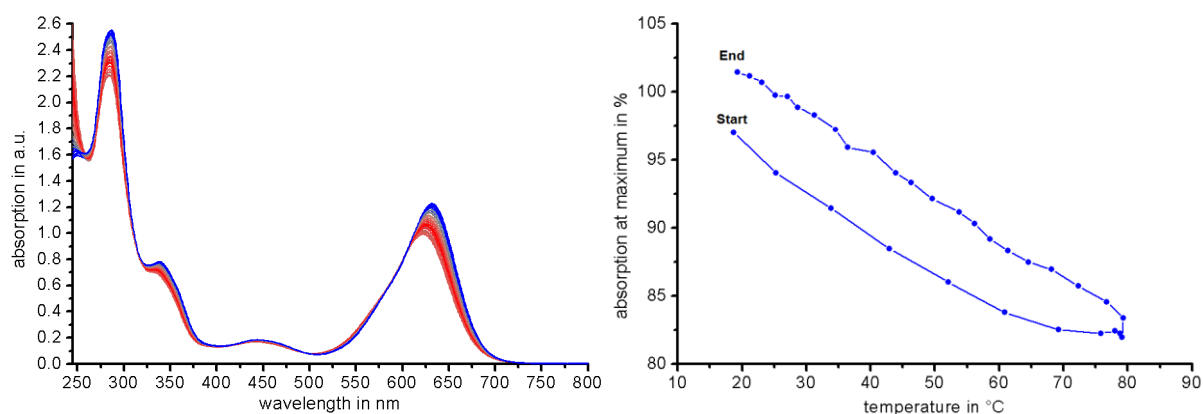


Figure 206: UV-Vis spectra (left) and plot of absorption maximum vs. temperature (right) for the di-*ortho*-tolyl substituted indigo **64** in chloroform. A thermochromic shift of about 20 nm can be seen. Also, a steady decline in absorption to 80 °C can be observed. The initial absorbance can be completely restored upon cooling.

## 2.4.1 INDIGO - THE ASPECT OF THERMOCHROMISM

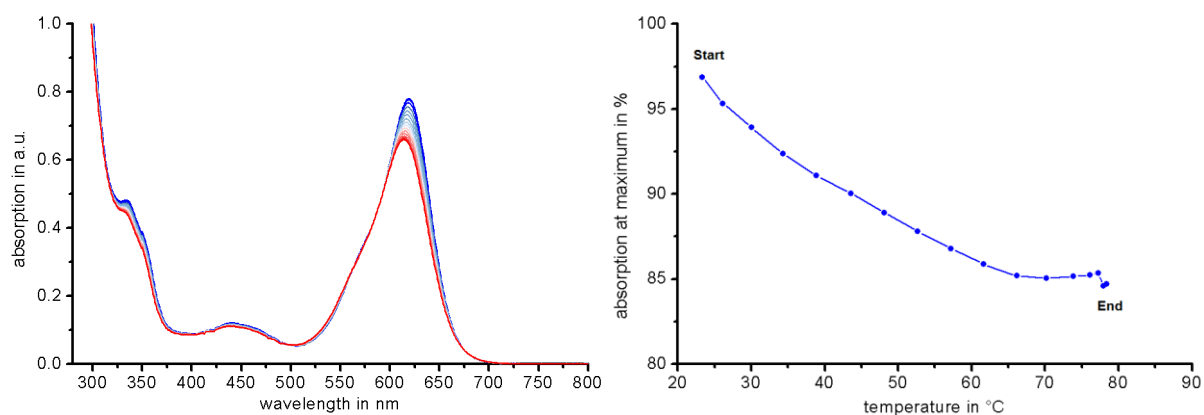


Figure 207: UV-Vis spectra (left) and plot of absorption maximum vs. temperature (right) for the di-*ortho*-tolyl substituted indigo **64** in chloroform. A thermochromic shift of about 10 nm can be seen. Also, a steady decline in absorption to 80 °C can be observed.

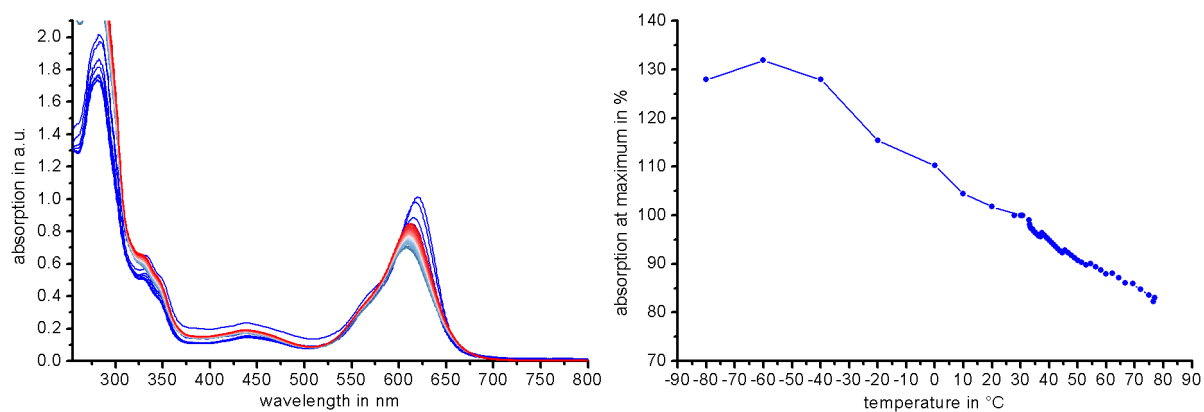


Figure 208: UV-Vis spectra (left) and plot of absorption maximum vs. temperature (right) for the di-*ortho*-tolyl substituted indigo **64** in 83 / 17 heptane / ethyl acetate. A thermochromic shift of about 20 nm can be seen. Also, a steady and linear increase towards -80 °C and a decline in absorption to 80 °C can be observed.



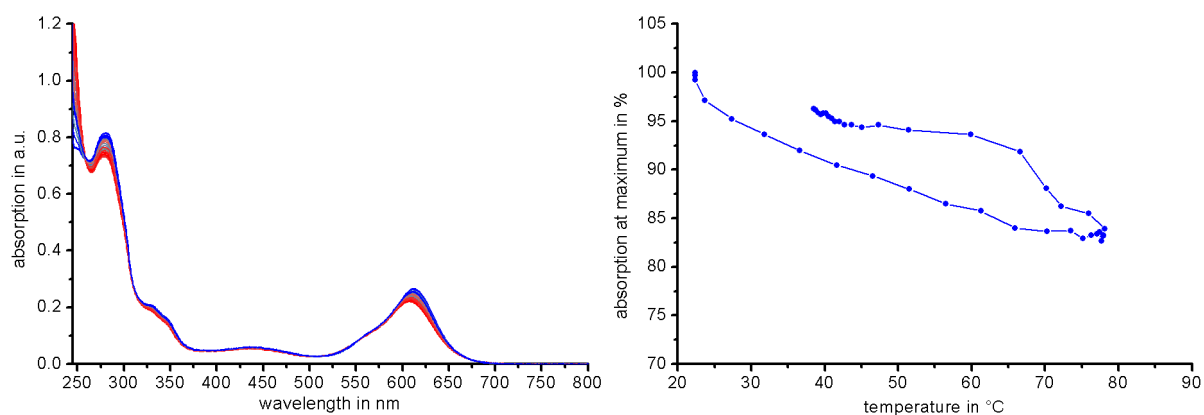
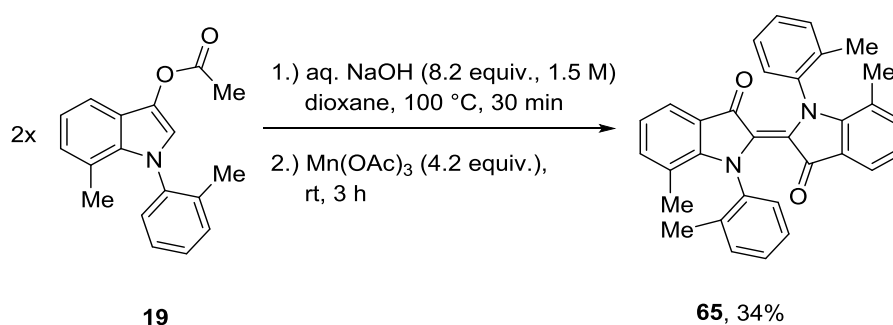


Figure 209: UV-Vis spectra (left) and plot of absorption maximum vs. temperature (right) for the di-*ortho*-tolyl substituted indigo **64** in 83 / 17 heptane / ethyl acetate at 1 / 5 of the concentration as shown in Figure 208. A thermochromic shift of about 20 nm can be seen. Also, a steady and linear decline in absorption to 80 °C can be observed. The initial absorbance can be completely restored upon cooling.

The synthesis of indigo **65** from indoxyl acetate **19** is shown in Scheme 35 below. The synthesis of **19** is shown in Section 2.2.7



Scheme 35: Deacylation of **19** according to *U. Burger et al.*<sup>[88]</sup> with dioxane as co-solvent and subsequent oxidation with manganese(III) acetate to furnish indigo **65** in low yield.

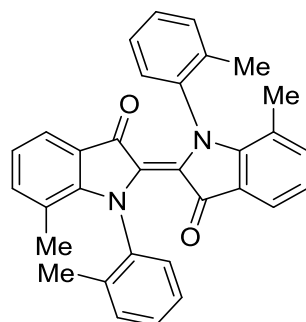


Figure 210: Lewis-formula of di-*ortho*-tolyl-indigo **65**.

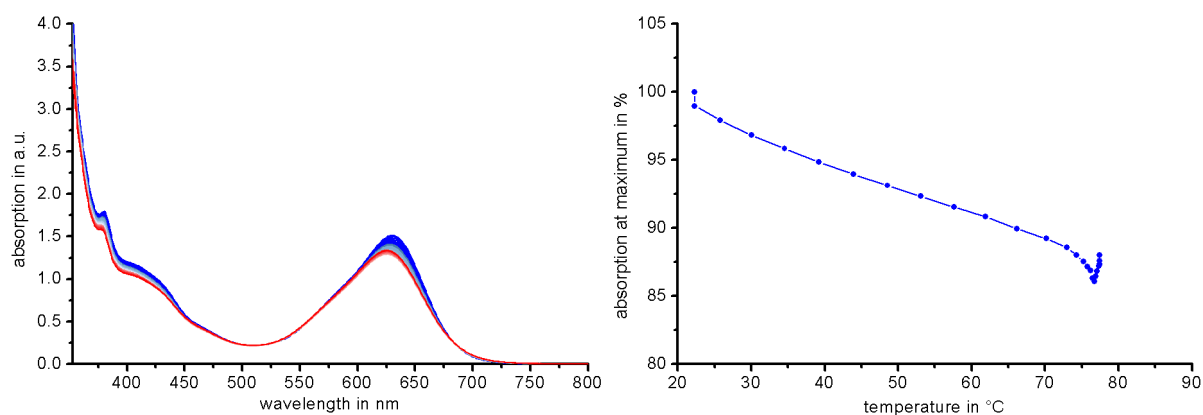


Figure 211: UV-Vis spectra (left) and plot of absorption maximum vs. temperature (right) for the di-*ortho*-tolyl di-7-methyl-substituted indigo **65** in 83 / 17 heptane / ethyl acetate. A thermochromic shift of about 15 nm can be seen. Also, a steady and linear decline in absorption to 80 °C can be observed.

These thermochromic effects of *N*-substituted indigos in solution suggest a temperature dependent change in the structure, electronics or hydrogen bonding strength of the unsubstituted indigo chromophore. As di-substitution eliminates the effect of hydrogen bonding and introduces enhanced skewing / bending / torsion to the core chromophore,<sup>[116]</sup> temperature dependent effects caused by structural changes become more likely. This can be explained by different geometries within and adjacent to the crucial central double bond, which, in combination with the donor / acceptor setups, is responsible for the color of indigo. A hypsochromic shift combined with a loss of absorptivity hints towards twisting of the double bond as the cross-talk of donors and acceptors is reduced. The latter trend is reversed upon cooling up to -80 °C without observable non-linearities within this measurement range. This can also be explained via *Boltzmann*-distributions at different temperatures, populating the increasingly planarized conformers at lower temperatures.

## 2.4.2 Axially chiral indigos

The synthesis of axially chiral hemiindigos described in section 2.2.7 yielded axially chiral indigo **65** as side product upon oxidation of unreacted starting materials on air during workup. The synthetic procedure was optimized by using manganese(III) acetate or potassium permanganate as oxidant to synthesize the desired indigo compounds efficiently and in higher yields.

This first generation of disubstituted chiral indigos was expected to show very interesting properties and characteristics especially with regard to molecular motors, machinery and complex molecular motions, driven by highly desirable red light.

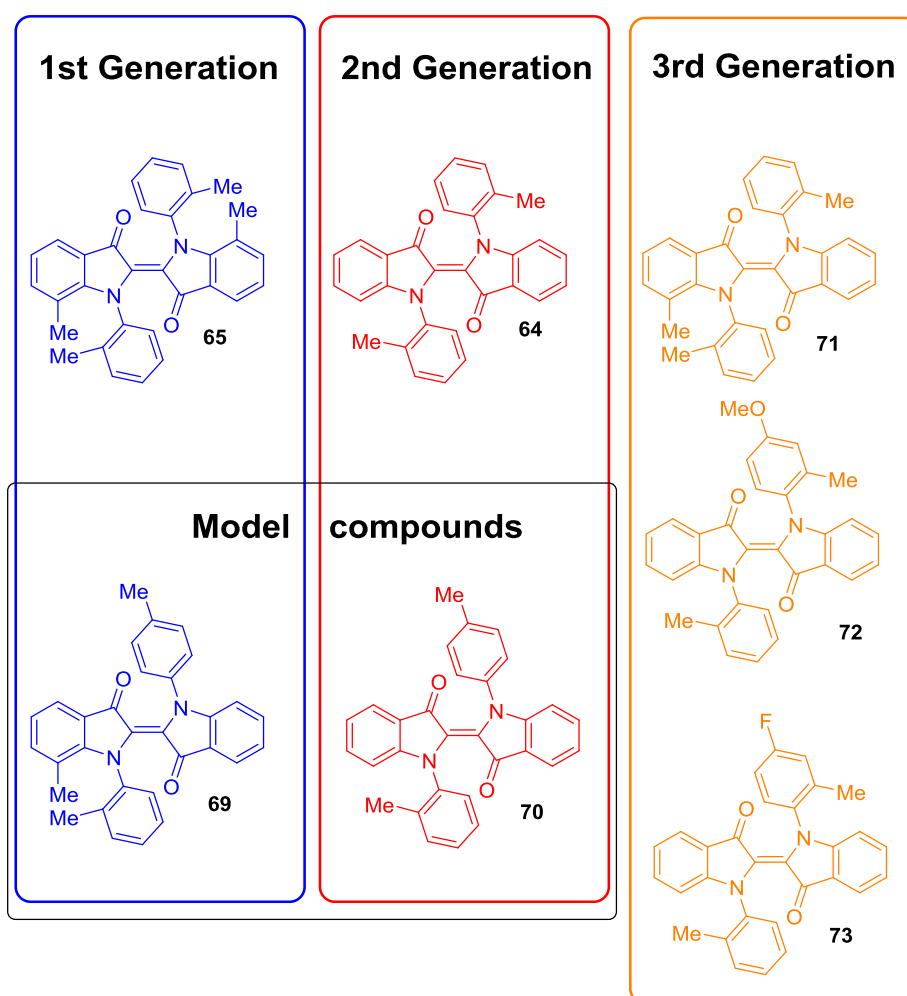


Figure 212: Overview of 1<sup>st</sup> (**65** and **69**), 2<sup>nd</sup> (**64** and **70**) and 3<sup>rd</sup> (**71**, **72** and **73**) generation of axially chiral di-*N*-substituted indigos.

The following sections describe the evolution and investigation of hemiindigo **64** and other axially chiral indigo (model) compounds (1<sup>st</sup> to 3<sup>rd</sup> Generation) and the concurrent progress

made in the interpretation of experimental data to give explanations for the intriguing motional behavior of the second generation indigo **64**.

Unidirectional single- and double bond motor rotations, photoinduced/thermal extended Hula-Twist, geared processes and pumping of bistable states against the thermal equilibrium, all fueled by red light, can be interpreted into the obtained experimental and theoretical data for **64**. An extensive computational DFT assessment was carried out on conformation, transition states, ECD / UV-Vis spectra and  $^1\text{H-NMR}$ -shifts to model the experimental data.

Desymmetrization of di-arylated indigos was carried out via different approaches, which are found in Section 2.4.27 and are still investigated to date. The non-symmetrical derivatives are expected to give further experimental proof of the underlying light-induced motions and trajectories of this class of compounds via predominantly NMR studies.

### 2.4.3 Symmetric chiral indigos - First generation indigo 65

Indigo **65** was the first compound of this class, which was initially obtained as synthetic side product. Its optimized synthesis is shown in Scheme 35, Section 2.4.1.

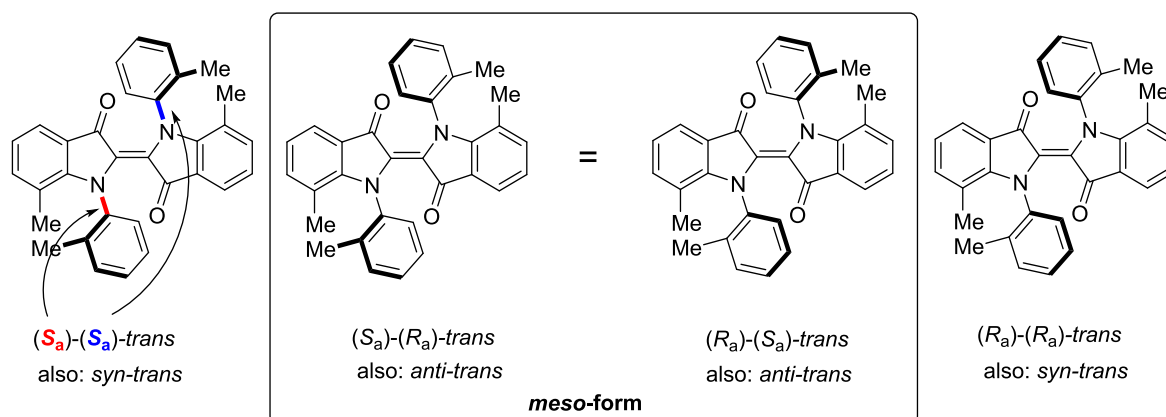


Figure 213: Overview of the three *trans* rotamers of indigo **65**. Formally, the same amount of rotamers is expected for the less stable *cis* form. Two-fold stereo descriptors like e.g.  $(S_a)-(S_a)$ -*syn-trans* emphasize the *syn-trans* forms to be enantiomeric whereas the *anti*-forms are *meso*-forms.

7,7'-Dimethyl-*N,N'*-di(*ortho*-tolyl)indigo **65** was isolated as turquoise oxidative side product of a condensation reaction between *ortho*-tolyl-arylated indoxyl acetate **19** and aldehydes. Besides its unexpected low solubility in various solvents, photoirradiation experiments followed via UV-Vis, NMR or chiral HPLC experiments did not show any *trans-cis* photoisomerization properties.

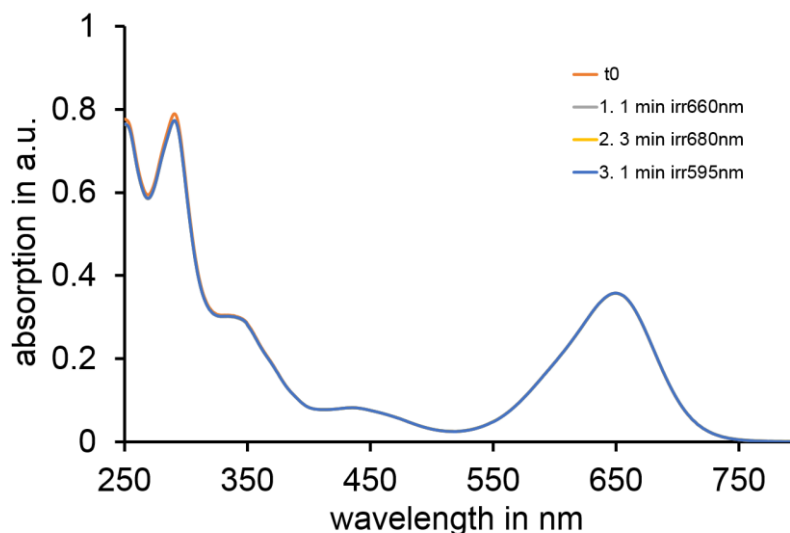


Figure 214: UV-Vis spectra of indigo **65** are shown exemplarily in dichloromethane. No change during longer irradiations (30 min) in dimethyl sulfoxide, acetonitrile, tetrahydrofuran or toluene could be observed.

Separation of rotamers was also impossible at different temperatures ranging from 40 °C to 0 °C, which is intriguing, as split signal sets for *syn*- and *anti* diastereomers are observed by NMR spectroscopy. Additionally, only one extremely broad peak (10 min compared to expected 30 s) could be eluted via achiral reversed phase (RP) and chiral normal phase HPLC under similar conditions as for indigo **64** (see Figure 230).

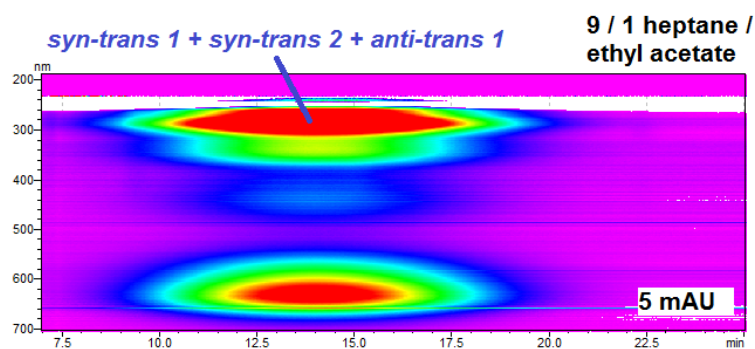


Figure 215: Chiral HPLC separation attempt on indigo **65** at 0 °C with 9 / 1 heptane / ethyl acetate as solvent. No rotamers or peak shoulders are visible. Very high solvent polarities (50 - 100% ethyl acetate) yielded one single sharp peak.

Oddly, the solubility of compound **65** is drastically reduced in organic solvents compared to all other arylated indigo chromophores, which can be quickly dissolved in e.g. toluene. Sonication and heating is necessary to obtain solutions suitable for NMR measurements.

A low rotational barrier for the *ortho*-aryl axis below 20 kcal/mol is expected as the isomers are inseparable via HPLC at 0 °C. The barrier of the *cis* to *trans* isomerization should also amount to less than 18 kcal/mol as no photoisomerization products can be observed because of the presumably fast thermal recovery of the *trans* state observed at 0 °C. Additionally, low quantum yields or the indigo not undergoing photoisomerization caused by the *cis*-isomer being highly thermodynamically disfavored could not be ruled out at this stage.

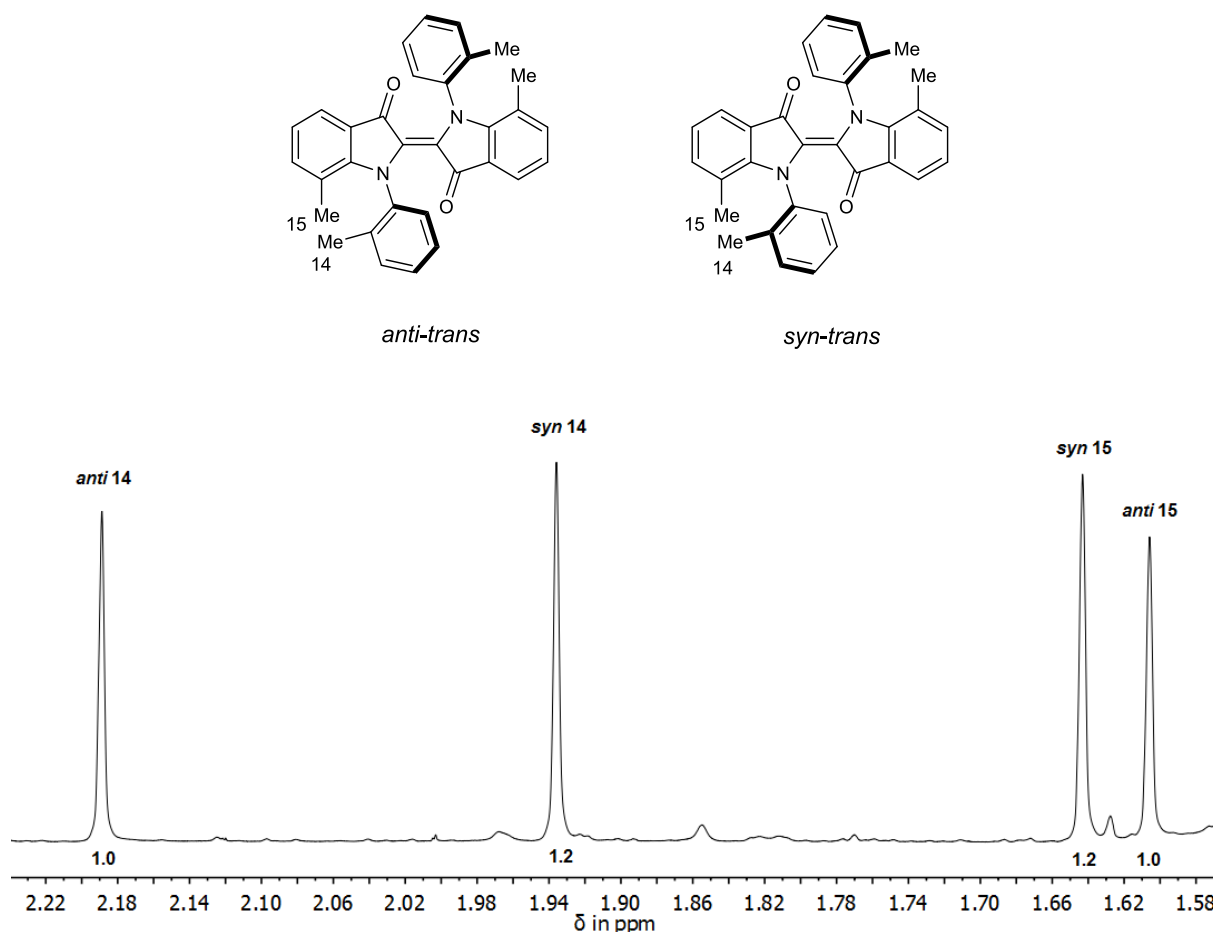


Figure 216: Aliphatic section of the  $^1\text{H-NMR}$  spectrum of *trans*-**65** (dichloromethane- $d_2$ , 600 MHz, 27 °C). The *syn* isomer is preferred by 10% over the *anti*-form. *Syn*- and *anti*-diastereomers show distinct shifts for indigo-core- (15) and rotatable *ortho*-tolyl methyl group protons (14). Assignments by 2D NMR spectroscopy are shown starting from Figure 219.

As the insights by photoisomerization experiments were very limited, a theoretical assessment was carried out.

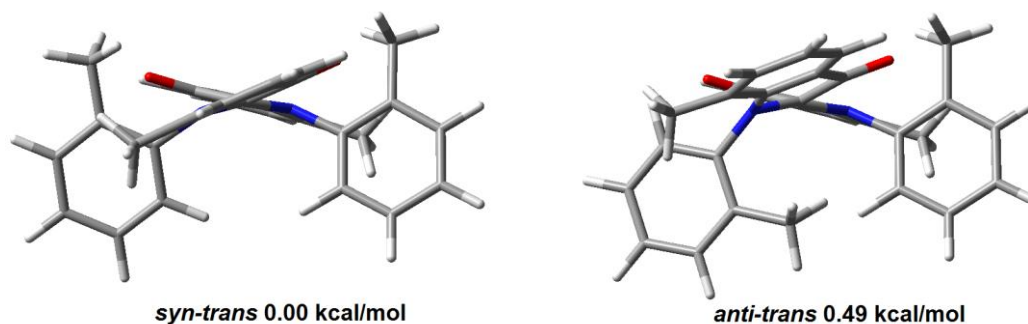


Figure 217: Comparison of obtained minimum geometries of *syn*(left)- and *anti*(right)-*trans* indigo **65** at the B3LYP/6-311+G(d,p) level of theory, view along the central double bond.

Both diastereomers show torsion around their central double bond, the *anti* form, however, experiences additional bending at this position to lower the strain induced by the methyl group pointing towards the other aryl moiety. The obtained minimum energies are in good agreement to the observed 1.2 / 1.0 *syn*- / *anti-trans* ratio observed via  $^1\text{H-NMR}$  spectroscopy in Figure 216 when taking into account the *Gibbs-Helmholtz* equation.

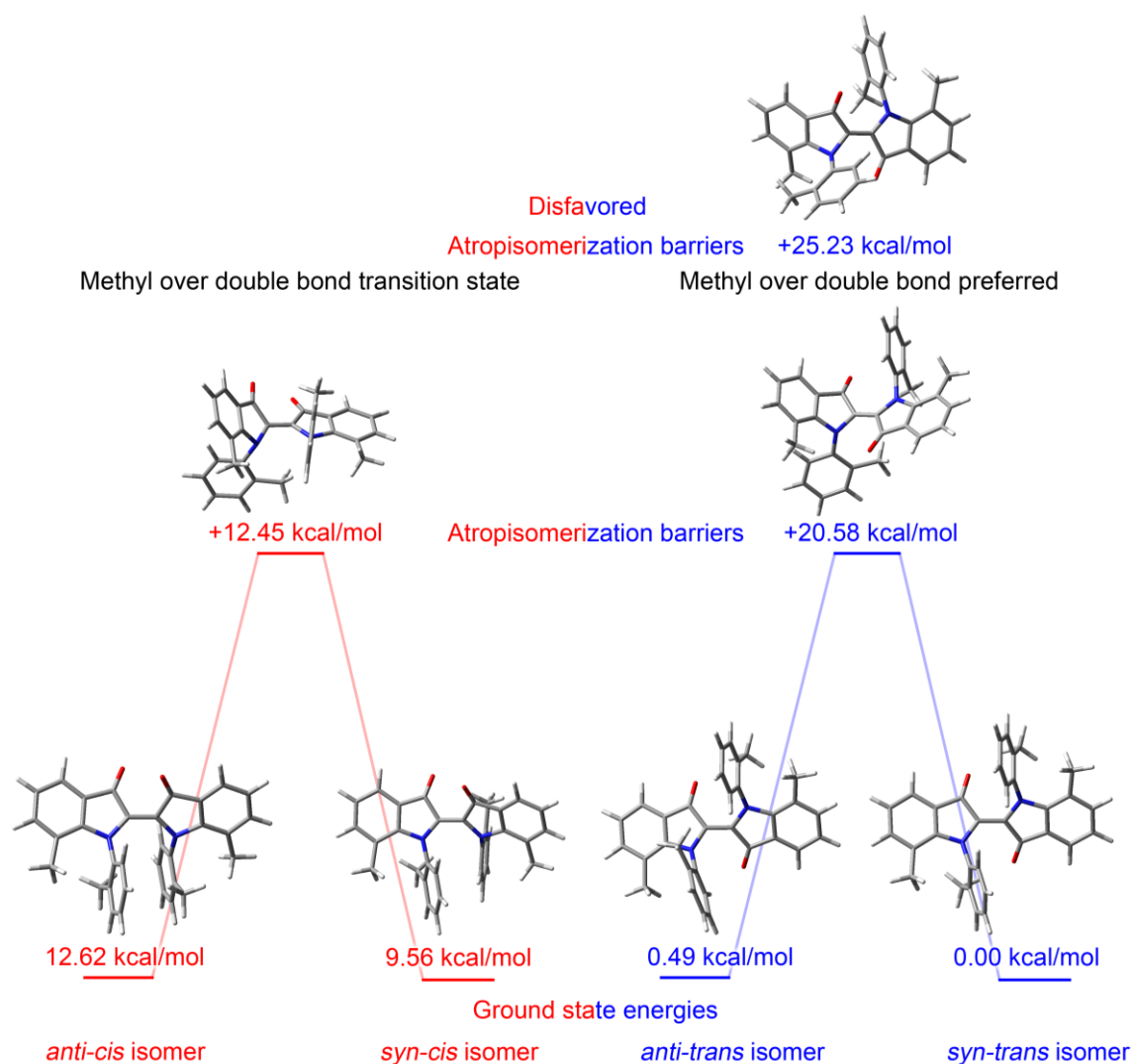


Figure 218: Calculated ground and transition state structures and energies of indigo **65** at the B3LYP/6-311+G(d,p) level of theory. Transition states for three of eight possible atropisomerizations could be found. The other possible transition state for the *cis* isomer did not converge after several attempts and tweaks. The “+” sign in front of transition state values indicates the energy difference with respect to the lower ground state of the respective *cis* or *trans* isomers. Missing experimental data for the *cis* isomer makes it difficult to assign the reported transition state to be high or low in energy or to address the preferred directionality for this rotation.

The favored atropisomerization energy barrier for the *trans* state of **65** was determined at relatively low values of about  $\Delta G^* = 20$  kcal/mol. Besides the comparably long retention times of this compound, chiral HPLC separation at 0 °C is expected to be difficult because of this fast thermal racemization. The *cis* state is strongly disfavored by 9 - 13 kcal/mol according to the theoretical description, which could explain the lack of photochemistry taking place for this



compound. The atropisomerization barrier in the *cis* state is calculated at even lower values compared to the *trans* state, with 12.6 kcal/mol higher in energy than the respective *syn-cis*-ground state, making kinetic observations not feasible at -80 °C.

$^1\text{H}$ -nuclear *Overhauser* effect spectroscopy (NOESY) NMR experiments were carried out with **65** at ambient temperatures. Positive NOEs indicate fast dynamics which support the low atropisomerization barriers found via DFT calculations.

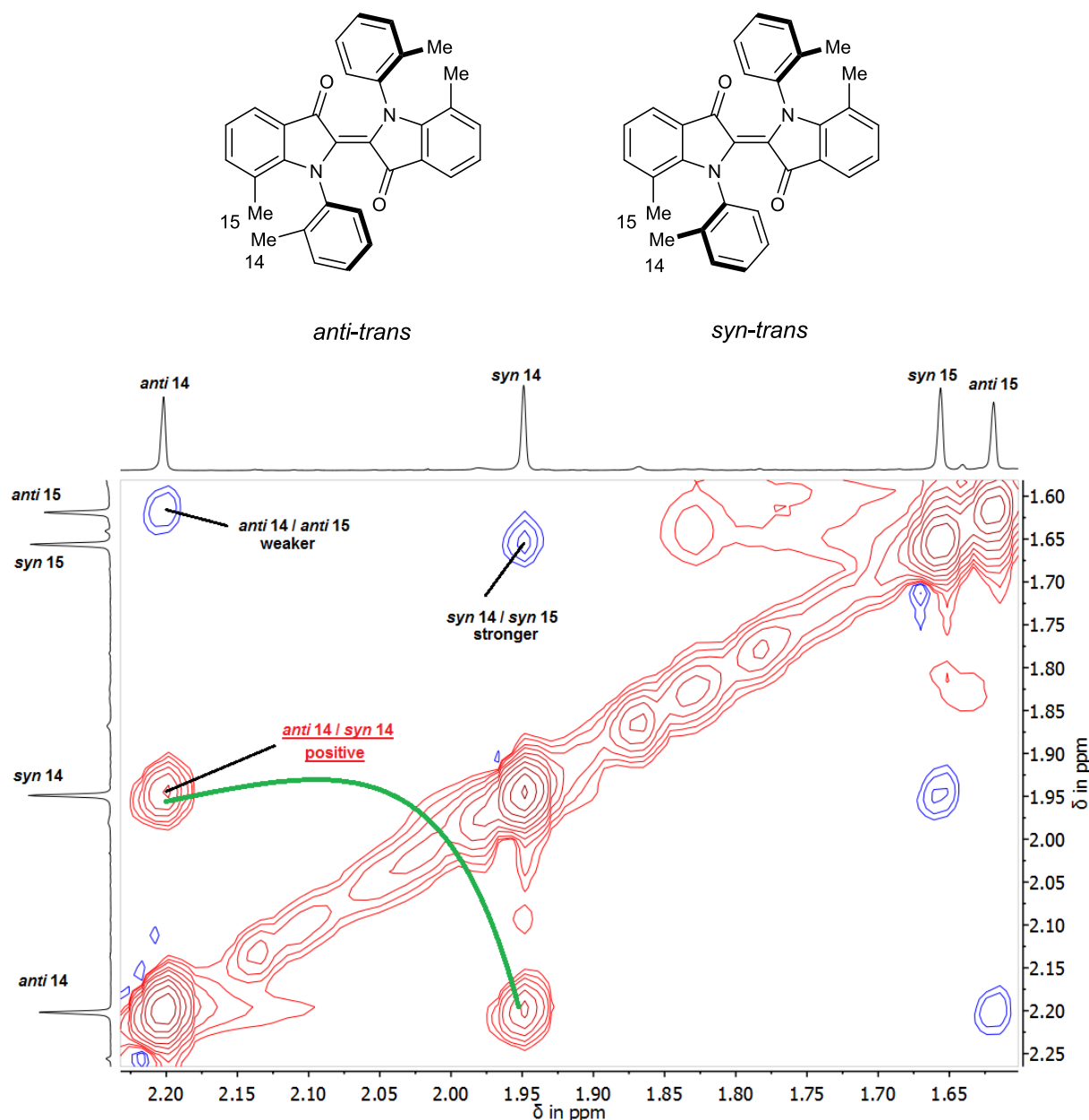


Figure 219: Aliphatic section of the  $^1\text{H}$  NOESY (dichloromethane- $d_2$ , 600 MHz, 27 °C) of *trans*-**65**. Expected cross peaks for *syn* / *anti* 14 / 15 can be observed. Signals of *anti* 14 and *syn* 14 show one of two positive NOE signals (see Figure 221), while the rest of the molecule shows negative NOEs if the diagonal signals are set to

positive values according to convention. This strongly indicates fast dynamics in between *syn*- and *anti* molecules as NOESY utilizes the same pulse sequence as exchange spectroscopy (EXSY) and the used mixing time of 1.2 s is much longer than the exchange of respective nuclei, hinting towards an atropisomerization barrier between 17- and 20 kcal/mol.

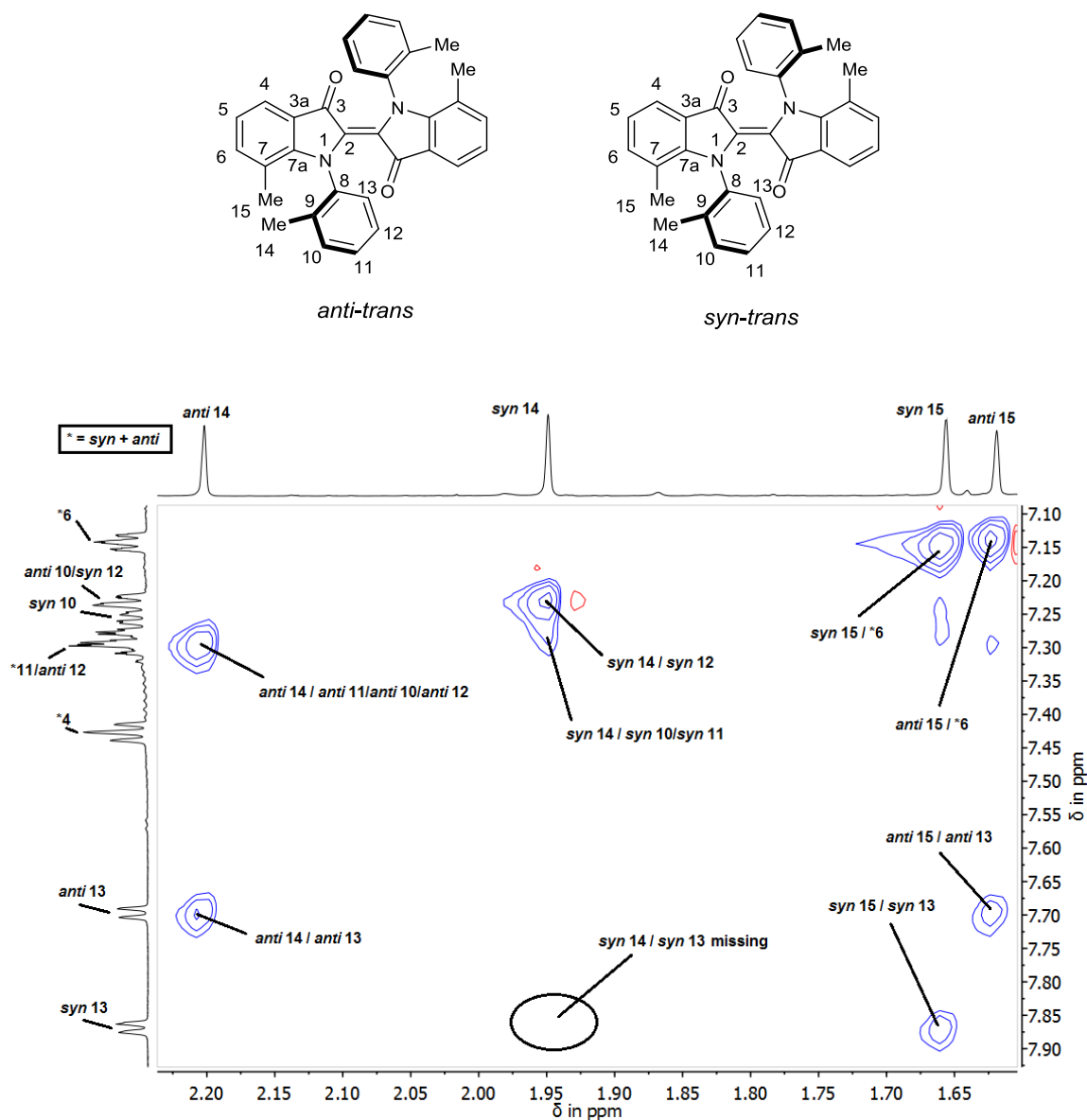


Figure 220: Aliphatic / aromatic <sup>1</sup>H NOESY spectrum (dichloromethane-*d*<sub>2</sub>, 600 MHz, 27 °C) of *trans*-65. *Syn*- and *anti* form can be distinguished by the NOE signal of *anti* 14 / 13 and the non-existent signal for *syn* 14 / 13. This indicates the proximity of methyl group *anti* 14 to the back of the other *ortho*-tolyl (proton *anti* 13) on the opposite side of the central double bond.

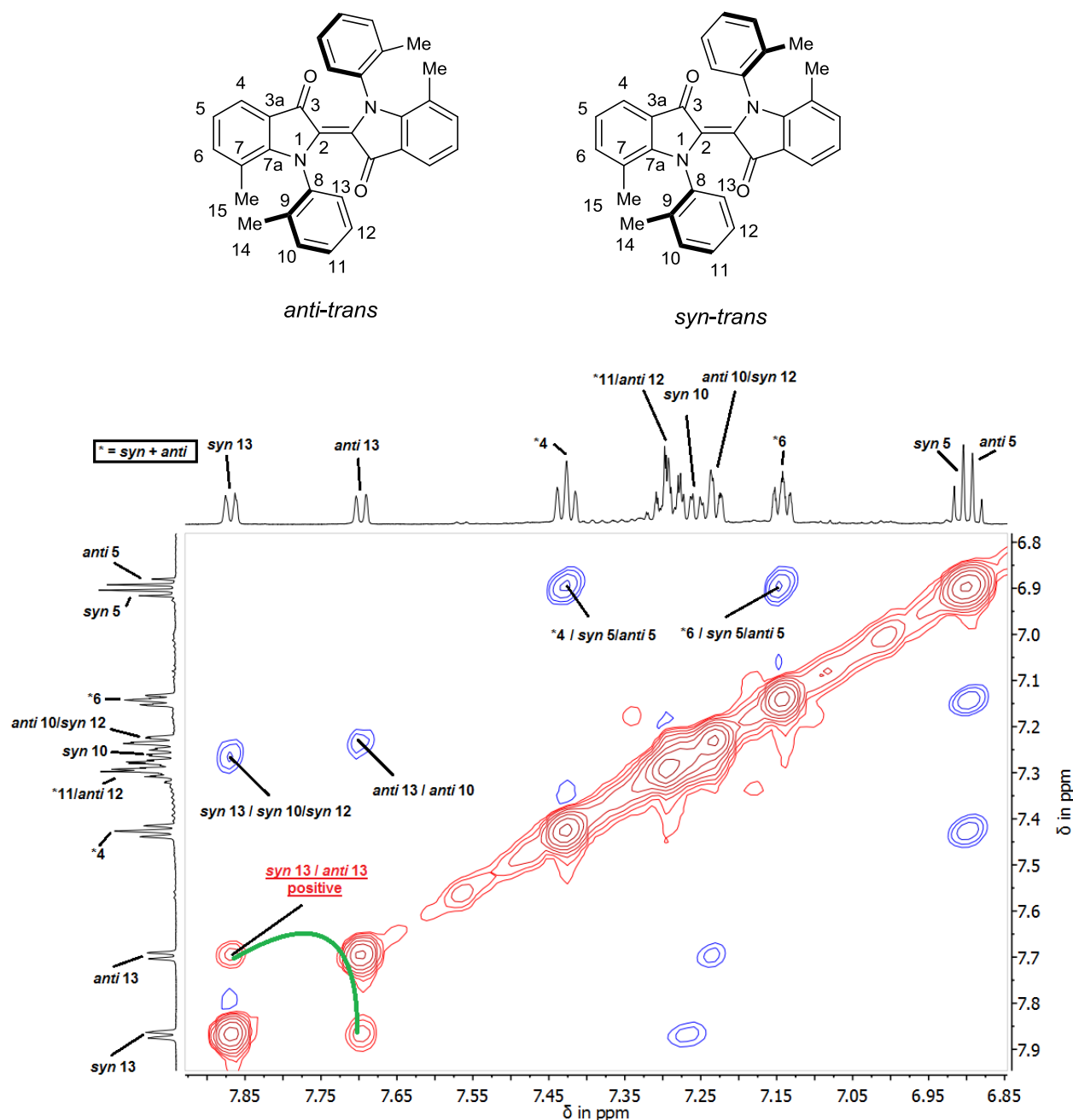


Figure 221: Aromatic section of the  $^1\text{H}$  NOESY spectrum (dichloromethane- $d_2$ , 600 MHz, 27  $^\circ\text{C}$ ) of *trans*-**65**. No indicative signals to prove *syn*- or *anti* configuration can be found. Signals of *anti* 13 and *syn* 13 show one of two positive NOE signals (see Figure 219), while the rest of the molecule shows negative NOEs. This is in accordance to fast dynamics in between *syn* and *anti* molecules as NOESY uses the same pulse sequence as EXSY and the used mixing time of 1.2 s is much longer than the exchange of respective nuclei.

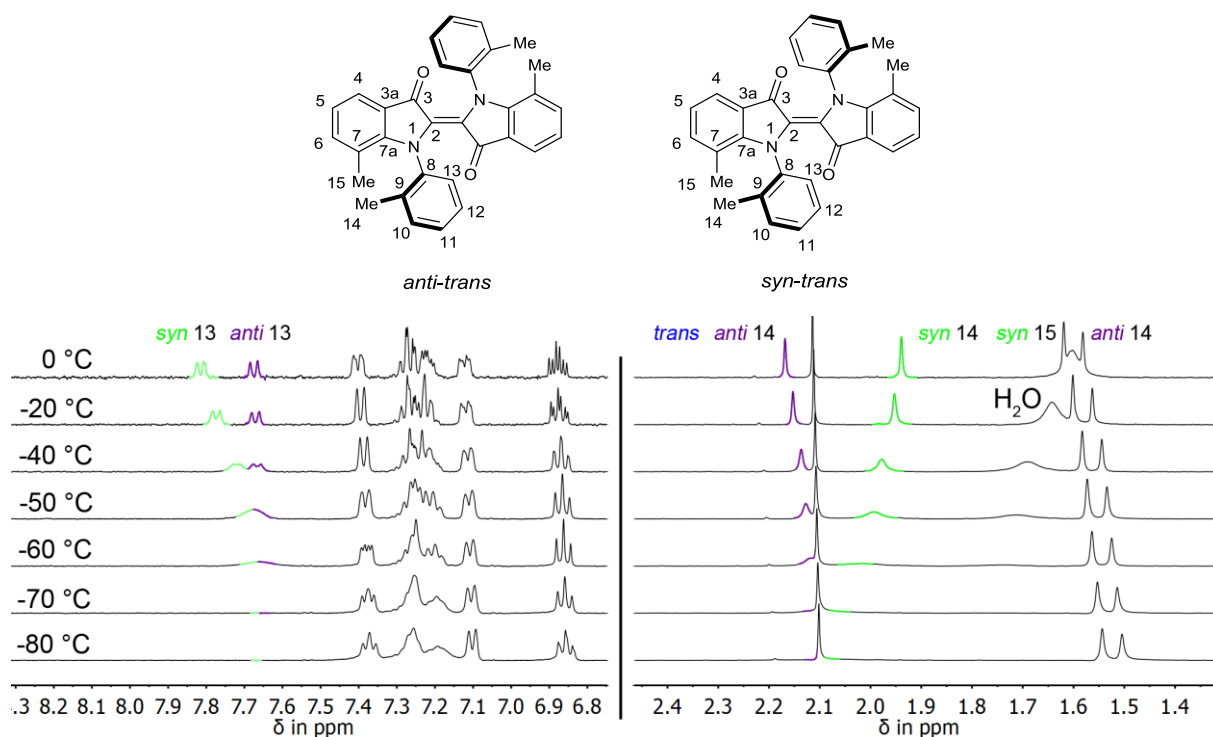


Figure 222: Aromatic (left) and aliphatic (right) sections of  $^1\text{H-NMR}$  spectra of *trans-65* from  $-80\text{ }^\circ\text{C}$  (start) to  $0\text{ }^\circ\text{C}$ , starting after 60 min of *in situ* irradiation with 625nm at  $-80\text{ }^\circ\text{C}$  (dichloromethane- $d_2$ , 400 MHz). The diagnostic signals 13 / 14 disappear completely at about  $-60\text{ }^\circ\text{C}$  due to signal broadening, making low temperature analysis of the (photo) kinetics of this compound inaccurate or impossible.

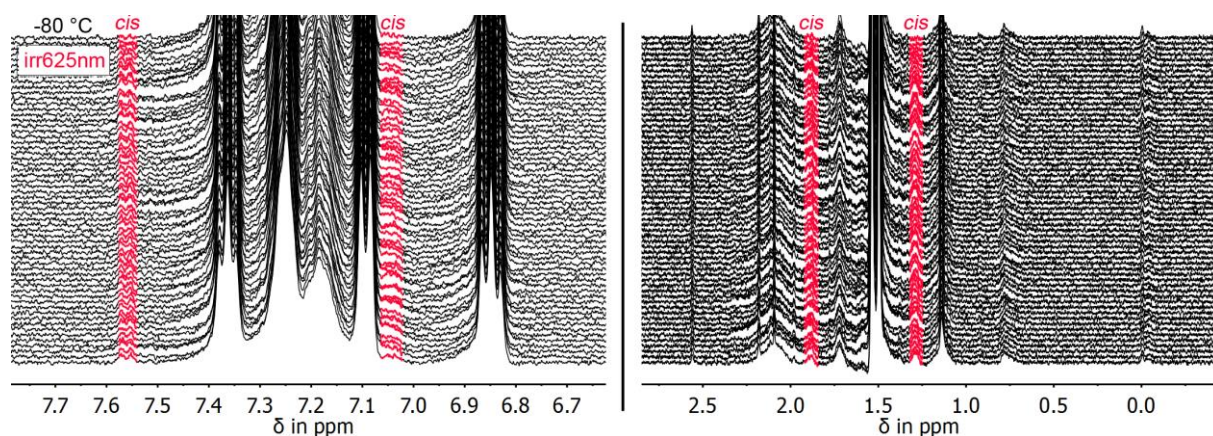


Figure 223: Aromatic (left) and aliphatic (right) sections of  $^1\text{H-NMR}$  spectra of *trans-65* with *in situ* irradiation at 625 nm (dichloromethane- $d_2$ , 600 MHz,  $-80\text{ }^\circ\text{C}$ ). Spectra were recorded in 1 minute intervals. A fast but small increase of one or multiple accumulated *cis* isomers can be observed. Apolar solvents increase the thermal stability of *cis* isomers for indigo **64** (see Section 2.4.13), which should be tried with this compound despite its overall low solubility.

## 2.4.4 Symmetric chiral indigos - Second generation indigo **64** - Achiral aspects

As indigo **65** did not possess the optimal photophysical properties to be examined in dichloromethane and probably other solvents, indigo **64** was synthesized without the “stopper” methyl groups at the aromatic indigo core structure (see Sections 2.2.7 and Section 2.4.1).

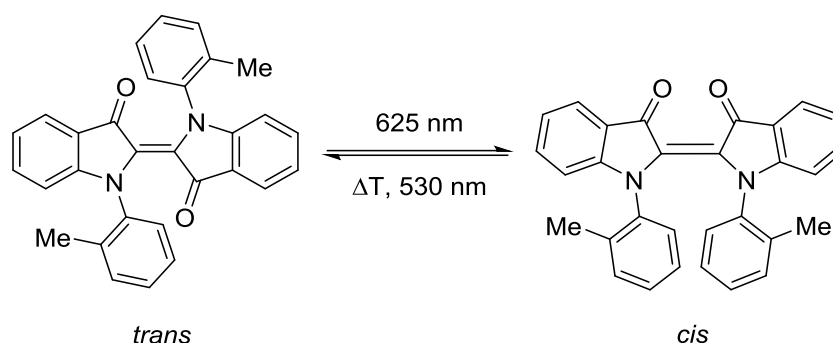


Figure 224: Photo- and thermally induced *cis-trans* isomerization of indigo **64**.

The synthesis of **64** is described in Scheme 34, Section 2.4.1 in detail. This compound shows significantly increased photoswitching activity at ambient temperatures in comparison to derivative **65**. First, racemic mixtures of enantiomers and mixtures of *syn-* / *anti* diastereomers are investigated, later these mixtures could be separated and the enantiomers are examined individually to gain insights in the mechanism of their photochemistry.

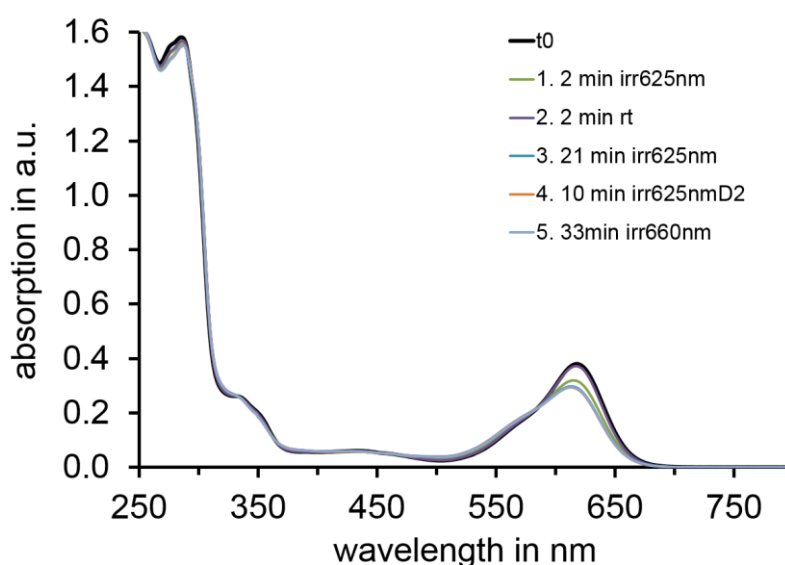


Figure 225: UV-Vis spectra of *N,N'*-di(*o*-tolyl)indigo **64** in THF, irradiation yields 20 - 30% of *cis* isomer (estimated by low temperature NMR and UV-Vis spectroscopy in

aprotic, apolar solvents, (see Section 2.4.13) which quickly returns to its *trans* state within a few minutes.

The thermal *cis-trans* isomerization barriers can be estimated by tracing the thermal *cis-* to *trans* isomerization at 600 nm observer wavelength in the UV-Vis spectrometer at 24 °C.

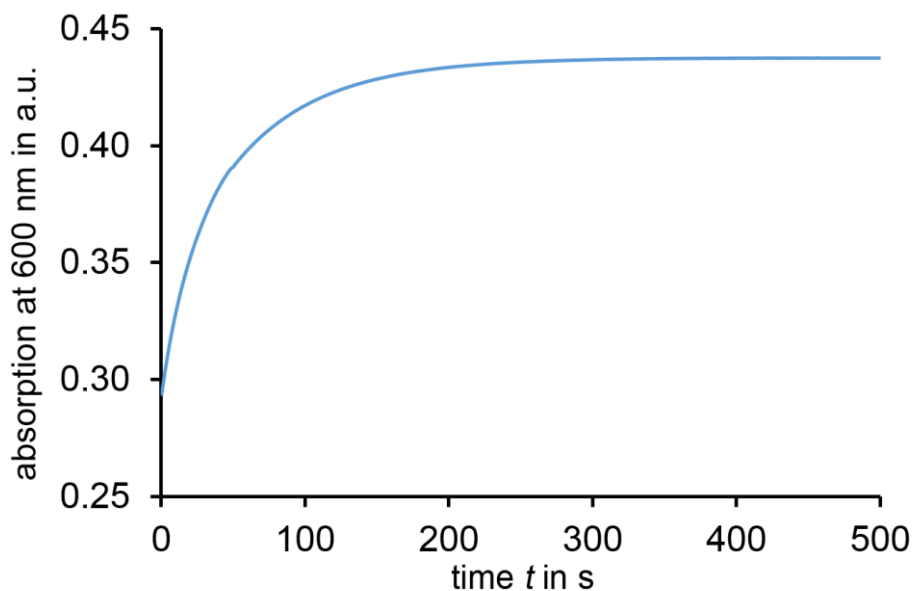


Figure 226: Immediate tracking of the thermal *cis* to *trans* isomerization of indigo **64** after 625 nm irradiation in THF at 24 °C. An estimated thermal *cis* to *trans* barrier between 20- and 21 kcal/mol can be regarded as reasonable from the data displayed in this measurement course. Precise evaluation and determination of isomerization barriers via  $^1\text{H-NMR}$  spectroscopy can be found in Section 2.4.19.

The thermal *cis* to *trans* barrier for indigo **64** is estimated to lie between 20 and 21 kcal/mol. The reduced sterical hindrance in the *cis* states of this chiral derivative provides detectable photoisomerization yields of the *cis* isomer at ambient temperatures for the first time.

## 2.4.5 Symmetric chiral indigos - Second generation indigo **64** - Assignment of *trans* isomers - NMR experiments

$^1\text{H}$ -NMR experiments on indigo **65** revealed the *syn* isomer to be thermodynamically preferred by about 20%. The bias for indigo **64** is unexpectedly increased four-fold to 80% *syn* isomer. The combination of different spectroscopic methods and synthesis of several model compounds was necessary to unambiguously assign the signals of *syn*- and *anti* diastereomers in the symmetric systems **65** and **64**, see Figure 227 to Figure 234.

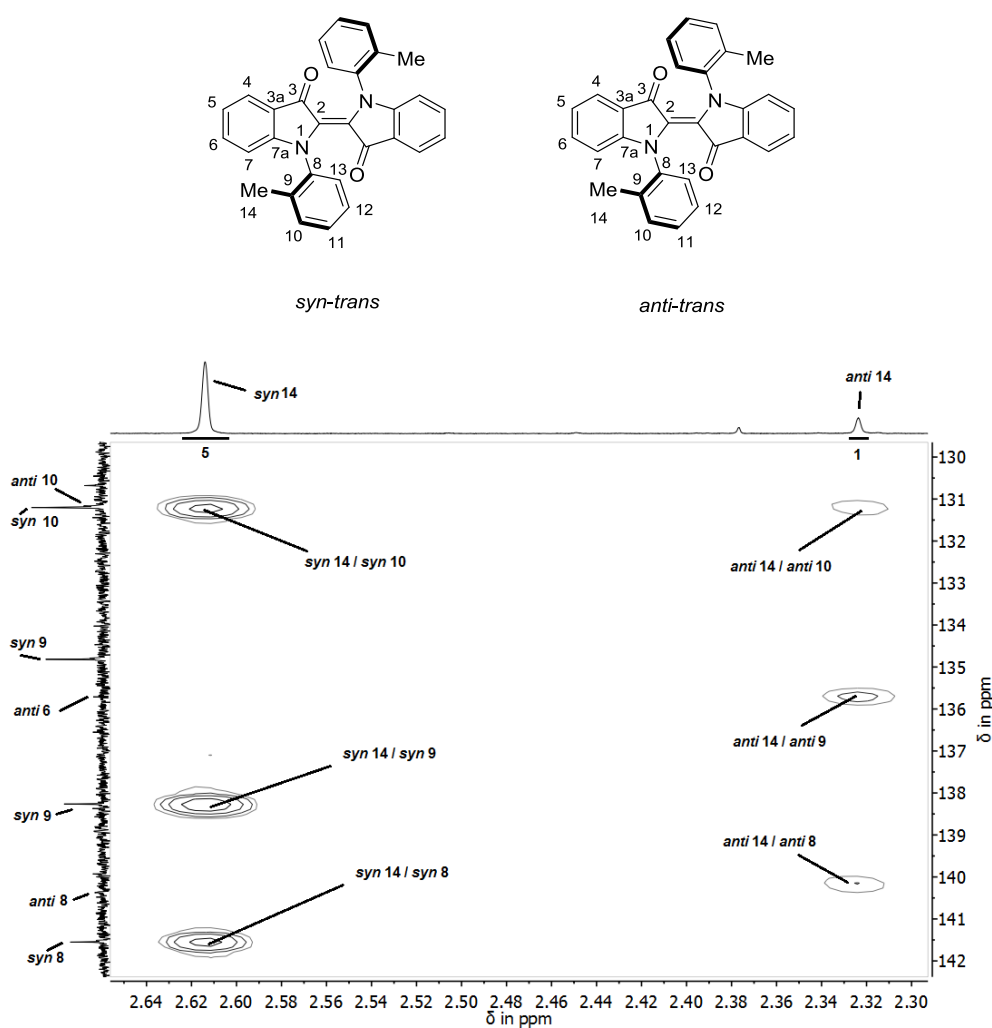


Figure 227: Aliphatic / aromatic section of the  $^1\text{H}$ - /  $^{13}\text{C}$ -HMBC NMR spectrum of *trans*-**64** (dichloromethane- $d_2$ , 600 MHz, 27 °C). Integrals for *anti*- and *syn* isomer are shown at the top,  $^3J$  proton couplings to carbon atoms are displayed for *anti*- and *syn* isomers. A comparable chemical shift of the methyl groups can be seen for indigo **64** as observed with indigo **65**. The ratio between *anti*- / *syn* isomer (1 / 5) is strongly shifted favoring the *syn* diastereomer for indigo **64** compared to *anti*- / *syn* isomer (1.0 / 1.2) for indigo **65**.

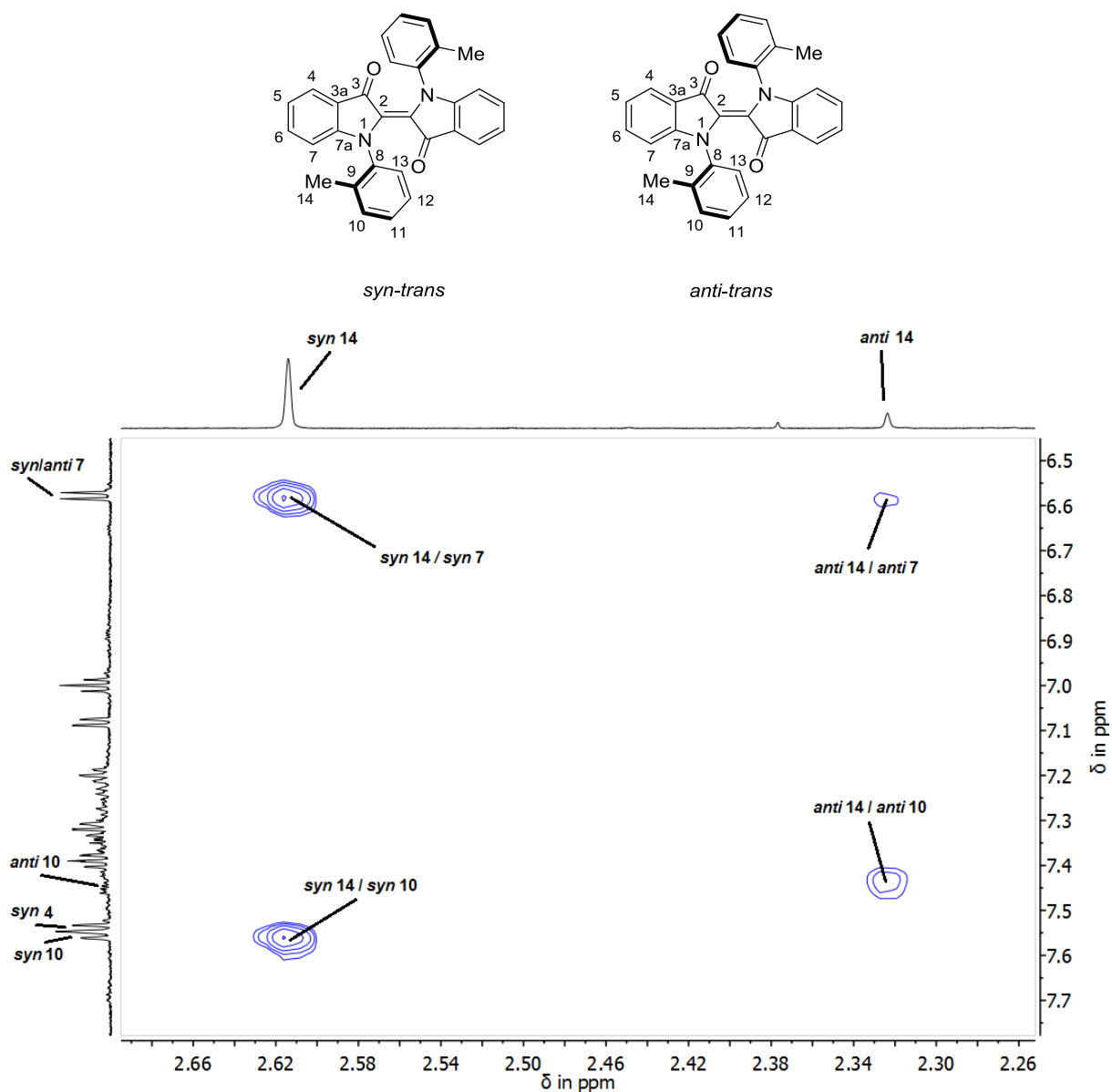


Figure 228: Aliphatic / aromatic section of the <sup>1</sup>H-NOESY NMR spectrum of *trans*-**64** (dichloromethane-*d*<sub>2</sub>, 600 MHz, 27 °C). No signals for unambiguous determination of *anti*- / *syn* conformations can be seen. Assignment was done according to separated peaks by HPLC and subsequent ECD and NMR analyses. The aromatic region (not shown) does not yield indicative signals as well. Repetition of this experiment with an 800 MHz NMR device did not yield any new indicative signals. Positive signals between *syn*- and *anti-trans* isomers were not observed, as the atropisomerization barrier of 23.6 kcal/mol is too high in energy to show a proton exchange for a mixing time of 1.2 s.



## 2.4.6 Symmetric chiral indigos - Second generation indigo **64** - Assignment of *trans* isomers - HPLC experiments

After obtaining the promising results for racemic indigo **64**, separation of rotamers via chiral HPLC was carried out.

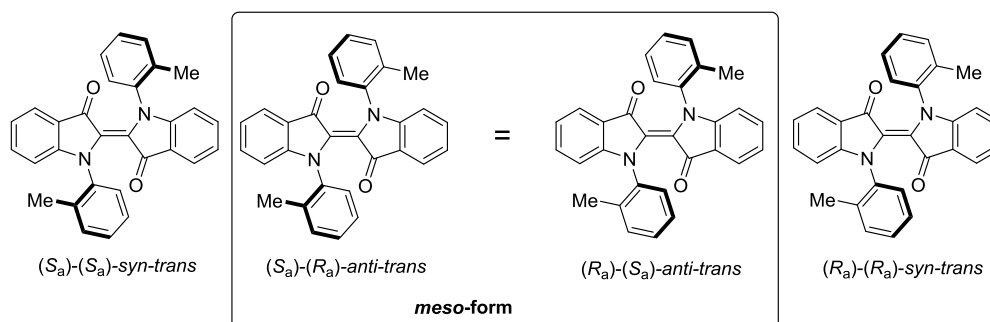


Figure 229: Overview of the three *trans* rotamers of indigo **64**. Formally, the same number of rotamers is expected in the less stable *cis* form.

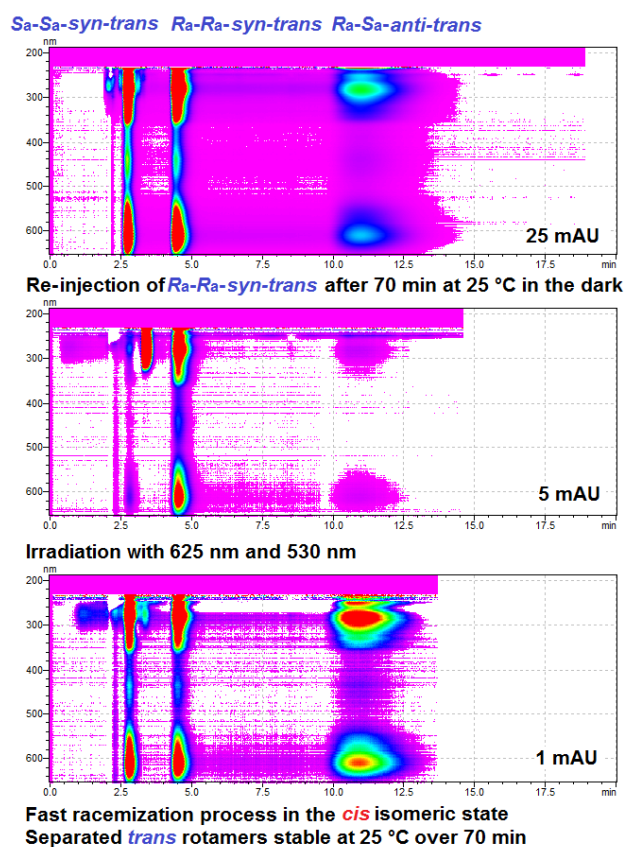


Figure 230: Separation of *trans*-**64** rotamers via chiral HPLC with 83 / 17 heptane / ethyl acetate as eluent at 0 °C displayed three peaks with the corresponding relative intensity in square brackets:  $(S_a)-(S_a)$ -syn-trans [2.5],  $(R_a)-(R_a)$ -syn-trans [2.5] and the  $(S_a)-(R_a)$ -anti-trans [1] (*meso* form) in this order. Thermal racemization

of the pure (*R<sub>a</sub>*)-(*R<sub>a</sub>*)-*syn-trans* fraction at 25 °C over 70 min yielded (*S<sub>a</sub>*)-(*S<sub>a</sub>*)-*syn-trans* and (*S<sub>a</sub>*)-(*R<sub>a</sub>*)-*anti-trans* in small and equal quantities. Photoswitching to the *cis* state and back to the *trans* isomer gave all three fractions again, hinting towards a lower thermal atropisomerization barrier in the *cis* state or an underlying photoreaction.

The (*S<sub>a</sub>*)-(*R<sub>a</sub>*)-*anti-trans* peak in the chromatogram shown in Figure 230 was initially interpreted as *cis* isomer with inseparable rotamers as NMR measurements and DFT calculations on di-*para*-tolyl indigo **63** by *L. Huber* suggested a 9 / 1 *trans* / *cis* equilibrium for compound **63** in chlorinated organic solvents.<sup>[66]</sup> Nonetheless, chiral HPLC separation at 0 °C of indigo **63** did not show a clearly identifiable 9 / 1 *trans* / *cis* ratio (Figure 231), which could be caused by isomerization of the *cis* isomer while interacting with the stationary phase or due to changed isomer stabilities induced by different solvent properties.

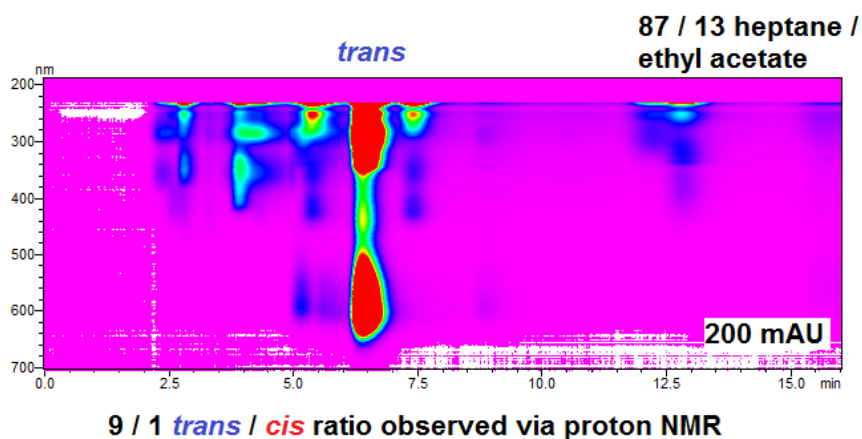


Figure 231: Injection of indigo **63** by *L. Huber* onto a chiral HPLC column at 0 °C with 83 / 17 heptane / ethyl acetate as eluent. No clearly identifiable *cis* isomer can be observed. The retention times of the *syn* isomers of indigo **64** amount to 2.5 min and 5.0 min for applied conditions, indigo **63** elutes at 6.5 min.

Solvent polarity effects or residual acidic impurities in chlorinated organic solvents might cause the invisibility of the *cis* isomer of **63** due to shifting of the *cis-trans* equilibrium towards 100% *trans* isomer. The possibly low stability of the *cis* isomer might also play a role for not observing this species.

However, NMR studies in dichloromethane-*d*<sub>2</sub> at 27 °C (Figure 227) suggest the *syn* form of **64** to be thermodynamically favored with a *syn* / *anti* equilibrium of 5 / 1 without any *cis* isomer signals. Favored torsion / bending / skewing of the indigo core and steric repulsion of the methyl groups might be responsible for the energy differences between *syn-trans* and *anti-*

*trans* forms. Fractions (*S<sub>a</sub>*)-(*S<sub>a</sub>*)-*syn-trans* and (*R<sub>a</sub>*)-(*R<sub>a</sub>*)-*syn-trans* show mirrored ECD spectra while (*S<sub>a</sub>*)-(*R<sub>a</sub>*)-*anti-trans* shows no ECD signal at all, which is expected for the *meso* form as the establishment of enantiomers is impossible for this diastereomer.

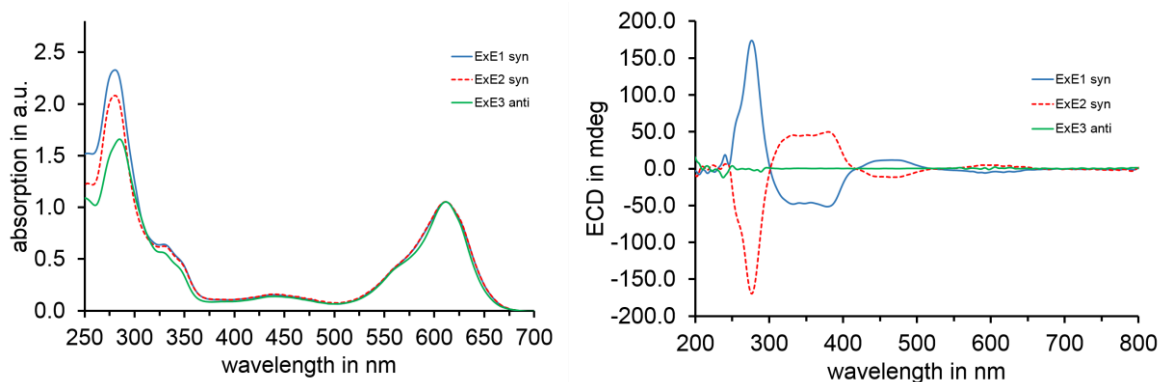


Figure 232: Scaled UV-Vis and corresponding ECD spectra of all peaks obtained from chiral HPLC separation ((*S<sub>a</sub>*)-(*S<sub>a</sub>*)-*syn-trans* (ExE1) (*R<sub>a</sub>*)-(*R<sub>a</sub>*)-*syn-trans* (ExE2) and (*S<sub>a</sub>*)-(*R<sub>a</sub>*)-*anti-trans*-1 (ExE3)) of *N,N'*-di(*o*-tolyl)indigo **64** in 83 / 17 heptane / ethyl acetate at 0 °C. Both *syn* isomers (solid blue and broken red spectrum) show strong ECD responses while the *anti* (*meso*, solid green spectrum) form shows no ECD signal at all.

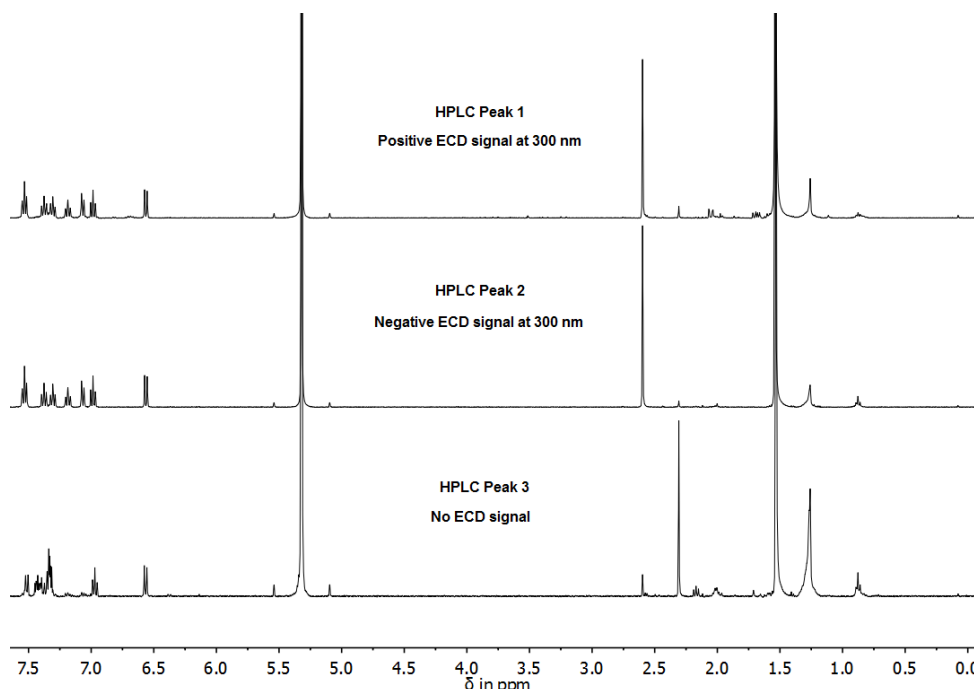


Figure 233: NMR Spectra for all three HPLC separable peaks ((*S<sub>a</sub>*)-(*S<sub>a</sub>*)-*syn-trans* (Peak 1) (*R<sub>a</sub>*)-(*R<sub>a</sub>*)-*syn-trans* (Peak 2) and (*S<sub>a</sub>*)-(*R<sub>a</sub>*)-*anti-trans*-1 (Peak 3)) of *N,N'*-di(*o*-tolyl)indigo **64** (dichloromethane-*d*<sub>2</sub>, 400 MHz, 27 °C).

With all combined data from UV-Vis, ECD and NMR spectroscopy, the *syn*- and *anti* form of indigo **64** can be unambiguously assigned without observing indicative NOESY signals.

Separation of one *syn*-rotamer and tracing of the thermal decrease in ECD signal intensity (area) in the dark yields the kinetic plot shown in Figure 234 below. Evaluation via  $^1\text{H-NMR}$  measurements for the atropisomerization of a racemic *syn-trans* mixture to the *anti-trans* diastereomer is also possible and should result in the same energy value, which is to be tested to date.

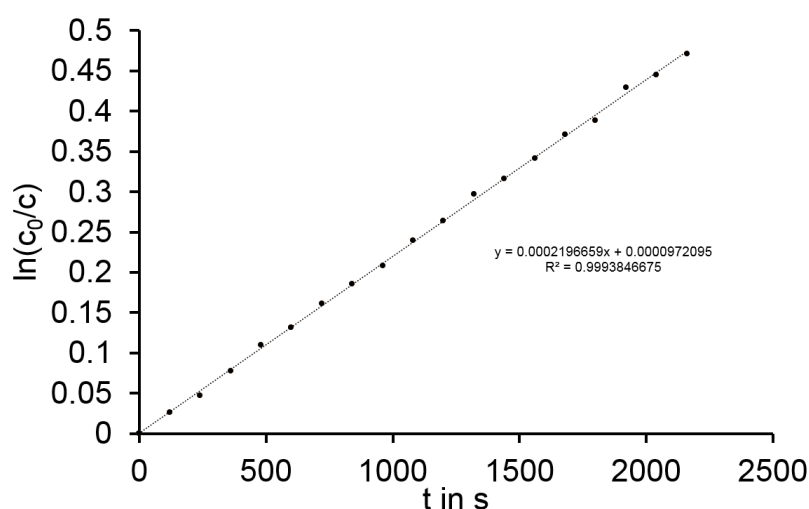


Figure 234: Linearization of the first order kinetics for the atropisomerization of *N,N'*-di(*o*-tolyl)indigo **64** at 40 °C in 83 / 17 heptane / ethyl acetate. A barrier of 23.6 kcal/mol and a half-life of 6.23 h at 25 °C could be determined. Used formulas and equations can be found in Section 2.2.19.

## 2.4.7 Symmetric chiral indigos - Second generation indigo 64 - Assignment of *trans* and *cis* isomers - ECD experiments

Low temperature ECD spectroscopy at -80 °C was carried out in an apolar 83 / 17 heptane / ethyl acetate solvent mixture to scrutinize the chiral behavior of indigo **64** invisible for NMR spectroscopy. *In-situ* irradiations within the ECD spectrometer in toluene at 0 °C showed similar results (omitted here).

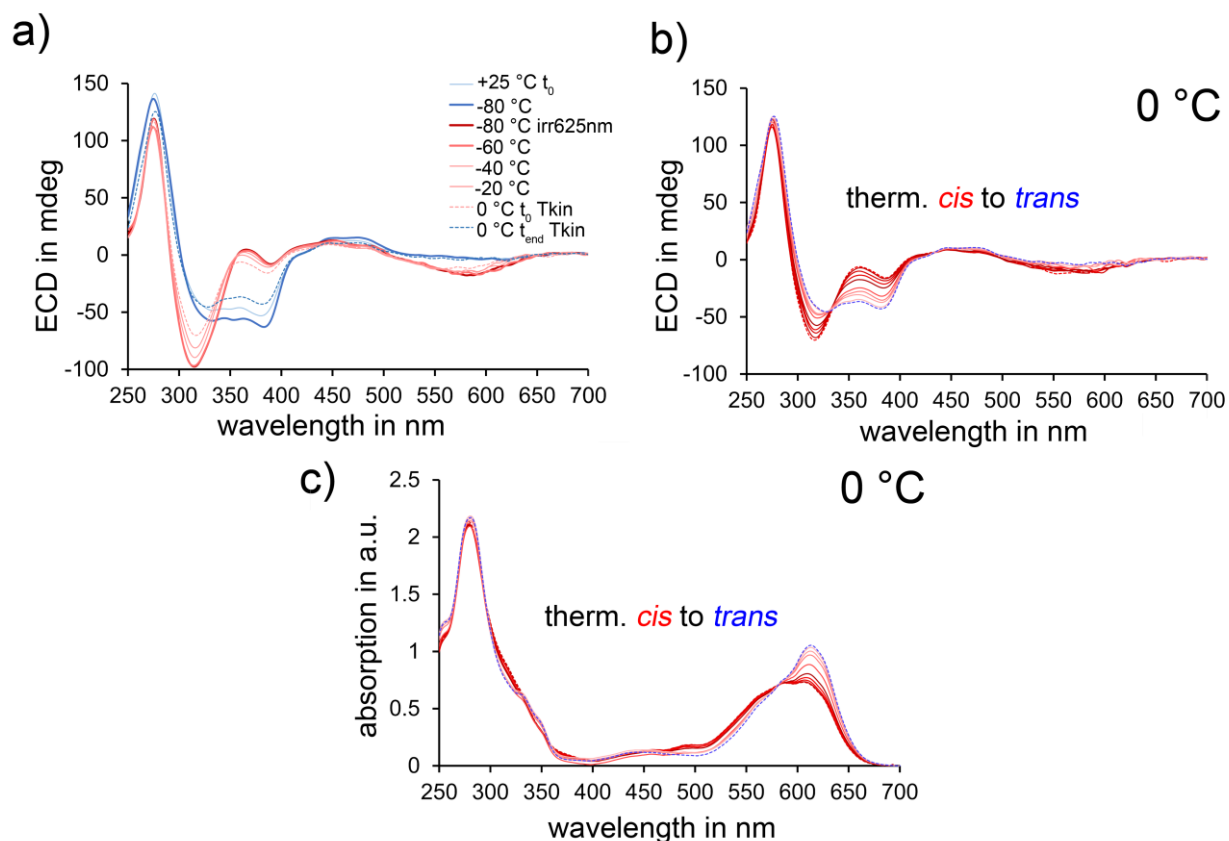


Figure 235: a) ECD spectra for different temperatures, irradiation- and thermal annealing steps of enantiopure *syn-trans* isomer of indigo **64**. The sample was irradiated *in situ* at  $-80\text{ }^{\circ}\text{C}$  with 625 nm LED light for 8 minutes to an estimated PSS consisting of 70-80% of *cis* isomer b) Kinetic ECD measurement for the thermal isomerization from the *anti-cis*- to the *syn-trans* isomer at  $0\text{ }^{\circ}\text{C}$  in the dark, c) Corresponding UV-Vis spectra for b) at  $0\text{ }^{\circ}\text{C}$  (starting point dashed red spectrum, end point after 22 min. dashed blue spectrum). All spectra were recorded from the same sample in an 83 / 17 heptane / ethyl acetate solvent mixture.

When starting from the enantiopure ( $S_a$ )-( $S_a$ )-*syn-trans* isomer, ECD- and UV-Vis measurements as depicted in Figure 235 show that no racemization towards the *syn-cis*- or *anti-trans* isomers takes place at low temperatures, which is agreement with a high rotational atropisomerization barrier for **64**. When comparing the  $t_0$  state with the  $t_{\text{end}}$  state at  $0\text{ }^{\circ}\text{C}$  in Figure 235 a), however, incomplete restoration of the initial ECD signal could be observed. It is impossible for this compound to show thermal atropisomerization reactions with the previously determined barrier of 23.6 kcal/mol for the *trans*-isomer at these temperatures during the time period of the measurement, which indicates a significantly lower rotational barrier in the *anti-cis* isomer. The latter thermally branches into to the *syn-cis* state (loss of ECD

signal) and the enantiopure ( $S_a$ )-( $S_a$ )-*syn-trans* state (restoration of ECD signal). Finally the populated *syn-cis* isomer is thermally converted into the *anti-trans* isomer (loss of ECD signal). The two latter molecules cannot show an ECD signal - even in their pure forms - as both derivatives constitute a *meso* form. This behavior is further elaborated via NMR studies shown in Section 2.4.13. For apolar solvents (toluene), the *anti-cis*- to *syn-trans* isomer barrier was determined at 18.5 kcal/mol, which is comparable to the observed UV-Vis kinetics at 0 °C in 83 / 17 heptane / ethyl acetate. However, the thermal *anti-cis*- to *syn-cis* isomer reaction trajectory is followed only on a small scale, as this atropisomerization barrier was determined at 19.11 kcal/mol at the B3LYP/6-311+G(d,p) level of theory. These ECD measurements prove that within the thermal branching process of the *anti-cis* isomer(s), the thermal double bond isomerization is preferred, as majorly restoration of the ECD signal was observed.

## 2.4.8 Symmetric chiral indigos - Second generation indigo **64** - Assignment of *trans* and *cis* isomers - DFT calculations

Besides the two observable *trans* species of indigo **64**, only one respective *cis*-species was experimentally confirmed via low temperature ECD spectroscopy (see Figure 235). The decrease in signal intensity after irradiation at low temperatures was ascribed to the generation of ECD-invisible *syn-cis*- and *anti-trans*- isomers. DFT calculations, however, suggested multiple isomers as local minimum structures (Figure 236).

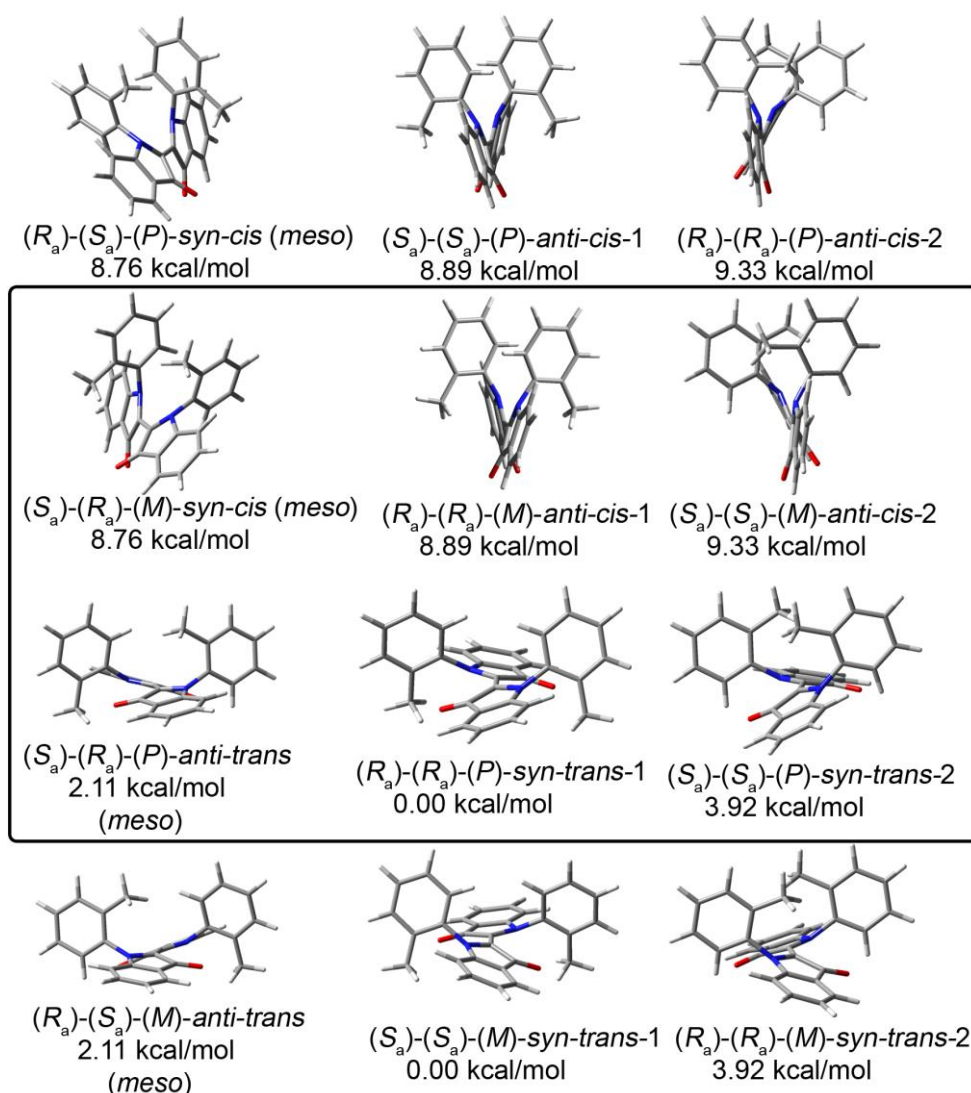


Figure 236: All possible diastereomers (inside box) and respective enantiomers for indigo **64** calculated at the B3LYP/6-311+G(d,p) level of theory. Energies are given corresponding to the lowest ground state energy of the *syn-trans-1* isomers.

Comparison of the measured to the calculated ECD spectra can help with the assignment or confirmation of the prevalent *anti-cis* species in solution.

To assign the ECD spectrum of the *anti-cis* signal in Figure 235, a comparison of the calculated ECD spectra at the B3LYP/6-311+G(d,p) level of theory of the different isomers of **64** as shown in Figure 236 is given in Figure 237 below. The *syn-cis (meso)* form is expected to show fast interconversion of its helicity as only one set of aromatic  $^1\text{H-NMR}$  signals and no ECD signal can be observed experimentally. The aliphatic methyl signals are completely invisible via  $^1\text{H-NMR}$  spectroscopy due to signal broadening below  $-20\text{ }^\circ\text{C}$  (Section 2.4.14, Figure 263). The *anti-trans (meso)* “forms” do not exist as separable enantiomers as they represent the same molecule.

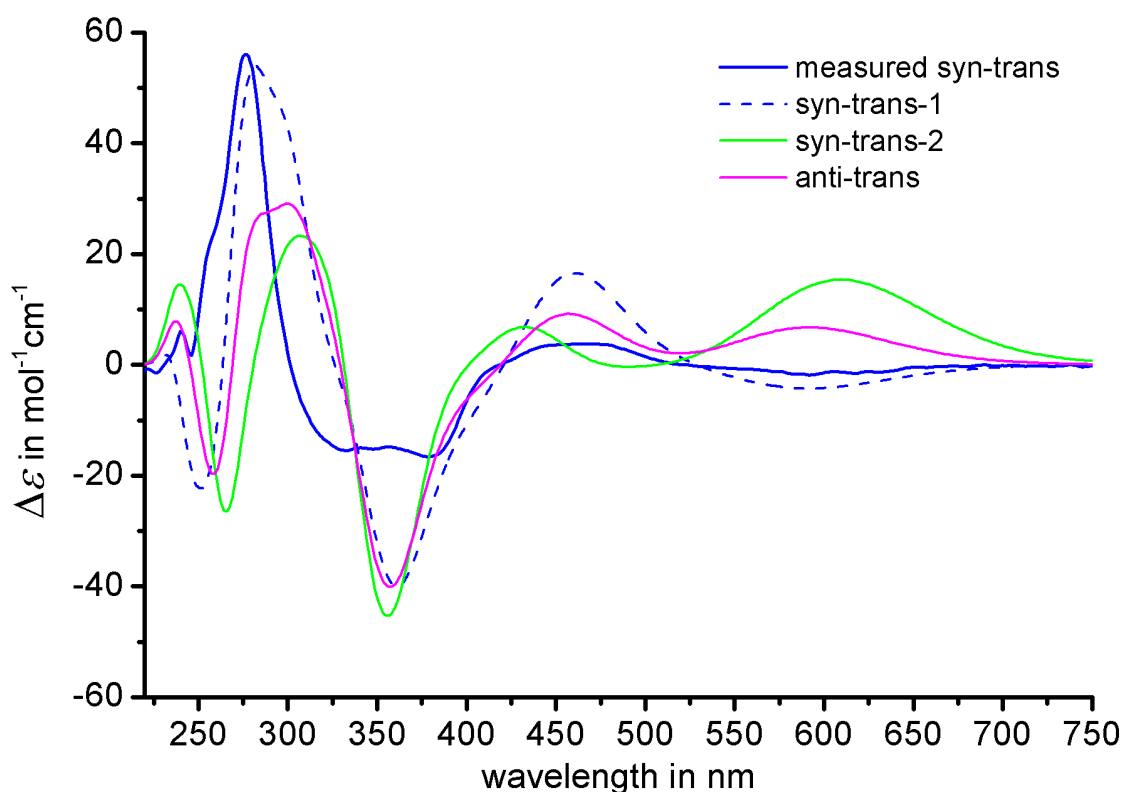


Figure 237: Measured, 100% enantiopure *trans* isomer (solid blue line) and calculated *trans* isomer ECD spectra of indigo **64** at the B3LYP/6-311+G(d,p) level of theory, the measured spectrum was scaled in intensity to the calculated values. The spectrum shown in the broken blue line represent the best fitting calculated spectrum. Signal intensities at and below 250 nm are not reliable experimentally as solvent absorptions (83 / 17 heptane / ethyl acetate) are obscuring the measurements.

The assignment in Figure 237 for the measured *syn-trans* isomer spectrum to be associated to the  $(S_a)-(S_a)-(M)$ -*syn-trans-1* structure of indigo **64** is based on the observation at the 600 nm region, where  $(S_a)-(S_a)-(M)$ -*syn-trans-1* is the only *trans* isomer that shows a negative ECD



response as observed for the measured sample. The *syn-trans-2* isomer shows a pronounced trend towards the opposite sign of the ECD absorption. The *anti-trans* isomer is out of consideration because it represents a *meso* form that yields no ECD signal (see Figure 232). The 275 nm region shows a good fit to the experimental measurement as well.

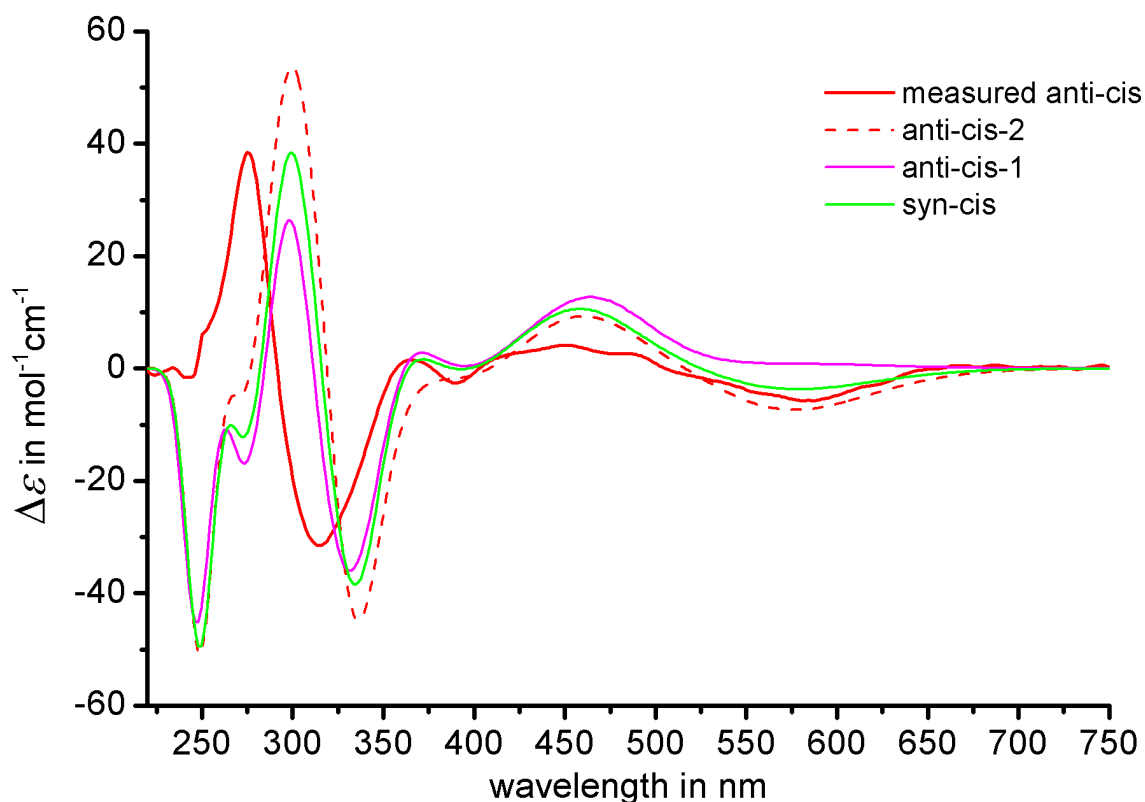


Figure 238: Measured, 70-80% *cis* isomer, estimated (solid red line) and calculated *cis* isomer ECD spectra of indigo **64** at the B3LYP/6-311+G(d,p) level of theory, measured spectra were scaled in intensity to the calculated values. The spectrum shown in the broken red line represents the best fitting calculated spectrum. Signal intensities at and below 250 nm are not reliable experimentally as solvent absorptions (83 / 17 heptane / ethyl acetate) are obscuring the measurements.

The *anti-cis* isomer (Figure 238) was assigned to be (*S<sub>a</sub>*)-(*S<sub>a</sub>*)-(*M*)-*anti-cis-2* by the 600 nm - 450 nm region, as the general shape of *anti-cis-1* shows a less matching graph to the experiment than (*S<sub>a</sub>*)-(*S<sub>a</sub>*)-(*M*)-*anti-cis-2*, especially in the 500 - 650 nm region. The *syn-cis* isomer is out of consideration because it represents a *meso* form that yields no ECD spectrum.

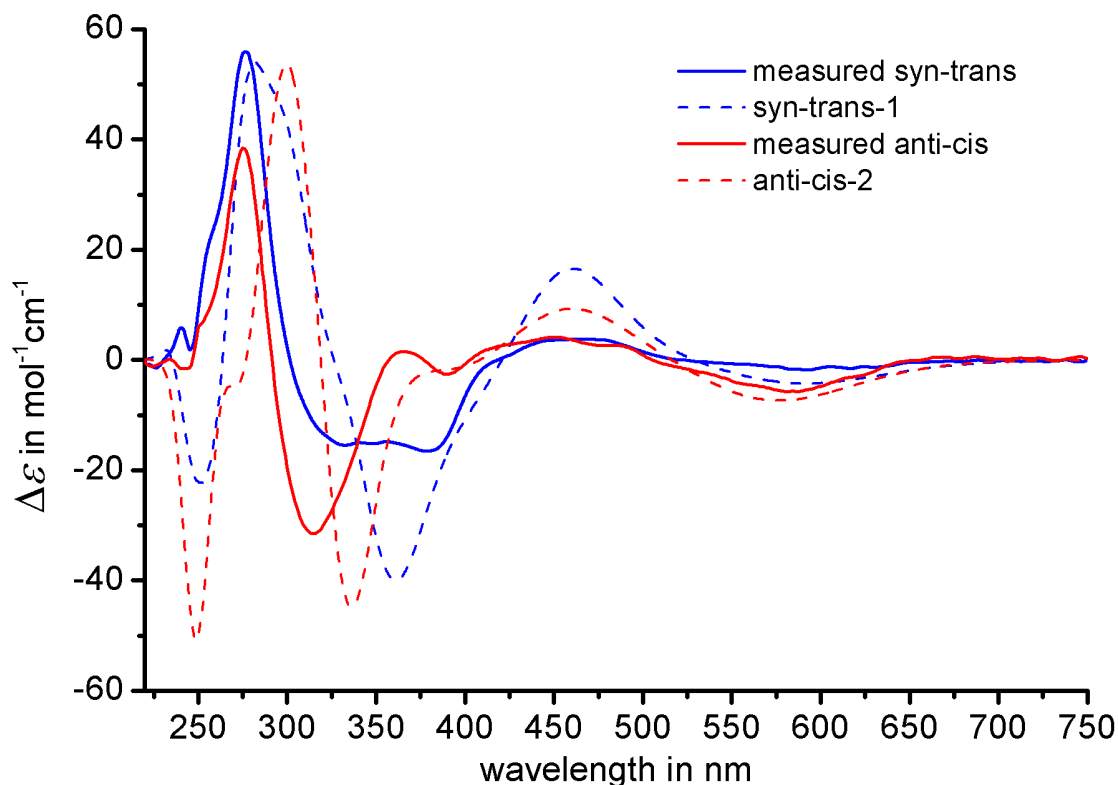


Figure 239: Comparison of measured (solid blue (100% enantiopure *trans* isomer) and red (70-80% *cis* isomer, estimated) lines) and best fitting calculated ECD spectra (broken blue- and red lines) of indigo **64** at the B3LYP/6-311+G(d,p) level of theory, measured spectra were scaled in intensity to the calculated values. Signal intensities at and below 250 nm are not reliable experimentally as solvent absorptions (83 / 17 heptane / ethyl acetate) are obscuring the measurements.

Comparison of both *trans* and *cis* isomers shows that no helix inversion around the aryl axes as well as within the indigo core takes place as this would result in a mirrored ECD response, which is not observed.

This assignment and the observed effects suggests a photoinduced *trans* to *cis* isomerization supporting solely a 180° rotation of the central double bond from the lowest energy ( $S_a$ )-( $S_a$ )-( $M$ )-*syn-trans-1*- to the highest energy ( $S_a$ )-( $S_a$ )-( $M$ )-*anti-cis-2* isomer without any additional single bond rotations of the chiral axes, which is in accordance to the  $^1\text{H-NMR}$  spectroscopic results shown in Section 2.4.13. A 147° rotation of the central double bond would result in the *anti-cis-1* isomer and hence a more positive ECD signal, especially in the 500 - 650 nm region. This is important to consider for the proposed two-step double motor motion of indigo **64** discussed in Section 2.4.21.

### 2.4.9 Non-symmetric chiral indigos - Second generation chimeric model compound indigo 70 - Disentanglement of chiral axes

At this point it was not certain if the kinetic plot in Figure 234 represented a cooperative process by the influence of both chiral axes or the independent but simultaneous atropisomerization of each chiral axis. To discern these two possibilities, chimeric model compound **70** was synthesized by *F. Binder* during his research internship. Another possibility, the simultaneous two-fold rotation of both axes for indigo **64** can be generally ruled out as this would suggest an experimental free activation enthalpy larger than  $\Delta G^* = 2 * 23.6 \text{ kcal/mol}$  for the same transition state geometry as calculated for a singular atropisomerization reaction. This is not feasible as a temperature of 313.2 °C is necessary to achieve the same thermal half-life of 6.35 h which is shown by the 23.6 kcal/mol atropisomerization barrier at 25 °C. Considering the *Boltzmann* distribution of the energies within molecules in bulk conditions, it is extremely unlikely for a simultaneous rotation of both axes to take place.

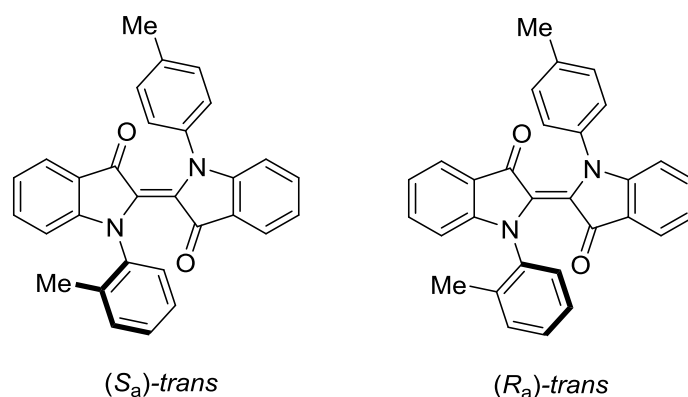
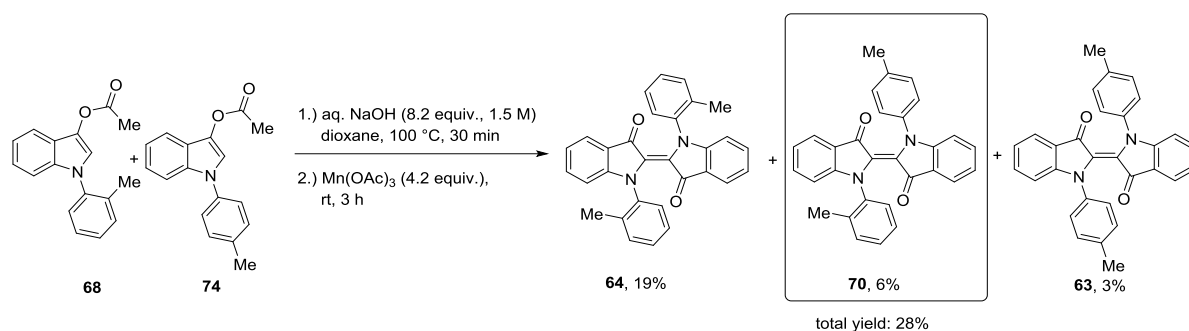


Figure 240: *Lewis*-formula of indigo **70**.

As the determined atropisomerization barrier of 23.6 kcal/mol for indigo **64** represents the loss of ECD signal area in a molecular setup with two atropisomeric *ortho*-tolyl axes, indigo **70** was synthesized to examine the properties of a single chiral aryl axis for this class of compounds. The synthesis follows established protocols from *U. Burger et al.*<sup>[88]</sup> using dioxane as co-solvent and subsequent oxidation with manganese(III) acetate to yield **70** in a mixture of products (Scheme 36).

2.4.9 NON-SYMMETRIC CHIRAL INDIGOS - SECOND GENERATION CHIMERIC MODEL COMPOUND INDIGO 70 -  
DISENTANGLEMENT OF CHIRAL AXES



Scheme 36: Simultaneous deacylation of **68** and **74** according to *U. Burger et al.*<sup>[88]</sup> with dioxane as co-solvent and subsequent oxidation with manganese(III) acetate yielding indigos **64**, **70** and **63**. The low yields can be attributed to the increased sterical hindrance of the more planarized *para*-tolyl moiety.

The use of potassium permanganate for the general oxidation reaction of arylated indoxyls to indigo is also possible, dropping the reaction times to 10 minutes. The expected statistical product distribution of 1 / 2 / 1 *ortho-ortho*- (**64**) / *ortho-para*- (**70**) / *para-para*- (**63**) indigo was not obtained by this reaction, instead, a 6 / 2 / 1 ratio was observed. The formation of dimers from twisted precursors is highly favored while the planar starting material **74** reacts at a slower rate. This can be attributed to increased sterical hindrance at the  $\alpha$ -position of the indoxyl caused by the protruding planarized *para*-tolyl substituent. The chimeric indigo **70** is obtained in a doubled yield compared to **63**.

Chiral HPLC separation yielded the two expected rotamers of **63** in (*S<sub>a</sub>*)- and (*R<sub>a</sub>*) configuration (Figure 241, chromatogram not shown).

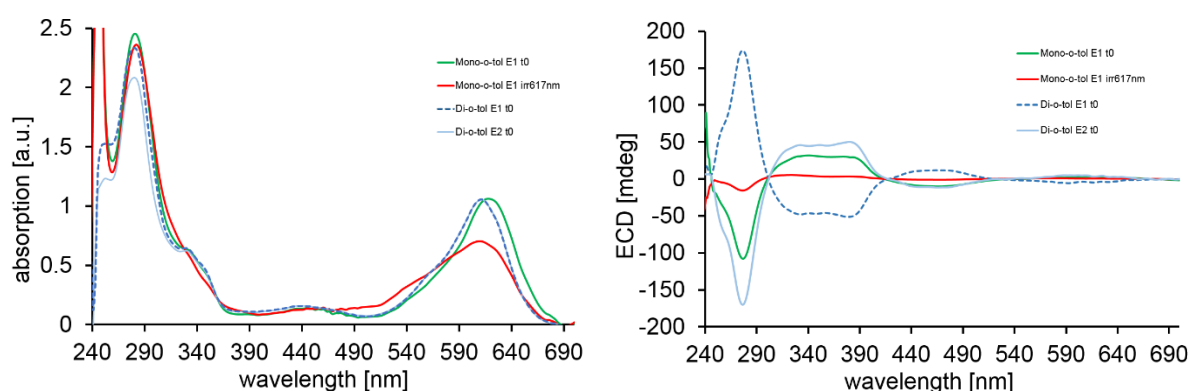


Figure 241: Scaled UV-Vis (left) and ECD (right) spectra of (*R<sub>a</sub>*)-*N*-(*o*-tolyl)-*N'*-(*p*-tolyl)indigo **70** in 83 / 17 heptane / ethyl acetate at 0 °C (green), after 5 min of irradiation with 617 nm (red). (*S<sub>a</sub>*)-(*S<sub>a</sub>*)-*Syn-trans*-1 (E1) and (*R<sub>a</sub>*)-(*R<sub>a</sub>*)-*syn-trans*-1 (E2) of *N,N'*-di(*o*-tolyl)indigo **64** (broken blue and light blue lines) are added for comparison. Irradiation of **70** gives slightly better *cis* isomer yields compared to **64**.

The comparison of the ECD spectra intensities of **70** to **64** (scaled by the absorption maxima at the red part of the spectra) shows that the area of the ECD signal is decreased by approximately 50% from 240 nm to 400 nm, which is in accordance to the removal of one chiral aryl axis. Interestingly, the range from 400 nm to 650 nm shows the same signal intensity, hinting towards the twisted indigo core absorbing circularly polarized light (CPL) as the *ortho*-aryls are not capable of absorbing green, yellow and red light. Photoisomerization of **70** at ambient temperatures suggests a fast racemization in the *cis* state because of the nearly complete loss of ECD signal intensity - a behavior also seen with indigo **64**. This shows that racemization in the *cis* state is accelerated because of a lower rotational energy barrier, regardless of the presence of a secondary chiral axis present in indigo **64**. At this stage, it cannot be discerned if the racemization takes place thermally or during a photostep, although experiments on chiral hemiindigos showed entirely thermal processes to be responsible for atropisomerization reactions (see Section 2.3.8).

With molecule **70** at hand, subtraction of the ECD signal of (*R<sub>a</sub>*)-(*M*)-*N*-(*o*-tolyl)-*N'*-(*p*-tolyl)indigo **70** from (*R<sub>a</sub>*)-(*R<sub>a</sub>*)-*syn-trans*-*N,N'*-di-(*o*-tolyl)indigo **64** is possible, which gives the spectrum of one *ortho*-tolyl group attached to the indigo core (Figure 242).

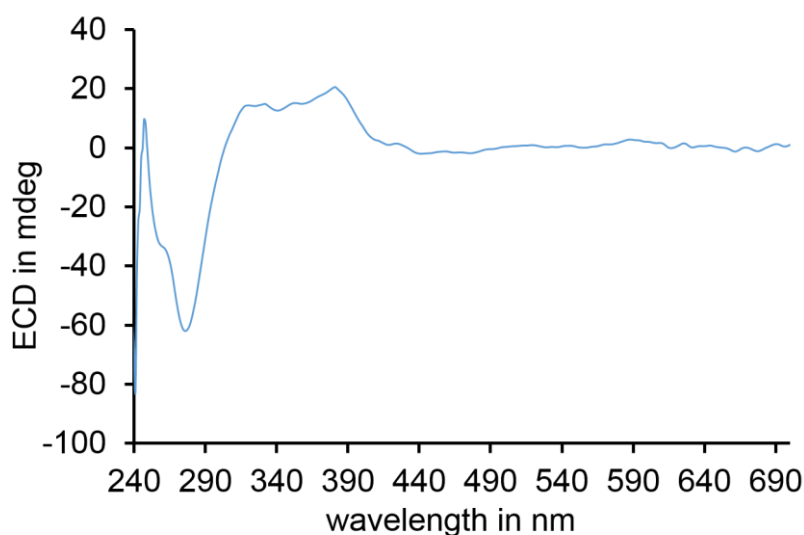


Figure 242: Spectra subtraction of the ECD response of (*R<sub>a</sub>*)-**70** from (*R<sub>a</sub>*)-(*R<sub>a</sub>*)-*syn-trans*-**64**. The influence of the additional *ortho*-tolyl moiety of **64** can be observed in the range from 240 nm to 400 nm.

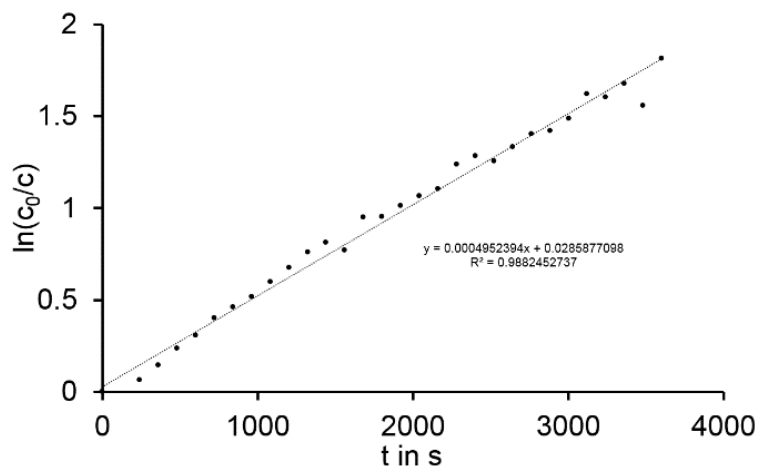


Figure 243: Linearized first order kinetics of the racemization of **70** (E1) in 83 / 17 heptane / ethyl acetate solution at 40 °C. The free activation enthalpy of thermal atropisomerization  $\Delta G^*$  was determined to be 23.1 kcal/mol with a thermal half-life of 2.7 h at 25 °C. Used formulas and equations can be found in Section 2.2.19.

The determined barriers for *trans*-**70** (23.1 kcal/mol) and *trans*-**64** (23.6 kcal/mol) are in good agreement, which indicates no or insignificant cooperativity during rotation of diarylated chiral indigo *trans*-**64**.

### 2.4.10 Non-symmetric chiral indigos - First generation chimeric model compound indigo **69** - Disentanglement of chiral axes

As the model compound **70** proved as a successful probe for identifying the properties of a singular chiral aryl axis attached to a diarylated indigo chromophore, chimeric model compound **69** was prepared as shown in Scheme 37 by *F. Binder*.

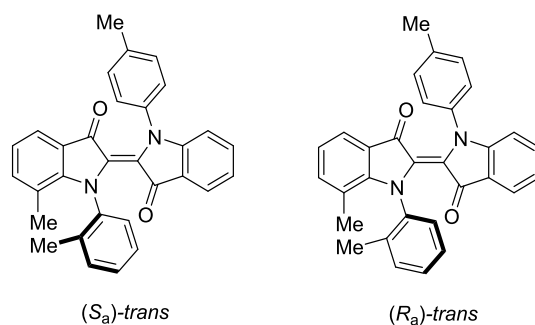
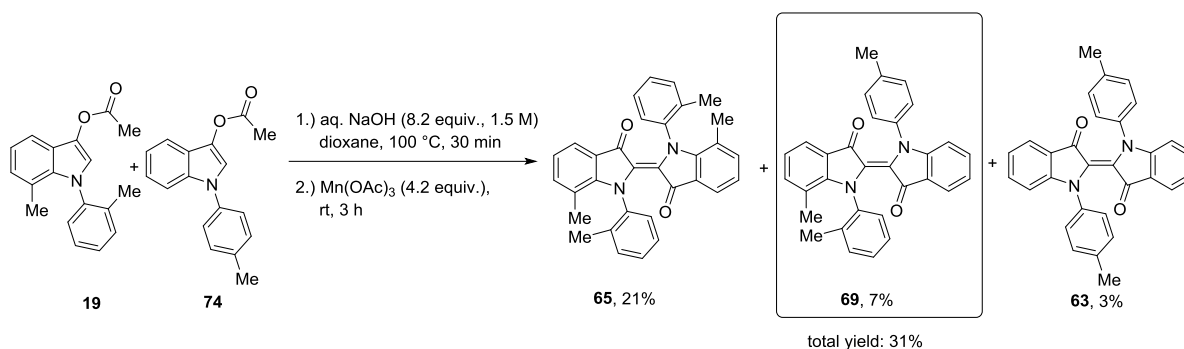


Figure 244: *Lewis*-formula of indigo **69**.

In order to scrutinize the behavior of symmetric 7,7'-dimethyl-*N,N'*-di(*o*-tolyl)indigo **65**, indigo **69** was prepared and characterized.



Scheme 37: Simultaneous deacylation of **19** and **74** according to *U. Burger et al.*<sup>[88]</sup> with dioxane as co-solvent and subsequent oxidation with manganese(III) acetate to yield indigos **65**, **69** and **63**. The low yields can be attributed to the increased sterical hindrance of the planar *para*-tolyl moiety.

The use of potassium permanganate for the general oxidation reaction of arylated indoxyls to indigo is also possible, dropping the reaction times to 10 minutes. The expected statistical product distribution of 1 / 2 / 1 *ortho-ortho-* (**65**) / *ortho-para-* (**69**) / *para-para-* (**63**) indigo was not obtained in this reaction, instead, a 6 / 2 / 1 ratio was observed. The formation of dimers from twisted precursors is strongly favored while the planar products represent minor species. The chimeric indigo **69** is obtained in twofold yield compared to **63**.

Separation with chiral HPLC at 0 °C was feasible for indigo **69**, two rotamers (*S<sub>a</sub>*)-*trans*-**69** and (*R<sub>a</sub>*)-*trans*-**69** could be isolated.

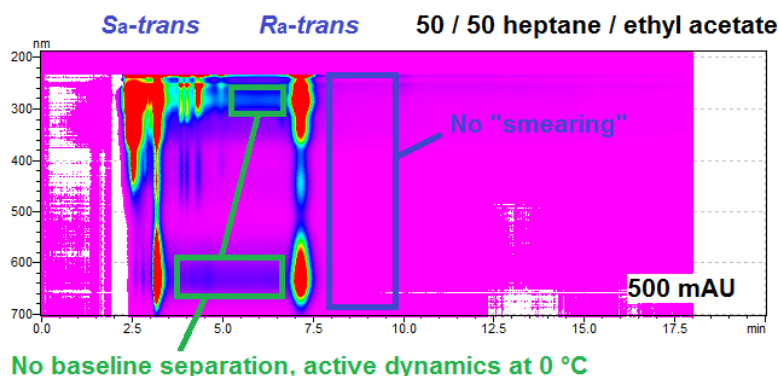


Figure 245: Chiral HPLC separation of the (*S<sub>a</sub>*)-*trans*-**69** and (*R<sub>a</sub>*)-*trans*-**69** indigo rotamers at 0 °C with 50 / 50 heptane / ethyl acetate as eluents. The two expected rotamers can be seen. The streaks between the two peaks indicate an active atropisomerization reaction taking place, interconverting one rotamer to the other while on the chiral column. The immediate stop of this “streaking” after the complete elution of the (*R<sub>a</sub>*)-*trans*-**69** underlines these findings. The polarity of the eluent mixture was significantly increased compared to the separation of **70** to yield an acceptable difference in retention times.

*O. Trapp* showed that the observed “streaking” during HPLC separation of **69** can be used to obtain kinetic data for the interconversion of molecular species via liquid- and gas chromatography.<sup>[95, 117]</sup> This should also be applicable in this case, as the difference in peak retention times should decrease while the intensity of the streaking level should increase for higher separation temperatures or molecules with lower interconversion barriers.

Immediate cooling and ECD measurement of the obtained fractions furnished the remaining ECD areas in Figure 246 below.



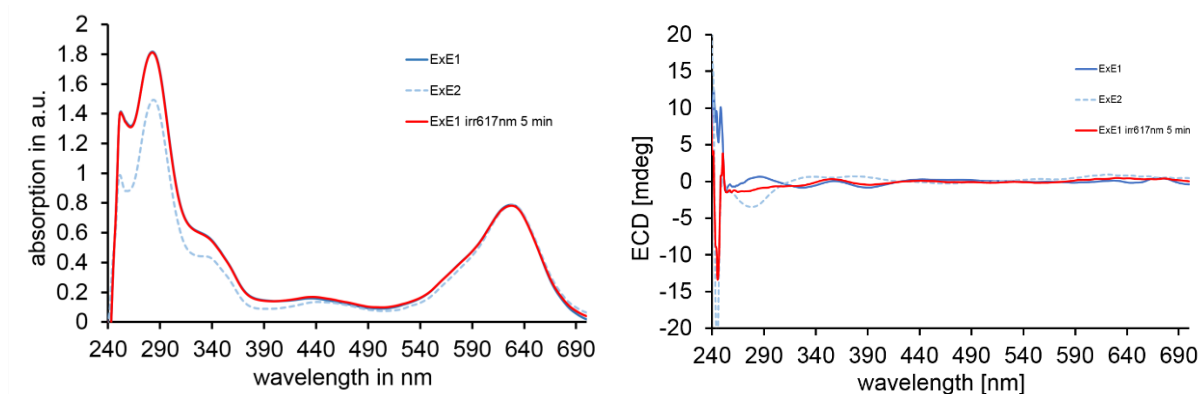


Figure 246: Scaled UV-Vis (left) and ECD (right) spectra of 7-methyl-*N*-(*o*-tolyl)-*N'*-(*p*-tolyl)indigo **69** in 83 / 17 heptane / ethyl acetate at 0 °C (fraction 1, blue and fraction 2 broken light blue) and after 5 min of 617 nm irradiation (red).

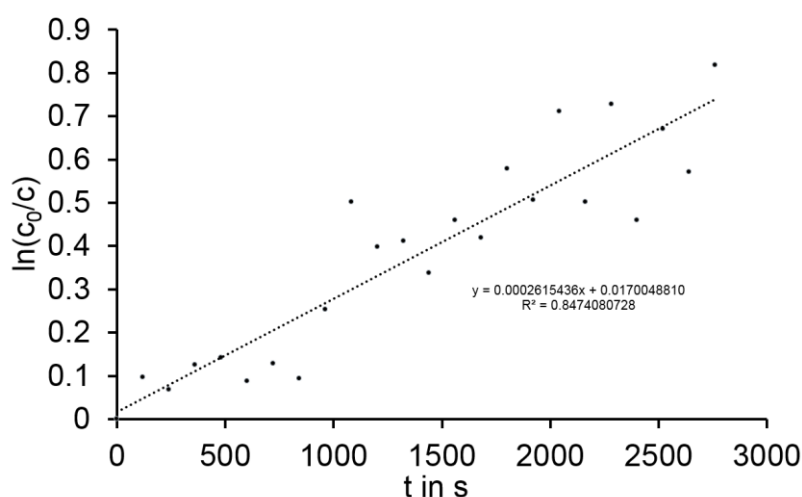


Figure 247: Linearized first order kinetics of the thermal atropisomerization of (*R<sub>a</sub>*)-*trans*-**69** in 50 / 50 heptane / ethyl acetate at 0 °C. The free activation enthalpy  $\Delta G^*$  for this process was determined to be 20.4 kcal/mol resulting half-lives of 1.73 min at 25 °C and 44.4 min at 0 °C. Used formulas and equations can be found in Section 2.2.19.

The low ECD signal of “pure” **69** can be attributed to an intrinsic property of the molecule to show less ECD response or due to the low free activation energy for the thermal atropisomerization ( $\Delta G^* = 20.4$  kcal/mol with half-lives of 1.73 min at 25 °C and 44.4 min at 0 °C) resulting in significant racemization before ECD measurement. Fast sample handling with immediate cooling in total absence of light is crucial for bridging the large spatial distances between the available analytical devices within our laboratory. Measurement at night and utilization of a scooter for fast sample transfer is advised under given circumstances. However, most of the ECD response of separated samples might have vanished due to the HPLC detector

and outlet tubing not being coolable to 0°C. No photoswitching could be observed after irradiation of *trans*-**69** with 617 nm for 5 min at 0 °C, which resembles the behavior of compound **65**. Irradiation to the non-observable *cis* isomer (quick thermal *cis* to *trans* isomerization) and thermal atropisomerization of the chiral axis in this unstable *cis* state quickly decreases the ECD signal of **69** as seen with other chiral indigo derivatives **64** and **70**.

The additional methyl group in position 7 of the indoxyl fragment adds sterical hindrance to the *ortho*-aryl group, which gets wedged in between the methyl group and carbonyl oxygen of the opposite indoxyl fragment. This reduces the stability of the chiral *ortho*-aryl axis as seen with all *Z* isomers of chiral hemiindigo derivatives (see Section 2.3.6) and indigo **65**.

Indigo **65** possesses two adjacent methyl groups next to its chiral axes and should show similar atropisomerization barriers as indigo **69**. The barriers of **65** cannot be measured via ECD spectroscopy as separation of atropisomers is not possible with the available equipment to date. However, suggestions by *R. Linser* supported EXSY NMR spectroscopy as possible method to obtain quantitative kinetic data for indigo **65**.

The synthesis, characterization and kinetic measurements of indigos **70** and **69** underlined the theories for the behavior of symmetric indigos **64** and **65**. These experiments also hinted towards the *cis* / *trans* / *syn* / *anti* assignments and gave the initial ideas for further low temperature ECD and NMR experiments to unambiguously assign the obtained signals to the correct molecular structure.

### 2.4.11 Symmetric chiral indigos - Second generation indigo 64 - Experimental photophysical data

The goal of the following sections consists of supporting the proposed (uni-)directional motional cycles of indigo **64** experimentally and with the help of DFT theory. The developed molecular setup allows for several different kinds of (uni-)directional motional cascades at different temperatures and was tested in dichloromethane and toluene as solvents. Keeping a physical molecular model from a building kit at hand is highly advised to keep track of the proposed geometrical changes within this molecule. The experimental data is presented coherently for two types of proposed unidirectional motors, thermally reversible photoinduced pumping of isomers and photoinduced- / thermal extended Hula-Twist / geared steps, as most of the proofs are redundant for each motion. Further interpretation of the data is given starting from Section 2.4.19.

The generally applied color code for the isomers is defined as following: *syn-trans* + *anti-trans* isomers = blue, *syn-cis* + *anti-cis* isomers = red, *syn-trans* + *syn-cis* isomers = green, *anti-cis* + *anti-trans* = violet. If *syn*- and *anti* forms are discernable from each other - regardless if a *cis*- or *trans* indigo core structure is present - the *syn*- / *anti* colors are chosen for respective signals. Blue- and red signals indicate the presence of combined *syn*- / *anti* signals within the respective *trans* or *cis* form.

## 2.4.12 Symmetric chiral indigos - Second generation indigo 64 - Photoinduced *trans* to *cis* double bond isomerizations

As starting point, the simplified photoinduced central double bond isomerization of different isomers of indigo **64** is shown with *Lewis*-formulas in Figure 248.

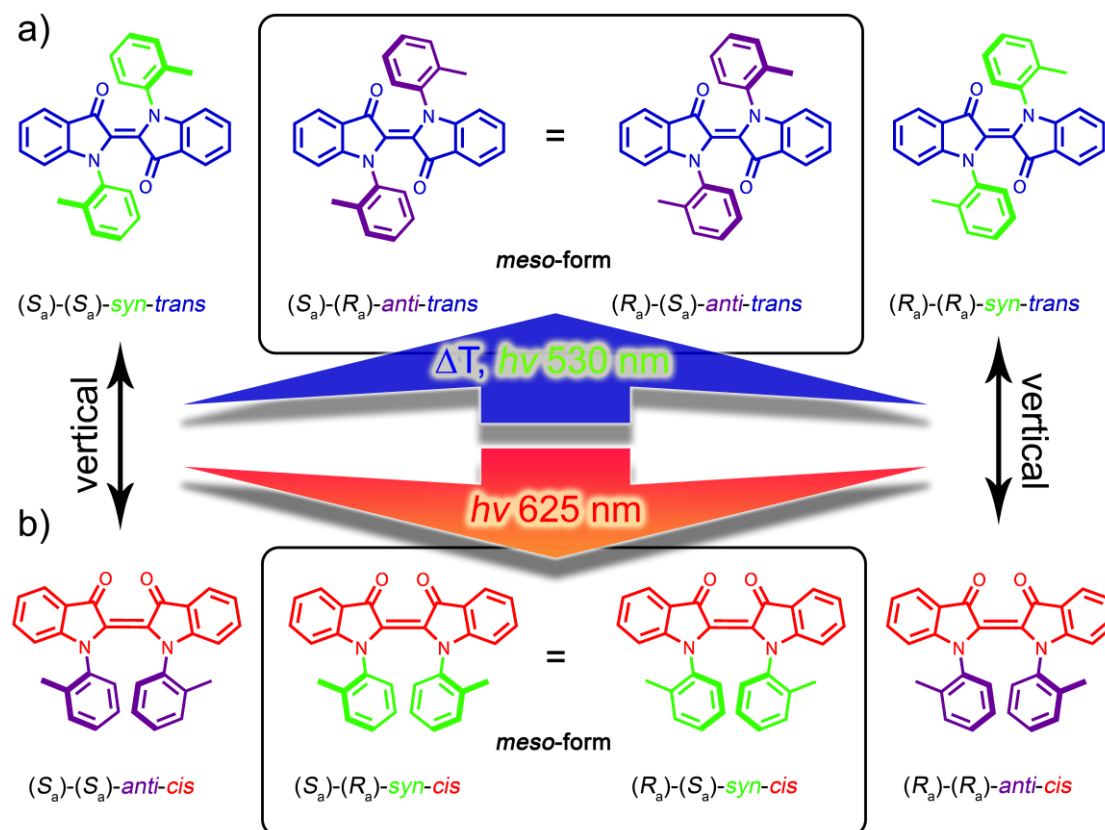


Figure 248: a) Rota- and diastereomers of *trans*-**64**, b) photoinduced rota- and diastereomers of *cis*-isomers by irradiation with red light. A rotation around the central double bond within the indigo core plane for the *meso* form *(S<sub>a</sub>)-(R<sub>a</sub>)-anti-trans-64* gives *(R<sub>a</sub>)-(S<sub>a</sub>)-anti-trans-64*, proving both projections to be the same molecule. The *meso* form of the *cis*-isomer supports a mirror plane between both *ortho*-arylated indoxyls, proving both projections to be the same molecule. The *trans* to *cis* isomerizations (and *vice versa*) to the respective products can be followed by the indicated vertical (de-) excitations.

The *meso* forms are invisible by ECD spectroscopy while enantiomers cannot be discerned by NMR spectroscopy without chiral alignment media. The two possible diastereomers for the *anti-cis* isomers (namely -1 and -2, caused by the freezing of helicity at -60 °C) and two diastereomers of the *syn-trans* isomers (namely -1 and -2, caused by the freezing of helicity at

-60 °C) are not discerned in Figure 248, as indication of the helicity around the central double bond is not done for clarity reasons and is discussed below and in Section 2.4.16.

As previously shown in Figure 230, indigo **64** can be separated via chiral HPLC into (*S<sub>a</sub>*)-(*S<sub>a</sub>*)-*syn-trans*-, (*R<sub>a</sub>*)-(*R<sub>a</sub>*)-*syn-trans*- and (*S<sub>a</sub>*)-(*R<sub>a</sub>*)-*anti-trans* isomers with a ratio of 2.5 / 2.5 / 1 in 83 / 17 heptane / ethyl acetate. A 5 / 1 *syn*- / *trans* isomer ratio is also observed via <sup>1</sup>H-NMR spectroscopy in dichloromethane-*d*<sub>2</sub>. Irradiation with a 625 nm LED light provides the corresponding *cis* isomers at temperatures below 0 °C. The *meso* forms possess an inversion center in the *trans* state and a mirror plane in the *cis* form, converting (*S<sub>a</sub>*)-(*S<sub>a</sub>*)- and (*R<sub>a</sub>*)-(*R<sub>a</sub>*)- enantiomers into one single (*S<sub>a</sub>*)-(*R<sub>a</sub>*) species upon atropisomerization.

The vertical, photoinduced double bond isomerizations from e.g. (*S<sub>a</sub>*)-(*S<sub>a</sub>*)-*syn-trans*- to the (*S<sub>a</sub>*)-(*S<sub>a</sub>*)-*anti-cis* isomer etc. and also the thermally- or photoinduced back reaction to the *trans* state are *always* observed experimentally e.g. at -5 °C in toluene. Higher temperatures allow for the thermal *cis* to *trans* central double bond isomerization to proceed, at e.g. 40 °C, however, the reaction rate is too fast for detection via NMR or stationary UV-Vis spectroscopy. If these vertical *trans* to *cis* to *trans* reactions would be the only observable pathways, the thermodynamic equilibrium ratio of 5 / 1 *syn*- / *anti-trans* isomer *cannot be changed under any circumstances* (within a closed system and no photodegradation). If a change in these ratios is observed, *other occurring photochemical or thermal reactions are mandatory* to shift the system out of its thermal equilibrium.

*Lewis*-formulas make visualization of the prevalent molecular helicities and diastereomers very confusing, therefore, the computationally optimized molecular structures are shown from now on. An overview of all experimentally- and computationally observed species and their properties is given in Table 12, Section 2.4.16, including short explanations. This is done to outline the complex motions and observed bistable intermediates to avoid confusion along the increasing number of experiments.

Table 12 shows the converged structures upon optimization (DFT) of respective isomers. The depicted structure is postulated, as a still unexplained additional signal set is observed upon irradiation of the *anti-trans* isomer at -60 °C in toluene-*d*<sub>8</sub> and dichloromethane-*d*<sub>2</sub>. These unexplainable signals show the same thermal stability as the *anti-cis*-1 and -2 isomers in dichloromethane-*d*<sub>2</sub> and are converted to the *anti-cis*-1 signal in toluene-*d*<sub>8</sub> at -20 °C. This hints towards another *anti-cis* species or a coalescence for split signals of the *anti-cis*-1 form, (see Section 2.4.14 for details).

### 2.4.13 Symmetric chiral indigos - Second generation indigo 64 - Low temperature NMR Data starting from the *syn-trans-1* isomers

To clarify which processes are responsible for the enrichment of respective isomers of indigo **64**, low temperature kinetic NMR studies were conducted on a 400 MHz NMR device with a glass fiber coupled to a high power 625 nm LED and are shown in this section.

In the case of dichloromethane, the free activation enthalpies for the thermal double bond isomerization from *anti-cis-* to *syn-trans-* and *syn-cis-* to *anti-trans* isomers differ vastly by 5 kcal/mol, as shown in Figure 249 and Figure 250 below.

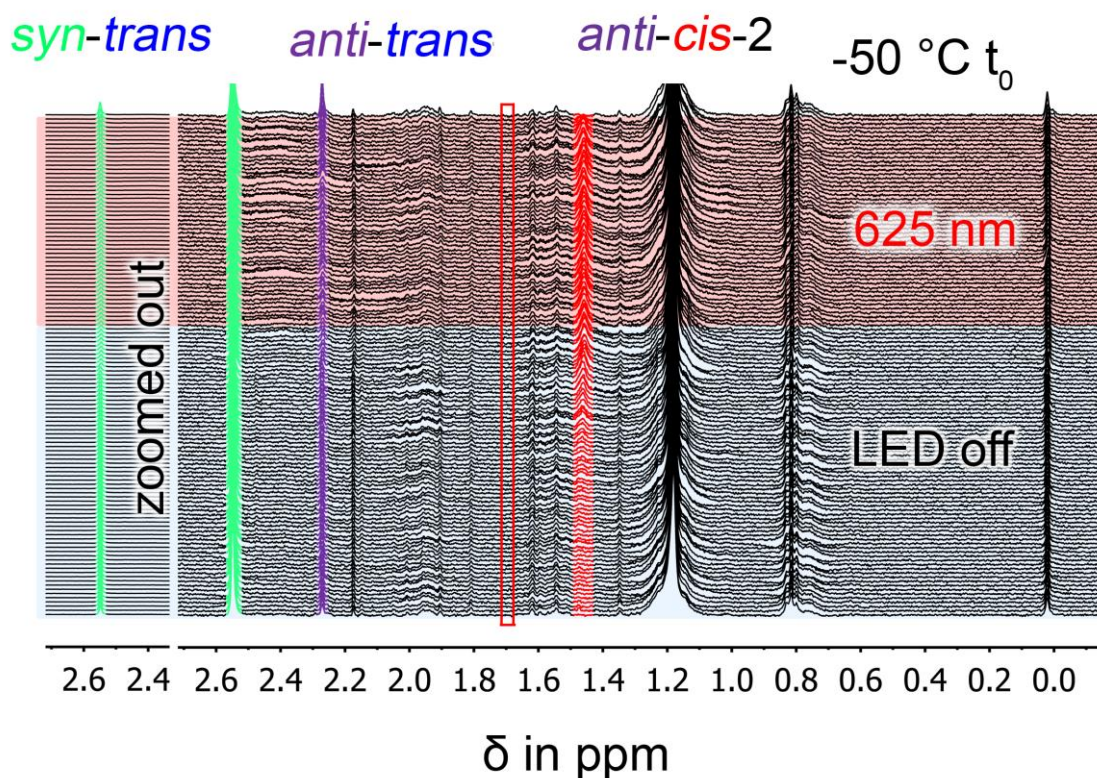


Figure 249: Irradiation of a 5 / 1 *syn-* / *anti* mixture of indigo **64** yields mainly the *anti-cis-2* isomer in dichloromethane-*d*<sub>2</sub> followed by <sup>1</sup>H-NMR spectroscopy at -50 °C. 52% of *anti-cis-2* isomer could be obtained in the PSS at 625 nm irradiation. Subsequent measurements of the decaying *cis* isomers in the dark gave a free activation enthalpy  $\Delta G^* = 15.8$  kcal/mol. The decreasing *anti-cis-2* isomer was fully converted back to the rising *syn-trans-1* isomer. No second signal for the *anti-cis-1* form at 1.9 ppm can be observed (see Figure 261). The signal at 1.72 ppm (red rectangle) of the thermally stable *syn-cis* isomer population - generated from the minor *anti-trans* isomer - is also not visible due to signal

broadening and subsequent shifting towards 1.45 ppm (see Figure 258 and Figure 222 for indigo **65**).

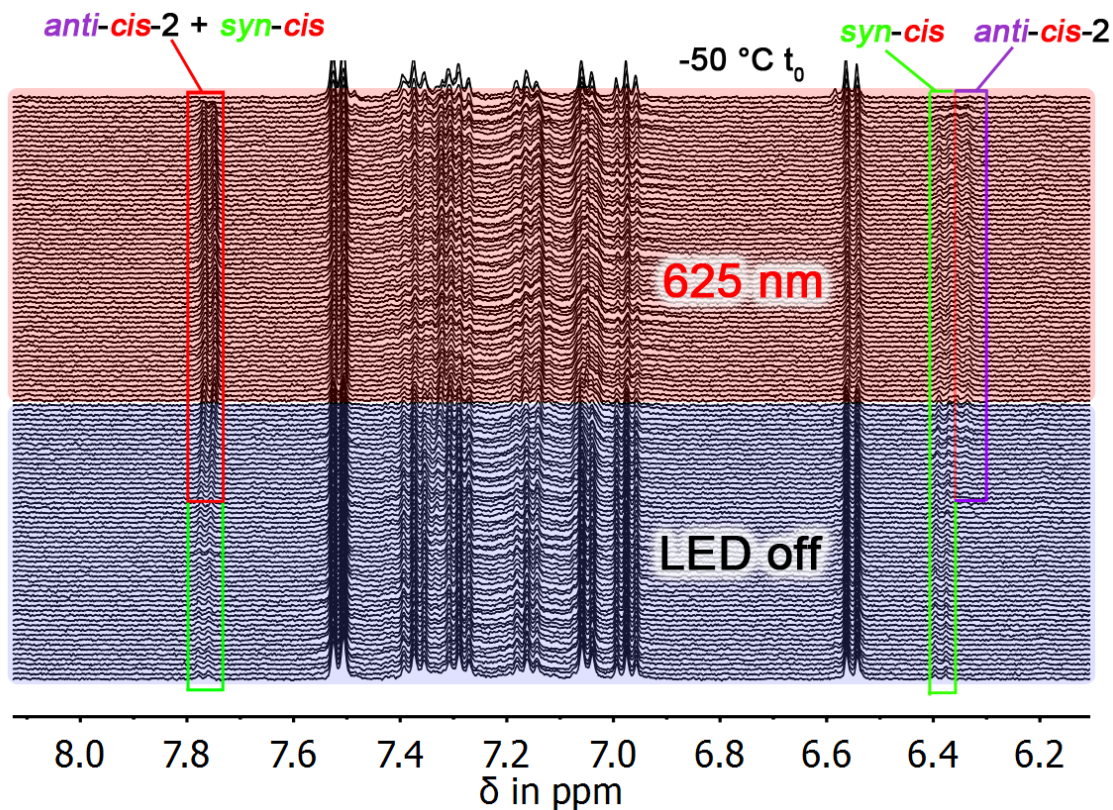


Figure 250: Aromatic part of the irradiation of a 5 / 1 *syn-* / *anti* mixture of indigo **64** to the *anti-cis-2* (violet) and *syn-cis* (green) isomers in dichloromethane- $d_2$  followed by  $^1\text{H-NMR}$  spectroscopy at  $-50\text{ }^\circ\text{C}$ . Subsequent measurements of the decaying *anti-cis-2* isomer in the dark gave a free activation enthalpy  $\Delta G^* = 15.8\text{ kcal/mol}$ . The decreasing *anti-cis-2* isomer was not converted to the stable *syn-cis* isomer, only the *syn-trans-1* isomer population was restored during the decay of the *anti-cis-2* isomer. The integrals of the *anti-cis-2* signals are underrepresented, especially in the aromatic region, as the total amount of *cis*-isomers reported at the signal located at 7.78 ppm exceeds the combined integral value located at 6.38 ppm.

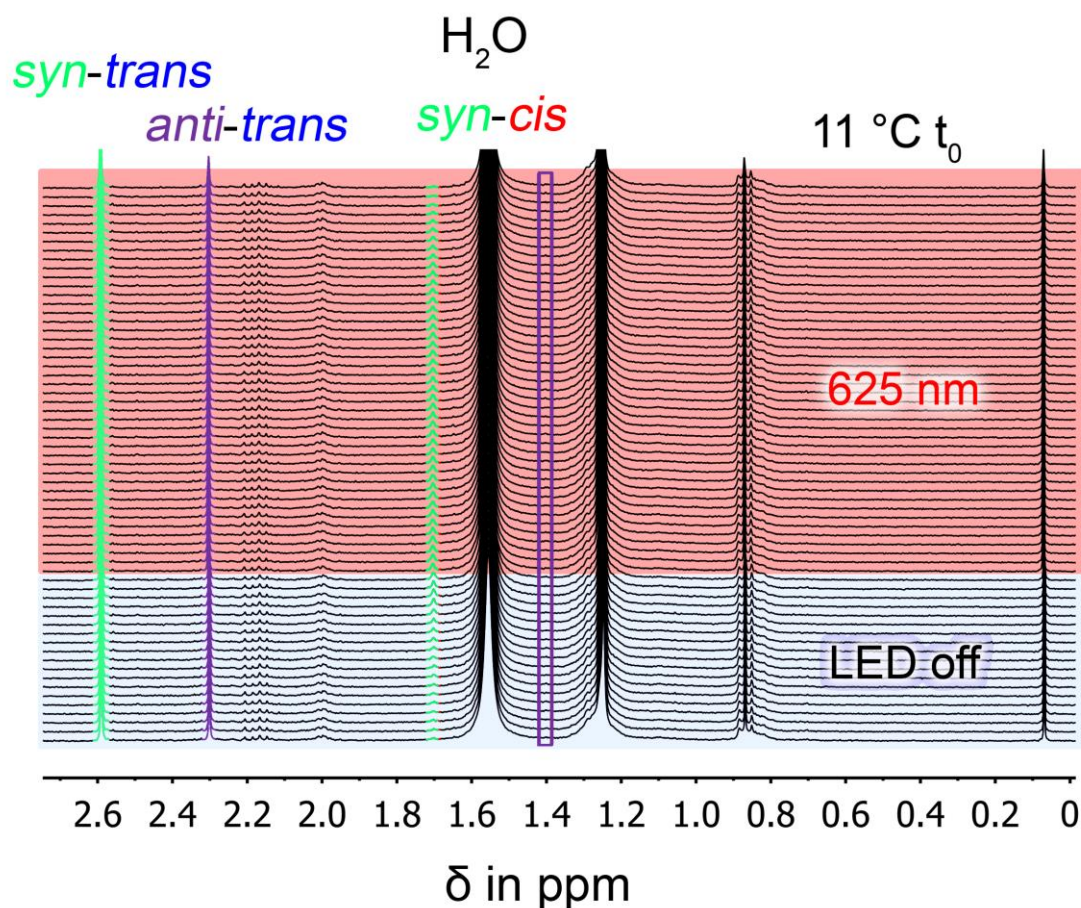


Figure 251: Irradiation of a 5 / 1 *syn-* / *anti* mixture of indigo **64** to the *syn-cis* isomer (green) in dichloromethane- $d_2$  followed by  $^1\text{H}$ -NMR spectroscopy at 11 °C. 20% of *syn-cis* isomer could be obtained at this temperature in the PSS (77% at -80 °C, Figure 253), which can be explained by the low thermal stability of the *anti-cis-2* isomer, which represents the mayor photoproduct. However, minor amounts of *anti-trans* isomer are responsible for the photogeneration of the *syn-trans-1* isomer population. Subsequent measurements of the decaying *cis* isomers in the dark gave a free activation enthalpy  $\Delta G^* = 20.7$  kcal/mol for this thermal reaction. The decreasing *syn-cis* isomer is thermally converted at a slow rate to the rising *anti-trans* isomer at this temperature. The violet rectangle at 1.45 ppm indicates the absence of the *anti-cis-2* isomer at 11 °C, which is to be expected because of its low thermal stability.

Irradiation of a 5 / 1 *syn-* / *anti* mixture of indigo **64** at -50 °C yields the product derived from a double bond isomerization starting from the *syn-trans-1* isomer, namely the *anti-cis-2* isomer. However, the thermally more stable *syn-cis* isomer, which is generated from the *anti-trans-2* isomer, remains static throughout the course of the kinetic measurement. The situation is



changed for irradiations at 11 °C, as it is impossible to observe the *anti-cis-2* isomer at this temperature. Irradiation yields solely the *syn-cis* isomer as photoproduct but, surprisingly, a rise in *anti-trans* isomer can also be observed during irradiation (Figure 251).

A hypothetical reaction pathway towards the *anti-trans* isomer consists of a temperature independent photoinduced single bond rotation, which can be most likely ruled out as a rise of *anti-trans* isomer at -50 °C or -80 °C is not observed. The reaction pathway shown in the cycle described in Figure 279, Section 2.4.19, is suggested as the *syn-trans-* to *anti-cis-2* isomer pathway branches into two thermally available reactions at 11 °C. These consist of the *anti-cis-2-* to *syn-trans-1* double bond isomerization towards the thermodynamic minimum represented by the *syn-trans-1* state and the atropisomerization of *anti-cis-2* towards the thermodynamically more favored *syn-cis* state. The latter is thermally converted back to the *anti-trans* state via double bond isomerization, accumulating this specific isomer against its thermal equilibrium. The atropisomerization barrier of 23.6 kcal/mol allows for restoring of the initial *syn-trans-1* isomer population, closing the motional cycle.

Figure 250 unambiguously shows that both *cis* isomers exhibit very different thermal barriers in dichloromethane-*d*<sub>2</sub> and can be populated by irradiation with 625 nm red light in a single experiment despite very different ratios of the starting *trans* isomers. It could also be shown that the decrease of *anti-cis-2* does not increase the amount of *syn-cis* isomer, proving that the thermal *anti-cis-2* to *syn-cis* barrier is not overcome at this temperature while the *anti-cis-2* to *syn-trans-1* double bond isomerization takes place readily.

Figures reporting the integration results like Figure 252 below show the distributions at the beginning or end of each measurement array under given conditions. Spectra without changes of representing key points of the measurement are omitted for clarity. The overall *cis* to *trans* ratios were determined with the non-shifting / unbroadened *syn+anti-cis* signals at 7.75 ppm (red) and *syn+anti-trans* signals at 6.55 ppm (blue). The *syn* / *anti* ratios of *cis* and *trans* isomers were determined within the aliphatic or aromatic region, depending on visibility and estimated degree of signal broadening. The methyl signal of the thermodynamically most stable *syn-anti* state (green) were used as internal integration reference (normalized to 1) to facilitate analysis.

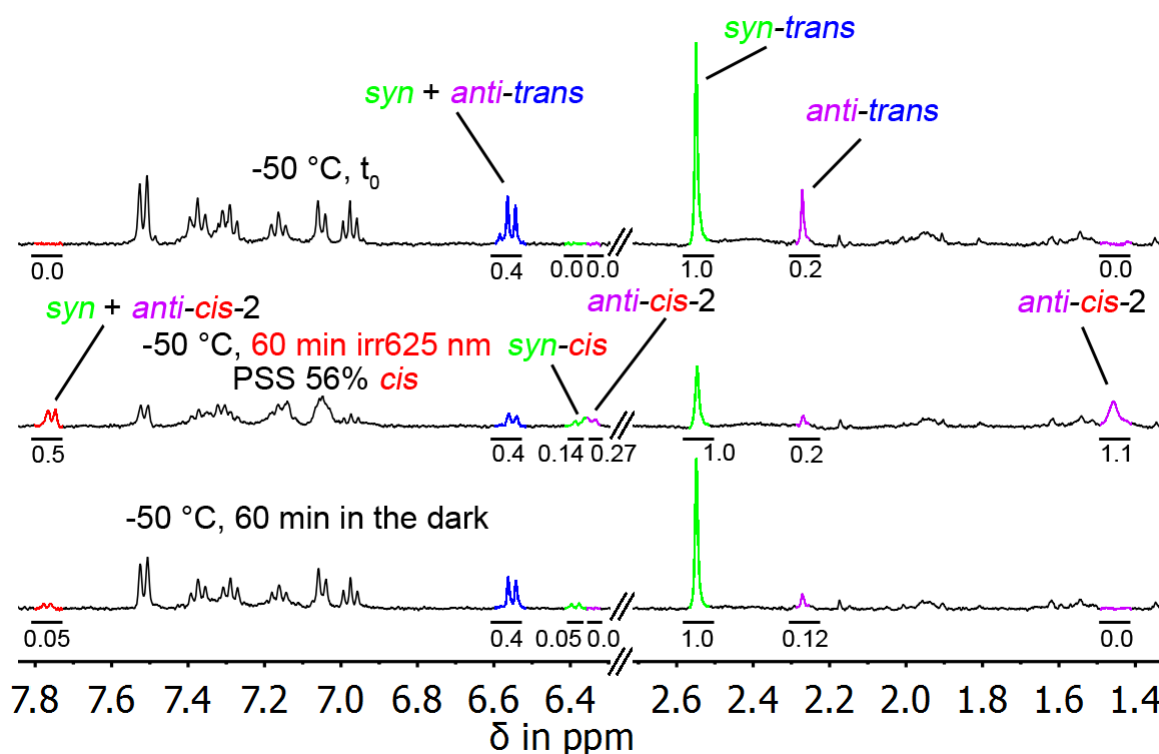


Figure 252: Selected <sup>1</sup>H-NMR spectra recorded during the irradiation of a 5.0 / 1.0 *syn*- / *anti-trans* mixture of indigo **64** populating the *anti-cis-2* and *syn-cis* isomers (dichloromethane-*d*<sub>2</sub> at -50 °C). The Spectra were taken from the irradiation and thermal annealing experiments shown in Figure 249 and Figure 250. A PSS consisting of 56% *cis* isomers (compared to all *trans* isomers) can be obtained at -50 °C. Relative normalized (to the *syn-anti* isomer methyl group signals) integrals for indicated signal areas are given below the respective peak. The integrals of the *anti-cis-2* signals are underrepresented, especially in the aromatic region, as the total amount of *cis*-isomers reported at the signal located at 7.78 ppm exceeds the combined integral value located at 6.38 ppm.

Irradiation at  $-50\text{ }^{\circ}\text{C}$  yields the signals for *anti-cis-2* and *syn-cis* isomers at 6.38 ppm and 6.34 ppm and after switching off the light source, the *anti-cis-2* signal thermally disappears after several minutes at  $-50\text{ }^{\circ}\text{C}$  while the *syn-cis* signals remain unchanged. Switching to an 8.3 / 1.0 *syn-* / *anti-trans* isomer ratio after the thermal annealing at  $-50\text{ }^{\circ}\text{C}$  can be explained by selective thermal isomerization from *anti-cis-2* to *syn-trans* isomers while the *syn-cis* isomer remains and functions as a “storage” of the missing *anti-trans* isomer population. The *syn-cis* isomer is converted to the *anti-trans* isomer starting above  $0\text{ }^{\circ}\text{C}$ . For the measurement shown in Figure 249, Figure 250 and Figure 251, however, thermal annealing at higher temperatures was not carried out.

To disentangle thermal- and photochemical reaction kinetics, *in situ* irradiations at  $-80\text{ }^{\circ}\text{C}$  with subsequent thermal annealing steps at increasingly higher temperatures were carried out (Figure 253).

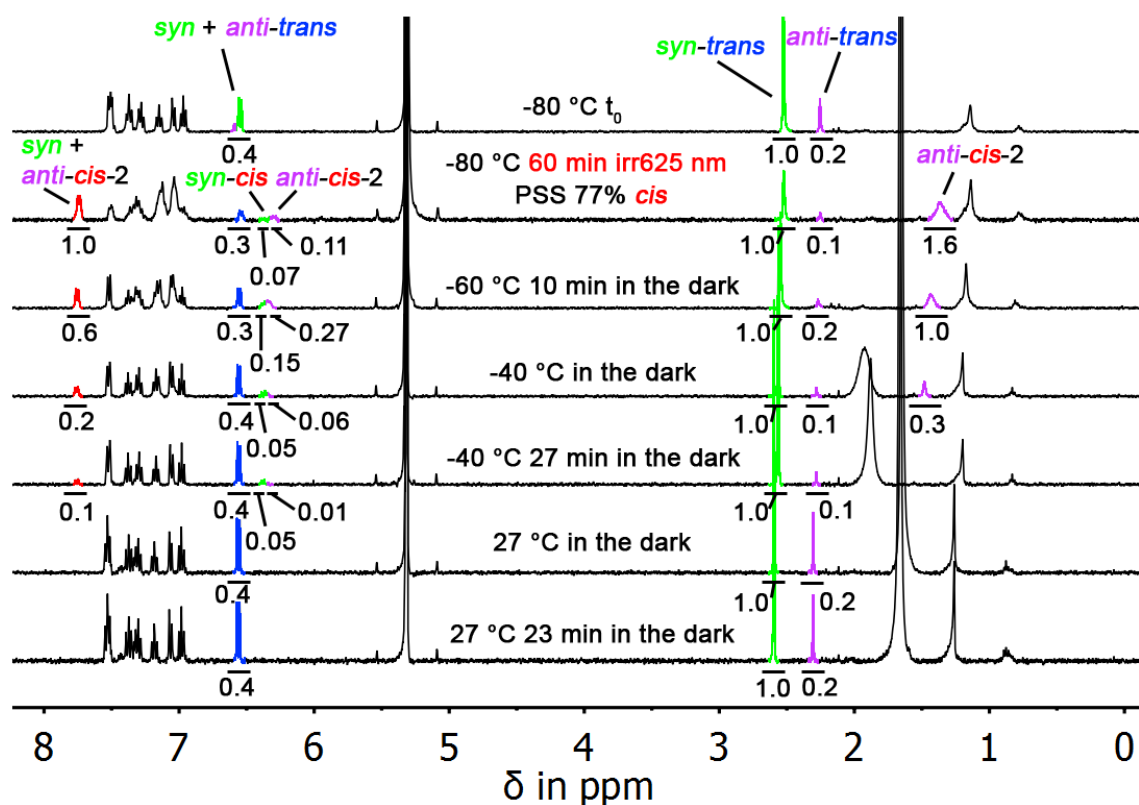


Figure 253:  $^1\text{H}$ -NMR spectra recorded during 625 nm the irradiation of a 5.0 / 1.0 *syn-* / *anti-trans* mixture of indigo **64** to the *anti-cis-* and *syn-cis* isomers in dichloromethane- $d_2$  at  $-80\text{ }^{\circ}\text{C}$  and stepwise annealing at higher temperatures. A PSS containing 77% *cis* isomers (relative to all *trans* isomers) can be obtained at  $-80\text{ }^{\circ}\text{C}$ . Integrals for indicated signal areas are given below the respective peak. Thermal decay in the dark is clearly seen at around  $-40\text{ }^{\circ}\text{C}$ . The integrals

of the *anti-cis-2* signals are underrepresented, especially in the aromatic region, as the total amount of *cis*-isomers reported at the signal located at 7.78 ppm exceeds the combined integral value located at 6.38 ppm.

Figure 253 shows the photoinduced population of *syn-* and *anti-cis-2* isomers with red light at -80 °C. Both isomers can be observed in the aromatic region at 6.38 ppm (*syn-cis* form) and 6.34 ppm (*anti-cis-2* form). The methyl signals of the *syn-cis* isomer cannot be observed because of signal broadening at low temperatures (see Figure 254 for the traced signals at different temperatures). The lower thermal stability of the *anti-cis-2* isomer can also be observed at -40 °C as the corresponding signal of this species decreases in intensity while the *syn-cis* signal remains unchanged (Figure 253). After full thermal conversion of the *cis* isomers back to the *trans* isomers at ambient temperatures, the initial composition of *syn-* to *anti-trans* isomers is restored which is consistent with the other low temperature measurements.

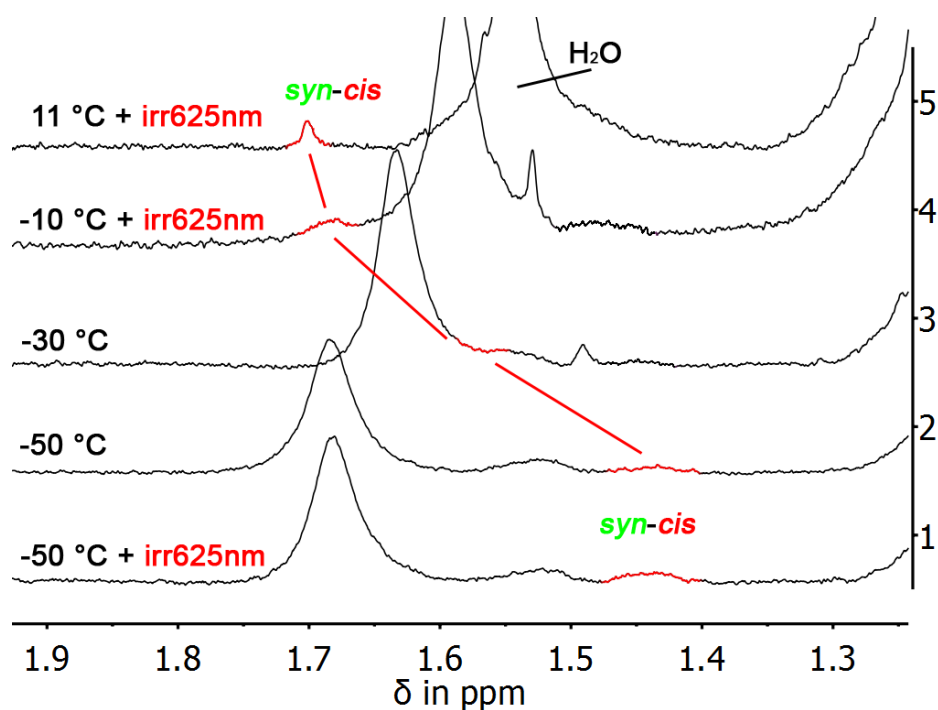


Figure 254: Temperature dependence of the *syn-cis* isomer *ortho*-methyl signal of indigo **64** in the range of 11 °C to -50 °C. Irradiation at 11 °C yielded the previously observed *syn-cis* isomer with the methyl-group signal residing at 1.69 ppm, cooling to -10 °C showed a slight upfield shift and signal broadening. Cooling to -30 °C strongly shifts the *syn-cis* methyl group signal under the also shifted water peak, while cooling to -50 °C gives another separate signal. Irradiation at -50 °C increases the broad signal of the methyl group of the *anti-cis-2* isomer at 1.43 ppm.

The assignments of the methyl-group signals in Figure 254 are not unambiguous as the shifts cannot be followed conclusively. However, it could be demonstrated that shifting and signal broadening takes place at different rates for the methyl signals of *syn-cis* isomers, which explains why the *syn-cis* and possibly other isomers cannot be observed simultaneously at low temperatures. This broadening might be caused by a constant change in helicity of the on average symmetric *syn-cis* isomer. This effect can also be observed for the fast motions of indigo **65** (Section 2.4.3, Figure 222).

As experiments in dichloromethane as solvent showed vast differences between the thermal stabilities for *anti-cis*- and *syn-cis* isomers, the experiments were repeated in toluene solution where the *anti-cis-2* isomer can already be observed at 0 °C instead of -50 °C (Figure 255).

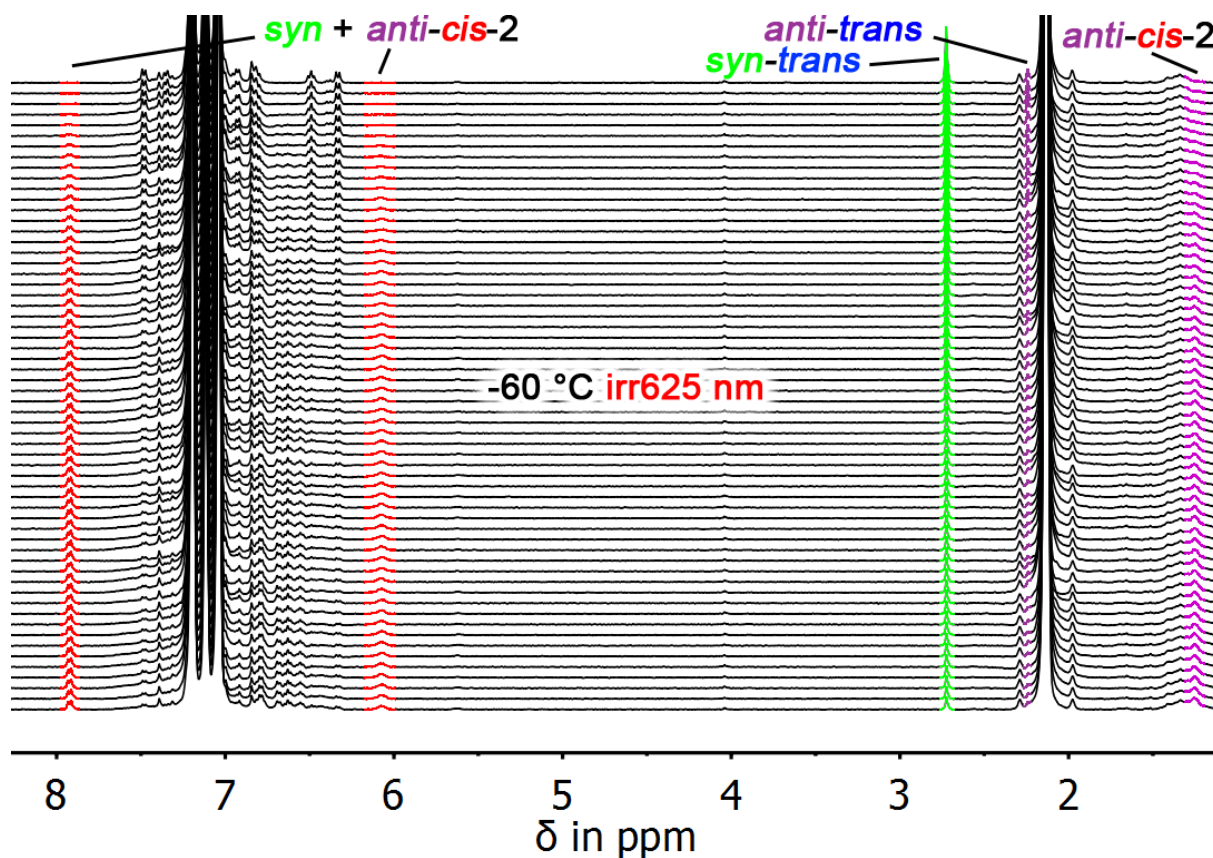


Figure 255: Irradiation of a 5.0 / 1.0 *syn*- / *anti* mixture of indigo **64** with 625 nm LED light to the *anti-cis-2* and *syn-cis* isomers in toluene-*d*<sub>8</sub> at -60 °C. Spectra were recorded in one minute intervals. Generation of *cis* isomers can be observed, the *syn-cis* species is expected to show broad signals for its methyl protons at low temperatures (see Figure 254), which leaves the *anti-cis-2* isomer as the only visible new species in the aliphatic part of each spectrum. Discerning of *syn*- and *anti-cis-2* isomers is impossible at -60 °C in this solvent as signal overlap and / or -broadening at in the aromatic part of the spectrum causes inseparable signals.

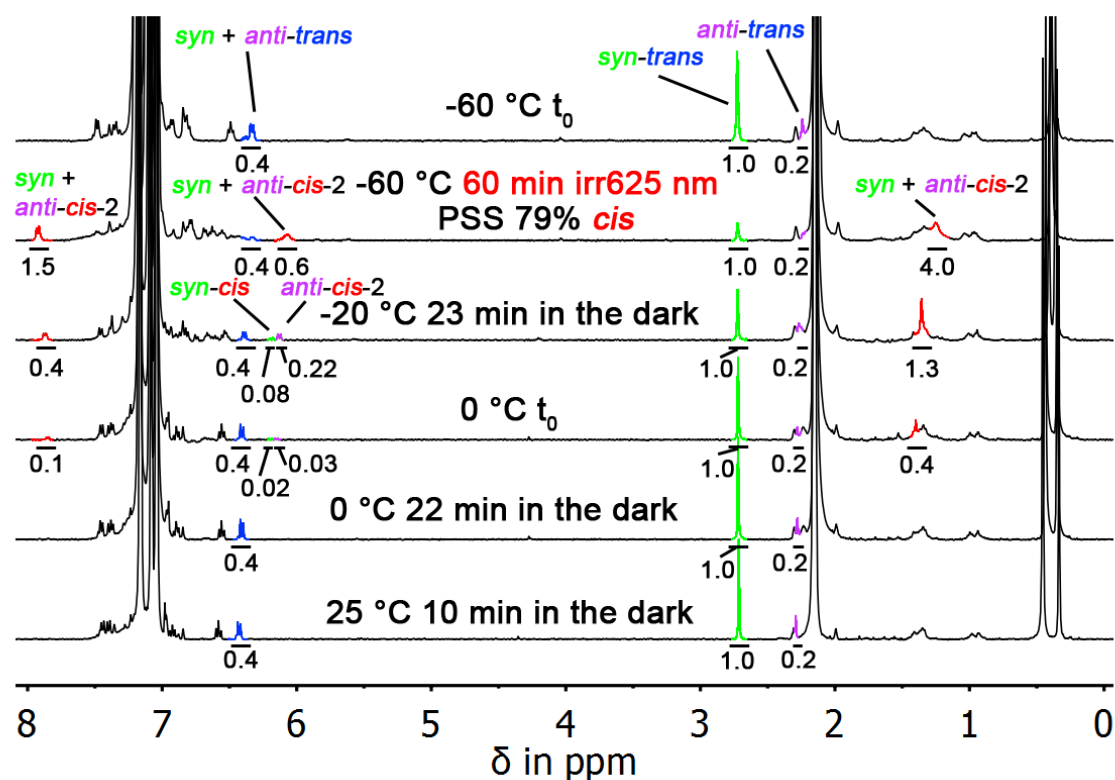


Figure 256:  $^1\text{H}$ -NMR spectra of the irradiation of a 5.0 / 1.0 *syn* / *anti* mixture of indigo **64** to the *anti-cis-2* and *syn-cis* isomers in toluene- $d_8$  at  $-60\text{ }^\circ\text{C}$  and subsequent behavior in the dark at various temperatures. A PSS consisting of 79% *cis* isomers (relative to all *trans* isomers) can be obtained during irradiation at  $-60\text{ }^\circ\text{C}$ . Integrals for indicated signal areas are given below the respective peak. The integrals of the *anti-cis-2* signals are underrepresented, especially in the aromatic region, as the total amount of *cis*-isomers reported at the signal located at 7.78 ppm exceeds the combined integral values located at 6.34 ppm.

Figure 255 shows the photoinduced population of *syn*- and *anti-cis-2* isomers with red light at  $-60\text{ }^\circ\text{C}$  in toluene solution and the subsequent species development at different temperatures in the dark. Both *cis* isomers can be observed in the aromatic region at 6.38 ppm (*syn-cis* form) and 6.34 ppm (*anti-cis-2* form) after irradiation while the methyl signals of the *syn-cis* isomer cannot be seen because of signal broadening at low temperatures. The *syn*- / *anti-trans* isomeric ratio remains unchanged, showing equal turn-over rates for *syn*- and *anti-cis-2* isomers. The lower thermal stability of the *anti-cis-2* isomer can be observed at  $0\text{ }^\circ\text{C}$  (in contrast to  $-50\text{ }^\circ\text{C}$  in dichloromethane- $d_2$ ) and the corresponding signals of this species now decrease only at a slightly faster rate than the *syn-cis* signal (Figure 256).

## 2.4.14 Symmetric chiral indigos - Second generation indigo 64 - Low temperature NMR Data starting from the *anti-trans* isomer

*In situ* irradiation of an *anti-trans*-**64** enriched isomeric mixture (obtained by low temperature HPLC separation of the *trans* isomers) yielded the <sup>1</sup>H-NMR spectra shown in Figure 257 below.

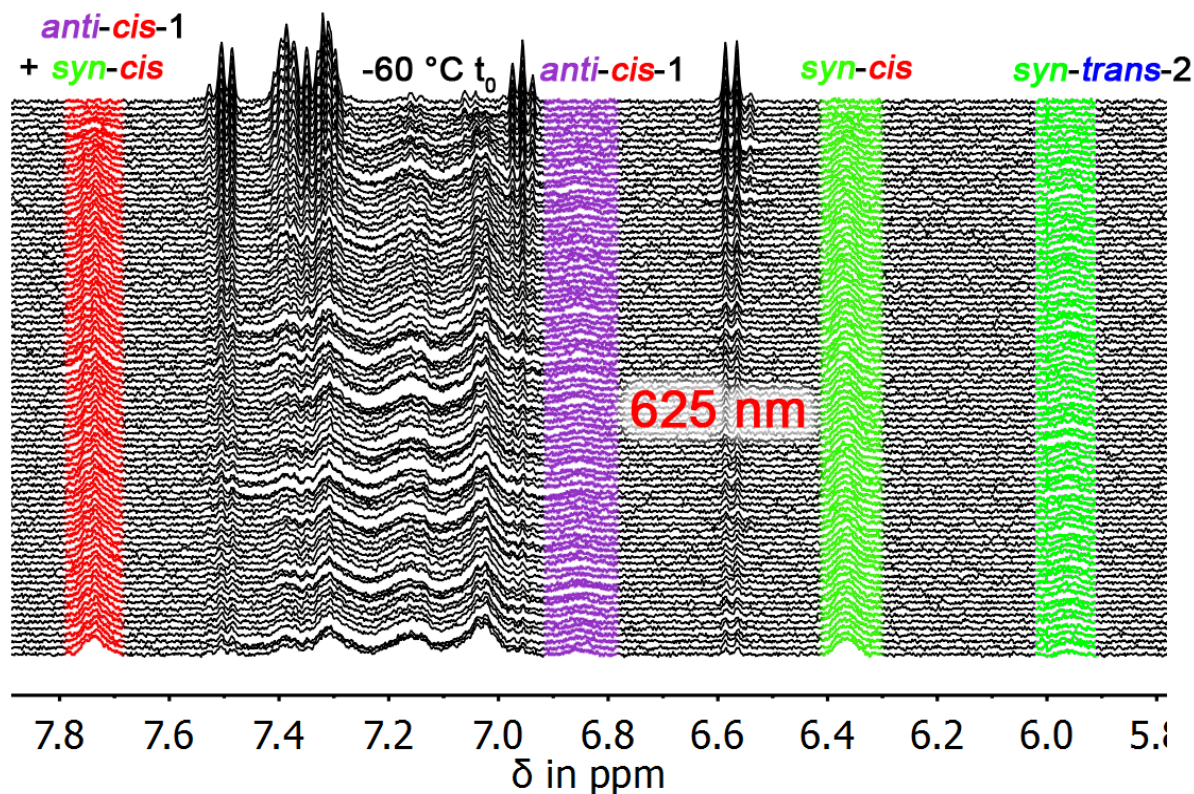


Figure 257: Aromatic part of the <sup>1</sup>H NMR spectra recorded during 625 nm irradiation of a 1.0 / 6.5 *syn* / *anti* mixture of indigo **64** to yield *syn-cis*, *anti-cis-1* and *syn-trans-2* signals in dichloromethane-*d*<sub>2</sub> at -60 °C. Coincident generation of *syn*-, *anti-cis-1* and *syn-trans-2* signals can be observed. The rate of the photoreactions can be seen to be faster for the *syn-cis* isomer and slower for the *anti-cis* isomer as the *syn-trans-1* isomer represents as minor species for the photoreaction and generates *anti-cis-1*- / *syn-trans-2* signals in lower quantities, respectively. The previously generated *anti-cis-2* isomer is not observed (Figure 250).

Figure 257 shows that *anti-cis-1* / *syn-trans-2* signals are generated exclusively and no *anti-cis-2* signal at 6.34 ppm can be observed. This suggests skipping of the *anti-cis-1* and *syn-trans-2* state within the photoinduced trajectory of the *syn-trans-* to the *anti-cis-2* isomer. Additionally, the *anti-cis-2* state is never populated when starting from the *anti-trans* isomer.



The aromatic region of *anti-trans* indigo **64** is clearly responsible for generating a new signal at 6.85 ppm and 5.96 ppm within  $^1\text{H-NMR}$  *in situ* irradiation experiments. The comparison of the aliphatic parts of the  $^1\text{H-NMR}$  spectra recorded during irradiation of either *syn-trans* or *anti-trans* enriched solutions in different solvents is shown in Figure 258.

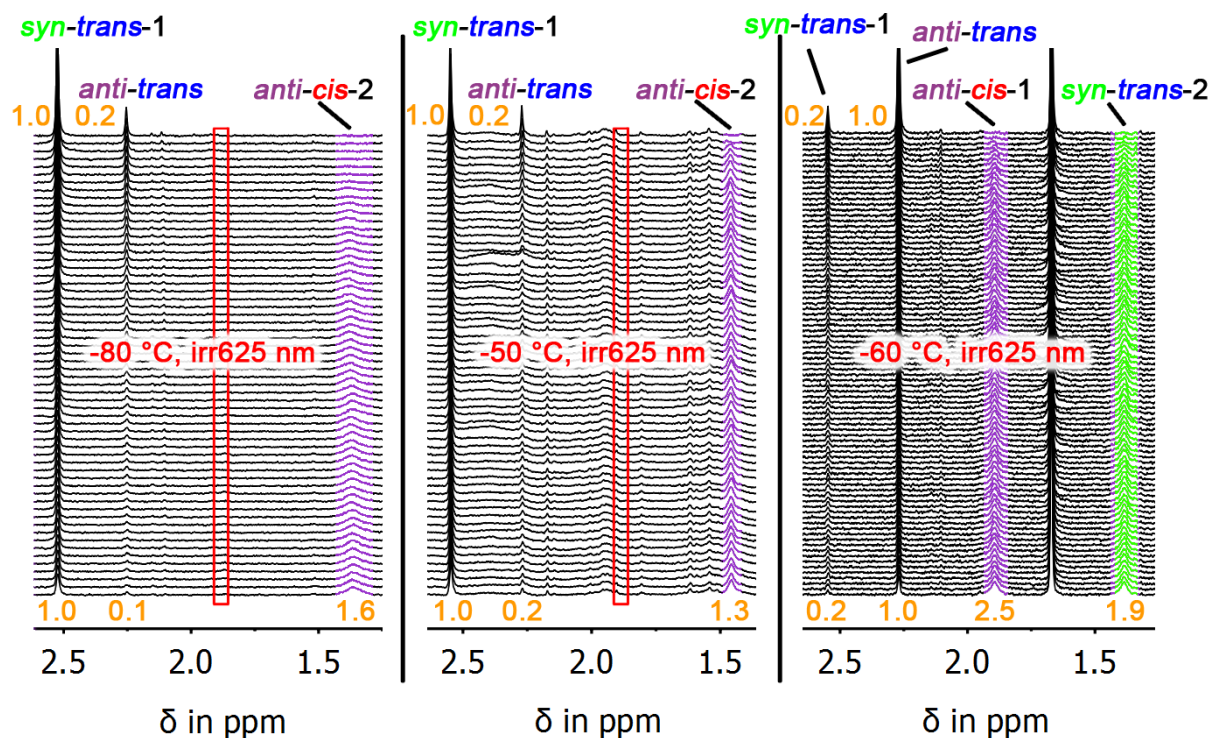


Figure 258: Comparison of three *in situ* irradiation experiments of indigo **64** with 625 nm LED light at low temperatures in dichloromethane- $d_2$ . The spectra were taken at a 1 minute time interval. The relative integrals for start and end of each photoreaction course are given in orange. The plots on the left and middle start with a 1.0 / 0.2 *syn-* / *anti-trans* mixture, the plot on the right with a 0.2 / 1.0 *syn-* / *anti-trans* mixture. The rise of novel signals at 1.89 ppm (*anti-cis-1*) and 1.38 ppm (*syn-trans-2*) with comparable estimated photokinetics as the signal at 1.46 ppm (*anti-cis-2* generated from the *syn-trans-1* isomer) can be observed. The *syn-cis* isomer is the major photoproduct originating from the *anti-trans* isomer but shows broad aliphatic signals at these temperatures and can only be observed in the aromatic region or at temperatures above  $-20\text{ }^\circ\text{C}$ , see Figure 253 and Figure 254.

With *anti-trans* being the initial major species at the start of the irradiation experiment (which undergoes only little atropisomerization to equal amounts of ( $S_a$ )-( $S_a$ )-*syn-* or ( $R_a$ )-( $R_a$ )-*syn-trans-1* isomer during sample handling), the two concomitantly arising signals at 1.90 ppm

(*anti-cis-1*) and 1.38 ppm (*syn-trans-2*) are unexpected because majorly the *syn-cis* isomer should be generated within this experiment if the isomerization mechanism would consist of a sole double bond photoisomerization. A possible explanation for the experimental observation is a photoreaction from *anti-trans* to *anti-cis-1*, which is not visible when only low amounts of *anti-trans* are present (see experiments starting with enriched *syn-trans* isomers as described above). This photoreaction could be described as a *photoinduced extended Hula-Twist (PEHT)* and rotates both the central double bond and one spatially close chiral aryl axis concertedly. This hitherto unknown reaction pathway might be the key step for the selective generation of the *anti-cis-1* / *syn-trans-2* isomer instead of the previously observed *anti-cis-2* isomer (Figure 253).

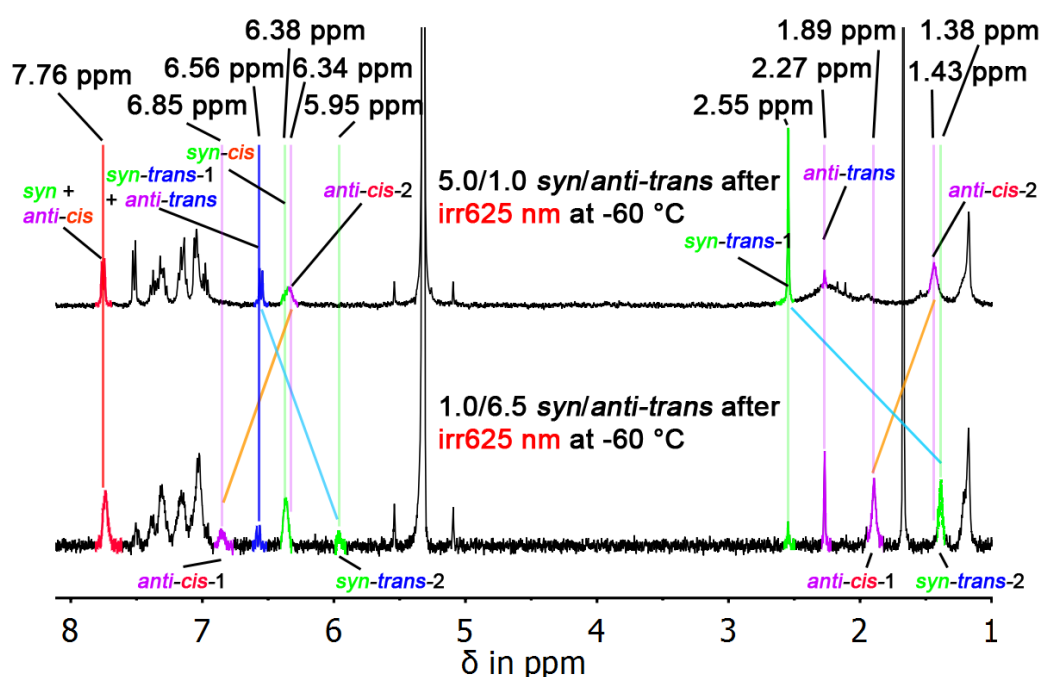


Figure 259: Comparison of  $^1\text{H}$ -NMR spectra obtained after irradiation of a 5.0 / 1.0 *syn* / *trans*- (top) and a 1.0 / 6.5 *syn* / *anti-trans* isomer (bottom) of indigo **64** at  $-60\text{ }^\circ\text{C}$  in dichloromethane- $d_2$ . If the *syn-trans-1* isomer is the major initial species, single signals at 6.34 and 1.43 ppm can be observed for the *anti-cis-2* isomer. When the *anti-trans* isomer represents the major initial species, two emerging signal sets at 6.85 ppm, 5.95 ppm and 1.89 ppm, 1.38 ppm can be observed after irradiation for the *anti-cis-1* / *syn-trans-2* isomers, which could be populated by a photoinduced extended Hula-Twist motion as the *anti-cis-1* isomer cannot be generated by solely double bond isomerizations from the *anti-trans* isomer, which is also true for *syn-trans-2*. The *syn-trans-1* isomer is too low in quantity to yield the significant amounts of (underrepresented) *anti-cis-2* isomer in the second experiment (bottom).

Two novel signals at 1.89 ppm and 1.38 ppm appear with the same rate and integral height during irradiation and decrease in population at -50 °C in the dark. Regarding their low thermal stability, these signals should correspond to the *anti-cis*-1 / 2 isomers, which also show by three-fold enlarged integrals for the methyl signal compared to a singular proton intensity in the aromatic region. One of the two emerging signals for the *anti-trans*-enriched measurement course can be explained by two possible diastereomers of the chiral axes for the *anti-cis*-1 and *anti-cis*-2 states, which is also backed by DFT calculations, see Section 2.4.8, Figure 236 and Section 2.4.16, Figure 269 for details. The *syn-trans*-2 signal was assigned to best knowledge, but highly speculative suggestions consist in a coalescence between the signals of interconverting edge-to-face configurations depicted in Figure 260 and the local minimum of *anti-cis*-1, which is highly unlikely. Nonetheless, calculational efforts were taken to estimate the stability of these isomeric forms.



Figure 260: Both hypothetical edge-to-face conformations of indigo **64** that are experimentally stable solely at -60 °C. DFT optimizations at the M05-2x/6-31+G(d) level of theory did not yield local minimum structures.

The M05-2x functional with 6-31+G(d) basis set was chosen as reports by *E. Wheeler* showed that it predicts edge-to-face energies and interactions of benzene very closely to the CCSD(T)/AVDZ level of theory with a fraction of required computational resources.<sup>[118]</sup>

Irradiation of the *anti-trans* isomer at -60 °C also confirmed the simultaneous generation of *three cis- or two cis- and one trans isomer*. Examining of the <sup>1</sup>H-NMR proton signal area intensities at key steps over the course of the experiment showed that the *anti-cis*-1 signal was in part thermally converted into the *syn-cis* isomer during irradiation. The rates and kinetic barriers could not be determined as all relevant signals disappeared during the change in temperature from -60 °C to -50 °C over 15 minutes. However, the major product of this irradiation was the *syn-trans*-1 isomer, which can only be generated from *anti-cis*-1 / -2- or *syn-trans*-2 isomers from a thermal isomerization around the central double bond or thermal helix inversion. This was observed by the product amounts at 25 °C. Measurements in toluene-*d*<sub>8</sub> observed the *anti-cis*-1 signal at -20 °C to 0 °C while *syn-trans*-2 disappeared completely at -40 °C (due to its low thermal stability or caused by signal broadening, see Figure 263).

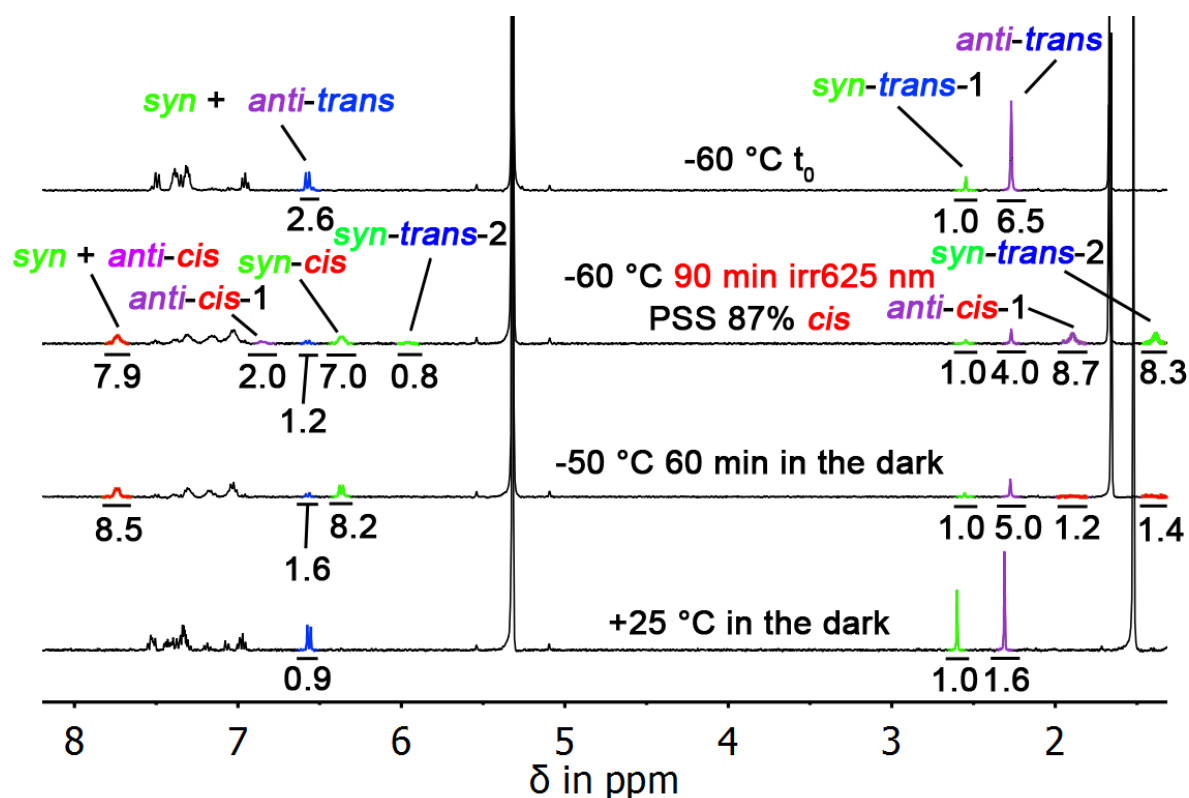


Figure 261: <sup>1</sup>H-NMR spectra obtained after the irradiation of a 1.0 / 6.5 *syn* / *anti* isomer mixture of indigo **64** to the *anti-cis* and *syn-cis* isomers in dichloromethane-*d*<sub>2</sub> at -60 °C and subsequent behavior in the dark at various temperatures. Integrals for indicated signal areas are given below the respective peak. A PSS consisting of 87% *cis* isomers can be obtained (relative to all *trans* isomers).

Coincident generation of *syn*- and *anti-cis-1* / *syn-trans-2* isomers can be observed. Starting from 1.0 / 6.5 *syn*- / *anti-trans* (87%), a 1.0 / 4.0 ratio of *syn*- / *anti-trans* (80%) can be obtained after irradiation, indicating a faster photoinduced turn-over rate for the *anti-trans* isomer which can be caused by its higher abundance or quantum yield. Thermal annealing of the *anti-cis-1* / *syn-trans-2* isomers at -50 °C showed a slight shift towards a 1.0 / 5.0 ratio of *syn*- / *anti-trans* (83%), which indicates back-conversion of *anti-cis-1*- or *syn-trans-2*- towards the *anti-trans* isomer. This is suggested by the *syn-cis* isomer not being able to contribute to the *anti-trans* isomer at this temperature due to its 20.7 kcal/mol double bond isomerization barrier. After irradiation, 13% of *syn*- + *anti-trans* isomers ( $1.2 / (1.2 + 7.9) * 100 = 13\%$ ) are obtained and subsequent thermal annealing step at -50 °C yielded 16% of *syn*- + *anti-trans* isomers ( $1.6 / (1.6 + 8.5) * 100 = 16\%$ ). The rise of the *anti-trans* isomer population by 3% (80% *anti-trans* at -60 °C, 83% *anti-trans* at -50 °C) can be quantitatively accounted to the 3% decrease of 25% *anti-cis-1* / *syn-trans-2* species ( $(2.0 + 0.8) / (7.0 + 2.0 + 0.8) * 0.87 * 100$ ) to 22% of *anti-cis*

1 / *syn-trans-2* species. This suggests a *photoinduced extended Hula-Twist (PEHT)* motion, as all other reaction trajectories would not lead to the observed products.

The *syn-cis-* to *syn-* + *anti-trans* isomer ratio remains constant at ~81% *syn-cis* isomer ( $7.0 * 3 / (7.0 * 3 + 1.0 + 4.0) * 100 = 80.8\%$ ), ( $8.2 * 3 / (8.2 * 3 + 1.0 + 5.0) * 100 = 80.4\%$ ) throughout the thermal reaction at -50 °C in the dark. This supports a *thermal extended Hula-Twist (TEHT)* reaction of 3% *anti-cis-1* / *syn-trans-2* isomers to the *anti-trans* isomer. The residual 22% of *anti-cis-1* / *syn-trans-2* isomer are converted to the *syn-trans-1* isomer between -50 °C and 25 °C. The *syn-trans-1* isomer was the observed product at -50 °C starting from irradiation of the *syn-trans-1* to the *anti-cis-2* isomer. For *anti-trans*, this is not the case as *anti-cis-1* / *syn-trans-2* is directly formed and partially converted back to the *anti-trans* state. A selectivity of the photo- and thermal reactions to the respective start- and end states can be observed.

Heating to 25 °C in the dark resulted in a large population shift from 83% *anti-trans* to 61% *anti-trans* isomer, which could not be obtained by a thermal atropisomerization under these conditions, as the barrier in the *trans* state amounts to 23.6 kcal/mol. These results suggest the *syn-trans-1* isomer being generated from the residual 22% *anti-cis-1* / *syn-trans-2* isomers over a *cis* to *trans* double bond isomerization, which shifted the *syn-* / *anti-trans* ratio from 17% to 39% *syn-trans-1* isomer at 25 °C. *This shows that a minimum of 22% of anti-trans isomers was converted to the anti-cis-1- / syn-trans-2 form via PEHT.*

The methyl signals of the stable *syn-cis* isomer with expected relative peak intensities of 21.0 - 24.0 cannot be observed due to signal broadening (see Figure 254). Prolonged thermal stability at -50 °C and complete back reaction from *cis* to *trans* at 25 °C suggests the aromatic signals at 7.73 ppm and 6.36 ppm (green) to be associated towards the more stable *syn-cis* isomer.

Low temperature NMR measurements starting from an enriched *anti-trans* mixture of **64** in toluene-*d*<sub>8</sub> were carried out as this solvent showed shifting of the *anti-cis-1*- and disappearing of the *syn-trans-2* signals, resulting in presumably only the *anti-cis-1* signal between -60 °C and -20 °C (see Figure 263).

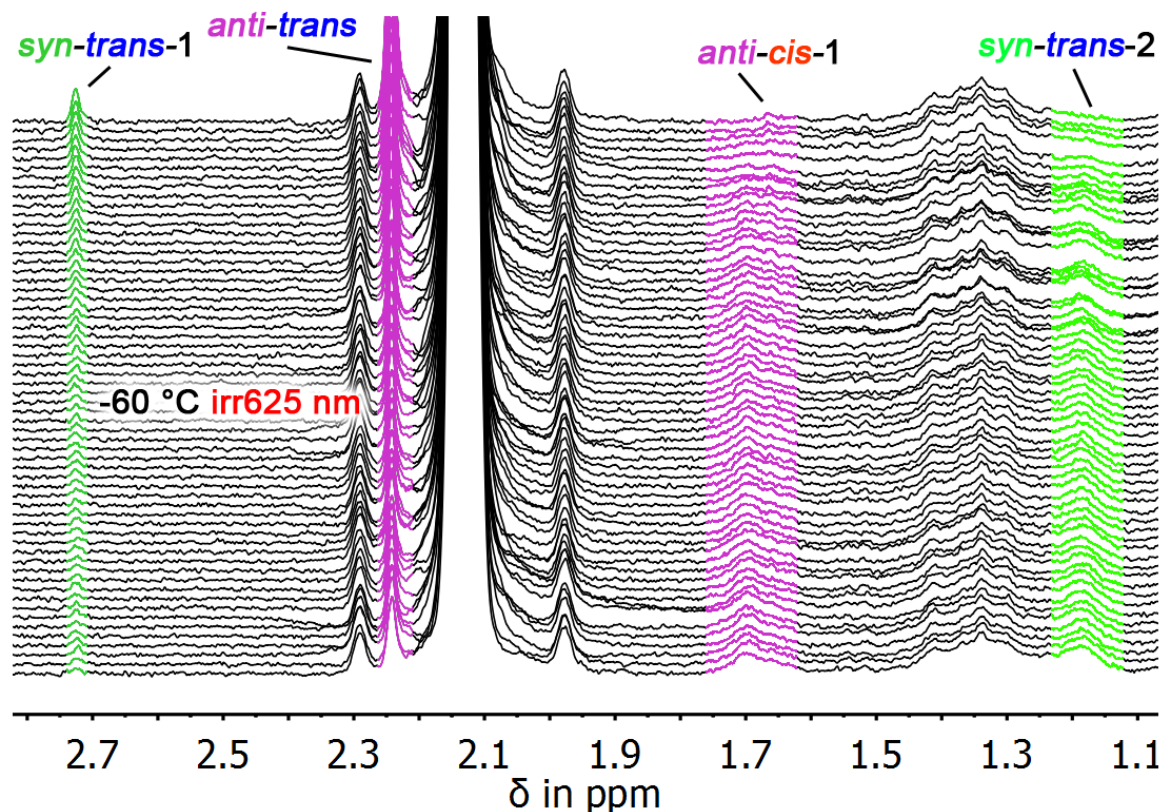


Figure 262: Aliphatic part after the irradiation of a 1.0 / 11.1 *syn-* / *anti* mixture of indigo **64** to the *anti-cis-* and *syn-cis* isomers in toluene-*d*<sub>8</sub> at -60 °C with 625 nm LED light. Two peaks can be observed, which is similar to the experiments in dichloromethane (see Figure 261). The detailed explanation of this behavior is given in Section 2.4.16, as two helicities are assumed to exist for *anti-cis-* and *syn-trans-* isomers.

Low temperature measurements at -60 °C in toluene showed the same population of both *anti-cis-1* and *syn-trans-2* isomers (see Figure 274). The *syn-cis* isomers cannot be observed due to signal broadening at low temperatures. Nonetheless, *syn-cis* isomer signals can be seen at -20 °C or 0 °C (Figure 263).

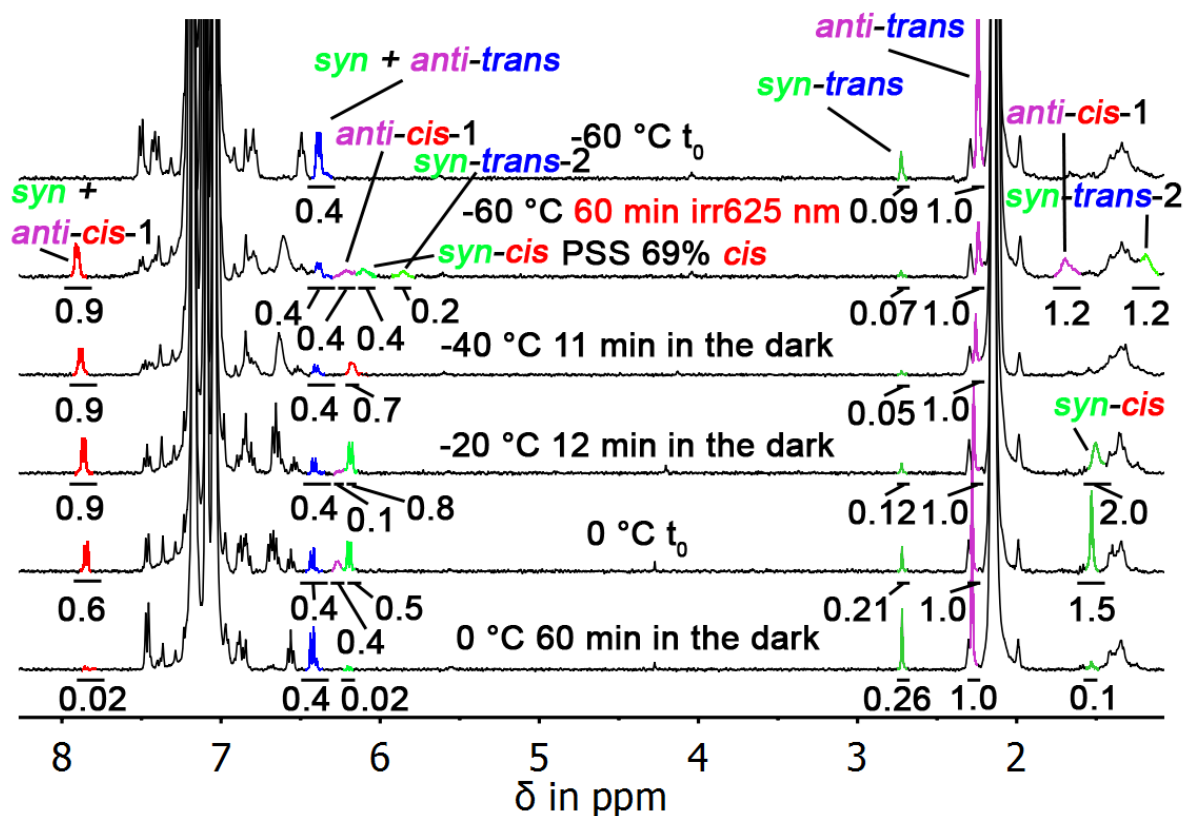


Figure 263:  $^1\text{H}$ -NMR spectra obtained after the irradiation of a 1.0 / 11.1 *syn*- / *anti* mixture of indigo **64** to the *anti-cis*- and *syn-cis* isomers in toluene- $d_8$  at  $-60\text{ }^\circ\text{C}$  and subsequent behavior in the dark at various temperatures. A PSS consisting of 69% *cis* isomers (relative to *syn-trans*-1 and *anti-trans* isomers) can be obtained at  $-60\text{ }^\circ\text{C}$ . Integrals for indicated signal areas are given below the respective peak.

Figure 263 shows the low temperature irradiation experiments with subsequent thermal annealing steps. A PSS consisting of 69% *cis* isomers can be reached. For the *anti-cis* isomers, two methyl group- (1.70 ppm = *anti-cis*-1, 1.19 ppm = *syn-trans*-2) and two indicative aromatic signals (6.21 ppm = *anti-cis*-1, 5.85 ppm = *syn-trans*-2) can be observed at  $-60\text{ }^\circ\text{C}$ . This pattern is also observed in dichloromethane (Figure 257). Starting from a 0.09 / 1.0 *syn*- / *anti-trans* (92%) isomer mixture, irradiation with 625 nm LED light at  $-60\text{ }^\circ\text{C}$  yielded a 0.07 / 1.0 *syn*- / *anti-trans* (94%) isomer mixture. Also, a slightly broadened *syn-cis* signal can be observed at 6.12 ppm at  $-60\text{ }^\circ\text{C}$ . The *anti-cis*-1 and *syn-cis* isomers amount to 28% each ( $((0.4) / (0.2 + 0.4 + 0.4)) * 0.69 * 100 = 28\%$ ) and the *anti-cis* isomer to 14% ( $((0.2) / (0.2 + 0.4 + 0.4)) * 0.69 * 100 = 14\%$ ) after irradiation. After heating to  $-40\text{ }^\circ\text{C}$ , all *anti-cis* signals disappear and the aliphatic *syn-cis* signal is still not visible due to signal broadening. However, the *syn*- to *anti-trans* ratio changed from 0.07 / 1.0 *syn*- / *anti-trans* (94%) to 0.05 / 1.0 *syn*- / *anti-trans* (95%). This could

be addressed in dichloromethane, as 3% of *anti-cis-1* / *syn-trans-2* isomers were converted to solely the *anti-trans* isomer. This should not be the case in toluene as the *anti-cis-1* isomer is stable up to 0 °C in contrast to the observations at -50 °C in dichloromethane. Heating to -20 °C shows only one signal for *anti-cis-1*- (6.18 ppm) and a novel signal for the *syn-cis* isomer (1.44 ppm), indicating that the *syn-trans-2* species to be thermally less stable than the *anti-cis-1* isomer. The *cis*-isomers remain at 69% ( $0.9 / (0.9 + 0.4) * 100 = 69\%$ ) with 61% *syn-cis* isomer ( $0.8 / 0.9 * 0.69 * 100 = 61\%$ ) and 8% of visible, broadened *anti-cis-1* isomer. The *syn-trans-2* signals disappeared completely, which can be attributed to its lower thermal energy barrier for the helix inversion compared to a double bond isomerization. Increasing the temperature to 0 °C enables the thermal *cis* to *trans* double bond isomerization. At the start of the 0 °C thermal annealing experiment, the *cis*-isomers amount to 60% ( $0.6 / (0.4 + 0.6) * 100 = 60\%$ ) with 27% of *anti-cis-1* isomer ( $0.4 / (0.4 + 0.5) * 0.6 * 100 = 27\%$ ) and 33% of *syn-cis* isomer ( $0.5 / (0.4 + 0.5) * 0.6 * 100 = 33\%$ ). The initial 42% (28% + 14%) of *anti-cis-1* - / *syn-trans-2* - and 28% of *syn-cis* isomer ratio was shifted to 27% *anti-cis*- and 33% *syn-cis* isomer, which is in accordance to the overall lower thermal stability of the *anti-cis-1*- and *syn-trans-2*-isomer compared to the *syn-cis* isomer. After 60 minutes of thermal annealing at 0 °C, an increase of *syn-trans-1* isomer from a 0.12 / 1.0 *syn*- / *anti-trans* (89%) to a 0.26 / 1.0 *syn*- / *anti-trans* (79%) ratio can be observed after the initial 60 minutes of irradiation at -60 °C. This suggests that a minimum of 10% *anti-cis-1* and/or *syn-trans-2* isomer was generated via PEHT at -60 °C, which is in accordance to the experiments in dichloromethane (Figure 261).



### 2.4.15 Symmetric chiral indigos - Second generation indigo **64** - Low temperature NMR Data - *Syn-trans-1* to *anti-trans* kinetic analysis

As measurements in toluene allowed for parallel generation and depletion of *syn-cis* and *anti-cis-2* isomers of indigo **64**, a temperature of  $-5\text{ }^{\circ}\text{C}$  was chosen to track all four isomers simultaneously.

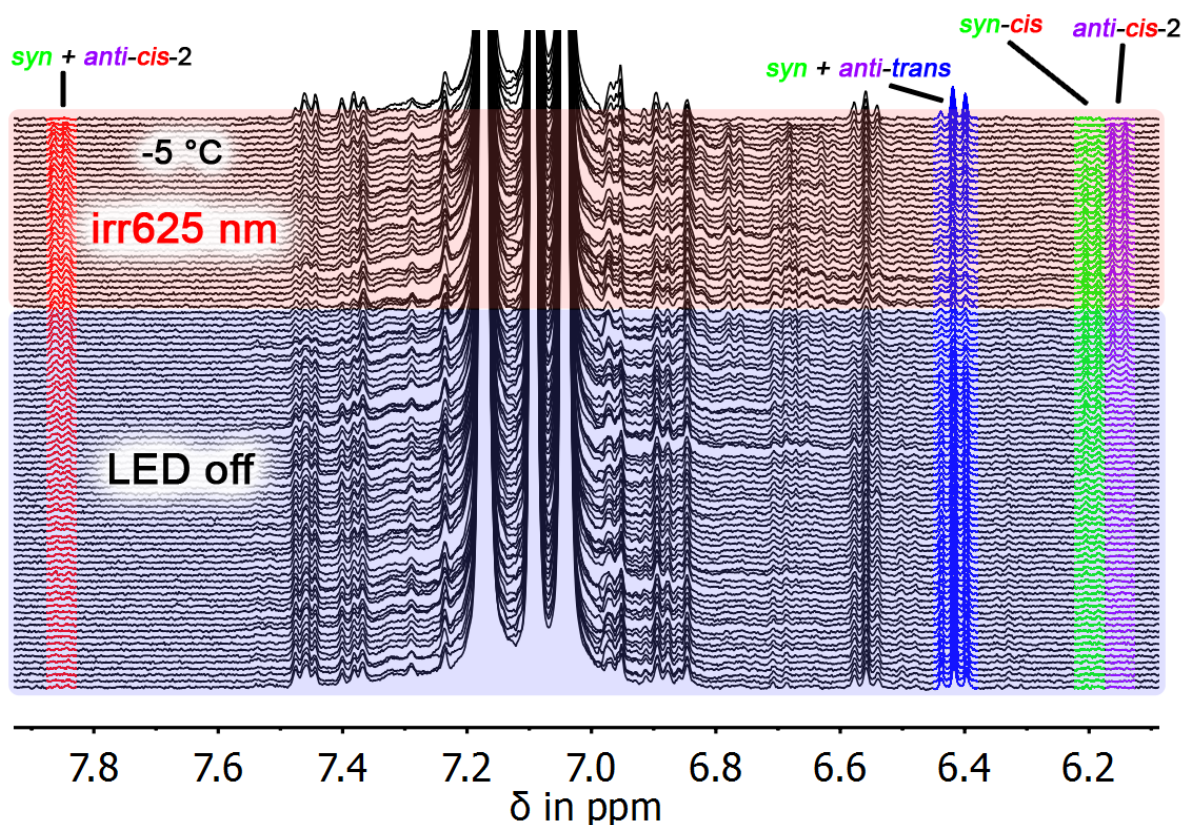


Figure 264:  $^1\text{H}$ -NMR spectra (aromatic part) of the irradiation and subsequent behavior in the dark of a 5 / 1 *syn-* / *anti-trans* isomer mixture of indigo **64** in toluene- $d_8$  at  $-5\text{ }^{\circ}\text{C}$  measured on a 400 MHz spectrometer. Each spectrum was measured with a 1 minute time interval. A PSS consisting of 73% *cis* isomers could be obtained. Subsequent measurements of the differently decaying *cis* isomers in the dark gave free activation enthalpies  $\Delta G^* = 18.5\text{ kcal/mol}$  with a half-life of 4.15 s at  $25\text{ }^{\circ}\text{C}$  for the *anti-cis-2*- and  $\Delta G^* = 19.4\text{ kcal/mol}$  with a half-life of 19.0 s at  $25\text{ }^{\circ}\text{C}$  for the *syn-cis* isomer. The decreasing *cis* isomer signals were assigned to the increasing *trans* isomer signals after the LED was turned off. Accumulation of the *anti-trans*- compared to the *syn-trans-1* isomer can be observed at 6.44 ppm.

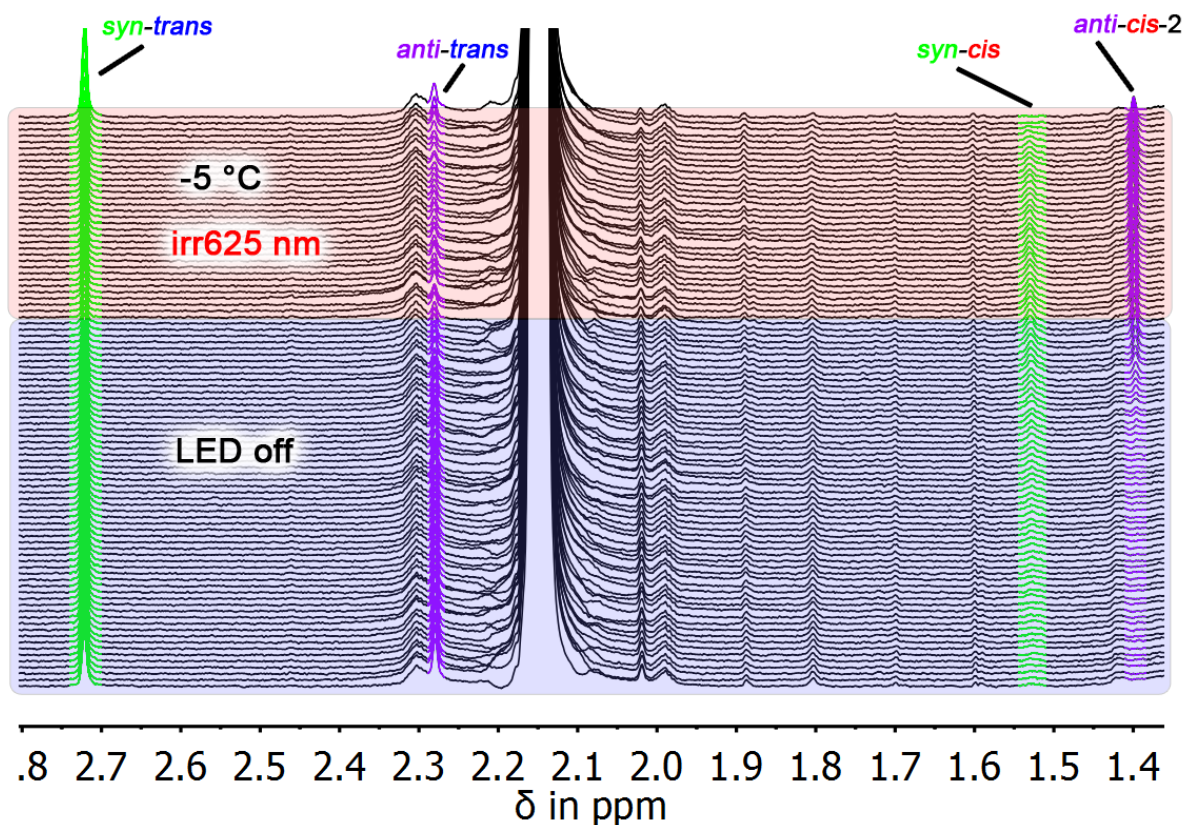


Figure 265: <sup>1</sup>H-NMR spectra (aliphatic part) of the irradiation and subsequent behavior in the dark of a 5 / 1 *syn-* / *anti-trans* isomer mixture of indigo **64** in toluene-*d*<sub>8</sub> at -5 °C measured on a 400 MHz spectrometer. Each spectrum was measured with a 1 minute time interval. A PSS consisting of 73% *cis* isomers could be obtained. Subsequent measurements of the differently decaying *cis* isomers in the dark gave free activation enthalpies  $\Delta G^* = 18.5$  kcal/mol with a half-life of 4.15 s at 25 °C for the *anti-cis-2* and  $\Delta G^* = 19.4$  kcal/mol with a half-life of 19.0 s at 25 °C for the *syn-cis* isomer. The decreasing *cis* isomer signals were assigned to the increasing *trans* isomer signals after the LED was turned off. Accumulation of *anti-trans* isomer can be observed at 2.28 ppm.

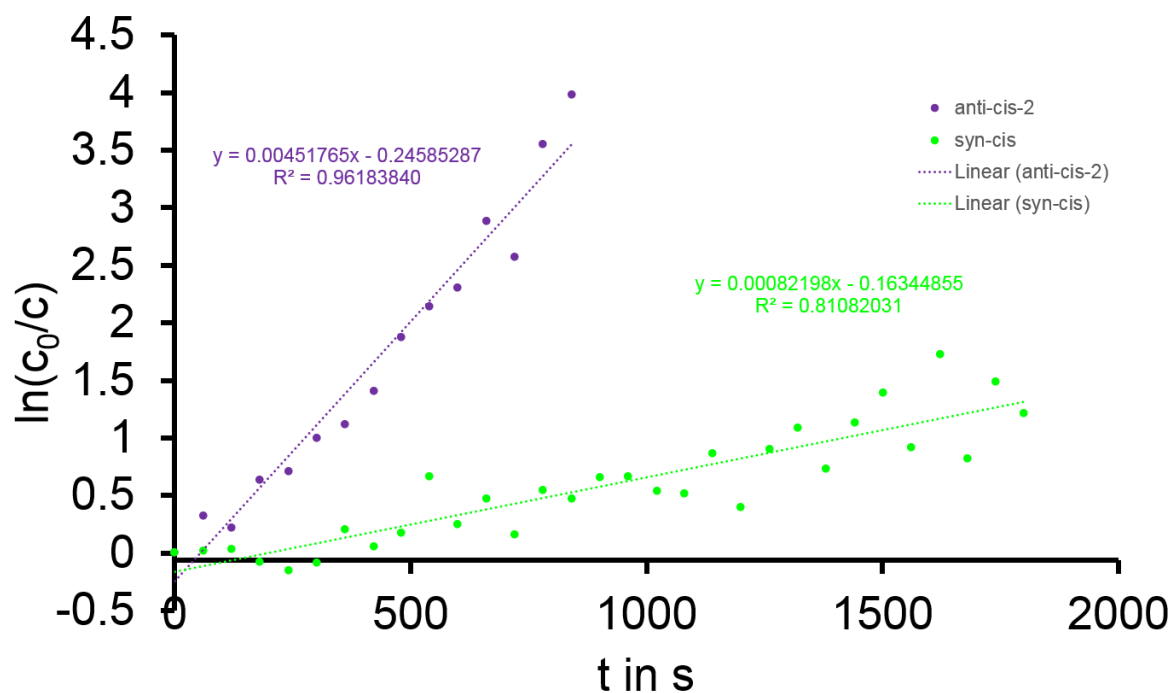


Figure 266: Linearized first order kinetic plots of *anti-cis-* (violet) and *syn-cis-64* (green) in toluene- $d_8$  at 0 °C derived from Figure 265 above. The thermal *cis* to *trans* isomerization barriers were determined at 18.5 kcal/mol with a half-life of 4.15 s at 25 °C for the *anti-cis-* and 19.4 kcal/mol with a half-life of 19.0 s at 25 °C for the *syn-cis* isomer. Used formulas and equations are given in Section 2.2.20.

As previously shown, a large increase of the thermal *cis* to *trans* isomerization barrier from 15.8 kcal/mol to 18.5 kcal/mol for the *anti-cis-2* isomer can be observed in toluene or other non-chlorinated, apolar solvents like 83 / 17 heptane / ethyl acetate mixtures.

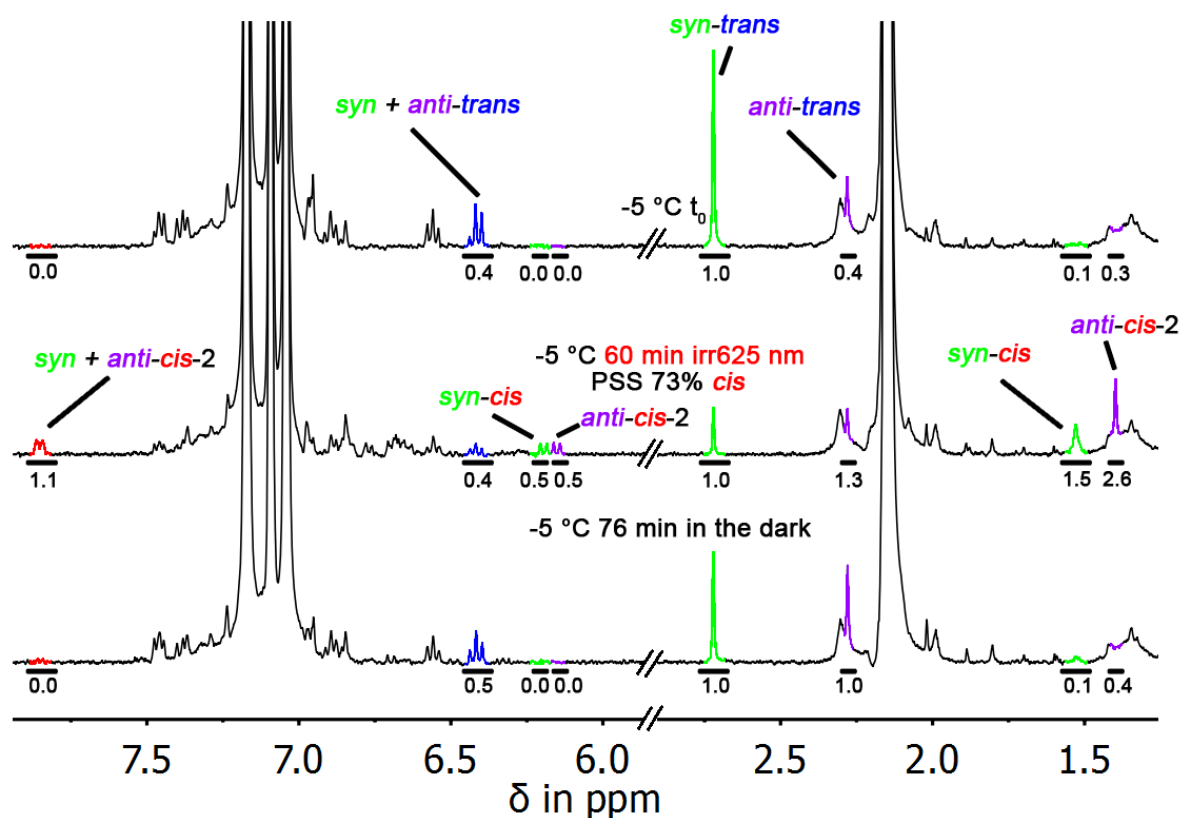


Figure 267:  $^1\text{H}$ -NMR spectra obtained after the irradiation of a 5.0 / 1.0 *syn*- / *anti* mixture of indigo **64** to the *anti-cis* and *syn-cis* isomers in toluene- $d_8$  at  $-5\text{ }^\circ\text{C}$  and subsequent behavior in the dark. A PSS consisting of 73% *cis* isomers can be obtained at  $-5\text{ }^\circ\text{C}$ , which is comparable to the observed PSS consisting of 77% *cis* isomers in dichloromethane- $d_2$  at  $-80\text{ }^\circ\text{C}$ . Integrals for indicated signal areas are given below the respective peak.

Figure 267 shows the low temperature irradiation NMR experiments with subsequent thermal annealing steps. After irradiation at  $-5\text{ }^\circ\text{C}$ , a PSS consisting of 73% *cis* isomers can be obtained. An (almost) 1 / 1 *syn-cis*- / *anti-cis-2* isomer ratio can be obtained at 6.19 - 6.15 ppm after 60 min of irradiation, which can also be observed regardless if starting from the *syn-trans*- or *anti-trans* isomers. These 1 / 1 equilibria are supposedly obtained as the reaction trajectory of the fast photokinetic and the thermally less stable *anti-cis-2* isomer (see Figure 249 and Figure 255, generated from the more abundant *syn-trans-1* isomer) branches towards the more stable *syn-cis* isomer and the *syn-trans* isomer as starting point. Figure 268 shows these findings in detail.

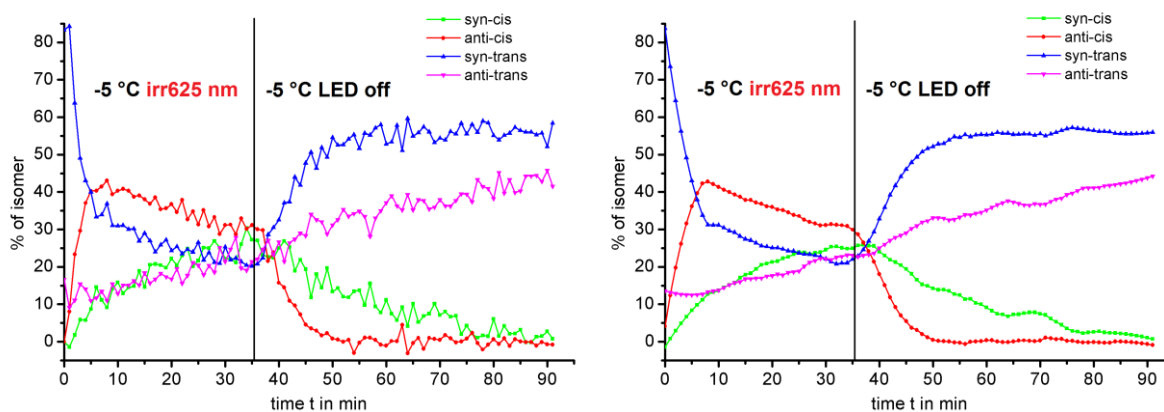


Figure 268: Plots of the respective percentages of all four isomers from  $^1\text{H-NMR}$  measurements with *in situ* irradiation and subsequent thermal annealing conditions of indigo **64** in toluene- $d_8$  recorded on a 400 MHz NMR spectrometer at  $-5\text{ }^\circ\text{C}$ . Raw data (left) and smoothed data (right, *Savitzky-Golay-Filter*, 20 points of window) is shown for easier visibility of the reaction rates, the immediate stopping of the photokinetics in the dark can be better demonstrated with the raw data.

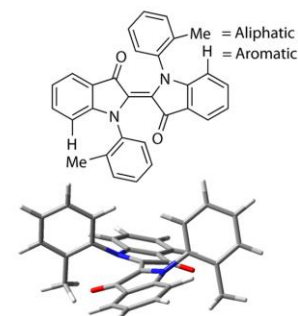
Figure 268 shows the fast *anti-cis-2* isomer (red) generation from the rapidly decreasing *syn-trans-1* isomer (blue) when irradiated with 625 nm LED light. The *syn-cis* isomer (green) is immediately generated from the *anti-cis-2* isomer (violet), which peaks at 45% total abundance after 10 minutes of irradiation. Subsequently, a photostationary *anti-cis-2* to *syn-trans-1* isomeric ratio is established. Both populations decrease at roughly the same rate as the *anti-cis-2* isomer population is branched towards the stable *syn-cis* isomer, which is hence converted to the steadily increasing *anti-trans* isomer population. Switching off the LED immediately stops the *syn-cis* isomer generation and the thermal *anti-cis-2*- to *syn-trans-1* isomer reaction pathway gains full speed (Better visible in Figure 268, left). The *syn-cis*- to *anti-trans* isomer reaction proceeds at a slower rate and generates only *anti-trans* isomer as long as *syn-cis* isomers are available.

If the calculated atropisomerization barrier of 19.11 kcal/mol from the *anti-cis-2*- to the *syn-cis* isomer is assumed to be correct and the favored *anti-cis-2*- to *syn-trans-1* isomer double bond isomerization barrier amounts to 18.5 kcal/mol, then a by 0.61 kcal/mol increased transition state energy barrier towards the disfavored *anti-cis-2*- to *syn-cis* isomer trajectory must be overcome. The  $k$  values for both pathways amount to  $0.045\text{ s}^{-1}$  (DBI) and  $0.015\text{ s}^{-1}$  (SBR), suggesting a three-fold faster *anti-cis-2*- to *syn-trans-1* reaction rate, quickly depleting the available *anti-cis-2* isomer towards the *syn-trans-1* isomer, showing only a little thermal

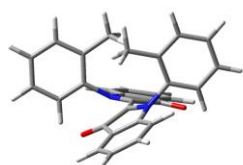
conversion rate towards the *syn-cis* state in the dark. This is seen in Figure 268 above, as no or just minimal amounts of *syn-cis* isomer are generated after the switching off the light source. Another indication for this pathway is its strong thermal dependence as the *anti-cis-2* to *syn-cis* isomer trajectory is not observed at lower temperatures, which is indicative for a thermal reaction.

## 2.4.16 Symmetric chiral indigos - Second generation indigo 64 - DFT

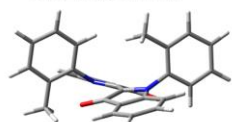
## overview



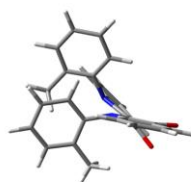
$(R_a)-(R_a)-(P)$ -*syn-trans*-1  
0.00 kcal/mol



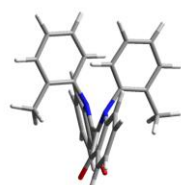
$(S_a)-(S_a)-(P)$ -*syn-trans*-2  
3.92 kcal/mol



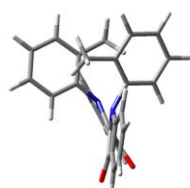
$(S_a)-(R_a)-(P)$ -*anti-trans*  
2.11 kcal/mol  
(*meso*)



$(S_a)-(R_a)-(P)$ -*syn-cis* (*meso*)  
8.76 kcal/mol



$(R_a)-(R_a)-(M)$ -*anti-cis*-1  
8.89 kcal/mol



$(S_a)-(S_a)-(M)$ -*anti-cis*-2  
9.33 kcal/mol

Table 12: Overview of the observed and calculated properties of the indigo **64** isomers (Measurements in toluene).

ECD	Ar ms.	Ar. cl.	Al. ms.	Al. cl.	Atrop.	DB
Yes	6.36	6.51	2.65	2.73	23.6 ms.	-
Global thermodynamic minimum, 5 / 1 <i>syn-</i> / <i>anti-trans</i> mixture, 625 nm irradiation at -60 °C yields exclusively <i>anti-cis</i> -2 isomer (DBI).						
Yes*	5.85	6.44	1.19	1.61	26.8 cl.	-
Disfavored <i>syn-trans</i> isomer, generated at -60 °C from a possibly incomplete PEHT or direct photoinduced SBR.						
No	6.38	6.43	2.23	2.32	24.5 cl.	-
Local minimum <i>trans</i> structure 5 / 1 <i>syn-</i> / <i>anti-trans</i> mixture, generated from <i>syn-cis</i> (DBI) and <i>anti-cis</i> -1 (TEHT).						
No	6.19	6.26	1.47	1.68	19.1 cl.	19.4 ms.
Global thermodynamic minimum for all <i>cis</i> isomers, generated from <i>anti-trans</i> (DBI) or <i>anti-cis</i> isomers (SBR).						
Yes*	6.27	6.45	1.65	1.92	19.1 cl.	18.5 ms.
Favored <i>anti-cis</i> isomer, generated exclusively from the <i>anti-trans</i> isomer (PEHT).						
Yes	6.09	6.18	1.43	1.39	20.1 cl.	18.5 ms.
Higher energy <i>anti-cis</i> isomer, generated exclusively from <i>syn-trans</i> (DBI).						

Ar. = aromatic-, Al. = aliphatic NMR shift in ppm, ms. = measured, cl. = calculated, Atrop. = Atropisomerization energy barrier ( $\Delta G^*$  in kcal/mol), DB = *cis-trans* energy barrier ( $\Delta G^*$  in kcal/mol)

Explanation of the abbreviations in Table 12: ms. = measured, cl. = calculated, ECD = electronic circular dichroism visible, Ar. = aromatic-, Al. = aliphatic NMR shift in ppm, \* = theoretically visible if isolated, can only be generated as racemate by a photoreaction, DBI = central double bond isomerization, SBR = chiral single bond rotation = atropisomerization, TEHT = thermal extended Hula-Twist, PEHT = photoinduced extended thermal Hula-Twist.

DFT calculations of transition states of indigo **64** are shown in Figure 269 below.

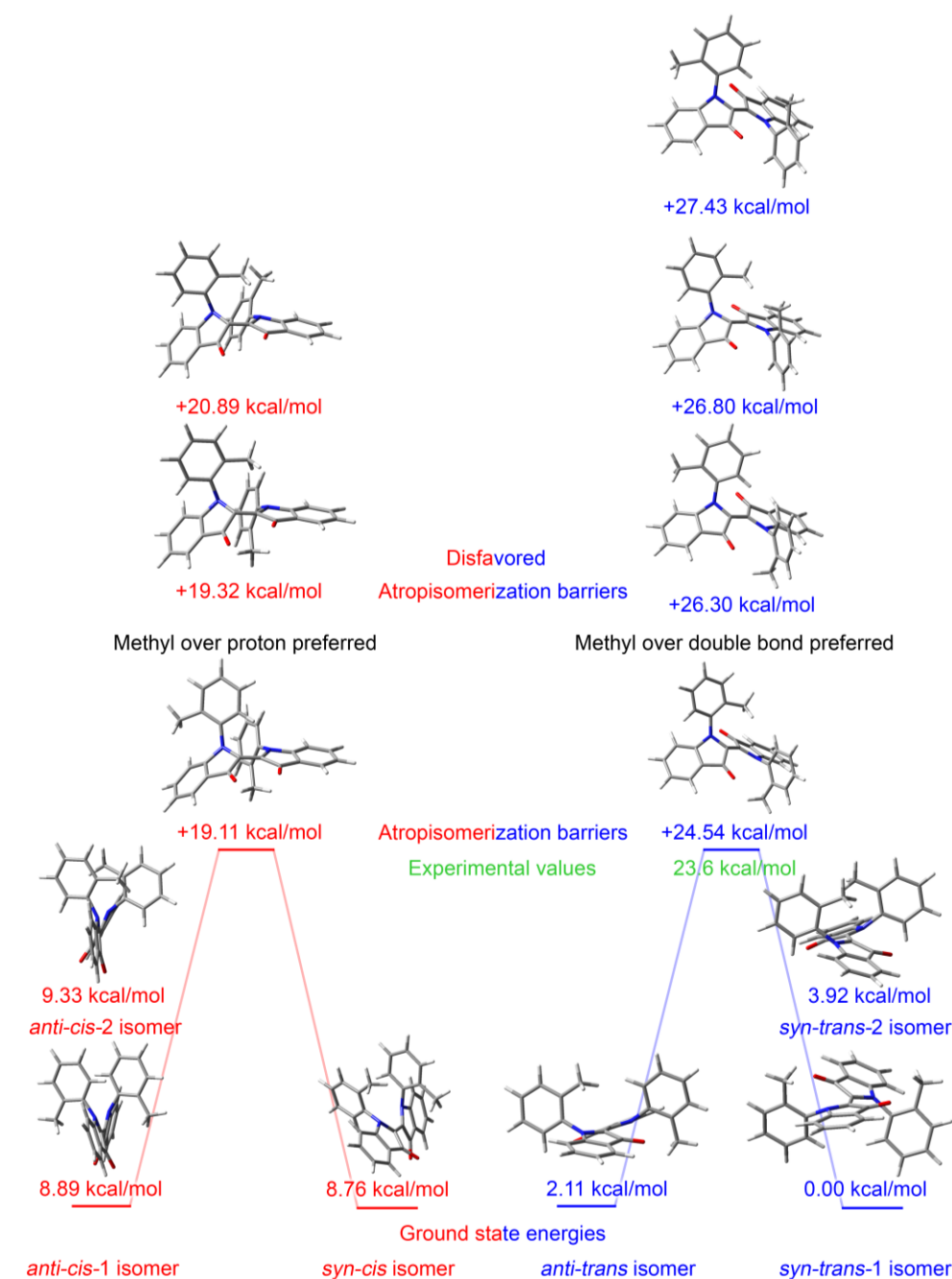


Figure 269: Calculated ground and transition state structures and energies of indigo **64** at the B3LYP/6-311+G(d,p) level of theory. Transition states for seven out of eight possible atropisomerizations could be found. The other possible transition state



for the *cis* isomer did not converge after several attempts and tweaks. The “+” sign in front of transition state values indicates the energy difference with respect to the lowest ground state of respective *cis* or *trans* isomers. Missing experimental data for the *cis* isomer makes it difficult to assign the reported transition state to be high or low in energy or to address the preferred directionality for this rotation.

Benchmarking of different functionals was carried out to test the robustness of the applied calculational methods.

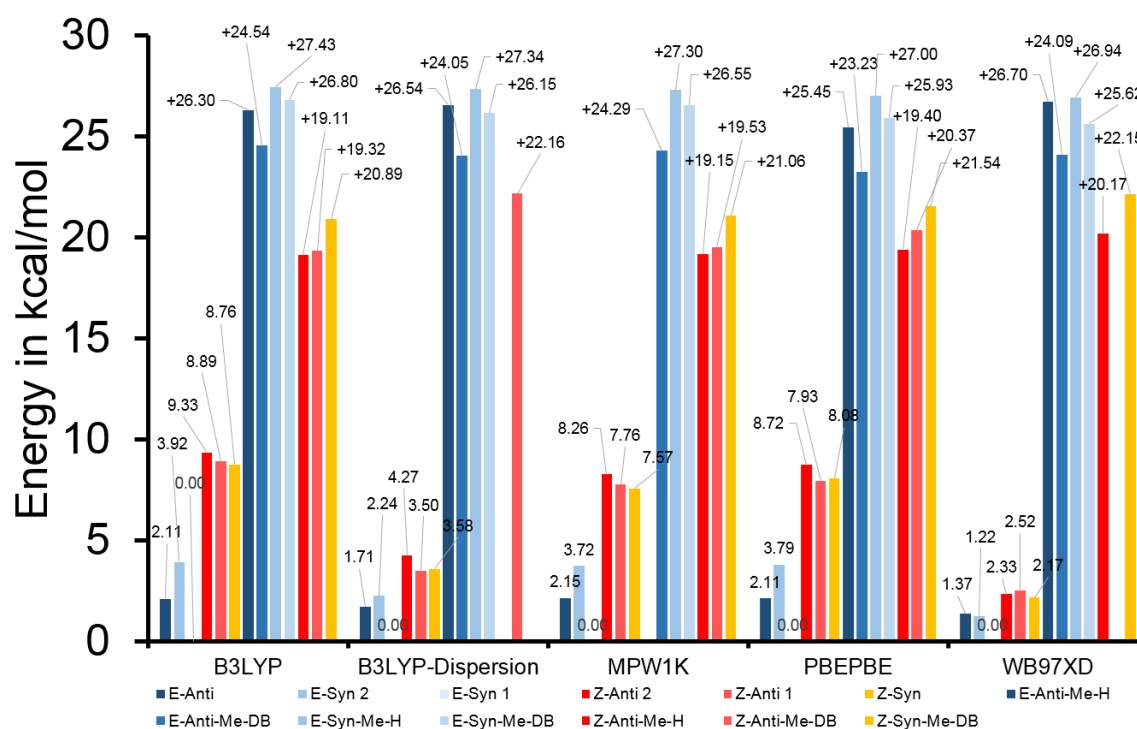


Figure 270: Benchmarking results for ground and transition states of indigo **64** using different DFT functionals for the 6-311+G(d,p) basis set. The “+” sign in front of transition state values indicates the energy difference with respect to the lowest ground state of respective *cis* or *trans* isomers. Missing transition states did not converge after several attempts and tweaks. “E” represents the *trans*- and “Z” the *cis* isomeric state. “E-Syn-1” represents the lowest ground state for all functionals in the *trans* state while “Z-Syn” constitutes the lowest energy *cis* state in most cases. “E-anti-Me-DB” shows the lowest transition state energy in all cases and suggests a rotation of an *ortho*-methyl group over the central double bond in the *trans* state. “Z-Anti-Me-H” shows the energetically lowest transition state for the *cis* isomers and suggests that the *ortho*-methyl group is rotated over its adjacent indoxyl core proton.

Benchmarking of different functionals and basis sets was carried out on the ground states to test the robustness of the applied calculational methods.

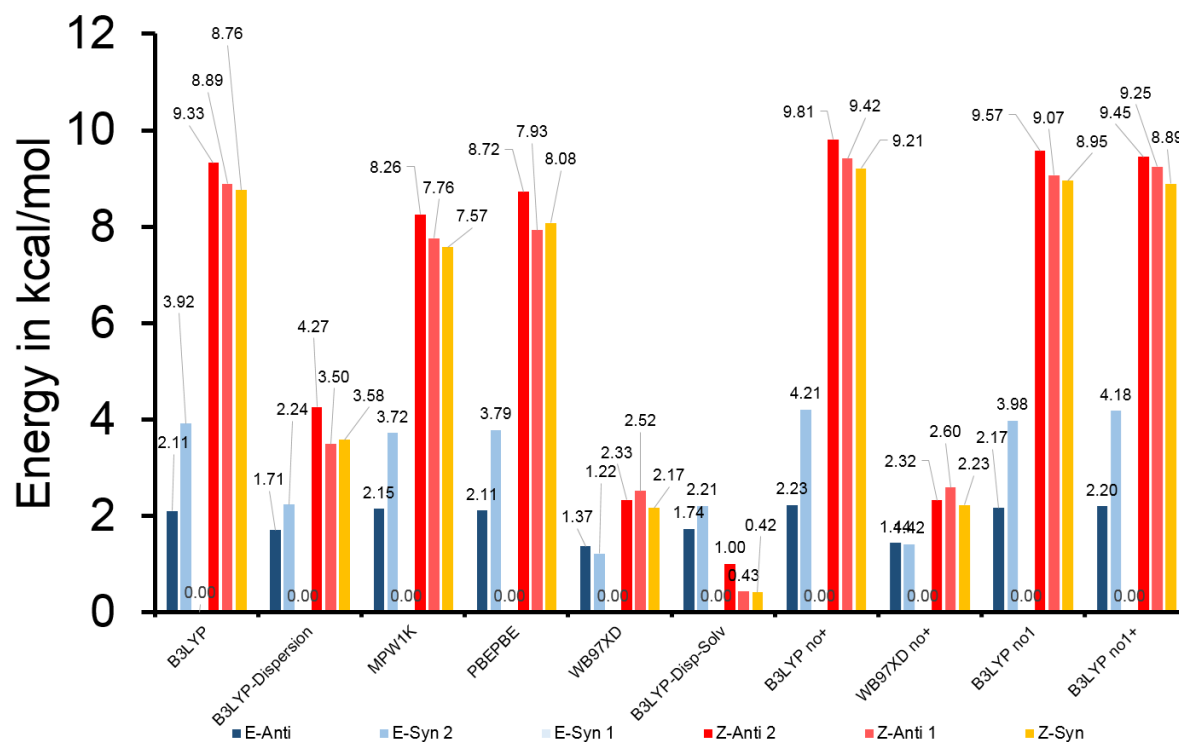


Figure 271: Benchmarking results for ground states of indigo **64** using different DFT functionals and basis sets. “E” represents the *trans*- and “Z” the *cis* isomeric state. “E-Syn-1” represents the lowest ground state for all functionals in the *trans* state while “Z-Syn” constitutes the lowest energy *cis* state in most cases. The “no+” indicator represents the 6-311G(d,p) *Pople* basis set, the “no1” indicator the 6-31+G(d,p) basis set and the “no1+” indicator the 6-31G(d,p) basis set. Functionals with dispersive corrections ( $\omega$ B97XD, B3LYP-GD3BJ, indicated as “Dispersion”, “Disp”) and PCM solvent modelling (“B3LYP-Disp-Solv”, dichloromethane) show lower differences between the *trans* and *cis* isomer ground states.

Overall, a good consistency of ground- and transition state values over all tested functionals and basis sets can be observed. The experimental values are also consistent with the calculated ground states and free activation enthalpies.

## 2.4.17 Symmetric chiral indigos - Second generation indigo **64** - DFT NMR

To further approve the assignment of *syn-trans*-1-, *syn-trans*-2-, *anti-trans*, *syn-cis*- and *anti-cis*-1- and -2 signals of indigo **64**, DFT calculations of the  $^1\text{H-NMR}$  shifts was carried out utilizing the gauge-including atomic orbital (GIAO) method.

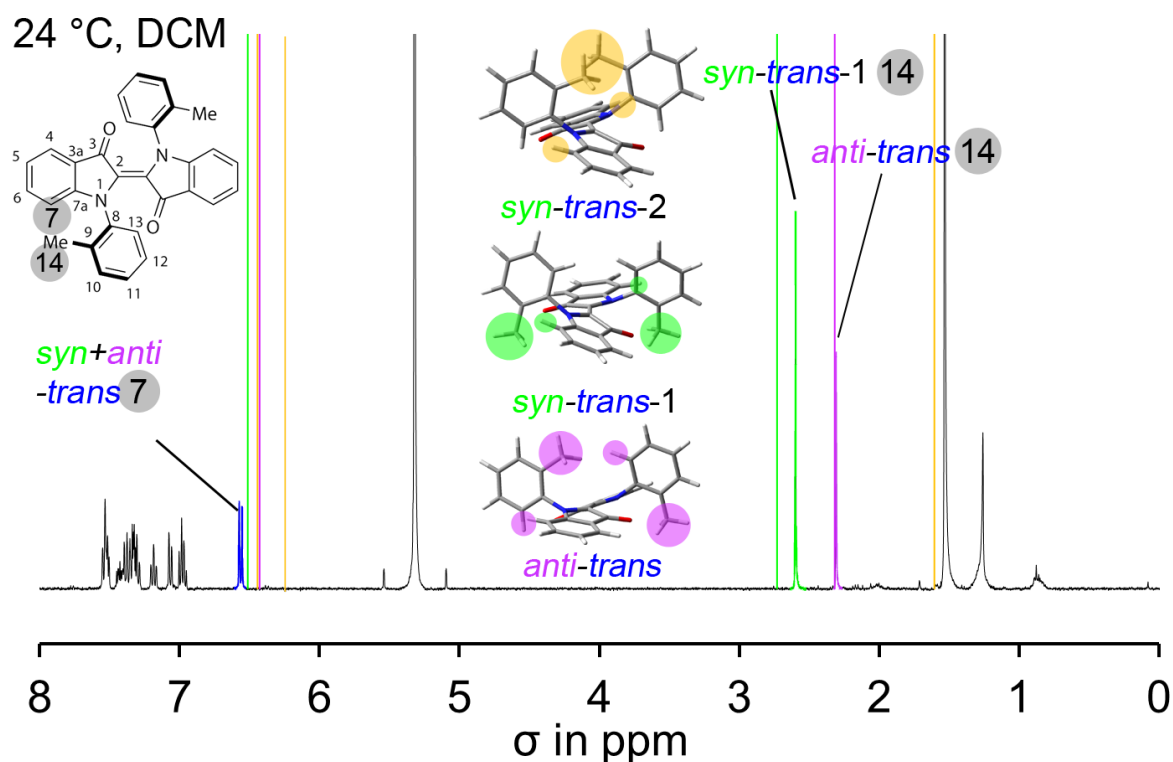


Figure 272:  $^1\text{H-NMR}$  spectra of a 3 / 2 *syn*- / *anti-trans* isomer mixture of **64** in dichloromethane- $d_2$  (24 °C) with overlaid calculated  $^1\text{H-NMR}$  shifts (colored lines) at the B3LYP/6-311+G(d,p) level of theory using the gauge-including atomic orbital (GIAO) method (TMS B3LYP/6-311+G(2d,p), GIAO as reference for zero). The reported shifts agree well with the experimentally obtained signals and the previous assignment of *trans* isomers. The signals corresponding to the yellow line should not be observable as the *syn-trans*-2 isomer is supposedly not stable at 24 °C. The yellow and violet lines within the aromatic part are almost overlapping.

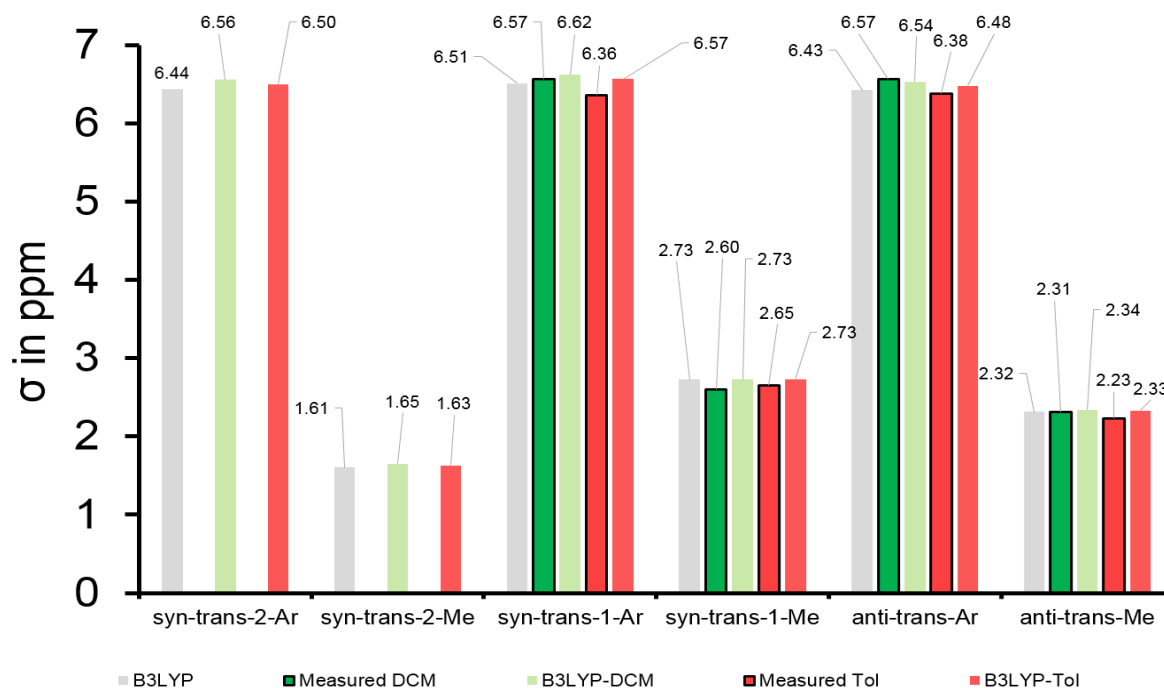


Figure 273: Benchmarking of  $^1\text{H}$ -NMR shifts at the B3LYP/6-311+G(d,p) level of theory using the gauge-including atomic orbital (GIAO) method (TMS B3LYP/6-311+G(2d,p), GIAO as reference for zero) and comparison to measured  $\sigma$ -values (framed in black). The shifts for *syn-trans-2* could not be measured as this species is not stable at ambient temperatures and was not observed at low temperatures as thermal- or photoproduct in dichloromethane or toluene. Overall, a good agreement for polarizable continuum model (PCM) solvent corrections (dichloromethane, toluene) was obtained.

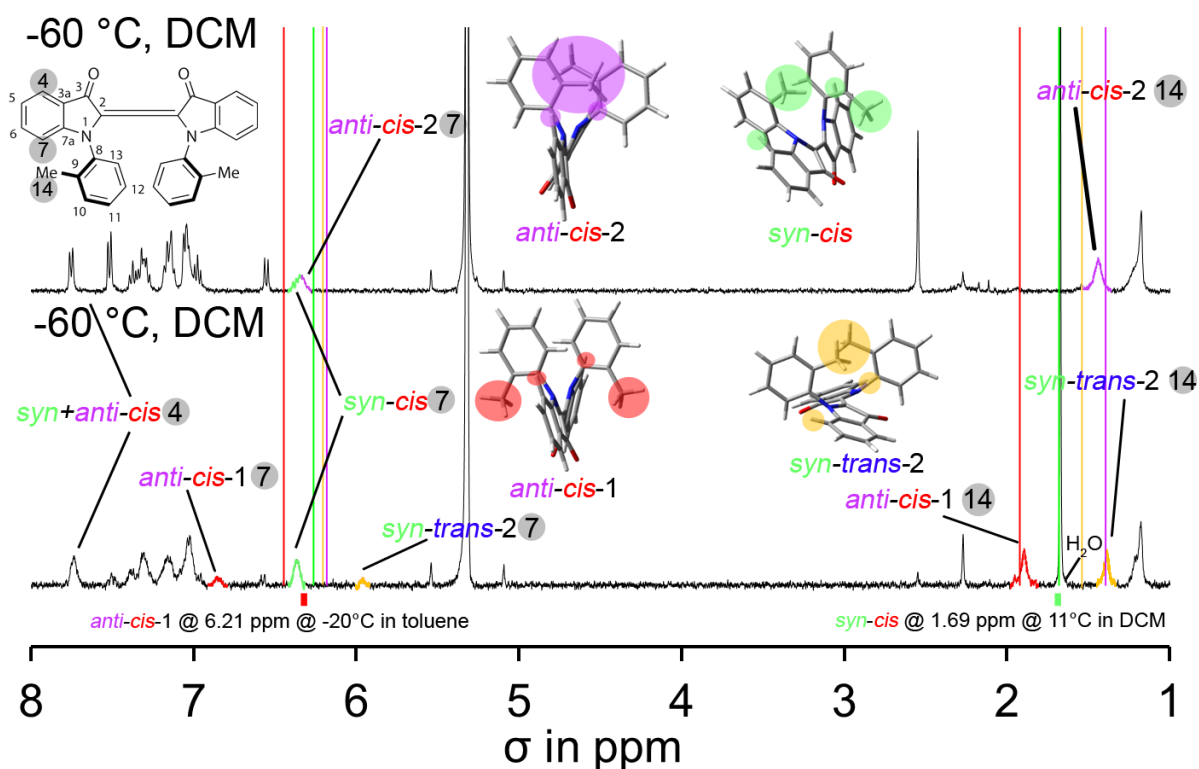


Figure 274: <sup>1</sup>H-NMR spectra of an irradiated 5 / 1 *syn*- / *anti-trans* isomer mixture (top) and an irradiated 1 / 6.5 *syn*- / *anti-trans* isomer mixture (bottom) of **64** in dichloromethane-*d*<sub>2</sub> (-60 °C) with overlaid calculated <sup>1</sup>H-NMR shifts (colored lines) at the B3LYP/6-311+G(d,p) level of theory using the gauge-including atomic orbital (GIAO) method (TMS B3LYP/6-311+G(2d,p), GIAO as reference for zero). The reported shifts agree well with the experimentally obtained signals and the previous assignment of both *cis* isomers in the aliphatic region. The signals in the aromatic regions agree qualitatively to the calculation with a matching order of observed and calculated shifts. The aliphatic signal for the *syn-cis* isomer can only be observed at temperatures above -20 °C (Figure 263, toluene and Figure 251, dichloromethane) at 1.69 ppm due to signal broadening and is indicated below the spectrum. The signals of *anti-cis-1* can only be observed in toluene (from -20 °C to 0°C, Figure 263) and are indicated below the spectrum. The *syn-trans-2* signal disappears at -50 °C.

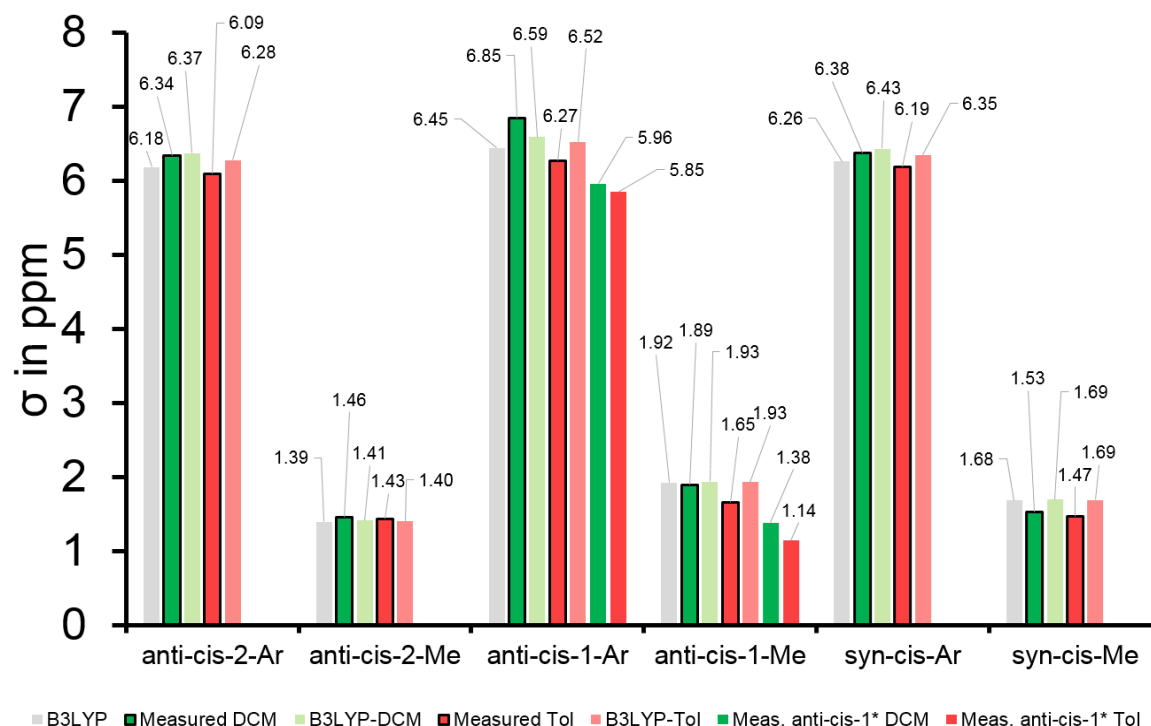


Figure 275: Benchmarking of  $^1\text{H}$ -NMR shifts of indigo **64** at the B3LYP/6-311+G(d,p) level of theory using the gauge-including atomic orbital (GIAO) method (TMS B3LYP/6-311+G(2d,p), GIAO as reference for zero) and comparison to measured  $\sigma$ -values (framed in black). The additional signals of *anti-cis-1* aromatic (green, red, not framed) for and aliphatic regions is also displayed. Overall, a good agreement for polarizable continuum model (PCM) solvent corrections (dichloromethane, toluene) was obtained.

The calculated  $^1\text{H}$ -NMR shifts are in accordance to the previous assignment of isomers, the additionally observed *syn-trans-2* signal is assumed to be populated by a single bond rotation caused by an incomplete photoinduced extended Hula-Twist, see Section 2.4.22. Another possible explanation is an edge-to-face conformation of the chiral aryls (see Figure 260) of the *anti-cis-1* isomer, which are accessed exclusively by the photoinduced extended Hula-Twist reaction trajectory and are only stable below  $-60\text{ }^\circ\text{C}$ . This can be observed in Figure 263, as annealing the sample from  $-60\text{ }^\circ\text{C}$  to  $-20\text{ }^\circ\text{C}$  (toluene) converts both aromatic *anti-cis-1* / *syn-trans-2* signals at 6.16 ppm and 5.81 ppm into one signal at 6.18 ppm from  $-20$  to  $0\text{ }^\circ\text{C}$ .

Besides the very good correlation of measured and calculated ECD spectra and measured and calculated NMR shifts, chemical intuition also supports the proposed assignment.

### 2.4.18 Symmetric chiral indigos - Second generation indigo 64 - $^1\text{H}$ -NMR-Shifts

Besides utilizing calculational assignments, the observation of  $^1\text{H}$ -NMR chemical shifts can also give substantial arguments for assigning *syn-cis*, *anti-cis-1* and *anti-cis-2* isomers to their respective signals. This is discussed by reference to Figure 274.

The *anti-cis-1* methyl groups are downfield shifted because of their proximity towards both electron-withdrawing carbonyls. The *syn-cis* methyl groups show an intermediate shift because on average, only one methyl group is in proximity of a carbonyl functionality and only one is adjacent to the shielding effect of the ring current of the other *ortho*-tolyl-moiety. At last, the *anti-cis-2* isomer methyl groups both experience a ring current from its folded conformation, leading to an upfield shift.

The diagnostic proton 7 can also serve as an indicator for the torsional strain on the *ortho*-tolyl moieties because of its different shift values for *syn-cis*, *anti-cis-1*-, *syn-trans-2* and *anti-cis-2* signals. Here, the outwards-pushing of methyl groups in close proximity to proton 7 will cause an upfield shift of proton 7. This is observed for *anti-cis-2*, which shows the overall largest upfield shift. The intermediate *syn-cis* isomer has the possibility for sterical evasion of one methyl group. The *anti-cis-1* isomer shows the farthest distance of its methyl groups towards proton 7 and is thus downfield shifted in comparison. These findings are in accordance to the calculated NMR parameters. However, the calculated energies suggest the *syn-cis* isomer as the energetically most stable conformer by 0.13 kcal/mol compared to the *anti-cis-1* isomer. The *anti-cis-2* isomer is disfavored by 0.57 kcal/mol compared to the *syn-cis* form.

These assessments are in accordance the theoretical and experimental observations for the occurrences of *cis*- isomers.

The *syn-trans-2* isomer is expected to display strongly upfield shifted methyl signals caused by the maximum methyl - carbonyl distance of all possible isomers. The sterical repulsion of both methyl groups should also cause significant upfield shifting of protons 7, which is, however, not predicted by the calculation. The latter does not differ in shift value for protons 7 compared to the other *trans* isomers. DFT energies, however, predict this isomer to be more stable by approx. 5 kcal/mol compared to all observed *cis*-isomers, which supports its existence energetically.

Additionally,  $^1\text{H}$ -NOESY spectroscopy at  $-60\text{ }^\circ\text{C}$  or  $-80\text{ }^\circ\text{C}$  could also show indications for the assignment of *anti-cis-2*, *anti-cis-1* and *syn-trans-2* signals to the respective isomers.

## 2.4.19 Symmetric chiral indigos - Second generation indigo 64 - Photoinduced *syn-trans*-1 to *anti-trans* pumping

Irradiation of a 5 / 1 *syn* / *anti-trans* isomer containing solution of indigo **64** with 625 nm at 27 °C yielded the <sup>1</sup>H-NMR spectra shown in Figure 276.

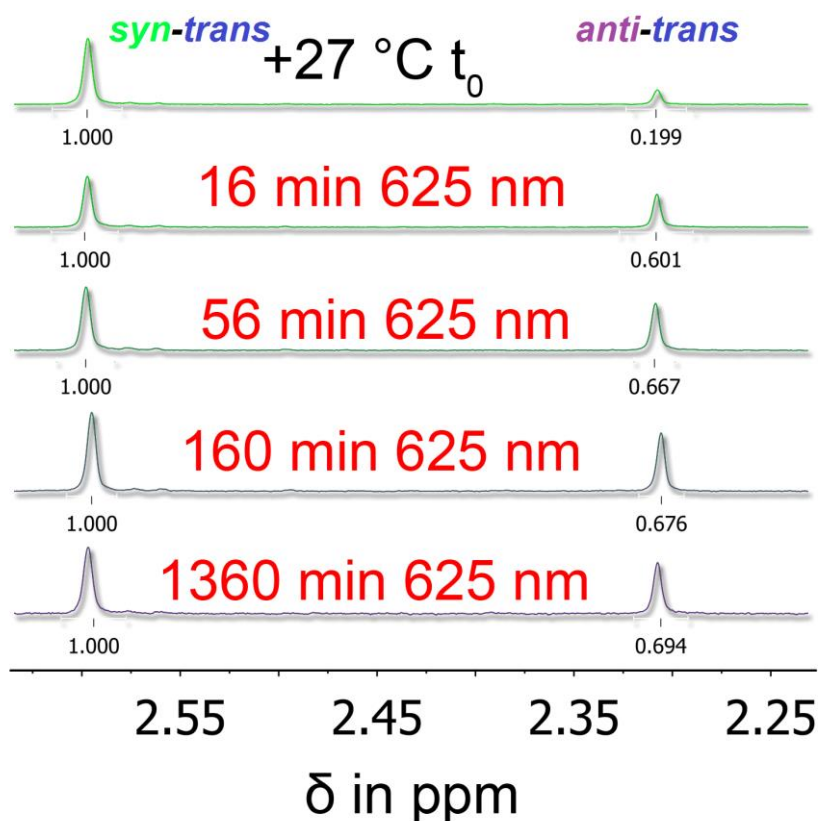


Figure 276: Irradiation of a thermally equilibrated 1.0 / 0.2 *syn*- / *anti* mixture of indigo **64** with 625 nm red light at 27 °C in dichloromethane-*d*<sub>2</sub>. A shift in population towards the *anti-trans* form can be observed, as a PSS consisting of a 1.0 / 0.7 *syn*- / *anti* ratio is obtained.

As indigo **64** showed photoinduced enrichment of its *anti-trans* isomer with red light against the thermal equilibrium in dichloromethane, toluene was also tested as solvent and yielded slightly better PSS ratios favoring the *anti-trans* isomer, see Figure 277 below.



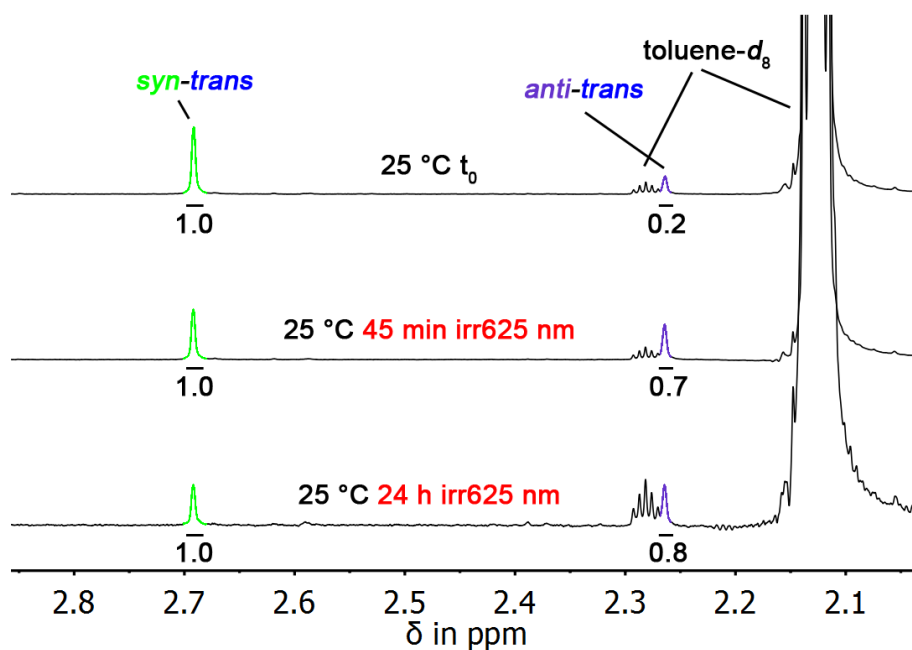


Figure 277: Irradiation of indigo **64** with 625 nm LED light in toluene- $d_8$  at 25 °C. An increase in *anti-trans* isomer population with slightly better photoinduced yields of the *anti-trans* isomer compared to dichloromethane solutions can be observed.

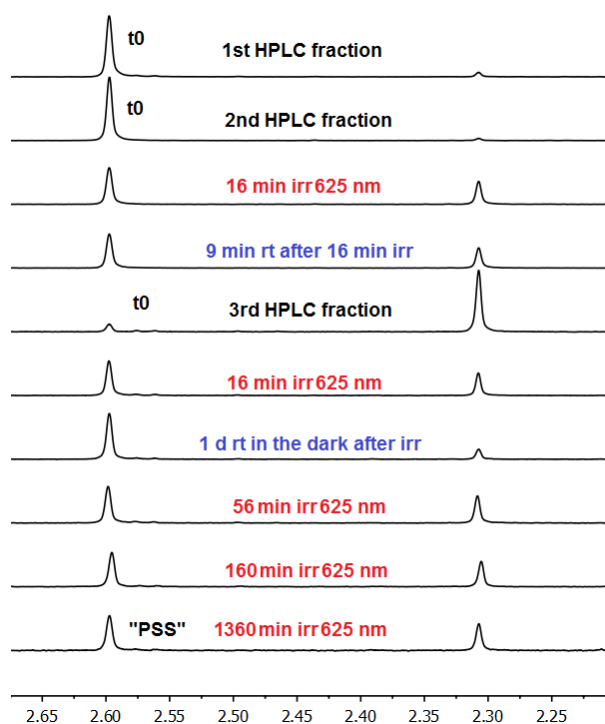


Figure 278: Overview of the aliphatic region of the  $^1\text{H}$ -NMR experiments on *syn-trans*-1 (1<sup>st</sup> and 2<sup>nd</sup> HPLC fraction) and *anti-trans* isomers (3<sup>rd</sup> HPLC fraction) at 27 °C in dichloromethane- $d_2$ . A clear rise in population of the *anti-trans* isomer at 2.31 ppm after 16 min of 625 nm irradiation can be observed. 9 minutes at ambient temperatures in the dark did not change the signal ratio, suggesting the

absence of *cis* isomers. Irradiation of majorly *anti-trans* isomer with 625 nm light reaches the previously observed PSS at a higher rate than the previously determined thermal reaction alone, suggesting the photoinduced extended Hula-Twist reaction as the major trajectory (see Figure 261) at 25 °C. Thermal annealing over 1 day at ambient temperatures restores the 5 / 1 *syn- / anti-trans* isomer thermodynamic equilibrium. Prolonged irradiation with 625 nm light, again, yields the previously observed PSS.

As stated before, a simple *trans* to *cis* back to *trans* reaction for all three observed *trans* ground states is never able to shift the thermal equilibrium between *syn-trans*- and *anti-trans* states (a photoinduced single bond rotation is only proposed for the generation of the *syn-trans*-2 isomer and never observed elsewhere). Figure 276 and Figure 277 show the opposite behavior (generation of *anti-trans*- from *syn-trans* isomers) with surprisingly high yields, which indicates feasible conversion rates of the following proposed reaction pathways. The unexpected observations depicted in Figure 276 can be explained by the reaction cycle shown in Figure 279 below.

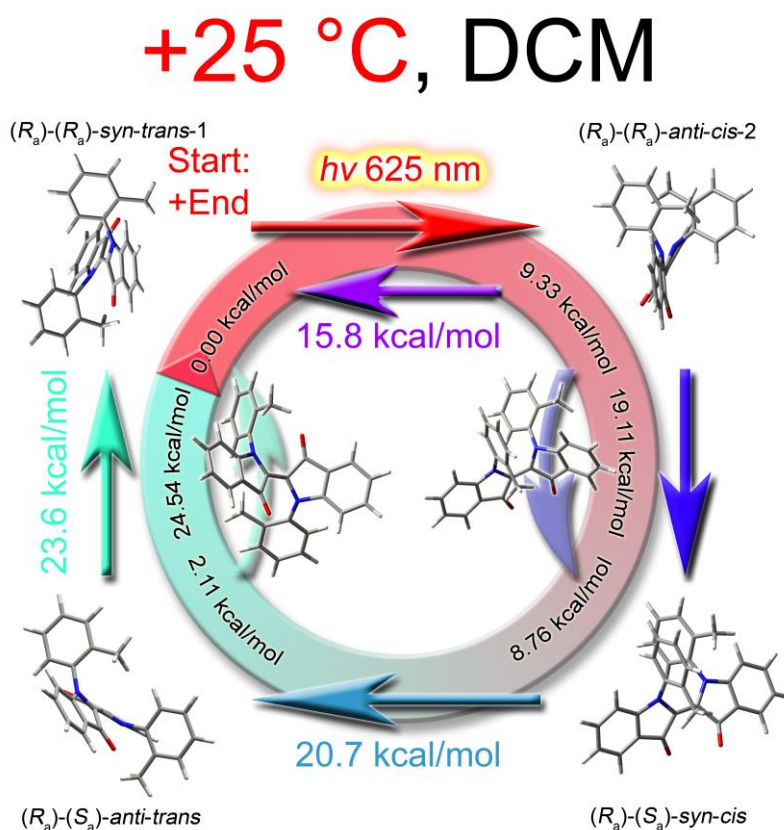


Figure 279: Proposed reaction pathway by irradiation of indigo **64** at 25 °C in dichloromethane *d*<sub>2</sub> enriching the *anti-trans*-**64** starting from majorly *syn-trans*-**64** isomer out of the thermodynamic equilibrium. Optimized ground- and

transition states calculated at the B3LYP/6-311+G(d,p) level of theory are shown, calculated values are placed within the circular graphic in black, measured values and transition state barriers are shown in the respective colors adjacent to the arrows.

At 25 °C in dichloromethane- $d_2$ , the motional cycle can be broken down into four steps: First, a photoinduced 180° *trans* to *cis* isomerization of the thermodynamically favored *syn-trans*- towards the *anti-cis-2* isomer takes place. Secondly, the *anti-cis-2* isomer is thermally branched into the *cis* to *trans* double bond isomerization pathway and the single bond rotation of one *ortho*-tolyl axis from the *anti-cis-2*- to the *syn-cis* state. Thirdly, a thermal *cis*- to *trans* isomerization from the *syn-cis*- to the *anti-trans* diastereomer takes place. Fourthly, a thermal atropisomerization from the *anti-trans*- to the *syn-trans-1* state closes the cycle.

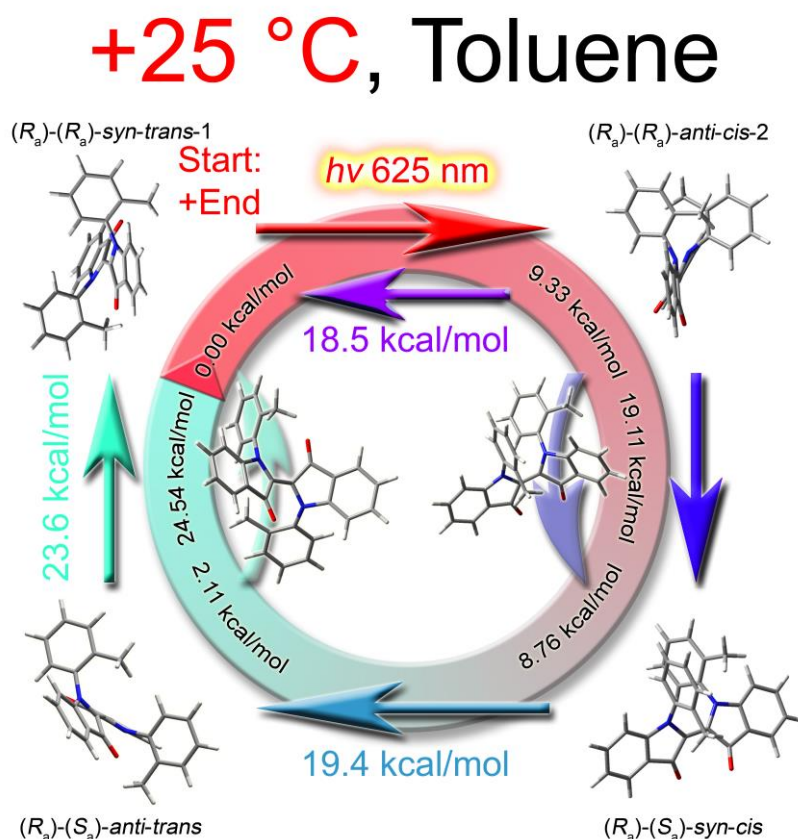


Figure 280: Proposed reaction pathway by irradiation of indigo **64** at 25 °C in toluene- $d_8$  enriching the *anti-trans-64*- starting from majorly *syn-trans-64* isomer out of the thermodynamic equilibrium. Optimized ground- and transition states calculated at the B3LYP/6-311+G(d,p) level of theory are shown, calculated values are placed within the circular graphic in black, measured values and transition state barriers are shown in the respective colors adjacent to the arrows.

The motional cycle of **64** can also be observed in toluene with a significantly enlarged *anti-cis-2* isomer barrier of 18.5 kcal/mol (15.8 kcal/mol in dichloromethane), accumulating the *anti-trans* isomer. The *syn-trans-1* isomer is populated at -50 °C when starting from the *anti-trans* isomer (see Section Figure 263), which changes the preferably accumulated isomer from previously *anti-trans*- (25 °C) to the *syn-trans-1* isomer (-50 °C).

## 2.4.20 Symmetric chiral indigos - Second generation indigo **64** - Photoinduced unidirectional single bond motor

### Trajectories for the prospective one-photon-four-step single bond motor

Theoretical calculations were carried out on indigo **64** to address their possible reaction trajectories towards unidirectional motion. For simplicity, one chiral axis of the molecule is considered as fixed, in reality, both axes undergo the same motions at equal rates. However, two-fold reactions of both axes could be ruled out via low temperature NMR- and ECD experiments as well by energetic criteria described in Section 2.4.9. The first example below discusses the *syn-trans*-1 isomer as starting point and considers the experimentally observed intermediates and their products after thermal annealing at ambient temperatures in toluene and dichloromethane. The second evaluation of the trajectories in Figure 283 considers the *anti-trans* isomer as starting point to explain the experimentally observed intermediates and their products after thermal annealing from -50 °C to ambient temperatures.

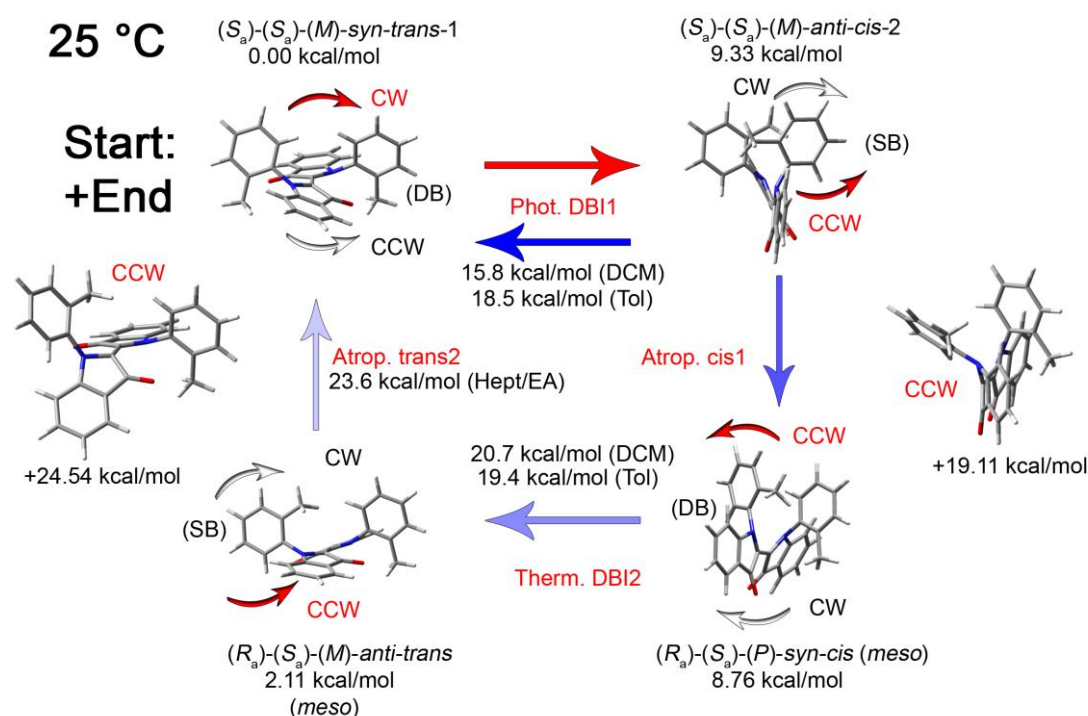


Figure 281: All possible theoretical trajectories for the reaction cycle of the *syn-trans*-1 isomer of indigo **64** at ambient temperatures. CW = clockwise rotation, CCW = counter clockwise rotation. (SB) = Single bond rotation, (DB) = Double bond rotation. The rotational direction is defined by the view alongside of the respective single or double bond axis. Rotational directions marked in red represent the favored rotations for single- and double bonds. The two lowest

energy transition states are shown for each respective reaction path. Calculated energies at the B3LYP/6-311+G(d,p) level of theory are given below the stereodescriptors respective to the lowest ground state energy, which was set to 0.00 kcal/mol.

### Arguments for assigning the CW / CCW directions for each respective state

Starting from the *syn-trans*-1 state of indigo **64** (Figure 281), a clockwise (CW) and a counter clockwise (CCW) rotation (R) can be postulated for the photoinduced central double bond isomerization. Section 2.2.26 elaborated why pre-twisting of a molecule leads to higher quantum yields towards its metastable state. Pre-twisting is assumed to shape the potential energy surface (PES) to a steeper gradient, leading towards the conical intersection for the respective photoisomerization product. This argument can be considered to explain why a CWR is preferred over a CCWR in this case, however, detailed and exhaustive excited state calculations have to be carried out to address this further by theory.

The other possibility, namely a photoinduced CCW double bond rotation would assume a PES gradient that either populates or skips the by ~4 kcal/mol (calculated) disfavored *syn-trans*-2 isomer against the pre-twisted conformation of the *syn-trans*-1 state. This is energetically possible within a photostep, but highly unlikely due to experimental observations on pre-twisted hemiindigo chromophores.

Interestingly, the formation of *anti-cis*-1 / *syn-trans*-2 signals could not be observed for the *syn-trans*-1 starting material, as exclusively the higher energy *anti-cis*-2 isomer is produced by a 180° rotation of the double bond. The energy of the excited state is assumed to dissipate by this extensive motion, resulting in skipping over the lower energy local minimum and geometrically closer *anti-cis*-1 isomers as their characteristic signals could not be observed via NMR spectroscopy. This shows that the CW double bond rotation covers a dihedral angle of 180° (Instead of 147°) and does not thermally convert back to the *anti-cis*-1 state, but solely to the *syn-trans*-1 form.

The *anti-cis*-2 state prefers a CCWR with the rotatable methyl group passing over one indigo core proton as lowest energy transition state.

The *syn-cis* isomer exhibits a thermal CCWR due to the pre-twisting argument. The thermal isomerization, however, does not proceed as forcefully as the photoreaction, leading to the geometrically closer *anti-trans* isomer. Experimentally, all generated *anti-trans* isomers are congruent, as this species represents a *meso* form.

The *anti-trans* isomer prefers a CCWR with the rotatable methyl group passing over the central indigo double bond as lowest energy transition state.

These arguments support a nominal back-and-forth motion for the central double bond and a unidirectional motion considering one rotatable- and one fixed chiral axis. Possible trajectories are shown in Table 13 below.

Table 13: Permutation of possible theoretical trajectories for the reaction cycle of the *syn-trans-64* isomer at ambient temperatures for Figure 281. Preferred rotations are marked in red. “T1” stands for “Trajectory1”. DBR = Double bond rotation, SBR = single bond rotation.

	Phot. DBI1 180°	Atrop. <i>cis</i> 1 180°	Therm. DBI2 180°	Atrop. <i>trans</i> 2 180°	Resulting trajectory
T1: DBR	CW		CW		Unidirectional
T1: SBR		CW		CW	Unidirectional
T2: DBR	CCW		CW		Not unidirectional
T2: SBR		CW		CW	Unidirectional
T3: DBR	CCW		CW		Not unidirectional
T3: SBR		CCW		CW	Not unidirectional
T4: DBR	CCW		CCW		Unidirectional
T4: SBR		CCW		CW	Not unidirectional
T4: DBR	CCW		CCW		Unidirectional
T4: SBR		CCW		CCW	Unidirectional
T5: DBR	CW		CCW		Not unidirectional
T5: SBR		CCW		CCW	Unidirectional
T6: DBR	CW		CCW		Not unidirectional
T6: SBR		CW		CCW	Not unidirectional
T7: DBR	CW		CW		Unidirectional
T7: SBR		CW		CCW	Not unidirectional
T8: DBR	CW		CCW		Not unidirectional
T8: SBR		CCW		CW	Not unidirectional
T9: DBR	CCW		CW		Not unidirectional
T9: SBR		CW		CCW	Not unidirectional
T10: SBR	CCW		CCW		Unidirectional
T10: DBR		CW		CW	Unidirectional
T11: SBR	CW		CW		Unidirectional
T11: DBR		CCW		CCW	Unidirectional
T12: SBR	CCW		CCW		Unidirectional
T12: DBR		CW		CCW	Not unidirectional
T13: SBR	CCW		CW		Not unidirectional
T13: DBR		CCW		CCW	Unidirectional
T14: SBR	CW		CW		Unidirectional
T14: DBR		CCW		CW	Not unidirectional
T15: SBR	CW		CCW		Not unidirectional
T15: DBR		CW		CW	Unidirectional

Table 12 shows that trajectory 5 is preferred by the arguments based on experimental and theoretical data for Figure 281 above. This suggests the trajectory of the single bond to be unidirectional, which prospectively makes the major *syn-trans*-1 indigo **64** species *a one photon driven, red-light fueled, four step single bond motor that rotates with a frequency of  $3 \times 10^{-5}$  Hz at 25 °C (23.6 kcal/mol, 83 / 17 heptane / ethyl acetate)*.

## 2.4.21 Symmetric chiral indigos - Second generation indigo 64 - Photoinduced unidirectional double bond motor

Besides the proposed four-step single bond motor trajectory, a unidirectional, one photon, two-step motor cycle for *syn-trans*-1-indigo-**64** can be postulated.

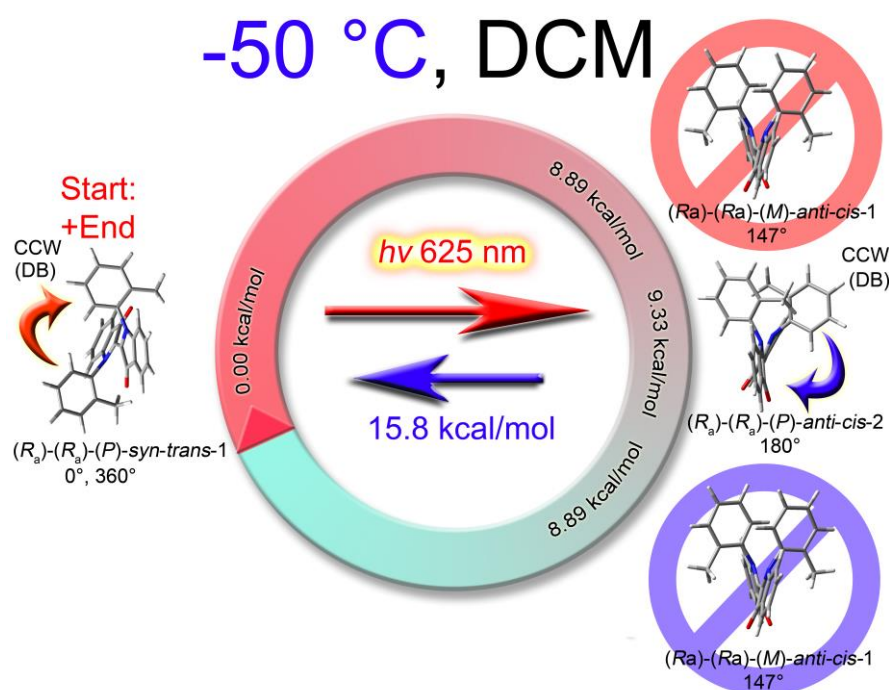


Figure 282: The photoinduced 180° double bond isomerization of indigo **64** at -50 °C in dichloromethane-*d*<sub>2</sub> yields the *anti-cis*-2 isomer starting from majorly *syn-trans*-1 isomer. The subsequent thermal back-reaction takes place over a free activation enthalpy of  $\Delta G^* = 15.8$  kcal/mol. The *anti-cis*-1 states are skipped in both cases. CCW = counter clockwise, DB = double bond. Optimized ground states calculated at the B3LYP/6-311+G(d,p) level of theory are shown, calculated values are placed within the circular graphic in black, the measured value is shown in blue.



### Arguments for assigning the CCW / CW directions for each respective state

Starting from the *syn-trans*-1 state of indigo **64** (Figure 281), a clockwise (CCW) and a counter clockwise (CW) rotation (R) can be postulated for the photoinduced central double bond isomerization. Section 2.2.26 elaborated why pre-twisting of a molecule leads to higher quantum yields towards its metastable state. Pre-twisting is assumed to shape the potential energy surface (PES) to a steeper gradient leading towards the conical intersection for the respective photoisomerization product. This argument can be considered to explain why a CCWR is preferred over a CWR in Figure 282, however, detailed and exhaustive excited state calculations have to be carried out to address this further by theory.

The other possibility, namely a photoinduced CW double bond rotation, would assume a PES gradient that either populates or skips the by  $\sim 4$  kcal/mol (calculated) disfavored *syn-trans*-2 isomer against the pre-twisted conformation of the *syn-trans*-1 state. This is energetically possible for a photostep, but highly unlikely due to experimental observations on pre-twisted hemiindigo chromophores and shaping of the (electronic) structure towards the transition state (see Section 1.1, Figure 3). This would also assume that solely a back-and-forth motion between the most disfavored (and experimentally invisible) *trans* state (*syn-trans*-2) and the globally most disfavored *cis* state (*anti-cis*-2) state takes place, which is also highly unlikely as the signals corresponding to the *syn-trans*-2 isomer cannot be observed by irradiation of the *syn-trans*-1 isomer. The surprising circumstance of three experimentally visible states for a single *trans* to *cis* photoisomerization and the skipping of two of them suggests indigo **64** to serve as an extremely rare example of a prospective photodriven, unidirectional two-step motor. In general, it is impossible to prove the (uni-) directionality of a two-step motor directly, as a simple photoisomerization consists only of two observable steps or states. In this case, however, the entirely different behavior of the interconvertible *syn-trans*- and *anti-trans* isomers makes indirect observation of the proposed two-step motor possible, as no chemical modifications of the chromophore are needed to e.g. capture intermediate states, as these steps can be generated simply via irradiation of the *anti-trans* isomer.

The prevalence of pre-twisting in the *syn-trans*-1 ground state,  $180^\circ$  rotation of the powerstroke (which is also observed within the four-step motor system published by *M. Güntner*<sup>[82]</sup>) and hereby skipping of the local minimum at  $147^\circ$  rotation angle, however, enable the determination of the unidirectionality for this system if a CCWR of the double bond is assumed.

The two 180° CCW rotation steps yield a 360° double bond isomerization rotation, supporting indigo **64** to be a red light driven, one photon, unidirectional, two-step double bond isomerization motor that rotates with 16 Hz at 25 °C (15.8 kcal/mol, DCM) and with  $4 \times 10^{-2}$  Hz at 25 °C (19.4 kcal/mol, toluene).

*J. M. Lehn* proposed a mechanism for light-driven, unidirectional two-step motors based on chiral imines in 2006.<sup>[119]</sup> In 2015, *L. Greb* of the *Lehn* group published experimental findings on these systems by utilization of the stereochemical bias of camphorquinone imines to introduce diastereomeric excess via cyclization reactions towards spirocyclic pyrrolines.<sup>[120]</sup> The bias observed by *L. Greb* amounts to 58/42 *endo/exo* form and represents trapping of a biradical S<sub>1</sub> state towards the locked intermediate steps, again subdividing the rotational motion into four discrete (and two hypothetical) states.

For the chiral indigo system at hand, the argument for stereochemical bias shifts from whether the rotation direction can be (directly) proven towards the predominant helicity as bias for a CCWR of the central double bond. The latter could be possibly proven via transient ECD spectroscopy in a direct fashion while the two-step cycle of the motion is proposed by the experiments shown in this work.

### 2.4.22 Symmetric chiral indigos - Second generation indigo 64 - Photoinduced and thermal extended Hula-Twist

For the discussion of the possible Hula-Twist motion in Figure 283, virtual trajectories based on theoretical calculations of atropisomerization directions, pre-twisting directionalities and the observed  $147^\circ$  angle of the photoinduced powerstroke are used as arguments. The presumably concerted nature of the extended Hula-Twist motion argues against a stepwise progression of this motion. However, for the sake of arguing towards possible directionalities of the entire trajectory, hypothetical intermediates based on the previously obtained data and calculations are considered, as experimental proof of the exact motion is impossible to obtain with our available resources at this time. The instantaneous transformation of significant amounts of *anti-trans* isomer signals to *anti-cis-1* isomer signals at  $-60^\circ\text{C}$  suggests a photoinduced extended Hula-Twist to take place (Section 2.4.14, Figure 261 and Figure 263). Also, thermal annealing of the *anti-cis-1* product yields small amounts of the unexpected *anti-trans* isomer signals and branches the remaining *anti-cis-1* population towards the expected *syn-trans-1* isomer. (Section 2.4.14, Figure 261 and Figure 263) This reaction pathway is thermally impossible at  $-60^\circ\text{C}$  and the opposite is observed when irradiating the *syn-trans-1* isomer at  $25^\circ\text{C}$  (Section 2.4.13).

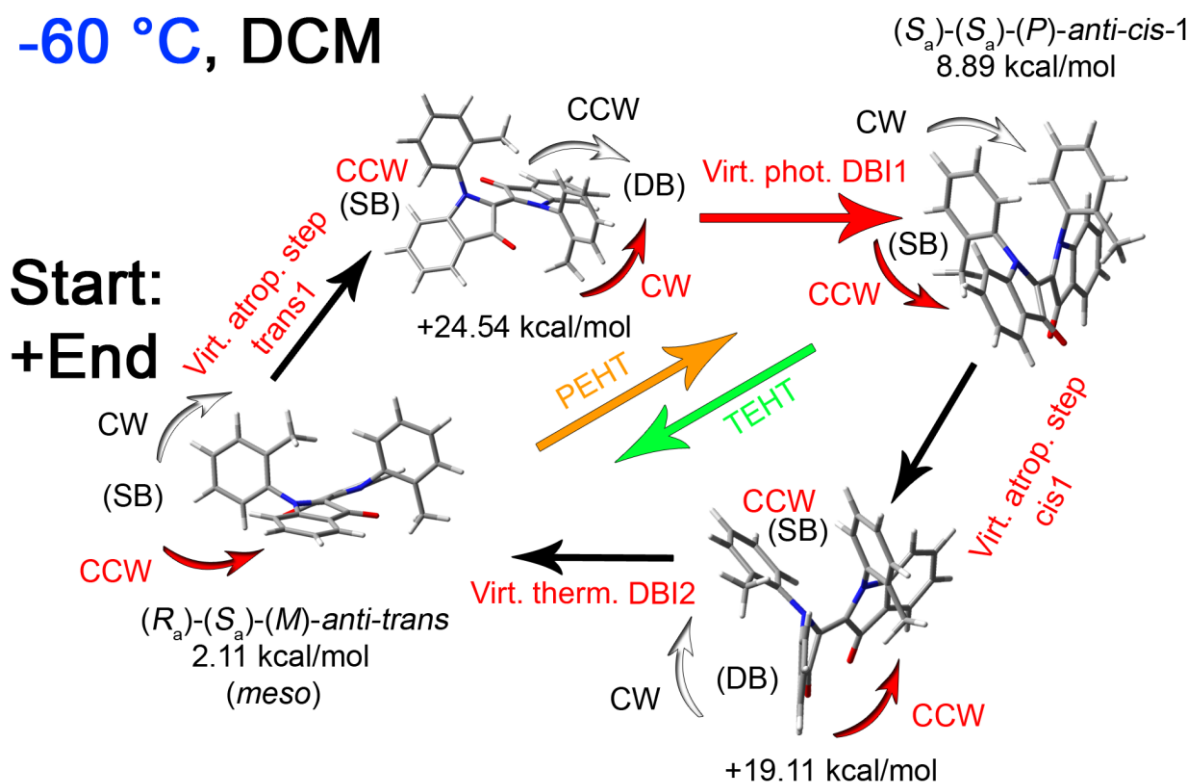


Figure 283: Possible theoretical trajectories of indigo **64** for the reaction cycle of the *anti-trans* isomer between -60 °C, -50 °C and 25 °C. CW = clockwise rotation, CCW = counter clockwise rotation, PEHT = photoinduced extended Hula-Twist, TEHT = thermal extended Hula-Twist. The rotational direction is defined by the view on top of the respective single or double bond axis. Rotational directions marked in red represent the favored rotations for single- and double bonds. The two lowest energy transition states are shown for respective reaction path. Calculated energies at the B3LYP/6-311+G(d,p) level of theory are given below the stereodescriptors respective to the lowest ground state energy. (SB) = rotation directions for the single bond, (DB) = rotation directions for the central double bond.

### Arguments for assigning the CW / CCW directions for each respective (virtual) state in Figure 283

The concerted rotational motions are split into virtual atropisomerization- and thermal- or photoinduced double bond isomerization steps as an attempt to model the trajectories of the *anti-trans* isomer at -50 °C in dichloromethane. The virtual atropisomerization step (*trans*1) passes its rotatable methyl group CCW over the central double bond according to the lowest

energy transition state. The 24.54 kcal/mol (calcd.) or 23.6 kcal/mol (measured) barrier can only be overcome photochemically at -60 °C.

The virtual subsequent photoinduced double bond isomerization is assumed to take place in a CWR because of the pre-twisting argument. This step is assumed to push the methyl group of the single bond transition state backwards in a CCWR, if the assumed concerted photoreaction is split into virtual steps. It is also important that the virtual atropisomerization “has to take place first” for a PEHT, as the generated *syn-cis* isomer is also observed starting from irradiation of the *anti-trans* isomer.

Interestingly, the previously observed photodriven 180° motion with the *syn-trans-1* isomer (when *anti-cis-2* is formed) is not completed in the *anti-trans* case, which stops after 147° of CCWR (*anti-cis-1* is formed). This can be explained by deexcitation upon concertedly rotating the single bond, giving the extended Hula-Twist trajectory, this can be described as a *photodriven geared motion* (see Section 2.4.23)

Table 14 below shows the resulting directionalities for the postulated rotation directions.

Table 14: Permutations of possible theoretical trajectories for the photodriven / thermal extended Hula-Twist reaction cycle of the *anti-trans-64* isomer at -60 °C, -50 °C for Figure 283. Preferred rotations are marked in red. “T1” stands for “Trajectory1”. DBR = Double bond rotation, SBR = single bond rotation.

	Atrop. <i>trans</i> 1 180°	Phot. DBI1 147°	Atrop. <i>cis</i> 1 180°	Therm. DBI2 180°	Resulting trajectory
T1: SBR	CW		CW		Unidirectional
T1: DBR		CW		CW	Unidirectional
T2: SBR	CCW		CW		Not unidirectional
T2: DBR		CW		CW	Unidirectional
T3: SBR	CCW		CW		Not unidirectional
T3: DBR		CCW		CW	Not unidirectional
T4: SBR	CCW		CCW		Unidirectional
T4: DBR		CCW		CW	Not unidirectional
T4: SBR	CCW		CCW		Unidirectional
T4: DBR		CCW		CCW	Unidirectional
T5: SBR	CW		CCW		Not unidirectional
T5: DBR		CCW		CCW	Unidirectional
T6: SBR	CW		CCW		Not unidirectional
T6: DBR		CW		CCW	Not unidirectional
T7: SBR	CW		CW		Unidirectional
T7: DBR		CW		CCW	Not unidirectional
T8: SBR	CW		CCW		Not unidirectional
T8: DBR		CCW		CW	Not unidirectional
T9: SBR	CCW		CW		Not unidirectional

T9: DBR		CW		CCW	Not unidirectional
T10: SBR	CCW		CCW		Unidirectional
T10: DBR		CW		CW	Unidirectional
T11: SBR	CW		CW		Unidirectional
T11: DBR		CCW		CCW	Unidirectional
T12: SBR	CCW		CCW		Unidirectional
T12: DBR		CW		CCW	Not unidirectional
T13: SBR	CCW		CW		Not unidirectional
T13: DBR		CCW		CCW	Unidirectional
T14: SBR	CW		CW		Unidirectional
T14: DBR		CCW		CW	Not unidirectional
T15: SBR	CW		CCW		Not unidirectional
T15: DBR		CW		CW	Unidirectional

Table 14 suggests a geared, unidirectional, red light-driven, one photon, two-step (PEHT, TEHT) single bond motor assembly with undeterminable rotational speed.

### 2.4.23 Symmetric chiral indigos - Second generation indigo **64** - Photodriven extended Hula-Twist gear

The evaluation by virtual steps in Section 2.4.22 suggests a unidirectional rotation of one axially chiral single bond caused by the “virtual atropisomerization step *cis1*” for the thermal single bond rotation by a small margin (19.11 kcal/mol, CCW versus 19.32 kcal/mol, CW).

Chemical intuition, however, suggests the PEHT and TEHT motion to follow the trajectory displayed in Figure 284 below:

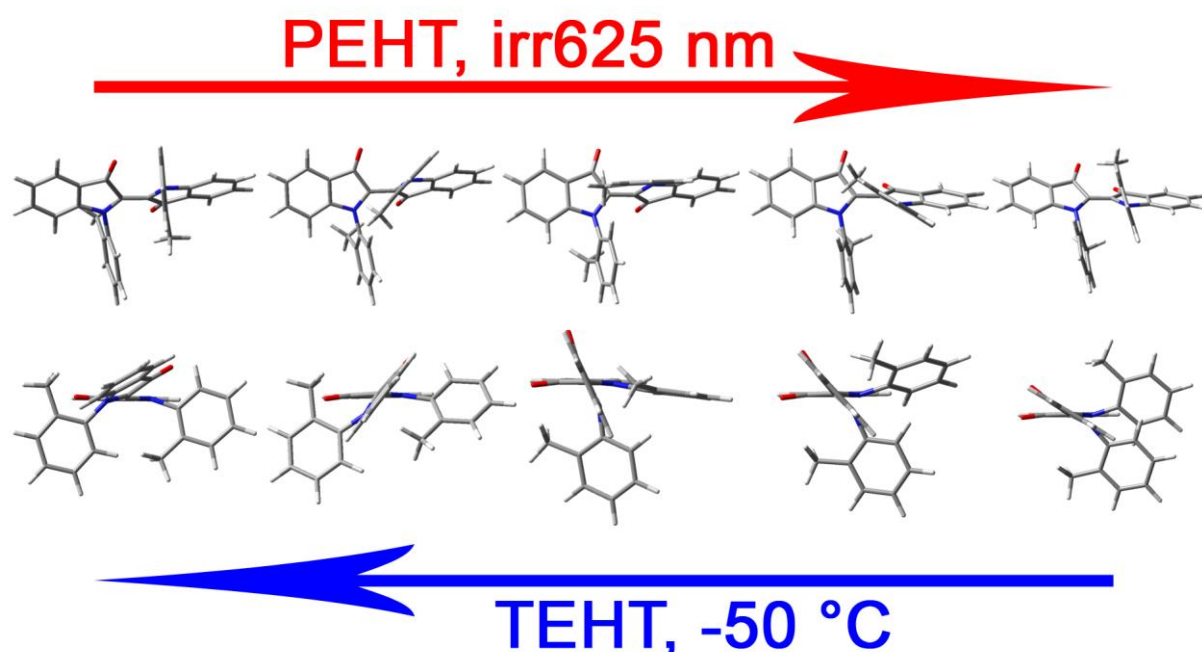


Figure 284: Suggestion of the PEHT and TEHT motion of indigo **64** based on chemical intuition. The first state on the left and the last state on the right represent minimum structures calculated at the B3LYP/6-311+G(d,p) level of theory, intermediate geometries represent arbitrary structures to visualize the proposed geared Hula-Twist motion. Top: view along a single bond, bottom: view along the central double bond.

As the introduced virtual steps are highly speculative and pose no significance in reality, an intuitive suggestion for the PEHT and TEHT trajectory is given in Figure 284. The depicted concerted Hula-Twist motions show no 360° rotations and thus no unidirectionality, as solely a back-and-forth motion is assumed. The chiral aryl axes are decoupled from the electronic influences of the central double bond and are assumed to rotate without the influence of the photochemistry taking place. This can be observed for the *syn-trans-1* isomer showing no single

bond rotations or racemizations when irradiated (see Section 2.4.13). The sterically “charged” state of the *anti-trans* isomer supports a “pocket” between the central double bond and the opposing aryl axis. This suggests the methyl group to engage with the electronic surface of this cavity, being pushed by the light-driven powerstroke into the backside of the opposing aryl moiety. This constitutes in a 147° double bond rotation and a formal 180° single bond rotation of electronically independent and remote systems within one photostep. This behavior can be interpreted as a geared motion to populate and depopulate the energetically intermediate *anti-cis-1* state from / to the *anti-trans* state.

Figure 284 also implies another photoinduced motion that could take place at an equal rate, namely the rotation of the aryl axis that was kept fixed in Figure 284. Starting from the left molecule, the rotation of the single bond over the central double bond is hindered upon photoisomerization, resulting in a rotation over the disfavored trajectory bypassing proton 7 of the indigo core. This sterical clash might lead to the deexcitation of the excited state, terminating the PEHT motion midway, which results in a single bond rotation without changing of the helicity at -60 °C and without *trans* to *cis* photoisomerization, exclusively giving the *syn-trans-2* isomer. This could explain the additional signal set besides *anti-cis-1* isomer signals that is only stable at -60 °C (or heavily broadened) and populates the *syn-cis-1* isomer upon thermal annealing.



## 2.4.24 Symmetric chiral indigos - Second generation indigo 64 - Overview of trajectories

Figure 281 is extended in Figure 285 below to visualize all possible and non-redundant trajectories in the photoswitching system of indigo **64** for the sake of completeness.

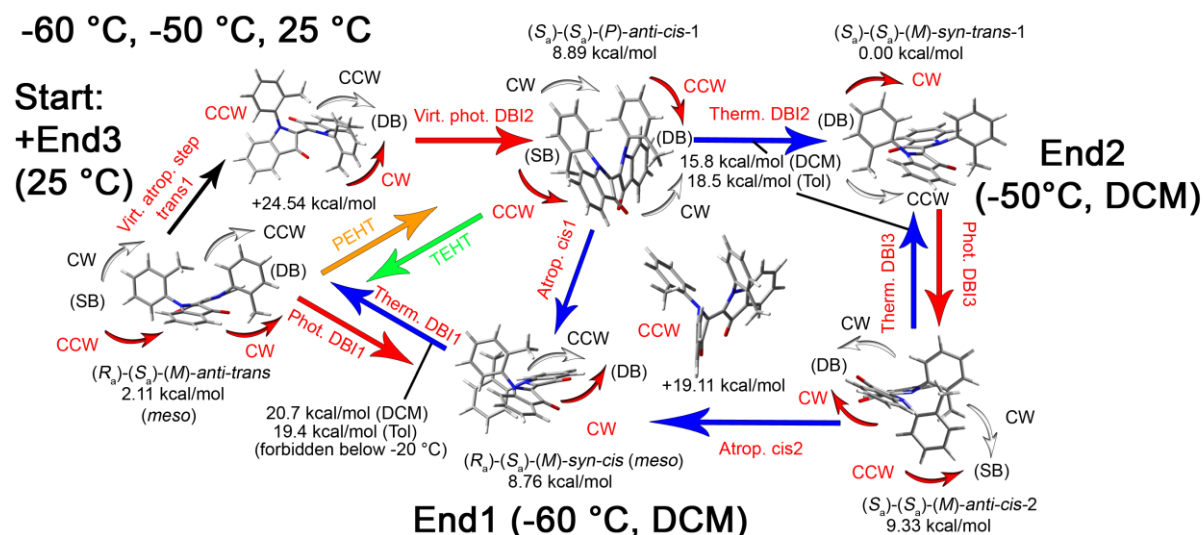


Figure 285: Possible theoretical trajectories for the reaction cycle of the *anti-trans* isomer between -60 °C, -50 °C and 25 °C. CW = clockwise rotation, CCW = counter clockwise rotation. The rotational direction is defined by the view on top of the respective single or double bond axis. Rotational directions marked in red represent the favored rotations for single- and double bonds. The two lowest energy transition states are shown for respective reaction path. Calculated energies at the B3LYP/6-311+G(d,p) level of theory are given below the stereodescriptors respective to the lowest ground state energy, which is set to 0.00 kcal/mol. (SB) = rotation directions for the single bond, (DB) = rotation directions for the central double bond.

### Overview and explanation of the possible trajectories in Figure 285

Starting from the *anti-trans* isomer, photoinduced branching towards the *syn-cis* and *anti-cis-1* isomers can be observed at -60 °C. The *anti-trans*- to *syn-cis* isomer trajectory follows a photoinduced double bond isomerization at -60 °C (End1) which is reversed at -5 - +25 °C, yielding the *anti-trans* starting material (End3). The *anti-trans* to *anti-cis-1* trajectory follows a photoinduced extended Hula-Twist (PEHT, orange) motion. The PEHT is broken down into a preferably CCW virtual atropisomerization- and a CW double bond isomerization step to

permutatively address its directionality. A more elaborated assessment of the trajectory for this photoreaction taking place at  $-60\text{ }^{\circ}\text{C}$  can only be assessed by detailed and exhaustive excited state calculations. The generated *anti-cis*-1 isomer is partially converted to the *anti-trans* isomer at  $-50\text{ }^{\circ}\text{C}$ , which can only take place via a thermal extended Hula-Twist trajectory (TEHT), as a simple CW thermal double bond isomerization would lead towards the *syn-trans*-1 isomer (End2). This supposedly concerted thermal reaction pathway is split into a preferably CCW atropisomerization and CW double bond isomerization to permutatively address its directionality, as observed with the PEHT trajectory. Continuing from the slowly accumulated *syn-trans*-1 isomer, the previously shown cycle would be active at  $-5\text{ }^{\circ}\text{C}$  to  $25\text{ }^{\circ}\text{C}$ . However, at  $-50\text{ }^{\circ}\text{C}$ , the *anti-cis*-2 isomer is the main photoproduct by a CW double bond isomerization. It is thermally branched back towards the *syn-trans*-1- (End2) via CW thermal double bond isomerization and *syn-cis* isomer (End1) via CCW atropisomerization over the favored transition state (methyl group passes over indigo core proton). Continuing from *anti-cis*-1, thermal branching to a CWR around the central double bond (pre-twisting) to the *syn-trans*-1 and a CCWR around the single bond (lowest *cis* transition state passes its methyl group over the indigo core proton) to the *syn-cis* isomer can be postulated.

Continuing from the slowly accumulating *syn-trans*-1 isomer, thermal branching to the previously described prospective unidirectional double bond motor rotation cycle (2x CWR at double bond) and CCW atropisomerization towards the *syn-cis* isomer takes place (lowest *cis* transition state passes its methyl group over the indigo core proton).

CW double bond isomerization from the *syn-cis*- to the *anti-trans* state with subsequent CCW atropisomerization to the *syn-trans*-1 state (arrow not shown) above  $0\text{ }^{\circ}\text{C}$  engages the prospective *syn-trans*-1 unidirectional single bond motor cycle shown in Figure 279.

The sequences of all trajectories for the *anti-trans* isomer starting point at  $25\text{ }^{\circ}\text{C}$  are given in Table 15

Table 15 below for a few examples, as a table with 720 entries would be necessary to display all possible ordered unique permutations.

Table 15: Permutation of seven possible theoretical trajectories for the photodriven / thermal extended reaction cycle of the *anti-trans*-64 isomer at  $25\text{ }^{\circ}\text{C}$  for Figure 285. Preferred rotations are marked in red. “T1” stands for “Trajectory1”. DBR = Double bond rotation, SBR = single bond rotation.

Atrop.	Phot.	Therm.	Phot.	Atrop.	Therm.	Resulting trajectory
<i>trans</i> 1	DBI2	DBI2	DBI3	<i>cis</i> 2	DBI1	
180°	147°	147°	180°	180°	180°	

T1: DBR		CW	CCW	CW		CCW	Not unidirectional
T1: SBR	CCW				CCW		Unidirectional
T2: DBR		CCW	CCW	CCW		CCW	1xUnidirectional
T2: SBR	CW				CCW		Not unidirectional
T3: DBR		CW	CCW	CCW		CCW	1xUnidirectional
T3: SBR	CW				CCW		Not unidirectional
T4: DBR		CW	CW	CCW		CCW	Not unidirectional
T4: SBR	CW				CCW		Not unidirectional
T4: DBR		CW	CW	CW		CCW	1xUnidirectional
T4: SBR	CW				CCW		Not unidirectional
T5: DBR		CW	CW	CW		CCW	1xUnidirectional
T5: SBR	CW				CW		Unidirectional
T6: DBR		CW	CW	CW		CW	2xUnidirectional
T6: SBR	CW				CW		Unidirectional
T7: DBR		CCW	CCW	CCW		CW	1xUnidirectional
T7: SBR	CCW				CCW		Unidirectional

Table 15 suggests a geared, unidirectional, red light, one photon-driven, six- or respectively two-step (PEHT, Atrop. *cis2*) prospective single bond motor assembly that rotates at  $6 \times 10^{-2}$  Hz at 25 °C (19.11 kcal/mol, calculated).

The directionality of this cycle is based on the two energetically favored transition states changing their rotational preference between the *trans* and *cis* state, as seen with the single bond rotational cycle proposed in Figure 279.

## 2.4.25 Symmetric chiral indigos - Second generation indigo 64 - Temperature- and solvent dependence of cyclic trajectories

Table 16 shows an overview of the prospective cyclic motor / machine properties of the axially chiral disubstituted indigo **64**.

Table 16: Overview of the direction of thermally switchable pumping against the thermal equilibrium and prospective unidirectional 2-step double- (DBI) / 4-step single bond (SBR) isomerization motor properties for indigo **64** in various solvents. HEA = 83 / 17 heptane / ethyl acetate

	25 °C	-50 °C
Pumping direction	<i>syn-</i> to <i>anti-trans</i> (DCM, Tol)	<i>anti-</i> to <i>syn-trans</i> (DCM, Tol)
Prospective 2-step DBI motor	$1.6 \times 10^1$ Hz (DCM) $3.7 \times 10^{-2}$ Hz (Tol)	$1.5 \times 10^{-3}$ Hz (DCM) $4.5 \times 10^{-7}$ Hz (Tol)
Prospective 4-step SBR motor	$3.0 \times 10^{-5}$ Hz (HEA)	$3.5 \times 10^{-11}$ Hz (HEA)

In summary, the combination of a (relatively) temperature independent single photoisomerization step with several (branched) thermal steps makes gating of the reaction pathways possible by disfavoring energetically higher thermal barriers at low temperatures. The latter is observed with the *anti-cis-2* to *syn-cis* atropisomerization as key step for the pumping of the *syn-trans-1* to the *anti-trans* isomer against its equilibrium ratio. Cooling to -50 °C completely cancels this pathway, favoring the photoinduced extended Hula-Twist reaction, which converts the *anti-trans-* to the *anti-cis-1-* / *syn-trans-2* signals. The *anti-cis-1* isomer is then thermally converted to the *syn-trans-1* isomer at -50 °C in dichloromethane, reversing the pumping direction when cooled down.

## 2.4.26 Symmetric chiral indigos - Second generation indigo 64 - Conclusion

The complex motional cascades of a red light-driven, one photon powered, unidirectional two-step double bond- or four-step single bond axially chiral indigo motor that shows thermally switchable enrichment of one of its two different *trans* states against the thermodynamic equilibrium could be proposed. The underlying thermal *anti-trans-2* to *syn-cis* step was shown to play a key role for the *syn-trans-* to *anti-trans* isomer enrichment at 25 °C. Also, a novel photoinduced- and thermal Hula-Twist motion spanning over three bonds could be demonstrated. The latter is proposed to show a geared motion between its two chiral aryl axes and represents the key step at -50 °C for the *anti-trans* to *syn-trans-1* enrichment. An unexpected selectivity for the *syn-cis* isomer to photochemically yield only the *anti-cis-2* isomer with the *anti-trans* isomer yielding only the *syn-cis-* and *anti-cis-1* / *syn-trans-2* signals could be shown via low temperature <sup>1</sup>H-NMR spectroscopy and DFT theory.

Further experiments on non-symmetric derivatives of this class compound should be carried out to scrutinize the intriguing motional behavior of this molecular setup.

These unprecedented motions utilizing the indigo scaffold expand the scope of designing and understanding future molecular motors and machines towards mechanical transmission of force and demonstrates the possibility of their usage within biological systems.

## 2.4.27 Non-symmetric chiral indigos - Third generation chimeric indigo 71

Experiments on indigo **69** in Section 2.4.10 determined a thermal atropisomerization barrier of 20.4 kcal/mol for indigo **69**, which led to another chimeric indigo derivative **71** which was synthesized and characterized by *F. Binder* during his research internship.

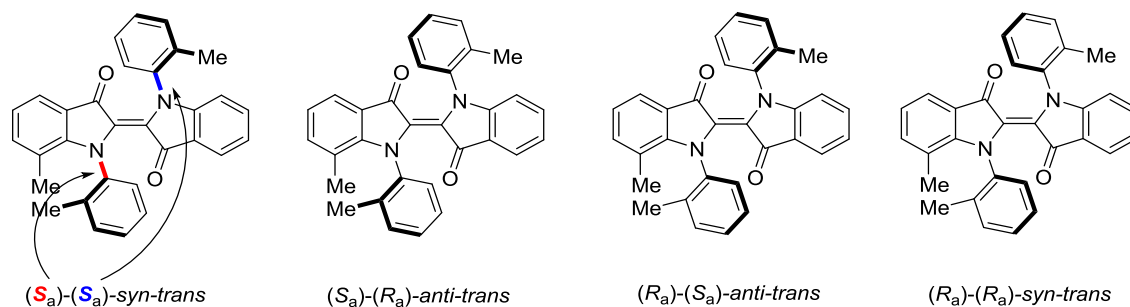


Figure 286: Overview of the *trans* forms of indigo **71**. The same amount of enantio and diastereomers is expected for the *cis* state.

The hybrid between chiral indigos **65** and **64** supports two chiral axes with potentially different thermal barriers and properties. 7-Methyl-*N,N'*-di(*o*-tolyl)indigo **71** supports two chiral *ortho*-aryl axes with one being sterically encumbered by a methyl group attached to the indoxyl core. Eight enantio- / diastereomers are expected for this molecule when *cis* isomers are taken into consideration (not shown).

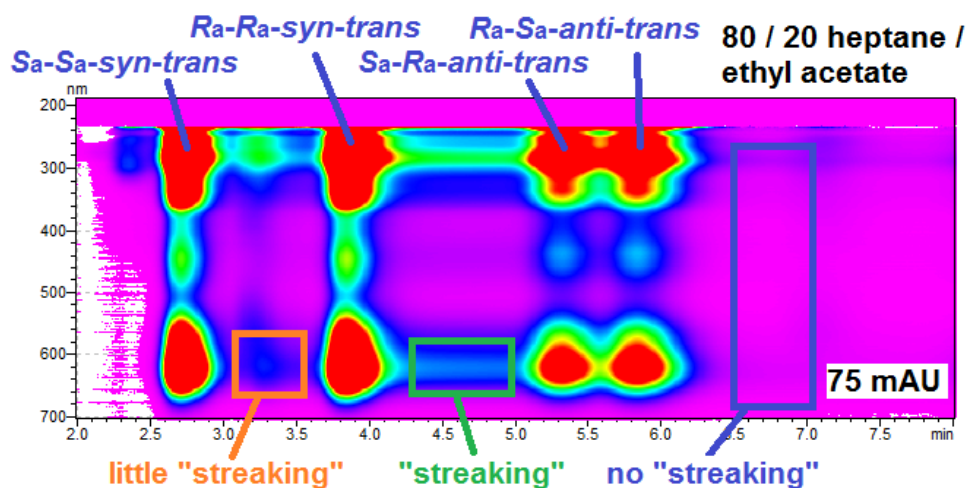


Figure 287: Chiral HPLC separation of the  $(S_a)-(S_a)$ -syn-trans-,  $(R_a)-(R_a)$ -syn-trans-,  $(S_a)-(R_a)$ -anti-trans- and  $(R_a)-(S_a)$ -anti-trans indigo **71** rota- and diastereomers at 0 °C with an 8 / 2 heptane / ethyl acetate mixture as eluent, the four separated rotamers can be observed.

The streaks between peaks indicate atropisomerization reactions taking place, which interconvert one rotamer to the other during elution from the chiral column. As the rotational barrier of the chiral axis adjacent to the core methyl group is expected to be below 21 kcal/mol, streaking between all isomers should be observable. This can be seen as the first streak between (*S*<sub>a</sub>)-(*S*<sub>a</sub>)- and (*S*<sub>a</sub>)-(*R*<sub>a</sub>) isomer is low in intensity while the (*R*<sub>a</sub>)-(*R*<sub>a</sub>) to (*R*<sub>a</sub>)-(*S*<sub>a</sub>) streak is added in intensity. A (*S*<sub>a</sub>)-(*S*<sub>a</sub>)- to (*R*<sub>a</sub>)-(*R*<sub>a</sub>)- as well as a (*R*<sub>a</sub>)-(*S*<sub>a</sub>) to (*S*<sub>a</sub>)-(*R*<sub>a</sub>) streak should not be visible at 0 °C. Latter is hard to observe because of the close proximity of both peaks. The immediate stop of the streaking after the complete elution of the (*R*<sub>a</sub>)-(*R*<sub>a</sub>)-*trans*-**71** isomer underlines these findings.

Separation by chiral HPLC at 0 °C yielded four peaks with relative intensities in square brackets: ExE1 (*S*<sub>a</sub>)-(*S*<sub>a</sub>)-*syn-trans*- [2], ExE2 (*R*<sub>a</sub>)-(*R*<sub>a</sub>)-*syn-trans*- [2], E3 (*S*<sub>a</sub>)-(*R*<sub>a</sub>)-*anti-trans*- [1] and E4 (*R*<sub>a</sub>)-(*S*<sub>a</sub>)-*anti-trans*- [1] isomer.

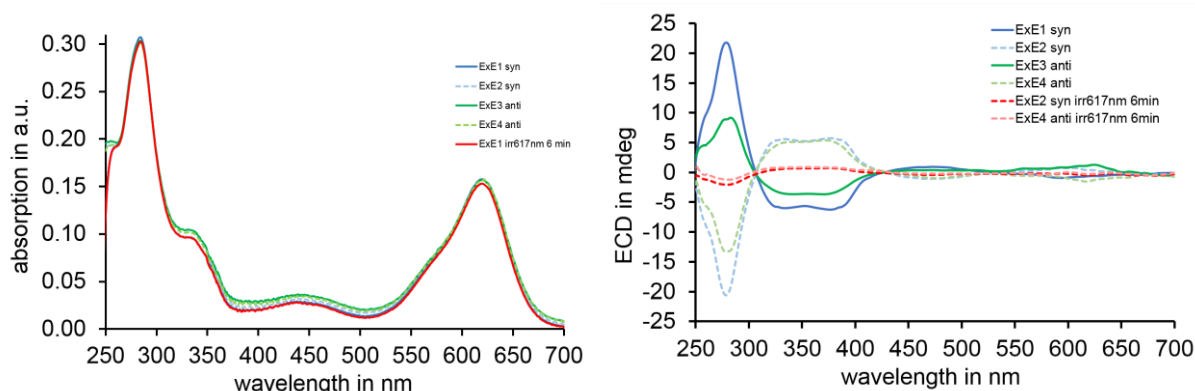


Figure 288: Scaled UV-Vis (left) and ECD (right) spectra of 7-methyl-*N,N'*-di(*o*-tolyl)indigo **71** in 8 / 2 heptane / ethyl acetate at 0 °C (blue / green and broken light blue / green) and after 6 min of 617 nm irradiation (red and broken light red).

E1 and E2 can be assigned to the *syn* isomers and E3 / E4 to both *anti* isomers. Lower ECD signal intensities for E1 / 2 of **71** were measured compared to the ones of E1 / 2 for **64** or **70**. Nonetheless, higher ECD responses than **65** and **69** could be obtained. E3 and E4 also show lower ECD intensity compared to E1 and E2 which is consistent to the observations for the *meso* form of **64**. The fact that removing one chiral axis yields half of the ECD response and the observation that chiral axes adjacent to the core methyl group also show only low ECD responses confirms the assignment.

When two chiral *o*-aryl axes motions are assumed for indigo **71**, two different free activation enthalpies should be measurable, first the one of model compound **69** at 0 °C with  $\Delta G^* =$

20.4 kcal/mol and second one that corresponds to model compound **70** at 40 °C with  $\Delta G^* = 23.1$  kcal/mol. Irradiation shows no visible photoswitching at ambient temperatures except for the racemization of the sample, which is also seen for chiral indigos **65** and **69**.

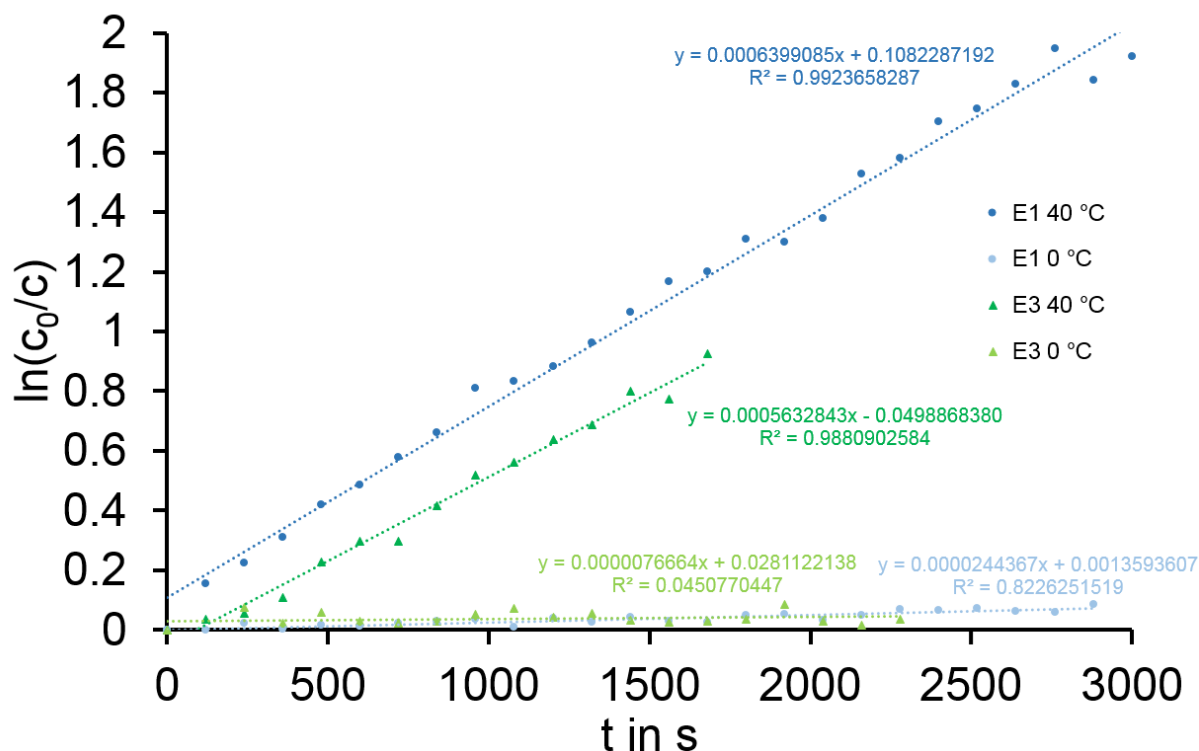


Figure 289: Linearized first order kinetics of **71** E1 and E3 in 8 / 2 heptane / ethyl acetate at 0 °C and 40 °C. The thermal atropisomerization barriers were determined as follows: E1 at 40 °C: 22.9 kcal/mol with a half-life of 1.98 h, E3 at 40 °C: 23.0 kcal/mol with a half-life of 2.32 h, E1 at 0 °C: 21.7 kcal/mol with a half-life of 15.2 min and E3 at 0 °C: 22.3 kcal/mol with a half-life of 44.0 min. Half-lives are given for a temperature of 25 °C. Used formulas and equations are described in Section 2.2.19.

The smaller barrier corresponding to the 7-methyl substituted *ortho*-aryl axis of indigo **71** as seen in model compound **69** is difficult to measure because of the bad signal-to-noise ratio of the ECD spectrophotometer for small signal intensities. The higher barrier corresponding to the sterically less encumbered chiral axis can be determined at almost the same values for **64** and **70**. The values measured at 0 °C correspond to the more stable chiral axis as values differ substantially from the previously determined 20 kcal/mol. Plots following the *Eyring* equation tend to vary with different measurement temperatures, giving slightly lower barriers for lower measurement temperatures and vice versa.



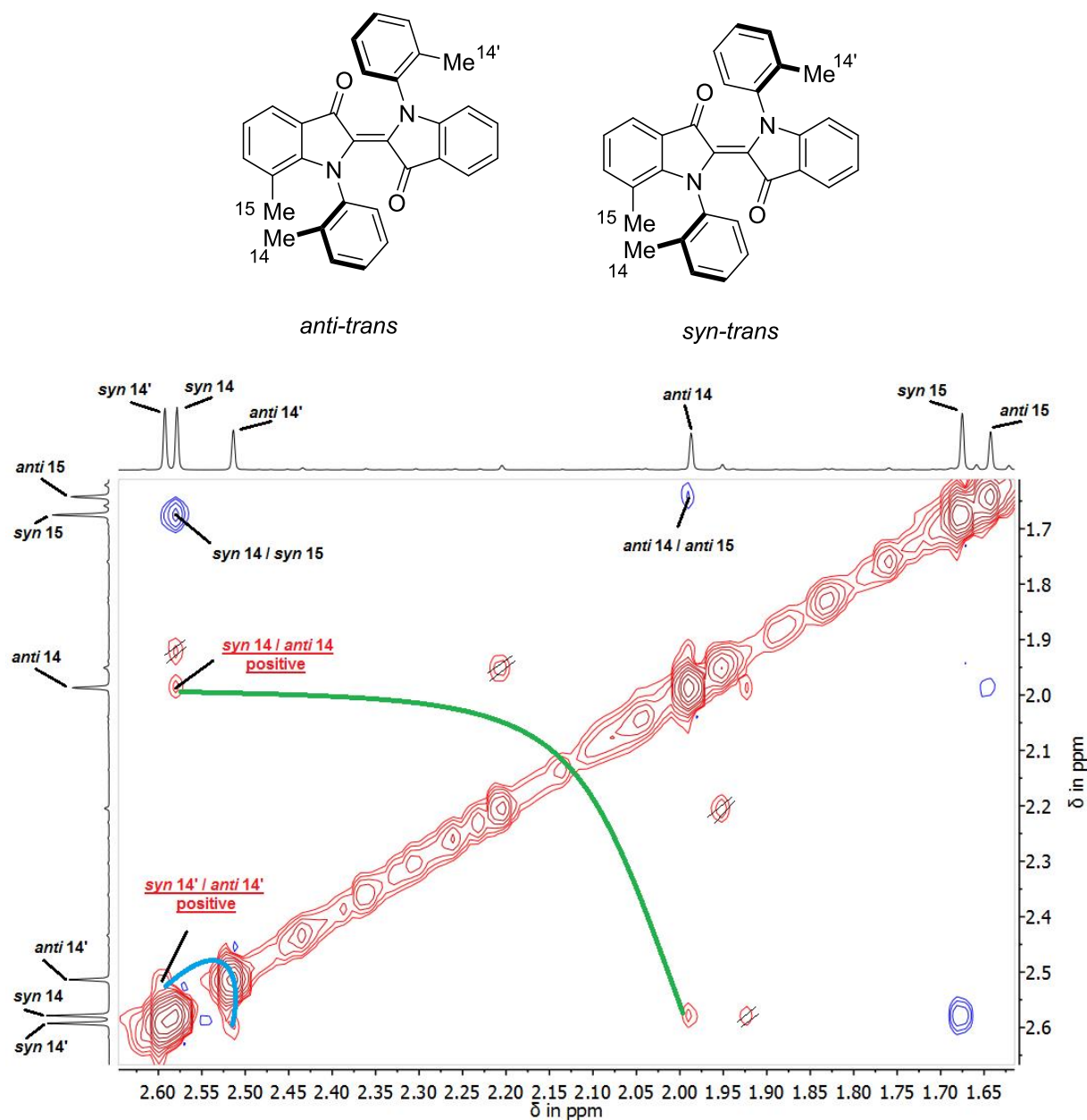


Figure 290: Aliphatic <sup>1</sup>H-NOESY NMR-spectrum of the *syn*- and *anti*-rotamer of 7-methyl-*N,N*-di(*o*-tolyl)indigo **71**, (600 MHz, dichloromethane-*d*<sub>2</sub>, 27 °C). Signals of protons *anti* 14 and *syn* 14 show positive NOE signals, while the rest of the molecule shows negative NOEs when the diagonal line is set to positive values according to convention. This confirms the expected fast dynamics between *syn*- and *anti* diastereomers (see indigo **65**, Section 2.4.3) as the used mixing time of 1.2 s is longer than the exchange of respective nuclei. Signal *syn* 14 / *syn* 15 shows stronger intensity than *anti* 14 / *anti* 15, which hints towards steric repulsion between methyl groups *syn* 14 / *syn* 14' (NOE not visible due to diagonal peak overlap) forcing methyl group 14 closer towards methyl group 15.

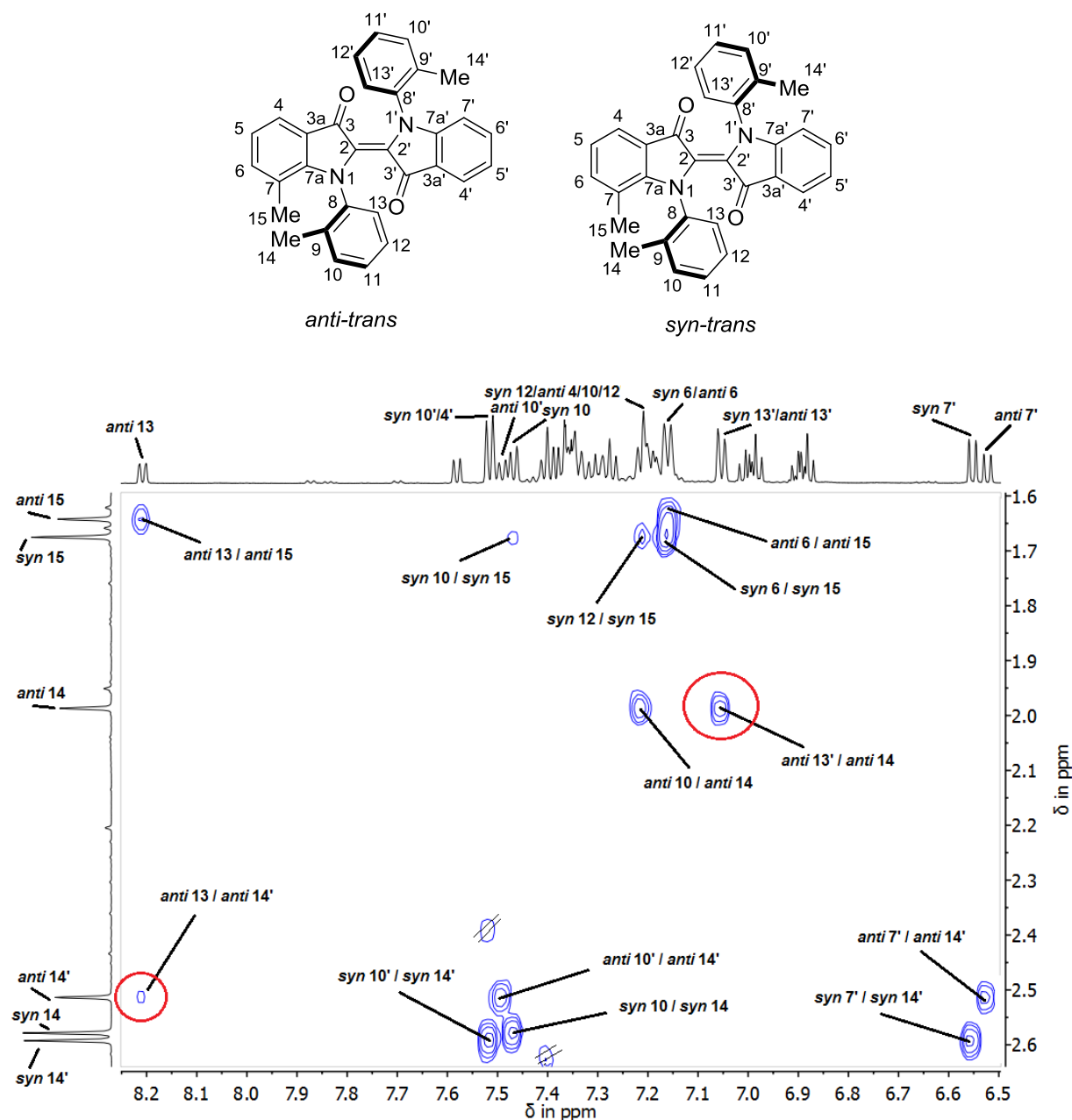


Figure 291: Aromatic / aliphatic  $^1\text{H}$ -NOESY NMR-spectrum of the *syn*- and *anti*-rotamer of 7-methyl-*N,N*-di(*o*-tolyl)indigo **71**, measured at 27 °C, 600 MHz, dichloromethane- $d_2$ , 27 °C). The *anti* conformation can be unambiguously assigned as cross-signals *anti* 13' / *anti* 14 and *anti* 13 / *anti* 14' can be observed. The difference intensity of these signals supports a twisted conformation of the molecule with aryl edge 13' closer to methyl group 14.

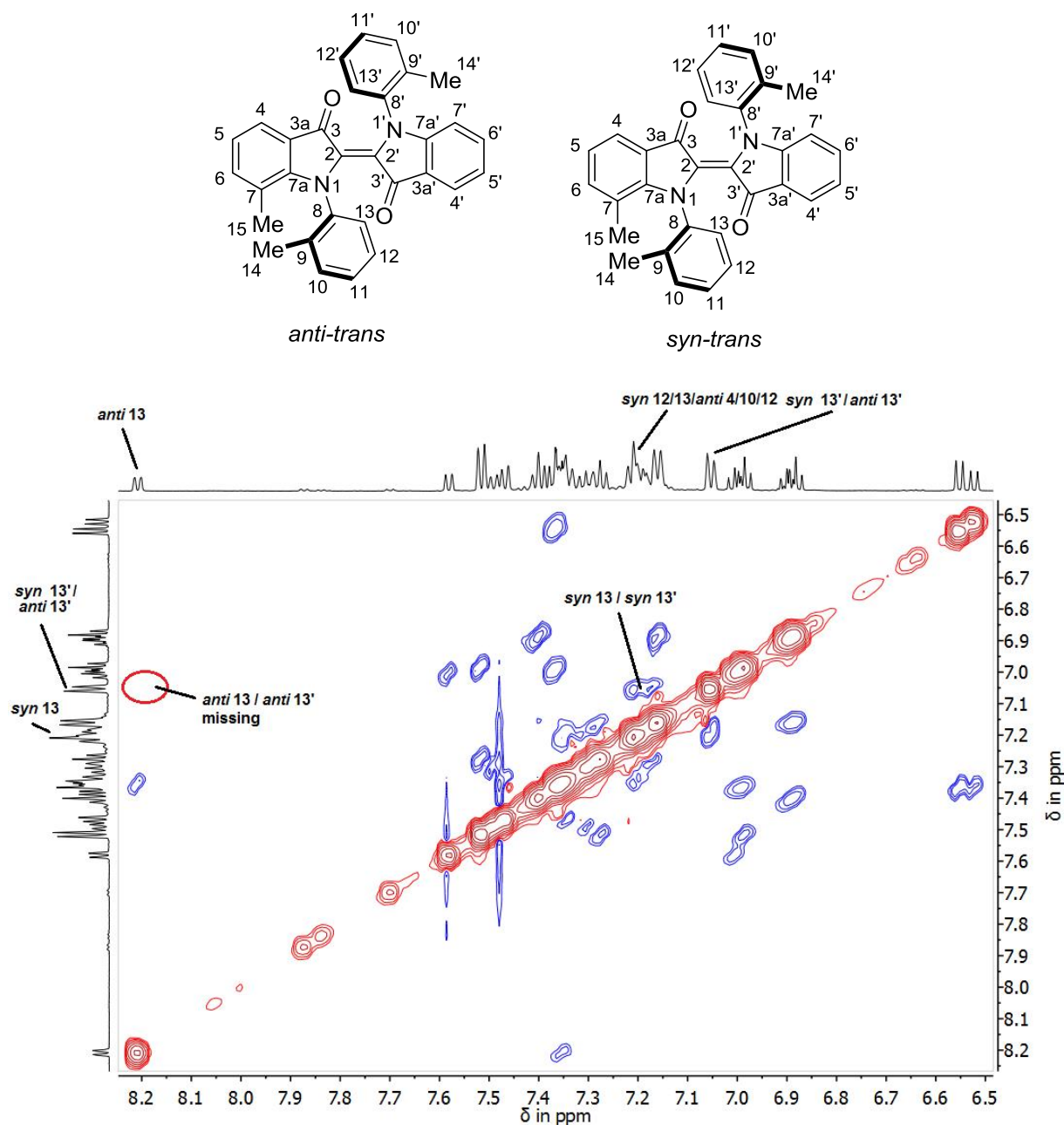


Figure 292: Aromatic  $^1\text{H}$ -NOESY NMR-spectrum of the *syn*- and *anti* rotamer of 7-methyl-*N,N'*-di(*o*-tolyl)indigo **71**, measured at (600 MHz, dichloromethane- $d_2$ , 27 °C). Signals *syn* 13 / *syn* 13' are visible while signals *anti* 13 / *anti* 13' are not visible, which underlines this assignment to be correct.

Further low temperature  $^1\text{H-NMR}$  experiments were carried out on this compound to scrutinize its photoisomerization behavior.

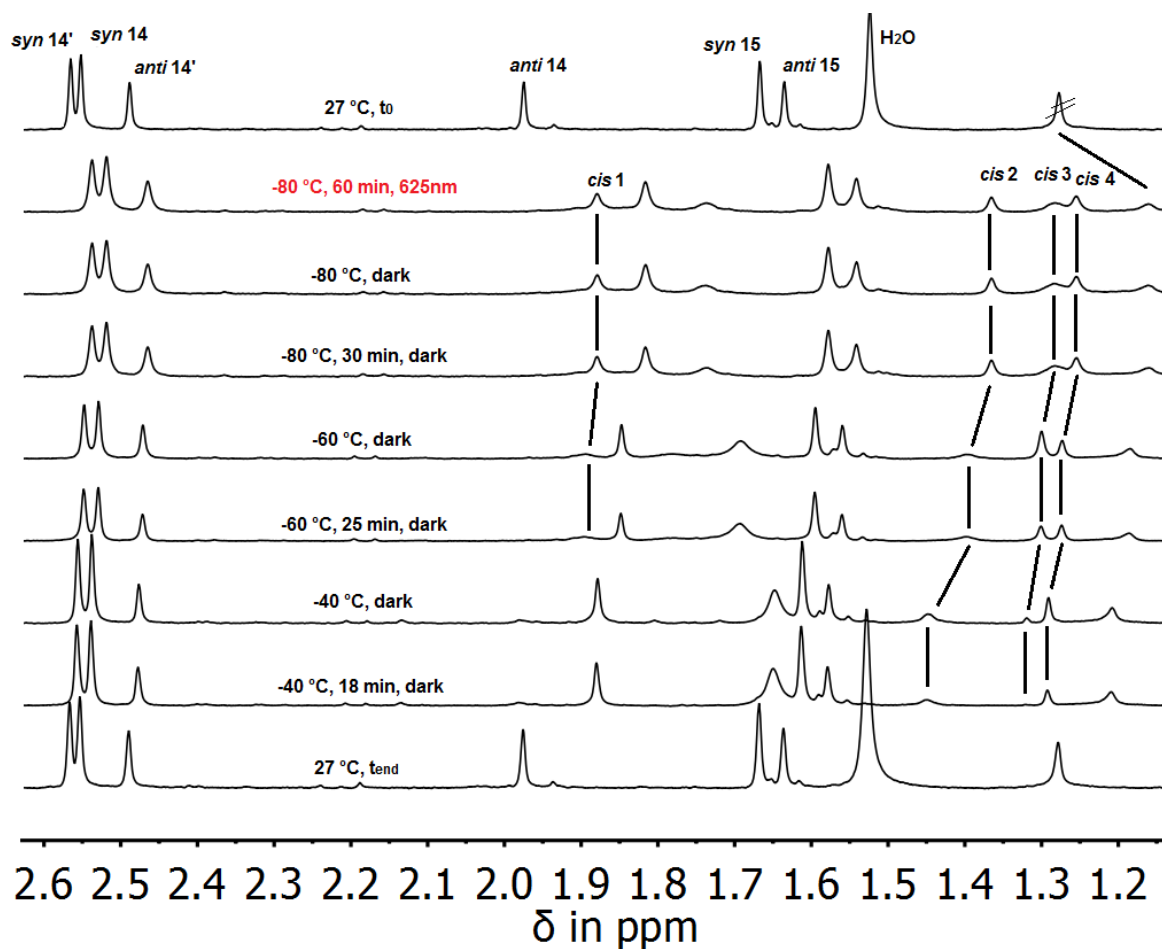


Figure 293: Irradiation of a 1.6 / 1.0 *syn-* / *anti-trans* mixture of indigo **71** in dichloromethane- $d_2$  (400 MHz) after irradiation at various temperatures. The generation of stable *cis* isomers can be observed at  $-80\text{ }^\circ\text{C}$ .

Increasing the temperature to  $-60\text{ }^\circ\text{C}$  showed no thermal reactions, only changing- / disappearing peak shapes of the *cis* isomers can be observed. When heating to  $-40\text{ }^\circ\text{C}$ , the observed *cis* isomers start to disappear thermally, which is shown in Figure 294 below.

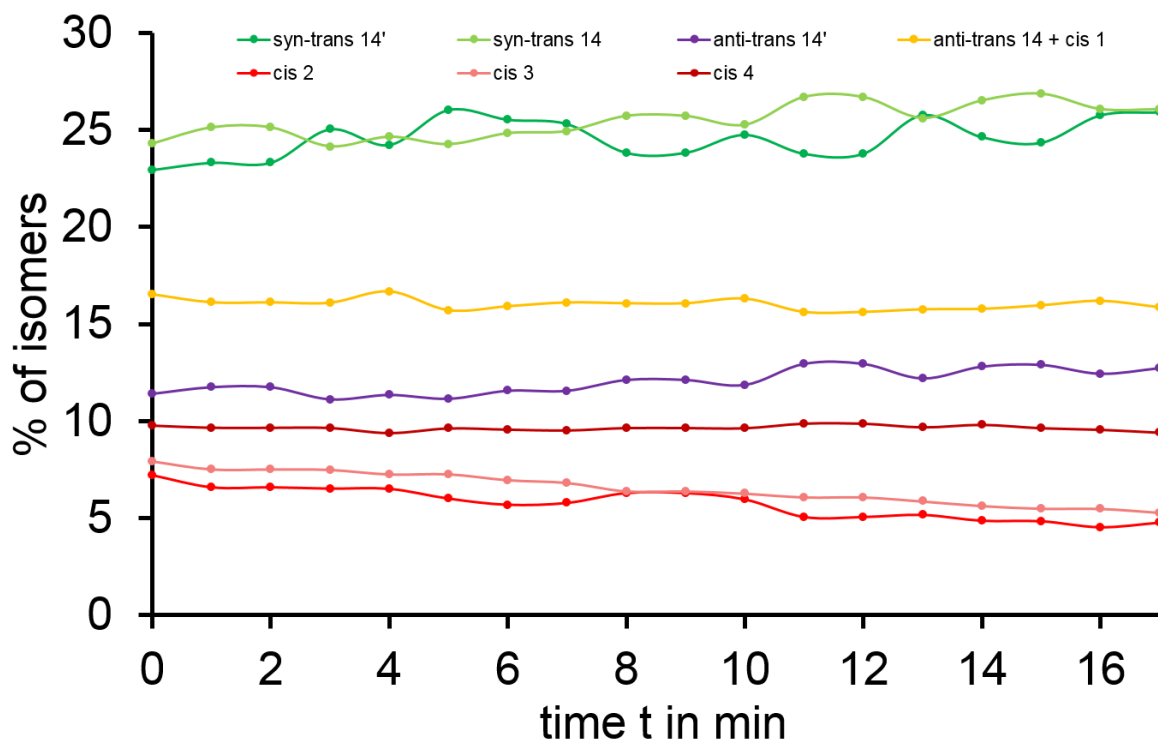


Figure 294: Kinetic plots for the thermal *cis* to *trans* isomerization of indigo **71** at -40 °C. An increase of all *trans* isomers can be observed while the *cis* states are depopulated.

The yellow line remains relatively constant as the *anti-trans* 14 signal is overlapped with the *cis* 1 peak, see Figure 293. A temperature of -30 °C or longer acquisition times should be tried for tracking of the kinetics to obtain more defined slopes for analysis of the prevalent barriers. Also, the *anti-trans* isomer should be isolated and irradiated at low temperatures. Future experiments have to be carried out on this intriguing system.

## 2.4.28 Non-symmetric chiral indigos - Third generation chimeric indigo 72

The synthesis and characterization of second generation non-symmetric chiral indigo **71** proved as success. Another approach desymmetrize the axially chiral indigo scaffold consisted in introduction of a functional group at the periphery of one chiral axis of this molecular setup. The goal of this project was to leave the atropisomerization barriers and photoinduced- / thermal trajectories of indigo **64** unchanged. *K. Jordan* synthesized *N*-(4-methoxy-2-methylphenyl)-*N'*-(*o*-tolyl)indigo **72** during his master's thesis to explore the properties of these systems.

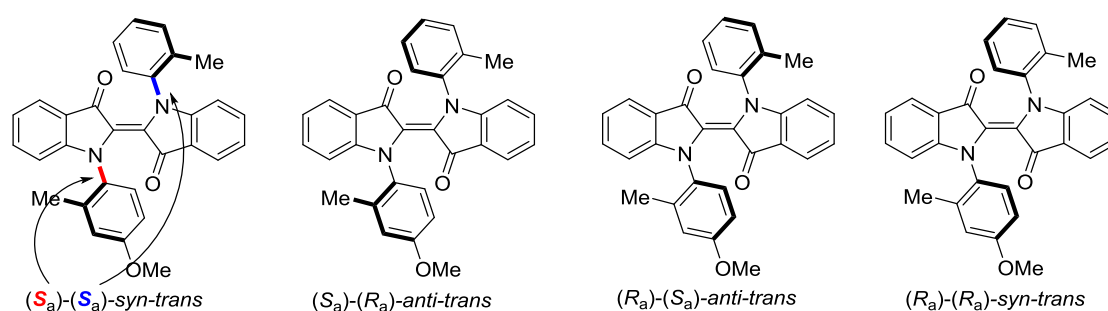
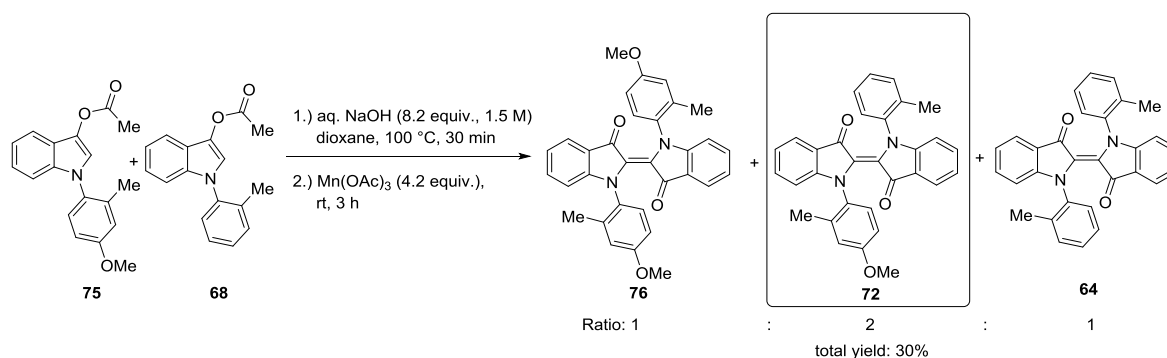


Figure 295: Overview of the *trans* forms of *N*-(4-methoxy-2-methylphenyl)-*N'*-(*o*-tolyl)indigo **72**. The same amount of enantio and diastereomers is expected for the *cis* state.



Scheme 38: Simultaneous deacylation of indoxyl acetates **75** and **68** was carried out according to *U. Burger et al.* with dioxane as co-solvent. Subsequent oxidation using manganese(III) acetate furnished **76**, **72** and **64** in low yields.

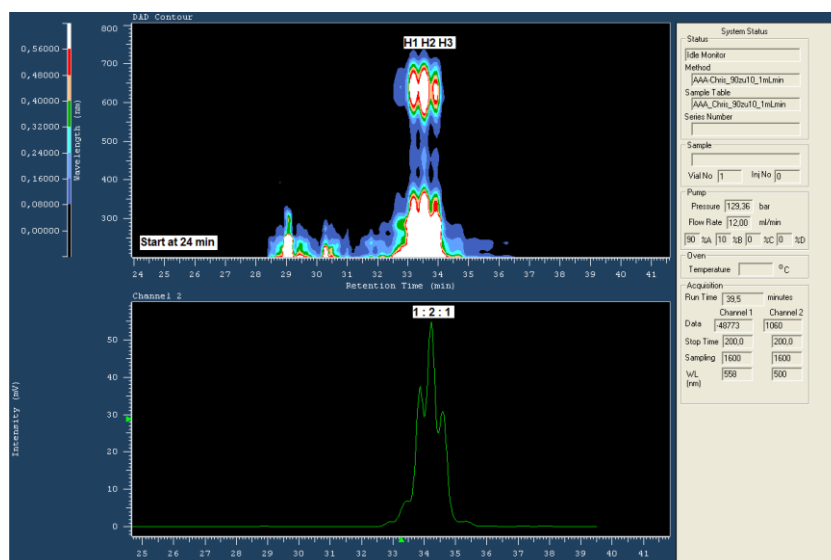


Figure 296: Optimized reversed-phase HPLC separation of indigo **72** with 9 / 1 acetonitrile / water as eluent. The difference in retention times proved as unfeasible for separation and changing of eluent(s) and / or composition, temperature and column phase did not yield satisfactory results. The expected 1 / 2 / 1 pattern for this statistical reaction can be observed.

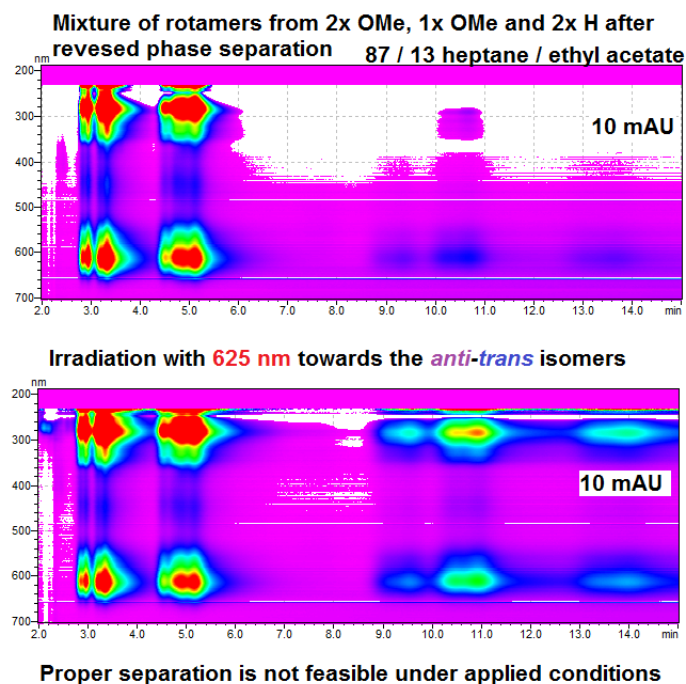


Figure 297: Injection of the H2 peak of indigo **72** from the preceding reversed-phase HPLC run onto a chiral HPLC column at 0 °C with 83 / 17 heptane / ethyl acetate as eluent. Poor separation and carry-over of the three different molecules with three to four rotamers each make obtaining of enantiopure fractions impossible.

The dissatisfactory separations lead to abandoning the methoxy substitution pattern. Ether cleavage with borontrihalides did not yield the hydroxyl derivatives.

### 2.4.29 Non-symmetric chiral indigos - Third generation chimeric indigo 73

As the methoxy substitution (indigo **72**) proved as unsuccessful approach towards measurements on third generation non-symmetric chiral indigos, *N*-(4-fluoro-2-methylphenyl)-*N'*-(*o*-tolyl)indigo **73** was synthesized and purified by *K. Jordan* during his master's thesis.

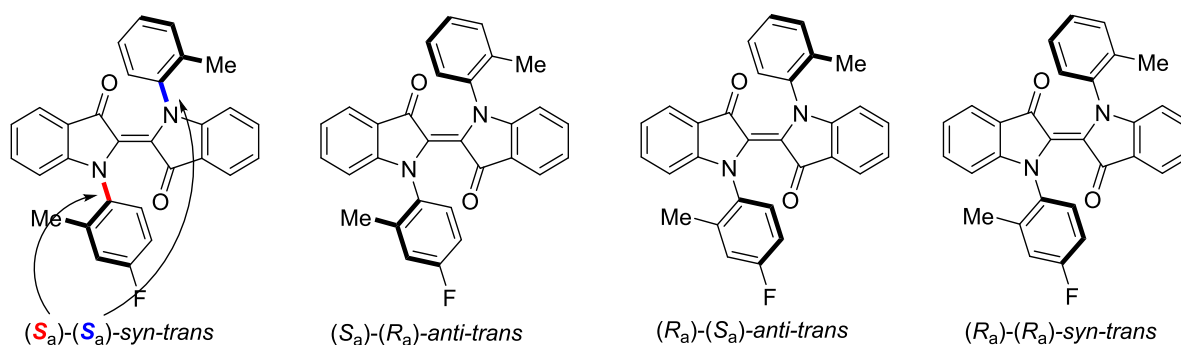
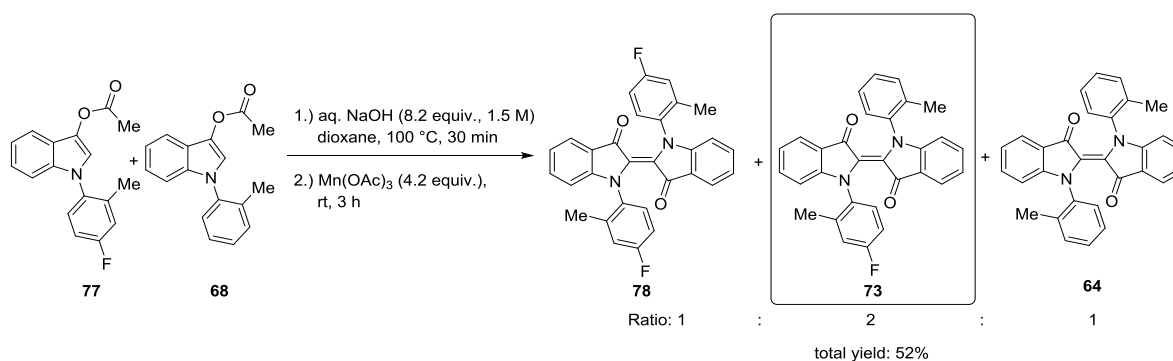


Figure 298: Overview of the *trans* forms of *N*-(4-fluoro-2-methylphenyl)-*N'*-(*o*-tolyl)indigo **73**. The same amount of enantio and diastereomers is expected for the *cis* state.



Scheme 39: Simultaneous deacylation of indoxyl acetates **77** and **68** was carried out according to *U. Burger et al.* with dioxane as co-solvent. Subsequent oxidation using manganese(III) acetate furnished indigos **78**, **73** and **64** in moderate yields.



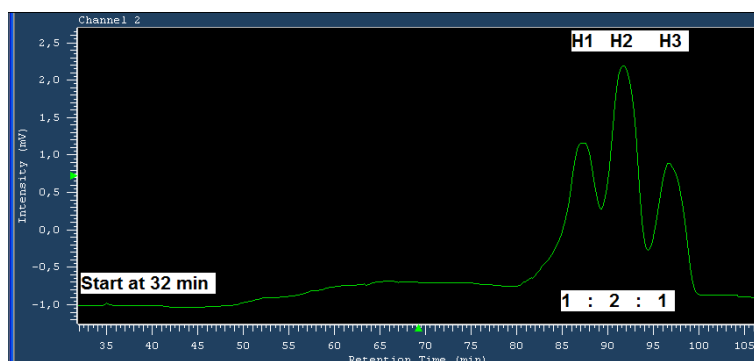


Figure 299: Optimized reversed-phase HPLC separation of indigo **73** with 6 / 4 acetonitrile / water as eluent. The expected 1 / 2 / 1 pattern for this statistical reaction can be observed.

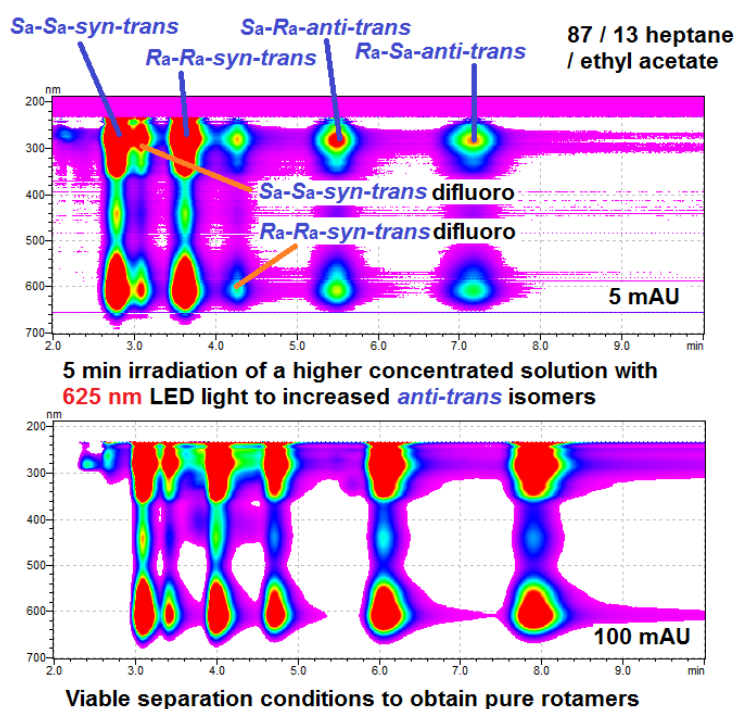


Figure 300: Injection of the H2 peak of indigo **73** from the preceding reversed-phase HPLC run onto a chiral HPLC column at 0 °C with 83 / 17 heptane / ethyl acetate as eluent. The expected four rotamers can be observed, however, the rotamers of residual difluorated indigo **79** from fraction H1 can also be seen.

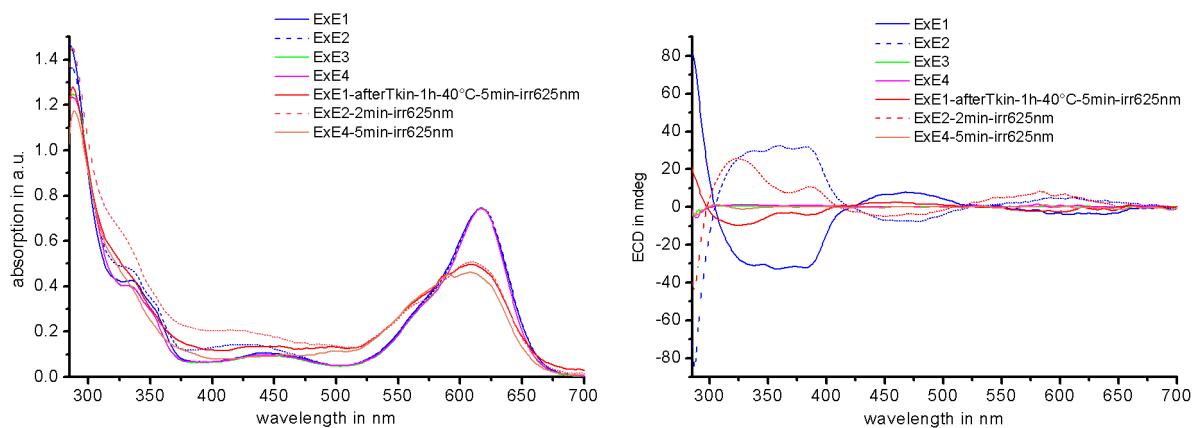


Figure 301: Scaled UV-Vis (left) and corresponding ECD spectra (right) of all four peaks obtained from chiral HPLC separation (*syn-trans*-1 (ExE1), *syn-trans*-2 (ExE2), *anti-trans*-1 (ExE3) and *anti-trans*-2 (ExE4)) of *N*-(4-fluoro-2-methylphenyl)-*N'*-(*o*-tolyl)indigo **73** in 83 / 17 heptane / ethyl acetate at 0 °C. Samples were irradiated and measured within the ECD spectrophotometer at 0 °C, which records UV-Vis spectra with poor quality. This was done because the other UV-Vis spectrophotometer cannot be cooled to 0 °C. Both *syn* isomers (blue and broken blue lines) show strong ECD responses while the *anti* forms (green and pink lines) show no ECD signal at all. This can be explained by the cancellation of ECD signal for a ( $R_a$ )- and a ( $S_a$ ) chiral axis in the same molecule, see Section 2.4.9. Irradiation at 0 °C shows the *anti-cis* isomers (red and broken red lines).

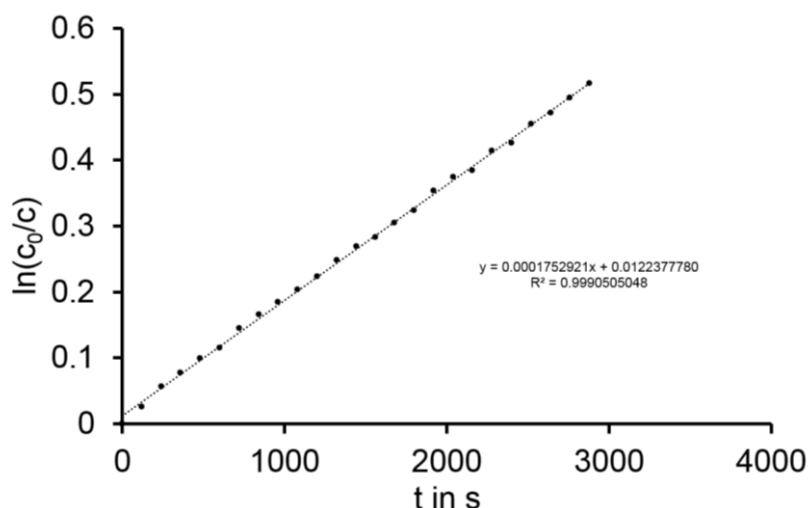


Figure 302: Linearization of the first order kinetics for the atropisomerization of *N*-(4-fluoro-2-methylphenyl)-*N'*-(*o*-tolyl)indigo **73** at 40 °C in 83 / 17 heptane / ethyl acetate. A barrier of 23.7 kcal/mol with a half-life of 7.90 h at 25 °C could be determined. Used formulas and equations can be found in Section 2.2.19.

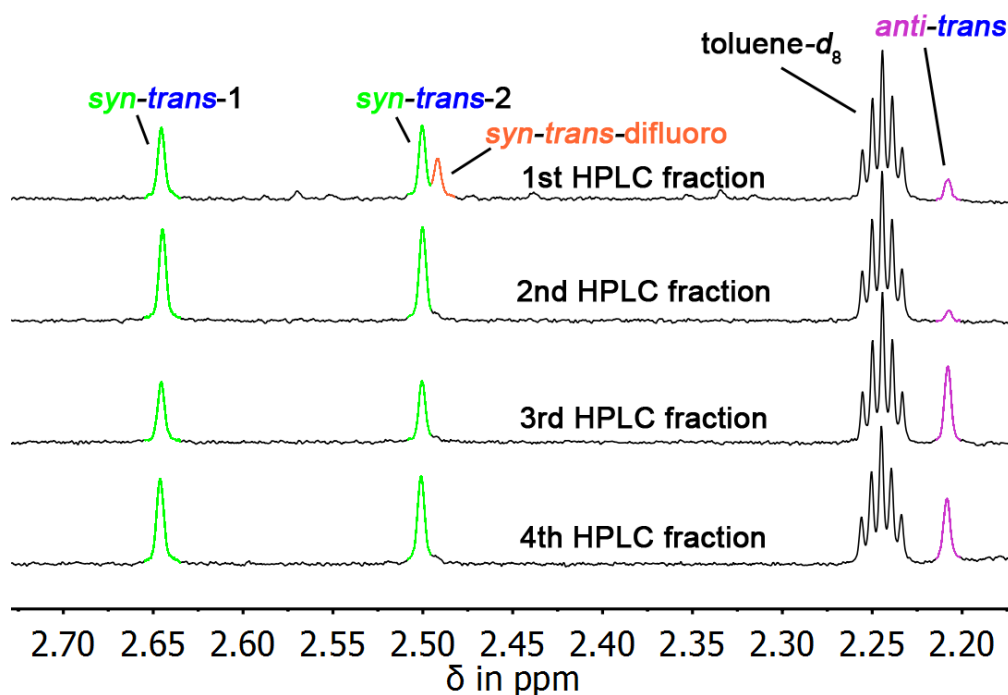


Figure 303:  $^1\text{H-NMR}$  spectra of all four isolated rotamers of indigo **73**. 1<sup>st</sup> and 2<sup>nd</sup> HPLC fractions can be regarded as enantiomers, which is also true for the 3<sup>rd</sup> and 4<sup>th</sup> fraction as they show the same spectra. Residual difluorated indigo **78** can only be observed in the 1<sup>st</sup> fraction, which shows that the separation of rotamers for this compound is feasible compared to indigo **72**.

To obtain insight in the motional behavior of this compound, further low temperature  $^1\text{H-NMR}$  measurements are carried out in the time of writing. The non-symmetric molecular setup should allow the recording of EXSY NMR spectra for separated dynamic signals to scrutinize their dynamics.

### 2.4.30 Conclusion: Axially chiral indigos

The presented axially chiral molecular setups based in the diarylated indigo scaffold show vastly different behaviors upon their substitution patterns by changing the position and number of methyl groups at crucial positions.

The first generation of this molecule class could not be easily analyzed due to its unexpectedly fast conversion rates and  $^1\text{H-NMR}$  signal broadening at low temperatures.

The second generation avoided the indigo core methyl groups, giving higher atropisomerization rates, enabling the separation of isomers for their individual analyses. Their complex motions could be determined to prospective unidirectional double- and single bond motors, thermally switchable enriching of *syn-* / *anti-trans* states against the thermal equilibrium and photochemically- / thermally induced, geared Hula-Twist motions.

Several non-symmetric axially chiral model compounds were successfully synthesized and characterized by *F. Binder* to disentangle and verify the observed properties shown by the symmetric derivatives. A novel chimeric compound supporting two different chiral axis setups was also explored.

The third generation of axially chiral indigos was successfully synthesized and characterized by *K. Jordan* to gain further insights on the exhibited motional cascades within these molecules, further experiments are carried out at the time of writing.

Overall, the unexpected behavior of these fairly small and formally simple looking molecules was scrutinized. Their potential as prospective molecular motors and -machines was demonstrated, giving insights into novel photoinduced- and thermal motions, which is crucial for the design of nanomachines and molecular robots. Also, addressability within the biooptical window was achieved, as all photosteps can be driven with low energy, 625 nm LED light, making the application of likewise systems available on biological tissues *in vitro* and *in vivo*.

- [53] N. Koumura, R. W. J. Zijlstra, R. A. van Delden, N. Harada, B. L. Feringa, *Light-driven unidirectional molecular rotor*, *Nature* **1999**, *401*, 152.
- [55] W. R. Browne, B. L. Feringa, *Making molecular machines work*, *Nature Nanotechnology* **2006**, *1*, 25.
- [66] L. A. Huber, P. Mayer, H. Dube, *Photoisomerization of Mono-Arylated Indigo and Water-Induced Acceleration of Thermal cis-to-trans Isomerization*, *ChemPhotoChem* **2018**, *2*, 458.
- [69] C. Y. Huang, A. Bonasera, L. Hristov, Y. Garmshausen, B. M. Schmidt, D. Jacquemin, S. Hecht, *N,N'-Disubstituted Indigos as Readily Available Red-Light Photoswitches with Tunable Thermal Half-Lives*, *J. Am. Chem. Soc.* **2017**, *139*, 15205.
- [80] B. L. Feringa, *In Control of Motion: From Molecular Switches to Molecular Motors*, *Acc. Chem. Res.* **2001**, *34*, 504.
- [81] A. Coskun, M. Banaszak, R. D. Astumian, J. F. Stoddart, B. A. Grzybowski, *Great expectations: can artificial molecular machines deliver on their promise?*, *Chem. Soc. Rev.* **2012**, *41*, 19.
- [82] M. Guentner, M. Schildhauer, S. Thumser, P. Mayer, D. Stephenson, P. J. Mayer, H. Dube, *Sunlight-powered kHz rotation of a hemithioindigo-based molecular motor*, *Nat Commun* **2015**, *6*, 8406.
- [88] U. Burger, A. O. Bringhen, *Cyclization Studies with N-Munnich Bases of 2-Substituted Indoles*, *Helv. Chim. Acta* **1989**, *72*, 93.
- [91] J. C. Antilla, A. Klapars, S. L. Buchwald, *The Copper-Catalyzed N-Arylation of Indoles*, *J. Am. Chem. Soc.* **2002**, *124*, 11684.
- [92] P. Y. Choy, C. P. Lau, F. Y. Kwong, *Palladium-catalyzed direct and regioselective C-H bond functionalization/oxidative acetoxylation of indoles*, *J. Org. Chem.* **2011**, *76*, 80.
- [95] O. Trapp, S. Bremer, S. K. Weber, *Accessing reaction rate constants in on-column reaction chromatography: an extended unified equation for reaction educts and products with different response factors*, *Analytical and Bioanalytical Chemistry* **2009**, *395*, 1673.
- [112] A. Gerwien, P. Mayer, H. Dube, *Green light powered molecular state motor enabling eight-shaped unidirectional rotation*, *Nature Communications* **2019**, *10*, 4449.
- [113] O. Lavinda, I. Mironova, S. Karimi, F. Pozzi, J. Samson, H. Ajiki, L. Massa, K. Ramig, *Singular thermochromic effects in dyeings with indigo, 6-bromoindigo, and 6,6'-dibromoindigo*, *Dyes and Pigments* **2013**, *96*, 581.
- [114] K. Ramig, O. Lavinda, D. J. Szalda, I. Mironova, S. Karimi, F. Pozzi, N. Shah, J. Samson, H. Ajiki, L. Massa, D. Mantzouris, I. Karapanagiotis, C. Cooksey, *The nature of thermochromic effects in dyeings with indigo, 6-bromoindigo, and 6,6'-dibromoindigo, components of Tyrian purple*, *Dyes and Pigments* **2015**, *117*, 37.
- [115] G. M. Wyman, W. R. Brode, *The Relation between the Absorption Spectra and the Chemical Constitution of Dyes XXII. cis-trans Isomerism in Thioindigo Dyes I*, *J. Am. Chem. Soc.* **1951**, *73*, 1487.
- [116] J. H. Porada, J.-M. Neudörfl, D. Blunk, *Planar and distorted indigo as the core motif in novel chromophoric liquid crystals*, *New J. Chem.* **2015**, *39*, 8291.
- [117] F. Maier, O. Trapp, *Effects of the Stationary Phase and the Solvent on the Stereodynamics of biphenyl Ligands Quantified by Dynamic Three-Column HPLC*, *Angew. Chem. Int. Ed.* **2012**, *51*, 2985.
- [118] S. Wheeler, K. Houk, *Origin of Substituent Effects in Edge-to-Face Aryl-Aryl Interactions*, *Mol. Phys.* **2009**, *107*, 749.
- [119] J. M. Lehn, *Conjecture: imines as unidirectional photodriven molecular motors-motional and constitutional dynamic devices*, *Chemistry* **2006**, *12*, 5910.

- [120] L. Greb, A. Eichhofer, J. M. Lehn, *Synthetic Molecular Motors: Thermal N Inversion and Directional Photoinduced C=N Bond Rotation of Camphorquinone Imines*, *Angew. Chem. Int. Ed. Engl.* **2015**, *54*, 14345.

## 2.5 Ionic hemiindigos - Photoswitching of collision cross-sections in the gas phase - Introduction

Achieving rational- and cost-effective design strategies for indigoid and other photoswitches requires a detailed understanding - both experimentally as well as theoretically - of their fundamental photochemical- and physical properties by exploring the underlying mechanisms. Most commonly, these properties are experimentally probed in solution or the solid state, i.e. in situations where the influence of the surrounding medium is important. Techniques that enable probing of the structure and photoinduced changes of an isolated molecule in the gas phase are still quite exotic despite offering unique insights into crucial intrinsic molecular properties. Such methods allow one to disentangle the influences of the surrounding medium and have the advantage of providing data directly comparable to theoretical descriptions.<sup>[121, 122, 123, 124, 125]</sup>

Hemiindigo photoswitches show almost quantitative isomer accumulation, high thermal bistabilities, good quantum yields and independence of solvent polarity upon photoswitching. Isolation of the hemiindigo photoswitches from the solvent matrix was scrutinized during gas phase experiments carried out by *E. Carrascosa*, *M. Schulz* and *J. Bull* from the *Bieske* group located at the University of Melbourne, Australia. Permanent charge tags were attached to hemiindigo photoswitches to further investigate the mechanistic properties and expanding the scope of their photoswitchability in both solution and the gas phase.<sup>[126]</sup> The use of ion mobility mass spectrometry coupled to laser spectroscopy enabled the observation of photochromism and reversible *Z*- / *E* isomer photoswitching in a solvent-free environment. This method provides direct experimental evidence for significant light-induced changes in the collision cross-section of these novel hemiindigos in the gas phase. As the influences of a surrounding medium can be eliminated, the resulting measured physical properties are directly relatable to theoretical descriptions. The combination of solution NMR and UV-Vis absorption spectroscopies with gas phase action spectroscopy delivers insights into the environmental influences on the photoswitching properties of hemiindigos. It could be shown that this approach represents a powerful and generally applicable strategy for studying the photoisomerization mechanisms and structural changes of isolated molecular switches.

An experimental approach combining ion mobility mass spectrometry with laser spectroscopy was developed by the *Bieske* group to obtain electronic action spectra of specific isomer ions, which has been applied successfully to a range of photoswitches and biochromophores.<sup>[127]</sup> Separation and photochemical characterization of the *Z* and *E* isomers of

three newly developed and permanently charged hemiindigo photoswitches **80**, **81** and **82** (Figure 304) could be carried out in the gas phase by utilization of this setup. The photochemical behavior of the isolated isomers was compared to the corresponding behavior in solution as well as to quantum chemical calculations.

Time-resolved collision cross-section experiments were carried out on the synthesized ionic hemiindigo photoswitches by mass filtering specific isomers and submitting them to a low pressure collision gas area within the tandem mass spectrometer. The collision gas decelerates the larger molecular conformers while the smaller ones travel less hindered at faster speeds towards the detector. This technique allows for the observation of delicate conformational changes of molecules that cannot be examined within solution or solid state in which *Brownian* motion is dominating.

The measurement course consists of *in situ* laser irradiation of isomer compositions to yield *Z*- or *E* isomer enriched and isomer specific arrival time distributions (ATDs) as photoproducts. The comparison of the *in situ* generated ATDs to the ATDs for samples which were previously enriched outside of the mass spectrometer to the *Z*- or *E* isomeric states makes an unambiguous assignment of the *in situ* generated ATDs possible, as the irradiation behavior in solution is known by UV-Vis and NMR spectroscopy. The photoswitches were irradiated outside the spectrometer and the isomerically enriched solutions were submitted to electrospray ionization (ESI), showing the same differences in arrival times as the *in situ* irradiated samples (Figure 307).

The comparison of the experimental datasets with the theoretical evaluation of the findings done by *E. Carrascosa* and *M. Scholz* gives insights in otherwise non-observable conformational effects within ionic hemiindigo photoswitches.

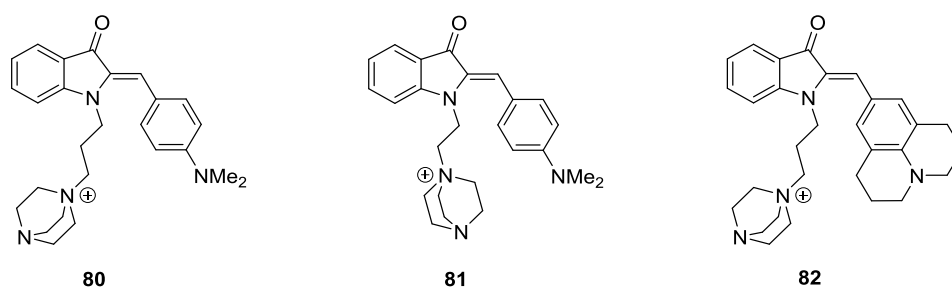


Figure 304: Overview of synthesized and investigated hemiindigos **80**, **81** and **82**. Only *Z* isomers are shown.

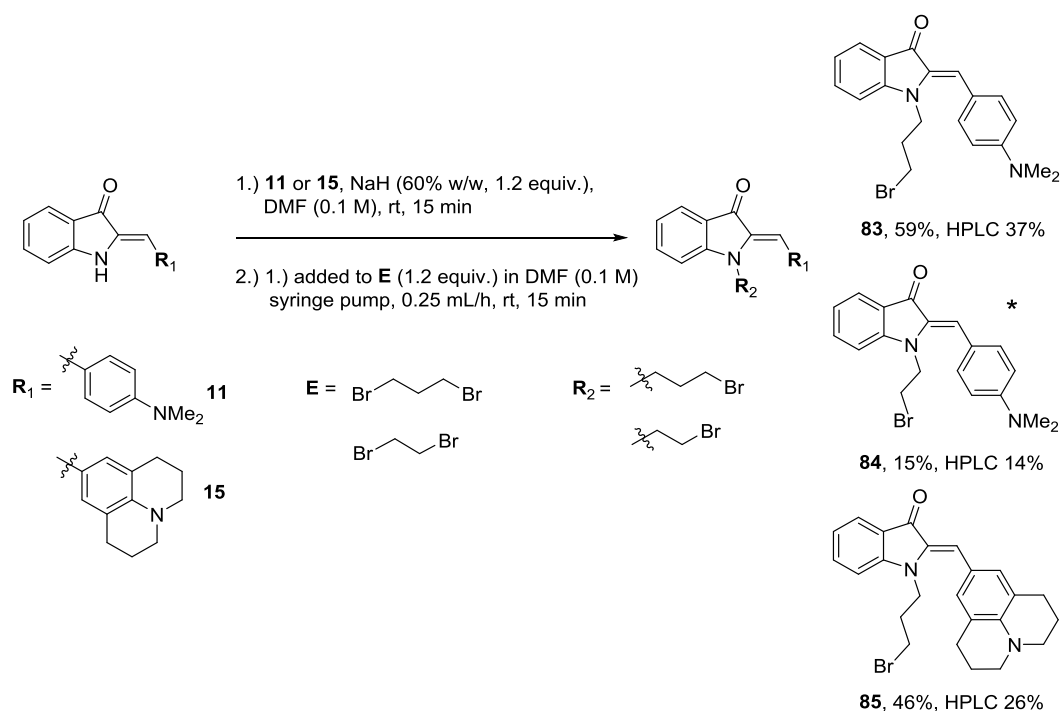
For hemiindigos **80**, **81** and **82** the charge-tag is peripherally attached to the chromophore via an alkyl chain, which is meant to minimize the electronic communication to the photoswitch



(Figure 304). While hemiindigo **80** and **81** only differ in the length of the charge-tag chain, hemiindigo **82** incorporates a stronger electron donating julolidine moiety.

### 2.5.1 Ionic hemiindigos - Synthesis

Hemiindigos **11** and **15** were prepared according to Section 2.2.4 or literature procedures.<sup>[74, 88]</sup> Sodium hydride, 1,2-dibromoethane and 1,3-dibromopropane were purchased from *Sigma-Aldrich* and used as received. Hemiindigos **83**, **84** and **85** were synthesized according to *V. Velezheva et al.* with changes to addition order and -speed.<sup>[90, 128]</sup>



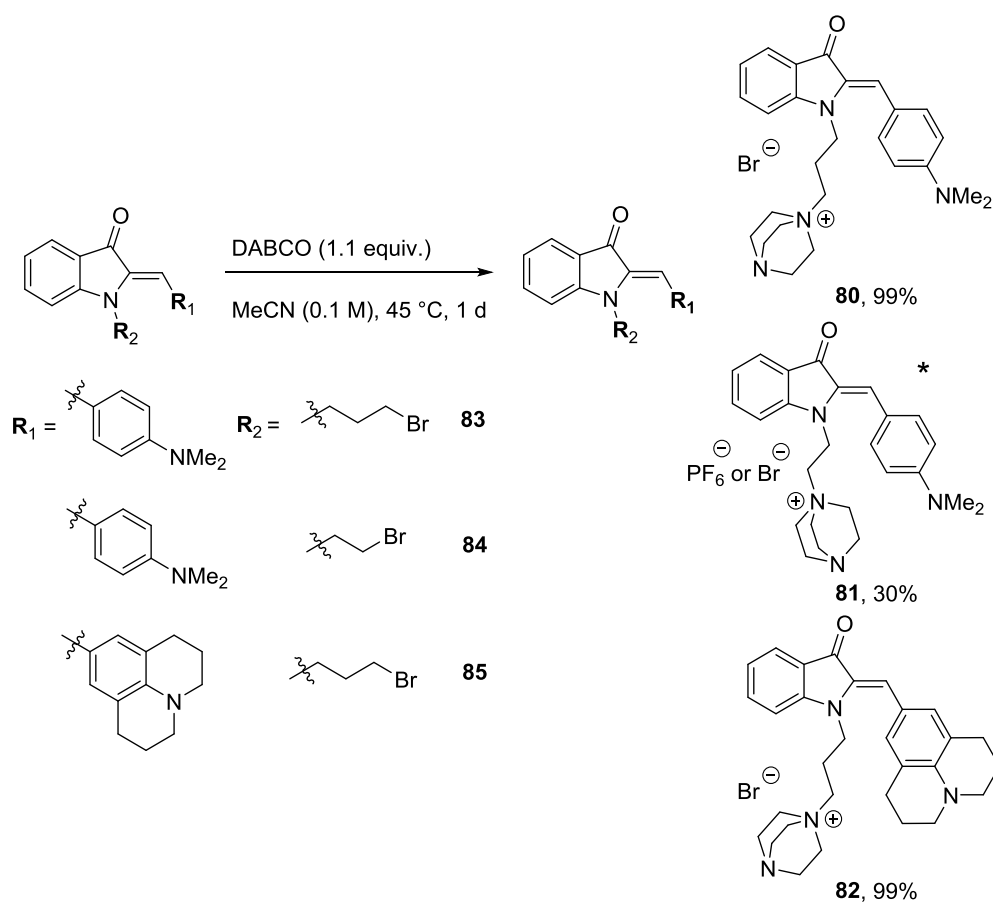
Scheme 40: Preparation of alkylated photoswitches **83**, **84** and **85** supporting a terminal bromine functionality starting from hemiindigo derivatives **11** and **15**. Hemiindigos **83**, **84** and **85** were obtained by deprotonation with sodium hydride and a subsequent S<sub>N</sub>2 reaction with terminal dibromoalkanes by addition via syringe pump at ambient temperatures. Lower HPLC yields are caused by loss of material<sup>86</sup> upon injection and / or isolation of only one isomer peak starting from a *Z* / *E* mixture.

\* 1.5 equivalents sodium hydride and 5.0 equivalents of 1,2-dibromoethane were used. Addition of 1,2-dibromoethane to a basified mixture of **11** in *N,N*-dimethylformamide was done rapidly without syringe pump.

Excess of base tends to eliminate bromine for entries **83** and **85** via an E1cB mechanism, leaving hemiindigo switches with 1-propenyl attached to the indoxyl nitrogen as side product (approx. 10 - 20%).

The introduction of a charge tag to the hemiindigo photoswitch is necessary for proving photoswitchability within ion mobility experiments in the gas phase. 1,4-Diazabicyclo[2.2.2]octane (DABCO) was chosen as charge tag because of its superior ionization yields reported by *M. Cydzik* compared to imidazolium and alkyl ammonium tags.<sup>[129]</sup>

1,4-Diazabicyclo[2.2.2]octane was purchased from *Sigma-Aldrich* and was used as received. Hemiindigos **80**, **81** and **82** were prepared according to *B. Almarzouqi* et al. at elevated temperatures.<sup>[130]</sup>



Scheme 41: Preparation of charge-tagged hemiindigos *Z* / *E* **80**, **81** and **82**. 1,4-Diazabicyclo[2.2.2]octane reacts almost quantitatively to its quaternary bromide salts with hemiindigos **83** and **85** via a *Menschutkin* reaction at 45 °C in one day. \*Hemiindigo **81** was prepared with 5.0 equivalents of 1,4-diazabicyclo[2.2.2]octane and showed no quantitative reaction.

The hexafluorophosphate salt of **81** was prepared because the low solubility of the bromine salt in dichloromethane with minor success, as the hexafluorophosphate salt did not increase the solubility of **81** substantially. Therefore, (deuterated) acetonitrile was further used as suitable solvent for NMR- and UV-Vis measurements.

### 2.5.2 Ionic hemiindigos - Gas phase photoisomerization experiments

To investigate the photoisomerization of the isolated charge-tagged hemiindigos **80**, **81** and **82**, a homebuilt tandem ion-mobility mass spectrometer (IMS) was employed by *E. Carrascosa* from the *Bieske* group.<sup>[123]</sup> The principle of ion-mobility spectrometry is based on the spatial separation of isomeric molecular ions due to differences in their drift mobilities.

To study the photoisomerization reactions of the assigned isomers in the gas phase, a specific mobility separated ion distribution was selected using a pulsed ion gate located halfway along the ion mobility spectrometer. Exposure of the initial isomer composition to wavelength- and intensity tunable laser light promotes photoisomerization reactions, which separate the resulting *Z*- or *E* enriched isomer mixtures from its precursor composition in the second drift region. Monitoring the isomeric intensities as a function of wavelength in a *laser on-laser off* experiment (see Figure 309, upper row) yields the *Z* to *E* and *E* to *Z* photoisomerization action spectra (Figure 309, middle row). It is found that all three hemiindigos undergo *Z* to *E* and *E* to *Z* photoisomerization in the absence of surrounding solvent. This observation is in contrast to a recent work on a hemithioindigo derivative, where reversible photoisomerization was only found in solution and the gas phase allowed only *Z* to *E* photoswitching.<sup>[122]</sup> The maxima of the *Z* to *E* photoisomerization action spectra of hemiindigos **80**, **81** and **82** appear at 450 nm, 410 nm, and 470 nm, respectively, while the corresponding *E* to *Z* photoisomerization response peaks are found at 505 nm, 490 nm, and 530 nm. The significant red-shift observed in the photoisomerization band of **82** can be explained by the presence of the strong electron donating julolidine group, as seen for hemiindigo **3** in Section 2.2.5. The absorption wavelengths of all hemiindigos **80**, **81** and **82** were calculated at the df-CC2/aug-cc-pVDZ level of theory using the MRCC software. The experimentally obtained photoisomerization spectra may represent a convolution of the photoresponses of several conformers that interconvert as they pass through the drift region, leading to a single ATD peak. Absorption wavelengths were only calculated for the previously identified low energy conformers.

An ions' mobility  $K$  can be expressed by the *Mason-Schamp* equation<sup>[131]</sup> (eq. 20):

$$K = \frac{3ze}{16N} \sqrt{\frac{2\pi}{\mu k_b T}} \left(\frac{1}{\Omega}\right) = \frac{l^2}{t_d V} \quad \text{eq. 20}$$

Here,  $z$  is the ion's charge number,  $e$  the electron charge,  $N$  the density of the buffer gas,  $\mu$  the reduced mass of the collision partners and  $k_b$  the *Boltzmann* constant.  $\Omega$  represents the integral collision cross-section and depends on the interaction between ion and buffer gas molecule, so that it is dependent on the molecular arrangement of the given ion. Bulky, unfolded molecules have larger collision cross-sections and therefore drift more slowly (larger  $t_d$ ) than compact molecules. Figure 305 shows a schematic representation of the experimental arrangement.

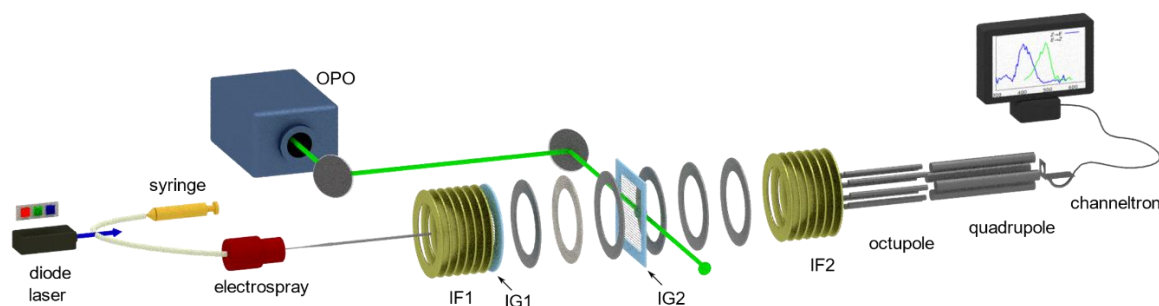


Figure 305: Schematic representation of the homebuilt tandem ion mobility mass spectrometer. Adapted with permission from<sup>[126]</sup>. Copyright 2020 Wiley VCH.

Hemiindigos **80**, **81** and **82** were electro sprayed from  $\sim 0.1$  mM solutions of the respective precursor in acetonitrile. The ions were then transferred through a heated capillary into a first radiofrequency (RF) driven ion funnel (IF1) for radial confinement. No significant effect of the RF drive voltage amplitude on the relative peak intensities in the arrival time distributions was observed. The absence of collisionally induced rearrangements suggests the existence of large thermal *Z/E* isomerization barriers for all three compounds. After confinement along the first ion funnel, the ions were injected as pulsed packets into a two-stage drift region filled with  $N_2$  buffer gas at  $\approx 6.2$  Torr using an electrostatic ion gate (IG1). The ion gate was pulsed for  $120 \mu s$  at a rate of 40 Hz. The drift tube consists of a series of ring electrodes which established an electric field (44 V/cm) that propelled the ions through the drift region. OPO = optical parametric oscillator, a wavelength- and intensity tuneable pulsed laser light source.

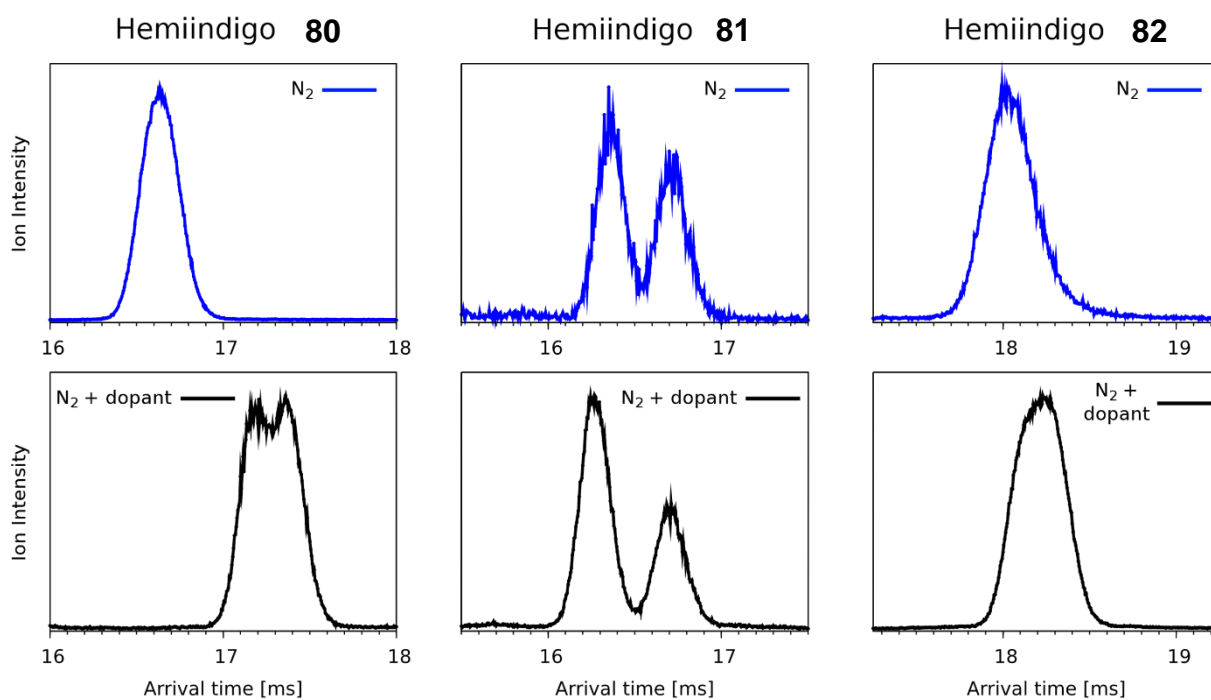


Figure 306: Arrival time distributions (ATDs) for the three investigated hemiindigo ions **80**, **81** and **82** recorded with N<sub>2</sub> buffer gas (upper row) and with N<sub>2</sub> doped with 1% 2-propanol (lower row). Adapted with permission from <sup>[126]</sup>. Copyright 2020 Wiley VCH.

While two almost baseline resolved peaks were obtained for hemiindigo **81** in N<sub>2</sub>, only one broad arrival time distribution was observed for compounds **80** and **82** with N<sub>2</sub> buffer gas (see Figure 306, upper row). Better separation was achieved by seeding the N<sub>2</sub> buffer gas with ≈1% 2-propanol (Figure 306, lower row). This allowed separating the *E*- and *Z* isomers for hemiindigos **80** and **82**, which was necessary to isolate and irradiate individual isomers.

### 2.5.3 Ionic hemiindigos - ATD peak assignments and determination of isomeric yields upon irradiation in solution

To assign the ATD peaks to specific isomers, a series of pre-irradiation experiments in solution were carried out by *E. Carrascosa* in the syringe connected to the electrospray source (see Figure 307). ATDs were monitored after irradiation of the sample with blue (*Laserglow LRS-473-TM-30-5*, 39.5mW, 430-473nm), green (*Thorlabs CPS533*, 4.5mW, 532nm) or red (*Melles Griot He-Ne Laser, 25-LHP-151-249*, <15mW, 632.8nm) cw lasers for 5-10 minutes, establishing a photostationary state (PSS) and comparing the irradiated samples to the distribution of the non-irradiated solution (see Figure 307). The resulting effect of light irradiation on the ATD peak intensities are shown in Figure 307 below. The obtained distributions were Gaussian fitted, constraining the width of both peaks to be equivalent.

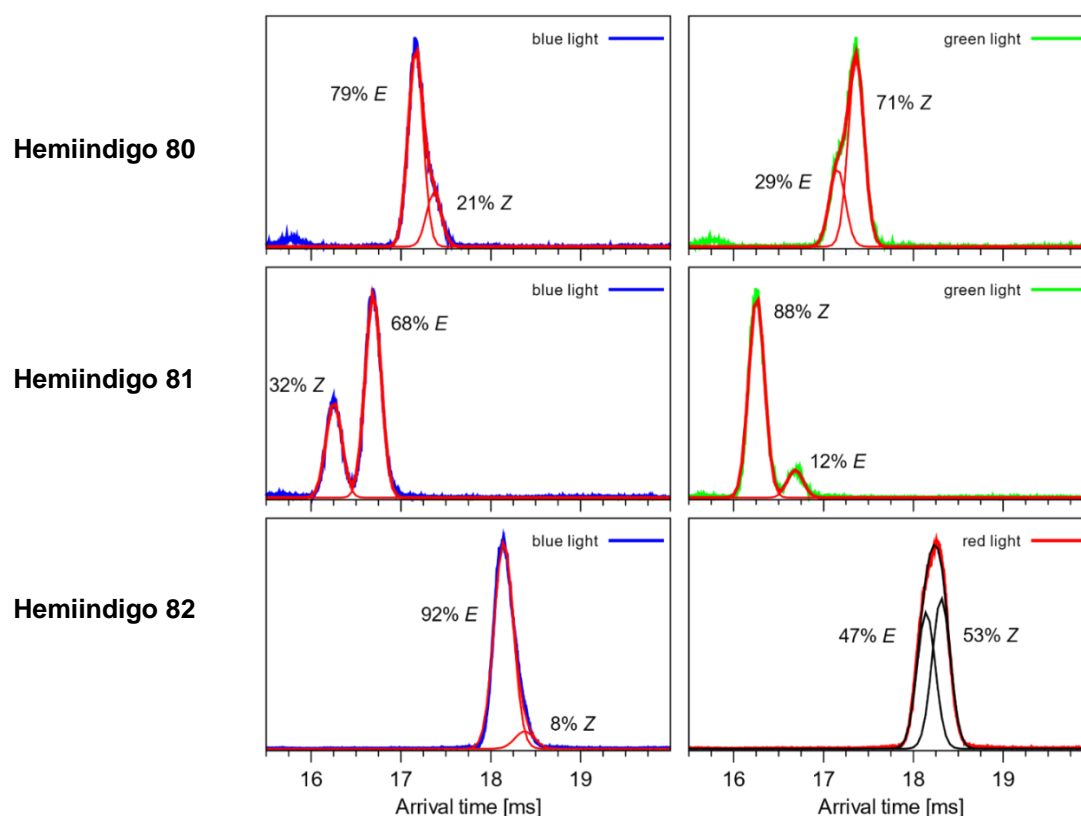


Figure 307: Fitted arrival time distributions (ATDs) for the three investigated hemiindigo ions **80**, **81** and **82** with different solution irradiation conditions. The left column shows the resulting ATD after 5 minutes irradiation of each sample with blue light, whereas the right column shows the ATDs after irradiation with green or red light prior to electrospray. The fitted contributions of each isomer are given under the obtained curves. Adapted with permission from <sup>[126]</sup>. Copyright 2020 Wiley VCH.

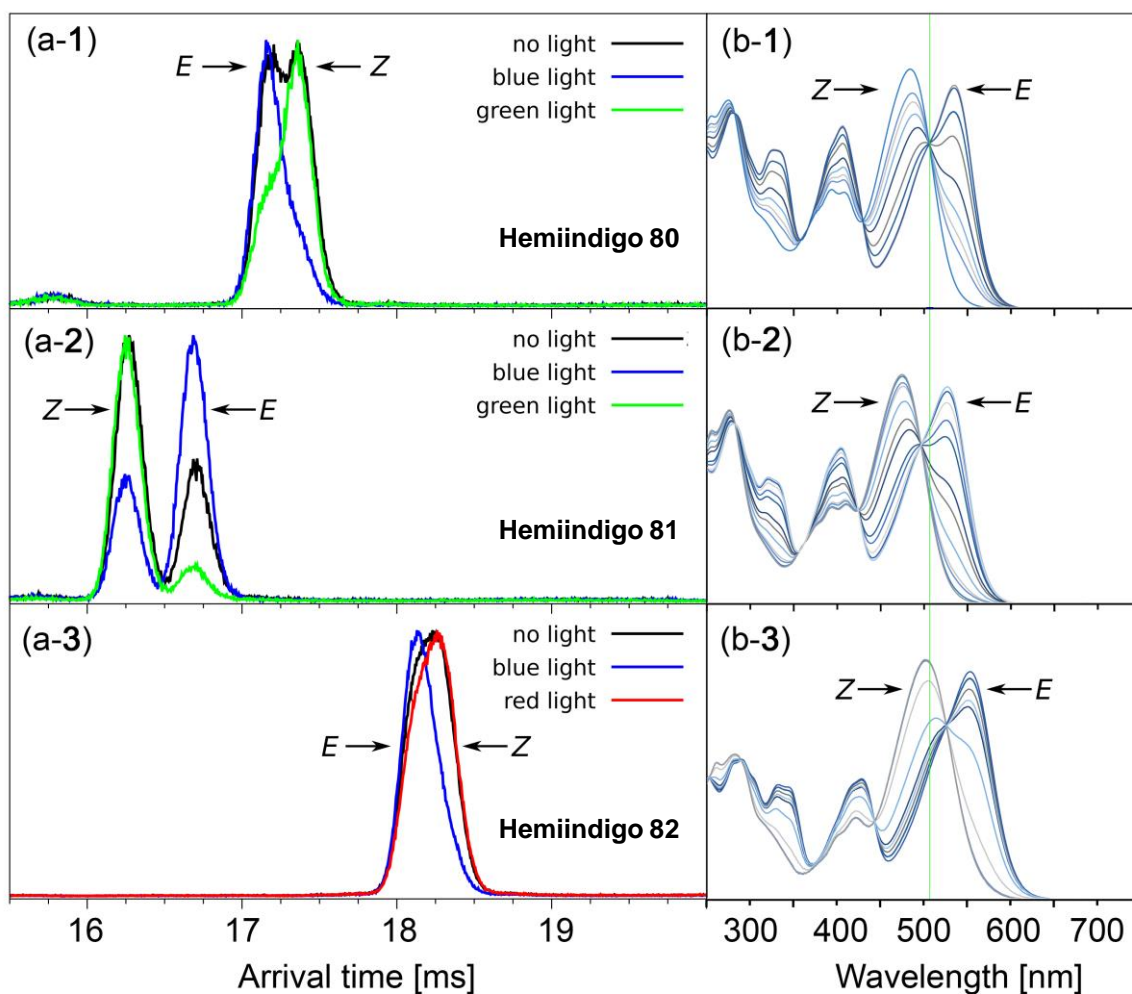


Figure 308: (a) ATDs showing mobility-separated *Z* and *E* isomers of hemiindigos **80**, **81** and **82**. The black traces show the ATDs of the electrosprayed samples shielded from light, whereas colored traces represent the distributions after exposure of each hemiindigo solution to the indicated wavelength of light. (b) Solution absorption spectra of an isomeric mixture of hemiindigos **80**, **81** and **82** after irradiation with different wavelengths of light promoting formation of either *Z* or *E* isomers. A reversal of the arrival times of *Z* and *E* isomers for hemiindigo **81** compared to **80** and **82** can be observed. Adapted with permission from <sup>[126]</sup>. Copyright 2020 Wiley VCH.

The resulting isomer PSS abundances compare well with the values obtained in solution. This comparison relies on the same PSS being established in both sets of measurements. The contribution of conformers associated with each isomer can be different for *E* and *Z*, thus causing a different broadening in the *E*- and *Z* ATDs. Therefore, assuming the same widths for

each Gauss-distribution may induce a small uncertainty in the isomer abundances shown in Figure 307.

## 2.5.4 Ionic hemiindigos - Photoisomerization action spectroscopy experiments

Photoisomerization experiments in the gas phase were carried out by *E. Carrascosa* and *M. Scholz* by selecting an ion distribution using a *Bradbury-Nielsen*-type ion gate (IG2) situated midway along the drift region which was opened for 100  $\mu$ s at an appropriate delay with respect to IG1 (see Figure 305). Shortly after being gated, the ions were irradiated with a light pulse from a tuneable optical parametric oscillator (OPO, EKSPLA NT342B, 20 Hz, 5 ns pulse width). The photoproducts were separated from the parent isomers in the second stage of the drift region and were then guided through a second ion funnel (IF2) followed by a differentially pumped octupole ion guide, a quadrupole for mass selection and a channel electron multiplier (*Channeltron*) detector. The OPO was fired at 20 Hz and overlapped every second ion packet allowing ‘light on’ and ‘light off’ ATDs to be collected, the difference between ATDs reflects the effect of light on the parent cation. Thus, a given photoisomer appeared as a separate peak in the ‘light on’ ATD.

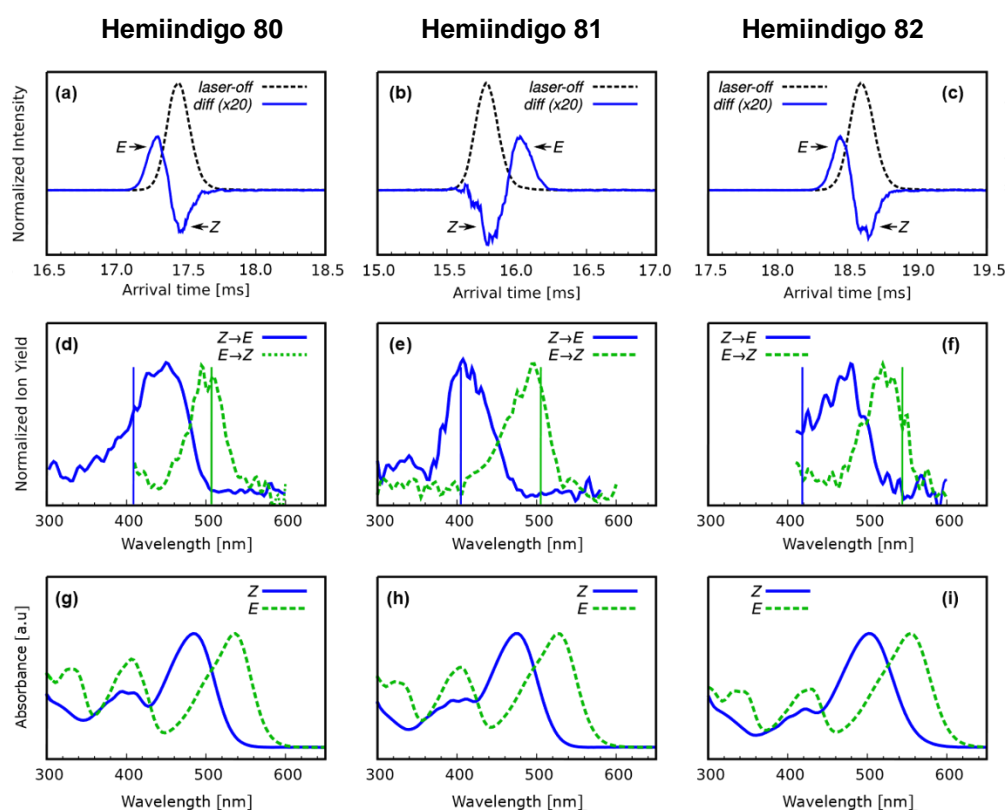


Figure 309: Example Z isomer photoaction ATDs (a-c), gas-phase action spectra (d-f) and solution absorption spectra (g-i) for the Z and E isomers of hemiindigos 80 (left



column), **81** (middle column) and **82** (right column). For the isolated hemiindigo isomers, the calculated absorption wavelengths are marked with bars of the corresponding color. Adapted with permission from <sup>[126]</sup>. Copyright 2020 Wiley VCH.

For the *E* isomers, the calculated absorption wavelengths (506 nm, 504 nm, and 543 nm for **80**, **81** and **82**) agree well with the experimental results (see Figure 309, middle row). For the *Z* isomers, the calculated absorption wavelength is blue-shifted by about 50 nm with respect to the experimental band maxima for **80** and **82** (409 nm and 419 nm), whereas it agrees with the experimental value for **81** (405 nm). Despite these slight deviations for some *Z* isomers, the calculated values lie in the wavelength range of the experimentally obtained photoisomerization response. While the photoisomerization action spectra potentially suffer from conformational broadening, this effect does not account for the observed slight disagreement between the *Z* to *E* photoisomerization action spectra maxima of hemiindigos **80** and **82** and the theoretically obtained absorptions.

The measured gas phase photoisomerization action spectra can be compared to the solution absorption spectra of the pure hemiindigo isomers (Figure 309, lower row). In all cases, the solution absorption spectra are red-shifted relative to the gas phase action spectra. While the shift between the *Z* to *E* and *E* to *Z* photoisomerization maxima does not change from solution compared to the gas phase for hemiindigos **80** and **82** ( $\Delta = \sim 50 - 70$  nm), it significantly increases for hemiindigo **81** in the gas phase ( $\Delta = 80 - 90$  nm).

## 2.5.5 Ionic hemiindigos - Power dependence

To evaluate the effect of light intensity on the photoisomerization yield, the *Z* isomer of hemiindigos **80**, **81** and **82** were irradiated at different light fluences at 450 / 430nm by *E. Carrascosa*. Resulting power dependence plots are shown in Figure 310. A linear fit of the data points shows that the photoinduced isomeric yield is directly proportional to light fluence for hemiindigos **80** and **81**, which is consistent to a single-photon isomerization. For hemiindigo **82**, the linear dependence is not followed at fluences above 1 mJ/pulse/cm<sup>2</sup>, suggesting saturation / multiphoton processes above this light fluence. All photoisomerization measurements were performed at fluences below 0.8 mJpulse<sup>-1</sup>cm<sup>-2</sup>. Similar power dependence measurements were not performed for the *E* to *Z* photoisomerization channels due to the significantly lower photoisomerization response. However, similar behavior as seen in the *Z* to *E* power dependences can be expected.

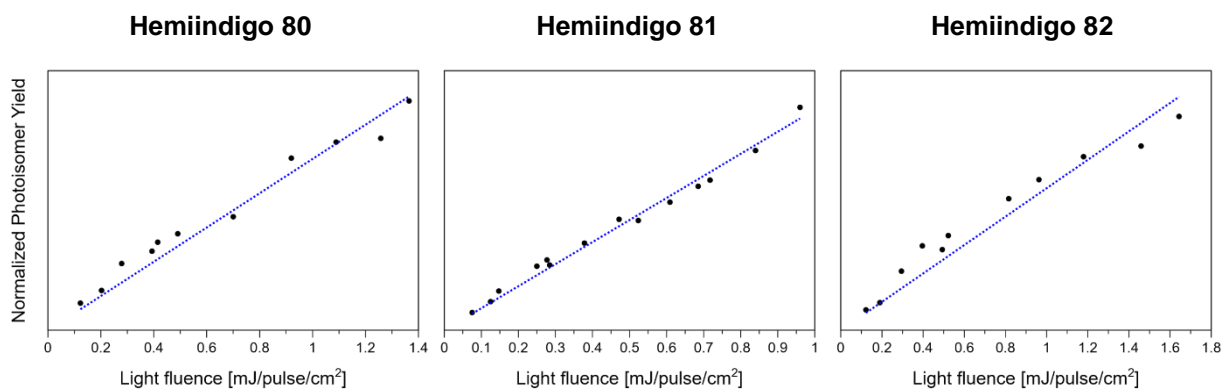


Figure 310: Normalized yield of *E* photoisomer as a function of light fluence. The experiments were performed at 450nm (Hemiindigos **80** and **81**) and 430nm (Hemiindigo **82**), respectively. All photoisomerization experiments were performed at a light fluence of <0.8 mJpulse<sup>-1</sup>cm<sup>-2</sup>. Adapted with permission from <sup>[126]</sup>. Copyright 2020 Wiley-VCH.

## 2.5.6 Ionic hemiindigos - Conformer evaluation in the gas phase

To identify the potential contribution of several conformations of the alkyl chain and aniline / julolidine moiety in each ATD peak, a non-exhaustive conformer search was performed by *E. Carrascosa* and *M. Scholz* using the Force Field tool in Avogadro. Conformations with relative energies <40 kJ/mol were re-optimized at the  $\omega$ B97XD/cc-pVDZ level of theory using the Gaussian16 package.<sup>[132]</sup> These geometries were then used as input for theoretical collision cross-section calculations using a version of the MOBCAL package parametrized for N<sub>2</sub> buffer gas.<sup>[133]</sup> Electronic excitation energies were calculated at the df-CC2/aug-cc-pVDZ level of theory using the MRCC program.<sup>[134]</sup> Figure 311 shows the optimized three-dimensional structures of *Z* and *E* conformers of hemiindigos **80**, **81** and **82**, respectively. Associated calculated energies, transition wavelengths and collision cross-sections for these conformers are given in Table 17.

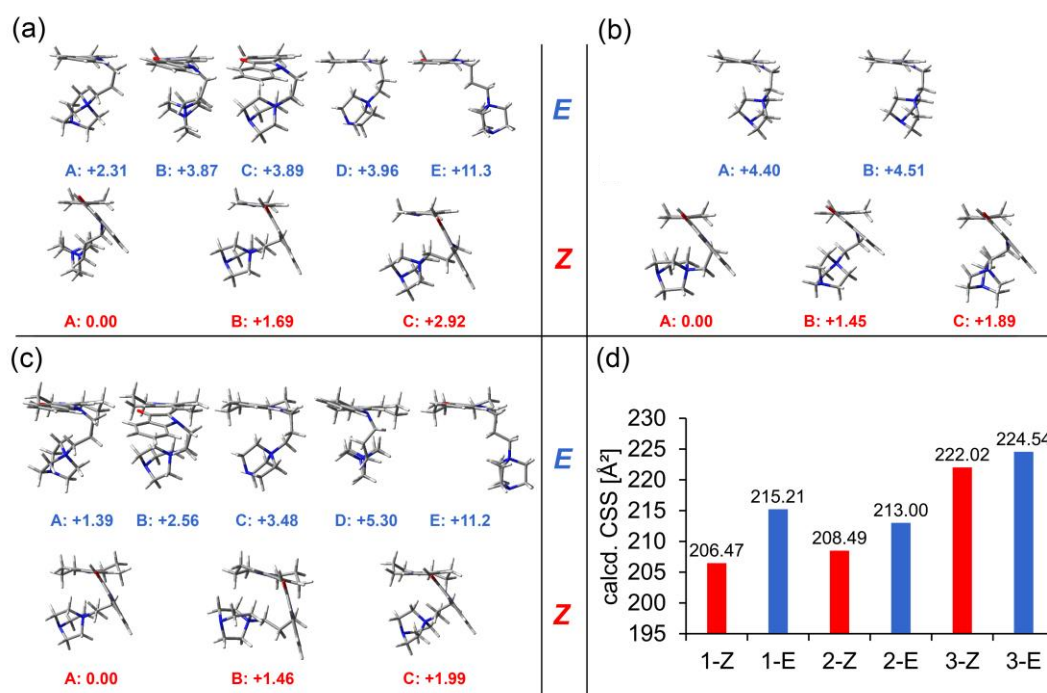


Figure 311: Calculated geometries and relative energies for representative low-energy *E* and *Z* conformers of hemiindigos **80** (a), **81** (b), and **82** (c) calculated at the  $\omega$ B97XD/cc-pVDZ level of theory. The energies are given in kcal/mol with respect to the most stable conformer. (d) Calculated averaged collision cross-section (CCS) for *E* and *Z* isomers in **80**, **81** and **82**, assuming a *Boltzmann* distribution of the individual conformers shown in (a-c) at a temperature of 300 K. Adapted with permission from <sup>[126]</sup>. Copyright 2020 Wiley VCH.

Table 17: Optimized ground state energies, transition wavelengths and theoretical collision cross-sections in pure N<sub>2</sub> buffer gas for a series of *Z* / *E* conformers of hemiindigos **80**, **81** and **82**.

Hemiindigo	Conformer	Optimized energy [kcal/mol]	Transition wavelength [nm]	CCS [Å <sup>2</sup> ]
<b>Z-80</b>	A	0.00	409  364	206
	B	1.69	405  362	214
	C	2.92	398  355	211
<b>E-80</b>	A	2.31	506  399	216
	B	3.87	502  396	206
	C	3.89	497  393	211
	D	3.96	517  387	218
	C	11.29	478  367	233
<b>Z-81</b>	A	0.00	405  365	208
	B	1.45	440  385	213
	C	1.89	398  366	211
<b>E-81</b>	A	4.40	504  391	213
	B	4.51	504  390	213
<b>Z-82</b>	A	0.00	419  372	222
	B	1.46	439  374	221
	C	1.99	418  371	225
<b>E-82</b>	A	1.39	543  417	225
	B	2.56	527  415	220
	C	3.48	559  402	231
	D	5.30	515  417	218
	E	11.16	518  397	247

All calculated and *Boltzmann* averaged collision cross-sections of hemiindigos **80**, **81** and **82**. Figure 311, (d) shows smaller values for their respective *Z*- compared to their *E* isomers. This, however, is only reflected with the ATDs of hemiindigo **81**, photoswitches **80** and **82** show faster arriving *E* instead of *Z* isomers. Nonetheless, the trend within the *E* isomers is reflected well, as hemiindigo **81** generally arrives first. The *Z* isomer of **81** should travel faster through the collision gas compared to **80** according to the collision cross-section value. Hemiindigo **82** shows the latest ATDs, which is in accordance to the biggest collision cross-sections of its isomers.

## 2.5.7 Ionic hemiindigos - Conformational analysis in solution

To correctly assign *Z* and *E* isomeric states to absorption spectra and ATDs, the respective *Z* and *E* isomers were investigated via  $^1\text{H}$ -NOESY NMR spectroscopy. The 2D NOESY spectra of the julolidine derivative **82** show similar respective signals compared to **80** and are omitted here.

### Aromatic / aliphatic NOEs of hemiindigo **80**

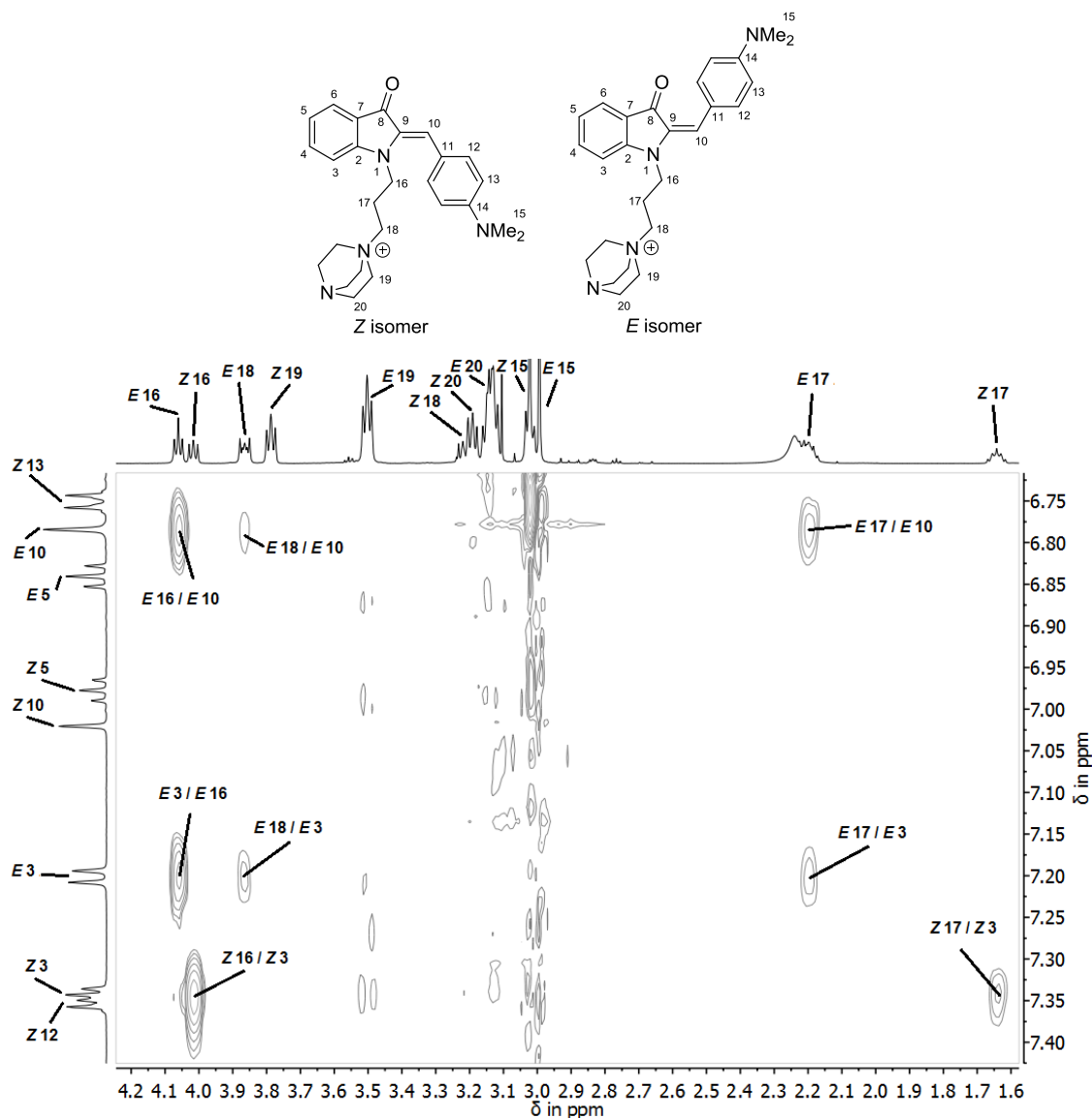


Figure 312: Section of the 2D NOESY NMR spectrum (dichloromethane- $d_2$ , 600 MHz, 27 °C) of hemiindigo **80**. The strong NOE cross signals between protons *E* 16 / 17 / *E* 10 and the weak signal of *E* 18 indicates their assignment to the *E* isomer to be correct. *Z* 10 shows no cross peaks with the chain protons. *Z* 16 / 17 show overlapping cross signals with protons *Z* 3 / 12, resolving the *Z* 12 / *Z* 3 signals

determines the preferred conformer in proximity of proton 3 instead of 12.  
Adapted with permission from [126]. Copyright 2020 Wiley VCH.

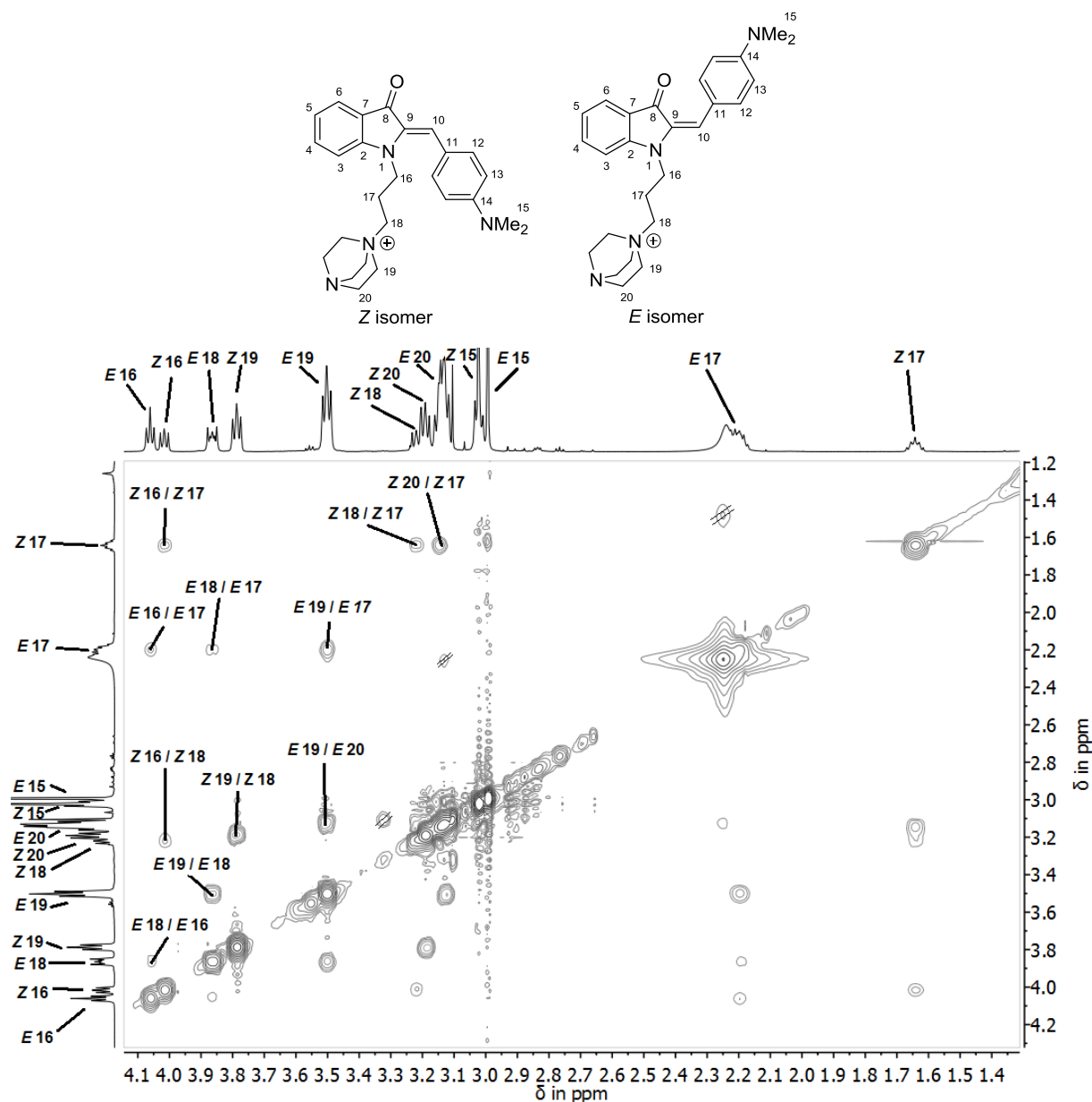


Figure 313: Section of the 2D NOESY NMR spectrum (dichloromethane- $d_2$ , 600 MHz, 27 °C) of hemiindigo **80**. The expected signals for the alkyl chain and diazabicyclo[2.2.2]octane can be identified. Adapted with permission from [126]. Copyright 2020 Wiley VCH.

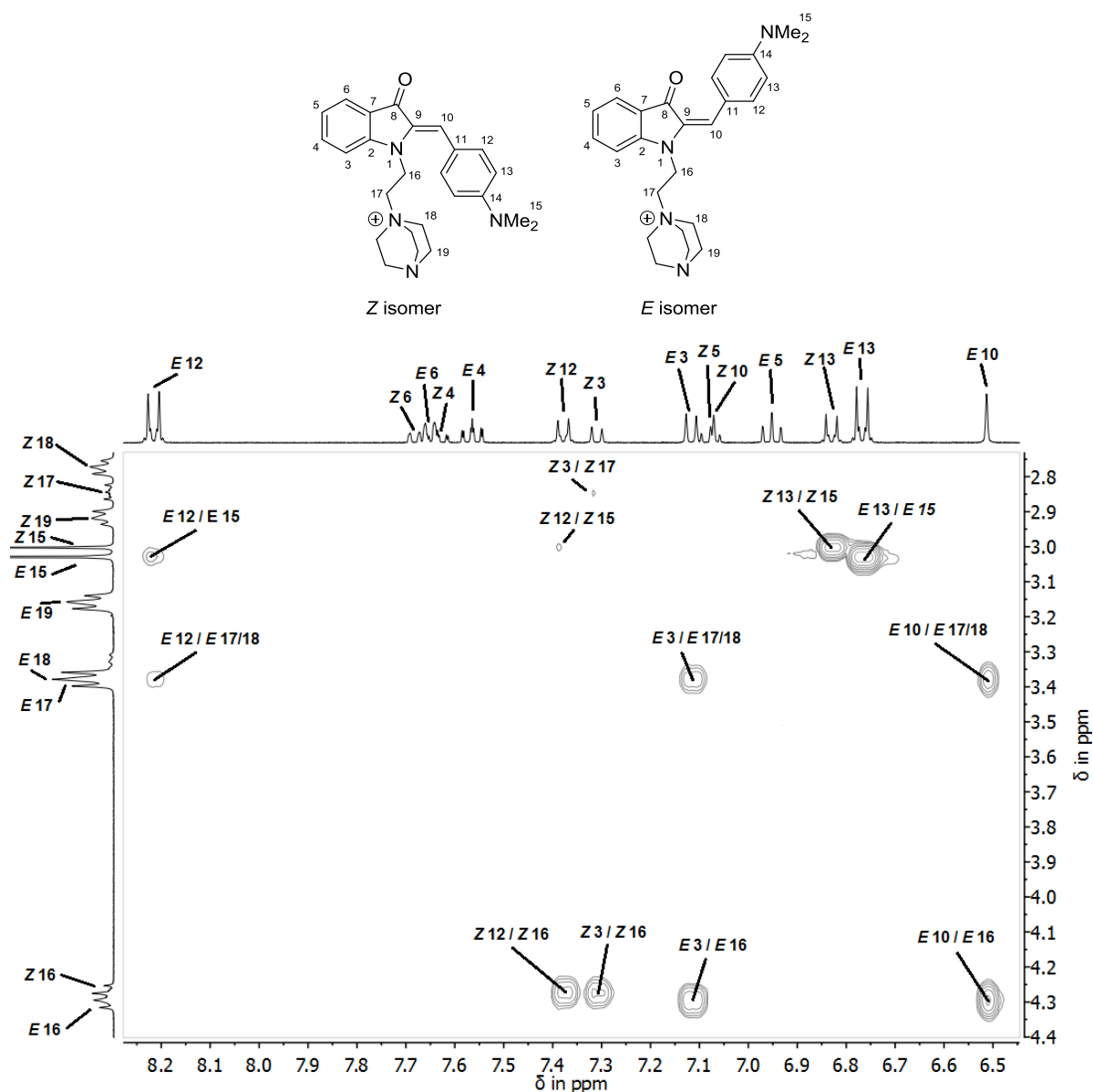
Aromatic/aliphatic NOEs of hemiindigo **81**

Figure 314: Section of the 2D-NOESY NMR spectrum (acetonitrile- $d_3$ , 400 MHz, 27 °C) of hemiindigo **81**. Strong cross signals of *E* 10 with protons *E* 16 and overlapped protons *E* 17 / 18 support their correct assignment to the *E* isomer. *Z* 10 shows no NOEs with alkyl chain protons. *Z* 12 shows strong signals with proton *Z* 16 but no cross signal with *Z* 17 / 18 / 19 while proton *Z* 3 shows signals with *Z* 16 and *Z* 17. This suggests a preferred chain conformer population in proximity of proton 3, although in a less pronounced manner than observed for *Z*-**80**. *E* 12 exhibits weak overlapped cross signals for protons *E* 17 / 18, which cannot be seen for *E* 18 / 19 in hemiindigo *E*-**80** as the elongated chain negates significant NOE signals to the peripheral diazabicyclo[2.2.2]octane tag. Adapted with permission from <sup>[126]</sup>. Copyright 2020 Wiley VCH.

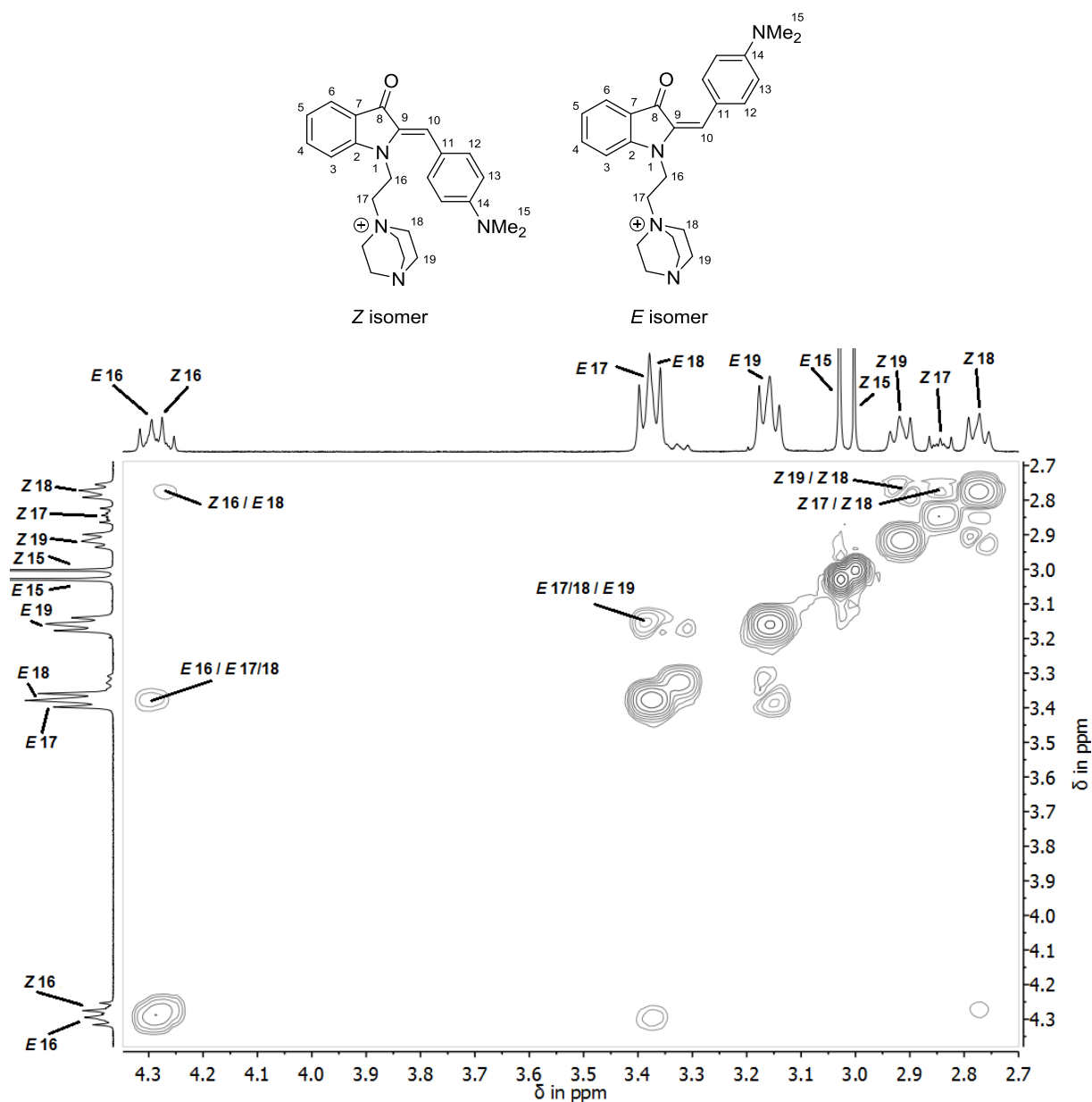


Figure 315: Section of the 2D NOESY NMR spectrum (acetonitrile- $d_3$ , 400 MHz, 27 °C) of hemiindigo **81**. The expected signals of the alkyl chain and diazabicyclo[2.2.2]octane can be identified. Adapted with permission from <sup>[126]</sup>. Copyright 2020 Wiley VCH.



### 2.5.8 Ionic hemiindigos - PSS UV-Vis spectra

To compare gas phase experiments to solution, ionic hemiindigos **80**, **81** and **82** were dissolved and irradiated in acetonitrile at different wavelengths. The photoswitching performance and photochromism is similar to the respective neutral hemiindigos **8** and **3**, see Section 2.2.6.

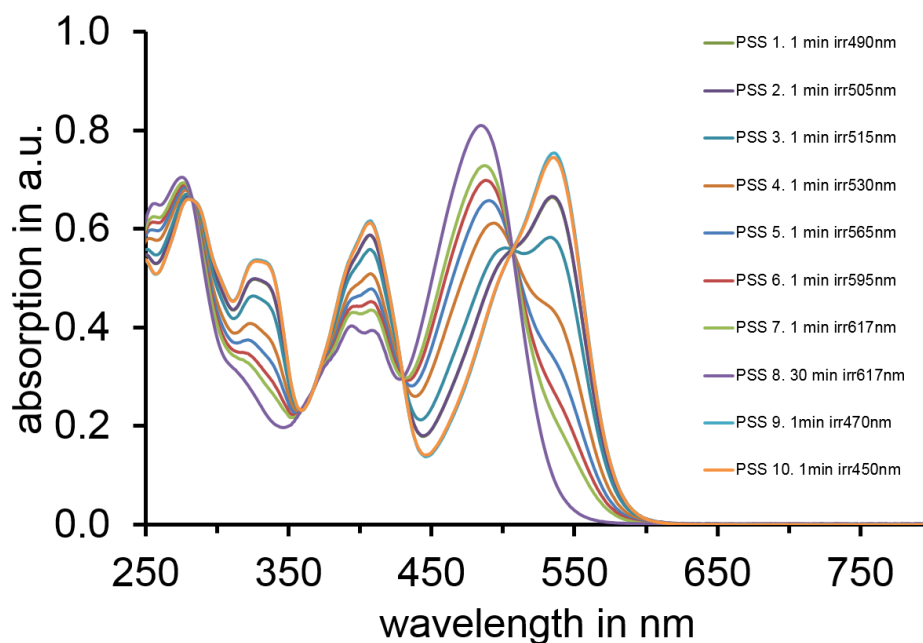


Figure 316: PSS UV-Vis spectra at different irradiation wavelengths for *Z*- / *E*-**80** in acetonitrile. Adapted with permission from <sup>[126]</sup>. Copyright 2020 Wiley VCH.

As ionic hemiindigo **80** is completely water soluble, photoisomerization in pure water (deionized, from laboratory tap) was tested as well. However, no photoswitchability of this compound could be observed in water at ambient temperatures (not shown).

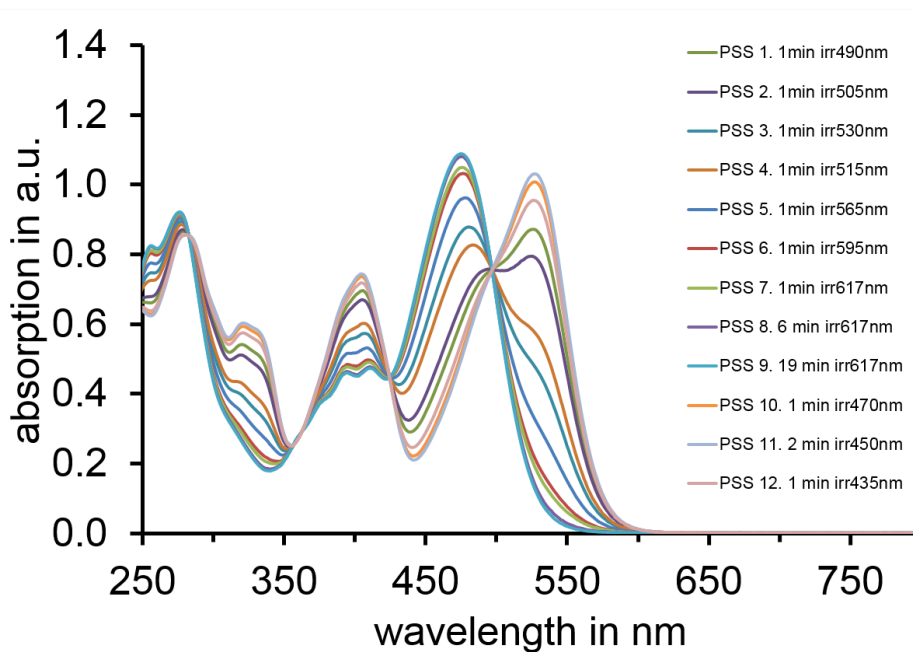


Figure 317: PSS UV-Vis spectra at different irradiation wavelengths for *Z*- / *E*-**81** in acetonitrile. Adapted with permission from <sup>[126]</sup>. Copyright 2020 Wiley VCH.

As ionic hemiindigo **81** is completely water soluble, photoisomerization in pure water was tested as well. However, no photoswitchability of this compound could be observed in water at ambient temperatures (not shown).

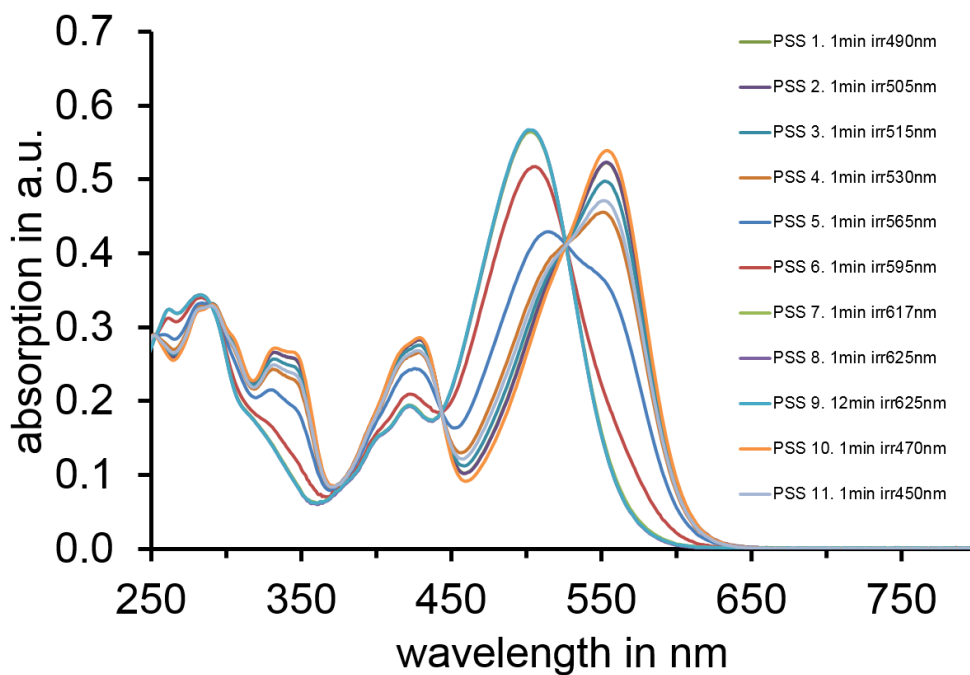


Figure 318: PSS UV-Vis spectra at different irradiation wavelengths for *Z*- / *E*-**82** in acetonitrile. Adapted with permission from <sup>[126]</sup>. Copyright 2020 Wiley VCH.

As ionic hemiindigo **82** is completely water soluble, photoisomerization in pure water was tested as well. However, no photoswitchability of this compound could be observed in water at ambient temperatures (not shown).

The lack of photoswitchability of hemiindigos substituted with electron-rich stilbene fragments can be overcome by utilization of less electron-donating groups than the dimethylamino moiety, which is addressed in Section 2.6.

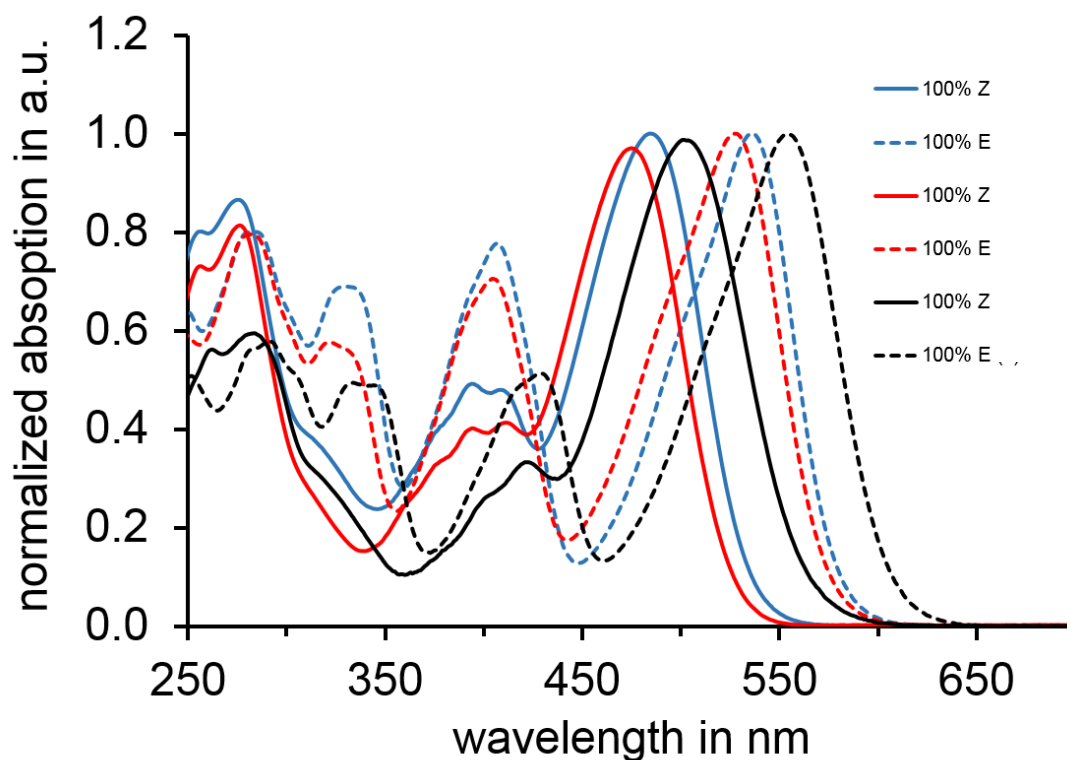


Figure 319: Absorbance normalized 100% *Z* / *E* UV-Vis spectra for **80** (blue), **81** (red) and **82** (black) in acetonitrile. Adapted with permission from <sup>[126]</sup>. Copyright 2020 Wiley VCH.

The expected red-shift from dimethylamino substituted phenyl (**80** and **81**) to julolidine stilbene fragment (**82**) can also be observed for this class of ionic hemiindigos. The blue-shift of the short chain substitution **81**, however, was unexpected. See the following section for possible explanations.

## 2.5.9 Ionic hemiindigos - Evaluation of chain length effects

Besides spectroscopic differences between ethyl- and *n*-propyl chains, varying chemical and physical properties are observed for the short chain hemiindigo **81**. First, the reaction yields for the alkylation step drop from 59% or 45% to 15% and yields of the subsequent *Menschutkin* reaction drop from 99% to 30% for this compound. Second, overall solubility in polar organic solvents is drastically decreased. Ionic hemiindigos supporting *n*-propyl chains are soluble in ethyl acetate (relative polarity: 0.288) as the generally less soluble bromine salts. This stands in contrast to the short chain derivative, which is insoluble in dichloromethane (relative polarity: 0.309) as the generally more soluble hexafluorophosphate salt. Acetonitrile (relative polarity: 0.460) had to be used to obtain NMR data of this compound as hexafluorophosphate salt. This can be explained by a stronger tendency of **81** to precipitate, which is caused by increased electrostatic effects or by a less flexible alkyl chain, which is not able to keep the molecules in solution.

The UV-Vis assessment in solution and action spectroscopy in the gas phase showed a blue-shift and ATD inversion of *Z* and *E* isomers for hemiindigo **81** compared to **80**. One explanation of the blue-shift is the closer proximity of the bulky diazabicyclo[2.2.2]octane moiety in the *Z* isomeric state, forcing the stilbene fragment out of the indoxyl plane, decreasing the *pi*-delocalization of the chromophore. This is also observed for twisted hemiindigos **30** and **33**, Section 2.2.7. However, the molecular geometries obtained by quantum chemical calculations suggest a reversed trend, showing slightly more pronounced twisting of the stilbene fragment for the *Z* isomers of hemiindigo **80** and **82** compared to **81** (Figure 321).

Another explanation is the closer proximity of the positive ion charge towards the electron rich stilbene fragment, which decreases its electron donating strength towards the central double bond (see molecular electrostatic potentials (MEPs) and explanation of Figure 322). Nonetheless, the *E* isomer should be completely planar and unaffected by shortening of the alkyl chain, as the distance to the positive ion charge is increased from the *Z*- to the *E* isomeric state. However, the two most red-shifted *Z*- and *E* maxima for **81** experience an equal hypsochromic shift by 8 nm from 484 nm to 476 nm (*Z* isomer) and 537 nm to 529 nm (*E* isomer) compared to **80**. This finding suggests a mostly *Z* / *E* isomer-independent cause of the blue-shift, which can be obtained by substitution of the indoxyl N-H proton with electron withdrawing groups, e.g. acetyls, see hemiindigo **12**, Section 2.2.9.

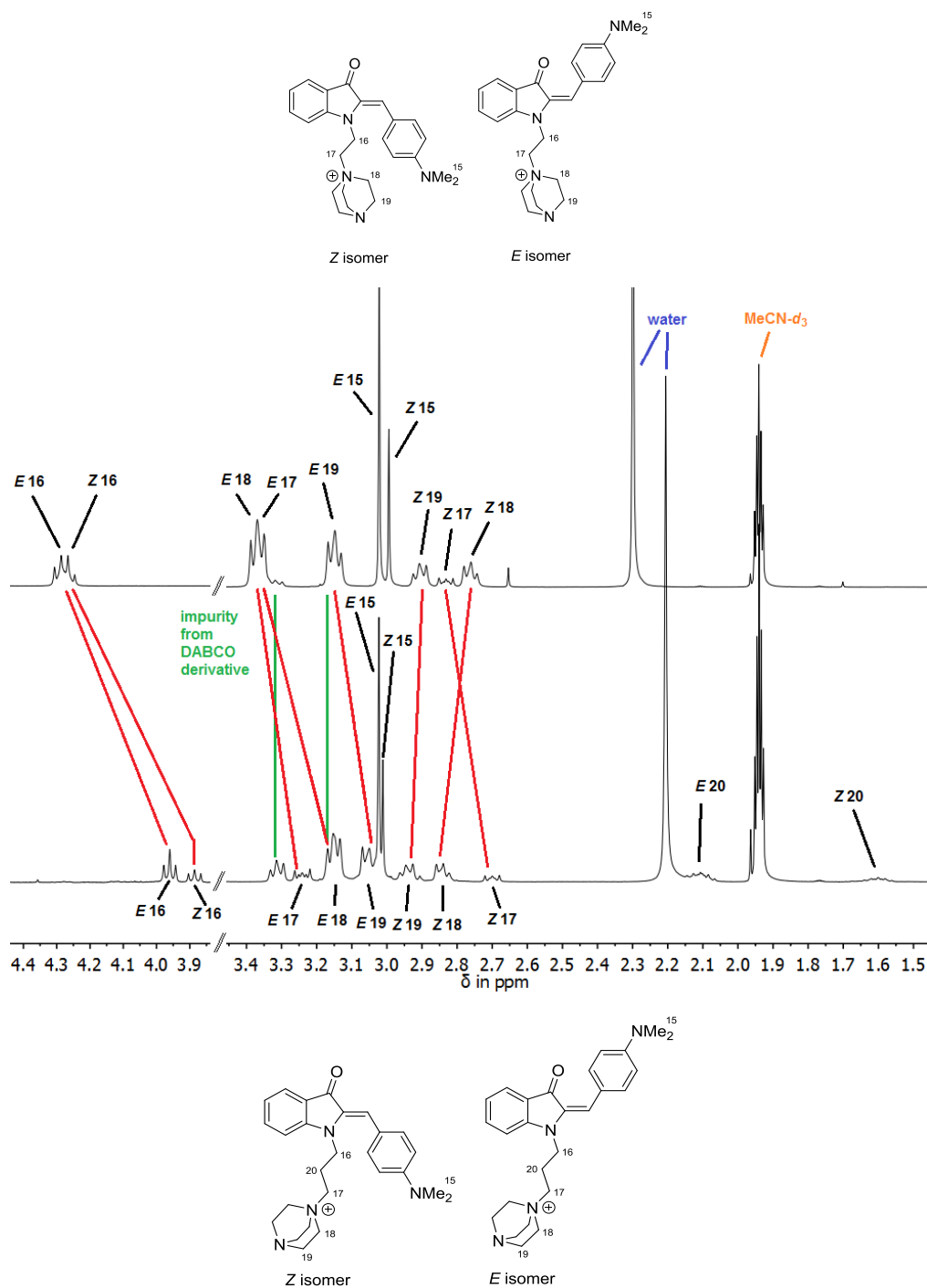


Figure 320:  $^1\text{H-NMR}$  spectra of *Z*/*E* **81** (top) and *Z*/*E* **80** (bottom) in acetonitrile- $d_3$ , only the aliphatic section is shown. Corresponding *Lewis*-formula are shown at the top and bottom. Adapted with permission from <sup>[126]</sup>. Copyright 2020 Wiley VCH.

$^1\text{H-NOESY}$  spectroscopy did not show unexpected or indicative signals for hemiindigos **80**, **81** and **82** and is therefore omitted here.

The diazabicyclo[2.2.2]octane substitution introduces a permanent positive charge at the quaternary nitrogen, which could be responsible for the electron density withdrawal from the electron-poor indoxyl fragment. This is hindered for hemiindigo **80**, as the additional aliphatic chain CH<sub>2</sub> group 20 (Figure 322) could act as an electronic decoupler between the photoswitch and the positive charge. For hemiindigo **81**, both aliphatic chain CH<sub>2</sub> groups 16 and 17 are connected to electron-poor nitrogen centers, which is also reflected by their <sup>1</sup>H-NMR downfield-shifted signals, see Figure 320. The central chain CH<sub>2</sub> group 20 of compound **80** experiences less downfield-shift because it is not connected to a heteroatom. However, switching from the *Z*- to the *E* isomeric state induces a strong downfield shift on CH<sub>2</sub> group 20, which can be caused by increased electron withdrawal of the carbonyl group and / or by the lack of the shielding ring-current of the stilbene fragment. The latter argument is supported by the pronounced shifting of CH<sub>2</sub> signals 18 and 19, as these positions also experience a large downfield shift when switched to the *E* isomer. It is unlikely that an electron-withdrawing effect originating from the indoxyl fragment causes downfield-shifts of up to 0.5 ppm in the periphery over four to six unconjugated covalent bonds for the *E* isomer. Nonetheless, the shifts of signals 16 do not change drastically during *Z* / *E* isomerization. This can be caused by the misalignment of the stilbene ring current towards these protons, which is responsible for significant shielding in the *Z*- compared to the *E* isomeric state.

Considering all signal positions, deshielding occurs in the *Z* to *E* isomerization direction for both molecules with downfield shifts ranging from 0.2 to 0.7 ppm. Compared to hemiindigo **80**, the shifting of signals 16, 17, 18 and 19 between *Z*- and *E* isomers is significantly pronounced for the shorter chain of hemiindigo **81**. This can be attributed to the proximity of the positive ion charge towards the electron-withdrawing hemiindigo chromophore, especially in the *E* state. The electron-rich stilbene moiety can donate electron density towards the carbonyl function in the *Z* state, which is impeded in the *E* state and compensated by electron-withdrawal from the substituted alkyl chain. Deshielding of all signals except for protons *Z* 19 and *Z* 18 can be observed for **81** when compared to **80**. The slight deshielding of diazabicyclo[2.2.2]octane protons 18 and 19 for the *Z* isomer of hemiindigo **80** can be explained by less influence of the stilbene ring-current as the alkyl chain is able to move freely.

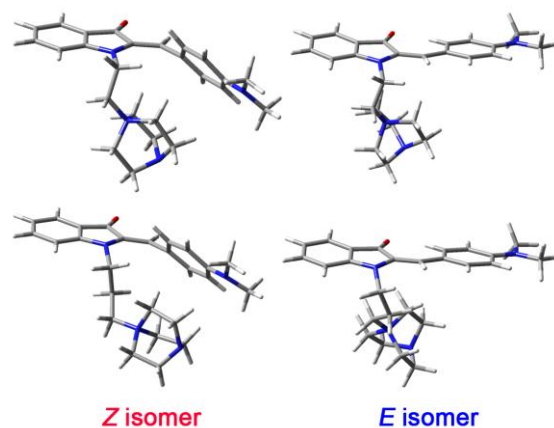


Figure 321: Energetically favored *Z* and *E* isomers of hemiindigo **81** (top) and **80** (bottom) calculated at the  $\omega$ B97XD/cc-pVDZ level of theory.

Figure 321 shows the calculated lowest energy conformers of hemiindigo **81** and **80**. Overall, very similar conformations can be observed, with a twisted stilbene fragment for the *Z* isomers and planar *E* isomers. The difference in  $^1\text{H-NMR}$  shifts seen in Figure 320 can be explained by the varying influence on the aliphatic protons caused by the aromatic ring current at the stilbene fragment, which is well aligned towards the positive charge on the side chain in the *Z* isomeric state.

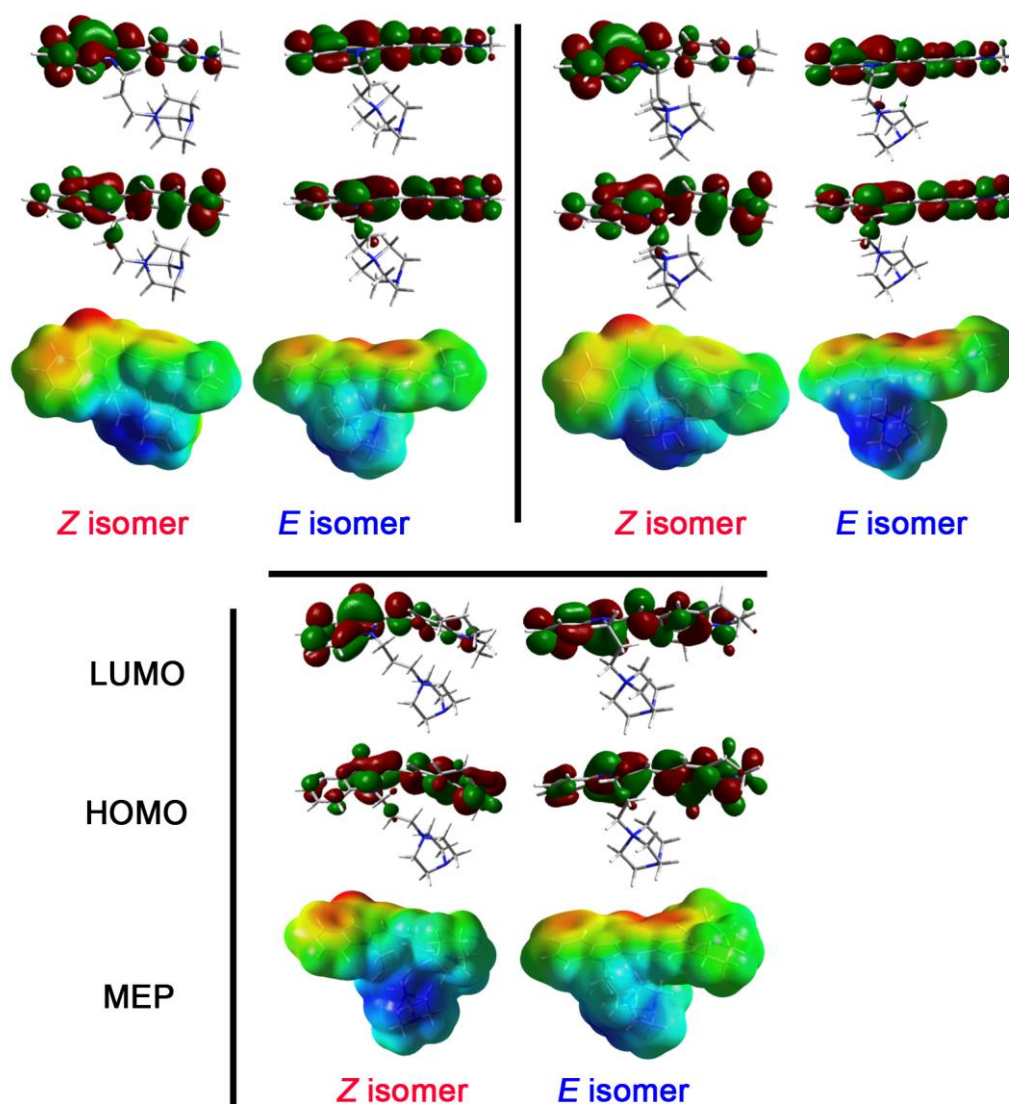


Figure 322: Molecular electrostatic potentials (MEPs), highest occupied molecular orbitals (HOMOs) and lowest unoccupied molecular orbitals (LUMOs) of hemiindigos **80** (top, left), **81** (top right) and **82** (bottom) calculated at the  $\omega$ B97XD/cc-pVDZ level of theory. Only the conformers with the lowest respective energy are shown. The MEPs show the affinity towards a positive test charge, red areas show high and blue areas low affinities. The same color margin values of -0.01 and +0.18 were used for all MEPs.

Visualization of HOMOs and LUMOs for hemiindigos **80**, **81** and **82** show comparable orbital shapes to previously obtained computational results.<sup>[74]</sup> The HOMOs show significant electron densities at the indoxyl nitrogen and along the alkyl chains, which disappear in the LUMO state. As a side note, this electron density at the alkyl chain might explain the low (photo-)stability of the methyl- (**13**) and ethyl (**14**) hemiindigo derivatives (see Section 2.2.3). For the ionic compound **81**, the electron density on the shorter chain is adjacent to the permanent positive



charge, which might also contribute to the immobilization of the side chain, decreasing its reactivity and solubility. The LUMO of the *E* isomeric state of **81** is the only molecular orbital where electron density is localized on the diazabicyclo[2.2.2]octane tag. Examination of the MEPs shows reduced charge separations for the *E* isomeric states of **80** and **81** compared to their respective *Z* states. A decrease in negative charge of the stilbene fragment can be observed for the *Z* isomers, which is in accordance to the shielding effects on aliphatic protons seen in <sup>1</sup>H-NMR spectra (see Figure 320). When comparing hemiindigos **80** and **82** to **81**, overall increased positive charges can be observed for **81**. Especially the *E* isomeric state shows no significant reduction in positive charge from the initial *Z* isomer as seen with **80** and **82**. These observations hint towards another explanation of the reversed ATDs: The slight difference in charge distribution between *Z* and *E* isomers and hemiindigos **80**, **81** and **82** interplays with their collision cross-section, more positively charged isomers experience a stronger force towards the negatively charged accelerators of the mass spectrometer, respectively reducing their ATD (see influence of charge *z* in eq. 20). Collision cross-section should be relatively independent from charge differences. With this theory at hand, the obtained ATDs represent the averaged effect between acceleration of more positively charged isomers and their deceleration caused by bigger collision cross-sections. As these effects are hard to disentangle experimentally, the outweighing effect cannot be unambiguously determined. However, the trend of faster arriving *E* isomers for **80** and **82** compared to *Z* isomers is not reproduced when an increasingly exposed positive charge is correlated to higher acceleration and faster ATDs. Nonetheless, acceleration and swapping of ATDs for hemiindigo **81** compared to **80** and **82**, which also shows unexpected behavior in solution, can be explained by this suggestion.

## 2.5.10 Conclusion: Ionic hemiindigos

In conclusion, three permanently charged thermally bistable hemiindigos were synthesized and their photochemical properties in the gas phase and in solution were investigated. It is shown that gas-phase experiments agree with the theoretical description and capture essential intrinsic molecular properties, including absorption wavelengths or collision cross-sections. Describing the influence of polar solvents on the photochemical behavior on the other hand is still challenging using this theoretical approach. Additionally, a novel way of separating stable hemiindigo isomers from an isomeric mixture to obtain isomer-specific photoisomerization responses without the need for spectral deconvolution of mixtures in solution is presented. It is further demonstrated, that reversible photoisomerization and strong photochromism for all isolated gas-phase hemiindigos is shown upon exposure to visible light. The influence of the shorter chain-length on absorption wavelengths, photoisomerization properties, overall reactivity and solubility were elaborated further. Possible explanations for the reversal of ATDs of *Z* and *E* isomers of the short-chain hemiindigo **81** are given.

The use of ion mobility mass spectrometry coupled to laser spectroscopy offers unique insights into the subtle effects of intrinsic molecular constitution and electronic structure - separated from environment influences - of photoactive molecules. Such fundamental investigations can be useful for rationally designing better molecular photoswitches and serve as a benchmark for developing accurate theoretical models for their photoisomerization dynamics / and mechanisms.

- [74] C. Petermayer, S. Thumser, F. Kink, P. Mayer, H. Dube, *Hemiindigo: Highly Bistable Photoswitching at the Biooptical Window*, *J. Am. Chem. Soc.* **2017**, *139*, 15060.
- [88] U. Burger, A. O. Bringhen, *Cyclization Studies with N-Munnich Bases of 2-Substituted Indoles*, *Helv. Chim. Acta* **1989**, *72*, 93.
- [90] V. S. Velezheva, P. J. Brennan, V. Y. Marshakov, *Novel Pyridazino[4,3-b]indoles with Dual Inhibitory Activity against Mycobacterium tuberculosis and Monoamine Oxidase*, *J. Med. Chem.* **2004**, *47*, 3455.
- [121] J. N. Bull, E. Carrascosa, N. Mallo, M. S. Scholz, G. da Silva, J. E. Beves, E. J. Bieske, *Photoswitching an Isolated Donor–Acceptor Stenhouse Adduct*, *The Journal of Physical Chemistry Letters* **2018**, *9*, 665.
- [122] R. Navratil, S. Wiedbrauk, J. Jasik, H. Dube, J. Roithova, *Transforming hemithioindigo from a two-way to a one-way molecular photoswitch by isolation in the gas phase*, *Phys. Chem. Chem. Phys.* **2018**, *20*, 6868.
- [123] B. D. Adamson, N. J. A. Coughlan, P. B. Markworth, R. E. Continetti, E. J. Bieske, *An ion mobility mass spectrometer for investigating photoisomerization and photodissociation of molecular ions*, *Rev. Sci. Instrum.* **2014**, *85*, 123109.
- [124] M. S. Scholz, J. N. Bull, E. Carrascosa, B. D. Adamson, G. K. Kosgei, J. J. Rack, E. J. Bieske, *Linkage Photoisomerization of an Isolated Ruthenium Sulfoxide Complex: Sequential versus Concerted Rearrangement*, *Inorg. Chem.* **2018**, *57*, 5701.
- [125] E. Carrascosa, J. N. Bull, M. S. Scholz, N. J. A. Coughlan, S. Olsen, U. Wille, E. J. Bieske, *Reversible Photoisomerization of the Isolated Green Fluorescent Protein Chromophore*, *The Journal of Physical Chemistry Letters* **2018**, *9*, 2647.
- [126] E. Carrascosa, C. Petermayer, M. S. Scholz, J. N. Bull, H. Dube, E. J. Bieske, *Reversible Photoswitching of Isolated Ionic Hemiindigos with Visible Light*, *ChemPhysChem* **2020**, *21*, 680.
- [127] J. N. Bull, M. S. Scholz, E. Carrascosa, G. da Silva, E. J. Bieske, *Double Molecular Photoswitch Driven by Light and Collisions*, *Phys. Rev. Lett.* **2018**, *120*, 223002.
- [128] V. S. Velezheva, P. J. Brennan, V. Y. Marshakov, D. V. Gusev, I. N. Lisichkina, A. S. Peregudov, L. N. Tchernousova, T. G. Smirnova, S. N. Andreevskaya, A. E. Medvedev, *Novel pyridazino[4,3-b]indoles with dual inhibitory activity against Mycobacterium tuberculosis and monoamine oxidase*, *J. Med. Chem.* **2004**, *47*, 3455.
- [129] M. Cydzik, M. Rudowska, P. Stefanowicz, Z. Szewczuk, *Derivatization of peptides as quaternary ammonium salts for sensitive detection by ESI-MS*, *J. Pept. Sci.* **2011**, *17*, 445.
- [130] B. Almarzoqi, A. V. George, N. S. Isaacs, *The Quaternisation of Tertiary Amines with Dihalomethane*, *Tetrahedron* **1986**, *42*, 601.
- [131] H. E. Revercomb, E. A. Mason, *Theory of plasma chromatography/gaseous electrophoresis. Review*, *Anal. Chem.* **1975**, *47*, 970.
- [132] Gaussian 16, Revision B.01, M. J. Frisch, G. W. Trucks, H. B. Schlegel, G. E. Scuseria, M. A. Robb, J. R. Cheeseman, G. Scalmani, V. Barone, G. A. Petersson, H. Nakatsuji, X. Li, M. Caricato, A. V. Marenich, J. Bloino, B. G. Janesko, R. Gomperts, B. Mennucci, H. P. Hratchian, J. V. Ortiz, A. F. Izmaylov, J. L. Sonnenberg, Williams, F. Ding, F. Lipparini, F. Egidi, J. Goings, B. Peng, A. Petrone, T. Henderson, D. Ranasinghe, V. G. Zakrzewski, J. Gao, N. Rega, G. Zheng, W. Liang, M. Hada, M. Ehara, K. Toyota, R. Fukuda, J. Hasegawa, M. Ishida, T. Nakajima, Y. Honda, O. Kitao, H. Nakai, T. Vreven, K. Throssell, J. A. Montgomery Jr., J. E. Peralta, F. Ogliaro, M. J. Bearpark, J. J. Heyd, E. N. Brothers, K. N. Kudin, V. N. Staroverov, T. A. Keith, R. Kobayashi, J. Normand, K. Raghavachari, A. P. Rendell, J. C. Burant, S. S. Iyengar, J. Tomasi, M. Cossi, J. M. Millam, M. Klene, C. Adamo, R. Cammi, J. W. Ochterski, R. L. Martin, K. Morokuma, O. Farkas, J. B. Foresman, D. J. Fox, Gaussian, Inc., Wallingford CT, **2016**.

- [133] A. A. Shvartsburg, M. F. Jarrold, *An exact hard-spheres scattering model for the mobilities of polyatomic ions*, *Chem. Phys. Lett.* **1996**, 261, 86.
- [134] M. Kállay, P. R. Nagy, Z. Rolik, D. Mester, G. Samu, J. Csontos, J. Csóka, B. P. Szabó, L. Gyevi-Nagy, I. Ladjánszki, L. Szegedy, B. Ladóczki, K. Petrov, M. Farkas, P. D. Mezei, a. B. Hégyel, *Mrcc, a quantum chemical program suite*, *J. Chem. Phys.* **2013**, 139, [www.mrcc.hu](http://www.mrcc.hu).

## 2.6 Hemiindigos in water - Photoswitchable interactions with DNA / RNA biomolecules

Experiments on various hemiindigos in Section 2.2.5 and Section 2.5 showed either no solubility in pure water or no photoswitchability of ionic hemiindigos with electron-rich stilbene fragments. *D. Berdnikova* of the *Ihmels* group in Siegen, Germany recently reported on a water soluble hemiindigo derivative that is able to photoswitch in pure water. Furthermore, binding of this compound towards parts of the human immunodeficiency virus type 1 (HIV-1) ribonucleic acid (RNA) with a fluorescent response could be shown. The occurring fluorescence could be switched off by visible light without decreasing affinity of the hemiindigo to the RNA complex.<sup>[40]</sup>

As part of a collaboration with *D. Berdnikova*, various hemiindigo derivatives were synthesized to examine if (ionic) hemiindigos show binding towards deoxyribonucleic acid (DNA) or RNA target sites. This was done with the goal to establish a photoswitchable therapeutic handle for the HIV-1 translation rates at the RNA level. A possible strategy to achieve this is the design of photoswitches that exhibit specific Tat (Trans-activator of transcription) protein binding or by (specific) RNA binding to e.g. the transactivation response element (TAR) or the Rev-response element region IIB (RRE-IIB). Photoisomerization of the bound photoswitch with preferably visible light could be able to modulate the proliferation rate of the HIV-1 virus *in vitro* and *in vivo*.

This project is still in progress to date and the herein presented preliminary results are meant to give a brief overview of possible substitution patterns and their effects on water solubility, photoswitchability and DNA / RNA binding properties. Full analytical data is not given for all compounds as most of the synthesized molecules did not meet the requirements for photoswitching upon binding to DNA / RNA, which makes further investigation pointless regarding the objective of this project. However, some of the permanently charged compounds were also sent to *E. Carrascosa* (see Section 2.5) for vibrational tandem mass spectrometry at cryogenic temperatures to the *L'Ecole polytechnique fédérale de Lausanne*, Switzerland for scrutinizing the properties of these compounds in the gas phase.

The ability of small molecules to exhibit binding or to modulate protein binding affinities and conformational changes to RNA is reported by recent literature.<sup>[96, 135, 136]</sup> *N,N*-dimethylamino alkyl chains are often found in RNA / DNA binders.<sup>[137]</sup> Three design examples of compounds that show related motifs to the introduced *N,N*-dimethylamino alkyl chains and hemiindigo photoswitch are given in Figure 323 below.

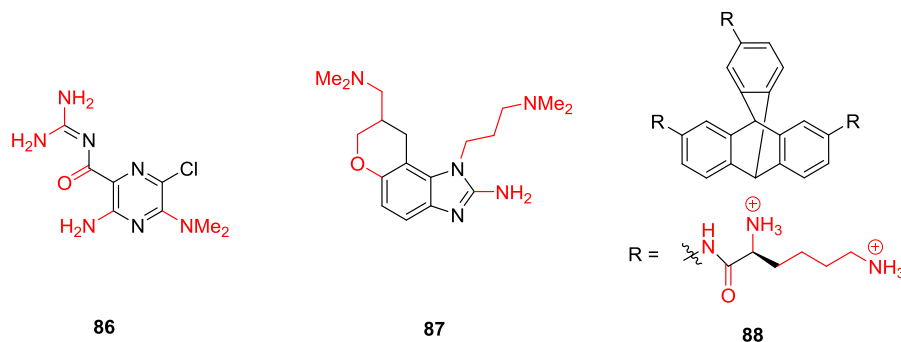


Figure 323: Three small molecules (**86**, **87** and **88**) that show affinities and conformational / regulatory changes at the RNA level in biological assemblies. Similarities of functional groups to the investigated hemiindigo photoswitches are marked red.

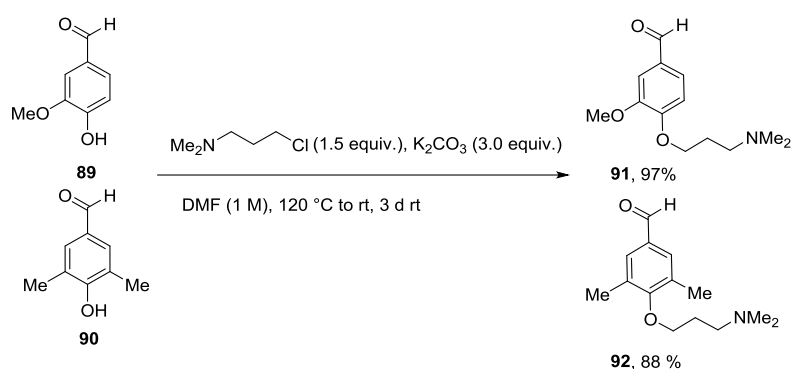
Compound **86** (Figure 323, left) selectively targets a pocket within the HIV-1 TAR hairpin loop with high affinity, which is rarely observed for small molecules.<sup>[135]</sup> Molecule **87** (middle) shows affinity towards the internal ribosome entry site (IRES) RNA of the hepatitis C virus (HCV), which inhibits translation within HCV infected cells.<sup>[138]</sup> The compound on the right (**88**) is able to modulate the heat shock response (HSR) in *E. coli* bacteria by stabilizing a messenger RNA (mRNA) three-way junction (3WJ) within the sigma factor 32 ( $\sigma^{32}$ ) mRNA inhibiting translation of heat shock proteins (HSP).<sup>[136]</sup>

The design of the hemiindigo photoswitches relies on the relatively easy introduction of *n*-propyl *N,N*-dimethylamino chains, which can be optionally converted to a permanently charged quaternary trimethylammonium species. These patterns - in conjunction to the hemiindigo photoswitch itself - try to integrate aspects of the aforementioned RNA-binding molecules in structure and / or type and abundance of functional groups. The vast amount of RNA / DNA binders and their structural / chemical similarities to hemiindigos cannot be shown with in its entirety in this work. The purpose of mimicking known DNA / RNA binders is the addition of controllability of their binding affinities by visible light.

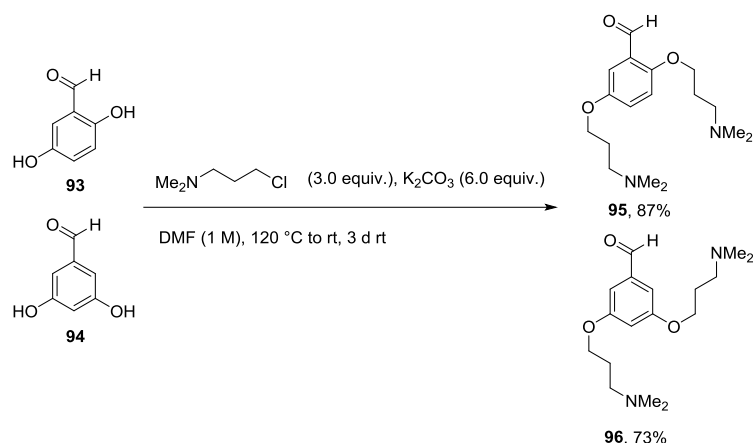
According to the rationale for hemiindigo substitution patterns, N-H unsubstituted and non-electron-rich derivatives show poor photostability and less red-shifted absorptions than their electron-rich, N-H substituted counterparts. This was also addressed within a series of synthesized hemiindigo photoswitches.

### 2.6.1 Hemiindigos in water - Synthesis

As the synthesis of hemiindigos with electron-neutral stilbene fragments proved as challenging in Section 2.2.1, commercially available aldehydes with high degrees of substitutions by methyl- or methoxy groups and one or two hydroxyl groups for functionalization with 1-*N,N*-dimethylaminopropyl moieties were chosen as starting materials. Anthracene as lipophilic stilbene fragment was tested as well. The detailed elution parameters for flash column chromatographic- and / or HPLC separation are given in this section to estimate the effects on polarity, solubility and overall “stickiness” of varying numbers of 1-*N,N*-dimethylaminopropyl groups to the respective solid phases during chromatography. The influence of the N-H group on elution and solubility of the hemiindigo photoswitch can also be estimated.



Scheme 42:  $S_N2$  reaction of the phenolic hydroxyl group of **89** and **90** with 3-chloro-1-(*N,N*-dimethyl)propylamine in *N,N*-dimethylformamide (DMF) at 120 °C with potassium carbonate as base. Aldehydes **91** and **92** could be obtained in good to excellent yields.

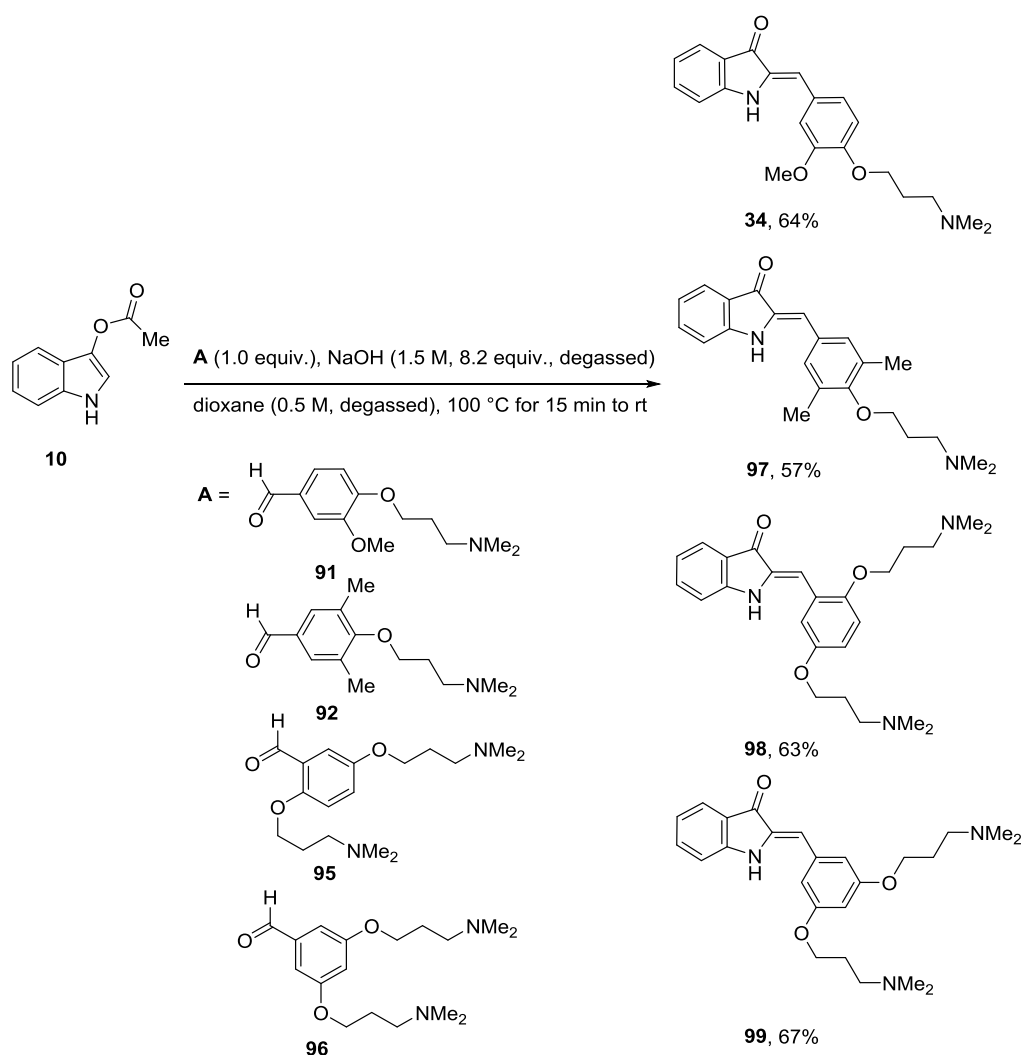


Scheme 43:  $S_N2$  reaction of two phenolic hydroxyl groups of **93** and **94** with two equivalents of 3-chloro-1-(*N,N*-dimethyl)propylamine in *N,N*-dimethylformamide at 120 °C

with potassium carbonate as base. Aldehydes **95** and **96** could be obtained in good yields.

The 1-*N,N*-dimethylaminopropyl disubstituted aldehydes **95** and **96** were purified by column chromatography with very polar eluent mixtures: 68 / 30 / 2 (silica) or 98 / 1 / 1 (aluminium(III) oxide, *Brockmann* III) dichloromethane / methanol / triethylamine.

The prepared aldehydes supporting one or two 1-*N,N*-dimethylaminopropyl chains were condensed with indoxyl acetate according to a procedure by *U. Burger et al.* to yield hemiindigo photoswitches.<sup>[88]</sup>



Scheme 44: Condensation reaction of different aldehydes (Aldehydes **91**, **92**, **95** and **96**) with indoxyl acetate **10** in to furnish hemiindigos **34**, **97**, **98** and **99** in moderate yields.

The stilbene 1-*N,N*-dimethylaminopropyl substituted hemiindigo photoswitches **34** and **97** were purified by column chromatography with 84 / 14 / 2 (silica) or 98 / 1 / 0 (aluminium(III) oxide, *Brockmann* III) dichloromethane / methanol / triethylamine mixtures. The stilbene 1-*N,N*-

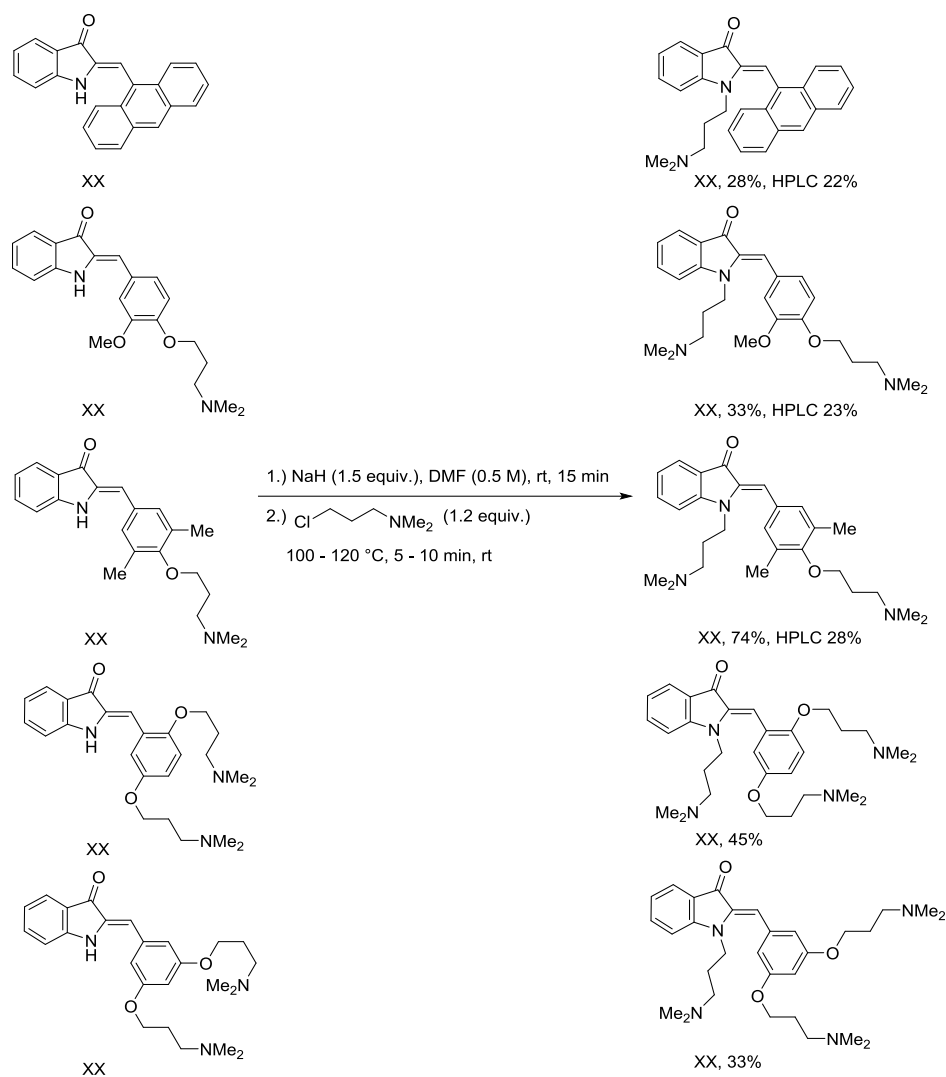


dimethylaminopropyl disubstituted hemiindigo photoswitches **98** and **99** were purified by silica column chromatography with 33 / 33 / 31 / 2 dichloromethane / methanol / *n*-hexane / triethylamine mixtures.

Hemiindigo **34** was prepared and characterized by *D. Berdnikova* for RNA binding studies, it was reproduced for further functionalization at the indoxyl nitrogen. The N-H unsubstituted hemiindigo photoswitches are soluble in water and show viable photoswitching behavior, in contrast to the ionic, electron-rich derivatives shown in Section 2.5.

The substitution at the indoxyl nitrogen with another 1-*N,N*-dimethylaminopropyl chain anticipated more mechanical leverage upon photoswitching. This is caused by e.g. the binding site attached to the stilbene fragment, which experiences a large geometrical change respective to the 1-*N,N*-dimethylaminopropyl chain at the indoxyl fragment. This might be crucial to photochemically control its regioselectivity, binding mode and ability to promote or hinder RNA / DNA-Protein complex formations at different rates between *Z*- and *E* isomers. The synthesis was carried out according to a modified procedure by *V. Velezheva et al.*<sup>[90]</sup>

## 2.6.1 HEMIINDIGOS IN WATER - SYNTHESIS



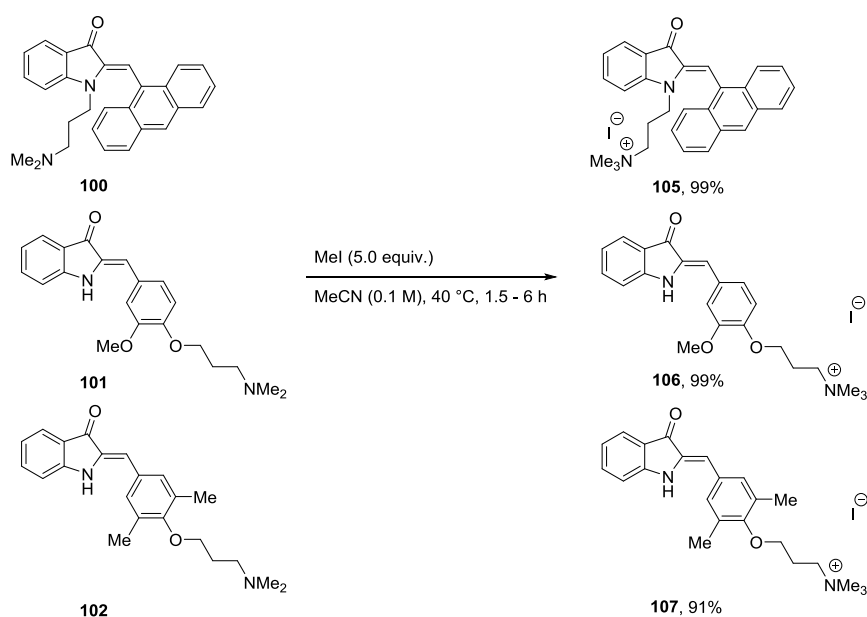
Scheme 45:  $S_N2$  reaction of N-H unsubstituted hemiindigo photoswitches (**51**, **34**, **97**, **98** and **99**) with 3-chloro-1-(*N,N*-dimethyl)propylamine in *N,N*-dimethylformamide at 100 - 120 °C with sodium hydride as base. Low to good yields of hemiindigos **100**, **101**, **102**, **103** and **104** could be obtained.

The indoxyl nitrogen 1-*N,N*-dimethylaminopropyl substituted hemiindigo photoswitch **100** was purified by silica column chromatography with 88 / 10 / 2 dichloromethane / methanol / triethylamine mixture. The 1-*N,N*-dimethylaminopropyl disubstituted photoswitches **101** and **102** were purified by column chromatography with 35 / 25 / 40 / 2 (silica) or 98 / 1 / 0 / 0 (aluminium(III) oxide, *Brockmann* III) dichloromethane / methanol / *n*-hexane / triethylamine mixtures. The 1-*N,N*-dimethylaminopropyl trisubstituted photoswitches **103** and **104** were purified by silica column chromatography with 61 / 35 / 4 dichloromethane / methanol / triethylamine mixtures.

The first reversed-phase- (RP) HPLC purifications of the 1-*N,N*-dimethylaminopropyl disubstituted photoswitches **101** and **102** were carried out on a preparative *Machery-Nagel* VP 250/21 *NUCLEODUR Sphinx* 5  $\mu\text{m}$  column under acidic / basic / neutral / ionic eluent conditions with varying organic modifiers, showing no success as mostly streaking of the desired peaks was observed. Obtaining of a preparative *Agilent XDB* 100/21 *Zorbax* 5  $\mu\text{m}$  column yielded acceptable peak separations for stilbene 1-*N,N*-dimethylaminopropyl substituted hemiindigo photoswitch **101** with a 9 / 1 / 0.01 methanol / water / triethylamine mixture as eluent and for 1-*N,N*-dimethylaminopropyl disubstituted photoswitch **102** with a 8 / 2 / 0.01 methanol / water / triethylamine mixture as eluent.

The *tris*-alkyl-dimethylamino compounds **103** and **104** were not submitted to RP-HPLC because of their high polarity and a high chance of contaminating the columns.

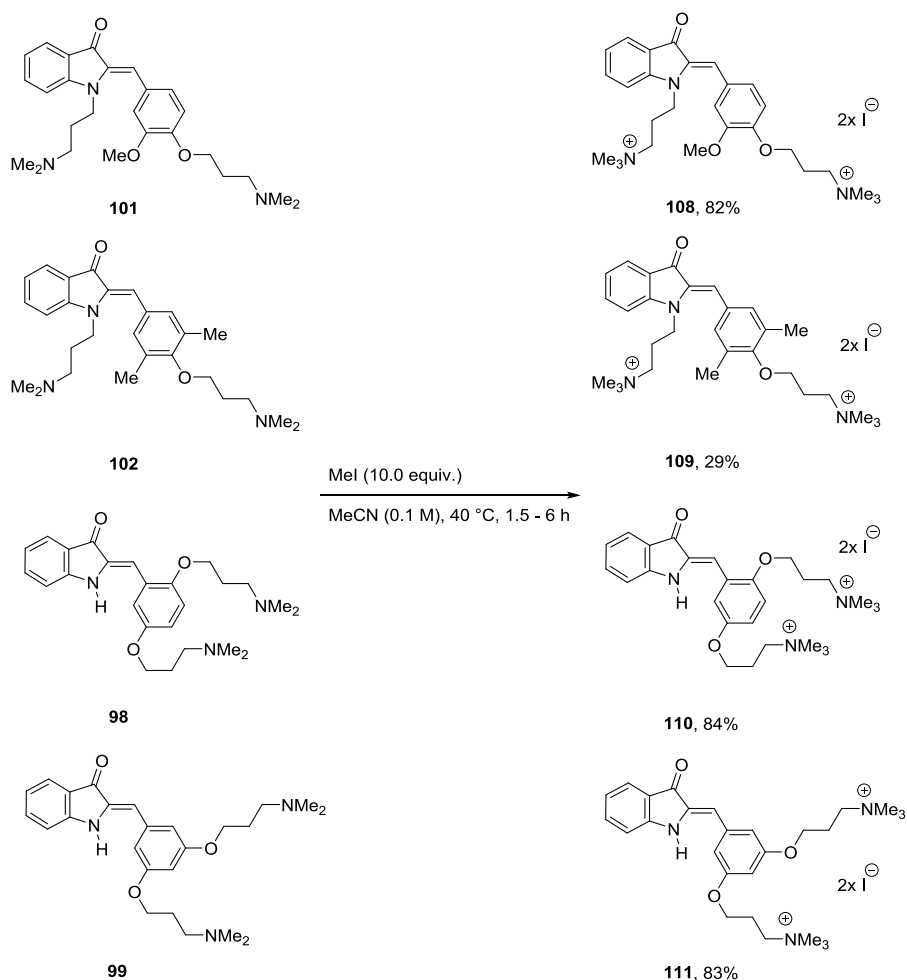
The loss of the N-H proton reduced the general water solubility of these compounds. This does not interfere with the objectives of the project, as a subsequent introduction of permanent charges by a *Menschutkin* reaction was planned.<sup>[139]</sup>



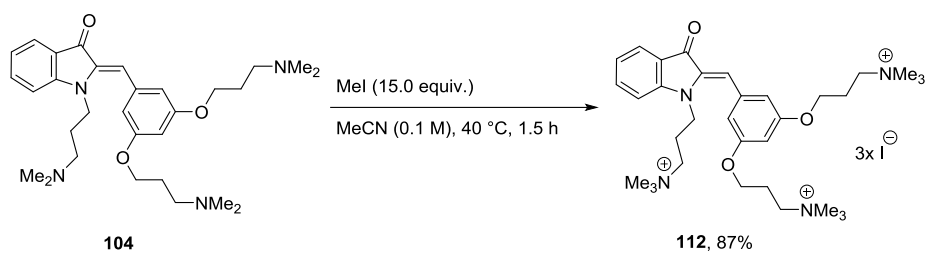
Scheme 46: *Menschutkin* reaction of excess methyl iodide in acetonitrile with dimethylamino alkyl chain substituted hemiindigos **100**, **101** and **102** yielding quaternary ammonium ion substituted hemiindigos **105**, **106** and **107**. This reaction introduces a permanent charge-tag to the hemiindigo photoswitch.

Purification of the ionic compounds was previously tried with minor success as these compounds are very hard to elute from RP-HPLC columns. Buffers, basic and acidic conditions were tried, with minor success. Large streaks of elution peaks over 20 minutes up to hours could

be observed. The use of anion exchange resins was tested, successfully changing iodide to hexafluorophosphate. This, however, introduces residual hexafluorophosphate salts upon evaporation, which makes yield determination or submitting these sample to elemental analysis or binding studies not feasible. The use of ammonium formate as volatile buffer did not yield satisfactory results as the salt could not be completely sublimated from the samples without destroying the photoswitches. The remaining salts pose no difficulties for NMR analysis or mass spectrometry, however, elemental analysis cannot be passed this way.



Scheme 47: *Menschutkin* reaction of excess methyl iodide in acetonitrile with dimethylamino alkyl chain substituted hemiindigos **101**, **102**, **98** and **99** yielding two quaternary ammonium ions, introducing permanent charge-tags to the hemiindigo photoswitches **108**, **109**, **110** and **111**. Low to good yields could be obtained.



Scheme 48: *Menschutkin* reaction of excess methyl iodide in acetonitrile with three dimethylamino alkyl chain substituted hemiindigo **104** yielding three quaternary ammonium ions, introducing permanent charge-tags to hemiindigo **112**.

The reaction of **103** with methyl iodide was not carried out as the triple charged photoswitches showed very unspecific binding to the highly anionic DNA backbone.

## 2.6.2 Hemiindigos in water - Photoswitching of non-ionic compounds

The general photoswitching behavior of the novel, water soluble hemiindigo compounds was tested. The dimethylamino alkyl chains were attached to achieve binding towards DNA / RNA and to introduce permanent charge-tags upon quaternization of the 1-*N,N*-dimethylamino moiety. The bare 1-*N,N*-dimethylamino moieties, the unsubstituted N-H functionality on the indoxyl core and especially permanent charge-tags promote the solubility of hemiindigo photoswitches in pure water. However, in some cases, the neutral compounds need additives in forms of buffer salt, acidity or water miscible polar organic solvents to dissolve.

This section deals with designing hemiindigo photoswitches that are able to switch in water, which is mandatory to show a modulation of affinity towards DNA / RNA. As the variability of substitution patterns is basically limitless, few molecular substitution patterns were tested by *D. Berdnikova* in Section 2.6.4 for their binding and photoswitching properties when introduced to biomolecules. Compounds that show dissatisfactory results were not looked into further, some molecules showed decomposition when stored in sealed vials at ambient temperatures in the dark over several weeks.

Baseline drifts seen in UV-Vis spectra are caused by air bubbles and / or precipitation, compounds with low solubility got dissolved over time, which can cause unexpected increases of absorption values during the measurement course. The used cuvettes supported a light-path of 1 cm and a volume of 2.5 - 3.0 mL.

Compound **34** was synthesized, characterized and published by *D. Berdnikova*.<sup>[40]</sup> This compound was revisited to pose as precursor for the attachment of a second alkyl chain.

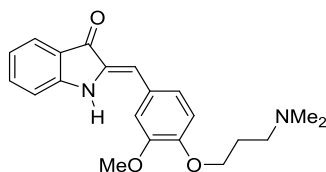


Figure 324: Lewis-formula of hemiindigo **34**.

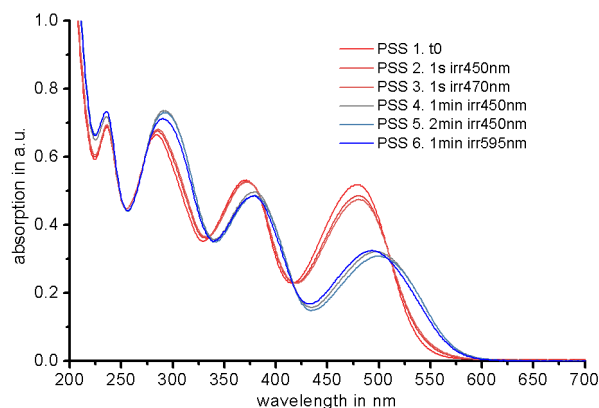


Figure 325: UV-Vis spectra of hemiindigo **34** in pure water under different irradiation conditions.

The PSS for irradiation with 470 nm LED light was reported at 80% *E* isomer and at 97% *Z* isomer for 590 nm LED light. Molar extinction coefficients were reported at  $10456 \text{ L mol}^{-1} \text{ cm}^{-1}$  (478 nm, *Z* isomer) and  $6289 \text{ L mol}^{-1} \text{ cm}^{-1}$  (501 nm, *E* isomer). The thermal *E* to *Z* isomerization barrier was determined at 23.7 kcal/mol with a thermal half-life of 10.8 h at 25 °C. The quantum yields were determined at 2.7% for *Z* to *E* and 0.2% for *E* to *Z* isomerization direction. Photodegradation over prolonged irradiation courses seems to be an issue with this compound. The photophysical data is reported according to the publication by *D. Berdnikova* for comparison with the following synthesized molecular substitution patterns.<sup>[40]</sup>

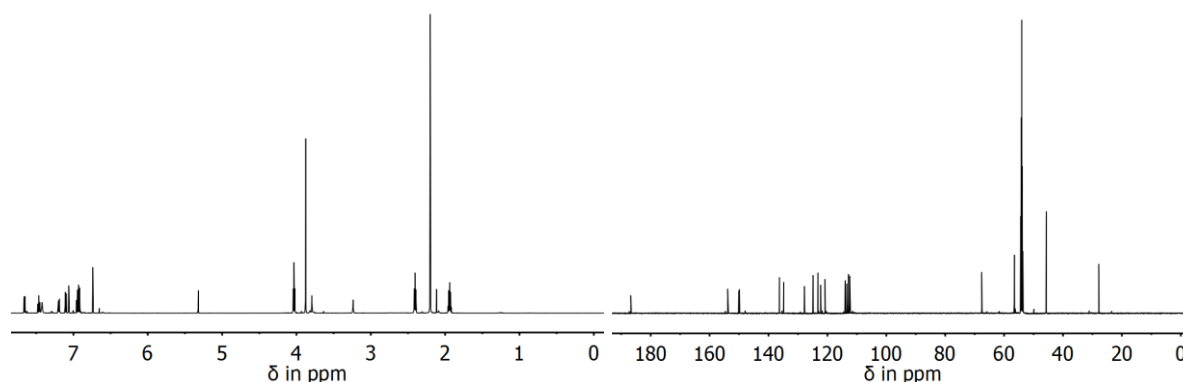
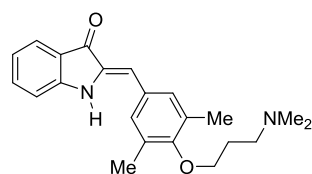
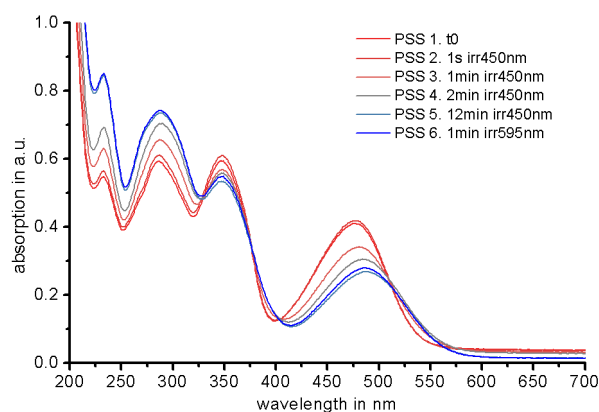
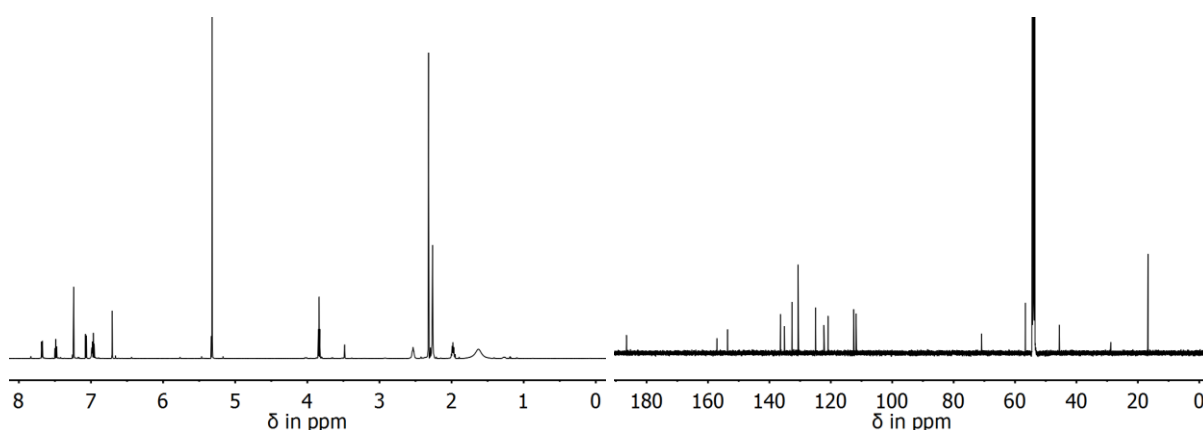


Figure 326:  $^1\text{H}$ - (left) and  $^{13}\text{C}$ -NMR spectra (right) of hemiindigo **34** (600 MHz, dichloromethane- $d_2$ , 27 °C).

Figure 327: Lewis-formula of hemiindigo **97**.Figure 328: UV-Vis spectra of hemiindigo **97** in pure water under different irradiation conditions.

Solubility in water is reduced for compound **97** compared to **34**, the quantum yields can be estimated at 1-3% for the *Z* to *E*- and below 1% for *E* to *Z* isomerization direction because of the elapsed time until the respective PSS is reached. The most red-shifted absorption maximum for the *Z* isomer remains at 478 nm while the *E* isomer shifts from 501 nm to 492 nm, which might cause a reduction of the isomeric yield for the *E* form caused by spectral overlap. Photodegradation over prolonged irradiation courses seems to be an issue with this compound.

Figure 329:  $^1\text{H}$ - (left) and  $^{13}\text{C}$ -NMR spectra (right) of hemiindigo **97** (600 MHz, dichloromethane- $d_2$ , 27 °C).



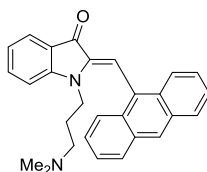


Figure 330: Lewis-formula of hemiindigo **100**.

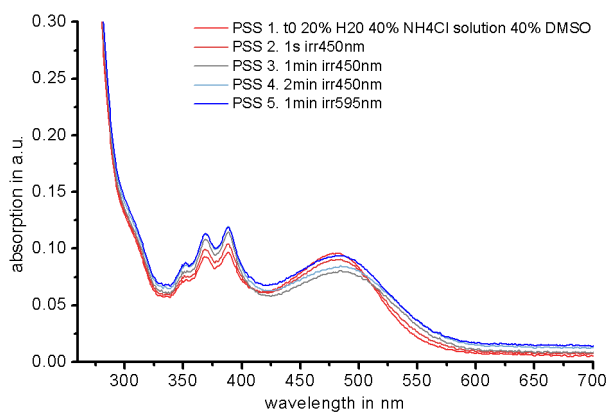


Figure 331: UV-Vis spectra of hemiindigo **100** in a 2 / 4 / 4 water / sat. aq. ammonium chloride / dimethyl sulfoxide mixture under different irradiation conditions.

Solubility in water is drastically reduced for compound **100** compared to **34** and **97**, which can be explained by the hydrophobicity of the anthracene moiety and the loss of the hydrophilic N-H proton. The quantum yields can be estimated at 1-2% for the *Z* to *E*- and below 1% for *E* to *Z* isomerization direction. The most red-shifted absorption maximum for the *Z* isomer shifts from 478 nm to 482 nm and the *E* isomer changes from 501 nm (for hemiindigo **34**) to 495 nm. The low solubility and usage of additives show bubbles and precipitation of the photoswitch within the cuvette, which causes drifting of the baseline and the isosbestic points.

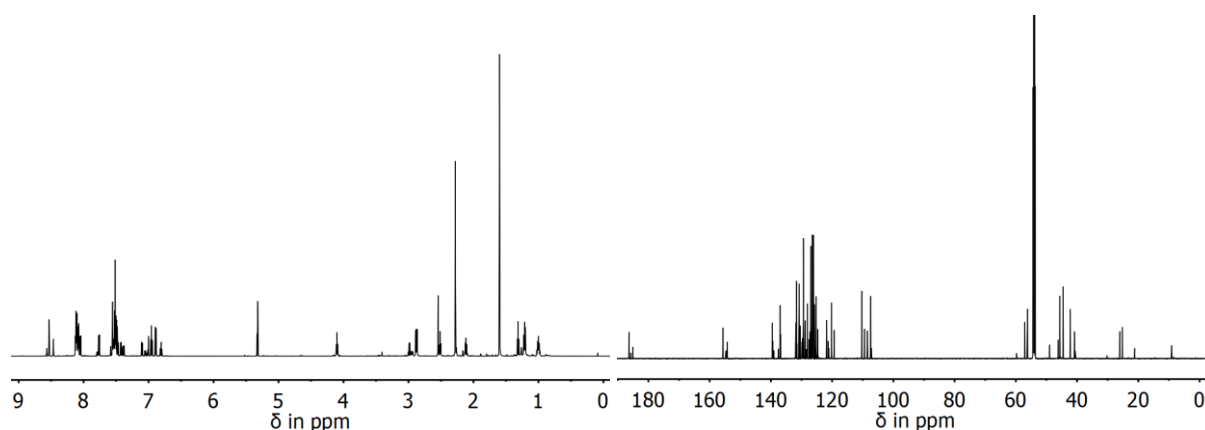
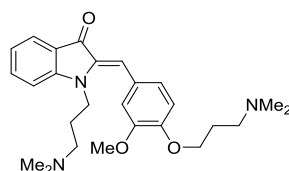
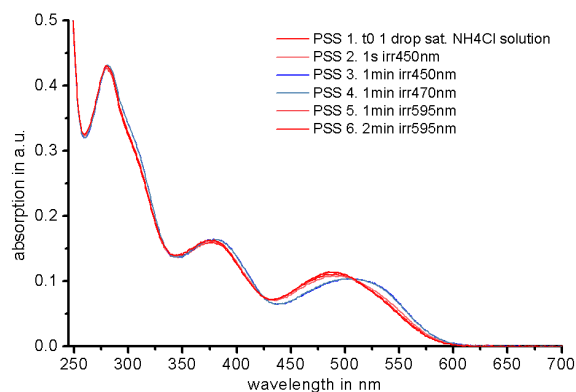
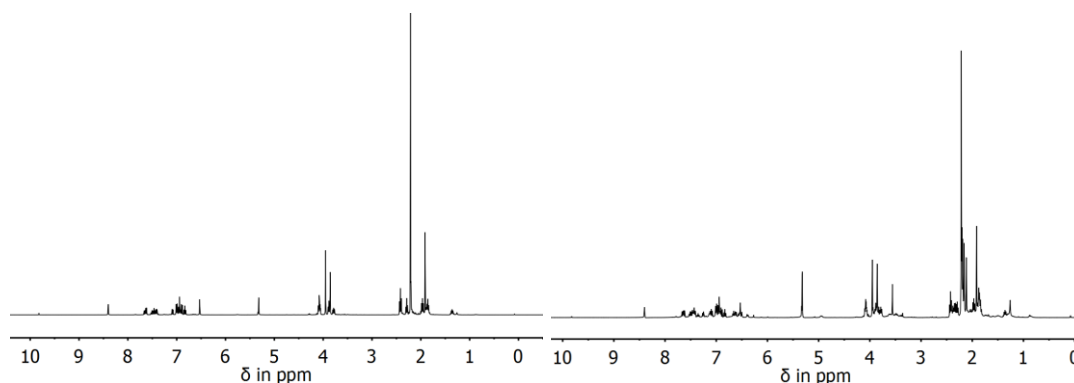


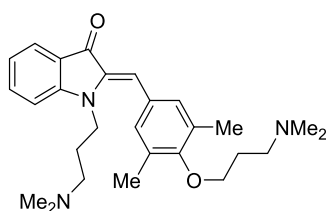
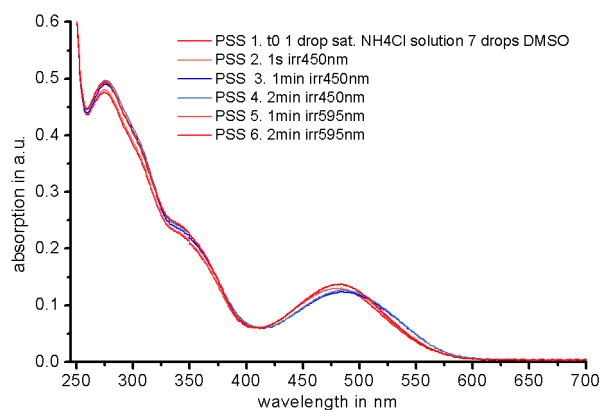
Figure 332:  $^1\text{H}$ - (left) and  $^{13}\text{C}$ -NMR spectra (right) of hemiindigo **100** (600 MHz, dichloromethane- $d_2$ , 27 °C).

Figure 333: *Lewis*-formula of hemiindigo **101**.Figure 334: UV-Vis spectra of hemiindigo **101** in water with one drop of sat. aq. ammonium chloride as additive under different irradiation conditions.

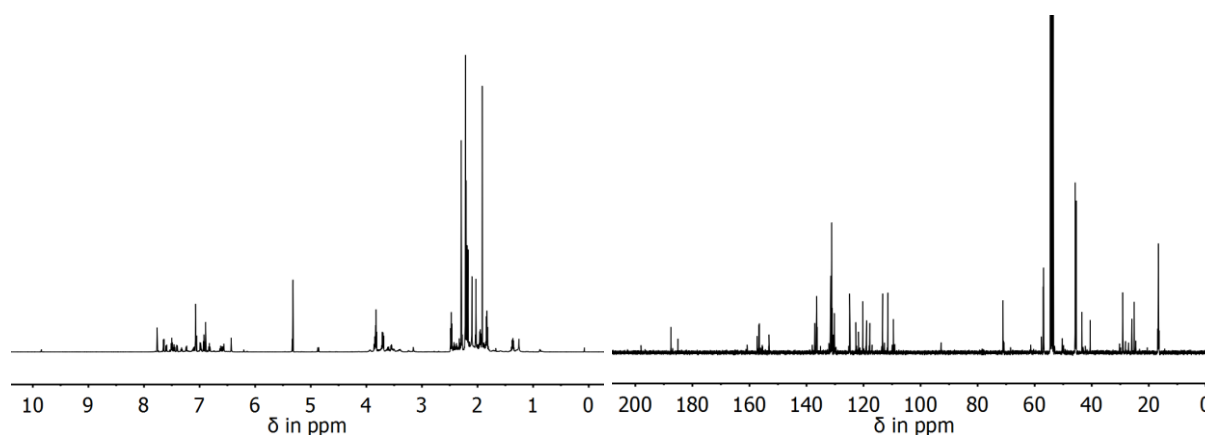
Solubility in water is increased for **101** in comparison to derivative **100** but reduced compared to **34** according to the absorptivity of qualitatively saturated solutions. Removal of the anthracene moiety reduces hydrophobicity while dimethylamino propyl substitution at the indoxyl N-H also lowers the hydrophilicity of this molecule. Addition of ammonium chloride protonates the basic dimethylamino functionality and increases its water solubility as salt. The quantum yields can be estimated at 1-2% for the *Z* to *E*- and below 1% for *E* to *Z* isomerization direction. The most red-shifted absorption maximum for the *Z* isomer shifts from 478 nm (for hemiindigo **34**) to 490 nm and the *E* isomer shifts from 501 nm (for hemiindigo **34**) to 510 nm. Photodegradation cannot be observed within this short irradiation experiment.

Figure 335:  $^1\text{H}$ -NMR spectra of hemiindigo **101** (400 MHz, dichloromethane- $d_2$ , 27 °C). RP-HPLC purification (right) yielded more signals than the precedent silica column separation (left), suggesting stability issues with this compound.

$^{13}\text{C}$ - and 2D-NMR spectra were not recorded as another purification protocol had to be found at that time. However, from preparation to shipment of this compound to *D. Berdnikova*, significant degradation of the sample was visible after one month, making it not viable for quantitative binding studies. This might be caused by oxidation of the basic dimethylamino side-chains and / or their reaction with the photoswitch. Also, gradually proceeding cleavage of the aldehyde can be observed via the signal at 9.8 ppm in the  $^1\text{H}$ -NMR spectrum after several weeks. The low shelf-life of the compound led to its discardment.

Figure 336: Lewis-formula of hemiindigo **102**.Figure 337: UV-Vis spectra of hemiindigo **102** in water with one drop of sat. aq. ammonium chloride and seven drops of dimethyl sulfoxide as additives under different irradiation conditions.

Solubility in water is increased for **102** in comparison to derivative **100** but reduced compared to **34** and **101**. Addition of ammonium chloride protonates the basic dimethylamino functionality and increases its water solubility as salt. The quantum yields can be estimated at 1-2% for the *Z* to *E*- and below 1% for *E* to *Z* isomerization direction. The most red-shifted absorption maximum for the *Z* isomer shifts from 478 nm (for hemiindigo **34**) to 484 nm and the *E* isomer shifts from 501 nm (for hemiindigo **34**) to 497 nm.

Figure 338:  $^1\text{H}$ - (left) and  $^{13}\text{C}$ -NMR spectra (right) of hemiindigo **102** (600 MHz, dichloromethane- $d_2$ , 27 °C).

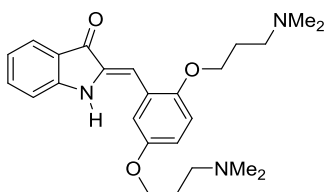


Figure 339: *Lewis*-formula of hemiindigo **98**.

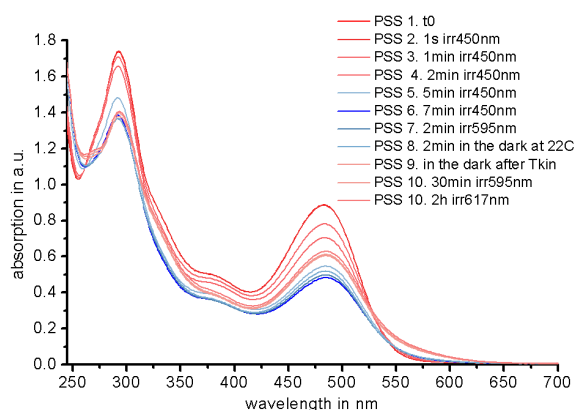


Figure 340: UV-Vis spectra of hemiindigo **98** in pure water at different irradiation conditions.

Solubility in water is increased for **98** in comparison to derivative **102** but lowered compared to **34**. The most red-shifted absorption maximum for the *Z* isomer shifts from 478 nm (for hemiindigo **34**) to 482 nm. Photodegradation and slow dissolution is mostly observed for this compound after a thermal kinetic experiment showed irregular absorption increases in the dark without isomerization reactions taking place (not shown).

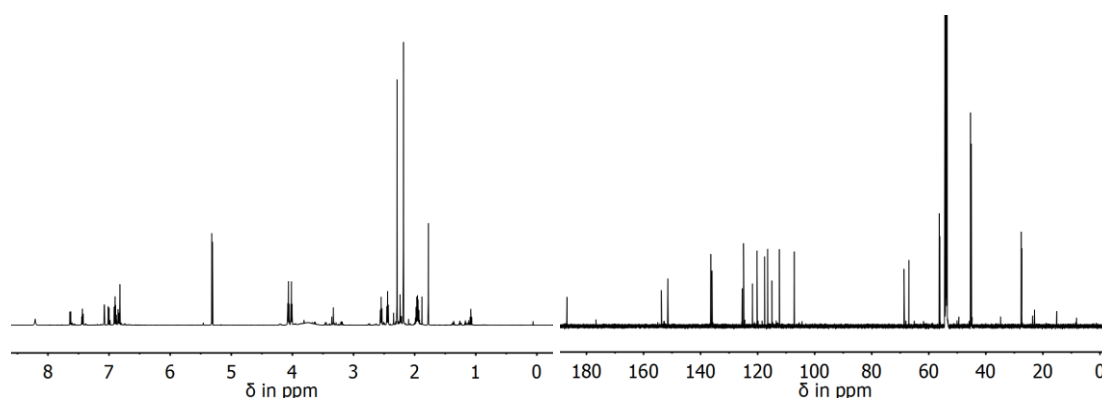


Figure 341:  $^1\text{H}$ - (left) and  $^{13}\text{C}$ -NMR spectra (right) of hemiindigo **98** (600 MHz, dichloromethane- $d_2$ , 27 °C).

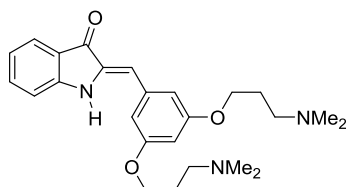


Figure 342: *Lewis*-formula of hemiindigo **99**.

Almost identical photophysical properties are expected for compound **99** compared to hemiindigo **98**.

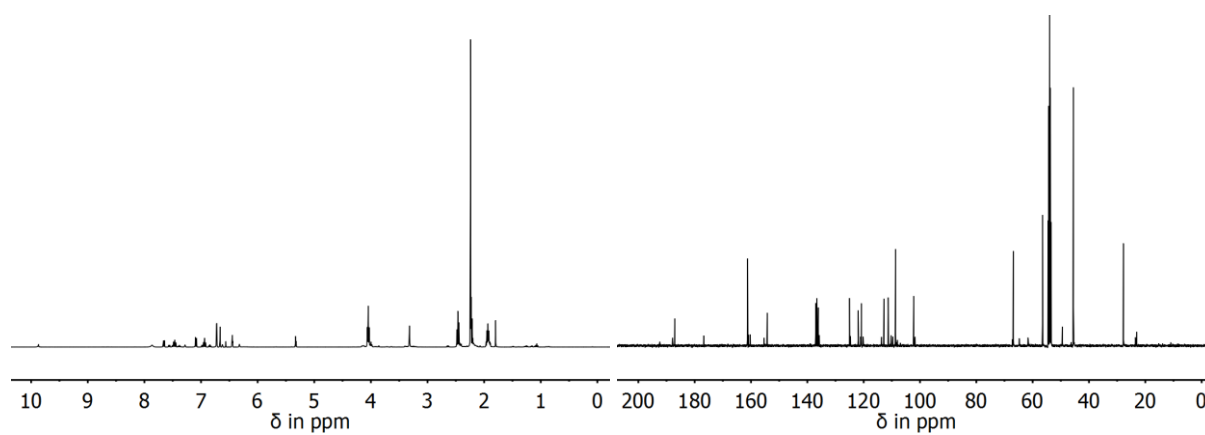


Figure 343:  $^1\text{H}$ - (left) and  $^{13}\text{C}$ -NMR spectra (right) of hemiindigo **99** (400 MHz, dichloromethane- $d_2$ , 27 °C).

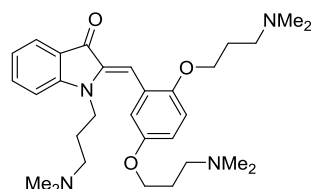


Figure 344: *Lewis*-formula of hemiindigo **103**.

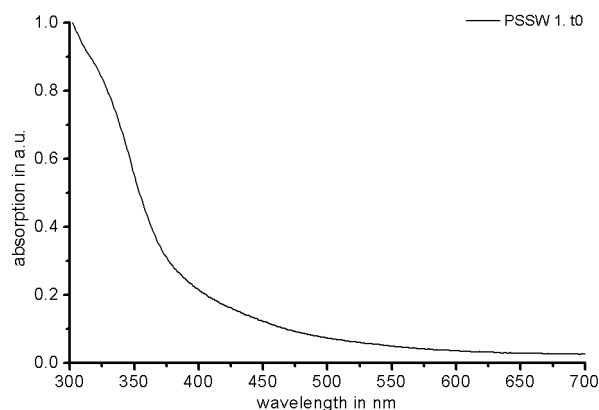


Figure 345: UV-Vis spectra of the degradation products of hemiindigo **103** in water after three months shelf storage in the dark at ambient temperatures. This compound was not measured via UV-Vis spectroscopy before degradation, spectra of **101** and **102** should be similar in shape.

The chromophore is completely degraded, which led to discardment of this substitution pattern.

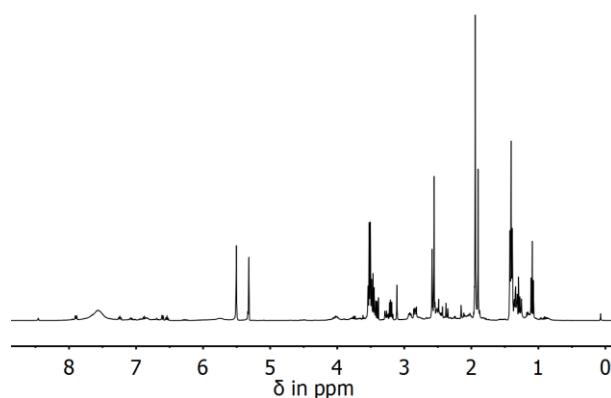


Figure 346:  $^1\text{H-NMR}$  spectra of hemiindigo **103** (400 MHz, dichloromethane- $d_2$ , 27 °C). Purification issues because of the high polarity of this compound yielded unclean products in low abundance.

The  $^1\text{H-NMR}$  spectrum recorded directly after synthesis and purification showed a set of desired and additional signals, indicating that purification is not optimized yet. The very polar nature of this compound makes it hard to elute from most stationary phases.

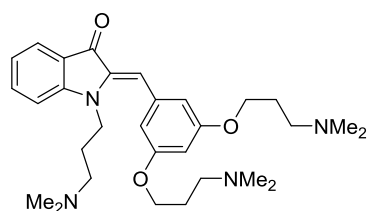


Figure 347: *Lewis*-formula of hemiindigo **104**.

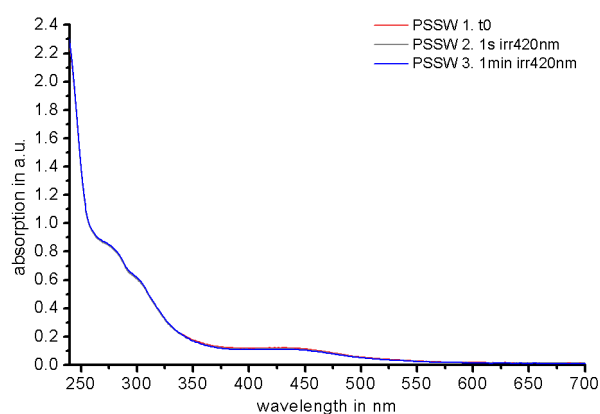


Figure 348: UV-Vis spectra of the degradation products of hemiindigo **104** in water after three months shelf storage in the dark at ambient temperatures. This compound was not measured via UV-Vis spectroscopy before degradation, spectra of **101** and **102** should be similar in shape.

The chromophore is almost completely degraded, attempts on photoswitching showed almost no modulation. This led to discardment of this substitution pattern.

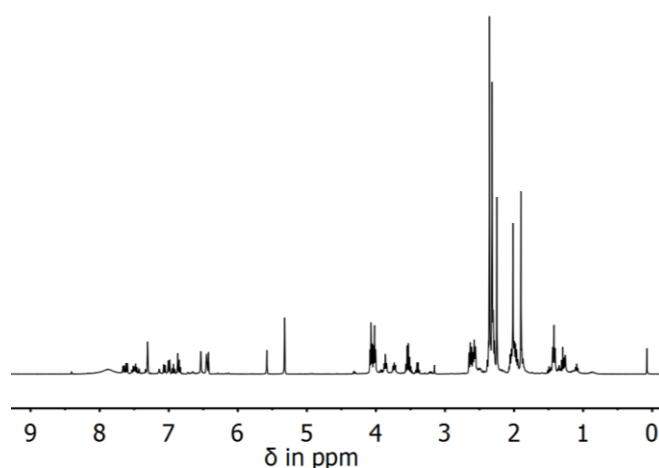


Figure 349:  $^1\text{H}$ -NMR spectra of hemiindigo **104** (400 MHz, dichloromethane- $d_2$ , 27 °C). Purification issues because of the high polarity of this compound yielded unclean products.



The  $^1\text{H}$ -NMR spectrum recorded directly after synthesis and purification showed a set of desired and additional signals, indicating that purification is not optimized yet. The very polar nature of this compound makes it hard for elution from most stationary phases.

### 2.6.3 Hemiindigos in water - Photoswitching of ionic compounds

One goal of this project was to supply *D. Berdnikova* with permanently charged, water soluble hemiindigo photoswitches for submission to quantitative binding studies on biomolecules. As synthesis and purification of the neutral compounds is already difficult and labor-intensive, the addition of a permanent charge-tag makes things worse. Elution from the available stationary RP-HPLC phases did not yield satisfactory peak separations and proceeded over 20 minutes to hours. Basic or acidic buffer systems improved this streaking but yielded no clean products as e.g. the cleaved, charge-tagged aldehydes could not be separated from the products. Another problem of the usage of buffers or ion exchange chromatography is the buffer salt solution itself as it is mixed with the desired photoswitch salt in undefinable amounts after evaporation. This makes weighing of the photoswitch for the preparation of defined solutions for titration in binding experiments very inaccurate. Ammonium formate as volatile buffer system was tested as well with minor success, as sublimation under high vacuum could not remove it entirely without degrading the photoswitchable compound.

The most practical way of preparing pure compounds with stoichiometric photoswitch to anion ratios was synthesizing the permanently charged compounds directly from HPLC purified starting materials (if possible) by quantitative reaction (if applicable) with methyl iodide in a *Menschutkin* type reaction in acetonitrile. Removal of excess methyl iodide and acetonitrile gives the pure desired compounds as iodine salts. Weighting of starting materials and products confirmed 99% reaction progress, as reacted methyl iodide contributes to the product mass while unreacted methyl iodide is removed *in vacuo*. However, small scale reactions with <10 mg of starting material and / or incomplete reaction progress introduced systematic errors for the yield determination. This was not crucial at this stage of the project, as testing of the binding properties of the various hemiindigo photoswitches was carried out with DNA samples to estimate the binding- and photoswitching properties of the molecules. The compounds showing positive results were synthesized in larger quantities for further investigation.

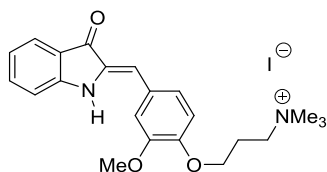


Figure 350: *Lewis*-formula of hemiindigo **106**.

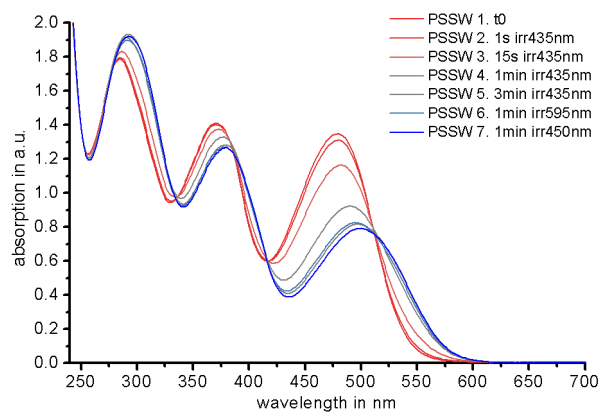
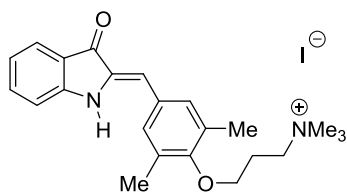
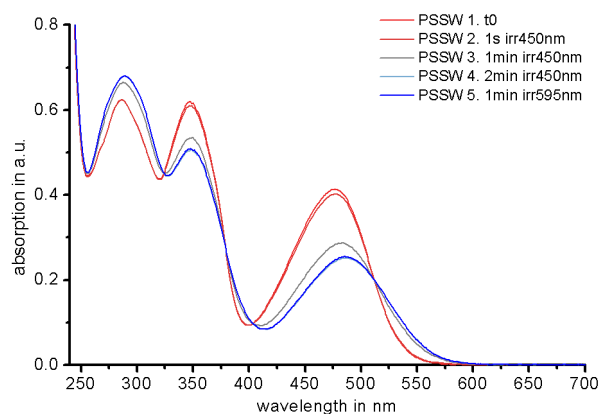


Figure 351: UV-Vis spectra of hemiindigo **106** in pure water under different irradiation conditions.

The (photo) physical data according to the publication by *D. Berdnikova* should be similar for this ionic compound as the permanent charge-tag is electronically decoupled from the  $\pi$ -system. The tripled amount of dissolved photoswitch compared to **34** showed no solubility issues.

Figure 352: *Lewis*-formula of hemiindigo **107**.Figure 353: UV-Vis spectra of hemiindigo **107** in pure water under different irradiation conditions.

The (photo) physical data of this compound should be similar to its precursor **97** as the permanent charge-tag is electronically decoupled from the  $\pi$ -system. Solubility and photostability in water increased for this molecule compared to **97**.

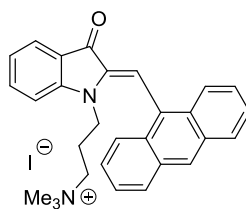


Figure 354: Lewis-formula of hemiindigo **105**.

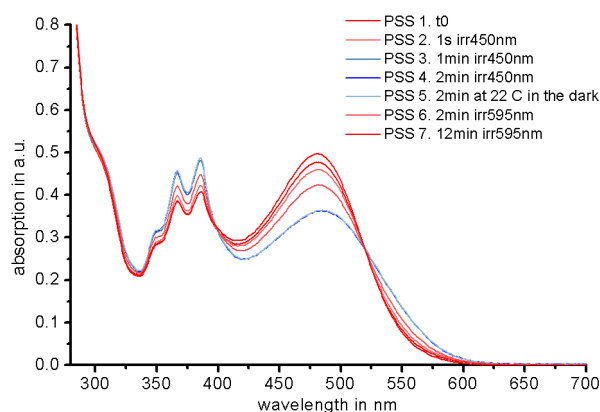


Figure 355: UV-Vis spectra of hemiindigo **105** in pure water under different irradiation conditions.

The (photo) physical data of this compound should be similar to its precursor **100** as the permanent charge-tag is electronically decoupled from the  $\pi$ -system. Solubility and photostability in water is drastically increased for this molecule compared to **100** as no additives (2 / 4 / 4 water / sat. aq. ammonium chloride / dimethyl sulfoxide mixture) are needed to dissolve this ionic photoswitch. It can also be stated that the introduction of one positive charge with iodine as counter anion outperforms the hydrophilicity of the N-H or a dimethylamino moiety. Also, an increase in photostability and quantum yields, especially for the *E* to *Z* isomerization direction can be observed. The thermal bistability was tested at 25 °C for 24 h, which showed no change in absorption, yielding a free activation enthalpy  $\Delta G^* > 25$  kcal/mol and minimal thermal half-lives in the range of days to weeks. The most red-shifted absorption maximum for the *Z* isomer is located at 481 nm and at 487 nm for the *E* isomer.

*D. Berdnikova* showed that **105** binds to ct DNA, maintaining its photoswitchability, while binding to the HIV-1 RNA on the TAR and RRE sites could be observed as well. This was the indication for upscaling and purification of this compound to obtain 40 mg for quantitative binding studies. Further photophysical measurements of this compound have to be carried out after completion of the binding studies to do further research on this system.

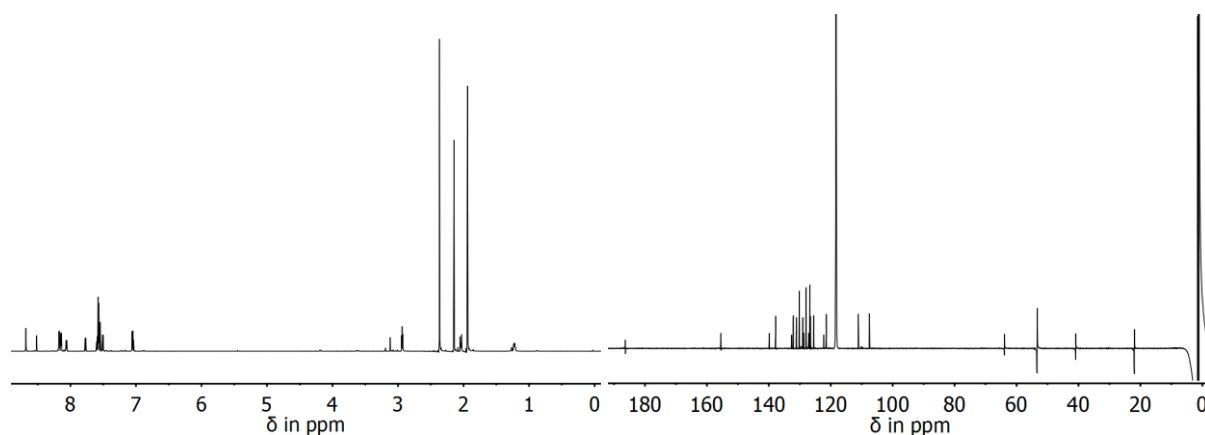


Figure 356:  $^1\text{H}$ - (left) and  $^{13}\text{C}$ -NMR spectra (right) of hemiindigo **105** (800 MHz, dichloromethane- $d_2$ , 27 °C).

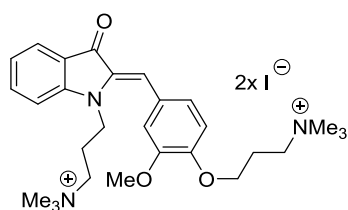


Figure 357: *Lewis*-formula of hemiindigo **108**.

This compound was abandoned for its poor shelf-life of its precursor of only a few weeks within sealed conditions in the dark at ambient temperatures. It is listed here for the discussion of all iterations of designed molecules.

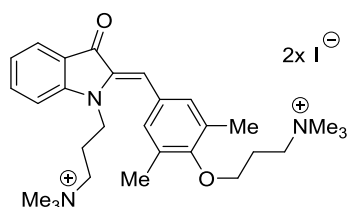


Figure 358: *Lewis*-formula of hemiindigo **109**.

This compound was abandoned for the poor shelf-life of its precursor of only a few months within sealed conditions in the dark at ambient temperatures. It is listed here for the discussion of all iterations of designed molecules.

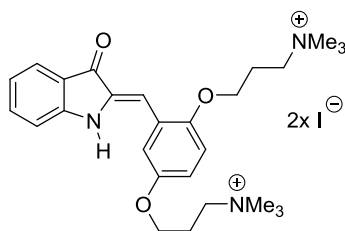


Figure 359: Lewis-formula of hemiindigo **110**.

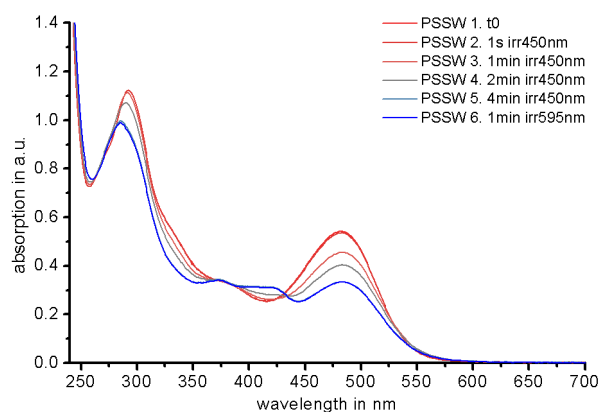


Figure 360: UV-Vis spectra of hemiindigo **110** in pure water under different irradiation conditions.

The (photo) physical data of this compound should be similar to its precursor **98** as the permanent charge-tag is electronically decoupled from the  $\pi$ -system. Solubility and photostability in water increased for this molecule compared to **98**. Viable Photoswitching for this compound can now be observed in pure water, which was not the case for its precursor. The most red-shifted absorption maximum for the *Z* isomer shifts from 480 nm (for ionic hemiindigo **106**) to 487 nm while the *E* isomer shifts from 501 nm (for ionic hemiindigo **106**) to 489 nm.





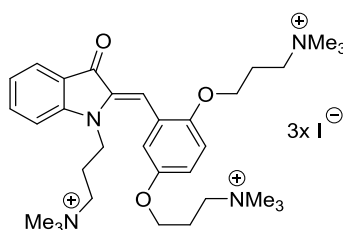


Figure 363: *Lewis*-formula of hemiindigo **113**.

The ionic derivative of this compound was not synthesized as binding studies with triple charged hemiindigo **112** showed excessively strong and unspecific interactions with the negatively charged phosphate backbone of DNA, which was not desired. It is listed here for the discussion of all iterations of designed molecules.

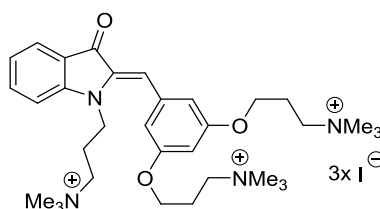


Figure 364: *Lewis*-formula of hemiindigo **112**.

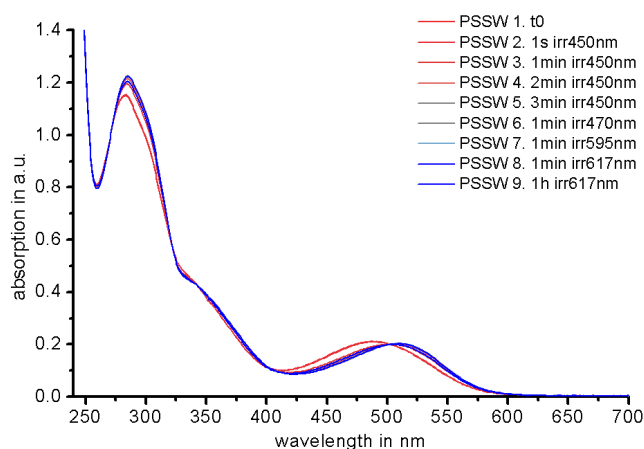


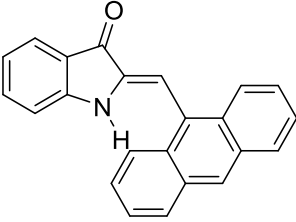
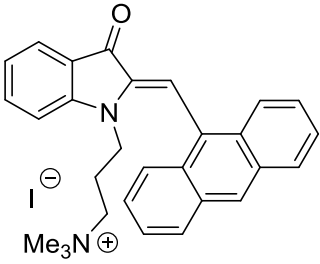
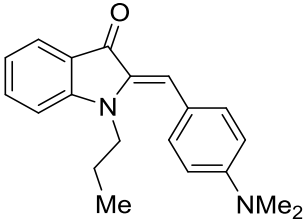
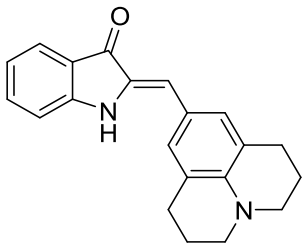
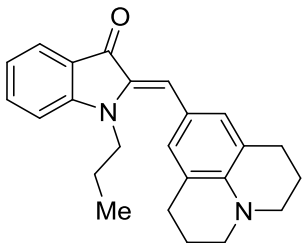
Figure 365: UV-Vis spectra of hemiindigo **112** in pure water under different irradiation conditions.

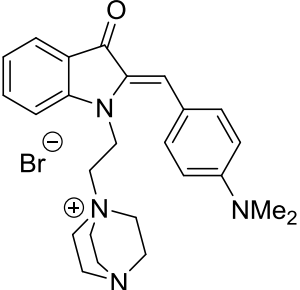
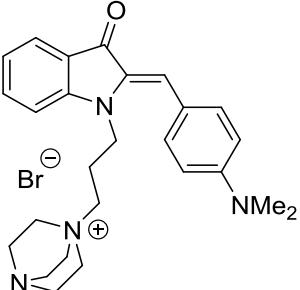
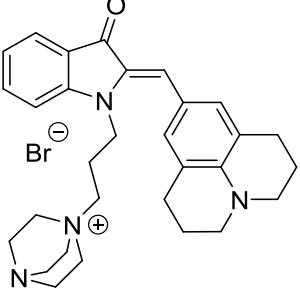
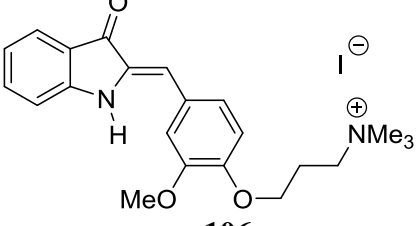
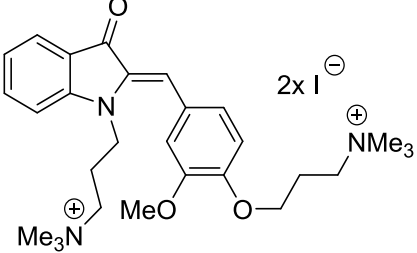
Surprisingly, this compound was stable over several months compared to its precursor, hinting towards the dimethylamino moieties being responsible for degradation of the compounds. Viable switching without photobleaching to good estimated isomeric yields can be contested. Also, the most red-shifted absorptions for *Z* (490 nm) and *E* isomers (514 nm) can be observed for this compound, which is caused by the N-H substitution with a dimethylamino alkyl chain.

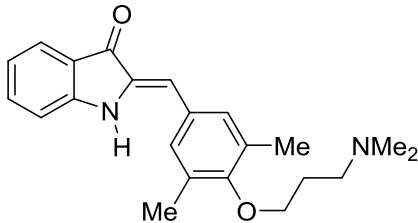
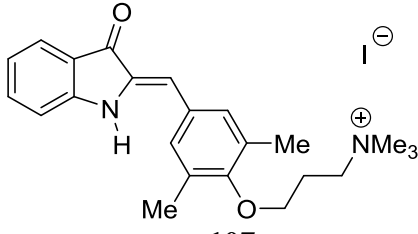
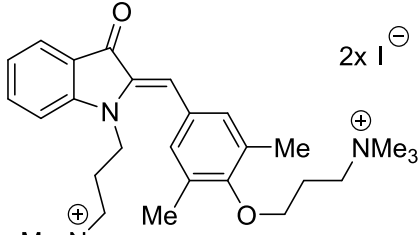
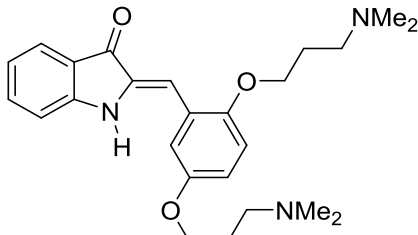
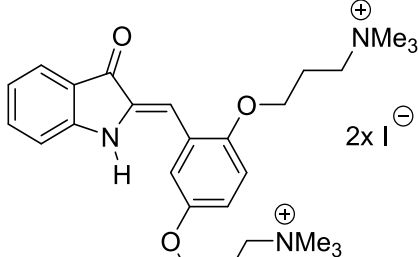
## 2.6.4 Hemiindigos in water - DNA / RNA binding

The main goal of this project consisted in finding suitable substitution patterns of hemiindigo photoswitches to show that hemiindigos are capable of interactions with nucleic acids while maintaining their photoswitching properties. Calf thymus DNA (ct DNA) and regulatory elements of HIV-1 RNA (TAR and RRE-IIB) were used for binding studies. Ct DNA is a natural DNA widely used in studies of DNA binding anti-cancer agents and DNA binding agents that modulate DNA structure and function. Ct DNA represents a linear polymeric chain comprising thousands of base pairs. The regulatory elements of HIV-1 RNA represent oligonucleotide fragments of the viral genome RNA with the length about 30 bases. The main goal was to find a ligand that would efficiently interact with a certain type of nucleic acids and would allow to control the structure and properties of DNA / RNA by photoswitching. The results of the binding studies of various neutral- and charge-tagged hemiindigos on DNA and RNA is shown in Table 18.

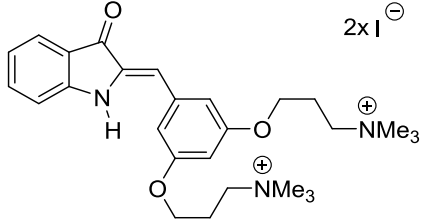
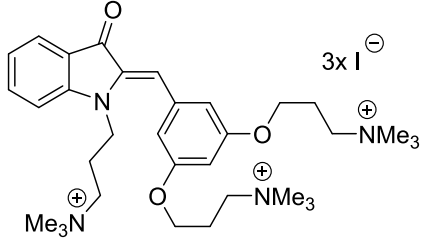
Table 18: Photoswitching and ct DNA + HIV-1 RNA binding studies by *D. Berdnikova* in water without buffer.

Compound	Photoswitching in water	Interaction & photoswitching with ct DNA	Interaction & photoswitching with HIV-1 RNA
 <b>51</b>	Switching: <b>No</b>	Interaction: <b>None</b> Switching: <b>No</b>	N/A
 <b>105</b>	Switching: <b>Z to E</b> <b>E to Z</b>	Interaction: <b>Binding</b> Switching: <b>Z to E</b> <b>E to Z</b>	TAR: <b>binds</b> RRE: <b>binds</b> Switching: To be tested
 <b>8</b>	Switching: <b>No</b> (precipitation and/or other photoprocess)	Interaction: <b>Some</b> Switching: <b>No</b>	N/A
 <b>15</b>	Switching: <b>No</b> (other photoprocess)	Interaction: <b>Some</b> Switching: <b>No</b> (other photoprocess)	N/A
 <b>3</b>	Switching: <b>No</b> (other photoprocess)	Interaction: <b>Binding</b> Switching: <b>No</b> (other photoprocess)	N/A

Compound	Photoswitching in water	Interaction & photoswitching with ct DNA	Interaction & photoswitching with HIV-1 RNA
 <p style="text-align: center;"><b>81</b></p>	<b>Switching:</b> <b>No</b>	<b>Interaction:</b> <b>Strong binding</b> <b>Switching:</b> <b>No</b> (other photoprocess)	N/A
 <p style="text-align: center;"><b>80</b></p>	<b>Switching:</b> <b>No</b>	<b>Interaction:</b> <b>Strong binding</b> <b>Switching:</b> <b>No</b>	<b>RRE: no or very          weak          interaction +          precipitation</b> <b>Switching:</b> <b>No</b>
 <p style="text-align: center;"><b>82</b></p>	<b>Switching:</b> <b>No</b>	<b>Interaction:</b> <b>Strong binding</b> <b>Switching:</b> <b>No</b> (other photoprocess)	N/A
 <p style="text-align: center;"><b>106</b></p>	<b>Switching:</b> <b>Z to E</b> <b>E to Z</b>	<b>Interaction:</b> <b>Binding</b> <b>Switching:</b> <b>Z to E</b>	N/A
 <p style="text-align: center;"><b>108</b></p>	<b>Switching:</b> <b>Z to E</b> <b>E to Z</b>	<b>Interaction:</b> <b>Binding</b> <b>Switching:</b> <b>Z to E</b>	N/A

Compound	Photoswitching in water	Interaction & photoswitching with ct DNA	Interaction & photoswitching with HIV-1 RNA
 <p style="text-align: center;"><b>97</b></p>	<b>Switching:</b> <i>Z to E</i> <i>E to Z</i>	<b>Interaction:</b> <b>Binding</b> <b>Switching:</b> <i>Z to E</i>	N/A
 <p style="text-align: center;"><b>107</b></p>	<b>Switching:</b> <i>Z to E</i> <i>E to Z</i>	<b>Interaction:</b> <b>Binding</b> <b>Switching:</b> <i>Z to E</i>	N/A
 <p style="text-align: center;"><b>109</b></p>	<b>Switching:</b> <i>Z to E</i> <i>E to Z</i>	<b>Interaction:</b> <b>Binding</b> <b>Switching:</b> <i>Z to E</i>	N/A
 <p style="text-align: center;"><b>98</b></p>	<b>Switching:</b> <b>No</b> (other photoprocess)	<b>Interaction:</b> <b>Some</b> <b>Switching:</b> <i>Z to E</i>	N/A
 <p style="text-align: center;"><b>110</b></p>	<b>Switching:</b> <b>No</b> (other photoprocess) <b>Reduced</b> <b>absorbance</b>	<b>Interaction:</b> <b>Binding</b> <b>Switching:</b> <b>Poorly</b> <i>Z to E</i>	N/A

---

 <p><b>111</b></p>	<b>Switching:</b> Slow / incomplete Z to E E to Z	<b>Interaction:</b> Some Switching: Poorly Z to E E to Z	N/A
 <p><b>112</b></p>	<b>Switching:</b> Some Z to E No / Slow E to Z	<b>Interaction:</b> Some Switching: Z to E	<b>TAR: no clear Interaction / switching</b>

---

Red = unfavored result, yellow = mediocre result, green = desired result

The results in Table 18 show that positively charged hemiindigos are expected to stick to the highly negatively charged RNA / DNA backbones. Increasing the permanent charges beyond a dicationic state yields unspecific binding at multiple and / or undesired sites. It should be mentioned that the basic functionalities of the non-ionic derivatives should experience protonation by surrounding water molecules under physiological conditions. This also renders them as ionic compounds within the binding experiments, although their binding affinity is not as pronounced as with the permanently charged derivatives. However, the particular binding modes cannot be determined at this stage. It can be stated that binding to DNA / RNA changes the photokinetics of hemiindigo with a general tendency for one-way or no photoswitching reactions. Derivatives that did not show photoswitching in water also show no photoswitching upon binding except for **98** and **110**. The most promising candidate is hemiindigo **105**, as switchability upon binding is observed. This compound was synthesized and purified at larger scale (40 mg) for submission to NMR binding studies carried out by *D. Berdnikova*. Further experiments will scrutinize the selectivity and binding affinity of this compound towards the regulatory elements of HIV-1 RNA.

## 2.6.5 Conclusion: Hemiindigos in water

As shown in Section 2.5, the ionic derivatives of highly bistable, red-shifted, electron rich hemiindigo photoswitches did not show photoisomerization reactions in pure water. *D. Berdnikova* of the *Ihmels* group in Siegen, Germany, synthesized the previously avoided hemiindigo derivatives featuring neutral stilbene fragments and made them water soluble by attaching a dimethylamino propyl chain at the stilbene fragment. This compound showed binding affinities towards HIV-1 TAR and RRE-IIB RNA and could be photoswitched in its fluorescent response.<sup>[40]</sup>

In accordance to the promising results of this therapeutic approach to potentially gain control of the HIV-1 proliferation apparatus, a series of hemiindigos with varying substitution patterns was synthesized and submitted to preliminary binding studies carried out by *D. Berdnikova*. Another promising candidate, namely hemiindigo **105**, was hereby found and synthesized at larger scale for further RNA binding studies followed with NMR spectroscopy by *D. Berdnikova*. These experiments will reveal the possible selectivity and binding constants of this photoswitch and its usability in controlling the HIV-1 activity.



- [40] D. V. Berdnikova, *Visible-range hemi-indigo photoswitch: ON–OFF fluorescent binder for HIV-1 RNA*, *Chem. Commun.* **2019**, 55, 8402.
- [88] U. Burger, A. O. Bringhen, *Cyclization Studies with N-Munnich Bases of 2-Substituted Indoles*, *Helv. Chim. Acta* **1989**, 72, 93.
- [90] V. S. Velezheva, P. J. Brennan, V. Y. Marshakov, *Novel Pyridazino[4,3-b]indoles with Dual Inhibitory Activity against Mycobacterium tuberculosis and Monoamine Oxidase*, *J. Med. Chem.* **2004**, 47, 3455.
- [96] C. M. Connelly, M. H. Moon, J. S. Schneekloth, *The Emerging Role of RNA as a Therapeutic Target for Small Molecules*, *Cell Chem Biol* **2016**, 23, 1077.
- [135] A. C. Stelzer, A. T. Frank, J. D. Kratz, M. D. Swanson, M. J. Gonzalez-Hernandez, J. Lee, I. Andricioaei, D. M. Markovitz, H. M. Al-Hashimi, *Discovery of selective bioactive small molecules by targeting an RNA dynamic ensemble*, *Nature chemical biology* **2011**, 7, 553.
- [136] S. A. Barros, I. Yoon, D. M. Chenoweth, *Modulation of the E. coli rpoH Temperature Sensor with Triptycene-Based Small Molecules*, *Angew. Chem. Int. Ed.* **2016**, 55, 8258.
- [137] C. M. Connelly, M. H. Moon, J. S. Schneekloth, *The Emerging Role of RNA as a Therapeutic Target for Small Molecules*, *Cell Chemical Biology* **2016**, 23, 1077.
- [138] J. Parsons, M. P. Castaldi, S. Dutta, S. M. Dibrov, D. L. Wyles, T. Hermann, *Conformational inhibition of the hepatitis C virus internal ribosome entry site RNA*, *Nature chemical biology* **2009**, 5, 823.
- [139] N. Menshutkin, in *Z. Phys. Chem., Vol. 5U*, **1890**, p. 589.

## 2.7 Photophysics - Improvements on the accuracy, repeatability and convenience of measurements

Automatization of repeating tasks and their analysis and interpretation is a key principle to increase productivity, repeatability and reliability. Several calculational tools were written in this work within *Microsoft Excel* to process the experimentally obtained photophysical data. The main purposes of these tools are automatized deconvolution of mixture UV-Vis spectra into pure spectra, determination of molar extinctions, photostationary isomeric yields, thermal kinetics and quantum yields. Additionally, this can be achieved by fast, resource-efficient UV-Vis experiments. UV-Vis spectrophotometers are fairly inexpensive, achieve fast measurement speeds, have no need for deuterated solvents and utilize only small quantities of valuable compounds. However, the usage of solvents is limited, as the observed molecules should absorb in different regions than the solvent matrix. This makes the herein presented methodology applicable for metastable photoswitches with barriers greater than 22 kcal/mol which absorb in the visible region of light. The compounds should also exhibit a photochromism greater than 10 nm between their most red shifted maxima.

### 2.7.1 Photophysics - Development of an “all-in-one” calculational *Excel* tool - 100% Z / E spectrum calculator

Observations of the key requirements of complete photophysical characterizations of photoswitches led to the development of an *Excel* tool that directly handles the spectrometer output files. The tool is able to calculate the following data: 100% Z / E spectra from two mixture spectra, molar extinction coefficients, photostationary states (PSS), multiple thermal kinetics via UV-Vis or NMR spectroscopy and quantum yields in both directions for up to four irradiation wavelengths. This requires meticulously obtained data and correctly determined analyte masses and measured solvent volumes with all photoswitches handled in absolute darkness over all the time. The benefits are reproducible results without copying tens of thousands of data points and handedly setting up their complicated calculations every time anew for each examined photoswitch in every utilized solvent.

When I began my PhD in the *Dube* group, quantitative kinetic- and PSS measurements were done largely via NMR spectroscopy. This leads to several shortcomings: At first, the irradiation duration of light increases with higher sample concentrations. The concentration difference between UV-Vis and NMR spectroscopy amounts to roughly a factor of 300 for acceptable signal-to-noise ratios of the measurements. This means that the amount of photons needed to

irradiate an NMR sample to the same isomeric ratio as an UV-Vis sample is increased by 300 for an ideal case, assuming the utilized LEDs are outputting a constant photon flux.

Secondly, the prolonged irradiation times within NMR tubes heat the sample and enable substantial contributions of possible thermal (back) reactions, giving inaccurate PSS results.

Thirdly, samples with very high molar absorptivities yield the same NMR peak intensities compared to samples with low molar absorptivities. This requires large amounts of photons and vigorous stirring to expose the entire sample volume to the incident light when used in high concentrations. The cause for this observation is the small penetration depth in highly concentrated solutions, as all present isomers absorb parts of the incoming light, shielding the inner region of the sample volume. This rendered some investigated photoswitches with quantum yields of about 20% as poorly photoswitchable at NMR concentrations at first. This observation also causes the inability to photoswitch large quantities, e.g. a 10 mmol reaction batch to the desired and potentially more reactive isomer. For example, the output of a 435 nm LED amounts to 257 mW, which translates to  $5.62 \times 10^{17}$  photons per second. Assuming a quantum yield of 20% and 10 mmol of photoswitch, irradiation has to be carried out for 14.9 h if every photon can always reach every molecule within the entire volume of the solution. This is not the case for optically dense solutions, as only a thin layer at the interface between air / glass and solution is efficiently irradiated, converting most of the incident light energy into heat. This could be overcome by higher photon outputs, which induce additional heating of the reaction mixture and cause potential photodamage.

These findings led to the conclusion that the lowest possible sample concentration that yields acceptable signal-to-noise ratios for a measurement is to be preferred for photoisomerization experiments. If viable molar absorptions are apparent, UV-Vis spectroscopy is very sensitive and yields excellent signal-to-noise ratios for little amounts of sample.

As UV-Vis spectroscopy is not able to give structural or quantitative information by itself, calibration needs to be done to determine isomeric ratios. One approach consists of purification and measurement of both pure isomers and mathematically scaling them to a common isosbestic point. This is often impractical and / or labor intensive, as almost all hemiindigo compounds require separation via HPLC. The usage of mixtures can avoid tedious separation of isomers. The first attempts on spectra deconvolution in the *Dube* group consisted in recording a UV-Vis spectrum of the pure hemithioindigo *Z* isomer (often obtained in its pure form) and subsequent irradiation to an estimated 50 / 50 *Z* / *E* ratio within an NMR tube. The irradiated mixture was kept in the dark (and sufficiently cooled) to measure if a 50 / 50 isomer composition was reached via NMR spectroscopy. Afterwards, this 50 / 50 mixture was measured via UV-Vis

spectroscopy and the product of pure *Z* spectrum and a factor *F* consisting of amount of *Z* isomer in the mixture (in %) divided by 50% was subtracted (eq. 21). The factor *F* which is desirably 1 in cases of a 50 / 50 *Z* / *E* ratio (eq. 22).

$$Abs(E) = Abs(Mix) - Abs(Z) * F \quad \text{eq. 21}$$

$$F = \frac{\%Z(Mix)}{50\%} \quad \text{eq. 22}$$

This, however, underestimates the absorptivity of the correct 100% *E* spectrum (see Figure 366 below), as absorption values were only subtracted from the spectrum and nothing was scaled up to make up for the loss of absorption.

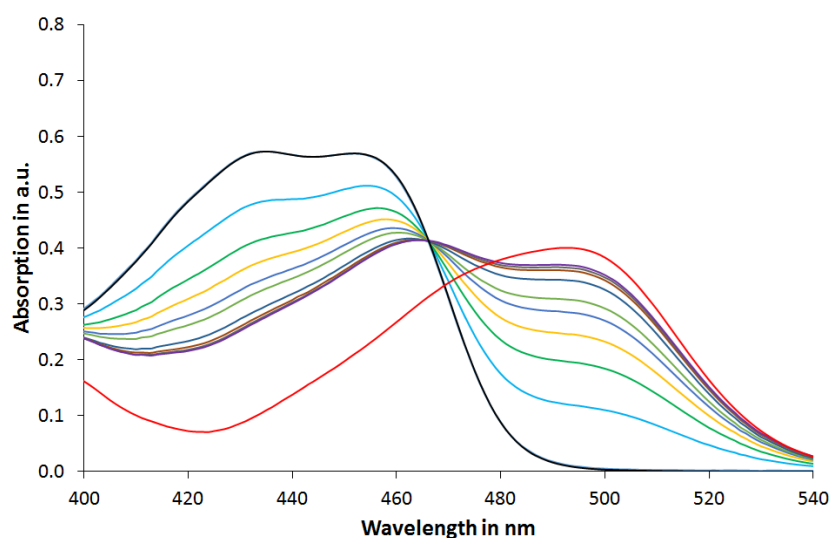


Figure 366: Example of an underestimated 100% *E* spectrum (red line) obtained by eq. 21 and eq. 22.

These observations led to a new mathematical approach by trial and error, which is described in the following section. The first major breakthrough was the possibility of using two mix spectra, as *N*-substituted hemiindigo compounds have their thermodynamic minima at variable *Z* / *E* equilibrium ratios. This circumvented the often impossible separation of *Z* and *E* isomers via reversed-phase HPLC and made it possible to utilize the generally very good (>90%) PSS yields of hemiindigos for the calculation of the 100% *Z*- and *E* spectra.

In general, UV-Vis spectra are recorded with the wavelength in nm as abscissa and absorption in a.u. (arbitrary units) as ordinate. The spectrophotometer, however, measures transmission, which is defined as (eq. 23):

$$\%T = \frac{I}{I_0} * 100\% \quad \text{eq. 23}$$

with  $I_0$  being the light intensity emitted by the light source and  $I$  being the transmitted light which was not absorbed by the sample.

$$A = -\log_{10} \left( \frac{I}{I_0} \right) \quad \text{eq. 24}$$

Calculation of the negative decadic logarithm of  $T$  yields the absorption  $A$  (eq. 24), which scales linearly with sample concentration.

To obtain the 100% spectra of solely  $Z$  or  $E$  isomers from two random isomeric mixtures, the exact composition of each mixture must be measured via NMR- and UV-Vis spectroscopy. For a successful spectra calculation, the required difference in isomer composition between the two measurement points is dependent on the photochromism of the compound. This translates to: more photochromism requires less difference in isomeric ratio between mixture A and B and vice versa. Also, thermal- and photoinduced reactions that shift the isomeric ratio within the NMR tube or the UV-Vis cuvette must be ruled out between the measurements. This allows to set up two UV-Vis spectra with exactly known isomeric compositions. However, it is not necessary to determine the sample concentrations if acceptable signal-to-noise ratios are prevalent, as all spectra will be scaled to a defined isosbestic point. The basic principle consists of calculating the spectrum  $A_{\text{calc.}}$  by subtracting the  $Z_{\text{mix}}$  spectrum from the  $E_{\text{mix}}$  spectrum and calculating the spectrum  $B_{\text{calc.}}$  by subtracting the  $E$  spectrum from the  $Z$  spectrum. The obtained  $A_{\text{calc.}}$  and  $B_{\text{calc.}}$  spectra are now multiplied with the respective isomer content determined via NMR spectroscopy. Subsequent multiplication of an upkeep factor is necessary to yield both 100% spectra that cross at the isosbestic points of the measured spectra.

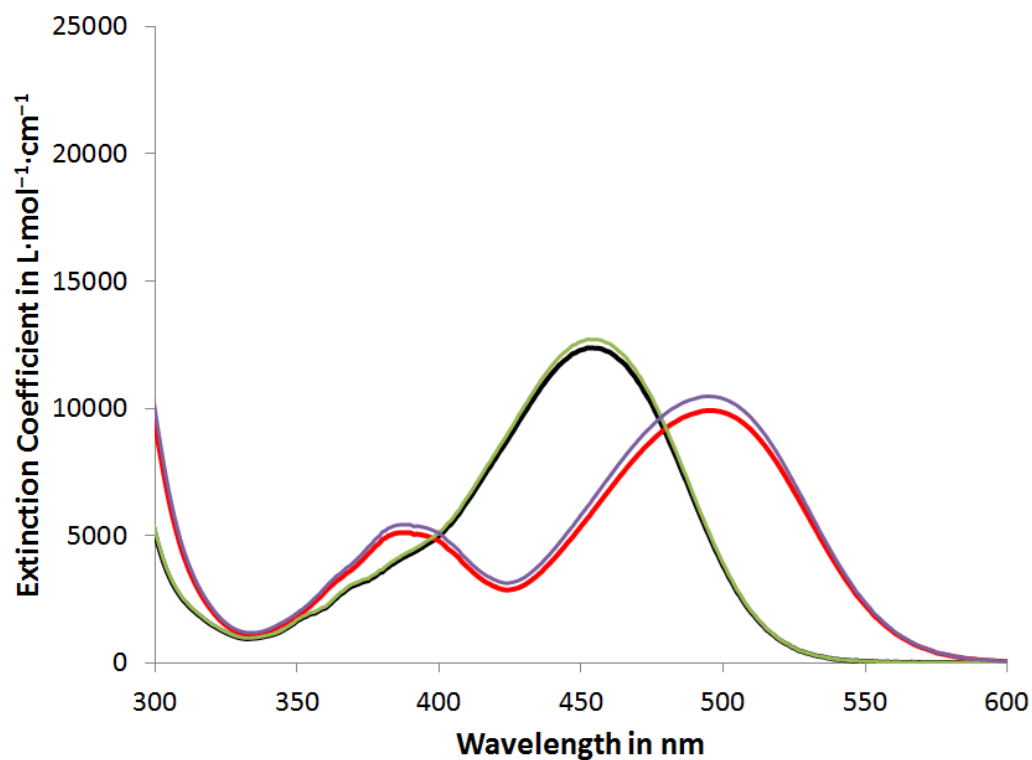


Figure 367: Example of the accuracy of the first generation of the 100% *Z / E* calculator, green and violet: measured 100% molar absorption spectra, black and red: calculated 100% molar absorption spectra.

A guide for successfully measuring and calculating 100% *Z/E* UV-Vis spectra was written to avoid potential mistakes beforehand, the section for the 100% spectrum calculator reads as follows (updated):

## “Determination of physical and photophysical properties of photoswitches via UV-Vis spectroscopy (suggestions)

### **0.) General considerations for UV-Vis measurements:**

Always clean your cuvettes prior to any measurement, use the soft tissues provided and double-check for fingerprints / solvent spillage. Use spectroscopic grade solvents filled into a separate beaker directly from the flask, no pipettes inside the flasks! Prevent solvent loss during (heated) measurements by plugging the cuvette. Try to use the same cuvette for the same compound and always face the cuvette in the same direction. Measure one baseline for every batch file you create and do not exceed 27 measurements per file. Choose an appropriate wavelength range for your measurements in your method and always use the same starting wavelength within your project, e.g. 800 nm (otherwise you will have to shift the wavelengths manually within the calculator, which does not save time at all!).

### **1.) Extinction coefficient measurements:**

Use the nanogram scale with an aluminium foil bowl (never touch it!) and the anti-electrostatic gun, weigh 0.2 mg to 2.0 mg depending on the expected molar absorption and mass of your chromophore. Use the anti-electrostatic gun again and drop the aluminium bowl without loss of compound into a 50 mL volumetric flask. Fill your flask with the desired solvent to the indicator in absence of light, plug it tightly and shake the flask thoroughly before taking out sample solution. Fill a clean cuvette with ~3 mL of the pure solvent and measure a baseline. Clean and dry your cuvette and fill it up with your compound solution, name your batch file “XX123\_SOLVENT\_ExCo” and the spectrum “ExCo 1. t0”. You should aim for a minimum of 0.3 Abs and maximum 1.5 Abs at the most red-shifted local maximum, repeat everything with more or less amount of compound if this is not the case. Choose a suitable wavelength to irradiate your

sample directly in the UV-Vis spectrometer. Irradiate in steps of 1, 5, 15, 30, 60, 120, 240... seconds until you reach the first PSS consisting of e.g. mainly *E* isomer, name your spectra "ExCo 2. 1s irrXXXnm", "ExCo 3. 5s irrXXXnm" etc. Change to another suitable wavelength and irradiate to the second PSS e.g. mainly *Z* isomer, adjust the times if necessary and use a continuous numbering throughout the batch file. Save the batch file as .BSW and .csv.

## 2.) UV-Vis - NMR correlation measurements:

Charge a NMR tube with 0.5 to 3.0 mg of your compound and dissolve it in ~0.6 mL of deuterated solvent. Fill a cuvette with the same kind of non-deuterated solvent, chose a fitting method, create "XXX123\_SOLVENT\_NMR.BSW" and measure a baseline. Turn off the light and proceed in absolute darkness from now on: Take a droplet from the NMR tube and add it to the solvent filled cuvette, measure an UV-Vis spectrum with at least 0.5 - 1.5 abs. Measure an NMR spectrum in absolute darkness (or black tube) on preferably a 400 MHz+ device as soon as possible and name it "XX123\_SOLVENT\_NMR\_XXXmin\_irrXXXnm". Irradiate your NMR tube (transfer the content of the black tube to a cuvette for irradiation) with the best suitable wavelength from your PSS measurement for *E* or *Z* isomers with the most powerful LED available to the respective PSS (~100 - 500x longer irradiation times than in the cuvette). Take a droplet from the irradiated NMR tube and add it to another clean and solvent filled cuvette, measure an UV-Vis spectrum with at least 0.5 - 1.5 abs. Save .BSW and .csv file. For pure compounds: Import UV-Vis spectra of pure *E* or *Z* isomer and set their NMR integrals to 99.99... % within the calculator. Import only baseline, isomer 1 and isomer 2, the isomer order can be changed with one click."

With the correctly measured data at hand, the next step consisted of manually importing the data (Wavelength / absorption,  $Z_{\text{meas.}}$  /  $E_{\text{meas.}}$ ) and the isomeric ratios measured via  $^1\text{H-NMR}$  spectroscopy ( $\%Z_{\text{NMR}}$  /  $\%E_{\text{NMR}}$  for both isomeric mixtures) into the first iteration of the calculational tool (see Figure 368).



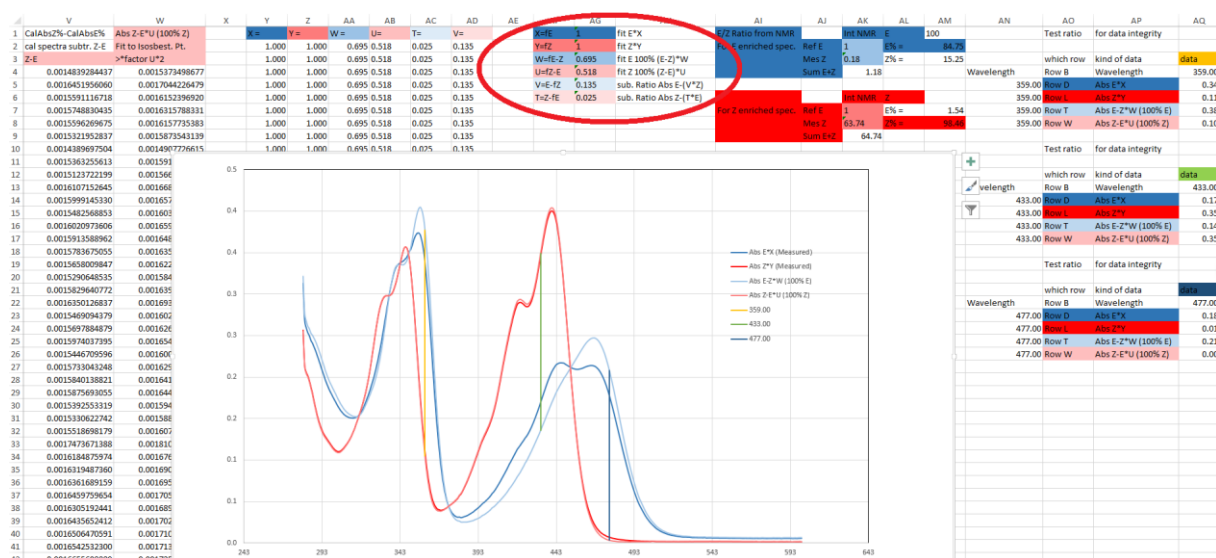


Figure 368: Screenshot of the spectra deconvolution *Excel* tool version 1.0 to obtain 100% *Z*- and *E* spectra from arbitrary mixtures. The red ellipsoid shows the three variable parameters for each *Z*- and *E* enriched isomer mixture. Vertical lines represent observation wavelengths to confirm the consistency of the calculated isomeric compositions from 359 nm to 477 nm, deviations below 1% were observed, which is dependent on the quality of data and the photochromism of the compound.

Adjusting the six parameters is done to obtain isosbestic points and thus correct 100% spectra by intuition, avoiding negative absorption values or unreasonable shapes. The three parameters consisted in:  $X / Y$  represent values which are multiplied with the respective measured absorption spectra ( $Z_{\text{meas.}} / E_{\text{meas.}}$ ) to roughly adjust for concentration differences,  $W / U$  represent values which are multiplied with  $(E_{\text{meas.}} \times \%E_{\text{NMR}} / 100 \times X - Z_{\text{meas.}} \times \%Z_{\text{NMR}} / 100 \times Y)$  or  $(Z_{\text{meas.}} \times \%Z_{\text{NMR}} / 100 \times Y - E_{\text{meas.}} \times \%E_{\text{NMR}} / 100 \times X)$  to adjust the magnitude of the spectra subtraction.  $V / T$  represent values which are multiplied with the previously obtained values to adjust the resulting data to the measured isosbestic points in concentration. This was done iteratively by hand to obtain reasonable spectra with already acceptable results as the calculated spectra represented the measurements in good agreement. This methodology could be seen as proof-of-concept that UV-Vis spectrum deconvolution is able to predict the pure spectra from two arbitrary mix spectra at arbitrary concentrations.

## 2.7.1 PHOTOPHYSICS - DEVELOPMENT OF AN “ALL-IN-ONE” CALCULATIONAL EXCEL TOOL - 100% Z / E SPECTRUM CALCULATOR

As this approach by trial and error was successful, a correct mathematical solution to this problem was implemented in version 2.0 of the calculational tool shown in Figure 369.

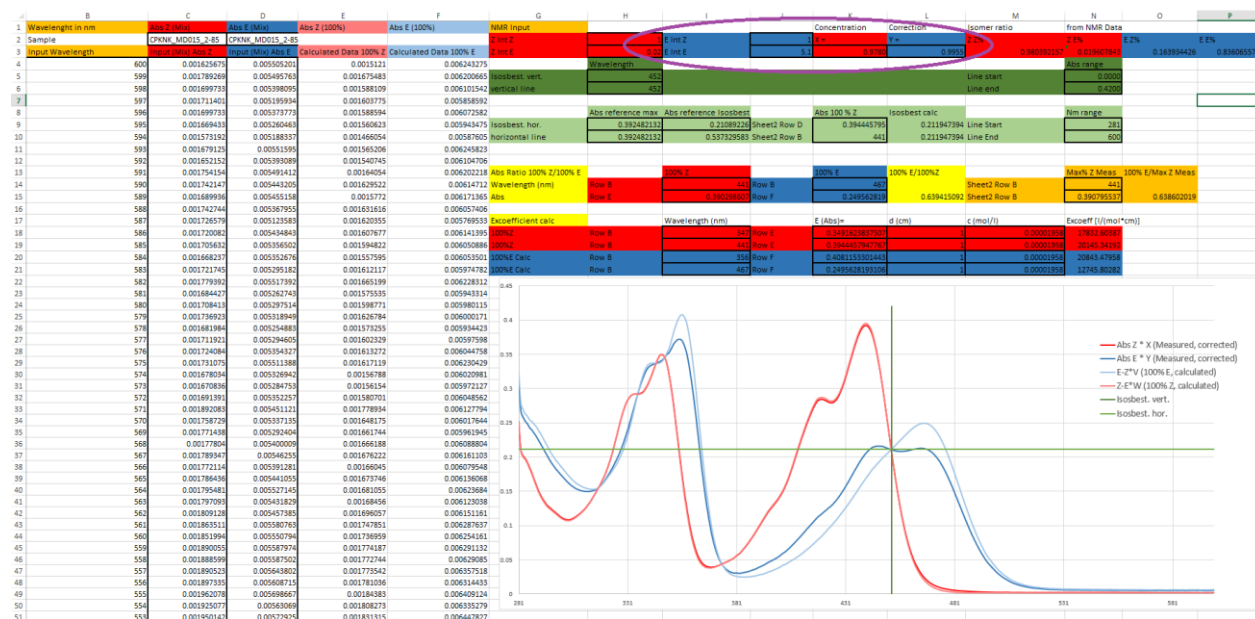


Figure 369: Screenshot of the spectra deconvolution *Excel* tool version 2.0 to obtain 100% Z- and E spectra from arbitrary mixtures. The violet ellipsoid shows that - besides the experimentally determined <sup>1</sup>H-NMR signal integral ratios of each isomer - only one variable parameter for each Z- and E enriched isomer mixture is needed to adjust for the respective measured concentration. The crosshair (green) marks the most red-shifted isosbestic point for concentration adjustment.

The second iteration of the calculational *Excel* tool shows similar results as version 1.0 without the time-consuming manual adjustments and the uncertainty of possible misalignments. The formulas for the Z / E isomer spectrum deconvolution employed by the calculator are shown in eq. 25 and eq. 26 below.

$$Z_{100\%} = \left( (Z_{\text{meas.}} \times X \times \frac{\%Z_{\text{NMR-Eenr.}}}{100}) - (E_{\text{meas.}} \times Y \times \frac{\%E_{\text{NMR-Zenr.}}}{100}) \right) \times \frac{1}{\left( \frac{1-(100-\%Z_{\text{NMR-Zenr.}})}{100} \right)} \quad \text{eq. 25}$$

$$E_{100\%} = \left( (E_{\text{meas.}} \times Y \times \frac{\%E_{\text{NMR-Eenr.}}}{100}) - (Z_{\text{meas.}} \times X \times \frac{\%Z_{\text{NMR-Eenr.}}}{100}) \right) \times \frac{1}{\left( \frac{1-(100-\%E_{\text{NMR-Eenr.}})}{100} \right)} \quad \text{eq. 26}$$

with Z / E<sub>100%</sub> being the deconvoluted 100% spectra values, Z / E<sub>meas.</sub> being the measured UV-Vis spectrum of the Z / E isomer, X / Y being the Z / E concentration factor and %Z<sub>NMR-Eenr.</sub>

being the e.g. percentage of *Z* isomer within the majorly *E* isomer enriched isomeric mixture determined via <sup>1</sup>H-NMR spectroscopy.

Rearrangement of eq. 25 and eq. 26 above initiated by A. Gerwien gave the following, tidied up mathematical description:

eq. 27 defines the spectrum *S* of the e.g. *E* isomer (*E*) as heaps of colligated numeric values:

$$S(E) = S(w_{E1,2,\dots}, a_{E1,2,\dots}) \quad \text{eq. 27}$$

with  $w_{E1}$  = wavelength 1 in nm as *x* value and  $a_{E1}$  = absorption 1 in a.u. as *y* value representing the absorption spectrum with eq. 28 and eq. 29 defining the measured *E* / *Z*-enriched mixture spectrum  $S_{mix}(E+/Z+)$  as a composite of pure *S*(*E*) and *S*(*Z*) spectra:

$$S_{mix}(E+) = S(E) \times f_1 + S(Z) \times f_2 \quad \text{eq. 28}$$

$$S_{mix}(Z+) = S(E) \times f_3 + S(Z) \times f_4 \quad \text{eq. 29}$$

with  $f_1, \dots$  being factors to account for the concentrations of each isomer in the mixture, which were determined by NMR measurements and the corresponding magnitudes of the absorption spectra. Solving the system of linear equations for *S*(*E*) and *S*(*Z*) results in eq. 30 / eq. 31:

$$S(E) = \frac{S_{mix}(Z+) \times f_2 - S_{mix}(E+) \times f_4}{f_2 \times f_3 - f_1 \times f_4} \quad \text{eq. 30}$$

$$S(Z) = \frac{S_{mix}(Z+) \times f_1 - S_{mix}(E+) \times f_3}{f_1 \times f_4 - f_2 \times f_3} \quad \text{eq. 31}$$

Factors  $f_1 - f_4$  were obtained from integrated indicative signals in the <sup>1</sup>H-NMR spectrum (percentage divided by 100) for the *E* or *Z* isomer in the *E* or *Z* enriched mixture according to the following matrix:

	<i>Z</i> isomer	<i>E</i> isomer
<i>Z</i> enriched mixture	$f_1$	$f_2$
<i>E</i> enriched mixture	$f_3$	$f_4$

The hereby determined spectra consist of 100% *E* isomer *S*(*E*) and 100% *Z* isomer *S*(*Z*), respectively.

## 2.7.1 PHOTOPHYSICS - DEVELOPMENT OF AN “ALL-IN-ONE” CALCULATIONAL EXCEL TOOL - 100% Z / E SPECTRUM CALCULATOR

To date, version 5.2 was released which utilizes only a few experimentally determined input parameters and automatically extracts spectrum data directly from the .csv output files of the *Varian Cary 5000* UV-Vis spectrophotometer software (see Figure 370). The only manual input parameter concerning the calculation is the observer wavelength, which should be chosen within an area of large UV-Vis spectral changes for the best signal-to-noise ratio of the processed data.

	A	B	C	D	E
1	Sample Name and Solvent:	CP348	87 /13 Heptane / Ethyl acetate		
2	Set Wavelength of Isosbestic point with largest red shift:	Isosbest. Pt. Wavelength:	456		<= Black outlined boxes = Edit or set v
3	Median Absorption is determined automatically:	Isosbest. Pt. Absorption:	0.228279023		DO NOT edit other boxes!
4	Desired Wavelength for % Determination (nm, global!)		492	= choose a value with huge differences between 100%Z and 100%E	
5	Determination of Concentration:	Weight from ExCo (mg)	0.8388		Spectra look strange? Delete the crap
6		Volume (mL)	50.0000		
7		Path length (cm)	1.0000		
8		Mol. Wt. (g/mol)	432.57		
9		c (mol/L)	3.87822E-05		
10	Determination of Composition via NMR:	Z enriched Integral of Z	99999	E enriched Integral of Z	1
11		Z enriched Integral of E	1.0000	E enriched Integral of E	99999.0000
12	Percentages (check):	Z Z%	99.999	E E%	99.999
13	Three UV-Vis NMR Headers:	Baseline 100%T			
14	Is this NMR coupled UV-Vis spectrum Z? (check for yes)	CD 3. ExE1	<input type="checkbox"/> Check Box 8		
15		CD 4. ExZ2		Best PSS @ Wavelengths:	
16		Max E:	83.23553566	PSS 1. 3s irr435nm	
17	PSS Calculation:	Max Z:	1.991503001	PSS 4. 1min irr530nm	
18	Copy Descriptor:	Baseline 100%T	PSS 1. 3s irr435nm	PSS 2. 30s irr505nm	PSS 3. 1min irr515nm
19	Copy Absorption:	0.215082487	0.22810528	0.041016266	0.034498736
20	Calculated PSS (in %E)	78.24923649	83.23553566	11.60099739	9.105499324

Figure 370: Screenshot of the spectra deconvolution *Excel* tool version 5.2 to obtain 100% Z- and E spectra from arbitrary mixtures. The violet ellipsoid shows that only a suitable observer wavelength needs to be set. The other parameters are needed for the calculation of molar absorption spectra and quantum yield determination, which are shown in sections 2.2.21 and 2.7.2.

The example in Figure 370 utilized pure, thermally stable isomers of hemiindigo **33** which were baseline separated via HPLC, no NMR measurements were needed to determine the isomeric ratios, which is why they were set to the respective 100% values. As the calculational *Excel* tool was expanded to be more versatile, a major part of the analysis and quantification of photophysical data could be carried out with it. This is the reason for using this tool even on pure compounds, as data importing, plotting and evaluation is done automatically and consistently, which is elaborated in Section 2.7.2 below.

Additionally, a web-based version of this tool was written in *javascript* by *Y. Ruppenthal* which is functional but still unfinished to date. Further efforts to implement photophysical analysis tools and input compatibility regarding different layouts of spectrometer output data need to be made to reach its full potential. Also, a detailed set of tooltips must be implemented for the ease of usage.

### Photophysikalischer-Rechner charts

1. NMR-Data?

A: Plot 1 ■
B: Plot 2 ■

Name

Stoff 1 Stoff 2

10.65% 89.34%

**Settings**

Stoff 1

Stoff 2

Weight (mg)

Volume (ml)

Path length (cm)

Mol. Wt. (g/mol)

c (mol/L)

2. ExCo-Data

Figure 371: Input page of the online based deconvolution tool by *Y. Ruppenthal*. The same functionality as the excel tool was achieved within this version.

## 2.7.2 Photophysics - Development of an “all-in-one” calculational Excel tool - Photophysical data evaluation

With the previously described deconvolution tool at hand, a precise determination of isomeric compositions for two interconverting compounds can be made at all times during an UV-Vis measurement course. This does not only save large amounts of compound but also irradiation- and measurement time as only a comparably small number of molecules need to be irradiated for a detectable shift in isomer composition. Additionally, UV-Vis spectroscopy is a rather fast and cheap measurement technique compared to NMR spectroscopy and can be utilized in online quantum yield measurements if a suitable setup is provided.

These features make PSS determinations, thermal kinetic measurements and quantum yield measurements fast, convenient and reproducible while wasting only little amounts of compounds and expensive deuterated solvents. The mathematical and physical formulas implemented within the calculator are given in Sections 2.2.20/2.2.21/2.7.1.

Examples of a UV-Vis equilibrium kinetic and a photoquantum yield measurement are shown in Figure 372 and Figure 373 below.

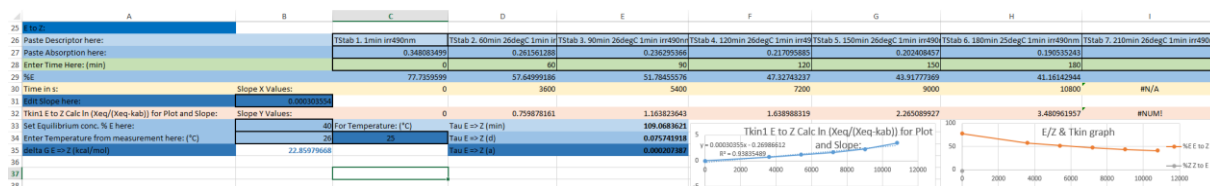


Figure 372: Kinetic analysis of the *E* to *Z* thermal isomerization of hemiindigo **8** in tetrahydrofuran measured at 26 °C over 180 minutes within the calculational Excel tool version 5.2.

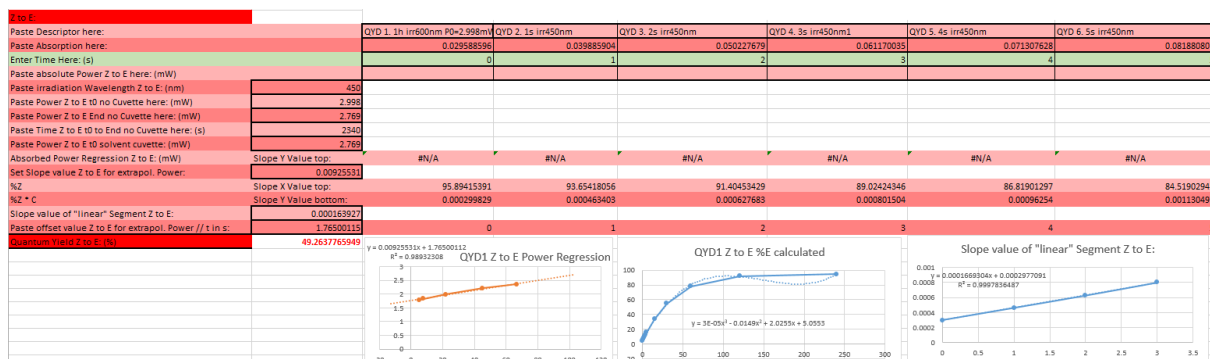


Figure 373: Photoquantum yield analysis of the *Z* to *E* photoisomerization of hemiindigo **20** in 83 / 17 heptane / ethyl acetate within the calculational Excel tool version 5.2.

If the suggested order of measurements is followed, all obtained data can be directly imported into the tool and results are calculated immediately with a minimal amount of manual input and adjustment.

The following sections of the guide provided with the calculational tool concern the required procedures for setting up photophysical measurements and read as following (continued from Section 2.7.1, updated):

### **“3.) PSS measurements:**

Copy the ExCo.BSW file, save it as “XX123\_SOLVENT\_PSS.BSW”, delete everything except the baseline, t0 and the two PSS spectra measured beforehand and rename them to “PSS 1. t0, PSS 2. XXXs irrXXXnm”, “PSS 3. XXXs irrXXXnm” etc. Sweep through all desired wavelengths and record the spectra assigning order of measurement, time and wavelength to each spectrum. Try to switch large amounts of *E* to *Z* or *Z* to *E*, take into account that the LEDs have optical powers ranging from 22 to 260 mW. Possibly low extinctions of your compound in the red part of the visible spectrum will call for irradiation times up to several hours or days. Save .BSW and .csv file.

### **4.) Thermal stability measurements of *Z* and *E* Isomers:**

Open a suitable method and record a baseline, measure your compound (0.5 - 1.5 abs), name the file “XX123\_SOLVENT\_Tkin1.BSW” and the first spectrum Tkin1 0. t0. Irradiate your compound to max. *E* or max. *Z* PSS, measure it and name your spectrum accordingly. Bring your cuvette to your desired constant temperature and measure UV-Vis spectra in reasonable time increments and indicate time and temperature in your spectra, e.g. “Tkin1 2. XXmin XX°C”. Type in absolute times, for 10 min increments type 0min, 10min, 20min etc. (don’t use “.” or “,”, it will mess up the import in excel!). Try to heat until you reach the equilibrium if applicable. Do the same for the other isomer, this can be done in the same file (max. 27 spectra), use continuous numbering. Save the .BSW and .csv file.

### **5.) Quantum Yield measurements:**

Get an instruction on how to set up the QYDS optics correctly and/or read the manual. Install the desired LED to the X/Y translation stage, let the fan blow onto the heatsink and open the case to some extent. Tilt the photometer slightly so that reflections will not enter the cuvette. Open the PowerMax software, choose the proper Powermeter device, press “start data collection”, zero the sensor in absolute darkness and set your desired wavelength in the software (does not make a observable difference). Use a reasonable  $P_0$  power value, depending on your absorption and estimated switching speed / quantum yield guess. Leave the LED to equilibrate for 10-30 min until you reach a standard deviation of about 4  $\mu$ W and write down this  $P_0$  power (mean value) and the absolute time e.g. “ $P_{0start}=4.523$  mW,  $\pm 4$  mW, 13:37”. Open a suitable method file at the UV-Vis device and measure a baseline with pure solvent. Put your solvent-filled cuvette in the QYDS and write down the  $P_{solv}$  power value. Proceed in absolute darkness from now on. Clean and dry the cuvette, add exactly 2.5 mL (or any defined volume from 1.5 to 3.0 mL) of your compound solution and a small magnetic stirring bar to your cuvette and put the cuvette lid on. Measure your sample (0.5 - 1.5 absorption), create the file “XX123\_SOLVENT\_QYD1.BSW” and name your spectrum “QYD1 1. t0”. Skip irradiation to the max. PSS if you have a pure compound. Put a piece of cardboard in the beam path of the QYDS in front of the cuvette. Sync yourself with a clock and remove the cardboard for 1s as fast as possible and put it back on. Measure UV-Vis without exposing the sample to room- or sunlight. Name your spectrum e.g. “QYD1 3. 1s irr467nm”. Repeat  $\sim 5$  times with 1s increments to get E/Z ratios for 1, 2, 3, 4 and 5s of

irradiation. Raise the time increment to 10s (15s total) and measure another UV-Vis spectrum. Raise the increment to 15s (30s total) and write down the power as close to the 15s mark as possible, e.g. "QYD1 9. 30s irr467nm P=4.232 mW, P0=4.492 mW", repeat with total times of 60, 120, 240s, 480s... not necessarily to the PSS, but accurate power readings at the end of each point are crucial. Remove the cuvette when finished, write down the  $P_0$  value and the absolute time, e.g. 14:07. Irradiate to the max. PSS consisting of the other isomer, change the LED in the QYDS and set it up properly (thermal equilibration of LED,  $P_0$  value at absolute time). Measure UV-Vis at the  $t_0$  value after irradiation in the same file and use continuous numbering (max. 27 spectra per file). Start with 5x 1s increments as in the previous measurement and proceed similarly. Take out the cuvette, write down the  $P_0$  value and the absolute time, empty the cuvette, clean it and fill it with pure solvent to measure  $P_{\text{soliv}}$  for the recent power and wavelength. Save the .BSW and .csv file.

## 6.) Calculations:

Set Excel to use "." as decimal separator in File > Options > Advanced. Import your raw data to the "Import ExCo/NMR/PSS/Tkin1/Tkin2/QYD1/QYD2" sheets in the calculator with "," as delimiter between columns. Go to the "Spectra" sheet to overview your raw data. If something seems wrong: Delete the text the UV-Vis software creates at the end of the data values, check if every set of columns starts with the same wavelength, e.g. 800 nm. If not, delete your data in the Import Sheet, open a new file in excel, import your data there and sort it properly. DO NOT SHIFT CELLS IN THE IMPORT SHEET, the calculator file will be useless afterwards. Zoom into your ExCo measurement and pick the wavelength at the most red-shifted isosbestic point, enter it in the first box (only natural digits), cross-check if the averaged absorption value matches the ExCo spectra. Every value in a black outlined box has to be entered or set by the user, do not change anything else! Set a wavelength at which all determinations will be carried out throughout the whole calculator, best done on the right side to the most red-shifted isosbestic point with large absorption changes. Enter mass, volume, cuvette path length and molecular weight.

### 6.1.) Calculated 100% Z and 100% E spectra: (boundaries for all other calculations)

Open your NMR spectra from the correlated UV-Vis - NMR measurements and enter your integrals for Z and E in the Z enriched spectrum and for Z and E in the E enriched spectrum. Look at the second of the three UV-Vis headers below and decide if this UV-Vis spectrum represents the Z enriched spectrum or not. Check the box if yes, uncheck if not. Go to the Spectra Sheet and look at the first graph for 100% Z and E spectra. Z should be red and on the left side, E blue and on the right side.

Troubleshoot: Do the extinctions make sense? If not: Are NMR integrals assigned correctly? Integration of other NMR signals? (Baseline and Phase correction? Solvent peak on reference for both spectra?) Check or uncheck the Check Box, parasitic irradiation from room lighting? Thermal isomerization in the time between UV-Vis and NMR measurement? Are the UV-Vis spectra of the right compound? Correct mass/volume/molecular weight in case of odd values for the molar absorption? If everything is alright, proceed to PSS calculation.

### 6.2.) PSS value determination:

Set the range of Max E and Max Z to valid values, the highest and lowest PSS value in %E should be shown and at which wavelength they occur. All other PSS values can be read from the table.

Troubleshoot: Negative or values over 100% indicate measurements close to the calculated boundaries. This indicates thermal/irradiative back isomerization within the NMR/UV-Vis correlation measurement or other issues as stated above. The automatic scaling process can create overshoot in these regions within ~1 - 2% or due to little photo destruction.



### 6.3.) Thermal stability determination:

Pull a rectangle around the extracted data in the UV-Vis Tkin section and paste one series of coherent measurements starting from  $t_0 = 0s$  in the black outlined boxes below according to  $E$  to  $Z$  or  $Z$  to  $E$  direction of isomerization. Read the times from the descriptors and enter them in minutes below. Double click the “Edit Slope here” box and choose all valid values except for the last ones in the series and hit enter. The slope should match the slope in the first graph. Double click “Set equilibrium conc. % $E$  here” and choose the last  $E\%$  value and hit enter. Set the temperature of your measurement in the box below. The thermal barrier can be read out in the last box and half-lives can be set for desired temperatures on the right. Repeat for the other isomerization direction and Tkin2 if applicable. NMR Integrals can be entered in the NMR Tkin section, the procedure stays the same.

Troubleshoot: The first graph should be a perfectly straight line. Curvature? Equilibrium not reached! If done correctly for  $E$  to  $Z$  and  $Z$  to  $E$  isomerization, the second graph should show both kinetics stopping at the same  $E$  to  $Z$  ratio, only then the true equilibrium was reached.

First order kinetics without equilibrium? No problem, the last point of the measurement gets discarded in comparison to the “normal” first order kinetics formula, the rest stays the same.

### 6.4.) Quantum yield determination:

QYD Section: Check if the automatic concentration adjustment makes sense “Conc. Factor (test):” for the same solution as the ExCo measurement it should be around “1”. Draw a rectangle around the extracted data in the QYD section and paste one series of coherent measurements starting from  $t_0 = 0s$  in the black outlined boxes below according to  $E$  to  $Z$  or  $Z$  to  $E$  direction of QY measurement. Read the time values from the descriptors and enter them in minutes below, do the same for power values. Enter volume, irradiation wavelength,  $P_{0start}$ ,  $P_{0end}$  and the time between these points from your absolute time values here. Enter  $P_{solv}$  below. Double click the “Set Slope value for extrapol. power” box and choose all valid values in the series and hit enter. The slope should match the slope in the first graph. Paste the read-out for the Y-Intercept from the first graph in the “Paste offset value for extrapol. Power” box. This will calculate the absorbed power of the sample at point  $t_0$  before the actual absorption of any light. Set the second slope to 0, 1s, 2s ... or more / less ((in)valid, “linear”) values, the quantum yield for the isomerization is shown below. Repeat for the other quantum yield measurements.

Troubleshoot: Too fast / too slow measurement? Too much / little power? Bad signal-to-noise ratio towards background / sample signal? Thermal LED drift taken into account correctly (times, values)? Everything done in darkness? Good 1s increment measurements? LED mounted and cooled correctly (no Tape etc., fan switched on? Case opened slightly)? Screw of the sample holder not within the beam path? Stirrer switched on? Powermeter tilted / equilibrated / zeroed / mean values used if possible? All parts of the assembly screwed to the breadboard? Feasible concentrations?

Happy measuring!”

With these suggestions taken into account, quantum yield- and other photophysical measurements can be conveniently carried out mainly via UV-Vis spectroscopy.

### 2.7.3 Photophysics - Building of an inexpensive quantum yield determination setup

A low-cost version of the published instrumental setup from the group of *E. Riedle* (see Section 2.2.23) was built as a prototype with the goal of cancelling thermal LED fluctuations to give accurate readings for the absorbed light energy.<sup>[98]</sup> The detection of light flux was done via photovoltaic diodes as suggested by *R. Wilcken*. The photovoltaic diodes scale the incident light power with their output current in a linear fashion. A simple transimpedance amplifier is able to convert the generated current into a linearly dependant voltage output. After calibration to an accurate thermal powermeter, the photodiode is able to translate the measured voltage into photon counts, which - besides reaction progress - is a key parameter to determine quantum efficiency.

The usage of LEDs as irradiation sources poses several (dis-) advantages. On one hand, LEDs are lightweight, cheap, relatively powerful, simple to use and easy to cool. On the other hand, they normally do not emit monochromatic light but wavelength distributions, which can complicate measurements. Furthermore, increasing heatsink temperatures decrease their light output gradually within a measurement, which leads to significantly false readouts. As a solution to this problem, the low-cost quantum yield determination prototype supports two photodiodes as detectors. The incident light path is split by a stack of several glass microscopic slides at a  $\sim 45^\circ$  angle before the sample. One of the two light rays is directed to the calibrated photovoltaic diode (reference diode) while the other light ray is sent towards the sample. The second calibrated photodiode (measurement diode) is located behind the sample and detects the absorbed power differentially towards the reference diode (see Figure 374). An *Arduino* microcontroller is used for data collection, calibration and calculation. The analog 10-bit inputs were used to detect the amplified output voltages between 0 V and 5 V, to compare them to changes at the reference photodiode and to calculate the absorbed power value  $P$  of the sample in mW at time  $t$ . Even significant short drops in LED light intensity do not affect the graph of the photokinetic as the absorbed power values are always relative to the reference power. Prolonged reduction of the light source intensity will slow down the progress of the photoreaction. This can also be compensated by tracking the changing power values of the reference photodiode as the physical property of quantum yield already implies a linear relationship of light intensity to reacted molecules, e.g. a quantum yield of 20% translates to 5 necessary photons to transform one starting molecule to one product molecule.

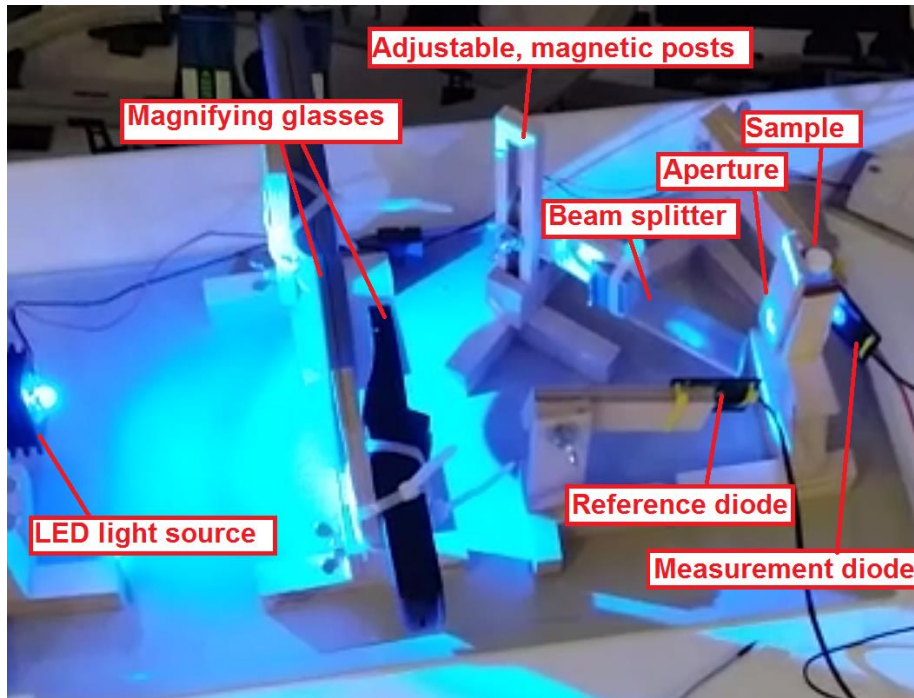


Figure 374: Low-cost quantum yield measurement prototype with differential read-out of absorbed power. The LED light is focused with two magnifying glasses onto a beam splitter made out of a stack of microscopy plates. One part of the light beam is measured with a calibrated reference diode, the other part of the beam is sent through the sample. The calibrated measurement diode reports the remaining light power which was not absorbed by the sample. The *Arduino* microcontroller subtracts the power values of the measurement diode from the reference diode, giving accurate absorbed power values even upon LED power fluctuations.

The parts for the device shown in Figure 374 were obtained for roughly 50 €, the *Coherent* thermal powermeter of the *Riedle* setup prices at roughly 1000 - 1500 € without optics, holders, light sources, computer hardware and software. The plywood holders are fixated on a scrap metal plate with three strong neodymium magnets each, making adjustments easy without easily shifting them by accident. Two transimpedance amplifiers convert the output current of the photodiodes into a linear voltage with an adjustable 0 V to 5 V output range that can be processed and quantized by the analog inputs of the *Arduino* microcontroller.

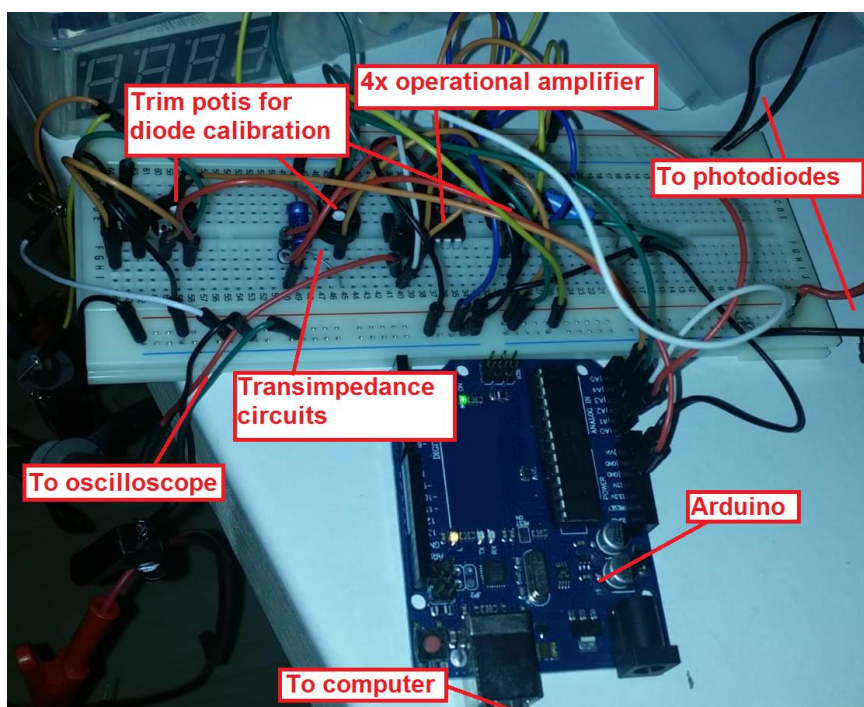


Figure 375: Circuit board and Arduino microcontroller of the inexpensive quantum yield determination setup. The current of the photodiodes is linearly converted into voltage and amplified utilizing two of the four operational amplifiers of the integrated circuit (IC) chip (MCP6004-I/P PDIP-14) wired as transimpedance amplifier. The amplification factor is adjusted individually for each photodiode by a trimmer potentiometer. A third trimmer potentiometer is used to normalize reference- and measurement photodiode when no sample is placed within the beam path prior to measurement. The *Arduino* microcontroller converts the measured voltage differences into light power according to a previously determined calibration curve and plots the absorbed power versus time on a computer screen for data acquisition.

One major drawback of this prototype are the 10-bit analog inputs of the *Arduino* microcontroller, which allow for analog to digital conversion of a 0 V to 5 V input voltage into values from 0 to 1023. The usage of 16- or 24 bit analog to digital converters should be considered as they will drastically improve signal resolution by dividing the 5 V measurement range into  $6.55 \times 10^4$  or  $1.68 \times 10^7$  steps, respectively. The code for the *Arduino* is shown below in Figure 376. Also, specialized quartz optics can be implemented to transmit light within the UV range. A magnetic stirrer was not yet implemented as it was not required for the proof-of-concept. Auto samplers for cuvette- or LED changes could also be implemented for further automatization.

```

#include <SoftwareSerial.h>
float refPin = 0;
float measPin = 1;
float refValue;
float refValue2;
float measValue;
float measValue2;
float diffValue;
float offsetPin = 2;
float gainPin = 3;
float gainValue;
float gainValue2;
float offsetValue;
float offsetValue2;

void setup() {
  Serial.begin(9600);
  delay(500);
}

void loop() {
  refValue = analogRead(refPin);
  measValue = analogRead(measPin);
  offsetValue = analogRead(offsetPin);
  offsetValue2 = (offsetValue/100)-5;
  gainValue = analogRead(gainPin);
  gainValue2 = 805+(825*(gainValue/25000));
  refValue2 = (refValue/gainValue)*(4/2.25)*5.103;
  measValue2 = (measValue/gainValue*5.103);
  diffValue = ((measValue2+offsetValue2)-refValue2);

  Serial.print(diffValue, DEC);
  Serial.println(" mW");
  delay(250);
}

```

**Figure 376:** Programming of the *Arduino* microcontroller in *C++* to measure the absorbed power of the sample with respect to the reference photodiode.

Additionally, a methodology for processing the obtained power data was developed in *Excel*, as it was found out that absorbed power and isomeric composition (e.g. in percent) give a linear correlation (most of the time) when plotted against each other, see Section 2.2.21. This makes it possible to record the entire photokinetic without obtaining more than two data points via UV-Vis (in theory). Additionally, the actual absorbed power values are given incidentally, allowing to fully automate quantum yield measurements by this methodology in the future. The novel calculator is not shown in this work as further experiments need to be carried out to test the robustness of its automatic output.

## 2.7.4 Photophysics - Building of an alternating irradiation device

To address the photofatigue of photoswitchable compounds, an automated alternating irradiation device was built to obtain data of almost arbitrary counts of photoswitching cycles. An *Arduino* microcontroller was used to control a relay board in order to switch the potentially high currents of the LED power supply. Two suitable LED wavelengths were set up into a homemade LED and cuvette holder with cooling fan. After calibration of the ideal irradiation times (e.g. reaching the PSS composition of a specific irradiation wavelength) for each LED, prolonged irradiation cycles can be run by measuring UV-Vis spectra at defined time intervals. Dividing the total elapsed time by the time needed for one cycle results in the total amount of switching cycles. The results for photoswitching of hemiindigo **8** can be seen in Section 2.2.5 and for switching of electronic circular dichroism of hemiindigo **33** in Section 2.3.8. Pictures of the setup are depicted in Figure 377 and Figure 378.

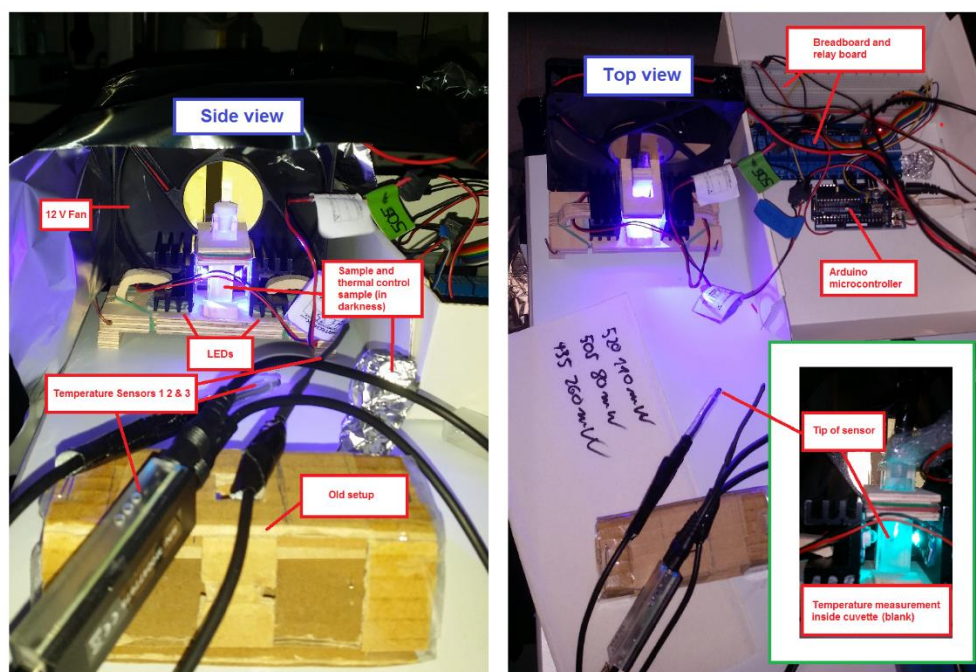


Figure 377: Improved setup for sample cooling during alternating irradiation experiments. During irradiation it was ensured that air gaps between LEDs and cuvette were present for effective fan-cooling (see Figure 377, top left corner). Direct temperature measurements inside a water filled cuvette determined temperature deviations of up to 1.23 °C during irradiation cycles in a control experiment (see inset in the right picture).

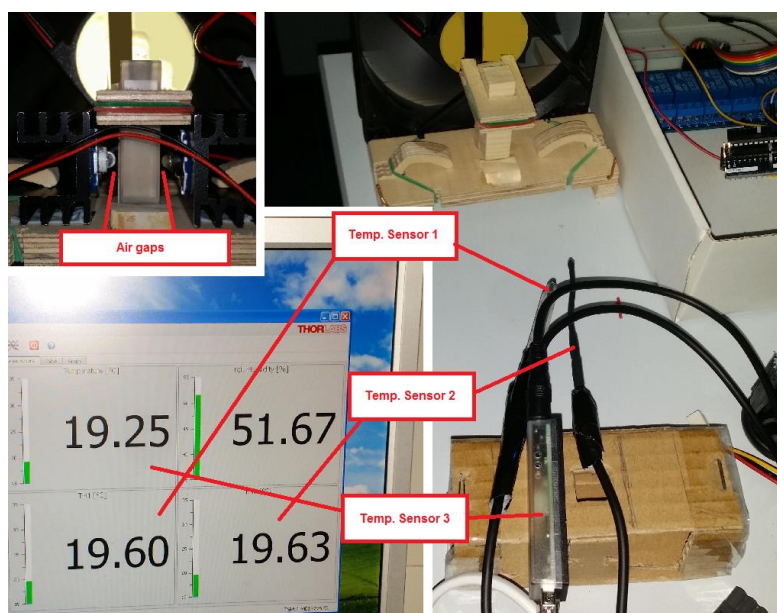


Figure 378: Depiction of the air gap between LEDs and sample (top left corner) and calibration of the different temperature sensors 1 to 3 within the air stream of the fan. The respective temperature deviations between the different sensors are very small. The surrounding room was not yet cooled to 18 °C at this time of measurement.

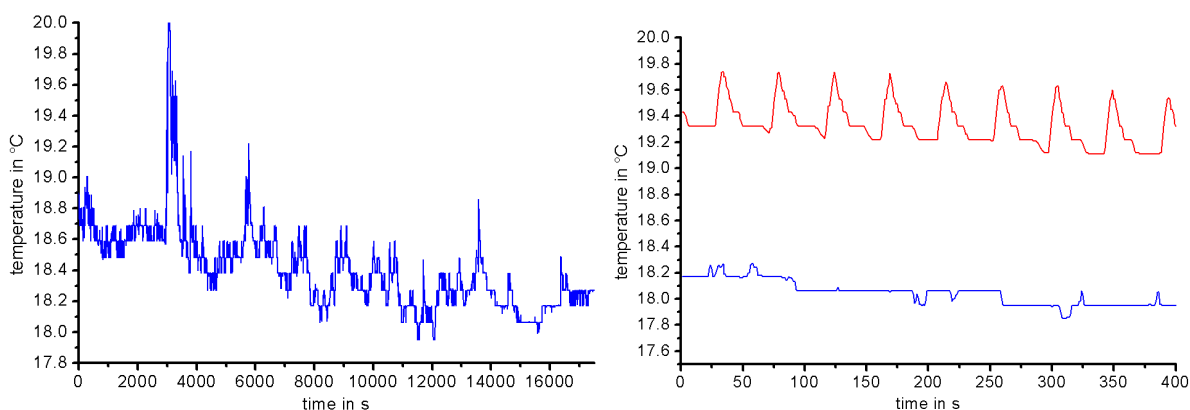


Figure 379: Monitored temperature of the surrounding air during 160 cycles of alternating irradiations of hemiindigo **33** (left). Spikes represent warming of the air stream during manual sample handling. Temperature difference (right) between the inside of the cuvette (red) and the surrounding room temperature (blue) measured for a water-filled cuvette during 9 cycles of alternating irradiations. On average, a 1.23 °C temperature difference was observed between irradiations for 7 s at 435 nm and 260 mW output power and 38 s at 505 nm and 80 mW output power. Spikes correspond to the flashing of the 435 nm LED, which dissipates more heat.



### 2.7.5 Photophysics - Building of a cuvette holder for cryogenic ECD measurements

Low temperature UV-Vis and ECD spectroscopy requires specialized equipment to avoid the condensation of water within the surrounding air. Because of the size of a cryogenic cuvette (cryostat), several problems arise when attempting to mount these devices within spectrophotometers. For UV-Vis spectroscopy, a sufficiently sized light path within the sample chamber and some height- and rotational adjustability is required. Adjustments can be made by dialing in the cuvette(s) position and minimizing the absorbance of a solvent filled cuvette as baseline priorly to the measurement of the sample itself. With ECD spectroscopy, however, differences in the angles of glass surfaces within the light path distort the circularly polarized light and add unwanted ellipticity as systematic error. This can be dialed in by minimizing the absorptivity as well for the solvent filled cuvette without sample. Nonetheless, without a proper cuvette holder and rigidity in the setup, sample change will relocate the cryostat, losing the adjusted positioning. Adjusting the cuvettes(s) anew with the sample in the light path is prone to give different results compared to the baseline measurement.

If *in-situ* irradiation by light is required, the attachment of LEDs within the spectrometer can also pose as a challenge due to the already limited space. This requires removing the cryostat from the spectrophotometer and losing the positioning again. As these drawbacks will add undefinable systematic errors, especially when only small signal changes need to be recorded, a homemade cuvette holder for an *Oxford Optistat DN* cryostat within a *Jasco J-810* ECD spectrometer was built from plywood (Figure 380). The cryostat and the aluminium mounting bracket were kindly supplied by the groups of *A. Ofial* and *H. Mayr*. This setup allows for rigid fastening of the aluminium holder with X / Y translation stage inside the sample chamber, which allows for removal and reinsertion of the cryostat without losing of the positioning. Also, repeatable adjustments in seven axes can be made towards a minimized absorptivity of the solvent filled cuvette for baseline measurement and positional calibration.

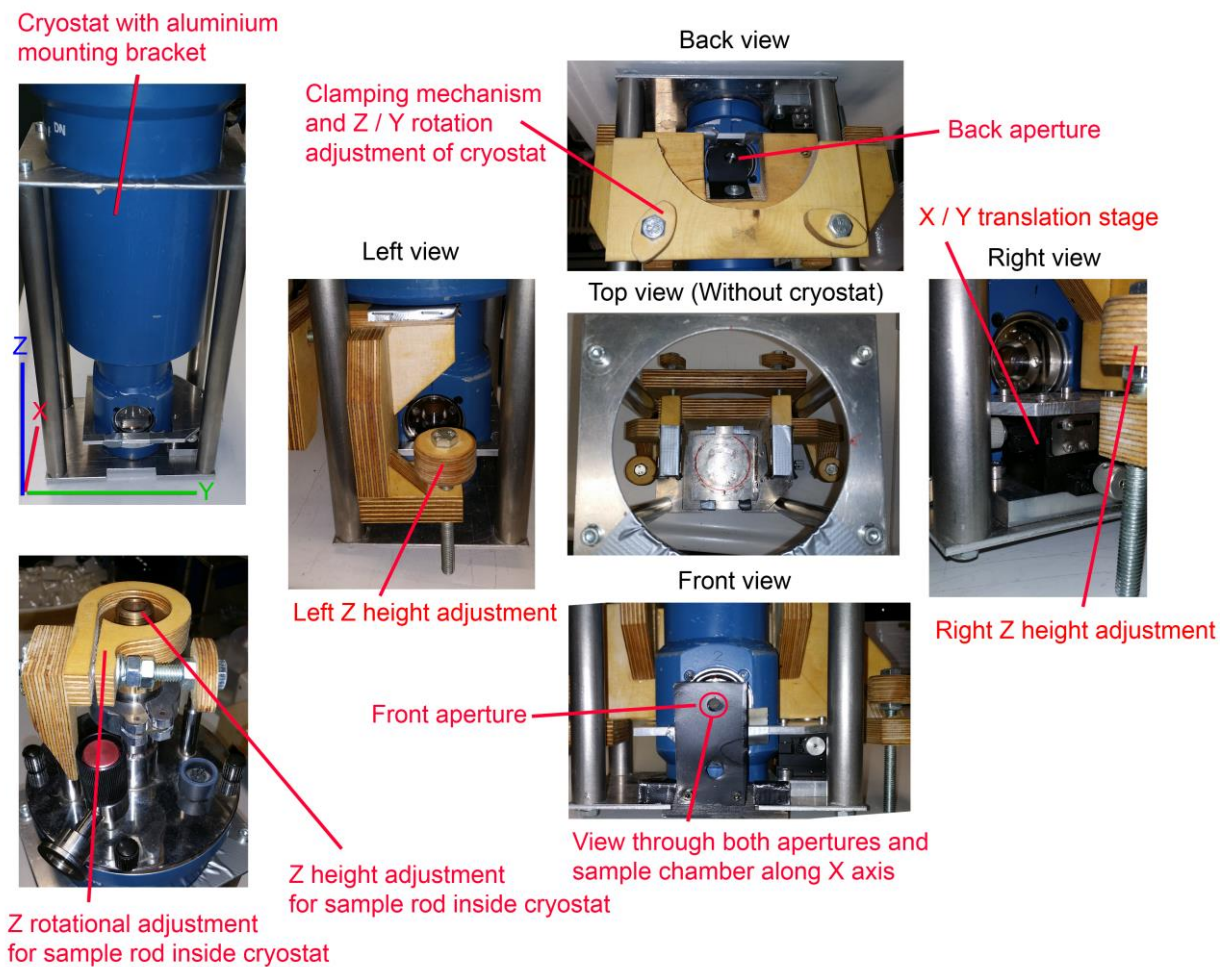


Figure 380: Different views of the homemade plywood cryostat mounting bracket outside the ECD spectrometer. The cryostat can be adjusted within five dimensions and the cuvette holder within the sample chamber can be moved in two dimensions.

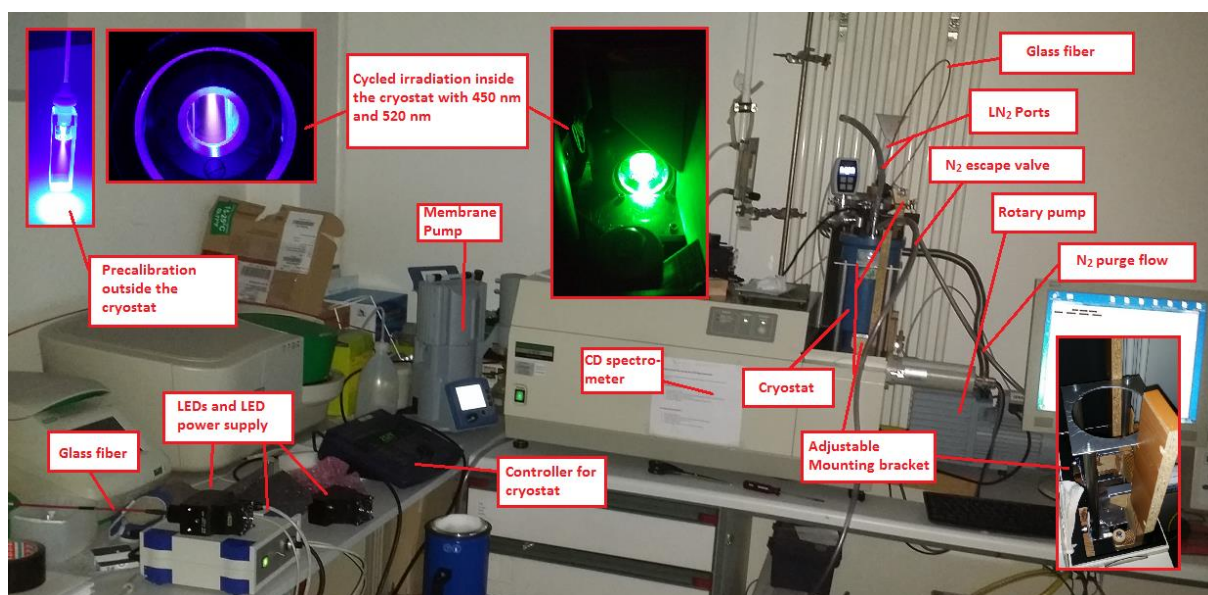


Figure 381: Instrumental setup used for repetitive ECD measurements in-between alternating irradiations of the  $(R_a)$ -**30** isomer at  $-20$  °C using an *Oxford instruments Optistat DN* cryostat. A rotary pump maintains a vacuum of  $3 \times 10^{-3}$  mbar for the isolation chamber of the cryostat to increase its operation time. The temperature controller was set to 253.2 K and maintained the temperature by successive heating pulses. A membrane pump is utilized for secondary control of temperature by regulating the exiting  $N_2$  gas stream and hence the coolant flow ( $LN_2$ ) respectively. Alternating irradiation inside the cryostat is realized by using two glass fiber-coupled LEDs, which can be exchanged at one end of the fiber without disturbing the sensitive setup (10 s 450 nm at 193 mW and 60 s 520 nm at 92 mW irradiations were used for each cycle). A home-made mounting bracket was used to ensure reproducible cryostat and sample holder alignments for each mechanical change in the setup (i.e. sample exchange for baseline measurements) as circularly polarized light gradually changes ellipticity if its beam is not passed through the cuvette windows perpendicularly.

The successfully obtained ECD data of hemiindigo **30** during cyclic switching experiments are depicted in Section 2.3.8.

## 2.7.6 Conclusion: Photophysics

The developed “all-in-one” *Excel* tool proved as a success as repetitive measurements of different photoswitches in various solvents require a robust and repeatable methodology to compare obtained datasets. Its ease of use and time- / compound savings for the required (photo) physical measurements (Molar absorptivity, PSS determination, thermal kinetics and quantum yield determination) was a major help in processing the acquired data via UV-Vis- and NMR spectroscopy.

The construction of a low-budget quantum yield measurement device with differential detection setup was a success and showed that even cheap components can be used for this kind of measurements as photodiodes are very sensitive towards minimal changes of light intensity and output a corresponding current in a linear fashion. Further improvements of the quantum yield measurement data processing are in preparation to date.

To consistently test the photofatigue of photoswitches, repeated cyclic measurements were set up by successfully building an alternating LED irradiation device controlled via a microcontroller. This allows for virtually infinite of switching cycles to be run, giving reliable degradation kinetics.

As ECD measurements are quite susceptible to angle changes of the cuvette(s) within the beam path of the circularly polarized light, a cryostat mount was built that allowed for adjustment in seven axes including removal and reinsertion of the cryostat / sample cuvette into the spectrometer without losing its positioning. Successful repeated ECD measurements proved the rigidity and usability of this setup.

- [98] U. Megerle, R. Lechner, B. König, E. Riedle, *Laboratory apparatus for the accurate, facile and rapid determination of visible light photoreaction quantum yields*, *Photochem Photobiol Sci* **2010**, 9, 1400.

### **3 EXPERIMENTAL SECTION**

The characterized compounds are sorted by reaction type. Synthetic schemes can be found within the respective “Results and discussion” sections.

### 3.1 General experimental

**Reagents and solvents** were obtained from *Acros*, *Aldrich*, *Fluka*, *Fluorochem*, *Merck*, or *Sigma-Aldrich* in the qualities *puriss.*, *p.a.*, or *purum* and used as received. Technical solvents were distilled before use for column chromatography and extraction on a rotary evaporator (*Vacuubrand CVC 3000*). Reactions were monitored on *Merck Silica 60 F<sub>254</sub>* or Aluminium(III) oxide 60 F<sub>254</sub> neutral TLC plates. Detection was done by irradiation with UV light (254 nm or 366 nm).

**Column chromatography** was performed with silica gel 60 (*Merck*, particle size 0.063 - 0.200 mm) or aluminium(III) oxide (*Sigma-Aldrich*, pore size 58 Å, *Brockmann III*, 6% water, w / w) and distilled technical solvents.

**<sup>1</sup>H-NMR and <sup>13</sup>C-NMR spectra** were measured on a *Varian Mercury 200 VX*, *Varian 300*, *Inova 400*, *Varian 600 NMR*, or *Bruker Avance III HD 800 MHz* spectrometer. Chemical shifts ( $\delta$ ) are given relative to tetramethylsilane as external standard. Deuterated solvents were obtained from *Cambridge Isotope Laboratories* and used without further purification. Residual solvent signals in the <sup>1</sup>H and <sup>13</sup>C-NMR spectra were used as internal reference: For <sup>1</sup>H-NMR: CD<sub>2</sub>Cl<sub>2</sub> = 5.32 ppm, CDCl<sub>3</sub> = 7.26 ppm, CD<sub>2</sub>Cl<sub>2</sub> = 5.32 ppm, toluene-*d*<sub>8</sub> = 2.08 ppm, cyclohexane-*d*<sub>12</sub> = 1.38 ppm, (CD<sub>3</sub>)<sub>2</sub>SO = 2.50 ppm, CD<sub>3</sub>CN = 1.94 ppm, THF-*d*<sub>8</sub> = 1.72, 3.58 ppm. For <sup>13</sup>C-NMR: CD<sub>2</sub>Cl<sub>2</sub> = 53.84 ppm. CDCl<sub>3</sub> = 77.16 ppm, CD<sub>2</sub>Cl<sub>2</sub> = 53.84 ppm, toluene-*d*<sub>8</sub> = 20.43, cyclohexane-*d*<sub>12</sub> = 26.43 ppm, CD<sub>3</sub>CN = 118.26, 1.32 ppm, THF-*d*<sub>8</sub> = 67.57, 23.37 ppm. The resonance multiplicity is indicated as *s* (singlet), *d* (doublet), *t* (triplet), *q* (quartet), *quin* (quintet), *sext* (sextet), and *m* (multiplet) and *br* (broad signal). The chemical shifts are given in parts per million (ppm) on the delta scale ( $\delta$ ) and the coupling constant values (*J*) are given in hertz (Hz). Signal assignments are given in the experimental part using the arbitrary numbering indicated.

**Electron Impact (EI) mass spectra** were measured on a *Finnigan MAT95Q* or on a *Finnigan MAT90* mass spectrometer.

**Electrospray ionization (ESI) mass spectra** were measured on a *Thermo Finnigan LTQ-FT*. The most important signals are reported in *m/z* units with *M* as the molecular ion.

**Elemental analysis** was performed in the micro analytical laboratory of the LMU department of chemistry on an *Elementar Vario EL* apparatus.

**Infrared spectra** were recorded on a *Perkin Elmer Spectrum BX-FT-IR* instrument equipped with a Smith *DuraSamplIR II* ATR-device. Transmittance values are qualitatively described by wavenumber ( $\text{cm}^{-1}$ ) as strong (*s*), medium (*m*), and weak (*w*).

**UV-vis spectra** were measured on a *Varian Cary 5000* spectrophotometer. The spectra were recorded in a quartz cuvette (10 mm path length). Solvents for spectroscopy were obtained from *VWR* and *Merck*. Absorption wavelength ( $\lambda$ ) are reported in nm and the extinction coefficients ( $\epsilon$ )  $\text{L}\cdot\text{mol}^{-1}\cdot\text{cm}^{-1}$  are given in brackets. Shoulders are declared as *sh*.

**Electronic circular dichroism spectra** were measured on a *Jasco J-810* CD spectropolarimeter equipped with a *Jasco* CDF-426S Peltier temperature controller. Baseline corrected spectra were recorded with standard sensitivity (100 mdeg), data pitch of 1 nm, 500 nm/min scanning speed, 1s response time and fivefold accumulation. Resulting spectra were smoothed via the adaptive- or *Savitzky-Golay* filter function.

**Low temperature UV-vis and electronic circular dichroism spectra** were measured with an *Oxford instruments Optistat DN* cryostat within an adjustable custom-made holder.

**Irradiation at low temperature** was carried out with a *Prizmatix UHP-T-LED Controller* powering collimated UHP-T-450-EP and UHT-T-520-DI LEDs coupled to a 3 m long coated glass fiber with 1.5 mm inner diameter.

**Melting points (m.p.)** were measured on a *Büchi B-540 melting point* apparatus in open capillaries.

**Gas chromatography - Mass spectrometry (GC-MS)** was performed on a *Shimadzu GC2010 Plus* gas chromatograph with a *Shimadzu QP2010SE* Mass detector, equipped with an *Agilent VF-5ms* Column (30 m length, 0.25 mm inner diameter, 0.25  $\mu\text{m}$  film thickness). Standard method: Injection: 250 °C liner temperature, 1  $\mu\text{L}$  injection volume, split ratio: 5.0, 45 cm/sec gas speed (linear velocity), carrier gas type: helium. Column program: hold 75 °C for 2 min, 50 °C/min heating ramp for 4.5 min, hold 300 °C for 14.5 min. MS detection: 200 °C ion source temperature, 250 °C interface temperature, 3.2 min solvent cut time, 0.15 s event time, scan speed: 5000s<sup>-1</sup>, start *m/z*: 35 u, end *m/z*: 700 u, 70 eV ionization energy.

**High performance liquid chromatography (HPLC)** was performed on a *Merck-Hitachi LaChrom* Series HPLC system consisting of a D-7000 interface, a L-7150 solvent delivery module, a L-7350 column oven, a L-7420 UV-vis detector and a L-7455 diode array detector



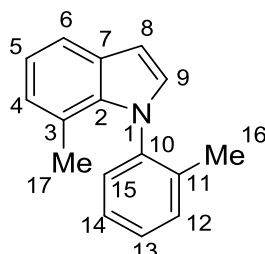
using a preparative *Machery-Nagel* VP 250/21 *NUCLEODUR Sphinx* RP (particle size 5  $\mu\text{m}$ ) column (7 / 3 to 1 / 0, acetonitrile / water, v / v, 12 to 15 mL/min, 35 °C column temperature) or on a *Shimadzu* HPLC system consisting of two LC-20AP solvent delivery modules, a CTO-20A column oven, a SPD-M20A photodiode array UV-vis detector, and a CBM-20A system controller using a semi preparative *Diacel CHIRALPAK® IC / ID* column (particle size 5  $\mu\text{m}$ ) cooled within an ice bath and HPLC grade solvents (ethyl acetate and *n*-heptane) from *Sigma-Aldrich* and *ROTH*.

**Theoretical DFT calculations** of optimizations of ground- and transition states were conducted at the B3LYP/6-311G+(d,p) level of theory using Gaussian 16 Rev. B.01 if not stated otherwise.<sup>[132]</sup> Frequency analysis confirmed all ground state structures to be stationary points since no imaginary frequencies were found. Transition states (TS) were found by scanning the minimized ground state structures around the N-C or stilbene single bond. The dihedral angle was rotated in steps of 2 degrees to complete one whole rotation. The respective maximum energy structures were subjected to a transition state optimization with the Berny, QST2 or QST3 algorithm,<sup>[140]</sup> first at the at B3LYP/3-21 level of theory, then at the B3LYP/6-311+G(d,p) level of theory. Undesired local minima (e.g. methyl group rotations) were frozen upon optimization. Converged transition state structures were checked for conclusiveness of their single imaginary vibrational mode. UV-vis and ECD spectra were calculated using TD-DFT at the B3LYP/6-311+G(d,p) level of theory, singlet excitations only, nstates=30, if not stated otherwise.<sup>[141]</sup> NMR spectra were calculated using the GIAO method.<sup>[142]</sup> Visualization of minimized structures, energies, oscillator strengths, electronic circular dichroism and NMR shifts was done with GaussView 6.0.16.<sup>[143]</sup>

### 3.2 Indole precursors - Copper-catalyzed *N*-arylations

Scheme 11 for the cross-coupling reaction can be found in Section 2.2.7.

#### 7-Methyl-1-(*o*-tolyl)-1*H*-indole (**17**)



To a sealable, N<sub>2</sub> purged pressure tube (40 mL total volume) equipped with a magnetic stirring bar 7-methyl-1*H*-indole (2.00 g, 15.3 mmol, 1.0 equiv.), copper iodide (0.146 g, 1.01 mmol, 0.05 equiv.) and anhydrous potassium phosphate (6.80 g, 32.0 mmol, 2.1 equiv.) were added. The pressure tube was evacuated and refilled with N<sub>2</sub> three times. Subsequently, 2-bromotoluene (2.61 g, 15.3 mmol, 1.0 equiv.), cyclohexane-1,2-diamine (0.348 g, 3.05 mmol, 0.2 equiv.) and toluene (15.3 mL, resulting in a 1 M solution) were added. The pressure tube was placed behind a blast shield and the mixture was vigorously stirred at 160 °C for 1 day. After cooling to 22 °C the mixture was neutralized with aq. sat. ammonium chloride solution, filtered through celite, extracted with ethyl acetate and washed with brine. The combined organic phases were dried over sodium sulfate and the volatiles were removed *in vacuo*. Subsequent purification by flash column chromatography (silica, hexanes) yielded 7-methyl-1-(*o*-tolyl)-1*H*-indole **17** (0.893 g, 4.04 mmol, 27%) as clear colorless oil.

*R<sub>f</sub>* = 0.39 (silica, hexanes).

**<sup>1</sup>H-NMR (600 MHz, CD<sub>2</sub>Cl<sub>2</sub>):**  $\delta$  (ppm) = 7.53 (d, <sup>3</sup>*J* = 8.3 Hz, 1H, H-C(6)), 7.40 (t, <sup>3</sup>*J* = 7.6 Hz, 1H, H-C(13)), 7.36 (d, <sup>3</sup>*J* = 7.9 Hz, 1H, H-C(15)), 7.33 (d, <sup>3</sup>*J* = 7.6 Hz, 1H, H-C(12)), 7.30 (t, <sup>3</sup>*J* = 7.9 Hz, 1H, H-C(14)), 7.06 (d, <sup>3</sup>*J* = 3.3 Hz, 1H, H-C(9)), 7.02 (t, <sup>3</sup>*J* = 7.6 Hz, 1H, H-C(5)), 6.90 (d, <sup>3</sup>*J* = 7.3 Hz, 1H, H-C(4)), 6.64 (dd, <sup>3</sup>*J* = 3.3 Hz, <sup>4</sup>*J* = 0.7 Hz, 1H, H-C(8)), 1.96 (s, 3H, H-C(16)), 1.90 (s, 3H, H-C(17)).

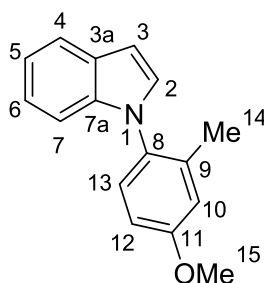
**<sup>13</sup>C-NMR (151 MHz, CD<sub>2</sub>Cl<sub>2</sub>):**  $\delta$  (ppm) = 140.61 (C(10)), 137.35 (C(11)), 135.48 (C(2)), 130.08 (C(12)), 129.50 (C(9)), 129.03 (C(15)), 128.93 (C(7)), 128.56 (C(13)), 126.07 (C(14)), 124.20 (C(4)), 121.58 (C(3)), 119.89 (C(5)), 118.80 (C(6)), 102.25 (C(8)), 17.97 (C(17)), 16.87 (C(16)).

**IR (Diamond ATR):**  $\tilde{\nu}$  (cm<sup>-1</sup>) = 3045 (w), 2952 (w), 2923 (w), 2859 (w), 2738 (w), 2557 (w), 1902 (w), 1828 (w), 1698 (w), 1599 (w), 1583 (w), 1520 (m), 1496 (s), 1483 (s), 1457 (s), 1440 (m), 1418 (m), 1381 (w), 1366 (w), 1331 (s), 1281 (m), 1245 (m), 1225 (s), 1197 (m), 1163 (w), 1139 (m), 1114 (w), 1075 (m), 1039 (w), 984 (w), 954 (m), 944 (w), 865 (w), 844 (m), 782 (s), 765 (s), 745 (s), 716 (s), 689 (s), 659 (w).

**MS (EI+, 70 eV):**  $m/z$  (%) = 221.1 (58), 220.1 (23), 206.1 (28), 204.1 (19), 70.0 (11), 61.0 (19), 45.0 (16), 43.0 (100).

**HRMS (EI+, C<sub>16</sub>H<sub>15</sub>N):** calcd.: 221.1204; found: 221.1202 (M<sup>+</sup>).

### 1-(4-methoxy-2-methylphenyl)-1*H*-indole (**114**)



A flame dried, N<sub>2</sub>-flushed Schlenk flask, equipped with a magnetic stirring bar, is charged with 1*H*-indole (0.500 g, 4.268 mmol, 1.0 equiv.), copper iodide (0.041 g, 0.213 mmol, 0.05 equiv.), potassium phosphate (1.902 g, 8.963 mmol, 2.1 equiv.), 1-bromo-4-methoxy-2-methylbenzene (0.858 g, 4.268 mmol, 1.0 equiv.), *N*1,*N*2-dimethylethane-1,2-diamine (0.075 g, 0.854 mmol, 0.2 equiv.) and toluene (4.268 mL, 1 M). The mixture was stirred at 110 °C for 18 h. The reaction was stopped with a sat. aq. ammonium chloride solution and extracted with ethyl acetate. The combined organic layers were dried over sodium sulfate. The mixture was filtrated and the solvents were removed *in vacuo*. Purification by flash column chromatography (silica, hexanes / ethyl acetate, 9 / 1, v / v) yielded 1-(4-methoxy-2-methylphenyl)-1*H*-indole **114** (0.789 g, 3.33 mmol, 78%) as colorless liquid.

$R_f$  = 0.43 (silica, hexanes / ethyl acetate, 9 / 1, v / v).

**<sup>1</sup>H-NMR (400 MHz, CD<sub>2</sub>Cl<sub>2</sub>):**  $\delta$  (ppm) = 7.71 - 7.67 (m, 1H, H-C(4)), 7.24 (d, <sup>3</sup>*J* = 8.6 Hz, 1H, H-C(13)), 7.20 - 7.11 (m, 3H, H-C(2, 5, 7)), 7.04 - 7.00 (m, 1H, H-C(6)), 6.94 (d, <sup>3</sup>*J* = 2.8 Hz, 1H, H-C(10)), 6.87 (dd, <sup>3</sup>*J* = 8.6 Hz, <sup>4</sup>*J* = 3.0 Hz, 1H, H-C(12)), 6.67 (dd, <sup>3</sup>*J* = 3.2 Hz, <sup>4</sup>*J* = 0.9 Hz, 1H, H-C(3)), 3.88 (s, 3H, H-C(15)), 2.02 (s, 3H, H-C(14)).

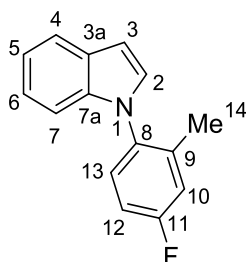
**$^{13}\text{C-NMR}$  (101 MHz,  $\text{CD}_2\text{Cl}_2$ ):**  $\delta$  (ppm) = 159.90 (C(11)), 137.98 (C(7a)), 137.96 (C(9)), 131.66 (C(8)), 129.64 (2C, C(2, 13)), 128.82 (3a), 122.41 (C(5)), 121.23 (C(4)), 120.20 (C(7)), 116.57 (C(10)), 112.38 (C(12)), 110.92 (C(6)), 102.54 (C(3)), 56.01 (C(15)), 18.07 (C(14)).

**IR (Diamond ATR):**  $\tilde{\nu}$  ( $\text{cm}^{-1}$ ) = 3050 (w), 2932 (w), 2836 (w), 1611 (m), 1581 (w), 1512 (s), 1502 (s), 1474 (m), 1457 (m), 1379 (w), 1332 (m), 1295 (m), 1281 (m), 1247 (m), 1226 (s), 1212 (m), 1159 (m), 1138 (m), 1121 (m), 1100 (m), 1062 (m), 1039 (m), 1009 (m), 960 (m), 929 (w), 915 (w), 882 (m), 847 (m), 810 (m), 763 (m), 739 (s), 716 (m), 658 (m).

**MS (EI+, 70 eV):**  $m/z$  (%) = 237.1 (97), 236.1 (62), 223.1 (15), 222.1 (100), 221.1 (10), 204.1 (21), 194.1 (30), 193.1 (23), 192.1 (21), 191.1 (21), 167.1 (10), 165.1 (15).

**HRMS (EI+,  $\text{C}_{16}\text{H}_{15}\text{NO}$ ):** calcd.: 237.1154; found: 237.1145 ( $\text{M}^+$ ).

### 1-(4-fluoro-2-methylphenyl)-1H-indole (115)



A flame dried,  $\text{N}_2$ -flushed Schlenk flask is charged with 1H-indole (0.100 g, 0.854 mmol, 1.0 equiv.), copper iodide (0.0008 g, 0.043 mmol, 0.05 equiv.), potassium phosphate (0.38 g, 1.79 mmol, 2.1 equiv.), 1-bromo-4-fluoro-2-methylbenzene (0.161 g, 0.854 mmol, 1.0 equiv.), *N*1,*N*2-dimethylethane-1,2-diamine (0.015 g, 0.171 mmol, 0.2 equiv.) and toluene (0.427 mL, 2 M). The mixture was stirred at 110 °C for 18 h. The reaction was stopped with a sat. aq. ammonium chloride solution and extracted with ethyl acetate. The combined organic layers were dried over sodium sulfate. The mixture was filtrated and the solvents were removed *in vacuo*. Purification by flash column chromatography (silica, hexanes / ethyl acetate, 9.5 / 0.5, v / v) yielded 1-(4-fluoro-2-methylphenyl)-1H-indole **115** (0.789 g, 3.33 mmol, 87%) as colorless liquid.

$R_f$  = 0.53 (silica, hexanes / ethyl acetate, 9.5 / 0.5, v / v).

**$^1\text{H-NMR}$  (400 MHz,  $\text{CD}_2\text{Cl}_2$ ):**  $\delta$  (ppm) = 7.68 (ddd,  $^3J = 7.1$  Hz,  $^4J = 2.0$  Hz,  $^4J = 0.8$  Hz, 1H, H-C(4)), 7.30 (dd,  $^3J = 8.6$  Hz,  $^4J = 5.4$  Hz, 1H, H-C(13)), 7.20 - 7.10 (m, 4H, H-C(2, 6, 5, 10)),

7.08 - 6.98 (m, 2H, H-C(12, 7)), 6.68 (dd,  $^3J = 3.2$  Hz,  $^4J = 0.8$  Hz, 1H, H-C(3)), 2.03 (s, 3H, H-C(14)).

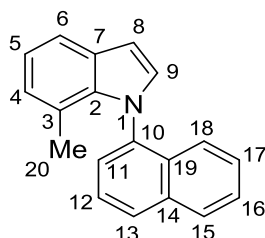
$^{13}\text{C-NMR}$  (101 MHz,  $\text{CD}_2\text{Cl}_2$ ):  $\delta$  (ppm) = 162.61 (d,  $^1J = 246.5$  Hz, 1C, C(11)), 139.21 (d,  $^3J = 8.5$  Hz, 1C, C(9)), 137.72 (C(7a)), 134.87 (d,  $^4J = 3.0$  Hz, 1C, C(8)), 130.31 (d,  $^3J = 9.1$  Hz, 1C, C(13)), 129.30 (C(2)), 128.89 (C(3a)), 122.65 (C(6)), 121.34 (C(4)), 120.45 (C(5)), 118.05 (d,  $^2J = 22.3$  Hz, 1C, C(10)), 114.03 (d,  $^2J = 22.4$  Hz, 1C, C(12)), 110.77 (C(7)), 103.06 (C(3)), 18.02 (d,  $^4J = 1.4$  Hz, 1C, C(14)).

**IR (Diamond ATR):**  $\tilde{\nu}$  ( $\text{cm}^{-1}$ ) = 3052 (w), 2922 (w), 2026 (w), 1891 (w), 1704 (w), 1612 (w), 1591 (w), 1512 (m), 1499 (s), 1474 (m), 1457 (m), 1381 (w), 1331 (m), 1307 (m), 1286 (w), 1268 (m), 1242 (m), 1220 (s), 1150 (m), 1135 (m), 1112 (w), 1096 (m), 1060 (w), 1036 (w), 1009 (m), 967 (m), 926 (m), 882 (m), 864 (m), 818 (m), 763 (m), 739 (s), 715 (m), 658 (m).

**MS (EI+, 70 eV):**  $m/z$  (%) = 225.1 (51), 224.1 (100), 222.1 (25), 204.1 (19).

**HRMS (EI+,  $\text{C}_{15}\text{H}_{12}\text{FN}$ ):** calcd.: 225.0945; found: 225.0942 (M+).

### 7-methyl-1-(naphthalen-1-yl)-1H-indole (31)



To a sealable,  $\text{N}_2$  purged round bottom flask equipped with a magnetic stirring bar, 7-methyl-1H-indole (2.00 g, 15.3 mmol, 1.0 equiv.), copper iodide (0.292 g, 1.52 mmol, 0.1 equiv.), anhydrous potassium phosphate (6.80 g, 32.0 mmol, 2.1 equiv.), and 1-bromonaphthalene (4.74 g, 22.9 mmol, 1.5 equiv.) were added. The flask was evacuated and refilled with  $\text{N}_2$  three times. Subsequently, cyclohexane-1,2-diamine (0.696 g, 6.10 mmol, 0.4 equiv.), and *p*-xylene (15.3 mL) were added. The mixture was heated to 160 °C and stirred for 1 day. After cooling to 22 °C the mixture was neutralized with aq. sat. ammonium chloride solution, filtered through celite, extracted with ethyl acetate and washed with brine. The combined organic phases were dried over sodium sulfate and the volatiles were removed *in vacuo*. Subsequent purification by flash column chromatography (silica, hexanes / ethyl acetate, 100 / 1, v / v) yielded 7-methyl-1-(naphthalen-1-yl)-1H-indole **31** (1.12 g, 4.65 mmol, 31%) as white solid.

**R<sub>f</sub>** = 0.18 (silica, hexanes / ethyl acetate, 100 / 1, v / v).

**m.p.** (°C): 118.

**<sup>1</sup>H-NMR (400 MHz, CD<sub>2</sub>Cl<sub>2</sub>):** δ (ppm) = 8.01 (dd, <sup>3</sup>J = 7.5 Hz, <sup>4</sup>J = 1.9 Hz, 1H, H-C(13)), 7.98 (d, <sup>3</sup>J = 8.3 Hz, 1H, H-C(15)), 7.62 - 7.59 (m, 1H, H-C(12)), 7.60 - 7.57 (m, 1H, H-C(11)), 7.59 - 7.56 (m, 1H, H-C(6)), 7.53 (ddd, <sup>3</sup>J = 8.2 Hz, <sup>3</sup>J = 7.0 Hz, <sup>4</sup>J = 1.3 Hz, 1H, H-C(16)), 7.39 (ddd, <sup>3</sup>J = 8.3 Hz, <sup>3</sup>J = 6.86 Hz, <sup>4</sup>J = 1.2 Hz, 1H, H-C(17)), 7.22 (d, <sup>3</sup>J = 3.2 Hz, 1H, H-C(9)), 7.15 (d, <sup>3</sup>J = 8.5 Hz, 1H, H-C(18)), 7.05 (dd, <sup>3</sup>J = 7.34 Hz, <sup>3</sup>J = 7.15 Hz, 1H, H-C(5)), 6.86 (d, <sup>3</sup>J = 7.15 Hz, 1H, H-C(4)), 6.72 (d, <sup>3</sup>J = 3.23 Hz, 1H, H-C(8)), 1.67 (s, 3H, H-C(20)).

**<sup>13</sup>C-NMR (101 MHz, CD<sub>2</sub>Cl<sub>2</sub>):** δ (ppm) = 138.79 (C(10)), 137.35 (C(2)), 134.25 (C(14)), 133.19 (C(19)), 131.48 (C(9)), 129.64 (C(7)), 129.33 (C(13)), 128.64 (C(15)), 127.81 (C(17)), 127.21 (C(16)), 126.92 (C(11)), 125.58 (C(12)), 124.95 (C(4)), 123.50 (C(18)), 122.38 (C(3)), 120.74 (C(5)), 119.49 (C(6)), 103.11 (C(8)), 18.62 (C(20)).

**IR (Diamond ATR):**  $\tilde{\nu}$  (cm<sup>-1</sup>) = 3359 (w), 3050 (w), 2971 (w), 1700 (w), 1576 (m), 1517 (w), 1505 (m), 1481 (m), 1451 (m), 1436 (m), 1421 (m), 1394 (m), 1382 (m), 1363 (w), 1340 (w), 1321 (m), 1279 (m), 1243 (m), 1226 (m), 1214 (m), 1181 (m), 1157 (m), 1140 (m), 1097 (w), 1072 (m), 1037 (m), 1014 (m), 951 (w), 933 (m), 880 (w), 866 (w), 852 (w), 843 (m), 814 (w), 802 (s), 776 (s), 745 (s), 737 (m), 714 (s), 680 (m).

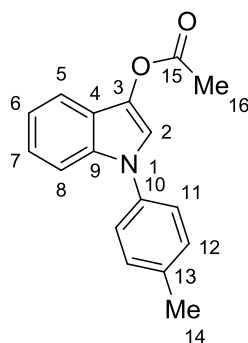
**MS (EI+, 70 eV):** *m/z* (%) = 258.1 (21), 257.1 (100), 256.1 (65), 254.1 (19), 242.1 (18), 241.1 (58), 127.6 (12), 127.1 (13), 120.5 (26).

**HRMS (EI+, C<sub>19</sub>H<sub>15</sub>N):** calcd.: 257.1205; found: 257.1199 (M+).

### 3.3 Indoxyl acetate precursors - Oxidative acetoxylation

Scheme 12 for the carbo acetylation reaction can be found in Section 2.2.7.

#### 1-(*p*-tolyl)-1*H*-indol-3-yl acetate (**74**)



A flame-dried Schlenk flask was charged with *N*-(*p*-tolyl)indole (0.590 g, 2.85 mmol, 1.0 equiv.), iodobenzene-*I,I*-diacetate (1.84 g, 5.70 mmol, 2.0 equiv.), palladium(II) acetate (0.032 g, 0.142 mmol, 0.05 equiv.) and potassium acetate (0.100 g, 2.85 mmol, 1.0 equiv.). After evacuating and refilling the flask with N<sub>2</sub> three times, degassed acetonitrile (12 mL) was added under N<sub>2</sub> atmosphere and the reaction mixture was stirred for 2 h at 70 °C. The reaction was stopped with an aq. sat. sodium bisulfite solution and water, filtered over celite, extracted with ethyl acetate and washed with brine. The combined organic layers were dried over sodium sulfate and evaporated to dryness *in vacuo*. Subsequently, the crude product was purified by flash column chromatography (silica, hexanes / ethyl acetate / triethylamine, 9.5 / 0.5 / 0.2, v / v / v). 1-(*p*-Tolyl)-1*H*-indol-3-yl acetate **74** (0.433 g, 1.63 mmol, 57%) was obtained as colorless oil.

$R_f$  = 0.40 (silica, hexanes / ethyl acetate / triethylamine, 9.5 / 0.5 / 0.2, v / v / v).

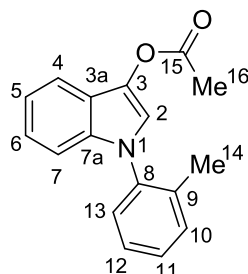
**<sup>1</sup>H-NMR (CD<sub>2</sub>Cl<sub>2</sub>, 600 MHz):**  $\delta$  (ppm) = 7.59 (dd, <sup>3</sup>*J* = 7.9 Hz, <sup>4</sup>*J* = 1.5 Hz, 1H, H-C(5)), 7.53 (dd, <sup>3</sup>*J* = 7.8 Hz, 1H, H-C(9)), 7.52 (s, 1H, H-C(2)), 7.41 (dd, <sup>3</sup>*J* = 8.5 Hz, 2H, H-C(11)), 7.35 (dd, <sup>3</sup>*J* = 8.5 Hz, 2H, H-C(12)), 7.25 (ddd, <sup>3</sup>*J* = 7.5 Hz, <sup>4</sup>*J* = 1.3 Hz, 1H, H-C(7)), 7.18 (ddd, <sup>3</sup>*J* = 7.5 Hz, <sup>4</sup>*J* = 1.0 Hz, 1H, H-C(6)), 2.44 (s, 3H, H-C(14)), 2.38 (s, 3H, H-C(16)).

**<sup>13</sup>C-NMR (CD<sub>2</sub>Cl<sub>2</sub>, 151 MHz):**  $\delta$  (ppm) = 168.49 (C(15)), 136.74 (C(10)), 136.56 (C(13)), 133.02 (C(9)), 131.19 (C(3)), 130.11 (C(12)), 124.21 (C(11)), 123.00 (C(7)), 121.17 (C(4)), 120.14 (C(6)), 117.62 (C(5)), 117.18 (C(2)), 110.53 (C(8)), 20.72 (C(14)), 20.70 (C(16)).

**MS (EI+, 70 eV):**  $m/z$  (%) = 265.1 (18), 224.1 (16), 223.1 (100), 222.1 (14), 194.1 (14), 180.1 (11), 43.1 (10).

**HRMS (EI+, C<sub>17</sub>H<sub>15</sub>NO<sub>2</sub>):** calcd.: 265.1103; found: 265.1101 (M+).

**1-(*o*-tolyl)-1*H*-indol-3-yl acetate (68)**



A flame dried, N<sub>2</sub>-flushed Schlenk flask is charged with 1-(*o*-tolyl)-1*H*-indole **66** (0.162 g, 0.782 mmol, 1.0 equiv.), iodobenzene-*I,I*-diacetate (0.503 g, 0.1563 mmol, 2.0 equiv.), palladium(II) acetate (0.009 g, 5 mol%), potassium acetate (0.044 g, 0.782 mmol, 1.0 equiv.) and acetonitrile (1.8 mL, 0.43 M). The contents were stirred at 70 °C for 2 h. The reaction was stopped with an aq. sodium bisulfate solution (1 M), filtered through celite and extracted with ethyl acetate. The combined organic layers were dried over sodium sulfate. The mixture was filtrated and the solvents were removed *in vacuo*. Purification by flash column chromatography (silica, hexanes / ethyl acetate / triethylamine, 88 / 10 / 2, v / v / v) yielded 1-(*o*-tolyl)-1*H*-indol-3-yl acetate **68** (0.071 g, 0.268 mmol, 34%) as colorless liquid.

$R_f$  = 0.42 (silica, hexanes / ethyl acetate / triethylamine, 88 / 10 / 2, v / v / v).

**<sup>1</sup>H-NMR (600 MHz, CD<sub>2</sub>Cl<sub>2</sub>):**  $\delta$  (ppm) = 7.60 (d, <sup>3</sup> $J$  = 7.6 Hz, 1H, H-C(4)), 7.41 - 7.36 (m, 3H, H-C(10, 12, 2)), 7.35 - 7.32 (m, 2H, H-C(11, 13)), 7.19 (ddd, <sup>3</sup> $J$  = 8.2 Hz, <sup>3</sup> $J$  = 7.0 Hz, <sup>4</sup> $J$  = 1.4 Hz, 1H, H-C(6)), 7.16 (ddd, <sup>3</sup> $J$  = 7.4 Hz, <sup>3</sup> $J$  = 7.0 Hz, <sup>4</sup> $J$  = 1.1 Hz, 1H, H-C(5)), 7.01 (d, <sup>3</sup> $J$  = 8.2 Hz, 1H, H-C(7)), 2.37 (s, 3H, H-C(16)), 2.08 (s, 3H, H-C(14)).

**<sup>13</sup>C-NMR (151 MHz, CD<sub>2</sub>Cl<sub>2</sub>):**  $\delta$  (ppm) = 169.01 (C(15)), 138.26 (C(9)), 136.51 (C(8)), 134.62 (C(7a)), 131.77 (C(10)), 131.20 (C(3)), 128.91 (C(12)), 128.72 (C(13)), 127.34 (C(11)), 123.40 (C(6)), 120.84 (C(3a)), 120.40 (C(5)), 118.49 (C(2)), 118.08 (C(4)), 111.13 (C(7)), 21.32 (C(16)), 17.92 (C(14)).

**IR (Diamond ATR):**  $\tilde{\nu}$  (cm<sup>-1</sup>) = 3055 (w), 2925 (w), 1968 (w), 1745 (m), 1614 (w), 1603 (w), 1582 (w), 1548 (w), 1498 (m), 1461 (m), 1364 (s), 1311 (m), 1235 (m), 1203 (s), 1162 (m),

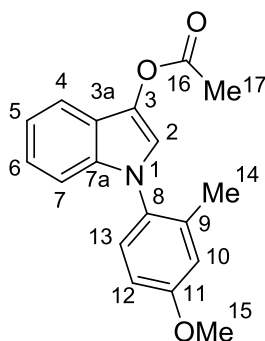


1124 (m), 1124 (m), 1076 (m), 1042 (m), 1008 (m), 938 (m), 892 (m), 844 (w), 774 (m), 737 (s), 720 (s), 688 (m).

**MS (EI+, 70 eV):**  $m/z$  (%) = 265.1 (15), 224.1 (15), 223.1 (100), 209.1 (10), 204.1 (14), 194.1 (26), 179.3 (18), 164.5 (11), 151.7 (10), 91.0 (13), 77.0 (17), 65.0 (14), 57.0 (26), 55.0 (15), 43.5 (36), 42.5 (18), 40.1 (13).

**HRMS (EI+, C<sub>17</sub>H<sub>15</sub>NO<sub>2</sub>):** calcd.: 265.1103; found: 265.1109 (M+).

### 1-(4-methoxy-2-methylphenyl)-1*H*-indol-3-yl acetate (**75**)



A flame dried, N<sub>2</sub>-flushed Schlenk flask is charged with 1-(4-methoxy-2-methylphenyl)-1*H*-indole **114** (0.050 g, 0.211 mmol, 1.0 equiv.), iodobenzene-*I,I*-diacetate (0.136 g, 0.421 mmol, 2.0 equiv.), palladium(II) acetate (0.002 g, 5 mol%), potassium acetate (0.012 g, 0.211 mmol, 1.0 equiv.) and acetonitrile (0.6 mL, 0.35 M). The contents were stirred at 70 °C for 2 h. The reaction was stopped with an aq. sodium bisulfate solution (1 M), filtered through celite and extracted with ethyl acetate. The combined organic layers were dried over sodium sulfate. The mixture was filtrated and the solvents were removed *in vacuo*. Purification by flash column chromatography (silica, hexanes / ethyl acetate / triethylamine, 88 / 10 / 2, v / v / v) yielded 1-(4-methoxy-2-methylphenyl)-1*H*-indol-3-yl acetate **75** (0.023 g, 0.078 mmol, 37%) as colorless liquid.

$R_f$  = 0.35 (silica, hexanes / ethyl acetate / triethylamine, 88 / 10 / 2, v / v / v).

**<sup>1</sup>H-NMR (400 MHz, CD<sub>2</sub>Cl<sub>2</sub>):**  $\delta$  (ppm) = 7.58 (dd, <sup>3</sup>*J* = 7.5 Hz, <sup>4</sup>*J* = 1.6 Hz, 1H, H-C(4)), 7.32 (s, 1H, H-C(2)), 7.24 (d, <sup>3</sup>*J* = 8.6 Hz, 1H, H-C(13)), 7.21 - 7.11 (m, 2H, H-C(6, 5)), 6.99 - 6.95 (m, 1H, H-C(7)), 6.91 (d, <sup>3</sup>*J* = 2.8 Hz, 1H, H-C(10)), 6.85 (dd, <sup>3</sup>*J* = 8.6 Hz, <sup>4</sup>*J* = 2.9 Hz, 1H, H-C(12)), 3.86 (s, 3H, H-C(15)), 2.36 (s, 3H, H-C(17)), 2.01 (s, 3H, H-C(14)).

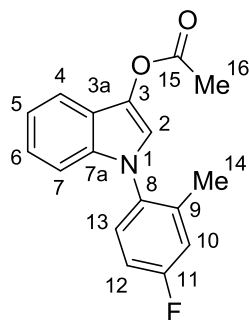
**$^{13}\text{C}$ -NMR (101 MHz,  $\text{CD}_2\text{Cl}_2$ ):**  $\delta$  (ppm) = 169.04 (C(16)), 159.99 (C(11)), 138.09 (C(9)), 135.00 (C(7)), 131.09 (C(8)), 130.93 (C(3)), 129.80 (C(13)), 123.28 (C(6)), 120.71 (C(3a)), 120.27 (C(5)), 118.79 (C(2)), 118.00 (C(4)), 116.58 (C(10)), 112.40 (C(12)), 111.07 (C(7)), 56.02 (C(15)), 21.31 (C(17)), 18.04 (C(14)).

**IR (Diamond ATR):**  $\tilde{\nu}$  ( $\text{cm}^{-1}$ ) = 2919 (w), 2849 (w), 2090 (w), 1745 (m), 1609 (m), 1579 (w), 1548 (w), 1505 (s), 1458 (m), 1366 (m), 1296 (m), 1283 (m), 1246 (m), 1200 (s), 1159 (m), 1122 (m), 1072 (m), 1040 (m), 1008 (m), 950 (m), 891 (m), 848 (m), 805 (m), 766 (m), 738 (s), 677 (m).

**MS (EI+, 70 eV):**  $m/z$  (%) = 295.1 (6), 254.1 (16), 253.1 (100), 252.1 (35), 238.1 (14), 224.1 (30), 210.1 (13), 180.1 (14), 122.1 (29).

**HRMS (EI+,  $\text{C}_{18}\text{H}_{17}\text{NO}_3$ ):** calcd.: 295.1208; found: 295.1200 ( $\text{M}^+$ ).

#### 1-(4-fluoro-2-methylphenyl)-1*H*-indol-3-yl acetate (**77**)



A flame dried,  $\text{N}_2$ -flushed Schlenk flask is charged with 1-(4-fluoro-2-methylphenyl)-1*H*-indole **115** (0.100 g, 0.444 mmol, 1.0 equiv.), iodobenzene-*I,I*-diacetate (0.286 g, 0.888 mmol, 2.0 equiv.), palladium(II) acetate (0.002 g, 2 mol%) and potassium acetate (0.025 g, 0.444 mmol, 1.0 equiv.) and acetonitrile (1.2 mL, 0.37 M). The contents were stirred at 70 °C for 2 h. The reaction was stopped with an aq. sodium bisulfate solution (1 M), filtered through celite and extracted with ethyl acetate. The combined organic layers were dried over sodium sulfate. The mixture was filtrated and the solvents were removed *in vacuo*. Purification by flash column chromatography (silica, hexanes / ethyl acetate / triethylamine, 97 / 1 / 2, v / v / v) yielded 1-(4-fluoro-2-methylphenyl)-1*H*-indol-3-yl acetate **77** (0.063 g, 0.222 mmol, 50%) as colorless liquid.

$R_f$  = 0.23 (silica, hexanes / ethyl acetate / triethylamine, 97 / 1 / 2, v / v / v).

**$^1\text{H-NMR}$  (400 MHz,  $\text{CD}_2\text{Cl}_2$ ):**  $\delta$  (ppm) = 7.60 (dd,  $^3J = 8.0$  Hz,  $^4J = 1.6$  Hz, 1H, H-C(4)), 7.34 (s, 1H, H-C(2)), 7.31 (dd,  $^3J = 8.6$  Hz,  $^4J = 5.4$  Hz, 1H, H-C(13)), 7.23 - 7.13 (m, 2H, H-C(13, 6)), 7.11 (dd,  $^3J = 9.4$  Hz,  $^4J = 2.9$  Hz, 1H, H-C(10)), 7.03 (dd,  $^3J = 8.1$  Hz,  $^4J = 3.0$  Hz, 1H, H-C(12)), 6.97 (dd,  $^3J = 7.7$  Hz,  $^4J = 1.6$  Hz, 1H, H-C(7)), 2.37 (s, 3H, H-C(16)), 2.04 (s, 3H, H-C(14)).

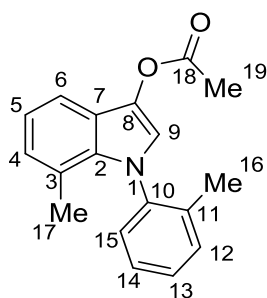
**$^{13}\text{C-NMR}$  (101 MHz,  $\text{CD}_2\text{Cl}_2$ ):**  $\delta$  (ppm) = 168.98 (C(15)), 162.68 (d,  $^1J = 246.7$  Hz, 1C, C(11)), 139.35 (d,  $^3J = 9.0$  Hz, 1C, C(9)), 134.81 (C(7a)), 134.34 (d,  $^4J = 3.0$  Hz, 1C, C(8)), 131.31 (C(3)), 130.49 (d,  $^3J = 9.2$  Hz, 1C, C(13)), 123.55 (C(6)), 120.86 (C(3a)), 120.52 (C(5)), 118.46 (C(2)), 118.14 (C(4)), 118.10 (d,  $^2J = 22.4$  Hz, 1C, C(10)), 114.09 (d,  $^2J = 22.4$  Hz) (C(12)), 110.93 (C(7)), 21.32 (C(16)), 18.02 (d,  $^4J = 1.3$  Hz, 1C, C(14)).

**IR (Diamond ATR):**  $\tilde{\nu}$  ( $\text{cm}^{-1}$ ) = 3057 (w), 2925 (w), 2852 (w), 1929 (w), 1746 (m), 1613 (w), 1549 (w), 1501 (s), 1458 (m), 1367 (m), 1312 (m), 1266 (m), 1234 (m), 1198 (s), 1150 (m), 1125 (m), 1100 (m), 1076 (m), 1041 (w), 1008 (m), 960 (m), 918 (w), 891 (m), 864 (m), 820 (m), 806 (m), 766 (w), 738 (s), 677 (m).

**MS (EI+, 70 eV):**  $m/z$  (%) = 283.1 (10), 242.1 (16), 241.1 (100), 240.1 (46), 212.1 (40), 198.1 (12), 196.1 (10).

**HRMS (EI+,  $\text{C}_{17}\text{H}_{14}\text{FNO}_2$ ):** calcd.: 283.1009; found: 283.1001 (M+).

### 7-Methyl-1-(*o*-tolyl)-1*H*-indol-3-yl acetate (19)



To a flame dried Schlenk flask, equipped with a magnetic stirring bar, 7-methyl-1-(*o*-tolyl)-1*H*-indole **17** (0.651 g, 2.94 mmol, 1.0 equiv.), iodobenzene-*I,I*-diacetate (1.90 g, 5.88 mmol, 2.0 equiv.), palladium(II) acetate (0.033 g, 0.147 mmol, 0.05 equiv.), and potassium acetate (2.94 g, 0.289 mmol, 1.0 equiv.) were added and the Schlenk flask was evacuated and refilled with  $\text{N}_2$  for three times. Then, acetonitrile (6.0 mL, 0.5 M, degassed with  $\text{N}_2$ ) was added and the mixture was stirred at 70 °C for 2 h. The mixture was treated with aq. sat. sodium bisulfite

solution, filtered through celite, extracted with ethyl acetate and washed with brine. The combined organic phases were dried over sodium sulfate and the volatiles were removed *in vacuo*. Subsequent purification by flash column chromatography (silica, hexanes / ethyl acetate / triethyl amine, 9.5 / 0.5 / 0.2, v / v / v) yielded 7-methyl-1-(*o*-tolyl)-1*H*-indol-3-yl acetate **19** (0.735 g, 2.63 mmol, 90%) as clear, colorless oil, which was stored under N<sub>2</sub> atmosphere.

**R<sub>f</sub>** = 0.50 (silica, hexanes / ethyl acetate / triethyl amine, 9.5 / 0.5 / 0.2, v / v / v).

**<sup>1</sup>H-NMR (600 MHz, CD<sub>2</sub>Cl<sub>2</sub>):** δ (ppm) = 7.43 (d, <sup>3</sup>*J* = 7.9 Hz, 1H, H-C(6)), 7.38 (dd, <sup>3</sup>*J* = 7.4 Hz, <sup>3</sup>*J* = 7.4 Hz, 1H, H-C(13)), 7.37 (d, <sup>3</sup>*J* = 7.4 Hz, 1H, H-C(15)), 7.31 (d, <sup>3</sup>*J* = 7.5 Hz, 1H, H-C(12)), 7.28 (dd, <sup>3</sup>*J* = 7.5 Hz, <sup>3</sup>*J* = 7.5 Hz, 1H, H-C(14)), 7.22 (s, 1H, H-C(9)), 7.03 (dd, <sup>3</sup>*J* = 7.1 Hz, <sup>3</sup>*J* = 7.1 Hz, 1H, H-C(5)), 6.92 (d, <sup>3</sup>*J* = 7.1 Hz, 1H, H-C(4)), 2.35 (s, 3H, H-C(19)), 1.96 (s, 3H, H-C(16)), 1.86 (s, 3H, H-C(17)).

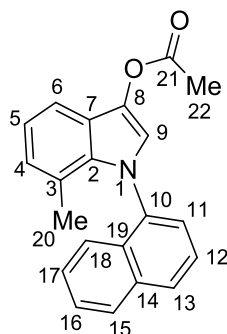
**<sup>13</sup>C-NMR (151 MHz, CD<sub>2</sub>Cl<sub>2</sub>):** δ (ppm) = 168.99 (C(18)), 140.63 (C(10)), 137.04 (C(11)), 138.04 (C(2)), 133.21 (C(8)), 131.03 (C(12)), 130.72 (C(15)), 129.31 (C(13)), 126.71 (C(14)), 125.61 (C(4)), 122.49 (C(3)), 121.43 (C(7)), 120.50 (C(5)), 119.17 (C(9)), 115.95 (C(6)), 21.32 (C(19)), 18.48 (C(17)), 17.42 (C(16)).

**IR (Diamond ATR):**  $\tilde{\nu}$  (cm<sup>-1</sup>) = 3157 (w), 3051 (w), 2953 (w), 2924 (w), 2860 (w), 2086 (w), 1908 (w), 1766 (s), 1747 (s), 1604 (w), 1582 (w), 1555 (w), 1497 (s), 1457 (m), 1417 (m), 1361 (s), 1290 (m), 1242 (m), 1205 (s), 1156 (s), 1128 (s), 1108 (m), 1073 (s), 1042 (m), 1019 (m), 1002 (m), 953 (w), 918 (m), 878 (m), 811 (w), 775 (s), 763 (s), 740 (s), 724 (s), 694 (m), 670 (m).

**MS (EI+, 70 eV):** *m/z* (%) = 279.1 (24), 238.1 (15), 237.1 (100), 236.1 (15), 222 (13), 91.1 (11), 42.9 (17).

**HRMS (EI+, C<sub>18</sub>H<sub>17</sub>NO<sub>2</sub>):** calcd.: 279.1259; found: 279.1256 (M+).

**EA (C<sub>18</sub>H<sub>17</sub>NO<sub>2</sub>):** calcd.: N, 5.01; C, 77.40; H, 6.13; found: N, 4.88; C, 77.31; H, 6.26.

**7-methyl-1-(naphthalen-1-yl)-1*H*-indol-3-yl acetate (32)**

To a flame dried Schlenk flask, equipped with a magnetic stirring bar, 7-methyl-1-(naphthalen-1-yl)-1*H*-indole **31** (0.500 g, 1.94 mmol, 1.0 equiv.), iodobenzene-*I,I*-diacetate (1.25 g, 3.89 mmol, 2.0 equiv.), palladium(II) acetate (0.022 g, 0.097 mmol, 0.05 equiv.), and potassium acetate (0.191 g, 1.94 mmol, 1.0 equiv.) were added and the Schlenk flask was evacuated and refilled with N<sub>2</sub> for three times. Then, acetonitrile (6.0 mL, 0.5 M, degassed with N<sub>2</sub>) was added and the mixture was stirred at 75 °C for 2 h. The mixture was treated with aq. sat. sodium bisulfite solution, filtered through celite, extracted with ethyl acetate and washed with brine. The combined organic phases were dried over sodium sulfate and the volatiles were removed *in vacuo*. Subsequent purification by flash column chromatography (silica, hexanes / ethyl acetate / triethyl amine, 9.5 / 0.5 / 0.2, v / v / v) yielded 7-methyl-1-(naphthalen-1-yl)-1*H*-indol-3-yl acetate **32** (0.297 g, 0.94 mmol, 49%) as clear colorless oil, which was stored under N<sub>2</sub> atmosphere and crystallizes to an off-white powder over time.

*R<sub>f</sub>* = 0.36 (silica, hexanes / ethyl acetate / triethyl amine, 9.5 / 0.5 / 0.2, v / v / v).

**m.p.** (°C): 116 - 117.

**<sup>1</sup>H-NMR (400 MHz, CD<sub>2</sub>Cl<sub>2</sub>):** δ (ppm) = 8.01 (d, <sup>3</sup>*J* = 8.1 Hz, 1H, H-C(13)), 7.97 (d, <sup>3</sup>*J* = 8.4 Hz, 1H, H-C(15)), 7.64 - 7.58 (m, 1H, H-C(11)), 7.60 - 7.56 (m, 1H, H-C(12)), 7.54 (ddd, <sup>3</sup>*J* = 8.1 Hz, <sup>3</sup>*J* = 6.9 Hz, <sup>4</sup>*J* = 1.3 Hz, 1H, H-C(16)), 7.50 (d, <sup>3</sup>*J* = 8.0 Hz, 1H, H-C(6)), 7.41 (ddd, <sup>3</sup>*J* = 8.3 Hz, <sup>3</sup>*J* = 7.0 Hz, <sup>4</sup>*J* = 1.2 Hz, 1H, H-C(17)), 7.39 (s, 1H, H-C(9)), 7.20 (d, <sup>3</sup>*J* = 8.49 Hz, 1H, H-C(18)), 7.08 (dd, <sup>3</sup>*J* = 7.60 Hz, <sup>3</sup>*J* = 7.19 Hz, 1H, H-C(5)), 6.90 (d, <sup>3</sup>*J* = 7.2 Hz, 1H, H-C(4)), 2.37 (s, 3H, H-C(22)), 1.66 (s, 3H, H-C(20)).

**<sup>13</sup>C-NMR (101 MHz, CD<sub>2</sub>Cl<sub>2</sub>):** δ (ppm) = 169.02 (C(21)), 138.22 (C(10)), 134.46 (C(2)), 134.27 (C(14)), 133.11 (C(19)), 131.29 (C(8)), 129.52 (C(13)), 128.69 (C(15)), 127.92 (C(17)),

127.25 (C(16)), 127.18 (C(11)), 125.80 (C(4)), 125.57 (C(12)), 123.37 (C(18)), 122.71 (C(3)), 121.67 (C(7)), 120.79 (C(5)), 120.56 (C(9)), 116.09 (C(6)), 21.34 (C(22)), 18.56 (C(20)).

**IR (Diamond ATR):**  $\tilde{\nu}$  (cm<sup>-1</sup>) = 3050 (w), 2953 (w), 2923 (w), 1907 (w), 1764 (s), 1745 (s), 1616 (w), 1596 (m), 1575 (w), 1558 (w), 1521 (w), 1508 (m), 1496 (w), 1466 (m), 1454 (m), 1436 (m), 1421 (s), 1396 (m), 1365 (s), 1342 (m), 1285 (m), 1241 (m), 1201 (s), 1154 (s), 1131 (s), 1070 (m), 1046 (m), 1016 (s), 999 (m), 955 (w), 940 (w), 913 (m), 878 (m), 822 (w), 802 (s), 791 (m), 771 (s), 739 (s), 701 (w), 684 (w), 675 (w).

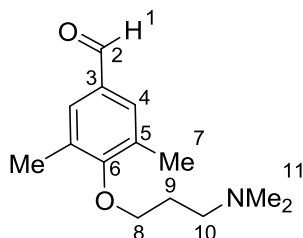
**MS (EI+, 70 eV):**  $m/z$  (%) = 315.1 (28), 274.1 (22), 273.1 (100), 272.1 (17), 244.1 (34), 128.1 (16), 127.1 (12), 43.0 (11).

**HRMS (EI+, C<sub>21</sub>H<sub>17</sub>NO<sub>2</sub>):** calcd.: 315.1259; found: 315.1255 (M+).

### 3.4 Aldehyde precursors - S<sub>N</sub>2 reactions

Scheme 42 for S<sub>N</sub>2 reactions with phenolic alcohols can be found in Section 2.6.1.

#### 4-(3-(dimethylamino)propoxy)-3,5-dimethylbenzaldehyde (**92**)



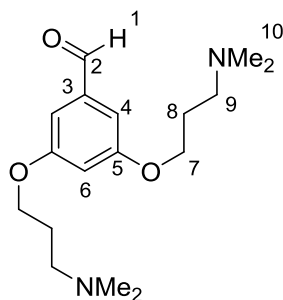
To a round bottom flask, equipped with a magnetic stirring bar, 4-hydroxy-3,5-dimethylbenzaldehyde (0.500 g, 3.33 mmol, 1.0 equiv.), 3-chloro-*N,N*-dimethylpropan-1-amine (0.607 g, 4.99 mmol, 1.5 equiv.), potassium carbonate (1.38 g, 9.99 mmol, 3.0 equiv.), and dimethylformamide (3.3 mL, 1 M) were added. The mixture was heated to 120 °C for 40 min and cooled to 23 °C. Afterwards, the mixture was filtered through celite, extracted with ethyl acetate and washed with brine. The combined organic phases were dried over sodium sulfate and the volatiles were removed *in vacuo*. This yielded 4-(3-(dimethylamino)propoxy)-3,5-dimethylbenzaldehyde **92** (0.691 g, 2.94 mmol, 88%) as clear colorless oil.

**<sup>1</sup>H-NMR (600 MHz, CD<sub>2</sub>Cl<sub>2</sub>):**  $\delta$  (ppm) = 9.84 (s, 1H, H-C(1)), 7.53 (s, 2H, H-C(4)), 3.86 (t, <sup>3</sup>*J* = 6.4 Hz, 2H, H-C(8)), 2.46 (t, <sup>3</sup>*J* = 7.1, 2H, H-C(10)), 2.33 (s, 6H, H-C(7)), 2.21 (s, 6H, H-C(11)), 1.95 (d, <sup>3</sup>*J* = 6.6 Hz, 2H, H-C(9)).

**<sup>13</sup>C-NMR (151 MHz, CD<sub>2</sub>Cl<sub>2</sub>):**  $\delta$  (ppm) = 192.01 (C(2)), 162.03 (C(6)), 132.66 (2C, C(5)), 132.71 (C(3)), 130.95 (2C, C(4)), 71.03 (C(8)), 56.55 (C(10)), 45.74 (2C, C(11)), 28.98 (C(9)), 16.65 (2C, C(7)).

**MS (EI+, 70 eV):** *m/z* (%) = 235.2 (4), 58.0 (100), 43.0 (45).

**HRMS (EI+, C<sub>14</sub>H<sub>21</sub>NO<sub>2</sub>):** calcd.: 235.1572; found: 235.1572 (M+).

**3,5-bis(3-(dimethylamino)propoxy)benzaldehyde 96**

To a round bottom flask, equipped with a magnetic stirring bar, 3,5-dihydroxybenzaldehyde (0.300 g, 2.17 mmol, 1.0 equiv.), 3-chloro-*N,N*-dimethylpropan-1-amine (0.792 g, 6.52 mmol, 3.0 equiv.), potassium carbonate (1.80 g, 13.0 mmol, 6.0 equiv.), and dimethylformamide (4.5 mL, 0.5 M) were added. The mixture was heated to 120 °C for 1 h and cooled to 23 °C. Afterwards, the mixture was filtered through celite, extracted with ethyl acetate and washed with brine. The combined organic phases were dried over sodium sulfate and the volatiles were removed *in vacuo*. Subsequent purification by flash column chromatography (silica, dichloromethane / methanol / triethyl amine, 69 / 29 / 2, v / v / v) yielded 3,5-bis(3-(dimethylamino)propoxy)benzaldehyde **96** (0.492 g, 1.60 mmol, 73%) as clear colorless oil.

**<sup>1</sup>H-NMR (400 MHz, CD<sub>2</sub>Cl<sub>2</sub>):**  $\delta$  (ppm) = 9.88 (s, 1H, H-C(1)), 6.99 (d, <sup>3</sup>*J* = 2.3 Hz, 2H, H-C(4)), 6.72 (t, <sup>3</sup>*J* = 2.3 Hz, 1H, H-C(6)), 4.05 (t, <sup>3</sup>*J* = 6.4 Hz, 4H, H-C(7)), 2.47 (t, <sup>3</sup>*J* = 7.2 Hz, 4H, H-C(9)), 2.24 (s, 12H, H-C(10)), 1.95 (*quin*, <sup>3</sup>*J* = 6.6 Hz, 4H, H-C(8)).

**<sup>13</sup>C-NMR (101 MHz, CD<sub>2</sub>Cl<sub>2</sub>):**  $\delta$  (ppm) = 192.36 (C(2)), 161.30 (2C, C(5)), 139.04 (C(3)), 108.30 (C(6)), 108.05 (2C, C(4)), 67.17 (2C, C(7)), 56.44 (2C, C(9)), 45.50 (4C, C(10)), 27.66 (2C, C(8)).

**MS (EI+, 70 eV):** *m/z* (%) = 263.2, (11), 86.1 (11), 85.1 (11), 84.1 (27), 59.1 (10). 58.1 (100), 42.9 (13), 41.9 (13).

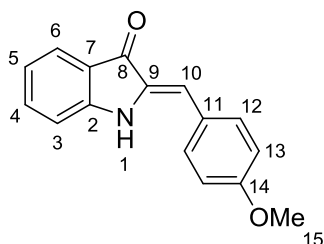
**HRMS (EI+, C<sub>17</sub>H<sub>28</sub>N<sub>2</sub>O<sub>3</sub>):** calcd.: 308.2100; found: 308.2101 (M+).



### 3.5 Condensation reactions of indoxyl acetates with aromatic aldehydes

Scheme 5 for the condensation reaction of indoxyl acetates with aldehydes can be found in Scheme 2.2.1.

#### (*Z*)-2-(4-methoxybenzylidene)indolin-3-one (**9**)



To a nitrogen-flushed Schlenk flask, equipped with a magnetic stirring bar and rubber septum, aq. sodium hydroxide solution (11.0 mL, 16.4 mmol, 1.5 M, 8.2 equiv., degassed with nitrogen) and 1*H*-indol-3-yl acetate (0.35 g, 2.00 mmol, 1.0 equiv.) were added and heated to 100 °C for 10 min. Then, 4-methoxybenzaldehyde (0.27 g, 2.00 mmol, 1.0 equiv.) in methanol (0.29 mL, 6.9 M, degassed) was added to the solution at 0 °C and stirred for 18 h from 0 °C to 23 °C. Filtration of the mixture and subsequent purification by flash column chromatography (silica, hexanes / ethyl acetate, 8 / 2, v / v) and recrystallization from ethanol / water yielded (*Z*)-2-(4-methoxybenzylidene)indolin-3-one **9** (0.364 g, 1.45 mmol, 72%) as orange crystals.

$R_f = 0.25$  (silica, hexanes / ethyl acetate, 4 / 1, v / v).

**m.p.** (°C): 186 - 187.

**<sup>1</sup>H-NMR (400 MHz, CDCl<sub>3</sub>):**  $\delta$  (ppm) = 7.75 (d, <sup>3</sup>*J* = 7.9 Hz, 1H, H-C(6)), 7.53 - 7.49 (m, 2H, H-C(12)), 7.46 (ddd, <sup>3</sup>*J* = 8.3 Hz, <sup>3</sup>*J* = 7.4 Hz, <sup>4</sup>*J* = 1.32 Hz, 1H, H-C(4)), 7.01 (dd, <sup>3</sup>*J* = 8.20 Hz, <sup>4</sup>*J* = 0.76 Hz, 1H, H-C(3)), 6.99 - 6.93 (m, 3H, H-C(13), H-C(5)), 6.86 (s, 1H, H-C(10)), 6.81 (s, 1H, H-N(1)), 3.85 (1s, 3H, H-C(15)).

**<sup>13</sup>C-NMR (101 MHz, CDCl<sub>3</sub>):**  $\delta$  (ppm) = 186.54 (C(8)), 160.08 (C(14)), 153.18 (C(2)), 135.97 (C(4)), 134.42 (C(9)), 131.35 (2C, C(12)), 127.42 (C(11)), 125.06 (C(6)), 122.21 (C(7)), 120.70 (C(5)), 114.94 (2C, C(13)), 112.34 (C(3)), 112.20 (C(10)), 55.55 (C(15)).

**IR (Diamond ATR):**  $\tilde{\nu}$  (cm<sup>-1</sup>) = 3325 (m), 2988 (w), 2974 (w), 2931 (w), 2851 (w), 2836 (w), 2568 (w), 2349 (w), 2293 (w), 2107 (w), 2005 (w), 1960 (w), 1928 (w), 1894 (w), 1806 (w),

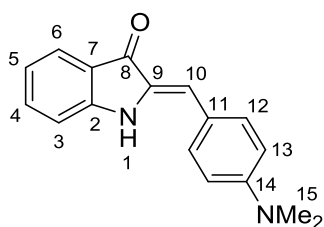
1760 (w), 1683 (m), 1619 (s), 1605 (s), 1581 (s), 1569 (s), 1511 (m), 1483 (m), 1461 (m), 1437 (w), 1427 (s), 1382 (s), 1317 (s), 1309 (s), 1297 (s), 1250 (s), 1193 (m), 1178 (s), 1159 (s), 1135 (s), 1115 (s), 1095 (s), 1027 (s), 1010 (m), 982 (w), 967 (m), 950 (m), 924 (w), 889 (m), 881 (s), 861 (m), 858 (m), 823 (s), 797 (s), 747 (s), 719 (m), 707 (s), 687 (s),

**MS (EI+, 70 eV):**  $m/z$  (%) = 252.1 (18), 251.1 (100), 250.1 (64), 236.1 (41), 220.1 (23), 208.1 (18).

**HRMS (EI+, C<sub>16</sub>H<sub>13</sub>NO<sub>2</sub>):** calcd.: 251.0946; found: 251.0941 (M+).

**EA (C<sub>16</sub>H<sub>13</sub>NO<sub>2</sub>):** calcd.: N, 5.57; C, 76.48; H 5.21; found: N, 5.50; C, 76.54; H 5.43.

**(Z)-2-(4-(dimethylamino)benzylidene)indolin-3-one (11)**



To a nitrogen-flushed Schlenk flask, equipped with a magnetic stirring bar and rubber septum, aq. sodium hydroxide solution (3.74 g, 93.6 mmol, 1.5 M, 8.2 equiv.) degassed with nitrogen and 1*H*-indol-3-yl acetate (2.00 g, 11.4 mmol, 1.0 equiv.) were added and heated to 100 °C for 15 min. Then, 4-(dimethylamino)benzaldehyde (1.70 g, 11.42 mmol, 1.0 equiv.) suspended in methanol (11.4 mL, 1 M, degassed) was added to the solution at 0 °C and stirred for 3 d at 23 °C. The mixture was neutralized with 1 M aq. hydrochloric acid and extracted with ethyl acetate. The combined organic layers were dried over sodium sulfate and the solvents were removed *in vacuo*. Subsequent purification by flash column chromatography (silica, hexanes / ethyl acetate, 1 / 1, v / v) and recrystallization from ethanol / water yielded (Z)-2-(4-(dimethylamino)-benzylidene)indolin-3-one **11** (2.47 g, 9.36 mmol, 82%) as deep violet crystals.

$R_f$  = 0.30 (silica, hexanes / ethyl acetate, 4 / 1, v / v).

**m.p.** (°C): 235 - 236 (decomposition).

**<sup>1</sup>H-NMR (400 MHz, CD<sub>2</sub>Cl<sub>2</sub>):**  $\delta$  (ppm) = 7.68 (d, <sup>3</sup>*J* = 7.7 Hz, 1H, H-C(6)), 7.51 - 7.47 (m, 2H, H-C(12)), 7.5 (ddd, <sup>3</sup>*J* = 8.4 Hz, <sup>3</sup>*J* = 7.3 Hz, <sup>4</sup>*J* = 1.3 Hz, 1H, H-C(4)), 7.06 (d, <sup>3</sup>*J* = 8.1 Hz, 1H, H-C(3)), 6.96 (ddd, <sup>3</sup>*J* = 8.0 Hz, <sup>3</sup>*J* = 7.34 Hz, <sup>4</sup>*J* = 0.9 Hz, 1H, H-C(5)), 6.99 (s, br, 1H, H-N(1)), 6.81 (s, 1H, H-C(10)), 6.79 - 6.74 (m, 2H, H-C(13)), 3.03 (s, 6H, H-C(15)).

**$^{13}\text{C}$ -NMR (400 MHz,  $\text{CD}_2\text{Cl}_2$ ):**  $\delta$  (ppm) = 186.07 (C(8)), 153.22 (C(2)), 151.16 (C(14)), 135.74 (C(4)), 133.43 (C(9)), 131.90 (2C, C(12)), 124.78 (C(6)), 122.86 (C(7)), 122.54 (C(11)), 120.69 (C(5)), 114.05 (C(10)), 112.86 (2C, C(13)), 112.71 (C(3)), 40.48 (2C, C(15)).

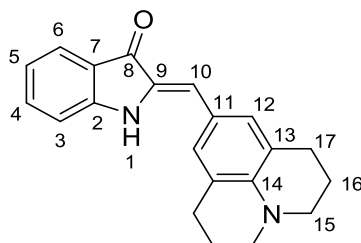
**IR (Diamond ATR):**  $\tilde{\nu}$  ( $\text{cm}^{-1}$ ) = 3227 (m), 3085 (w), 2919 (m), 2854 (m), 2817 (w), 2652 (w), 2551 (w), 2124 (w), 1997 (w), 1954 (w), 1922 (w), 1893 (w), 1656 (s), 1603 (s), 1548 (s), 1539 (s), 1524 (s), 1487 (s), 1462 (s), 1436 (m), 1392 (m), 1369 (s), 1319 (s), 1302 (m), 1262 (m), 1239 (m), 1230 (m), 1186 (s), 1157 (s), 1123 (s), 1097 (s), 1064 (s), 1011 (m), 965 (m), 947 (m), 932 (m), 893 (s), 857 (m), 828 (m), 807 (s), 790 (m), 781 (m), 753 (s), 727 (m), 707 (s), 687 (s).

**MS (EI+, 70 eV):**  $m/z$  (%) = 265.1 (19), 264.1 (100), 247.1 (14), 220.1 (21), 132.1 (9).

**HRMS (EI+,  $\text{C}_{17}\text{H}_{16}\text{N}_2\text{O}$ ):** calcd.: 264.1263; found: 264.1256 (M+).

**EA ( $\text{C}_{17}\text{H}_{16}\text{N}_2\text{O}$ ):** calcd.: N, 10.60; C, 77.25, H, 6.10; found: N, 10.38; C, 77.14, H 6.20.

**(Z)-2-((2,3,6,7-tetrahydro-1H,5H-pyrido[3,2,1-ij]quinolin-9-yl)methylene)indolin-3-one**  
**(15)**



To a nitrogen-flushed Schlenk flask, equipped with a magnetic stirring bar and rubber septum, aq. sodium hydroxide solution (0.41 g, 10.3 mmol, 1.5 M, 8.2 equiv.) degassed with nitrogen and 1H-indol-3-yl acetate (0.22 g, 1.26 mmol, 1.0 equiv.) were added and heated to 100 °C for 15 min. Then, 2,3,6,7-tetrahydro-1H,5H-pyrido[3,2,1-ij]quinoline-9-carbaldehyde (0.25 g, 1.26 mmol, 1.0 equiv.) suspended in methanol (4.2 mL, 0.3 M, degassed) was added to the solution at 0 °C and stirred for 3 d at 23 °C. The mixture was neutralized with 1 M aq. hydrochloric acid and extracted with ethyl acetate. The combined organic layers were dried over sodium sulfate and the solvents were removed *in vacuo*. Subsequent purification by flash column chromatography (silica, hexanes / ethyl acetate, 1 / 1, v / v) and recrystallization from ethanol / water yielded (Z)-2-(4-(dimethylamino)benzylidene)indolin-3-one **15** (0.28 g, 0.87 mmol, 69%) as deep red / green dichroic crystals.

$R_f = 0.14$  (silica, hexanes / ethyl acetate, 4 / 1, v / v).

**m.p.** (°C): 211- 212.

**$^1\text{H-NMR}$  (600 MHz,  $\text{CD}_2\text{Cl}_2$ ):**  $\delta$  (ppm) = 7.67 (d,  $^3J = 7.7$  Hz, 1H, H-C(6)), 7.45 (ddd,  $^3J = 8.2$  Hz,  $^3J = 7.2$  Hz,  $^4J = 1.1$  Hz, 1H, H-C(4)), 7.07 (d,  $^3J = 8.2$  Hz, 1H, H-C(3)), 7.03 (s, 2H, H-C(12)), 6.94 (dd,  $^3J = 7.5$  Hz,  $^3J = 7.4$  Hz, 1H, H-C(5)), 6.82 (s, br, 1H, H-N(1)), 6.72 (s, 1H, H-C(10)), 3.26 - 3.24 (m, 4H, H-C(15)), 2.77 (t, 4H, H-C(17)), 1.99 - 1.95 (m, 4H, H-C(16)).

**$^{13}\text{C-NMR}$  (151 MHz,  $\text{CD}_2\text{Cl}_2$ ):**  $\delta$  (ppm) = 185.86 (C(8)), 153.07 (C(2)), 144.54 (C(14)), 135.58 (C(4)), 132.94 (C(9)), 129.86 (2C, C(12)), 124.81 (C(6)), 123.17 (C(7)), 122.40 (2C, C(13)), 121.56 (C(11)), 120.68 (C(5)), 115.21 (C(10)), 112.83 (C(3)), 50.64 (2C, C(15)), 28.51 (2C, C(17)), 22.38 (2C, C(16)).

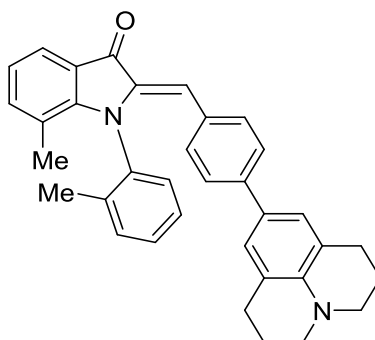
**IR (Diamond ATR):**  $\tilde{\nu}$  ( $\text{cm}^{-1}$ ) = 3230 (s), 2964 (w), 2942 (w), 2922 (m), 2836 (w), 2634 (w), 2128 (w), 1933 (w), 1906 (w), 1670 (m), 1621 (s), 1606 (s), 1569 (s), 1577 (s), 1516 (m), 1502 (s), 1486 (s), 1463 (s), 1443 (m), 1411 (m), 1391 (m), 1368 (s), 1338 (w), 1327 (m), 1313 (s), 1301 (s), 1278 (s), 1266 (s), 1213 (m), 1195 (m), 1181 (s), 1170 (s), 1150 (s), 1129 (s), 1097 (s), 1074 (s), 1050 (s), 1031 (m), 1012 (m), 1000 (s), 949 (m), 907 (s), 898 (s), 876 (s), 862 (s), 852 (m), 796 (m), 780 (m), 744 (s), 720 (m), 696 (s), 658 (s).

**MS (EI+, 70 eV):**  $m/z$  (%) = 317.2 (19), 316.2 (100), 315.2 (19).

**HRMS (EI+,  $\text{C}_{21}\text{H}_{20}\text{N}_2\text{O}$ ):** calcd.: 316.1576; found: 316.1571.

**EA ( $\text{C}_{21}\text{H}_{20}\text{N}_2\text{O}$ ):** calcd.: N, 8.85; C, 79.72, H, 6.37; found: N, 8.76; C, 79.72; H, 6.58.

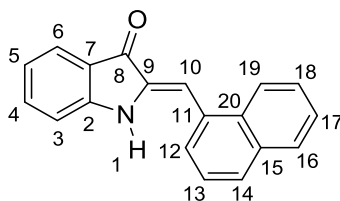
**(Z)-7-methyl-2-(4-(2,3,6,7-tetrahydro-1H,5H-pyrido[3,2,1-ij]quinolin-9-yl)benzylidene)-1-(o-tolyl)indolin-3-one (25)**



To a nitrogen-flushed Schlenk flask, equipped with a magnetic stirring bar and rubber septum, aq. sodium hydroxide solution (1.7 mL, 2.6 mmol, 1.5 M, 8.2 equiv.) degassed with nitrogen and 7-methyl-1-(*o*-tolyl)-1*H*-indol-3-yl acetate **19** (0.087 g, 0.31 mmol, 1.0 equiv.) were added and heated to 100 °C for 15 min and subsequently cooled to 23 °C. Then, 4-(2,3,6,7-tetrahydro-1*H*,5*H*-pyrido[3,2,1-*ij*]quinolin-9-yl)benzaldehyde **24** (0.086 g, 0.31 mmol, 1.0 equiv.) and dioxane (0.3 mL, 0.3 M, degassed) were added to the solution and it was stirred for 18 h at 23 °C. The mixture was neutralized with 1 M aq. hydrochloric acid, filtered through celite and extracted with ethyl acetate. The combined organic layers were dried over sodium sulfate and the solvents were removed *in vacuo*. Subsequent purification by flash column chromatography (aluminium(III) oxide, *Brockmann* III, 6% water, w / w, hexanes / ethyl acetate, 9 / 1, v / v) yielded crude (Z)-7-methyl-2-(4-(2,3,6,7-tetrahydro-1*H*,5*H*-pyrido[3,2,1-*ij*]quinolin-9-yl)benzylidene)-1-(*o*-tolyl)indolin-3-one **25** (0.030 g, 0.060 mmol, 19%) as orange solid. Purification via HPLC was omitted as the compound did not show sufficient red-shift of its absorption.

**MS (EI+, 70 eV):**  $m/z$  (%) = 498.3 (16), 497.3 (41), 496.3 (100), 495.3 (14), 263.2 (11), 262.2 (63), 223.1 (14).

**HRMS (EI+, C<sub>21</sub>H<sub>20</sub>N<sub>2</sub>O):** calcd.: 496.2515; found: 496.2508.

**(Z)-2-(naphthalen-1-ylmethylene)indolin-3-one (50)**

To a nitrogen-flushed Schlenk flask, equipped with a magnetic stirring bar and rubber septum, aq. sodium hydroxide solution (15.6 mL, 23.4 mmol, 1.5 M, 8.2 equiv., degassed with nitrogen) and 1*H*-indol-3-yl acetate (0.50 g, 2.85 mmol, 1.0 equiv.) were added and heated to 100 °C for 10 min. Then, 1-naphthaldehyde (0.45 g, 2.85 mmol, 1.0 equiv.) in methanol (0.41 mL, 6.9 M, degassed) was added to the solution at 0 °C and stirred for 3 h from 0 °C to 23 °C. The mixture was neutralized with 1 M aq. hydrochloric acid and extracted with ethyl acetate. The combined organic layers were dried over sodium sulfate and the solvents were removed *in vacuo*. Subsequent purification by flash column chromatography (silica, hexanes / ethyl acetate, 8 / 2, v / v) and recrystallization from ethanol / water yielded (Z)-2-(naphthalen-1-ylmethylene)indolin-3-one **50** (0.275 g, 0.101 mmol, 36%) as orange crystals.

$R_f$  = 0.42, (silica, hexanes / ethyl acetate, 8 / 2, v / v).

**m.p.** (°C): 215 (decomposition).

**<sup>1</sup>H-NMR (800 MHz, CDCl<sub>3</sub>):**  $\delta$  (ppm) = 8.15 (d,  $^3J$  = 8.3 Hz, 1H, H-C(19)), 7.89 (dd,  $^3J$  = 7.7 Hz,  $^4J$  = 1.6 Hz, 1H, H-C(16)), 7.86 (d,  $^3J$  = 8.2 Hz, 1H, H-C(14)), 7.78 (d,  $^3J$  = 7.7 Hz, 1H, H-C(6)), 7.74 (d,  $^3J$  = 7.0 Hz, 1H, H-C(12)), 7.58 - 7.54 (m, 3H, H-C(18, 13, 17)), 7.47 (s, 1H, H-C(10)), 7.46 (ddd,  $^3J$  = 8.2 Hz,  $^3J$  = 7.3 Hz,  $^4J$  = 1.3 Hz, 1H, H-C(4)), 6.96 (ddd,  $^3J$  = 7.7 Hz,  $^3J$  = 7.1 Hz,  $^4J$  = 0.6 Hz, 1H, H-C(5)), 6.92 (d,  $^3J$  = 8.0 Hz, 1 H, H-C(3)), 6.81 (s, 1H, H-N(1)).

**<sup>13</sup>C-NMR (201 MHz, CDCl<sub>3</sub>):**  $\delta$  (ppm) = 186.15 (C(8)), 153.21 (C(7)), 136.91 (C(9)), 136.37 (C(4)), 134.04 (C(15)), 132.05 (C(20)), 131.87 (C(11)), 129.26 (C(14)), 128.88 (C(16)), 126.99 (C(18)), 126.97 (C(12)), 126.66 (C(17)), 125.62 (C(13)), 125.31 (C(6)), 124.57 (C(19)), 121.98 (C(2)), 120.58 (C(5)), 111.81 (C(3)), 108.50 (C(10)).

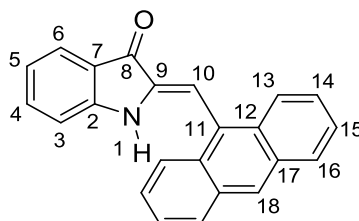
**IR (Diamond ATR):**  $\tilde{\nu}$  (cm<sup>-1</sup>) = 3350 (m), 3042 (w), 2921 (w), 1912 (w), 1688 (s), 1628 (s), 1591 (s), 1506 (m), 1489 (s), 1470 (s), 1405 (m), 1379 (s), 1366 (s), 1337 (s), 1314 (s), 1294 (s), 1252 (s), 1212 (w), 1198 (s), 1157 (s), 1135 (s), 1095 (s), 1021 (w), 957 (w), 889 (w), 873 (w), 849 (w), 837 (w), 812 (w), 788 (s), 763 (s), 743 (s), 699 (s), 678 (m), 655 (m).

**MS (EI+, 70 eV):**  $m/z$  (%) = 272.1 (19), 271.1 (82), 270.1 (100), 254.1 (13), 241.1 (19), 44.1 (12), 41.3 (15).

**HRMS (EI-, C<sub>19</sub>H<sub>13</sub>NO):** calcd.: 271.0997; found: 270.0914 (M-H<sup>+</sup>).

**EA (C<sub>19</sub>H<sub>13</sub>NO):** calcd.: C, 84.11; H, 4.83; N, 5.16; found: C, 84.28; N, 5.16; H 4.86.

**(Z)-2-(anthracen-9-ylmethylene)indolin-3-one (51)**



To a nitrogen-flushed Schlenk flask, equipped with a magnetic stirring bar and rubber septum, aq. sodium hydroxide solution (63.0 mL, 93.6 mmol, 1.5 M, 8.2 equiv., degassed with nitrogen) and 1*H*-indol-3-yl acetate (2.00 g, 11.4 mmol, 1.0 equiv.) were added and heated to 100 °C for 10 min. Then, 9-anthracenecarboxaldehyde (2.35 g, 11.4 mmol, 1.0 equiv.) in methanol (12 mL, 1.0 M, degassed) was added to the solution at 0 °C and stirred for 18 h from 0 °C to 23 °C. The mixture was neutralized with 1 M aq. hydrochloric acid and extracted with ethyl acetate. The combined organic layers were dried over sodium sulfate and the solvents were removed *in vacuo*. Subsequent purification by flash column chromatography (silica, hexanes / ethyl acetate 8 / 2, v / v) and recrystallization from ethanol / water yielded (Z)-2-(anthracen-9-ylmethylene)indolin-3-one **51** (2.93 g, 9.12 mmol, 80%) as orange crystals.

$R_f$  = 0.46 (silica, hexanes / ethyl acetate 8 / 2, v / v).

**m.p.** (°C): 255 °C.

**<sup>1</sup>H-NMR (800 MHz, CDCl<sub>3</sub>):**  $\delta$  (ppm) = 8.51 (s, 1H, H-C(18)), 8.14 - 8.13 (m, 2H, H-C(13)), 8.08 - 8.06 (m, 2H, H-C(16)), 7.80 (d, <sup>3</sup> $J$  = 7.7 Hz, 1H, H-C(6)), 7.73 (s, 1H, H-C(10)), 7.54 - 7.51 (m, 4H, H-C(14, 15)), 7.40 (ddd, <sup>3</sup> $J$  = 8.2 Hz, <sup>3</sup> $J$  = 6.9 Hz, <sup>4</sup> $J$  = 1.3 Hz, 1H, H-C(4)), 6.94 (dd, <sup>3</sup> $J$  = 7.5 Hz, <sup>3</sup> $J$  = 7.4 Hz, 1H, H-C(5)), 6.71 (d, <sup>3</sup> $J$  = 8.0 Hz, 1H, H-C(3)), 6.10 (s, 1H, H-N(1)).

**<sup>13</sup>C-NMR (201 MHz, CDCl<sub>3</sub>):**  $\delta$  (ppm) = 185.58 (C(8)), 152.87 (C(7)), 138.37(C(9)), 136.57 (C(4)), 131.59 (2C, C(17)), 129.77 (2C, C(12)), 129.22 (2C, C(16)), 128.35 (C(18)), 127.74

(C(11)), 126.74 (2C, C(15)), 125.86 (2C, C(13)), 125.73 (2C, C(14)), 125.34 (C(6)), 121.75 (C(2)), 120.38 (C(5)), 111.51 (C(3)), 107.79 (C(10)).

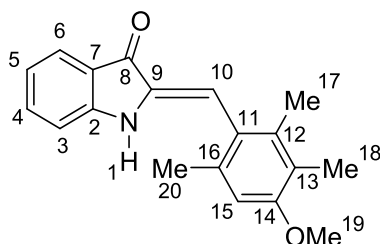
**IR (Diamond ATR):**  $\tilde{\nu}$  (cm<sup>-1</sup>) = 3426 (w), 3272 (m), 3047 (w), 2970 (w), 2925 (w), 2879 (w), 2360 (w), 1682 (s), 1669 (m), 1616 (s), 1587 (s), 1520, (w), 1485 (s), 1465 (s), 1442 (m), 1382 (m), 1363 (w), 1336 (m), 1310 (s), 1248 (s), 1195 (m), 1155 (s), 1127 (s), 1096 (s), 1037 (m), 1016 (m), 972 (w), 947 (m), 929 (w), 890 (m), 878 (s), 846 (w), 830 (m), 798 (w), 758 (m), 748 (s), 727 (s), 706 (s), 655 (m).

**MS (EI+, 70 eV):**  $m/z$  (%) = 322.1 (20), 321.1 (100), 320.1 (64), 319.1 (11), 304.1 (32), 292.1 (14), 291.1 (19), 290.1 (11), 202.1 (21), 160.6 (11), 160.1 (12), 145.5 (12).

**HRMS (EI+, C<sub>23</sub>H<sub>15</sub>NO):** calcd.: 321.1154; found: 321.1158 (M+).

**EA (C<sub>23</sub>H<sub>15</sub>NO):** calcd.: C, 85.96; H, 4.70; N, 4.36; found: C, 85.59; H, 4.84; N, 4.28.

**(Z)-2-(4-methoxy-2,3,6-trimethylbenzylidene)indolin-3-one (52)**



To a nitrogen-flushed Schlenk flask, equipped with a magnetic stirring bar and rubber septum, aq. sodium hydroxide solution (6.24 mL, 9.36 mmol, 1.5 M, 8.2 equiv., degassed with nitrogen) and 1*H*-indol-3-yl acetate (0.20 g, 1.14 mmol, 1.0 equiv.) were added and heated to 100 °C for 10 min. Then, 4-methoxy-2,3,6-trimethylbenzaldehyde (0.20 g, 1.14 mmol, 1.0 equiv.) in methanol (1.7 mL, 1.0 M, degassed) was added to the solution at 0 °C and stirred for 18 h from 0 °C to 23 °C. The mixture was neutralized with 1 M aq. hydrochloric acid and extracted with ethyl acetate. The combined organic layers were dried over sodium sulfate and the solvents were removed *in vacuo*. Subsequent purification by flash column chromatography (silica, hexanes / ethyl acetate, 85 / 15, v / v) and recrystallization from ethanol / water yielded (Z)-2-(4-methoxy-2,3,6-trimethylbenzylidene)indolin-3-one **52** (0.234 g, 0.798 mmol, 71%) as orange crystals.

$R_f$  = 0.46 (silica, hexanes / ethyl acetate, 85 / 15, v / v).



**m.p. (°C):** 188 - 190 °C.

**<sup>1</sup>H-NMR (800 MHz, CD<sub>2</sub>Cl<sub>2</sub>):**  $\delta$  (ppm) = 7.63 (d, <sup>3</sup>J = 7.8 Hz, 1H, H-C(6)), 7.4 (ddd, <sup>3</sup>J = 8.2 Hz, <sup>3</sup>J = 7.3 Hz, <sup>4</sup>J = 1.3 Hz, 1H, H-C(4)), 6.89 (ddd, <sup>3</sup>J = 7.8 Hz, <sup>3</sup>J = 7.3 Hz, <sup>4</sup>J = 0.7 Hz, 1H, H-C(5)), 6.87 - 6.86 (m, 2H, H-C(3), H-C(10)), 6.66 (s, 1H, H-C(15)), 6.42 (s, 1H, H-N(1)), 3.81 (s, 3H, H-C(19)), 2.26 (s, 3H, H-C(20)), 2.20 (s, 3H, H-C(17)), 2.14 (s, 3H, H-C(18)).

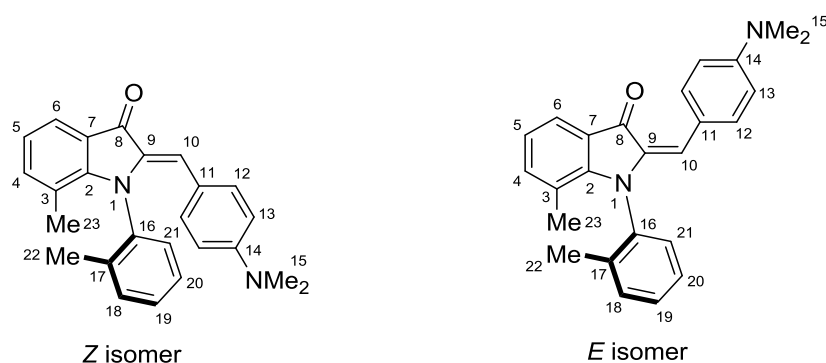
**<sup>13</sup>C-NMR (201 MHz, CD<sub>2</sub>Cl<sub>2</sub>):**  $\delta$  (ppm) = 185.79 (C(8)), 157.80 (C(14)), 153.56 (C(2)), 137.52 (C(16)), 136.83 (C(12)), 136.63 (C(4)), 135.43 (C(9)), 125.38 (C(11)), 125.08 (C(6)), 123.42 (C(13)), 122.38 (C(7)), 120.23 (C(5)), 112.00 (C(3)), 111.96 (C(10)), 110.48 (C(15)), 55.99 (C(19)), 21.13 (C(20)), 17.80 (C(17)), 12.03 (C(18)).

**IR (Diamond ATR):**  $\tilde{\nu}$  (cm<sup>-1</sup>) = 3403 (m), 3355 (w), 3046 (w), 3015 (w), 2920 (m), 2835 (w), 2359 (w), 1695 (s), 1632 (s), 1607 (s), 1468 (s), 1379 (s), 1353 (s), 1307 (s), 1283 (s), 1243 (m), 1229 (s), 1160 (m), 1136 (s), 1111 (s), 1012 (w), 992 (m), 957 (m), 886 (m), 832 (s), 750 (s), 702 (s), 675 (w).

**MS (EI+, 70 eV):** m/z (%) = 294.1 (11), 293.1 (39), 292.1 (20), 279.1 (17), 278.1 (100), 276.1 (58), 261.1 (28), 234.1 (14), 218.1 (12), 85.9 (14), 55.0 (13), 44.0 (96).

**HRMS (EI+, C<sub>19</sub>H<sub>19</sub>NO<sub>2</sub>):** calcd.: 293.1416; found: 293.1393 (M+).

**EA (C<sub>19</sub>H<sub>19</sub>NO<sub>2</sub>):** calcd.: C, 77.79; H, 6.53; N, 4.77; found: C, 77.64; H, 6.53; N, 4.65.

**(*R<sub>a</sub>/S<sub>a</sub>*)-(Z/E)-2-(4-(dimethylamino)benzylidene)-7-methyl-1-(*o*-tolyl)indolin-3-one (20)**

To a nitrogen-flushed Schlenk flask equipped with a magnetic stirring bar and a rubber septum 7-methyl-1-(*o*-tolyl)-1*H*-indol-3-yl acetate **19** (0.106 g, 0.379 mmol, 1.0 equiv.), 4-(dimethylamino)benzaldehyde (0.063 g, 0.422 mmol, 1.0 equiv.), aq. sodium hydroxide solution (0.124 g, 3.11 mmol, 1.5 M, 2.07 mL, 8.2 equiv., degassed with N<sub>2</sub>) and dioxane (0.4 mL, 1 M, degassed) were added and the resulting mixture was heated to 100 °C for 30 min. The mixture was cooled to 23 °C, neutralized with aq. hydrochloric acid (1.0 M), extracted with ethyl acetate and washed with brine. The combined organic phases were dried over sodium sulfate and the volatiles were removed *in vacuo*. Subsequent purification by flash column chromatography (aluminium(III) oxide, *Brockmann* III, 6% water, w / w), hexanes / ethyl acetate, 4 / 1, v / v) yielded (*R<sub>a</sub>/S<sub>a</sub>*)-(Z/E)-2-(4-(dimethylamino)benzylidene)-7-methyl-1-(*o*-tolyl)indolin-3-one **20** (0.129 g, 0.351 mmol, 93%) as deep red solid. Further purification was carried out via preparative HPLC (*Machery-Nagel* VP 250/21 *NUCLEODUR Sphinx* RP 5 μm column, acetonitrile / water, 4 / 1, v / v, 15 mL/min, 35 °C column temperature, retention times: 12.5 min, *E* isomer, 17.3 mg; 17% isolated yield).

$R_f = 0.18$  (silica, hexanes / ethyl acetate, 8 / 2, v / v).

**m.p.** (°C): 169 - 171 (decomposition).

**Z isomer:**

**<sup>1</sup>H-NMR (600 MHz, CD<sub>2</sub>Cl<sub>2</sub>):** δ (ppm) = 7.43 - 7.39 (m, 1H, H-C(20)), 7.37 (d, <sup>3</sup>*J* = 7.7 Hz, 1H, H-C(18)), 7.36 - 7.34 (m, 1H, H-C(21)), 7.34 - 7.32 (m, 1H, H-C(19)), 7.29 (d, <sup>3</sup>*J* = 7.6 Hz, 1H, H-C(6)), 7.20 (d, <sup>3</sup>*J* = 7.6 Hz, 1H, H-C(4)), 6.98 (s, 1H, H-C(10)), 6.86 (t, <sup>3</sup>*J* = 7.5, 1H, H-C(5)), 6.62 - 6.58 (m, 2H, H-C(12)), 6.30 - 6.27 (m, 2H, H-C(13)), 2.88 (s, 6H, H-C(15)), 2.03 (s, 3H, H-C(22)), 1.65 (s, 3H, H-C(23)).

**$^{13}\text{C-NMR}$  (201 MHz,  $\text{CD}_2\text{Cl}_2$ ):**  $\delta$  (ppm) = 186.53 (C(8)), 152.11 (C(2)), 150.36 (C(14)), 140.69 (C(16)), 139.56 (C(17)), 139.36 (C(4)), 134.96 (C(9)), 132.47 (2C, C(12)), 131.98 (C(21)), 131.10 (C(18)), 129.36 (C(19)), 126.83 (C(20)), 122.77 (C(6)), 122.69 (C(7)), 122.54 (C(3)), 121.00 (C(11)), 120.53 (C(5)), 116.27 (C(10)), 111.47 (2C, C(13)), 40.41 (2C, C(15)), 19.15 (C(23)), 18.06 (C(22)).

***E* isomer:**

**$^1\text{H-NMR}$  (600 MHz,  $\text{CD}_2\text{Cl}_2$ ):**  $\delta$  (ppm) = 8.08 - 8.04 (m, 2H, H-C(12)), 7.62 (d,  $^3J = 7.9$  Hz, 1H, H-C(6)), 7.43 - 7.39 (m, 1H, H-C(20)), 7.37 (d,  $^3J = 7.7$  Hz, 1H, H-C(18)), 7.36 - 7.34 (m, 1H, H-C(21)), 7.34 - 7.32 (m, 1H, H-C(19)), 7.15 (d,  $^3J = 7.4$  Hz, 1H, H-C(4)), 6.81 (t,  $^3J = 7.4$ , 1H, H-C(5)), 6.67 - 6.63 (m, 2H, H-C(13)), 5.89 (s, 1H, H-C(10)), 3.01 (s, 6H, H-C(15)), 2.14 (s, 3H, H-C(22)), 1.64 (s, 3H, H-C(23)).

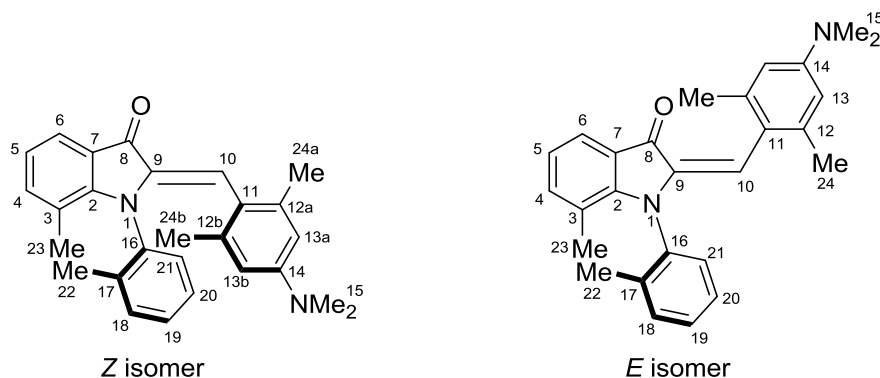
**$^{13}\text{C-NMR}$  (151 MHz,  $\text{CD}_2\text{Cl}_2$ ):**  $\delta$  (ppm) = 183.61 (C(8)), 151.45 (C(2)), 150.10 (C(14)), 139.51 (C(16)), 138.75 (C(17)), 137.85 (C(4)), 136.81 (C(9)), 132.89 (2C, C(12)), 131.49 (C(19)), 131.16 (C(18)), 129.26 (C(20)), 127.33 (C(21)), 123.05 (C(7)), 122.79 (C(10)), 122.70 (C(11)), 122.31 (C(6)), 121.58 (C(3)), 119.15 (C(5)), 111.40 (2C, C(13)), 40.26 (2C, C(15)), 18.16 (C(23)), 17.70 (C(22)).

**IR (Diamond ATR):**  $\tilde{\nu}$  ( $\text{cm}^{-1}$ ) = 2897 (w), 1655 (s), 1591 (s), 1553 (s), 1522 (s), 1489 (s), 1447 (s), 1391 (s), 1367 (s), 1348 (s), 1323 (s), 1278 (s), 1244 (m), 1212 (m), 1196 (s), 1147 (m), 1102 (m), 1027 (s), 986 (m), 933 (m), 899 (w), 868 (w), 823 (m), 755 (s), 731 (w), 670 (w).

**MS (EI+, 70 eV):**  $m/z$  (%) = 369.2 (26), 368.2 (100), 367.2 (26), 184.6 (11), 44.0 (16).

**HRMS (EI+,  $\text{C}_{25}\text{H}_{24}\text{N}_2\text{O}$ ):** calcd.: 368.1889; found: 368.1875 (M+).

**(*R<sub>a</sub>/S<sub>a</sub>*)-(Z/E)-2-(4-(dimethylamino)-2,6-dimethylbenzylidene)-7-methyl-1-(*o*-tolyl)-indolin-3-one (30)**



To a nitrogen-flushed Schlenk flask, equipped with a magnetic stirring bar and rubber septum, aq. sodium hydroxide solution (0.117 g, 2.94 mmol, 1.5 M, 2.00 mL, 8.2 equiv., degassed with N<sub>2</sub>), 7-methyl-1-(*o*-tolyl)-1*H*-indol-3-yl acetate **19** (0.100 g, 0.358 mmol, 1.0 equiv.), 4-(dimethylamino)-2,6-dimethylbenzaldehyde (0.063 g, 0.358 mmol, 1.0 equiv.), and dioxane (0.36 mL, 1 M, degassed) were added and the mixture was heated to 100 °C for 18 h. After cooling to 23 °C, the mixture was neutralized with aq. hydrochloric acid (1.0 M), extracted with ethyl acetate and washed with brine. The combined organic phases were dried over sodium sulfate and the volatiles were removed *in vacuo*. Subsequent purification by flash column chromatography (aluminium(III) oxide, *Brockmann* III, 6% water, w / w), hexanes / ethyl acetate, 4 / 1, v / v) yielded (*R<sub>a</sub>/S<sub>a</sub>*)-(Z/E)-2-(4-(dimethylamino)-2,6-dimethylbenzylidene)-7-methyl-1-(*o*-tolyl)indolin-3-one **30** (0.064 g, 0.161 mmol, 45%) as orange to red solid. Further purification was carried out via preparative HPLC (*Machery-Nagel* VP 250/21 *NUCLEODUR Sphinx* RP 5 μm column, acetonitrile / water, 8 / 2, v / v, 15 mL/min, 35 °C column temperature, retention times: 15.0 min, Z+E isomer, 14.1 mg; 16% isolated yield).

*R<sub>f</sub>* = 0.43 (silica, hexanes / ethyl acetate, 4 / 1, v / v).

**m.p.** (°C): 60 - 70.

**Z isomer:**

**<sup>1</sup>H-NMR (400 MHz, CD<sub>2</sub>Cl<sub>2</sub>):** δ (ppm) = 7.63 (d, <sup>3</sup>*J* = 7.5 Hz, 1H, H-C(6)), 7.17 (d, <sup>3</sup>*J* = 7.3 Hz, 1H, H-C(4)), 6.99 (d, <sup>3</sup>*J* = 8.1 Hz, 1H, H-C(21)), 6.97 (s, 1H, H-C(10)), 6.94 (t, <sup>3</sup>*J* = 7.2 Hz, 1H, H-C(19)), 6.92 - 6.90 (m, 1H, H-C(18)), 6.90 - 6.88 (m, 1H, H-C(5)), 6.72 (t, <sup>3</sup>*J* = 7.4 Hz, 1H, H-C(20)), 6.22 (d, <sup>3</sup>*J* = 2.3 Hz, 1H, H-C(13a)), 6.02 (d, <sup>3</sup>*J* = 2.2 Hz, 1H, H-C(13b)),

2.80 (s, 6H, H-C(15)), 2.16 (s, 3H, H-C(24a)), 1.87 (s, 3H, H-C(22)), 1.85 (s, 3H, H-C(24b)), 1.55 (s, 3H, H-C(23)).

**<sup>13</sup>C-NMR (151 MHz, CD<sub>2</sub>Cl<sub>2</sub>):**  $\delta$  (ppm) = 186.68 (C(8)), 154.56 (C(2)), 150.71 (C(14)), 140.97 (C(9)), 139.51 (C(16)), 139.45 (C(4)), 137.39 (C(17)), 137.01 (C(12a)), 136.88 (C(12b)), 131.55 (C(21)), 130.30 (C(18)), 128.30 (C(19)), 125.99 (C(20)), 123.66 (C(3)), 123.17 (C(7)), 122.88 (C(6)), 121.99 (C(11)), 121.11 (C(5)), 115.67 (C(10)), 112.02 (C(13a)), 111.95 (C(13b)), 41.11 (C(15)), 21.64 (C(24a)), 21.04 (C(24b)), 18.49 (C(23)), 18.13 (C(22)).

***E* isomer:**

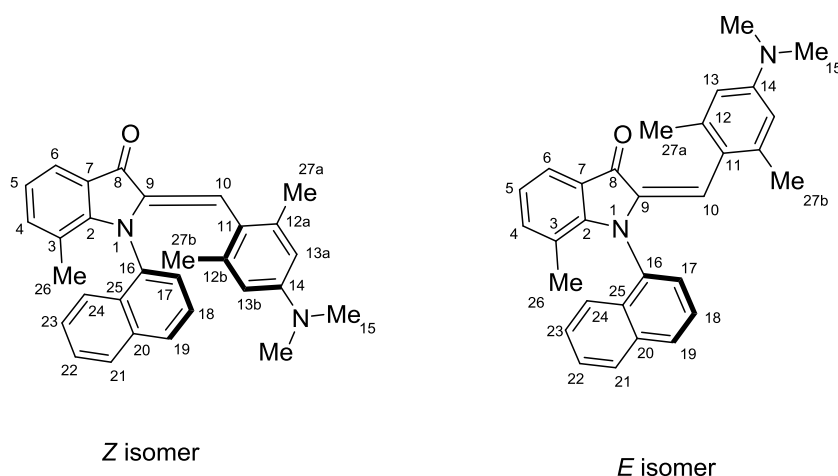
**<sup>1</sup>H-NMR (600 MHz, CD<sub>2</sub>Cl<sub>2</sub>):**  $\delta$  (ppm) = 7.52 (d, <sup>3</sup>J = 7.6 Hz, 1H, H-C(6)), 7.41 - 7.38 (m, 1H, H-C(19)), 7.40 - 7.37 (m, 1H, H-C(18)), 7.38 - 7.35 (m, 1H, H-C(21)), 7.35 - 7.33 (m, 1H, H-C(20)), 7.17 (d, <sup>3</sup>J = 7.4 Hz, 1H, H-C(4)), 6.81 (t, <sup>3</sup>J = 7.4 Hz, 1H, H-C(5)), 6.43 (s, 2H, H-C(13)), 5.84 (s, 1H, H-C(10)), 2.93 (s, 6H, H-C(15)), 2.25 (s, 3H, H-C(22)), 2.12 (s, br, 6H, H-C(24)), 1.68 (s, 3H, H-C(23)).

**<sup>13</sup>C-NMR (151 MHz, CD<sub>2</sub>Cl<sub>2</sub>):**  $\delta$  (ppm) = 184.96 (C(8)), 151.60 (C(2)), 150.38 (C(14)), 139.47 (C(9)), 139.26 (C(16)), 139.05 (C(17)), 138.73 (C(4)), 138.42 (C(12)), 131.42 (2C, C(18)), 130.98 (C(21)), 129.38 (C(19)), 127.67 (C(20)), 122.98 (C(7)), 122.48 (C(6)), 122.12 (C(11)), 121.82 (C(3)), 119.80 (C(5)), 116.56 (C(5)), 111.82 (C(10)), 40.77 (2C, C(15)), 21.19 (br, 2C, C(24)), 18.28 (C(23)), 17.94 (C(22)).

**IR (Diamond ATR):**  $\tilde{\nu}$  (cm<sup>-1</sup>) = 2918 (m), 2777 (m), 1691 (w), 1665 (m), 1652 (m), 1590 (s), 1540 (m), 1490 (m), 1456 (m), 1441 (m), 1421 (m), 1383 (w), 1355 (s), 1323 (m), 1281 (m), 1268 (m), 1242 (m), 1220 (m), 1191 (w), 1143 (s), 1070 (m), 1033 (m), 988 (w), 931 (w), 877 (w), 855 (w), 823 (s), 781 (s), 753 (m), 725 (w), 711(w).

**MS (EI+, 70 eV):**  $m/z$  (%) = 396.2 (47), 382.2 (13), 381.2 (24), 380.2 (24), 379.2 (72), 365.2 (19), 364.2 (30), 335.2 (17), 177.1 (14), 176.1 (26), 44.2 (100), 43.3 (16).

**HRMS (EI+, C<sub>27</sub>H<sub>28</sub>N<sub>2</sub>O):** calcd.: 396.2201; found: 396.2213 (M+).

**(*R<sub>a</sub>/S<sub>a</sub>*)-(Z/E)-2-(4-(dimethylamino)-2,6-dimethylbenzylidene)-7-methyl-1-(naphthalen-1-yl)indolin-3-one (33)**

To a nitrogen-flushed Schlenk flask, equipped with a magnetic stirring bar and rubber septum, aq. sodium hydroxide solution (0.119 g, 2.96 mmol, 1.5 M, 2.00 mL, 8.2 equiv., degassed with N<sub>2</sub>), 7-methyl-1-(naphthalen-1-yl)-1*H*-indol-3-yl acetate **32** (0.114 g, 0.361 mmol, 1.0 equiv.), 4-(dimethylamino)-2,6-dimethylbenzaldehyde (0.064 g, 0.361 mmol, 1.0 equiv.), and dioxane (0.36 mL, 1 M, degassed) were added and the mixture was heated to 100 °C for 18 h. After cooling to 23 °C, the mixture was neutralized with aq. hydrochloric acid (1.0 M), extracted with ethyl acetate and washed with brine. The combined organic phases were dried over sodium sulfate and the volatiles were removed *in vacuo*. Subsequent purification by flash column chromatography (aluminium(III) oxide, *Brockmann* III, 6% water, w / w), hexanes / ethyl acetate, 4 / 1, v / v) yielded (*R<sub>a</sub>/S<sub>a</sub>*)-(Z/E)-2-(4-(dimethylamino)-2,6-dimethylbenzylidene)-7-methyl-1-(naphthalen-1-yl)indolin-3-one **33** (0.076 g, 0.174 mmol, 47%) as orange to red solid. Further purification was carried out via preparative HPLC (*Machery-Nagel* VP 250/21 *NUCLEODUR Sphinx* RP 5 μm column, acetonitrile / water, 4 / 1, v / v, 15 mL/min, 35 °C column temperature, retention times: 9.5 min, Z+E isomer, 67.6 mg; 43% isolated yield).

*R<sub>f</sub>* = 0.54 (silica, hexanes / ethyl acetate, 4 / 1, v / v).

**m.p.** (°C): 141 - 150.

**Z isomer:**

**<sup>1</sup>H-NMR (600 MHz, CD<sub>2</sub>Cl<sub>2</sub>):** δ (ppm) = 7.79 (d, <sup>3</sup>*J* = 7.9 Hz, 1H, H-C(6)), 7.71 (d, <sup>3</sup>*J* = 7.2 Hz, 1H, H-C(21)), 7.56 - 7.53 (m, 1H, H-C(24)), 7.54 - 7.51 (m, 1H, H-C(19)), 7.39 (ddd, <sup>3</sup>*J* = 8.1 Hz, <sup>3</sup>*J* = 6.8 Hz, <sup>4</sup>*J* = 1.2 Hz, 1H, H-C(22)), 7.30 (ddd, <sup>3</sup>*J* = 8.3 Hz, <sup>3</sup>*J* = 6.7 Hz, <sup>4</sup>*J* =

1.2 Hz, 1H, H-C(23)), 7.30 (dd,  $^3J = 8.6$  Hz,  $^4J = 1.3$  Hz, 1H, H-C(17)), 7.13 (d,  $^3J = 7.3$  Hz, 1H, H-C(4)), 7.07 (dd,  $^3J = 8.3$  Hz,  $^3J = 7.3$  Hz, 1H, H-C(18)), 6.95 (s, 1H, H-C(10)), 6.93 (dd,  $^3J = 7.5$  Hz,  $^3J = 7.4$  Hz, 1H, H-C(5)), 6.05 (d,  $^4J = 2.6$  Hz, 1H, H-C(13a)), 5.60 (d,  $^4J = 2.5$  Hz, 1H, H-C(13b)), 2.72 (s, 6H, H-C(15)), 2.11 (s, 3H, H-C(27a)), 1.39 (s, 3H, H-C(26)), 1.37 (s, 3H, H-C(27b)).

**$^{13}\text{C-NMR}$  (151 MHz,  $\text{CD}_2\text{Cl}_2$ ):**  $\delta$  (ppm) = 186.60 (C(8)), 155.05 (C(2)), 150.25 (C(14)), 141.57 (C(9)), 139.63 (C(4)), 137.16 (C(16)), 136.71 (C(12a)), 136.24 (C(12b)), 134.36 (C(20)), 132.43 (C(25)), 128.89 (C(19)), 128.63 (C(21)), 128.62 (C(17)), 126.77 (C(23)), 126.38 (C(22)), 125.25 (C(18)), 123.70 (C(24)), 123.63 (C(3)), 123.10 (C(7)), 122.94 (C(6)), 121.57 (C(11)), 121.19 (C(5)), 115.90 (C(10)), 111.83 (C(13a)), 111.80 (C(13b)), 40.98 (2C, C(15)), 21.63 (C(27a)), 20.60 (C(27b)), 18.76 (C(26)).

***E* isomer:**

**$^1\text{H-NMR}$  (600 MHz,  $\text{CD}_2\text{Cl}_2$ ):**  $\delta$  (ppm) = 8.01 (d,  $^3J = 7.8$  Hz, 1H, H-C(21)), 7.99 (d,  $^3J = 7.9$  Hz, 1H, H-C(19)), 7.87 (d,  $^3J = 8.2$  Hz, 1H, H-C(24)), 7.66 - 7.63 (m, 1H, H-C(23)), 7.64 - 7.60 (m, 1H, H-C(18)), 7.59 (d,  $^3J = 7.6$  Hz, 1H, H-C(6)), 7.56 (ddd,  $^3J = 8.1$  Hz,  $^3J = 6.7$  Hz,  $^4J = 1.4$  Hz, 1H, H-C(22)), 7.51 (ddd,  $^3J = 8.5$  Hz,  $^3J = 7.1$  Hz,  $^4J = 1.2$  Hz, 1H, H-C(17)), 7.15 (d,  $^3J = 7.3$  Hz, 1H, H-C(4)), 6.86 (dd,  $^3J = 7.5$  Hz,  $^3J = 7.5$  Hz, 1H, H-C(5)), 6.38 (s, 2H, H-C(13)), 5.84 (s, 1H, H-C(13)), 2.91 (s, 6H, H-C(15)), 2.07 (s, br, 3H, H-C(27a)), 2.02 (s, br, 3H, H-C(27b)), 1.48 (s, 3H, H-C(26)).

**$^{13}\text{C-NMR}$  (151 MHz,  $\text{CD}_2\text{Cl}_2$ ):**  $\delta$  (ppm) = 184.98 (C(8)), 152.41 (C(2)), 150.37 (C(14)), 140.77 (C(9)), 138.78 (C(4)), 138.41 (br, 2C, C(12)), 137.19 (C(16)), 134.96 (C(20)), 133.17 (C(25)), 129.58 (C(21)), 129.11 (C(19)), 128.75 (C(23)), 127.83 (C(17)), 127.26 (C(22)), 126.26 (C(18)), 123.69 (C(24)), 123.25 (C(3)), 122.50 (C(6)), 122.11 (C(7)), 121.97 (C(11)), 120.11 (C(5)), 117.57 (C(10)), 111.74 (2C, C(13)), 40.73 (2C, C(15)), 21.10 (2C, C(27)), 18.40 (C(26)).

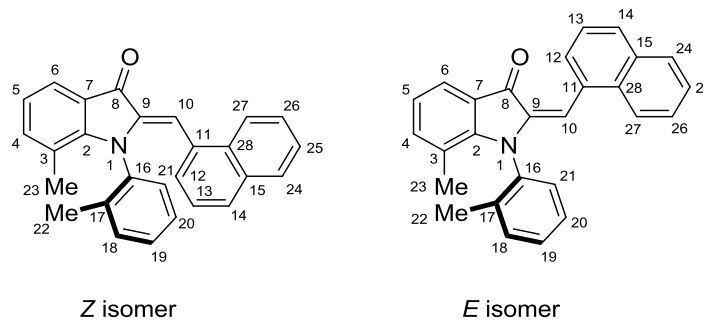
**IR (Diamond ATR):**  $\tilde{\nu}$  ( $\text{cm}^{-1}$ ) = 2912 (w), 2226 (w), 1690 (s), 1623 (m), 1600 (s), 1490 (s), 1456 (m), 1415 (m), 1394 (m), 1357 (s), 1309 (m), 1278 (s), 1245 (m), 1208 (m), 1172 (m), 1133 (s), 1077 (s), 1051 (m), 1031 (s), 988 (m), 936 (w), 900 (w), 890 (w), 827 (m), 796 (m), 775 (s), 755 (s), 714 (m), 698 (w).

**MS (EI+, 70 eV):**  $m/z$  (%) = 433.2 (23), 432.2 (55), 418.2 (11), 417.2 (35), 416.2 (34), 415.2 (100), 401.2 (18), 400.2 (25), 371.2 (18), 260.1 (15).

**HRMS (EI<sup>+</sup>, C<sub>30</sub>H<sub>28</sub>N<sub>2</sub>O):** calcd.: 432.2202; found: 432.2197 (M<sup>+</sup>).

**EA (C<sub>30</sub>H<sub>28</sub>N<sub>2</sub>O):** calcd.: N, 6.48; C, 83.30; H, 6.52; found: N, 6.42; C, 83.44; H, 6.34.

**(R<sub>a</sub>/S<sub>a</sub>)-(Z/E)-7-methyl-2-(naphthalen-1-ylmethylene)-1-(o-tolyl)indolin-3-one (60)**



To a nitrogen-flushed Schlenk flask, equipped with a magnetic stirring bar and rubber septum, aq. sodium hydroxide solution (0.117 g, 2.94 mmol, 1.5 M, 2.00 mL, 8.2 equiv., degassed with N<sub>2</sub>), 7-methyl-1-(*o*-tolyl)-1*H*-indol-3-yl acetate **19** (0.100 g, 0.358 mmol, 1.0 equiv.), 1-naphthaldehyde (0.056 g, 0.358 mmol, 1.0 equiv.) and dioxane (0.36 mL, 1 M, degassed) were added and the mixture was heated to 100 °C for 5 h. After cooling to 23 °C, the mixture was neutralized with aq. hydrochloric acid (1.0 M), extracted with ethyl acetate and washed with brine. The combined organic phases were dried over sodium sulfate and the volatiles were removed *in vacuo*. Subsequent purification by flash column chromatography (aluminium(III) oxide, *Brockmann* III, 6% water, w / w), hexanes / ethyl acetate, 4 / 1, v / v yielded (R<sub>a</sub>/S<sub>a</sub>)-(Z/E)-7-methyl-2-(naphthalen-1-ylmethylene)-1-(*o*-tolyl)indolin-3-one **60** (0.128 g, 0.342 mmol, 96%) as deep red solid. Further purification was carried out via preparative HPLC (*Machery-Nagel* VP 250/21 *NUCLEODUR Sphinx* RP 5 μm column, acetonitrile / water, 4 / 1, v / v, 15 mL/min, 35 °C column temperature, retention times: 18.5 min, *Z* isomer, 6.3 mg; 20.2 min, *E* isomer, 14.9 mg; 18.5 - 23.0 min, *Z+E* isomer, 37.4 mg; 67% overall yield.

**R<sub>f</sub>** = 0.63 (silica, hexanes / ethyl acetate, 8 / 2, v / v).

***E* isomer:**

**<sup>1</sup>H-NMR (800 MHz, CD<sub>2</sub>Cl<sub>2</sub>):** δ (ppm) = 8.04 (d, <sup>3</sup>*J* = 7.5 Hz, 1H, H-C(12)), 7.86 (d, <sup>3</sup>*J* = 8.1 Hz, 1H, H-C(24)), 7.83 (d, <sup>3</sup>*J* = 8.2 Hz, 1H, H-C(14)), 7.70 (d, <sup>3</sup>*J* = 8.6, 1H, H-C(27)), 7.54 (d, <sup>3</sup>*J* = 7.9 Hz, 1H, H-C(6)), 7.50 - 7.48 (m, 1H, H-C(13)), 7.49 - 7.47 (m, 1H, H-C(21)), 7.48 - 7.46 (m, 1H, H-C(19)), 7.46 - 7.45 (m, 1H, H-C(25)), 7.45 - 7.44 (m, 1H, H-C(18)), 7.44 - 7.42 (m, 1H, H-C(26)), 7.42 - 7.40 (m, 1H, H-C(20)), 7.21 (d, <sup>3</sup>*J* = 7.3 Hz, 1H, H-C(4)), 6.85



(t,  $^3J = 7.5$  Hz, 1H, H-C(5)), 6.40 (s, 1H, H-C(10)), 2.33 (s, 3H, H-C(22)), 1.71 (s, 3H, H-C(23)).

**$^{13}\text{C}$ -NMR (201 MHz,  $\text{CD}_2\text{Cl}_2$ ):**  $\delta$  (ppm) = 184.67 (C(8)), 151.01 (C(2)), 139.58 (C(9)), 138.83 (C(4)), 138.67 (C(17)), 138.17 (C(16)), 133.45 (C(11)), 131.75 (C(28)), 131.11 (C(18)), 130.53 (C(26)), 130.35 (C(15)), 129.17 (C(21)), 128.70 (C(14)), 128.58 (C(24)), 128.10 (C(12)), 127.36 (C(20)), 126.13 (C(25)), 125.64 (C(19)), 125.03 (C(13)), 123.95 (C(27)), 122.51 (C(7)), 122.29 (C(6)), 121.39 (C(3)), 119.74 (C(5)), 114.43 (C(10)), 17.67 (C(23)), 17.45 (C(22)).

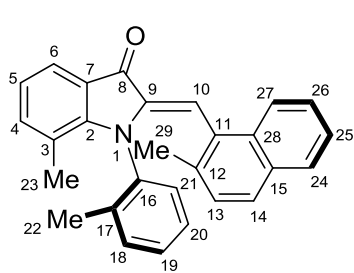
**Z isomer:  $^1\text{H}$ -NMR (600 MHz,  $\text{CD}_2\text{Cl}_2$ ):**  $\delta$  (ppm) = 7.92 - 7.87 (m, 1H, H-C(27)), 7.73 - 7.69 (m, 1H, H-C(24)), 7.68 (d,  $^3J = 8.1$  Hz, 1H, H-C(6)), 7.50,  $^3J = 8.1$  Hz, 1H, H-C(14)), 7.46 - 7.43 (m, 1H, H-C(26)), 7.43 - 7.41 (m, 1H, H-C(25)), 7.37 (s, 1H, H-C(10)), 7.18 (d,  $^3J = 7.4$  Hz, 1H, H-C(4)), 7.00 - 6.96 (m, 1H, H-C(13)), 6.94 (d,  $^3J = 8.0$  Hz, 1H, H-C(21)), 6.90 (dd,  $^3J = 7.5$  Hz,  $^3J = 7.5$  Hz, 1H, H-C(5)), 6.83 (dd,  $^3J = 7.5$  Hz,  $^3J = 7.5$  Hz, 1H, H-C(19)), 6.81 (d,  $^3J = 7.0$  Hz, 1H, H-C(12)), 6.68 (d,  $^3J = 7.5$  Hz, 1H, H-C(18)), 6.64 (t,  $^3J = 7.7$  Hz, 1H, H-C(20)), 1.87 (s, 3H, H-C(22)), 1.53 (s, 3H, H-C(23)).

**$^{13}\text{C}$ -NMR (151 MHz,  $\text{CD}_2\text{Cl}_2$ ):**  $\delta$  (ppm) = 186.89 (C(8)), 153.43 (C(2)), 140.11 (C(4)), 139.69 (C(9)), 139.26 (C(16)), 138.28 (C(17)), 133.38 (C(15)), 132.06 (C(28)), 131.17 (C(21)), 130.98 (C(11)), 130.35 (C(18)), 128.65 (C(19)), 128.58 (C(24)), 127.74 (C(14)), 127.43 (C(12)), 126.35 (C(26)), 126.19 (C(25)), 126.13 (C(20)), 125.94 (C(27)), 124.95 (C(13)), 123.10 (C(6)), 122.77 (C(3)), 122.35 (C(7)), 120.97 (C(5)), 111.54 (C(10)), 18.56 (C(23)), 17.94 (C(22)).

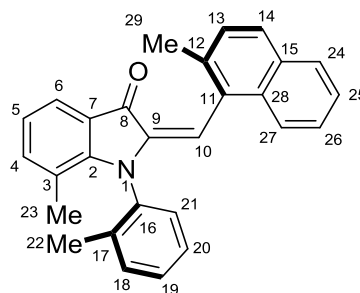
**MS (EI+, 70 eV):**  $m/z$  (%) = 376.2 (25), 375.2 (100), 374.2 (88), 234.1 (11).

**HRMS (EI+,  $\text{C}_{27}\text{H}_{21}\text{NO}$ ):** calcd.: 375.1623; found: 375.1610 (M+).

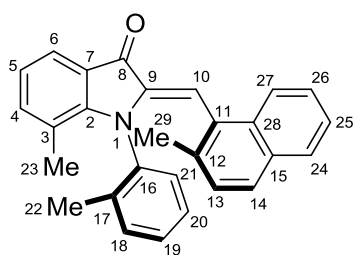
**(*R<sub>a</sub>/S<sub>a</sub>*)-(Z/E)-(syn/anti)-7-methyl-2-((2-methylnaphthalen-1-yl)methylene)-1-(*o*-tolyl)indolin-3-one (61)**



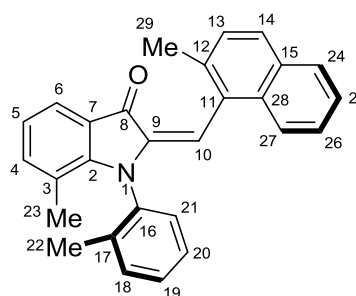
syn-Z isomer



anti-E isomer



anti-Z isomer



syn-E isomer

To a nitrogen-flushed Schlenk flask, equipped with a magnetic stirring bar and rubber septum, aq. sodium hydroxide solution (0.117 g, 2.94 mmol, 1.5 M, 2.00 mL, 8.2 equiv., degassed with N<sub>2</sub>), 7-methyl-1-(*o*-tolyl)-1*H*-indol-3-yl acetate **19** (0.100 g, 0.358 mmol, 1.0 equiv.), 2-methyl-1-naphthaldehyde (0.061 g, 0.358 mmol, 1.0 equiv.) and dioxane (0.36 mL, 1 M, degassed) were added and the mixture was heated to 100 °C for 18 h. After cooling to 23 °C, the mixture was neutralized with aq. hydrochloric acid (1.0 M), extracted with ethyl acetate and washed with brine. The combined organic phases were dried over sodium sulfate and the volatiles were removed *in vacuo*. Subsequent purification by flash column chromatography (aluminium(III) oxide, *Brockmann* III, 6% water, w / w), hexanes / ethyl acetate, 4 / 1, v / v) yielded (*R<sub>a</sub>/S<sub>a</sub>*)-(Z/E)-(syn/anti)-7-methyl-2-((2-methylnaphthalen-1-yl)methylene)-1-(*o*-tolyl)indolin-3-one **61** (0.105 g, 0.277 mmol, 78%) as orange to red solid. Further purification was carried out via preparative HPLC (*Machery-Nagel* VP 250/21 *NUCLEODUR Sphinx* RP 5 μm column, acetonitrile, 15 mL/min, 35 °C column temperature, retention times: 5.9 min, Z+E isomer, 28.1 mg; 37% overall yield).

*R<sub>f</sub>* = 0.79 (hexanes / ethyl acetate, 4 / 1, v / v).

**Note:** The obtained NMR data is displayed in Section 2.3.7, Figure 152. Even the spectra of the enantiopure compounds cannot be solved by hand due to signal splitting and -overlap within  $^1\text{H}$ - and  $^{13}\text{C}$ -NMR spectra. The amount of  $^{13}\text{C}$  signals cannot be determined properly (Figure 159 and Figure 160), which makes unambiguous solving of 2D HSQC- and HMBC NMR spectra (Figure 161) impossible by hand. The aliphatic signals were assigned via  $^1\text{H}$  2D NOESY NMR spectra (Figure 154 and Figure 156).

***Z* syn / -anti isomers:**

**$^1\text{H}$ -NMR (600 MHz,  $\text{CD}_2\text{Cl}_2$ ):**  $\delta$  (ppm) = 7.86 - 7.79 (m, 1H), 7.71 - 7.67 (m, 4H), 7.67 - 7.64 (m, 2H), 7.57 (dd,  $^3J = 7.8$  Hz,  $^4J = 1.5$  Hz, 1H), 7.44 - 7.41 (m, 3H), 7.41 - 7.36 (m, 2H), 7.28 (ddd,  $^3J = 8.1$  Hz,  $^3J = 6.8$  Hz,  $^4J = 1.5$  Hz, 1H), 7.26 (dd,  $^3J = 8.2$  Hz,  $^4J = 1.6$  Hz, 1H), 7.24 - 7.20 (m, 2H), 7.16 (ddd,  $^3J = 7.3$  Hz,  $^3J = 3.1$  Hz,  $^4J = 1.1$  Hz, 2H), 7.07 (d,  $^3J = 8.3$  Hz, 1H), 6.95 (d,  $^3J = 8.4$  Hz, 1H), 6.93 - 6.87 (m, 3H), 6.79 - 6.74 (m, 1H), 6.69 (dd,  $^3J = 7.5$  Hz,  $^4J = 1.4$  Hz, 1H), 6.61 - 6.55 (m, 1H), 6.54 (dd,  $^3J = 7.6$ ,  $^3J = 1.7$  Hz, 1H), 6.34 - 6.29 (m, 1H), 6.21 (dd,  $^3J = 7.9$  Hz,  $^4J = 1.3$  Hz, 1H), 6.09 (dd,  $^3J = 7.6$  Hz,  $^4J = 1.5$  Hz, 1H), 2.37 (s, 3H, H-C(*syn* 29)), 2.18 (s, 3H, H-C(*anti* 29)), 1.92 (s, 3H, H-C(*anti* 22)), 1.68 (s, 3H, H-C(*syn* 22)), 1.47 (s, 3H, H-C(*syn* 23)), 1.43 (s, 3H, H-C(*anti* 23)).

**$^{13}\text{C}$ -NMR (151 MHz,  $\text{CD}_2\text{Cl}_2$ ):**  $\delta$  (ppm) = 185.95, 185.90, 153.55, 153.43, 140.58, 140.57, 139.38, 139.34, 139.30, 139.26, 137.85, 137.69, 137.18, 136.79, 133.66, 133.21, 131.95, 131.61, 131.39, 131.31, 130.96, 130.86, 129.83, 129.81, 129.54, 129.29, 129.25, 129.22, 129.21, 129.16, 127.79, 127.76, 127.71, 127.64, 127.59, 127.47, 127.45, 127.44, 127.43, 127.34, 127.27, 126.95, 126.91, 126.87, 126.84, 126.06, 126.02, 125.72, 125.68, 125.64, 125.58, 125.04, 124.87, 124.84, 124.83, 124.69, 124.66, 124.65, 124.63, 124.56, 124.49, 122.65, 122.56, 122.55, 122.50, 122.49, 122.00, 121.93, 120.61, 120.56, 120.51, 120.47, 111.29, 111.20, 111.11, 53.77, 53.59, 53.48, 53.41, 53.34, 53.23, 53.17, 53.04, 20.73, 20.68, 20.28, 20.25, 17.78, 17.73, 17.68, 17.64, 17.59, 17.57, 17.53, 17.47, 17.46.

***E* syn / -anti isomers:**

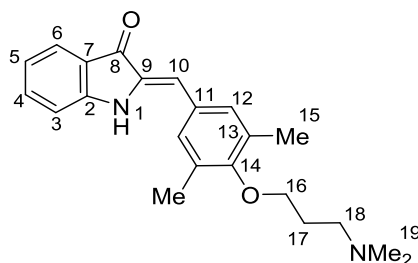
**$^1\text{H}$ -NMR (600 MHz,  $\text{CD}_2\text{Cl}_2$ ):**  $\delta$  (ppm) = 7.83 - 7.78 (m, 2H), 7.77 - 7.75 (m, 1H), 7.74 - 7.69 (m, 2H), 7.57 - 7.53 (m, 1H), 7.49 - 7.42 (m, 9H), 7.38 (m, 7H), 7.22 (m, 2H), 6.82 (m, 3H), 2.43 (s, 3H, H-C(*syn* 22)), 2.40 (s, 4H, H-C(*anti* 29)), 2.35 (s, 6H, H-C(*anti* 22, *syn* 29)), 1.73 (s, 6H, H-C (*anti*-, *syn* 23)).

**$^{13}\text{C}$ -NMR (151 MHz,  $\text{CD}_2\text{Cl}_2$ ):** 185.31, 152.15, 140.90, 140.77, 139.39, 139.33, 139.15, 138.86, 138.82, 135.05, 132.58, 132.55, 132.35, 131.68, 130.84, 130.47, 130.42, 129.63, 129.11, 129.04, 128.70, 127.88, 127.84, 126.39, 126.33, 125.26, 122.72, 122.67, 121.98, 120.30, 120.28, 113.01, 112.91, 20.89, 20.84, 20.81, 20.76, 18.26, 18.24, 18.21, 18.17, 18.06, 18.02.

**MS (EI+, 70 eV):**  $m/z$  (%) = 390.2 (17), 389.2 (53), 375.2 (28), 374.2 (100), 373.2 (25), 372.2 (93), 357.2 (19).

**HRMS (EI+,  $\text{C}_{28}\text{H}_{23}\text{NO}$ ):** calcd.: 389.1780; found: 389.1780 ( $\text{M}^+$ ).

**(Z)-2-(4-(3-(dimethylamino)propoxy)-3,5-dimethylbenzylidene)indolin-3-one (97)**



To a nitrogen-flushed Schlenk flask, equipped with a magnetic stirring bar and rubber septum, aq. sodium hydroxide solution (1.63 mL, 20.1 mmol, 1.5 M, 8.2 equiv., degassed with  $\text{N}_2$ ), 1*H*-indol-3-yl acetate (0.429 g, 2.45 mmol, 1.0 equiv.), 4-(3-(dimethylamino)propoxy)-3,5-dimethylbenzaldehyde **92** (0.576 g, 2.45 mmol, 1.0 equiv.) and dioxane (1.2 mL, 2 M, degassed) were added and the mixture was heated to 100 °C for 30 min. After cooling to 23 °C, the mixture was neutralized with aq. hydrochloric acid (1.0 M), filtered through celite, extracted with ethyl acetate and washed with brine. The combined organic phases were dried over sodium sulfate and the volatiles were removed *in vacuo*. Subsequent purification by flash column chromatography (silica, dichloromethane / methanol / triethylamine, 84 / 15 / 1, v / v / v) yielded (Z)-2-(4-(3-(dimethylamino)propoxy)-3,5-dimethylbenzylidene)indolin-3-one **97** (0.488 g, 1.391 mmol, 57%) as orange viscous oil.

$R_f$  = 0.25 (silica, 84 / 15 / 1, methanol / dichloromethane / triethylamine, v / v / v).

**Z isomer:**

**$^1\text{H}$ -NMR (600 MHz,  $\text{CD}_2\text{Cl}_2$ ):**  $\delta$  (ppm) = 7.68 (d,  $^3J$  = 7.6 Hz, 1H, H-C(6)), 7.49 (ddd,  $^3J$  = 8.3 Hz,  $^3J$  = 7.2 Hz,  $^4J$  = 1.3 Hz, 1H, H-C(4)), 7.24 (s, 2H, H-C(12)), 7.07 (d,  $^3J$  = 8.1 Hz, 1H, H-C(3)), 6.99 (s, br, 1H, H-N(1)), 6.97 (dd,  $^3J$  = 8.0 Hz,  $^3J$  = 7.1 Hz, 1H, H-C(5)), 6.71 (s, 1H,

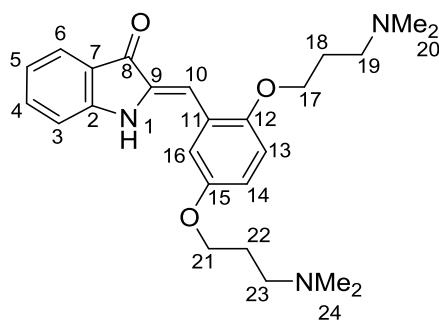
H-C(10)), 3.84 (t,  $^3J = 6.3$  Hz,  $^3J = 6.3$  Hz, 2H, H-C(16)), 2.53 (t,  $^3J = 6.5$  Hz, 2H, H-C(18)), 2.32 (s, 6H, H-C(15)), 2.26 (s, 6H, H-C(19)), 1.98 (p,  $^3J = 6.7$  Hz, 2H, H-C(17)).

$^{13}\text{C-NMR}$  (151 MHz,  $\text{CD}_2\text{Cl}_2$ ):  $\delta$  (ppm) = 186.02 (C(8)), 156.57 (C(14)), 153.06 (C(2)), 135.84 (C(4)), 134.57 (C(11)), 132.08 (2C, C(13)), 130.11 (2C, C(12)), 129.99 (C(9)), 124.43 (C(6)), 121.70 (C(7)), 120.36 (C(5)), 112.01 (C(3)), 111.22 (C(10)), 70.34 (C(16)), 56.07 (C(18)), 45.03 (2C, C(19)), 28.25 (C(17)), 16.16 (2C, C(15)).

**MS (EI+, 70 eV):**  $m/z$  (%) = 350.2 (4), 86.1 (37), 61.2 (11), 58.0 (62), 45.0 (12), 43.2 (100).

**HRMS (EI+,  $\text{C}_{22}\text{H}_{26}\text{N}_2\text{O}_2$ ):** calcd.: 350.1994; found: 350.1978 (M+).

**(Z)-2-(2,5-bis(3-(dimethylamino)propoxy)benzylidene)indolin-3-one (98)**



To a nitrogen-flushed Schlenk flask, equipped with a magnetic stirring bar and rubber septum, aq. sodium hydroxide solution (1.05 mL, 12.9 mmol, 1.5 M, 8.2 equiv., degassed with  $\text{N}_2$ ), 1*H*-indol-3-yl acetate (0.275 g, 1.57 mmol, 1.0 equiv.), 2,5-bis(3-(dimethylamino)propoxy)benzaldehyde **95** (0.808 g, 1.57 mmol, 1.0 equiv.) and dioxane (0.8 mL, 2.0 M, degassed) were added and the mixture was heated to 100 °C for 30 min. After cooling to 23 °C, the mixture was neutralized with aq. hydrochloric acid (1.0 M), filtered through celite, extracted with ethyl acetate and washed with brine. The combined organic phases were dried over sodium sulfate and the volatiles were removed *in vacuo*. Subsequent purification by flash column chromatography (silica, dichloromethane / methanol / hexanes / triethylamine, 33 / 33 / 31 / 2, v / v / v / v) yielded (Z)-2-(2,5-bis(3-(dimethylamino)propoxy)-benzylidene)indolin-3-one **98** (0.418 g, 0.986 mmol, 63%) as orange viscous oil.

$R_f$  = 0.29 (silica, 33 / 33 / 31 / 2, methanol / dichloromethane / hexanes / triethylamine, v / v / v / v).

**Z isomer:**

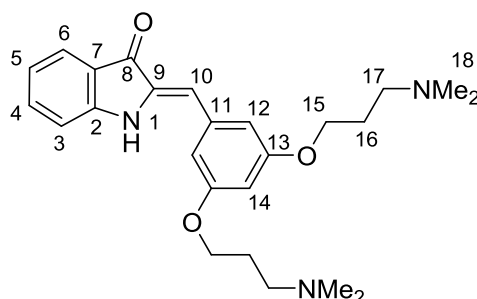
**<sup>1</sup>H-NMR (600 MHz, CD<sub>2</sub>Cl<sub>2</sub>):**  $\delta$  (ppm) = 8.22 (s, br, 1H, H-N(1)), 7.65 (d, <sup>3</sup>*J* = 7.7 Hz, 1H, H-C(6)), 7.45 (ddd, <sup>3</sup>*J* = 8.3 Hz, <sup>3</sup>*J* = 7.1 Hz, <sup>4</sup>*J* = 1.3 Hz, 1H, H-C(4)), 7.09 (d, <sup>3</sup>*J* = 2.9 Hz, 1H, H-C(16)), 7.02 (d, <sup>3</sup>*J* = 8.0 Hz, 1H, H-C(3)), 6.94 - 6.88 (m, 2H, H-C(5, 13)), 6.86 (dd, <sup>3</sup>*J* = 8.8 Hz, <sup>3</sup>*J* = 3.0 Hz, 1H, H-C(14)), 6.84 (s, 1H, H-C(10)), 4.08 (t, <sup>3</sup>*J* = 6.5 Hz, 2H, H-C(17)), 4.03 (t, *J* = 6.3 Hz, 2H, H-C(21)), 2.56 (t, *J* = 7.2 Hz, 2H, H-C(19)), 2.45 (t, *J* = 7.1 Hz, 2H, H-C(23)), 2.30 (s, 6H, H-C(20)), 2.20 (s, 6H, H-C(24)), 1.97 (m, 4H, H-C(18, 22)).

**<sup>13</sup>C-NMR (151 MHz, CD<sub>2</sub>Cl<sub>2</sub>):**  $\delta$  (ppm) = 186.85 (C(8)), 153.75 (C(15)), 153.66 (C(2)), 151.50 (C(12)), 136.44 (C(4)), 135.97 (C(9)), 125.41 (C(7)), 124.95 (C(6)), 121.81 (C(11)), 120.22 (C(10)), 117.55 (C(16)), 116.48 (C(14)), 115.00 (C(13)), 112.36 (C(3)), 107.16 (C(10)), 68.67 (C(17)), 66.98 (C(21)), 56.36 (C(23)), 56.12 (C(19)), 45.31 (2C, C(24)), 45.08 (2C, C(20)), 27.61 (C(18)), 27.40 (C(22)).

**MS (EI+, 70 eV):** *m/z* (%) = 423.2 (4), 86.1 (11), 84.1 (34), 61.2 (10), 58.1 (42), 45.1 (10), 43.2 (100).

**HRMS (EI+, C<sub>25</sub>H<sub>33</sub>N<sub>3</sub>O<sub>3</sub>):** calcd.: 423.2522; found: 423.2516 (M+).

**(Z)-2-(3,5-bis(3-(dimethylamino)propoxy)benzylidene)indolin-3-one (99)**



To a nitrogen-flushed Schlenk flask, equipped with a magnetic stirring bar and rubber septum, aq. sodium hydroxide solution (0.54 mL, 6.69 mmol, 1.5 M, 8.2 equiv., degassed with N<sub>2</sub>), 1*H*-indol-3-yl acetate (0.143 g, 0.816 mmol, 1.0 equiv.), 3,5-bis(3-(dimethylamino)propoxy)-benzaldehyde **96** (0.252 g, 0.816 mmol, 1.0 equiv.) and dioxane (0.4 mL, 2.0 M, degassed) were added and the mixture was heated to 100 °C for 30 min. After cooling to 23 °C, the mixture was neutralized with aq. hydrochloric acid (1.0 M), filtered through celite, extracted with ethyl acetate and washed with brine. The combined organic phases were dried over sodium sulfate and the volatiles were removed *in vacuo*. Subsequent purification by flash column chromatography (silica, dichloromethane / methanol / hexanes / triethylamine, 30 / 34 / 34 / 2,

v / v / v / v) yielded (*Z*)-2-(2,5-bis(3-(dimethylamino)propoxy)benzylidene)indolin-3-one **99** (0.231 g, 0.545 mmol, 67%) as orange viscous oil.

$R_f = 0.30$  (silica, 30 / 34 / 34 / 2, methanol / dichloromethane / hexanes / triethylamine, v / v / v / v).

**Z isomer:**

**$^1\text{H-NMR}$  (400 MHz,  $\text{CD}_2\text{Cl}_2$ ):**  $\delta$  (ppm) = 7.85 (s, br, 1H, (H-N(1))), 7.64 (d,  $^3J = 7.6$  Hz, 1H, H-C(6)), 7.45 (ddd,  $^3J = 8.4$  Hz,  $^3J = 7.2$  Hz,  $^3J = 1.4$  Hz, 1H, H-C(4)), 7.08 (d,  $^3J = 8.2$  Hz, 1H, H-C(3)), 6.92 (ddd,  $^3J = 7.5$  Hz,  $^3J = 7.5$  Hz,  $^3J = 0.8$  Hz, 1H, H-C(5)), 6.71 (d,  $^3J = 2.2$  Hz, 2H, H-C(12)), 6.65 (s, 1H, H-C(10)), 6.43 (t,  $^3J = 2.2$  Hz, 1H, H-C(14)), 4.03 (t,  $^3J = 6.4$  Hz, 4H, H-C(15)), 2.45 (t,  $^3J = 7.1$  Hz, 4H, H-C(17)), 2.23 (s, 12H, H-C(18)), 1.92 (*quin*,  $^3J = 6.7$  Hz, 4H, H-C(16)).

**$^{13}\text{C-NMR}$  (101 MHz,  $\text{CD}_2\text{Cl}_2$ ):**  $\delta$  (ppm) = 186.51 (C(8)), 160.64 (2C, C(13)), 153.67 (C(2)), 136.43 (C(11)), 136.04 (C(4)), 135.55 (C(9)), 124.46 (C(6)), 121.38 (C(7)), 120.23 (C(5)), 112.24 (C(3)), 110.74 (C(10)), 108.12 (2C, C(12)), 101.66 (C(14)), 66.31 (2C, C(15)), 55.89 (2C, C(17)), 44.98 (4C, C(18)), 27.22 (2C, C(16)).

**MS (EI+, 70 eV):**  $m/z$  (%) = 423.3 (9), 86.1 (11), 84.1 (36), 58.1 (100).

**HRMS (EI+,  $\text{C}_{25}\text{H}_{33}\text{N}_3\text{O}_3$ ):** calcd.: 423.2522; found: 423.2509 (M+).





(2C, C(10)), 128.49 (2C, C(11)), 125.60 (2C, C(12)), 123.42 (2C, C(7)), 122.78 (2C, C(3a)), 121.72 (2C, C(5)), 121.62 (2C, C(4)), 18.40 (2C, C(14)), 18.04 (2C, C(15)).

**Anti-trans isomer:**

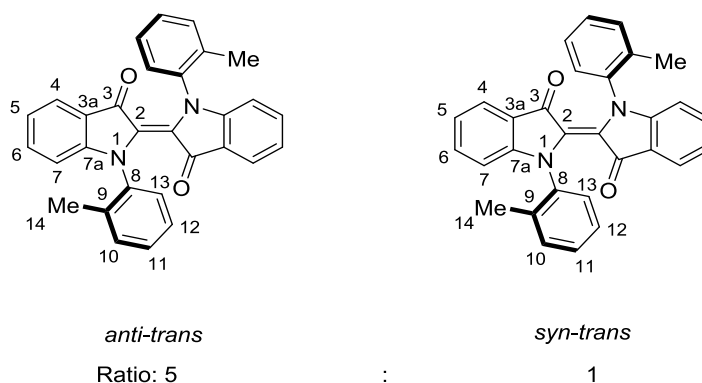
**$^1\text{H-NMR}$  (600 MHz,  $\text{CD}_2\text{Cl}_2$ ):**  $\delta$  (ppm) = 7.72 (d,  $^3J = 7.6$  Hz, 2H, H-C(13)), 7.43 (dd,  $^3J = 6.6$  Hz,  $^4J = 1.4$  Hz, 2H, H-C(4)), 7.33 - 7.21 (m, 6H, H-C(10, 11, 12)), 7.14 (m, 2H, H-C(6)), 6.90 (d,  $^3J = 7.2$  Hz, 2H, H-C(5)), 2.20 (s, 6H, H-C(14)), 1.62 (s, 6H, H-C(15)).

**$^{13}\text{C-NMR}$  (151 MHz,  $\text{CD}_2\text{Cl}_2$ ):**  $\delta$  (ppm) = 184.91 (2C, C(3')), 150.91 (2C, C(7a)), 141.94 (2C, C(8)), 138.37 (2C, C(6)), 138.30 (2C, C(9)), 131.24 (2C, C(13)), 130.79 (2C, C(2)), 130.45 (2C, C(10)), 128.45 (2C, C(11)), 125.34 (2C, C(12)), 123.29 (2C, C(7)), 122.70 (2C, C(3a)), 121.72 (2C, C(5)), 121.62 (2C, C(4)), 18.78 (2C, C(14)), 18.08 (2C, C(15)).

**MS (EI+, 70 eV):**  $m/z$  (%) = 472.2 (17), 471.2 (50), 470.2 (100), 456.2 (20), 427.2 (15), 425.2 (14), 246.1 (21), 245.2 (54), 237.1 (15), 236.1 (36), 235.1 (14), 224.1 (20), 223.1 (37), 208.1 (18), 206.1 (16), 204.1 (16), 194.1 (22), 91.0 (18), 71.1 (15), 69.1 (15), 57.1 (26), 55.0 (14), 44.1 (20), 43.2 (15), 43.1 (61), 41.2 (13).

**HRMS (EI+,  $\text{C}_{32}\text{H}_{26}\text{N}_2\text{O}_2$ ):** calcd.: 470.1994; found: 470.1989 ( $\text{M}^+$ ).

**(trans)-N,N'-Di(o-tolyl)indigo (64)**



To a flame dried Schlenk flask, indoxyl acetate **68** (0.140 g, 0.528 mmol, 1.0 equiv.), aq. sodium hydroxide solution (2.89 mL, 4.33 mmol, 1.5 M, 8.2 equiv., degassed) and dioxane (0.5 mL, 1 M, degassed) were added under  $\text{N}_2$  atmosphere. After stirring at 100 °C for 15 min and cooling of the reaction mixture to 23 °C, manganese(III) acetate (0.282 g, 1.05 mmol, 2.1 equiv.) was added. The suspension was stirred for 2 h at room temperature. Subsequently, the mixture was treated with aq. sat. ammonium chloride solution, filtered over celite, extracted

with ethyl acetate and washed with brine. The combined organic layers were dried over sodium sulfate and evaporated to dryness *in vacuo*. The crude product was purified by flash column chromatography (aluminium(III) oxide, *Brockmann III*, 6% water, w / w), hexanes / ethyl acetate, 4 / 1, v / v) to yield (*trans*)-*N,N*-di(*o*-tolyl)indigo **64** (0.096 g, 0.217 mmol, 82%) as green-blueish solid.

$R_f = 0.70$  (silica, hexanes / ethyl acetate, 4 / 1, v / v).

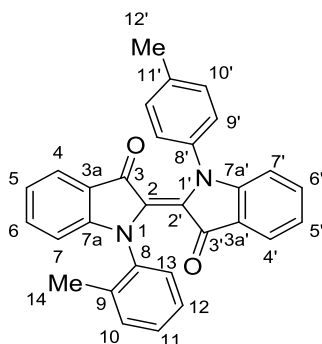
***Syn-trans-1 isomer:***

**$^1\text{H-NMR}$  (600 MHz,  $\text{CD}_2\text{Cl}_2$ ):**  $\delta$  (ppm) = 7.54 (d,  $^3J = 8.0$  Hz, 2H, H-C(10)), 7.53 (d,  $^3J = 8.1$  Hz, 2H, H-C(4)), 7.38 (ddd,  $^3J = 8.2$  Hz,  $^3J = 7.2$  Hz,  $^4J = 1.3$  Hz, 2H, H-C(6)), 7.32 - 7.29 (m, 2H, H-C(11)), 7.20 (ddd,  $^3J = 8.0$  Hz,  $^3J = 7.5$  Hz,  $^4J = 1.4$  Hz, 2H, H-C(12)), 7.08 (dd,  $^3J = 7.9$  Hz,  $^4J = 1.3$  Hz, 2H, H-C(13)), 6.99 (dd,  $^3J = 7.9$  Hz,  $^3J = 7.1$  Hz, 2H, H-C(5)), 6.56 (d,  $^3J = 8.3$  Hz, 2H, H-C(7)), 2.60 (s, 6H, H-C(14)).

**$^{13}\text{C-NMR}$  (151 MHz,  $\text{CD}_2\text{Cl}_2$ ):**  $\delta$  (ppm) = 185.03 (2C, C(3)), 152.93 (2C, C(7a)), 141.55 (2C, C(8)), 138.26 (2C, C(9)), 134.82 (2C, C(6)), 131.20 (2C, C(10)), 127.54 (2C, C(11)), 126.91 (2C, C(12)), 126.40 (2C, C(2)), 123.55 (2C, C(13)), 123.46 (2C, C(4)), 121.69 (2C, C(3a)), 121.49 (2C, C(5)), 111.73 (2C, C(7)), 18.97 (2C, C(14)).

**MS (EI+, 70 eV):**  $m/z$  (%) = 444.2 (13), 443.2 (35), 442.2 (100), 413.2 (15), 397.2 (14), 335.1 (10), 232.1 (18), 231.1 (53), 222.1 (11), 221.1 (12), 220.1 (10), 204.1 (17), 180.1 (14), 65.0 (11).

**HRMS (EI+,  $\text{C}_{30}\text{H}_{22}\text{N}_2\text{O}_2$ ):** calcd.: 442.1681; found: 442.1677 (M+).

**(trans)-N-(o-Tolyl)-N'-(p-tolyl)indigo (70)**

To a flame dried Schlenk flask, 1-(*o*-tolyl)-1*H*-indol-3-yl acetate **68** (0.050 g, 0.188 mmol, 1.0 equiv.), 1-(*p*-tolyl)-1*H*-indol-3-yl acetate **74** (0.050 g, 0.188 mmol, 1.0 equiv.), aq. sodium hydroxide solution (2.2 mL, 3.30 mmol, 1.5 M, 8.2 equiv., degassed) and dioxane (0.5 mL, 1 M, degassed) were added under N<sub>2</sub> atmosphere. After stirring at 100 °C for 30 min and cooling of the reaction mixture to 23 °C, manganese(III) acetate (0.212 g, 0.79 mmol, 4.2 equiv.) was added. The suspension was stirred for 3 h at room temperature. Subsequently, the mixture was treated with aq. sat. ammonium chloride solution, filtered over celite, extracted with ethyl acetate and washed with brine. The combined organic layers were dried over sodium sulfate and evaporated to dryness *in vacuo*. The crude product was purified by flash column chromatography (aluminium(III) oxide, *Brockmann* III, 6% water, w / w), hexanes / ethyl acetate, 4 / 1, v / v) to yield crude (*trans*)-*N*-(*o*-tolyl)-*N'*-(*p*-tolyl)indigo **70** (0.019 g, 0.043 mmol, 23%) as green-blueish solid. Further purification was carried out via preparative HPLC (*Machery-Nagel* VP 250/21 *NUCLEODUR Sphinx* RP 5 μm column, acetonitrile / water, 9 / 1, 15 mL/min, 35 °C column temperature, retention time: 7.5 min, 2.2 mg, 2% overall yield).

$R_f = 0.69$  (silica, hexanes / ethyl acetate, 4 / 1, v / v).

**<sup>1</sup>H-NMR (600 MHz, CD<sub>2</sub>Cl<sub>2</sub>):**  $\delta$  (ppm) = 7.59 - 7.50 (m, 3H, H-C(4, 10')), 7.44 - 7.35 (m, 4H, H-C(4', 6, 6', 10)), 7.30 - 7.35 (m, 3H, H-C(9', 11)), 7.27 - 7.22 (m, 1H, H-C(12)), 7.18 (dd, <sup>3</sup>*J* = 7.9 Hz, <sup>4</sup>*J* = 1.3 Hz, 1H, H-C(13)), 7.03 - 6.96 (m, 3H, H-C(5, 5', 7')), 6.60 (dd, <sup>3</sup>*J* = 8.2 Hz, <sup>4</sup>*J* = 0.8 Hz, 1H, H-C(7)), 2.56 (s, 3H, H-C(14)), 2.43 (s, 3H, H-C(14')).

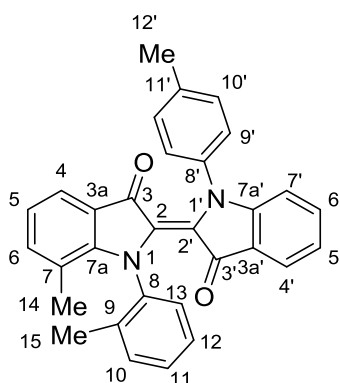
**<sup>13</sup>C-NMR (101 MHz, CD<sub>2</sub>Cl<sub>2</sub>):**  $\delta$  (ppm) = 184.92 (C(2)), 184.38 (C(2')), 153.63 (C(7a')), 152.93 (C(7a)), 141.23 (C(11')), 139.81 (C(8)), 136.70 (C(11)), 135.80 (C(3a)), 134.89 (C(5)), 134.83 (C(5')), 134.75 (C(6')), 134.69 (C(6)), 131.26 (2C, C(10')), 131.21 (C(12)), 129.80 (C(4')), 129.75 (C(9)), 128.13 (C(2)), 127.66 (2C, C(9')), 126.79 (C(8')), 125.74 (C(10)), 124.46

(C(13)), 123.55 (C(4)), 123.49 (C(2')), 121.73 (C(3a')), 111.73 (C(7)), 111.70 (C(5')), 20.91 (C(14)), 18.96 (C(12')).

**MS (EI+, 70 eV):**  $m/z$  (%) = 443.2 (29), 425.2 (11), 413.2 (24), 397.2 (15), 232.1 (17), 231.1 (55), 221.1 (15), 204.1 (17), 180.1 (11), 91.1 (10), 70.0 (12), 61.0 (14), 44.0 (28), 43.0 (83).

**HRMS (EI+, C<sub>30</sub>H<sub>22</sub>N<sub>2</sub>O<sub>2</sub>):** calcd.: 442.1679; found: 442.1677 (M+).

**(*trans*)-7-Methyl-*N*-(*o*-tolyl)-*N'*-(*p*-tolyl)indigo (**69**)**



To a flame dried Schlenk flask, 1-(*p*-tolyl)-1*H*-indol-3-yl acetate **74** (0.050 g, 0.188 mmol, 1.0 equiv.), 1-(*o*-tolyl)-1*H*-7-methylindol-3-yl acetate **19** (0.053 g, 0.188 mmol, 1.0 equiv.), aq. sodium hydroxide solution (2.2 mL, 3.30 mmol, 1.5 M, 8.2 equiv., degassed) and dioxane (0.5 mL, 1 M, degassed) were added under N<sub>2</sub> atmosphere. After stirring at 100 °C for 30 min and cooling of the reaction mixture to 23 °C, manganese(III) acetate (0.212 g, 0.79 mmol, 4.2 equiv.) was added. The suspension was stirred for 3 h at room temperature. Subsequently, the mixture was treated with aq. sat. ammonium chloride solution, filtered over celite, extracted with ethyl acetate and washed with brine. The combined organic layers were dried over sodium sulfate and evaporated to dryness *in vacuo*. The crude product was purified by flash column chromatography (aluminium(III) oxide, *Brockmann* III, 6% water, w / w), hexanes / ethyl acetate, 4 / 1, v / v) to yield crude (*trans*)-7-methyl-*N*-(*o*-tolyl)-*N'*-(*p*-tolyl)indigo **69** (0.027 g, 0.060 mmol, 33%) as green-blueish solid. Further purification was carried out via preparative HPLC (*Machery-Nagel* VP 250/21 *NUCLEODUR Sphinx* RP 5 μm column, acetonitrile / water, 9 / 1, 15 mL/min, 35 °C column temperature, retention time: 10.0 min, 2.2 mg, 2% overall yield).

$R_f$  = 0.70 (silica, hexanes / ethyl acetate, 4 / 1, v / v).

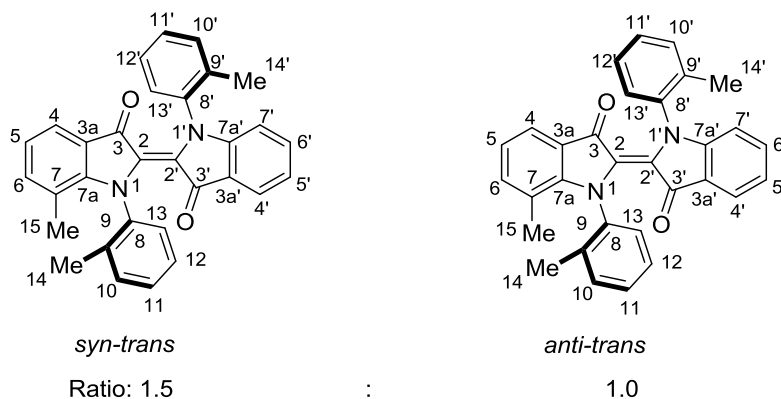
**$^1\text{H-NMR}$  (600 MHz,  $\text{CD}_2\text{Cl}_2$ ):**  $\delta$  (ppm) = 7.61 (dd,  $^3J = 7.8$  Hz,  $^4J = 1.3$  Hz, 1H, H-C(13)), 7.52 (dd,  $^3J = 7.7$  Hz,  $^4J = 1.4$  Hz, 1H, H-C(4')), 7.41 (dd,  $^3J = 7.6$  Hz,  $^4J = 1.4$  Hz, 1H, H-C(4)), 7.39 - 7.33 (m, 5H, H-C(6', 9', 10, 11)), 7.31 - 7.28 (m, 2H, H-C(10')), 7.26 (m, 1H, H-C(12)), 7.16 (dd,  $^3J = 7.3$  Hz,  $^4J = 1.5$  Hz, 1H, H-C(6)), 6.99 (dd,  $^3J = 7.4$  Hz,  $^4J = 0.8$  Hz, 1H, H-C(5')), 6.94 (dd,  $^3J = 8.3$  Hz,  $^4J = 0.8$  Hz, 1H, H-C(7')), 6.90 (ddd,  $^3J = 7.4$  Hz, 1H, H-C(5)), 2.40 (s, 3H, H-C(12')), 2.35 (s, 3H, H-C(14)), 1.67 (s, 3H, H-C(15)).

**$^{13}\text{C-NMR}$  (151 MHz,  $\text{CD}_2\text{Cl}_2$ ):**  $\delta$  (ppm) = 184.80 (C(3')), 184.53 (C(3)), 153.49 (C(7a')), 150.93 (C(7)), 141.93 (C(8)), 140.09 (C(8')), 139.14 (C(9)), 138.63 (C(6)), 136.69 (C(11')), 134.58 (C(6')), 130.47 (C(10)), 129.66(2C, C(10')), 129.55 (C(13)), 128.53 (C(11)), 128.52((C(2')), 126.66 (C(2)), 126.07 (2C, C(9')), 125.78 (C(12)), 123.44 (C(4')), 123.18 (C(7a)), 122.55(C(3a)), 121.85 (C(3a')), 121.70 (C(4)), 121.70 (C(5')), 121.61 (C(5)), 111.46 (C(7')), 20.86 (C(12')), 19.10 (C(14)), 17.88 (C(15)).

**MS (EI+, 70 eV):**  $m/z$  (%) = 458.2 (14), 457.2 (38), 456.2 (100), 442.2 (13), 439.2 (21), 428.2 (16), 427.2 (27), 413.2 (20), 411.2 (12), 245.1 (27), 236.1 (13), 228.1 (11), 223.1 (18), 61.0 (11), 45.1 (14), 44.1 (19), 43.2 (88).

**HRMS (EI+,  $\text{C}_{31}\text{H}_{24}\text{N}_2\text{O}_2$ ):** calcd.: 456.1838; found: 456.1838 (M+).

**(*trans*)-7-Methyl-*N,N'*-di(*o*-tolyl)indigo (71)**



To a flame dried Schlenk flask, 1-(*o*-tolyl)-1*H*-indol-3-yl acetate **68** (0.050 g, 0.188 mmol, 1.0 equiv.), 1-(*o*-tolyl)-1*H*-7-methylindol-3-yl acetate **19** (0.053 g, 0.188 mmol, 1.0 equiv.), aq. sodium hydroxide solution (2.2 mL, 3.30 mmol, 1.5 M, 8.2 equiv., degassed) and dioxane (0.5 mL, 1 M, degassed) were added under  $\text{N}_2$  atmosphere. After stirring at 100 °C for 30 min and cooling of the reaction mixture to 23 °C, manganese(III) acetate (0.212 g, 0.79 mmol, 4.2 equiv.) was added. The suspension was stirred for 3 h at room temperature. Subsequently,

the mixture was treated with aq. sat. ammonium chloride solution, filtered over celite, extracted with ethyl acetate and washed with brine. The combined organic layers were dried over sodium sulfate and evaporated to dryness *in vacuo*. The crude product was purified by flash column chromatography (aluminium(III) oxide, *Brockmann III*, 6% water, w / w), hexanes / ethyl acetate, 4 / 1, v / v) to yield crude (*trans*)-7-methyl-*N,N'*-di(*o*-tolyl)indigo **71** (0.045 g, 0.096 mmol, 51%) as green-blueish solid. Further purification was carried out via preparative HPLC (*Machery-Nagel VP 250/21 NUCLEODUR Sphinx RP 5 μm* column, acetonitrile / water, 9 / 1, 15 mL/min, 35 °C column temperature, retention time: 9.5 min, 4.0 mg, 5% overall yield).

$R_f = 0.70$  (silica, hexanes / ethyl acetate, 4 / 1, v / v).

***Syn-trans-1 isomer:***

**$^1\text{H-NMR}$  (600 MHz,  $\text{CD}_2\text{Cl}_2$ ):**  $\delta$  (ppm) = 7.52 (dd,  $^3J = 7.7$  Hz,  $^4J = 1.0$  Hz, 2H, H-C(4', 10')), 7.47 (d,  $^3J = 7.7$  Hz, 1H, H-C(10)), 7.42 - 7.38 (m, 1H, H-C(4)), 7.38 - 7.32 (m, 2H, H-C(6', 11)), 7.30 - 7.26 (m, 1H, H-C(11')), 7.23 - 7.17 (m, 1H, H-C(12)), 7.18 - 7.13 (m, 2H, H-C(6, 12')), 7.05 (dd,  $^3J = 7.9$  Hz,  $^4J = 1.5$  Hz, 1H, H-C(13)), 7.00 (m, 1H, H-C(5')), 6.92 - 6.86 (m, 2H, H-C(5, 13')), 6.55 (dd,  $^3J = 8.2$  Hz,  $^4J = 0.8$  Hz, 1H, H-C(7')), 2.59 (s, 3H, H-C(14')), 2.58 (s, 3H, H-C(14)), 1.68 (s, 3H, H-C(15)).

**$^{13}\text{C-NMR}$  (151 MHz,  $\text{CD}_2\text{Cl}_2$ ):**  $\delta$  (ppm) = 185.09 (C(3)), 184.86 (C(3')), 151.78 (C(7a)), 150.61 (C(3a)), 142.21 (C(9)), 141.88 (C(9')), 138.77 (C(6)), 138.39 (C(8')), 138.03 (C(8)), 137.65 (C(2)), 134.60 (C(6')), 134.46 (C(3a')), 131.27 (C(10')), 130.67 (C(10)), 128.76 (C(11)), 127.66 (C(11')), 126.83 (C(12')), 126.50 (C(12)), 123.66 (C(13)), 123.36 (C(4')), 121.90 (C(7a')), 121.76 (C(4)), 121.69 (C(5)), 121.65 (C(13')), 121.65 (C(2')), 121.56 (C(7)) 121.49 (C(5')), 111.81 (C(7')), 19.74 (C(14)), 18.99 (C(14')), 17.59 (C(15)).

***Anti-trans isomer:***

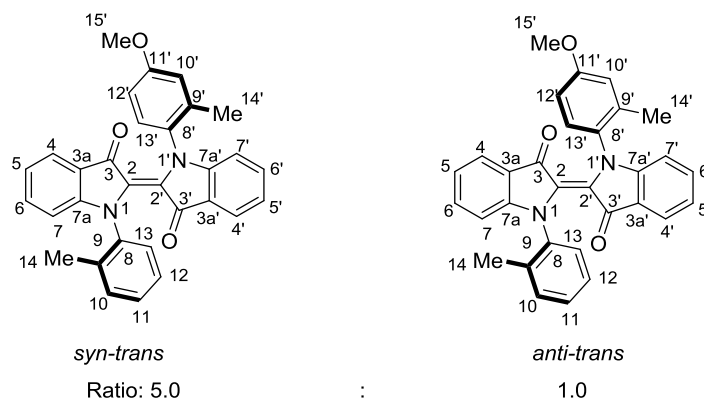
**$^1\text{H-NMR}$  (600 MHz,  $\text{CD}_2\text{Cl}_2$ ):**  $\delta$  (ppm) = 8.21 (dd,  $^3J = 7.7$  Hz,  $^4J = 1.7$  Hz, 1H, H-C(13)), 7.58 (dd,  $^3J = 7.7$  Hz,  $^4J = 1.1$  Hz, 1H, H-C(4')), 7.47 (d,  $^3J = 7.7$  Hz, 1H, H-C(10')), 7.38 - 7.32 (m, 2H, H-C(6', 12)), 7.31 (dd,  $^3J = 7.5$  Hz,  $^4J = 1.2$  Hz, 1H, H-C(11)), 7.30 - 7.26 (m, 2H, H-C(5, 11')), 7.23 - 7.17 (m, 3H, H-C(4, 10, 12')), 7.16 (dd,  $^3J = 8.2$  Hz,  $^4J = 1.5$  Hz, 1H, H-C(6)), 7.05 (dd,  $^3J = 7.9$  Hz,  $^4J = 1.5$  Hz, 1H, H-C(13')), 7.00 (dd,  $^3J = 7.4$  Hz,  $^4J = 0.9$  Hz, 1H, H-C(5')), 6.52 (dd,  $^3J = 8.2$  Hz,  $^4J = 0.8$  Hz, 1H, H-C(7')), 2.51 (s, 3H, H-C(14')), 1.99 (s, 3H, H-C(14)), 1.64 (s, 3H, H-C(15)).

**$^{13}\text{C}$ -NMR (151 MHz,  $\text{CD}_2\text{Cl}_2$ ):**  $\delta$  (ppm) = 185.16 (C(3)), 184.76 (C(3')), 151.79 (C(7)), 141.72 (C(9)), 141.06 (C(9')), 141.05 (C(2')), 138.38 (C(6)), 137.65 (C(8')), 136.24 (C(8)), 134.82 (C(3a')), 134.45 (C(13)), 131.27 (C(10')), 130.59 (C(11)), 130.24 (C(4)), 128.77 (C(2)), 128.66 (C(12)), 127.65 (C(11')), 127.64 (C(5)), 126.50 (C(10)), 126.10 (C(12')), 125.41 (C(13')), 125.24 (C(3a)), 123.80 (C(7a)), 123.47 (C(4')), 121.56 (C(5')), 121.48 (C(7a')) 121.44 (C(6')), 111.64 (C(7')), 18.98 (C(14')), 18.45 (C(15)), 18.10 (C(14)).

**MS (EI+, 70 eV):**  $m/z$  (%) = 458.2 (19), 457.2 (38), 456.2 (100), 442.2 (11), 427.2 (11), 349.1 (13), 245.1 (30), 236.1 (19), 232.1 (13), 231.1 (34), 223.1 (25), 220.1 (13), 209.1 (15), 206.1 (10), 205.1 (11), 204.1 (17), 194.1 (17), 180.1 (18), 91.1 (13), 69.1 (11), 65.0 (18), 57.1 (18), 55.1 (11), 44.0 (19), 43.1 (17), 43.0 (49).

**HRMS (EI+,  $\text{C}_{31}\text{H}_{24}\text{N}_2\text{O}_2$ ):** calcd.: 456.1838; found: 456.1836 (M+).

**(*trans*)-1-(4-methoxy-2-methylphenyl)-1'-(*o*-tolyl)-[2,2'-biindolinylidene]-3,3'-dione (72)**



A flame dried,  $\text{N}_2$ -flushed Schlenk flask is charged with 1-(*o*-tolyl)-1*H*-indol-3-yl acetate **68** (0.021 g, 0.078 mmol, 1.0 equiv.), 1-(4-methoxy-2-methylphenyl)-1*H*-indol-3-yl acetate **75** (0.023 g, 0.078 mmol, 1.0 equiv.), aq. sodium hydroxide solution (0.42 mL, 8.2 equiv. 1.5 M, degassed) and dioxane (0.2 mL, 0.3 M, degassed). The contents were stirred at 100 °C for 15 min, then manganese(III) acetate (0.038 g, 0.163 mmol, 2.1 equiv.) was added. The mixture was cooled to 23 °C and stirred for 2 h. The reaction was stopped with a sat. aq. ammonium chloride solution, filtered through celite and extracted with ethyl acetate. The combined organic layers were dried over sodium sulfate. The mixture was filtrated and the solvents were removed *in vacuo*. Purification by flash column chromatography (aluminium(III) oxide, *Brockmann* III, 6% water, w / w, hexanes / ethyl acetate, 9 / 1, v / v) yielded crude (*trans*)-1-(4-methoxy-2-methylphenyl)-1'-(*o*-tolyl)-[2,2'-biindolinylidene]-3,3'-dione **72** (0.011 g, 0.023 mmol, 30%) as blue solid. Purification via reversed phase- and chiral normal phase HPLC was not able to

separate axially chiral disubstituted indigo **64** without the *para*-methoxy group, product **72** and the *bis-para*-methoxy derivative **76**.

$R_f = 0.16$  (silica, hexanes / ethyl acetate, 9 / 1, v / v).

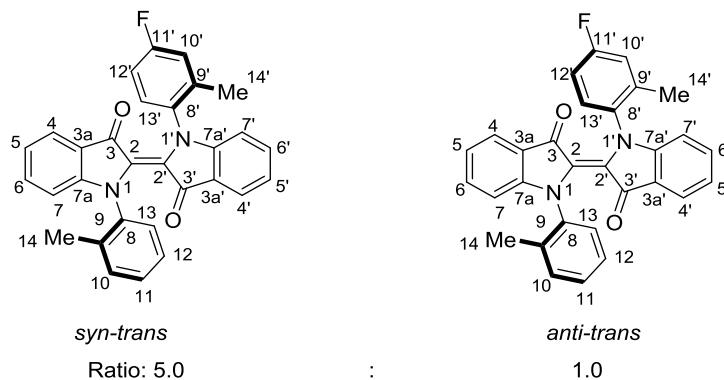
**m.p.** (°C): 303 (decomposition).

**IR (Diamond ATR):**  $\tilde{\nu}$  (cm<sup>-1</sup>) = 2956 (m), 2921 (m), 2851 (m), 2388 (w), 2176 (w), 1987 (w), 1740 (m), 1659 (m), 1600 (m), 1499 (m), 1461 (m), 1375 (m), 1319 (m), 1295 (m), 1257 (m), 1239 (m), 1182 (m), 1092 (m), 1039 (s), 923 (m), 908 (m), 854 (m), 840 (m), 797 (s), 749 (s), 718 (m), 698 (m).

**MS (EI+, 70 eV):**  $m/z$  (%) = 472.2 (100), 443.2 (26), 442.2 (47), 427.2 (12), 335.1 (13), 262.1 (14), 261.1 (38), 236.1 (26), 233.1 (11), 232.1 (16), 231.1 (41), 221.1 (13), 220.1 (21), 204.1 (25), 203.1 (12), 192.1 (13), 191.1 (11), 190.1 (14), 180.1 (18), 167.1 (11), 165.1 (14), 91.1 (16), 77.0 (14), 69.1 (13), 57.1 (17), 55.1 (13), 44.0 (45), 43.0 (17), 41.0 (13).

**HRMS (EI+, C<sub>31</sub>H<sub>24</sub>N<sub>2</sub>O<sub>3</sub>):** calcd.: 472.1787; found: 472.1797 (M<sup>+</sup>).

**(*trans*)-1-(4-fluoro-2-methylphenyl)-1'-(*o*-tolyl)-[2,2'-biindolinylidene]-3,3'-dione (**73**)**



A flame dried, N<sub>2</sub>-flushed Schlenk flask is charged with 1-(*o*-tolyl)-1*H*-indol-3-yl acetate **68** (0.059 g, 0.222 mmol, 1.0 equiv.), 1-(4-fluoro-2-methylphenyl)-1*H*-indol-3-yl acetate **77** (0.063 g, 0.222 mmol, 1.0 equiv.), aq. sodium hydroxide solution (1.21 mL, 8.2 equiv., 1.5 M, degassed) and dioxane (0.6 mL, 0.3 M, degassed). The contents were stirred at 100 °C for 15 min, then manganese(III) acetate (0.108 g, 0.465 mmol, 2.1 equiv.) was added. The mixture was cooled to 23 °C and stirred for 2 h. The reaction was stopped with a sat. aq. ammonium chloride solution, filtered through celite and extracted with ethyl acetate. The combined organic layers were dried over sodium sulfate. The mixture was filtrated and the solvents were removed *in vacuo*. Purification by flash column chromatography (aluminium(III) oxide,



*Brockmann III*, 6% water, w / w, hexanes / ethyl acetate, 9 / 1, v / v) yielded (*trans*)-1-(4-fluoro-2-methylphenyl)-1'-(*o*-tolyl)-[2,2'-biindolinylidene]-3,3'-dione **73** (0.053 g, 0.115 mmol, 52%) as blue solid. Further purification was carried out via preparative HPLC (*Machery-Nagel* VP 250/21 *NUCLEODUR Sphinx* RP 5  $\mu$ m column, acetonitrile / water 6 / 4, v / v, 15 mL/min, 35 °C column temperature, retention time: 59.0 min with 18% yield.

$R_f$  = 0.25 (silica, hexanes / ethyl acetate, 9 / 1, v / v).

**m.p.** (°C): 301 (decomposition).

**Syn- / anti-trans isomers:**

**$^1\text{H-NMR}$  (800 MHz,  $\text{CD}_2\text{Cl}_2$ ):**  $\delta$  (ppm) = 7.55 - 7.52 (m, 3H, H-C(4, 4', 10)), 7.41 - 7.37 (m, 2H, H-C(6, 6')), 7.31 (ddd,  $^3J = 7.5$  Hz,  $^3J = 7.5$  Hz,  $^4J = 1.3$  Hz, 1H, H-C(11)), 7.25 (dd,  $^3J = 9.5$  Hz,  $^4J = 3.0$  Hz, 1H, H-C(10')), 7.18 (ddd,  $^3J = 7.6$  Hz,  $^3J = 7.6$  Hz,  $^4J = 1.5$  Hz, 1H, H-C(12)), 7.05 - 7.02 (m, 2H, H-C(13, 13')), 7.02 - 6.99 (m, 2H, H-C(5, 5')), 6.89 (dd,  $^3J = 8.3$  Hz,  $^4J = 3.0$  Hz, 1H, H-C(12')), 6.58 - 6.54 (m, 2H, H-C(7, 7')), 2.60 (s, 5H, H-C(*syn* 14, *syn* 14')), 2.31 (s, 0.5 H, H-C(*anti* 14, *anti* 14')), 2.29 (s, 0.5 H, H-C(*anti* 14, *anti* 14')).

**$^{13}\text{C-NMR}$  (201 MHz,  $\text{CD}_2\text{Cl}_2$ ):**  $\delta$  (ppm) = 185.73 (C(3)), 185.45 (C(3')), 161.96 (d,  $^1J = 248.6$  Hz, 1C, (11')), 153.59 (C(7a)), 153.48 (C(7a')), 142.07 (C(8)), 141.68 (d,  $^3J = 8.8$  Hz, 1C, C(9')), 138.88 (C(9)), 138.13 (C(8)), 135.57 (C(6)), 135.52 (C(6')), 131.85 (C(10)), 128.81 (C(2)), 128.72 (C(2')), 128.21 (C(11)), 127.53 (C(12)), 125.75 (d,  $^3J = 8.8$  Hz, 1C, C(13')), 124.13 (C(4)), 124.11 (C(13)), 124.08 (C(4')), 122.28 (C(3a)), 122.24 (C(5)), 122.22 (C(3a')), 122.20 (C(5')), 118.18 (d,  $^2J = 22.4$  Hz, 1C, C(10')), 114.21 (d,  $^2J = 22.8$  Hz, 1C, C(12')), 112.37 (C(7)), 112.16 (C(7')), 19.79 (C(*syn* 14)), 19.58 (C(*syn* 14')), 19.42 (C(*anti* 14)), 19.39 (C(*anti* 14')).

**$^{19}\text{F-NMR}$  (377 MHz,  $\text{CD}_2\text{Cl}_2$ ):**  $\delta$  (ppm) = -115.07 (ddd,  $^3J = 9.4$  Hz,  $^3J = 8.0$  Hz,  $^4J = 5.3$  Hz, *anti*), -115.16 (ddd,  $^3J = 9.4$  Hz,  $^3J = 8.0$  Hz,  $^4J = 5.3$  Hz, *syn*).

**IR (Diamond ATR):**  $\tilde{\nu}$  ( $\text{cm}^{-1}$ ) = 2922 (m), 2852 (m), 2179 (w), 2026 (w), 1987 (w), 1951 (w), 1738 (w), 1660 (m), 1600 (m), 1538 (w), 1494 (m), 1461 (m), 1375 (m), 1332 (m), 1296 (s), 1256 (m), 1231 (m), 1183 (s), 1144 (m), 1092 (m), 1050 (s), 1013 (m), 959 (m), 933 (m), 916 (m), 852 (m), 814 (m), 763 (m), 749 (s), 720 (m), 697 (m), 665 (m).

**MS (EI+, 70 eV):**  $m/z$  (%) = 460.2 (17), 125.1 (14), 123.1 (15), 111.1 (28), 109.1 (23), 97.1 (43), 96.1 (17), 95.1 (34), 85.1 (35), 83.1 (50), 82.1 (17), 81.1 (39), 72.0 (23), 71.1 (54), 70.1

### 3.6 OXIDATIVE DIMERIZATION OF ARYLATED INDOXYL ACETATES

(22), 69.1 (68), 68.1 (13), 67.1 (28), 59.0 (35), 57.1 (100), 56.1 (28), 55.1 (83), 43.1 (99), 42.1 (14), 41.1 (57).

**HRMS (EI+, C<sub>30</sub>H<sub>21</sub>FN<sub>2</sub>O<sub>2</sub>):** calcd.: 460.1587; found: 460.1590 (M+).

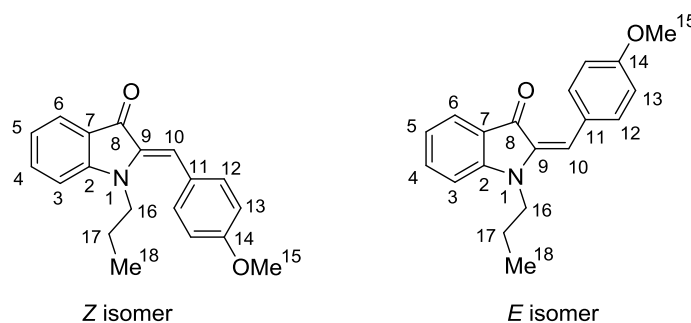
### 3.7 Late stage substitutions at the indoxyl-nitrogen

Introduction of various substituents at the hemiindigo nitrogen was furnished via  $S_N2$  reactions (Section 2.2.3, Scheme 9), *Buchwald-Hartwig* cross-couplings (Section 2.2.6, Scheme 10) or 4-dimethylaminopyridine (DMAP) catalyzed acylation reactions (Section 2.2.2, Scheme 6).

#### 3.7.1 N-Alkylations - $S_N2$ reactions

Scheme 9 for alkylation reactions can be found in Section 2.2.3.

##### (*Z/E*)-2-(4-(methoxy)benzylidene)-1-propylindolin-3-one (7)



A flame dried, nitrogen -flushed round bottom flask, equipped with a magnetic stirring bar was charged with sodium hydride (0.030 g, 0.758 mmol, 1.5 equiv., 60% w / w in paraffin oil), (*Z*)-2-(4-methoxybenzylidene)indolin-3-one **9** (0.127 g, 0.505 mmol, 1.0 equiv.) and dimethylformamide (1 mL, 0.5 M). The formed deep green solution was stirred at 23 °C for 15 min. 1-Iodopropane (0.103 g, 0.606 mmol, 1.2 equiv.) was added dropwise and it was stirred at 23 °C for 5 min until an orange solution emerged. The reaction was terminated with sat. aq. ammonium chloride solution, extracted with ethyl acetate, treated with sat. aq. sodium bisulfite solution and washed ten times with water. The combined organic layers were dried over sodium sulfate. Removal of the solvents *in vacuo* after filtration and subsequent purification by flash column chromatography (aluminium(III) oxide, *Brockmann* III, 6% water, w / w), hexanes / ethyl acetate, 9 / 1, v / v), yielded crude (*Z/E*)-2-(4-methoxybenzylidene)-1-propylindolin-3-one **7** (0.147 g, 0.501 mmol, 99%) as orange solid. Further purification was carried out via preparative HPLC (*Machery-Nagel* VP 250/21 *NUCLEODUR Sphinx* RP 5  $\mu$ m column, acetonitrile / water, 7 / 3, v / v, 15 mL/min, 35 °C column temperature, retention times: 9.1 min (*Z* isomer) and 10.2 min (*E* isomer)) with 77% overall yield.

$R_f$  = 0.61 (silica, hexanes / ethyl acetate, 4 / 1, v / v)

**m.p.** (°C): 92 - 93.

**Z isomer:**

**<sup>1</sup>H-NMR (400 MHz, CDCl<sub>3</sub>):**  $\delta$  (ppm) = 7.73 (d,  $^3J = 7.7$  Hz, 1H, H-C(6)), 7.48 (ddd,  $^3J = 8.4$  Hz,  $^3J = 7.3$  Hz,  $^4J = 1.3$  Hz, 1H, H-C(4)), 7.39 - 7.34 (m, 2H, H-C(12)), 7.02 (s, 1H, H-C(10)), 6.99 (d,  $^3J = 8.3$  Hz, 1H, H-C(3)), 6.96 - 6.90 (m, 3H, H-C(5), H-C(13)), 3.86 (s, 3H, H-C(15)), 3.74 (t,  $^3J = 7.69$  Hz, 2H, H-C(16)), 1.33 (*sext*,  $^3J = 7.69$  Hz, 2H, H-C(17)), 0.57 (t,  $^3J = 7.5$  Hz, 3H, H-C(18)).

**<sup>13</sup>C-NMR (101 MHz, CDCl<sub>3</sub>):**  $\delta$  (ppm) = 187.54 (C(8)), 159.63 (C(14)), 156.14 (C(2)), 136.67 (C(9)), 135.97 (C(4)), 131.79 (2C, C(12)), 126.88 (C(11)), 125.01 (C(6)), 122.54 (C(7)), 119.96 (C(5)), 113.90 (2C, C(13)), 113.56 (C(10)), 111.03 (C(3)), 55.48 (H-C(15)), 46.69 (H-C(16)), 20.20 (H-C(17)), 11.24 (H-C(18)).

**E isomer:**

**<sup>1</sup>H-NMR (400 MHz, CDCl<sub>3</sub>):**  $\delta$  (ppm) = 8.12 - 8.07 (m, 2H, H-C(12)), 7.67 (d,  $^3J = 7.7$  Hz, 1H, H-C(6)), 7.44 (ddd,  $^3J = 8.4$  Hz,  $^3J = 7.2$  Hz,  $^4J = 1.4$  Hz, 1H, H-C(4)), 6.96 - 6.90 (m, 2H, H-C(13)), 6.87 (d,  $^3J = 8.3$  Hz, 1H, H-C(3)), 6.83 (ddd,  $^3J = 7.7$  Hz,  $^3J = 7.2$  Hz,  $^4J = 0.7$  Hz, 1H, H-C(5)), 6.34 (s, 1H, H-C(10)), 3.86 (s, 3H, H-C(15)), 3.62 (t,  $^3J = 7.3$  Hz, 2H, H-C(16)), 1.78 (*sext*,  $^3J = 7.3$  Hz, 2H, H-C(17)), 1.02 (t,  $^3J = 7.5$  Hz, 3H, H-C(18)).

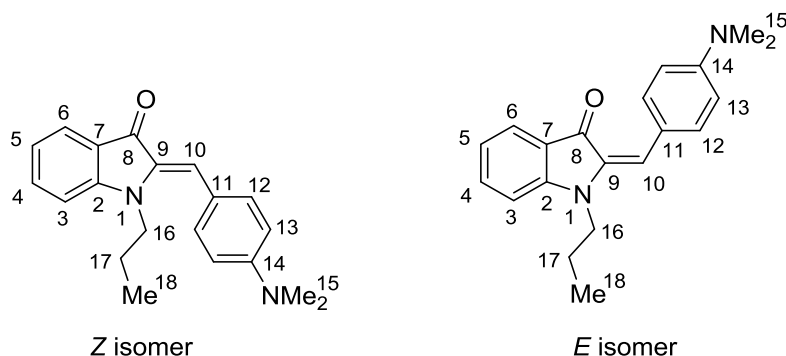
**<sup>13</sup>C-NMR (101 MHz, CDCl<sub>3</sub>):**  $\delta$  (ppm) = 184.68 (C(8)), 160.30 (C(14)), 152.51 (C(2)), 135.78 (C(4)), 135.63 (C(9)), 132.23 (2C, C(12)), 126.95 (C(11)), 124.86 (C(6)), 121.38 (C(7)), 118.59 (C(5)), 117.70 (C(10)), 113.67 (2C, H-C(13)), 108.74 (C(3)), 55.48 (H-C(15)), 44.17 (H-C(16)), 20.94 (H-C(17)), 11.86 (H-C(18)).

**IR (Diamond ATR):**  $\tilde{\nu}$  (cm<sup>-1</sup>) = 2966 (w), 2935 (w), 2874 (w), 2361 (w), 1693 (m), 1629 (m), 1600 (s), 1582 (m), 1569 (m), 1508 (m), 1474 (s), 1456 (m), 1417 (w), 1386 (m), 1366 (m), 1345 (s), 1311 (m), 1301 (m), 1289 (m), 1259 (s), 1245 (s), 1173 (s), 1156 (m), 1128 (s), 1109 (m), 1109 (m), 1095 (s), 1051 (s), 1021 (s), 966 (m), 909 (m), 887 (w), 859 (s), 843 (s), 829 (s), 812 (s), 779 (w), 750 (s), 702 (s), 674 (m).

**MS (EI+, 70 eV):**  $m/z$  (%) = 294.2 (19), 293.1 (100), 292.1 (13), 265.1 (16), 264.1 (88), 221.1 (10), 220.1 (11).

**HRMS (EI+, C<sub>19</sub>H<sub>19</sub>NO<sub>2</sub>):** calcd.: 293.1411; found: 293.1416 (M+).

**EA (C<sub>19</sub>H<sub>19</sub>NO<sub>2</sub>):** calcd.: N, 4.77; C, 77.79; H, 6.53; found: N, 4.77; C, 77.62; H, 6.56.

**(E)-2-(4-(dimethylamino)benzylidene)-1-propylindolin-3-one (8)**

A flame dried, nitrogen-flushed round bottom flask, equipped with a magnetic stirring bar was charged with sodium hydride (0.03 g, 0.76 mmol, 1.5 equiv., 60% w / w in paraffin oil), (*Z*)-2-(4-(dimethylamino)benzylidene)indolin-3-one **11** (0.13 g, 0.50 mmol, 1.0 equiv.) and dimethylformamide (1.00 mL, 0.5 M). The solution was stirred at 23 °C for 15 min. 1-Iodopropane (0.10 g, 0.60 mmol, 1.2 equiv.) was added dropwise and it was stirred at 23 °C for 5 min until a red solution emerged. The reaction was terminated with sat. aq. ammonium chloride solution, extracted with ethyl acetate, treated with sat. aq. sodium bisulfite solution, washed ten times with water and once with sat. aq. sodium chloride solution. The combined organic layers were dried over sodium sulfate. Removal of the solvents *in vacuo* after filtration and subsequent purification by flash column chromatography (aluminium(III) oxide, *Brockmann* III, 6% water, w / w), hexanes / ethyl acetate 9 / 1) yielded (*E*)-2-(4-(dimethylamino)benzylidene)-1-propylindolin-3-one **8** (0.142 g, 0.463 mmol, 92%) as deep violet crystals.

$R_f = 0.45$  (silica, hexanes / ethyl acetate, 4 / 1, v / v)

**m.p.** (°C): 105 - 106.

**Z isomer:**

**<sup>1</sup>H-NMR (800 MHz, CD<sub>2</sub>Cl<sub>2</sub>):**  $\delta$  (ppm) = 7.66 (d,  $^3J = 7.5$  Hz, 1H, H-C(6)), 7.49 (ddd,  $^3J = 8.0$  Hz,  $^3J = 7.0$  Hz,  $^4J = 1.1$  Hz, 1H, H-C(4)), 7.37 - 7.34 (m, 2H, H-C(12)), 7.08 (d,  $^3J = 8.3$  Hz, 1H, H-C(3)), 6.96 (s, 1H, H-C(10)), 6.94 - 6.92 (m, 1H, H-C(5)), 6.75 - 6.73 (m, 2H, H-C(13)), 3.73 (t,  $^3J = 7.6$  Hz, 2H, H-C(16)), 3.02 (s, 6H, H-C(15)), 1.35 (*sext*,  $^3J = 7.3$  Hz, 2H, H-C(17)), 0.59 (t,  $^3J = 7.5$  Hz, 3H, H-C(18)).

**$^{13}\text{C-NMR}$  (201 MHz,  $\text{CD}_2\text{Cl}_2$ ):**  $\delta$  (ppm) = 187.29 (C(8)), 156.46 (C(2)), 150.87 (C(14)), 134.66 (C(4)), 133.97 (C(9)), 132.62 (2C, C(12)), 124.73 (C(6)), 123.59 (C(7)), 121.96 (C(11)), 120.13 (C(5)), 115.79 (C(10)), 112.11 (2C, C(13)), 112.04 (C(3)), 47.49 (C(16)), 40.54 (2C, C(15)), 20.62 (C(17)), 11.52 (C(18)).

***E* isomer:**

**$^1\text{H-NMR}$  (800 MHz,  $\text{CD}_2\text{Cl}_2$ ):**  $\delta$  (ppm) = 8.17 - 8.14 (m, 2H, H-C(12)), 7.63 (d,  $^3J = 7.5$  Hz, 1H, H-C(6)), 7.43 (ddd,  $^3J = 8.3$  Hz,  $^3J = 7.3$  Hz,  $^4J = 1.2$  Hz, 1H, H-C(4)), 6.92 - 6.90 (m, 1H, H-C(3)), 6.81 (ddd,  $^3J = 7.5$  Hz,  $^3J = 7.2$  Hz,  $^4J = 0.8$  Hz, 1H, H-C(5)), 6.73 - 6.70 (m, 2H, H-C(13)), 6.39 (s, 1H, H-C(10)), 3.77 (t,  $^3J = 7.4$  Hz, 2H, H-C(16)), 3.06 (s, 6H, H-C(15)), 1.76 (sext,  $^3J = 7.5$  Hz, 2H, H-C(17)), 1.00 (t,  $^3J = 7.4$  Hz, 3H, H-C(18)).

**$^{13}\text{C-NMR}$  (201 MHz,  $\text{CD}_2\text{Cl}_2$ ):**  $\delta$  (ppm) = 184.13 (C(8)), 152.25 (C(2)), 151.51 (C(14)), 135.76 (C(9)), 135.45 (C(4)), 132.80 (2C, C(12)), 124.62 (C(6)), 122.98 (C(11)), 121.90 (C(7)), 120.20 (C(10)), 118.36 (C(5)), 111.74 (2C, C(13)), 109.27 (C(3)), 44.53 (C(16)), 40.50 (2C, C(15)), 21.48 (C(17)), 11.96 (C(18)).

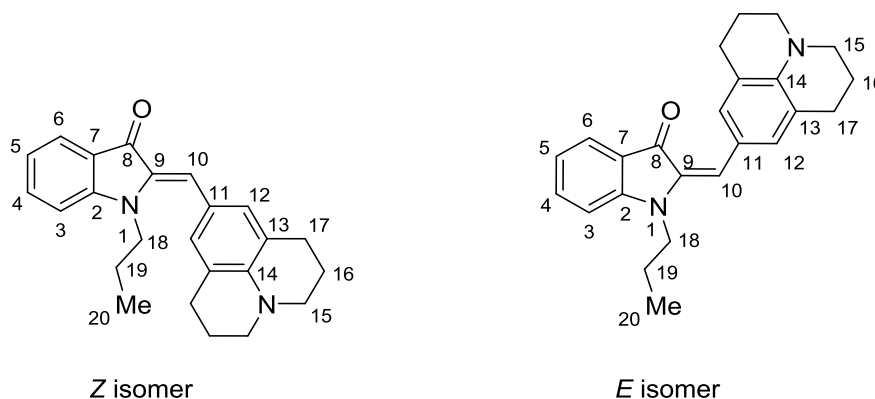
**IR (Diamond ATR):**  $\tilde{\nu}$  ( $\text{cm}^{-1}$ ) = 3854 (w), 2958 (m), 2922 (m), 2852 (m), 2361 (w), 1663 (s), 1603 (s), 1554 (s), 1524 (s), 1524 (s), 1472 (s), 1409 (w), 1360 (s), 1317 (s), 1293 (m), 1263 (m), 1228 (m), 1208 (s), 1188 (s), 1153 (s), 1124 (s), 1095 (s), 1064 (m), 1049 (s), 1024 (m), 972 (s), 946 (m), 906 (m), 894 (m), 880 (s), 848 (m), 818 (s), 743 (s), 716 (s), 703 (s).

**MS (EI+, 70 eV):**  $m/z$  (%) = 307.2 (28), 306.2 (100), 305.2 (13), 277.1 (52), 264.1 (11), 263.1 (38), 248.1 (16), 247.1 (14), 233.1 (15), 232.1 (17), 220.0 (15), 159.0 (14), 138.0 (10).

**HRMS (EI+,  $\text{C}_{20}\text{H}_{22}\text{N}_2\text{O}$ ):** calcd.: 306.1732; found: 306.1726 (M+).

**EA ( $\text{C}_{20}\text{H}_{22}\text{N}_2\text{O}$ ):** calcd.: N, 9.14; C, 78.40; H, 7.24; found: N, 8.81; C, 78.48; H, 7.24.

**(*Z/E*)-1-propyl-2-((2,3,6,7-tetrahydro-1*H*,5*H*-pyrido[3,2,1-*ij*]quinolin-9-yl)methylene)indolin-3-one (3)**



A flame dried, nitrogen-flushed round bottom flask, equipped with a magnetic stirring bar was charged with sodium hydride (0.03 g, 0.76 mmol, 1.5 equiv., 60% w / w in paraffin oil), (*Z*)-2-((2,3,6,7-tetrahydro-1*H*,5*H*-pyrido[3,2,1-*ij*]quinolin-9-yl)methylene)indolin-3-one **15** (0.16 g, 0.50 mmol, 1.0 equiv.) and dimethylformamide (4.00 mL, 0.13 M). The solution was stirred at 23 °C for 15 min. 1-Iodopropane (0.10 g, 0.60 mmol, 1.2 equiv.) was added dropwise and it was stirred at 23 °C for 5 min until a violet solution emerged. The reaction was terminated with sat. aq. ammonium chloride solution, extracted with ethyl acetate, treated with sat. aq. sodium bisulfite solution, washed ten times with water and once with sat. aq. sodium chloride solution. The combined organic layers were dried over sodium sulfate. Removal of the solvents *in vacuo* after filtration and subsequent purification by flash column chromatography (aluminium(III) oxide, *Brockmann* III, 6% water w / w), hexanes / ethyl acetate, 9 / 1, v / v) yielded (*Z/E*)-1-propyl-2-((2,3,6,7-tetrahydro-1*H*,5*H*-pyrido[3,2,1-*ij*]quinolin-9-yl)methylene)indolin-3-one **3** (0.105 g, 0.291 mmol, 87%) as deep violet solid. Further purification was carried out via preparative HPLC (*Machery-Nagel* VP 250/21 *NUCLEODUR Sphinx* RP 5  $\mu$ m column, acetonitrile / water 7 / 3, v / v, 15 mL/min, 35 °C column temperature, retention times: 25.5 min (*E* isomer) with 38% yield. Recrystallization from dichloromethane / ethyl acetate / heptane, ~5 / 15 / 80, v / v / v, yielded deep violet crystals.

$R_f$  = 0.42 (silica, hexanes / ethyl acetate, 4 / 1, v / v).

**m.p.** (°C): 160 - 161.

**Z isomer:**

**<sup>1</sup>H-NMR (600 MHz, CD<sub>2</sub>Cl<sub>2</sub>):**  $\delta$  (ppm) = 7.65 (d, <sup>3</sup>*J* = 7.2 Hz, 1H, H-C(6)), 7.48 (ddd, <sup>3</sup>*J* = 8.4 Hz, <sup>3</sup>*J* = 7.2 Hz, <sup>4</sup>*J* = 1.7 Hz, 1H, H-C(4)), 7.09 (d, <sup>3</sup>*J* = 8.5 Hz, 1H, H-C(3)), 6.94 - 6.91 (m, 3H, H-C(5), H-C(12)), 6.88 (s, 1H, H-C(10)), 3.78 - 3.71 (m, 2H, H-C(18)), 3.26 - 3.21 (m, 4H, H-C(15)), 2.79 - 2.74 (m, 4H, H-C(17)), 1.99 - 1.94 (m, 4H, H-C(16)), 1.42 (*sext*, <sup>3</sup>*J* = 7.7 Hz, 2H, H-C(19)), 0.63 (t, <sup>3</sup>*J* = 7.5 Hz, 3H, H-C(20)).

**<sup>13</sup>C-NMR (151 MHz, CD<sub>2</sub>Cl<sub>2</sub>):**  $\delta$  (ppm) = 187.05 (C(8)), 156.38 (C(2)), 143.89 (C(14)), 135.57 (C(9)), 135.43 (C(4)), 130.55 (2C, C(12)), 124.58 (C(6)), 123.88 (C(7)), 121.36 (2C, C(13)), 120.82 (C(11)), 120.06 (C(5)), 116.98 (C(10)), 112.21 (C(3)), 50.48 (2C, C(15)), 47.83 (C(18)), 28.24 (2C, C(17)), 22.34 (2C, C(16)), 20.87 (C(19)), 11.61 (C(20)).

**E isomer:**

**<sup>1</sup>H-NMR (600 MHz, CD<sub>2</sub>Cl<sub>2</sub>):**  $\delta$  (ppm) = 7.80 (s, 2H, H-C(12)), 7.62 (d, <sup>3</sup>*J* = 7.8 Hz, 1H, H-C(6)), 7.41 (ddd, <sup>3</sup>*J* = 8.3 Hz, <sup>3</sup>*J* = 7.1 Hz, <sup>4</sup>*J* = 1.0 Hz, 1H, H-C(4)), 6.92 - 6.90 (m, 1H, H-C(3)), 6.79 (dd, <sup>3</sup>*J* = 7.5 Hz, <sup>3</sup>*J* = 7.3 Hz, 1H, H-C(5)), 6.31 (s, 1H, H-C(10)), 3.78 - 3.71 (m, 2H, H-C(18)), 3.26 - 3.21 (m, 4H, H-C(15)), 2.79 - 2.74 (m, 4H, H-C(17)), 1.99 - 1.94 (m, 4H, H-C(16)), 1.74 (*sext*, <sup>3</sup>*J* = 7.7 Hz, 2H, H-C(19)), 0.98 (t, <sup>3</sup>*J* = 7.5 Hz, 3H, H-C(20)).

**<sup>13</sup>C-NMR (151 MHz, CD<sub>2</sub>Cl<sub>2</sub>):**  $\delta$  (ppm) = 183.52 (C(8)), 151.73 (C(2)), 144.78 (C(14)), 135.02 (C(4)), 133.92 (C(9)), 130.70 (2C, C(12)), 124.45 (C(6)), 122.08 (C(11)), 121.99 (C(7)), 121.54 (C(10)), 120.89 (2C, C(13)), 118.11 (C(5)), 109.23 (C(3)), 50.56 (2C, C(15)), 44.50 (C(18)), 28.32 (2C, C(17)), 22.42 (2C, C(16)), 21.55 (C(19)), 11.96 (C(20)).

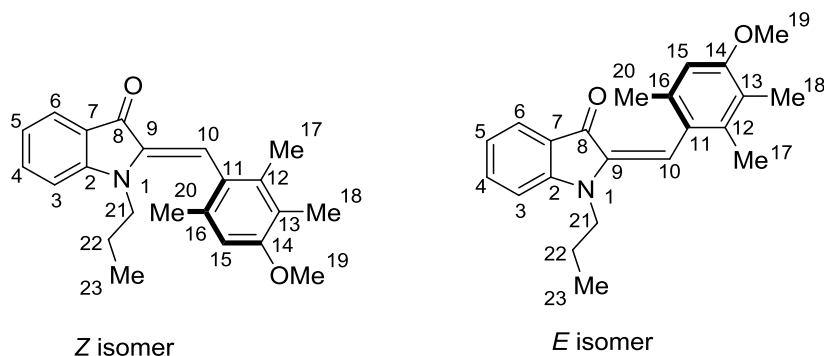
**IR (Diamond ATR):**  $\tilde{\nu}$  (cm<sup>-1</sup>) = 3058 (w), 2925 (s), 2873 (m), 2841 (m), 2128 (w), 1941 (w), 1625 (s), 1600 (s), 1565 (w), 1528 (s), 1509 (s), 1480 (s), 1461 (s), 1431 (s), 1357 (s), 1306 (s), 1268 (s), 1258 (s), 1207 (m), 1173 (s), 1156 (s), 1125 (s), 1088 (s), 1044 (s), 1030 (s), 1006 (s), 953 (s), 921 (s), 900 (s), 862 (m), 833 (m), 748 (s), 720 (s), 703 (s).

**MS (EI+, 70 eV):** *m/z* (%) = 359.2 (31), 358.2 (100), 287.1 (29).

**HRMS (EI+, C<sub>24</sub>H<sub>26</sub>N<sub>2</sub>O):** calcd.: 358.2045; found: 358.2041 (M+).

**EA (C<sub>24</sub>H<sub>26</sub>N<sub>2</sub>O):** calcd.: N, 7.81; C, 80.41; H, 7.31; found: N, 7.58; C, 80.41; H, 7.61.



**(Z/E)-2-(4-methoxy-2,3,6-trimethylbenzylidene)-1-propylindolin-3-one (28)**

A flame dried, nitrogen-flushed round bottom flask, equipped with a magnetic stirring bar was charged with sodium hydride (0.03 g, 0.76 mmol, 1.5 equiv., 60% w / w in paraffin oil), (*Z*)-2-(4-methoxy-2,3,6-trimethylbenzylidene)indolin-3-one **27** (0.149 g, 0.51 mmol, 1.0 equiv.) and dimethylformamide (4.00 mL, 0.13 M). The solution was stirred at 23 °C for 15 min. 1-Iodopropane (0.104 g, 0.61 mmol, 1.2 equiv.) was added dropwise and it was stirred at 23 °C for 5 min until a yellow solution emerged. The reaction was terminated with sat. aq. ammonium chloride solution, extracted with ethyl acetate, treated with sat. aq. sodium bisulfite solution, washed ten times with water and once with brine. The combined organic layers were dried over sodium sulfate. Removal of the solvents *in vacuo* after filtration and subsequent purification by flash column chromatography (aluminium(III) oxide, *Brockmann* III, 6% water w / w), hexanes / ethyl acetate, 9 / 1, v / v) yielded (*Z/E*)-2-(4-methoxy-2,3,6-trimethylbenzylidene)-1-propylindolin-3-one **28** (0.152 g, 0.453 mmol, 89%) as yellow solid.

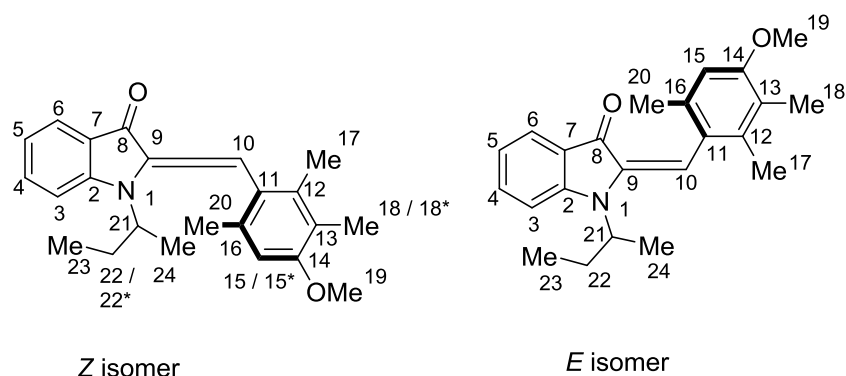
$R_f = 0.29$  (silica, hexanes / ethyl acetate, 9 / 1, v / v).

**Z isomer:**

**$^1\text{H-NMR}$  (400 MHz,  $\text{CD}_2\text{Cl}_2$ ):**  $\delta$  (ppm) = (d,  $^3J = 7.6$  Hz, 1H, H-C(6), 7.47 (dd,  $^3J = 7.5$  Hz, 7.5 Hz, 1H, H-C(4)), 6.90 (dd,  $^3J = 8.0$  Hz,  $^3J = 8.0$  Hz, 1H, H-C(5)), 6.88 (dd,  $^3J = 8.0$  Hz,  $^3J = 8.0$  Hz, 1H, H-C(3)), 6.64 (s, 1H, H-C(10)), 6.59 (s, 1H, H-C(15)), 3.86 (s, 3H, H-C(19)), 3.25 - 3.16 (m, 2H, H-C(21)) 2.57 (s, 3H, H-C(20)), 2.51 (s, 3H, H-C(17)), 2.14 (s, 3H, H-C(18)), 1.18 (sext,  $^3J = 7.3$  Hz, 2H, H-C(22)), 0.43 (t,  $^3J = 7.4$  Hz, 3H, H-C(23)).

**MS (EI+, 70 eV):**  $m/z$  (%) = 258.1 (11), 145.6 (13).

**HRMS (EI+,  $\text{C}_{22}\text{H}_{25}\text{NO}_2$ ):** calcd.: 335.1885; found: 335.1879 (M+).

**(Z/E)-1-(*sec*-butyl)-2-(4-methoxy-2,3,6-trimethylbenzylidene)indolin-3-one (58)**

A flame dried, nitrogen-flushed round bottom flask, equipped with a magnetic stirring bar was charged with sodium hydride (0.033 g, 0.793 mmol, 1.5 equiv., 60% w / w in paraffin oil), (*Z*)-2-(4-methoxy-2,3,6-trimethylbenzylidene)indolin-3-one **27** (0.155 g, 0.53 mmol, 1.0 equiv.) and dimethylformamide (4.5 mL, 0.13 M). The solution was stirred at 23 °C for 15 min. 2-Iodobutane (0.117 g, 0.61 mmol, 1.2 equiv.) was added and it was stirred at 60 °C for 15 h. The reaction was terminated with sat. aq. ammonium chloride solution, extracted with ethyl acetate, treated with sat. aq. sodium bisulfite solution, washed ten times with water and once with brine. The combined organic layers were dried over sodium sulfate. Removal of the solvents *in vacuo* after filtration and subsequent purification by flash column chromatography (aluminium(III) oxide, *Brockmann* III, 6% water w / w), hexanes / ethyl acetate, 9 / 1, v / v) yielded (*Z/E*)-1-(*sec*-butyl)-2-(4-methoxy-2,3,6-trimethylbenzylidene)indolin-3-one **58** (0.035 g, 0.099 mmol, 19%) as yellow solid. Further purification was carried out via preparative HPLC (*Machery-Nagel* VP 250/21 *NUCLEODUR Sphinx* RP 5  $\mu$ m column, acetonitrile / water 8 / 2, v / v, 15 mL/min, 35 °C column temperature, retention times: 11.5 min (*E* isomer, 8.0 mg), 13.5 min (*Z* isomer, 16 mg) with 13% overall yield.

$R_f$  = 0.30 (silica, hexanes / ethyl acetate, 9 / 1, v / v).

**Z isomer:**

**$^1\text{H-NMR}$  (600 MHz,  $\text{CD}_2\text{Cl}_2$ ):**  $\delta$  (ppm) = 7.68 (dd,  $^3J = 7.6$  Hz,  $^3J = 1.3$  Hz, 1H, H-C(6)), 7.42 (ddd,  $^3J = 8.4$  Hz,  $^3J = 7.2$  Hz,  $^3J = 1.4$  Hz, 1H, H-C(4)), 7.05 (d,  $^3J = 8.7$  Hz, 1H, H-C(3)), 6.89 (dd,  $^3J = 7.4$  Hz,  $^3J = 7.4$  Hz, 1H, H-C(5)), 6.85 (s, 0.5H, H-C(10)), 6.84 (s, 0.5H, H-C(10\*)), 6.65 (s, 1H, H-C(15)), 3.83 (s, 3H, H-C(19)), 3.56 - 3.47 (m, 1H, H-C(21)), 2.23 (s, 3H, H-C(18)), 2.19 (s, 3H, H-C(17)), 2.14 (s, 1.5 H, H-C(18)) 2.13 (s, 1.5H, H-C(18\*)), 1.82 - 1.72

(m, 1H, H-C(22)), 1.55 - 1.45 (m, 1H, H-C(22\*)), 1.24 - 1.19 (m, 3H, H-C(24)), 0.57 (t,  $^3J = 6.4$  Hz, 1.5H, H-C(23)), 0.54 (t,  $^3J = 6.4$  Hz, 1.5H, H-C(23\*)).

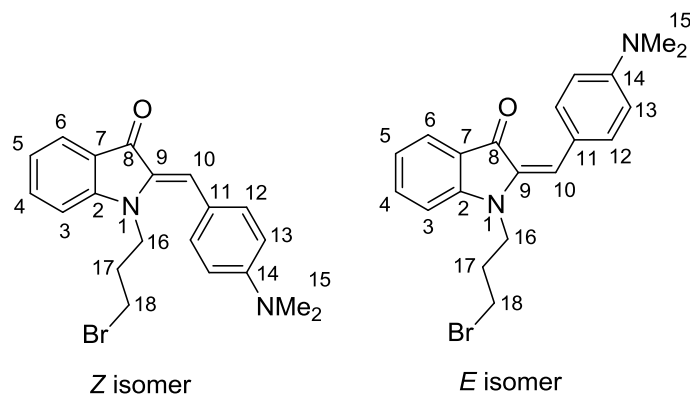
**$^{13}\text{C-NMR}$  (151 MHz,  $\text{CD}_2\text{Cl}_2$ ):**  $\delta$  (ppm) = 186.63 (0.5C, C(8)), 186.60 (0.5C, C(8\*)), 157.59 (0.5C, C(14)), 157.58 (0.5C, C(14\*)), 154.24 (0.5C, C(2)), 154.22 (0.5C, C(2\*)), 139.55 (0.5C, C(9)), 139.43 (0.5C, C(9\*)), 136.45 (0.5C, C(16)), 136.33 (0.5C, C(16\*)), 136.06 (0.5C, C(4)), 136.04 (0.5C, C(4\*)), 134.75 (0.5C, C(12)), 134.72 (0.5C, C(12\*)), 126.13 (0.5C, C(11)), 126.11 (0.5C, C(11\*)), 125.19 (C(6)), 123.38 (0.5C, C(3)), 123.37 (0.5C, C(3\*)), 123.02 (0.5C, C(13)), 123.00 (0.5C, C(13\*)), 119.68 (C(5)), 113.46 (0.5C, C(3)), 113.44 (0.5C, C(3\*)), 112.22 (0.5C, C(10)), 112.15 (0.5C, C(10\*)), 110.11 (0.5C, C(15)), 110.09 (0.5C, C(15\*)), 55.98 (0.5C, C(19)), 55.97 (0.5C, C(19\*)), 54.20 (0.5C, C(21)), 54.16 (0.5 C(21)) 27.78 (0.5C, C(22\*)), 27.71 (0.5C, C(22)), 21.35 (0.5C, C(20)), 21.30 (0.5C, C(20\*)), 18.68 (0.5C, C(24)), 18.60 (0.5C, C(24\*)), 18.02 (0.5C, C(17)), 18.01 (0.5C, C(17\*)), 12.00 (0.5C, C(18)), 11.91 (0.5C, C(18\*)), 11.83 (0.5C, C(23)), 11.76 (0.5C, C(23\*)).

***E* isomer:**

**$^1\text{H-NMR}$  (600 MHz,  $\text{CD}_2\text{Cl}_2$ ):**  $\delta$  (ppm) = 7.50 (dd,  $^3J = 7.8$  Hz, 1.2 Hz, 1H, H-C(6)), 7.43 (ddd,  $^3J = 8.5$  Hz,  $^3J = 7.2$  Hz,  $^3J = 1.5$  Hz, 1H, H-C(4)), 7.03 (d,  $^3J = 8.3$  Hz, 1H, H-C(2)), 6.78 (ddd,  $^3J = 7.4$  Hz,  $^3J = 7.4$  Hz,  $^3J = 0.7$  Hz, 1H, H-C(5)), 6.64 (s, 1H, H-C(15)), 6.44 (s, 1H, H-C(10)), 4.23 - 4.13 (m, 1H, H-C(21)), 3.83 (s, 3H, H-C(19)), 2.21 - 2.10 (m, 1H, H-C(22)), 2.19 (s, 3H, H-C(20)), 2.14 (s, 6H, H-C(17, 18)), 1.91 - 1.79 (m, 1H, H-C(22\*)), 1.56 (s, 1.5H, H-C(24)), 1.55 (s, 1.5H, H-C(24\*)), , 0.96 (t,  $^3J = 7.4$  Hz, 3H, H-C(24)).

**MS (EI+, 70 eV):**  $m/z$  (%) = 349.2 (43), 335.2 (25), 334.2 (100), 333.2 (13), 332.2 (48).

**HRMS (EI+,  $\text{C}_{23}\text{H}_{27}\text{NO}_2$ ):** calcd.: 349.2042; found: 349.2033 (M+).

**(Z/E)-1-(3-bromopropyl)-2-(4-(dimethylamino)benzylidene)indolin-3-one (83)**

To a sealable, N<sub>2</sub> purged round bottom flask, equipped with a magnetic stirring bar, (*Z*)-2-(4-(dimethylamino)benzylidene)indolin-3-one **11** (0.100 g, 0.378 mmol, 1.0 equiv.) sodium hydride (60% w / w, 0.018 g, 0.454 mmol, 1.2 equiv.) and dimethylformamide (4 mL, 0.1 M) were added and the deep green solution was stirred for 15 min at 23 °C. The mixture was taken up in a syringe and added via syringe pump (0.25 mL/h) to another N<sub>2</sub> purged round bottom flask, equipped with a magnetic stirring bar, filled with 1,3-dibromopropane (0.092 mg, 0.454 mmol, 1.2 equiv.) and dimethylformamide (4 mL, 0.1 M) at 23 °C. After completion of the addition, the mixture was neutralized with aq. sat. ammonium chloride solution, extracted with ethyl acetate, washed ten times with water and treated with brine once. The combined organic phases were dried over sodium sulfate and the volatiles were removed *in vacuo*. Subsequent purification by flash column chromatography (aluminium(III) oxide, *Brockmann*(III), hexanes / ethyl acetate, 4 / 1, v / v) yielded (*Z/E*)-1-(3-bromopropyl)-2-(4-(dimethylamino)benzylidene)indolin-3-one **83** (0.086 g, 0.22 mmol, 59%) as deep red solid. Further purification was carried out via preparative HPLC (*Machery-Nagel* VP 250/21 *NUCLEODUR Sphinx* RP 5 μm column, acetonitrile / water, 8 / 2, v / v, 15 mL/min, 35 °C column temperature, retention times: 9.8 min, 53 mg (37%) of an *E / Z* mixture was obtained.

*R<sub>f</sub>* = 0.37 (silica, hexanes / ethyl acetate, 4 / 1, v / v).

**Z isomer:**

**<sup>1</sup>H-NMR (600 MHz, CD<sub>2</sub>Cl<sub>2</sub>):** δ (ppm) = 7.68 (dd, <sup>3</sup>*J* = 7.6 Hz, <sup>4</sup>*J* = 1.4 Hz, 1H, H-C(6)), 7.52 (ddd, <sup>3</sup>*J* = 8.4 Hz, <sup>3</sup>*J* = 7.1 Hz, <sup>4</sup>*J* = 1.4 Hz, 1H, H-C(4)), 7.37 - 7.34 (m, 2H, H-C(12)), 7.14 (dd, <sup>3</sup>*J* = 8.2 Hz, <sup>4</sup>*J* = 0.8 Hz, 1H, H-C(3)), 7.02 (s, 1H, H-C(10)), 6.97 (ddd, <sup>3</sup>*J* = 7.7 Hz, <sup>3</sup>*J* = 7.3 Hz, <sup>4</sup>*J* = 0.8 Hz, 1H, H-C(5)), 6.76 - 6.73 (m, 2H, H-C(13)), 3.96 (t, <sup>3</sup>*J* = 7.1 Hz, 2H, H-

C(16)), 3.04 (t,  $^3J = 6.7$  Hz, 2H, H-C(18)), 3.03 (s, 6H, H-C(15)), 1.80 (*quin*,  $^3J = 6.9$  Hz, 2H, H-C(17)).

**$^{13}\text{C-NMR}$  (101 MHz,  $\text{CD}_2\text{Cl}_2$ ):**  $\delta$  (ppm) = 186.98 (C(8)), 155.87 (C(2)), 150.97 (C(14)), 135.90 (C(4)), 134.29 (C(9)), 132.71 (2C, C(12)), 124.79 (C(6)), 123.76 (C(7)), 121.47 (C(11)), 118.78 (C(5)), 116.54 (C(10)), 112.11 (C(3)), 112.11 (2C, C(13)), 44.07 (C(16)), 40.51 (2C, C(15)), 31.17 (C(18)), 30.17 (C(17)).

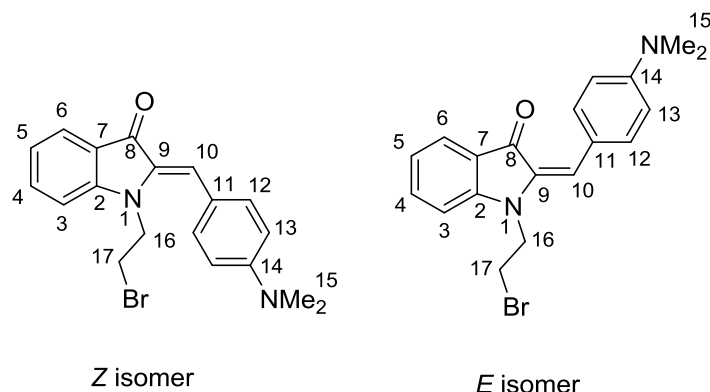
***E* isomer:**

**$^1\text{H-NMR}$  (600 MHz,  $\text{CD}_2\text{Cl}_2$ ):**  $\delta$  (ppm) = 8.20 - 8.17 (m, 2H, H-C(12)), 7.65 (dd,  $^3J = 7.5$  Hz,  $^4J = 1.3$  Hz, 1H, H-C(6)), 7.46 (ddd,  $^3J = 8.4$  Hz,  $^3J = 7.1$  Hz,  $^4J = 1.4$  Hz, 1H, H-C(4)), 7.01 (dd,  $^3J = 8.4$  Hz,  $^4J = 0.7$  Hz, 1H, H-C(3)), 6.85 (ddd,  $^3J = 7.7$  Hz,  $^3J = 7.2$  Hz,  $^3J = 0.8$  Hz, 1H, H-C(5)), 6.73 - 6.71 (m, 2H, H-C(13)), 6.48 (s, 1H, H-C(10)), 4.00 (t,  $^3J = 6.9$  Hz, 2H, H-C(16)), 3.50 (t,  $^3J = 6.2$  Hz, 2H, H-C(18)), 3.04 (s, 6H, H-C(15)), 2.30 (*quin*,  $^3J = 6.7$  Hz, 2H, H-C(17)).

**$^{13}\text{C-NMR}$  (151 MHz,  $\text{CD}_2\text{Cl}_2$ ):**  $\delta$  (ppm) = 183.85 (C(8)), 151.82 (C(14)), 151.57 (C(2)), 135.56 (C(4)), 132.93 (2C, C(12)), 132.71 (C(9)), 124.66 (C(6)), 122.71 (C(11)), 122.06 (C(7)), 120.62 (C(5)), 120.54 (C(10)), 111.67 (2C, C(13)), 109.20 (C(3)), 40.92 (C(16)), 40.46 (2C, C(15)), 31.85 (C(18)), 31.24 (C(17)).

**MS (EI+, 70 eV):**  $m/z$  (%) = 386.1 (20), 384.1 (22), 305.2 (24), 304.2 (100), 303.1 (16), 277.1 (17), 264.1 (17), 263.1 (83), 248.1 (30), 247.1 (20), 232.1 (14), 220.1 (19), 219.1 (19), 159.1 (11), 134.1 (14), 57 (12).

**HRMS (EI+,  $\text{C}_{20}\text{H}_{21}\text{BrN}_2\text{O}$ ):** calcd.: 384.0837; found: 384.0831(M+).

**(Z/E)-1-(2-bromoethyl)-2-(4-(dimethylamino)benzylidene)indolin-3-one (84)**

To a sealable, N<sub>2</sub> purged round bottom flask, equipped with a magnetic stirring bar, (*Z*)-2-(4-(dimethylamino)benzylidene)indolin-3-one **11** (0.200 g, 0.757 mmol, 1.0 equiv.) sodium hydride (60% w / w, 0.045 g, 1.135 mmol, 1.5 equiv.) and dimethylformamide (8 mL, 0.1 M) were added and the deep green solution was stirred for 15 min at 23 °C. 1,2-dibromoethane (0.711 g, 3.78 mmol, 5.0 equiv.) was added and the solution mixture was stirred for 30 min at 23 °C. The mixture was neutralized with aq. sat. ammonium chloride solution, extracted with ethyl acetate, washed ten times with water and treated with brine once. The combined organic phases were dried over sodium sulfate and the volatiles were removed *in vacuo*. Subsequent purification by flash column chromatography (aluminium(III) oxide, *Brockmann*(III), hexanes / ethyl acetate, 8 / 2, v / v) yielded (*Z/E*)-1-(3-bromoethyl)-2-(4-(dimethylamino)benzylidene)-indolin-3-one **84** (0.042 g, 0.113 mmol, 15%) as deep red solid. Further purification was carried out via preparative HPLC (*Machery-Nagel* VP 250/21 *NUCLEODUR Sphinx* RP 5 μm column, acetonitrile / water, 9 / 1, v / v, 15 mL/min, 35 °C column temperature, retention times: 5.4 min, 38 mg (14%) of an *E/Z* mixture was obtained.

$R_f = 0.34$  (silica, hexanes / ethyl acetate, 4 / 1, v / v).

**Z isomer:**

**<sup>1</sup>H-NMR (400 MHz, CD<sub>2</sub>Cl<sub>2</sub>):** δ (ppm) = 7.70 (dd, <sup>3</sup>*J* = 7.7 Hz, <sup>4</sup>*J* = 1.4 Hz, 1H, H-C(6)), 7.54 (ddd, <sup>3</sup>*J* = 8.4 Hz, 7.2 Hz, 1.4 Hz, 1H, H-C(4)), 7.39 - 7.33 (m, 2H, H-C(12)), 7.14 (d, <sup>3</sup>*J* = 8.3 Hz, 1H, H-C(3)), 7.04 (s, 1H, H-C(10)), 7.01 (ddd, <sup>3</sup>*J* = 7.4 Hz, <sup>3</sup>*J* = 6.3 Hz, <sup>4</sup>*J* = 0.9 Hz, 1H, H-C(5)), 6.78 - 6.74 (m, 2H, H-C(13)), 4.20 (t, <sup>3</sup>*J* = 7.4 Hz, 2H, H-C(16)), 3.16 (t, <sup>3</sup>*J* = 7.3 Hz, 7.1 Hz, 2H, H-C(17)), 3.05 (s, 6H, H-C(15)).

**<sup>13</sup>C-NMR (101 MHz, CD<sub>2</sub>Cl<sub>2</sub>):**  $\delta$  (ppm) = 186.79 (C(8)), 155.72 (C(2)), 151.10 (C(14)), 135.93 (C(4)), 134.97 (C(9)), 132.62 (2C, C(12)), 124.93 (C(6)), 123.92 (C(7)), 121.10 (C(11)), 119.39 (C(5)), 116.76 (C(10)), 112.24 (2C, C(13)), 111.96 (C(3)), 44.71 (C(16)), 40.47 (2C, C(15)), 28.26 (C(17)).

***E* isomer:**

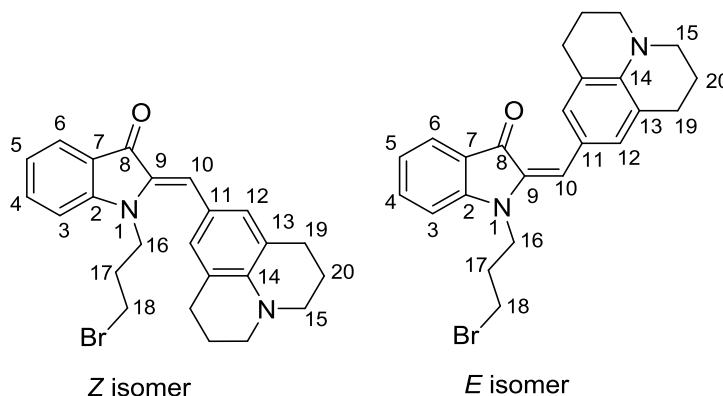
**<sup>1</sup>H-NMR (400 MHz, CD<sub>2</sub>Cl<sub>2</sub>):**  $\delta$  (ppm) = 8.21 - 8.13 (m, 2H, H-C(12)), 7.67 (dd, <sup>3</sup>*J* = 7.6 Hz, <sup>4</sup>*J* = 1.4 Hz, 1H, H-C(6)), 7.48 (ddd, <sup>3</sup>*J* = 8.4 Hz, <sup>3</sup>*J* = 7.2 Hz, <sup>4</sup>*J* = 1.4 Hz, 1H, H-C(4)), 7.00 (d, <sup>3</sup>*J* = 7.4 Hz, 1H, H-C(3)), 6.89 (ddd, <sup>3</sup>*J* = 7.8 Hz, <sup>3</sup>*J* = 7.3 Hz, <sup>4</sup>*J* = 0.8 Hz, 1H, H-C(5)), 6.74 - 6.69 (m, 2H, H-C(13)), 6.42 (s, 1H, H-C(10)), 4.23 (t, <sup>3</sup>*J* = 7.4 Hz, 2H, H-C(16)), 3.60 (t, <sup>3</sup>*J* = 7.3 Hz, 7.1 Hz, 2H, H-C(17)), 3.04 (s, 6H, H-C(15)).

**<sup>13</sup>C-NMR (101 MHz, CD<sub>2</sub>Cl<sub>2</sub>):**  $\delta$  (ppm) = 183.57 (C(8)), 151.73 (C(14)), 151.39 (C(2)), 135.57 (C(4)), 133.76 (C(9)), 133.03 (2C, C(12)), 124.76 (C(6)), 122.39 (C(11)), 122.30 (C(7)), 121.08 (C(5)), 120.56 (C(10)), 111.69 (2C, C(13)), 109.30 (C(3)), 47.01 (C(16)), 40.50 (2C, C(15)), 28.28 (C(17)).

**MS (EI+, 70 eV):** *m/z* (%) = 373.1 (23), 372.1 (100), 371.1 (29), 370.1 (95), 292.2 (16), 291.2 (27), 290.2 (60), 289.2 (21), 288.1 (29), 287.1 (12), 278.1 (10), 277.1 (53), 275.1 (10), 273.1 (11), 264.1 (16), 261.1 (12), 248.1 (26), 247.1 (21), 233.1 (18), 232.1 (15), 220.1 (20), 219 (17), 159.1 (12), 145.1 (10), 144.1 (12), 138.1 (18).

**HRMS (EI+, C<sub>19</sub>H<sub>19</sub>BrN<sub>2</sub>O):** calcd.: 372.0660; found: 372.0710(M+).

**(*Z/E*)-1-(3-bromopropyl)-2-((2,3,6,7-tetrahydro-1*H*,5*H*-pyrido[3,2,1-*ij*]quinolin-9-yl)methylene)indolin-3-one (85)**



To a sealable, N<sub>2</sub> purged round bottom flask, equipped with a magnetic stirring bar, (*Z*)-2-((2,3,6,7-tetrahydro-1*H*,5*H*-pyrido[3,2,1-*ij*]quinolin-9-yl)methylene)indolin-3-one **15** (0.050 g, 0.158 mmol, 1.0 equiv.) sodium hydride (60% w / w, 0.008 g, 0.190 mmol, 1.2 equiv.) and dimethylformamide (1.6 mL, 0.1 M) were added and the deep green solution was stirred for 15 min at 23 °C. The mixture was taken up in a syringe and added via syringe pump (0.25 mL/h) to another N<sub>2</sub> purged round bottom flask equipped with a magnetic stirring bar filled with 1,3-dibromopropane (0.038 g, 0.190 mmol, 1.2 equiv.) and dimethylformamide (1.6 mL, 0.1 M) at 23 °C. After completion of the addition, the mixture was neutralized with aq. sat. ammonium chloride solution, extracted with ethyl acetate, washed ten times with water and treated with brine once. The combined organic phases were dried over sodium sulfate and the volatiles were removed *in vacuo*. Subsequent purification by flash column chromatography (aluminium(III) oxide, *Brockmann*(III), hexanes / ethyl acetate, 8 / 2, v / v) yielded (*Z/E*)-1-(3-bromopropyl)-2-((2,3,6,7-tetrahydro-1*H*,5*H*-pyrido[3,2,1-*ij*]quinolin-9-yl)methylene)indolin-3-one **85** (0.032 g, 0.073 mmol, 46%) as deep violet solid. Further purification was carried out via preparative HPLC (*Machery-Nagel* VP 250/21 *NUCLEODUR Sphinx* RP 5 μm column, acetonitrile / water, 9 / 1, v / v, 15 mL/min, 35 °C column temperature, retention times: 7.6 min, 18 mg (26%) of an *E/Z* mixture was obtained.

**R<sub>f</sub>** = 0.29 (silica, hexanes / ethyl acetate, 8 / 2, v / v).

**Z isomer:**

**<sup>1</sup>H-NMR (400 MHz, CD<sub>2</sub>Cl<sub>2</sub>):** δ (ppm) = 7.67 (dd, <sup>3</sup>*J* = 7.6 Hz, <sup>4</sup>*J* = 1.3 Hz, 1H, H-C(6)), 7.44 (ddd, <sup>3</sup>*J* = 8.5 Hz, <sup>3</sup>*J* = 7.2 Hz, <sup>4</sup>*J* = 1.3 Hz, 1H, H-C(4)), 7.15 (d, <sup>3</sup>*J* = 8.3 Hz, 1H, H-C(3)), 6.96 (ddd, <sup>3</sup>*J* = 7.8 Hz, <sup>3</sup>*J* = 7.3 Hz, <sup>4</sup>*J* = 0.8 Hz, 1H, H-C(5)), 6.94 (s, 1H, H-C(10)), 6.91 (s, 2H, H-



C(12)), 3.97 (t,  $^3J = 6.7$  Hz, 2H, H-C(16)), 3.24 (t,  $^3J = 6.5$  Hz, 4H, H-C(15)), 3.07 (t,  $^3J = 6.4$  Hz, 2H, H-C(18)), 2.75 (t,  $^3J = 6.5$  Hz, 4H, H-C(19)), 1.96 (*quin*,  $^3J = 6.7$  Hz, 4H, H-C(20)), 1.84 (*quin*,  $^3J = 6.9$  Hz, 2H, H-C(17)).

**$^{13}\text{C-NMR}$  (101 MHz,  $\text{CD}_2\text{Cl}_2$ ):**  $\delta$  (ppm) = 186.77 (C(8)), 155.83 (C(2)), 144.08 (C(14)), 135.59 (C(4)), 135.03 (C(9)), 130.83 (2C, C(12)), 124.67 (C(6)), 124.10 (C(7)), 121.85 (2C, C(13)), 120.56 (C(5)), 120.40 (C(11)), 117.75 (C(10)), 112.27 (C(3)), 50.46 (2C, C(15)), 44.35 (C(16)), 31.31 (C(18)), 30.40 (C(17)), 28.26 (2C, C(19)), 22.29 (2C, C(20)).

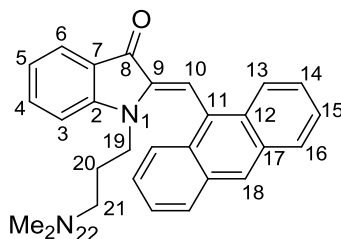
***E* isomer:**

**$^1\text{H-NMR}$  (400 MHz,  $\text{CD}_2\text{Cl}_2$ ):**  $\delta$  (ppm) = 7.82 (s, 2H, H-C(12)), 7.64 (dd,  $^3J = 7.6$  Hz,  $^4J = 1.3$  Hz, 1H, H-C(6)), 7.51 (ddd,  $^3J = 8.5$  Hz,  $^3J = 7.3$  Hz,  $^4J = 1.4$  Hz, 1H, H-C(4)), 7.01 (d,  $^3J = 8.3$  Hz, 1H, H-C(3)), 6.83 (ddd,  $^3J = 7.7$  Hz,  $^3J = 7.3$  Hz,  $^4J = 0.7$  Hz, 1H, H-C(5)), 6.30 (s, 1H, H-C(10)), 3.99 (t,  $^3J = 6.4$  Hz, 2H, H-C(16)), 3.48 (t,  $^3J = 6.1$  Hz, 2H, H-C(18)), 3.25 (t,  $^3J = 6.4$  Hz, 4H, H-C(15)), 2.78 (t,  $^3J = 6.5$  Hz, 4H, H-C(19)), 2.27 (*quin*,  $^3J = 6.6$  Hz, 2H, H-C(17)), 1.97 (*quin*,  $^3J = 6.6$  Hz, 4H, H-C(20)).

**$^{13}\text{C-NMR}$  (101 MHz,  $\text{CD}_2\text{Cl}_2$ ):**  $\delta$  (ppm) = 183.25 (C(8)), 151.37 (C(2)), 144.94 (C(14)), 135.14 (C(4)), 133.58 (C(9)), 130.62 (2C, C(12)), 124.51 (C(6)), 122.22 (C(7)), 121.86 (C(10)), 121.43 (C(11)), 120.88 (2C, C(13)), 118.57 (C(5)), 109.19 (C(3)), 50.56 (2C, C(15)), 40.96 (C(16)), 31.84 (C(18)), 31.30 (C(17)), 28.31 (2C, C(19)), 22.37 (2C, C(20)).

**MS (EI+, 70 eV):**  $m/z$  (%) = 439.1 (25), 438.1 (100), 437.1 (27), 436.1 (99), 357.2 (19), 356.2 (39), 355.2 (10), 329.1 (29), 315.1 (16), 288.1 (15), 287.1 (59), 186.1 (52), 173.1 (26), 164.6 (10), 164.1 (17), 150.1 (10), 57 (12), 44.0 (19).

**HRMS (EI+,  $\text{C}_{24}\text{H}_{25}\text{BrN}_2\text{O}$ ):** calcd.: 436.1150; found: 436.1146 (M+).

**(Z/E)-2-(anthracen-9-ylmethylene)-1-(3-(dimethylamino)propyl)indolin-3-one (100)**

To a sealable, N<sub>2</sub> purged round bottom flask, equipped with a magnetic stirring bar, (*Z*)-2-(anthracen-9-ylmethylene)indolin-3-one **51** (0.050 g, 0.156 mmol, 1.0 equiv.) sodium hydride (60% w / w, 0.009 g, 0.233 mmol, 1.5 equiv.) and dimethylformamide (0.3 mL, 0.5 M) were added and the deep green solution was stirred for 15 min at 23 °C. 3-chloro-*N,N*-dimethylpropan-1-amine (0.023 g, 0.187 mmol, 1.2 equiv.) was added and the mixture was heated to 120 °C for 5 min and slowly cooled to 23 °C. The reaction was treated with aq. sat. ammonium chloride solution, extracted with ethyl acetate, washed ten times with water and treated with brine once. The combined organic phases were dried over sodium sulfate and the volatiles were removed *in vacuo*. Subsequent purification by flash column chromatography (silica, dichloromethane / methanol / triethylamine, 88 / 10 / 2, v / v / v) yielded (*Z/E*)-2-(anthracen-9-ylmethylene)-1-(3-(dimethylamino)propyl)indolin-3-one **100** (0.018 g, 0.044 mmol, 28%) as viscous orange oil.

*R<sub>f</sub>* = 0.11 (silica, dichloromethane / methanol / triethylamine, 88 / 10 / 2, v / v / v).

**Z isomer:**

**<sup>1</sup>H-NMR (400 MHz, CD<sub>2</sub>Cl<sub>2</sub>):** δ (ppm) = 8.47 (s, 1H, H-C(18)), 8.15 - 8.07 (m, 4H, H-C(16, 13)), 7.76 (d, <sup>3</sup>*J* = 7.5 Hz, 1H, H-C(6)), 7.60 - 7.36 (m, 6H, H-C(10, 4, 15, 14)), 6.96 (ddd, <sup>3</sup>*J* = 7.5 Hz, <sup>3</sup>*J* = 7.5 Hz, <sup>4</sup>*J* = 0.8 Hz, 1H, H-C(5)), 6.89 (d, <sup>3</sup>*J* = 8.2 Hz, 1H, H-C(3)), 2.91 - 2.85 (m, 2H, H-C(19)), 1.60 (s, 6H, H-C(22)), 1.21 (t, <sup>3</sup>*J* = 8.3 Hz, 2H, H-C(21)), 1.00 (*quin*, <sup>3</sup>*J* = 8.2 Hz, 2H, H-C(20)).

**<sup>13</sup>C-NMR (101 MHz, CD<sub>2</sub>Cl<sub>2</sub>):** δ (ppm) = 186.34 (C(8)), 155.61 (C(2)), 139.56 (C(9)), 136.96 (C(4)), 131.84 (C(11)), 130.73 (2C, C(12)), 129.38 (2C, C(13)), 129.29 (C(18)), 126.91 (2C, C(15)), 126.52 (2C, C(16)), 126.51 (C(10)), 126.05 (2C, C(14)), 125.19 (C(6)), 126.21 (2C, C(17)), 120.22 (C(5)), 109.37 (C(3)), 107.39 (C(7)), 44.56 (2C, C(22)), 42.21 (C(19)), 25.18 (C(20)), 21.16 (C(21)).

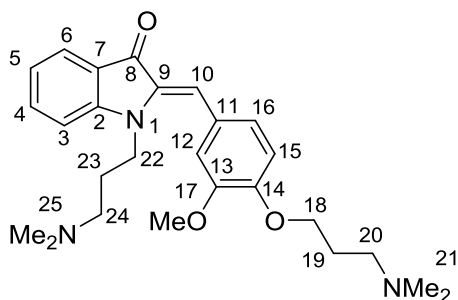
***E* isomer:**

**<sup>1</sup>H-NMR (400 MHz, CD<sub>2</sub>Cl<sub>2</sub>):**  $\delta$  (ppm) = 8.53 (s, 1H, H-C(18)), 8.15 - 8.07 (m, 4H, H-C(16, 13)), 7.78 (d, <sup>3</sup>*J* = 7.6 Hz, 1H, H-C(6)), 7.60 - 7.36 (m, 6H, H-C(10, 4, 15, 14)), 7.10 (d, <sup>3</sup>*J* = 8.0 Hz, 1H, H-C(3)), 6.81 (ddd, <sup>3</sup>*J* = 7.4 Hz, <sup>3</sup>*J* = 7.3 Hz, <sup>4</sup>*J* = 0.8 Hz, 1H, H-C(5)), 2.96 (m, <sup>3</sup>*J* = 6.7 Hz, 2H, H-C(19)), 2.28 (s, 6H, H-C(22)), 2.12 (*quin*, <sup>3</sup>*J* = 6.8 Hz, 2H, H-C(20)), 1.31 (t, <sup>3</sup>*J* = 6.7 Hz, 2H, H-C(21)).

**<sup>13</sup>C-NMR (101 MHz, CD<sub>2</sub>Cl<sub>2</sub>):**  $\delta$  (ppm) = 185.72 (C(8)), 154.67 (C(2)), 139.35 (C(9)), 137.51 (C(4)), 130.40 (2C, C(12)), 129.70 (2C, C(13)), 128.36 (C(11)), 127.57 (C(10)), 127.24 (C(18)), 126.25 (2C, 16), 126.09 (2C, C(17)), 126.03 (C(2C, 14)), 125.70 (C(2C, 15)), 125.39 (C(6)), 119.35 (C(5)), 108.46 (C(3)), 107.17 (C(7)), 45.67 (2C, C(22)), 40.70 (C(19)) 26.01 (C(20)), 9.14 (C(21)).

**MS (EI+, 70 eV):** *m/z* (%) = 406.2 (11), 335.1 (10), 215.1 (23), 208.1 (10), 191.1 (13), 180.1 (10), 178.1 (22), 61.0 (12), 58.1 (57), 45.0(13), 43.0 (100).

**HRMS (EI+, C<sub>28</sub>H<sub>26</sub>N<sub>2</sub>O):** calcd.: 406.2045; found: 406.2037 (M+).

**(Z/E)-2-(4-(3-(dimethylamino)propoxy)-3-methoxybenzylidene)-1-(3-(dimethylamino)propyl)indolin-3-one (101)**

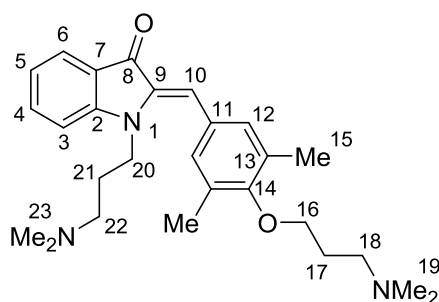
To a sealable, N<sub>2</sub> purged round bottom flask, equipped with a magnetic stirring bar, (Z)-2-(4-(3-(dimethylamino)propoxy)-3-methoxybenzylidene)indolin-3-one **34** (0.050 g, 0.142 mmol, 1.0 equiv.) sodium hydride (60% w / w, 0.009 g, 0.213 mmol, 1.5 equiv.) and dimethylformamide (0.3 mL, 0.5 M) were added and the deep green solution was stirred for 15 min at 23 °C. 3-chloro-*N,N*-dimethylpropan-1-amine (0.021 g, 0.170 mmol, 1.2 equiv.) was added and the mixture was heated to 120 °C for 5 min and slowly cooled to 23 °C. The reaction was treated with aq. sat. ammonium chloride solution, extracted with ethyl acetate, washed ten times with water and treated with brine once. The combined organic phases were dried over sodium sulfate and the volatiles were removed *in vacuo*. Subsequent purification by flash column chromatography (aluminium(III) oxide, *Brockmann* III, 6% water, w / w, dichloromethane / methanol, 99.5 / 0.5, v / v) yielded (Z/E)-2-(4-(3-(dimethylamino)propoxy)-3-methoxybenzylidene)-1-(3-(dimethylamino)propyl)indolin-3-one **101** (0.021 g, 0.047 mmol, 33%) as viscous orange oil. Further purification was carried out via preparative HPLC (*Machery-Nagel* VP 250/21 *NUCLEODUR Sphinx* RP 5 μm column, acetonitrile / water / triethylamine, 90 / 10 / 0.1, v / v / v, 10 mL/min, 35 °C column temperature, retention times: 13.0 min, 14 mg (23%) of an *E* / *Z* isomer mixture and cleaved aldehyde was obtained due to the low stability of the product.

**R<sub>f</sub>** = 0.68 (silica, dichloromethane / methanol, 99.5 / 0.5, v / v).

**MS (EI+, 70 eV):** *m/z* (%) = 435.3 (9), 215.1 (12), 86.1 (75), 84.1 (19), 58.1 (100), 42.8 (21).

**HRMS (EI+, C<sub>26</sub>H<sub>35</sub>N<sub>3</sub>O<sub>3</sub>):** calcd.: 437.2678; found: 437.2670 (M+).

**(*Z/E*)-2-(4-(3-(dimethylamino)propoxy)-3,5-dimethylbenzylidene)-1-(3-(dimethylamino)propyl)indolin-3-one (102)**



To a sealable, N<sub>2</sub> purged round bottom flask, equipped with a magnetic stirring bar, (*Z*)-2-(4-(3-(dimethylamino)propoxy)-3,5-dimethylbenzylidene)indolin-3-one **97** (0.050 g, 0.143 mmol, 1.0 equiv.) sodium hydride (60% w / w, 0.009 g, 0.214 mmol, 1.5 equiv.) and dimethylformamide (0.3 mL, 0.5 M) were added and the deep green solution was stirred for 15 min at 23 °C. 3-chloro-*N,N*-dimethylpropan-1-amine (0.021 g, 0.171 mmol, 1.2 equiv.) was added and the mixture was heated to 120 °C for 5 min and slowly cooled to 23 °C. The reaction was treated with aq. sat. ammonium chloride solution, extracted with ethyl acetate, washed ten times with water and treated with brine once. The combined organic phases were dried over sodium sulfate and the volatiles were removed *in vacuo*. Subsequent purification by flash column chromatography (aluminium(III) oxide, *Brockmann* III, 6% water, w / w, dichloromethane / methanol, 99.5 / 0.5, v / v) yielded (*Z/E*)-2-(4-(3-(dimethylamino)propoxy)-3,5-dimethylbenzylidene)-1-(3-(dimethylamino)propyl)indolin-3-one **102** (0.046 g, 0.106 mmol, 74%) as viscous orange oil. Further purification was carried out via preparative HPLC (*Machery-Nagel* VP 250/21 *NUCLEODUR Sphinx* RP 5 µm column, acetonitrile / water / triethylamine, 90 / 10 / 0.1, v / v / v, 10 mL/min, 35 °C column temperature, retention times: 20.0 min, 17 mg (28%) of an *E / Z* isomer mixture was obtained.

**R<sub>f</sub>** = 0.70 (silica, dichloromethane / methanol, 100 / 0.5, v / v).

**Z isomer:**

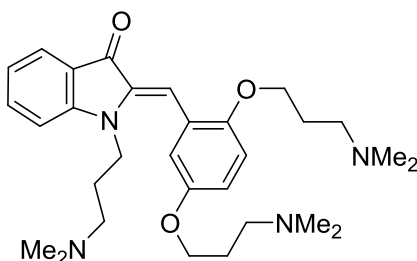
**<sup>1</sup>H-NMR (400 MHz, CD<sub>2</sub>Cl<sub>2</sub>):** δ (ppm) = 7.65 (dd, <sup>3</sup>*J* = 7.6 Hz, <sup>3</sup>*J* = 1.4 Hz, <sup>3</sup>*J* = 0.7 Hz, 1H, H-C(6)), 7.50 (ddd, <sup>3</sup>*J* = 8.4 Hz, <sup>3</sup>*J* = 7.2 Hz, <sup>3</sup>*J* = 1.4 Hz, 1H, H-C(4)), 7.07 (s, 2H, H-C(12)), 7.06 (d, <sup>3</sup>*J* = 8.6 Hz, 1H, H-C(3)), 6.92 (ddd, <sup>3</sup>*J* = 7.4 Hz, 7.3 Hz, 0.8 Hz, 1H, H-C(5)), 6.89 (s, 1H, H-C(10)), 3.87 - 3.81 (m, 2H, H-C(20)), 3.72 - 3.68 (m, 2H, H-C(16)), 2.47 (t, <sup>3</sup>*J* = 7.2 Hz,

2H, H-C(22)), 2.29 (s, 6H, H-C(15)), 2.22 (s, 6H, H-C(23)), 1.92 (s, 6H, H-C(19)), 1.95 (*quin*,  $^3J = 7.3$  Hz, 2H, H-C(21)), 1.85 - 1.81 (m, 2H, H-C(18)), 1.37 (*quin*,  $^3J = 7.3$  Hz, 2H, H-C(17)).

**MS (EI+, 70 eV):**  $m/z$  (%) = 437.3 (10), 86.1 (70), 84.1 (13), 58.1 (100), 43.0 (18).

**HRMS (EI+, C<sub>27</sub>H<sub>37</sub>N<sub>3</sub>O<sub>2</sub>):** calcd.: 435.2886; found: 435.2873 (M+).

**(Z/E)-2-(2,5-bis(3-(dimethylamino)propoxy)benzylidene)-1-(3-(dimethylamino)propyl)indolin-3-one (103)**

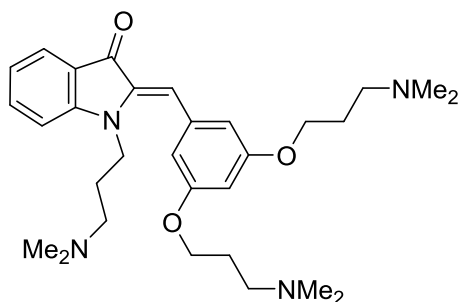


To a sealable, N<sub>2</sub> purged round bottom flask, equipped with a magnetic stirring bar, (*Z*)-2-(2,5-*bis*(3-(dimethylamino)propoxy)benzylidene)indolin-3-one **98** (0.033 g, 0.078 mmol, 1.0 equiv.) sodium hydride (60% w / w, 0.005 g, 0.117 mmol, 1.5 equiv.) and dimethylformamide (0.2 mL, 0.5 M) were added and the deep green solution was stirred for 15 min at 23 °C. 3-chloro-*N,N*-dimethylpropan-1-amine (0.011 g, 0.093 mmol, 1.2 equiv.) was added and the mixture was heated to 120 °C for 5 min and slowly cooled to 23 °C. The reaction was treated with aq. sat. ammonium chloride solution, extracted with ethyl acetate, washed ten times with water and treated with brine once. The combined organic phases were dried over sodium sulfate and the volatiles were removed *in vacuo*. Subsequent purification by flash column chromatography (silica, dichloromethane / methanol / triethylamine, 61 / 35 / 4, v / v / v) yielded crude (*Z/E*)-2-(2,5-*bis*(3-(dimethylamino)propoxy)benzylidene)-1-(3-(dimethylamino)propyl)indolin-3-one **103** (0.018 g, 0.035 mmol, 45%) as viscous orange oil. Purification via HPLC was not feasible for this compound.

**MS (EI+, 70 eV):**  $m/z$  (%) = 86.1 (11), 85.1 (10), 61.0 (13), 58.1 (47), 45.0 (14), 43.0 (100).

**HRMS (EI+, C<sub>30</sub>H<sub>44</sub>N<sub>4</sub>O<sub>3</sub>):** calcd.: 508.3413; found: 508.3420 (M+).

**(*Z/E*)-2-(3,5-bis(3-(dimethylamino)propoxy)benzylidene)-1-(3-(dimethylamino)propyl)indolin-3-one (104)**



To a sealable, N<sub>2</sub> purged round bottom flask, equipped with a magnetic stirring bar, (*Z*)-2-(3,5-bis(3-(dimethylamino)propoxy)benzylidene)indolin-3-one **99** (0.078 g, 0.184 mmol, 1.0 equiv.) sodium hydride (60% w / w, 0.011 g, 0.276 mmol, 1.5 equiv.) and dimethylformamide (0.4 mL, 0.5 M) were added and the deep green solution was stirred for 15 min at 23 °C. 3-chloro-*N,N*-dimethylpropan-1-amine (0.027 g, 0.221 mmol, 1.2 equiv.) was added and the mixture was heated to 120 °C for 5 min and slowly cooled to 23 °C. The reaction was treated with aq. sat. ammonium chloride solution, extracted with ethyl acetate, washed ten times with water and treated with brine once. The combined organic phases were dried over sodium sulfate and the volatiles were removed *in vacuo*. Subsequent purification by flash column chromatography (silica, dichloromethane / methanol / triethylamine, 61 / 35 / 4, v / v / v) yielded (*Z/E*)-2-(3,5-bis(3-(dimethylamino)propoxy)benzylidene)-1-(3-(dimethylamino)propyl)indolin-3-one **104** (0.031 g, 0.060 mmol, 33%) as viscous orange oil. Purification via HPLC was not feasible for this compound.

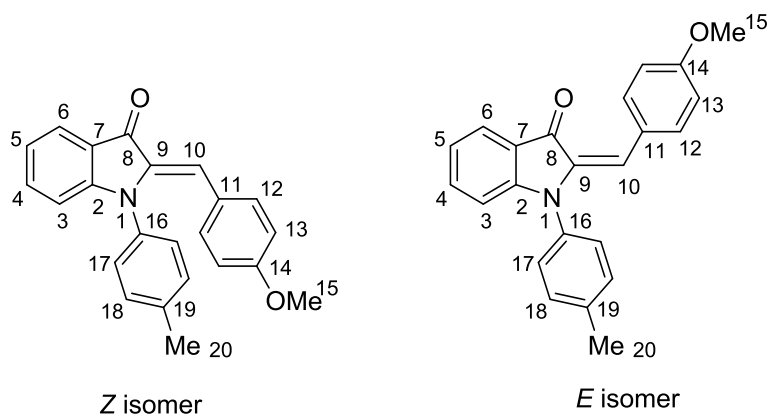
**MS (EI+, 70 eV):**  $m/z$  (%) = 508.3 (8), 215.1 (11), 127.9 (11), 86.1 (20), 84.1 (33), 61.0 (13), 58.1 (100), 45.1 (13), 44.1 (16), 43.1 (100), 42.2 (15).

**HRMS (EI+, C<sub>30</sub>H<sub>44</sub>N<sub>4</sub>O<sub>3</sub>):** calcd.: 508.3413; found: 508.3408 (M<sup>+</sup>).

### 3.7.2 *N*-Arylations - *Buchwald-Hartwig* cross-couplings

Scheme 10, Section 2.2.6 depicts a late-stage *Buchwald-Hartwig* cross-coupling reaction according to *Old et al.*<sup>[144]</sup>

#### (*Z/E*)-2-(4-(methoxy)benzylidene)-1-(*p*-tolyl)indolin-3-one (**116**)



A flame dried, nitrogen-flushed round bottom flask, equipped with a magnetic stirring bar, was charged with *tris*(dibenzylideneacetone)dipalladium(0) (0.009 g, 0.01 mmol, 0.02 equiv.), 2-dicyclohexylphosphino-2'-(*N,N*-dimethylamino)biphenyl (0.012 g, 0.03 mmol, 0.06 equiv.), dry toluene (4 mL, 0.125 M) and sodium *tert*-butoxide (0.068 g, 0.704 mmol, 1.40 equiv.). The mixture was stirred at 80 °C for 5 min. Then, (*Z*)-2-(4-methoxybenzylidene)indolin-3-one **9** (0.127 g, 0.505 mmol, 1.00 equiv.) was added to the suspension at 80 °C and it was stirred for 5 min. Subsequently, 4-bromotoluene (0.085 g, 0.495 mmol, 0.98 equiv.) was added to the reaction and it was stirred at 80 °C for 18 h. The reaction was stopped with sat. aq. ammonium chloride solution, filtered through celite, extracted with ethyl acetate and washed with sat. aq. sodium bisulfite solution. The combined organic layers were dried over sodium sulfate, filtered and the solvents were removed *in vacuo*. Subsequent purification by flash column chromatography (aluminium(III) oxide, *Brockmann* III, 6% water, w / w), hexanes / ethyl acetate, 9 / 1, v / v) yielded crude (*Z/E*)-2-(4-(methoxy)benzylidene)-1-(*p*-tolyl)indolin-3-one **116** (0.083 g, 0.244 mmol, 48%) as orange solid. Further purification was carried out via preparative HPLC (*Machery-Nagel* VP 250/21 *NUCLEODUR Sphinx* RP 5  $\mu$ m column, acetonitrile / water, 7 / 3, v / v, 15 mL/min, 35 °C column temperature, retention times: 15.1 min (*Z* isomer), 22.5 min (*E* isomer) with 29% yield.

$R_f = 0.55$  (*E* isomer), 0.38 (*Z* isomer), (silica, hexanes / ethyl acetate, 4 / 1, v / v)



**m.p. (°C):** 103 - 104.

**Z isomer:**

**<sup>1</sup>H-NMR (800 MHz, CD<sub>2</sub>Cl<sub>2</sub>):**  $\delta$  (ppm) = 7.75 (d, <sup>3</sup>*J* = 7.5 Hz, 1H, H-C(6)), 7.43 (ddd, <sup>3</sup>*J* = 8.0 Hz, <sup>3</sup>*J* = 7.0 Hz, <sup>4</sup>*J* = 1.3 Hz, 1H, H-C(4)), 7.09 - 7.07 (m, 2H, H-C(18)), 7.06 - 7.03 (m, 4H, H-C(17), H-C(10), H-C(3)), 7.01 (ddd, <sup>3</sup>*J* = 7.5 Hz, <sup>3</sup>*J* = 7.0 Hz, <sup>4</sup>*J* = 0.8 Hz, 1H, H-C(5)), 6.97 - 6.95 (m, 2H, H-C(12)), 6.55 - 6.52 Hz (m, 2H, H-C(13)), 3.71 (s, 3H, H-C(15)), 2.30 (s, 3H, H-C(20)).

**<sup>13</sup>C-NMR (201 MHz, CD<sub>2</sub>Cl<sub>2</sub>):**  $\delta$  (ppm) = 187.22 (C(8)), 160.17 (C(14)), 155.98 (C(2)), 137.37 (C(16)), 137.29 (C(19)), 136.28 (C(4)), 135.69 (C(9)), 132.83 (2C, C(12)), 130.35 (2C, C(18)), 127.09 (2C, C(17)), 126.21 (C(11)), 124.95 (C(6)), 122.65 (C(7)), 121.52 (C(5)), 114.74 (C(10)), 113.62 (2C, C(13)), 111.59 (C(3)), 55.89 (C(15)), 21.42 (C(20)).

**E isomer:**

**<sup>1</sup>H-NMR (800 MHz, CD<sub>2</sub>Cl<sub>2</sub>):**  $\delta$  (ppm) = 8.05 - 8.02 (m, 2H, H-C(12)), 7.71 (d, <sup>3</sup>*J* = 7.7 Hz, 1H, H-C(6)), 7.40 - 7.38 (m, 2H, H-C(18)), 7.37 (ddd, <sup>3</sup>*J* = 8.2 Hz, <sup>3</sup>*J* = 7.3 Hz, <sup>4</sup>*J* = 1.4 Hz, 1H, H-C(4)), 7.29 - 7.26 (m, 2H, H-C(17)), 6.90 (ddd, <sup>3</sup>*J* = 7.5 Hz, <sup>3</sup>*J* = 7.3 Hz, <sup>4</sup>*J* = 0.9, 1H, H-C(5)), 6.89 - 6.86 (m, 2H, H-C(13)), 6.65 (d, <sup>3</sup>*J* = 8.3 Hz, 1H, H-C(3)), 6.25 (s, 1H, H-C(10)), 3.83 (s, 3H, H-C(15)), 2.46 (s, 3H, H-C(20)).

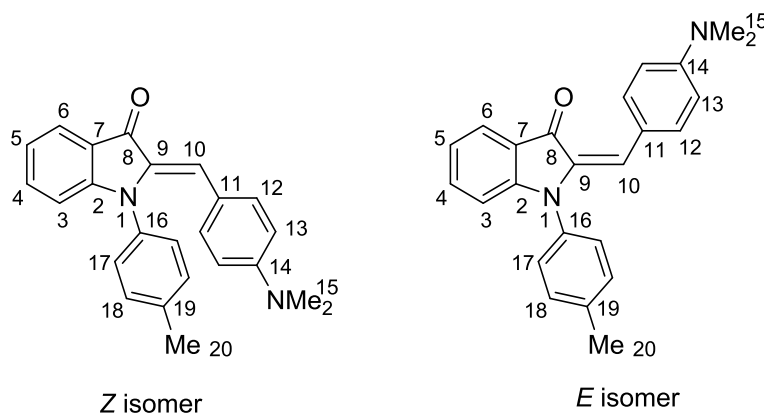
**<sup>13</sup>C-NMR (201 MHz, CD<sub>2</sub>Cl<sub>2</sub>):**  $\delta$  (ppm) = 184.71 (C(8)), 161.10 (C(14)), 153.34 (C(2)), 138.99 (C(19)), 138.34 (C(9)), 136.15 (C(4)), 135.11 (C(16)), 132.93 (2C, C(12)), 132.51 (2C, C(18)), 129.38 (2C, C(17)), 127.44 (C(11)), 124.89 (C(6)), 122.24 (C(7)), 120.45 (C(10)), 119.91 (C(5)), 114.10 (2C, C(13)), 110.57 (C(3)), 56.00 (C(15)), 21.68 (C(20)).

**IR (Diamond ATR):**  $\tilde{\nu}$  (cm<sup>-1</sup>) = 3032 (w), 2967 (w), 2927 (w), 2839 (w), 2361 (w), 1923 (w), 1671 (m), 1602 (s), 1577 (m), 1549 (m), 1510 (s), 1467 (s), 1445 (m), 1426 (m), 1395 (m), 1352 (m), 1313 (s), 1304 (s), 1255 (s), 1191 (m), 1177 (s), 1147 (m), 1136 (s), 1108 (m), 1096 (s), 1035(s), 978 (m), 947 (m), 931 (m), 884 (s), 828 (s), 810 (s), 802 (m), 790 (m), 746 (s), 713 (m), 702 (s).

**MS (EI+, 70 eV):** *m/z* (%) = 342.2 (29), 341.4 (100), 340.1 (45), 326.1 (29), 324.1 (12), 310 (10), 298.1 (10), 170.5 (11).

**HRMS (EI+, C<sub>23</sub>H<sub>19</sub>NO<sub>2</sub>):** calcd.: 341.1416; found: 341.1412 (M+).

**EA (C<sub>23</sub>H<sub>19</sub>NO<sub>2</sub>):** calcd.: N, 4.10; C, 80.92; H, 5.61; found: N, 3.97; C, 80.84; H, 5.70.

**(Z)-2-(4-(dimethylamino)benzylidene)-1-(p-tolyl)indolin-3-one (16)**

A flame dried, nitrogen-flushed round bottom flask, equipped with a magnetic stirring bar, was charged with *tris*(dibenzylideneacetone)dipalladium(0) (0.009 g, 0.01 mmol, 0.02 equiv.), 2-dicyclohexylphosphino-2'-(*N,N*-dimethylamino)biphenyl (0.012 g, 0.03 mmol, 0.06 equiv.), dry toluene (4 mL, 0.125 M) and sodium *tert*-butoxide (0.068 g, 0.704 mmol, 1.40 equiv.). The mixture was stirred at 80 °C for 5 min. Then, (*Z*)-2-(4-(dimethylamino)benzylidene)indolin-3-one **11** (0.133 g, 0.503 mmol, 1.00 equiv.) was added to the suspension at 80 °C and it was stirred for another 5 min. Subsequently, 4-bromotoluene (0.084 g, 0.493 mmol, 0.98 equiv.) was added to the reaction and it was stirred at 80 °C for 18 h. The reaction was stopped with sat. aq. ammonium chloride solution, filtered through celite, extracted with ethyl acetate and washed with sat. aq. sodium bisulfite solution. The combined organic layers were dried over sodium sulfate, filtered and the solvents were removed *in vacuo*. Subsequent purification by flash column chromatography (aluminium(III) oxide (*Brockmann* III, 6% water, w / w), hexanes / ethyl acetate 9 / 1, v / v, yielded crude (*Z/E*)-2-(4-(dimethylamino)benzylidene)-1-(*p*-tolyl)indolin-3-one **16** (0.122 g, 0.344 mmol, 68%) as orange to reddish solid. Further purification was carried out via preparative HPLC (*Machery-Nagel* VP 250/21 *NUCLEODUR Sphinx* RP 5  $\mu$ m column, acetonitrile / water, 7 / 3, v / v, 15 mL/min, 35 °C column temperature, retention times: 16.1 min (*Z* isomer) with 50% yield.

$R_f$  = 0.45 (silica, hexanes / ethyl acetate 4 / 1, v / v).

**m.p.** (°C): 146 - 148.

**Z isomer:**

**<sup>1</sup>H-NMR (800 MHz, CD<sub>2</sub>Cl<sub>2</sub>):**  $\delta$  (ppm) = 7.75 (d, <sup>3</sup>*J* = 7.7 Hz, 1H, H-C(6)), 7.41 (ddd, <sup>3</sup>*J* = 8.5 Hz, <sup>3</sup>*J* = 7.3 Hz, <sup>4</sup>*J* = 1.2 Hz, 1H, H-C(5)), 7.14 - 7.12 (m, 2H, H-C(18)), 7.11 - 7.09 (m,

3H, H-C(17, 16)), 7.07 (s, 1H, H-C(10)), 7.01 (ddd,  $^3J = 7.8$  Hz,  $^3J = 7.3$  Hz,  $^4J = 0.7$  Hz, 1H, H-C(4)), 6.95 - 6.92 (m, 2H, H-C(12)), 6.36 - 6.34 (m, 2H, H-C(13)), 2.90 (s, 6H, H-C(15)), 2.33 (s, 3H, H-C(20)).

**$^{13}\text{C-NMR}$  (201 MHz,  $\text{CD}_2\text{Cl}_2$ ):**  $\delta$  (ppm) = 186.73 (C(8)), 155.44 (C(2)), 150.75 (C(14)), 138.01 (C(16)), 136.95 (C(19)), 135.54 (C(4)), 133.97 (C(9)), 133.36 (2C, C(12)), 130.24 (2C, C(18)), 126.81 (2C, C(17)), 124.57 (C(6)), 123.08 (C(7)), 121.23 (C(5)), 120.94 (C(11)), 117.14 (C(10)), 111.67 (C(3)), 111.38 (2C, C(13)), 40.37 (2C, C(15)), 21.32 (C(20)).

***E* isomer:**

**$^1\text{H-NMR}$  (800 MHz,  $\text{CD}_2\text{Cl}_2$ ):**  $\delta$  (ppm) = 8.10 - 8.08 (m, 2H, H-C(12)), 7.7 (d,  $^3J = 7.8$  Hz, 1H, H-C(6)), 7.39 - 7.37 (m, 2H, H-C(18)), 7.35 (ddd,  $^3J = 8.2$  Hz,  $^3J = 7.0$  Hz,  $^4J = 1.3$  Hz, 1H, H-C(5)), 7.28 - 7.26 (m, 2H, H-C(17)), 6.89 (ddd,  $^3J = 7.8$  Hz,  $^3J = 7.4$  Hz,  $^4J = 0.7$  Hz, 1H, H-C(4)), 6.69 - 6.66 (m, 3H, H-C(13, 3)), 6.28 (s, 1H, H-C(10)), 3.02 (s, 6H, H-C(15)), 2.46 (s, 3H, H-C(20)).

**$^{13}\text{C-NMR}$  (201 MHz,  $\text{CD}_2\text{Cl}_2$ ):**  $\delta$  (ppm) = 183.69 (C(8)), 152.58 (C(2)), 151.70 (C(14)), 138.56 (C(19)), 136.81 (C(9)), 135.36 (C(16)), 135.27 (C(4)), 133.09 (2C, C(12)), 131.26 (2C, C(18)), 129.34 (2C, C(17)), 124.51 (C(6)), 122.79 (C(10)), 122.74 (C(11)), 122.39 (C(7)), 119.32 (C(5)), 111.67 (2C, C(13)), 110.38 (C(3)), 40.45 (2C, C(15)), 21.54 (C(20)).

**IR (Diamond ATR):**  $\tilde{\nu}$  ( $\text{cm}^{-1}$ ) = 2898 (w), 2362 (w), 1676 (w), 1660 (w), 1600 (s), 1559 (s), 1520 (s), 1475 (m), 1461 (m), 1444 (m), 1398 (w), 1359 (s), 1308 (s), 1295 (m), 1252 (w), 1228 (m), 1184 (s), 1169 (s), 1147 (m), 1110 (s), 1096 (s), 1062 (m), 1019 (m), 992 (m), 980 (m), 945 (m), 922 (s), 890 (m), 859 (w), 837 (w), 816 (s), 786 (m), 754 (s), 728 (m), 721 (m), 704 (s).

**MS (EI+, 70 eV):**  $m/z$  (%) = 355.2 (25), 354.2 (100), 353.2 (40), 337.2 (12), 337.1 (15), 310.1 (12), 177.5 (11).

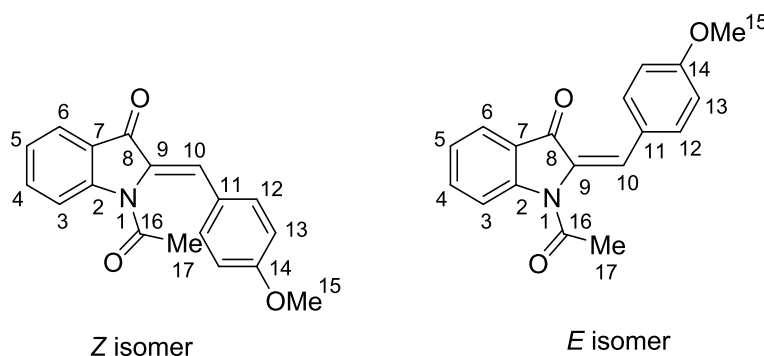
**HRMS (EI+,  $\text{C}_{24}\text{H}_{22}\text{N}_2\text{O}$ ):** calcd.: 354.1732; found: 354.1722 (M+).

**EA ( $\text{C}_{24}\text{H}_{22}\text{N}_2\text{O}$ ):** calcd.: N, 7.90; C, 81.33; H, 6.26; found: N, 7.82; C, 81.14; H, 6.41.

### 3.7.3 *N*-Acetylations - Nucleophilic catalysis

Scheme 6, Section 2.2.2 depicts a 4-dimethylaminopyridine (DMAP) catalyzed acylation reaction.

#### (*Z/E*)-1-acetyl-2-(4-(methoxy)benzylidene)indolin-3-one (**2**)



A flame dried, nitrogen-flushed round bottom flask, equipped with a magnetic stirring bar, was charged with (*Z*)-2-(4-methoxybenzylidene)indolin-3-one **9** (0.123 g, 0.489 mmol, 1.0 equiv.), 4-*N,N*-dimethylaminopyridine (0.006 g, 0.049 mmol, 0.1 equiv.), acetic anhydride (4.9 mL, 0.1 M) and *N,N*-diisopropylethylamine (0.127 g, 0.979 mmol, 2.0 equiv.). The mixture was stirred at 100 °C for 1 day. The remaining acetic anhydride was removed *in vacuo*, the residual slurr was extracted with ethyl acetate, basified with sat. aq. sodium hydrogen carbonate solution, washed ten times with water and sat. aq. sodium chloride solution. The combined organic layers were dried over sodium sulfate, filtered and the solvent was removed *in vacuo*. Subsequent purification by flash column chromatography (silica, hexanes / ethyl acetate, 9 / 1, v / v) yielded (*Z/E*)-1-acetyl-2-(4-methoxybenzylidene)indolin-3-one **2** (0.093 g, 0.318 mmol, 65%) as yellow solid. Further purification was carried out via preparative HPLC (*Machery-Nagel* VP 250/21 *NUCLEODUR Sphinx* RP 5  $\mu\text{m}$  column, acetonitrile / water, 7 / 3, v / v, 15 mL/min, 35 °C column temperature, retention times: 9.1 min (*Z* isomer) with 61% total yield.

$R_f$  = 0.30 (silica, hexanes / ethyl acetate, 9 / 1, v / v).

**m.p.** (°C): 135 - 136.

**Z isomer:**

**$^1\text{H-NMR}$  (800 MHz,  $\text{CD}_2\text{Cl}_2$ ):**  $\delta$  (ppm) = 8.24 (d,  $^3J$  = 8.3 Hz, 1H, H-C(6)), 7.81 (d,  $^3J$  = 7.5 Hz, 1H, H-C(3)), 7.67 (ddd,  $^3J$  = 8.3 Hz,  $^3J$  = 7.5 Hz,  $^4J$  = 1.4 Hz, 1H, H-C(4)), 7.55 - 7.52

(m, 2H, H-C(12)), 7.31 (ddd,  $^3J = 7.5$  Hz,  $^3J = 7.4$  Hz,  $^4J = 0.8$  Hz, 1H, H-C(5)), 7.28 (s, 1H, H-C(10)), 6.99 - 6.97 (m, 2H, H-C(13)), 3.86 (s, 3H, H-C(15)), 2.04 (s, 3H, H-C(17)).

**$^{13}\text{C-NMR}$  (201 MHz,  $\text{CD}_2\text{Cl}_2$ ):**  $\delta$  (ppm) = 186.38 (C(8)), 171.14 (C(16)), 161.68 (C(14)), 150.88 (C(2)), 136.57 (C(4)), 134.40 (C(9)), 133.03 (2C, C(12)), 126.92 (C(11)), 125.40 (C(5)), 125.09 (C(7)), 124.40 (C(6)), 123.73 (C(10)), 118.45 (C(3)), 115.31 (2C, C(13)), 56.14 (C(15)), 25.66 (C(17)).

***E* isomer:**

**$^1\text{H-NMR}$  (800 MHz,  $\text{CD}_2\text{Cl}_2$ ):**  $\delta$  (ppm) = 8.14 (d,  $^3J = 8.3$  Hz, 1H, H-C(6)), 7.98 - 7.95 (m, 2H, H-C(12)), 7.77 (d,  $^3J = 7.5$  Hz, 1H, H-C(3)), 7.64 (ddd,  $^3J = 8.6$  Hz,  $^3J = 7.3$  Hz,  $^4J = 1.5$  Hz, 1H, H-C(4)), 7.46 (s, 1H, H-C(10)), 7.26 (ddd,  $^3J = 7.5$  Hz,  $^3J = 7.5$  Hz,  $^4J = 0.7$  Hz, 1H, H-C(5)), 6.97 - 6.95 (m, 2H, H-C(13)), 3.88 (s, 3H, H-C(15)), 2.59 (s, 3H, H-C(17)).

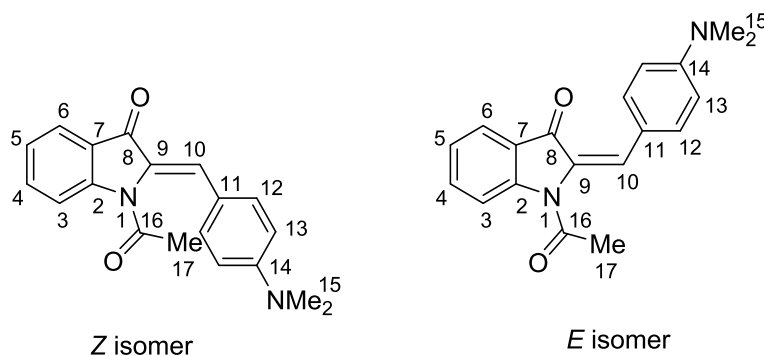
**$^{13}\text{C-NMR}$  (201 MHz,  $\text{CD}_2\text{Cl}_2$ ):**  $\delta$  (ppm) = 183.33 (C(8)), 169.94 (C(16)), 162.20 (C(14)), 148.73 (C(2)), 136.24 (C(4)), 134.45 (C(11)), 134.18 (2C, C(12)), 131.02 (C(10)), 125.59 (C(9)), 125.50 (C(7)), 125.02 (C(5)), 124.42 (C(6)), 117.94 (C(3)), 114.03 (2C, C(13)), 56.12 (C(15)), 26.86 (C(17)).

**IR (Diamond ATR):**  $\tilde{\nu}$  ( $\text{cm}^{-1}$ ) = 3066 (w), 2922 (m), 2852 (m), 2361 (w), 1706 (m), 1682 (s), 1629 (m), 1600 (s), 1509 (s), 1474 (w), 1456 (s), 1438 (m), 1361 (s), 1318 (m), 1303 (s), 1255 (s), 1231 (s), 1203 (m), 1177 (s), 1137 (m), 1098 (s), 1048 (m), 1030 (s), 1004 (s), 988 (s), 956 (m), 948 (m), 908 (m), 896 (m), 878 (s), 842 (s), 814 (s), 789 (m), 762 (s), 754 (s), 742 (m), 703 (s), 674 (m).

**MS (EI+, 70 eV):**  $m/z$  (%) = 293.1 (38), 252.1 (18), 251.1 (100), 250.1 (51), 236.1 (20), 235.1 (11), 220.1 (33).

**HRMS (EI+,  $\text{C}_{18}\text{H}_{15}\text{NO}_3$ ):** calcd.: 293.1052; found: 293.1045 (M+).

**EA ( $\text{C}_{18}\text{H}_{15}\text{NO}_3$ ):** calcd.: N, 4.78; C, 73.71; H 5.15; found: C, 73.44; N, 4.74; H 5.15.

**(Z/E)-1-acetyl-2-(4-(dimethylamino)benzylidene)indolin-3-one (12) CP181**

A flame dried, nitrogen-flushed round bottom flask, equipped with a magnetic stirring bar, was charged with (*Z*)-2-(4-(dimethylamino)benzylidene)indolin-3-one **11** (0.123 g, 0.465 mmol, 1.0 equiv.), 4-*N,N*-dimethylaminopyridine (0.047 mmol, 0.006 g, 0.1 equiv.), acetic anhydride (4.7 mL, 0.1 M) and *N,N*-diisopropylethylamine (0.120 g, 0.931 mmol, 2.0 equiv.). The mixture was stirred at 100 °C for 1 day. The remaining acetic anhydride was removed *in vacuo*, the residual slur was extracted with ethyl acetate, basified with sat. aq. sodium hydrogen carbonate solution, washed ten times with water and once with sat. aq. sodium chloride solution. The combined organic layers were dried over sodium sulfate, filtered and the solvent was removed *in vacuo*. Subsequent purification by flash column chromatography (silica, hexanes / ethyl acetate, 9 / 1, v / v) yielded (*Z*)-1-acetyl-2-(4-(dimethylamino)benzylidene)indolin-3-one **12** (0.139 g, 0.454 mmol, 98%) as violet solid. Further purification was carried out via preparative HPLC (*Machery-Nagel* VP 250/21 *NUCLEODUR Sphinx* RP 5  $\mu\text{m}$  column, acetonitrile / water, 7 / 3, v / v, 15 mL/min, 35 °C column temperature, retention times: 10.5 min (*Z* isomer) with 64% total yield.

$R_f = 0.19$  (silica, hexanes / ethyl acetate, 9 / 1, v / v).

**m.p.** (°C): 140 - 142.

**Z isomer:**

**$^1\text{H-NMR}$  (800 MHz,  $\text{CD}_2\text{Cl}_2$ ):**  $\delta$  (ppm) = 8.25 (d,  $^3J = 8.3$  Hz, 1H, H-C(6)), 7.79 (d,  $^3J = 7.5$  Hz, 1H, H-C(3)), 7.64 (ddd,  $^3J = 8.4$  Hz,  $^3J = 7.3$  Hz,  $^4J = 1.4$  Hz, 1H, H-C(5)), 7.49 - 7.47 (m, 2H, H-C(12)), 7.29 (ddd,  $^3J = 7.4$  Hz,  $^3J = 7.4$  Hz,  $^4J = 0.7$  Hz, 1H, H-C(4)), 7.27 (s, 1H, H-C(10)), 6.74 - 6.71 (m, 2H, H-C(13)), 3.05 (s, 6H, H-C(15)), 2.12 (s, 3H, H-C(17)).

**<sup>13</sup>C-NMR (201 MHz, CD<sub>2</sub>Cl<sub>2</sub>):**  $\delta$  (ppm) = 185.91 (C(8)), 171.55 (C(16)), 151.95 (C(14)), 150.27 (C(7)), 135.82 (C(5)), 133.37 (2C, C(12)), 132.28 (C(9)), 125.47 (C(2)), 125.01 (C(4)), 125.00 (C(10)), 123.94 (C(3)), 120.96 (C(11)), 118.23 (C(6)), 112.33 (2C, C(13)), 40.38 (2C, C(15)), 25.64 (C(17)).

***E* isomer:**

**<sup>1</sup>H-NMR (800 MHz, CD<sub>2</sub>Cl<sub>2</sub>):**  $\delta$  (ppm) = 8.18 (d, <sup>3</sup>*J* = 8.5 Hz, 1H, H-C(6)), 8.04 - 8.02 (m, 2H, H-C(12)), 7.77 (d, <sup>3</sup>*J* = 7.4 Hz, 1H, H-C(3)), 7.60 (ddd, <sup>3</sup>*J* = 8.6 Hz, <sup>3</sup>*J* = 7.2 Hz, <sup>3</sup>*J* = 1.4 Hz, 1H, H-C(5)), 7.3 (s, 1H, H-C(10)), 7.25 (ddd, <sup>3</sup>*J* = 7.4 Hz, <sup>3</sup>*J* = 7.4 Hz, <sup>4</sup>*J* = 0.7 Hz, 1H, H-C(4)), 6.75 - 6.73 (m, 2H, H-C(13)), 3.08 (s, 6H, H-C(15)), 2.57 (s, 3H, H-C(17)).

**<sup>13</sup>C-NMR (201 MHz, CD<sub>2</sub>Cl<sub>2</sub>):**  $\delta$  (ppm) = 182.09 (C(8)), 169.86 (C(16)), 152.73 (C(14)), 147.96 (C(7)), 135.36 (C(5)), 134.61 (2C, C(12)), 132.84 (C(10)), 132.26 (C(9)), 125.90 (C(2)), 124.61 (C(4)), 123.88 (C(3)), 120.50 (C(11)), 117.75 (C(6)), 111.34 (2C, C(13)), 40.44 (2C, C(15)), 26.65 (C(17)).

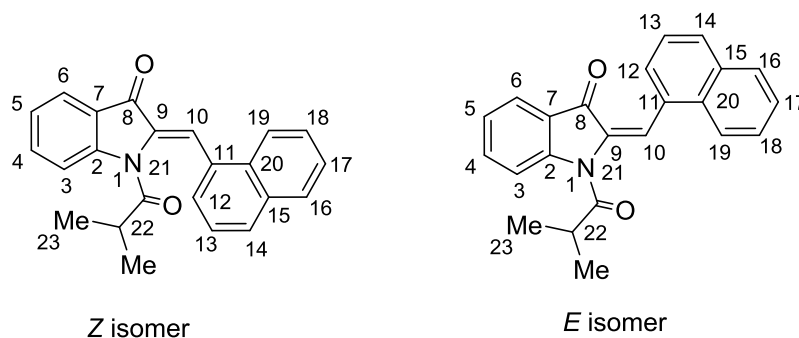
**IR (Diamond ATR):**  $\tilde{\nu}$  (cm<sup>-1</sup>) = 3087 (w), 3018 (w), 2986 (w), 2894 (w), 2816 (w), 2003 (w), 1979 (w), 1940 (w), 1889 (w), 1822 (w), 1681 (s), 1596 (s), 1586 (s), 1557 (m), 1524 (s), 1487 (w), 1474 (m), 1454 (s), 1411 (w), 1367 (s), 1358 (s), 1314 (m), 1302 (m), 1271 (s), 1243 (m), 1230 (m), 1211 (m), 1181 (s), 1170 (s), 1156 (m), 1140 (s), 1095 (s), 1067 (m), 1048 (m), 1036 (m), 1006 (s), 991 (m), 961 (w), 947 (m), 935 (m), 917 (w), 910 (w), 896 (s), 883 (m), 809 (s), 788 (m), 759 (s), 727 (m), 722 (m), 705 (s), 667 (m).

**MS (EI+, 70 eV):** *m/z* (%) = 307.1 (20), 306.1 (91), 265.1 (11), 248.1 (21), 247.1 (21), 220.1 (27), 219.1 (20), 159.1 (13).

**HRMS (EI+, C<sub>19</sub>H<sub>18</sub>N<sub>2</sub>O<sub>2</sub>):** calcd.: 306.1368; found: 306.1361 (M+).

**EA (C<sub>19</sub>H<sub>18</sub>N<sub>2</sub>O<sub>2</sub>):** calcd.: N, 9.14; C, 74.49; H 5.92; found: N, 9.04; C, 74.31; H 5.88.



**(Z/E)-1-isobutyryl-2-(naphthalen-1-ylmethylene)indolin-3-one (55)**

A flame dried, N<sub>2</sub>-flushed Schlenk flask, equipped with a magnetic stirring bar, is charged with triethylamine (0.082 g, 0.81 mmol, 1.1 equiv.), 4-(dimethylamino)-pyridine (0.009 g, 0.073 mmol, 0.1 equiv.), dichloroethane (3.0 mL, 0.25 M) and (Z)-2-(naphthalen-1-ylmethylene)indolin-3-one **50** (0.200 g, 0.737 mmol, 1.0 equiv.). The contents were stirred at 23 °C for 5 min, then isobutyryl chloride (0.086 g, 0.811 mmol, 1.1 equiv.) was added. The mixture was stirred at 80 °C for 18 h. The reaction was stopped with sat. aq. ammonium chloride solution and extracted with ethyl acetate. The combined organic layers were dried over sodium sulfate. The mixture was filtrated and the solvents were removed *in vacuo*. Purification by flash column chromatography (aluminium(III) oxide, *Brockmann* III, 6% water, w / w, hexanes / ethyl acetate, 9 / 1, v / v) yielded (Z/E)-1-isobutyryl-2-(naphthalen-1-ylmethylene)indolin-3-one **55** (0.204 g, 0.598 mmol, 81%) as yellow solid. Further purification was carried out via preparative HPLC (*Machery-Nagel* VP 250/21 *NUCLEODUR Sphinx* RP 5 μm column, acetonitrile / water 7 / 3, v / v, 15 mL/min, 35 °C column temperature, retention time: 10.0 min (Z isomer) with 38% yield.

$R_f$  = 0.36 (silica, hexanes / ethyl acetate, 9 / 1, v / v).

**m.p.** (°C): 69 - 71.

**Z isomer:**

**<sup>1</sup>H-NMR 600 MHz, CDCl<sub>3</sub>:** δ (ppm) = 8.21 (dd, <sup>3</sup>J = 8.4 Hz, <sup>4</sup>J = 0.7 Hz, 1H, H-C(6)), 8.12 (dd, <sup>3</sup>J = 8.3 Hz, <sup>4</sup>J = 0.9 Hz, 1H, H-C(19)), 7.93 - 7.88 (m, 4H, H-C(16, 10, 3, 14)), 7.69 - 7.60 (m, 3H, H-C(5, 12, 18)), 7.59 (ddd, <sup>3</sup>J = 6.8 Hz, <sup>3</sup>J = 5.6 Hz, <sup>4</sup>J = 1.3 Hz, 1H, H-C(17)), 7.51 (dd, <sup>3</sup>J = 8.2 Hz, <sup>3</sup>J = 7.2 Hz, 1H, H-C(13)), 7.29 (ddd, <sup>3</sup>J = 7.5 Hz, <sup>3</sup>J = 6.7 Hz, <sup>4</sup>J = 0.8 Hz, 1H, H-C(4)), 2.61 (sept, <sup>3</sup>J = 6.7 Hz, 1H, H-C(22)), 0.49 (d, <sup>3</sup>J = 6.8 Hz, 6H, H-C(23)).

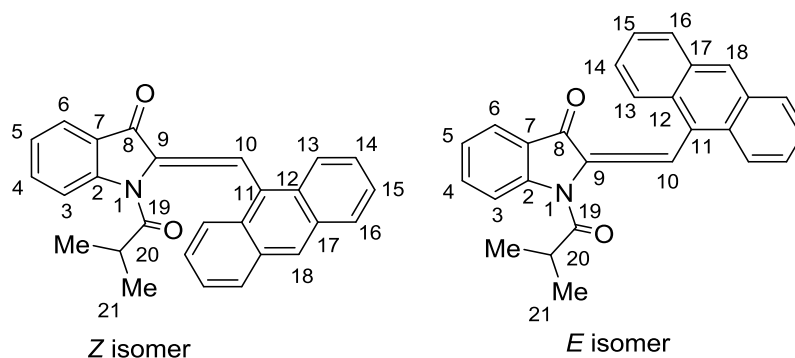
**$^{13}\text{C}$ -NMR (150 MHz,  $\text{CDCl}_3$ ):**  $\delta$  (ppm) = 185.17 (C(8)), 178.74 (C(21)), 150.75 (C(2)), 136.66 (C(4)), 136.08 (C(9)), 133.86 (C(15)), 131.46 (C(20)), 131.11 (C(11)), 130.20 (C(14)), 128.96 (C(16)), 127.54 (C(12)), 127.39 (C(18)), 126.76 (C(17)), 125.67 (C(13)), 124.41 (C(6)), 124.36 (C(5)), 123.98 (C(19)), 123.29 (C(7)), 118.92 (C(10)), 116.38 (C(3)), 35.14 (C(22)), 18.31 (C(23)).

**IR (Diamond ATR):**  $\tilde{\nu}$  ( $\text{cm}^{-1}$ ) = 3056 (w), 2965 (m), 2921 (m), 2850 (m), 2359 (w), 1682 (s), 1604 (s), 1584 (s), 1507 (w), 1457 (s), 1384 (s), 1355 (s), 1317 (m), 1298 (s), 1268 (m), 1242 (s), 1211 (m), 1181 (s), 1153 (m), 1127 (m), 1080 (s), 1043 (w), 1017 (w), 978 (m), 956 (m), 898 (m), 857 (w), 843 (w), 799 (s), 773 (s), 754 (s), 700 (s), 657 (w).

**MS (EI+, 70 eV):**  $m/z$  (%) = 341.1 (21), 272.1 (21), 271.1 (100), 270.1 (67), 241.1 (19), 71.0 (14), 43.0 (34).

**HRMS (EI+,  $\text{C}_{23}\text{H}_{19}\text{NO}_2$ ):** calcd.: 341.1416; found: 341.1412 (M+).

**EA ( $\text{C}_{23}\text{H}_{19}\text{NO}_2$ ):** calcd.: C, 80.92; H, 5.61; N, 4.10; found: C, 80.84; H, 5.86; N, 4.00.

**(Z/E)-2-(anthracen-9-ylmethylene)-1-isobutyrylindolin-3-one (56)**

A flame dried, N<sub>2</sub>-flushed Schlenk flask, equipped with a magnetic stirring bar, is charged with triethylamine (0.035 g, 0.342 mmol, 1.1 equiv.), 4-(dimethylamino)-pyridine (0.004 g, 0.031 mmol, 0.1 equiv.), dichloroethane (1.3 mL, 0.25 M) and (Z)-2-(anthracen-9-ylmethylene)indolin-3-one **51** (0.100 g, 0.311 mmol, 1.0 equiv.) were added. The contents were stirred at 23 °C for 5 min, then isobutyryl chloride (1.1 equiv.) was added. The mixture was stirred at 80 °C for 22 h. The reaction was stopped with sat. aq. ammonium chloride solution and extracted with ethyl acetate. The combined organic layers were dried over sodium sulfate. The mixture was filtrated and the solvents were removed *in vacuo*. Purification by flash column chromatography (aluminium(III) oxide, *Brockmann III*, 6% water, w / w, hexanes / ethyl acetate, 9 / 1, v / v) yielded (Z/E)-2-(anthracen-9-ylmethylene)-1-isobutyrylindolin-3-one **56** (0.063 g, 0.161 mmol, 52%) as orange solid. Further purification was carried out via preparative HPLC (*Machery-Nagel VP 250/21 NUCLEODUR Sphinx RP 5 μm* column, acetonitrile / water, 7 / 3, v / v, 15 mL/min, 35 °C column temperature, retention time: 12.5 min (*Z* isomer) with 56% yield.

$R_f = 0.28$  (hexanes / ethyl acetate, 4 / 1, v / v).

**m.p.** (°C): 54 - 56.

**Z isomer:**

**<sup>1</sup>H-NMR (600 MHz, CD<sub>2</sub>Cl<sub>2</sub>):**  $\delta$  (ppm) = 8.56 (s, 1H, H-C(18)), 8.20 (s, 1H, H-C(10)), 8.11 - 8.07 (m, 3H, H-C(6, 13)), 8.00 - 7.97 (m, 2H, H-C(15)), 7.95 (dd, <sup>3</sup>*J* = 7.6 Hz, <sup>4</sup>*J* = 0.9 Hz, 1H, H-C(3)), 7.69 (ddd, <sup>3</sup>*J* = 8.4 Hz, <sup>3</sup>*J* = 7.3 Hz, <sup>4</sup>*J* = 1.4 Hz, 1H, H-C(5)), 7.56 - 7.53 (m, 4H, H-C(16, 14)), 7.34 (ddd, <sup>3</sup>*J* = 8.0 Hz, <sup>3</sup>*J* = 7.5 Hz, <sup>4</sup>*J* = 0.7 Hz, 1H, H-C(4)), 2.27 (sept, <sup>3</sup>*J* = 6.8 Hz, 1H, H-C(20)), 0.07 (d, <sup>3</sup>*J* = 6.8 Hz, 6H, H-C(21)).

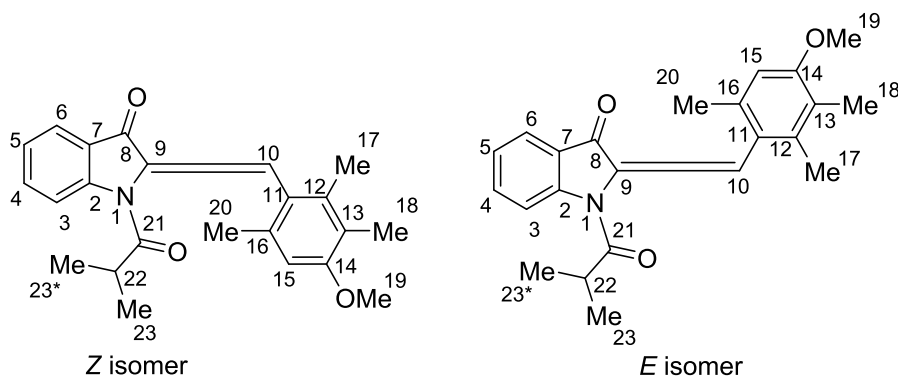
**$^{13}\text{C-NMR}$  (150 MHz,  $\text{CD}_2\text{Cl}_2$ ):**  $\delta$  (ppm) = 184.82 (C(8)), 177.41 (C(19)), 150.53 (C(2)), 136.63 (C(5)), 131.48 (2C, C(17)), 129.23 (2C, C(12)), 129.18 (2C, C(16)), 129.11 (C(18)), 128.88 (C(9)), 127.31 (C(11)), 127.15 (2C, C(14)), 125.69 (2C, C(13)), 124.94 (2C, C(15)), 124.35 (C(4)), 124.30 (C(3)), 123.43 (C(7)), 117.28 (C(10)), 116.43 (C(6)), 34.53 (C(20)), 17.93 (2C, C(21)).

**IR (Diamond ATR):**  $\tilde{\nu}$  ( $\text{cm}^{-1}$ ) = 3341 (w), 3049 (w), 2920 (s), 2850 (s), 2361 (w), 2340 (w), 1696 (s), 1604 (s), 1540 (w), 1520 (m), 1507 (w), 1457 (s), 1384 (m), 1363 (m), 1336 (m), 1312 (s), 1246 (s), 1184 (s), 1157 (s), 1131 (s), 1096 (s), 978 (w), 955 (m), 930 (w), 910 (w), 885 (s), 842 (m), 798 (w), 733 (s).

**MS (EI+, 70 eV):**  $m/z$  (%) = 391.2 (21), 374.1 (12), 322.1 (13), 321.1 (52), 320.1 (100), 319.1 (40), 304.1 (23), 290.1 (18), 57.1 (11), 44.0 (15), 43.0 (28), 41.0 (11).

**HRMS (EI+,  $\text{C}_{27}\text{H}_{21}\text{NO}_2$ ):** calcd.: 391.1572; found: 391.1569 (M+).

**EA ( $\text{C}_{27}\text{H}_{21}\text{NO}_2$ ):** calcd.: C, 82.84; H, 5.41; N, 3.58; found: C, 82.80; H, 5.62; N, 3.53.

**(Z/E)-1-isobutyryl-2-(4-methoxy-2,3,6-trimethylbenzylidene)indolin-3-one (57)**

A flame dried, N<sub>2</sub>-flushed Schlenk flask, equipped with a magnetic stirring bar, is charged with triethylamine (0.082 g, 0.81 mmol, 1.1 equiv.), 4-(dimethylamino)-pyridine (0.009 g, 0.074 mmol, 0.1 equiv.), dichloroethane (3 mL, 0.25 M) and (Z)-2-(4-methoxy-2,3,6-trimethylbenzylidene)indolin-3-one **52** (0.216 g, 0.737 mmol, 1.0 equiv.). The contents were stirred at 23 °C for 5 min, then isobutyryl chloride (0.086 g, 0.810 mmol, 1.1 equiv.) was added. The mixture was stirred at 80 °C until reaction was complete (indicated by GCMS analysis). The reaction was stopped with sat. aq. ammonium chloride solution and extracted with ethyl acetate. The combined organic layers were dried over sodium sulfate. The mixture was filtrated and the solvents were removed *in vacuo*. Purification by flash column chromatography (aluminium(III) oxide, *Brockmann* III, 6% water, w / w, hexanes / ethyl acetate, 9 / 1, v / v) yielded (Z/E)-1-isobutyryl-2-(4-methoxy-2,3,6-trimethylbenzylidene)indolin-3-one **57** (0.230 g, 0.632 mmol, 86%) as yellow solid. Further purification was carried out via preparative HPLC (*Machery-Nagel* VP 250/21 *NUCLEODUR Sphinx* RP 5 µm column, acetonitrile / water, 7 / 3, v / v, 15 mL/min, 35 °C column temperature, retention time: 11.0 min (Z isomer) with 42% yield.

*R<sub>f</sub>* = 0.63 (silica, hexanes / ethyl acetate, 8 / 2, v / v).

**m.p.** (°C): 64 - 66.

**Z isomer:**

**<sup>1</sup>H-NMR (800 MHz, CD<sub>2</sub>Cl<sub>2</sub>):** δ (ppm) = 8.21 (d, 1H, H-C(6)), 7.86 (dd, <sup>3</sup>*J* = 7.6 Hz, <sup>4</sup>*J* = 1.3 Hz, 1H, H-C(3)), 7.69 - 7.66 (m, 1H, H-C(4)), 7.42 (s, 1H, H-C(10)), 7.30 (ddd, <sup>3</sup>*J* = 7.4 Hz, <sup>3</sup>*J* = 6.7 Hz, <sup>4</sup>*J* = 0.8 Hz, 1H, H-C(5)), 6.71 (s, 1H, H-C(15)), 3.85 (s, 3H, H-C(19)), 2.47 (sept,

$^3J = 6.8$  Hz, 1H, H-C(22)), 2.21 (s, 3H, H-C(20)), 2.17 (s, 6H, H-C(17, 18)), 0.61 (d,  $^3J = 6.7$  Hz, 3H, H-C(23)), 0.54 (d,  $^3J = 6.7$  Hz, 3H, H-C(23\*)).

**$^{13}\text{C-NMR}$  (201 MHz,  $\text{CD}_2\text{Cl}_2$ ):**  $\delta$  (ppm) = 184.86 (C(8)), 178.21 (C(21)), 157.96 (C(14)), 150.33 (C(7)), 136.29 (C(4)), 136.14 (C(13)), 136.09 (C(16)), 134.72 (C(12)), 125.17 (C(11)), 124.16 (C(9)), 124.09 (C(5)), 123.92 (C(3)), 123.55 (C(2)), 121.34 (C(10)), 116.24 (C(6)), 110.52 (C(15)), 55.49 (C(19)), 34.97 (C(22)), 20.30 (C(20)), 18.68 (C(23\*)), 18.28 (C(23)), 17.06 (C(17)), 11.38 (C(18)).

***E* isomer:**

**$^1\text{H-NMR}$  800 MHz,  $\text{CD}_2\text{Cl}_2$ ):**  $\delta$  (ppm) = 8.20 (d,  $^3J = 8.2$  Hz, 1H, H-C(6)), 7.72 (dd,  $^3J = 7.5$  Hz,  $^4J = 1.4$  Hz, 1H, H-C(3)), 7.69 - 7.66 (m, 1H, H-C(4)), 7.44 (s, 1H, H-C(10)), 7.27 (ddd,  $^3J = 7.3$  Hz,  $^3J = 6.7$  Hz,  $^4J = 0.8$  Hz, 1H, H-C(5)), 6.71 (s, 1H, H-C(15)), 3.89 (s, 3H, H-C(19)), 3.56 (sept,  $^3J = 6.7$  Hz, 1H, H-C(22)), 2.29 (s, 3H, H-C(20)), 2.22 (s, 3H, H-C(17)), 2.20 (s, 3H, H-C(18)), 1.34 (d,  $^3J = 6.5$  Hz, 3H, H-C(23)), 1.33 (d,  $^3J = 6.5$  Hz, 3H, H-C(23\*)).

**$^{13}\text{C-NMR}$  (201 MHz,  $\text{CD}_2\text{Cl}_2$ ):**  $\delta$  (ppm) = 182.75 (C(8)), 177.29 (C(21)), 157.27 (C(14)), 148.65 (C(7)), 136.65 (C(16)), 135.73 (C(5)), 135.06 (C(13)), 135.01 (C(12)), 125.95 (C(10)), 124.76 (C(11)), 124.53 (C(2)), 123.75 (C(3)), 123.60 (C(4)), 122.16 (C(9)), 117.16 (C(6)), 109.39 (C(15)), 55.39 (C(19)), 34.06 (C(22)), 20.71 (C(20)), 19.78 (C(23\*)), 19.74 (C(23)), 17.12 (C(17)), 11.45 (C(18)).

**IR (Diamond ATR):**  $\tilde{\nu}$  ( $\text{cm}^{-1}$ ) = 3358 (w), 2968 (m), 2927 (m), 2853 (m), 1759 (m), 1694 (s), 1630 (s), 1588 (s), 1455 (s), 1383 (m), 1357 (m), 1315 (s), 1300 (s), 1262 (s), 1224 (m), 1181 (m), 1149 (w), 1119 (s), 1098 (s), 1043 (w), 1010 (w), 992 (w), 952 (w), 911 (m), 894 (m), 801 (w), 755 (s), 704 (m), 672 (m).

**MS (EI+, 70 eV):**  $m/z$  (%) = 433.2 (16), 364.2 (15), 363.2 (60), 349.2 (19), 348.2 (89), 293.1 (36), 292.1 (66), 279.1 (18), 278.1 (94), 277.1 (33), 276.1 (96), 262.1 (28), 261.1 (27), 260.1 (11), 234.1 (14), 190.1 (45), 151.1 (10), 150.1 (100), 120.0 (18), 71.0 (13), 43.1 (50).

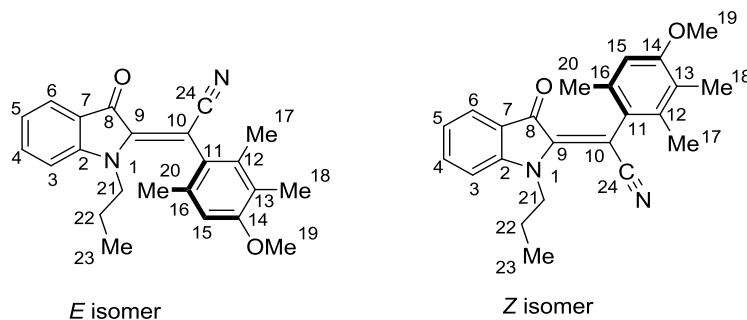
**HRMS (EI+,  $\text{C}_{23}\text{H}_{25}\text{NO}_3$ ):** calcd.: 363.1834; found: 363.1830 (M+).

**EA ( $\text{C}_{23}\text{H}_{25}\text{NO}_3$ ):** calcd.: C, 76.01; H, 6.93; N, 3.85; found: C, 75.80; H, 7.04; N, 3.85.

### 3.7.4 Vicarious nucleophilic substitution at the central double bond

Scheme 20, Section 2.2.10 depicts the substitution of the vinylic proton by a cyano group.

**(*E/Z*)-2-(4-methoxy-2,3,6-trimethylphenyl)-2-(3-oxo-1-propylindolin-2-ylidene)acetonitrile (26)**



To a round bottom flask, equipped with a magnetic stirring bar and a rubber septum, (*Z/E*)-2-(4-methoxy-2,3,6-trimethylbenzylidene)-1-propylindolin-3-one **28** (0.060 g, 0.179 mmol, 1.0 equiv.), potassium cyanide (0.035 g, 0.537 mmol, 3.0 equiv.) and dimethyl sulfoxide (3.0 mL, 0.04 M) were added and the solution was stirred at 23 °C for 5 d. The reaction treated with sodium bisulfite solution, filtered through celite, extracted with ethyl acetate and washed with brine. The combined organic layers were dried over sodium sulfate, filtered and the solvents were removed *in vacuo*. Subsequent purification by flash column chromatography (aluminium(III) oxide, *Brockmann* III, 6% water, w / w), hexanes / ethyl acetate, 9 / 1, v / v) yielded (*E/Z*)-2-(4-methoxy-2,3,6-trimethylphenyl)-2-(3-oxo-1-propylindolin-2-ylidene)acetonitrile **26** (0.028 g, 0.077 mmol, 43%) as orange solid.

$R_f = 0.12$  (silica, hexanes / ethyl acetate, 9 / 1, v / v).

**Z isomer:**

**$^1\text{H-NMR}$  (800 MHz,  $\text{CD}_2\text{Cl}_2$ ):**  $\delta$  (ppm) = 7.74 (dd,  $^3J = 7.6$  Hz,  $^3J = 1.4$  Hz, 1H, H-C(6)), 7.54 (ddd,  $^3J = 8.2$  Hz,  $^3J = 7.3$  Hz,  $^3J = 1.4$  Hz, 1H, H-C(4)), 7.04 (ddd,  $^3J = 7.5$  Hz,  $^3J = 7.5$  Hz,  $^3J = 0.7$  Hz, 1H, H-C(5)), 6.89 (d,  $^3J = 8.3$  Hz, 1H, H-C(3)), 6.69 (s, 1H, H-C(15)), 3.84 (s, 3H, H-C(19)), 3.14 - 2.97 (m, 2H, H-C(21)), 2.27 (s, 3H, H-C(20)), 2.24 (s, 3H, H-C(17)), 2.15 (s, 3H, H-C(18)), 0.89 (*quin*,  $^3J = 8.3$  Hz, 2H, H-C(22)), 0.44 (t,  $^3J = 7.4$  Hz, 3H, H-C(23)).

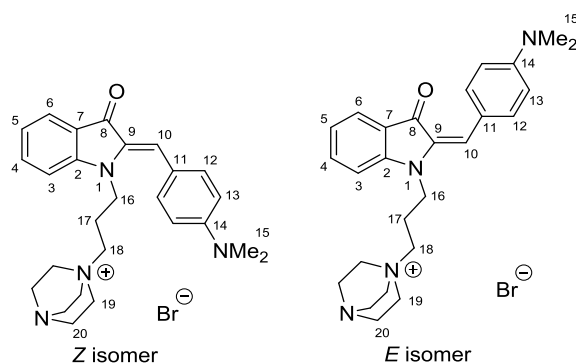
**MS (EI+, 70 eV):**  $m/z$  (%) = 360.2 (31), 346.2 (24), 345.2 (11), 343.2 (32), 328.2 (24), 320.2 (16), 315.1 (10), 303.1 (15), 299.1 (15), 281.1 (18), 225.0 (17).

**HRMS (EI+, C<sub>23</sub>H<sub>24</sub>N<sub>2</sub>O<sub>2</sub>):** calcd.: 360.1838; found: 360.1834 (M<sup>+</sup>).

### 3.7.5 Quaternary ammonium salts - *Menschutkin* reactions

Scheme 41, Section 2.5.1 shows the quaternization of 1,4-diazabicyclo[2.2.2]octane via S<sub>N</sub>2 reaction with an aliphatic halide substituted hemiindigo photoswitch.

**(*Z/E*)-1-(3-(2-(4-(dimethylamino)benzylidene)-3-oxoindolin-1-yl)propyl)-1,4-diazabicyclo[2.2.2]octan-1-ium bromide (80)**



To a round bottom flask, equipped with a magnetic stirring bar and a rubber septum, (*Z/E*)-1-(3-bromopropyl)-2-(4-(dimethylamino)benzylidene)indolin-3-one **83** (0.0154 g, 0.040 mmol, 1.0 equiv.), 1,4-diazabicyclo[2.2.2]octane (0.0067 g, 0.060 mmol, 1.5 equiv.) and acetonitrile (0.25 mL, 0.1 M) were added and the solution was heated to 45 °C for 1 d. The volatiles and 1,4-diazabicyclo[2.2.2]octane were removed *in vacuo* and 19.7 mg (0.0397 mmol, 99%) of (*Z/E*)-1-(3-(2-(4-(dimethylamino)benzylidene)-3-oxoindolin-1-yl)propyl)-1,4-diazabicyclo[2.2.2]octan-1-ium bromide **80** was obtained as deep red solid.

**Z isomer:**

**<sup>1</sup>H-NMR (600 MHz, CD<sub>2</sub>Cl<sub>2</sub>):** δ (ppm) = 7.66 (ddd, <sup>3</sup>J = 7.6 Hz, <sup>4</sup>J = 1.3 Hz, <sup>4</sup>J = 0.6 Hz, 1H, H-C(6)), 7.55 (ddd, <sup>3</sup>J = 8.4 Hz, <sup>3</sup>J = 7.2 Hz, <sup>4</sup>J = 1.4 Hz, 1H, H-C(4)), 7.37 - 7.33 (m, 2H, H-C(12)), 7.34 (d, <sup>3</sup>J = 8.2 Hz, 1H, H-C(3)), 7.02 (s, 1H, H-C(10)), 6.98 (ddd, <sup>3</sup>J = 7.8, <sup>3</sup>J = 7.5, <sup>4</sup>J = 0.7 Hz, 1H, H-C(5)), 6.77 - 6.73 (m, 2H, H-C(13)), 4.02 (t, <sup>3</sup>J = 7.5 Hz, 2H, H-C(16)), 3.79 (t, <sup>3</sup>J = 7.6 Hz, 6H, H-C(19)), 3.24 - 3.20 (m, 2H, H-C(18)), 3.14 - 3.11 (m, 6H, H-C(20)), 3.02 (s, 6H, H-C(15)), 1.64 (*quin*, <sup>3</sup>J = 7.6 Hz, 2H, H-C(17)).

**<sup>13</sup>C-NMR (151 MHz, CD<sub>2</sub>Cl<sub>2</sub>):** δ (ppm) = 186.83 (C(8)), 155.42 (C(2)), 151.01 (C(14)), 136.57 (C(4)), 135.16 (C(9)), 132.71 (2C, C(12)), 124.81 (C(6)), 123.47 (C(7)), 121.12 (C(11)),



121.08 (C(5)), 116.04 (C(10)), 112.49 (C(3)), 112.20 (2C, C(13)), 62.11 (C(18)), 52.95 (3C, C(19)), 45.70 (3C, C(20)), 42.49 (C(16)), 40.55 (2C, C(15)), 19.91 (C(17)).

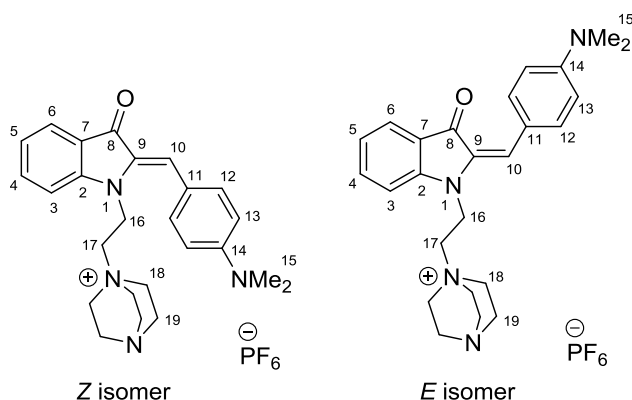
***E* isomer:**

**<sup>1</sup>H-NMR (600 MHz, CD<sub>2</sub>Cl<sub>2</sub>):**  $\delta$  (ppm) = 8.40 - 8.36 (m, 2H, H-C(12)), 7.63 (ddd, <sup>3</sup>*J* = 7.6 Hz, <sup>4</sup>*J* = 1.3 Hz, <sup>4</sup>*J* = 0.7 Hz, 1H, H-C(6)), 7.46 (ddd, <sup>3</sup>*J* = 8.3, <sup>3</sup>*J* = 7.1, <sup>4</sup>*J* = 1.4 Hz, 1H, H-C(4)), 7.20 (d, <sup>3</sup>*J* = 8.3 Hz, 1H, H-C(3)), 6.84 (ddd, <sup>3</sup>*J* = 7.8 Hz, <sup>3</sup>*J* = 7.2 Hz, <sup>4</sup>*J* = 0.6 Hz, 1H, H-C(5)), 6.78 (s, 1H, H-C(10)), 6.69 - 6.66 (m, 2H, H-C(13)), 4.06 (t, <sup>3</sup>*J* = 7.2 Hz, 2H, H-C(16)), 3.89 - 3.84 (m, 2H, H-C(18)), 3.50 (t, <sup>3</sup>*J* = 7.6 Hz, 6H, H-C(19)), 3.17 - 3.13 (m, 6H, H-C(20)), 2.99 (s, 6H, H-C(15)), 2.23 - 2.16 (m, 2H, H-C(17)).

**<sup>13</sup>C-NMR (151 MHz, CD<sub>2</sub>Cl<sub>2</sub>):**  $\delta$  (ppm) = 183.75 (C(8)), 151.66 (C(14)), 151.45 (C(2)), 135.93 (C(4)), 133.90 (C(9)), 133.52 (2C, C(12)), 124.58 (C(6)), 122.81 (C(11)), 122.11 (C(7)), 121.35 (C(10)), 119.08 (C(5)), 111.60 (2C, C(13)), 109.86 (C(3)), 62.21 (C(18)), 53.25 (3C, C(19)), 45.82 (3C, C(20)), 40.44 (2C, C(15)), 39.74 (C(16)), 21.16 (C(17)).

**HRMS (ESI+, C<sub>26</sub>H<sub>33</sub>N<sub>4</sub>O<sup>+</sup>):** calcd.: 417.26489; found: 417.26459 (M<sup>+</sup>).

**(*Z/E*)-1-(2-(2-(4-(dimethylamino)benzylidene)-3-oxoindolin-1-yl)ethyl)-1,4-diazabicyclo[2.2.2]octan-1-ium hexafluorophosphate (81)**



To a round bottom flask, equipped with a magnetic stirring bar and a rubber septum, (*Z/E*)-1-(3-bromoethyl)-2-(4-(dimethylamino)benzylidene)indolin-3-one **84** (0.036 g, 0.097 mmol, 1.0 equiv.), 1,4-diazabicyclo[2.2.2]octane (0.055 g, 0.485 mmol, 5.0 equiv.) and acetonitrile (0.1 mL, 0.1 M) were added and the solution was heated to 45 °C for 1 d. The volatiles and 1,4-diazabicyclo[2.2.2]octane were removed *in vacuo*. Water and diethyl ether were added and the extracted organic layers were combined, weighted and reused. The aqueous phase was charged onto a *Supleco* DSC-WCX ion exchange sorbent and eluted with a 30 mM water / acetonitrile

(7 / 3, v / v) potassium hexafluorophosphate solution and concentrated *in vacuo*. Subtraction of the previously weighted unreacted starting material yielded 0.016 g (0.029 mmol, 30% of (*Z/E*)-1-(2-(2-(4-(dimethylamino)benzylidene)-3-oxoindolin-1-yl)ethyl)-1,4-diazabicyclo-[2.2.2]octan-1-ium hexafluorophosphate **81** as deep red solid with potassium hexafluorophosphate as residue.

**Z isomer:**

**<sup>1</sup>H-NMR (400 MHz, CD<sub>3</sub>CN):**  $\delta$  (ppm) = 7.67 (d, <sup>3</sup>*J* = 7.6 Hz, 1H, H-C(6)), 7.63 (ddd, <sup>3</sup>*J* = 8.3 Hz, <sup>3</sup>*J* = 7.2 Hz, <sup>4</sup>*J* = 1.3 Hz, 1H, H-C(4)), 7.40 - 7.35 (m, 2H, H-C(12)), 7.31 (d, <sup>3</sup>*J* = 8.3 Hz, 1H, H-C(3)), 7.07 (ddd, <sup>3</sup>*J* = 7.8, <sup>3</sup>*J* = 7.3 Hz, 0.9 Hz, 1H, H-C(5)), 7.06 (s, 1H, H-C(10)), 6.85 - 6.80 (m, 2H, H-C(13)), 4.27 (t, <sup>3</sup>*J* = 8.7 Hz, 2H, H-C(16)), 3.00 (s, 6H, H-C(15)), 2.91 (t, <sup>3</sup>*J* = 7.2 Hz, 6H, H-C(19)), 2.87 - 2.81 (m, 2H, H-C(17)), 2.77 (t, <sup>3</sup>*J* = 7.2 Hz, 6H, H-C(18)).

**<sup>13</sup>C-NMR (101 MHz, CD<sub>2</sub>Cl<sub>2</sub>):**  $\delta$  (ppm) = 186.52 (C(8)), 155.15 (C(2)), 151.82 (C(14)), 136.97 (C(4)), 134.69 (C(9)), 132.93 (2C, C(12)), 124.93 (C(6)), 123.78 (C(7)), 121.93 (C(5)), 120.42 (C(11)), 117.07 (C(10)), 112.74 (2C, C(13)), 112.15 (C(3)), 59.20 (C(17)), 52.84 (3C, C(18)), 45.11 (3C, C(19)), 40.11 (2C, C(15)), 37.47 (C(16)).

**E isomer:**

**<sup>1</sup>H-NMR (400 MHz, CD<sub>3</sub>CN):**  $\delta$  (ppm) = 8.24 - 8.19 (m, 2H, H-C(12)), 7.64 (d, <sup>3</sup>*J* = 7.6 Hz, 1H, H-C(6)), 7.56 (ddd, <sup>3</sup>*J* = 8.4 Hz, <sup>3</sup>*J* = 7.2 Hz, <sup>4</sup>*J* = 1.3 Hz, 1H, H-C(4)), 7.11 (d, <sup>3</sup>*J* = 8.3 Hz, 1H, H-C(3)), 6.95 (ddd, <sup>3</sup>*J* = 7.8, <sup>3</sup>*J* = 7.2 Hz, <sup>4</sup>*J* = 0.6 Hz, 1H, H-C(5)), 6.79 - 6.74 (m, 2H, H-C(13)), 6.51 (s, 1H, H-C(10)), 4.29 (t, <sup>3</sup>*J* = 8.4 Hz, 2H, H-C(16)), 3.38 (t, <sup>3</sup>*J* = 7.8 Hz, 2H, H-C(17)), 3.37 (t, <sup>3</sup>*J* = 7.8 Hz, 6H, H-C(18)), 3.15 (t, <sup>3</sup>*J* = 7.1 Hz, 6H, H-C(19)), 3.03 (s, 6H, H-C(15)).

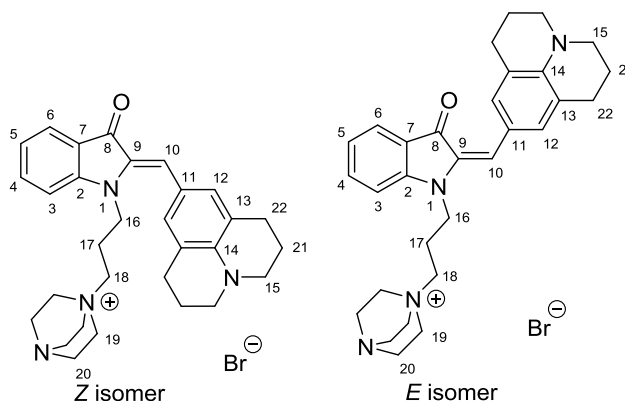
**<sup>13</sup>C-NMR (101 MHz, CD<sub>2</sub>Cl<sub>2</sub>):**  $\delta$  (ppm) = 183.58 (C(8)), 152.26 (C(14)), 151.06 (C(2)), 136.25 (C(4)), 133.53 (2C, C(12)), 133.30 (C(9)), 124.77 (C(6)), 122.67 (C(7)), 122.36 (C(11)), 121.79 (C(10)), 120.06 (C(5)), 111.88 (2C, C(13)), 109.78 (C(3)), 59.58 (C(17)), 53.29 (3C, C(18)), 45.37 (3C, C(19)), 40.02 (2C, C(15)), 35.42 (C(16)).

**<sup>19</sup>F-NMR (376 MHz, CD<sub>3</sub>CN):**  $\delta$  (ppm) = -72.99 (d, <sup>1</sup>*J* = 706.0 Hz, 6F, F-P).

**<sup>31</sup>P-NMR (162 MHz, CD<sub>3</sub>CN):**  $\delta$  (ppm) = -144.67 (sept, <sup>1</sup>*J* = 706.2 Hz, 1P, P-F).

**HRMS (ESI+, C<sub>25</sub>H<sub>31</sub>N<sub>4</sub>O<sup>+</sup>):** calcd.: 403.24924, found: 403.24925 (M<sup>+</sup>).

**(*Z/E*)-1-(3-(3-oxo-2-((2,3,6,7-tetrahydro-1*H*,5*H*-pyrido[3,2,1-*ij*]quinolin-9-yl)methylene)-indolin-1-yl)propyl)-1,4-diazabicyclo[2.2.2]octan-1-ium bromide (82)**



To a round bottom flask, equipped with a magnetic stirring bar and a rubber septum, (*Z/E*)-1-(3-bromopropyl)-2-((2,3,6,7-tetrahydro-1*H*,5*H*-pyrido[3,2,1-*ij*]quinolin-9-yl)methylene)-indolin-3-one **85** (0.0182 g, 0.0416 mmol, 1.0 equiv.), 1,4-diazabicyclo[2.2.2]octane (0.0051 g, 0.046 mmol, 1.0 equiv.) and acetonitrile (0.42 mL, 0.1 M) were added and the solution was heated to 45 °C for 1 d. The volatiles and 1,4-diazabicyclo[2.2.2]octane were removed *in vacuo* and 22.6 mg (0.0411 mmol, 99%) of (*Z/E*)-1-(3-(3-oxo-2-((2,3,6,7-tetrahydro-1*H*,5*H*-pyrido[3,2,1-*ij*]quinolin-9-yl)methylene)-indolin-1-yl)propyl)-1,4-diazabicyclo[2.2.2]octan-1-ium bromide **82** was obtained as deep violet solid.

**Z isomer:**

**<sup>1</sup>H-NMR (600 MHz, CD<sub>2</sub>Cl<sub>2</sub>):**  $\delta$  (ppm) = 7.66 (dd, <sup>3</sup>*J* = 7.6 Hz, <sup>4</sup>*J* = 1.2 Hz, 1H, H-C(6)), 7.54 (ddd, <sup>3</sup>*J* = 8.4 Hz, <sup>3</sup>*J* = 7.2 Hz, <sup>4</sup>*J* = 1.4 Hz, 1H, H-C(4)), 7.32 (d, <sup>3</sup>*J* = 8.3 Hz, 1H, H-C(3)), 6.98 (ddd, <sup>3</sup>*J* = 7.8 Hz, <sup>3</sup>*J* = 7.3, <sup>4</sup>*J* = 0.8 Hz, 1H, H-C(5)), 6.96 (s, 1H, H-C(10)), 6.91 (s, 2H, H-C(12)), 4.05 (t, <sup>3</sup>*J* = 7.5 Hz, 2H, H-C(16)), 3.26 - 3.24 (m, 4H, H-C(15)), 3.23 - 3.20 (m, 2H, H-C(18)), 3.18 (t, <sup>3</sup>*J* = 7.5 Hz, 6H, H-C(19)), 3.04 (t, <sup>3</sup>*J* = 7.7 Hz, 6H, H-C(20)), 2.75 (t, <sup>3</sup>*J* = 6.2 Hz, 4H, H-C(22)), 1.98 - 1.94 (m, 4H, H-C(21)), 1.65 (*quin*, <sup>3</sup>*J* = 8.0 Hz, 2H, H-C(17)).

**<sup>13</sup>C-NMR (151 MHz, CD<sub>2</sub>Cl<sub>2</sub>):**  $\delta$  (ppm) = 186.65 (C(8)), 155.29 (C(2)), 144.32 (C(14)), 136.22 (C(4)), 134.45 (C(9)), 130.64 (2C, C(12)), 124.39 (C(6)), 123.93 (C(7)), 121.58 (2C, C(13)), 121.06 (C(5)), 119.96 (C(11)), 117.52 (C(10)), 112.71 (C(3)), 62.16 (C(18)), 52.94 (3C, C(19)), 50.43 (2C, C(15)), 45.82 (3C, C(20)), 42.60 (C(16)), 28.23 (2C, C(22)), 22.17 (2C, C(21)), 19.78 (C(17)).

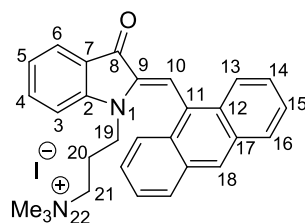
***E* isomer:**

**<sup>1</sup>H-NMR (600 MHz, CD<sub>2</sub>Cl<sub>2</sub>):**  $\delta$  (ppm) = 7.99 (s, 2H, H-C(12)), 7.62 (dd, <sup>3</sup>*J* = 7.6 Hz, <sup>4</sup>*J* = 1.3 Hz, 1H, H-C(6)), 7.45 (ddd, <sup>3</sup>*J* = 8.3 Hz, <sup>3</sup>*J* = 7.2 Hz, <sup>4</sup>*J* = 1.4 Hz, 1H, H-C(4)), 7.20 (d, <sup>3</sup>*J* = 8.3 Hz, 1H, H-C(3)), 6.83 (<sup>3</sup>*J* = 7.7 Hz, <sup>3</sup>*J* = 7.3 Hz, <sup>4</sup>*J* = 0.6 Hz, 1H, H-C(5)), 6.59 (s, 1H, H-C(10)), 4.03 (t, <sup>3</sup>*J* = 7.4 Hz, 2H, H-C(16)), 3.84 - 3.77 (m, 2H, H-C(18)), 3.50 (t, <sup>3</sup>*J* = 8.3 Hz, 6H, H-C(19)), 3.24 - 3.22 (m, 4H, H-C(15)), 3.13 (t, <sup>3</sup>*J* = 7.7 Hz, 6H, H-C(20)), 2.74 (t, <sup>3</sup>*J* = 6.1 Hz, 4H, H-C(22)), 2.22 - 2.15 (m, 2H, H-C(17)), 1.94 - 1.90 (m, 4H, H-C(21)).

**<sup>13</sup>C-NMR (151 MHz, CD<sub>2</sub>Cl<sub>2</sub>):**  $\delta$  (ppm) = 183.06 (C(8)), 150.96 (C(2)), 145.11 (C(14)), 135.53 (C(4)), 133.09 (C(9)), 131.30 (2C, C(12)), 124.70 (C(6)), 122.49 (C(10)), 122.21 (C(7)), 121.80 (C(11)), 120.79 (2C, C(13)), 118.90 (C(5)), 109.87 (C(3)), 62.25 (C(18)), 53.23 (3C, C(19)), 50.52 (2C, C(15)), 45.75 (3C, C(20)), 39.71 (C(16)), 28.25 (2C, C(22)), 22.30 (2C, C(21)), 21.26 (C(17)).

**HRMS (ESI+, C<sub>30</sub>H<sub>37</sub>N<sub>4</sub>O<sup>+</sup>):** calcd.: 469.29619; found: 469.29606 (M<sup>+</sup>).

**(*Z*)-3-(2-(anthracen-9-ylmethylene)-3-oxoindolin-1-yl)-*N,N,N*-trimethylpropan-1-aminium iodide (105)**



To a round bottom flask, equipped with a magnetic stirring bar and a rubber septum, (*Z/E*)-2-(anthracen-9-ylmethylene)-1-(3-(dimethylamino)propyl)indolin-3-one **100** (0.050 g, 0.119 mmol, 1.0 equiv.), iodomethane (0.025 g, 0.597 mmol, 5.0 equiv.) and acetonitrile (1.2 mL, 0.1 M) were added and the solution was heated to 40 °C for 90 min. The volatiles were removed *in vacuo* and 65.6 mg (0.119 mmol, 99%) of (*Z*)-3-(2-(anthracen-9-ylmethylene)-3-oxoindolin-1-yl)-*N,N,N*-trimethylpropan-1-aminium iodide **105** was obtained as orange solid.

**m.p.** (°C): 198 (decomposition).

**Z isomer:**

**<sup>1</sup>H-NMR (800 MHz, CD<sub>3</sub>CN):**  $\delta$  (ppm) = 8.68 (s, 1H, H-C(18)), 8.20 - 8.11 (m, 4H, H-C(16, 13)), 7.77 (d, <sup>3</sup>*J* = 7.7 Hz, 1H, H-C(6)), 7.63 - 7.53 (m, 6H, H-C(4, 15, 14, 10)), 7.05 (d, <sup>3</sup>*J* = 8.7 Hz, 1H, H-C(3)), 7.04 (dd, <sup>3</sup>*J* = 8.2 Hz, 7.4 Hz, 1H, H-C(5)), 2.93 (t, <sup>3</sup>*J* = 7.4 Hz, 2H, H-C(19)), 2.36 (s, 9H, H-C(22)), 2.08 - 1.99 (m, 2H, H-C(21)), 1.26 - 1.18 (m, 2H, H-C(20)).

**<sup>13</sup>C-NMR (201 MHz, CD<sub>3</sub>CN):**  $\delta$  (ppm) = 185.90 (C(8)), 155.03 (C(2)), 139.40 (C(9)), 137.37 (C(4)), 131.65 (C(11)), 130.67 (2C, C(12)), 129.73 (2C, C(16)), 128.73 (C(18)), 127.53 (2C, C(14)), 126.41 (2C, C(15)), 126.36 (2C, C(13)), 126.10 (2C, C(17)), 125.12 (C(6)), 121.88 (C(7)), 121.03 (C(5)), 110.70 (C(3)), 107.12 (C(10)), 63.50 (C(21)), 52.95 (3C, C(22)), 40.46 (C(19)), 21.54 (C(20)).

**IR (Diamond ATR):**  $\tilde{\nu}$  (cm<sup>-1</sup>) = 3751 (w), 2916 (w), 1698 (s), 1607 (s), 1474 (s), 1370 (m), 1338 (m), 1309 (m), 1134 (m), 1101 (m), 1056 (w), 882 (w), 849 (w), 752 (s), 735 (s).

**HRMS (ESI+, C<sub>29</sub>H<sub>29</sub>N<sub>2</sub>O<sup>+</sup>):** calcd.: 421.22744; found: 421.22729 (M<sup>+</sup>).

- [132] Gaussian 16, Revision B.01, M. J. Frisch, G. W. Trucks, H. B. Schlegel, G. E. Scuseria, M. A. Robb, J. R. Cheeseman, G. Scalmani, V. Barone, G. A. Petersson, H. Nakatsuji, X. Li, M. Caricato, A. V. Marenich, J. Bloino, B. G. Janesko, R. Gomperts, B. Mennucci, H. P. Hratchian, J. V. Ortiz, A. F. Izmaylov, J. L. Sonnenberg, Williams, F. Ding, F. Lipparini, F. Egidi, J. Goings, B. Peng, A. Petrone, T. Henderson, D. Ranasinghe, V. G. Zakrzewski, J. Gao, N. Rega, G. Zheng, W. Liang, M. Hada, M. Ehara, K. Toyota, R. Fukuda, J. Hasegawa, M. Ishida, T. Nakajima, Y. Honda, O. Kitao, H. Nakai, T. Vreven, K. Throssell, J. A. Montgomery Jr., J. E. Peralta, F. Ogliaro, M. J. Bearpark, J. J. Heyd, E. N. Brothers, K. N. Kudin, V. N. Staroverov, T. A. Keith, R. Kobayashi, J. Normand, K. Raghavachari, A. P. Rendell, J. C. Burant, S. S. Iyengar, J. Tomasi, M. Cossi, J. M. Millam, M. Klene, C. Adamo, R. Cammi, J. W. Ochterski, R. L. Martin, K. Morokuma, O. Farkas, J. B. Foresman, D. J. Fox, Gaussian, Inc., Wallingford CT, **2016**.
- [140] C. Gonzalez, H. B. Schlegel, *An improved algorithm for reaction path following*, *The Journal of Chemical Physics* **1989**, *90*, 2154.
- [141] M. Petersilka, U. J. Gossmann, E. K. U. Gross, *Excitation Energies from Time-Dependent Density-Functional Theory*, *Phys. Rev. Lett.* **1996**, *76*, 1212.
- [142] K. Wolinski, J. F. Hinton, P. Pulay, *Efficient implementation of the gauge-independent atomic orbital method for NMR chemical shift calculations*, *J. Am. Chem. Soc.* **1990**, *112*, 8251.
- [143] GaussView, Version 6.1, R. Dennington, T. A. Keith, J. M. Millam, Semichem Inc., Shawnee Mission, KS, **2016**.
- [144] D. W. Old, M. C. Harris, S. L. Buchwald, *Efficient Palladium-Catalyzed N-Arylation of Indoles*, *Org. Lett* **2000**, *2*, 1403.

## 4 SUMMARY

## 4.1 Hemiindigo - Rationale of substitution patterns

It could be shown that hemiindigos are a class of virtually unexplored, potent photoswitches supporting high photoisomerization ratios with blue over green to yellow and red light, high thermal bistabilities, good quantum yields and high tolerance of the photoreactions towards solvent polarity changes. The effects of different substitutions at the indoxyl- and stilbene fragments could be shown, with electron donating substituents being beneficial for red-shifted absorptions and twisted aryl axes at the indoxyl-nitrogen increasing thermal bistability while maintaining its red-shift. Increase of conjugation strength at the stilbene fragment did not yield desired red-shifted hemiindigos. The thermal bistabilities of *Z* and *E* isomers can be increased by electron withdrawing groups at the indoxyl nitrogen or by electron-neutral stilbene fragments. The thermal bistabilities of *N*-arylated hemiindigos profit from twisting of the *N*-aryl moiety and from decreasing sterical bulk between the indoxyl core methyl group and the stilbene fragment by substituting an *ortho*-tolyl group with a naphthyl group.



## 4.2 Hemiindigo - Solvent, Water and pH influence

The effects of solvent polarity on hemiindigo photoswitches could be demonstrated. Generally, red-shift is increased and quantum yields are slightly decreased for polar solvents, these trends are reversed for apolar solvents, with few exceptions. Photoswitching in water can only be realized by addition of 2.5 - 30% of water miscible organic solvent for hemiindigos supporting electron rich stilbene fragments.<sup>[74]</sup> Water soluble, ionic hemiindigos can only photoisomerize if the stilbene fragment features weak electron donating groups like methoxy or methyl (see section 2.2.5 and Section 2.6 for details). Acidic or basic conditions do not show visible photoswitching of hemiindigo chromophores.

## 4.3 Quantum yields

A general trend towards higher quantum yields especially for the *Z* to *E* direction when changing from polar to apolar solvents can be observed. This could be explained by a highly polar excited state structure similar to charge-transfer (CT) states, which would be stabilized by a polar environment. Such CT states would lead to competing deexcitation channels, which reduce the photoisomerization quantum yield - similar to the twisted intramolecular charge transfer (TICT) state behavior of donor-substituted twisted hemithioindigos.<sup>[87, 102]</sup> In theory, if the conical intersection shows symmetric pathways towards *Z* or *E* isomer, the maximum obtainable quantum yield should amount 50%. However, sterical pre-twisting of a molecule or specific electronic structures can prearrange and favor the trajectory of the desired photoreaction leading to quantum yields beyond 50%. Rational design of quantum yield efficiencies is therefore very challenging, as these effects cannot be easily predicted.

The introduction of a twisted *ortho*-tolyl aryl axis (hemiindigo **20**) increases the *Z* to *E* quantum yield by 10% compared to the *para*-toluene axis supported by hemiindigo **16** and the *n*-propyl residue found with hemiindigo **8**. The significant drop of photoisomerization efficiency to 2% observed with hemiindigo **16** could be circumvented by remotely twisting the aryl axis away from the stilbene fragment. A possible explanation for this low quantum yield is the collision of the stilbene fragment with the *para*-tolyl residue which tries to planarize to extend its *pi*-conjugation towards the indoxyl core. With the twisted *N*-aryl axis in hemiindigo **20** its quantum yield rises 4.5-fold from 2 to 9%. This also indicates that the *E* to *Z* isomerization power stroke is barely able to twist the conjugated *para*-tolyl out of its way.

It would also be possible for the *para*-tolyl hemiindigo **16** to twist the stilbene fragment around its single bond, which can be discarded as this would cause a significant bathochromic shift, which cannot be observed compared to the *ortho*-tolyl derivative **20** (see Figure 46, Section 2.2.7 for comparison). These findings suggest that the torsion of the *N*-aryl axis is favored, while the stilbene single bond remains within the conjugated indoxyl plane. The stilbene fragment could be regarded as a torsion sensor that reports increased twisting with a bathochromic shift.

## 4.4 Axially chiral hemiindigos

The introduction of a chiral acyl or aryl axis on hemiindigo chromophores at the indoxyl nitrogen was tested with various substitution patterns to explore the influence of electronics and sterics on the photoswitching behavior and motion of the passive chiral axes.

First experiments were carried out with acyl residues as the *pi*-delocalization of the amide bond was thought to be stable enough for low temperature measurements. This could not be achieved and the low thermal barriers of this atropisomerization are only reported by theory. Changing the acetyl to an isobutyryl group increased the sterical bulk and yielded presumably higher rotational barriers as split signals could be observed via  $^1\text{H}$  NMR spectroscopy when sterically hindered, asymmetrical stilbene fragments are introduced to the hemiindigo photoswitch. This splitting, however, is not caused by the high rotational barrier of the isobutyryl group but by the averaged asymmetric environment induced by the stilbene fragment. The rotational barrier of the stilbene fragment could be determined via temperature dependent  $^1\text{H}$ -NMR coalescence measurements.

The introduction of a chiral aryl axis to the hemiindigo chromophore was done utilizing a novel synthetic route coupling sterically demanding 2-bromotoluene to 7-methyl indole as precursor. The resulting chiroptical switches were scrutinized via chiral HPLC,  $^1\text{H}$  NMR, UV-Vis and (low temperature) electronic circular dichroism (ECD) spectroscopy. In general, a by 3 kcal/mol lowered atropisomerization barrier for the *Z* isomers compared to the *E* isomers could be observed. For all non-*ortho* stilbene substituted derivatives, the calculated transition states of *Z* isomers show passing of the *ortho*-tolyl methyl group over the indoxyl core methyl group while *E* isomer transition states prefer rotation of said methyl group over the central double bond, introducing directionality of the thermal atropisomerization. Furthermore, a strong modulation of ECD signals could be observed between *Z* and *E* isomers for derivatives **30** and **33**. Cyclic experiments showed that the atropisomerization is not influenced by the photoswitching motion, making these materials viable chiroptical switches addressable by visible light. The drawback of the fast racemization of **33** in its *Z* state could be improved by the introduction of a naphthyl moiety which makes the chiroptical properties of these switches usable for prolonged times at 25 °C.

Derivative **58** (see Section 2.3.4) supports a permanent stereocenter and shows similar magnitudes of ECD modulation as derivatives **30** and **33** while maintaining its UV-Vis absorption profile. This type of compounds could be used for prolonged data storage applications beyond 1s and 0s and advanced chiroptical filter systems.

## 4.5 Axially chiral indigos

The presented axially chiral molecular setups based in the diarylated indigo scaffold show vastly different behaviors upon their substitution patterns by changing the position and number of methyl groups at crucial positions.

The first generation of this molecule class could not be easily analyzed due to its unexpectedly fast conversion rates and  $^1\text{H-NMR}$  signal broadening at low temperatures.

The second generation avoided the indigo core methyl groups, giving higher atropisomerization rates, enabling the separation of isomers for their individual analyses. Their complex motions could be determined to prospective unidirectional double- and single bond motors, thermally switchable enriching of *syn-* / *anti-trans* states against the thermal equilibrium and photochemically- / thermally induced, geared Hula-Twist motions.

Several non-symmetric axially chiral model compounds were successfully synthesized and characterized by *F. Binder* to disentangle and verify the observed properties shown by the symmetric derivatives. A novel chimeric compound supporting two different chiral axis setups was also explored.

The third generation of axially chiral indigos was successfully synthesized and characterized by *K. Jordan* to gain further insights on the exhibited motional cascades within these molecules, further experiments are carried out at the time of writing.

Overall, the unexpected behavior of these fairly small and formally simple looking molecules was scrutinized. Their potential as prospective molecular motors and -machines was demonstrated, giving insights into novel photoinduced- and thermal motions, which is crucial for the design of nanomachines and molecular robots. Also, addressability within the biooptical window was achieved, as all photosteps can be driven with low energy, 625 nm LED light, making the application of likewise systems available on biological tissues *in vitro* and *in vivo*.

## 4.6 Ionic hemiindigos

In conclusion, three permanently charged thermally bistable hemiindigos were synthesized and their photochemical properties in the gas phase and in solution were investigated. It is shown that gas-phase experiments agree with the theoretical description and capture essential intrinsic molecular properties, including absorption wavelengths or collision cross-sections. Describing the influence of polar solvents on the photochemical behavior on the other hand is still challenging using this theoretical approach. Additionally, a novel way of separating stable hemiindigo isomers from an isomeric mixture to obtain isomer-specific photoisomerization responses without the need for spectral deconvolution of mixtures in solution is presented. It is further demonstrated, that reversible photoisomerization and strong photochromism for all isolated gas-phase hemiindigos is shown upon exposure to visible light. The influence of the shorter chain-length on absorption wavelengths, photoisomerization properties, overall reactivity and solubility were elaborated further. Possible explanations for the reversal of ATDs of *Z* and *E* isomers of the short-chain hemiindigo **81** are given.

The use of ion mobility mass spectrometry coupled to laser spectroscopy offers unique insights into the subtle effects of intrinsic molecular constitution and electronic structure - separated from environment influences - of photoactive molecules. Such fundamental investigations can be useful for rationally designing better molecular photoswitches and serve as a benchmark for developing accurate theoretical models for their photoisomerization dynamics / and mechanisms.

## 4.7 Hemiindigos in water

As shown in Section 2.5, the ionic derivatives of highly bistable, red-shifted, electron rich hemiindigo photoswitches did not show photoisomerization reactions in pure water. *D. Berdnikova* of the *Ihmels* group in Siegen, Germany, synthesized the previously avoided hemiindigo derivatives featuring neutral stilbene fragments and made them water soluble by attaching a dimethylamino propyl chain at the stilbene fragment. This compound showed binding affinities towards HIV-1 TAR and RRE-IIB RNA and could be photoswitched in its fluorescent response.<sup>[40]</sup>

In accordance to the promising results of this therapeutic approach to potentially gain control of the HIV-1 proliferation apparatus, a series of hemiindigos with varying substitution patterns was synthesized and submitted to preliminary binding studies carried out by *D. Berdnikova*. Another promising candidate, namely hemiindigo **105**, was hereby found and synthesized at larger scale for further RNA binding studies followed with NMR spectroscopy by *D. Berdnikova*. These experiments will reveal the possible selectivity and binding constants of this photoswitch and its usability in controlling the HIV-1 activity.

## 4.8 Photophysics

The developed “all-in-one” *Excel* tool proved as a success as repetitive measurements of different photoswitches in various solvents require a robust and repeatable methodology to compare obtained datasets. Its ease of use and time- / compound savings for the required (photo) physical measurements (Molar absorptivity, PSS determination, thermal kinetics and quantum yield determination) was a major help in processing the acquired data via UV-Vis- and NMR spectroscopy.

The construction of a low-budget quantum yield measurement device with differential detection setup was a success and showed that even cheap components can be used for this kind of measurements as photodiodes are very sensitive towards minimal changes of light intensity and output a corresponding current in a linear fashion. Further improvements of the quantum yield measurement data processing are in preparation to date.

To consistently test the photofatigue of photoswitches, repeated cyclic measurements were set up by successfully building an alternating LED irradiation device controlled via a microcontroller. This allows for virtually infinite of switching cycles to be run, giving reliable degradation kinetics.

As ECD measurements are quite susceptible to angle changes of the cuvette(s) within the beam path of the circularly polarized light, a cryostat mount was built that allowed for adjustment in seven axes including removal and reinsertion of the cryostat / sample cuvette into the spectrometer without losing its positioning. Successful repeated ECD measurements proved the rigidity and usability of this setup.

- [40] D. V. Berdnikova, *Visible-range hemi-indigo photoswitch: ON–OFF fluorescent binder for HIV-1 RNA*, *Chem. Commun.* **2019**, 55, 8402.
- [74] C. Petermayer, S. Thumser, F. Kink, P. Mayer, H. Dube, *Hemiindigo: Highly Bistable Photoswitching at the Biooptical Window*, *J. Am. Chem. Soc.* **2017**, 139, 15060.
- [87] S. Wiedbrauk, B. Maerz, E. Samoylova, A. Reiner, F. Trommer, P. Mayer, W. Zinth, H. Dube, *Twisted Hemithioindigo Photoswitches: Solvent Polarity Determines the Type of Light-Induced Rotations*, *J. Am. Chem. Soc.* **2016**, 138, 12219.
- [102] S. Wiedbrauk, B. Maerz, E. Samoylova, P. Mayer, W. Zinth, H. Dube, *Ingredients to TICT Formation in Donor Substituted Hemithioindigo*, *The Journal of Physical Chemistry Letters* **2017**, 8, 1585.

## **5 APPENDIX**



## 5.1 List of Abbreviations

$\delta$	chemical shift
$\Delta T$	temperature difference
$\lambda_{\max}$	absorption maximum
calcd.	calculated
ECD	electronic circular dichroism
EI	electron ionization
ESI	electrospray ionisation
equiv.	equivalent
ESPT	excited-state proton transfer
<i>et al.</i>	<i>et alii</i> (and others)
GC-MS	gas chromatography–mass spectrometry
HMBC	heteronuclear multiple-bond correlation spectroscopy
HOMO	highest occupied molecular orbital
HPLC	high-performance liquid chromatography
HRMS	high-resolution mass spectrometry
<i>hν</i>	light
kcal	kilocalorie
LUMO	lowest unoccupied molecular orbital
<i>m/z</i>	mass/charge
MS	mass spectrometry
NMR	nuclear magnetic resonance
NOE	nuclear <i>Overhauser</i> effect
NOESY	nuclear <i>Overhauser</i> effect spectroscopy
<i>o</i>	<i>ortho</i>
<i>m</i>	<i>meta</i>
<i>p</i>	<i>para</i>
ppm	parts per million
PSS	photostationary state
$R_f$	retardation factor
UV	ultraviolet
vis	visible

Further abbreviations used in the text are explained in the corresponding passages.

## 5.2 Table of Figures

Figure 1:	Simplified <i>Jablonski</i> diagram. Absorption of a photon results in excitation of the molecule e.g. into the singlet state 1 or 2 ( $S_1$ or $S_2$ , blue arrow) within an accessible vibronic state. Lower lying vibronic states can be populated by phononic de-excitations, which can be simplified as cooling of an excited vibrating molecule towards a state of lower energy (wavy lines). The lowest energy vibronic mode of the excited state (here: $S_{1-0}$ ) must be in phase with at least one vibronic mode $x$ (in most cases not the lowest vibronic mode) of the ground state (singlet state 0 or $S_0$ ) to emit a photon (fluorescence). This photon has the same energy as the energy gap between $S_{1-0}$ and $S_{0-x}$ . The same principle can be applied to the triplet states with the additional aspect that the required changes in spin polarization from triplet to singlet states are forbidden. This circumstance can trap molecules in long-lasting triplet states for time periods that extend fluorescent phenomena by several orders of magnitude.	4
Figure 2:	Overview of different classes of photoswitches. In general, thermodynamically stable forms are shown on the left, metastable products are shown on the right. Rule-of-thumb performances with regard to red-shifted photoswitching and long thermal half-lives at 25 °C are shown for a respective isomerization direction. Very fast = ns to s, fast = s to min, medium fast = min to h, medium slow = h to days, slow = days to years, very slow = years to millennia. NIR = near infrared	8
Figure 3:	Simplified depiction of a conical intersection for a <i>Z</i> / <i>E</i> double bond isomerization, $X$ represents the reaction coordinate. The excited state $S_1$ rapidly de-excites towards the $S_0$ state of the <i>Z</i> - or <i>E</i> isomer with a 1 to 1 probability.	9
Figure 4:	Indigo and its reduced <i>leuco</i> form.	11
Figure 5:	Irradiation of biological tissue with 405 nm (100 mW of light power, left) and 625 nm (130 mW of light power, right) light emitting diodes (LEDs). The lower measured power (~30%) for the LED on the left is not the main cause for the significant transmission difference (>> 30%) when compared to the right.	13
Figure 6:	Overview of increasing thermal half-lives for different indigoid photoswitches at 25 °C.	14
Figure 7:	Energy profile of the unidirectional rotational cycle of the molecular motor as published by <i>M. Güntner</i> . <sup>[82]</sup> Black lines represent theoretically obtained values calculated at the MPW1K/6-31+G(d,p) level of theory, blue values indicate experimentally measured values.	18
Figure 8:	Simplified motional cycle of an axially chiral di- <i>N</i> -arylated indigo derivative.	19
Figure 9:	Nomenclature and fundamental switching processes of a hemiindigo photoswitch induced by visible light or thermal excitation.	24
Figure 10:	Transient absorption spectra of hemiindigo <b>2</b> recorded after 45 femtosecond photoexcitation of the <i>Z</i> isomer with 400 nm light.	27
Figure 11:	<i>Lewis</i> -formulas of hemithioindigos <b>E-4</b> , <b>5</b> , <b>6</b> (top) and hemiindigos <b>E-7</b> , <b>8</b> , <b>3</b> (bottom) and their free activation enthalpies $\Delta G^\ddagger$ for the respective <i>E</i> to <i>Z</i> isomerizations in toluene.	29
Figure 12:	Rationale for the substitution and selection of solvents for tailoring hemiindigo photoswitches. EWG = Electron withdrawing group, EDG = electron donating group. Electron donating moieties at the <i>N</i> -R position result in red-shifted chromophores, the same can be seen for the <i>para</i> -position of the stilbene fragment. Electron withdrawing groups will result in blue-shifted absorptions, this includes the proton substitution at the central double bond. Introduction of bulk at the <i>ortho</i> -positions of the stilbene fragment or at the central double bond will result in twisting of the adjacent single bond and loss of <i>p</i> -conjugation along the chromophore, which also blue-shifts absorptions. Polar solvents will red-shift absorptions and enhance thermal bistabilities while lowering quantum efficiencies upon switching. Apolar solvents will reverse these trends.	30
Figure 13:	Crystals (left) and structure of hemiindigo <b>Z-9</b> (left) in the crystalline state. An almost planar conformation of the single bond with a dihedral angle of 9.26° for C8-C9-C10-C11 can be observed. The double bond (red) measures 1.352 Å in length and the stilbene single bond (green) at 1.451 Å.	31
Figure 14:	<i>Lewis</i> -formula of hemiindigo <b>9</b> .	32
Figure 15:	Photoswitching of hemiindigo <b>9</b> in toluene (left) and dimethyl sulfoxide (right) at different wavelengths. <i>Z</i> isomer enriched states are colored in red, <i>E</i> isomer enriched states are colored in blue. Comparable amounts of photodestruction can be seen over this broad range of solvent polarity. The estimated increase in isomeric yields of the <i>E</i> isomer in toluene can be attributed to the overall improved quantum yields of hemiindigos in apolar solvents, which is discussed in Section 2.2.25. Exact quantification of thermal bistabilities, isomeric ratios and quantum efficiencies were not carried out as the constant degradation of this molecule would not yield accurate results.	32
Figure 16:	Fluorescence spectra of hemiindigo <b>9</b> in toluene (left) and dimethyl sulfoxide (right). This strong fluorescence is exclusive to <i>N</i> -H unsubstituted and stilbene <i>para</i> -proton, -methyl and -methoxy substituted hemiindigos. Fluorescence is lost upon photoswitching and by exposure to atmospheric conditions.	33
Figure 17:	Structure of hemiindigo <b>Z-2</b> in the crystalline state. The viewing angle on the right emphasizes the strong helical twisting within the <i>Z</i> isomer with a dihedral torsion angle of 52.97° for C1-N1-C10-C11. The stilbene single bond is twisted by 23.24° for C10-C11-C12-C13. The length of the double bond (red) is contracted from 1.352 to 1.344 Å and the single bond (green) elongated from 1.451 to 1.459 Å compared to hemiindigo <b>9</b> .	34
Figure 18:	<i>Lewis</i> -formula of hemiindigo <b>2</b> .	35
Figure 19:	Molar absorption (left) and PSS (right) spectra of hemiindigo <b>2</b> in dichloromethane. A blue shifted absorption compared to the <i>N</i> -H substituted compound <b>9</b> can be observed resulting from acetylation of the indoxyl nitrogen (Figure 15). Defined isosbestic points can be seen at 260 nm, 320 nm, 360 nm and 430 nm, which indicates good photostability of this compound. Highest isomeric yields were obtained at 385 nm irradiation (88% <i>E</i> isomer) and at 505 nm irradiation (87% <i>Z</i> isomer). Energy barriers for thermal double bond isomerizations were determined to be 24.4 kcal/mol for the <i>Z</i> to <i>E</i> and 24.0 kcal/mol for the <i>E</i> to <i>Z</i> direction at 24 °C, which translates to thermal half-lives of 12.5 h and 24.5 h at 25 °C, for the respective isomers.	35
Figure 20:	Molar absorption (left) and PSS (right) spectra of hemiindigo <b>2</b> in toluene. Almost similar absorption profiles can be observed compared to dichloromethane as solvent (Figure 19). The isosbestic points are well defined, verifying the photostability of this compound. Highest isomeric yields were obtained at 385 nm irradiation (89% <i>E</i> isomer) and at 490 nm irradiation (99% <i>Z</i> isomer). Energy barriers for thermal double bond isomerizations were determined to be 32.6 kcal/mol for the <i>Z</i> to <i>E</i> and 31.4 kcal/mol for the <i>E</i> to <i>Z</i> direction at 100 °C, which translates to thermal half-lives of 2895 years and 381 years at 25 °C, for the respective isomers.	36
Figure 21:	Structure of hemiindigo <b>13</b> in the crystalline state in its <i>E</i> isomeric form. Full planarity for the <i>E</i> isomer can be observed, which is seen for all hemiindigos with <i>ortho</i> -unsubstituted stilbene fragments. The double (red) and single bond (green) are elongated from 1.352 to 1.354 Å and 1.451 to 1.455 Å, respectively, compared to <i>N</i> -H substituted chromophore <b>2</b> . This can be caused by the +I effect of the methyl group or the overall electronically different <i>E</i> isomeric form.	37
Figure 22:	Unexpected dipolar [2+4] cycloaddition product upon recrystallization of <i>N</i> -ethyl substituted hemiindigo <b>14</b> at approximately 100 °C in ethanol / water. Bond lengths are shown in respective colors.	38
Figure 23:	Structure of hemiindigo <b>7</b> in the crystalline state. The viewing angle on the right emphasizes the strong single bond twisting of the stilbene fragment. The stilbene single bond dihedral torsion angle amounts to 43.47° for C8-C9-C10-C15 in the <i>Z</i> isomeric state and the dihedral helical torsion angle amounts to 8.73° for C17-N1-C8-C9. The double bond (red) is contracted from 1.352 to 1.346 Å and the single bond (green) is highly elongated from 1.451 to 1.467 Å compared to the <i>N</i> -H unsubstituted chromophore <b>9</b> .	39
Figure 24:	Comparison of helical torsion and stilbene single bond rotation for alkylated hemiindigo <b>7</b> (left) and acetylated hemiindigo <b>2</b> (right)	40
Figure 25:	<i>Lewis</i> -formula of hemiindigo <b>7</b> .	41
Figure 26:	Molar absorption (left) and PSS (right) spectra of hemiindigo <b>7</b> in dichloromethane. The isosbestic points are well defined, verifying the photostability of this compound. Highest isomeric yields were obtained at 435 nm irradiation (96% <i>E</i> isomer) and at 565 nm irradiation (54% <i>Z</i> isomer). Energy barriers for thermal double bond isomerizations were determined to be 23.8 kcal/mol for the <i>Z</i> to <i>E</i> and 23.7 kcal/mol for the <i>E</i> to <i>Z</i> direction at 100 °C, which translates to thermal half-lives of 8.9 h and 7.5 h at 25 °C, for the respective isomers. Quantum yields were determined at 17 ±3% (449 nm) for <i>Z</i> to <i>E</i> and 3.2 ±1% (565 nm) for <i>E</i> to <i>Z</i> direction.	41
Figure 27:	Molar absorption (left) and PSS (right) spectra of hemiindigo <b>7</b> in toluene. Similar spectra can be observed compared to dichloromethane as solvent (see Figure 26). The isosbestic points are well defined, verifying the photostability of this compound. Highest isomeric yields were obtained at 435 nm irradiation (97% <i>E</i> isomer) and at 530 nm irradiation (18% <i>Z</i> isomer). Energy barriers for thermal double bond isomerizations were determined to be 31.5 kcal/mol for the <i>Z</i> to <i>E</i> and 29.8 kcal/mol for the <i>E</i> to <i>Z</i> direction at 100 °C, which translates to thermal half-lives of 452 years and 25.6 years at 25 °C, for the respective isomers.	42
Figure 28:	Structure of hemiindigo <b>Z-11</b> (left) and <b>Z-15</b> (right) in the crystalline state. Both derivatives remain planar in the <i>Z</i> form, as no bulk is introduced at the indoxyl nitrogen. The double (red) and single bond (green) lengths change from 1.352 to 1.357 to 1.347 Å and 1.451 to 1.438 to 1.449 Å for the methoxy, dimethylamino and julolidine derivatives <b>9</b> , <b>11</b> and <b>15</b> , respectively.	44
Figure 29:	Dichroic crystals of hemiindigo <b>15</b> obtained in lengths from 5 to 10 mm. Adapted with permission from <sup>[74]</sup> . Copyright 2017 American Chemical Society.	44
Figure 30:	<i>Lewis</i> -formula of hemiindigo <b>11</b> .	45
Figure 31:	Molar absorption spectra of pure <i>Z</i> and <i>E</i> isomers of <b>11</b> measured in solvents of increasing polarity (toluene, tetrahydrofuran and dimethyl sulfoxide). PSS and switching spectra are omitted for clarity reasons and can be found in the literature. <sup>[74]</sup> A clear correlation between rising solvent polarity and red-shift of absorptions can be observed, evidencing moderate solvatochromism. Adapted with permission from <sup>[74]</sup> . Copyright 2017 American Chemical Society.	45
Figure 32:	<i>Lewis</i> -formula of hemiindigo <b>15</b> .	46
Figure 33:	Molar absorption spectra of pure <i>Z</i> and <i>E</i> isomers of <b>15</b> measured in solvents of increasing polarity (toluene, tetrahydrofuran and dimethyl sulfoxide). PSS and switching spectra are omitted for clarity reasons and can be found in the literature. <sup>[74]</sup> A clear correlation between rising solvent polarity and red-shift of absorptions can be observed, evidencing moderate solvatochromism. Adapted with permission from <sup>[74]</sup> . Copyright 2017 American Chemical Society.	46
Figure 34:	Structure of hemiindigo <b>E-8</b> (left) and <b>E-3</b> (right) in the crystalline state. Both derivatives remain planar in the <i>E</i> isomeric form. The double (red) and single bond (green) lengths change from 1.354 to 1.363 to 1.362 Å and 1.455 to 1.450 to 1.445 Å for the <i>N</i> -methyl methoxy, dimethylamino and julolidine derivatives <b>7</b> , <b>8</b> and <b>8</b> , respectively. A clear trend for stilbene-single-bond-shortening can be observed by increasing electron donor strength in the <i>para</i> -position.	47

Figure 35:	<i>Lewis</i> -formula of hemiindigo <b>8</b> .	48
Figure 36:	Molar absorption spectra of pure <i>Z</i> and <i>E</i> isomers of <b>8</b> measured in solvents of increasing polarity (toluene, tetrahydrofuran and dimethyl sulfoxide). PSS and switching spectra are omitted for clarity reasons and can be found in the literature. <sup>[74]</sup> A clear correlation between rising solvent polarity and red-shift of absorptions can be observed, evidencing moderate solvatochromism. Adapted with permission from <sup>[74]</sup> . Copyright 2017 American Chemical Society.	48
Figure 37:	Prolonged photoswitching of hemiindigo <b>8</b> from <i>Z</i> PSS (590 nm) to <i>E</i> PSS (470 nm) and vice versa in dimethyl sulfoxide over 50 cycles. Only minor amounts of photodestruction could be observed. Adapted with permission from <sup>[76]</sup> . Copyright 2018 American Chemical Society.	49
Figure 38:	Absorption spectra during photoswitching of hemiindigo <b>8</b> in 4 / 1 water / <i>N,N</i> -dimethylformamide. Visually unhampered photoswitchability remains even at high water contents. Adapted with permission from <sup>[74]</sup> . Copyright 2017 American Chemical Society.	50
Figure 39:	Poly(methyl methacrylate) piece treated with a solution of hemiindigo <b>8</b> in dichloromethane. Photoswitchability was preserved within the polymer. Experiments with UV curable clear resins for 3D printing by <i>Formlabs</i> were also successful, which makes it possible to print photoswitches favorably within translucent polymer materials.	51
Figure 40:	<i>Lewis</i> -formula of hemiindigo <b>3</b> .	52
Figure 41:	Molar absorption spectra of pure <i>Z</i> and <i>E</i> isomers of <b>3</b> measured in solvents of increasing polarity (toluene, tetrahydrofuran and dimethyl sulfoxide). PSS and switching spectra are omitted for clarity reasons and can be found in the literature. <sup>[74]</sup> A clear correlation between rising solvent polarity and red-shift of absorptions can be observed, evidencing moderate solvatochromism. Adapted with permission from <sup>[74]</sup> . Copyright 2017 American Chemical Society.	52
Figure 42:	Photoswitching of hemiindigo <b>3</b> in 4 / 1 water / <i>N,N</i> -dimethylformamide. Excellent photoswitching performance can be observed even at high water contents. Adapted with permission from <sup>[74]</sup> . Copyright 2017 American Chemical Society.	53
Figure 43:	<i>Lewis</i> -formula of hemiindigo <b>16</b> .	55
Figure 44:	Molar absorption spectra of pure <i>Z</i> and <i>E</i> isomers of <b>16</b> measured in solvents of increasing polarity (toluene, tetrahydrofuran and dimethyl sulfoxide). PSS and switching spectra are omitted for clarity reasons and can be found in the literature. <sup>[74]</sup> A clear correlation between rising solvent polarity and red-shift of absorptions can be observed, evidencing moderate solvatochromism. Adapted with permission from <sup>[74]</sup> . Copyright 2017 American Chemical Society.	55
Figure 45:	Molar absorption spectra of pure isomers (left) and spectra recorded at the PSS at different wavelengths of irradiation PSS (right) spectra of hemiindigo <b>20</b> in dimethyl sulfoxide. The isosbestic points are well defined, verifying the photostability of this compound. Highest isomeric yields were obtained at 470 nm irradiation (93% <i>E</i> isomer) and at 625 nm irradiation (97% <i>Z</i> isomer). Energy barriers for thermal double bond isomerizations were determined to be 30.6 kcal/mol for the <i>Z</i> to <i>E</i> and 32.1 kcal/mol for the <i>E</i> to <i>Z</i> direction at 114 °C, which translates to thermal half-lives of 99 years and 1140 years at 25 °C, for the respective isomers. Quantum yields were determined at 33 ±2% (467 nm) for <i>Z</i> to <i>E</i> and 9 ±1% (600 nm) for <i>E</i> to <i>Z</i> photoisomerizations. In 83 / 17 heptane / ethyl acetate, the quantum yields increase up to 49 ±2% (450 nm) for <i>Z</i> to <i>E</i> and 12 ±2% (520 nm) for <i>E</i> to <i>Z</i> photoisomerization. Adapted with permission from <sup>[75]</sup> . Copyright 2018 American Chemical Society.	57
Figure 46:	Comparison of molar absorption spectra for less twisted <i>para</i> -tolyl ( <b>16</b> ) and strongly twisted <i>ortho</i> -tolyl derivative <b>20</b> in dimethyl sulfoxide. No significant batho- or hypsochromic shift can be observed. Thus the wavelengths of absorption are mainly determined by the stilbene-fragment and much less so by the twisting of the <i>N</i> -indoxyl substituent. A reduction of $\epsilon$ by 30% can be observed. However, this does not hamper the responsiveness of the twisted system, as even higher quantum yields are reported for hemiindigo <b>20</b> .	58
Figure 47:	UV-Vis spectrum of hemiindigo <b>25</b> in dimethyl sulfoxide.	60
Figure 48:	<i>Lewis</i> -formula of hemiindigo <b>12</b> .	61
Figure 49:	Molar absorption spectra of pure isomers (left) and spectra recorded at the PSS at different wavelengths of irradiation PSS (right) spectra of hemiindigo <b>12</b> in dichloromethane that was filtered through aluminium(III) oxide to reduce prevalent amounts of hydrochloric acid. The isosbestic points are well defined, verifying the photostability of this compound. Highest isomeric yields were obtained at 420 nm irradiation (79% <i>E</i> isomer) and at 625 nm irradiation (99% <i>Z</i> isomer). Energy barriers for thermal double bond isomerizations were determined to be 25.9 kcal/mol for the <i>Z</i> to <i>E</i> and 27.9 kcal/mol for the <i>E</i> to <i>Z</i> direction at 100 °C, which translates to thermal half-lives of 13 days and 1 year at 25 °C, for the respective isomers.	61
Figure 50:	Molar absorption spectra of pure isomers (left) and spectra recorded at the PSS at different wavelengths of irradiation PSS (right) spectra of hemiindigo <b>12</b> in dichloromethane that was filtered through aluminium(III) oxide to reduce prevalent amounts of hydrochloric acid. The isosbestic points are well defined, verifying the photostability of this compound. Highest isomeric yields were obtained at 420 nm irradiation (77% <i>E</i> isomer) and at 530 nm irradiation (96% <i>Z</i> isomer). Energy barriers for thermal double bond isomerizations were determined to be 29.8 kcal/mol for the <i>Z</i> to <i>E</i> and 30.3 kcal/mol for the <i>E</i> to <i>Z</i> direction at 100 °C, which translates to thermal half-lives of 26 years and 60 years at 25 °C, for the respective isomers. Unprecedented behavior of this compound can be seen as the only intermediate <i>Z</i> / <i>E</i> composition is obtained with 470 nm irradiation (broken light blue line). For previous compounds, a more or less continuous distribution of PSS compositions was obtained when sweeping through all available wavelengths for irradiation. In this case, however, a sharp discrimination for wavelengths below 470 nm and above 470 nm can be observed, which strongly favor one or the other isomer in the PSS.	62
Figure 51:	UV-Vis spectra of irradiation experiments on hemiindigo <b>26</b> in cyclohexane (left) and dichloromethane (right). Photoswitching can be seen in cyclohexane. The initial <i>Z</i> / <i>E</i> composition is switched with 435 nm LED light and can be recovered by irradiation with 530 nm. Little photoswitching is observed in dichloromethane, which was also assessed via NMR in Figure 53.	64
Figure 52:	UV-Vis spectra of irradiation experiments on hemiindigo <b>26</b> in dimethyl sulfoxide. Little photoswitching can be seen. This kind of substitution pattern seems to perform poorly within polar solvents, in contrast to derivatives possessing only a threefold substituted double bond.	65
Figure 53:	<sup>1</sup> H-NMR spectra recorded during irradiation experiments on hemiindigo <b>26</b> in dichloromethane- <i>d</i> <sub>2</sub> at 25 °C, 400 MHz. The initial <i>Z</i> / <i>E</i> composition before irradiation is the same as observed in the spectrum on top and is not shown. 91% of the <i>Z</i> isomer are present in the thermal equilibrium and photoswitching to 23% <i>E</i> isomer content is possible.	65
Figure 54:	Chromatogram of hemiindigo <b>26</b> recorded via gas chromatography - mass spectrometry. Only the mass trace with an <i>m/z</i> of 360 corresponding to the product <b>26</b> is shown. Two distinct peaks connected by a streaking area can be observed at 300 °C, suggesting interconversion of <i>Z</i> - and <i>E</i> isomers during elution.	66
Figure 55:	<i>Lewis</i> -formula of hemiindigo <b>29</b> .	67
Figure 56:	UV-Vis spectra of photoswitching experiments of hemiindigo <b>29</b> in dimethyl sulfoxide (left) and comparison to the dimethylamino derivative <b>20</b> . The absorption maximum of the <i>Z</i> isomer (red) is not shifted but the <i>E</i> isomer (blue) exhibits a hypsochromic shift beyond the most red-shifted <i>Z</i> isomer maximum.	67
Figure 57:	<i>Lewis</i> -formula of hemiindigo <b>30</b> .	68
Figure 58:	Molar absorption spectra of pure isomers (left) and spectra recorded at the PSS at different wavelengths (right) of hemiindigo <b>30</b> in dimethyl sulfoxide. The isosbestic points are well defined, verifying the photostability of this compound. Highest isomeric yields were obtained at 450 nm irradiation (56% <i>E</i> isomer) and at 617 nm irradiation (96% <i>Z</i> isomer). Energy barriers for thermal double bond isomerizations were determined to be 30.5 kcal/mol for the <i>Z</i> to <i>E</i> and 31.7 kcal/mol for the <i>E</i> to <i>Z</i> direction at 114 °C, which translates to thermal half-lives of 78 years and 614 years at 25 °C, for the respective isomers. Quantum yields were determined at 12 ±2% (450 nm) for <i>Z</i> to <i>E</i> and 12 ±2% (520 nm) for <i>E</i> to <i>Z</i> direction. In 83 / 17 heptane / ethyl acetate the quantum yield rises to 33 ±2% (435 nm) for <i>Z</i> to <i>E</i> and is lowered to 10 ±2% (520 nm) for <i>E</i> to <i>Z</i> photoisomerizations. This increase in quantum yield of the <i>Z</i> isomer over the <i>E</i> isomer improves the photoisomerization yields to 98% <i>Z</i> isomer (530 nm) and 84% <i>E</i> isomer (435 nm) in apolar medium. Adapted with permission from <sup>[75]</sup> . Copyright 2018 American Chemical Society.	68
Figure 59:	Comparison of molar absorption spectra for less ( <b>20</b> ) and highly stilbene single bond-twisted hemiindigo <b>30</b> in 83 / 17 heptane / ethyl acetate. A strong hypsochromic shift of the twisted derivative <b>30</b> can be observed and its molar absorptivity $\epsilon$ is lowered by 70%.	69
Figure 60:	Structure of naphthylated indole <b>31</b> in the crystalline state. The perspective on the right emphasizes the nearly orthogonal planes of indole and naphthyl. The dihedral angle between the indole and naphthyl plane is close to 90° with 86.28° for the angle C8-N1-C10-C19. This proves that the introduction of the 7-methyl group alone twists the aryl axis to nearly its maximum in the crystalline state, which is also reproduced by DFT calculations (see Section 2.3.7). Chiral HPLC at 0 °C did not show a separation of rotamers for <b>31</b> , which indicates a low thermal stability of its rotational axis suggesting a rotational energy barrier of less than 20 kcal/mol.	70
Figure 61:	<i>Lewis</i> -formula of hemiindigo <b>33</b> .	72
Figure 62:	Molar absorption spectra of pure isomers (left) and spectra recorded at the PSS at different wavelengths of irradiation PSS (right) spectra of hemiindigo <b>33</b> in dimethyl sulfoxide. The isosbestic points are well defined, verifying the photostability of this compound. Highest isomeric yields were obtained at 450 nm irradiation (43% <i>E</i> isomer) and at 595 nm irradiation (98% <i>Z</i> isomer). Energy barriers for thermal double bond isomerizations were determined to be 31.8 kcal/mol for the <i>Z</i> to <i>E</i> and 32.7 kcal/mol for the <i>E</i> to <i>Z</i> direction at 114 °C, which translates to thermal half-lives of 750 years and 3427 years at 25 °C, for the respective isomers. Quantum yields were determined at 5 ±1% (450 nm) for <i>Z</i> to <i>E</i> and 8 ±2% (520 nm) for <i>E</i> to <i>Z</i> photoisomerizations. In 83 / 17 heptane / ethyl acetate, quantum yields were determined at 27 ±2% (435 nm) for <i>Z</i> to <i>E</i> and 9 ±2% (520 nm) for <i>E</i> to <i>Z</i> photoisomerizations. This increase in quantum yield of the <i>Z</i> isomer over the <i>E</i> isomer improves the photoisomerization yields to 98% <i>Z</i> isomer (530 nm) and 83% <i>E</i> isomer (435 nm) in apolar medium. Adapted with permission from <sup>[75]</sup> . Copyright 2018 American Chemical Society.	72
Figure 63:	Comparison of molar absorption spectra of <i>N</i> -naphthyl substituted hemiindigo <b>33</b> and <i>N</i> - <i>ortho</i> -tolyl substituted hemiindigo <b>30</b> . The shape of absorption spectra is almost identical whereas the molar absorptivity $\epsilon$ is increased by 20% for the naphthyl derivative.	73
Figure 64:	UV-Vis spectra of hemiindigo <b>33</b> dissolved in <i>Formlabs</i> clear resin (left) and photograph of prepared samples (right). Photoswitchability between >95% <i>Z</i> isomer and >83% <i>E</i> isomer can be seen, which equals the performance of hemiindigo <b>33</b> in apolar solvent mixtures of 87 / 13 heptane / ethyl acetate. The black circle on sample "348-H 1" served as positional marker for circularly polarized light (CPL) irradiations and ECD measurements.	74
Figure 65:	Calculated UV-Vis spectra at the B3LYP/6-311+G(d,p) level of theory, (TD-DFT, <i>n</i> states = 30) for a potentially red-shifted hemiindigo derivative, <i>Z</i> isomer (top) and <i>E</i> isomer (bottom) are shown. Absorption maxima of 625 nm ( <i>Z</i> ) and 660 nm ( <i>E</i> ) can be observed, an increase towards longer wavelengths is expected for the experiment, as DFT calculations tend to underestimate the red-shift. <sup>[74]</sup>	75
Figure 66:	Hemiindigo derivative <b>34</b> was synthesized by <i>D. Berdnikova</i> . Photoswitching and unspecified binding to HIV-1 TAR RNA, HIV-1 RRE-IIB RNA and HIV-1 TAR Tat complexes with fluorescent responses could be shown. <sup>[40]</sup>	77
Figure 67:	<i>Lewis</i> -formula of hemiindigo <b>9</b> .	78

## 5.2 TABLE OF FIGURES

Figure 68:	Impact of acids and base additions on the absorption of hemiindigo <b>9</b> in toluene. Photoswitchability without additives was ensured first (broken blue line and solid red line). Addition of 8 drops of trifluoroacetic acid to 2 mL of toluene volume yielded spectrum shown in green. Irradiation in this state did not induce any spectral changes. This can be caused by low thermal barriers in between <i>Z</i> and <i>E</i> isomer or due to deexcitation trough ESPT. An increase of molar absorptivity can be seen although the photoswitch concentration was diluted throughout this experiment. Neutralizing the solution yielded the bright blue line. In this state photoswitchability could be restored (broken violet line). Addition of a few drops of triethylamine yielded the pink spectrum.	78
Figure 69:	Lewis-formula of hemiindigo <b>11</b> .	79
Figure 70:	Impact of acids and base addition on the absorption of hemiindigo <b>11</b> in toluene. Photoswitchability without additives was ensured first (dashed blue line and solid red line). Addition of 4 drops of trifluoroacetic acid to 2 mL of toluene solution yielded the spectrum shown in green. Irradiation in this state did not induce any spectral changes. This can be caused by low thermal barriers in between <i>Z</i> and <i>E</i> isomer or due to deexcitation trough ESPT. A strong decrease of molar absorptivity can be seen as the photoswitch was not diluted by a factor of three by the small volumes of acid / base added. Excess triethylamine (violet line) restores proper photoswitchability (broken violet line, pink line) and results in a defined isosbestic point shifted by approximately 10 nm to the red part of the visible light spectrum compared to the neutral solution. A decrease in molar absorptivity by 20% can be observed.	79
Figure 71:	A first order kinetic analysis of the thermal <i>E</i> to <i>Z</i> isomerization of hemiindigo <b>15</b> in toluene (black, 22 °C), tetrahydrofuran (red, 25 °C), and dimethyl sulfoxide (grey, 51 °C) gives a linear relationship. The slope <i>m</i> can be translated into the rate constant <i>k</i> for this process. The corresponding Gibbs energies of activation are given in Table 8. Adapted with permission from [74]. Copyright 2017 American Chemical Society.	90
Figure 72:	Exemplary illustration of the decaying ECD response of <i>Z</i> -( <i>R<sub>a</sub></i> )- <b>30</b> at 40 °C in 93 / 7 heptane / ethyl acetate. The red spectrum with strongest ECD response represents <i>t</i> = 0 s and was set to 100% (added absolute spectral area for positive and negative signals). Correspondingly, the blue spectrum with weakest ECD response represents <i>t</i> = 3720 s at the end of the measurement. Kinetic plots were conducted within these respective margins. Yellow and green represent intermediate time points within the measurement. Adapted with permission from [75]. Copyright 2018 American Chemical Society.	92
Figure 73:	First order kinetic analyses of the thermal racemization via atropisomerization of hemiindigo <b>30</b> in 93 / 7 heptane / ethyl acetate in the dark. The slopes <i>m</i> can be translated into the rate constant <i>k</i> for each process. Racemization in the <i>Z</i> isomeric state (red, see also Figure 72) was measured at 40 °C and gives an energy barrier of 23.1 kcal/mol. Racemization in the <i>E</i> isomeric state (blue) was measured at 60 °C and proceeds over an energy barrier of 26.1 kcal/mol. Poor <i>R</i> <sup>2</sup> values are based on bad signal to noise ratios caused by the weak ECD response of the <i>E</i> isomer. Adapted with permission from [75]. Copyright 2018 American Chemical Society.	93
Figure 74:	Kinetics of the thermal isomer interconversion of hemiindigo <b>20</b> at 103 °C in dimethyl sulfoxide- <i>d</i> <sub>6</sub> in the dark starting from either 92% <i>E</i> - <b>20</b> (blue) or 96% <i>Z</i> - <b>20</b> (red). After prolonged heating, a stable 87 / 13 <i>E</i> / <i>Z</i> isomer mixture is obtained independently for both experiments. Adapted with permission from [75]. Copyright 2018 American Chemical Society.	95
Figure 75:	First order kinetic analysis of the thermal <i>E</i> to <i>Z</i> and <i>Z</i> to <i>E</i> isomerization of hemiindigo <b>20</b> in dimethyl sulfoxide- <i>d</i> <sub>6</sub> at 103 °C starting from either 92% <i>E</i> - <b>20</b> (blue) or 96% <i>Z</i> - <b>20</b> (red). After prolonged heating in the dark, a stable 87/13 <i>E</i> / <i>Z</i> isomer composition is observed in both experiments. Linearized plots according to eq. 5 are shown. The slopes <i>m</i> can be translated into the rate constant <i>k</i> for each isomerization direction. Analysis of the thermal <i>Z</i> to <i>E</i> equilibration reaction (red) gave energy barriers of 30.6 for <i>Z</i> / <i>E</i> - and 32.0 kcal/mol for the <i>E</i> / <i>Z</i> isomerizations. Analysis of the thermal <i>E</i> to <i>Z</i> equilibration reaction (blue) gave energy barriers of 30.6 for <i>Z</i> / <i>E</i> - and 32.1 kcal/mol for <i>E</i> / <i>Z</i> isomerizations, respectively. The close agreements of these two independent experiments can be seen by the almost similar slopes for the <i>Z</i> to <i>E</i> and <i>E</i> to <i>Z</i> isomerization experiments. Adapted with permission from [75]. Copyright 2018 American Chemical Society.	96
Figure 76:	Chromatogram of the HPLC separation of diarylethene <b>35</b> in pure acetonitrile. 3D plot of the diode array detector (DAD, top), trace of the Vis detector at 500 nm (bottom). A baseline resolved separation could be obtained.	100
Figure 77:	Lewis-formula of <b>35</b> .	100
Figure 78:	<sup>1</sup> H-NMR spectrum of the HPLC separated diarylethene <b>35</b> (closed form) in dichloromethane- <i>d</i> <sub>2</sub> . No open form is visible.	100
Figure 79:	Molar absorption spectra of diarylethene <b>35</b> in <i>n</i> -hexane. The molar absorptions reported by Sumi et al. of 28400 Lmol <sup>-1</sup> cm <sup>-1</sup> at 268 nm for the open form and 10900 Lmol <sup>-1</sup> cm <sup>-1</sup> at 562 nm for the closed form match very well with the recorded data (28517 Lmol <sup>-1</sup> cm <sup>-1</sup> (blue) at 268 nm and 11123 Lmol <sup>-1</sup> cm <sup>-1</sup> at 562 nm (red)).	101
Figure 80:	Photoisomerization progress of the ring-opening reaction of diarylethene <b>35</b> at different time points in <i>n</i> -hexane.	102
Figure 81:	Recorded photokinetic (blue) and polynomial fit (dotted blue) during the photoswitching of diarylethene <b>35</b> from 100% closed to 80% open form in <i>n</i> -hexane.	103
Figure 82:	Starting points / linear segment of the photokinetic shown in Figure 81 measured during the photoswitching of diarylethene <b>35</b> from 100% closed to 8% open form in <i>n</i> -hexane	104
Figure 83:	Regression of the weighted power factor versus the percentage of 100% closed diarylethene <b>35</b> in <i>n</i> -hexane to extrapolate the power value <i>P<sub>0</sub>f</i> the time <i>t<sub>0</sub></i> . Linear approximation (broken blue line) and polynomial fit (broken orange line) which improves the obtained quantum yield by 4.6% compared to the linear regression value.	105
Figure 84:	Quantum yield measurement, photokinetic, and polynomial fit for the ring-opening photoswitching reaction of diarylethene <b>35</b> at 520 nm irradiation starting from a 60% to 40% closed to open form mixture in <i>n</i> -hexane.	106
Figure 85:	Regression to calculate the power value <i>P<sub>0</sub>f</i> at the time <i>t<sub>0</sub></i> for the ring-opening photoswitching reaction of diarylethene <b>35</b> at 520 nm irradiation starting from a 60% to 40% closed to open form mixture in <i>n</i> -hexane. The linear approximation is shown in broken orange lines.	107
Figure 86:	Initial linear part (orange) and slope (blue) for the photoisomerization from 100% closed to open form recorded with the <i>Zinith</i> laser setup. Only the part from 10 s to 180 s is shown, as the first seconds gave inaccurate results because of laser adjustment.	109
Figure 87:	Complete plot for measurements (orange) and slope <i>t<sub>0</sub></i> (blue and green dotted line) for the photoisomerization from 100% closed to open form recorded with the <i>Zinith</i> laser setup. Slope <i>t<sub>0</sub></i> considers only the data points shown in Figure 86 and is added for comparison.	109
Figure 88:	Overlay of the <i>t<sub>0</sub></i> spectrum of diarylethene <b>35</b> in <i>n</i> -hexane (yellow), <i>t<sub>end</sub></i> spectrum (green), irradiation wavelength (473 nm, blue), absorption profile of the low pass filter glass, which was installed between the irradiated cuvette and the detector and readout wavelength (650 nm dark red).	110
Figure 89:	Quantum yield measurement of the <i>Z</i> to <i>E</i> photoisomerization of hemiindigo <b>20</b> in 83 / 17 heptane / ethyl acetate (blue dots) using a 467 nm LED for irradiation and starting from 95.9% <i>Z</i> - <b>20</b> and 4.1% <i>E</i> - <b>20</b> . The whole photoconversion kinetic was fitted with a fourth order polynomial (blue broken line). The polynomial formula is given in blue. Extrapolation of the polynomial to <i>y</i> = % <i>E</i> isomer = 0, differentiation and insertion of the corresponding <i>x</i> -value gives an initial slope <i>m<sub>0</sub></i> = 2.408%Es <sup>-1</sup> (orange formula). Adapted with permission from [75]. Copyright 2018 American Chemical Society.	111
Figure 90:	Quantum yield measurement of the <i>E</i> to <i>Z</i> photoisomerization of hemiindigo <b>20</b> in 83 / 17 heptane / ethyl acetate (blue dots) using a 520 nm LED for irradiation and starting from 95.8% <i>E</i> - <b>20</b> and 4.2% <i>Z</i> - <b>20</b> . The whole photoconversion kinetic was fitted with a fourth order polynomial (blue broken line). The polynomial formula is given in blue. Extrapolation of the polynomial to <i>y</i> = % <i>Z</i> isomer = 0, differentiation and insertion of the corresponding <i>x</i> -value gives an initial slope of <i>m<sub>0</sub></i> = 0.4682%Zs <sup>-1</sup> (orange formula). Adapted with permission from [75]. Copyright 2018 American Chemical Society.	113
Figure 91:	Initial design idea for a unidirectional molecular gearbox (top middle, <b>36</b> ). A, B and C pose as different substituents to yield a stereocenter at the indoxyl nitrogen. Indanone (top left, <b>37</b> ) and fluorenone (top right, <b>38</b> ) stilbene fragments could be used as rigid paddles to drive the adjacent N-C axis. Triptycyl moieties (bottom, <b>39</b> and <b>40</b> ) could provide better geared engagement between the photochemically driven stilbene fragment and the coupled, mechanically driven, single bond rotation attached to the nitrogen.	118
Figure 92:	Sequence for a geared, photodriven motion of the triptycyl residue at the indoxyl nitrogen of a model hemiindigo chromophore. One intermeshing step is shown in the sequence from 1 - 5. Calculations were done at the PM6 level of theory, the central double bond was rotated in 90 steps of two degrees each for the full 180° rotation of the double bond.	119
Figure 93:	Lewis-formula of hemiindigo <b>2</b> .	122
Figure 94:	Calculated ground and transition state structures of hemiindigo <b>2</b> at the B3LYP/6-311+G(d,p) level of theory. Transition states for the atropisomerizations and the stilbene single bond rotations were found for <i>Z</i> and <i>E</i> isomers. The disfavored transition state for the <i>E</i> isomer did not converge after several attempts and tweaks. The "+" sign in front of transition state values indicates the energy difference with respect to the lowest ground state of respective <i>Z</i> or <i>E</i> isomers. Structures in the box both correspond to the transition states of the stilbene rotational barriers of the <i>anti</i> - <i>Z</i> isomer.	122
Figure 95:	Lewis-formula of hemiindigo <b>50</b> .	125
Figure 96:	Structure of hemiindigo <b>50</b> in the crystalline state. The viewing angle on the right emphasizes the pronounced stilbene single bond twisting. The stilbene single bond dihedral torsion angle amounts to 42.05° for C8-C9-C10-C11 in the <i>E</i> isomeric state. The double bond (red) length amounts to 1.345 Å and the single bond (green) to 1.468 Å.	125
Figure 97:	Molar absorption (left) and PSS (right) UV-Vis spectra of hemiindigo <b>50</b> in toluene. The isosbestic points are not well defined, verifying the photolability of this compound. The <i>Z</i> state cannot be recovered upon irradiation, which could be caused by a low quantum yield for the <i>E</i> to <i>Z</i> photoisomerization.	125
Figure 98:	Lewis-formula of hemiindigo <b>51</b> .	126
Figure 99:	Structure of hemiindigo <b>51</b> in the crystalline state. The viewing angle on the right emphasizes the pronounced single bond twisting of the anthracene. The anthracene single bond dihedral torsion angle amounts to -59.61° for C8-C9-C10-C11 in the <i>Z</i> isomeric state, which is about 17° larger than the value of the corresponding torsion angle in the <i>E</i> state of naphthyl derivative <b>50</b> . The double bond (red) length amounts to 1.331 Å and the single bond (green) to 1.472 Å. Comparison to the <i>E</i> form of the naphthyl derivative <b>50</b> does not allow for unambiguous conclusions as electronic effects in between <i>Z</i> and <i>E</i> form might outweigh the influence of the added phenyl core resulting in the observed torsional differences.	126
Figure 100:	Molar absorption in dichloromethane (left) and PSS (right) UV-Vis spectra of hemiindigo <b>51</b> in toluene. The isosbestic points are well defined in dichloromethane, which is not true for toluene, verifying the solvent dependent photolability of this compound as mainly photodegradation can be observed in latter case.	127
Figure 101:	Lewis-formula of hemiindigo <b>52</b> .	128
Figure 102:	Structure of hemiindigo <b>52</b> in the crystalline state. The viewing angle on the right emphasizes the strong stilbene single bond twisting. The stilbene single bond dihedral torsion angle amounts to 58.25° for C8-C9-C10-C15 in the <i>Z</i> isomeric state, the double bond (red) length amounts to 1.342 Å and the single bond (green) to 1.477 Å.	128

Figure 103:	Molar absorption (left) and PSS (right) UV-Vis spectra of hemiindigo <b>52</b> in toluene. The isosbestic points are well-defined compared to previously synthesized derivatives <b>50</b> and <b>51</b> as viable photoswitchability can be observed.	129
Figure 104:	Lewis-formula of hemiindigo <b>55</b> .	131
Figure 105:	<sup>1</sup> H-NMR spectrum of HPLC separated <i>Z</i> and <i>E</i> isomers of hemiindigo <b>55</b> in chloroform- <i>d</i> at 27 °C.	131
Figure 106:	Calculated ground and transition state structures of hemiindigo <b>55</b> at the B3LYP/6-311+G(d,p) level of theory. Transition states for the atropisomerizations for <i>Z</i> and <i>E</i> isomers and the naphthyl single bond rotation for <i>anti</i> -diastereomers were found. The "+" sign in front of transition state values indicates the energy difference with respect to the lowest ground state of the respective <i>Z</i> or <i>E</i> isomers. The <i>syn</i> -transition states of the stilbene single bond rotation, however, did not converge after several attempts and tweaks. The isopropyl C-C single bond rotation and the methyl group rotation (+7.26 kcal/mol when adjacent to the carbonyl group, not shown) were found only for the <i>Z</i> isomer.	132
Figure 107:	Molar absorption (left) and PSS (right) UV-Vis spectra of hemiindigo <b>55</b> in toluene. The isosbestic points are not well defined, verifying the photolability of this compound. The <i>Z</i> state cannot be recovered upon irradiation.	133
Figure 108:	Lewis-formula of hemiindigo <b>56</b> .	133
Figure 109:	Molar absorption (left) and PSS (right) UV-Vis spectra of hemiindigo <b>56</b> in toluene. The isosbestic points are well defined, verifying the restored photostability of this compound after acylation. Photoswitching proceeds readily in both directions and a strong red-shift of about 60 nm compared to the naphthyl derivative <b>55</b> can be observed.	134
Figure 110:	Lewis-formula of hemiindigo <b>57</b> .	134
Figure 111:	Molar absorption (left) and PSS (right) UV-Vis spectra of hemiindigo <b>57</b> in toluene. The isosbestic points are well defined, verifying the photostability of this compound. Photoswitching proceeds readily in both directions, a large blue-shift of approx. 60 nm can be observed compared to the anthracene derivative. A fine structure can be seen for the <i>Z</i> isomer, which can be attributed to multiple, discernable oscillation modes with smaller full widths at half maximum (FWHM).	135
Figure 112:	Comparison of <sup>1</sup> H-NMR spectra of hemiindigo <b>55</b> in chloroform- <i>d</i> (600 MHz, 27 °C) and <b>57</b> in dichloromethane- <i>d</i> <sub>2</sub> (800 MHz, 27 °C), only the aliphatic region is shown. A pronounced splitting of the isobutyl methyl signals (2) can be observed which is enlarged in the <i>Z</i> state by almost one order of magnitude from 5.70 Hz to 52.36 Hz at 800 MHz NMR spectrometer frequency.	136
Figure 113:	<sup>1</sup> H-NMR spectra of a mixture of <i>Z</i> and <i>E</i> isomers of hemiindigo <b>57</b> in toluene- <i>d</i> <sub>6</sub> measured at different temperatures on a 400 MHz NMR spectrometer.	138
Figure 114:	Calculated ground and transition state structures of hemiindigo <b>57</b> at the B3LYP/6-311+G(d,p) level of theory. Transition states for the atropisomerizations for <i>Z</i> and <i>E</i> isomers and two stilbene single bond rotation for the <i>anti</i> - <i>Z</i> isomer were found. The "+" sign in front of transition state values indicates the energy difference with respect to the lowest ground state of respective <i>Z</i> or <i>E</i> isomers. The <i>E</i> -transition states of the stilbene single bond rotation, however, did not converge after several attempts and tweaks. The isopropyl single bond rotation was found only for the <i>Z</i> isomer. The calculated value of the stilbene single bond rotation in the <i>Z</i> state is in good agreement to the experimentally determined value of 17.06 kcal/mol.	140
Figure 115:	<sup>1</sup> H-NMR spectra of enantiopure HPLC fractions of hemiindigo <b>58</b> in dichloromethane- <i>d</i> <sub>2</sub> at ambient temperatures. The matching signals prove the separated HPLC fractions to be enantiomers.	142
Figure 116:	Structures of the enantiopure crystallization batches for <i>E</i> isomers of hemiindigo <b>58</b> in the crystalline state. The structure on the left (inside rectangle) was crystallized from the first enantiomeric fraction, the structure on the right from the second one, respectively. The chiral nature of the compound requires four molecules to determine its unit cell. Both crystal structures purposely show the <i>R</i> configuration at the stereocenter as the evaluation of the structural data done by <i>P. Mayer</i> was not unambiguous to assign the enantiomers to their respective stereodescriptors. This is generally difficult to achieve if the molecules do not contain at least one heavy atom, for example sulphur, or if only small crystals can be obtained. The stilbene single bond dihedral torsion angle amounts to 78.20° for C54-C55-C56-C57 in the <i>E</i> isomeric state. The double bond (red) length amounts to 1.337 Å and the single bond (green) to 1.488 Å.	143
Figure 117:	PSS (left) UV-Vis and ECD spectra of hemiindigo <b>58</b> in dimethyl sulfoxide. The isosbestic points are well defined, verifying the photostability of this compound after alkylation. Photoswitching proceeds readily in both directions. A red-shift of approximately 40 nm can be observed compared to the absorption of the acylated derivative <b>57</b> . A strong modulation of the ECD signal can be seen in between <i>Z</i> and <i>E</i> isomer. Adapted with permission from [75]. Copyright 2018 American Chemical Society.	144
Figure 118:	Setup for alternatively irradiating liquid samples with right or left handed circularly polarized light (CPL) and non-polarized light. LED 1 is focused with a lens on a stack of microscopy plates at the Brewster angle of 56°. The reflected linearly polarized light (LPL) was tested with sunglasses (which can pose as linear polarizers) and could be extinguished upon turning the glasses within the plane of the lens, which proved successful linear polarization. The addition of a Fresnel rhomb (which poses also as a quarter wave plate) with its optical axis turned at 45° to the light path led to a non-extinguishable ray of CPL. When another quarter wave plate (like the Fresnel rhomb) is added to the beam path, CPL is again transformed to extinguishable LPL, which proves the successful circular polarization of the LED light. A microcontroller can be used for actuating a relay board to run cyclic experiments where a sample is repeatedly irradiated with CPL and normal, unpolarized light to its initial state.	145
Figure 119:	Design principles of axially chiral hemiindigo photoswitches. The chiral axis together with a methyl group in 7-position of the indoxyl core yield HPLC-separable rotamers for specific stilbene substitution patterns in <i>Z</i> and <i>E</i> isomeric forms.	147
Figure 120:	Overview of selected axially chiral hemiindigos <b>20</b> , <b>59</b> , <b>29</b> , <b>25</b> , <b>60</b> , <b>61</b> , <b>30</b> and <b>33</b> . Only respective <i>E</i> isomers are shown. The properties of compound <b>25</b> were discussed in Section 2.2.7, as no chiral HPLC separation was performed on this molecule.	148
Figure 121:	First generation of synthesized axially chiral hemiindigo derivatives <b>20</b> , <b>59</b> and <b>29</b> .	150
Figure 122:	Section of the 2D <sup>1</sup> H-NOESY NMR spectrum (dichloromethane- <i>d</i> <sub>2</sub> , 600 MHz, 27 °C) of hemiindigo <b>20</b> . An unambiguous assignment of the double bond configuration can be done with this spectrum. A strong NOE cross signal between <i>Z</i> 12 and <i>Z</i> 22 evidences the <i>Z</i> isomeric state. The strong NOE cross signal between proton <i>E</i> 10 and protons <i>E</i> 22 evidences the <i>E</i> isomer. The corresponding cross signal of <i>Z</i> 10 and <i>Z</i> 22 is very weak, indicating a farther distance of the methyl group associated to the <i>ortho</i> -tolyl residue to the double bond proton in the <i>Z</i> isomeric state.	151
Figure 123:	Aromatic section of the <sup>1</sup> H-NMR spectra (dichloromethane- <i>d</i> <sub>2</sub> , 800 / 600 MHz, 27 °C) of <i>E</i> (top) and <i>Z</i> isomer (bottom) enriched mixtures of hemiindigo <b>20</b> . Large upfield shifts can be observed upon transition from <i>E</i> to <i>Z</i> isomer, which indicate proximity of the shielding aniline ring-current to the chiral <i>ortho</i> -tolyl residue in the <i>Z</i> state. Adapted with permission from [75]. Copyright 2018 American Chemical Society.	152
Figure 124:	3D UV-Vis Chromatograms of hemiindigo <b>20</b> on a chiral HPLC column recorded at 0 °C in 87 / 13 heptane / ethyl acetate. The peak intensity scale is given in mAU (milli a.u., arbitrary units).	153
Figure 125:	Molar absorption coefficients (left) of <b>20</b> in 83 / 17 heptane / ethyl acetate with the <i>Z</i> isomer shown in red and the <i>E</i> isomer in blue. Spectral changes recorded after different irradiation times show clear isosbestic points (right). Adapted with permission from [75]. Copyright 2018 American Chemical Society.	154
Figure 126:	ECD spectrum measurement of <i>Z</i> - <b>20</b> at 25 °C (left). Because of the low energy barrier of 19.9 kcal/mol for atropisomerization via <i>N</i> -(indoxyl)- <i>o</i> -tolyl single-bond rotation (corresponding to a half-life of 43 s at 25 °C) the ECD signal has almost completely vanished at 0 °C. Molar ellipticity ECD spectra of <i>E</i> - <b>20</b> in 83 / 17 heptane/ethyl acetate at 25 °C (right), ( <i>R</i> <sub>s</sub> )- <i>E</i> - <b>20</b> shown in blue, ( <i>S</i> <sub>s</sub> )- <i>E</i> - <b>20</b> shown in red. Adapted with permission from [75]. Copyright 2018 American Chemical Society.	154
Figure 127:	UV-Vis absorption (left) and ECD spectrum (right) of <b>20</b> in 83 / 17 heptane / ethyl acetate recorded for one switching cycle starting from pure ( <i>R</i> <sub>s</sub> )- <i>E</i> - <b>20</b> (solid blue), which was photoisomerized to <i>Z</i> - <b>20</b> (5 min, 595 nm, solid red) and then switched back to <i>E</i> - <b>20</b> (1 min, 470 nm, light blue, dashed) in high isomeric yields at 23 °C. The low free activation enthalpy Δ <i>G</i> <sup>‡</sup> = 19.9 kcal/mol for thermal atropisomerization in the <i>Z</i> isomeric state leads to fast racemization in this state within ~2 minutes (thermal half-life of 43 s at 25 °C) under the applied measurement conditions. Consequently, the ECD signal is already lost in the <i>Z</i> isomeric state (right, red spectra) and photoisomerization back to the thermally more stable <i>E</i> - <b>20</b> therefore shows no leftover ECD signal for the <i>E</i> isomer (right, light blue, dashed line). Adapted with permission from [75]. Copyright 2018 American Chemical Society.	155
Figure 128:	First order kinetic analyses of the thermal racemization via atropisomerization of hemiindigo <b>20</b> in 83 / 17 heptane / ethyl acetate in the dark. The slopes <i>m</i> can be translated into the rate constants <i>k</i> for each process. Racemization in the <i>Z</i> isomeric state (red) was measured at -20 °C and proceeds over an energy barrier of 19.9 kcal/mol. Racemization in the <i>E</i> isomeric state (blue) was measured at 40 °C and proceeds over an energy barrier of 23.4 kcal/mol. Poor <i>R</i> <sup>2</sup> values are based on bad signal to noise ratios caused by weak ECD responses. Adapted with permission from [75]. Copyright 2018 American Chemical Society.	156
Figure 129:	Calculated ground and transition state structures of hemiindigo <b>20</b> at the B3LYP/6-311+G(d,p) level of theory. Transition states for the atropisomerization and the stilbene single bond rotation were found. The disfavored atropisomerization transition states did not converge after several attempts and tweaks. The calculated energies are in good agreement to the experimental values. The "+" sign in front of transition state values indicates the energy difference with respect to the lowest ground state of respective <i>Z</i> or <i>E</i> isomers.	157
Figure 130:	Benchmarking results for hemiindigo <b>20</b> using different DFT functionals for the 6-311+G(d,p) basis set. " <i>Z</i> " and " <i>E</i> " represent the ground states and " <i>Z</i> Me-Me" and " <i>E</i> Me-DB" the energetically lowest transition state for the rotation around the <i>ortho</i> -tolyl axis with the respective double bond configuration (see Figure 129). The "+" sign in front of transition state values indicates the energy difference with respect to the lowest ground state of respective <i>Z</i> or <i>E</i> isomers.	158
Figure 131:	Lewis-formula of hemiindigo <b>59</b> .	160
Figure 132:	3D UV-Vis Chromatograms of hemiindigo <b>59</b> on a chiral HPLC column (Diacel Chiralpak IC, 5µm, 8 mL/min) recorded at 0 °C in 95 / 5 heptane / ethyl acetate. Injection of a <i>Z</i> / <i>E</i> mixture gives three separable peaks, <i>E</i> 1 <i>E</i> 2 and <i>Z</i> 1. The peak intensity scale is given in mAU (milli a.u., arbitrary units).	160
Figure 133:	Lewis-formula of hemiindigo <b>29</b> .	161
Figure 134:	3D UV-Vis Chromatograms of hemiindigo <b>29</b> on a chiral HPLC column (Diacel Chiralpak IC, 5µm, 8 mL/min) recorded at 0 °C in 83 / 17 heptane / ethyl acetate. Injection of a <i>Z</i> / <i>E</i> mixture gives mainly two separable peaks, <i>E</i> 1 and <i>E</i> 2. The peak intensity scale is given in mAU (milli a.u., arbitrary units).	161
Figure 135:	Second generation of synthesized axially chiral hemiindigo derivatives <b>60</b> and <b>61</b> .	163
Figure 136:	Lewis-formula of hemiindigo <b>60</b> .	164
Figure 137:	3D UV-Vis Chromatograms of hemiindigo <b>60</b> on a chiral HPLC column (Diacel Chiralpak IC, 5µm, 8 mL/min) recorded at 0 °C in 95 / 5 heptane / ethyl acetate. Injection of a <i>Z</i> / <i>E</i> mixture gives four separable peaks, <i>Z</i> 1, <i>Z</i> 2, <i>E</i> 1 and <i>E</i> 2, which is a novelty compared to the previously synthesized	

## 5.2 TABLE OF FIGURES

- hemiindigos substituted with chiral axes. The peak intensity scale is given in mAU (milli a.u., arbitrary units). Collection and re-injection of *E* 1 (left) gives the pure *E* peak. Collection and re-injection of *Z* 1 (right) gives the pure peak and some unknown side product, which is probably a residue from a previous run. Irradiation of *Z* 1 to the *E* state yielded the *E* 1 isomer almost quantitatively. *E* 1 and *Z* 1 left in the dark did not noticeably racemize, heating to 100 °C for 25 minutes, however, yielded the racemates (not shown).
- Figure 138: Structure of hemiindigo **60** in the crystalline state. The viewing angle on the right emphasizes the strong twisting of the naphthyl stilbene fragment and the *ortho*-tolyl chiral axis within the *Z* form. Latter is strongly twisted with a dihedral torsion angle of 102.71° for C25-C20-N1-C1. The twist around the stilbene single bond amounts to 72.49° for C8-C9-C10-C19. The length of the double bond (red) amounts to 1.342 Å and the single bond (green) amounts to 1.482 Å. 164
- Figure 139: Section of the NOESY <sup>1</sup>H-NMR spectrum (dichloromethane-*d*<sub>2</sub>, 800 MHz, 27 °C) of hemiindigo *E*-**60**. The strong NOE cross signal between proton *E* 10 and protons *E* 22 and the weak interaction between *E* 12 and *E* 22 suggest the *E* conformation. Cross signal *E* 27 / *E* 22 and the downfield shift of *E* 12 and *E* 27 suggest the naphthyl moiety to face away from the carbonyl oxygen while maintaining rotatability at the carbon-carbon single bond (weak signals *E* 12 / *E* 22). Cross signals *E* 21 / *E* 23, *E* 18 / *E* 23 and *E* 20 / *E* 23 exemplify the proximity of methyl group *E* 23 towards the ring system of the chiral aryl axis. 165
- Figure 140: Section of the NOESY <sup>1</sup>H-NMR spectrum (dichloromethane-*d*<sub>2</sub>, 600 MHz, 27°C) of hemiindigo *Z*-**60**. The missing NOE cross signal between proton *Z* 10 and protons *Z* 22 and the strong interaction between *Z* 12 and *Z* 22 suggest the *Z* conformation. Cross signal *Z* 27 / *Z* 22 suggests twisting of the stilbene and the downfield shift of *Z* 27 suggest the naphthyl moiety to face towards the carbonyl oxygen while maintaining rotatability at the carbon-carbon single bond. Signal *Z* 12 shows a strong upfield shift, hinting towards increased distance towards the carbonyl oxygen. Cross signal *Z* 21 / *Z* 23, exemplifies the proximity of methyl group *Z* 23 towards the ring system of the chiral aryl axis. 166
- Figure 141: Section of the <sup>1</sup>H-NMR spectra (dichloromethane-*d*<sub>2</sub>, 800 / 600 MHz, 27 °C) of *E* (top) and *Z* isomer (bottom) enriched mixtures of hemiindigo **60**. Strong chemical shifts can be observed upon transition from *E* to *Z* isomer, which indicates proximity of the stilbene ring current towards the *N*-aryl chiral axis in the *Z* state as the signals for the *E* isomer are separated from each other and tend to shift upfield in the *Z* isomer. The large upfield shifts of signals 12, 18, 19, 20 and 21 from *E* to *Z* and the downfield shift of signal 27 indicates transition from a mostly planar stilbene fragment in *E* configuration to pronounced twisting of the naphthalene in the *E* state. 167
- Figure 142: Molar absorption (left) and PSS (right) spectra of hemiindigo **60** in 95 / 5 heptane / ethyl acetate. The isosbestic points remain defined, verifying the photostability of this compound. Best isomeric yields were determined at 95% *E* isomer (435 nm) and 39% *Z* isomer (617 nm). 168
- Figure 143: Molar electronic circular dichroism spectra of hemiindigo **60** for the *Z* (left) and *E* isomer (right) in 95 / 5 heptane / ethyl acetate at 0 °C. Fractions *Z* 1 and *E* 1 yielded the red spectra (*ortho*-tolyl *S*<sub>0</sub> configurations) while *Z* 2 and *E* 2 yielded the blue spectra (*R*<sub>0</sub> configurations). 169
- Figure 144: UV-Vis (left) and ECD spectrum (right) of **60** in 95 / 5 heptane / ethyl acetate after one cycle of switching of *E* (blue) and *Z* (red) isomers at 0 °C. Isomerization from *E* to *Z* was not feasible with all wavelengths available in this solvent mixture (irradiation in dimethyl sulfoxide yielded the *Z* isomer). The mediocre thermal barrier of the chiral aryl axis in the *Z* isomer (right, red) prevents racemization at 0 °C and irradiation from *Z* to the *E* isomer (blue) yielded almost exactly the ECD spectrum of the isolated pure *E* isomer (light blue, dotted line). Irradiation with 530 nm for 5 min did not yield the *Z* isomer but did also not change the ECD spectrum (light blue, dashed line). (*Z* to *E* irradiation: 2 min 470 nm) 170
- Figure 145: First order kinetic analyses of hemiindigo **60** in 95 / 5 heptane / ethyl acetate for the atropisomerization of *Z* isomer (red) and *E* isomer (blue). The data points are fitted with a linear relationship. The slope *m* can be translated into the rate constant *k* for this process. For the *Z* isomer, a rotational barrier of 21.7 kcal/mol was determined at 10 °C, which translates into a thermal half-life of 15 min at 25 °C. For the *E* isomer, a rotational barrier of 24.3 kcal/mol was determined at 60 °C, which translates into a thermal half-life of 21 h at 25 °C. 170
- Figure 146: Calculated ground and transition state structures of hemiindigo **60** at the B3LYP/6-311+G(d,p) level of theory. All transition states for the atropisomerization and one for the stilbene single bond rotation were found. The transition state of the stilbene single bond did not converge after several attempts and tweaks. The "+" sign in front of transition state values indicates the energy difference with respect to the lowest ground state of respective *Z* or *E* isomers. The calculated energies are in good agreement to the experimental values for the *Z* isomer, however the lowest transition state of the *E* isomer is undershot by about 4 kcal/mol compared to the experimental values. The methyl-over-methyl transition state is disfavored by 4 kcal/mol in the *E* isomer and the methyl over central double bond transition state is disfavored by 1 kcal/mol in the *Z* state. A by 2.6 kcal/mol lowered atropisomerization barrier for the *Z* isomers can be measured. The transition state structures suggest a rotation of the *ortho*-tolyl axis methyl group over the indoxyl core methyl group in the *Z* state while the *E* form prefers passing of the methyl group over its central double bond. These findings show that gating of thermal barriers as well as their directionality are possible for these chiroptical photoswitches. 171
- Figure 147: Benchmarking results for hemiindigo **60** using different DFT functionals for the 6-311+G(d,p) basis set. "*Z*-anti/syn" and "*E*-anti/syn" represent the ground states and "*Z*-Anti-Me-Me" and "*E*-Syn-Me-DB" the energetically lowest transition state for respective isomer and rotation pathway in all cases without dispersive corrections except for the PBE/PBE functional. The "+" sign in front of transition state values indicates the energy difference with respect to the lowest ground state of respective *Z* or *E* isomers. 172
- Figure 148: Lewis-formula of hemiindigo **61**. 173
- Figure 149: 3D UV-Vis Chromatograms of hemiindigo **61** on a chiral HPLC column (*Diacel Chiralpak* IC, 5µm, 8 mL/min) recorded at 0 °C in 95 / 5 heptane / ethyl acetate. Injection of a *Z* / *E* mixture gives four separable peaks, *Z* 1, *Z* 2, *E* 1 and *E* 2, which shows similar results to hemiindigo **60** with the addition that eight peaks were expected, see Figure 151. The peak intensity scale is given in mAU (milli a.u., arbitrary units). 173
- Figure 150: Structure of (*S*<sub>A</sub>)-(*S*<sub>A</sub>)-*anti*-*E*-**61** in the crystalline state. The *anti* form is defined by the higher oxidized carbon position in the phenyl ring opposing the *ortho*-tolyl methyl group. This means that in the *anti* form both methyl groups involved in axial chirality are configured *syn* to each other. The viewing angle on the right emphasizes the strong twisting of the naphthyl stilbene fragment and the *ortho*-tolyl chiral axis within the *E* form. Latter is strongly twisted with a dihedral torsion angle of 84.09° for C25-C20-N1-C1. The stilbene single bond is twisted by 53.58° for C8-C9-C10-C11. The length of the double bond (red) amounts to 1.340 Å and the single bond (green) amounts to 1.469 Å. 174
- Figure 151: Overview of all possible conformations of hemiindigo **61**. 175
- Figure 152: <sup>1</sup>H-NMR spectra (dichloromethane-*d*<sub>2</sub>, 600 MHz, 27 °C) of all four separable *Z* and *E* isomers of hemiindigo **61**. Six distinct methyl group signals can be observed for the *Z* isomer, three of them each belong to the respective *anti*- or *syn* diastereomers. In the *E* form, overlapping signals can be observed as the chemical shift between diastereomers is too small / similar to cause distinct signal shifts. 176
- Figure 153: Lewis-formula of hemiindigo **61**. 177
- Figure 154: <sup>1</sup>H-NOESY 2D NMR spectrum of *syn*- and *anti*-*Z*-**61** (dichloromethane-*d*<sub>2</sub>, 600 MHz, 27 °C). An unambiguous assignment can be made as cross-signal 22 / 23 is observable for *syn* and *anti* forms but signal 29 / 22 is only visible in the *anti* form in which both rotatable methyl groups are closest together. As NOESY and EXSY share the same pulse sequence, positive (red) signals between *syn* and *anti* forms prove an observable fast exchange of nuclei for these positions caused by the dynamics being faster than the used mixing time of 1.2 s. 177
- Figure 155: Lewis-formula of hemiindigo **61**. 178
- Figure 156: <sup>1</sup>H-NOESY 2D NMR spectrum of *syn*- and *anti*-*E*-**61** (dichloromethane-*d*<sub>2</sub>, 600 MHz, 27 °C). An unambiguous *syn* / *anti* assignment cannot be made. However, the crystallized *E* isomer resides in the *anti* form (Figure 150), hinting towards its higher thermodynamic stability or crystal packing effects. The signals of 22 can be seen for the *syn*- and *anti* form and very pronounced positive (red) signals for *syn* to *anti* transitions of signals 22 and 29 can be observed. This proves faster dynamics of the stilbene single bond rotation in the *E* isomer compared to the *Z* state (see Figure 154). 178
- Figure 157: Lewis-formula of hemiindigo **61**. 179
- Figure 158: <sup>1</sup>H-HSQC 2D NMR spectrum of *syn*- and *anti*-*E*-**61** (dichloromethane-*d*<sub>2</sub>, 600 MHz, 27 °C). An unambiguous *syn* / *anti* assignment cannot be made. However, the superimposing signals can be differentiated, suggesting the <sup>1</sup>H-NOESY assignment regarding the positions of the methyl groups to be correct. 179
- Figure 159: <sup>13</sup>C-NMR spectrum of *syn*- and *anti*-*Z*-**61** (dichloromethane-*d*<sub>2</sub>, 600 MHz, 27 °C). The two insets above magnify the large amounts of signals and multiplets. 180
- Figure 160: <sup>13</sup>C-NMR spectrum of *syn*- and *anti*-*E*-**61** (dichloromethane-*d*<sub>2</sub>, 600 MHz, 27 °C). The insets above visualize the large amounts of signals and multiplets. Four proton signals could be obtained for the methyl groups of these compounds while two respective multiplets are observed in the <sup>13</sup>C-NMR spectrum. 181
- Figure 161: <sup>1</sup>H-HMBC 2D NMR spectrum of *syn*- and *anti*-*Z*-**61** (dichloromethane-*d*<sub>2</sub>, 600 MHz, 27 °C). An unambiguous assignment of all protons and carbons cannot be made, as interpretation by hand is impossible with this large amount of overlapping signals and ghost peaks which were observed with multiple sample preparations on 600 and 800 MHz NMR devices. 182
- Figure 162: Molar absorption (left) and PSS (right) UV-Vis spectra of hemiindigo **61** in 95 / 5 heptane / ethyl acetate. The isosbestic points remain defined, verifying the photostability of this compound. Best isomeric yields were determined at 98% *E* isomer (470 nm) and 25% *Z* isomer (505 nm). 183
- Figure 163: Molar electronic circular dichroism spectra of hemiindigo **61** for the *Z* (left) and *E* isomer (right) in 95 / 5 heptane / ethyl acetate at 0 °C. Fractions *Z* 1 and *E* 1 yielded the red spectra (*ortho*-tolyl *S*<sub>0</sub> configurations) while *Z* 2 and *E* 2 yielded the blue spectra (*R*<sub>0</sub> configurations). 183
- Figure 164: UV-Vis (left) and CD spectrum (right) of hemiindigo **61** in 95 / 5 heptane / ethyl acetate after one cycle of switching from *Z* (red) to *E* (blue) to little *Z* contents (blue, dashed line) at 0 °C. The high thermal barrier for the chiral aryl axis in the *Z* isomer (right, red) prevents racemization from 0 °C up to ambient temperatures and irradiation to the *E* isomer (blue) yielded almost exactly the ECD spectrum of the isolated pure *E* isomer (light blue, dotted line). Irradiation with 505 nm for 10 min did yield the *Z* isomer in low contents but did also not change the ECD spectrum (blue, dashed line), which shifts proportionally towards the *Z* state. (*Z* to *E* irradiation: 5 min 470 nm) 184
- Figure 165: First order kinetic analyses of hemiindigo **61** in 95 / 5 heptane / ethyl acetate for the atropisomerization of *Z* isomer (red) and *E* isomer (blue). The data points are fitted with a linear relationship. The slope *m* can be translated into the rate constant *k* for this process. For the *Z* isomer, a rotational barrier of 24.6 kcal/mol was determined at 40 °C, which translates into a thermal half-life of 35 h at 25 °C. For the *E* isomer, a rotational barrier of 26.8 kcal/mol was determined at 80 °C, which translates into a thermal half-life of 59 d at 25 °C. Used formulas and equations can be found in Section 2.2.19. 184
- Figure 166: Calculated ground and transition state structures of hemiindigo **61** at the B3LYP/6-311+G(d,p) level of theory. Transition states for the atropisomerization and the stilbene single bond rotation were found. The disfavored atropisomerization transition state for the *Z* isomer and the stilbene rotation in the *E* isomer did not converge after several attempts and tweaks. The "+" sign in front of transition state values indicates the energy difference with respect to the lowest ground state of respective *Z* or *E* isomers. 185

- Figure 167: Benchmarking results for hemiindigo **61** using different DFT functionals for the 6-311+G(d,p) basis set. "Z-anti/syn" and "E-anti/syn" represent the ground states and "Z-Anti-Me-Me" and "E-Syn-Me-DB" the energetically lowest transition state for respective isomer and rotation pathway (see Figure 166). The "+" sign in front of transition state values indicates the energy difference with respect to the lowest ground state of respective Z or E isomers. 186
- Figure 168: Third generation of axially chiral hemiindigos **30** and **33**. 187
- Figure 169: Lewis-formula of hemiindigo **30**. 187
- Figure 170: Molar absorption coefficients of **30** in 93 / 7 heptane / ethyl acetate (left) with the Z isomer shown in red and the E isomer in blue. Spectral changes recorded after different irradiation times show clear isosbestic points (right). Adapted with permission from [75]. Copyright 2018 American Chemical Society. 187
- Figure 171: Molar ellipticity ECD spectra of Z-**30** in 93 / 7 heptane / ethyl acetate (left), ( $R_a$ )-Z-**30** shown in blue, ( $S_a$ )-Z-**30** shown in red. Molar ellipticity ECD spectra of E-**30** in 93 / 7 heptane / ethyl acetate (right), ( $R_a$ )-E-**30** shown in blue, ( $S_a$ )-E-**30** shown in red. Adapted with permission from [75]. Copyright 2018 American Chemical Society. 188
- Figure 172: UV-Vis absorption (left) and ECD spectrum (right) of **30** in 93 / 7 heptane / ethyl acetate recorded for one switching cycle starting from pure ( $R_a$ )-Z-**30** (solid red), which was photoisomerized to ( $R_a$ )-E-**30** (1 min 435 nm, solid blue) and then switched back to ( $R_a$ )-Z-**30** (1 min 530 nm, pale red, dashed) in high isomeric yields at 0 °C. The high free activation enthalpies  $\Delta G^\ddagger = 24.0$  kcal/mol for thermal atropisomerization in the Z isomeric state and  $\Delta G^\ddagger = 26.1$  kcal/mol in the E isomeric state prevent any racemization at 0 °C and even ambient temperatures. Therefore, the initial ECD spectrum of the pure Z isomer is fully recovered after a complete photoswitching cycle (solid red and pale red dashed spectra). Adapted with permission from [75]. Copyright 2018 American Chemical Society. 188
- Figure 173: First order kinetic analyses of the thermal racemization via atropisomerization of hemiindigo **30** in 93 / 7 heptane / ethyl acetate in the dark. The slopes  $m$  can be translated into the rate constant  $k$  for each process. Racemization in the Z isomeric state (red, see also Figure 174) was measured at 40 °C and proceeds over an energy barrier of 23.1 kcal/mol. Racemization in the E isomeric state (blue) was measured at 60 °C and proceeds over an energy barrier of 26.1 kcal/mol. Poor  $R^2$  values are based on bad signal to noise ratios caused by the weak ECD response of the E isomer. Adapted with permission from [75]. Copyright 2018 American Chemical Society. 189
- Figure 174: Repetitive photoswitching of the ECD spectrum of hemiindigo **30** (solid lines: ( $S_a$ ) configuration) and thermal decay of the ECD spectrum in the dark (broken lines: ( $R_a$ ) configuration) in 93 / 7 heptane / ethyl acetate. Spectra of Z isomers are shown in red and of E isomers in blue (light blue after 36 cycles / 90 minutes). The ( $S_a$ ) and ( $R_a$ ) configured samples were handled at 18 °C within an air-conditioned room. The ( $S_a$ )-**30** isomer was photoswitched 12 times between its two PSS' at 435 nm (30 s irradiation time at 260 mW per cycle to reach the PSS) and 505 nm (120 s irradiation time at 80 mW per cycle to reach the PSS) within 30 minutes. An ECD spectrum was recorded at this time interval and the procedure was repeated for two times (red solid line spectra, total of 36 photoswitching cycles within 90 min). The ( $R_a$ )-Z-**30** isomer was kept in the dark at 18 °C and was also measured in 30 min intervals to show the thermal racemization of the chiral axis (red broken line spectra). ECD measurements were conducted at 0 °C and samples were put on ice (0 °C) during transfer of samples and waiting times in complete darkness. The slightly faster decline of the photoswitched sample (red solid line spectra) results from additional heating effects of the LED irradiations, which were measured to result in 6.15 °C higher sample temperature compared to the surrounding 18 °C. Adapted with permission from [75]. Copyright 2018 American Chemical Society. 190
- Figure 175: Repetitive photoswitching of the ECD spectrum of ( $S_a$ )-**30** (red, see also Figure 174) and thermal decay of ( $R_a$ )-Z-**30** (violet) in 93 / 7 heptane / ethyl acetate. Photoirradiation was performed at 24.15 °C (red for the Z state, blue for the E state). The ECD signal at 420 nm is used exemplarily because at this spectral position signal intensity for the PSS solution enriched in E isomer (84% E-**30** and 16% Z-**30** in the PSS at 435 nm) is zero. The thermal decay of the Z-**30** ECD signal was measured at 18 °C and then extrapolated to 24.15 °C to ensure comparability (solid violet line). The residual loss of ECD signal is attributed to irreversible photodegradation (green) over 36 photoswitching cycles and was determined from the corresponding experimental absorption spectra (5% after 36 cycles). Adapted with permission from [75]. Copyright 2018 American Chemical Society. 191
- Figure 176: Fully reversible photoswitching of the ECD spectrum of ( $S_a$ )-**30** (red for the Z state, blue for the E state) in 93 / 7 heptane / ethyl acetate is seen after correction for thermal ECD decay of ( $S_a$ )-Z-**30**. No racemization of the chiral *N*-indoxyl-*ortho*-tolyl axis by photoinduced double-bond isomerization is observed over 36 switching cycles excluding light induced coupled motions between the aniline fragment and the *ortho*-tolyl residue. Photodegradation is plotted in green for comparison. Adapted with permission from [75]. Copyright 2018 American Chemical Society. 192
- Figure 177: Repetitive photoswitching of the ECD spectrum of hemiindigo **30** (solid lines: ( $R_a$ ) configuration) 93 / 7 heptane / ethyl acetate. Spectra of Z isomers are shown in red and of E isomers in blue (light blue at the start). The ( $R_a$ ) configured sample was irradiated and measured at -20 °C within a cryostat mounted inside the ECD spectrometer equipped with a glass fiber directly inserted into the sample cuvette inside the cryostat (see Section 2.7.5 for the newly built setup for this purpose). The ( $R_a$ )-**30** isomer was photoswitched 7 times between its two PSS' at 450 nm (10 s irradiation time at 193 mW per cycle to reach the PSS) and 520 nm (60 s irradiation time at 92 mW per cycle to reach the PSS). An ECD spectrum was recorded after every irradiation step. Adapted with permission from [75]. Copyright 2018 American Chemical Society. 193
- Figure 178: 3D plot showing modulation of the ECD of hemiindigo **30** by repetitive photoswitching between the PSS at 435 nm (weak signals) and the PSS at 520 nm (strong signals) at -20 °C. Adapted with permission from [75]. Copyright 2018 American Chemical Society. 194
- Figure 179: Repetitive photoswitching of the ECD spectrum of ( $R_a$ )-**30** (red) in 93 / 7 heptane / ethyl acetate. Photoirradiation was performed at -20 °C (red for the Z enriched state at 520 nm, blue for the E enriched state at 450 nm). No thermal racemization or photodegradation could be observed over the course of the experiment at -20 °C. The ECD signal at 420 nm is used exemplarily because at this spectral position signal intensity for the PSS solution enriched in E isomer (83% E-**30** and 17% Z-**30** in the PSS at 450 nm) is almost zero. Adapted with permission from [75]. Copyright 2018 American Chemical Society. 194
- Figure 180: Photoswitching of the  $g$  factors of hemiindigo **30** in 93 / 7 heptane / ethyl acetate (blue: E isomers, red: Z isomers, solid lines: ( $S_a$ ) configuration, broken lines: ( $R_a$ ) configuration). Adapted with permission from [75]. Copyright 2018 American Chemical Society. 195
- Figure 181: Calculated ground and transition state structures of hemiindigo **30** at the B3LYP/6-311+G(d,p) level of theory. Transition states for all atropisomerization and the stilbene single bond rotation in the Z state were found. The "+" sign in front of transition state values indicates the energy difference with respect to the lowest ground state of respective Z or E isomers. 196
- Figure 182: Benchmarking results for hemiindigo **30** using different DFT functionals for the 6-311+G(d,p) basis set. "Z" and "E" represent the ground states and "Z-Me-DB" and "E-Me-DB" the energetically lowest transition state for respective isomer and rotation pathway (see Figure 181). The "+" sign in front of transition state values indicates the energy difference with respect to the lowest ground state of respective Z or E isomers. 197
- Figure 183: Lewis-formula of hemiindigo **33**. 198
- Figure 184: Molar absorption coefficients of **33** in 87 / 13 heptane / ethyl acetate (left) with the Z isomer shown in red and the E isomer in blue. Spectral changes recorded after different irradiation times show clear isosbestic points (right). Adapted with permission from [75]. Copyright 2018 American Chemical Society. 198
- Figure 185: Molar ellipticity ECD spectra of Z-**33** (left) in 87 / 13 heptane / ethyl acetate, ( $R_a$ )-Z-**33** shown in blue, ( $S_a$ )-Z-**33** shown in red. Determination of the absolute configuration is based on the theoretical description. Molar ellipticity ECD spectra of E-**33** (right) in 87 / 13 heptane / ethyl acetate, ( $R_a$ )-E-**33** shown in blue, ( $S_a$ )-E-**33** shown in red. Adapted with permission from [75]. Copyright 2018 American Chemical Society. 199
- Figure 186: UV-Vis absorption (left) and ECD spectrum (right) of **33** in 87 / 13 heptane / ethyl acetate recorded for one switching cycle starting from pure ( $R_a$ )-Z-**33** (solid red), which was photoisomerized to ( $R_a$ )-E-**33** (30 s, 435 nm, solid blue) and then switched back to ( $R_a$ )-Z-**33** (2 min, 505 nm, pale red, dashed) in high isomeric yields at 0 °C. The further increased free activation enthalpies  $\Delta G^\ddagger = 24.8$  kcal/mol for thermal atropisomerizations in the Z isomeric state and  $\Delta G^\ddagger = 27.6$  kcal/mol in the E isomeric state prevent any racemization also at ambient temperatures. Therefore, the initial ECD spectrum of the pure Z isomer is fully recovered after a complete photoswitching cycle (solid red and pale red dashed spectra). Adapted with permission from [75]. Copyright 2018 American Chemical Society. 199
- Figure 187: First order kinetic analyses of the thermal racemization via atropisomerization of hemiindigo **33** in 87 / 13 heptane/ethyl acetate in the dark. The slopes  $m$  can be translated into the rate constant  $k$  for each process. Racemization in the Z isomeric state (red) was measured at 40 °C and proceeds over an energy barrier of 24.8 kcal/mol. Racemization in the E isomeric state (blue) was measured at 90 °C and proceeds over an energy barrier of 27.6 kcal/mol. Adapted with permission from [75]. Copyright 2018 American Chemical Society. 200
- Figure 188: Repetitive photoswitching of the ECD spectrum of hemiindigo **33** (solid lines: ( $S_a$ ) configuration) and thermal decay of the ECD spectrum in the dark (broken lines: ( $R_a$ ) configuration) in 87 / 13heptane / ethyl acetate. Spectra of Z isomers are shown in red and of E isomers in blue (light blue after 160 cycles/120 min). The ( $S_a$ ) and ( $R_a$ ) configured samples were handled at 18 °C within an air-conditioned room. The ( $S_a$ )-**33** isomer was photoswitched 40 times between its two PSS' at 435 nm (7 s irradiation time at 260 mW per cycle to reach the PSS) and 505 nm (38 s irradiation time at 80 mW per cycle to reach the PSS) within 30 minutes. A spectrum was recorded after this time interval and this procedure was repeated for three times (red solid line spectra, total of 160 photoswitching cycles within 120 min). The ( $R_a$ )-Z-**33** isomer was kept in the dark at 18 °C and was also measured in 30 min intervals to show the thermal racemization of the chiral axis (red broken line spectra). ECD measurements were conducted at 0 °C and samples were kept at 22 °C during transfer of samples and waiting times in complete darkness. The slightly faster decline of the photoswitched sample (red solid line spectra) results from heat dissipation of the LEDs, which were measured to result in 1.23 °C higher sample temperature with respect to the surrounding 18 °C. A new fan equipped irradiation setup was built to cool LEDs and sample during irradiation and is depicted in Section 2.7.4. Adapted with permission from [75]. Copyright 2018 American Chemical Society. 202
- Figure 189: Repetitive photoswitching of the ECD spectrum of ( $S_a$ )-**33** (red, see Figure 190), thermal decay of ( $R_a$ )-Z-**33** (violet) extrapolated to 19.2 °C and photodegradation (green) in 87 / 13 heptane / ethyl acetate. Photoirradiation was performed at 19.2 °C (red for the Z state, blue for the E state). The ECD signal at 435 nm is used exemplarily because at this spectral position signal intensity for the PSS solution enriched in E isomer (83% E-**33** and 17% Z-**33** in the PSS at 435 nm) is close to zero. The thermal decay of the Z-**33** ECD signal was measured at 18 °C and extrapolated to the actual 19.2 degrees of the irradiation sample temperature (violet). The residual loss of ECD signal after correcting for thermal decay is attributed to irreversible photodegradation over 160 photoswitching cycles and amounts to 2% (green, derived from absorption loss during UV-Vis measurements). Adapted with permission from [75]. Copyright 2018 American Chemical Society. 203
- Figure 190: Fully reversible photoswitching of the ECD spectrum of ( $S_a$ )-**33** in 83 / 17 heptane / ethyl acetate (red for the Z state, blue for the E state) is observed after correction for thermal ECD decay of ( $S_a$ )-Z-**33**. No racemization of the chiral *N*-indoxyl-naphthyl axis by photoinduced double-bond isomerization

## 5.2 TABLE OF FIGURES

	is observed over 160 cycles excluding light induced coupled motions between the aniline fragment and the naphthyl residue. Photodegradation is plotted in green for comparison. Adapted with permission from [75]. Copyright 2018 American Chemical Society.	203
Figure 191:	Photoswitching of the <i>g</i> factors of hemiindigo <b>33</b> in 83 / 17 heptane / ethyl acetate (blue: <i>E</i> isomers, red: <i>Z</i> isomers, solid lines: ( <i>S<sub>a</sub></i> ) configuration, broken lines: ( <i>R<sub>a</sub></i> ) configuration). Adapted with permission from [75]. Copyright 2018 American Chemical Society.	204
Figure 192:	Calculated ground and transition state structures of hemiindigo <b>33</b> at the B3LYP/6-311+G(d,p) level of theory. Transition states for all atropisomerizations were found. The stilbene rotation transition states did not converge after several attempts and tweaks. The "+" sign in front of transition state values indicates the energy difference with respect to the lowest ground state of respective <i>Z</i> or <i>E</i> isomers.	205
Figure 193:	Benchmarking results for hemiindigo <b>33</b> using different DFT functionals for the 6-311+G(d,p) basis set. " <i>Z</i> " and " <i>E</i> " represent the ground states and " <i>Z</i> -Nph-DB" and " <i>E</i> -Nph-DB" the energetically lowest transition state for respective isomer and rotation pathway (see Figure 192). The "+" sign in front of transition state values indicates the energy difference with respect to the lowest ground state of respective <i>Z</i> or <i>E</i> isomers. The " <i>Z</i> -Nph-DB" transition state did not converge with the $\omega$ B97XD functional after several attempts and tweaks.	206
Figure 194:	Conformational analysis of hemiindigos <b>20</b> , <b>30</b> and <b>33</b> . a) - c) Molecular structures of ( <i>R<sub>a</sub></i> )- <i>Z</i> - and ( <i>R<sub>a</sub></i> )- <i>E</i> -isomers of <b>20</b> , <b>30</b> and <b>33</b> from left to right optimized at the DFT B3LYP/6-311+G(d,p) level of theory. d) Aliphatic region of the <sup>1</sup> H NMR spectrum (400 MHz, dichloromethane- <i>d</i> <sub>2</sub> , 27 °C) of <b>Z-20</b> (violet) and <b>E-20</b> (black). Indicative signals of the methyl groups are upfield shifted in <b>Z-20</b> compared to <b>E-20</b> . Signals of protons 24a and 24b are split and strongly separated for <b>Z-30</b> . In the corresponding <b>E-30</b> isomer the signal of protons 24 are broadened. e) Aliphatic region of the <sup>1</sup> H NMR spectrum of <b>Z-30</b> (red) and <b>E-30</b> (blue). Indicative signals of the methyl groups are upfield shifted in <b>Z-30</b> compared to <b>E-30</b> . f) Aliphatic region of the <sup>1</sup> H NMR spectrum of <b>Z-33</b> (green) and <b>E-33</b> (brown). Indicative signals of the methyl groups are upfield shifted in <b>Z-33</b> compared to <b>E-33</b> . Signals of protons 24a and 24b are split and strongly separated for <b>Z-33</b> . In the corresponding <b>E-33</b> isomer the corresponding signals are also already split at ambient temperature (see inset 600 MHz, dichloromethane- <i>d</i> <sub>2</sub> , 27 °C). The "*" symbol represents the water peak. Adapted with permission from [75]. Copyright 2018 American Chemical Society.	207
Figure 195:	All atropisomerization and <i>Z</i> / <i>E</i> isomerization barriers for hemiindigos <b>20</b> , <b>30</b> and <b>33</b> . Changes are indicated with +/- over the respective arrows. A clear tendency towards higher atropisomerization barriers from <b>20</b> over <b>30</b> to <b>33</b> can be seen. A slight drop the <i>Z</i> / <i>E</i> isomerization barrier can be seen for hemiindigo <b>30</b> compared to <b>20</b> and <b>33</b> . Adapted with permission from [75]. Copyright 2018 American Chemical Society.	209
Figure 196:	Overview of investigated compounds <b>62</b> , <b>63</b> , <b>64</b> and <b>65</b> regarding their UV-Vis spectra at different temperatures. Compound <b>63</b> was synthesized and characterized by L. Huber.[66] The <i>syn</i> - / <i>anti</i> -stereodescriptors are explained in detail within Section 2.4.5.	213
Figure 197:	Lewis-formula of <i>trans</i> -indigo <b>62</b> .	214
Figure 198:	UV-Vis spectra (left) and plot of absorption maximum (right) against temperature for the parent indigo <b>62</b> in chloroform. A thermochromic shift of about 20 nm can be seen. Also, a decline in absorption to about 60 °C can be observed with a subsequent sharp increase in absorbance starting at 78 °C probably caused by boiling chloroform. The initial absorbance is not lost upon cooling, but the higher values at the end can be explained by increasingly dissolved chromophore, as this compound tends to be very insoluble in most solvents.	214
Figure 199:	UV-Vis spectra (left) and plot of absorption maximum vs. temperature (right) for the parent indigo <b>62</b> in <i>N,N</i> -dimethylformamide. A thermochromic shift of about 10 nm can be seen. Also, a steady decline in absorption to 78 °C can be observed with a subsequent sharp drop in absorbance starting from 78 °C. The initial absorbance can be partially restored upon cooling, however, a permanent decline of 44% can be observed. This thermal degradation can also be observed for arylated derivatives for this solvent.	214
Figure 200:	DFT calculations at the B3LYP/6-311+G(d,p) level of theory for indigo <b>62</b> . UV-Vis spectra including oscillator energies (left) and ECD spectra (right) were calculated using TD-DFT, <i>n</i> states = 20 or * = 30 (the other enantiomer was calculated for 135°). The <i>trans</i> -form of indigo represents its global minimum, while dihedral torsion of the central double bond by 180° gives the <i>cis</i> -state. Incremental torsion in 15° - 45° steps yields two red-shifted maxima for a 45° and a 135° torsion angle.	215
Figure 201:	Lewis-formula of di- <i>para</i> -tolyl-indigo <b>63</b> .	216
Figure 202:	UV-Vis spectra (left) and plot of absorption maximum vs. temperature (right) for the di- <i>para</i> -tolyl substituted indigo <b>63</b> in chloroform. A thermochromic shift of about 30 nm can be seen. Also, a steady and linear decline in absorption to 80 °C can be observed. The initial absorbance can be completely restored upon cooling.	217
Figure 203:	UV-Vis spectra (left) and plot of absorption maximum vs. temperature (right) for the di- <i>para</i> -tolyl substituted indigo <b>63</b> in <i>N,N</i> -dimethylformamide. A thermochromic shift of about 20 nm can be seen. Also, a steady decline in absorption to 80 °C can be observed. The initial absorbance can be partially restored upon cooling, although the same kind of loss of absorbance can be seen with the parent indigo chromophore <b>62</b> in <i>N,N</i> -dimethylformamide.	217
Figure 204:	UV-Vis spectra (left) and plot of absorption maximum vs. temperature for the di- <i>para</i> -tolyl substituted indigo <b>63</b> in toluene. A thermochromic shift of about 20 nm can be seen. Also, a steady and linear decline in absorption to 80 °C can be observed.	218
Figure 205:	Lewis-formula of di- <i>ortho</i> -tolyl-indigo <b>64</b> .	219
Figure 206:	UV-Vis spectra (left) and plot of absorption maximum vs. temperature (right) for the di- <i>ortho</i> -tolyl substituted indigo <b>64</b> in chloroform. A thermochromic shift of about 20 nm can be seen. Also, a steady decline in absorption to 80 °C can be observed. The initial absorbance can be completely restored upon cooling.	219
Figure 207:	UV-Vis spectra (left) and plot of absorption maximum vs. temperature (right) for the di- <i>ortho</i> -tolyl substituted indigo <b>64</b> in chloroform. A thermochromic shift of about 10 nm can be seen. Also, a steady decline in absorption to 80 °C can be observed.	220
Figure 208:	UV-Vis spectra (left) and plot of absorption maximum vs. temperature (right) for the di- <i>ortho</i> -tolyl substituted indigo <b>64</b> in 83 / 17 heptane / ethyl acetate. A thermochromic shift of about 20 nm can be seen. Also, a steady and linear increase towards -80 °C and a decline in absorption to 80 °C can be observed.	220
Figure 209:	UV-Vis spectra (left) and plot of absorption maximum vs. temperature (right) for the di- <i>ortho</i> -tolyl substituted indigo <b>64</b> in 83 / 17 heptane / ethyl acetate at 1 / 5 of the concentration as shown in Figure 208. A thermochromic shift of about 20 nm can be seen. Also, a steady and linear decline in absorption to 80 °C can be observed. The initial absorbance can be completely restored upon cooling.	221
Figure 210:	Lewis-formula of di- <i>ortho</i> -tolyl-indigo <b>65</b> .	221
Figure 211:	UV-Vis spectra (left) and plot of absorption maximum vs. temperature (right) for the di- <i>ortho</i> -tolyl di-7-methyl-substituted indigo <b>65</b> in 83 / 17 heptane / ethyl acetate. A thermochromic shift of about 15 nm can be seen. Also, a steady and linear decline in absorption to 80 °C can be observed.	222
Figure 212:	Overview of 1 <sup>st</sup> ( <b>65</b> and <b>69</b> ), 2 <sup>nd</sup> ( <b>64</b> and <b>70</b> ) and 3 <sup>rd</sup> ( <b>71</b> , <b>72</b> and <b>73</b> ) generation of axially chiral di- <i>N</i> -substituted indigos.	223
Figure 213:	Overview of the three <i>trans</i> rotamers of indigo <b>65</b> . Formally, the same amount of rotamers is expected for the less stable <i>cis</i> form. Two-fold stereo descriptors like e.g. ( <i>S<sub>a</sub></i> )-( <i>S<sub>a</sub></i> )- <i>syn-trans</i> emphasize the <i>syn-trans</i> forms to be enantiomeric whereas the <i>anti</i> -forms are <i>meso</i> -forms.	224
Figure 214:	UV-Vis spectra of indigo <b>65</b> are shown exemplarily in dichloromethane. No change during longer irradiations (30 min) in dimethyl sulfoxide, acetonitrile, tetrahydrofuran or toluene could be observed.	225
Figure 215:	Chiral HPLC separation attempt on indigo <b>65</b> at 0 °C with 9 / 1 heptane / ethyl acetate as solvent. No rotamers or peak shoulders are visible. Very high solvent polarities (50 - 100% ethyl acetate) yielded one single sharp peak.	225
Figure 216:	Aliphatic section of the <sup>1</sup> H-NMR spectrum of <i>trans</i> - <b>65</b> (dichloromethane- <i>d</i> <sub>2</sub> , 600 MHz, 27 °C). The <i>syn</i> isomer is preferred by 10% over the <i>anti</i> -form. <i>Syn</i> - and <i>anti</i> -diastereomers show distinct shifts for indigo-core- (15) and rotatable <i>ortho</i> -tolyl methyl group protons (14). Assignments by 2D NMR spectroscopy are shown starting from Figure 219.	226
Figure 217:	Comparison of obtained minimum geometries of <i>syn</i> (left)- and <i>anti</i> (right)- <i>trans</i> indigo <b>65</b> at the B3LYP/6-311+G(d,p) level of theory, view along the central double bond.	227
Figure 218:	Calculated ground and transition state structures and energies of indigo <b>65</b> at the B3LYP/6-311+G(d,p) level of theory. Transition states for three of eight possible atropisomerizations could be found. The other possible transition state for the <i>cis</i> isomer did not converge after several attempts and tweaks. The "+" sign in front of transition state values indicates the energy difference with respect to the lower ground state of the respective <i>cis</i> or <i>trans</i> isomers. Missing experimental data for the <i>cis</i> isomer makes it difficult to assign the reported transition state to be high or low in energy or to address the preferred directionality for this rotation.	228
Figure 219:	Aliphatic section of the <sup>1</sup> H NOESY (dichloromethane- <i>d</i> <sub>2</sub> , 600 MHz, 27 °C) of <i>trans</i> - <b>65</b> . Expected cross peaks for <i>syn</i> / <i>anti</i> 14 / 15 can be observed. Signals of <i>anti</i> 14 and <i>syn</i> 14 show one of two positive NOE signals (see Figure 221), while the rest of the molecule shows negative NOEs if the diagonal signals are set to positive values according to convention. This strongly indicates fast dynamics in between <i>syn</i> - and <i>anti</i> molecules as NOESY utilizes the same pulse sequence as exchange spectroscopy (EXSY) and the used mixing time of 1.2 s is much longer than the exchange of respective nuclei, hinting towards an atropisomerization barrier between 17- and 20 kcal/mol.	229
Figure 220:	Aliphatic / aromatic <sup>1</sup> H NOESY spectrum (dichloromethane- <i>d</i> <sub>2</sub> , 600 MHz, 27 °C) of <i>trans</i> - <b>65</b> . <i>Syn</i> - and <i>anti</i> form can be distinguished by the NOE signal of <i>anti</i> 14 / 13 and the non-existent signal for <i>syn</i> 14 / 13. This indicates the proximity of methyl group <i>anti</i> 14 to the back of the other <i>ortho</i> -tolyl (proton <i>anti</i> 13) on the opposite side of the central double bond.	230
Figure 221:	Aromatic section of the <sup>1</sup> H NOESY spectrum (dichloromethane- <i>d</i> <sub>2</sub> , 600 MHz, 27 °C) of <i>trans</i> - <b>65</b> . No indicative signals to prove <i>syn</i> - or <i>anti</i> configuration can be found. Signals of <i>anti</i> 13 and <i>syn</i> 13 show one of two positive NOE signals (see Figure 219), while the rest of the molecule shows negative NOEs. This is in accordance to fast dynamics in between <i>syn</i> and <i>anti</i> molecules as NOESY uses the same pulse sequence as EXSY and the used mixing time of 1.2 s is much longer than the exchange of respective nuclei.	231
Figure 222:	Aromatic (left) and aliphatic (right) sections of <sup>1</sup> H-NMR spectra of <i>trans</i> - <b>65</b> from -80 °C (start) to 0 °C, starting after 60 min of <i>in situ</i> irradiation with 625nm at -80 °C (dichloromethane- <i>d</i> <sub>2</sub> , 400 MHz). The diagnostic signals 13 / 14 disappear completely at about -60 °C due to signal broadening, making low temperature analysis of the (photo) kinetics of this compound inaccurate or impossible.	232
Figure 223:	Aromatic (left) and aliphatic (right) sections of <sup>1</sup> H-NMR spectra of <i>trans</i> - <b>65</b> with <i>in situ</i> irradiation at 625 nm (dichloromethane- <i>d</i> <sub>2</sub> , 600 MHz, -80 °C). Spectra were recorded in 1 minute intervals. A fast but small increase of one or multiple accumulated <i>cis</i> isomers can be observed. Apolar solvents increase the thermal stability of <i>cis</i> isomers for indigo <b>64</b> (see Section 2.4.13), which should be tried with this compound despite its overall low solubility.	232
Figure 224:	Photo- and thermally induced <i>cis-trans</i> isomerization of indigo <b>64</b> .	233
Figure 225:	UV-Vis spectra of <i>N,N</i> -di( <i>o</i> -tolyl)indigo <b>64</b> in THF, irradiation yields 20 - 30% of <i>cis</i> isomer (estimated by low temperature NMR and UV-Vis spectroscopy in aprotic, apolar solvents, (see Section 2.4.13) which quickly returns to its <i>trans</i> state within a few minutes.	233



- Figure 226: Immediate tracking of the thermal *cis* to *trans* isomerization of indigo **64** after 625 nm irradiation in THF at 24 °C. An estimated thermal *cis* to *trans* barrier between 20- and 21 kcal/mol can be regarded as reasonable from the data displayed in this measurement course. Precise evaluation and determination of isomerization barriers via <sup>1</sup>H-NMR spectroscopy can be found in Section 2.4.19. 234
- Figure 227: Aliphatic / aromatic section of the <sup>1</sup>H- / <sup>13</sup>C-HMBC NMR spectrum of *trans*-**64** (dichloromethane-*d*<sub>2</sub>, 600 MHz, 27 °C). Integrals for *anti*- and *syn* isomer are shown at the top, <sup>3</sup>J proton couplings to carbon atoms are displayed for *anti*- and *syn* isomers. A comparable chemical shift of the methyl groups can be seen for indigo **64** as observed with indigo **65**. The ratio between *anti*- / *syn* isomer (1 / 5) is strongly shifted favoring the *syn* diastereomer for indigo **64** compared to *anti*- / *syn* isomer (1.0 / 1.2) for indigo **65**. 235
- Figure 228: Aliphatic / aromatic section of the <sup>1</sup>H-NOESY NMR spectrum of *trans*-**64** (dichloromethane-*d*<sub>2</sub>, 600 MHz, 27 °C). No signals for unambiguous determination of *anti*- / *syn* conformations can be seen. Assignment was done according to separated peaks by HPLC and subsequent ECD and NMR analyses. The aromatic region (not shown) does not yield indicative signals as well. Repetition of this experiment with an 800 MHz NMR device did not yield any new indicative signals. Positive signals between *syn*- and *anti*-*trans* isomers were not observed, as the atropisomerization barrier of 23.6 kcal/mol is too high in energy to show a proton exchange for a mixing time of 1.2 s. 236
- Figure 229: Overview of the three *trans* rotamers of indigo **64**. Formally, the same number of rotamers is expected in the less stable *cis* form. 237
- Figure 230: Separation of *trans*-**64** rotamers via chiral HPLC with 83 / 17 heptane / ethyl acetate as eluent at 0 °C displayed three peaks with the corresponding relative intensity in square brackets: (S<sub>a</sub>)-(S<sub>a</sub>)-*syn-trans* [2.5], (R<sub>a</sub>)-(R<sub>a</sub>)-*syn-trans* [2.5] and the (S<sub>a</sub>)-(R<sub>a</sub>)-*anti-trans* [1] (*meso* form) in this order. Thermal racemization of the pure (R<sub>a</sub>)-(R<sub>a</sub>)-*syn-trans* fraction at 25 °C over 70 min yielded (S<sub>a</sub>)-(S<sub>a</sub>)-*syn-trans* and (S<sub>a</sub>)-(R<sub>a</sub>)-*anti-trans* in small and equal quantities. Photoswitching to the *cis* state and back to the *trans* isomer gave all three fractions again, hinting towards a lower thermal atropisomerization barrier in the *cis* state or an underlying photoreaction. 237
- Figure 231: Injection of indigo **63** by *L. Huber* onto a chiral HPLC column at 0 °C with 83 / 17 heptane / ethyl acetate as eluent. No clearly identifiable *cis* isomer can be observed. The retention times of the *syn* isomers of indigo **64** amount to 2.5 min and 5.0 min for applied conditions, indigo **63** elutes at 6.5 min. 238
- Figure 232: Scaled UV-Vis and corresponding ECD spectra of all peaks obtained from chiral HPLC separation ((S<sub>a</sub>)-(S<sub>a</sub>)-*syn-trans* (ExE1) (R<sub>a</sub>)-(R<sub>a</sub>)-*syn-trans* (ExE2) and (S<sub>a</sub>)-(R<sub>a</sub>)-*anti-trans*-1 (ExE3)) of *N,N*-di(*o*-tolyl)indigo **64** in 83 / 17 heptane / ethyl acetate at 0 °C. Both *syn* isomers (solid blue and broken red spectrum) show strong ECD responses while the *anti* (*meso*, solid green spectrum) form shows no ECD signal at all. 239
- Figure 233: NMR Spectra for all three HPLC separable peaks ((S<sub>a</sub>)-(S<sub>a</sub>)-*syn-trans* (Peak 1) (R<sub>a</sub>)-(R<sub>a</sub>)-*syn-trans* (Peak 2) and (S<sub>a</sub>)-(R<sub>a</sub>)-*anti-trans*-1 (Peak 3)) of *N,N*-di(*o*-tolyl)indigo **64** (dichloromethane-*d*<sub>2</sub>, 400 MHz, 27 °C). 239
- Figure 234: Linearization of the first order kinetics for the atropisomerization of *N,N*-di(*o*-tolyl)indigo **64** at 40 °C in 83 / 17 heptane / ethyl acetate. A barrier of 23.6 kcal/mol and a half-life of 6.23 h at 25 °C could be determined. Used formulas and equations can be found in Section 2.2.19. 240
- Figure 235: a) ECD spectra for different temperatures, irradiation- and thermal annealing steps of enantiopure *syn-trans* isomer of indigo **64**. The sample was irradiated *in situ* at -80 °C with 625 nm LED light for 8 minutes to an estimated PSS consisting of 70-80% of *cis* isomer b) Kinetic ECD measurement for the thermal isomerization from the *anti-cis*- to the *syn-trans* isomer at 0 °C in the dark, c) Corresponding UV-Vis spectra for b) at 0 °C (starting point dashed red spectrum, end point after 22 min. dashed blue spectrum). All spectra were recorded from the same sample in an 83 / 17 heptane / ethyl acetate solvent mixture. 241
- Figure 236: All possible diastereomers (inside box) and respective enantiomers for indigo **64** calculated at the B3LYP/6-311+G(d,p) level of theory. Energies are given corresponding to the lowest ground state energy of the *syn-trans*-1 isomers. 243
- Figure 237: Measured, 100% enantiopure *trans* isomer (solid blue line) and calculated *trans* isomer ECD spectra of indigo **64** at the B3LYP/6-311+G(d,p) level of theory, the measured spectrum was scaled in intensity to the calculated values. The spectrum shown in the broken blue line represent the best fitting calculated spectrum. Signal intensities at and below 250 nm are not reliable experimentally as solvent absorptions (83 / 17 heptane / ethyl acetate) are obscuring the measurements. 244
- Figure 238: Measured, 70-80% *cis* isomer, estimated (solid red line) and calculated *cis* isomer ECD spectra of indigo **64** at the B3LYP/6-311+G(d,p) level of theory, measured spectra were scaled in intensity to the calculated values. The spectrum shown in the broken red line represents the best fitting calculated spectrum. Signal intensities at and below 250 nm are not reliable experimentally as solvent absorptions (83 / 17 heptane / ethyl acetate) are obscuring the measurements. 245
- Figure 239: Comparison of measured (solid blue (100% enantiopure *trans* isomer) and red (70-80% *cis* isomer, estimated) lines) and best fitting calculated ECD spectra (broken blue- and red lines) of indigo **64** at the B3LYP/6-311+G(d,p) level of theory, measured spectra were scaled in intensity to the calculated values. Signal intensities at and below 250 nm are not reliable experimentally as solvent absorptions (83 / 17 heptane / ethyl acetate) are obscuring the measurements. 246
- Figure 240: *Lewis*-formula of indigo **70**. 247
- Figure 241: Scaled UV-Vis (left) and ECD (right) spectra of (R<sub>a</sub>)-*N*-(*o*-tolyl)-*N'*-(*p*-tolyl)indigo **70** in 83 / 17 heptane / ethyl acetate at 0 °C (green), after 5 min of irradiation with 617 nm (red). (S<sub>a</sub>)-(S<sub>a</sub>)-*Syn-trans*-1 (E1) and (R<sub>a</sub>)-(R<sub>a</sub>)-*syn-trans*-1 (E2) of *N,N*-di(*o*-tolyl)indigo **64** (broken blue and light blue lines) are added for comparison. Irradiation of **70** gives slightly better *cis* isomer yields compared to **64**. 248
- Figure 242: Spectra subtraction of the ECD response of (R<sub>a</sub>)-**70** from (R<sub>a</sub>)-(R<sub>a</sub>)-*syn-trans*-**64**. The influence of the additional *ortho*-tolyl moiety of **64** can be observed in the range from 240 nm to 400 nm. 249
- Figure 243: Linearized first order kinetics of the racemization of **70** (E1) in 83 / 17 heptane / ethyl acetate solution at 40 °C. The free activation enthalpy of thermal atropisomerization ΔG<sup>‡</sup> was determined to be 23.1 kcal/mol with a thermal half-life of 2.7 h at 25 °C. Used formulas and equations can be found in Section 2.2.19. 250
- Figure 244: *Lewis*-formula of indigo **69**. 251
- Figure 245: Chiral HPLC separation of the (S<sub>a</sub>)-*trans*-**69** and (R<sub>a</sub>)-*trans*-**69** indigo rotamers at 0 °C with 50 / 50 heptane / ethyl acetate as eluents. The two expected rotamers can be seen. The streaks between the two peaks indicate an active atropisomerization reaction taking place, interconverting one rotamer to the other while on the chiral column. The immediate stop of this "streaking" after the complete elution of the (R<sub>a</sub>)-*trans*-**69** underlines these findings. The polarity of the eluent mixture was significantly increased compared to the separation of **70** to yield an acceptable difference in retention times. 252
- Figure 246: Scaled UV-Vis (left) and ECD (right) spectra of 7-methyl-*N*-(*o*-tolyl)-*N'*-(*p*-tolyl)indigo **69** in 83 / 17 heptane / ethyl acetate at 0 °C (fraction 1, blue and fraction 2 broken light blue) and after 5 min of 617 nm irradiation (red). 253
- Figure 247: Linearized first order kinetics of the thermal atropisomerization of (R<sub>a</sub>)-*trans*-**69** in 50 / 50 heptane / ethyl acetate at 0 °C. The free activation enthalpy ΔG<sup>‡</sup> for this process was determined to be 20.4 kcal/mol resulting half-lives of 1.73 min at 25 °C and 44.4 min at 0 °C. Used formulas and equations can be found in Section 2.2.19. 253
- Figure 248: a) Rota- and diastereomers of *trans*-**64**, b) photoinduced rota- and diastereomers of *cis*-isomers by irradiation with red light. A rotation around the central double bond within the indigo core plane for the *meso* form (S<sub>a</sub>)-(R<sub>a</sub>)-*anti-trans*-**64** gives (R<sub>a</sub>)-(S<sub>a</sub>)-*anti-trans*-**64**, proving both projections to be the same molecule. The *meso* form of the *cis*-isomer supports a mirror plane between both *ortho*-arylated indoxyls, proving both projections to be the same molecule. The *trans* to *cis* isomerizations (and *vice versa*) to the respective products can be followed by the indicated vertical (de-) excitations. 256
- Figure 249: Irradiation of a 5 / 1 *syn*- / *anti* mixture of indigo **64** yields mainly the *anti-cis*-2 isomer in dichloromethane-*d*<sub>2</sub> followed by <sup>1</sup>H-NMR spectroscopy at -50 °C. 52% of *anti-cis*-2 isomer could be obtained in the PSS at 625 nm irradiation. Subsequent measurements of the decaying *cis* isomers in the dark gave a free activation enthalpy ΔG<sup>‡</sup> = 15.8 kcal/mol. The decreasing *anti-cis*-2 isomer was fully converted back to the rising *syn-trans*-1 isomer. No second signal for the *anti-cis*-1 form at 1.9 ppm can be observed (see Figure 261). The signal at 1.72 ppm (red rectangle) of the thermally stable *syn-cis* isomer population - generated from the minor *anti-trans* isomer - is also not visible due to signal broadening and subsequent shifting towards 1.45 ppm (see Figure 258 and Figure 222 for indigo **65**). 258
- Figure 250: Aromatic part of the irradiation of a 5 / 1 *syn*- / *anti* mixture of indigo **64** to the *anti-cis*-2 (violet) and *syn-cis* (green) isomers in dichloromethane-*d*<sub>2</sub> followed by <sup>1</sup>H-NMR spectroscopy at -50 °C. Subsequent measurements of the decaying *anti-cis*-2 isomer in the dark gave a free activation enthalpy ΔG<sup>‡</sup> = 15.8 kcal/mol. The decreasing *anti-cis*-2 isomer was not converted to the stable *syn-cis* isomer, only the *syn-trans*-1 isomer population was restored during the decay of the *anti-cis*-2 isomer. The integrals of the *anti-cis*-2 signals are underrepresented, especially in the aromatic region, as the total amount of *cis*-isomers reported at the signal located at 7.78 ppm exceeds the combined integral value located at 6.38 ppm. 259
- Figure 251: Irradiation of a 5 / 1 *syn*- / *anti* mixture of indigo **64** to the *syn-cis* isomer (green) in dichloromethane-*d*<sub>2</sub> followed by <sup>1</sup>H-NMR spectroscopy at 11 °C. 20% of *syn-cis* isomer could be obtained at this temperature in the PSS (77% at -80 °C, Figure 253), which can be explained by the low thermal stability of the *anti-cis*-2 isomer, which represents the mayor photoproduct. However, minor amounts of *anti-trans* isomer are responsible for the photogeneration of the *syn-trans*-1 isomer population. Subsequent measurements of the decaying *cis* isomers in the dark gave a free activation enthalpy ΔG<sup>‡</sup> = 20.7 kcal/mol for this thermal reaction. The decreasing *syn-cis* isomer is thermally converted at a slow rate to the rising *anti-trans* isomer at this temperature. The violet rectangle at 1.45 ppm indicates the absence of the *anti-cis*-2 isomer at 11 °C, which is to be expected because of its low thermal stability. 260
- Figure 252: Selected <sup>1</sup>H-NMR spectra recorded during the irradiation of a 5.0 / 1.0 *syn*- / *anti-trans* mixture of indigo **64** populating the *anti-cis*-2 and *syn-cis* isomers (dichloromethane-*d*<sub>2</sub> at -50 °C). The Spectra were taken from the irradiation and thermal annealing experiments shown in Figure 249 and Figure 250. A PSS consisting of 56% *cis* isomers (compared to all *trans* isomers) can be obtained at -50 °C. Relative normalized (to the *syn-anti* isomer methyl group signals) integrals for indicated signal areas are given below the respective peak. The integrals of the *anti-cis*-2 signals are underrepresented, especially in the aromatic region, as the total amount of *cis*-isomers reported at the signal located at 7.78 ppm exceeds the combined integral value located at 6.38 ppm. 262
- Figure 253: <sup>1</sup>H-NMR spectra recorded during 625 nm irradiation of a 5.0 / 1.0 *syn*- / *anti-trans* mixture of indigo **64** to the *anti-cis*- and *syn-cis* isomers in dichloromethane-*d*<sub>2</sub> at -80 °C and stepwise annealing at higher temperatures. A PSS containing 77% *cis* isomers (relative to all *trans* isomers) can be obtained at -80 °C. Integrals for indicated signal areas are given below the respective peak. Thermal decay in the dark is clearly seen at around -40 °C. The integrals of the *anti-cis*-2 signals are underrepresented, especially in the aromatic region, as the total amount of *cis*-isomers reported at the signal located at 7.78 ppm exceeds the combined integral value located at 6.38 ppm. 263
- Figure 254: Temperature dependence of the *syn-cis* isomer *ortho*-methyl signal of indigo **64** in the range of 11 °C to -50 °C. Irradiation at 11 °C yielded the previously observed *syn-cis* isomer with the methyl-group signal residing at 1.69 ppm, cooling to -10 °C showed a slight upfield shift and signal

## 5.2 TABLE OF FIGURES

	broodening. Cooling to -30 °C strongly shifts the <i>syn-cis</i> methyl group signal under the also shifted water peak, while cooling to -50 °C gives another separate signal. Irradiation at -50 °C increases the broad signal of the methyl group of the <i>anti-cis-2</i> isomer at 1.43 ppm.	264
Figure 255:	Irradiation of a 5.0 / 1.0 <i>syn- / anti</i> mixture of indigo <b>64</b> with 625 nm LED light to the <i>anti-cis-2</i> and <i>syn-cis</i> isomers in toluene- <i>d</i> <sub>6</sub> at -60 °C. Spectra were recorded in one minute intervals. Generation of <i>cis</i> isomers can be observed, the <i>syn-cis</i> species is expected to show broad signals for its methyl protons at low temperatures (see Figure 254), which leaves the <i>anti-cis-2</i> isomer as the only visible new species in the aliphatic part of each spectrum. Discerning of <i>syn-</i> and <i>anti-cis-2</i> isomers is impossible at -60 °C in this solvent as signal overlap and / or -broodening at in the aromatic part of the spectrum causes inseparable signals.	266
Figure 256:	<sup>1</sup> H-NMR spectra of the irradiation of a 5.0 / 1.0 <i>syn / anti</i> mixture of indigo <b>64</b> to the <i>anti-cis-2</i> and <i>syn-cis</i> isomers in toluene- <i>d</i> <sub>6</sub> at -60 °C and subsequent behavior in the dark at various temperatures. A PSS consisting of 79% <i>cis</i> isomers (relative to all <i>trans</i> isomers) can be obtained during irradiation at -60 °C. Integrals for indicated signal areas are given below the respective peak. The integrals of the <i>anti-cis-2</i> signals are underrepresented, especially in the aromatic region, as the total amount of <i>cis</i> -isomers reported at the signal located at 7.78 ppm exceeds the combined integral values located at 6.34 ppm.	267
Figure 257:	Aromatic part of the <sup>1</sup> H NMR spectra recorded during 625 nm irradiation of a 1.0 / 6.5 <i>syn / anti</i> mixture of indigo <b>64</b> to yield <i>syn-cis</i> , <i>anti-cis-1</i> and <i>syn-trans-2</i> signals in dichloromethane- <i>d</i> <sub>2</sub> at -60 °C. Coincident generation of <i>syn-</i> , <i>anti-cis-1</i> and <i>syn-trans-2</i> signals can be observed. The rate of the photoreactions can be seen to be faster for the <i>syn-cis</i> isomer and slower for the <i>anti-cis</i> isomer as the <i>syn-trans-1</i> isomer represents as minor species for the photoreaction and generates <i>anti-cis-1- / syn-trans-2</i> signals in lower quantities, respectively. The previously generated <i>anti-cis-2</i> isomer is not observed (Figure 250).	268
Figure 258:	Comparison of three <i>in situ</i> irradiation experiments of indigo <b>64</b> with 625 nm LED light at low temperatures in dichloromethane- <i>d</i> <sub>2</sub> . The spectra were taken at a 1 minute time interval. The relative integrals for start and end of each photoreaction course are given in orange. The plots on the left and middle start with a 1.0 / 0.2 <i>syn- / anti-trans</i> mixture, the plot on the right with a 0.2 / 1.0 <i>syn- / anti-trans</i> mixture. The rise of novel signals at 1.89 ppm ( <i>anti-cis-1</i> ) and 1.38 ppm ( <i>syn-trans-2</i> ) with comparable estimated photokinetics as the signal at 1.46 ppm ( <i>anti-cis-2</i> generated from the <i>syn-trans-1</i> isomer) can be observed. The <i>syn-cis</i> isomer is the major photoproduct originating from the <i>anti-trans</i> isomer but shows broad aliphatic signals at these temperatures and can only be observed in the aromatic region or at temperatures above -20 °C, see Figure 253 and Figure 254.	269
Figure 259:	Comparison of <sup>1</sup> H-NMR spectra obtained after irradiation of a 5.0 / 1.0 <i>syn- / trans-</i> (top) and a 1.0 / 6.5 <i>syn- / anti-trans</i> isomer (bottom) of indigo <b>64</b> at -60 °C in dichloromethane- <i>d</i> <sub>2</sub> . If the <i>syn-trans-1</i> isomer is the major initial species, single signals at 6.34 and 1.43 ppm can be observed for the <i>anti-cis-2</i> isomer. When the <i>anti-trans</i> isomer represents the major initial species, two emerging signal sets at 6.85 ppm, 5.95 ppm and 1.89 ppm, 1.38 ppm can be observed after irradiation for the <i>anti-cis-1 / syn-trans-2</i> isomers, which could be populated by a photoinduced extended Hula-Twist motion as the <i>anti-cis-1</i> isomer cannot be generated by solely double bond isomerizations from the <i>anti-trans</i> isomer, which is also true for <i>syn-trans-2</i> . The <i>syn-trans-1</i> isomer is too low in quantity to yield the significant amounts of (underrepresented) <i>anti-cis-2</i> isomer in the second experiment (bottom).	270
Figure 260:	Both hypothetical edge-to-face conformations of indigo <b>64</b> that are experimentally stable solely at -60 °C. DFT optimizations at the M05-2x/6-31+G(d) level of theory did not yield local minimum structures.	271
Figure 261:	<sup>1</sup> H-NMR spectra obtained after the irradiation of a 1.0 / 6.5 <i>syn / anti</i> isomer mixture of indigo <b>64</b> to the <i>anti-cis</i> and <i>syn-cis</i> isomers in dichloromethane- <i>d</i> <sub>2</sub> at -60 °C and subsequent behavior in the dark at various temperatures. Integrals for indicated signal areas are given below the respective peak. A PSS consisting of 87% <i>cis</i> isomers can be obtained (relative to all <i>trans</i> isomers).	272
Figure 262:	Aliphatic part after the irradiation of a 1.0 / 11.1 <i>syn- / anti</i> mixture of indigo <b>64</b> to the <i>anti-cis-</i> and <i>syn-cis</i> isomers in toluene- <i>d</i> <sub>6</sub> at -60 °C with 625 nm LED light. Two peaks can be observed, which is similar to the experiments in dichloromethane (see Figure 261). The detailed explanation of this behavior is given in Section 2.4.16, as two helicities are assumed to exist for <i>anti-cis-</i> and <i>syn-trans-</i> isomers.	274
Figure 263:	<sup>1</sup> H-NMR spectra obtained after the irradiation of a 1.0 / 11.1 <i>syn- / anti</i> mixture of indigo <b>64</b> to the <i>anti-cis-</i> and <i>syn-cis</i> isomers in toluene- <i>d</i> <sub>6</sub> at -60 °C and subsequent behavior in the dark at various temperatures. A PSS consisting of 69% <i>cis</i> isomers (relative to <i>syn-trans-1</i> and <i>anti-trans</i> isomers) can be obtained at -60 °C. Integrals for indicated signal areas are given below the respective peak.	275
Figure 264:	<sup>1</sup> H-NMR spectra (aromatic part) of the irradiation and subsequent behavior in the dark of a 5 / 1 <i>syn- / anti-trans</i> isomer mixture of indigo <b>64</b> in toluene- <i>d</i> <sub>6</sub> at -5 °C measured on a 400 MHz spectrometer. Each spectrum was measured with a 1 minute time interval. A PSS consisting of 73% <i>cis</i> isomers could be obtained. Subsequent measurements of the differently decaying <i>cis</i> isomers in the dark gave free activation enthalpies $\Delta G^\ddagger = 18.5$ kcal/mol with a half-life of 4.15 s at 25 °C for the <i>anti-cis-2-</i> and $\Delta G^\ddagger = 19.4$ kcal/mol with a half-life of 19.0 s at 25 °C for the <i>syn-cis</i> isomer. The decreasing <i>cis</i> isomer signals were assigned to the increasing <i>trans</i> isomer signals after the LED was turned off. Accumulation of the <i>anti-trans-</i> compared to the <i>syn-trans-1</i> isomer can be observed at 6.44 ppm.	277
Figure 265:	<sup>1</sup> H-NMR spectra (aliphatic part) of the irradiation and subsequent behavior in the dark of a 5 / 1 <i>syn- / anti-trans</i> isomer mixture of indigo <b>64</b> in toluene- <i>d</i> <sub>6</sub> at -5 °C measured on a 400 MHz spectrometer. Each spectrum was measured with a 1 minute time interval. A PSS consisting of 73% <i>cis</i> isomers could be obtained. Subsequent measurements of the differently decaying <i>cis</i> isomers in the dark gave free activation enthalpies $\Delta G^\ddagger = 18.5$ kcal/mol with a half-life of 4.15 s at 25 °C for the <i>anti-cis-2</i> and $\Delta G^\ddagger = 19.4$ kcal/mol with a half-life of 19.0 s at 25 °C for the <i>syn-cis</i> isomer. The decreasing <i>cis</i> isomer signals were assigned to the increasing <i>trans</i> isomer signals after the LED was turned off. Accumulation of <i>anti-trans</i> isomer can be observed at 2.28 ppm.	278
Figure 266:	Linearized first order kinetic plots of <i>anti-cis-</i> (violet) and <i>syn-cis-64</i> (green) in toluene- <i>d</i> <sub>6</sub> at 0 °C derived from Figure 265 above. The thermal <i>cis</i> to <i>trans</i> isomerization barriers were determined at 18.5 kcal/mol with a half-life of 4.15 s at 25 °C for the <i>anti-cis-</i> and 19.4 kcal/mol with a half-life of 19.0 s at 25 °C for the <i>syn-cis</i> isomer. Used formulas and equations are given in Section 2.2.20.	279
Figure 267:	<sup>1</sup> H-NMR spectra obtained after the irradiation of a 5.0 / 1.0 <i>syn- / anti</i> mixture of indigo <b>64</b> to the <i>anti-cis</i> and <i>syn-cis</i> isomers in toluene- <i>d</i> <sub>6</sub> at -5 °C and subsequent behavior in the dark. A PSS consisting of 73% <i>cis</i> isomers can be obtained at -5 °C, which is comparable to the observed PSS consisting of 77% <i>cis</i> isomers in dichloromethane- <i>d</i> <sub>2</sub> at -80 °C. Integrals for indicated signal areas are given below the respective peak.	280
Figure 268:	Plots of the respective percentages of all four isomers from <sup>1</sup> H-NMR measurements with <i>in situ</i> irradiation and subsequent thermal annealing conditions of indigo <b>64</b> in toluene- <i>d</i> <sub>6</sub> recorded on a 400 MHz NMR spectrometer at -5 °C. Raw data (left) and smoothed data (right, Savitzky-Golay-Filter, 20 points of window) is shown for easier visibility of the reaction rates, the immediate stopping of the photokinetics in the dark can be better demonstrated with the raw data.	281
Figure 269:	Calculated ground and transition state structures and energies of indigo <b>64</b> at the B3LYP/6-311+G(d,p) level of theory. Transition states for seven out of eight possible atropisomerizations could be found. The other possible transition state for the <i>cis</i> isomer did not converge after several attempts and tweaks. The "+" sign in front of transition state values indicates the energy difference with respect to the lowest ground state of respective <i>cis</i> or <i>trans</i> isomers. Missing experimental data for the <i>cis</i> isomer makes it difficult to assign the reported transition state to be high or low in energy or to address the preferred directionality for this rotation.	284
Figure 270:	Benchmarking results for ground and transition states of indigo <b>64</b> using different DFT functionals for the 6-311+G(d,p) basis set. The "+" sign in front of transition state values indicates the energy difference with respect to the lowest ground state of respective <i>cis</i> or <i>trans</i> isomers. Missing transition states did not converge after several attempts and tweaks. "E" represents the <i>trans-</i> and "Z" the <i>cis</i> isomeric state. "E-Syn-1" represents the lowest ground state for all functionals in the <i>trans</i> state while "Z-Syn" constitutes the lowest energy <i>cis</i> state in most cases. "E-anti-Me-DB" shows the lowest transition state energy in all cases and suggests a rotation of an <i>ortho</i> -methyl group over the central double bond in the <i>trans</i> state. "Z-Anti-Me-H" shows the energetically lowest transition state for the <i>cis</i> isomers and suggests that the <i>ortho</i> -methyl group is rotated over its adjacent indoxyl core proton.	285
Figure 271:	Benchmarking results for ground states of indigo <b>64</b> using different DFT functionals and basis sets. "E" represents the <i>trans-</i> and "Z" the <i>cis</i> isomeric state. "E-Syn-1" represents the lowest ground state for all functionals in the <i>trans</i> state while "Z-Syn" constitutes the lowest energy <i>cis</i> state in most cases. The "no+" indicator represents the 6-311G(d,p) <i>Popple</i> basis set, the "no1" indicator the 6-31+G(d,p) basis set and the "no1+" indicator the 6-31G(d,p) basis set. Functionals with dispersive corrections ( $\omega$ B97XD, B3LYP-GD3BJ, indicated as "Dispersion", "Disp") and PCM solvent modelling ("B3LYP-Disp-Solv", dichloromethane) show lower differences between the <i>trans</i> and <i>cis</i> isomer ground states.	286
Figure 272:	<sup>1</sup> H-NMR spectra of a 3 / 2 <i>syn- / anti-trans</i> isomer mixture of <b>64</b> in dichloromethane- <i>d</i> <sub>2</sub> (24 °C) with overlaid calculated <sup>1</sup> H-NMR shifts (colored lines) at the B3LYP/6-311+G(d,p) level of theory using the gauge-including atomic orbital (GIAO) method (TMS B3LYP/6-311+G(2d,p), GIAO as reference for zero). The reported shifts agree well with the experimentally obtained signals and the previous assignment of <i>trans</i> isomers. The signals corresponding to the yellow line should not be observable as the <i>syn-trans-2</i> isomer is supposedly not stable at 24 °C. The yellow and violet lines within the aromatic part are almost overlapping.	287
Figure 273:	Benchmarking of <sup>1</sup> H-NMR shifts at the B3LYP/6-311+G(d,p) level of theory using the gauge-including atomic orbital (GIAO) method (TMS B3LYP/6-311+G(2d,p), GIAO as reference for zero) and comparison to measured $\sigma$ -values (framed in black). The shifts for <i>syn-trans-2</i> could not be measured as this species is not stable at ambient temperatures and was not observed at low temperatures as thermal- or photoproduct in dichloromethane or toluene. Overall, a good agreement for polarizable continuum model (PCM) solvent corrections (dichloromethane, toluene) was obtained.	288
Figure 274:	<sup>1</sup> H-NMR spectra of an irradiated 5 / 1 <i>syn- / anti-trans</i> isomer mixture (top) and an irradiated 1 / 6.5 <i>syn- / anti-trans</i> isomer mixture (bottom) of <b>64</b> in dichloromethane- <i>d</i> <sub>2</sub> (-60 °C) with overlaid calculated <sup>1</sup> H-NMR shifts (colored lines) at the B3LYP/6-311+G(d,p) level of theory using the gauge-including atomic orbital (GIAO) method (TMS B3LYP/6-311+G(2d,p), GIAO as reference for zero). The reported shifts agree well with the experimentally obtained signals and the previous assignment of both <i>cis</i> isomers in the aliphatic region. The signals in the aromatic regions agree qualitatively to the calculation with a matching order of observed and calculated shifts. The aliphatic signal for the <i>syn-cis</i> isomer can only be observed at temperatures above -20 °C (Figure 263, toluene and Figure 251, dichloromethane) at 1.69 ppm due to signal broadening and is indicated below the spectrum. The signals of <i>anti-cis-1</i> can only be observed in toluene (from -20 °C to 0°C, Figure 263) and are indicated below the spectrum. The <i>syn-trans-2</i> signal disappears at -50 °C.	289
Figure 275:	Benchmarking of <sup>1</sup> H-NMR shifts of indigo <b>64</b> at the B3LYP/6-311+G(d,p) level of theory using the gauge-including atomic orbital (GIAO) method (TMS B3LYP/6-311+G(2d,p), GIAO as reference for zero) and comparison to measured $\sigma$ -values (framed in black). The additional signals of <i>anti-cis-1</i> aromatic (green, red, not framed) for and aliphatic regions is also displayed. Overall, a good agreement for polarizable continuum model (PCM) solvent corrections (dichloromethane, toluene) was obtained.	290
Figure 276:	Irradiation of a thermally equilibrated 1.0 / 0.2 <i>syn- / anti</i> mixture of indigo <b>64</b> with 625 nm red light at 27 °C in dichloromethane- <i>d</i> <sub>2</sub> . A shift in population towards the <i>anti-trans</i> form can be observed, as a PSS consisting of a 1.0 / 0.7 <i>syn- / anti</i> ratio is obtained.	292

- Figure 277: Irradiation of indigo **64** with 625 nm LED light in toluene- $d_6$  at 25 °C. An increase in *anti-trans* isomer population with slightly better photoinduced yields of the *anti-trans* isomer compared to dichloromethane solutions can be observed. 293
- Figure 278: Overview of the aliphatic region of the  $^1\text{H-NMR}$  experiments on *syn-trans*-1 (1<sup>st</sup> and 2<sup>nd</sup> HPLC fraction) and *anti-trans* isomers (3<sup>rd</sup> HPLC fraction) at 27 °C in dichloromethane- $d_2$ . A clear rise in population of the *anti-trans* isomer at 2.31 ppm after 16 min of 625 nm irradiation can be observed. 9 minutes at ambient temperatures in the dark did not change the signal ratio, suggesting the absence of *cis* isomers. Irradiation of majorly *anti-trans* isomer with 625 nm light reaches the previously observed PSS at a higher rate than the previously determined thermal reaction alone, suggesting the photoinduced extended Hula-Twist reaction as the major trajectory (see Figure 261) at 25 °C. Thermal annealing over 1 day at ambient temperatures restores the 5 / 1 *syn* / *anti-trans* isomer thermodynamic equilibrium. Prolonged irradiation with 625 nm light, again, yields the previously observed PSS. 293
- Figure 279: Proposed reaction pathway by irradiation of indigo **64** at 25 °C in dichloromethane  $d_2$  enriching the *anti-trans*-**64**- starting from majorly *syn-trans*-**64** isomer out of the thermodynamic equilibrium. Optimized ground- and transition states calculated at the B3LYP/6-311+G(d,p) level of theory are shown, calculated values are placed within the circular graphic in black, measured values and transition state barriers are shown in the respective colors adjacent to the arrows. 294
- Figure 280: Proposed reaction pathway by irradiation of indigo **64** at 25 °C in toluene- $d_6$  enriching the *anti-trans*-**64**- starting from majorly *syn-trans*-**64** isomer out of the thermodynamic equilibrium. Optimized ground- and transition states calculated at the B3LYP/6-311+G(d,p) level of theory are shown, calculated values are placed within the circular graphic in black, measured values and transition state barriers are shown in the respective colors adjacent to the arrows. 295
- Figure 281: All possible theoretical trajectories for the reaction cycle of the *syn-trans*-1 isomer of indigo **64** at ambient temperatures. CW = clockwise rotation, CCW = counter clockwise rotation. (SB) = Single bond rotation, (DB) = Double bond rotation. The rotational direction is defined by the view alongside of the respective single or double bond axis. Rotational directions marked in red represent the favored rotations for single- and double bonds. The two lowest energy transition states are shown for each respective reaction path. Calculated energies at the B3LYP/6-311+G(d,p) level of theory are given below the stereodescriptors respective to the lowest ground state energy, which was set to 0.00 kcal/mol. 297
- Figure 282: The photoinduced 180° double bond isomerization of indigo **64** at -50 °C in dichloromethane- $d_2$  yields the *anti-cis*-2 isomer starting from majorly *syn-trans*-1 isomer. The subsequent thermal back-reaction takes place over a free activation enthalpy of  $\Delta G^\ddagger = 15.8$  kcal/mol. The *anti-cis*-1 states are skipped in both cases. CCW = counter clockwise, DB = double bond. Optimized ground states calculated at the B3LYP/6-311+G(d,p) level of theory are shown, calculated values are placed within the circular graphic in black, the measured value is shown in blue. 300
- Figure 283: Possible theoretical trajectories of indigo **64** for the reaction cycle of the *anti-trans* isomer between -60 °C, -50 °C and 25 °C. CW = clockwise rotation, CCW = counter clockwise rotation, PEHT = photoinduced extended Hula-Twist, TEHT = thermal extended Hula-Twist. The rotational direction is defined by the view on top of the respective single or double bond axis. Rotational directions marked in red represent the favored rotations for single- and double bonds. The two lowest energy transition states are shown for respective reaction path. Calculated energies at the B3LYP/6-311+G(d,p) level of theory are given below the stereodescriptors respective to the lowest ground state energy. (SB) = rotation directions for the single bond, (DB) = rotation directions for the central double bond. 304
- Figure 284: Suggestion of the PEHT and TEHT motion of indigo **64** based on chemical intuition. The first state on the left and the last state on the right represent minimum structures calculated at the B3LYP/6-311+G(d,p) level of theory, intermediate geometries represent arbitrary structures to visualize the proposed geared Hula-Twist motion. Top: view along a single bond, bottom: view along the central double bond. 307
- Figure 285: Possible theoretical trajectories for the reaction cycle of the *anti-trans* isomer between -60 °C, -50 °C and 25 °C. CW = clockwise rotation, CCW = counter clockwise rotation. The rotational direction is defined by the view on top of the respective single or double bond axis. Rotational directions marked in red represent the favored rotations for single- and double bonds. The two lowest energy transition states are shown for respective reaction path. Calculated energies at the B3LYP/6-311+G(d,p) level of theory are given below the stereodescriptors respective to the lowest ground state energy, which is set to 0.00 kcal/mol. (SB) = rotation directions for the single bond, (DB) = rotation directions for the central double bond. 309
- Figure 286: Overview of the *trans* forms of indigo **71**. The same amount of enantio and diastereomers is expected for the *cis* state. 314
- Figure 287: Chiral HPLC separation of the ( $S_S$ )-( $S_S$ )-*syn-trans*-, ( $R_S$ )-( $R_S$ )-*syn-trans*-, ( $S_S$ )-( $R_S$ )-*anti-trans*- and ( $R_S$ )-( $S_S$ )-*anti-trans* indigo **71** rota- and diastereomers at 0 °C with an 8 / 2 heptane / ethyl acetate mixture as eluent, the four separated rotamers can be observed. 314
- Figure 288: Scaled UV-Vis (left) and ECD (right) spectra of 7-methyl-*N,N*-di(*o*-tolyl)indigo **71** in 8 / 2 heptane / ethyl acetate at 0 °C (blue / green and broken light blue / green) and after 6 min of 617 nm irradiation (red and broken light red). 315
- Figure 289: Linearized first order kinetics of **71** E1 and E3 in 8 / 2 heptane / ethyl acetate at 0 °C and 40 °C. The thermal atropisomerization barriers were determined as follows: E1 at 40 °C: 22.9 kcal/mol with a half-life of 1.98 h, E3 at 40 °C: 23.0 kcal/mol with a half-life of 2.32 h, E1 at 0 °C: 21.7 kcal/mol with a half-life of 15.2 min and E3 at 0 °C: 22.3 kcal/mol with a half-life of 44.0 min. Half-lives are given for a temperature of 25 °C. Used formulas and equations are described in Section 2.2.19. 316
- Figure 290: Aliphatic  $^1\text{H-NOESY}$  NMR-spectrum of the *syn*- and *anti*-rotamer of 7-methyl-*N,N*-di(*o*-tolyl)indigo **71**, (600 MHz, dichloromethane- $d_2$ , 27 °C). Signals of protons *anti* 14 and *syn* 14 show positive NOE signals, while the rest of the molecule shows negative NOEs when the diagonal line is set to positive values according to convention. This confirms the expected fast dynamics between *syn*- and *anti* diastereomers (see indigo **65**, Section 2.4.3) as the used mixing time of 1.2 s is longer than the exchange of respective nuclei. Signal *syn* 14 / *syn* 15 shows stronger intensity than *anti* 14 / *anti* 15, which hints towards steric repulsion between methyl groups *syn* 14 / *syn* 14' (NOE not visible due to diagonal peak overlap) forcing methyl group 14 closer towards methyl group 15. 317
- Figure 291: Aromatic / aliphatic  $^1\text{H-NOESY}$  NMR-spectrum of the *syn*- and *anti*-rotamer of 7-methyl-*N,N*-di(*o*-tolyl)indigo **71**, measured at 27 °C, 600 MHz, dichloromethane- $d_2$ , 27 °C). The *anti* conformation can be unambiguously assigned as cross-signals *anti* 13' / *anti* 14 and *anti* 13 / *anti* 14' can be observed. The difference intensity of these signals supports a twisted conformation of the molecule with aryl edge 13' closer to methyl group 14. 318
- Figure 292: Aromatic  $^1\text{H-NOESY}$  NMR-spectrum of the *syn*- and *anti* rotamer of 7-methyl-*N,N*-di(*o*-tolyl)indigo **71**, measured at (600 MHz, dichloromethane- $d_2$ , 27 °C). Signals *syn* 13 / *syn* 13' are visible while signals *anti* 13 / *anti* 13' are not visible, which underlines this assignment to be correct. 319
- Figure 293: Irradiation of a 1.6 / 1.0 *syn* / *anti-trans* mixture of indigo **71** in dichloromethane- $d_2$  (400 MHz) after irradiation at various temperatures. The generation of stable *cis* isomers can be observed at -80 °C. 320
- Figure 294: Kinetic plots for the thermal *cis* to *trans* isomerization of indigo **71** at -40 °C. An increase of all *trans* isomers can be observed while the *cis* states are depopulated. 321
- Figure 295: Overview of the *trans* forms of *N*-(4-methoxy-2-methylphenyl)-*N*-(*o*-tolyl)indigo **72**. The same amount of enantio and diastereomers is expected for the *cis* state. 322
- Figure 296: Optimized reversed-phase HPLC separation of indigo **72** with 9 / 1 acetonitrile / water as eluent. The difference in retention times proved as unfeasible for separation and changing of eluent(s) and / or composition, temperature and column phase did not yield satisfactory results. The expected 1 / 2 / 1 pattern for this statistical reaction can be observed. 323
- Figure 297: Injection of the H2 peak of indigo **72** from the preceding reversed-phase HPLC run onto a chiral HPLC column at 0 °C with 83 / 17 heptane / ethyl acetate as eluent. Poor separation and carry-over of the three different molecules with three to four rotamers each make obtaining of enantiopure fractions impossible. 323
- Figure 298: Overview of the *trans* forms of *N*-(4-fluoro-2-methylphenyl)-*N*-(*o*-tolyl)indigo **73**. The same amount of enantio and diastereomers is expected for the *cis* state. 324
- Figure 299: Optimized reversed-phase HPLC separation of indigo **73** with 6 / 4 acetonitrile / water as eluent. The expected 1 / 2 / 1 pattern for this statistical reaction can be observed. 325
- Figure 300: Injection of the H2 peak of indigo **73** from the preceding reversed-phase HPLC run onto a chiral HPLC column at 0 °C with 83 / 17 heptane / ethyl acetate as eluent. The expected four rotamers can be observed, however, the rotamers of residual difluorated indigo **79** from fraction H1 can also be seen. 325
- Figure 301: Scaled UV-Vis (left) and corresponding ECD spectra (right) of all four peaks obtained from chiral HPLC separation (*syn-trans*-1 (ExE1), *syn-trans*-2 (ExE2), *anti-trans*-1 (ExE3) and *anti-trans*-2 (ExE4)) of *N*-(4-fluoro-2-methylphenyl)-*N*-(*o*-tolyl)indigo **73** in 83 / 17 heptane / ethyl acetate at 0 °C. Samples were irradiated and measured within the ECD spectrophotometer at 0 °C, which records UV-Vis spectra with poor quality. This was done because the other UV-Vis spectrophotometer cannot be cooled to 0 °C. Both *syn* isomers (blue and broken blue lines) show strong ECD responses while the *anti* forms (green and pink lines) show no ECD signal at all. This can be explained by the cancellation of ECD signal for a ( $R_S$ )- and a ( $S_S$ ) chiral axis in the same molecule, see Section 2.4.9. Irradiation at 0 °C shows the *anti-cis* isomers (red and broken red lines). 326
- Figure 302: Linearization of the first order kinetics for the atropisomerization of *N*-(4-fluoro-2-methylphenyl)-*N*-(*o*-tolyl)indigo **73** at 40 °C in 83 / 17 heptane / ethyl acetate. A barrier of 23.7 kcal/mol with a half-life of 7.90 h at 25 °C could be determined. Used formulas and equations can be found in Section 2.2.19. 326
- Figure 303:  $^1\text{H-NMR}$  spectra of all four isolated rotamers of indigo **73**. 1<sup>st</sup> and 2<sup>nd</sup> HPLC fractions can be regarded as enantiomers, which is also true for the 3<sup>rd</sup> and 4<sup>th</sup> fraction as they show the same spectra. Residual difluorated indigo **78** can only be observed in the 1<sup>st</sup> fraction, which shows that the separation of rotamers for this compound is feasible compared to indigo **72**. 327
- Figure 304: Overview of synthesized and investigated hemiindigos **80**, **81** and **82**. Only *Z* isomers are shown. 332
- Figure 305: Schematic representation of the homebuilt tandem ion mobility mass spectrometer. Adapted with permission from <sup>[126]</sup>. Copyright 2020 Wiley VCH. 336
- Figure 306: Arrival time distributions (ATDs) for the three investigated hemiindigo ions **80**, **81** and **82** recorded with  $\text{N}_2$  buffer gas (upper row) and with  $\text{N}_2$  doped with 1% 2-propanol (lower row). Adapted with permission from <sup>[126]</sup>. Copyright 2020 Wiley VCH. 337
- Figure 307: Fitted arrival time distributions (ATDs) for the three investigated hemiindigo ions **80**, **81** and **82** with different solution irradiation conditions. The left column shows the resulting ATD after 5 minutes irradiation of each sample with blue light, whereas the right column shows the ATDs after irradiation with green or red light prior to electrospray. The fitted contributions of each isomer are given under the obtained curves. Adapted with permission from <sup>[126]</sup>. Copyright 2020 Wiley VCH. 338
- Figure 308: (a) ATDs showing mobility-separated *Z* and *E* isomers of hemiindigos **80**, **81** and **82**. The black traces show the ATDs of the electrosprayed samples shielded from light, whereas colored traces represent the distributions after exposure of each hemiindigo solution to the indicated wavelength of light. (b) Solution absorption spectra of an isomeric mixture of hemiindigos **80**, **81** and **82** after irradiation with different wavelengths of light promoting

## 5.2 TABLE OF FIGURES

	formation of either <i>Z</i> or <i>E</i> isomers. A reversal of the arrival times of <i>Z</i> and <i>E</i> isomers for hemiindigo <b>81</b> compared to <b>80</b> and <b>82</b> can be observed. Adapted with permission from [126]. Copyright 2020 Wiley VCH.	339
Figure 309:	Example Z isomer photoaction ATDs ( <b>a-c</b> ), gas-phase action spectra ( <b>d-f</b> ) and solution absorption spectra ( <b>g-i</b> ) for the <i>Z</i> and <i>E</i> isomers of hemiindigos <b>80</b> (left column), <b>81</b> (middle column) and <b>82</b> (right column). For the isolated hemiindigo isomers, the calculated absorption wavelengths are marked with bars of the corresponding color. Adapted with permission from [126]. Copyright 2020 Wiley VCH.	340
Figure 310:	Normalized yield of <i>E</i> photoisomer as a function of light fluence. The experiments were performed at 450nm (Hemiindigo <b>80</b> and <b>81</b> ) and 430nm (Hemiindigo <b>82</b> ), respectively. All photoisomerization experiments were performed at a light fluence of <math>\sim 0.8 \text{ mJ pulse}^{-1} \text{ cm}^{-2}</math>. Adapted with permission from [126]. Copyright 2020 Wiley-VCH.	342
Figure 311:	Calculated geometries and relative energies for representative low-energy <i>E</i> and <i>Z</i> conformers of hemiindigos <b>80</b> (a), <b>81</b> (b), and <b>82</b> (c) calculated at the $\omega$ B97XD/cc-pVDZ level of theory. The energies are given in kcal/mol with respect to the most stable conformer. (d) Calculated averaged collision cross-section (CCS) for <i>E</i> and <i>Z</i> isomers in <b>80</b> , <b>81</b> and <b>82</b> , assuming a Boltzmann distribution of the individual conformers shown in (a-c) at a temperature of 300 K. Adapted with permission from [126]. Copyright 2020 Wiley VCH.	343
Figure 312:	Section of the 2D NOESY NMR spectrum (dichloromethane- $d_2$ , 600 MHz, 27 °C) of hemiindigo <b>80</b> . The strong NOE cross signals between protons <i>E</i> 16 / 17 / <i>E</i> 10 and the weak signal of <i>E</i> 18 indicates their assignment to the <i>E</i> isomer to be correct. <i>Z</i> 10 shows no cross peaks with the chain protons. <i>Z</i> 16 / 17 show overlapping cross signals with protons <i>Z</i> 3 / 12, resolving the <i>Z</i> 12 / <i>Z</i> 3 signals determines the preferred conformer in proximity of proton 3 instead of 12. Adapted with permission from [126]. Copyright 2020 Wiley VCH.	345
Figure 313:	Section of the 2D NOESY NMR spectrum (dichloromethane- $d_2$ , 600 MHz, 27 °C) of hemiindigo <b>80</b> . The expected signals for the alkyl chain and diazabicyclo[2.2.2]octane can be identified. Adapted with permission from [126]. Copyright 2020 Wiley VCH.	346
Figure 314:	Section of the 2D-NOESY NMR spectrum (acetonitrile- $d_3$ , 400 MHz, 27 °C) of hemiindigo <b>81</b> . Strong cross signals of <i>E</i> 10 with protons <i>E</i> 16 and overlapped protons <i>E</i> 17 / 18 support their correct assignment to the <i>E</i> isomer. <i>Z</i> 10 shows no NOEs with alkyl chain protons. <i>Z</i> 12 shows strong signals with proton <i>Z</i> 16 but no cross signal with <i>Z</i> 17 / 18 / 19 while proton <i>Z</i> 3 shows signals with <i>Z</i> 16 and <i>Z</i> 17. This suggests a preferred chain conformer population in proximity of proton 3, although in a less pronounced manner than observed for <i>Z</i> - <b>80</b> . <i>E</i> 12 exhibits weak overlapped cross signals for protons <i>E</i> 17 / 18, which cannot be seen for <i>E</i> 18 / 19 in hemiindigo <i>E</i> - <b>80</b> as the elongated chain negates significant NOE signals to the peripheral diazabicyclo[2.2.2]octane tag. Adapted with permission from [126]. Copyright 2020 Wiley VCH.	347
Figure 315:	Section of the 2D NOESY NMR spectrum (acetonitrile- $d_3$ , 400 MHz, 27 °C) of hemiindigo <b>81</b> . The expected signals of the alkyl chain and diazabicyclo[2.2.2]octane can be identified. Adapted with permission from [126]. Copyright 2020 Wiley VCH.	348
Figure 316:	PSS UV-Vis spectra at different irradiation wavelengths for <i>Z</i> - / <i>E</i> - <b>80</b> in acetonitrile. Adapted with permission from [126]. Copyright 2020 Wiley VCH.	349
Figure 317:	PSS UV-Vis spectra at different irradiation wavelengths for <i>Z</i> - / <i>E</i> - <b>81</b> in acetonitrile. Adapted with permission from [126]. Copyright 2020 Wiley VCH.	350
Figure 318:	PSS UV-Vis spectra at different irradiation wavelengths for <i>Z</i> - / <i>E</i> - <b>82</b> in acetonitrile. Adapted with permission from [126]. Copyright 2020 Wiley VCH.	350
Figure 319:	Absorbance normalized 100% <i>Z</i> / <i>E</i> UV-Vis spectra for <b>80</b> (blue), <b>81</b> (red) and <b>82</b> (black) in acetonitrile. Adapted with permission from [126]. Copyright 2020 Wiley VCH.	351
Figure 320:	<sup>1</sup> H-NMR spectra of <i>Z</i> / <i>E</i> <b>81</b> (top) and <i>Z</i> / <i>E</i> <b>80</b> (bottom) in acetonitrile- $d_3$ , only the aliphatic section is shown. Corresponding Lewis-formula are shown at the top and bottom. Adapted with permission from [126]. Copyright 2020 Wiley VCH.	353
Figure 321:	Energetically favored <i>Z</i> and <i>E</i> isomers of hemiindigo <b>81</b> (top) and <b>80</b> (bottom) calculated at the $\omega$ B97XD/cc-pVDZ level of theory.	355
Figure 322:	Molecular electrostatic potentials (MEPs), highest occupied molecular orbitals (HOMOs) and lowest unoccupied molecular orbitals (LUMOs) of hemiindigos <b>80</b> (top, left), <b>81</b> (top right) and <b>82</b> (bottom) calculated at the $\omega$ B97XD/cc-pVDZ level of theory. Only the conformers with the lowest respective energy are shown. The MEPs show the affinity towards a positive test charge, red areas show high and blue areas low affinities. The same color margin values of -0.01 and +0.18 were used for all MEPs.	356
Figure 323:	Three small molecules ( <b>86</b> , <b>87</b> and <b>88</b> ) that show affinities and conformational / regulatory changes at the RNA level in biological assemblies. Similarities of functional groups to the investigated hemiindigo photoswitches are marked red.	362
Figure 324:	Lewis-formula of hemiindigo <b>34</b> .	371
Figure 325:	UV-Vis spectra of hemiindigo <b>34</b> in pure water under different irradiation conditions.	371
Figure 326:	<sup>1</sup> H- (left) and <sup>13</sup> C-NMR spectra (right) of hemiindigo <b>34</b> (600 MHz, dichloromethane- $d_2$ , 27 °C).	371
Figure 327:	Lewis-formula of hemiindigo <b>97</b> .	372
Figure 328:	UV-Vis spectra of hemiindigo <b>97</b> in pure water under different irradiation conditions.	372
Figure 329:	<sup>1</sup> H- (left) and <sup>13</sup> C-NMR spectra (right) of hemiindigo <b>97</b> (600 MHz, dichloromethane- $d_2$ , 27 °C).	372
Figure 330:	Lewis-formula of hemiindigo <b>100</b> .	373
Figure 331:	UV-Vis spectra of hemiindigo <b>100</b> in a 2 / 4 / 4 water / sat. aq. ammonium chloride / dimethyl sulfoxide mixture under different irradiation conditions.	373
Figure 332:	<sup>1</sup> H- (left) and <sup>13</sup> C-NMR spectra (right) of hemiindigo <b>100</b> (600 MHz, dichloromethane- $d_2$ , 27 °C).	373
Figure 333:	Lewis-formula of hemiindigo <b>101</b> .	374
Figure 334:	UV-Vis spectra of hemiindigo <b>101</b> in water with one drop of sat. aq. ammonium chloride as additive under different irradiation conditions.	374
Figure 335:	<sup>1</sup> H-NMR spectra of hemiindigo <b>101</b> (400 MHz, dichloromethane- $d_2$ , 27 °C). RP-HPLC purification (right) yielded more signals than the precedent silica column separation (left), suggesting stability issues with this compound.	374
Figure 336:	Lewis-formula of hemiindigo <b>102</b> .	376
Figure 337:	UV-Vis spectra of hemiindigo <b>102</b> in water with one drop of sat. aq. ammonium chloride and seven drops of dimethyl sulfoxide as additives under different irradiation conditions.	376
Figure 338:	<sup>1</sup> H- (left) and <sup>13</sup> C-NMR spectra (right) of hemiindigo <b>102</b> (600 MHz, dichloromethane- $d_2$ , 27 °C).	376
Figure 339:	Lewis-formula of hemiindigo <b>98</b> .	377
Figure 340:	UV-Vis spectra of hemiindigo <b>98</b> in pure water at different irradiation conditions.	377
Figure 341:	<sup>1</sup> H- (left) and <sup>13</sup> C-NMR spectra (right) of hemiindigo <b>98</b> (600 MHz, dichloromethane- $d_2$ , 27 °C).	377
Figure 342:	Lewis-formula of hemiindigo <b>99</b> .	378
Figure 343:	<sup>1</sup> H- (left) and <sup>13</sup> C-NMR spectra (right) of hemiindigo <b>99</b> (400 MHz, dichloromethane- $d_2$ , 27 °C).	378
Figure 344:	Lewis-formula of hemiindigo <b>103</b> .	379
Figure 345:	UV-Vis spectra of the degradation products of hemiindigo <b>103</b> in water after three months shelf storage in the dark at ambient temperatures. This compound was not measured via UV-Vis spectroscopy before degradation, spectra of <b>101</b> and <b>102</b> should be similar in shape.	379
Figure 346:	<sup>1</sup> H-NMR spectra of hemiindigo <b>103</b> (400 MHz, dichloromethane- $d_2$ , 27 °C). Purification issues because of the high polarity of this compound yielded unclean products in low abundance.	379
Figure 347:	Lewis-formula of hemiindigo <b>104</b> .	380
Figure 348:	UV-Vis spectra of the degradation products of hemiindigo <b>104</b> in water after three months shelf storage in the dark at ambient temperatures. This compound was not measured via UV-Vis spectroscopy before degradation, spectra of <b>101</b> and <b>102</b> should be similar in shape.	380
Figure 349:	<sup>1</sup> H-NMR spectra of hemiindigo <b>104</b> (400 MHz, dichloromethane- $d_2$ , 27 °C). Purification issues because of the high polarity of this compound yielded unclean products.	380
Figure 350:	Lewis-formula of hemiindigo <b>106</b> .	383
Figure 351:	UV-Vis spectra of hemiindigo <b>106</b> in pure water under different irradiation conditions.	383
Figure 352:	Lewis-formula of hemiindigo <b>107</b> .	384
Figure 353:	UV-Vis spectra of hemiindigo <b>107</b> in pure water under different irradiation conditions.	384
Figure 354:	Lewis-formula of hemiindigo <b>105</b> .	385
Figure 355:	UV-Vis spectra of hemiindigo <b>105</b> in pure water under different irradiation conditions.	385
Figure 356:	<sup>1</sup> H- (left) and <sup>13</sup> C-NMR spectra (right) of hemiindigo <b>105</b> (800 MHz, dichloromethane- $d_2$ , 27 °C).	386
Figure 357:	Lewis-formula of hemiindigo <b>108</b> .	386
Figure 358:	Lewis-formula of hemiindigo <b>109</b> .	386
Figure 359:	Lewis-formula of hemiindigo <b>110</b> .	387
Figure 360:	UV-Vis spectra of hemiindigo <b>110</b> in pure water under different irradiation conditions.	387
Figure 361:	Lewis-formula of hemiindigo <b>111</b> .	388
Figure 362:	UV-Vis spectra of hemiindigo <b>111</b> in pure water under different irradiation conditions.	388
Figure 363:	Lewis-formula of hemiindigo <b>113</b> .	389
Figure 364:	Lewis-formula of hemiindigo <b>112</b> .	389
Figure 365:	UV-Vis spectra of hemiindigo <b>112</b> in pure water under different irradiation conditions.	389
Figure 366:	Example of an underestimated 100% <i>E</i> spectrum (red line) obtained by eq. 21 and eq. 22.	400
Figure 367:	Example of the accuracy of the first generation of the 100% <i>Z</i> / <i>E</i> calculator, green and violet: measured 100% molar absorption spectra, black and red: calculated 100% molar absorption spectra.	402
Figure 368:	Screenshot of the spectra deconvolution <i>Excel</i> tool version 1.0 to obtain 100% <i>Z</i> - and <i>E</i> spectra from arbitrary mixtures. The red ellipsoid shows the three variable parameters for each <i>Z</i> - and <i>E</i> enriched isomer mixture. Vertical lines represent observation wavelengths to confirm the consistency of the calculated isomeric compositions from 359 nm to 477 nm, deviations below 1% were observed, which is dependent on the quality of data and the photochromism of the compound.	405
Figure 369:	Screenshot of the spectra deconvolution <i>Excel</i> tool version 2.0 to obtain 100% <i>Z</i> - and <i>E</i> spectra from arbitrary mixtures. The violet ellipsoid shows that - besides the experimentally determined <sup>1</sup> H-NMR signal integral ratios of each isomer - only one variable parameter for each <i>Z</i> - and <i>E</i> enriched isomer mixture is needed to adjust for the respective measured concentration. The crosshair (green) marks the most red-shifted isosbestic point for concentration adjustment.	406
Figure 370:	Screenshot of the spectra deconvolution <i>Excel</i> tool version 5.2 to obtain 100% <i>Z</i> - and <i>E</i> spectra from arbitrary mixtures. The violet ellipsoid shows that only a suitable observer wavelength needs to be set. The other parameters are needed for the calculation of molar absorption spectra and quantum yield determination, which are shown in sections 2.2.21 and 2.7.2.	408
Figure 371:	Input page of the online based deconvolution tool by <i>Y. Ruppenthal</i> . The same functionality as the excel tool was achieved within this version.	409

Figure 372:	Kinetic analysis of the <i>E</i> to <i>Z</i> thermal isomerization of hemiindigo <b>8</b> in tetrahydrofuran measured at 26 °C over 180 minutes within the calculational <i>Excel</i> tool version 5.2.	410
Figure 373:	Photoquantum yield analysis of the <i>Z</i> to <i>E</i> photoisomerization of hemiindigo <b>20</b> in 83 / 17 heptane / ethyl acetate within the calculational <i>Excel</i> tool version 5.2.	410
Figure 374:	Low-cost quantum yield measurement prototype with differential read-out of absorbed power. The LED light is focused with two magnifying glasses onto a beam splitter made out of a stack of microscopy plates. One part of the light beam is measured with a calibrated reference diode, the other part of the beam is sent through the sample. The calibrated measurement diode reports the remaining light power which was not absorbed by the sample. The <i>Arduino</i> microcontroller subtracts the power values of the measurement diode from the reference diode, giving accurate absorbed power values even upon LED power fluctuations.	415
Figure 375:	Circuit board and <i>Arduino</i> microcontroller of the inexpensive quantum yield determination setup. The current of the photodiodes is linearly converted into voltage and amplified utilizing two of the four operational amplifiers of the integrated circuit (IC) chip (MCP6004-I/P PDIP-14) wired as transimpedance amplifier. The amplification factor is adjusted individually for each photodiode by a trimmer potentiometer. A third trimmer potentiometer is used to normalize reference- and measurement photodiode when no sample is placed within the beam path prior to measurement. The <i>Arduino</i> microcontroller converts the measured voltage differences into light power according to a previously determined calibration curve and plots the absorbed power versus time on a computer screen for data acquisition.	416
Figure 376:	Programming of the <i>Arduino</i> microcontroller in C++ to measure the absorbed power of the sample with respect to the reference photodiode.	417
Figure 377:	Improved setup for sample cooling during alternating irradiation experiments. During irradiation it was ensured that air gaps between LEDs and cuvette were present for effective fan-cooling (see Figure 377, top left corner). Direct temperature measurements inside a water filled cuvette determined temperature deviations of up to 1.23 °C during irradiation cycles in a control experiment (see inset in the right picture).	419
Figure 378:	Depiction of the air gap between LEDs and sample (top left corner) and calibration of the different temperature sensors 1 to 3 within the air stream of the fan. The respective temperature deviations between the different sensors are very small. The surrounding room was not yet cooled to 18 °C at this time of measurement.	420
Figure 379:	Monitored temperature of the surrounding air during 160 cycles of alternating irradiations of hemiindigo <b>33</b> (left). Spikes represent warming of the air stream during manual sample handling. Temperature difference (right) between the inside of the cuvette (red) and the surrounding room temperature (blue) measured for a water-filled cuvette during 9 cycles of alternating irradiations. On average, a 1.23 °C temperature difference was observed between irradiations for 7 s at 435 nm and 260 mW output power and 38 s at 505 nm and 80 mW output power. Spikes correspond to the flashing of the 435 nm LED, which dissipates more heat.	420
Figure 380:	Different views of the homemade plywood cryostat mounting bracket outside the ECD spectrometer. The cryostat can be adjusted within five dimensions and the cuvette holder within the sample chamber can be moved in two dimensions.	422
Figure 381:	Instrumental setup used for repetitive ECD measurements in-between alternating irradiations of the ( <i>R<sub>s</sub></i> )- <b>30</b> isomer at -20 °C using an <i>Oxford instruments Optistat DN</i> cryostat. A rotary pump maintains a vacuum of $3 \times 10^{-3}$ mbar for the isolation chamber of the cryostat to increase its operation time. The temperature controller was set to 253.2 K and maintained the temperature by successive heating pulses. A membrane pump is utilized for secondary control of temperature by regulating the exiting N <sub>2</sub> gas stream and hence the coolant flow (LN <sub>2</sub> ) respectively. Alternating irradiation inside the cryostat is realized by using two glass fiber-coupled LEDs, which can be exchanged at one end of the fiber without disturbing the sensitive setup (10 s 450 nm at 193 mW and 60 s 520 nm at 92 mW irradiations were used for each cycle). A home-made mounting bracket was used to ensure reproducible cryostat and sample holder alignments for each mechanical change in the setup (i.e. sample exchange for baseline measurements) as circularly polarized light gradually changes ellipticity if its beam is not passed through the cuvette windows perpendicularly.	423

## 5.3 Table of Schemes

Scheme 1:	Photoisomerization of <i>trans</i> stilbene to <i>cis</i> stilbene by irradiation with UV-light.	6
Scheme 2:	Photoisomerization of pyrrole-substituted hemiindigo 1 by <i>T. Arai</i> .	26
Scheme 3:	Photoswitching and thermal isomerization pathways of hemiindigo 2.	27
Scheme 4:	Exemplary <i>Z/E</i> isomerization of hemiindigo 3 with nominal green 530 nm LED light to 93% <i>E</i> isomer and nominal red 680 nm LED light to 99% <i>Z</i> isomer in dimethyl sulfoxide. The <i>Z</i> isomer has a thermal half-life of 0.7 years and the <i>E</i> isomer of 0.9 years at 25 °C.	28
Scheme 5:	Condensation of indoxyl acetate and an aldehyde to obtain hemiindigo 9.	31
Scheme 6:	Acetylation of hemiindigos 9 and 11 utilizing acetic anhydride, 4-dimethylaminopyridine as nucleophilic catalyst and <i>Hünig's</i> base ( <i>N,N</i> -diisopropylethylamine) at 100 °C. Moderate yields of 61% for 2 and 64% for the dimethyl amino derivative 12 are obtained after purification by high performance liquid chromatography (HPLC). Subsequent crystallization yielded yellow needles.	34
Scheme 7:	Alkylation of hemiindigo 9 via an $S_N2$ mechanism to obtain compound 7 in excellent yields.	39
Scheme 8:	Synthesis of hemiindigos 11 and 15 from indoxyl acetate 10 and electron-rich aldehydes in good to moderate yields. The products can be crystallized as violet needles (dimethylamino moiety) or red / green dichroic crystals (julolidine derivative).	43
Scheme 9:	Alkylation of <i>N</i> -protonated hemiindigos 11 and 15 via an $S_N2$ mechanism to yield alkylated compounds 8 and 3.	47
Scheme 10:	Palladium catalyzed <i>Buchwald-Hartwig</i> cross-coupling reaction of an electron-poor aromatic secondary amine, i.e. hemiindigo 11 and <i>para</i> -bromotoluene utilizing <i>DavePhos</i> as ligand <b>L</b> . <b>SM</b> = Starting Material.	54
Scheme 11:	Preparation of <i>N</i> -arylated indole 17.	56
Scheme 12:	Preparation of <i>N</i> -arylated indoxyl acetate 19.	57
Scheme 13:	Preparation of hemiindigo 20. Low yields after HPLC separation are caused by injection loss and the collection of only one isomer peak.	57
Scheme 14:	Cyclization reaction of 1,2,3,4-tetrahydroquinoline 22 and 1-bromo-3-chloropropane.	59
Scheme 15:	Bromination of julolidine 21.	59
Scheme 16:	<i>Suzuki</i> cross-coupling of bromojulolidine 23 and 4-formylphenylboronic acid.	60
Scheme 17:	Condensation reaction between arylated indoxyl acetate 19 and an extended electron-rich aldehyde 24.	60
Scheme 18:	Condensation reaction of indoxyl acetate 10 and 4-methoxy-2,3,6-trimethylbenzaldehyde according to the procedure of <i>U. Burger et al.</i> to yield hemiindigo 27.	63
Scheme 19:	$S_N2$ reaction of 1-propyl iodide with the deprotonated nitrogen of hemiindigo 27 according to the procedure of <i>V. Velezheva et al.</i> to yield compound 28. <sup>[90]</sup>	63
Scheme 20:	Vicarious $S_NAr$ reaction of the protonated central double bond position of hemiindigo 28 with potassium cyanide according to the procedure of <i>V. Velezheva et al.</i> to yield hemiindigo 26. <sup>[90]</sup>	64
Scheme 21:	Preparation of hemiindigo 30 from indoxyl acetate 19. Moderate to low yields were obtained after HPLC purification, which was caused by losses during injection and discarded fractions due to elution overlap with other compounds.	68
Scheme 22:	Preparation of <i>N</i> -arylated indole 31.	70
Scheme 23:	Preparation of <i>N</i> -arylated indoxyl acetate 32.	71
Scheme 24:	Preparation of hemiindigo 33 in moderate yields. Loss of substance during HPLC injection was minimized by recovery and re-injection of spilled material.	71
Scheme 25:	Introduction of tertiary alkyl substituents at the indole nitrogen atom. * = yield reported in the literature.	120
Scheme 26:	Synthesis of the <i>N</i> -acetylated indoxyl building block 44.	120
Scheme 27:	Synthetic route to the 2-thio ketone precursor. * = yield reported by literature. <sup>[104]</sup>	121
Scheme 28:	Proposed coupling conditions of the 2-thio ketone indoxyl 45 by <i>V. Velezheva</i> with the diazofluorenone 47 by <i>M. Ramana</i> utilizing the conditions of <i>N. Ruangsapichat</i> yielding intermediate 48 and model system 49 (top). The desired triptycyl derivative 39 is shown below.	121
Scheme 29:	Synthesis of hemiindigos with asymmetric and / or bulky stilbene fragments.	124
Scheme 30:	Introduction of an isobutryl moiety via 4-dimethylaminopyridine (DMAP) mediated nucleophilic catalysis in dichloroethane (DCE) utilizing triethylamine (TEA) as base. The introduction of a pivaloyl residue did not yield products 53.	130
Scheme 31:	Introduction of a secondary alkyl residue to the hemiindigo chromophore. Elevated temperatures are necessary for the reaction to progress and only low yields of 58 could be obtained.	141
Scheme 32:	Preparation of <i>N</i> -arylated indole 66.	218
Scheme 33:	Preparation of <i>N</i> -arylated indoxyl acetate 68.	218
Scheme 34:	Deacylation of indoxyl acetate 68 according to <i>U. Burger et al.</i> <sup>[98]</sup> with dioxane as co-solvent and subsequent oxidation with manganese(III) acetate to furnish indigo 64 in good yield.	219
Scheme 35:	Deacylation of 19 according to <i>U. Burger et al.</i> <sup>[98]</sup> with dioxane as co-solvent and subsequent oxidation with manganese(III) acetate to furnish indigo 65 in low yield.	221
Scheme 36:	Simultaneous deacylation of 68 and 74 according to <i>U. Burger et al.</i> <sup>[98]</sup> with dioxane as co-solvent and subsequent oxidation with manganese(III) acetate yielding indigos 64, 70 and 63. The low yields can be attributed to the increased sterical hindrance of the more planarized <i>para</i> -tolyl moiety.	248
Scheme 37:	Simultaneous deacylation of 19 and 74 according to <i>U. Burger et al.</i> <sup>[98]</sup> with dioxane as co-solvent and subsequent oxidation with manganese(III) acetate to yield indigos 65, 69 and 63. The low yields can be attributed to the increased sterical hindrance of the planar <i>para</i> -tolyl moiety.	251
Scheme 38:	Simultaneous deacylation of indoxyl acetates 75 and 68 was carried out according to <i>U. Burger et al.</i> with dioxane as co-solvent. Subsequent oxidation using manganese(III) acetate furnished 76, 72 and 64 in low yields.	322
Scheme 39:	Simultaneous deacylation of indoxyl acetates 77 and 68 was carried out according to <i>U. Burger et al.</i> with dioxane as co-solvent. Subsequent oxidation using manganese(III) acetate furnished indigos 78, 73 and 64 in moderate yields.	324
Scheme 40:	Preparation of alkylated photoswitches 83, 84 and 85 supporting a terminal bromine functionality starting from hemiindigo derivatives 11 and 15. Hemiindigos 83, 84 and 85 were obtained by deprotonation with sodium hydride and a subsequent $S_N2$ reaction with terminal dibromoalkanes by addition via syringe pump at ambient temperatures. Lower HPLC yields are caused by loss of material <sup>86</sup> upon injection and / or isolation of only one isomer peak starting from a <i>Z/E</i> mixture.	333
Scheme 41:	Preparation of charge-tagged hemiindigos <i>Z/E</i> 80, 81 and 82. 1,4-Diazabicyclo[2.2.2]octane reacts almost quantitatively to its quaternary bromide salts with hemiindigos 83 and 85 via a <i>Menschutkin</i> reaction at 45 °C in one day.	334
Scheme 42:	$S_N2$ reaction of the phenolic hydroxyl group of 89 and 90 with 3-chloro-1-( <i>N,N</i> -dimethyl)propylamine in <i>N,N</i> -dimethylformamide (DMF) at 120 °C with potassium carbonate as base. Aldehydes 91 and 92 could be obtained in good to excellent yields.	363
Scheme 43:	$S_N2$ reaction of two phenolic hydroxyl groups of 93 and 94 with two equivalents of 3-chloro-1-( <i>N,N</i> -dimethyl)propylamine in <i>N,N</i> -dimethylformamide at 120 °C with potassium carbonate as base. Aldehydes 95 and 96 could be obtained in good yields.	363
Scheme 44:	Condensation reaction of different aldehydes (Aldehydes 91, 92, 95 and 96) with indoxyl acetate 10 in to furnish hemiindigos 34, 97, 98 and 99 in moderate yields.	364
Scheme 45:	$S_N2$ reaction of <i>N</i> -H unsubstituted hemiindigo photoswitches (51, 34, 97, 98 and 99) with 3-chloro-1-( <i>N,N</i> -dimethyl)propylamine in <i>N,N</i> -dimethylformamide at 100 - 120 °C with sodium hydride as base. Low to good yields of hemiindigos 100, 101, 102, 103 and 104 could be obtained.	366
Scheme 46:	<i>Menschutkin</i> reaction of excess methyl iodide in acetonitrile with dimethylamino alkyl chain substituted hemiindigos 100, 101 and 102 yielding quaternary ammonium ion substituted hemiindigos 105, 106 and 107. This reaction introduces a permanent charge-tag to the hemiindigo photoswitch.	367
Scheme 47:	<i>Menschutkin</i> reaction of excess methyl iodide in acetonitrile with dimethylamino alkyl chain substituted hemiindigos 101, 102, 98 and 99 yielding two quaternary ammonium ions, introducing permanent charge-tags to the hemiindigo photoswitches 108, 109, 110 and 111. Low to good yields could be obtained.	368
Scheme 48:	<i>Menschutkin</i> reaction of excess methyl iodide in acetonitrile with three dimethylamino alkyl chain substituted hemiindigo 104 yielding three quaternary ammonium ions, introducing permanent charge-tags to hemiindigo 112.	369

## 5.4 List of Tables

Table 1:	Photophysical properties of hemiindigo <b>11</b> in different solvents. ....	45
Table 2:	Photophysical properties of hemiindigo <b>15</b> in different solvents. ....	46
Table 3:	Photophysical properties of hemiindigo <b>8</b> in different solvents. ....	48
Table 4:	Photophysical properties of hemiindigo <b>3</b> in different solvents. ....	52
Table 5:	Photophysical properties of hemiindigo <b>16</b> in different solvents. ....	55
Table 6:	Isomer yields obtained in the PSS after <i>Z/E</i> and <i>E/Z</i> photoisomerization of the respective hemiindigo in different solvents at different wavelengths. Isomer yields were determined via UV-Vis measurements at $\sim 2.5 \cdot 10^{-6}$ M concentration. ....	82
Table 7:	Overview of different incorrectly determined free activation enthalpies (exemplary values) and the respective correction of systematic error. ....	89
Table 8:	Free activation enthalpies $\Delta G^\ddagger$ and corresponding half-lives at 25 °C for the thermal <i>E/Z</i> as well as <i>Z/E</i> isomerizations of hemiindigos <b>11</b> and <b>15</b> without entering equilibria. ....	91
Table 9:	Free activation enthalpies $\Delta G^\ddagger$ for the thermal <i>Z/E</i> and <i>E/Z</i> isomerizations of selected hemiindigos and corresponding extrapolated half-lives at 25 °C. ....	97
Table 10:	Overview of measured quantum yields and experimental measurement parameters using the <i>Riedle</i> setup. ....	113
Table 11:	Free activation enthalpies $\Delta G^\ddagger$ for thermal racemizations of the chiral axes of hemiindigos <b>20</b> , <b>30</b> and <b>33</b> measured separately for <i>Z</i> and <i>E</i> isomers in heptane / ethyl acetate mixtures. Corresponding half-lives in a = years, d = days, min = minutes and s = seconds were extrapolated to 25 °C. ....	201
Table 12:	Overview of the observed and calculated properties of the indigo <b>64</b> isomers (Measurements in toluene). ....	283
Table 13:	Permutation of possible theoretical trajectories for the reaction cycle of the <i>syn-trans-64</i> isomer at ambient temperatures for Figure 281. Preferred rotations are marked in red. "T1" stands for "Trajectory1". DBR = Double bond rotation, SBR = single bond rotation. ....	299
Table 14:	Permutations of possible theoretical trajectories for the photodriven / thermal extended Hula-Twist reaction cycle of the <i>anti-trans-64</i> isomer at -60 °C, -50 °C for Figure 283. Preferred rotations are marked in red. "T1" stands for "Trajectory1". DBR = Double bond rotation, SBR = single bond rotation. ....	305
Table 15:	Permutation of seven possible theoretical trajectories for the photodriven / thermal extended reaction cycle of the <i>anti-trans-64</i> isomer at 25 °C for Figure 285. Preferred rotations are marked in red. "T1" stands for "Trajectory1". DBR = Double bond rotation, SBR = single bond rotation. ....	310
Table 16:	Overview of the direction of thermally switchable pumping against the thermal equilibrium and prospective unidirectional 2-step double- (DBI) / 4-step single bond (SBR) isomerization motor properties for indigo <b>64</b> in various solvents. HEA = 83 / 17 heptane / ethyl acetate. ....	312
Table 17:	Optimized ground state energies, transition wavelengths and theoretical collision cross-sections in pure N <sub>2</sub> buffer gas for a series of <i>Z/E</i> conformers of hemiindigos <b>80</b> , <b>81</b> and <b>82</b> . ....	344
Table 18:	Photoswitching and ct DNA + HIV-1 RNA binding studies by <i>D. Berdnikova</i> in water without buffer. ....	391

## 5.5 Table of Equations

eq. 1	87
eq. 2	88
eq. 3	88
eq. 4	88
eq. 5	94
eq. 6	95
eq. 7	95
eq. 8	95
eq. 9	98
eq. 10	98
eq. 11	105
eq. 12	106
eq. 13	108
eq. 14	108
eq. 15	111
eq. 16	111
eq. 17	112
eq. 18	112
eq. 19	139
eq. 20	336
eq. 21	400
eq. 22	400
eq. 23	401
eq. 24	401
eq. 25	406
eq. 26	406
eq. 27	407
eq. 28	407
eq. 29	407
eq. 30	407
eq. 31	407



## 5.6 References

- [1] M. Calvin, A. A. Benson, *The Path of Carbon in Photosynthesis*, *Science* **1948**, 107, 476.
- [2] R. Hill, *Oxygen Evolved by Isolated Chloroplasts*, *Nature* **1937**, 139, 881.
- [3] J. Ingenhousz, *Experiments upon vegetables discovering their great power of purifying the common air in the sunshine and of injuring it in the shade and at night*, **1779**.
- [4] G. Wald, *Carotenoids and the vitamin A cycle in vision*, *Nature* **1934**, 134, 65.
- [5] T. D. Lamb, *Gain and kinetics of activation in the G-protein cascade of phototransduction*, *Proc. Natl. Acad. Sci. U.S.A.* **1996**, 93, 566.
- [6] A. Gerwien, M. Schildhauer, S. Thumser, P. Mayer, H. Dube, *Direct evidence for hula twist and single-bond rotation photoproducts*, *Nature Communications* **2018**, 9, 2510.
- [7] P. Nogly, T. Weinert, D. James, S. Carbajo, D. Ozerov, A. Furrer, D. Gashi, V. Borin, P. Skopintsev, K. Jaeger, K. Nass, P. B ath, R. Bosman, J. Koglin, M. Seaberg, T. Lane, D. Kekilli, S. Br unle, T. Tanaka, W. Wu, C. Milne, T. White, A. Barty, U. Weierstall, V. Panneels, E. Nango, S. Iwata, M. Hunter, I. Schapiro, G. Schertler, R. Neutze, J. Standfuss, *Retinal isomerization in bacteriorhodopsin captured by a femtosecond x-ray laser*, *Science* **2018**, 361, 127.
- [8] W. F. Loomis, *Skin-pigment regulation of vitamin-D biosynthesis in man*, *Science* **1967**, 157, 501.
- [9] J. Itten, *Kunst der Farbe: Subjektives Erleben und objektives Erkennen als Wege zur Kunst*, Otto Maier Verlag, Ravensberg, **1961**.
- [10] J. Joly, *A quantum theory of colour vision*, *Proceedings of the Royal Society of London. Series B, Containing Papers of a Biological Character* **1921**, 92, 219.
- [11] H. Ley, * ber die Beziehungen zwischen Lichtabsorption und chemischer Konstitution bei organischen Verbindungen*, *Angew. Chem.* **1907**, 20, 1303.
- [12] P. W. Atkins, d. P. Julio, *Physikalische Chemie*, 4th ed., Wiley-VCH Verlag GmbH & Co. KGaA, **2006**.
- [13] J. Wisotzky, *Phosphorescence of teeth cooled in liquid nitrogen*, *The Journal of the American Dental Association* **1963**, 67, 392.
- [14] Y.-K. Lee, *Fluorescence properties of human teeth and dental calculus for clinical applications*, *Journal of biomedical optics* **2015**, 20, 40901.
- [15] M. Born, R. Oppenheimer, *Zur Quantentheorie der Molekeln*, *Annalen der Physik* **1927**, 389, 457.
- [16] E. Schr odinger, *An Undulatory Theory of the Mechanics of Atoms and Molecules*, *Phys. Rev.* **1926**, 28, 1049.
- [17] E. Schr odinger, *Quantisierung als Eigenwertproblem*, *Annalen der Physik* **1926**, 384, 361.
- [18] E. Schr odinger, *Quantisierung als Eigenwertproblem*, *Annalen der Physik* **1926**, 385, 437.
- [19] A. Jablonski, *Efficiency of Anti-Stokes Fluorescence in Dyes*, *Nature* **1933**, 131, 839.
- [20] F. A. Carey, R. J. Sundberg, *Photochemistry. In: Advanced Organic Chemistry. Advanced Organic Chemistry.*, Springer, Boston, MA, **2007**.
- [21] G. N. Lewis, M. Kasha, *Phosphorescence and the Triplet State*, *J. Am. Chem. Soc.* **1944**, 66, 2100.
- [22] M. Frizot, *Neue Geschichte der Fotografie*, Koenemann.com, **1998**.

- [23] H. Remane, W. Girnus, *Meilensteine der Chemie 2009, Nachrichten aus der Chemie* **2009**, 57, 11.
- [24] E. Bequerel, *Mémoire sur les effets électriques produits sous l'influence des rayons solaires, Comptes Rendus* **1839**, 9, 561
- [25] R. S. Ohl, *Light-sensitive electric device* **1941**, US2402662A.
- [26] D. A. Nicewicz, D. W. C. MacMillan, *Merging Photoredox Catalysis with Organocatalysis: The Direct Asymmetric Alkylation of Aldehydes, Science* **2008**, 322, 77.
- [27] K. Nakamaru, *Synthesis, Luminescence Quantum Yields, and Lifetimes of Trischelated Ruthenium(II) Mixed-ligand Complexes Including 3,3'-Dimethyl-2,2'-bipyridyl, Bull. Chem. Soc. Jpn.* **1982**, 55, 2697.
- [28] M. A. Cismesia, T. P. Yoon, *Characterizing chain processes in visible light photoredox catalysis, Chemical Science* **2015**, 6, 5426.
- [29] H. Trommsdorf, *Über Santonin, Ann. Chem. Pharm.* **1834**, 11, 190.
- [30] A. Natarajan, C. K. Tsai, S. I. Khan, P. McCarren, K. N. Houk, M. A. Garcia-Garibay, *The Photoarrangement of  $\alpha$ -Santonin is a Single-Crystal-to-Single-Crystal Reaction: A Long Kept Secret in Solid-State Organic Chemistry Revealed, J. Am. Chem. Soc.* **2007**, 129, 9846.
- [31] J. Saltiel, *Perdeuteriostilbene. The Role of Phantom States in the cis-trans Photoisomerization of Stilbenes, J. Am. Chem. Soc.* **1967**, 89, 1036.
- [32] J. B. Birks, *The photo-isomerization of stilbene, Chem. Phys. Lett.* **1976**, 38, 437.
- [33] M. Irie, *Diarylethenes for Memories and Switches, Chem. Rev.* **2000**, 100, 1685.
- [34] G. Berkovic, V. Krongauz, V. Weiss, *Spiropyrans and Spirooxazines for Memories and Switches, Chem. Rev.* **2000**, 100, 1741.
- [35] S. Helmy, F. A. Leibfarth, S. Oh, J. E. Poelma, C. J. Hawker, J. Read de Alaniz, *Photoswitching Using Visible Light: A New Class of Organic Photochromic Molecules, J. Am. Chem. Soc.* **2014**, 136, 8169.
- [36] K. Hull, J. Morstein, D. Trauner, *In Vivo Photopharmacology, Chem. Rev.* **2018**, 118, 10710.
- [37] W. A. Velema, W. Szymanski, B. L. Feringa, *Photopharmacology: Beyond Proof of Principle, J. Am. Chem. Soc.* **2014**, 136, 2178.
- [38] I. S. Park, Y.-S. Jung, K.-J. Lee, J.-M. Kim, *Photoswitching and sensor applications of a spiropyran-polythiophene conjugate, Chem. Commun.* **2010**, 46, 2859.
- [39] M. Ikegami, T. Arai, *Photochromic and Fluorescence Properties of a Hemiindigo in the Presence of Bovine Serum Albumin, Chem. Lett.* **2005**, 34, 492.
- [40] D. V. Berdnikova, *Visible-range hemi-indigo photoswitch: ON-OFF fluorescent binder for HIV-1 RNA, Chem. Commun.* **2019**, 55, 8402.
- [41] F. Kink, M. P. Collado, S. Wiedbrauk, P. Mayer, H. Dube, *Bistable Photoswitching of Hemithioindigo with Green and Red Light: Entry Point to Advanced Molecular Digital Information Processing, Chemistry – A European Journal* **2017**, 23, 6237.
- [42] J.-R. Colard-Itté, Q. Li, D. Collin, G. Mariani, G. Fuks, E. Moulin, E. Buhler, N. Giuseppone, *Mechanical behaviour of contractile gels based on light-driven molecular motors, Nanoscale* **2019**, 11, 5197.
- [43] S. Kassem, A. T. L. Lee, D. A. Leigh, V. Marcos, L. I. Palmer, S. Pisano, *Stereodivergent synthesis with a programmable molecular machine, Nature* **2017**, 549, 374.
- [44] S. M. Douglas, I. Bachelet, G. M. Church, *A Logic-Gated Nanorobot for Targeted Transport of Molecular Payloads, Science* **2012**, 335, 831.
- [45] B. Osterby, R. D. McKelvey, L. Hill, *Photochromic sunglasses: A patent-based advanced organic synthesis project and demonstration, J. Chem. Educ.* **1991**, 68, 424.

- [46] M. Borowiak, W. Nahaboo, M. Reynders, K. Nekolla, P. Jalinot, J. Hasserodt, M. Rehberg, M. Delattre, S. Zahler, A. Vollmar, D. Trauner, O. Thorn-Seshold, *Photoswitchable Inhibitors of Microtubule Dynamics Optically Control Mitosis and Cell Death*, *Cell* **2015**, 162, 403.
- [47] J. Broichhagen, J. A. Frank, D. Trauner, *A Roadmap to Success in Photopharmacology*, *Acc. Chem. Res.* **2015**, 48, 1947.
- [48] P. Urban, S. D. Pritzl, D. B. Konrad, J. A. Frank, C. Pernpeintner, C. R. Roeske, D. Trauner, T. Lohmüller, *Light-Controlled Lipid Interaction and Membrane Organization in Photolipid Bilayer Vesicles*, *Langmuir* **2018**, 34, 13368.
- [49] P. Glock, J. Broichhagen, S. Kretschmer, P. Blumhardt, J. Mücksch, D. Trauner, P. Schwille, *Optical Control of a Biological Reaction–Diffusion System*, *Angew. Chem. Int. Ed.* **2018**, 57, 2362.
- [50] Z. Tian, A. D. Q. Li, *Photoswitching-Enabled Novel Optical Imaging: Innovative Solutions for Real-World Challenges in Fluorescence Detections*, *Acc. Chem. Res.* **2013**, 46, 269.
- [51] E. National Academies of Sciences, Medicine, *Quantum Computing: Progress and Prospects*, The National Academies Press, Washington, DC, **2019**.
- [52] T. R. Kelly, H. De Silva, R. A. Silva, *Unidirectional rotary motion in a molecular system*, *Nature* **1999**, 401, 150.
- [53] N. Koumura, R. W. J. Zijlstra, R. A. van Delden, N. Harada, B. L. Feringa, *Light-driven monodirectional molecular rotor*, *Nature* **1999**, 401, 152.
- [54] J. Chen, S. J. Wezenberg, B. L. Feringa, *Intramolecular transport of small-molecule cargo in a nanoscale device operated by light*, *Chem. Commun.* **2016**, 52, 6765.
- [55] W. R. Browne, B. L. Feringa, *Making molecular machines work*, *Nature Nanotechnology* **2006**, 1, 25.
- [56] C. Song, Z.-G. Wang, B. Ding, *Smart Nanomachines Based on DNA Self-Assembly*, *Small* **2013**, 9, 2382.
- [57] M. Kathan, S. Hecht, *Photoswitchable molecules as key ingredients to drive systems away from the global thermodynamic minimum*, *Chem. Soc. Rev.* **2017**, 46, 5536.
- [58] W. Fuß, *Previtamin D: Z–E photoisomerization via a Hula-twist conical intersection*, *PCCP* **2019**, 21, 6776.
- [59] B. Maerz, S. Wiedbrauk, S. Oesterling, E. Samoylova, A. Nenov, P. Mayer, R. de Vivie-Riedle, W. Zinth, H. Dube, *Making Fast Photoswitches Faster—Using Hammett Analysis to Understand the Limit of Donor–Acceptor Approaches for Faster Hemithioindigo Photoswitches*, *Chemistry – A European Journal* **2014**, 20, 13984.
- [60] R. Wilcken, M. Schildhauer, F. Rott, L. A. Huber, M. Guentner, S. Thumser, K. Hoffmann, S. Oesterling, R. de Vivie-Riedle, E. Riedle, H. Dube, *Complete Mechanism of Hemithioindigo Motor Rotation*, *J. Am. Chem. Soc.* **2018**, 140, 5311.
- [61] C. Redwood, M. Bayda, J. Saltiel, *Photoisomerization of Pre- and Provitamin D3 in EPA at 77 K: One-Bond-Twist, Not Hula-Twist*, *The Journal of Physical Chemistry Letters* **2013**, 4, 716.
- [62] A. Baeyer, A. Emmerling, *Reduction des Isatins zu Indigblau*, *Berichte der deutschen chemischen Gesellschaft* **1870**, 3, 514.
- [63] A. Baeyer, *Ueber die Verbindungen der Indigogruppe*, *Berichte der deutschen chemischen Gesellschaft* **1883**, 16, 2188.
- [64] H. Schmidt, *Indigo – 100 Jahre industrielle Synthese*, *Chem. unserer Zeit* **1997**, 31, 121.
- [65] S. Yamazaki, A. L. Sobolewski, W. Domcke, *Molecular mechanisms of the photostability of indigo*, *PCCP* **2011**, 13, 1618.

- [66] L. A. Huber, P. Mayer, H. Dube, *Photoisomerization of Mono-Arylated Indigo and Water-Induced Acceleration of Thermal cis-to-trans Isomerization*, *ChemPhotoChem* **2018**, *2*, 458.
- [67] H. S. Correa, E. Ortiz, V. H. Uc, I. D. B. Quintal, J. L. H. Avila, *Indigo stability: an ab initio study*, *Molecular Simulation* **2011**, *37*, 1085
- [68] J. Seixas de Melo, A. P. Moura, M. J. Melo, *Photophysical and Spectroscopic Studies of Indigo Derivatives in Their Keto and Leuco Forms*, *The Journal of Physical Chemistry A* **2004**, *108*, 6975.
- [69] C. Y. Huang, A. Bonasera, L. Hristov, Y. Garmshausen, B. M. Schmidt, D. Jacquemin, S. Hecht, *N,N'-Disubstituted Indigos as Readily Available Red-Light Photoswitches with Tunable Thermal Half-Lives*, *J. Am. Chem. Soc.* **2017**, *139*, 15205.
- [70] P. Friedlaender, *Ueber Thionaphtenderivate und Thioindigo*, *Justus Liebigs Annalen der Chemie* **1907**, *351*, 390.
- [71] P. Friedländer, *Zeitschr. f. Farben- und Textilchemie* **1904**, *3*, 333.
- [72] M. Dittmann, F. F. Graupner, B. Maerz, S. Oesterling, R. de Vivie-Riedle, W. Zinth, M. Engelhard, W. Lüttke, *Photostability of 4,4'-Dihydroxythioindigo, a Mimetic of Indigo*, *Angew. Chem. Int. Ed.* **2014**, *53*, 591.
- [73] S. Wiedbrauk, H. Dube, *Hemithioindigo—an emerging photoswitch*, *Tetrahedron Lett.* **2015**, *56*, 4266.
- [74] C. Petermayer, S. Thumser, F. Kink, P. Mayer, H. Dube, *Hemiindigo: Highly Bistable Photoswitching at the Biooptical Window*, *J. Am. Chem. Soc.* **2017**, *139*, 15060.
- [75] C. Petermayer, H. Dube, *Circular Dichroism Photoswitching with a Twist: Axially Chiral Hemiindigo*, *J. Am. Chem. Soc.* **2018**, *140*, 13558.
- [76] C. Petermayer, H. Dube, *Indigoid Photoswitches: Visible Light Responsive Molecular Tools*, *Acc. Chem. Res.* **2018**, *51*, 1153.
- [77] B. Kahr, K. Claborn, *The Lives of Malus and His Bicentennial Law*, *ChemPhysChem* **2008**, *9*, 43.
- [78] F. A. Carey, R. J. Sundberg, *Stereochemistry, Conformation, and Stereoselectivity*. In: *Advanced Organic Chemistry. Advanced Organic Chemistry*, Springer, Boston, MA, **2007**.
- [79] A. Homberg, E. Brun, F. Zinna, S. Pascal, M. Górecki, L. Monnier, C. Besnard, G. Pescitelli, L. Di Bari, J. Lacour, *Combined reversible switching of ECD and quenching of CPL with chiral fluorescent macrocycles*, *Chemical Science* **2018**, *9*, 7043.
- [80] B. L. Feringa, *In Control of Motion: From Molecular Switches to Molecular Motors*, *Acc. Chem. Res.* **2001**, *34*, 504.
- [81] A. Coskun, M. Banaszak, R. D. Astumian, J. F. Stoddart, B. A. Grzybowski, *Great expectations: can artificial molecular machines deliver on their promise?*, *Chem. Soc. Rev.* **2012**, *41*, 19.
- [82] M. Guentner, M. Schildhauer, S. Thumser, P. Mayer, D. Stephenson, P. J. Mayer, H. Dube, *Sunlight-powered kHz rotation of a hemithioindigo-based molecular motor*, *Nat Commun* **2015**, *6*, 8406.
- [83] T. Kudernac, N. Ruangsapapichat, M. Parschau, B. Maciá, N. Katsonis, S. R. Harutyunyan, K.-H. Ernst, B. L. Feringa, *Electrically driven directional motion of a four-wheeled molecule on a metal surface*, *Nature* **2011**, *479*, 208.
- [84] W. Szymański, J. M. Beierle, H. A. V. Kistemaker, W. A. Velema, B. L. Feringa, *Reversible Photocontrol of Biological Systems by the Incorporation of Molecular Photoswitches*, *Chem. Rev.* **2013**, *113*, 6114.

- [85] M. Ikegami, T. Suzuki, Y. Kaneko, T. Arai, *Photochromism of Hydrogen Bonded Compounds, Molecular Crystals and Liquid Crystals Science and Technology. Section A. Molecular Crystals and Liquid Crystals* **2006**, 345, 113.
- [86] B. Maerz, S. Wiedbrauk, S. Oesterling, E. Samoylova, A. Nenov, P. Mayer, R. de Vivie-Riedle, W. Zinth, H. Dube, *Making fast photoswitches faster--using Hammett analysis to understand the limit of donor-acceptor approaches for faster hemithioindigo photoswitches*, *Chemistry* **2014**, 20, 13984.
- [87] S. Wiedbrauk, B. Maerz, E. Samoylova, A. Reiner, F. Trommer, P. Mayer, W. Zinth, H. Dube, *Twisted Hemithioindigo Photoswitches: Solvent Polarity Determines the Type of Light-Induced Rotations*, *J. Am. Chem. Soc.* **2016**, 138, 12219.
- [88] U. Burger, A. O. Bringhen, *Cyclization Studies with N-Munnich Bases of 2-Substituted Indoles*, *Helv. Chim. Acta* **1989**, 72, 93.
- [89] M. J. Moon, S. K. Lee, J. W. Lee, W. K. Song, S. W. Kim, J. I. Kim, C. Cho, S. J. Choi, Y. C. Kim, *Synthesis and structure-activity relationships of novel indirubin derivatives as potent anti-proliferative agents with CDK2 inhibitory activities*, *Bioorg. Med. Chem.* **2006**, 14, 237.
- [90] V. S. Velezheva, P. J. Brennan, V. Y. Marshakov, *Novel Pyridazino[4,3-b]indoles with Dual Inhibitory Activity against Mycobacterium tuberculosis and Monoamine Oxidase*, *J. Med. Chem.* **2004**, 47, 3455.
- [91] J. C. Antilla, A. Klapars, S. L. Buchwald, *The Copper-Catalyzed N-Arylation of Indoles*, *J. Am. Chem. Soc.* **2002**, 124, 11684.
- [92] P. Y. Choy, C. P. Lau, F. Y. Kwong, *Palladium-catalyzed direct and regioselective C-H bond functionalization/oxidative acetoxylation of indoles*, *J. Org. Chem.* **2011**, 76, 80.
- [93] H. Katayama, E. Abe, K. Kaneko, *Synthesis of julolidines from anilines*, *J. Heterocyclic Chem.* **1982**, 19, 925.
- [94] N. Miyaura, A. Suzuki, *Stereoselective synthesis of arylated (E)-alkenes by the reaction of alk-1-enylboranes with aryl halides in the presence of palladium catalyst*, *J. Chem. Soc., Chem. Commun.* **1979**, 866.
- [95] O. Trapp, S. Bremer, S. K. Weber, *Assessing reaction rate constants in on-column reaction chromatography: an extended unified equation for reaction educts and products with different response factors*, *Analytical and Bioanalytical Chemistry* **2009**, 395, 1673.
- [96] C. M. Connelly, M. H. Moon, J. S. Schneekloth, *The Emerging Role of RNA as a Therapeutic Target for Small Molecules*, *Cell Chem Biol* **2016**, 23, 1077.
- [97] C. Reichardt, *Solvatochromic Dyes as Solvent Polarity Indicators*, *Chem. Rev.* **1994**, 94, 2319.
- [98] U. Megerle, R. Lechner, B. König, E. Riedle, *Laboratory apparatus for the accurate, facile and rapid determination of visible light photoreaction quantum yields*, *Photochem Photobiol Sci* **2010**, 9, 1400.
- [99] T. Sumi, Y. Takagi, A. Yagi, M. Morimoto, M. Irie, *Photoirradiation wavelength dependence of cycloreversion quantum yields of diarylethenes*, *Chem Commun (Camb)* **2014**, 50, 3928.
- [100] S. Wiedbrauk, B. Maerz, E. Samoylova, A. Reiner, F. Trommer, P. Mayer, W. Zinth, H. Dube, *Twisted Hemithioindigo Photoswitches: Solvent Polarity Determines the Type of Light-Induced Rotations*, *J. Am. Chem. Soc.* **2016**, 138, 12219.
- [101] U. Megerle, R. Lechner, B. König, E. Riedle, *Laboratory apparatus for the accurate, facile and rapid determination of visible light photoreaction quantum yields*, *Photochem. Photobiol. Sci.* **2010**, 9, 1400.
- [102] S. Wiedbrauk, B. Maerz, E. Samoylova, P. Mayer, W. Zinth, H. Dube, *Ingredients to TICT Formation in Donor Substituted Hemithioindigo*, *The Journal of Physical Chemistry Letters* **2017**, 8, 1585.

- [103] A. J. Fletcher, M. N. Bax, M. C. Willis, *Palladium-catalysed N-annulation routes to indoles: the synthesis of indoles with sterically demanding N-substituents, including demethylasterriquinone A1*, *Chem Commun (Camb)* **2007**, 4764.
- [104] V. S. Velezheva, A. I. Mel'man, Y. I. Smushkevich, V. I. Pol'shakov, O. S. Anisimova, *1-Acetyl-2-bromo-3-indolinone in nucleophilic substitution reactions and the synthesis of pyrrolo[3,2-b]indoles*, *Pharm. Chem. J.* **1990**, 24, 917.
- [105] I. Shcherbakova, Y. Nikolyukin, *Indoloquinoline compounds as Calcium Channel Blockers*, **2007**, CA20072662185.
- [106] M. M. V. Ramana, P. V. Potnis, *A Simple Approach to the Synthesis of Fluoren-9-Ones*, *Synth. Commun.* **1995**, 25, 1751.
- [107] N. Ruangsupapichat, M. M. Pollard, S. R. Harutyunyan, B. L. Feringa, *Reversing the direction in a light-driven rotary molecular motor*, *Nature Chemistry* **2011**, 3, 53.
- [108] B. L. Feringa, R. A. van Delden, *Absolute Asymmetric Synthesis: The Origin, Control, and Amplification of Chirality*, *Angew. Chem. Int. Ed.* **1999**, 38, 3418.
- [109] P. K. Hashim, R. Thomas, N. Tamaoki, *Induction of molecular chirality by circularly polarized light in cyclic azobenzene with a photoswitchable benzene rotor*, *Chemistry* **2011**, 17, 7304.
- [110] K. Rijeesh, P. K. Hashim, S. I. Noro, N. Tamaoki, *Dynamic induction of enantiomeric excess from a prochiral azobenzene dimer under circularly polarized light*, *Chem Sci* **2015**, 6, 973.
- [111] B. Luy, *Disinction of enantiomers by NMR spectroscopy using chiral orienting media*, *Journal of the Indian Institute of Science* **2010**, 90, 119.
- [112] A. Gerwien, P. Mayer, H. Dube, *Green light powered molecular state motor enabling eight-shaped unidirectional rotation*, *Nature Communications* **2019**, 10, 4449.
- [113] O. Lavinda, I. Mironova, S. Karimi, F. Pozzi, J. Samson, H. Ajiki, L. Massa, K. Ramig, *Singular thermochromic effects in dyeings with indigo, 6-bromoindigo, and 6,6'-dibromoindigo*, *Dyes and Pigments* **2013**, 96, 581.
- [114] K. Ramig, O. Lavinda, D. J. Szalda, I. Mironova, S. Karimi, F. Pozzi, N. Shah, J. Samson, H. Ajiki, L. Massa, D. Mantzouris, I. Karapanagiotis, C. Cooksey, *The nature of thermochromic effects in dyeings with indigo, 6-bromoindigo, and 6,6'-dibromoindigo, components of Tyrian purple*, *Dyes and Pigments* **2015**, 117, 37.
- [115] G. M. Wyman, W. R. Brode, *The Relation between the Absorption Spectra and the Chemical Constitution of Dyes XXII. cis-trans Isomerism in Thioindigo Dyes I*, *J. Am. Chem. Soc.* **1951**, 73, 1487.
- [116] J. H. Porada, J.-M. Neudörfl, D. Blunk, *Planar and distorted indigo as the core motif in novel chromophoric liquid crystals*, *New J. Chem.* **2015**, 39, 8291.
- [117] F. Maier, O. Trapp, *Effects of the Stationary Phase and the Solvent on the Stereodynamics of biphep Ligands Quantified by Dynamic Three-Column HPLC*, *Angew. Chem. Int. Ed.* **2012**, 51, 2985.
- [118] S. Wheeler, K. Houk, *Origin of Substituent Effects in Edge-to-Face Aryl-Aryl Interactions*, *Mol. Phys.* **2009**, 107, 749.
- [119] J. M. Lehn, *Conjecture: imines as unidirectional photodriven molecular motors-motional and constitutional dynamic devices*, *Chemistry* **2006**, 12, 5910.
- [120] L. Greb, A. Eichhofer, J. M. Lehn, *Synthetic Molecular Motors: Thermal N Inversion and Directional Photoinduced C=N Bond Rotation of Camphorquinone Imines*, *Angew. Chem. Int. Ed. Engl.* **2015**, 54, 14345.

- [121] J. N. Bull, E. Carrascosa, N. Mallo, M. S. Scholz, G. da Silva, J. E. Beves, E. J. Bieske, *Photoswitching an Isolated Donor–Acceptor Stenhouse Adduct*, *The Journal of Physical Chemistry Letters* **2018**, *9*, 665.
- [122] R. Navratil, S. Wiedbrauk, J. Jasik, H. Dube, J. Roithova, *Transforming hemithioindigo from a two-way to a one-way molecular photoswitch by isolation in the gas phase*, *Phys. Chem. Chem. Phys.* **2018**, *20*, 6868.
- [123] B. D. Adamson, N. J. A. Coughlan, P. B. Markworth, R. E. Continetti, E. J. Bieske, *An ion mobility mass spectrometer for investigating photoisomerization and photodissociation of molecular ions*, *Rev. Sci. Instrum.* **2014**, *85*, 123109.
- [124] M. S. Scholz, J. N. Bull, E. Carrascosa, B. D. Adamson, G. K. Kosgei, J. J. Rack, E. J. Bieske, *Linkage Photoisomerization of an Isolated Ruthenium Sulfoxide Complex: Sequential versus Concerted Rearrangement*, *Inorg. Chem.* **2018**, *57*, 5701.
- [125] E. Carrascosa, J. N. Bull, M. S. Scholz, N. J. A. Coughlan, S. Olsen, U. Wille, E. J. Bieske, *Reversible Photoisomerization of the Isolated Green Fluorescent Protein Chromophore*, *The Journal of Physical Chemistry Letters* **2018**, *9*, 2647.
- [126] E. Carrascosa, C. Petermayer, M. S. Scholz, J. N. Bull, H. Dube, E. J. Bieske, *Reversible Photoswitching of Isolated Ionic Hemiindigos with Visible Light*, *ChemPhysChem* **2020**, *21*, 680.
- [127] J. N. Bull, M. S. Scholz, E. Carrascosa, G. da Silva, E. J. Bieske, *Double Molecular Photoswitch Driven by Light and Collisions*, *Phys. Rev. Lett.* **2018**, *120*, 223002.
- [128] V. S. Velezheva, P. J. Brennan, V. Y. Marshakov, D. V. Gusev, I. N. Lisichkina, A. S. Peregudov, L. N. Tchernousova, T. G. Smirnova, S. N. Andreevskaya, A. E. Medvedev, *Novel pyridazino[4,3-*b*]indoles with dual inhibitory activity against *Mycobacterium tuberculosis* and monoamine oxidase*, *J. Med. Chem.* **2004**, *47*, 3455.
- [129] M. Cydzik, M. Rudowska, P. Stefanowicz, Z. Szewczuk, *Derivatization of peptides as quaternary ammonium salts for sensitive detection by ESI-MS*, *J. Pept. Sci.* **2011**, *17*, 445.
- [130] B. Almarzoqi, A. V. George, N. S. Isaacs, *The Quaternisation of Tertiary Amines with Dihalomethane*, *Tetrahedron* **1986**, *42*, 601.
- [131] H. E. Revercomb, E. A. Mason, *Theory of plasma chromatography/gaseous electrophoresis. Review*, *Anal. Chem.* **1975**, *47*, 970.
- [132] Gaussian 16, Revision B.01, M. J. Frisch, G. W. Trucks, H. B. Schlegel, G. E. Scuseria, M. A. Robb, J. R. Cheeseman, G. Scalmani, V. Barone, G. A. Petersson, H. Nakatsuji, X. Li, M. Caricato, A. V. Marenich, J. Bloino, B. G. Janesko, R. Gomperts, B. Mennucci, H. P. Hratchian, J. V. Ortiz, A. F. Izmaylov, J. L. Sonnenberg, Williams, F. Ding, F. Lipparini, F. Egidi, J. Goings, B. Peng, A. Petrone, T. Henderson, D. Ranasinghe, V. G. Zakrzewski, J. Gao, N. Rega, G. Zheng, W. Liang, M. Hada, M. Ehara, K. Toyota, R. Fukuda, J. Hasegawa, M. Ishida, T. Nakajima, Y. Honda, O. Kitao, H. Nakai, T. Vreven, K. Throssell, J. A. Montgomery Jr., J. E. Peralta, F. Ogliaro, M. J. Bearpark, J. J. Heyd, E. N. Brothers, K. N. Kudin, V. N. Staroverov, T. A. Keith, R. Kobayashi, J. Normand, K. Raghavachari, A. P. Rendell, J. C. Burant, S. S. Iyengar, J. Tomasi, M. Cossi, J. M. Millam, M. Klene, C. Adamo, R. Cammi, J. W. Ochterski, R. L. Martin, K. Morokuma, O. Farkas, J. B. Foresman, D. J. Fox, Gaussian, Inc., Wallingford CT, **2016**.
- [133] A. A. Shvartsburg, M. F. Jarrold, *An exact hard-spheres scattering model for the mobilities of polyatomic ions*, *Chem. Phys. Lett.* **1996**, *261*, 86.
- [134] M. Kállay, P. R. Nagy, Z. Rolik, D. Mester, G. Samu, J. Csontos, J. Csóka, B. P. Szabó, L. Gyevi-Nagy, I. Ladjászki, L. Szegedy, B. Ladóczki, K. Petrov, M. Farkas, P. D. Mezei, a. B. Hégyely, *Mrcc, a quantum chemical program suite*, *J. Chem. Phys.* **2013**, *139*, [www.mrcc.hu](http://www.mrcc.hu).

- [135] A. C. Stelzer, A. T. Frank, J. D. Kratz, M. D. Swanson, M. J. Gonzalez-Hernandez, J. Lee, I. Andricioaei, D. M. Markovitz, H. M. Al-Hashimi, *Discovery of selective bioactive small molecules by targeting an RNA dynamic ensemble*, *Nature chemical biology* **2011**, *7*, 553.
- [136] S. A. Barros, I. Yoon, D. M. Chenoweth, *Modulation of the E. coli rpoH Temperature Sensor with Triptycene-Based Small Molecules*, *Angew. Chem. Int. Ed.* **2016**, *55*, 8258.
- [137] C. M. Connelly, M. H. Moon, J. S. Schneekloth, *The Emerging Role of RNA as a Therapeutic Target for Small Molecules*, *Cell Chemical Biology* **2016**, *23*, 1077.
- [138] J. Parsons, M. P. Castaldi, S. Dutta, S. M. Dibrov, D. L. Wyles, T. Hermann, *Conformational inhibition of the hepatitis C virus internal ribosome entry site RNA*, *Nature chemical biology* **2009**, *5*, 823.
- [139] N. Menschutkin, in *Z. Phys. Chem., Vol. 5U*, **1890**, p. 589.
- [140] C. Gonzalez, H. B. Schlegel, *An improved algorithm for reaction path following*, *The Journal of Chemical Physics* **1989**, *90*, 2154.
- [141] M. Petersilka, U. J. Gossmann, E. K. U. Gross, *Excitation Energies from Time-Dependent Density-Functional Theory*, *Phys. Rev. Lett.* **1996**, *76*, 1212.
- [142] K. Wolinski, J. F. Hinton, P. Pulay, *Efficient implementation of the gauge-independent atomic orbital method for NMR chemical shift calculations*, *J. Am. Chem. Soc.* **1990**, *112*, 8251.
- [143] GaussView, Version 6.1, R. Dennington, T. A. Keith, J. M. Millam, Semichem Inc., Shawnee Mission, KS, **2016**.
- [144] D. W. Old, M. C. Harris, S. L. Buchwald, *Efficient Palladium-Catalyzed N-Arylation of Indoles*, *Org. Lett* **2000**, *2*, 1403.



